

Biological and Medical Physics, Biomedical Engineering

Bharat Bhushan

Biomimetics

Bioinspired Hierarchical-Structured
Surfaces for Green Science and
Technology

Second Edition

 Springer

**BIOLOGICAL AND MEDICAL PHYSICS,
BIOMEDICAL ENGINEERING**

BIOLOGICAL AND MEDICAL PHYSICS, BIOMEDICAL ENGINEERING

The fields of biological and medical physics and biomedical engineering are broad, multidisciplinary and dynamic. They lie at the crossroads of frontier research in physics, biology, chemistry, and medicine. The Biological and Medical Physics, Biomedical Engineering Series is intended to be comprehensive, covering a broad range of topics important to the study of the physical, chemical and biological sciences. Its goal is to provide scientists and engineers with textbooks, monographs, and reference works to address the growing need for information.

Books in the series emphasize established and emergent areas of science including molecular, membrane, and mathematical biophysics; photosynthetic energy harvesting and conversion; information processing; physical principles of genetics; sensory communications; automata networks, neural networks, and cellular automata. Equally important will be coverage of applied aspects of biological and medical physics and biomedical engineering such as molecular electronic components and devices, biosensors, medicine, imaging, physical principles of renewable energy production, advanced prostheses, and environmental control and engineering.

Editor-in-Chief:

Elias Greenbaum, Oak Ridge National Laboratory, Oak Ridge, Tennessee, USA

Editorial Board:

Masuo Aizawa, Department of Bioengineering,
Tokyo Institute of Technology, Yokohama, Japan

Olaf S. Andersen, Department of Physiology,
Biophysics and Molecular Medicine,
Cornell University, New York, USA

Robert H. Austin, Department of Physics,
Princeton University, Princeton, New Jersey, USA

James Barber, Department of Biochemistry,
Imperial College of Science, Technology
and Medicine, London, England

Howard C. Berg, Department of Molecular
and Cellular Biology, Harvard University,
Cambridge, Massachusetts, USA

Victor Bloomfield, Department of Biochemistry,
University of Minnesota, St. Paul, Minnesota, USA

Robert Callender, Department of Biochemistry,
Albert Einstein College of Medicine,
Bronx, New York, USA

Britton Chance, University of Pennsylvania
Department of Biochemistry/Biophysics
Philadelphia, USA

Steven Chu, Lawrence Berkeley National
Laboratory, Berkeley, California, USA

Louis J. DeFelice, Department of Pharmacology,
Vanderbilt University, Nashville, Tennessee, USA

Johann Deisenhofer, Howard Hughes Medical
Institute, The University of Texas, Dallas,
Texas, USA

George Feher, Department of Physics,
University of California, San Diego, La Jolla,
California, USA

Hans Frauenfelder,
Los Alamos National Laboratory,
Los Alamos, New Mexico, USA

Ivar Giaever, Rensselaer Polytechnic Institute,
Troy, New York, USA

Sol M. Gruner, Cornell University,
Ithaca, New York, USA

Judith Herzfeld, Department of Chemistry,
Brandeis University, Waltham, Massachusetts, USA

Mark S. Humayun, Doheny Eye Institute,
Los Angeles, California, USA

Pierre Joliot, Institute de Biologie
Physico-Chimique, Fondation Edmond
de Rothschild, Paris, France

Lajos Keszthelyi, Institute of Biophysics, Hungarian
Academy of Sciences, Szeged, Hungary

Robert S. Knox, Department of Physics
and Astronomy, University of Rochester, Rochester,
New York, USA

Aaron Lewis, Department of Applied Physics,
Hebrew University, Jerusalem, Israel

Stuart M. Lindsay, Department of Physics
and Astronomy, Arizona State University,
Tempe, Arizona, USA

David Mauzerall, Rockefeller University,
New York, New York, USA

Eugenie V. Mielczarek, Department of Physics
and Astronomy, George Mason University, Fairfax,
Virginia, USA

Markolf Niemz, Medical Faculty Mannheim,
University of Heidelberg, Mannheim, Germany

V. Adrian Parsegian, Physical Science Laboratory,
National Institutes of Health, Bethesda,
Maryland, USA

Linda S. Powers, University of Arizona,
Tucson, Arizona, USA

Earl W. Prohovsky, Department of Physics,
Purdue University, West Lafayette, Indiana, USA

Andrew Rubin, Department of Biophysics, Moscow
State University, Moscow, Russia

Michael Seibert, National Renewable Energy
Laboratory, Golden, Colorado, USA

David Thomas, Department of Biochemistry,
University of Minnesota Medical School,
Minneapolis, Minnesota, USA

Bharat Bhushan

Biomimetics

Bioinspired Hierarchical-Structured Surfaces
for Green Science and Technology

Second Edition

 Springer

Bharat Bhushan
Nanoprobe Laboratory for Bio- and
Nanotechnology and Biomimetics
(NLBB)
The Ohio State University
Columbus, OH
USA

ISSN 1618-7210 ISSN 2197-5647 (electronic)
Biological and Medical Physics, Biomedical Engineering
ISBN 978-3-319-28282-4 ISBN 978-3-319-28284-8 (eBook)
DOI 10.1007/978-3-319-28284-8

Library of Congress Control Number: 2016930053

1st edition: © Springer-Verlag Berlin Heidelberg 2012

2nd edition: © Springer International Publishing Switzerland 2016

This work is subject to copyright. All rights are reserved by the Publisher, whether the whole or part of the material is concerned, specifically the rights of translation, reprinting, reuse of illustrations, recitation, broadcasting, reproduction on microfilms or in any other physical way, and transmission or information storage and retrieval, electronic adaptation, computer software, or by similar or dissimilar methodology now known or hereafter developed.

The use of general descriptive names, registered names, trademarks, service marks, etc. in this publication does not imply, even in the absence of a specific statement, that such names are exempt from the relevant protective laws and regulations and therefore free for general use.

The publisher, the authors and the editors are safe to assume that the advice and information in this book are believed to be true and accurate at the date of publication. Neither the publisher nor the authors or the editors give a warranty, express or implied, with respect to the material contained herein or for any errors or omissions that may have been made.

Printed on acid-free paper

This Springer imprint is published by SpringerNature
The registered company is Springer International Publishing AG Switzerland

*To my sons Ankur and Corrado, daughters
Noopur and Subha, granddaughters Sahana
and Joya, and my grandson Ashwin.*



Foreword

Our planet has a unique biological diversity of about 1.8 million different species of living organisms that have been scientifically documented. The overwhelming diversity of plants and animals in shape, color, and function has fascinated students and scientists. What is more, it is estimated that the real number of species is much higher; on the order of 10 million species.

Each of these approximately 10 million species has optimized “technical” solutions to particular environmental conditions. The results of millions of years of biological evolution of millions of species are freely available to scientists that begin looking to nature’s solutions for ideas. The most exciting of these solutions happen on surfaces, the boundary layer, and interface between solids and their gaseous or liquid environment. Surfaces define the boundaries for the well-structured world of solids, and it is surfaces that define their interactions.

Concise and systematic research in biology and technical innovations started only in the 1970s. “Bionics,” “biomimicry,” and “biomimetics” are the terms used for this field. Until the 1980s, bionics concentrated on mechanical functions such as robotics and airplane development. Surfaces did not really play a role—despite the fact that surfaces are an essential part of all solids.

In 1977, when I discovered the functions of biological hierarchical structuring and the self-cleaning abilities of certain plant surfaces such as lotus leaves, I published the results in German in a purely academic journal—exotic for an engineering audience. Nobody took any notice. Then, it was difficult for scientists to talk across disciplines: different languages and seemingly different aims. Today, the cross-disciplinary field of biomimetics has changed this situation dramatically for the better: engineers listen to biologists—and biologists are aware of technical potentials in their research and discuss them with materials scientists.

There is one outstanding scientist who has reinforced this process: Professor Bharat Bhushan. Bharat, a materials engineer/physicist by education and practice and not a botanist, became interested in bionics in the 1990s. He recognized the enormous importance of biomimetic materials and their surfaces for technical applications. When the first edition of his “Biomimetics—Bioinspired Hierarchical-Structured

Surfaces” appeared in 2012, it was an inspiration to scientists; for students this was the first time a comprehensive textbook was available.

Now, the amended second edition is available that recapitulates and expands on the first edition to provide a comprehensive review of the field. It covers not only topics such as lotus leaves, rose petals, and salvinia leaves, but is pushing boundaries looking at low drag and antifouling properties of shark skin, rice leaves, and butterfly wings. The book covers broad biomimetic topics from solid explanations of superphobic/superphilic, self-cleaning, and antifouling surfaces (lotus, rose petal, salvinia, rice leaf, and butterfly wings), to more discrete topics including structural coloration (butterfly wings), mechanical toughness and durability (nacre), and reversible adhesion (gecko feet). The book even ventures beyond the sciences to discuss the influence of biomimetics on art and architecture. As a biologist, I congratulate him and I am convinced it will be a great success and an important resource for all scholars of biomimetics.

Bonn

Dr. Wilhelm Barthlott
Professor Emeritus of Botany and Former Director
of the Nees Institute for Biodiversity of Plants
University of Bonn
Member of the National Academy of Sciences Leopoldina
Member of the Academy of Sciences and Literature Mainz
Foreign Member of the Linnean Society of London

Preface (Second Edition)

The field of biomimetics or bioinspired hierarchically structured surfaces started to take off in the late 1990s with major developments in nanoscience and nanotechnology. The latter made it possible to create natural surfaces with features ranging from the molecular scale to the macroscale. The interest in green science and technology has also provided impetus for advancement. The field is highly interdisciplinary, spanning from biology, physics, chemistry, materials science, and engineering. As of 2015, the field contains only a handful of visionaries and contributors.

Since the early 2000s, there have been significant advances in research, and many ideas have started to be commercialized. With continued understanding of the mechanisms relevant in species of living nature and development of new materials and nanofabrication techniques, rapid advancements are expected in the next decade and beyond. It is expected that new inventions will play a major role in human life. This author is fortunate to be one of the early pioneers in the field.

The second edition of the book provides a state of the art of the biomimetics field primarily related to interface science. The book is targeted to various audiences including novices as well as experts in the field, practitioners, solution seekers, and the curious. It should help in advancement of the field.

The book is based on the work of past and present collaborators. These include the following:

Past and present students:

Zach Burton, Yong Chae Jung, James Hunt, Robert A. Sayer, and Eun Kyu Her (Seoul National University, Korea); Brian Dean, Daniel Ebert, Gregory D. Bixler, and Srimala Perara (University of Moratuwa, Sri Lanka); Andrew Theiss and Shan Peng (Wuhan University of Science and Technology, China); and Samuel Martin.

Past and present postdoctoral fellows and visitors:

Dr. Michael Nosonovsky (University of Wisconsin, Milwaukee), Dr. Andrei G. Peressadko (Russia), Dr. Tae-Wan Kim (Pukyong National University, Korea),

Prof. Kerstin Koch (University of Bonn, Germany), Dr. Manuel L. B. Palacio (Western Digital Corp., San Jose, California), Dr. Hyungoo Lee, Dr. P.K. Muthiah, Dr. Yongxin Wang, and Dr. Philip S. Brown.

External Collaborators:

Professor Wilhelm Barthlott (University of Bonn, Germany), Dr. E.S. Yoon (KIST, Korea), Dr. Patrick Hoffman (EPFL, Lausanne, Switzerland), Dr. Andre Meister (CSEM, Switzerland), Prof. Scott. C. Schricker (Ohio State University, Columbus, Ohio), Prof. Joao F. Mano (University of Minho, Guimaraes, Portugal), Dr. Jiyu Sun (Jilin University, China), Prof. Shunsuke Nishimoto (Okayama University, Japan), Prof. Stanislav N. Gorb (University of Kiel, Germany), Prof. Eduard Arzt (Max Planck Institute for Metals Research, Stuttgart, Germany), and Prof. Stephen C. Lee (Ohio State University, Columbus, Ohio).

Next, the author would like to thank Renee L. Ripley for many important contributions during preparation of the manuscript including major edits in the manuscript, architectural content, figure drawings, and constant input based on her vast experience. Finally, author would like to thank his wife Sudha for her constant support and encouragement.

Columbus, Ohio

Bharat Bhushan

Preface (First Edition)

Nature has developed materials, objects, and processes that function from the macroscale to the nanoscale. The emerging field of biomimetics allows one to mimic biology or nature to develop nanomaterials, nanodevices, and processes which provide desirable properties. Hierarchical structures with dimensions of features ranging from the macroscale to the nanoscale are extremely common in nature to provide properties of interest. The biologically inspired materials and structured surfaces are eco-friendly or green with minimum human impact on the environment and are being explored for various commercial applications. This recognition has led to “Green Science and Technology,” the term used for the first time in this book.

There are a large number of objects including bacteria, plants, land and aquatic animals, and seashells with properties of commercial interest. The book presents an overview of the general field of biomimetics and biomimetics-inspired surfaces. It deals with various examples of biomimetics, which include surfaces with roughness-induced superomniphobicity, self-cleaning, antifouling, and controlled adhesion. It primarily focuses on the lotus effect which exhibits superhydrophobicity, self-cleaning, antifouling, low adhesion, and drag reduction. The book also includes the floating water fern which floats over water, rose petal effect which can provide either low adhesion or high adhesion, oleophobic/oleophilic surfaces inspired from aquatic animals, shark skin which exhibits low drag and antifouling, and gecko feet which exhibits reversible adhesion.

The book provides theoretical background, characterization of natural objects, and relevant mechanisms and inspired structured surface of commercial interest. We hope the book would serve as a catalyst for further innovations as well as serve as a useful reference in the emerging field of biomimetics. The book should also serve as an excellent text for a one-semester graduate course in biomimetics or as a companion text for a general course in nanotechnology. Given the interdisciplinary nature of the discipline, the appeal of the book is expected to be broad.

The work reported in the book is largely based on the pioneering contributions made by former and present students, postdoctoral fellows, and visiting scholars.

Special mention is deserved by Dr. Yong Chae Jung, a former Ph.D. student working in fabrication and characterization; Prof. Michael Nosonovsky, a former visiting scholar and an ongoing collaborator in theoretical modeling; and Prof. Kerstin Koch of Nees Institute for Biodiversity of Plants at University of Bonn, Germany, who spent a sabbatical year in the author's laboratory. All of them contributed immensely to the research on the lotus effect. Dr. Tae-Wan Kim, a visiting scholar, contributed immensely on theoretical modeling of Gecko Adhesion. Brian Dean, a graduate student, contributed to the understanding of the mechanisms of the shark skin effect. Other postdoctoral fellows and students who have contributed include Dr. Andrei G. Peressadko (gecko adhesion), Zack Burton (lotus effect), Eun Kyu Her (rose petal effect), Robert Sayer (gecko adhesion), James Hunt (salvinia effect), Daniel Ebert (lotus effect), and Dr. Hyungoo Lee (gecko adhesion). Finally, the author would like to thank Caterina Runyon-Spears for administrative support.

My special thanks go to my wife Sudha, who has been forbearing of my 24/7 commitment to science.

Columbus, Ohio

Bharat Bhushan

Contents

1	Introduction	1
1.1	Introduction	1
1.2	Biodiversity	2
1.3	Lessons from Nature	2
1.4	Golden Ratio and Fibonacci Numbers	7
1.5	Biomimetics in Art and Architecture—Bioarchitecture	12
1.6	Industrial Significance	16
1.7	Research Objective and Approach	19
1.8	Organization of the Book	19
	References	19
2	Roughness-Induced Superliquiphilic/phobic Surfaces: Lessons from Nature	23
2.1	Introduction	23
2.2	Wetting States	23
2.3	Applications	25
2.4	Natural Superhydrophobic, Self-cleaning, Low Adhesion/Drag Reduction Surfaces with Antifouling	27
2.5	Natural Superhydrophobic and High Adhesion Surfaces	28
2.6	Natural Superoleophobic Self-cleaning and Low Drag Surfaces with Antifouling	29
2.7	Closure	30
	References	30
3	Modeling of Contact Angle for a Liquid in Contact with a Rough Surface for Various Wetting Regimes	35
3.1	Introduction	35
3.2	Contact Angle Definition	35
3.3	Homogeneous and Heterogeneous Interfaces and the Wenzel, Cassie-Baxter and Cassie Equations	37

3.3.1	Limitations of the Wenzel and Cassie-Baxter Equations	42
3.3.2	Range of Applicability of the Wenzel and Cassie-Baxter Equations	45
3.4	Contact Angle Hysteresis	49
3.5	Stability of a Composite Interface and Role of Hierarchical Structure with Convex Surfaces	51
3.6	The Cassie-Baxter and Wenzel Wetting Regime Transition	55
3.7	Closure	59
	References	60
4	Lotus Effect Surfaces in Nature	63
4.1	Introduction	63
4.2	Plant Leaves	63
4.3	Characterization of Superhydrophobic and Hydrophilic Leaf Surfaces	66
4.3.1	Experimental Techniques	66
4.3.2	SEM Micrographs	67
4.3.3	Contact Angle Measurements	67
4.3.4	Surface Characterization Using an Optical Profiler	70
4.3.5	Surface Characterization, Adhesion, and Friction Using an AFM	71
4.3.6	Role of the Hierarchical Roughness	77
4.3.7	Summary	79
4.4	Various Self-cleaning Approaches	79
4.4.1	Comparison Between Superhydrophobic and Superhydrophilic Surface Approaches for Self-cleaning	80
4.4.2	Summary	82
4.5	Closure	82
	References	83
5	Nanofabrication Techniques Used for Lotus-Like Structures	85
5.1	Introduction	85
5.2	Roughening to Create One-Level Structure	86
5.3	Coatings to Create One-Level Structures	90
5.4	Methods to Create Two-Level (Hierarchical) Structures	92
5.5	Closure	93
	References	94
6	Fabrication and Characterization of Micro-, Nano- and Hierarchically Structured Lotus-Like Surfaces	97
6.1	Introduction	97
6.2	Experimental Techniques	99

6.2.1	Contact Angle, Surface Roughness, and Adhesion.	99
6.2.2	Droplet Evaporation Studies	100
6.2.3	Bouncing Droplet Studies	100
6.2.4	Vibrating Droplet Studies	100
6.2.5	Microdroplet Condensation and Evaporation Studies Using ESEM	101
6.2.6	Generation of Submicron Droplets	101
6.2.7	Waterfall/Jet Tests	104
6.2.8	Wear and Friction Tests	105
6.2.9	Transmittance Measurements	106
6.3	Micro- and Nanopatterned Polymers.	106
6.3.1	Contact Angle	108
6.3.2	Effect of Submicron Droplet on Contact Angle	109
6.3.3	Adhesive Force	110
6.3.4	Summary	111
6.4	Micropatterned Si Surfaces	111
6.4.1	Cassie-Baxter and Wenzel Transition Criteria.	114
6.4.2	Effect of Pitch Value on the Transition	116
6.4.3	Observation of Transition During the Droplet Evaporation.	118
6.4.4	Another Cassie-Baxter and Wenzel Transition for Different Series.	122
6.4.5	Contact Angle Hysteresis and Wetting/Dewetting Asymmetry	124
6.4.6	Contact Angle Measurements During Condensation and Evaporation of Microdroplets on Micropatterned Surfaces	128
6.4.7	Observation of Transition During the Bouncing Droplet	132
6.4.8	Summary	136
6.5	Ideal Surfaces with Hierarchical Structure	136
6.6	Hierarchically Structured Surfaces with Wax Platelets and Tubules Using Nature's Route.	137
6.6.1	Effect of Nanostructures with Various Wax Platelet Crystal Densities on Superhydrophobicity	142
6.6.2	Effect of Hierarchical Structure with Wax Platelets on the Superhydrophobicity	146
6.6.3	Effect of Hierarchical Structure with Wax Tubules on Superhydrophobicity	150
6.6.4	Self-cleaning Efficiency of Hierarchically Structured Surfaces	156

6.6.5	Observation of Transition During the Bouncing Droplet	157
6.6.6	Observation of Transition During the Vibrating Droplet	162
6.6.7	Measurement of Fluid Drag Reduction	167
6.6.8	Summary	168
6.7	Mechanically Durable Superhydrophobic Surfaces	169
6.7.1	CNT Composites	170
6.7.2	Nanoparticle Composites with Hierarchical Structure	179
6.7.3	Nanoparticle Composites for Optical Transparency	186
6.8	Superhydrophobic Paper Surfaces.	197
6.9	Closure	197
	References	198
7	Fabrication and Characterization of Micropatterned Structures Inspired by <i>Salvinia molesta</i>	205
7.1	Introduction.	205
7.2	Characterization of Leaves and Fabrication of Inspired Structural Surfaces	207
7.3	Measurement of Contact Angle and Adhesion	209
7.3.1	Observation of Pinning and Contact Angle	209
7.3.2	Adhesion.	210
7.4	Closure.	212
	References	212
8	Characterization of Rose Petals and Fabrication and Characterization of Superhydrophobic Surfaces with High and Low Adhesion	213
8.1	Introduction.	213
8.2	Characterization of Two Kinds of Rose Petals and Their Underlying Mechanisms	214
8.3	Fabrication of Surfaces with High and Low Adhesion for Understanding of Rose Petal Effect	221
8.4	Fabrication of Mechanically Durable, Superhydrophobic Surfaces with High Adhesion.	230
8.4.1	Samples with Hydrophilic ZnO Nanoparticles (Before ODP Modification)	231
8.4.2	Samples with Hydrophobic ZnO Nanoparticles (After ODP Modification)	233
8.4.3	Wear Resistance in AFM Wear Experiment.	237
8.5	Closure.	239
	References	240

9	Modeling, Fabrication, and Characterization of Superoleophobic/Philic Surfaces	243
9.1	Introduction.	243
9.2	Strategies to Achieve Superoleophobicity in Air.	247
9.2.1	Fluorination Techniques	248
9.2.2	Re-entrant Geometry.	250
9.3	Model to Predict Oleophobic/Philic Nature of Surfaces	252
9.4	Validation of Oleophobicity/Philicity Model for Oil Droplets in Air and Water	255
9.4.1	Experimental Techniques.	255
9.4.2	Fabrication of Oleophobic/Philic Surfaces	256
9.4.3	Characterization of Oleophobic/Philic Surfaces.	257
9.4.4	Summary	264
9.5	Mechanically Durable Nanoparticle Composite Coatings for Superoleophobicity	264
9.5.1	Experimental Details.	271
9.5.2	Results and Discussion	273
9.5.3	Summary	281
9.6	Mechanically Durable Nanoparticle Composite Coatings for Superliquiphilicity and Superliquiphobicity Using Layer-by-Layer Technique.	282
9.6.1	Experimental Details.	285
9.6.2	Results and Discussion	288
9.6.3	Summary	297
9.7	Mechanically Durable Superoleophobic Aluminum Surfaces	299
9.7.1	Experimental Details.	303
9.7.2	Results and Discussion	305
9.7.3	Summary	314
9.8	Mechanically Durable Superoleophobic Polymer Surfaces	314
9.8.1	Experimental Details.	315
9.8.2	Results and Discussion	316
9.8.3	Summary	319
9.9	Closure.	319
	References	320
10	Shark-Skin Surface for Fluid-Drag Reduction in Turbulent Flow	327
10.1	Introduction.	327
10.2	Fluid Drag Reduction	329
10.2.1	Mechanisms of Fluid Drag	329
10.2.2	Shark Skin	331
10.3	Experimental Studies	332
10.3.1	Flow Visualization Studies	334
10.3.2	Riblet Geometries and Configurations	334

- 10.3.3 Riblet Fabrication 336
- 10.3.4 Drag Measurement Techniques 341
- 10.3.5 Riblet Results and Discussion 346
- 10.3.6 Summary 361
- 10.4 Fluid Flow Modeling 362
 - 10.4.1 Riblet Geometry Models 364
 - 10.4.2 Results and Discussion 367
 - 10.4.3 Summary 370
- 10.5 Application of Riblets for Drag Reduction and Antifouling 373
- 10.6 Closure 376
- References 377
- 11 Rice Leaf and Butterfly Wing Effect 383**
 - 11.1 Introduction 383
 - 11.2 Inspiration from Living Nature 383
 - 11.2.1 Ambient Species—Lotus Effect 383
 - 11.2.2 Aquatic Species—Shark Skin and Fish Scales Effect 384
 - 11.2.3 Ambient Species—Rice Leaf and Butterfly Wing Effect 384
 - 11.3 Sample Fabrication 386
 - 11.3.1 Actual Sample Replicas 386
 - 11.3.2 Rice Leaf Inspired Surfaces 387
 - 11.4 Pressure Drop Measurement Technique 392
 - 11.5 Results and Discussion 395
 - 11.5.1 Surface Characterization 396
 - 11.5.2 Pressure Drop Measurements 400
 - 11.5.3 Wettability 411
 - 11.5.4 Drag Reduction Models 413
 - 11.6 Closure 420
 - References 420
- 12 Bio- and Inorganic Fouling 423**
 - 12.1 Introduction 423
 - 12.2 Fields Susceptible to Fouling 423
 - 12.3 Biofouling and Inorganic Fouling Formation Mechanisms 427
 - 12.3.1 Biofouling Formation 428
 - 12.3.2 Inorganic Fouling Formation 430
 - 12.3.3 Surface Factors 430
 - 12.4 Antifouling Strategies from Living Nature 433
 - 12.5 Antifouling: Current Prevention and Cleaning Techniques 437
 - 12.5.1 Prevention Techniques 437
 - 12.5.2 Self-cleaning Surfaces and Cleaning Techniques 440
 - 12.6 Bioinspired Rice Leaf Surfaces for Antifouling 441

12.6.1	Fabrication of Micropatterned Samples	443
12.6.2	Anti-biofouling Measurements	444
12.6.3	Anti-inorganic Fouling Measurements	445
12.6.4	Results and Discussion	446
12.6.5	Anti-biofouling and Anti-inorganic Fouling Mechanisms.	449
12.7	Closure	452
	References	452
13	Gecko Adhesion	457
13.1	Introduction	457
13.2	Hairy Attachment Systems	458
13.3	Tokay Gecko	462
13.3.1	Construction of Tokay Gecko	462
13.3.2	Adhesion Enhancement by Division of Contacts and Multilevel Hierarchical Structure	464
13.3.3	Peeling	466
13.3.4	Self Cleaning	470
13.4	Attachment Mechanisms	472
13.4.1	van der Waals Forces	473
13.4.2	Capillary Forces	474
13.5	Adhesion Measurements and Data	476
13.5.1	Adhesion Under Ambient Conditions	476
13.5.2	Effects of Temperature	478
13.5.3	Effects of Humidity	479
13.5.4	Effects of Hydrophobicity	479
13.6	Adhesion Modeling of Fibrillar Structures	480
13.6.1	Single Spring Contact Analysis	482
13.6.2	The Multi-level Hierarchical Spring Analysis	484
13.6.3	Adhesion Results of the Multi-level Hierarchical Spring Model.	488
13.6.4	Capillary Effects.	494
13.7	Adhesion Data Base of Fibrillar Structures	498
13.7.1	Fiber Model.	499
13.7.2	Single Fiber Contact Analysis	499
13.7.3	Constraints	500
13.7.4	Non-fiber Fracture Condition	502
13.7.5	Numerical Simulation	504
13.7.6	Results and Discussion	505
13.8	Fabrication of Gecko Skin-Inspired Structures	509
13.8.1	Single Level Roughness Structures	510
13.8.2	Multi-level Hierarchical Structures	517
13.9	Closure	522
	References	524

14	Structure and Mechanical Properties of Nacre	531
14.1	Introduction	531
14.2	Hierarchical Structure	533
14.2.1	Columnar and Sheet Structure	533
14.2.2	Mineral Bridges	535
14.2.3	Polygonal Nanograins	536
14.2.4	Inter-Tile Toughening Mechanism	537
14.3	Mechanical Properties	538
14.4	Bioinspired Structures	542
14.5	Closure	545
	References	545
15	Structural Coloration	549
15.1	Introduction	549
15.2	Physical Mechanisms of Structural Colors	552
15.2.1	Film Interference	552
15.2.2	Diffraction Gratings	554
15.2.3	Scattering	555
15.2.4	Photonic Crystals	555
15.2.5	Coloration Changes	556
15.3	Lessons from Living Nature	557
15.3.1	Film Interference	558
15.3.2	Diffraction Grating	562
15.3.3	Scattering	565
15.3.4	Photonic Crystals	566
15.3.5	Coloration Changes	569
15.4	Bioinspired Fabrication and Applications	571
15.5	Closure	572
	References	573
16	Outlook	581
	Index	583

Biography and Photograph of Author



Dr. Bharat Bhushan received an M.S. in mechanical engineering from the Massachusetts Institute of Technology in 1971, an M.S. in mechanics and a Ph.D. in mechanical engineering from the University of Colorado at Boulder in 1973 and 1976, respectively; an MBA from Rensselaer Polytechnic Institute at Troy, NY, in 1980; Doctor Technicae from the University of Trondheim at Trondheim, Norway, in 1990; a Doctor of Technical Sciences from the Warsaw University of Technology at Warsaw, Poland, in 1996; and Doctor Honouris Causa from the National Academy of Sciences at Gomel, Belarus, in

2000, and University of Kragujevac, Serbia, in 2011. He is a registered professional engineer. He is presently an Ohio Eminent Scholar and The Howard D. Winbigger Professor in the College of Engineering, and the Director of the Nanoprobe Laboratory for Bio- and Nanotechnology and Biomimetics (NLBB) and affiliated faculty in John Glenn College of Public Affairs at the Ohio State University, Columbus, Ohio. In 2013–14, he served as an ASME/AAAS Science and Technology Policy Fellow, House Committee on Science, Space and Technology, United States Congress, Washington, DC. His research interests include fundamental studies with a focus on scanning probe techniques in the interdisciplinary areas of bio/nanotribology, bio/nanomechanics and bio/nanomaterials characterization and applications to bio/nanotechnology, and biomimetics. He is an internationally recognized expert of bio/nanotribology and bio/nanomechanics using scanning probe microscopy and is one of the most prolific authors. He is considered by some a pioneer of the tribology and mechanics of magnetic storage devices. He has authored 8 scientific books, 90+ handbook chapters, 800+ scientific papers (h-index—76+; ISI Highly Cited Researcher in Materials Science since 2007 and in Biology and Biochemistry since 2013; ISI Top 5 % Cited Authors for Journals in Chemistry since 2011), and 60+ technical reports. He has also edited 50+ books and

holds 20 US and foreign patents. He is co-editor of Springer NanoScience and Technology Series and co-editor of Microsystem Technologies, and member of editorial board of PNAS. He has given more than 400 invited presentations on six continents and more than 200 keynote/plenary addresses at major international conferences.

Dr. Bhushan is an accomplished organizer. He organized the 1st Symposium on Tribology and Mechanics of Magnetic Storage Systems in 1984 and the 1st Int. Symposium on Advances in Information Storage Systems in 1990, both of which are now held annually. He organized two international NATO institutes in Europe. He is the founder of an ASME Information Storage and Processing Systems Division founded in 1993 and served as the founding chair during 1993–1998. His biography has been listed in over two dozen Who's Who books including Who's Who in the World and has received more than two dozen awards for his contributions to science and technology from professional societies, industry, and US government agencies including Life Achievement Tribology Award and Institution of Chemical Engineers (UK) Global Award. His research was listed as the top ten science stories of 2015. He is also the recipient of various international fellowships including the Alexander von Humboldt Research Prize for Senior Scientists, Max Planck Foundation Research Award for Outstanding Foreign Scientists, and Fulbright Senior Scholar Award. He is a foreign member of the International Academy of Engineering (Russia), Byelorussian Academy of Engineering and Technology, and the Academy of Triboengineering of Ukraine; an honorary member of the Society of Tribologists of Belarus and STLE; a fellow of ASME, IEEE, and the New York Academy of Sciences; and a member of ASEE, Sigma Xi, and Tau Beta Pi.

Dr. Bhushan has previously worked for Mechanical Technology Inc., Latham, NY; SKF Industries Inc., King of Prussia, PA; IBM, Tucson, AZ; and IBM Almaden Research Center, San Jose, CA. He has held visiting professorship at University of California at Berkeley; University of Cambridge, UK; Technical University Vienna, Austria; University of Paris, Orsay; ETH Zurich; EPFL Lausanne; Univ. of Southampton, UK; Univ. of Kragujevac, Serbia; Tsinghua Univ., China; Harbin Inst., China; and KFUPM, Saudi Arabia.

Chapter 1

Introduction

Look deep into nature and you will understand everything.

—Albert Einstein

Nature always tends to act in the simplest way.

—Bernoulli

(In nature,) Nothing is lacking and nothing is superfluous.

—Leonardo da Vinci

1.1 Introduction

Biomimetics is derived from the Greek word biomimesis. It means mimicking biology or living nature, or living organisms, and is also called biomimicry. The word biomimetics was coined by polymath Otto Schmitt in 1957, who, in his doctoral research, developed a physical device that mimicked the electrical action of a nerve. Another word often used in Europe and Asia is bionics, coined by Jack Steele of Wright-Patterson Air Force Base in Dayton, Ohio in 1960. Bionics combines two words, biology and technology/electronics. It translates to the creation of products, devices, and processes by using materials and processes found in living nature. Bionics today is referred to as robotics and replacement or enhancement of living matter, tissue, body parts, and organs. An example of bionics would be the “bionic man.” Finally, another word used is biognis, which is defined as the scientific investigation of life.

The word biomimetics is most commonly used in the English-speaking world. It first appeared in Webster’s dictionary in 1974, and is defined as “the study of the formation, structure or function of biologically produced substances and materials (as enzymes or silk) and biological mechanisms and processes (as protein synthesis or photosynthesis) especially for the purpose of synthesizing similar products by artificial mechanisms which mimic natural ones.” The field of biomimetics is highly interdisciplinary. It involves the understanding of biological functions, structures, and principles of various objects found in nature by biologists, physicists, chemists, and material scientists, and can lead to the biologically-inspired design, adaptation,

or derivation from living nature (Bhushan 2009). Bioinspiration or biodesign would be a more appropriate term for the field, as it applies to engineering. Various materials, structures, and devices have been fabricated for commercial interest by engineers, material scientists, chemists, and biologists, and for beauty, structure, and design by artists and architects (Bhushan 2009).

Nature has gone through evolution over the 3.8 billion years since life is estimated to have appeared on the Earth (Gordon 1976). It has evolved species with high performance using commonly found materials. Surfaces of solids interact with other surfaces and the environment and derive the properties of materials. Biological materials are highly organized from the molecular to the nano-, micro-, and macroscales, often in a hierarchical manner with intricate nanoarchitecture that ultimately makes up a myriad of different functional elements (Alberts et al. 2008; Nosonovsky and Bhushan 2008; Bhushan 2009). Properties of materials and surfaces result from a complex interplay between surface structure and morphology and physical and chemical properties. Many materials, surfaces, and objects in general provide multi-functionality.

Major benefits of biomimetics research is that it may allow derivation of optimal designs benefitting from improvements made during evolution of living nature and efficient use of natural resources in a more sustainable and environmentally friendly (green) manner. Biologically inspired materials and surfaces have generated significant interest and are helping to shape green science and technology.

1.2 Biodiversity

It is estimated that about 1.7 million different living organisms have been discovered. According to some estimates, Earth is home to some 10 million different species (Mora et al. 2011). About 83 % of these species are yet to be discovered. Given the loss of biodiversity, which began with the industrial era, some of the undiscovered organisms may be lost forever. Major groups of organisms account for very different proportions of biodiversity. Barthlott et al. (2014) report that arthropods make up the largest category, with roughly 5 million species, followed by bacteria (~2 million), other animals (~1.8 million), fungi (~600,000), and terrestrial plants (~370,000). The number of species per area vary considerably in different geographical regions. The highest diversity occurs in subtropical areas, and especially in the tropics.

1.3 Lessons from Nature

The understanding of the functions provided by species and processes found in living nature can guide us to design and produce nanomaterials, nanodevices, and processes (Bhushan 2009). There are a large number of flora and fauna with

properties of commercial interest. Molecular scale devices, superhydrophobicity, self-cleaning, drag reduction in fluid flow, antifouling, superhydrophilicity, energy conversion and conservation, reversible adhesion, aerodynamic lift, materials and fibers with high mechanical strength, biological self-assembly, anti-reflection, structural coloration, thermal insulation, self-healing, and sensory aid mechanisms are examples of functionalities found in living nature that are of commercial interest (Bhushan 2009; Bar-Cohen 2011).

Figure 1.1 provides an overview of various species and objects from living nature and their properties of interest (Bhushan 2009). These include bacteria (Jones and Aizawa 1991), plants (Koch et al. 2008, 2009), insects/spiders/lizards/frogs (Autumn et al. 2000; Gorb 2001; Bhushan 2007, 2010), aquatic animals (Bechert et al. 1997, 2000; Dean and Bhushan 2010; Bixler and Bhushan 2013a, 2015), birds

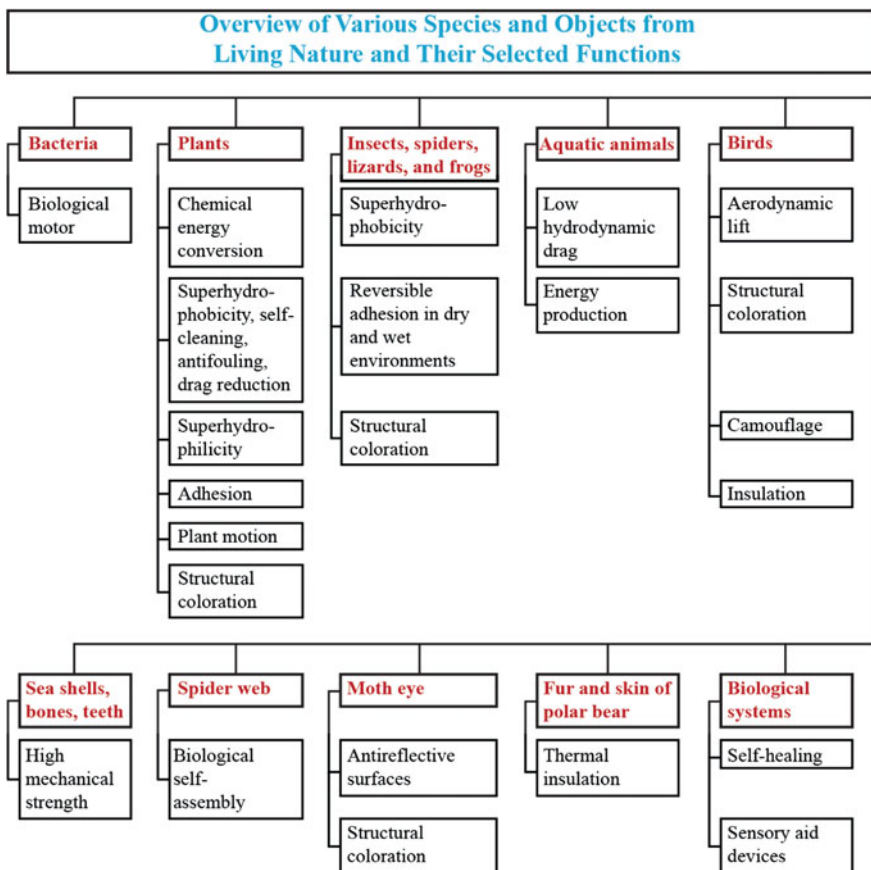


Fig. 1.1 An overview of various species and objects from living nature and their selected function (Adapted from Bhushan 2009)

(Jakab 1990), seashells/bones/teeth (Lowenstam and Weiner 1989; Sarikaya and Aksay 1995; Mann 2001; Alexander and Diskin 2004; Meyers et al. 2006, 2008; Sun and Bhushan 2012), spider web (Jin and Kaplan 2003; Bar-Cohen 2011), moth eye (Genzer and Efimenko 2006; Mueller 2008), structural coloration (Parker 2009; Sun et al. 2013), the fur and skin of polar bears (Stegmaier et al. 2009), biological systems with a self-healing capability (Fratzl and Weinkamer 2007; Nosonovsky and Bhushan 2009), and sensory-aid devices (Barth et al. 2003; Bar-Cohen 2011).

Figure 1.2 shows a montage of some examples from living nature (Bhushan 2009). Many bacteria propel themselves by a type of extremely miniature motor called a flagellum motor. These motors rotate up to 100,000 rpm (Jones and Aizawa 1991). These are similar to an electrical motor and have a starter, rotor, and drive shaft with a bushing. The diameter of the bushing is approximately 20–30 nm with a clearance of approximately 1 nm. The flagellum motor is driven by the proton flow caused by the electrochemical potential difference across the cell membrane.

The diversity of the structure and morphology of plant leaf surfaces provides multifunctional properties (Koch et al. 2008, 2009). Plants use photosynthesis to harness solar energy to support plant life. Plant leaves can exhibit superhydrophobicity, self-cleaning, antifouling, drag reduction, superhydrophilicity, adhesion, and plant motion. Leaves of water-repellent plants, such as *Nelumbo nucifera* (lotus), are known to be superhydrophobic, self-cleaning, and antifouling, due to hierarchical roughness (microbumps superimposed with a nanostructure) and the presence of a hydrophobic wax coating (Neinhuis and Barthlott 1997; Barthlott and Neinhuis 1997; Wagner et al. 2003; Burton and Bhushan 2006; Bhushan and Jung 2006, 2011; Bhushan 2009, 2011; Bhushan et al. 2009). Water droplets on these surfaces readily sit on the apex of nanostructures because air bubbles fill in the valleys of the structure under the droplet (Bhushan et al. 2009). Therefore, these leaves exhibit considerable superhydrophobicity.

Two strategies used by plants for catching insects for digestion are having either sticky or slippery surfaces. Slippery surfaces are created by the pitcher plant (carnivorous, genus *Nepenthes*) using surface wetting, which causes insects to aquaplane into the digestion area (Bohn and Federle 2004; Bhushan 2009; Koch et al. 2009). The pitcher rim (peristome) consists of microstructure with radial ridges of smooth overlapping epidermal cells, which forms a series of steps toward the pitcher inside. This anisotropic surface is completely wettable by nectar secreted at the inner margin of the peristome and by rain water, so a water film covers the surface under humid conditions. The wet surface is slippery and causes the aquaplaning effect, forcing insects to slip inside the pitcher plants.

Insects, spiders, lizards, and frogs can exhibit superhydrophobicity, reversible adhesion in dry and wet environments, and structural coloration. Water striders (*Gerris remigis*) have the ability to stand and walk upon a water surface without getting wet. Even the impact of rain droplets with a size greater than the water strider's size does not immerse it in the water. The water strider's legs consist of a hierarchical structure with a large number of oriented tiny hairs (microsetae) with fine nanogrooves and covered with cuticle wax that makes the leg surfaces

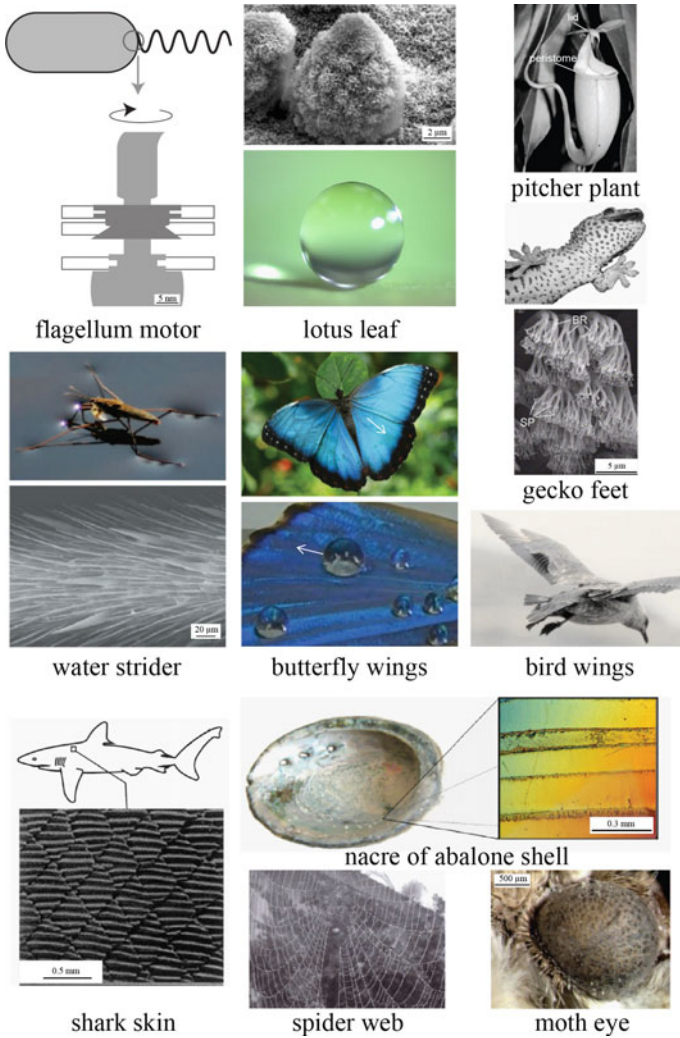


Fig. 1.2 Montage of some examples from living nature: schematic of bacteria and flagellum motor; lotus leaf (Bhushan et al. 2009); The slippery rim (peristome) of the pitcher plant captures insects by insect aquaplaning; water strider walking on water (Gao and Jiang 2004); butterfly wing effect (Bixler and Bhushan 2013b); gecko foot exhibiting reversible adhesion (Gao et al. 2005); scale structure of shark reducing drag (Jung and Bhushan 2010); wings of a bird in landing approach; nacre of the inner abalone shell showing mesostructure with mesolayers (Meyers et al. 2006); spider web made of silk material (Bar-Cohen 2011); and antireflective moth’s eye (Genzer and Efimenko 2006)

superhydrophobic and is responsible for their water resistance. Because of these structures, water striders can stand and walk quickly on the water surface (Gao and Jiang 2004).

Wings of butterflies, a family of insects, exhibit superhydrophobicity, self-cleaning, antifouling, and low drag (Bixler and Bhushan 2012b, 2015). The wings have a hierarchical structure consisting of shingle-like scales covered by microgrooves oriented radially outward from the main body of the butterfly. The hierarchical scales create a superhydrophobic and self-cleaning surface, similar to lotus effects. Superhydrophobicity and anisotropic grooves, similar to those in shark skin, lead to low drag. Thus, the wing surface combines both the lotus and shark skin effects. Brilliant iridescent colors of the wings are created by coherent scattering across the wings' nanostructures, known as structural coloration, rather than the use of color pigments (Sun et al. 2013).

A gecko is the largest animal that can produce high (dry) adhesion to support its weight with a high factor of safety. Gecko skin is comprised of a complex hierarchical structure of lamellae, setae, branches, and spatula (Autumn et al. 2000; Gao et al. 2005; Bhushan 2007). The attachment pads on two feet of the Tokay gecko have an area of approximately 220 mm². Approximately 3 million setae on their toes that branch off into about three billion spatula on two feet can produce a clinging ability of approximately 20 N (vertical force required to pull a lizard down a nearly vertical (85°) surface) and allow them to climb vertical surfaces at speeds of over 1 m/s, with the capability to attach or detach their toes in milliseconds (Bhushan 2007).

Shark skin, which is a model from nature for a low drag surface, is covered by very small individual tooth-like scales called dermal denticles (little skin teeth), ribbed with longitudinal grooves (aligned parallel to the local flow direction of the water). These grooved scales lift vortices to the tips of the scales, resulting in water moving efficiently over their surface (Bechert et al. 1997, 2000; Dean and Bhushan 2010; Jung and Bhushan 2010; Bixler and Bhushan 2013a). The spacing between these dermal denticles is such that microscopic aquatic organisms have difficulty adhering to the surface, making the skin surface antifouling (Genzer and Efimenko 2006; Bixler and Bhushan 2012a, 2013a).

Birds' wings consist of several consecutive rows of covering feathers that are flexible. These movable flaps develop the aerodynamic lift necessary for flight. When a bird lands, a few feathers are deployed in front of the leading edges of the wings, which help to reduce the drag on the wings (Jakob 1990). The beautiful colors in birds' feathers are created by structural coloration (Sun et al. 2013).

Seashells, bones, and teeth are biomaterials that are nanocomposites with a laminated, hierarchical structure that exhibit superior mechanical properties to their constituents (Lowenstam and Weiner 1989; Sarikaya and Aksay 1995; Mann 2001; Alexander and Diskin 2004; Meyer et al. 2006, 2008; Sun and Bhushan 2012). This is because biological organisms produce composites in complex, layered structures. The nacre of the inner abalone shell (*Haliotis*) derives high hardness and high toughness (as compared to the lower toughness of monolithic CaCO₃) from a hierarchically organized structure starting with single crystals of the aragonite polymorph of CaCO₃, consisting of 0.5–10 μm thick bricks (microstructure) and finishing with 0.3 μm thick layers (nanostructure). Between the layers, there exists a 20–30 nm thick organic protein substance. The mixture of brittle platelets and thin

layers of elastic biomaterials inhibit transverse crack propagation and make the material strong and resilient.

A spider generates silk fiber and has a sufficient supply of raw material for its silk to span great distances (Jin and Kaplan 2003; Bar-Cohen 2011). A spider web is a structure built of a one-dimensional fiber. The fiber is very strong and continuous and is insoluble in water. The web can hold a significant amount of water droplets, and it is resistant to rain, wind, and sunlight (Sarıkaya and Aksay 1995).

The eyes of moths are antireflective to visible light as they consist of hundreds of hexagonally organized nanoscopic pillars, each approximately 200 nm in diameter and height, which result in the very low reflectance for visible light (Genzer and Efimenko 2006; Mueller 2008). These nanostructures' optical surfaces make the eye surface nearly antireflective in any direction.

These examples show the bounty of properties living nature has to offer scientists and engineers. These properties, and others yet undiscovered, hold the keys to solving science and engineering problems.

1.4 Golden Ratio and Fibonacci Numbers

To understand the secrets of the order that nature imposes, researchers have studied the so-called “Golden Ratio” and “Fibonacci numbers.” These describe unique patterns found throughout not only our terrestrial environment, but the universe as well (Vajda 1989; Livio 2002; Posamentier and Lehmann 2007). Scientists and mathematicians began to study the Golden Ratio around 450 B.C., though it was used for some time before by the Greeks, and Egyptians even before them, in art and architecture (Wittkower 1960). Leonardo da Pisa, nicknamed Fibonacci (1175–1230), discovered that a certain sequence of numbers, the Fibonacci numbers, approached the Golden Ratio, and he began studying the preponderance of examples of those numbers in nature around 1200 A.D. (Wittkower 1960; Bixler and Bhushan 2013b, 2015).

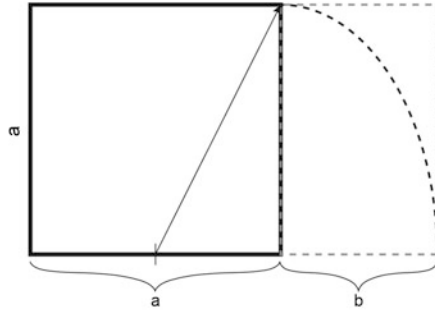
The Golden Ratio is a unique ratio whose proportions are considered to represent a functional and aesthetic ideal. It is defined as $\frac{\text{length } 1}{\text{length } 2} \approx 1.618$, where length 1 and length 2 are larger and smaller dimensions of a rectangle, respectively. A rectangle produced using the Golden Ratio is called the Golden Rectangle, consisting of a square combined with another Golden Rectangle, as shown in Fig. 1.3. A Golden Rectangle is produced by drawing a line from the midpoint of one side of the square to an opposite corner, then using that line as the radius to draw an arc that defines the height of the rectangle. Each Golden Rectangle contains an infinite sequence of squares and adjacent Golden Rectangles. The figure also shows how the Golden Spiral can be produced from the Golden Rectangle by drawing an arc tangent to the square, from the bottom corner of the square to the opposite corner, where it meets the square encompassed in the adjacent encompassed Golden Rectangle (Wittkower 1960).

Fig. 1.3 The Golden Ratio, and the construction of the Golden Rectangle and the Golden Spiral, as derivations of the Golden Ratio

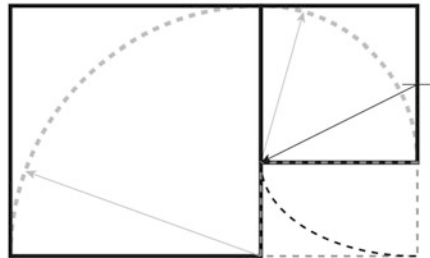
The Golden Ratio and the construction of a Golden Rectangle and Golden Spiral

The Golden Ratio is given by: $\frac{a+b}{a} = \frac{a}{b} = 1.618$

where a is the side of the square, b is the short side of an adjacent Golden Rectangle, and $a+b$ gives the long side of the encompassing rectangle

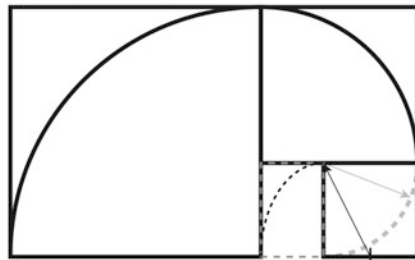


By drawing a line from the midpoint of a side of a square, a , to an opposite corner, and using the line as the radius of an arc that determines the endpoint of b , a Golden Rectangle is constructed with a Golden Ratio.



Each Golden Rectangle encompasses an infinite number of squares with adjacent Golden Rectangles.

By drawing an arc tangent to the square, from one corner to the opposite corner, and connecting these together, a Golden Spiral is created.



The Golden Ratio is found throughout nature, with examples ranging from the proportions of the human body to the spiral shapes of the Milky Way galaxy and seashells. Inspired by beauty found in nature, famous artists have included the

Golden Ratio in their works, such as Leonardo da Vinci's paintings "A Head of an Old Man" and the "Mona Lisa." Architects have also relied on the Golden Ratio for functional aesthetics since its discovery (Wittkower 1960). The "mystical" beauty found using the golden section is exemplified in the proportions of the Parthenon (Zeising 1854), the construction of medieval churches (Zeising 1854; Wittkower 1960), and, more recently in the mid-20th century, in the work of Le Corbusier (Wittkower 1960), who used the Golden Ratio to define his oeuvre.

Moreover, Fibonacci numbers describe geometries of various structures found in nature. While these whole numbers do not produce the Golden Ratio precisely, the ratios of the numbers quickly approach the Golden Ratio, as the sequence continues into infinity (Wittkower 1960). The Fibonacci numbers are described by the mathematical expression $F_n = F_{n-1} + F_{n-2}$. The sequence begins with the seed values of $F_0 = 0$ and $F_1 = 1$, then, the recursive expression provides the values following, resulting in 0, 1, 1, 2, 3, 5, 8, 13, 21, 34,... and so on (Wittkower 1960; Vajda 1989; Posamentier and Lehman 2007). Figure 1.4 shows how the sequence is created out of these whole numbers, and how their ratios approach the Golden Ratio. In the figure, the Fibonacci sequence, F_n , is placed to the left; in the center, the sequence is displaced by one number, F_{n-1} , and to the right, displaced by 2 numbers, F_{n-2} . This shows how the sequence is calculated. Examples of the Fibonacci numbers in nature include the number and sequence of patterns on pineapples and sunflower heads, as well as the number of petals on flowers.

Figure 1.5 illustrates examples that demonstrate the prevalence of the Fibonacci numbers and the Golden Ratio in nature and art (Bixler and Bhushan 2013b, 2015). Shown are the Milky Way galaxy, a sunflower head, flower petals, a nautilus seashell, the Mona Lisa, and pineapples. The Mona Lisa highlights the Golden Rectangle, as well as the Golden spiral, which draws the eye to the focus of the art. The Golden Spiral is demonstrated in the images of the Milky Way galaxy, the seed growth in the sunflower head, and a nautilus seashell. When the Golden Rectangle height is divided by its width, the Golden Ratio of 1.618 is calculated, as demonstrated with the galaxy, sunflower head, sea shell, and Mona Lisa painting. Furthermore, Fibonacci numbers are present in the arrangement of petals in a dahlia flower, and interlocking helices of 0, 5, 8, and 13 wrapping around the skin of a pineapple (Vajda 1989; Livio 2002; Posamentier and Lehman 2007).

The Golden Ratio and Fibonacci numbers also are present in shark skin, a rice leaf, and butterfly wings, to be discussed in Chaps. 10 and 12. It has been found that riblets from the mako (*Isurus oxyrinchus*) and the dogfish (*Squalus acanthias*) shark species contain five and three riblets per dermal denticle, respectively. These values represent Fibonacci numbers (Bixler and Bhushan 2013b). Furthermore, it has been reported that butterfly wing scales are approximately 75 μm wide by 125 μm long (Bixler and Bhushan 2013b). Such scales exhibit a ratio value approximately equating to Fibonacci ratios, $\frac{125 \mu\text{m}}{75 \mu\text{m}} = \frac{12.5 \text{ mm}}{7.5 \text{ mm}} \approx \frac{13}{8}$, which approach the Golden Ratio, 1.618.

Fig. 1.4 Fibonacci sequence shows how the sequence is calculated from whole numbers, and how the ratios of these numbers in sequence approach the Golden Ratio (adapted from Wittkower 1960)

Fibonacci sequence

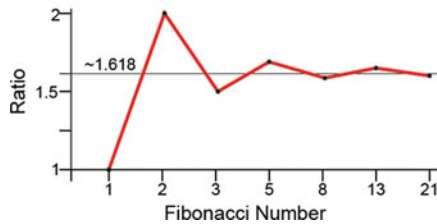
The Fibonacci sequence is defined by:

$$F_n = F_{n-1} + F_{n-2}$$

Seed Values	F ₀	0	0	0
	F ₁	1	0	0
Recursive Values	F ₂	1	1	0
	F ₃	2	1	1
	F ₄	3	2	1
	F ₅	5	3	2
	F ₆	8	5	3
	F ₇	13	8	5
	F ₈	21	13	8

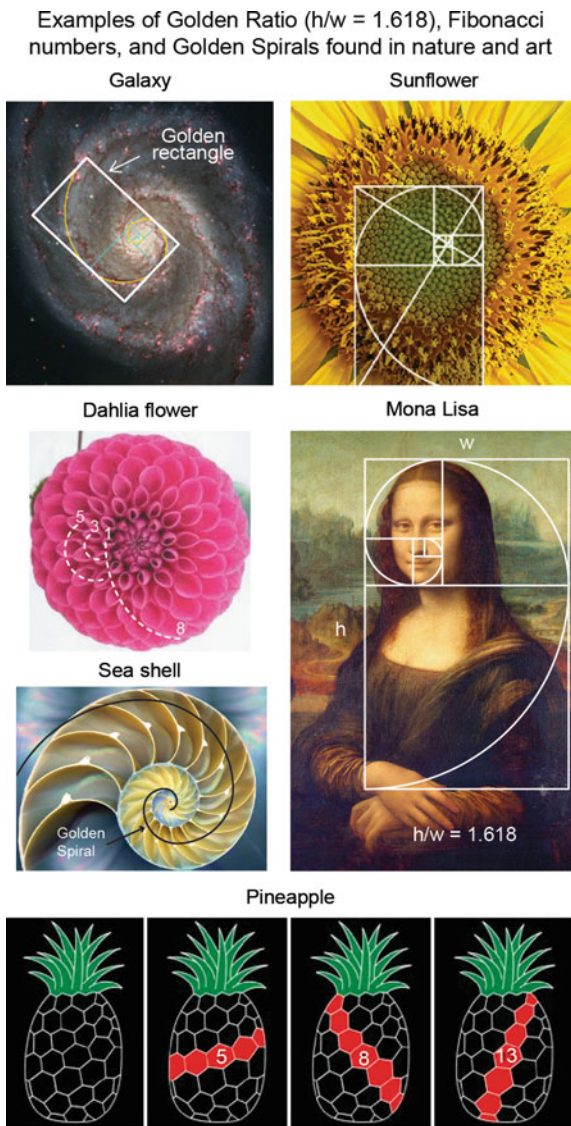
The ratio of each number in the sequence to its preceding number rapidly approaches the Golden Ratio:

$$\frac{1}{1}, \frac{2}{1}, \frac{3}{2}, \frac{5}{3}, \frac{8}{5}, \frac{13}{8}, \frac{21}{13} \text{ gives:}$$



To help explain the significance of these numbers, possible explanations have been developed (Bixler and Bhushan 2013b, 2015). For shark skin, it is believed that each riblet must be large enough to properly lift and pin the turbulent vortices to lower drag, yet be small enough to easily flex with the shark. Furthermore, it is suspected that dermal denticles with fewer than three riblets would be too disjointed and not effectively control the vortices. Conversely, it is suspected that dermal denticles with more than five riblets would be too large to flex with the shark. As

Fig. 1.5 Montage of images showing examples of the Golden Ratio, Golden Rectangle, and Fibonacci numbers found in nature and art. Examples include galaxies, sunflower heads, flower petals, sea shells, Mona Lisa painting, and pineapple fruit (from *top left* to *bottom right*). The Golden Rectangle and Fibonacci or Golden spiral are superimposed on select images. Such proportions and patterns are considered aesthetically pleasing and are believed to enhance performance of systems found throughout nature (adapted from Bixler and Bhushan 2013b)



for the butterfly wings, it is believed that the scales exhibit the Golden Ratio to create effective overlapping shingle-like structures, with the longer edge in the fluid flow direction. This arrangement is suspected to help encourage the desired anisotropic flow away from the butterfly body, which leads to self-cleaning. It is believed that scales veering from the Golden Ratio may not effectively direct the fluid flow.

Since Fibonacci numbers and the Golden Ratio are found throughout nature, it is believed such findings may hold clues for designing low drag and self-cleaning surfaces (Bixler and Bhushan 2013b, 2015).

1.5 Biomimetics in Art and Architecture—Bioarchitecture

Scientists and engineers take inspiration from living nature for the purpose of functionality and commercial applications. Artists and architects take inspiration from nature for the purpose of beauty, as well as design and functionality. They incorporate many biomimetic ideas in both ornamental and functional ways. Various patterns found in nature are used by artists for beauty and design. Further, structural coloration from nanostructured surfaces is being developed for use by artists to produce vivid, durable colors that may not be possible by color pigments. Architects develop design strategies by incorporating patterns and organization found in natural forms (Gruber 2011; Imhof and Gruber 2013). Moreover, as nanostructured surfaces or materials with functional hierarchy are developed, these, too, are being incorporated into design practice ranging from nanoscale to the

Fig. 1.6 Examples of biomimetics in art: antique jewelry pieces crafted by Van Cleef and Arpels in the early 1900s

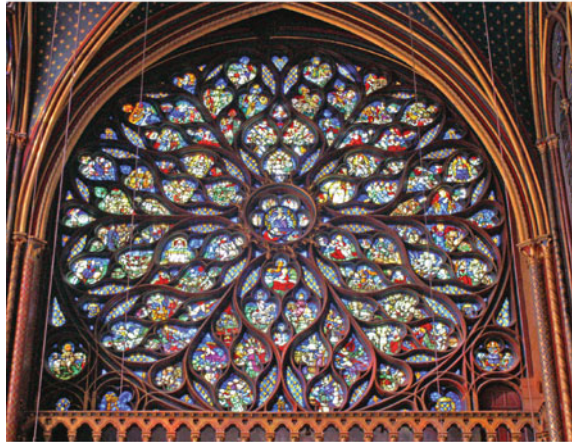


macroscale. There is a field of emerging contemporary architectural design practice based on patterns and processes found in living nature, we would like to call “bioarchitecture.” Another term “biornametics” has also been used (Imhof and Gruber 2013).

At its most basic, biomimetics is the mimicking of living nature. At a macro-scale, art accomplishes this through direct copying of natural figures. Figure 1.6 shows four examples of bioinspired antique jewelry pieces crafted by Van Cleef and Arpels in the early 1900s. The figure shows four brooches inspired by a snowflake, butterfly, orchid, and sycamore leaf. Architects, too, accomplish this direct representation in various ornamental motifs. Figure 1.7 shows examples of the rose window of the gothic Sainte Chapelle Cathedral designed for King Louis IX (1248) in Paris, France, inspired by the color and shape of a flower (Watkin 2005), and an art nouveau staircase incorporating vines, flowers, and other

Fig. 1.7 Examples of biomimetics in architecture: the rose window of the gothic Sainte Chapelle Cathedral in Paris, France, for King Louis IX (1248), and an art nouveau staircase incorporating vines, flowers, and other plant forms in the Horta Museum in Brussels, Belgium, by Victor Horta (1898)

Examples of biomimetics in architecture



Rose Window, Sainte Chappelle, Paris, France (1248)



Victor Horta Museum, Brussels, Belgium, Horta (1898)

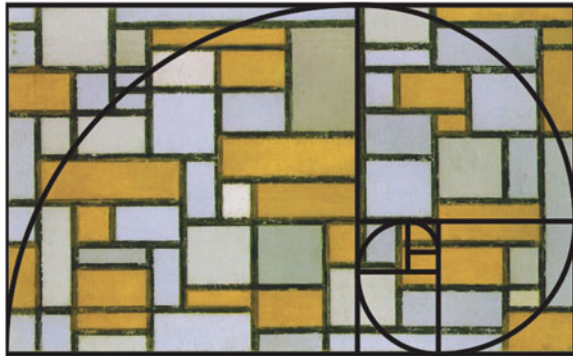
plant forms, located within the Horta Museum in Brussels, Belgium, designed by Victor Horta (1898) (Watkin 2005; Curtis 2012).

However, direct representation is a fairly facile way to incorporate nature into design without actually delving into the organization or properties nature provides. Artists and architects alike strive to derive these properties and incorporate this organization into their work in this manner; not as merely direct representation or ornament to the design, but as an integral part of the making of the work.

Figure 1.8 shows *Composition in Gray and Light Brown* by Piet Mondrian (1918) and *Bone Armchair* by Joris Laarman (2006). *Composition in Gray and*

Fig. 1.8 Examples of bioinspiration in art: *Composition in Gray and Light Brown* by Piet Mondrian (1918), incorporating the golden ratio to structure the composition of the painting; and *Bone Armchair* by Joris Laarman (2006), using an understanding of how the interior structure of bone grows, as a way to create a novel construction for a chair

Examples of bioinspiration in art



Composition in Gray and Light Brown
Piet Mondrian (1918) (with overlay)



Bone Armchair, Joris Laarman (2006)

Light Brown incorporates the Golden Spiral into the arrangement of the various rectangles in the composition. This spiral, while not obvious without overlay, serves to draw the viewer's eye around the painting to a focus, much the same way that the Golden Spiral does for the Mona Lisa. Without a direct representation of the spiral, the composition still incorporates it as an integral part of the organization. For the Bone Armchair, Joris Laarman studied the way that the interior structure of bones grow, and, using sophisticated software, created the structure for his chair in

Fig. 1.9 Examples of bioinspiration in architecture: gothic rib vaulting from the Durham Cathedral in Durham, England, by William of S. Carilef (c. 1100), relying on an understanding of the relationship between bones and the thin tissues between them to reduce the weight of the traditionally thick stone or timber ceiling; and the Nakagin Capsule Tower in Tokyo, Japan, by Kisho Kurakawa (1972), using cellular discoveries of the time to reduce the essential living requirements to discrete, replicable, and interconnected blocks suitable for rapid growth and expansion

Examples of bioinspiration in architecture



Durham Cathedral, Durham, England (c. 1100)



Nakagin Capsule Tower, Tokyo, Japan (1972)

much the same way; reducing material where the structure could be light and increasing it where the structure needed to be strong (Fairs 2006). This created a chair that is structurally very strong and sturdy, yet light, both in actual weight and in appearance.

Figure 1.9 shows the Durham Cathedral in Durham, England, by William of St. Carilef (completed c. 1100) (Watkin 2005); and the Nakagin Capsule Tower in Tokyo, Japan, by Kisho Kurakawa (1972). The construction of Durham Cathedral relied on an understanding of the relationship between bones and the thin tissues between them to reduce the weight of the traditionally thick stone or timber ceiling (Watkin 2005). Historically, heavy stone or timber ceilings necessitated building walls that were very thick and relatively short to support the weight, and the ceilings were prone to collapse, either from the weight or from fire. By reducing the weight of the ceiling, rib vaulting ushered in a new era of cathedral buildings that resulted in soaring heights, thinner walls pierced by many windows, and structures less likely to collapse under the weight of the ceiling (Watkin 2005). Nakagin Capsule Tower, produced out of the Metabolist movement in Japan, used cellular discoveries of the time to reduce the essential living requirements to discrete, replicable, and interconnected blocks suitable for rapid growth and expansion (von Richthofen 2007). The Metabolists were fascinated by new scanning electron microscope (SEM) images of metabolic and cellular organizations. They extracted out of these images ideas of cellular replication, organization, and efficiency of function. From these ideas, they scaled up and created projects that addressed rapid, post-war urban growth (von Richthofen 2007).

Through these projects, biomimetics transcends mimicry, and approaches what has been previously called bioinspiration. No longer are the works mere copies of living nature, but instead, they extract a principle from nature, seek to understand that principle, and then incorporate the principle into a new medium, design, or other end result.

1.6 Industrial Significance

The understanding of the functions provided by species and processes found in living nature can guide us to produce nanomaterials, nanodevices, and processes with desirable functionality. Living nature has a limited toolbox and uses rather basic materials and routine fabrication methods. The objective of biomimetics is not to simply mimic nature. Once one understands how nature does its job, one can then fabricate optimum structures and devices using smart materials and fabrication techniques. One does not do biomimicry, but instead develops bioinspired designs, adaptation, or derivation from living nature. This may be referred to as biodesign.

Although the word biomimetics is relatively new, our ancestors looked to living nature for inspiration and development of various materials and devices many centuries ago (Ball 2002; Anonymous 2007; Meyers et al. 2008; Bar-Cohen 2011). For example, the Chinese tried to make artificial silk some 3000 years ago.

Leonardo da Vinci, a genius of his time, studied how birds fly and proposed designs of flying machines. In the twentieth century, various products, including the design of aircraft, have been inspired by nature. Since the 1980s, the artificial intelligence and neural networks in information technology have been inspired by the desire to mimic the human brain. The existence of biocells and deoxyribonucleic acid (DNA) serves as a source of inspiration for nanotechnologists who hope to one day build self-assembled molecular-scale devices. In molecular biomimetics, proteins are being utilized in controlling materials formation in practical engineering towards self-assembled, hybrid, functional materials structure (Grunwald et al. 2009; Tamerler and Sarikaya 2009).

Superhydrophobic surfaces can be used for water repellency, drag reduction in fluid flow, energy conservation, and energy conversion. Self-cleaning surfaces are of interest in various applications, including self-cleaning windows, windshields, exterior paint for buildings, utensils, roof tiles, textiles, solar panels, and exterior surfaces in transportation. Low adhesion/drag surfaces also exhibits anti-fouling of interest. Examples include biomedical and membranes for desalination and water purification.

Since the mid-1990s, the lotus effect has been used to develop a variety of surfaces for superhydrophobicity, self-cleaning, low adhesion, and drag reduction in fluid flow, as well as antifouling (Bhushan 2009; Bhushan and Jung 2011; Bixler and Bhushan 2012a). Self-cleaning products include hydrophobic façade paints Lotusan[®], introduced by Sto in 1999, and Erlus Lotus roof tiles and NanoSphere[®] fabric by Schoeller Technologies. Self-cleaning hydrophilic SunClean[®] glass by PPG Industries contains a titanium dioxide coating, which uses the sheeting action of water to efficiently gather and remove contaminants (Bixler and Bhushan 2015).

Replication of the dynamic climbing and peeling ability of geckos has been carried out to develop treads of wall-climbing robots (Cutkosky and Kim 2009).

Low drag is of interest in both internal and external flow. Examples of internal flow include pipelines, catheters, and micro/nano channels such as in micro/nanofluidic based sensors (Bhushan 2010, 2012). A major example of external flow is transportation—ships, airplanes, and automobiles. According to the U.N. International Maritime Organization, about 90 % of worldwide goods are carried by sea-faring vessels, and about 35–70 % of energy consumed in transportation is estimated to be lost due to drag. In airplanes and automobiles, energy losses due to drag are also important. In the oil industry, pipeline flow must overcome high drag due to viscous effects and sludge fouling. Low drag surfaces often equate to energy conservation and less fouling. Shark skin-inspired surfaces have been created to reduce drag (Dean and Bhushan 2010; Bixler and Bhushan 2013a). Shark skin-inspired experimental vinyl sawtooth riblets have been developed by 3M Corp. (Marentic and Morris 1992). They have been reported to reduce drag by 3 % when 70 % of the Airbus plane surface was covered by these sheets. Their major commercial application is in the Speedo FastSkin[®] racing swimsuit. It was worn by American Swimmer Michael Phelps, who won 8 gold medals, the most of any athlete in any single Olympic showing, and broke 8 Olympic and 7 World records.

Table 1.1 Selected examples of objects and desired properties including mechanical durability for industrial applications

Objects	Materials	Desired properties
<i>(a) Automotive applications</i>		
Windshield, window glass, side/rear view mirrors, camera lens (back of car)	Glass	Superoleophobic, self-cleaning, anti-smudge, antifouling, optically transparent/antireflective
Display, headlights	PMMA for temperature sensitive, transparent, capacitive touch material; polycarbonate	Superoleophobic, self-cleaning, anti-smudge, antifouling, optically transparent/antireflective
Door liners, fabric, carpet, leather	Polypropylene (door liner)	Superoleophobic, self-cleaning, anti-smudge, antifouling
Car body	Painted steel	Self-cleaning, anti-smudge, low drag
<i>(b) Plastic bottles and caps</i>		
Bottles	High-density polyethylene, polyethylene terephthalate, polypropylene	Superoleophobic, superhydrophobic
Caps	Polypropylene	Superoleophobic, superhydrophobic
<i>(c) Smart screens for electronic display</i>		
Screens	Soda-lime glass, polyethylene terephthalate, polycarbonate	Superoleophobic, self-cleaning, anti-smudge, antifouling, optically transparent

In the field of biomimetic materials, bioinspired ceramics have been fabricated based on sea shells and other biomimetic materials. Two-component biological materials such as bones, teeth, and abalone shells exhibit high mechanical strength, as well as fracture toughness, responsible for durability. Nanoscale architecture used in nature for optical reflection and anti-reflection has been used to develop reflecting and anti-reflecting surfaces, as well as structural coloration. Inspired by the fur of the polar bear, artificial furs and textiles have been developed. Self-healing of biological systems found in nature is of interest for self-repair. Biomimetics is also guiding in the development of sensory-aid devices.

The major emphasis on nanoscience and nanotechnology since the early 1990s has provided a significant impetus in mimicking nature using nanofabrication techniques for commercial applications (Bhushan 2010). Biomimetics has spurred interest across many disciplines. Revenues from biomimetic products in 2015 were estimated to be several billion dollars annually. Annual sales are expected to continue to increase dramatically.

Table 1.1 shows selected examples of objects and desired properties in some industrial applications.

1.7 Research Objective and Approach

The objective of biomimetics research is to develop biologically-inspired materials and surfaces of commercial interest. The approach is threefold:

1. Species are selected from nature which provide functionality of commercial interest.
2. The species are characterized to understand how a natural species provides functionality. Then it is modeled and structures are generally fabricated in the lab using nature's route to verify one's understanding. Modeling is used to develop optimum structures.
3. Nature has a limited toolbox and uses rather basic materials and routine fabrication methods for species, and it capitalizes on hierarchical structures. Once one understands how nature does it, one can then fabricate optimum structures using smart materials and fabrication techniques to provide functionality of interest.

1.8 Organization of the Book

After a broad introduction, the book starts with roughness-induced superomniphobicity, lessons from living nature, and the lotus effect, which exhibits superhydrophobicity, self-cleaning, low adhesion/drag reduction, and antifouling. Next follows the floating water fern, which floats over water; the rose petal effect, which can provide either low adhesion or high adhesion; superoleophobic/philic surfaces; shark skin, which exhibits low drag and antifouling, the rice leaf and butterfly wing effect, which exhibits a combination of the lotus effect and shark skin effect and antifouling; gecko adhesion, which exhibit reversible adhesion; nacre with high mechanical strength; and structural coloration.

References

- Alberts, B., Johnson, A., Lewis, J., Raff, M. Roberts, K., Walter, P. (eds.) (2008) *Molecular Biology of the Cell*, Garland Science, New York.
- Alexander, R. M. and Diskin, A. (2004), *Human Bones: A Scientific and Pictorial Investigation*, Pi Press, New York.
- Anonymous (2007), *Biomimetics: Strategies for Product Design Inspired by Nature*, Dept. of Trade and Industry, UK.
- Autumn, K., Liang, Y. A., Hsieh, S. T., Zesch, W., Chan, W. P., Kenny, T. W., Fearing, R. and Full, R. J. (2000), "Adhesive Force of a Single Gecko Foot-Hair," *Nature* 405, 681–685.
- Ball, P. (2002), "Natural Strategies for the Molecular Engineer," *Nanotechnology* 13, R15-R28.
- Bar-Cohen, Y. (2011), *Biomimetics: Nature-Based Innovation*, CRC Press, Boca Raton, FL.

- Barth, F. G., Humphrey, J. A. C., and Secomb, T. W. (2003), *Sensors and Sensing in Biology and Engineering*, Springer-Verlag, New York.
- Barthlott, W. and Neinhuis, C. (1997), "Purity of the Sacred Lotus, or Escape from Contamination in Biological Surfaces," *Planta* 202, 1-8.
- Barthlott, W., Erdelen, W. R., and Rafiqpoor, M. D. (2014), "Biodiversity and Technical Innovations: Bionics," in *Concepts and Values in Biodiversity* (Lanzerath, D. and Friele, M. (eds.), Routledge, London.
- Bechert, D. W., Bruse, M., Hage W., Van Der Hoeven J. G. T., and Hoppe G. (1997), "Experiments on Drag-Reducing Surfaces and Their Optimization with an Adjustable Geometry," *J. Fluid Mech.* 338, 59-87.
- Bechert, D. W., Bruse, M., and Hage, W. (2000), "Experiments with Three-Dimensional Riblets as an Idealized Model of Shark Skin," *Exp. Fluids* 28, 403-412.
- Bhushan, B. (2007), "Adhesion of Multi-Level Hierarchical Attachment Systems in Gecko Feet," *J. Adhes. Sci. Technol.* 21, 1213-1258.
- Bhushan, B. (2009), "Biomimetics: Lessons from Nature – An Overview," *Phil. Trans. R. Soc. A* 367, 1445-1486.
- Bhushan, B. (2010), *Springer Handbook of Nanotechnology*, third ed., Springer, Heidelberg, Germany.
- Bhushan, B. (2011), "Biomimetics Inspired Surfaces for Drag Reduction and Oleophobicity/philicity," *Beilstein J. Nanotechnol.* 2, 66-84.
- Bhushan, B. (2012), *Encyclopedia of Nanotechnology*, Vols. 1-4, Springer, Heidelberg, Germany.
- Bhushan, B. and Jung, Y. C. (2006), "Micro and Nanoscale Characterization of Hydrophobic and Hydrophilic Leaf Surface," *Nanotechnology* 17, 2758-2772.
- Bhushan, B. and Jung, Y. C. (2011), "Natural and Biomimetic Artificial Surfaces for Superhydrophobicity, Self-Cleaning, Low Adhesion, and Drag Reduction," *Prog. Mater. Sci.* 56, 1-108.
- Bhushan, B., Jung, Y. C., and Koch, K. (2009), "Micro-, Nano- and Hierarchical Structures for Superhydrophobicity, Self-Cleaning and Low Adhesion," *Phil. Trans. R. Soc. A* 367, 1631-1672.
- Bixler, G. D. and Bhushan, B. (2012a), "Biofouling: Lessons from Nature," *Phil. Trans. R. Soc. A* 370, 2381-2417.
- Bixler, G. D. and Bhushan, B. (2012b), "Bioinspired Rice Leaf and Butterfly Wing Surface Structures Combining Shark Skin and Lotus Effects," *Soft Matter* 9, 1620-1635.
- Bixler, G. D. and Bhushan, B. (2013a), "Fluid Drag Reduction with Shark-skin Riblet Inspired Microstructured Surfaces," *Adv. Func. Mater.* 23, 4507-4528.
- Bixler, G. D. and Bhushan, B. (2013b), "Fluid Drag Reduction and Efficient Self-Cleaning with Rice Leaf and Butterfly Wing Bioinspired Surfaces," *Nanoscale* 5, 7685-7710.
- Bixler, G. D. and Bhushan, B. (2015), "Rice- and Butterfly-Wing Effect Inspired Low Drag and Antifouling Surfaces: A Review," *Crit. Rev. in Solid State Mater. Sci.* 40, 1-37.
- Bohn, H. F. and Federle, W. (2004), "Insect Aquaplaning: Nepenthes Pitcher Plants Capture Prey with the Peristome, A Fully Wettable Water-lubricated Anisotropic Surface," *PNAS* 101, 14138-14143.
- Burton, Z. and Bhushan, B. (2006), "Surface Characterization and Adhesion and Friction Properties of Hydrophobic Leaf Surfaces," *Ultramicroscopy* 106, 709-719.
- Curtis, W. J. R. (2012), *Modern Architecture Since 1900, 3rd Ed.*, Phaidon Press, Ltd., London.
- Cutkosky, M. R. and Kim, S. (2009), "Design and Fabrication of Multi-Materials Structures for Bio-Inspired Robots," *Philos. Trans. R. Soc. A* 367, 1799-1813.
- Dean, B. and Bhushan, B. (2010), "Shark-Skin Surfaces for Fluid-Drag Reduction in Turbulent Flow: A Review," *Phil. Trans. R. Soc. A* 368, 4775-4806; 368, 5737.
- Fairs, M. (2006), "Joris Laarman Works with Opel," *Dezeen Magazine* (<http://www.dezeen.com/2006/12/27/joris-laarman-works-with-open/>).
- Fratzl, P. and Weinkamer, R. (2007), "Nature's Hierarchical Materials," *Prog. Mat. Sci.* 52, 1263-1334.

- Gao, X. F. and Jiang, L. (2004), "Biophysics: Water-repellent Legs of Water Striders," *Nature* 432, 36.
- Gao, H., Wang, X., Yao, H., Gorb, S. and Arzt, E. (2005), "Mechanics of Hierarchical Adhesion Structures of Geckos," *Mech. Mater.* 37, 275–285.
- Genzer, J. and Efimenko, K. (2006), "Recent Developments in Superhydrophobic Surfaces and Their Relevance to Marine Fouling: A Review," *Biofouling* 22, 339-360.
- Gorb, S. (2001), *Attachment Devices of Insect Cuticle*, Kluwer Academic, Dordrecht, Netherlands.
- Gordon, J. E. (1976), *The New Science of Strong Materials, or Why You Don't Fall Through the Floor*, second ed., Pelican–Penguin, London, UK.
- Gruber, P. (2011), *Biomimetics in Architecture*, Springer-Verlag, Germany.
- Grunwald, I., Rischka, K., Kast, S. M., Scheibel, T., and Bargel, H. (2009), "Mimicking Biopolymers on a Molecular Scale: Nano(bio)technology Based on Engineering Proteins," *Phil. Trans. R. Soc. A* 367, 1727-1726.
- Imhof, B. and Gruber, P. (2013), *What is the Architect Doing in the Jungle?*, Springer Wein, New York.
- Jakab, P. L. (1990), *Vision of a Flying Machine*, Smithsonian Institution Press, Washington D.C.
- Jin, H. -J. and Kaplan, D. L. (2003), "Mechanism of Silk Processing in Insects and Spiders," *Nature* 424, 1057–1061.
- Jones, C. J. and Aizawa, S. (1991), "The Bacterial Flagellum and Flagellar Motor: Structure, Assembly, and Functions," *Adv. Microb. Physiol.* 32, 109-172.
- Jung, Y. C. and Bhushan, B. (2010), "Biomimetic Structures for Fluid Drag Reduction in Laminar and Turbulent Flows," *J. Phys.: Condens. Matter* 22, 035104.
- Koch, K., Bhushan, B., and Barthlott, W. (2008), "Diversity of Structure, Morphology, and Wetting of Plant Surfaces (invited)," *Soft Matter* 4, 1943-1963.
- Koch, K., Bhushan, B., and Barthlott, W. (2009), "Multifunctional Surface Structures of Plants: An Inspiration for Biomimetics (invited)," *Prog. Mater. Sci.* 54, 137-178.
- Livio, M. (2002), *The Golden Ratio: The Story of Phi, the World's Most Astonishing Number*, Broadway Books, New York.
- Lowenstam, H. A. and Weiner, S. (1989), *On Biomineralization*, Oxford University Press, Oxford, UK.
- Mann, S. (2001), *Biomineralization*, Oxford Univ. Press, Oxford, U.K.
- Marentic, F. J. and Morris, T. L. (1992), "Drag Reducing Article," U.S. Patent No. 5,133,516.
- Meyers, M. A., Lin, A. Y. M., Seki, Y., Chen, P. Y., Kad, B. K., and Bodde, S. (2006), "Structural Biological Composites: An Overview," *JOM* 58, 35-41.
- Meyers, M. A., Chen, P. Y., Lin, A. Y. M., and Seki, Y. (2008), "Biological Materials: Structure and Mechanical Properties," *Prog. Mater. Sci.* 53, 1-206.
- Mora, C., Tittensor, D. P., Adl, S., Simpson, A. G. B., and Worm, B. (2011), "How Many Species Are There on Earth and in the Ocean?," *PLoS Biology* 9(8), e1001127.
- Mueller, T. (2008), "Biomimetics Design by Natures," *National Geographic* April 2008, 68–90.
- Neinhuis, C., and Barthlott, W. (1997), "Characterization and Distribution of Water-Repellent, Self-Cleaning Plant Surfaces," *Annals of Botany* 79, 667-677.
- Nosonovsky, M and Bhushan, B. (2008), *Multiscale Dissipative Mechanisms and Hierarchical Surfaces*, Springer, Heidelberg, Germany.
- Nosonovsky, M. and Bhushan, B. (2009), "Thermodynamics of Surface Degradation, Self-Organization, and Self-Healing for Biomimetic Surfaces," *Phil. Trans. R. Soc. A* 367, 1607-1627.
- Parker, A. R. (2009), "Natural Photonics for Industrial Applications," *Phil. Trans. R. Soc. A* 367, 1759-1782.
- Posamentier, A. S. and Lehmann, I. (2007), *The Fabulous Fibonacci Numbers*, Prometheus Books, New York.
- Sarikaya, M. and Aksay, I. A. (1995), *Biomimetic Design and Processing of Materials*, American Institute of Physics, Woodbury, NY.
- Stegmaier, T., Linke, M., and Planck, H. (2009), "Bionics in Textiles: Flexible and Translucent Thermal Insulations for Solar Thermal Applications," *Phil. Trans. R. Soc. A* 367, 1749-1758.

- Sun, J. and Bhushan, B. (2012), "Hierarchical Structure and Mechanical Properties of Nacre: A Review," *RSC Adv.* 2, 7617-7632.
- Sun, J., Bhushan, B., and Tong, J. (2013), "Structural Coloration in Nature," *RSC Adv.* 3, 14862-14899.
- Tamerler, C. and Sarikaya, M. (2009), "Molecular Biomimetics: Nanotechnology and Molecular Medicine Utilizing Genetically Engineered Peptides," *Phil. Trans. R. Soc. A* 367, 1705-1726.
- Vajda, S. (1989), *Fibonacci & Lucas Numbers, and the Golden Section: Theory and Applications*, Halsted Press, New York.
- von Richthofen, A. (2007), "3 m's of Metabolism," *Pidgin Magazine* 3.
- Wagner, P., Fürstner, R., Barthlott, W. and Neinhuis, C. (2003), "Quantitative Assessment to the Structural Basis of Water Repellency in Natural and Technical Surfaces," *J. Exper. Botany* 54, 1295-1303.
- Watkin, D. (2005) *A History of Western Architecture, 4th Ed.*, Watson-Guptill Publications, New York.
- Wittkower, R. (1960), "The Changing Concept of Proportion," *Daedalus* 89, 199-215.

Chapter 2

Roughness-Induced Superliquiphilic/phobic Surfaces: Lessons from Nature

God created solids, but the devil made their surfaces.
—Wolfgang Pauli, Nobel Laureate in Physics

2.1 Introduction

A solid surface, or more exactly a solid-gas or solid-liquid interface, has a complex structure and properties dependent upon nature of solids, the method of preparation, and the interaction between the surface and the environment. Physical and chemical properties of surfaces affect their interaction with other surfaces.

The wetting state of a surface (i.e., whether it is -philic or -phobic to a liquid) depends on a variety of surface characteristics, including surface roughness. Surface roughness affects the angle at which a liquid contacts a surface, called the contact angle. If there is a high contact angle, the liquid is less likely to wet the surface. If the contact angle is low, the liquid is more likely to wet the surface. Contact angle depends not only on roughness, but also surface energy and cleanliness of the surface (Adamson 1990; Israelachvili 1992; Nosonovsky and Bhushan 2008a). Contact angle is the parameter that is most important for characterizing the wetting state. Various flora and fauna found in living nature exhibit a variety of wetting states that can be of interest in commercial applications.

2.2 Wetting States

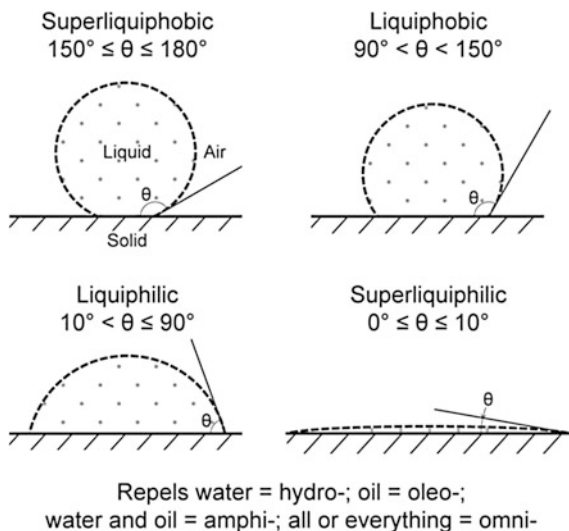
To define various wetting states of surfaces, we start with the definition of a few Greek words of interest for liquids: hydro- = water, oleo- = oil, amphi- = both (water and oil in this context), and omni- = all or everything. Within oils, edible oils have a

surface tension larger than 30 mN/m and alkanes-based oils have a surface tension 20–30 mN/m. Greek suffixes of interest are: -philic = friendly or attracting, and -phobic = afraid of or repelling.

If a liquid wets a surface, it is referred to as a wetting liquid and the value of the static contact angle is $0 \leq \theta \leq 90^\circ$. A surface that is wetted by a wetting liquid is referred to as hydrophilic if that wetting liquid is water, oleophilic if it is oil, amphiphilic if it can be wetted by water and oil, and omniphilic if all liquids wet the surface. If the liquid does not wet the surface, it is referred to as a non-wetting liquid, and the value of the contact angle is $90^\circ < \theta \leq 180^\circ$. A surface that repels a liquid is referred to as hydrophobic if it repels water, oleophobic for oil, amphiphobic if it repels both water and oil, and omniphobic if it repels all liquids. If the liquid is not specified, the surface is simply referred to as -philic or -phobic, dependent upon the contact angle. Surfaces with a contact angle of less than 10° are called super-philic, while surfaces with a contact angle between 150° and 180° are called super-phobic. Figure 2.1 shows schematics of various wetting regimes.

Surfaces with high energy with polar molecules, tend to be -philic to liquids with lower surface tension. Conversely, those with low energy with non-polar molecules tend to be -phobic to those with higher surface tension. It should be noted that by using low surface energy, generally fluorinated materials, the highest water contact angles that can be achieved are on the order of 120° . The contact angle is even lower for liquids with lower surface energy, such as oils. In order to achieve a contact angle higher than 120° , and certainly super-phobicity with a contact angle over 150° , a suitable roughness distribution needs to be introduced. This design approach is referred to as “roughness-induced” superliquiphobicity.

Fig. 2.1 Schematics of liquid droplets in contact with superliquiphobic, liquiphobic, liquiphilic, and superliquiphilic solid surfaces



2.3 Applications

For liquid repellent and self-cleaning surfaces, high contact angle is required. In fluid flow, in order to have low drag and for applications requiring the self-cleaning feature, in addition to the high contact angle, super-phobic surfaces should also have very low liquid contact angle hysteresis. The contact angle at the front of the droplet (advancing contact angle) is greater than that at the back of the droplet (receding contact angle), resulting in contact angle hysteresis (CAH), which is the difference between the advancing and receding contact angles, representing two stable values. It occurs due to surface roughness and surface heterogeneity. CAH reflects the irreversibility of the wetting/dewetting cycle. In a surface with high CAH, the receding contact angle is low and may pin the liquid and provide resistance to flow. CAH is a measure of energy dissipation during the flow of a droplet along a solid surface. At a low value of CAH, the droplets may roll, in addition to slide, and take contaminants from the surface with them, providing a self-cleaning ability known as the “lotus effect.” Surfaces with low CAH have a low liquid roll-off (tilt) angle, which denotes the angle to which a surface must be tilted for liquid drops to roll off (Extrand 2002; Kijlstra et al. 2002; Bhushan and Jung 2008; Nosonovsky and Bhushan 2007, 2008a, b, c; Bhushan et al. 2009a). The tangent of the tilt angle is equal to the coefficient of friction of a droplet sliding/rolling on a surface. Therefore, surfaces with CAH or a tilting angle of less than $<10^\circ$ are self-cleaning surfaces and with low adhesion/drag and antifouling.

Superliquiphobic surfaces can be used for drag reduction in fluid flow, energy conservation, and conversion (Nosonovsky and Bhushan 2008a, d, 2009a, b, 2010). Self-cleaning surfaces are of interest in various applications, including self-cleaning windows, windshields, exterior paints for buildings, utensils, roof tiles, textiles, solar panels, and exterior surfaces in transportation (Bhushan and Jung 2011). They also exhibit antifouling of interest in various applications including biomedical and membranes used in desalination and water purification (Bixler and Bhushan 2012a).

Recent advances in super-phobic surfaces make such applications possible. Selection of a proper super-phobic surface allows the reduction of energy dissipation, and, therefore, energy conservation. Reversible super-phobicity provides potential for new means of energy conversion, such as the microscale capillary engine.

Wetting may lead to the formation of concave shaped menisci at the interface between hydrophilic solid bodies during static or sliding contact, shown in Fig. 2.2. These menisci develop a negative pressure leading to an intrinsic attractive force, which increases adhesion and friction. In some cases, the wet friction force can be greater than the dry friction force, which is usually undesirable (Bhushan 1996, 1998, 2001, 2003, 2010, 2011a, 2012, 2013). In some cases, high wet adhesion/friction may lead to sticking of two surfaces, referred to as stiction. On the other

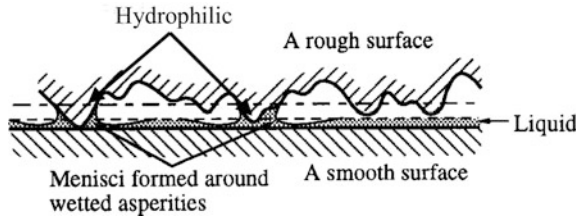


Fig. 2.2 A schematic diagram of condensed water vapor from the environment forming meniscus bridges at asperity contacts, which lead to an intrinsic attractive force

hand, high adhesion is desirable in some applications, such as adhesive tapes and adhesion of cells to biomaterial surfaces. Therefore, enhanced wetting would be desirable in these applications.

Numerous applications, such as magnetic storage devices and micro/nanoelectromechanical systems (MEMS/NEMS), require surfaces with low adhesion and stiction (Bhushan et al. 1995; Bhushan 1996, 1998, 2001, 2003, 2010, 2011a, 2012). As the size of these devices decreases, surface forces tend to dominate over the volume forces, and adhesion and stiction constitute a challenging problem for proper operation of these devices. This makes the development of superhydrophobic surfaces with non-adhesive characteristics crucial for many of these emerging applications.

A related wetting problem is icing. Icing may occur due to sticking of super-cooled water droplets onto a solid surface, also known as freezing rain or atmospheric icing. It is undesirable, as it leads to glazed roadways, broken tree limbs and power lines, and stalled aircraft airfoils. Icephobicity is defined as a surface's ability to prevent ice formation or to have very low adhesion to form ice. Anti-icing surfaces are typically superhydrophobic, as super-cooled droplets of water are able to roll off the surface before freezing, and any ice formed is weakly adhered compared to a hydrophilic surface, due to an air cushion (Cao et al. 2009; Wang et al. 2013; Brown and Bhushan 2015). Freezing time scale is about 15 ms so time of contact of droplet during bouncing should be about 15 ms or larger.

Another related wetting problem is fogging. Fogging occurs due to condensation of water in the form of small droplets on a surface. Antifogging is of interest in transparent glass or plastic surfaces used in optical applications. Hydrophilic surfaces are useful for anti-fogging applications, as they spread out any water into a thin film, thereby maintaining transparency. This is more favorable than hydrophobic surfaces for antifogging, as these require a surface to be tilted for the droplets to roll off, in order to maintain transparency. Various superhydrophilic surfaces have been fabricated using polymer-nanoparticle coatings (Grosu et al. 2004; Cebeci et al. 2006; Brown and Bhushan 2015).

2.4 Natural Superhydrophobic, Self-cleaning, Low Adhesion/Drag Reduction Surfaces with Antifouling

In the 1990s, biologists and materials scientists started to study natural superhydrophobic surfaces. It has been reported that all superhydrophobic and self-cleaning leaves consist of an intrinsic hierarchical structure (Koch et al. 2008, 2009a). Hierarchical structure provides air pocket formation, leading to a low contact area for an applied water droplet, shown in Fig. 2.3. Air pocket formation results in a reduction of the CAH, tilt angle, and adhesive force responsible for self-cleaning, low adhesion, and antifouling (Bhushan and Jung 2011; Nosonovsky and Bhushan 2008a; Bhushan et al. 2009b; Bixler and Bhushan 2012a).

The leaves of water-repellent plants, such as *Nelumbo nucifera*, (lotus), are the most studied plant leaves (Neinhuis and Barthlott 1997; Barthlott and Neinhuis 1997; Wagner et al. 2003; Burton and Bhushan 2006; Bhushan and Jung 2006, 2011; Bhushan 2009; Koch et al. 2008, 2009a). The lotus leaf was known as sacred for some 2000 years by Hindus and Buddhists due to its self-cleaning ability. It was scientifically examined in 1997. The leaf surface is rough due to so-called papillose epidermal cells, which form papillae or microasperities. In addition to the micro-scale roughness, the surface of the papillae is also rough, with nanoscale asperities composed of three-dimensional epicuticular waxes which are long chain hydrocarbons and are hydrophobic, Fig. 2.4 (adapted from Bhushan et al. 2009b). The wax on the lotus leaf self-assembles as tubules, but on other leaves, waxes exist also in the form of platelets or other morphologies (Koch et al. 2008, 2009a). The hierarchical structure of these leaves has been studied by Burton and Bhushan (2006) and Bhushan and Jung (2006). The water droplets on these surfaces readily sit on the apex of the nanostructures because air bubbles fill in the valleys of the structure under the droplet. Therefore, these leaves exhibit considerable superhydrophobicity and extremely low CAH. Static contact angle and CAH of a lotus leaf are about 164° and 3° , respectively (Fig. 2.4) (Bhushan et al. 2009b; Koch et al. 2009b). Simply, wax makes the surface hydrophobic, and hierarchical structure

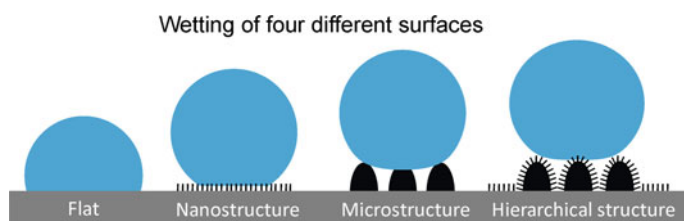


Fig. 2.3 Schematic and wetting of the four different surfaces. The largest contact area between the droplet and the surface is given in flat and microstructured surfaces, but is reduced in nanostructured surfaces and is minimized in hierarchical structured surfaces

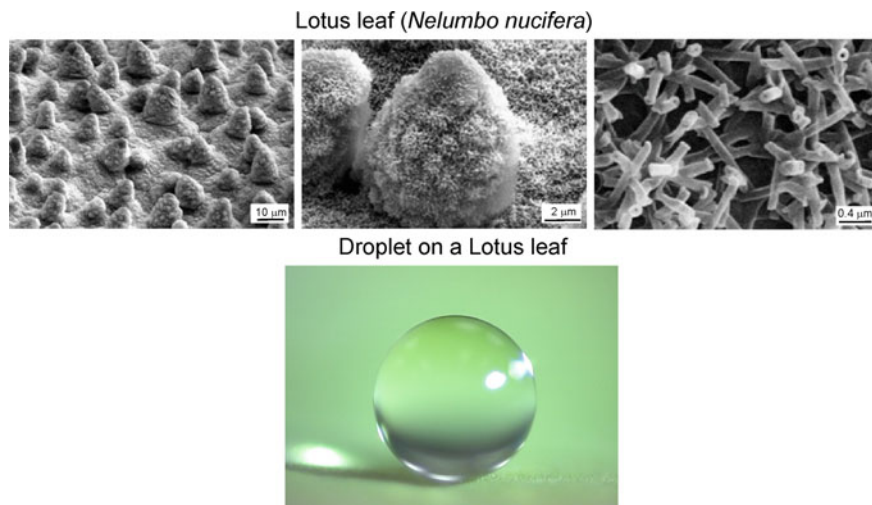


Fig. 2.4 SEM micrograph of a lotus (*Nelumbo nucifera*) leaf surface, consisting of microstructure formed by papillose epidermal cells covered with 3-D epicuticular wax tubules on surface, which create nanostructure, and an image of a water droplet sitting on a lotus leaf (adapted from Bhushan et al. 2009b)

makes it superhydrophobic with low CAH. Because of the latter, the water droplets on the leaves remove any contaminant particles from their surfaces when they roll off, leading to self-cleaning (Neinhuis and Barthlott 1997).

Other examples of superhydrophobicity in biological objects include rice leaves and butterfly wings (Bixler and Bhushan 2012b), water striders (*Gerris remigis*) (Gao and Jiang 2004), and mosquito (*Culex pipiens*) eyes (Gao et al. 2007). Their superhydrophobicity results from hierarchical structures. Duck feathers also provide superhydrophobicity (Bhushan 2009). Their corrugated surfaces provide air pockets that prevent water from completely touching the surface.

2.5 Natural Superhydrophobic and High Adhesion Surfaces

Unlike the lotus leaf, some rose petals (*rosea Rehd*), scallions, and garlic exhibit superhydrophobicity with high CAH (Feng et al. 2008; Chang et al. 2009; Bhushan and Her 2010; Ebert and Bhushan 2012). While a water droplet can easily roll off the surface of a lotus leaf, it stays pinned to the surface of these leaves. The different behavior of wetting between the lotus leaf and the rose petal can be explained by different designs in the surface hierarchical micro- and nanostructure. Since the rose petal's microstructures have a larger pitch value than those of the lotus leaf, the

liquid is allowed to impregnate between the microstructure, and partially penetrates into the nanostructure. This is referred to as the Cassie impregnating wetting regime, in which the wetted surface area is less than that in the Wenzel regime but greater than that in the Cassie–Baxter regime, to be described later. Such an explanation implies that the extent of CAH increases with increasing wetted surface area, which is governed by surface micro- and nanostructure. These surfaces exhibit high adhesion.

2.6 Natural Superoleophobic Self-cleaning and Low Drag Surfaces with Antifouling

A model surface for superoleophobicity in water and self-cleaning is provided by sea animals such as fish (including carp and trout) and sharks, which are known to be protected from contamination by oil pollution although they are wetted by water (Jung and Bhushan 2009; Liu et al. 2009; Bixler and Bhushan 2012b). Fish are covered with oriented scales with concentric rings overlapping and hinged that promote anisotropic flow from head to tail (Bixler and Bhushan 2012b). Shark skin, which is a model from nature for a low drag surface, is covered by very small individual tooth-like scales called dermal denticles (little skin teeth), shaped like small riblets with longitudinal grooves (aligned parallel to the local flow direction of the water). When a shark swims fast during turbulent flow, vortices form on the surface that cause high stresses across the entire surface, leading to high drag. The riblets on the skin lift the vortices to the tips of the grooves and constrain them, resulting in water moving efficiently over their surface (Bechert et al. 2000; Bhushan 2009, 2011b; Jung and Bhushan 2009, 2010; Dean and Bhushan 2010; Bixler and Bhushan 2013a). The space between these dermal denticles is such that microscopic aquatic organisms have difficulty adhering to and colonizing the surface (Genzer and Efimenko 2006; Jung and Bhushan 2009, 2010; Dean and Bhushan 2010; Bixler and Bhushan 2012a, 2013a). If oil is present on the surfaces of sea animals, the scales repel the oil and it is superoleophobic (Bixler and Bhushan 2013b). Hydrophilic surfaces exhibit superoleophobicity underwater as it is difficult for water to dewet the surface.

The lower side of the lotus leaf also provides a model surface for superoleophobicity in water. The lower side does not contain three-dimensional wax crystals (Neinhuis and Barthlott 1997) and consists of rather flat, tubular, and slightly convex papillae (Koch et al. 2009a). Therefore, the bottom surface is superhydrophilic but superoleophobic in water (Chang et al. 2011).

Model surfaces in living nature with superoleophobicity in air are rare. Examples include certain species of insects such as some leafhoppers (Rakitov and Gorb 2013) and springtails (Hensel et al. 2013). Superoleophobic surfaces are of interest for drag reduction in oil pipelines and antifouling.

2.7 Closure

The term omniphobic/philic is used with regard to wetting by all liquids of scientific interest. The term amphiphobic/philic is used with regard to wetting by water and oil. If liquid is not specified, the surface is simply referred to as -philic or-phobic, dependent upon the contact angle. A surface is super-phobic if it has a liquid contact angle above 150° . These surfaces are liquid repellent. These surfaces with low contact angle hysteresis (less than 10°) also have a self-cleaning effect, called the "lotus effect." Liquid droplets roll off the surface and take contaminants with them.

The wetting state of a surface depends on a variety of factors, including surface roughness, surface energy, and cleanliness of the surface. Various flora and fauna found in living nature exhibit a variety of wetting states. A model surface for superhydrophobicity is the lotus leaf. Water repellent and self-cleaning surfaces with low adhesion/drag are of interest in various applications. Low adhesion and drag reduction in fluid flow is also of interest in many applications. Also, superhydrophobic surfaces can be used for energy conservation and energy conversion. Surfaces with low adhesion/drag also exhibit antifouling properties. Superhydrophobic surfaces are also desirable in the ambient environment to minimize stiction.

Unlike lotus leaves, some rose petals, scallions, and garlic exhibit superhydrophobicity with high contact angle hysteresis. These surfaces exhibit high adhesion.

Oleophobic/philic is the term used with regard to wetting by oil and other organic liquids. A model surface for superoleophobicity in water and self-cleaning is provided by many sea animals including fish and sharks, which are known to be well protected from contaminants from oil pollution although they are wetted by water. Microstructured surfaces of sea animals also exhibit antifouling. Another model surface for superoleophobicity in water is the lower side of the lotus leaf. Model surfaces for superoleophobicity in air is rare and include certain species of insects such as some leafhoppers and springtails.

References

- Adamson A. V. (1990), *Physical Chemistry of Surfaces*, Wiley, New York.
- Barthlott, W. and Neinhuis, C. (1997), "Purity of the Sacred Lotus, or Escape from Contamination in Biological Surfaces," *Planta* **202**, 1-8.
- Bechert, D. W., Bruse, M., and Hage, W. (2000), "Experiments with Three-Dimensional Riblets as an Idealized Model of Shark Skin," *Exp. Fluids* **28**, 403-412.
- Bhushan, B. (1996), *Tribology and Mechanics of Magnetic Storage Systems*, second ed., Springer-Verlag, New York.
- Bhushan, B. (1998), *Tribology Issues and Opportunities in MEMS*, Kluwer Academic Publishers, Dordrecht, Netherlands.

- Bhushan, B. (2001), *Modern Tribology Handbook, Vol. 1 – Principles of Tribology; Vol. 2 – Materials, Coatings, and Industrial Applications*, CRC Press Inc., Boca Raton, Florida.
- Bhushan, B. (2003), “Adhesion and Stiction: Mechanisms, Measurement Techniques and Methods for Reduction,” *J. Vac. Sci. Technol. B* **21**, 2262-2296.
- Bhushan, B. (2007), “Adhesion of Multi-Level Hierarchical Attachment Systems in Gecko Feet,” *J. Adhes. Sci. Technol.* **21**, 1213–1258.
- Bhushan, B. (2009), “Biomimetics: Lessons from Nature – An Overview,” *Phil. Trans. R. Soc. A* **367**, 1445-1486.
- Bhushan, B. (2010), *Springer Handbook of Nanotechnology*, third ed., Springer, Heidelberg, Germany.
- Bhushan B. (2011a) *Nanotribology and Nanomechanics I – Measurement Techniques, II – Nanotribology, Biomimetics, and Industrial Applications*, third ed., Springer-Verlag, Heidelberg, Germany.
- Bhushan, B. (2011b), “Biomimetics Inspired Surfaces for Drag Reduction and Oleophobicity/philicity,” *Beilstein J. Nanotechnol.* **2**, 66-84.
- Bhushan, B. (2012), *Encyclopedia of Nanotechnology, Vols. 1-4*, Springer, Heidelberg, Germany.
- Bhushan, B. (2013), *Introduction to Tribology, 2nd Ed.*, Wiley, New York.
- Bhushan, B. and Her, E. K. (2010), “Fabrication of Superhydrophobic Surfaces with High and Low Adhesion Inspired from Rose Petal,” *Langmuir* **26**, 8207-8217.
- Bhushan, B. and Jung, Y. C. (2006), “Micro and Nanoscale Characterization of Hydrophobic and Hydrophilic Leaf Surface,” *Nanotechnology* **17**, 2758-2772.
- Bhushan, B. and Jung, Y. C. (2008), “Wetting, Adhesion and Friction of Superhydrophobic and Hydrophilic Leaves and Fabricated Micro/nanopatterned Surfaces,” *J. Phys.: Condens. Matter* **20**, 225010.
- Bhushan, B. and Jung, Y. C. (2011), “Natural and Biomimetic Artificial Surfaces for Superhydrophobicity, Self-Cleaning, Low Adhesion, and Drag Reduction,” *Prog. Mater. Sci.* **56**, 1-108.
- Bhushan, B., Israelachvili, J. N., and Landman, U. (1995), “Nanotribology: Friction, Wear and Lubrication at the Atomic Scale,” *Nature* **374**, 607-616.
- Bhushan, B., Jung, Y. C., and Koch, K. (2009a), “Self-Cleaning Efficiency of Artificial Superhydrophobic Surfaces,” *Langmuir* **25**, 3240-3248.
- Bhushan, B., Jung, Y. C., and Koch, K. (2009b), “Micro-, Nano- and Hierarchical Structures for Superhydrophobicity, Self-Cleaning and Low Adhesion,” *Phil. Trans. R. Soc. A* **367**, 1631-1672.
- Bixler, G. D. and Bhushan, B. (2012a), “Biofouling: Lessons from Nature,” *Phil. Trans. R. Soc. A* **370**, 2381-2417.
- Bixler, G. D. and Bhushan, B. (2012b), “Bioinspired Rice Leaf and Butterfly Wing Surface Structures Combining Shark Skin and Lotus Effects,” *Soft Matter* **9**, 1620-1635.
- Bixler, G. D. and Bhushan, B. (2013a), “Fluid Drag Reduction with Shark-skin Riblet Inspired Microstructured Surfaces,” *Adv. Func. Mater.* **23**, 4507-4528.
- Bixler, G. D. and Bhushan, B. (2013b), “Fluid Drag Reduction and Efficient Self-Cleaning with Rice Leaf and Butterfly Wing Bioinspired Surfaces,” *Nanoscale* **5**, 7685-7710.
- Brown, P. S., and Bhushan, B. (2015), “Bioinspired, Roughness-induced, Water and Oil Super-philic and Super-phobic Coatings Prepared by Adaptable Layer by Layer Technique,” *Sci. Rep.* **5**, 14030.
- Burton, Z. and Bhushan, B. (2006), “Surface Characterization and Adhesion and Friction Properties of Hydrophobic Leaf Surfaces,” *Ultramicroscopy* **106**, 709-719.
- Cao, L., Jones, A. K., Sikka, V. K., Wu, J., and Gao, D. (2009), “Anti-Icing Superhydrophobic Surfaces,” *Langmuir* **25**, 12444-12448.
- Cebeci, F. C., Zhizhang, W., Zhai, L., Cohen, R. E., and Rubner, M. F. (2006), “Nanoporosity-driven Superhydrophilicity: A Means to Create Multifunctional Antifogging Coatings,” *Langmuir* **22**, 2856-2862.
- Chang, F. M., Hong, S. J., Sheng, Y. J. and Tsao, H. K. (2009), “High Contact Angle Hysteresis of Superhydrophobic Surfaces: Hydrophobic Defects,” *Appl. Phys. Lett.* **95**, 064102.

- Cheng, Q., Li, M., Zheng, Y., Su, B., Wang, S., and Jiang, L. (2011), "Janus Interface Materials: Superhydrophobic Air/Solid Interface and Superoleophobic Water/Solid Interface Inspired by a Lotus Leaf," *Soft Matter* **7**, 5948-5951.
- Dean, B. and Bhushan, B. (2010), "Shark-Skin Surfaces for Fluid-Drag Reduction in Turbulent Flow: A Review," *Phil. Trans. R. Soc. A* **368**, 4775-4806; **368**, 5737.
- Ebert, D. and Bhushan, B. (2012), "Wear-Resistant Rose Petal-Effect Surfaces with Superhydrophobicity and High Droplet Adhesion Using Hydrophobic and Hydrophilic Nanoparticles," *J. Colloid Interf. Sci.* **384**, 183-188.
- Extrand, C. W. (2002), "Model for Contact Angle and Hysteresis on Rough and Ultraphobic Surfaces," *Langmuir* **18**, 7991-7999.
- Feng, L., Zhang, Y., Xi, J., Zhu, Y., Wang, N., Xia, F., and Jiang, L. (2008), "Petal Effect: A Superhydrophobic State with High Adhesive Force," *Langmuir* **24**, 4114-4114.
- Gao, X. F. and Jiang, L. (2004), "Biophysics: Water-repellent Legs of Water Striders," *Nature* **432**, 36.
- Gao, X., Yan, X., Yao, X., Xu, L., Zhang, K., Zhang, J., Yang, B., and Jiang, L. (2007), "The Dry-Style Antifogging Properties of Mosquito Compound Eyes and Artificial Analogues Prepared by Soft Lithography," *Adv. Mater.* **19**, 2213-2217.
- Genzer, J. and Efimenko, K. (2006), "Recent Developments in Superhydrophobic Surfaces and Their Relevance to Marine Fouling: A Review," *Biofouling* **22**, 339-360.
- Grosu, G., Andrzejewski, L., Veilleux, G., and Ross, G. G. (2004), "Relation Between the Size of Fog Droplets and their Contact Angles with CR39 Surfaces," *J. Phys. D* **37**, 3350-3355.
- Hensel, R., Helbig, R., Aland, S., Braun, H. G., Voigt, A., Neinhuis, C., and Werner, C. (2013) "Wetting Resistance at Its Topographical Limit: The Benefit of Mushroom and Serif T Structures," *Langmuir* **29**, 1100-1112.
- Israelachvili, J. N. (1992), *Intermolecular and Surface Forces*, second edition, Academic Press, London.
- Jung, Y. C. and Bhushan, B. (2009), "Wetting Behavior of Water and Oil Droplets in Three Phase Interfaces for Hydrophobicity/phillicity and Oleophobicity/phillicity," *Langmuir* **25**, 14165-14173.
- Jung, Y. C. and Bhushan, B. (2010), "Biomimetic Structures for Fluid Drag Reduction in Laminar and Turbulent Flows," *J. Phys.: Condens. Matter* **22**, 035104.
- Kijlstra, J., Reihs, K., and Klami, A. (2002), "Roughness and Topology of Ultra-Hydrophobic surfaces," *Colloid Surf. A-Physicochem. Eng. Asp.* **206**, 521-529.
- Koch, K., Bhushan, B., and Barthlott, W. (2008), "Diversity of Structure, Morphology, and Wetting of Plant Surfaces (invited)," *Soft Matter* **4**, 1943-1963.
- Koch, K., Bhushan, B., and Barthlott, W. (2009a), "Multifunctional Surface Structures of Plants: An Inspiration for Biomimetics (invited)," *Prog. Mater. Sci.* **54**, 137-178.
- Koch, K., Bhushan, B., Jung, Y. C., and Barthlott, W. (2009b), "Fabrication of Artificial Lotus Leaves and Significance of Hierarchical Structure for Superhydrophobicity and Low Adhesion," *Soft Matter* **5**, 1386-1393.
- Liu, M., Wang, S., Wei, Z., Song, Y., and Jiang, L. (2009), "Bioinspired Design of a Superoleophobic and Low Adhesive Water/Solid Interface," *Adv. Mater.* **21**, 665-669.
- Neinhuis, C., and Barthlott, W. (1997), "Characterization and Distribution of Water-Repellent, Self-Cleaning Plant Surfaces," *Annals of Botany* **79**, 667-677.
- Nosonovsky, M. and Bhushan, B. (2007), "Multiscale Friction Mechanisms and Hierarchical Surfaces in Nano- and Bio-Tribology," *Mater. Sci. Eng.:R* **58**, 162-193.
- Nosonovsky, M. and Bhushan, B. (2008a), *Multiscale Dissipative Mechanisms and Hierarchical Surfaces: Friction, Superhydrophobicity, and Biomimetics*, Springer-Verlag, Heidelberg, Germany.
- Nosonovsky, M. and Bhushan, B. (2008b), "Roughness-Induced Superhydrophobicity: A Way to Design Non-Adhesive Surfaces," *J. Phys.: Condens. Matter* **20**, 225009.
- Nosonovsky, M. and Bhushan, B. (2008c), "Biologically-Inspired Surfaces: Broadening the Scope of Roughness," *Adv. Func. Mater.* **18**, 843-855.

- Nosonovsky, M. and Bhushan, B. (2008d), "Superhydrophobicity for Energy Conversion and Conservation Applications," *J. Adhesion Sci. Tech.* **22**, 2105-2115.
- Nosonovsky, M. and Bhushan, B. (2009a), "Multiscale Effects and Capillary Interactions in Functional Biomimetic Surfaces for Energy Conversion and Green Engineering," *Phil. Trans. R. Soc. A* **367**, 1511-1539.
- Nosonovsky, M. and Bhushan, B. (2009b), "Superhydrophobic Surfaces and Emerging Applications: Non-Adhesion, Energy, Green Engineering," *Curr. Opin. Colloid Interface Sci.* **14**, 270-280.
- Nosonovsky, M. and Bhushan, B. (2010), "Green Tribology: Principles, Research Areas and Challenges," *Phil. Trans. R. Soc. A* **368**, 4677-4694.
- Rakitov, R. and Gorb, S. N. (2013), "Brochosomal Coats Turn Leafhopper (*Insecta, Hemiptera, Cicadellidae*) Integument to Superhydrophobic State," *Proc. R. Soc. B.* **280**, 20122391.
- Wagner, P., Füstner, R., Barthlott, W. and Neinhuis, C. (2003), "Quantitative Assessment to the Structural Basis of Water Repellency in Natural and Technical Surfaces," *J. Exper. Botany* **54**, 1295-1303.
- Wang, Y. Xue, J., Wang, Q., Chen, Q., and Ding, J. (2013), "Verification of Icephobic/Anti-icing Properties of a Superhydrophobic Surface," *ACS Appl. Mater. Interf.* **5**, 3370-3381.

Chapter 3

Modeling of Contact Angle for a Liquid in Contact with a Rough Surface for Various Wetting Regimes

3.1 Introduction

The roughness distribution affects contact angle and surface wetting. Three surface wetting regimes are discussed, which include Wenzel, Cassie-Baxter, and Cassie regimes. In the Wenzel regime, a liquid droplet completely wets the rough surface with a homogeneous interface. In the Cassie-Baxter regime, a heterogeneous or composite interface with air pockets trapped between the asperities is formed. In a Cassie regime, a liquid film impregnates some of the cavities in an area surrounding the droplet as well.

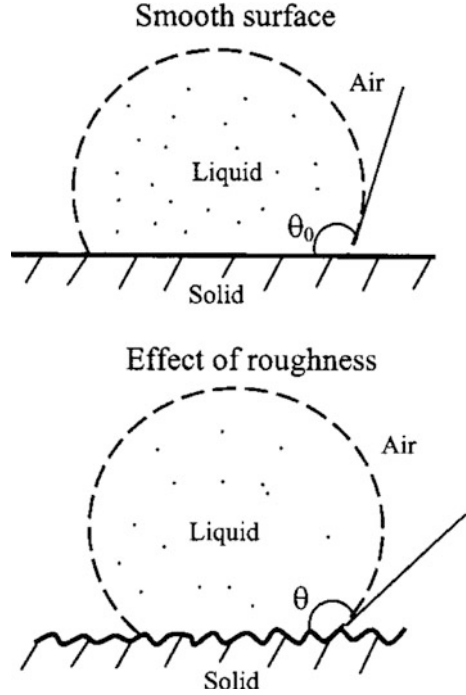
3.2 Contact Angle Definition

The surface atoms or molecules of liquids or solids have fewer bonds with neighboring atoms. Therefore, they have higher energy than similar atoms and molecules in the interior. This additional energy is characterized quantitatively by the surface tension or free surface energy γ , which is equal to the work that is required to create a unit area of the surface at a constant pressure and temperature. The unit of γ is J/m^2 or N/m , and it can be interpreted either as energy per unit surface area or as tension force per unit length of a line at the surface. When a solid is in contact with liquid, the molecular attraction will reduce the energy of the system below that for the two separate surfaces. This is expressed by the Dupré equation,

$$W_{SL} = \gamma_{SA} + \gamma_{LA} - \gamma_{SL} \quad (3.1)$$

where W_{SL} is the work of adhesion per unit area, γ_{SA} , γ_{SL} , and γ_{LA} are the solid-air, solid-liquid, and liquid-air surface tensions, respectively.

Fig. 3.1 Schematic of a liquid droplet in contact with a smooth solid surface (contact angle θ_0) and with a rough solid surface (contact angle θ)



If a liquid droplet is placed on a smooth solid surface, the liquid and solid surfaces come together under equilibrium at a characteristic angle called the static contact angle θ_0 (Fig. 3.1). This contact angle can be determined by minimizing the net surface free energy of the system (Adamson 1990; Israelachvili 1992; Nosonovsky and Bhushan 2008a; Bhushan 2013a, b). The total energy E_{tot} is given by,

$$E_{tot} = \gamma_{LA}(A_{LA} + A_{SL}) - W_{SL}A_{SL} \quad (3.2)$$

where A_{SL} and A_{LA} are the contact areas of the liquid with the solid and air, respectively. It is assumed that the droplet of density ρ is smaller than the capillary length, $(\gamma_{LA}/\rho g)^{1/2}$, so that the gravitational potential energy can be neglected. It is also assumed that the volume and pressure are constant, so that the volumetric energy does not change. At the equilibrium $dE_{tot} = 0$, which yields,

$$\gamma_{LA}(dA_{LA} + dA_{SL}) - W_{SL}dA_{SL} = 0 \quad (3.3)$$

For a droplet of constant volume, it is easy to show using geometrical considerations that,

$$dA_{LA}/dA_{SL} = \cos \theta_0 \quad (3.4)$$

Combining (3.1), (3.3) and (3.4), the well-known Young's equation for the contact angle is obtained,

$$\cos \theta_0 = \frac{\gamma_{SA} - \gamma_{SL}}{\gamma_{LA}} \quad (3.5)$$

Equation (3.5) provides an expression for the static contact angle for given surface tensions.

Note that, although the term "air" is used, the analysis does not change in the case of another gas, such as water vapor.

3.3 Homogeneous and Heterogeneous Interfaces and the Wenzel, Cassie-Baxter and Cassie Equations

In this section, the equations that govern the contact angle of liquid with a rough surface for homogeneous and heterogeneous interfaces are introduced and discussed. First, we consider a liquid droplet on a rough surface with a homogeneous interface. The interface area increases with respect to that for a smooth surface. Using the surface force balance and empirical considerations, the contact angle of a liquid droplet upon a rough solid surface, θ , is related to that upon a smooth surface, θ_0 for a homogeneous interface (Fig. 3.1), through the non-dimensional surface roughness factor, $R_f > 1$, which is equal to the ratio of the rough surface area, A_{SL} , to its flat projected area, A_F (Wenzel 1936),

$$\cos \theta = \frac{dA_{LA}}{dA_F} = \frac{A_{SL}}{A_F} \frac{dA_{LA}}{dA_{SL}} = R_f \cos \theta_0 \quad (3.6)$$

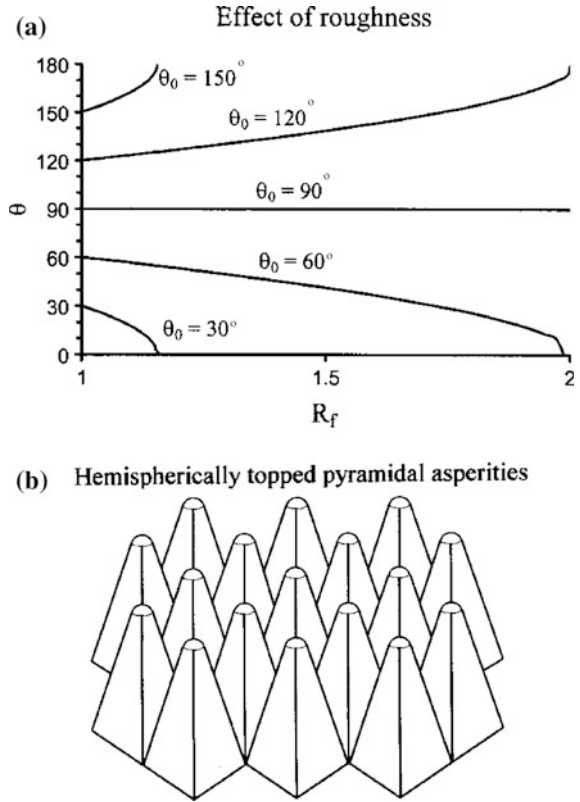
where,

$$R_f = \frac{A_{SL}}{A_F} \quad (3.7)$$

This is called the Wenzel equation.

The dependence of the contact angle on the roughness factor is presented in Fig. 3.2a for different values of θ_0 (Nosonovsky and Bhushan 2005). The Wenzel model predicts that a liquiphobic surface ($\theta_0 > 90^\circ$) becomes more liquiphobic with an increase in R_f , while a liquiphilic surface ($\theta_0 < 90^\circ$) becomes more liquiphilic with an increase in R_f (Nosonovsky and Bhushan 2005; Jung and Bhushan 2006). As an example, Fig. 3.2b shows a geometry with square-based hemispherically-topped pyramidal asperities with a rounded top, which has complete packing. The size and shape of the asperities can be optimized for a desired roughness factor.

Fig. 3.2 a Contact angle for a rough surface (θ) as a function of the roughness factor (R_f) for various contact angles of the smooth surface (θ_0), and **b** schematic of square-based hemispherically-topped pyramidal asperities with complete packing (Nosonovsky and Bhushan 2005)



Next, we consider a liquid droplet on a rough surface with a heterogeneous interface. For a heterogeneous interface composed of two fractions, one with the fractional area f_1 and the contact angle θ_1 and the other with f_2 and θ_2 , respectively (so that $f_1 + f_2 = 1$), the contact angle is given by the Cassie equation (Cassie 1948),

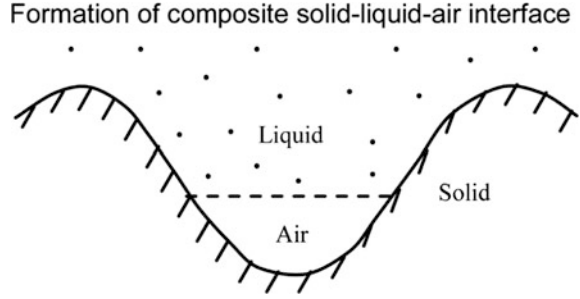
$$\cos \theta = f_1 \cos \theta_1 + f_2 \cos \theta_2 \quad (3.8)$$

A composite interface (Fig. 3.3), consists of a fractional geometrical area of the solid-liquid interface under the droplet ($f_1 = f_{SL}$, $\theta_1 = \theta$) and of the liquid-air interface ($f_2 = f_{LA} = 1 - f_{SL}$, $\cos \theta_2 = -1$). For this case, combining (3.7) and (3.8) yields the so-called Cassie-Baxter equation (Cassie and Baxter 1944),

$$\begin{aligned} \cos \theta &= R_f f_{SL} \cos \theta_0 - 1 + f_{SL} \\ \text{or, } \cos \theta &= R_f \cos \theta_0 - f_{LA} (R_f \cos \theta_0 + 1) \end{aligned} \quad (3.9)$$

Another interface in which liquid film impregnates some of the cavities in an area surrounding the liquid droplet, while the top of the rough surface remains dry (Cassie 1948). It consists of two fractions – solid-liquid homogeneous interface

Fig. 3.3 Schematic of the formation of a composite solid-liquid-air interface for a rough surface



(Wenzel interface) and some of the neighboring cavities filled with liquid with dry tops. The energy of such a rough surface with filled cavities is different from the energy of the surface with empty cavities. Filled cavities correspond to the liquid-liquid interface with $\cos \theta_2 = 1$ ($\theta_2 = 0^\circ$). Using (3.8) and (3.6) for this case, one gets,

$$\cos \theta = 1 + f_{SL}(R_f \cos \theta_0 - 1) \quad (3.10)$$

A liquid film filling the cavities surrounding the droplet is possible when $\theta_0 < \theta_c$, where θ_c is the critical contact angle given by (de Gennes et al. 2003),

$$\cos \theta_c = \frac{1 - f_{SL}}{R_f - f_{SL}} \quad (3.11)$$

This wetting interface is referred to as the Cassie-impregnated interface or simply the Cassie interface.

Pure Cassie-Baxter and Wenzel wetting situations rarely occur. An intermediate state between the Wenzel and Cassie-Baxter interfaces is more common. In this interface, underneath the droplet, liquid penetrates and the cavities are partially impregnated or filled, and is referred to as the mixed/impregnated state (Marmur 2003; Bhushan and Nosonovsky 2010). This state is metastable.

For easy comparison, Fig. 3.4 schematically shows liquid sitting on rough surfaces showing the Wenzel, Cassie-Baxter, Cassie-impregnated, and mixed/impregnated interfaces. An extension of these three regimes to nine different regimes for surfaces with hierarchical roughness has been presented by Bhushan and Nosonovsky (2010).

Equation (3.9) for the composite interface was derived using (3.6) and (3.8), and it could also be obtained independently. For this purpose, two sets of interfaces are considered: a liquid-air interface, and a composite interface under the droplet, which itself involves solid-liquid, liquid-air, and solid-air interfaces. For fractional flat geometrical areas of the solid-liquid and liquid-air interfaces under the droplet, f_{SL} and f_{LA} ($f_{SL} = 1 - f_{LA}$), the flat area of the composite interface is (Nosonovsky and Bhushan 2008a)

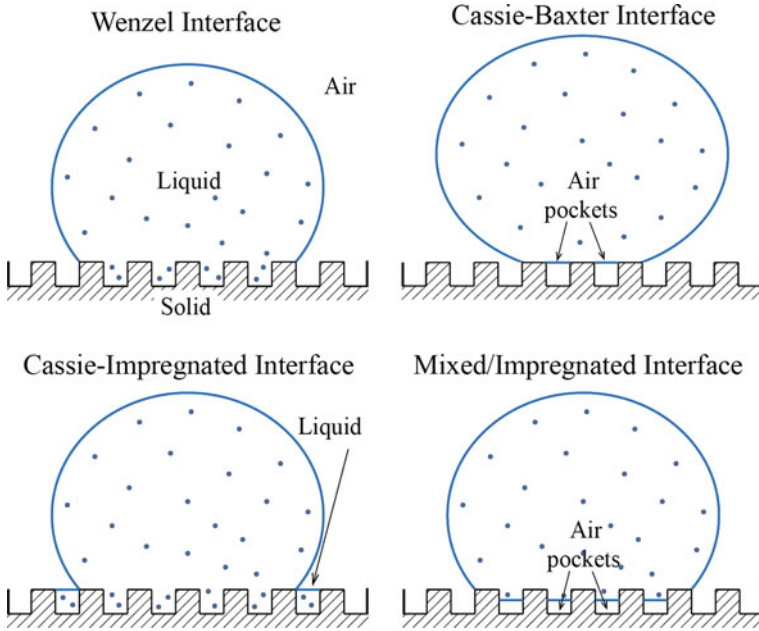


Fig. 3.4 Schematics of four configurations showing the Wenzel interface [homogeneous interface, (3.6)], Cassie-Baxter interface [composite interface with air pockets, (3.9)], Cassie-impregnated interface [homogeneous interface and some of the neighboring cavities filled with liquid, also referred to as simply the Cassie interface, (3.10)], and mixed/impregnated interface (in which the cavities under the droplet are partially filled)

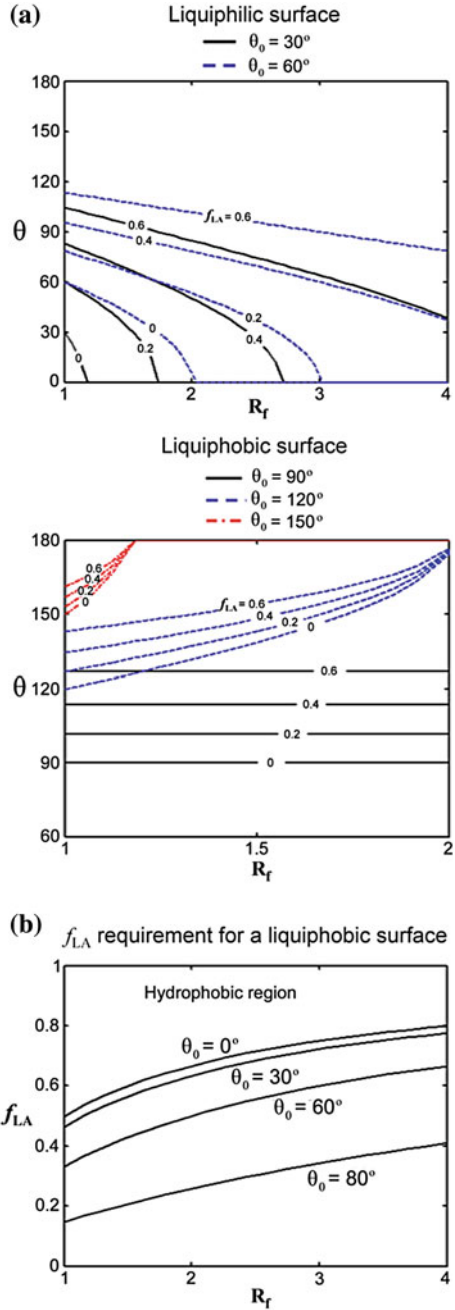
$$A_F = f_{SL}A_F + f_{LA}A_f = R_f A_{SL} + f_{LA}A_F \quad (3.12)$$

In order to calculate the contact angle in a manner similar to the derivation of (3.6), the differential area of the liquid-air interface under the droplet, $f_{LA}dA_F$, should be subtracted from the differential of the total liquid-air area dA_{LA} , which yields the Cassie-Baxter equation (3.9),

$$\begin{aligned} \cos \theta &= \frac{dA_{LA} - f_{LA}dA_F}{dA_F} = \frac{A_{SL}}{A_F} \frac{dA_{LA}}{dA_{SL}} - f_{LA} = R_f f_{SL} \cos \theta_0 - f_{LA} \\ &= R_f \cos \theta_0 - f_{LA} (R_f \cos \theta_0 + 1) \end{aligned}$$

The dependence of the contact angle on the roughness factor and fractional liquid-air area for hydrophilic and hydrophobic surfaces with a composite interface is presented in Fig. 3.5a (Jung and Bhushan 2006). According to (3.9), even for a liquiphilic surface, the contact angle increases with an increase of f_{LA} . At a high value of f_{LA} , a surface can become liquiphobic; however, the value required may be unachievable, or the formation of air pockets may become unstable. Using the Cassie-Baxter equation, the value of f_{LA} at which a liquiphilic surface could turn into a liquiphobic one is given as (Jung and Bhushan 2006)

Fig. 3.5 a Contact angle for a rough surface (θ) as a function of the roughness factor (R_f) for various f_{LA} values on a liquiphilic surface and a liquiphobic surface, and **b** f_{LA} requirement for a liquiphilic surface to be liquiphobic as a function of the roughness factor (R_f) and θ_0 (Jung and Bhushan 2006)



$$f_{LA} \geq \frac{R_f \cos \theta_0}{R_f \cos \theta_0 + 1} \quad \text{for } \theta_0 < 90^\circ \quad (3.13)$$

Figure 3.5b shows the value of f_{LA} required as a function of R_f for four surfaces with different contact angles, θ_0 . Hydrophobic surfaces can be achieved above a certain f_{LA} value, as predicted by (3.13). The upper part of each contact angle line is the hydrophobic region. For the hydrophobic surface, contact angle increases with an increase in f_{LA} , both for smooth and rough surfaces.

For high f_{LA} , a nanopattern is desirable because whether a liquid-air interface is generated depends upon the ratio of distance between two adjacent asperities and droplet radius. Furthermore, asperities can pin liquid droplets and thus prevent liquid from filling the valleys between asperities. High R_f can be achieved by both micropatterns and nanopatterns.

Based on Nosonovsky and Bhushan (2008a, 2009), spreading of a liquid over a rough solid surface continues until (3.5) (Young's equation) is satisfied locally at the triple line (the line of contact of the solid, liquid, and air interfaces) and, simultaneously, the surface area is minimized over the entire liquid-air interface. The minimal surface area condition states that the sum of the inverse of the principal radii of curvature R_1 and R_2 of the liquid surface along the two mutually orthogonal planes (mean curvature) is constant at any point, which governs the shape of the liquid-air interface. The same condition is also the consequence of the Laplace equation, which relates pressure change through an interface, ΔP , with its mean curvature (Nosonovsky and Bhushan 2008a),

$$\frac{1}{R_1} + \frac{1}{R_2} = \frac{\Delta P}{\gamma_{LA}} \quad (3.14)$$

Note that at the thermodynamic equilibrium (when condensation and evaporation occurs at the same speed), ΔP is dependent on the partial vapor pressure. For contact with saturated vapor the mean curvature of the liquid-air interface is zero at equilibrium. A convex interface ($1/R_1 + 1/R_2 > 0$) results in evaporation prevailing over condensation. This is why small droplets tend to evaporate. However, a concave interface ($1/R_1 + 1/R_2 < 0$) results in condensation of saturated vapor prevailing over evaporation. Since the condensation prevails, a concave interface may be in thermodynamic equilibrium with undersaturated vapor. This is why concave menisci tend to condense even when the relative humidity is less than 100 % (Nosonovsky and Bhushan 2008a, 2009).

3.3.1 Limitations of the Wenzel and Cassie-Baxter Equations

Based on Nosonovsky and Bhushan (2008a, d), the Cassie-Baxter equation (3.8) is based on the assumption that the heterogeneous surface is composed of

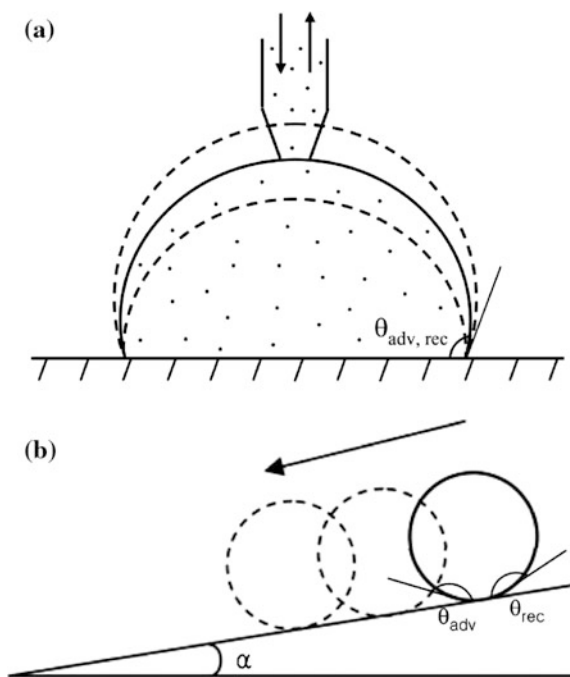
well-separated distinct patches of different material, so that the free surface energy can be averaged. It has been argued also that when the size of the chemical heterogeneities is very small (of atomic or molecular dimensions), the quantity that should be averaged is not the energy, but the dipole moment of a macromolecule (Israelachvili and Gee 1989). Furthermore, (3.8) should be replaced by (Nosonovsky and Bhushan 2008d),

$$(1 + \cos \theta)^2 = f_1(1 + \cos \theta_1)^2 + f_2(1 + \cos \theta_2)^2 \quad (3.15)$$

Experimental studies of polymers with different functional groups showed a good agreement with (3.15) (Tretinnikov 2000).

Based on Nosonovsky and Bhushan (2008a, d), later investigations put the Wenzel and Cassie-Baxter equations into a thermodynamic framework. However, they also showed that there is no one single value of the contact angle for a rough or heterogeneous surface (Johnson and Dettre 1964; Marmur 2003; Li and Amirfazli 2006). The contact angle can be in a range of values between the receding contact angle, θ_{rec} , and the advancing contact angle, θ_{adv} . The system tends to achieve the receding contact angle when liquid is removed (for example, at the rear end of a moving droplet), whereas the advancing contact angle is achieved when the liquid is added (for example, at the front end of a moving droplet) (Fig. 3.6a). When the liquid is neither added nor removed, the system tends to have a static or “most stable” contact angle, which is given approximately by (3.5), (3.6), (3.8), and (3.10).

Fig. 3.6 **a** Liquid droplet in contact with a rough surface with liquid added or removed (advancing and receding contact angles are θ_{adv} and θ_{rec} , respectively) and **b** tilted surface profile (tilt angle, α with a moving liquid droplet)



Another way to define θ_{adv} and θ_{rec} is to consider a moving liquid droplet over a tilted surface as shown in Fig. 3.6b. The liquid is pumped at the leading edge, and the contact angle at this edge corresponds to the advancing contact angle. The liquid is pumped away from the trailing edge, and the angle at the trailing edge corresponds to the receding contact angle.

The contact angle provided by (3.5), (3.6), (3.8), and (3.10) is a macroscale parameter, so it is sometimes called “the apparent contact angle.” Based on Nosonovsky and Bhushan (2008a, c), the actual angle under which the liquid-air interface comes in contact with the solid surface at the micro- and nanoscale can be different. There are several reasons that this is the case. First, liquid molecules tend to form a thin layer upon the surfaces of many materials. This is because of a long-distance van der Waals adhesion force that creates the so-called disjoining pressure (Derjaguin and Churaev 1974). This pressure is dependent upon the liquid layer thickness and may lead to the formation of stable thin films. In this case, the shape of the droplet near the triple line (line of contact of the solid, liquid and air, to be shown later in Fig. 3.8) transforms gradually from the spherical surface into a precursor layer, and thus the nanoscale contact angle is much smaller than the apparent contact angle. In addition, adsorbed liquid monolayers and multilayers are common for many materials. Second, even carefully prepared atomically smooth surfaces exhibit a certain roughness and chemical heterogeneity. Liquid tends first to cover the liquiphilic spots with high surface energy and low contact angle (Checco et al. 2003). The tilt angle due to roughness can also contribute to the apparent contact angle. Third, the very concept of the static contact angle is not well defined. For practical purposes, the contact angle, which is formed after a droplet is gently placed upon a surface and stops propagating, is considered the static contact angle. However, depositing the droplet involves adding liquid while leaving it involves evaporation, so it is difficult to avoid dynamic effects. Fourth, for small droplets and curved triple lines, the effect of the contact line tension may be significant. Molecules at the surface of a liquid or solid phase have higher energy because they are bonded to fewer molecules than those in the bulk. This is responsible for surface tension and surface energy. In a similar manner, molecules at the concave surface and, especially, at the edge have fewer bonds than those at the surface, which leads to line tension and curvature dependence of the surface energy. This effect becomes important when the radius of curvature is comparable with the so-called Tolman’s length, normally of the molecular size (Anisimov 2007). However, the triple line at the nanoscale can be curved so that the line tension effects become important (Pompe et al. 2000).

The contact angle, accounting for the contact line effect, for a droplet with radius R is given by $\cos \theta = \cos \theta_0 + 2\tau/(R\gamma_{LA})$, where τ is the contact line tension, and θ_0 is the value given by Young’s equation (Boruvka and Neumann 1977). Thus, while the contact angle is a convenient macroscale parameter, wetting is governed by interactions at the micro- and nanoscale, which determine the contact angle hysteresis and other wetting properties. Table 3.1 shows various scale levels, which affect wetting of a superhydrophobic surface.

Table 3.1 Wetting of a superhydrophobic surface as a multiscale process (Nosonovsky and Bhushan 2007c, 2008c)

Scale level	Characteristic length	Parameters	Phenomena	Interface
Macroscale	Droplet radius (mm)	Contact angle, droplet radius	Contact angle hysteresis	2-D
Microscale	Roughness detail (μm)	Shape of the droplet, position of the liquid-air interface (h)	Kinetic effects	3-D solid surface, 2-D liquid surface
Nanoscale	Molecular heterogeneity (nm)	Molecular description	Thermodynamic and dynamic effects	3-D

3.3.2 Range of Applicability of the Wenzel and Cassie-Baxter Equations

Gao and McCarthy (2007) showed experimentally that the contact angle of a droplet is defined by the triple line and does not depend upon the roughness under the bulk of the droplet. A similar result for chemically heterogeneous surfaces was obtained by Extrand (2003). Gao and McCarthy (2007) concluded that the Wenzel and Cassie-Baxter equations “should be used with the knowledge of their fault.” However the question remains, under what circumstances the Wenzel and Cassie-Baxter equations can be used safely and under what circumstances they become irrelevant?

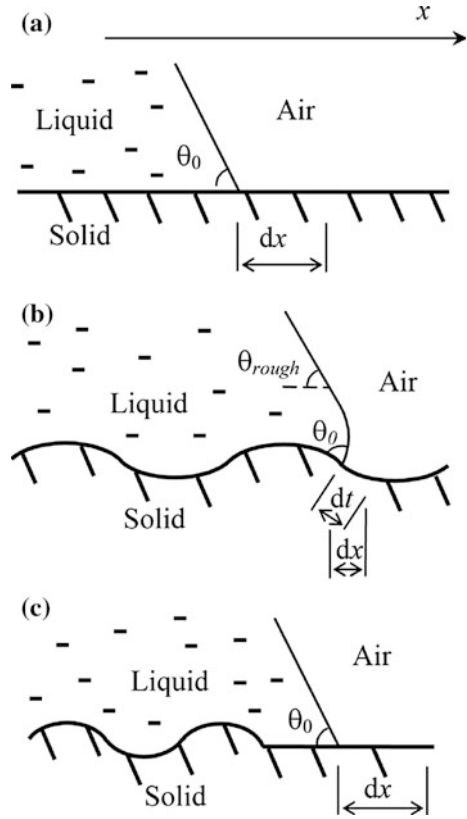
Based on Nosonovsky (2007c) and Nosonovsky and Bhushan (2008a), for a liquid front propagating along a rough two-dimensional profile (Fig. 3.7a, b), the derivative of the free surface energy (per liquid front length), W , by the profile length, t , yields the surface tension force $\sigma = dW/dt = \gamma_{SL} - \gamma_{SA}$ (Nosonovsky 2007c). The quantity of practical interest is the component of the tension force that corresponds to the advancing of the liquid front in the horizontal direction for dx . This component is given by $dW/dx = (dW/dt)(dt/dx) = (\gamma_{SL} - \gamma_{SA})dt/dx$. It is noted that the derivative dt/dx is equal to Wenzel’s roughness factor (R_f), in the case when the roughness factor is constant throughout the surface. Therefore, Young’s equation (3.5), which relates the contact angle with solid, liquid, and air interface tensions, is modified as (Nosonovsky 2007c)

$$\gamma_{LA} \cos \theta = R_f(\gamma_{SA} - \gamma_{SL}) \quad (3.16)$$

The empirical Wenzel equation (3.6) is a consequence of (3.16) combined with Young’s equation.

Nosonovsky (2007c) and Nosonovsky and Bhushan (2008a) showed that for a more complicated case of a non-uniform roughness given by the profile $z(x)$, the local value of derivative $r(x) = dt/dx = (1 + (dz/dx)^2)^{1/2}$ matters. In the cases that were studied experimentally by Gao and McCarthy (2007) and Extrand (2003), the

Fig. 3.7 Liquid front in contact with **a** a smooth solid surface and **b** a rough solid surface. Propagation for a distance dt along the curved surface corresponds to the distance dx along the horizontal surface. **c** Surface roughness under the bulk of the droplet does not affect the contact angle (Nosonovsky 2007c)



roughness was present ($r > 1$) under the bulk of the droplet, but there was no roughness ($r = 0$) at the triple line, and the contact angle was given by (3.6) (Fig. 3.7c). In the general case of a 3-D rough surface $z(x, y)$, the roughness factor can be defined as a function of the coordinates $r(x, y) = (1 + (dz/dx)^2 + (dz/dy)^2)^{1/2}$.

Equation (3.6) is valid for uniformly rough surfaces, that is, surfaces with $r = \text{constant}$, and for non-uniformly rough surfaces, the generalized Wenzel equation is formulated to determine the local contact angle (a function of x and y) with rough surfaces at the triple line (Nosonovsky 2007c; Nosonovsky and Bhushan 2008a, b)

$$\cos \theta = r(x, y) \cos \theta_0 \quad (3.17)$$

The difference between the Wenzel equation (3.6) and the Nosonovsky-Bhushan equation (3.17) is that the latter is valid for a non-uniform roughness with the roughness factor as the function of the coordinates. Equation (3.17) is consistent with the experimental results of the researchers who showed that roughness beneath the droplet does not affect the contact angle, since it predicts that only roughness at the triple line matters. It is also consistent with the results of the researchers who confirmed the Wenzel equation (for the case of the uniform roughness) and of those

who reported that only the triple line matters (for non-uniform roughness). A summary of experimental results for uniform and non-uniform rough and chemically heterogeneous surfaces is shown in Table 3.2.

The Cassie equation for the composite surface can be generalized in a similar manner introducing the spatial dependence of the local densities, f_1 and f_2 of the solid-liquid interface with the contact angle, as a function of x and y . It is given as (Nosonovsky 2007c),

$$\cos \theta_{composite} = f_1(x, y) \cos \theta_1 + f_2(x, y) \cos \theta_2 \quad (3.18)$$

where $f_1 + f_2 = 1$, and θ_1 and θ_2 are contact angles of the two components.

According to Nosonovsky (2007c) and Nosonovsky and Bhushan (2008a), the important question remains, what should be the typical size of roughness/heterogeneity details in order for the generalized Wenzel and Cassie equations (3.17)–(3.18) to be valid? Some scholars have suggested that roughness/heterogeneity details should be comparable with the thickness of the liquid-air interface and thus “the roughness would have to be of molecular dimensions to alter the equilibrium conditions” (Bartell and Shepard 1953). Conversely, others have claimed that roughness/heterogeneity details should be small compared with the linear size of the droplet (Johnson and Dettre 1964; Li and Amirfazli 2006; Bhushan and Jung 2007, 2008; Jung and Bhushan 2006, 2007, 2008a, b; Bhushan et al. 2007; Barbieri et al. 2007). The interface in the analysis proposed earlier is an idealized 2-D object, which has no thickness. In reality, the triple line zone has two characteristic dimensions: the thickness (of the order of molecular dimensions) and the length (of the order of the droplet size).

According to Nosonovsky and Bhushan (2008a, b), the apparent contact angle, given by (3.17)–(3.18), may be viewed as the result of averaging of the local contact angle at the triple line over its length, and thus the size of the roughness/heterogeneity details should be small compared to the length (and not the thickness) of the triple line (Nosonovsky and Bhushan 2008b). A rigorous definition of the generalized equation requires the consideration of several length scales. The length dx needed for the averaging of the energy gives the length over which the averaging is performed to obtain $r(x, y)$. This length should be larger than the roughness details. However, it is still smaller than the droplet size, and the length scale at which the apparent contact angle is observed (at which local variations of the contact angle level out). Since of these lengths (the roughness size, dx , the droplet size), the first and the last are of practical importance, it is concluded that the roughness details should be smaller than the droplet size. When the liquid-air interface is studied at the length scale of roughness/heterogeneity details, the local contact angle, θ_0 , is given by (3.6)–(3.10). The liquid-air interface at that scale has perturbations caused by the roughness/heterogeneity, and the scale of the perturbations is the same as the scale of the roughness/heterogeneity details. However, when the same interface is studied at a larger scale, the effect of the perturbation vanishes, and apparent contact angle is given by (3.17)–(3.18) (Fig. 3.7c).

Table 3.2 Summary of experimental results for uniform and non-uniform rough and chemically heterogeneous surfaces

Experiment	Roughness/hydrophobicity at the triple line and at the rest of the surface	Roughness at the bulk (under the droplet)	Experimental contact angle (compared with that at the rest of the surface)	Theoretical contact angle, Wenzel/Cassie equations	Theoretical contact angle, generalized Wenzel-Cassie (3.17)–(3.18)
Gao and McCarthy (2007)	Hydrophobic Rough Smooth	Hydrophilic Smooth Rough	Not changed Not changed Not changed	Decreased Decreased Increased	Not changed Not changed Not changed
Extrand (2003)	Hydrophilic Hydrophobic	Hydrophobic Hydrophilic	Not changed Not changed	Increased Decreased	Not changed Not changed
Bhushan et al. (2007)	Rough	Rough	Increased	Increased	Increased
Barbieri et al. (2007)	Rough	Rough	Increased	Increased	Increased

For non-uniform surfaces, the results are shown for droplets larger than the islands of non-uniformity. Detailed quantitative values of the contact angle in various sets of experiments can be found in the referred sources (Nosonovsky 2007c)

This apparent contact angle is defined at the length scale for which the small perturbations of the liquid-air interface vanish, and the interface can be treated as a smooth surface. The values of $r(x, y)$, $f_1(x, y)$, $f_2(x, y)$ in (3.17)–(3.18) are average values over an area (x, y) with a size larger than a typical roughness/heterogeneity detail size. Therefore, the generalized Wenzel and Cassie equations can be used at the scale at which the effect of the interface perturbations vanish, in other words, when the size of the solid surface roughness/heterogeneity details is small compared with the size of the liquid-air interface, which is of the same order as the size of the droplet (Nosonovsky and Bhushan 2008b).

Nosonovsky and Bhushan (2008a, d) used the surface energy approach to find the domain of validity of the Wenzel and Cassie equations (uniformly rough surfaces) and generalized it for a more complicated case of non-uniform surfaces. The generalized equations explain a wide range of existing experimental data, which could not be explained by the original Wenzel and Cassie equations.

3.4 Contact Angle Hysteresis

Contact angle hysteresis is another important characteristic of a solid-liquid interface. Contact angle hysteresis occurs due to surface roughness and heterogeneity. Although for surfaces with roughness carefully controlled on the molecular scale it is possible to achieve contact angle hysteresis as low as $<1^\circ$ (Gupta et al. 2005), hysteresis cannot be eliminated completely, since even atomically smooth surfaces have a certain roughness and heterogeneity. Contact angle hysteresis reflects the irreversibility of the wetting/dewetting cycle. In a surface with high contact angle hysteresis, the receding contact angle is low and pins the liquid, providing resistance to flow. Contact angle hysteresis is a measure of energy dissipation during the flow of a droplet along a solid surface. Low contact angle hysteresis results in a very low tilt angle, the angle to which a surface may be tilted for roll-off of liquid drops (i.e., very low drag) (Extrand 2002; Kijlstra et al. 2002; Bhushan and Jung 2007, 2008, 2011; Jung and Bhushan 2007, 2008a) (Fig. 3.6b). Low tilt angle is important in liquid flow applications and surfaces with self-cleaning ability.

Certain conclusions about the relationship of contact angle hysteresis to roughness can be made. It is known that the energy gained for surfaces during contact is greater than the work of adhesion for separating the surfaces, due to so called adhesion hysteresis. Factors that affect contact angle hysteresis include adhesion hysteresis, surface roughness, and inhomogeneity. Bhushan et al. (2007) and Nosonovsky and Bhushan (2007b) assumed that contact angle hysteresis is equal to the adhesion hysteresis term and the term corresponding to the effect of roughness, H_r . They further noted that adhesion hysteresis can be assumed to be proportional to the fractional solid-liquid area $(1 - f_{LA})$. Using (3.9), the difference of cosines of the advancing and receding angles is related to the difference of those for a nominally smooth surface, θ_{adv0} and θ_{rec0} , as

$$\cos \theta_{adv} - \cos \theta_{rec} = R_f(1 - f_{LA})(\cos \theta_{adv0} - \cos \theta_{rec0}) + H_r \quad (3.19)$$

The first term in the right-hand part of the equation, which corresponds to the inherent contact angle hysteresis of a smooth surface, is proportional to the fraction of the solid-liquid contact area, $1 - f_{LA}$. The second term, H_r , is the effect of surface roughness, which is equal to the total perimeter of the asperity per unit area, or in other words, to the length density of the triple line (Bhushan et al. 2007). Thus (3.19) involves both the term proportional to the solid-liquid interface area and to the triple line length. It is observed from (3.9) and (3.19) that increasing $f_{LA} \rightarrow 1$ results in increasing the contact angle ($\cos \theta \rightarrow -1, \theta \rightarrow \pi$) and decreasing the contact angle hysteresis ($\cos \theta_{adv} - \cos \theta_{rec} \rightarrow 0$). In the limiting case of very small solid-liquid fractional contact area under the droplet, when the contact angle is large ($\cos \theta \approx -1 + (\pi - \theta)^2/2, \sin \theta \approx \theta - \pi$) and the contact angle hysteresis is small ($\theta_{adv} \approx \theta \approx \theta_{rec}$), based on (3.9) and (3.19) (Nosonovsky and Bhushan 2007b),

$$\pi - \theta = \sqrt{2(1 - f_{LA})(R_f \cos \theta_0 + 1)} \quad (3.20)$$

$$\theta_{adv} - \theta_{rec} = (1 - f_{LA})R_f \frac{\cos \theta_{a0} - \cos \theta_{r0}}{-\sin \theta} = \left(\sqrt{1 - f_{LA}}\right)R_f \frac{\cos \theta_{r0} - \cos \theta_{a0}}{\sqrt{2(R_f \cos \theta_0 + 1)}} \quad (3.21)$$

For the homogeneous interface, $f_{LA} = 0$, whereas for the composite interface f_{LA} is a non-zero number. It is observed from (3.20) to (3.21) that for a homogeneous interface, increasing roughness (high R_f) leads to increasing the contact angle hysteresis (high values of $\theta_{adv} - \theta_{rec}$), while for the composite interface, an approach to unity of f_{LA} provides both high contact angle and small contact angle hysteresis (Jung and Bhushan 2006; Bhushan et al. 2007; Nosonovsky and Bhushan 2007b, d). Therefore, the composite interface is desirable for low contact angle hysteresis.

A sharp edge can pin the line of contact of the solid, liquid, and air (or the “triple line”) at a position far from stable equilibrium, i.e., at contact angles different from θ_0 (Eustathopoulos et al. 1999). This effect is illustrated in Fig. 3.8, which shows a droplet propagating along a solid surface with grooves (Nosonovsky and Bhushan 2005). Based on Nosonovsky and Bhushan (2005, 2008a), at the edge point, the contact angle is not defined and can have any value between the values corresponding to contact with the horizontal and inclined surfaces. For a droplet moving from left to right, the triple line will be pinned at the edge point until it will be able to proceed to the inclined plane. As it is observed from Fig. 3.8, the change of the surface slope (α) at the edge is the cause of the pinning. Because of the pinning, the value of the contact angle at the front of the droplet (dynamic maximum advancing contact angle or $\theta_{adv} = \theta_0 + \alpha$) is greater than θ_0 , whereas the value of the contact angle at the back of the droplet (dynamic minimum receding contact angle or $\theta_{rec} = \theta_0 - \alpha$) is smaller than θ_0 . A hysteresis domain of the dynamic contact angle

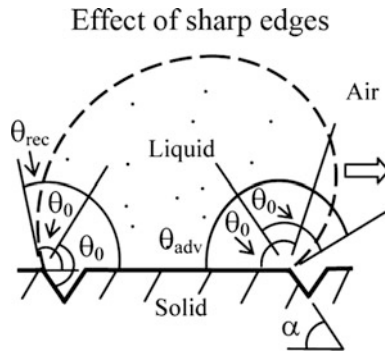


Fig. 3.8 A liquid droplet in contact with a surface with sharp edges. For a droplet moving from left to right on a sharp edge (shown by *arrow*), the contact angle at a sharp edge may take any value between the contact angle with the horizontal and inclined planes. This effect results in the difference between advancing ($\theta_{adv} = \theta_0 + \alpha$) and receding ($\theta_{rec} = \theta_0 - \alpha$) contact angles (Nosonovsky and Bhushan 2005)

is thus defined by the difference $\theta_{adv} - \theta_{rec}$. The liquid can travel easily along the surface if the contact angle hysteresis is small. It is noted that the static contact angle lies within the hysteresis domain. Therefore, increasing the static contact angle up to the values of a superliquiphobic surface (approaching 180°) will also result in a reduction of the contact angle hysteresis. In a similar manner, contact angle hysteresis can also exist even if the surface slope changes smoothly, without sharp edges. There is an analogy between the two mechanisms leading to contact angle hysteresis (energy dissipation at the solid-liquid interface and pinning of the triple line) and dissipation mechanisms of dry friction (adhesion and deformation) (Nosonovsky 2007b; Nosonovsky and Bhushan 2008a).

3.5 Stability of a Composite Interface and Role of Hierarchical Structure with Convex Surfaces

Stability of the composite interface is an important issue. Even though it may be geometrically possible for the system to become composite, it may be energetically profitable for the liquid to penetrate into the valleys between asperities and form a homogeneous interface. Marmur (2003) formulated geometrical conditions for a surface under which the energy of the system has a local minimum and the composite interface may exist. Patankar (2004) pointed out that whether the homogeneous or composite interface exists depends on the system's history, i.e., on whether the droplet was formed at the surface or deposited.

Based on Nosonovsky and Bhushan (2007b, 2008a), formation of a composite interface is a multiscale phenomenon that depends upon the relative sizes of the liquid droplet and roughness details. The composite interface is fragile and can be

irreversibly transformed into the homogeneous interface, thus damaging superhydrophobicity. In order to form a stable composite interface with air pockets between solid and liquid, the destabilizing factors such as capillary waves, nanodroplet condensation, surface inhomogeneity, and liquid pressure should be avoided. A description of these destabilizing factors follows.

- First, the capillary waves at the liquid-air interface may destabilize the composite interface. Due to an external perturbation, a standing capillary wave can form at the liquid-air interface. If the amplitude of the capillary wave is greater than the height of the asperity, the liquid can touch the valley between the asperities, and if the angle under which the liquid comes in contact with the solid is greater than θ_0 , it is energetically profitable for the liquid to fill the valley (Nosonovsky and Bhushan 2005, 2006a). When the composite interface is destroyed and space between the asperities is filled with liquid, it is highly unlikely that the composite interface will be formed again because the transition from the non-composite solid-liquid interface to a composite interface would require a large activation energy. Such a transition has never been observed. The effect of capillary waves is more pronounced for small asperities with height comparable with wave amplitude.
- Second, nanodroplets may condense and accumulate in the valleys between asperities and eventually destroy the composite interface. Cheng et al. (2005) observed condensation of submicron sized droplets on a lotus leaf surface, and found that droplets tend to condense at areas adjacent to bumps (i.e. in the valleys) and have a contact angle of less than 90° , whereas larger droplets have higher contact angles, thus demonstrating that the contact angle is scale dependent. The scale effect is observed for small droplets or at small distances near the triple line. Scale dependence of the contact angle has been reported by Nosonovsky and Bhushan (2007b, 2008a). At nanoscale distances from the triple line, the liquid touches the solid under a much lower contact angle.
- Third, even hydrophobic surfaces are usually not chemically homogeneous and can have hydrophilic spots. It is known from experiments that for droplets of submicron size, the value of the contact angle is usually smaller than for droplets at the macroscale (Lafuma and Quéré 2003). Checco et al. (2003) suggested that surface inhomogeneity is responsible for this scale effect, since nanodroplets tend to sit at the highest free surface energy (most hydrophilic) spots and thus have lower contact angles. Their phenomenological numerical simulations showed good agreement with experimental data.

Nosonovsky and Bhushan (2007a, b, c, d, 2008a, b, c, e) have demonstrated that a combination of microroughness and nanoroughness (multiscale roughness) with convex surfaces can help resist the destabilization by pinning the interface. It also helps in preventing the gaps between the asperities from filling with liquid, even in the case of a hydrophilic material. The effect of roughness on wetting is scale dependent, and the mechanisms that lead to destabilization of a composite interface are also scale-dependent. To effectively resist these scale-dependent mechanisms, it is expected that a multiscale roughness is optimum for superhydrophobicity.

Nosonovsky and Bhushan (2008a) considered a two-dimensional structure with rectangular pillars of height h separated by distance b , covered with small semi-circular bumps (convex) and grooves (concave surface) in between of radius r (Fig. 3.9a). It is referred to as a geometry with re-entrant curvature. If the distance between the pillars is small in comparison with the capillary length, the effect of gravity is negligible, it can be assumed that the liquid-air interface is a horizontal plane, and its position is characterized by the vertical coordinate z . The free energy is given by (Nosonovsky 2007a; Nosonovsky and Bhushan 2008a)

$$W = A_{SL}\gamma_{SL} + A_{SA}\gamma_{SA} + A_{LA}\gamma_{LA} = rL\gamma_{LA}(\sin \alpha - \alpha \cos \theta_0), \quad 0 < z < h \quad (3.22)$$

where $\alpha = a \cos((r - z)/r) + 2\pi N$ is the angle corresponding to vertical position of the interface z , N is the number of ridges or grooves, and L is length of the grooves in the y -direction, which is required based on the dimensional considerations.

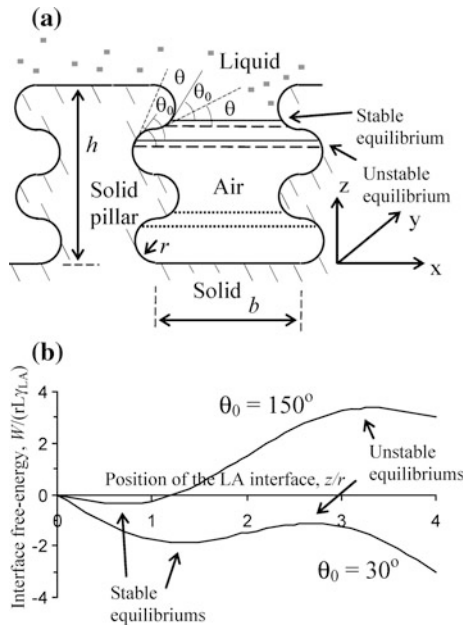


Fig. 3.9 Two-dimensional pillars with semi-circular bumps/grooves. **a** Schematics of the structure. The bumps may pin the triple line, because an advance of the LA interface results in a decrease of the contact angle ($\theta < \theta_0$), making the equilibrium stable. Grooves provide equilibrium positions, which satisfy Young’s equation. However, the equilibrium is unstable because an advance of the LA interface results in an increase of the contact angle ($\theta > \theta_0$). **b** Energy profiles for configurations in Fig. 3.9a with bumps and grooves for liquiphilic ($\theta_0 = 30^\circ$) and liquiphobic ($\theta_0 = 150^\circ$) materials. Energy (normalized by $Lr\gamma_{LA}$) is shown as a function of vertical position of the interface z (normalized by the radius of bumps/grooves r). Bumps result in stable equilibriums (energy minima), whereas grooves result in unstable equilibriums (energy maxima) (Nosonovsky and Bhushan 2008a)

The dependence is presented in Fig. 3.9b, for the cases of liquiphobic ($\theta_0 = 150^\circ$) and—philic ($\theta_0 = 30^\circ$) materials for both the convex surface (with bumps) and concave surface (with grooves). It is seen that for the convex surface, there are many states of stable equilibrium (shown in Fig. 3.9a with dotted lines), separated by energy barriers which correspond to every ridge, whereas for the concave surface, equilibrium states are unstable. Therefore, the ridges can pin the triple line and thus lead to a composite interface. In the case of a liquiphilic surface, each lower position of the equilibrium state corresponds to a lower value of W . Therefore, when the liquid advances from one equilibrium state to the next, the total energy decreases, and the liquid's advance is energetically profitable. When the liquid reaches the bottom of the valley and completely fills the space between the pillars forming a homogeneous interface, the total energy decreases dramatically by the value of (Nosonovsky 2007a; Nosonovsky and Bhushan 2008a)

$$\Delta W = bL(\gamma_{SA} + \gamma_{LA} - \gamma_{SL}) = bL\gamma_{LA}(1 + \cos \theta_0) \quad (3.23)$$

The opposite transition from a homogeneous interface to a composite interface requires high activation energy ΔW , and is thus unlikely, making the transition from composite interface to homogeneous interface irreversible. If the distance between the pillars b is much greater than r , the energy barriers that separate the equilibrium states, $2\pi rL\gamma_{LA} \cos \theta_0$, will be relatively small compared to ΔW , and low activation energy will be required for the liquid to spread and propagate from one equilibrium state to the other (Nosonovsky and Bhushan 2007b, d).

For the interface to be stable, the value of the contact angle should decrease when the liquid-air interface advances, whereas for receding liquid the contact angle should increase. For a two-dimensional surface, the change of angle is equal to the change of the slope of the surface, and whether the configuration is stable or not depends on the sign of curvature of the surface. As indicated earlier, the convex surface (with bumps) leads to a stable interface, whereas a concave surface (with grooves) leads to an unstable interface. A structure consisting of bumps and grooves, a re-entrant surface structure, initially proposed by Nosonovsky and Bhushan (2008a), has been used by various researchers to create superoleophobic surfaces, since the surface tension of oil and other organic liquids is much lower than that of water, and it is difficult to create a surface not wetted by oil.

Sun et al. (2005) conducted an experiment to verify that the sign of curvature is indeed important for hydrophobicity. They produced both a positive and a negative replica of a lotus leaf surface by nanocasting using poly(dimethylsiloxane), which has a contact angle with water of about 105° . This value is close to the contact angle of the wax which covers lotus leaves [about 103° as reported by Kamusewitz et al. (1999)]. The positive and negative replicas have the same roughness factor and thus should produce the same contact angle in the case of a homogeneous interface, according to (3.6). However, the values of surface curvature are opposite. The value of contact angle for the positive replica was found to be 160° (same as for lotus leaf), while for the negative replica it was only 110° . This result suggests that the high contact angle for lotus leaf is due to the composite, rather than homogeneous

interface, and that the sign of surface curvature indeed plays a critical role in the formation of the composite interface.

3.6 The Cassie-Baxter and Wenzel Wetting Regime Transition

Since superhydrophobicity requires a stable composite interface, it is important to understand the destabilization mechanisms for the Cassie-Baxter and Wenzel wetting transition. Based on Nosonovsky and Bhushan (2008a, d), it is known from experimental observations that the transition from the Cassie-Baxter to the Wenzel regime can be an irreversible event. Such a transition can be induced, for example, by applying pressure or force to the droplet (Jung and Bhushan 2008b; Nosonovsky and Bhushan 2008f), electric voltage (Krupenkin et al. 2004; Bahadur and Garimella 2007), light for a photocatalytic texture (Feng et al. 2004), and vibration (Bormashenko et al. 2007). However, the opposite transition is never observed.

Several approaches have been proposed for investigation of the transition between the metastable Cassie-Baxter and Wenzel regimes, referred to as “the Cassie-Wenzel transition.” It has been suggested that the transition takes place when the net surface energy of the Wenzel regime becomes equal to that of the Cassie-Baxter regime, in other words, when the contact angle predicted by the Cassie-Baxter equation is equal to that predicted by the Wenzel equation. Lafuma and Quéré (2003) noticed that in certain cases the transition does not occur even when it is energetically profitable, and considered such a Cassie-Baxter state metastable. Extrand (2003) suggested that the weight of the droplet is responsible for the transition and proposed the contact line density model, according to which the transition takes place when the weight exceeds the surface tension force at the triple line. Patankar (2004) proposed a transition criterion based on energy balance. There is an energy barrier in going from a higher energy Cassie-Baxter droplet to a lower energy Wenzel droplet. The most probable mechanism is that the decrease in the gravitational potential energy during the transition helps in overcoming the energy barrier. This energy barrier was estimated by considering an intermediate state in which the liquid fills the grooves below the contact area of a Cassie-Baxter droplet but the liquid-solid contact is yet to be formed at the bottom of the valleys. Quéré (2005) also suggested that the droplet curvature (which depends upon the pressure difference between the inside and the outside of the droplet) governs the transition. Nosonovsky and Bhushan (2005, 2006a, b) proposed a probabilistic model for wetting of rough surfaces with a certain probability associated with every equilibrium state. According to their model, the overall contact angle with a two-dimensional rough profile is calculated by assuming that the overall configuration of a droplet occurs as a result of superposition of numerous metastable states. Numerous experimental results support many of these approaches, however, it is not clear which particular mechanism prevails.

Based on Nosonovsky and Bhushan (2008a, d), there is an asymmetry between the wetting and dewetting processes, since less energy is released during wetting than the amount required for dewetting due to adhesion hysteresis. Adhesion hysteresis is one of the reasons that leads to contact angle hysteresis, and it also results in the hysteresis of the Wenzel and Cassie-Baxter state transition. Figure 3.10 shows the contact angle of a rough surface as a function of surface roughness parameter, given by (3.9) (Nosonovsky and Bhushan 2008d). Here it is assumed that $R_f \sim 1$ for a Cassie-Baxter regime with a stable composite interface, and the liquid droplet sits flat over the surface. It is noted that, at a certain point, the contact angles given by the Wenzel and Cassie-Baxter equations are the same, and $R_f = (1 - f_{LA}) - f_{LA} / \cos\theta_0$. At this point, the lines corresponding to the Wenzel and Cassie-Baxter regimes intersect. This point corresponds to an equal net energy of the Cassie-Baxter and Wenzel regimes. For a lower roughness (e.g., larger pitch between the asperities) the Wenzel state is more energetically profitable, whereas for a higher roughness, the Cassie-Baxter regime is more energetically profitable.

It is observed from Fig. 3.10 that an increase of roughness may lead to the transition between the Wenzel and Cassie-Baxter regimes at the intersection point. With decreasing roughness, the system is expected to transition to the Wenzel state. However, experiments show that, despite the energy in the Wenzel regime being lower than that in the Cassie-Baxter regime, the transition does not necessarily occur, and the droplet may remain in the metastable Cassie-Baxter regime (Bhushan and Jung 2007, 2008; Jung and Bhushan 2007, 2008a, b; Bhushan et al. 2007; Barbieri et al. 2007). This is because there are energy barriers associated with the transition, which occurs due to destabilization by dynamic effects (such as waves and vibration) (Nosonovsky and Bhushan 2008a, d).

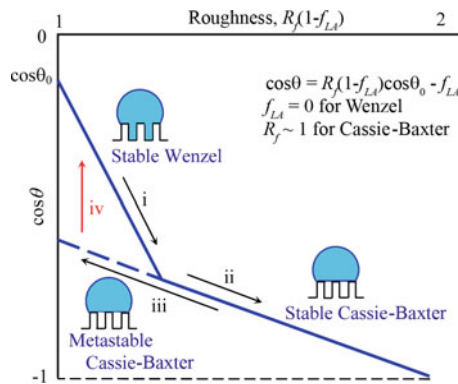
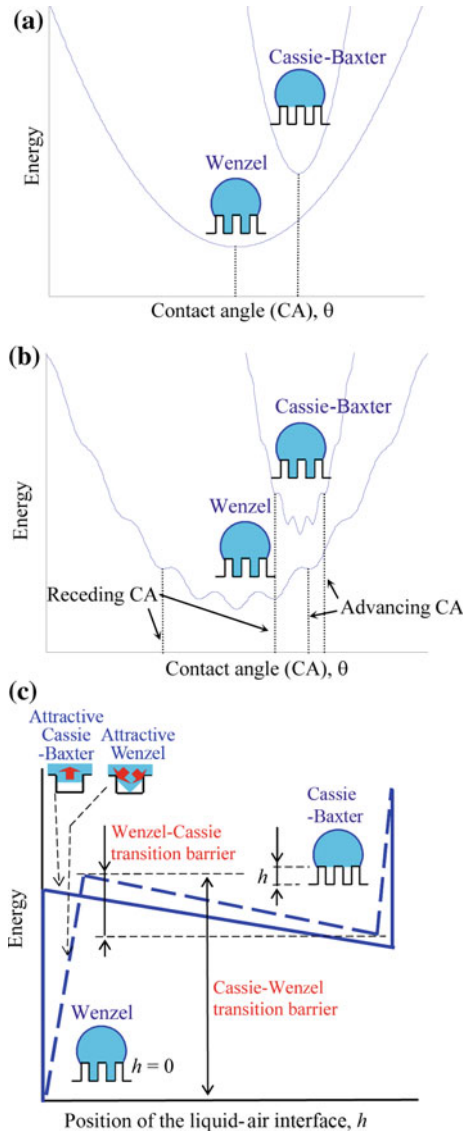


Fig. 3.10 Wetting hysteresis for a superliquiphobic surface. Contact angle as a function of roughness. The stable Wenzel state (*i*) can transform into the stable Cassie-Baxter state with increasing roughness (*ii*). The metastable Cassie-Baxter state (*iii*) can abruptly transform (*iv*) into the stable Wenzel state. The transition *i*–*ii* corresponds to equal Wenzel and Cassie-Baxter states free energies, whereas the transition *iii*–*iv* corresponds to a significant energy dissipation, and thus it is irreversible (adapted from Nosonovsky and Bhushan 2008d)

In order to understand contact angle hysteresis and the transition between the Cassie-Baxter and Wenzel regimes, Nosonovsky and Bhushan (2008a, d) analyzed the shape of the free surface energy profile. The free surface energy of a droplet upon a smooth surface as a function of the contact angle has a distinct minimum which corresponds to the most stable contact angle. As shown in Fig. 3.11a, the macroscale profile of the net surface energy allows us to find the contact angle (corresponding to energy minimums). However it fails to predict contact angle

Fig. 3.11 Schematics of net free energy profiles.

a Macroscale description; energy minimums correspond to the Wenzel and Cassie states. **b** Microscale description with multiple energy minimums due to surface texture. Largest and smallest values of the energy minimum correspond to the advancing and receding contact angles, respectively. **c** Origin of the two branches (Wenzel and Cassie-Baxter) is found when a dependence of energy upon h (air layer thickness or vertical position of the liquid-air interface) is considered for the microscale description (solid line) and nanoscale imperfectness (dashed line) (adapted from Nosonovsky and Bhushan 2008d). When the nanoscale imperfectness is introduced, it is observed that the Wenzel state corresponds to an energy minimum and the energy barrier for the Wenzel-Cassie transition is much smaller than for the opposite transition



hysteresis and the Cassie-Baxter and Wenzel transition, which are governed by micro- and nanoscale effects (Nosonovsky and Bhushan 2008d). As soon as microscale substrate roughness is introduced, the droplet shape cannot be considered as an ideal truncated sphere anymore, and energy profiles have multiple energy minimums, corresponding to the location of the asperities (Fig. 3.11b). The microscale energy profile (solid line) has numerous energy maxima and minima due to surface asperities. While exact calculation of the energy profile for a 3-D droplet is complicated, a qualitative shape may be obtained by assuming a periodic sinusoidal dependence (Johnson and Dettre 1964), superimposed upon the macroscale profile, as shown in Fig. 3.11b (Nosonovsky and Bhushan 2008a, d). Thus, the advancing and receding contact angles can be identified as the maximum and minimum possible contact angles corresponding to energy minimum points. However, the transition between the Wenzel and Cassie-Baxter branches still cannot be explained. Note also that Fig. 3.11b explains qualitatively the hysteresis due to the kinetic effect of the asperities, but not the inherited adhesion hysteresis, which is characterized by the molecular length scale and cannot be captured by the microscale model.

Based on Nosonovsky and Bhushan (2008a, d), the energy profile as a function of the contact angle does not provide information on how the transition between the Cassie-Baxter and Wenzel regimes occurs, because their two states correspond to completely isolated branches of the energy profile in Fig. 3.11a, b. However, the energy may depend not only upon the contact angle, but also upon micro/nanoscale parameters such as, for example, the vertical position of the liquid-air interface under the droplet, h (assuming that the interface is a horizontal plane) or similar geometrical parameters (assuming a more complicated shape of the interface). In order to investigate the Wenzel and Cassie-Baxter transition, Nosonovsky and Bhushan (2008a, d) studied the dependence of the energy upon these parameters. They assume that the liquid-air interface under the droplet is a flat horizontal plane. When such air layer thickness or the vertical position of the liquid-air interface, h , is introduced, the energy can be studied as a function of the droplet's shape, the contact angle, and h (Fig. 3.11c). For an ideal situation, the energy profile has an abrupt minimum at the point corresponding to the Wenzel state, which corresponds to the sudden net energy change due to the destruction of the solid-air and liquid-air interfaces ($\gamma_{SL} - \gamma_{SA} - \gamma_{LA} = -\gamma_{LA}(\cos \theta + 1)$) times the interface area) (Fig. 3.11c). In a more realistic case, the liquid-air interface cannot be considered horizontal due to nanoscale imperfectness or dynamic effects such as the capillary waves (Nosonovsky and Bhushan 2006a). A typical size of the imperfectness is much smaller than the size of details of the surface texture and thus belongs to the molecular scale level. The height of the interface, h , can now be treated as an average height. The energy dependence upon h is now not as abrupt as in the idealized case. For example, for the "triangular" shape as shown in Fig. 3.11c, the Wenzel state may become the second attractor for the system. It is seen that there are two equilibriums that correspond to the Wenzel and Cassie-Baxter regimes, with the Wenzel state corresponding to a much lower energy level. The energy dependence upon h governs the transition between the two states, and it is observed

that a much larger energy barrier exists for the transition from Wenzel to Cassie-Baxter regime than for the opposite transition. This is why the first transition has never been observed experimentally (Nosonovsky and Bhushan 2007c).

3.7 Closure

The modeling of wetting of rough surfaces is presented. There are two primary wetting regimes—Wenzel and Cassie-Baxter regimes. In the Wenzel regime, a liquid droplet completely wets the rough surface with a homogeneous interface. The contact angle of a rough surface is altered by the roughness details—roughness factor R_f , which is a ratio of the surface area to its flat projected area. The Wenzel equation predicts that a liquiphobic surface becomes more liquiphobic, while a liquiphilic surface becomes more liquiphilic with an increase in roughness. In the Cassie-Baxter regime, a heterogeneous or composite interface with air pockets trapped between the asperities is formed. The contact angle is altered by the roughness details and fractional liquid-air area (f_{LA}). The Cassie-Baxter equation predicts that, even for a liquiphilic surface, the surface can become liquiphobic with an increase of f_{LA} . However, the f_{LA} value required may be very high, or the formation of air pockets may become unstable. Whether a liquid-air interface is generated depends upon the ratio of distance between two adjacent asperities and droplet radius.

In an intermediate wetting regime, referred to as the Cassie-impregnated regime, or simply the Cassie regime, a liquid film impregnates some of the cavities in an area surrounding the droplet as well. It consists of two interfaces—a Wenzel interface and some of the neighboring cavities filled with liquid. Pure Cassie-Baxter and Wenzel wetting situations rarely occur. An intermediate state between the Wenzel and Cassie-Baxter interfaces is more common. In this interface, underneath the droplet, liquid penetrates and the cavities are partially impregnated or filled, and is referred to as the mixed/impregnated state.

Another property of interest in fluid flow is contact angle hysteresis, which is the difference between the advancing and receding contact angles. It occurs due to surface roughness and heterogeneity. Hysteresis cannot be eliminated completely, since even atomically smooth surfaces have a certain roughness and heterogeneity. Contact angle hysteresis is a measure of energy dissipation during the flow of a droplet along a solid surface. Low contact angle hysteresis results in a very low tilt or roll-off angle, implying low drag and self-cleaning ability. It turns out that it is efficient to increase both contact angle and reduce contact angle hysteresis by having a moderate roughness and large fractional liquid-air area.

A composite interface is metastable, and its stability is an important issue. The formation of a composite interface is a multiscale phenomenon that depends on the relative sizes of the liquid droplet and the roughness details. Destabilizing factors include capillary wave, condensation and accumulation of nanodroplets, and surface inhomogeneity (with hydrophilic spots). A microstructure resists capillary

waves present at the liquid-air interface. A nanostructure prevents nanodroplets from filling the valleys between asperities and pin the droplet. A combination of microstructure and nanostructure with convex surfaces can help resist the destabilization by pinning the interface. Based on the modeling and observation of natural objects (present in the next chapter), it is widely understood that a hierarchical surface structure is needed to develop a composite interface with high stability. A so-called re-entrant geometry is useful in creating superoleophobic surfaces.

References

- Adamson A. V. (1990), *Physical Chemistry of Surfaces*, Wiley, New York.
- Anisimov, M. A. (2007), "Divergence of Tolman's Length for a Droplet Near the Critical Point," *Phys. Rev. Lett.* **98**, 035702.
- Bahadur, V. and Garimella, S. V. (2007), "Electrowetting-Based Control of Static Droplet States on Rough Surfaces," *Langmuir* **23**, 4918-4924.
- Barbieri, L., Wagner, E., and Hoffmann, P. (2007), "Water Wetting Transition Parameters of Perfluorinated Substrates with Periodically Distributed Flat-Top Microscale Obstacles," *Langmuir* **23**, 1723-1734.
- Bartell, F.E. and Shepard, J. W. (1953), "Surface Roughness as Related to Hysteresis of Contact Angles" *J. Phys. Chem.* **57**, 455-458.
- Bhushan, B. (2013a), *Principles and Applications of Tribology*, 2nd Ed., Wiley, New York.
- Bhushan, B. (2013b), *Introduction to Tribology*, 2nd Ed., Wiley, New York.
- Bhushan, B. and Jung, Y. C. (2007), "Wetting Study of Patterned Surfaces for Superhydrophobicity," *Ultramicroscopy* **107**, 1033-1041.
- Bhushan, B. and Jung, Y. C. (2008), "Wetting, Adhesion and Friction of Superhydrophobic and Hydrophilic Leaves and Fabricated Micro/nanopatterned Surfaces," *J. Phys.: Condens. Matter* **20**, 225010.
- Bhushan, B. and Jung, Y. C. (2011), "Natural and Biomimetic Artificial Surfaces for Superhydrophobicity, Self-Cleaning, Low Adhesion, and Drag Reduction," *Prog. Mater. Sci.* **56**, 1-108.
- Bhushan, B. and Nosonovsky, M. (2010), "The Rose Petal Effect and the Modes of Superhydrophobicity," *Phil. Trans. R. Soc. A* **368**, 4713-4728.
- Bhushan, B., Nosonovsky, M., and Jung, Y. C. (2007), "Towards Optimization of Patterned Superhydrophobic Surfaces" *J. R. Soc. Interf.* **4**, 643-648.
- Bormashenko, E., Pogreb, R., Whyman, G., and Erlich, M. (2007), "Cassie-Wenzel Wetting Transition in Vibrated Drops Deposited on the Rough Surfaces: Is Dynamic Cassie-Wenzel Transition 2D or 1D Affair?" *Langmuir* **23**, 6501-6503.
- Boruvka, L. and Neumann, A. W. (1977), "Generalization of the Classical Theory of Capillarity," *J. Chem. Phys.* **66**, 5464-5476.
- Cassie, A. B. D. (1948), "Contact Angles," *Discuss. Faraday Soc.* **3**, 11-16.
- Cassie, A. B. D. and Baxter, S. (1944), "Wettability of Porous Surfaces," *Trans. Faraday Soc.* **40**, 546-551.
- Checco, A., Guenoun, P., and Daillant, J. (2003), "Nonlinear Dependence of the Contact Angle of Nanodroplets on Contact Line Curvatures," *Phys. Rev. Lett.* **91**, 186101.
- Cheng, Y. T., Rodak, D. E., Angelopoulos, A., and Gacek, T. (2005), "Microscopic Observations of Condensation of Water on Lotus Leaves," *Appl. Phys. Lett.* **87**, 194112.
- de Gennes, P. G., Brochard-Wyart, F., and Quéré, D. (2003) *Capillarity and Wetting Phenomena*, Springer, Berlin.

- Derjaguin, B. V. and Churaev, N. V. (1974), "Structural Component of Disjoining Pressure," *J. Colloid Interface Sci.* **49**, 249-255.
- Eustathopoulos N., Nicholas, M. G., Drevet, B. (1999), *Wettability at High Temperatures*, Pergamon, Amsterdam.
- Extrand, C. W. (2002), "Model for Contact Angle and Hysteresis on Rough and Ultraphobic Surfaces," *Langmuir* **18**, 7991-7999.
- Extrand, C. W. (2003), "Contact Angle Hysteresis on Surfaces with Chemically Heterogeneous Islands," *Langmuir* **19**, 3793-3796.
- Feng, X. J., Feng, L., Jin, M. H., Zhai, J., Jiang, L., Zhu, D. B. (2004), "Reversible Super-hydrophobicity to Super-hydrophilicity Transition of Aligned ZnO Nanorod Films," *J. Am. Chem. Soc.* **126**, 62-63.
- Gao, L. and McCarthy, T. J. (2007). "How Wenzel and Cassie Were Wrong," *Langmuir* **23**, 3762-3765.
- Gupta, P., Ulman, A., Fanfan, F., Korniaikov, A., and Loos, K. (2005), "Mixed Self-Assembled Monolayer of Alkanethiolates on Ultrasoother Gold do not Exhibit Contact Angle Hysteresis," *J. Am. Chem. Soc.* **127**, 4-5.
- Israelachvili, J. N. (1992), *Intermolecular and Surface Forces*, second edition, Academic Press, London.
- Israelachvili, J. N. and Gee, M. L. (1989), "Contact Angles on Chemically Heterogeneous Surfaces," *Langmuir* **5**, 288-289.
- Johnson, R. E. and Dettre, R. H. (1964), "Contact Angle Hysteresis," *Contact Angle, Wettability, and Adhesion, Adv. Chem. Ser.*, Vol. 43, Ed. F. M. Fowkes, pp. 112-135, American Chemical Society, Washington, D. C.
- Jung, Y. C. and Bhushan, B. (2006), "Contact Angle, Adhesion, and Friction Properties of Micro- and Nanopatterned Polymers for Superhydrophobicity," *Nanotechnology* **17**, 4970-4980.
- Jung, Y. C. and Bhushan, B. (2007), "Wetting Transition of Water Droplets on Superhydrophobic Patterned Surfaces," *Scripta Mater.* **57**, 1057-1060.
- Jung, Y. C. and Bhushan, B. (2008a), "Wetting Behavior During Evaporation and Condensation of Water Microdroplets on Superhydrophobic Patterned Surfaces" *J. Micros.* **229**, 127-140.
- Jung, Y. C. and Bhushan, B. (2008b), "Dynamic Effects of Bouncing Water Droplets on Superhydrophobic Surfaces," *Langmuir* **24**, 6262-6269.
- Kamusewitz, H., Possart, W., and Paul, D. (1999), "The Relation Between Young's Equilibrium Contact Angle and the Hysteresis on Rough Paraffin Wax Surfaces," *Colloid Surf. A-Physicochem. Eng. Asp.* **156**, 271 - 279.
- Kijlstra, J., Reihs, K., and Klami, A. (2002), "Roughness and Topology of Ultra-Hydrophobic surfaces," *Colloid Surf. A-Physicochem. Eng. Asp.* **206**, 521-529.
- Krupenkin, T. N., Taylor, J. A., Schneider, T. M., and Yang, S. (2004), "From Rolling Ball to Complete Wetting: The Dynamic Tuning of Liquids on Nanostructured Surfaces," *Langmuir* **20**, 3824-3827.
- Lafuma, A. and Quéré, D. (2003), "Superhydrophobic States," *Nature Materials* **2**, 457-460.
- Li, W. and Amirfazli, A. (2006), "A Thermodynamic Approach for Determining the Contact Angle Hysteresis for Superhydrophobic Surfaces," *J. Colloid. Interface Sci.* **292**, 195-201.
- Marmur, A. (2003), "Wetting on Hydrophobic Rough Surfaces: to be Heterogeneous or Not to be?" *Langmuir* **19**, 8343-8348.
- Nosonovsky, M. (2007a), "Multiscale Roughness and Stability of Superhydrophobic Biomimetic Interfaces," *Langmuir* **23**, 3157-3161.
- Nosonovsky, M. (2007b), "Model for Solid-Liquid and Solid-Solid Friction for Rough Surfaces with Adhesion Hysteresis," *J. Chem. Phys.* **126**, 224701.
- Nosonovsky, M. (2007c), "On the Range of Applicability of the Wenzel and Cassie Equations" *Langmuir* **23** 9919-9920.
- Nosonovsky, M. and Bhushan, B. (2005), "Roughness Optimization for Biomimetic Superhydrophobic Surfaces," *Microsyst. Technol.* **11**, 535-549.
- Nosonovsky, M. and Bhushan, B. (2006a), "Stochastic Model for Metastable Wetting of Roughness-Induced Superhydrophobic Surfaces," *Microsyst. Technol.* **12**, 231-237.

- Nosonovsky, M. and Bhushan, B. (2006b), "Wetting of Rough Three-Dimensional Superhydrophobic Surfaces," *Microsyst. Technol.* **12**, 273-281.
- Nosonovsky, M. and Bhushan, B. (2007a), "Multiscale Friction Mechanisms and Hierarchical Surfaces in Nano- and Bio-Tribology," *Mater. Sci. Eng.:R* **58**, 162-193.
- Nosonovsky, M. and Bhushan, B. (2007b), "Hierarchical Roughness Makes Superhydrophobic Surfaces Stable," *Microelectronic Eng.* **84**, 382-386.
- Nosonovsky, M. and Bhushan, B. (2007c), "Biomimetic Superhydrophobic Surfaces: Multiscale Approach," *Nano Lett.* **7**, 2633-2637.
- Nosonovsky, M. and Bhushan, B. (2007d), "Hierarchical Roughness Optimization for Biomimetic Superhydrophobic Surfaces," *Ultramicroscopy* **107**, 969-979.
- Nosonovsky, M. and Bhushan, B. (2008a), *Multiscale Dissipative Mechanisms and Hierarchical Surfaces: Friction, Superhydrophobicity, and Biomimetics*, Springer-Verlag, Heidelberg, Germany.
- Nosonovsky, M. and Bhushan, B. (2008b), "Roughness-Induced Superhydrophobicity: A Way to Design Non-Adhesive Surfaces," *J. Phys.: Condens. Matter* **20**, 225009.
- Nosonovsky, M. and Bhushan, B. (2008c), "Biologically-Inspired Surfaces: Broadening the Scope of Roughness," *Adv. Func. Mater.* **18**, 843-855.
- Nosonovsky, M. and Bhushan, B. (2008d), "Patterned Non-Adhesive Surfaces: Superhydrophobicity and Wetting Regime Transitions," *Langmuir* **24**, 1525-1533.
- Nosonovsky, M. and Bhushan, B. (2008e), "Do Hierarchical Mechanisms of Superhydrophobicity Lead to Self-Organized Criticality?," *Scripta Mater.* **59**, 941-944.
- Nosonovsky, M. and Bhushan, B. (2008f), "Energy Transitions in Superhydrophobicity: Low Adhesion, Easy Flow and Bouncing," *J. Phys.: Condens. Matter* **20**, 395005.
- Nosonovsky, M. and Bhushan, B. (2009), "Superhydrophobic Surfaces and Emerging Applications: Non-Adhesion, Energy, Green Engineering," *Curr. Opin. Colloid Interface Sci.* **14**, 270-280.
- Patankar, N. A. (2004), "Transition between Superhydrophobic States on Rough Surfaces" *Langmuir* **20**, 7097-7102.
- Pompe, T., Fery, A., and Herminghaus, S. (2000), "Measurement of Contact Line Tension by Analysis of the Three-Phase Boundary with Nanometer Resolution," in *Apparent and Microscopic Contact Angles* pp. 3-12 (Drelich, J., Laskowski, J.S., and Mittal, K.L., eds.) VSP, Utrecht.
- Quéré, D. (2005), "Non-Sticking Drops," *Rep. Prog. Phys.* **68**, 2495-2535.
- Sun, M., Luo, C., Xu, L., Ji, H., Ouyang, Q., Yu, D., and Chen, Y. (2005), "Artificial Lotus Leaf by Nanocasting," *Langmuir* **21**, 8978-8981.
- Tretinnikov, O. N. (2000), "Wettability and Microstructure of Polymer Surfaces: Stereochemical and Conformational Aspects" in *Apparent and Microscopic Contact Angles* pp. 111-128 (Drelich, J., Laskowski, J.S., and Mittal, K.L., eds.) VSP, Utrecht.
- Wenzel, R. N. (1936), "Resistance of Solid Surfaces to Wetting by Water," *Indust. Eng. Chem.* **28**, 988-994.

Chapter 4

Lotus Effect Surfaces in Nature

*brahmany adhaya karmani
sangam tyaktva karoti yah
lipyate na sa papena
padma-patram ivambhasa.*

Translation—One who performs his duty without attachment, surrendering the results unto the Supreme God, is not affected by sinful action, as the lotus leaf is untouched by water.

—Bhagwat Gita, Chapter 5 Text 10

4.1 Introduction

Many biological surfaces are known to be superhydrophobic and self-cleaning with low adhesion/low drag. The lotus leaf is the most studied leaf surface that exhibits superhydrophobicity and self-cleaning. Many such surfaces also exhibit antifouling properties. In this chapter, various plant leaves, their roughness, and wax coatings in relation to their hydrophobic/hydrophilic and self-cleaning properties (Bhushan and Jung 2011; Bhushan 2012) will be discussed. Surface characterization of hydrophobic and hydrophilic leaves on the micro- and nanoscale is presented to understand the role of microbumps and nanobumps. In addition, the contact angle and adhesion and friction properties of these leaves are considered. The knowledge gained by examining these properties of the leaves and by quantitatively analyzing the surface structure helps in the design of superhydrophobic and self-cleaning surfaces. Finally, various self-cleaning approaches are presented.

4.2 Plant Leaves

Hydrophobic and water-repellent abilities of many plant leaves have been long known. Scanning electron microscope (SEM) studies since the 1970s have revealed that the hydrophobicity of the leaf surface is related to its microstructure. The outer

cells covering a plant, especially the leaf, are called epidermis cells. The epidermis in all plant surfaces is covered by a thin extracellular membrane, called a cuticle. The plant cuticle is a composite material mainly built up of a cutin network and hydrophobic waxes (Barthlott and Neinhuis 1997; Koch et al. 2008, 2009a). The chemical structure of the epicuticular waxes has been studied extensively by plant scientists and lipid chemists (Baker 1982; Jetter et al. 2006). The epicuticular waxes can be thin with a 2-D structure, thicker with a 3-D structure, or a combination thereof. It is believed that waxes diffuse through the cuticle via a lipidic pathway, and after diffusion of the wax, the tubular or platelet type wax morphologies grow by crystallization or self-assembly (Koch et al. 2009c). The plants are able to repair the wax layer by self-assembly.

Neinhuis and Barthlott (1997) studied the surfaces and wetting properties of about 200 water-repellent plants; for comprehensive reviews, see Koch et al. (2008, 2009a). Among the epidermal relief features are the papillose epidermal cells with either every epidermal cell forming a single papilla or cells being divided into papillae. The scale of the epidermal relief features ranges from 5 μm in multi-papillate cells to 100 μm in large epidermal cells. Some cells also are convex (rather than having real papillae) and/or had hairs (trichomes). Various types and shapes of wax crystals are also found at the surface (Neinhuis and Barthlott 1997; Koch et al. 2008, 2009a). Interestingly, the hairy surfaces with a thin film of wax exhibited water-repellency for short periods (minutes), after which water penetrated between the hairs. Conversely, hairs with a thick film led to strong water-repellency. The wax crystal creates nanoroughness, in addition to the microroughness created by the papillae. Hierarchical roughness with microroughness superimposed with nanoroughness plays the dominant role in self-cleaning leaves.

The hydrophobicity of the leaves is related to another important effect: the ability to remain clean after being immersed in dirty water, known as self-cleaning. This ability is best known from the lotus (*Nelumbo nucifera*) leaf, which has been considered by Hindus and Buddhists as sacred due to its purity for some 2000 years. Not surprisingly, the self-cleaning and water repellent abilities of lotus-like surfaces was dubbed the “lotus effect”. As far as the biological implications of the lotus effect, self-cleaning plays an important role in the defense against pathogens binding to the leaf surface. Many spores and conidia of pathogenic organisms—most fungi—require water for germination and can infect leaves only in the presence of water. The lotus effect also provides antifouling for leaf surfaces.

SEM micrographs of a lotus leaf are shown in Fig. 4.1. The lotus leaf surface is covered by “bumps,” more exactly called papillae (papillose epidermal cells), which, in turn, are covered by an additional layer of three-dimensional epicuticular waxes (Barthlott and Neinhuis 1997). The wax is present in crystalline tubules, composed of a mixture of long-chain aliphatic compounds, principally nonacosanol and nonacosanediols (Koch et al. 2006, 2008, 2009a). The wax on the lotus leaf self-assembles as tubules, but on other leaves, waxes exist also in the form of platelets or other morphologies (Koch et al. 2008, 2009a). The wax is hydrophobic with a water contact angle of about 95° – 110° , and the hierarchical structure present

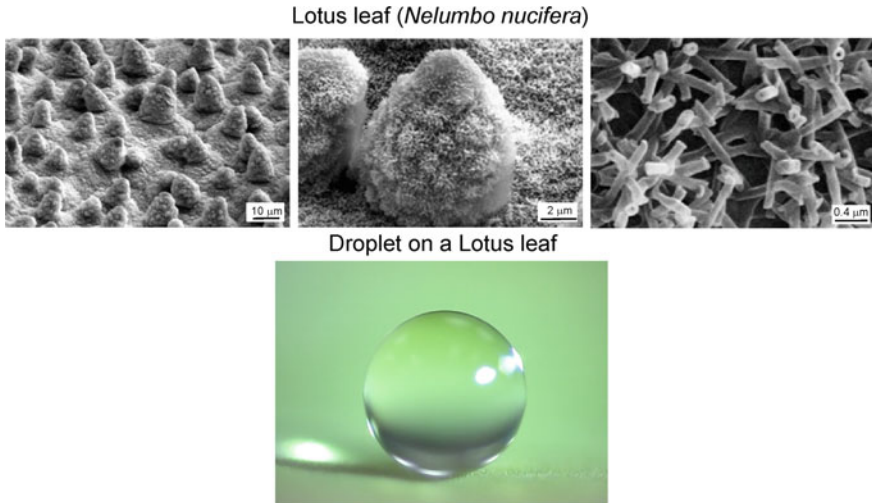
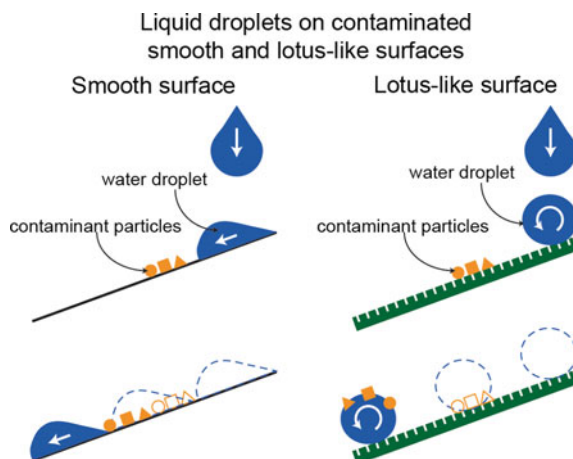


Fig. 4.1 SEM micrographs (shown at three magnifications) of a lotus (*Nelumbo nucifera*) leaf surface, consisting of microstructure formed by papillose epidermal cells covered with 3-D epicuticular wax tubules on surface, which create nanostructure, and an image of a water droplet sitting on a lotus leaf with a contact angle of about 164° (Bhushan et al. 2009a)

results in a high contact angle, making the surface superhydrophobic with a low contact angle hysteresis, based on the Wenzel and Cassie-Baxter models discussed in the preceding chapter. The experimental value of the static water contact angle with the lotus leaf was reported to be about 164° and a contact angle hysteresis of 3° (Bhushan et al. 2009a; Koch et al. 2009b). Taking the papillae density of 3400 per square millimeter, the average radius of the hemispherical asperities equal to $10\ \mu\text{m}$, and the aspect ratio (height/radius) equal to 1, provides the value of the roughness factor $R_f \approx 4$ based on Wenzel's equation (Nosonovsky and Bhushan 2005). Taking the value of the contact angle for wax, $\theta_0 = 104^\circ$ (Kamusewitz et al. 1999), the calculation with the Wenzel equation yields $\theta = 165^\circ$, which is close to the experimentally observed values (Nosonovsky and Bhushan 2005). However, the simple Wenzel model is not sufficient to explain the lotus effect, as the roughness structure forms a composite interface, represented by the Cassie-Baxter equation. Moreover, its structure has hierarchical roughness and models have been developed to study the role of hierarchical roughness on contact angle (Nosonovsky and Bhushan 2008).

The self-cleaning ability of the lotus leaf is derived from the low contact angle hysteresis or a tilt angle of about 3° with low adhesion/drag. A qualitative explanation for self-cleaning is that on a smooth surface, the droplet slides on the surface and contaminant particles are mainly redistributed by the sliding droplet. Conversely, on a rough, lotus-like surface, contaminant particles adhere to the droplet and are removed from the surface when the droplet rolls off because of low adhesion/drag, Fig. 4.2.

Fig. 4.2 Schematic showing a droplet sliding on a smooth surface, leading to redistribution of contaminant particles, and a droplet rolling on a lotus-like surface with low contact angle hysteresis and low adhesion/drag, removing contaminant particles from the leaf surface



4.3 Characterization of Superhydrophobic and Hydrophilic Leaf Surfaces

In order to understand the mechanisms of hydrophobicity in plant leaves, a comprehensive comparative study of various superhydrophobic and hydrophilic leaf surfaces and their properties was carried out by Bhushan and Jung (2006) and Burton and Bhushan (2006). Below is a discussion of the findings of the study.

4.3.1 *Experimental Techniques*

The static contact angles were measured using a Rame-Hart model 100 contact angle goniometer with droplets of deionized (DI) water (Bhushan and Jung 2006; Burton and Bhushan 2006). Droplets of about 5 μL in volume (with diameter of a spherical droplet about 2.1 mm) were gently deposited on the substrate using a microsyringe for the static contact angle. All measurements were made at five different points for each sample at 22 ± 1 $^{\circ}\text{C}$ and 50 ± 5 % relative humidity (RH). The measurement results were reproducible within $\pm 3^{\circ}$.

An optical profiler was used to measure surface roughness for different surface structures (Bhushan and Jung 2006; Burton and Bhushan 2006). A greater Z-range of the optical profiler of 2 mm is a distinct advantage over the surface roughness measurements with an atomic force microscope (AFM), which has a Z-range on the order of 7 μm , but an AFM has only a maximum lateral resolution of approximately 0.6 μm (Bhushan 2013a, b). A commercial AFM was used for additional surface roughness measurements with a high lateral resolution (sub nm) and for adhesion and friction measurements (Burton and Bhushan 2005; Bhushan and Jung 2006). The measurements for surface roughness were performed in the tapping mode with

a square pyramidal Si(100) tip with a native oxide layer, which had a nominal radius of 20 nm, on a rectangular Si(100) cantilever with a spring constant of 3 N m^{-1} .

Adhesion and friction force at various relative RH were measured using a $15 \mu\text{m}$ radius borosilicate ball (Bhushan 2011, 2013a, b). A large tip radius was used to measure contributions from several microbumps and a large number of nanobumps. Friction force was measured under a normal load ranging from 20 to 250 nN using a 90° scan angle. It was measured at a velocity of $100 \mu\text{m/s}$ in a $50 \mu\text{m}$ scan and at a velocity of $4 \mu\text{m/s}$ in a $2 \mu\text{m}$ scan. The quantitative measurement of friction force was calibrated by the method described by Bhushan (2011). The normal load was varied (20–250 nN), and a friction force measurement was taken at each increment. By plotting the friction force as a function of normal load, an average coefficient of friction was obtained from the slope of the fit line of the data. The adhesive force was measured using the force distance curve approach. In this technique, the AFM tip is brought into contact with the sample by extending the piezo vertically, then retracting the piezo and calculating the force required to separate the tip from the sample. The adhesive force is obtained by multiplying the cantilever spring constant with the cantilever deflection during the retraction between zero value and the maximum negative value. The method is described in detail by Bhushan (2011, 2013a, b).

4.3.2 SEM Micrographs

Figure 4.3 shows the SEM micrographs of two superhydrophobic leaves and two hydrophilic leaves. The two superhydrophobic leaves are the lotus (*N. nucifera*) and the elephant ear or taro plant (*Colocasia esculenta*), referred to as lotus and colocasia, respectively. The two hydrophilic leaves are the beech (*Fagus sylvatica*) and Magnolia (*Magnolia grandiflora*), referred to as fagus and magnolia, respectively (Bhushan and Jung 2006). Lotus and colocasia are characterized by papillose epidermal cells responsible for the creation of papillae or microbumps on the surfaces, and an additional layer of 3-D epicuticular waxes. These waxes are a mixture of very long chain fatty acids molecules (compounds with chains >20 carbon atoms) and create nanostructure on the entire surface. Fagus and magnolia are characterized to be rather flat, tabular cells with a thin wax film with a 2-D structure (Barthlott and Neinhuis 1997). The leaves don't repel water, are not self-cleaning, and contaminant particles from ambient conditions are accumulated.

4.3.3 Contact Angle Measurements

Figure 4.4a shows the contact angles for the superhydrophobic and hydrophilic leaves before and after applying acetone. The acetone was applied in order to

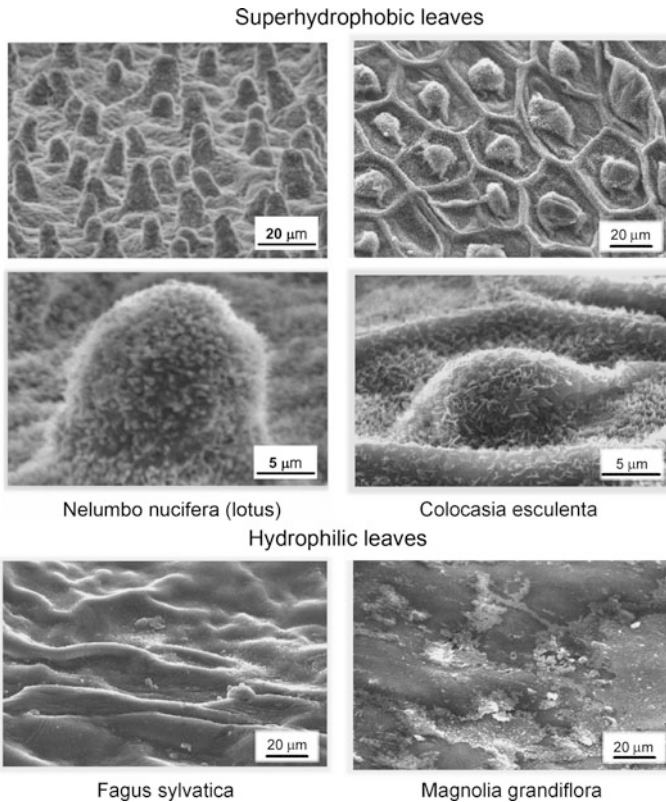
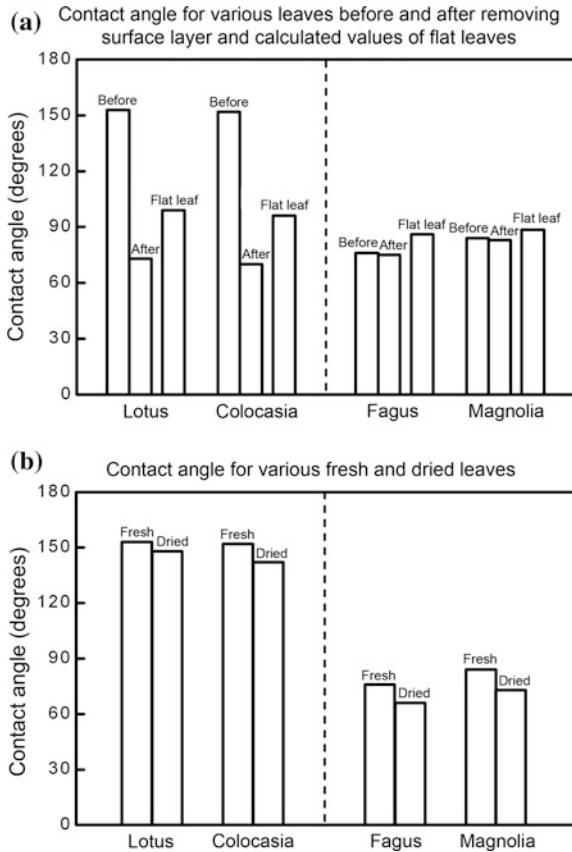


Fig. 4.3 Scanning electron micrographs of the relatively rough, water-repellent leaf surfaces of *Nelumbo nucifera* (lotus) and *C. esculenta* and the relatively smooth, wettable leaf surfaces of *F. sylvatica* and *M. grandiflora* (Bhushan and Jung 2006)

remove any wax present on the surface. As a result, for the superhydrophobic leaves, the contact angle dramatically reduced, whereas for the hydrophilic leaves, the contact angle was almost unchanged. It is known that there is a very thin 2-D wax layer on the hydrophilic leaves, which introduces little roughness. In contrast, superhydrophobic leaves are known to have a 3-D wax layer on their surface consisting of nanoscale roughness over microroughness created by the papillae, which results in a hierarchical roughness. The combination of this wax and the roughness of the leaf creates a superhydrophobic surface.

Bhushan and Jung (2006) calculated the contact angles for leaves with smooth surfaces using the Wenzel equation and the calculated R_f and the contact angle of the four leaves. The results are presented in Fig. 4.4a. The approximate values of R_f for lotus and colocasia are 5.6 and 8.4 and for fagus and magnolia are 3.4 and 3.8, respectively. Based on the calculations, the contact angles on smooth surfaces were approximately 99° for lotus and 96° for colocasia. For both fagus and magnolia, the

Fig. 4.4 Contact angle measurements and calculations for the leaf surfaces, **a** before and after removing the surface layer as well as calculated values, and **b** fresh and dried leaves. The contact angle on a smooth surface for the four leaves was obtained using the roughness factor calculated (Bhushan and Jung 2006)



contact angles for the smooth surfaces were found to be approximately 86° and 88° . A further discussion on the effect of R_f on the contact angle will be presented later.

Figure 4.4b shows the contact angles for both fresh and dried states for the four leaves. There is a decrease in the contact angle for all four leaves when they are dried. For lotus and colocasia, this decrease is present because it is found that a fresh leaf has taller bumps than a dried leaf (data to be presented later), which will give a larger contact angle according to the Wenzel equation. When the surface area is at a maximum compared to the footprint area, as with a fresh leaf, the roughness factor will be at a maximum and will only reduce when shrinking has occurred after drying. To understand the reason for the decrease of contact angle after drying of hydrophilic leaves, dried Magnolia leaves were also measured using an AFM. It is found that the dried leaf (peak-valley (P-V) height = $7 \mu\text{m}$, mid-width = $15 \mu\text{m}$, and peak radius = $18 \mu\text{m}$) has taller bumps than a fresh leaf (P-V height = $3 \mu\text{m}$, mid-width = $12 \mu\text{m}$, and peak radius = $15 \mu\text{m}$), which increases the roughness, and the contact angle decreases, leading to a more hydrophilic surface. The mid-width is defined as the width of the bump at a height equal to half of the peak to mean line value.

4.3.4 Surface Characterization Using an Optical Profiler

The use of an optical profiler allows measurements to be made on fresh leaves, which have a large P-V distance. Three different surface height maps for superhydrophobic and hydrophilic leaves are shown in Figs. 4.5 and 4.6 (Bhushan and Jung 2006). In each figure, a 3-D map and a flat map along with a 2-D profile in a given location of the flat 3-D map are shown. A scan size of $60 \times 50 \mu\text{m}$ was used to obtain a sufficient amount of bumps to characterize the surface but also to maintain enough resolution to get an accurate measurement.

The structures found with the optical profiler correlate well with the SEM images shown in Fig. 4.3. The bumps on the lotus leaf are distributed on the entire surface, but the colocasia leaf shows a very different structure to that of the lotus. The surface structure for colocasia not only has bumps similar to lotus, but surrounding each bump there is also a ridge that keeps the bumps separated. With these ridges, the bumps have a hexagonal (honeycomb) packing geometry that allows for the maximum number of bumps in a given area. The bumps of lotus and both bumps and ridges of colocasia contribute to the superhydrophobic nature, since they both increase the R_f factor and result in air pockets between the droplet of water and the surface. In fagus and magnolia height maps, short bumps can be seen on the surface. This means that with decreased bump height, the probability of air pocket formation decreases, and bumps have a less beneficial effect on the contact angle.

As shown in 2-D profiles of superhydrophobic and hydrophilic leaves in Figs. 4.5 and 4.6, a curve has been fitted to each profile to calculate dimensions of

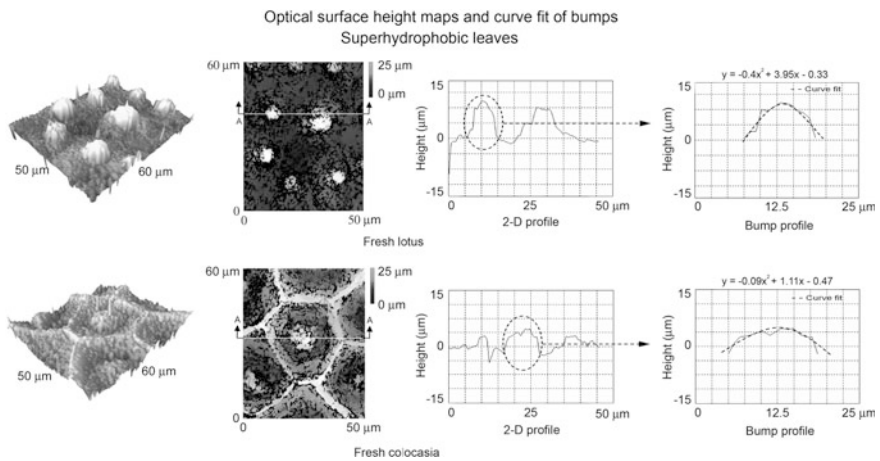


Fig. 4.5 Surface height maps and 2-D profiles of superhydrophobic leaves using an optical profiler. For lotus leaf, a microbump is defined as a single, independent microstructure protruding from the surface. For colocasia leaf, a microbump is defined as the single, independent protrusion from the leaf surface, whereas a ridge is defined as the structure that surrounds each bump and is completely interconnected on the leaf. A curve has been fitted to each profile to calculate dimensions of the bump. The radius of curvature is calculated from the parabolic curve fit of the bump (Bhushan and Jung 2006)

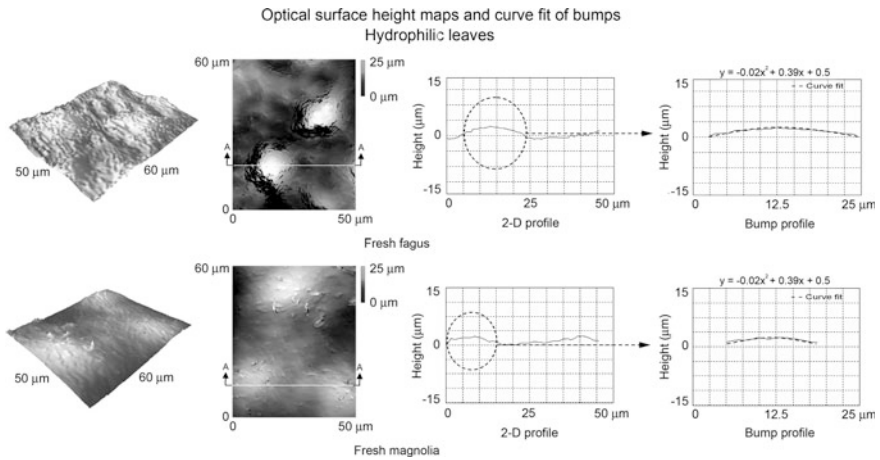


Fig. 4.6 Surface height maps and 2-D profiles of hydrophilic leaves using an optical profiler. For fagus and magnolia leaves, a microbump is defined as a single, independent microstructure protruding from the surface. A curve has been fitted to each profile to calculate dimensions of the bump. The radius of curvature is calculated from the parabolic curve fit of the bump (Bhushan and Jung 2006)

the bump. For each leaf, a second order curve fit has been given to the profiles to show how closely the profile is followed. By using the second order curve fitting of the profiles, the radius of curvature can be found (Bhushan and Jung 2006; Burton and Bhushan 2006).

Using these optical surface height maps, different statistical parameters of bumps and ridges can be found to characterize the surface: P-V height, mid-width, and peak radius (Bhushan 2013a, b). Table 4.1 shows these quantities found in the optical height maps for the four leaves. Comparing the superhydrophobic and hydrophilic leaves, it can be seen that the P-V height for the bumps of lotus and colocasia is much taller than that for the bumps of fagus and magnolia. The peak radius for the bumps of lotus and colocasia is also smaller than that for the bumps of fagus and magnolia. However, the values of mid-width for the bumps of the four leaves are similar.

4.3.5 Surface Characterization, Adhesion, and Friction Using an AFM

4.3.5.1 Comparison of Two AFM Measurement Techniques

To measure topographic images of the leaf surfaces, both the contact and tapping modes were first used (Bhushan and Jung 2006). Figure 4.7 shows surface height maps of dried lotus obtained using the two techniques. In the contact mode, local

Table 4.1 Microbump and nanobump map statistics for superhydrophobic and hydrophilic leaves, measured both fresh and dried using an optical profiler and AFM (Bhushan and Jung 2006)

Leaf	Microbump			Nanobump			
	Scan size (50 × 50 μm)			Scan size (2 × 2 μm)			
	P-V height (μm)	Mid-width (μm)	Peak radius (μm)	P-V height (μm)	Mid-width (μm)	Peak radius (μm)	
<i>Lotus</i>							
Fresh	13 ^a	10 ^a	3 ^a	0.78 ^b	0.40 ^b	0.15 ^b	
Dried	9 ^b	10 ^b	4 ^b	0.67 ^b	0.25 ^b	0.10 ^b	
<i>Colocasia</i>							
Fresh	Bump	9 ^a	15 ^a	5 ^a	0.53 ^b	0.25 ^b	0.07 ^b
	Ridge	8 ^a	7 ^a	4 ^a	0.68 ^b	0.30 ^b	0.12 ^b
Dried	Bump	5 ^b	15 ^b	7 ^b	0.48 ^b	0.20 ^b	0.06 ^b
	Ridge	4 ^b	8 ^b	4 ^b	0.57 ^b	0.25 ^b	0.11 ^b
<i>Fagus</i>							
Fresh	5 ^a	10 ^a	15 ^a	0.18 ^b	0.04 ^b	0.01 ^b	
	4 ^b	5 ^b	10 ^b				
<i>Magnolia</i>							
Fresh	4 ^a	13 ^a	17 ^a	0.07 ^b	0.05 ^b	0.04 ^b	
	3 ^b	12 ^b	15 ^b				

^aData measured using optical profiler^bData measured using AFM

height variation for a lotus leaf was observed in a 50 μm scan size. However, little height variation was obtained in a 2 μm scan, even at loads as low as 2 nN. This could be due to the substantial frictional force generated as the probe scanned over the sample. Frictional force can damage the sample. The tapping mode technique allows high-resolution topographic imaging of sample surfaces that are easily damaged, loosely held to their substrate, or difficult to image by other AFM techniques (Bhushan 2013a, b). As shown in Fig. 4.7, with the tapping mode technique, the soft and fragile leaves were imaged successfully. Therefore, the tapping mode technique was used to examine the surface roughness of the superhydrophobic and hydrophilic leaves using an AFM.

4.3.5.2 Surface Characterization

The AFM has a Z-range on the order of 7 μm and cannot be used for measurements in a conventional way because of the high P-V distances of a lotus leaf. Burton and Bhushan (2006) developed a new method to fully determine the bump profiles. In order to compensate for the large P-V distance, two scans were made for each height: one measurement that scans the tops of the bumps and another measurement that scans the bottom or valleys of the bumps. The total height of the bumps is

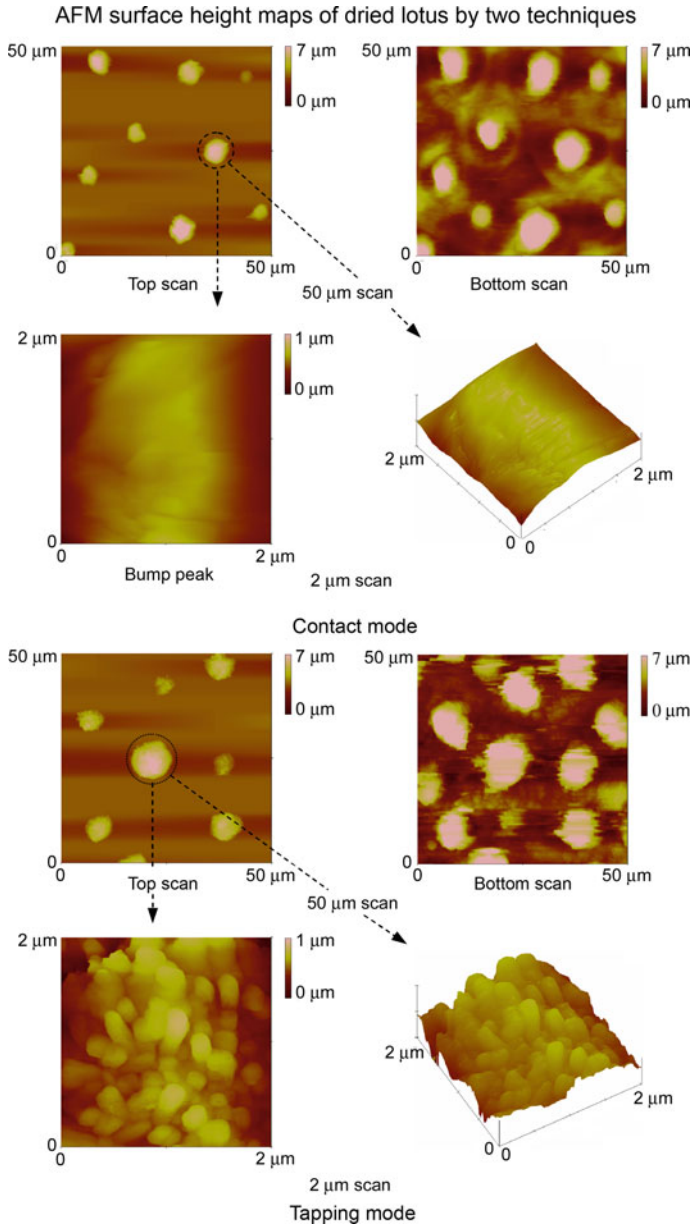


Fig. 4.7 Surface height maps showing the top scan and bottom scan in a 50 μm scan size and the bump peak scan selected in a 2 μm scan size for a lotus leaf using an AFM in contact mode and tapping mode. Two methods were used to determine a suitable method to obtain high resolution of nanotopography for a lotus leaf (Bhushan and Jung 2006)

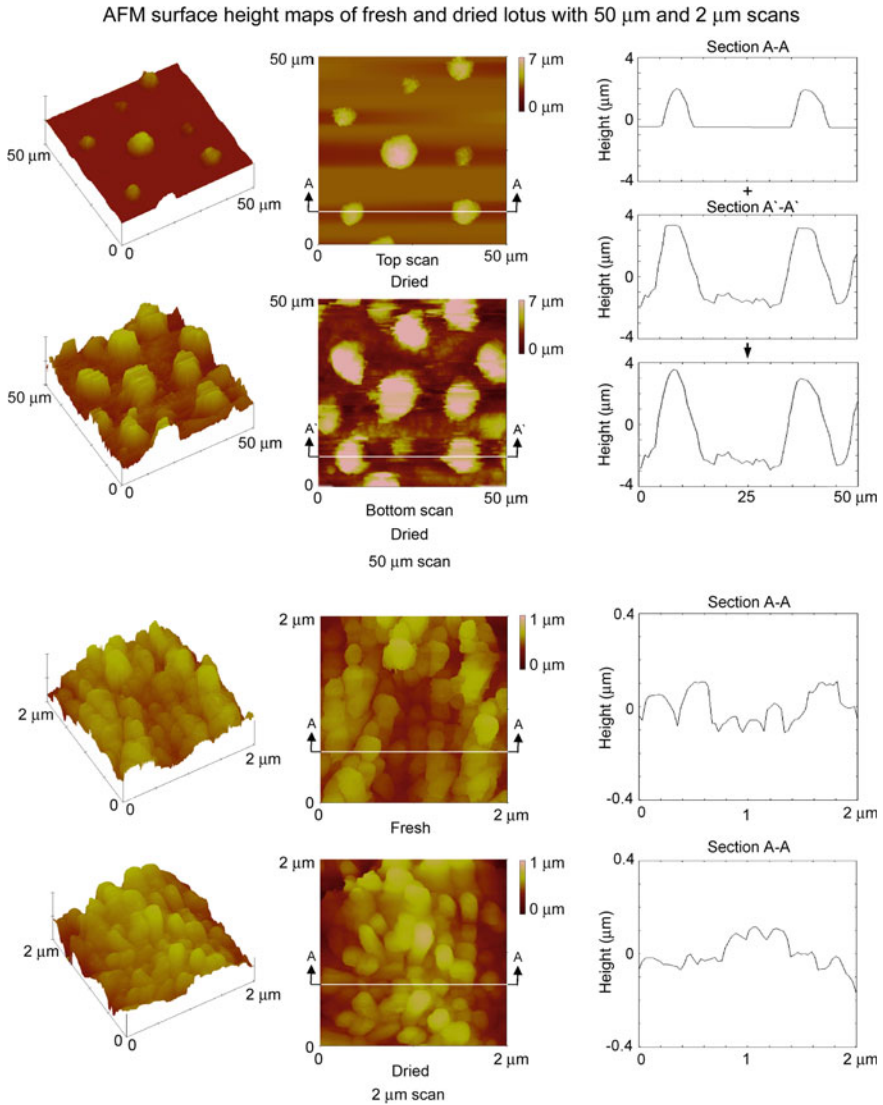


Fig. 4.8 Surface height maps and 2-D profiles showing the top scan and bottom scan of a dried lotus leaf in 50 μm scan (because the P-V distance of a dried lotus leaf is greater than the Z-range of an AFM), and the top scan of both fresh and dried lotus in a 2 μm scan (Bhushan and Jung 2006). A splicing technique was used to determine the bump profiles. In order to compensate for the large P-V distance, the total height of the bumps is embedded within the top scan and bottom scan

embedded within the two scans. Figure 4.8 shows the 50 μm surface height maps obtained using this method (Bhushan and Jung 2006). The 2-D profiles in the right column take the profiles from the top scan and the bottom scan for each scan size

and splice them together to get the total profile of the leaf. The 2 μm surface height maps for both fresh and dried lotus can also be seen in Fig. 4.8. This scan area was selected on the top of a microbump obtained in the 50 μm surface height map. It can be seen that nanobumps are randomly and densely distributed on the entire surface of the lotus leaf.

Bhushan and Jung (2006) also measured the surface height maps for hydrophilic leaves in both 50 and 2 μm scan sizes as shown in Fig. 4.9. For fagus and magnolia,

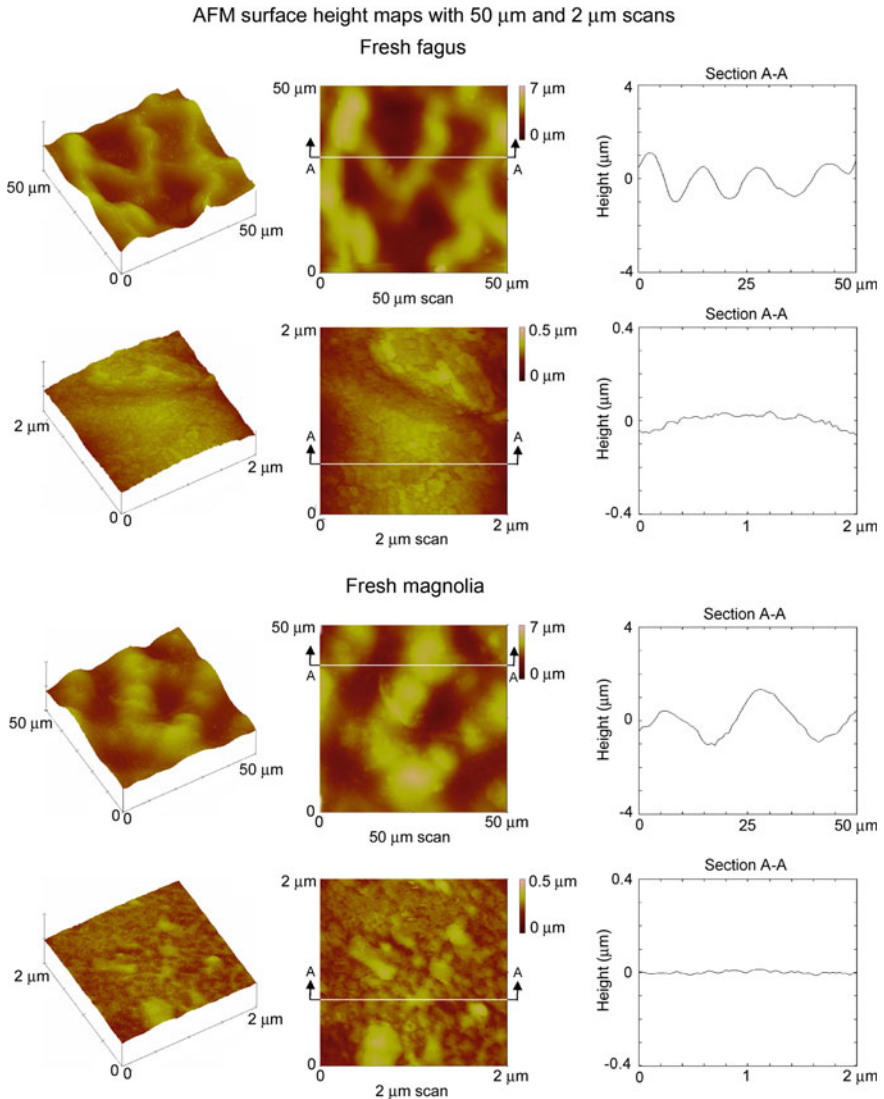


Fig. 4.9 Surface height maps and 2-D profiles of fagus and magnolia using an AFM in both 50 μm and 2 μm scans (Bhushan and Jung 2006)

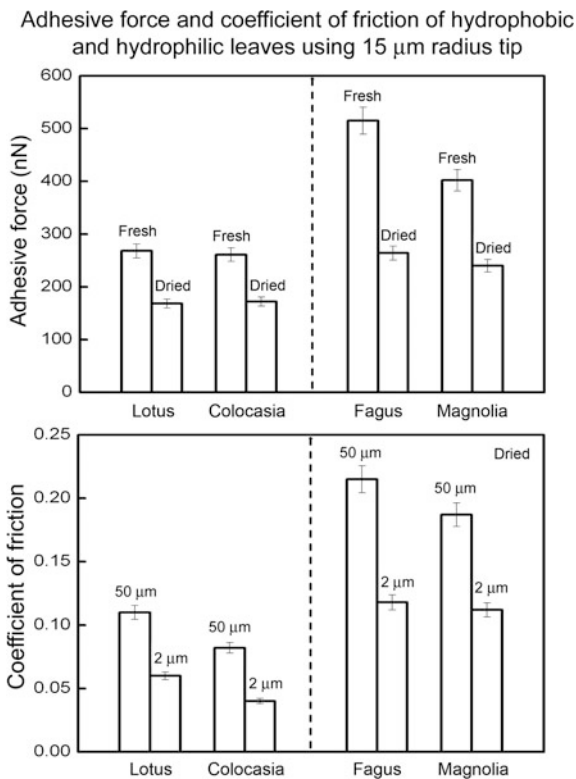
microbumps were found on the surface, and the P-V distance of these leaves is lower than that of lotus and colocasia. It can be seen in the 2 μm surface height maps that nanobumps selected on the peak of the microbump have an extremely low P-V distance.

Using the AFM surface height maps, different statistical parameters of bumps and ridges can be obtained: P-V height, mid-width, and peak radius. These quantities for the four leaves are listed in Table 4.1. It can be seen that the values correlate well with the values obtained from optical profiler scans except for the bump height, which decreased by more than half because of leaf shrinkage.

4.3.5.3 Adhesive Force and Friction

Adhesive force and the coefficients of friction of superhydrophobic and hydrophilic leaves obtained using an AFM are presented in Fig. 4.10 (Bhushan and Jung 2006). For each type of leaf, adhesive force measurements were made for both fresh and dried leaves using a 15 μm radius tip. It was found that the dried leaves had a lower adhesive force than the fresh leaves. Adhesive force arises from several sources in changing the presence of a thin liquid film, such as an adsorbed water layer that

Fig. 4.10 Adhesive force for fresh and dried leaves, and the coefficient of friction for dried leaves for 50 and 2 μm scan sizes for hydrophobic and hydrophilic leaves. All measurements were made using an AFM with 15 μm radius borosilicate tip. Reproducibility for both adhesive force and coefficient of friction is $\pm 5\%$ for all measurements (Bhushan and Jung 2006)



causes meniscus bridges to build up around the contacting and near contacting bumps as a result of surface energy effects (Bhushan 2013a, b). When the leaves are fresh, there is moisture within the plant material that causes the leaf to be soft. When the tip comes into contact with the fresh leaf sample, the sample will deform, a larger real area of contact between the tip and sample will occur, and the adhesive force will increase. After the leaf has dried, the moisture that was in the plant material is gone, and there is not as much deformation of the leaf when the tip comes into contact with the leaf sample. Hence, the adhesive force is decreased because the real area of contact has decreased.

The adhesive force of fagus and magnolia is higher than that of lotus and colocasia because the real area of contact between the tip and leaf surface is expected to be higher in hydrophilic leaves than in superhydrophobic leaves. Fagus and magnolia are hydrophilic, and thus, have a high affinity to water. The combination of a large real area of contact and an affinity to water are responsible for higher meniscus forces (Bhushan 2013a, b). The coefficient of friction was only measured on a dried plant surface using the same sliding velocity (10 $\mu\text{m/s}$) in different scan sizes. Fresh surfaces were not included because their P-V was too large to scan back and forth with the AFM to obtain friction force. As expected, the coefficient of friction for superhydrophobic leaves is lower than that for hydrophilic leaves due to the real area of contact between the tip and leaf sample, similar to the adhesive force results. When the scan size decreases from microscale to nanoscale, the coefficient of friction also decreases in each leaf. The reason for such dependence is the scale dependent nature of the roughness of the leaf surface. Figures 4.8 and 4.9 show AFM topography images and 2-D profiles of the surfaces for different scan sizes. The scan size dependence of the coefficient of friction has been reported previously (Poon and Bhushan 1995; Koinkar and Bhushan 1997; Tambe and Bhushan 2004).

4.3.6 *Role of the Hierarchical Roughness*

The approximation of the roughness factor for the leaves on the micro- and nanoscale was made using AFM scan data (Bhushan and Jung 2006). Roughness factors for various leaves are presented in Table 4.2. As mentioned earlier, the open space between asperities on a surface has the potential to collect air, and its probability appears to be higher in nanobumps as the distance between bumps in the nanoscale is smaller than those in the microscale. The contact angle (θ_0) for smooth surfaces can be calculated using roughness factor values and contact angles (θ) from both superhydrophobic and hydrophilic surfaces, 153° and 152° in lotus and colocasia, and 76° and 84° in fagus and magnolia, respectively. The Wenzel equation (Chap. 3) is used for microbumps and the Cassie-Baxter equation (Chap. 3) for nanobumps. The contact angle ($\Delta\theta$) calculated using R_f on the smooth surface can be found in Table 4.2. It can be seen that the roughness factors and the differences

Table 4.2 Roughness factor and contact angle ($\Delta\theta = \theta - \theta_0$) calculated using R_f on the smooth surface for hydrophobic and hydrophilic leaves measured using an AFM, both microscale and nanoscale (Bhushan and Jung 2006)

Leaf (contact angle)	Scan size	State	R_f	$\Delta\theta$ ($^\circ$)
Lotus (153 $^\circ$)	50 μm	Dried	5.6	54 ^a
	2 μm	Fresh	20	61 ^b
		Dried	16	60 ^b
Colocasia (152 $^\circ$)	50 μm	Dried	8.4	56 ^a
	2 μm bump	Fresh	18	60 ^b
		Dried	14	59 ^b
	2 μm ridge	Fresh	18	60 ^b
		Dried	15	59 ^b
	Fagus (76 $^\circ$)	50 μm	Fresh	3.4
50 μm		Fresh	5.3	2 ^b
Magnolia (84 $^\circ$)	50 μm	Fresh	3.8	-4 ^a
	2 μm	Fresh	3.6	14 ^b

^aCalculations made using Wenzel equation

^bCalculations made using Cassie–Baxter equation. It is assumed that the contact area between the droplet and air is the half of the whole area of the rough surface

($\Delta\theta$) between θ and θ_0 on the nanoscale are higher than those on the microscale. This means that nanobumps on the top of a microbump increase contact angle more effectively than microbumps alone. In the case of hydrophilic leaves, the values of R_f and $\Delta\theta$ change very little on both scales.

Based on the data in Fig. 4.10, the coefficient of friction values on the nanoscale are much lower than those on the microscale. It is observed that friction values are scale dependent. The height of a bump and the distance between bumps on the microscale is much larger than those on the nanoscale, which may be responsible for larger values of friction force on the microscale.

One difference between microbumps and nanobumps for surface enhancement of water repellency is the effect on contact angle hysteresis, which is the ease with which a droplet of water can roll on the surface. It has been stated earlier that contact angle hysteresis decreases and contact angle increases due to the decreased contact with the solid surface caused by the air pockets beneath the droplet. The surface with nanobumps has a high roughness factor compared with that of microbumps. With large distances between microbumps, the probability of air pocket formation decreases and is responsible for high contact angle hysteresis. Therefore, on the surface with nanobumps, the contact angle is high and contact angle hysteresis is low. Drops rebound easily and can begin to roll motion with a small tilt angle (Bhushan and Jung 2006).

Natural water-repellent and self-cleaning surfaces, such as the lotus leaf (Koch et al. 2008, 2009a) or water strider leg (Gao and Jiang 2004), have a hierarchical structure. However, the functionality of this hierarchical roughness remains a subject of discussion, and several explanations have been suggested. Nosonovsky and Bhushan (2008) showed that the mechanisms involved in superhydrophobicity

are scale dependent, and thus, the roughness must be hierarchical in order to respond to these mechanisms. The surface must be able to repel both macroscopic and microscopic droplets. Fürstner et al. (2005) pointed out that artificial surfaces with one level of roughness can well repel large “artificial rain” droplets, but they cannot repel small “artificial fog” droplets trapped in the valleys between the bumps. Thus, the hierarchy may have to do with the ability to repel droplets of various size ranges. According to Gao and McCarthy (2006), large bumps allow a surface to maintain a composite interface, while small ones enhance the contact angle in accordance with the Wenzel model. Jung and Bhushan (2008) showed that a droplet with a radius of about 100–400 μm on a micropatterned surface goes through transition from the composite interface to the solid-liquid interface as the pitch increases. Bhushan et al. (2008, 2009b, c) showed that hierarchical structure can prevent the gaps between the pillars from filling with liquid until the droplet evaporated completely.

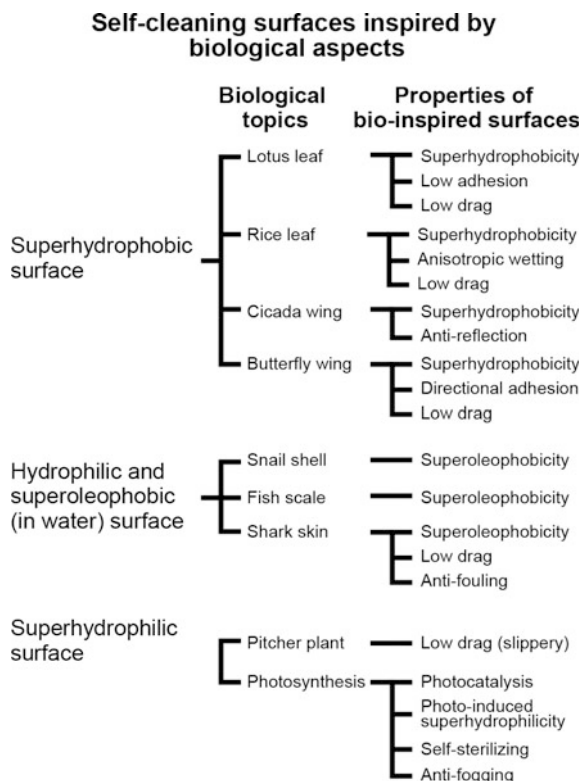
4.3.7 Summary

Various leaf surfaces on the micro- and nanoscale have been characterized, and attempts are made to separate out the effect of micro- and nanobumps and epicuticular wax on hydrophobicity. For the superhydrophobic lotus and colocasia leaves, the leaf surface consists of microbumps formed by convex papilla epidermal cells covered with a 3-D epicuticular wax (crystalline tubules composed of a mixture of secondary alcohol nonacosan-10-01 and nonacosanedoils), which self-assemble as nanotubules. A hierarchical surface and the presence of wax creates a superhydrophobic and self-cleaning surface with low adhesion and antifouling. Hydrophilic fagus and magnolia have rather flat tabular cells with a 2-D thin wax film (not continuous) on the surface.

4.4 Various Self-cleaning Approaches

In addition to the lotus effect approach for self-cleaning, other self-cleaning approaches have been developed (Nishimoto and Bhushan 2013). The self-cleaning surfaces can be divided into three wettability regimes: superhydrophobicity, superoleophobicity, and superhydrophilicity. An overview of nine examples from living nature is provided in Fig. 4.11: lotus leaves, rice leaves, cicada wings, butterfly wings, snail shell, fish scale, shark skin, pitcher plant, and photosynthesis. An example of a photosynthesis-inspired self-cleaning surface is a TiO_2 photocatalyst coated surface, which has been developed by mimicking the photosynthesis process of green leaves.

Fig. 4.11 Overview of self-cleaning surfaces inspired by biological objects (adapted from Nishimoto and Bhushan 2013)

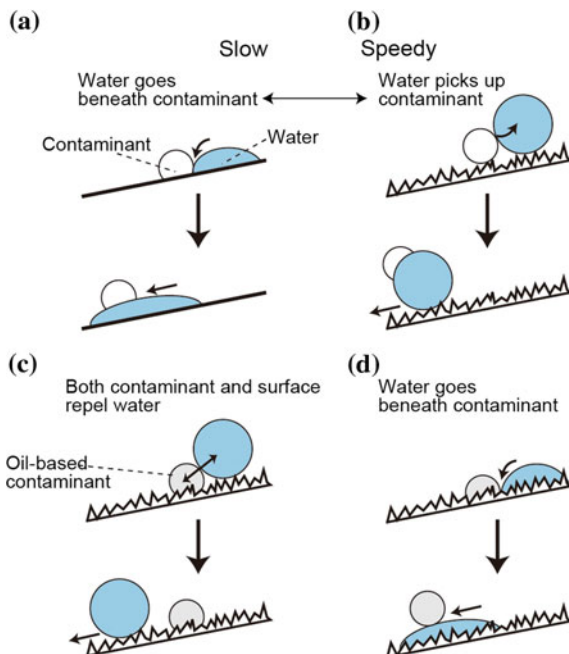


4.4.1 Comparison Between Superhydrophobic and Superhydrophilic Surface Approaches for Self-cleaning

Several types of self-cleaning surfaces have been developed for practical applications. In particular, two types of surfaces, i.e. superhydrophobic surface (lotus) and superhydrophilic surfaces (TiO_2 photocatalyst), are notably important (Nishimoto and Bhushan 2013). We briefly describe the comparison between superhydrophobic and superhydrophilic surface approaches.

Nishimoto and Bhushan (2013) presented a comparison of the self-cleaning processes on superhydrophilic, superhydrophobic, and hydrophilic and superoleophobic surfaces, as shown in Fig. 4.12. On the superhydrophilic surface shown in Fig. 4.12a, the water droplets go beneath the contaminant and wash it away. Water on this surface spreads quickly creating no streaks. The thin film of water produced on the surface may evaporate rapidly. Water film moves the contaminants out during spreading. However, the surface may remain wet for a longer period in this

Fig. 4.12 Schematic illustrations of self-cleaning processes on **a** superhydrophilic surface, **b** superhydrophobic surface, **c** superhydrophobic surface with oil-based contaminant, and **d** hydrophilic and superoleophobic (in water) surface with oil-based contaminant (adapted from Nishimoto and Bhushan 2013)



case, as compared to that for superhydrophobic surfaces, which may be undesirable in some applications.

On the superhydrophobic surface shown in Fig. 4.12b, water is repelled from the surface and water droplets may roll off the surface taking contaminant particles with them. In this case, considering low adhesion of superhydrophobic surfaces, it would seem that higher self-cleaning efficiency would be obtained with a superhydrophobic surface than a superhydrophilic one.

On the superhydrophobic surface with oil-based contaminant shown in Fig. 4.12c, because both the contaminants and the superhydrophobic surface repel the water droplet, the contaminants cannot be removed by the water droplet. On the other hand, as shown in Fig. 4.12a, the oil-based contaminants, such as printing ink, can be washed away on a superhydrophilic surface. Nishimoto et al. (2009) observed that the oil-based ink that was adhered to the superhydrophilic area on the superhydrophobic-superhydrophilic pattern could be easily removed by water supply, while the ink was stable on the superhydrophobic area. The water droplets can go beneath an oil-based contaminant on the superhydrophilic surfaces, raise it up, and wash it away. It should be noted that most hydrophilic surfaces exhibit oleophobicity in water.

On the hydrophilic and superoleophobic (in water) surfaces shown in Fig. 4.12d, an oil-based contaminant could be efficiently washed away. Due to the superoleophobicity in water, the water droplets efficiently go beneath an oil-based

contaminant and raise it up. However, the hydrophilic and superoleophobic (in water) surfaces may suffer from hydrophilic contaminants, because a certain amount of water would be necessary to wash the contaminants away.

It should be noted that the superhydrophobic and superhydrophilic surfaces have different surface roughnesses. For a surface to be superhydrophobic, the surface should have some roughness. On the other hand, a TiO_2 photocatalyst surface becomes superhydrophilic even if the surface is quite smooth. A superhydrophilic flat surface has the advantage of protecting the surface from contamination, and may compensate in some degree for its high adhesion as compared with a superhydrophobic surface.

Because of the differences in the self-cleaning mechanisms between the two surfaces, the self-cleaning effect for each would depend on the environment in which the surface is used, e.g. rainfall level, contaminant species, and amounts. There are some parameters to be compared for practical applications. For example, in the use of the TiO_2 photocatalyst, UV light is necessary, which would be the most significant drawback of this material. Furthermore, since the TiO_2 photocatalyst decomposes most organic materials, special care is necessary for the coating if it is used with the organic materials. However, the photocatalytic oxidation activity offers additional benefits such as self-sterilizing property. The durability of the smooth TiO_2 photocatalyst coating may be superior to that of the rough superhydrophobic coatings. However, recent studies show that superhydrophobic coatings also can be fabricated with high durability.

4.4.2 Summary

Superhydrophobic and superhydrophilic surfaces are commonly considered for self-cleaning properties. Both surfaces exhibit efficient self-cleaning properties in their own manner, and have been developed for practical applications. In addition to superhydrophobicity and superhydrophilicity, superoleophobicity is also a promising characteristic for self-cleaning surfaces, which can be easily achieved in hydrophilic surfaces in water. Moreover, anisotropic wetting, low drag, anti-fouling, slippery surfaces, and photocatalytic oxidation activity play an important role for the self-cleaning effect.

4.5 Closure

The lotus effect results in surfaces that are superhydrophobic and self-cleaning with low adhesion/drag. Various biological surfaces found in living nature that exhibit this effect are presented, with a focus on the lotus leaf. Finally, various self-cleaning approaches using superhydrophobic and superhydrophilic surfaces are presented.

References

- Baker, E. A. (1982), "Chemistry and Morphology of Plant Epicuticular Waxes," in *The Plant Cuticle*, (Cutler, D. F., Alvin, K. L., and Price, C. E., Eds.), Academic Press, London, pp. 139-165.
- Barthlott, W. and Neinhuis, C. (1997), "Purity of the Sacred Lotus, or Escape from Contamination in Biological Surfaces," *Planta* **202**, 1-8.
- Bhushan B. (2011), *Nanotribology and Nanomechanics I – Measurement Techniques, II – Nanotribology, Biomimetics, and Industrial Applications*, third ed., Springer-Verlag, Heidelberg, Germany.
- Bhushan, B. (2012) Bioinspired Structured Surfaces," *Langmuir* **28**, 1698-1714.
- Bhushan, B. (2013a), *Principles and Applications of Tribology, 2nd Ed.*, Wiley, New York.
- Bhushan, B. (2013b), *Introduction to Tribology, 2nd Ed.*, Wiley, New York.
- Bhushan, B. and Jung, Y. C. (2006), "Micro and Nanoscale Characterization of Hydrophobic and Hydrophilic Leaf Surface," *Nanotechnology* **17**, 2758-2772.
- Bhushan, B. and Jung, Y. C. (2011), "Natural and Biomimetic Artificial Surfaces for Superhydrophobicity, Self-Cleaning, Low Adhesion, and Drag Reduction," *Prog. Mater. Sci.* **56**, 1-108.
- Bhushan, B., Koch, K., and Jung, Y. C. (2008), "Nanostructures for Superhydrophobicity and Low Adhesion," *Soft Matter* **4**, 1799-1804.
- Bhushan, B., Jung, Y. C., and Koch, K. (2009a), "Micro-, Nano- and Hierarchical Structures for Superhydrophobicity, Self-Cleaning and Low Adhesion," *Phil. Trans. R. Soc. A* **367**, 1631-1672.
- Bhushan, B., Jung, Y. C., Niemietz, A., and Koch, K. (2009b), "Lotus-like Biomimetic Hierarchical Structures Developed by the Self-assembly of Tubular Plant Waxes," *Langmuir* **25**, 1659-1666.
- Bhushan, B., Koch, K., and Jung, Y. C. (2009c), "Fabrication and Characterization of the Hierarchical Structure for Superhydrophobicity," *Ultramicroscopy* **109**, 1029-1034.
- Burton, Z. and Bhushan, B. (2005), "Hydrophobicity, Adhesion, and Friction Properties of Nanopatterned Polymers and Scale Dependence for Micro- and Nanoelectromechanical Systems," *Nano Lett.* **5**, 1607-1613.
- Burton, Z. and Bhushan, B. (2006), "Surface Characterization and Adhesion and Friction Properties of Hydrophobic Leaf Surfaces," *Ultramicroscopy* **106**, 709-719.
- Fürstner, R., Barthlott, W., Neinhuis, C., and Walzel, P. (2005), "Wetting and Self-Cleaning Properties of Artificial Superhydrophobic Surfaces," *Langmuir* **21**, 956-961.
- Gao, X. F. and Jiang, L. (2004), "Biophysics: Water-repellent Legs of Water Striders," *Nature* **432**, 36.
- Gao, L. and McCarthy, T. J. (2006), "The Lotus Effect Explained: Two Reasons Why Two Length Scales of Topography are Important," *Langmuir* **22**, 2966-2967.
- Jetter, R., Kunst, L., and Samuels, A. L. (2006), "Composition of Plant Cuticular Waxes," in *Biology of the Plant Cuticle* (Riederer, M. and Müller, C., Eds.), Blackwell Publishing, Oxford, pp. 145-181.
- Jung, Y. C. and Bhushan, B. (2008), "Wetting Behavior during Evaporation and Condensation of Water Microdroplets on Superhydrophobic Patterned Surfaces" *J. Micros.* **229**, 127-140.
- Kamusewitz, H., Possart, W., and Paul, D. (1999), "The Relation between Young's Equilibrium Contact Angle and the Hysteresis on Rough Paraffin Wax Surfaces," *Colloid Surf. A-Physicochem. Eng. Asp.* **156**, 271 – 279.
- Koch, K., Domnisse, A., and Barthlott, W. (2006), "Chemistry and Crystal Growth of Plant Wax Tubules of Lotus (*Nelumbo nucifera*) and *Nasturtium* (*Tropaeolum majus*) Leaves on Technical Substrates," *Crystl. Growth Des.* **6**, 2571-2578.
- Koch, K., Bhushan, B., and Barthlott, W. (2008), "Diversity of Structure, Morphology, and Wetting of Plant Surfaces (invited)," *Soft Matter* **4**, 1943-1963.

- Koch, K., Bhushan, B., and Barthlott, W. (2009a), "Multifunctional Surface Structures of Plants: An Inspiration for Biomimetics (invited)," *Prog. Mater. Sci.* **54**, 137-178.
- Koch, K., Bhushan, B., Jung, Y. C., and Barthlott, W. (2009b), "Fabrication of Artificial Lotus Leaves and Significance of Hierarchical Structure for Superhydrophobicity and Low Adhesion," *Soft Matter* **5**, 1386-1393.
- Koch, K., Bhushan, B., Eniskat, H. -J., and Barthlott, W. (2009c), "Self-Healing of Voids in the Wax Coating on Plant Surfaces," *Phil. Trans. R. Soc. A* **367**, 1673-1688.
- Koinkar, V. N. and Bhushan, B. (1997) "Effect of Scan Size and Surface Roughness on Microscale Friction Measurements," *J. Appl. Phys.* **81**, 2472-2479.
- Neinhuis, C., and Barthlott, W. (1997), "Characterization and Distribution of Water-Repellent, Self-Cleaning Plant Surfaces," *Annals of Botany* **79**, 667-677.
- Nishimoto, S. and Bhushan, B. (2013), "Bioinspired Self-cleaning Surfaces with Superhydrophobicity, Superoleophobicity, and Superhydrophilicity," *RSC Adv.* **3**, 671-690.
- Nishimoto, S., Kubo, A., Nohara, K. Zhang, X., Taneichi, N., Okui, T., Liu, Z., Nakata, K., Sakai, H., Murakami, T., Abe, M., Komine, T. and Fujishima, A. (2009b), "TiO₂-based superhydrophobic-superhydrophilic patterns: Fabrication via an ink-jet technique and application in offset printing," *Appl. Surf. Sci.* **255**, 6221-6225.
- Nosonovsky, M. and Bhushan, B. (2005), "Roughness Optimization for Biomimetic Superhydrophobic Surfaces," *Microsyst. Technol.* **11**, 535-549.
- Nosonovsky, M. and Bhushan, B. (2008), *Multiscale Dissipative Mechanisms and Hierarchical Surfaces: Friction, Superhydrophobicity, and Biomimetics*, Springer-Verlag, Heidelberg, Germany.
- Poon, C. Y. and Bhushan, B. (1995), "Comparison of Surface Roughness Measurements by Stylus Profiler, AFM and Non-Contact Optical Profiler," *Wear* **190**. 76-88.
- Tambe, N. S. and Bhushan, B. (2004), "Scale Dependence of Micro/Nano-Friction and Adhesion of MEMS/NEMS Materials, Coatings and Lubricants," *Nanotechnology* **15**, 1561-1570.

Chapter 5

Nanofabrication Techniques Used for Lotus-Like Structures

5.1 Introduction

Nanofabrication of superhydrophobic surfaces has been an area of active research since the mid-1990s. In general, the same techniques that are used for micro- and nanostructure fabrication, such as lithography, etching, deposition, and self-assembly, have been utilized for producing superhydrophobic surfaces (Fig. 5.1). Typical materials and fabrication techniques used to produce micro/nanoroughness are summarized in Table 5.1. The pros and cons of these techniques are summarized in Table 5.2.

Among especially interesting developments is the creation of switchable surfaces that can be turned from hydrophobic to hydrophilic. This is done by surface energy modification through electrowetting, light and X-ray irradiation, dynamic effects, optical effects (e.g., the transparency, reflectivity, or non-reflectivity) combined with the lotus effect, hydrophobic interactions, and so on (Feng et al. 2004; Xu et al. 2005; Shirtcliffe et al. 2005; Wang et al. 2007; Krupenkin et al. 2007). An important requirement for potential applications for optics and self-cleaning glasses is the creation of transparent superhydrophobic surfaces. In order for the surface to be transparent, roughness details should be smaller than a quarter of the wavelength of visible light (about 100 nm or less) (Nakajima et al. 1999).

Two main requirements for a superhydrophobic surface are that the surface should be rough and that it should be hydrophobic (low surface energy). These two requirements lead to two methods of producing a superhydrophobic surface: first, it is possible to start with a hydrophobic material and make it rough or, second, to start with a rough surface that may be hydrophilic and turn it hydrophobic by modifying the surface chemistry or applying a hydrophobic material to the surface. Note that roughness is usually a more critical property than low surface energy, since both moderately hydrophobic and very hydrophobic materials can exhibit similar wetting behavior when roughened.

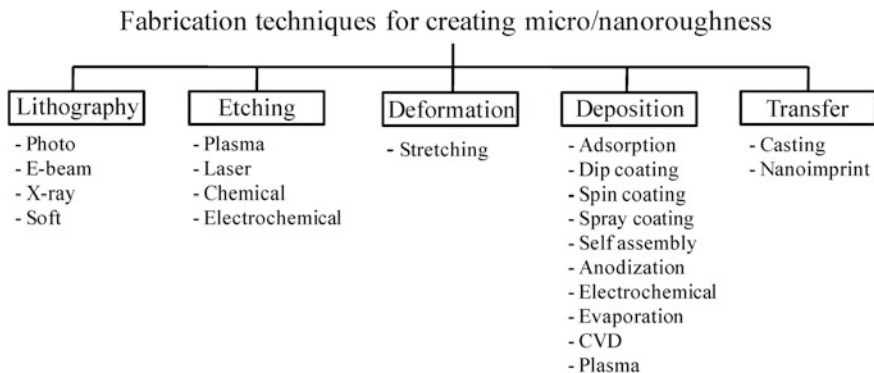


Fig. 5.1 Various methods for creating micro/nanoroughened surfaces

5.2 Roughening to Create One-Level Structure

Lithography is a well-established technique, used for creating a large area of periodic micro/nanopatterns. It includes photo, electron beam (E-beam), X-ray, and soft lithography. Bhushan and Jung (2007) produced micropatterned Si using photolithography. To obtain a sample that is hydrophobic, a self-assembled monolayer (SAM) of 1,1,-2,2,-tetrahydroperfluorodecyltrichlorosilane (PF_3) was deposited on the sample surface using a vapor phase deposition technique. They obtained a superhydrophobic surface with a contact angle up to 170° . Martines et al. (2005) fabricated ordered arrays of nanopits and nanopillars by using E-beam lithography. They obtained a superhydrophobic surface with a static contact angle of 164° and contact angle hysteresis of 1° after hydrophobization with octadecyltrichlorosilane (OTS) on a surface consisting of tall pillars with cusped tops. Fürstner et al. (2005) created silicon wafers with regular patterns of spikes by X-ray lithography. The wafer was hydrophobized by sputtering a layer of gold and subsequent immersion in a hexadecanethiol solution. AFM can be used in nanolithography to produce a nanostructure with the aid of a solvent on polystyrene (PS) (Cappella and Bonaccorso 2007) or an electric field on polymethylmethacrylate (PMMA) (Martin et al. 2005). Jung and Bhushan (2006) created low aspect ratio asperities (LAR, 1:1 height-to-diameter ratio), high aspect ratio asperities (HAR, 3:1 height-to-diameter ratio), and a lotus pattern (replica from the lotus leaf), all on a PMMA surface using soft lithography. A SAM of perfluorodecyltriethoxysilane (PFDTES) was deposited on the patterned surfaces using a vapor phase deposition technique.

One well-known and effective way to make rough surfaces is etching using either plasma, laser, chemical, or electrochemical techniques (Ma and Hill 2006). Jansen et al. (1995) etched a silicon wafer using a fluorine-based plasma by using the black silicon method to obtain isotropic, positively and negatively tapered, and vertical walls with smooth surfaces. Coulson et al. (2000) described an approach in

Table 5.1 Typical materials and fabrication techniques to produce micro/nanoroughness

Material	Technique	Contact angle (°)	Notes	Source
Teflon	Plasma	168		Zhang et al. (2004a), Shiu et al. (2004)
Fluorinated block polymer solution	Casting under humid environment	160	Transparent	Yabu and Shimomura (2005)
PFOS	Electro- and chemical polymerization	152	Reversible (electric potential)	Xu et al. (2005)
PDMS	Laser treatment	166		Khorasani et al. (2005)
PS-PDMS	Electrospinning	>150		Ma et al. (2005)
Block copolymer				
PS, PC, PMMA	Evaporation	>150		Bormashenko et al. (2006)
PS nanofiber	Nanoimprint	156		Lee et al. (2004)
Polyaniline nanofiber	Chemical polymerization	175		Chiou et al. (2007)
Polypropylene nanofibers	Porous nanomembrane patterning technique	173	Hierarchical	Lee and Bhushan (2012)
PET	Oxygen plasma etching	>150		Teshima et al. (2005)
Organo-triethoxysilanes	Sol-gel	155	Reversible (temperature)	Shirtcliffe et al. (2005)
Al	Chemical etching	>150		Qian and Shen (2005)
Copper	Electrodeposition	160	Hierarchical	Shirtcliffe et al. (2004)
Si	Photolithography	170		Bhushan and Jung (2007)
Si	E-beam lithography	164		Martines et al. (2005)
Si	X-ray lithography	>166		Fürstner et al. (2005)
PS, PMMA	AFM nanolithography			Martin et al. (2005), Cappella and Bonaccorso (2007)
Si	Casting	158	Plant leaf replica	Sun et al. (2005), Fürstner et al. (2005)

(continued)

Table 5.1 (continued)

Material	Technique	Contact angle (°)	Notes	Source
Si (Black Si)	Plasma etching	>150	For liquid flow	Jansen et al. (1995)
Silica	Sol-gel	150		Hikita et al. (2005), Shang et al. (2005)
Silica	Layer-by-layer assembly	160	Hierarchical	Zhao et al. (2008)
Silica	Replication and spray coating	168	Hierarchical	Ebert and Bhushan (2012a)
Polyelectrolyte multilayer surface overcoated with silica nanoparticles	Self-assembly	168		Zhai et al. (2004)
Epoxy resin with synthetic and plant waxes	Replication and self-assembly	173	Hierarchical	Bhushan et al. (2008a, b, 2009a, b), Koch et al. (2009)
Nano-silica spheres	Dip coating	105		Klein et al. (2003)
Silica colloidal particles in PDMS	Spin coated	165	Hierarchical	Ming et al. (2005)
Au clusters	Electrochemical deposition	>150		Zhang et al. (2004b)
Carbon nanotubes	Chemical vapor deposition	>165		Lau et al. (2003)
Carbon nanotubes	Chemical vapor deposition	159	Hierarchical	Huang et al. (2005)
Carbon nanotubes	Replication and spray coating	170	Hierarchical	Jung and Bhushan (2009)
ZnO, TiO ₂ Nanorods	Sol-gel	>150	Reversible (UV irradiation)	Feng et al. (2004)
ZnO and ITO	Spray coating	165	Transparent	Ebert and Bhushan (2012b)

Table 5.2 Pros and cons of various fabrication techniques

Techniques	Pros	Cons
Lithography	Accuracy, large area	Slow process, high cost
Etching	Fast	Chemical contamination, less control
Deposition	Flexibility, cheap	Can be high temperature, less control
Self-assembly	Flexibility, cheap	Require suitable precursor

plasma chemical roughening of poly(tetrafluoroethylene) (PTFE) substrates followed by the deposition of low surface energy plasma polymer layers, which give rise to high repellency towards polar and nonpolar probe liquids. A different approach was taken by Shiu et al. (2004), who treated a Teflon film with oxygen plasma and obtained a superhydrophobic surface with a contact angle of 168° . Fluorinated materials have a limited solubility, which makes it difficult to roughen them. However, they may be linked or blended with other materials, which are often easier to roughen, in order to make superhydrophobic surfaces. Teshima et al. (2005) obtained a transparent superhydrophobic surface from a poly(ethylene terephthalate) (PET) substrate via selective oxygen plasma etching followed by plasma-enhanced chemical vapor deposition using tetramethylsilane (TMS) as the precursor. Khorasani et al. (2005) produced porous polydimethylsiloxane (PDMS) surfaces with the contact angle of 175° using the CO_2 -pulsed laser etching method as an excitation source for the surface. Qian and Shen (2005) described a simple surface roughening method by chemical etching on polycrystalline metals such as aluminum. After treatment with fluoroalkylsilane, the etched metallic surfaces exhibited superhydrophobicity. Xu et al. (2005) fabricated a reversible superhydrophobic surface with a double-roughened perfluorooctanesulfonate (PFOS) doped conducting polypyrrole (PPy) film by a combination of electropolymerization and chemical polymerization. Reversibility was achieved by switching between superhydrophobic doped or oxidized states and superhydrophilicity dedoped or neutral states by changing the applied electrochemical potential.

A stretching method can be used to produce a superhydrophobic surface. Zhang et al. (2004a) stretched a Teflon film and converted it into fibrous crystals with a large fraction of void space in the surface, leading to high roughness and the superhydrophobicity.

Deposition methods can also be used to make a substrate rough, including adsorption, dip coating, electrospinning, anodization, electrochemical, evaporation, chemical vapor deposition (CVD), and plasma. Solidification of wax can be used to produce a superhydrophobic surface. Shibuichi et al. (1996) used alkylketene dimer (AKD) wax on a glass plate to spontaneously form a fractal structure in its surfaces. They obtained a surface with a contact angle larger than 170° without any fluorination treatments. Klein et al. (2003) obtained superhydrophobic surfaces by simply dip-coating a substrate with a slurry containing nano-silica spheres, which adhered to the substrate after a low temperature heat treatment. After reaction of the surface with a fluoroalkyltrichlorosilane, the hydrophobicity increased with a decreasing area fraction of spheres. Ma et al. (2005) produced block copolymer poly(styrene-*b*-dimethylsiloxane) fibers with submicrometer diameters in the range of 150–400 nm by electrospinning from a solution in tetrahydrofuran and dimethylformamide. They obtained superhydrophobic, nonwoven fibrous mats with a contact angle of 163° . Shiu et al. (2004) produced self-organized, close-packed superhydrophobic surfaces by spin-coating a monodispersed polystyrene beads solution on a substrate surface. Abdelsalam et al. (2005) studied the wetting of

structured gold surfaces formed by electrodeposition through a template of sub-micrometer spheres, and discussed the role of the pore size and shape in controlling wetting. Bormashenko et al. (2006) used evaporated polymer solutions of polystyrene (PS), polycarbonate (PC) and polymethylmethacrylate (PMMA) dissolved in chlorinated solvents, dichloromethane (CH_2Cl_2) and chloroform (CHCl_3), to obtain a self-assembled structure with hydrophobic properties.

Chemical/physical vapor deposition (CVD/PVD) has been used for the modification of surface chemistry as well. Lau et al. (2003) created superhydrophobic carbon nanotube forests by modifying the surface of vertically aligned nanotubes with plasma enhanced chemical vapor deposition (PECVD). Superhydrophobicity was achieved down to the microscopic level where essentially spherical, micrometer-sized water droplets can be suspended on top of the nanotube forest. Zhu et al. (2005), Huang et al. (2005) prepared surfaces with two-scale roughness by the controlled growth of carbon nanotube (CNT) arrays by CVD. Zhao et al. (2006) also synthesized vertically aligned multiwalled carbon nanotube (MWCNT) arrays by chemical-vapor deposition on Si substrates using a thin film of iron (Fe) as catalyst layer and aluminum (Al) film.

Attempts to create superhydrophobic surfaces by casting and nanoimprint methods have also been successful. Yabu and Shimomura (2005) prepared a porous superhydrophobic transparent membrane by casting a fluorinated block polymer solution in a humid environment. Transparency was achieved because the honeycomb-patterned films had a sub-wavelength pore size. Sun et al. (2005) reported a nanocasting method to make a superhydrophobic PDMS surface. They first made a negative PDMS template using a lotus leaf as an original template and then used the negative template to make a positive PDMS template—a replica of the original lotus leaf. Zhao et al. (2005) prepared a superhydrophobic surface by casting a micellar solution of a copolymer poly(styrene-*b*-dimethylsiloxane) (PS-PDMS) in humid air based on the cooperation of vapor-induced phase separation and surface enrichment of PDMS block. Lee et al. (2004) produced vertically aligned PS nanofibers by using nanoporous anodic aluminum oxide as a replication template in a heat- and pressure-driven nanoimprint pattern transfer process. As the aspect ratio of the polystyrene (PS) nanofibers increased, the nanofibers could not stand upright but formed twisted bundles resulting in a three-dimensionally rough surface with a contact angle of about 155° .

5.3 Coatings to Create One-Level Structures

Modifying the surface chemistry with a hydrophobic coating widens the potential applications of superhydrophobic surfaces. There are several ways to modify the chemistry of a surface including sol-gel, dip coating, self-assembly, electrochemical and chemical/physical vapor deposition. Shirtcliffe et al. (2005) prepared porous

sol–gel foams from organo-triethoxysilanes which exhibited switching between superhydrophobicity and superhydrophilicity when exposed to different temperatures. Hikita et al. (2005) used colloidal silica particles and fluoroalkylsilane as the starting materials and prepared a sol–gel film with superliquid-repellency by hydrolysis and condensation of alkoxysilane compounds. Feng et al. (2004) produced superhydrophobic surfaces by sol-gel method using ZnO nanorods. They showed that superhydrophobic surfaces can be switched into hydrophilic surfaces by alternation of ultraviolet (UV) irradiation. Shang et al. (2005) did not blend low surface energy materials in the sols, but described a procedure to make transparent superhydrophobic surfaces by modifying silica based gel films with a fluorinated silane. In a similar way, Wu et al. (2005) made a microstructured, ZnO-based surface via a wet chemical process, and obtained superhydrophobicity after coating the surface with long-chain alkanolic acids. Chiou et al. (2007) fabricated polyaniline nanofibers using chemical oxidative polymerization to produce uniform, aligned nanofibers and treated with CF_4 plasma treatment to create superhydrophobic surfaces with a contact angle of 175° .

Zhai et al. (2004) used a layer-by-layer (LBL) self-assembly technique to create a poly(allylamine hydrochloride)/poly(acrylic acid) (PAH/PAA) multilayer which formed a honeycomb-like structure on the surface after an appropriate combination of acidic treatments. After cross-linking the structure, they deposited silica nanoparticles on the surface via alternating dipping of the substrates into an aqueous suspension of the negatively charged nanoparticles and an aqueous PAH solution, followed by a final dipping into the nanoparticle suspension. Superhydrophobicity was obtained after the surface was modified by a chemical vapor deposition of (tridecafluoro-1,1,2,2-tetrahydrooctyl)-1-trichlorosilane followed by a thermal annealing.

Zhang et al. (2004b) showed that the surface covered with dendritic gold clusters, which was formed by electrochemical deposition onto an indium tin oxide (ITO) electrode modified with a polyelectrolyte multilayer, showed superhydrophobic properties after further deposition of a *n*-dodecanethiol monolayer. Han et al. (2005) described the fabrication of lotus leaf-like superhydrophobic metal surfaces by using electrochemical reaction of Cu or Cu–Sn alloy plated on steel sheets with sulfur gas, and subsequent perfluorosilane treatment. Chemical bath deposition (CBD) has also been used to make nanostructured surfaces. Hosono et al. (2005) fabricated a nanopin film of brucite-type cobalt hydroxide (BCH) and achieved the contact angle of 178° after further modification of lauric acid (LA). Shi et al. (2006) described the use of galvanic cell reaction as a facile method to chemically deposit Ag nanostructures on the *p*-silicon wafer on a large scale. When the Ag covered silicon wafer was further modified with a self-assembled monolayer of *n*-dodecanethiol, a superhydrophobic surface was obtained with a contact angle of about 154° and a tilt angle lower than 5° .

Ebert and Bhushan (2012b) produced a mechanically durable, transparent structure using SiO_2 , ZnO and ITO (Indium Tin Oxide) nanoparticles bonded with methylphenyl silicone. This was accomplished using a spray coating technique.

5.4 Methods to Create Two-Level (Hierarchical) Structures

Two-level (hierarchical) roughness structures are typical for superhydrophobic surfaces in nature, as was discussed above. Many efforts have been devoted to fabricating these hierarchical structures in various ways. Shirtcliffe et al. (2004) prepared a hierarchical (double-roughened) copper surface by electrodeposition from acidic copper sulfate solution onto flat copper and a patterning technique of coating with a fluorocarbon hydrophobic layer.

Another way to obtain a rough surface for superhydrophobicity is assembly from colloidal systems. Ming et al. (2005) prepared a hierarchical (double roughened) surface consisting of silica-based raspberry-like particles. First was the attachment of epoxy and amino groups onto the silica microparticles of about 700 nm and nanoparticles of about 70 nm, respectively, using established synthetic procedures. Two suspensions in ethanol were created, one with microparticles and another one with nanoparticles. In the next step, the suspension with the silica microparticles was added dropwise to the suspension with the nanoparticles. The nanoparticles attached to the microparticles due to the reaction between the epoxy and amino groups present on the surface of the particles. Then, the suspension was centrifuged to separate any unreacted particles. The next step involved depositing these micro/nanostructured particles into an epoxy film (on silicon). Finally, since the resulting micro/nanoparticle surface was initially hydrophilic, it was made hydrophobic by a deposition of monoepoxy-end-capped poly(dimethylsiloxane) (PDMS).

Northen and Turner (2005) fabricated arrays of flexible silicon dioxide platforms supported by single high aspect ratio silicon pillars down to 1 μm in diameter and with heights up to $\sim 50 \mu\text{m}$. When these platforms were coated with polymeric organorods of approximately 2 μm tall and 50–200 nm in diameter, it showed that the surface is highly hydrophobic with a water contact angle of 145°.

Chong et al. (2006) fabricated hierarchically ordered nanowire arrays with periodic voids at the microscale and hexagonally packed nanowires at the nanoscale. This hierarchical surface was created by selective electrodeposition using nanoporous anodic alumina as a template and a porous gold film as a working electrode that was patterned by microsphere monolayers. Wang et al. (2006) also developed a novel precursor hydrothermal redox method with $\text{Ni}(\text{OH})_2$ as the precursor to fabricate a hierarchical structure consisting of nickel hollow microspheres with nickel nanoparticles in situ. The hierarchical hollow structure created exhibited enhanced coercivity and remnant magnetization as compared with hollow nickel submicrometer spheres, hollow nickel nanospheres, bulk nickel, and free Ni nanoparticles.

Kim et al. (2007) fabricated a hierarchical structure that looks like the same structures as the lotus leaf. First, the nanoscale porosity was generated by anodic aluminum oxidation. Then, the anodized porous alumina surface was replicated by polytetrafluoroethylene. The polymer sticking phenomenon during the replication created the sub-microstructures on the negative polytetrafluoroethylene

nanostructure replica. The contact angle of the hierarchical structure created was about 160° and the tilt angle was less than 1° . Del Campo and Greiner (2007) reported that SU-8 hierarchical patterns comprised of features with lateral dimensions ranging from 5 to 2 mm and heights from 10 to 500 μm were obtained by photolithography, which is comprised of a step of layer-by-layer exposure in soft contact printed shadow masks embedded into the SU-8 multilayer.

Bhushan et al. (2008a, b, 2009a, b) and Koch et al. (2009) produced hierarchical structures by replication of a micropatterned silicon surface and a lotus leaf microstructure using an epoxy resin and by self-assembly of synthetic and plant waxes as thin hydrophobic three-dimensional crystals to create hydrophobic nanostructures. The fabrication technique used is a low cost two-step process, which provides flexibility in the fabrication of a variety of hierarchical structures. They showed that a hierarchical structure has a high propensity for air pocket formation and leads to a static contact angle of 173° and contact angle hysteresis and tilt angle of $\sim 2^\circ$.

Zhao et al. (2008) fabricated a hierarchical structure by using layer-by-layer assembly of silica nanoparticles on a microsphere-patterned polyimide precursor substrate combined with the fluoroalkylsilane treatment. The microstructures were created by replica molding of polyamide using two-dimensional PS microsphere arrays. They obtained a superhydrophobic surface with a static contact angle of 160° and tilt angle of less than 10° . Cortese et al. (2008) applied plasma CF_4 treatment on micropattern PDMS and obtained contact angle of 170° . Kuan et al. (2009) produced a hierarchical structure by imprinting ZnO precursor films using gratings with 830 nm and 50 μm dimensions. They achieved a contact angle of 141° by nanostructures deposited on sawtooth patterns without modifying the surface chemistry. Lee and Bhushan (2012) fabricated a hierarchical structure made of polypropylene fibers using two stacked porous membranes as a template.

Jung and Bhushan (2009) produced mechanically durable carbon nanotube composite hierarchical structures with a static contact angle of 170° and a contact angle hysteresis of 2° by replication of a micropatterned silicon surface using an epoxy resin and by deposition of the carbon nanotube composite using a spray method. They showed that carbon nanotube composite structure had high mechanical strength and wear resistance as a result of the uniform distribution and strong bonding of the carbon nanotube on the substrates. Ebert and Bhushan (2012a) produced a mechanically durable silica composite hierarchical structure with a static contact angle of 168° and a contact angle hysteresis of 1° fabrication using spray method.

5.5 Closure

Various nanofabrication techniques have been used to create superhydrophobic surfaces. These include roughening at one or two levels and/or chemical modification that affect surface energy. These techniques have been used to create lotus-like structures and surfaces for a variety of applications.

References

- Abdelsalam, M. E., Bartlett, P. N., Kelf, T., and Baumberg, J. (2005), "Wetting of Regularly Structured Gold Surfaces," *Langmuir* **21**, 1753-1757.
- Bhushan, B. and Jung, Y. C. (2007), "Wetting Study of Patterned Surfaces for Superhydrophobicity," *Ultramicroscopy* **107**, 1033-1041.
- Bhushan, B., Koch, K., and Jung, Y. C. (2008a), "Nanostructures for Superhydrophobicity and Low Adhesion," *Soft Matter* **4**, 1799-1804.
- Bhushan, B., Koch, K., and Jung, Y. C. (2008b), "Biomimetic Hierarchical Structure for Self-Cleaning," *Appl. Phys. Lett.* **93**, 093101.
- Bhushan, B., Jung, Y. C., Niemietz, A., and Koch, K. (2009a), "Lotus-like Biomimetic Hierarchical Structures Developed by the Self-assembly of Tubular Plant Waxes," *Langmuir* **25**, 1659-1666.
- Bhushan, B., Koch, K., and Jung, Y. C. (2009b), "Fabrication and Characterization of the Hierarchical Structure for Superhydrophobicity," *Ultramicroscopy* **109**, 1029-1034.
- Bormashenko E., Stein, T., Whyman, G., Bormashenko, Y., and Pogreb, E. (2006), "Wetting Properties of the Multiscaled Nanostructured Polymer and Metallic Superhydrophobic Surfaces," *Langmuir* **22**, 9982-9985.
- Cappella, B. and Bonaccorso, E. (2007), "Solvent-Assisted Nanolithography on Polystyrene Surfaces using the Atomic Force Microscope," *Nanotechnology* **18**, 155307.
- Chiou, N., Lu, C., Guan, J., Lee, L. J., and Epstein, A. J. (2007), "Growth and Alignment of Polyaniline Nanofibres with Superhydrophobic, Superhydrophilic and Other Properties," *Nature Nanotechnol.* **2**, 354-357.
- Chong, M. A. S., Zheng, Y. B., Gao, H., and Tan, L. K. (2006), "Combinational Template-Assisted Fabrication of Hierarchically Ordered Nanowire Arrays on Substrates for Device Applications," *Appl. Phys. Lett.* **89**, 233104.
- Cortese, B., Amone S. D., Manca, M., Viola, I., Cingolani, R., and Gigli, G. (2008), "Superhydrophobicity Due to the Hierarchical Scale Roughness of PDMS Surfaces," *Langmuir* **24**, 2712-2718.
- Coulson, S. R., Woodward, I., Badyal, J. P. S., Brewer, S. A., and Willis, C. (2000), "Super-Repellent Composite Fluoropolymer Surfaces," *J. Phys. Chem. B* **104**, 8836-8840.
- del Campo, A., Greiner, C. (2007), "SU-8: a Photoresist for High-Aspect-Ratio and 3D Submicron Lithography," *J. Micromech. Microeng.* **17**, R81-R95.
- Ebert, D. and Bhushan, B. (2012a), "Durable Lotus-Effect Surfaces with Hierarchical Structure Using Micro- and Nanosized Hydrophobic Silica Particles," *J. Colloid Interf. Sci.* **368**, 584-591.
- Ebert, D. and Bhushan, B. (2012b), "Transparent, Superhydrophobic, and Wear-Resistant Coatings on Glass and Polymer Substrates using SiO₂, ZnO, and ITO Nanoparticles," *Langmuir* **28**, 11391-11399.
- Feng, X. J., Feng, L., Jin, M. H., Zhai, J., Jiang, L., Zhu, D. B. (2004), "Reversible Super-hydrophobicity to Super-hydrophilicity Transition of Aligned ZnO Nanorod Films," *J. Am. Chem. Soc.* **126**, 62-63.
- Fürstner, R., Barthlott, W., Neinhuis, C., and Walzel, P. (2005), "Wetting and Self-Cleaning Properties of Artificial Superhydrophobic Surfaces," *Langmuir* **21**, 956-961.
- Han, J. T., Jang, Y., Lee, D. Y., Park, J. H., Song, S. H., Ban, D. Y., and Cho, K. (2005), "Fabrication of a Bionic Superhydrophobic Metal Surface by Sulfur-Induced Morphological Development," *J. Mater. Chem.* **15**, 3089-3092.
- Hikita, M., Tanaka, K., Nakamura, T., Kajiyama, T., and Takahara, A. (2005), "Superliquid-Repellent Surfaces Prepared by Colloidal Silica Nanoparticles Covered with Fluoroalkyl Groups," *Langmuir* **21**, 7299-7302.
- Hosono, E., Fujihara, S., Honma, I., and Zhou, H. (2005), "Superhydrophobic Perpendicular Nanopin Film by the Bottom-Up Process," *J. Am. Chem. Soc.* **127**, 13458-13459.

- Huang, L., Lau, S. P., Yang, H. Y., Leong, E. S. P., and Yu, S. F. (2005), "Stable Superhydrophobic Surface via Carbon Nanotubes Coated with a ZnO Thin Film," *J. Phys. Chem.* **109**, 7746-7748.
- Jansen, H., de Boer, M., Legtenberg, R., and Elwenspoek, M. (1995), "The Black Silicon Method: a Universal Method for Determining the Parameter Setting of a Fluorine-Based Reactive Ion Etcher in Deep Silicon Trench Etching with Profile Control," *J. Micromech. Microeng.* **5**, 115-120.
- Jung, Y. C. and Bhushan, B. (2006), "Contact Angle, Adhesion, and Friction Properties of Micro- and Nanopatterned Polymers for Superhydrophobicity," *Nanotechnology* **17**, 4970-4980.
- Jung, Y. C. and Bhushan, B. (2009), "Mechanically Durable CNT-Composite Hierarchical Structures with Superhydrophobicity, Self-Cleaning, and Low-Drag," *ACS Nano* **3**, 4155-4163.
- Khorasani, M. T., Mirzadeh, H., and Kermani, Z. (2005), "Wettability of Porous Polydimethylsiloxane Surface: Morphology Study," *Appl. Surf. Sci.* **242**, 339-345.
- Kim, D., Hwang, W., Park, H. C., and Lee, K. H. (2007), "Superhydrophobic Micro- and Nanostructures Based on Polymer Sticking," *Key Eng. Mat.* **334-335**, 897-900.
- Klein, R. J., Biesheuvel P. M., Yu, B. C., Meinhart, C. D., and Lange, F. F. (2003), "Producing Super-Hydrophobic Surfaces with Nano-Silica Spheres," *Z. Metallkd.* **94**, 377-380.
- Koch, K., Bhushan, B., Jung, Y. C., and Barthlott, W. (2009), "Fabrication of Artificial Lotus Leaves and Significance of Hierarchical Structure for Superhydrophobicity and Low Adhesion," *Soft Matter* **5**, 1386-1393.
- Krupenkin, T. N., Taylor, J. A., Wang, E. N., Kolodner, P., Hodes, M., and Salamon, T. R. (2007), "Reversible Wetting-Dewetting Transitions on Dielectrically Tunable Superhydrophobic Nanostructured Surfaces," *Langmuir* **23**, 9128-9133.
- Kuan, C. Y., Hon, M. H., Chou, J. M., and Leu, I. C. (2009), "Wetting Characteristics on Micro/Nanostructured Zinc Oxide Coatings," *J. Electrochem. Soc.* **156**, J32-J36.
- Lau, K. K. S., Bico, J., Teo, K. B. K., Chhowalla, M., Amaratunga, G. A. J., Milne, W. I., McKinley, G. H., and Gleason, K. K. (2003), "Superhydrophobic Carbon Nanotube Forests," *Nano Lett.* **3**, 1701-1705.
- Lee, H. and Bhushan, B. (2012), "Fabrication and Characterization of Hierarchical Nanostructured Smart Adhesion Surfaces," (unpublished).
- Lee, W., Jin, M., Yoo, W., and Lee, J. (2004), "Nanostructuring of a Polymeric Substrate with Well-Defined Nanometer-Scale Topography and Tailored Surface Wettability," *Langmuir* **20**, 7665-7669.
- Ma, M. and Hill, R. M. (2006), "Superhydrophobic Surfaces," *Curr. Opin. Colloid Interface Sci.* **11**, 193-202.
- Ma, M., Hill, R. M., Lowery, J. L., Fridrikh, S. V., and Rutledge, G. C. (2005), "Electrospun Poly (styrene-block-dimethylsiloxane) Block Copolymer Fibers Exhibiting Superhydrophobicity," *Langmuir* **21**, 5549-5554.
- Martin, C., Rius, G., Borriase, X., and Perez-Murano, F. (2005), "Nanolithography on Thin Layers of PMMA using Atomic Force Microscopy," *Nanotechnology* **16**, 1016-1022.
- Martines, E., Seunarine, K., Morgan, H., Gadegaard, N., Wilkinson, C. D. W., and Riehle, M. O. (2005), "Superhydrophobicity and Superhydrophilicity of Regular Nanopatterns," *Nano Lett.* **5**, 2097-2103.
- Ming, W., Wu, D., van Benthem, R., and de With, G. (2005), "Superhydrophobic Films from Raspberry-Like Particles," *Nano Lett.* **5**, 2298-2301.
- Nakajima, A., Fujishima, A., Hashimoto, K., and Watanabe, T. (1999), "Preparation of Transparent Superhydrophobic Boehmite and Silica Films by Sublimation of Aluminum Acetylacetonate," *Adv. Mater.* **11**, 1365-1368.
- Northen, M. T. and Turner, K. L. (2005), "A Batch Fabricated Biomimetic Dry Adhesive," *Nanotechnology* **16**, 1159-1166.
- Qian, B. and Shen, Z. (2005), "Fabrication of Superhydrophobic Surfaces by Dislocation-Selective Chemical Etching on Aluminum, Copper, and Zinc Substrates," *Langmuir* **21**, 9007-9009.

- Shang, H. M., Wang, Y., Limmer, S. J., Chou, T. P., Takahashi, K., and Cao, G. Z. (2005) "Optically Transparent Superhydrophobic Silica-Based Films," *Thin Solid Films* **472**, 37-43.
- Shi, F., Song, Y., Niu, J., Xia, X., Wang, Z., and Zhang, X. (2006), "Facile Method To Fabricate a Large-Scale Superhydrophobic Surface by Galvanic Cell Reaction," *Chem. Mater.* **18**, 1365-1368.
- Shibuichi, S., Onda, T., Satoh, N., and Tsujii, K. (1996), "Super-Water-Repellent Surfaces Resulting from Fractal Structure," *J. Phys. Chem.* **100**, 19512-19517.
- Shirtcliffe, N. J., McHale, G., Newton, M. I., Chabrol, G., Perry, C. C. (2004). "Dual-Scale Roughness Produces Unusually Water-Repellent Surfaces," *Adv. Mater.* **16**, 1929-1932.
- Shirtcliffe, N. J., McHale, G., Newton, M. I., Perry, C. C., and Roach, P. (2005), "Porous Materials Show Superhydrophobic to Superhydrophilic Switching," *Chem. Commun.* 3135-3137.
- Shiu, J., Kuo, C., Chen, P., and Mou, C. (2004), "Fabrication of Tunable Superhydrophobic Surfaces by Nanosphere Lithography," *Chem. Mater.* **16**, 561-564.
- Sun, M., Luo, C., Xu, L., Ji, H., Ouyang, Q., Yu, D., and Chen, Y. (2005), "Artificial Lotus Leaf by Nanocasting," *Langmuir* **21**, 8978-8981.
- Teshima, K., Sugimura, H., Inoue, Y., Takai, O., and Takano, A. (2005), "Transparent Ultra Water-Repellent Poly(ethylene terephthalate) Substrates Fabricated by Oxygen Plasma Treatment and Subsequent Hydrophobic Coating," *Appl. Surf. Sci.* **244**, 619-622.
- Wang, Y., Zhu, Q., and Zhang, H. (2006), "Fabrication and Magnetic Properties of Hierarchical Porous Hollow Nickel Microspheres," *J. Mater. Chem.* **16**, 1212-1214.
- Wang, S., Liu, H., Liu, D., Ma, X., Fang, X., and Jiang, L. (2007), "Enthalpy Driven Three State Switching of a Superhydrophilic/Superhydrophobic Surfaces," *Angew. Chem. Int. Ed.* **46**, 3915-3917.
- Wu, X., Zheng, L., and Wu, D. (2005), "Fabrication of Superhydrophobic Surfaces from Microstructured ZnO-Based Surfaces via a Wet-Chemical Route," *Langmuir* **21**, 2665-2667.
- Xu, L., Chen, W., Mulchandani, A., and Yan, Y. (2005), "Reversible Conversion of Conducting Polymer Films from Superhydrophobic to Superhydrophilic," *Angew. Chem. Int. Ed.* **44** 6009-6012.
- Yabu, H. and Shimomura, M. (2005), "Single-Step Fabrication of Transparent Superhydrophobic Porous Polymer Films," *Chem. Mater.* **17**, 5231-5234.
- Zhai, L., Cebeci, F. C., Cohen, R. E., and Rubner, M. F. (2004), "Stable Superhydrophobic Coatings from Polyelectrolyte Multilayers," *Nano Lett.* **4**, 1349-1353.
- Zhang, J. L., Li, J. A., and Han, Y. C. (2004a), "Superhydrophobic PTFE Surfaces by Extension," *Macromol. Rapid Commun.* **25**, 1105-1108.
- Zhang, X., Feng, S., Yu, X., Liu, H., Fu, Y., Wang, Z., Jiang, L., and Li, X. (2004b), "Polyelectrolyte Multilayer as Matrix for Electrochemical Deposition of Gold Clusters: Toward Super-Hydrophobic Surface," *J. Am. Chem. Soc.* **126**, 3064-3065.
- Zhao, N., Xie, Q. D., Weng, L. H., Wang, S. Q., Zhang, X. Y., and Xu, J. (2005), "Superhydrophobic Surface from Vapor-Induced Phase Separation of Copolymer Micellar Solution," *Macromolecules* **38**, 8996-8999.
- Zhao, Y., Tong, T., Delzeit, L., Kashani, A., Meyyappan, M., and Majumdar, A. (2006), "Interfacial Energy and Strength of Multiwalled-Carbon-Nanotube-Based Dry Adhesive," *J. Vac. Sci. Technol. B* **24**, 331-335.
- Zhao, Y., Li, M., Lu, Q., and Shi, Z. (2008), "Superhydrophobic Polyimide Films with a Hierarchical Topography: Combined Replica Molding and Layer-by-Layer Assembly," *Langmuir* **24**, 12651-12657.
- Zhu, L., Xiu, Y., Xu, J., Tamirisa, P. A., Hess, D. W., and Wong C. (2005), "Superhydrophobicity on Two-Tier Rough Surfaces Fabricated by Controlled Growth of Aligned Carbon Nanotube Arrays Coated with Fluorocarbon," *Langmuir* **21**, 11208-11212.

Chapter 6

Fabrication and Characterization of Micro-, Nano- and Hierarchically Structured Lotus-Like Surfaces

6.1 Introduction

It has been demonstrated experimentally that roughness changes contact angle (CA) in accordance with the Wenzel model or the Cassie-Baxter model, depending upon whether the surface is hydrophilic or hydrophobic (Bhushan and Jung 2011). Yost et al. (1995) found that roughness enhances wetting of a copper surface with Sn-Pb eutectic solder, which has a contact angle of 15–20° for a smooth surface. Shibuichi et al. (1996) measured the contact angle of various liquids (mixtures of water and 1,4-dioxane) on alkylketene dimmer (AKD) substrate (contact angle not larger than 109° for a smooth surface). They found that with increasing roughness, the contact angle decreases for wetting liquids and increases for non-wetting liquids. Semal et al. (1999) investigated the effect of surface roughness on contact angle hysteresis (CAH) by studying a sessile droplet of squalane spreading dynamically on multilayer substrates (behenic acid on glass). They found that an increase in microroughness slows the rate of droplet spread. Erbil et al. (2003) measured the contact angle of polypropylene (contact angle of 104° for smooth surface) and found that the contact angle increases with increasing roughness. Burton and Bhushan (2005) and Jung and Bhushan (2006) measured the contact angle of various micro- and nanopatterned polymer surfaces with hydrophilicity and hydrophobicity. They found that for an increasing roughness factor, contact angle decreases for hydrophilic surfaces and increases for hydrophobic surfaces. Nanopatterned surfaces benefit from air pocket formation. Jung and Bhushan (2008c) studied the effect of submicron droplets on contact angle.

The contact angle on selected patterned surfaces has been measured to understand the role of pitch value on contact angle, as well as on the transition between the Cassie-Baxter and Wenzel regimes (Bhushan and Jung 2007, 2008; Jung and Bhushan 2007, 2008a, b). Evaporation studies are useful in characterizing the role of droplet size. During evaporation, droplets with decreasing sizes exist and are used to evaluate the transition criterion on a given patterned surface (Bourges-Monnier and

Shanahan 1995; Rowan et al. 1995; Erbil et al. 2002; McHale et al. 2005; Jung and Bhushan 2007, 2008a; Nosonovsky and Bhushan 2007a, c, 2008b, c, d; Bhushan et al. 2008a, 2009b, c, d). It was found that the wetting state changes from the Cassie-Baxter to the Wenzel state as the droplet becomes smaller than a critical value, and the pitch value becomes larger than a critical value on patterned surfaces.

Another important phenomenon related to wetting behavior is the bouncing of droplets. When a droplet hits a surface, it can bounce, spread, or stick. In practical applications of superhydrophobic surfaces, surfaces should maintain their ability to repel penetrating droplets under dynamic conditions. Whether or not a droplet transitions between bouncing or remaining on the surface can be determined from the impact of a droplet at a critical velocity on a patterned surface with a given geometric parameter (Richard et al. 2002; Lafuma and Quere 2003; Bartolo et al. 2006; Reyssat et al. 2006; Jung and Bhushan 2008b, 2009a; Nosonovsky and Bhushan 2008e).

An environmental scanning electron microscope (ESEM) can be used to condense or evaporate water droplets on surfaces by adjusting the pressure of the water vapor in the specimen chamber and the temperature of the cooling stage. Transfer of the water droplet has been achieved by a specially designed micro-injector device on wool fibers and then imaged at room temperature in ESEM (Danilatos and Brancik 1986). Images of water droplets show strong topographic contrast in ESEM such that reliable contact angle measurements can be made on the surfaces (Stelmashenko et al. 2001). Water condensation and evaporation studies on patterned surfaces have been carried out by Jung and Bhushan (2008a), where the change of static contact angle and contact angle hysteresis was related with the surface roughness.

Bhushan and Jung (2007, 2008), Jung and Bhushan (2006, 2007, 2008a, b), Bhushan et al. (2007, 2008a, b, 2009b, c, d), and Koch et al. (2009) used nature's route to fabricate hierarchical structures. These were created by replication of micropatterns and by self-assembly of hydrophobic alkanes and plant waxes. They studied the static contact angle, contact angle hysteresis, tilt angle, air pocket formation, and adhesive force, as well as efficiency of self-cleaning. Hierarchical structures exhibited superhydrophobicity with static contact angles of about 171° , low contact angle hysteresis of about 2° , and self-cleaning properties comparable to that of the lotus (*Nelumbo nucifera*) leaf. This verified their understanding of the wetting mechanisms of the lotus leaf. Jung and Bhushan (2008b, 2009a) performed bouncing and vibrating droplet experiments to study the effect of impact velocity and vibration amplitude on the transition from the composite solid-air-liquid interface to the homogeneous solid-liquid interface.

By using smart materials and nanofabrication techniques, Jung and Bhushan (2009b) produced mechanically durable carbon nanotube (CNT) composite hierarchical structures with a static contact angle of 170° and a contact angle hysteresis of 2° . This was done by replication of a micropatterned silicon surface using an epoxy resin and by deposition of the CNT composite using a spray method. Based on durability experiments, they showed that the CNT composite structure had high mechanical strength and wear resistance from the uniform distribution and strong

bonding of CNT on substrates. Ebert and Bhushan (2012a, b) have produced mechanically durable hierarchical structures using micro/nanoparticles and mechanically durable structures with optical transparency.

In this chapter, characterization of various micro-, nano-, and hierarchically patterned surfaces is provided to verify theoretical models, to understand the transition between the Wenzel and Cassie-Baxter wetting regimes, and to understand the role of contact angle hysteresis and hierarchical roughness. Details on fabricated surfaces using nature's route are presented which was used to verify one's understanding, and then details are presented on optimum structures fabricated based on the models using smart materials and fabrication techniques.

6.2 Experimental Techniques

6.2.1 Contact Angle, Surface Roughness, and Adhesion

Static and dynamic (advancing and receding) contact angles were measured using a Rame-Hart model 100 contact angle goniometer and droplets of DI water (Burton and Bhushan 2005; Bhushan and Jung 2007, 2008; Jung and Bhushan 2006, 2007; Bhushan et al. 2008a, b, 2009c, d; Koch et al. 2009). For measurement of the static contact angle, the droplet size should be smaller than the capillary length but larger than the dimension of the structures present on the surfaces. Droplets of about 5 μL in volume (with the diameter of a spherical droplet about 2.1 mm) were deposited on the substrate using a microsyringe for measurement of the static contact angle. The advancing and receding contact angles were measured by the addition and removal of water from a DI water sessile droplet using a microsyringe. The contact angle hysteresis was calculated as the difference between the measured advancing and receding contact angles, and the tilt angle was measured by using a tilting stage (Bhushan and Jung 2007, 2008; Bhushan et al. 2008a, b, 2009c, d; Koch et al. 2009). All measurements were made at five different points for each sample at 22 ± 1 $^{\circ}\text{C}$ and 50 ± 5 % RH. The measurements were reproducible to within $\pm 3^{\circ}$.

For surface roughness measurement, an optical profiler was used for different surface structures (Burton and Bhushan 2006; Bhushan and Jung 2006, 2007, 2008). The optical profiler has an advantage due to its greater Z-range (2 mm) over an atomic force microscope (AFM) (Z-range about 7 μm), but it has a maximum lateral resolution of only approximately 0.6 μm (Bhushan 2011, 2013a, b).

Adhesive force was measured with an AFM using a force distance curve approach (Bhushan 2011). Experiments were performed using three different radii tips to study the effect of scale dependence. A borosilicate ball with 15 μm radius and a silica ball with 3.8 μm radius were mounted on a gold-coated triangular Si_3N_4 cantilever with a nominal spring constant of 0.58 N m^{-1} . A square pyramidal Si_3N_4 tip with a nominal radius of 30–50 nm on a triangular Si_3N_4 cantilever with a nominal spring constant of 0.58 N m^{-1} was used for the smaller radius tip.

6.2.2 Droplet Evaporation Studies

Droplet evaporation was observed and recorded by a digital camcorder with a 10× optical and 120× digital zoom for every run of the experiment. Then the decrease in the diameter of the droplets with time was determined (Jung and Bhushan 2007, 2008a; Bhushan et al. 2008a, 2009c). The frame speed of the camcorder was 0.03 s per frame. An objective lens placed in front of the camcorder during recording gave a total magnification of 10× to 20×. Droplet diameter as small as a few hundred microns could be measured with this method. Droplets were deposited on the substrate using a microsyringe, and the whole process of evaporation was recorded. Images obtained were analyzed using Imagetool[®] software (University of Texas Health Science Center) for the contact angle. To find the dust trace remaining after droplet evaporation, an optical microscope with a charge-coupled device (CCD) camera was used. All measurements were made in a controlled environment at 22 ± 1 °C and 45 ± 5 % RH (Jung and Bhushan 2007, 2008a; Bhushan et al. 2008a, 2009c, d).

6.2.3 Bouncing Droplet Studies

The process of dynamic impact was recorded by a high speed camera (Kodak Ektapro HS Motion Analyzer, Model 4540) operated at 500 frames/s for each experimental run and then measuring the dynamic impact behavior of the droplet as a function of time. The impact velocity was calculated by varying the droplet release height. Droplets of about 5 μ L in volume with a diameter of a spherical droplet of about 2.1 mm were used. All measurements were made in a controlled environment at 22 ± 1 °C and 45 ± 5 % RH (Jung and Bhushan 2008b).

6.2.4 Vibrating Droplet Studies

The process of dynamic behavior was obtained by a system producing vertical vibrations (Jung and Bhushan 2009a). The system consists of an electrodynamic shaker (Labworks Inc. Model ET-126A/B) connected with a signal generator and power amplifier, a digital camcorder with an objective lens, and a lamp for a light source. The specimen was placed on the top of the shaker, and a droplet was deposited using a microsyringe. Droplets of about 5 μ L in volume with a diameter of a spherical droplet of about 2.1 mm were used. The vibration frequency was controlled between 0 and 300 Hz at 0.4 mm amplitude for measurement of the resonance frequency of a droplet. For wetting behavior of a droplet on the surface, a frequency of 30 Hz, which was less than the resonance frequency, was chosen, and the vibration amplitude was controlled between 0 and 3 mm. The vibration time

applied to the droplet was 1 min for each experiment. All measurements were made in a controlled environment at 22 ± 1 °C and 45 ± 5 % RH (Jung and Bhushan 2009a).

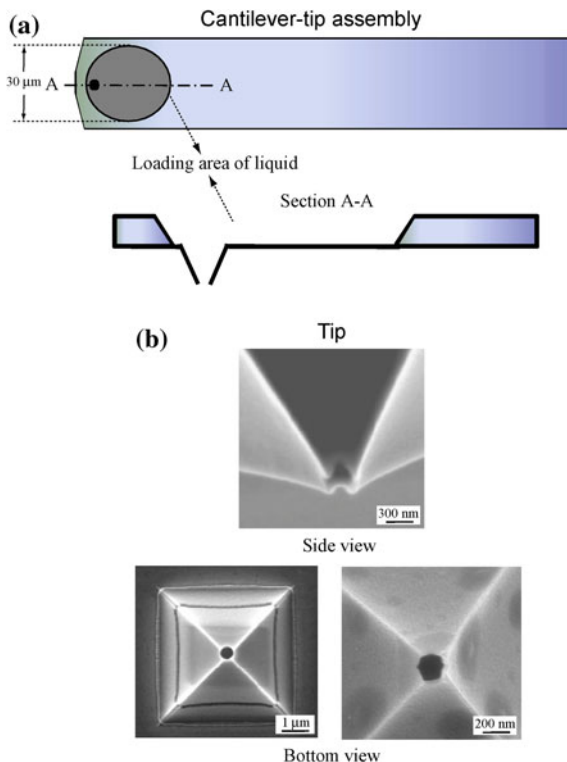
6.2.5 Microdroplet Condensation and Evaporation Studies Using ESEM

A Philips XL30 ESEM equipped with a Peltier cooling stage was used to study smaller droplets (Jung and Bhushan 2008a). ESEM uses a gaseous secondary electron detector (GSED) for imaging. The ESEM column is equipped with a multistage differential pressure-pumping unit. The pressure in the upper part is about 10^{-6} – 10^{-7} Torr, but a pressure of about 1–15 Torr can be maintained in the observation chamber. When the electron beam (primary electrons) ejects secondary electrons from the surface of the sample, the secondary electrons collide with gas molecules in the ESEM chamber, which in turn acts as a cascade amplifier, delivering the secondary electron signal to the positively biased GSED. The positively charged ions are attracted to the specimen to neutralize the negative charge produced by the electron beam. Therefore, the ESEM can be used to examine electrically isolated specimens in their natural state. In ESEM, adjusting the pressure of the water vapor in the specimen chamber and the temperature of the cooling stage allows the water to condense on the sample in the chamber. For the measurement of the static and dynamic contact angles on patterned surfaces, video images were recorded. The voltage of the electron beam was 15 kV, and the distance of the specimen from the final aperture was about 8 mm. If the angle of observation is not parallel to the surface, the electron beam is not parallel to the surface but inclined at an angle, this will produce a distortion in the projection of the droplet profile. A mathematical model to calculate the real contact angle from the ESEM images was used to correct the tilting of the surfaces during imaging (Brugnara et al. 2006; Jung and Bhushan 2008a).

6.2.6 Generation of Submicron Droplets

In order to generate submicron droplets, Jung and Bhushan (2008c) developed an AFM-based technique using a modified nanoscale dispensing (NADIS) probe as shown in Fig. 6.1. The NADIS probe was fabricated by modifying a commercially available silicon nitride (Si_3N_4) cantilever (Olympus OMCL-RC800) with lengths of 100 and 200 μm , spring constants of 0.8 and 0.1 N/m, and resonance frequencies of 68.94 and 122.02 kHz, respectively (Swiss Center for Electronics and Microtechnology). The probe consisted of a loading area (30 μm diameter) for the liquid on the upper side of the cantilever. The loading area was produced by

Fig. 6.1 **a** Schematic of modified nanoscale dispensing (NADIS) probe for generation of submicron size droplets. The loaded liquid is limited to the loading area ($30\ \mu\text{m}$ diameter circle), **b** scanning electron micrograph of tip in *side view* and *bottom view* with different aperture sizes (500 and 200 nm) at its apex (Jung and Bhushan 2008c)



removing the material locally in and around the tip with a reflective gold layer using focused ion beam milling. The remaining gold was made hydrophobic using hexadecanethiol (in liquid phase) whereas the bare silicon nitride in the milling area remained hydrophilic. The hydrophilic–hydrophobic transition prevents spreading of the loaded liquid over the entire cantilever.

A droplet of volume V is deposited on the surface. Figure 6.2 shows an idealized spherical capped droplet. Based on the thickness of the droplet h and contact diameter d , the contact angle is obtained by the following equation for a simple spherical capped geometry of droplet (Jung and Bhushan 2008c).

$$\theta = \sin^{-1} \left(\frac{3d}{2 \left(\frac{3V}{\pi h^2} + h \right)} \right) \quad (6.1)$$

For calculation of the contact angle of the droplet, Jung and Bhushan (2008c) use the following three steps:

- (1) For the measurement of the volume of a droplet deposited on the surface, the change in resonance frequency of the cantilever before and after depositing the droplet on the surface is measured. The resonance frequency of the cantilever

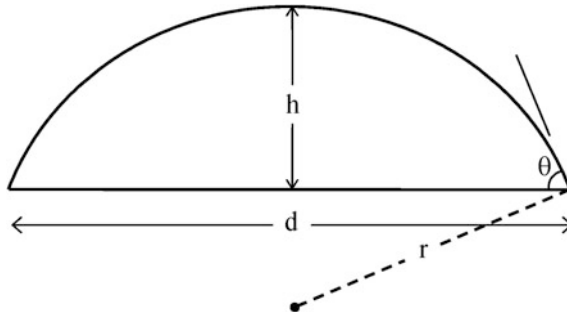


Fig. 6.2 Droplet of liquid in contact with a surface, contact angle θ . The thickness of droplet is h . The contact diameter between droplet and surface is d . The radius of curvature of droplet is r (Jung and Bhushan 2008c)

is measured by performing a frequency sweep of the voltage driven oscillations by a thermal tune method (Palacio and Bhushan 2010).

- (2) For the measurement of the thickness of a droplet deposited on the surface, the distance between the tip snap-in and the position where the tip is in contact with the surface is measured in the force calibration mode.
- (3) For the measurement of the contact diameter between a droplet and surface, the image of the droplet after evaporation is measured using an Si tip.

For measurement of the thickness of a droplet deposited on the surface, a force distance curve was used (Bhushan 2011, 2013a, b). The droplet was deposited in the first approach. The force distance curve was obtained during a second approach to measure the thickness of the droplet (Bhushan and Blackman 1991; Chen and Bhushan 2006; Lodge and Bhushan 2006). The cantilever deflection is plotted on the vertical axis against the Z-position of the piezo scanner in a force distance curve as shown in Fig. 6.3. The measurement starts at a large separation (point A), where there is no deflection of the cantilever. As the piezo moves to the sample, a sudden mechanical instability occurs between point B and point C, and the droplet jumps into contact with the tip and wicks up around the tip to form a meniscus. The cantilever bends downward because of the attractive meniscus force acting on the tip. As the piezo further approaches the surface, the deflection of the cantilever increases while the tip travels the thickness of the droplet and eventually contacts the underlying surface at point D, and the cantilever starts to bend upward. Once the piezo reaches the end of its designated ramp size at point E, it is retracted to its starting position. The tip goes beyond zero deflection and enters the adhesion region. At point F, the elastic force of the cantilever becomes equivalent to the adhesive force, causing the cantilever to snap back to point G. As the tip travels in the liquid, it is deflected as well. The tip deflection occurs in the same direction as the piezo travels for the AFM used in this study. The liquid film thickness (h) is the sum of the travel distance of the piezo (described as h_1 in Fig. 6.3) and the deflection of the cantilever (described as h_2 in Fig. 6.3). Though previous studies

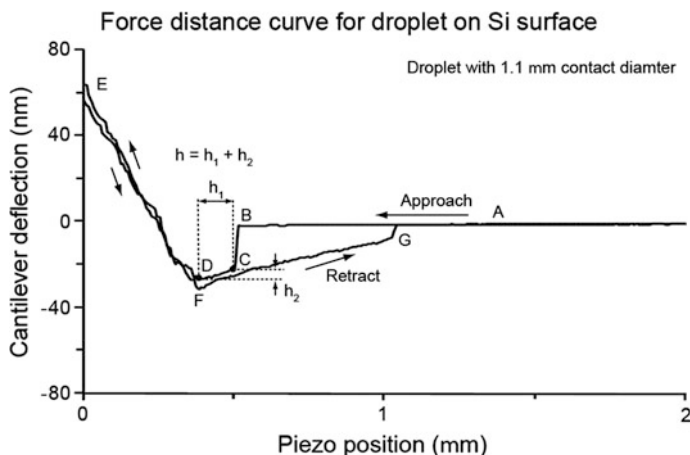


Fig. 6.3 Force distance curve for a droplet with 1.1 μm contact diameter on Si surface. The h is a measure of droplet thickness on the surface

show that h overestimates the actual liquid film thickness, it still provides a good measurement of the thickness of the droplet (Bhushan and Blackman 1991; Chen and Bhushan 2006; Lodge and Bhushan 2006).

The resolution of volume (mass) was about $1 \times 10^{-4} \mu\text{m}^3$ (0.12 fg). This resolution of volume was calculated with the measured data of the shift in the resonance frequency of the cantilever from 122.01 to 122.02 kHz during the evaporation time of 10 min. The resolutions of thickness was about 0.1 nm. This was measured from the calibration data of the z piezo by AFM (Veeco). The resolution of the contact diameter was <1 nm. This was measured from the calibration data of the x-y piezo by AFM (Veeco). The accuracy of volume, thickness, and contact diameter measurements was about $\pm 10\%$, 10% and <1 nm, respectively.

6.2.7 Waterfall/Jet Tests

To investigate the durability of the created surfaces in long-term exposure to water and different kinetic energies of water, a setup was constructed to provide a waterfall/jet flow, as shown in Fig. 6.4 (Jung and Bhushan 2009b). Water from the laboratory faucet flowed through a pipe. Specimens were fixed on the stage using a double-sided adhesive tape. Specimens were placed 2 mm below the four holes in the pipe. In order to minimize flow interruption on the specimens, the runoff plate was tilted to 45° . Waterfall/jet experiments are composed of two different setups. First, water pressure was fixed at 10 kPa. Then, specimens were exposed for 24 h. Next, in order to apply different kinetic energies of the water, the water pressure

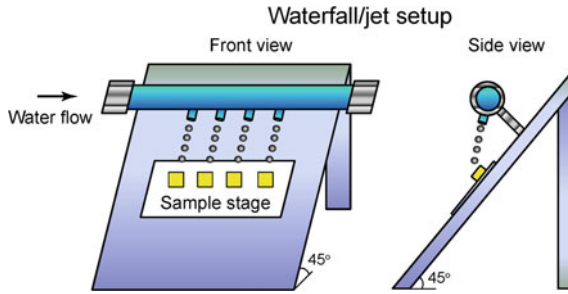


Fig. 6.4 Schematics of waterfall/jet setup shown in *front* and *side* views (Jung and Bhushan 2009b)

was controlled between 0 and 45 kPa. The exposure time applied to the specimens was 20 min for each experiment. During the tests, the change of static contact angle was measured using droplets of about 5 μL in volume (with radius of a spherical droplet about 1 mm) deposited on the substrate using a microsyringe. For contact angle hysteresis, the advancing and receding contact angles were measured at the front and back of the droplet moving along the tilted surface, respectively. The image of the droplet is obtained by a digital camcorder with a 10 \times optical and 120 \times digital zoom. Images obtained were analyzed using Imagetool[®] software (University of Texas Health Science Center) for the contact angle.

6.2.8 Wear and Friction Tests

To investigate the durability of structured surfaces, wear tests on the surfaces were performed using a commercial AFM (Jung and Bhushan 2009b). With the AFM in contact mode, the surfaces were worn using a 15 μm radius borosilicate ball mounted on a triangular Si_3N_4 cantilever with a nominal spring constant of 0.58 N m^{-1} . Wear scars with dimensions of 50 \times 50 μm^2 were created and scanned for 1 cycle at two different loads of 100 and 10 μN . In order to analyze the changes in the morphology of structured surfaces before and after wear tests, surface height maps were obtained in dimensions of 100 \times 100 μm^2 using a square pyramidal Si(100) tip with a native oxide layer which has a nominal radius of 20 nm on a rectangular Si(100) cantilever with a spring constant of 3 N m^{-1} and at a natural frequency of 76 kHz in tapping mode.

In order to investigate durability at a high load, macroscale wear and friction tests on the structured surfaces were conducted based on an established procedure of using a ball-on-flat tribometer under reciprocating motion (Jung and Bhushan 2009b). A sapphire ball with a diameter of 3 mm and surface finish of about 2 nm RMS was fixed on a stationary holder. A normal load of 10 mN was applied, and the frictional forces were measured with semiconductor strain gauges, which were

then digitized and collected on a computer. Typical test conditions were: stroke length = 800 μm , average linear speed = 1 mm/s, temperature = 22 ± 1 $^{\circ}\text{C}$, and relative humidity = 45 ± 5 %. Wear was characterized by imaging the resulting scar with an optical microscope with a CCD camera before and after wear tests. The number of cycles to failure was determined by identifying the point where a sudden change in the friction force is observed.

6.2.9 Transmittance Measurements

Transmittance measurements were performed using an incandescent light bulb as a point source, an Ocean Optics USB400 spectrometer (Ocean Optics Inc., Dunedin, FL) with a 200 μm aperture width, and an intensified CCD camera. All transmittance data was obtained for a one-sided coating as a percentage of the transmittance of the uncoated substrate in the visible spectrum (400–700 nm).

6.3 Micro- and Nanopatterned Polymers

To investigate the effects of microstructure and nanostructure on contact angle and adhesion, Jung and Bhushan (2006) studied micro- and nanopatterned surfaces made with two types of polymers: poly(methyl methacrylate) (PMMA) and polystyrene (PS). PMMA and PS were chosen because they are widely used in MEMS/NEMS devices (Bhushan 2010). Both hydrophilic and hydrophobic surfaces can be produced by using these two polymers, as PMMA has polar (hydrophilic) groups with high surface energy while PS has electrically neutral and nonpolar (hydrophobic) groups with low surface energy. Furthermore, a PMMA structure can be made hydrophobic by treating it appropriately, for example by coating with a hydrophobic self-assembled monolayer (SAM).

Four types of surface patterns were fabricated from PMMA: a flat film, low aspect ratio asperities (LAR, 1:1 height-to-diameter ratio), high aspect ratio asperities (HAR, 3:1 height-to-diameter ratio), and a replica of the lotus leaf (the lotus pattern). Two types of surface patterns were fabricated from PS: a flat film and the lotus pattern. Figure 6.5 shows SEM images of the two types of nanopatterned structures, LAR and HAR, and the one type of micropatterned structure, lotus pattern, all on a PMMA surface (Burton and Bhushan 2005; Jung and Bhushan 2006). Both micro- and nanopatterned structures were manufactured using soft lithography. For nanopatterned structures, PMMA film was spin-coated on a silicon wafer. A UV-cured mold of polyurethane acrylate (PUA) resin with nanopatterns of interest was made which enables one to create sub-100-nm patterns with a high aspect ratio (Choi et al. 2004). The mold was placed on the PMMA film, and a slight pressure of ~ 10 g/cm² (~ 1 kPa) was applied and annealed at 120 $^{\circ}\text{C}$. Finally, the PUA mold was removed from the PMMA film. For micropatterned

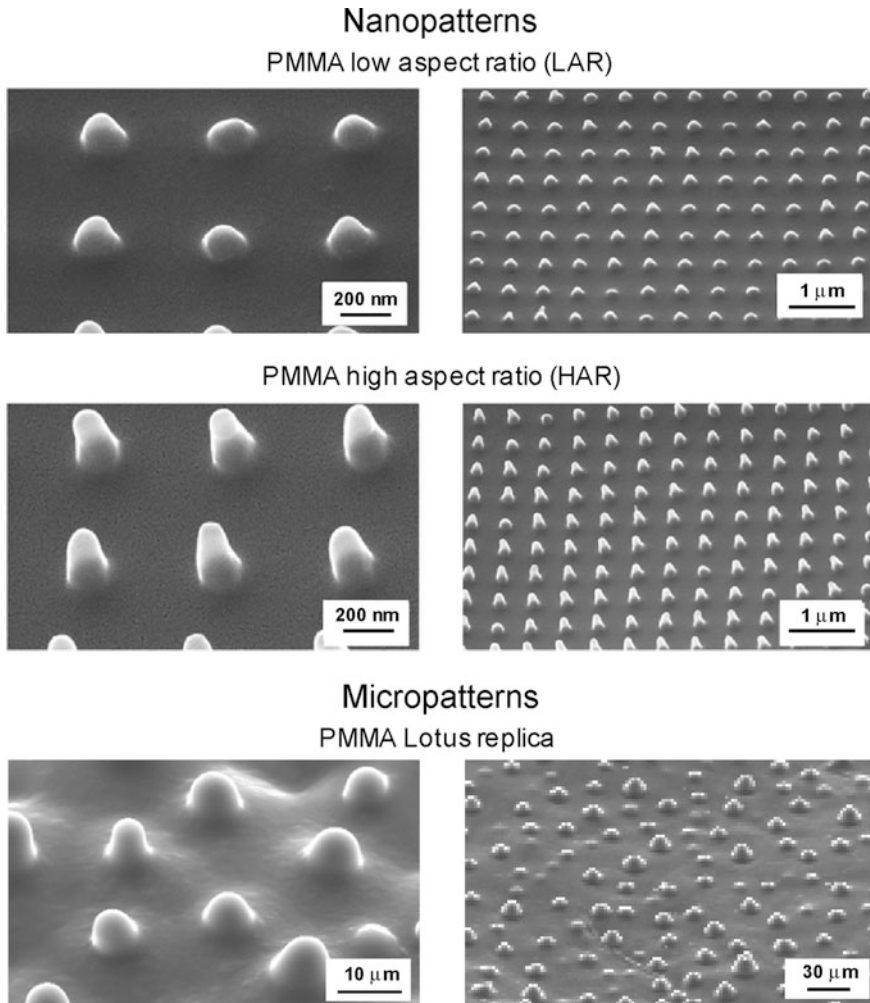


Fig. 6.5 Scanning electron micrographs of the two nanopatterned polymer surfaces (shown using two magnifications to see both the *asperity shape* and the *asperity pattern* on the surface) and the micropatterned polymer surface (*lotus pattern*, which has only microstructures on the surface) (Burton and Bhushan 2005; Jung and Bhushan 2006)

structures, a polydimethylsiloxane (PDMS) mold was first made by casting PDMS against a lotus leaf after the wax had been removed (left with only microstructure), followed by heating. Then, the mold was placed on the PMMA and PS film to create a positive replica of lotus leaf. As shown in Fig. 6.5, it can be seen that only microstructures exist on the surface of lotus pattern (Jung and Bhushan 2006).

Since PMMA by itself is hydrophilic, in order to obtain a hydrophobic sample, a self-assembled monolayer (SAM) of perfluorodecyltriethoxysilane (PFDTES) was

deposited on the sample surfaces using a vapor phase deposition technique. PFDTES was chosen because of its hydrophobic nature. The deposition conditions for PFDTES were 100 °C temperature, 400 Torr pressure, 20 min deposition time, and 20 min annealing time. The polymer surface was exposed to an oxygen plasma treatment (40 W, O₂ 187 Torr, 10 s) prior to coating (Bhushan et al. 2006). The oxygen plasma treatment is necessary to oxidize any organic contaminants on the polymer surface and to alter the surface chemistry to allow for enhanced bonding between the SAM and the polymer surface.

6.3.1 Contact Angle

Jung and Bhushan (2006) measured the static contact angle of water with the micro- and nanopatterned PMMA and PS structures; see Fig. 6.6. Since the Wenzel roughness factor is the parameter that often determines wetting behavior, the

Fig. 6.6 Contact angles for various micro- and nanopatterned surfaces on PMMA and PS polymers and calculated values using Wenzel equation (Jung and Bhushan 2006)

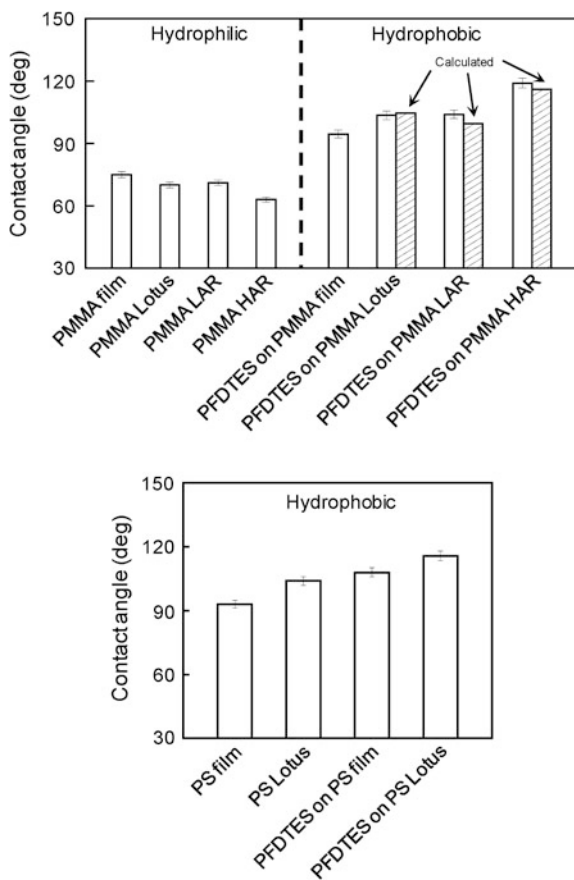


Table 6.1 Roughness factor for micro- and nanopatterned polymers (Jung and Bhushan 2006)

	LAR	HAR	Lotus
R_f	2.1	5.6	3.2

roughness factor was calculated, and it is presented in Table 6.1 for various samples. The data show that the contact angle of the hydrophilic materials decreases with an increase in the roughness factor, as predicted by the Wenzel model. When the polymers were coated with PFDTES, the film surface became hydrophobic. Figure 6.6 also shows the contact angle for various PMMA samples coated with PFDTES. For a hydrophobic surface, the standard Wenzel model predicts an increase of contact angle with roughness factor, which is what happens in the case of patterned samples. The calculated values of the contact angle for various micro- and nanopatterned samples based on the contact angle of the smooth film and Wenzel equation are also presented. The measured contact angle values for the lotus pattern were comparable with the calculated values, whereas for the LAR and HAR patterns, they are higher. It suggests that nanopatterns benefit from air pocket formation. Furthermore, pinning at the top of the nanopatterns may stabilize the droplet. For the PS material (hydrophobic), the contact angle of the lotus pattern also increased with increased roughness factor.

6.3.2 Effect of Submicron Droplet on Contact Angle

Wetting phenomena have been studied and understood at the macroscale. However, micro- and nanoscale wetting mechanisms require further investigation. The actual contact angle under which the liquid-vapor interface comes in contact with the solid surface at the micro- and nanoscale is expected to be a function of the droplet size. Jung and Bhushan (2008c) measured the contact angle of micro- and nanodroplets on various surfaces using an AFM-based technique. The contact angle for different droplet sizes on various hydrophilic and hydrophobic, nanopatterned surfaces is summarized in Fig. 6.7. The data for the microdroplets with 2.4–8.1 μm diameter and nanodroplets with 0.22–1.1 μm diameter were compared with conventional contact angle measurements obtained with a droplet with 2.1 mm diameter (5 μL volume). The measured values of micro- and nanodroplets using an AFM were found to be lower than those of the macrodroplet (Pompe and Herminghaus 2000; Checco et al. 2003). There are several reasons for the scale dependence, such as the effect of contact line tension of a three-phase system (solid-liquid-vapor), which is the excess free energy of a solid-liquid-vapor system per unit length of the contact line (Pompe and Herminghaus 2000; Checco et al. 2003; Quere 2004; Nosonovsky and Bhushan 2007d). Another reason can be surface heterogeneity (Checco et al. 2003). For a thin fluid film present on a surface, the disjoining pressure of a film is repulsive, analogous to the repulsive van der Waals force across a film, and it

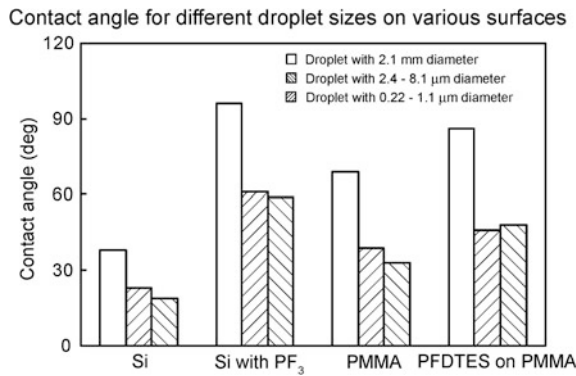


Fig. 6.7 Contact angle measurements for different droplet sizes on various nanopatterned surfaces (Jung and Bhushan 2008c)

causes a film to spread on surfaces. It decreases with the liquid layer thickness (Israelachvili 1992). This pressure may lead to a smaller contact angle at the nanoscale.

6.3.3 Adhesive Force

Adhesion force depends, among other factors, on the hydrophobic/hydrophilic nature of the surfaces, surface structure, and AFM tip radii. Figure 6.8 shows the scale dependence of adhesive force on tip radius for PMMA (hydrophilic) and PFDTES coated on PMMA (hydrophobic) surfaces with various micro- and nanopatterns (Jung and Bhushan 2006). The left bar chart in Fig. 6.8 is for hydrophilic PMMA film and lotus, LAR, and HAR patterns. For increasing radius, the adhesive force increases for each material. With a larger radius, the real area of contact and the meniscus contribution increase, resulting in increased adhesion.

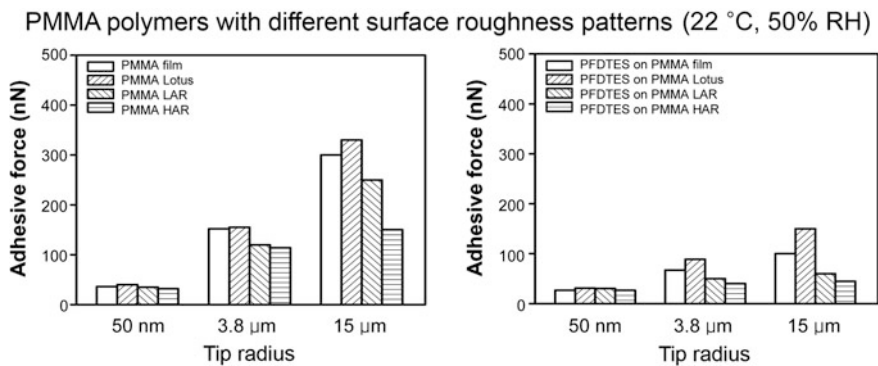


Fig. 6.8 Scale dependence of adhesive force for various micro- and nanopatterned surfaces measured using AFM tips of various radii (Jung and Bhushan 2006)

Adhesive force is the lowest for a nanopattern with the highest bump height. The right bar chart in Fig. 6.8 shows the results for hydrophobic PFDTES coated on each material. These samples show the same trends as the film samples, but the change in adhesion is not as dramatic. The hydrophobicity of PFDTES on material reduces meniscus forces, which in turn reduces adhesion from the surface. The dominant mechanism for the hydrophobic material is real area of contact and not meniscus force, whereas with hydrophilic material there is a combination of real area of contact and meniscus forces (Jung and Bhushan 2006).

6.3.4 Summary

The contact angle data on micro- and nanopatterned polymers show that on hydrophilic surfaces, contact angle decreases with roughness. On hydrophobic surfaces, contact angle increases with roughness, consistent with the Wenzel and Cassie-Baxter equations. The measured contact angles of nanopatterned samples are higher than the calculated values using the Wenzel equation. It suggests that nanopatterns benefit from air pocket formation. The contact angle for micro- and nanodroplets on various hydrophilic and hydrophobic nanopatterned surfaces was found to be scale dependent.

Adhesive force decreases with an increase of the contact angle. The AFM tip radius affects the adhesion because the tip/sample interfaces area changes with tip size. The adhesive force increases with tip size for all samples because of an increased number of contacting asperities (real area of contact) and increased meniscus contribution.

6.4 Micropatterned Si Surfaces

It was reported earlier that the Cassie-Baxter regime is desirable to achieve high contact angle and low contact angle hysteresis. The relevant regime is dependent upon the micro/nanostructure and droplet radius. A criterion transition from the Cassie-Baxter to the Wenzel regime has been proposed. Using micropatterned surfaces, Jung and Bhushan (2007, 2008a) investigated the role of distance between micropillars (pitch) and droplet radius on the contact angle and contact angle hysteresis. The effect of droplet radius has been studied using evaporation studies. To provide insight into the formation of microdroplets on micropatterned surfaces, condensation and evaporation studies of microdroplets over patterned surfaces have been carried out using an ESEM. Jung and Bhushan (2008b) also studied the transition during the bouncing droplet.

Micropatterned surfaces produced from single-crystal silicon (Si) by photolithography and coated with a SAM were used by Jung and Bhushan (2007, 2008a, b) in their study. Silicon has traditionally been the most commonly used

structural material for micro/nanocomponents. A Si surface can be made hydrophobic by coating it with a SAM. One purpose of this investigation was to study the transition from the Cassie-Baxter to the Wenzel regime by changing the distance between the pillars. To create micropatterned Si, two series of nine samples each were fabricated using photolithography. Series 1 had 5- μm diameter and 10- μm height flat-top, cylindrical pillars with different pitch values (7, 7.5, 10, 12.5, 25, 37.5, 45, 60, and 75 μm), and series 2 had 14- μm diameter and 30- μm height flat-top, cylindrical pillars with different pitch values (21, 23, 26, 35, 70, 105, 126, 168, and 210 μm). The pitch is the spacing between the centers of two adjacent pillars. The SAM of 1,1-,2,2-,tetrahydroperfluorodecyltrichlorosilane (PF_3) was deposited on the Si sample surfaces using a vapor phase deposition technique. PF_3 was chosen because of the hydrophobic nature of the surface. The thickness and RMS roughness of the SAM of PF_3 were 1.8 and 0.14 nm, respectively (Kasai et al. 2005).

An optical profiler was used to measure the surface topography of the micropatterned surfaces (Bhushan and Jung 2007, 2008; Jung and Bhushan 2008a, b). One sample each from the two series was chosen to characterize the surfaces. Two different surface height maps can be seen for the micropatterned Si in Fig. 6.9. In each case, a 3-D map and a flat map along with a 2-D profile in a given location of the flat 3-D map are shown. A scan size of 100 $\mu\text{m} \times 90 \mu\text{m}$ was used to obtain a sufficient number of pillars to characterize the surface but also to maintain sufficient resolution to get an accurate measurement.

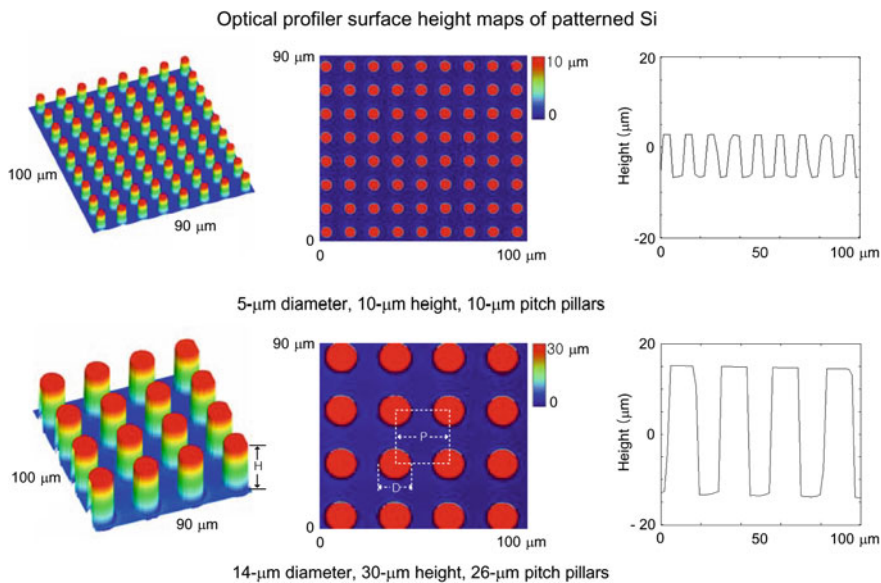


Fig. 6.9 Surface height maps and 2-D profiles of the micropatterned surfaces using an optical profiler (Bhushan and Jung 2007)

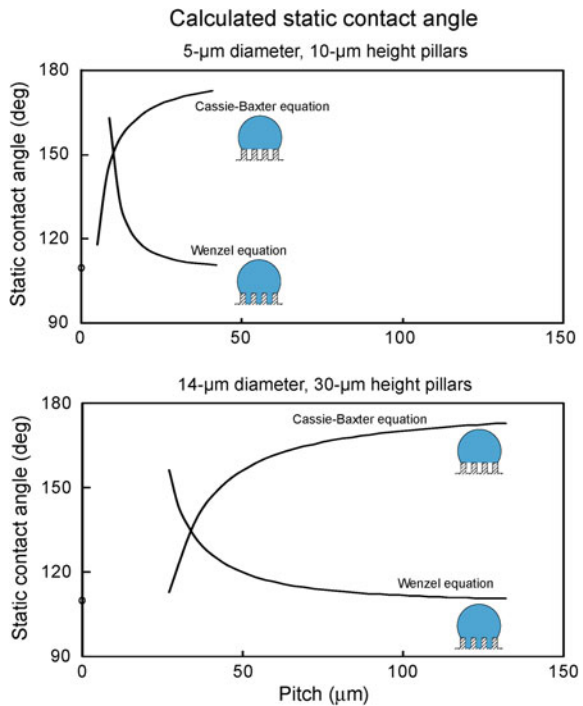
Consider the geometry of flat-top, cylindrical pillars of diameter D , height H , and pitch P , distributed in a regular square array as shown in Fig. 6.9. For the special case of a droplet size much larger than P (of interest in this study), a droplet contacts the flat-top of the pillars forming the composite interface, and the cavities are filled with air. For this case, $f_{LA} = 1 - \frac{\pi D^2}{4P^2} = 1 - f_{SL}$. Further assume that the flat tops are smooth with $R_f = 1$. The contact angles are given by the Wenzel and Cassie-Baxter equations (Bhushan and Jung 2007),

$$\text{Wenzel: } \cos \theta = \left(1 + \frac{\pi DH}{P^2} \right) \cos \theta_0 \tag{6.2}$$

$$\text{Cassie-Baxter: } \cos \theta = \frac{\pi D^2}{4P^2} (\cos \theta_0 + 1) - 1 \tag{6.3}$$

Geometrical parameters of the flat-top, cylindrical pillars in series 1 and 2 are used for calculating the contact angle for the above-mentioned two cases. Figure 6.10 shows the plot of the predicted values of the contact angle as a function of pitch between the pillars for the two cases. The Wenzel and Cassie-Baxter equations present two possible equilibrium states for a water droplet on the surface. This indicates that there is a critical pitch below which the composite interface dominates and above which the homogeneous interface dominates the wetting

Fig. 6.10 Calculated static contact angle as a function of geometric parameters for a given value of θ_0 using the Wenzel and Cassie-Baxter equations for two series of the micropatterned surfaces with different pitch values (Bhushan and Jung 2007)



behavior. Therefore, one needs to find the critical point that can be used to design superhydrophobic surfaces. Furthermore, even in cases where the liquid droplet does not contact the bottom of the cavities, the water droplet can be in a metastable state and can become unstable, with the transition from the Cassie-Baxter to Wenzel regime occurring if the pitch is large.

6.4.1 Cassie-Baxter and Wenzel Transition Criteria

A stable composite interface is essential for the successful design of superhydrophobic surfaces. However, the composite interface is fragile, and it may transform into the homogeneous interface. What triggers the transition between the regimes remains a subject of argument, although a number of explanations have been suggested. Nosonovsky and Bhushan (2007b) have studied destabilizing factors for the composite interface and found that a convex surface (with bumps) leads to a stable interface and high contact angle. Also, they have suggested the effects of a droplet's weight and curvature among the factors which affect the transition.

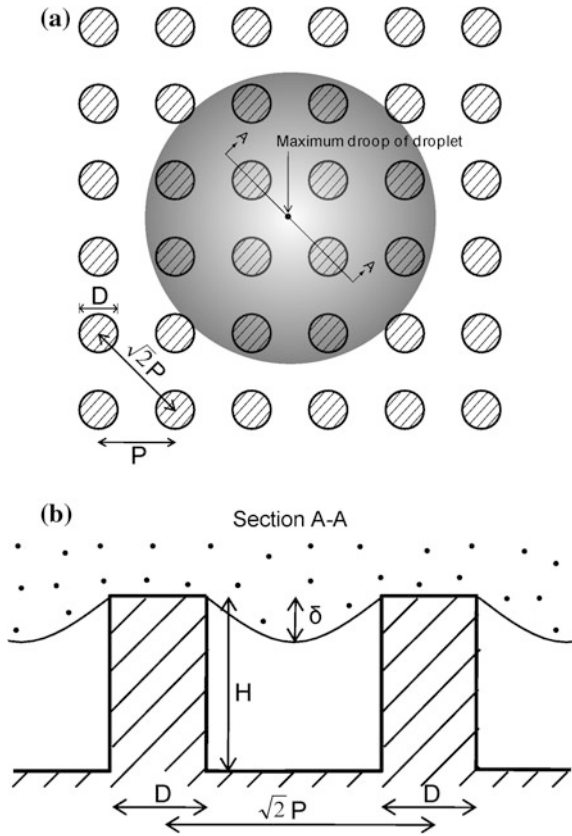
Bhushan and Jung (2007, 2008) and Jung and Bhushan (2007, 2008a, b) investigated the effect of droplet curvature on the Cassie-Baxter and Wenzel regime transition. First, they considered a small water droplet suspended on a superhydrophobic surface consisting of a regular array of circular pillars with diameter D , height H , and pitch P , as shown in Fig. 6.11. The local deformation for small droplets is governed by surface effects, rather than gravity. The curvature of a droplet is governed by the Laplace equation, which relates the pressure inside the droplet to its curvature (Adamson 1990). Therefore, the curvature is the same at the top and at the bottom of the droplet (Nosonovsky and Bhushan 2007d). For the micropatterned surface considered here, the maximum droop of the droplet occurs in the center of the square formed by the four pillars as shown in Fig. 6.11a. Therefore, the maximum droop of the droplet (δ) in the recessed region can be found in the middle of two pillars which are diagonally across as shown in Fig. 6.11b, which is $(\sqrt{2}P - D)^2 / (8R)$. If the droop is greater than the depth of the cavity, then the droplet will just contact the bottom of the cavities between pillars. If it is much greater, transition from the Cassie-Baxter to Wenzel regime occurs,

$$\left(\sqrt{2}P - D\right)^2 / R \geq H \quad (6.4)$$

Equation (6.4) shows that geometry (P and H) and droplet radius R govern the transition. A droplet with a large radius, lower pitch, or larger height is desirable for the Cassie-Baxter regime.

To investigate the dynamic effect of a bouncing water droplet on the Cassie-Baxter and Wenzel regime transition, Jung and Bhushan (2008b) considered a water droplet hitting a superhydrophobic surface as shown in Fig. 6.11. As the

Fig. 6.11 A liquid droplet suspended on a superhydrophobic surface consisting of a regular array of circular pillars. **a** *Plan view*. The maximum droop of droplet occurs in the center of square formed by four pillars. **b** *Side view* in section A-A. The maximum droop of droplet (δ) can be found in the middle of *two pillars* which are diagonally across (Jung and Bhushan 2007)



droplet hits the surface at velocity V , a liquid-air interface below the droplet is formed when the dynamic pressure is less than the Laplace pressure. The Laplace pressure can be written as,

$$p_L = 2\gamma/R = 16\gamma\delta/(\sqrt{2}P - D)^2 \tag{6.5}$$

where γ is the surface tension of the liquid-air interface, and the dynamic pressure of the droplet is equal to,

$$p_d = \frac{1}{2}\rho V^2 \tag{6.6}$$

where ρ is the mass density of the liquid droplet. If the maximum droop of the droplet (δ) is larger than the height of the pillar (H), the droplet contacts the bottom of the cavities between pillars. Determination of the critical velocity at which the droplet touches the bottom is obtained by equating the Laplace pressure to the

dynamic pressure. To develop a composite interface, velocity should be smaller than the critical velocity given as,

$$V < \sqrt{\frac{32\gamma H}{\rho(\sqrt{2}P - D)^2}} \quad (6.7)$$

Furthermore, in the case of large distances between the pillars, the liquid-air interface can easily be destabilized due to dynamic effects. This leads to the formation of the homogeneous solid-liquid interface (Nosonovsky and Bhushan 2007b). Equation (6.7) shows that critical velocity increases with a decrease of pitch or an increase of pillar height.

Nosonovsky and Bhushan (2008e) used the energy barrier approach to study the Cassie-Baxter and Wenzel transition. The energy barrier is given by the product of the height of the pillars (H), pillar perimeter (πD), pillar density ($1/P^2$), and the area (A_0) required to initiate the transition, and the corresponding change in the surface energy,

$$\Delta E = A_0 \frac{\pi H D}{P^2} (\gamma_{SL} - \gamma_{SA}) = -A_0 \frac{\pi H D}{P^2} \cos \theta_0 \quad (6.8)$$

where $A_0 = \pi(R \sin \theta)^2$.

For a short pitch, the net energy of the Cassie-Baxter state is lower than that of the Wenzel state, whereas for larger pitch values, the energy of the Wenzel state is lower (Fig. 3.10c). However, due to the energy barriers, a metastable Cassie-Baxter state with a higher energy than the Wenzel state may be found.

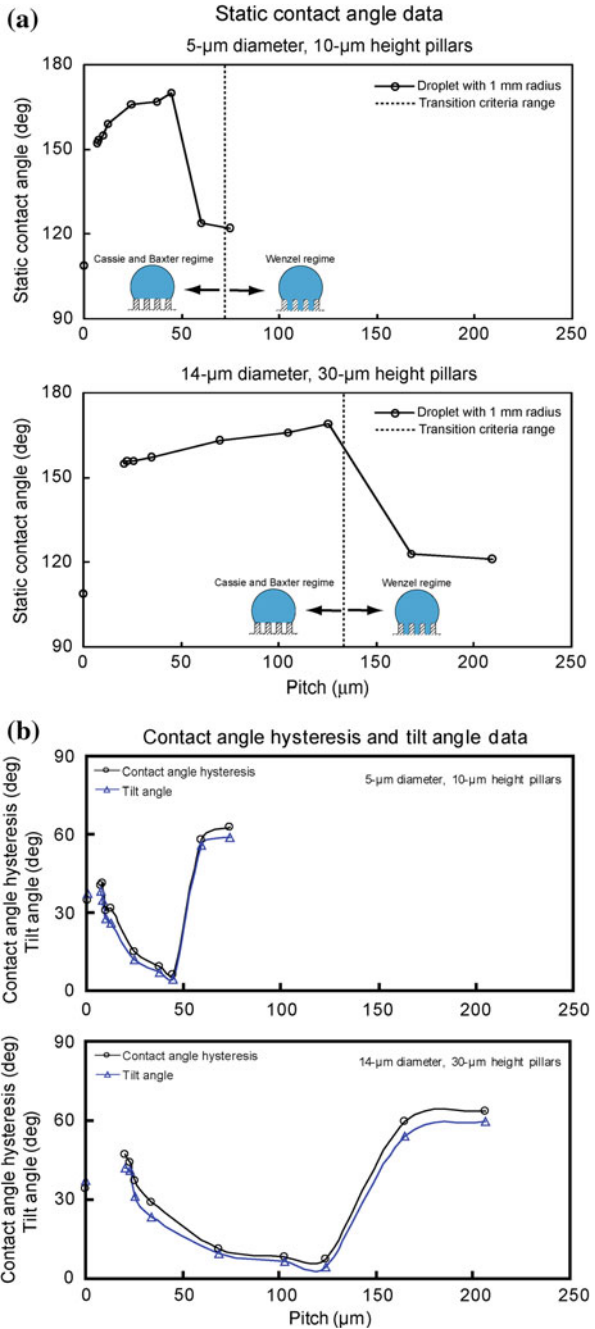
The energy barrier of the Cassie-Baxter and Wenzel transition can be estimated as the kinetic energy of the droplet. The kinetic energy of a droplet of radius R_0 , mass m , density ρ , and velocity V is given by,

$$E_{kin} = \frac{(4/3)\pi\rho R^3 V^2}{2}. \quad (6.9)$$

6.4.2 Effect of Pitch Value on the Transition

In order to study the effect of pitch value on the transition from the Cassie-Baxter to the Wenzel regime, the static contact angles were measured on the micropatterned Si coated with PF_3 , and the data are plotted as a function of pitch between the pillars in Fig. 6.12a (Bhushan and Jung 2007, 2008; Jung and Bhushan 2007, 2008a, b). A dotted line represents the transition criteria range obtained using (6.4). The flat Si coated with PF_3 showed a static contact angle of 109° . The contact angle of selected micropatterned surfaces is much higher than that of the flat surfaces. It first increases with an increase in the pitch values, then drops rapidly to a value slightly

Fig. 6.12 **a** Static contact angle [a dotted line represents the transition criteria range obtained using (6.4)] and **b** contact angle hysteresis and tilt angle as a function of geometric parameters for two series of the micropatterned surfaces with different pitch values for a droplet with 1 mm in radius ($5 \mu\text{L}$ volume). Data at zero pitch correspond to a flat sample (Bhushan and Jung 2007; Jung and Bhushan 2007)



higher than that of the flat surfaces. In the first portion, it jumps to a high value of 152° corresponding to a superhydrophobic surface and continues to increase to 170° at a pitch of $45\ \mu\text{m}$ in series 1 and $126\ \mu\text{m}$ in series 2. Open air space increases with an increase in pitch, which is responsible for the propensity of air pocket formation. The sudden drop at about a pitch value of $50\ \mu\text{m}$ in series 1, and $150\ \mu\text{m}$ in series 2, corresponds to the transition from the Cassie-Baxter to the Wenzel regime. In series 1, the value predicted from the curvature transition criteria (6.4) is a little higher than the experimental observations. However, in series 2, there is a good agreement between the experimental data and the values theoretically predicted by Jung and Bhushan (2007, 2008a, b) for the Cassie-Baxter and Wenzel transition.

Figure 6.12b shows contact angle hysteresis and tilt angle as a function of pitch between the pillars (Bhushan and Jung 2007, 2008). Both angles are comparable. The flat Si coated with PF_3 showed a contact angle hysteresis of 34° and tilt angle of 37° . The angle first increases with an increase of pitch value, which has to do with pinning of the droplet at the sharp edges of the micropillars. Figure 6.13 shows droplets on micropatterned Si with $5\ \mu\text{m}$ diameter and $10\ \mu\text{m}$ height pillars with different pitch values. The asymmetrical shape of the droplet signifies pinning. The pinning on the micropatterned surfaces can be observed as compared to the flat surface. The micropatterned surface with low pitch ($7\ \mu\text{m}$) has more pinning than the micropatterned surface with high pitch ($37.5\ \mu\text{m}$), because the micropatterned surface with low pitch has more sharp edges in contact with a droplet. As the pitch increases, there is a higher propensity of air pocket formation and fewer numbers of sharp edges per unit area, which is responsible for the sudden drop in the angle. The lowest contact angle hysteresis and tilt angle are 5° and 3° , respectively, which were observed on the micropatterned Si with pitch values of $45\ \mu\text{m}$ in series 1 and $126\ \mu\text{m}$ in series 2. Above a pitch value of $50\ \mu\text{m}$ in series 1 and $150\ \mu\text{m}$ in series 2, the angle increases very rapidly because of transition to the Wenzel regime.

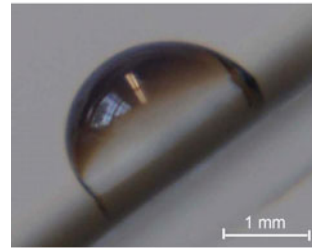
These results suggest that air pocket formation and the reduction of pinning in the micropatterned surface play an important role for a surface with both low contact angle hysteresis and tilt angle (Bhushan and Jung 2007, 2008). Hence, to create superhydrophobic surfaces, it is important that they are able to form a stable composite interface with air pockets between solid and liquid.

6.4.3 *Observation of Transition During the Droplet Evaporation*

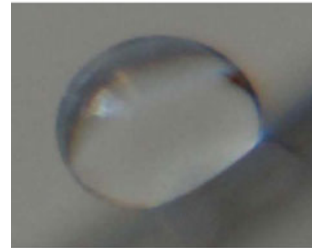
In order to study the effect of droplet size on the transition from a composite state to a wetted state, Jung and Bhushan (2007, 2008a) performed droplet evaporation experiments to observe the Cassie-Baxter and Wenzel transition on two different micropatterned Si surfaces coated with PF_3 . The series of four images in Fig. 6.14 shows the successive photos of a droplet evaporating on the two micropatterned

Fig. 6.13 Optical micrographs of droplets on the inclined micropatterned surfaces with different pitch values. The images were taken when the droplet started to move down. Data at zero pitch correspond to a flat sample (Bhushan and Jung 2007)

Patterned surfaces with 5- μm diameter and 10- μm height pillars with different pitch values



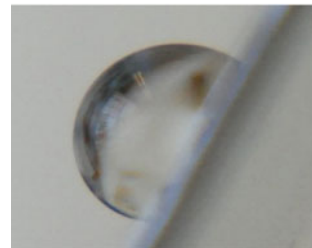
0 μm pitch



7 μm pitch



37.5 μm pitch



75 μm pitch

surfaces. The initial radius of the droplet was about 700 μm . The time interval between first two photos was 180 s, and between the latter two was 60 s. In the first three photos, the droplet is shown in a Cassie-Baxter state, and its size gradually decreases with time. However, the transition from the Cassie-Baxter to Wenzel

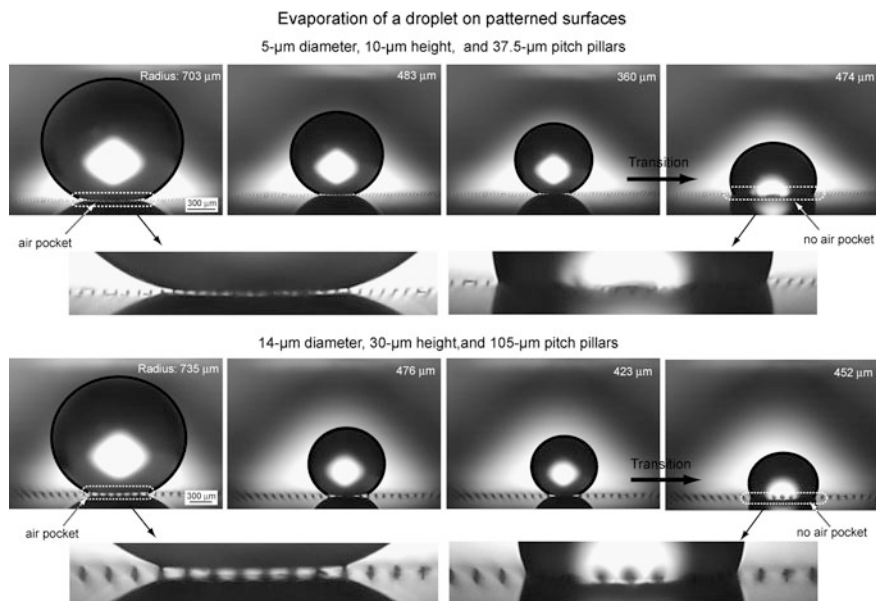
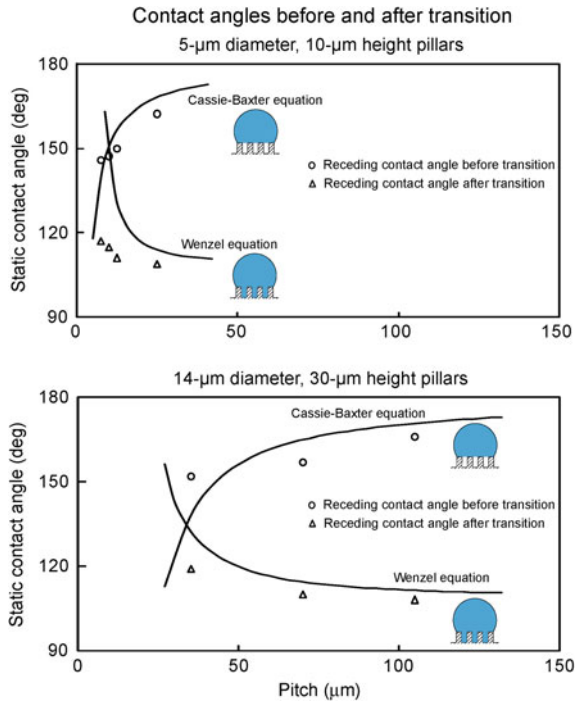


Fig. 6.14 Evaporation of a droplet on two different micropatterned surfaces. The initial radius of the droplet is about 700 μm , and the time interval between the first two photos was 180 s and between the latter two was 60 s. As the radius of the droplet reaches 360 μm on the surface with 5- μm diameter, 10- μm height, and 37.5- μm pitch pillars, and 420 μm on the surface with 14- μm diameter, 30- μm height, and 105- μm pitch pillars, the transition from the Cassie-Baxter regime to Wenzel regime occurs, as indicated by the *arrow*. Before the transition, an air pocket is clearly visible at the *bottom* area of the droplet, but after the transition, an air pocket is not found at the *bottom* area of the droplet (Jung and Bhushan 2008a)

regime occurred as the radius of the droplet reached 360 μm on the surface with 5 μm diameter, 10 μm height, and 37.5 μm pitch pillars, and 423 μm on the surface with 14 μm diameter, 30 μm height, and 105 μm pitch pillars, as indicated by the arrow. The light passes below the first droplet, indicating that air pockets exist, so that the droplet is in the Cassie-Baxter state. However, an air pocket is not visible below the last droplet, so it is in the Wenzel state. This could result from an impalement of the droplet in the micropatterned surface, characterized by a smaller contact angle.

To find the contact angle before and after the transition, the values of the contact angle are plotted against the theoretically predicted value, based on the Wenzel and Cassie-Baxter (Chap. 3) models. Figure 6.15 shows the static contact angle as a function of geometric parameters for the experimental contact angles before (circle) and after (triangle) the transition compared to the Wenzel and Cassie-Baxter equations (solid lines) with a given value of θ_0 for two series' of micropatterned Si with different pitch values coated with PF_3 (Jung and Bhushan 2008a). The fit is good between the experimental data and the theoretically predicted values for the contact angles before and after transition.

Fig. 6.15 Receding contact angle as a function of geometric parameters before (circle) and after (triangle) transition compared with predicted static contact angle values obtained using the Wenzel and Cassie-Baxter equations (solid lines) with a given value of θ_0 for two series of the micropatterned surfaces with different pitch values (Jung and Bhushan 2008a)



To prove the validity of the transition criteria in terms of droplet size, the critical radius of a droplet deposited on the micropatterned Si with different pitch values coated with PF_3 is measured during the evaporation experiment (Jung and Bhushan 2007, 2008a). Figure 6.16 shows the radius of a droplet as a function of geometric parameters for the experimental results (circle) compared with the transition criterion (6.4) from the Cassie-Baxter regime to Wenzel regime (solid lines) for two series of micropatterned Si with different pitch values coated with PF_3 . It is found that the critical radius of impalement is in good quantitative agreement with the predictions. The critical radius of the droplet increases linearly with the geometric parameter (pitch). For a surface with small a pitch, the critical radius of droplet can become quite small.

To verify the transition, Jung and Bhushan (2007, 2008a) used another approach using dust mixed in water. Figure 6.17 presents the dust trace remaining after a droplet with 1 mm radius (5 μL volume) has evaporated on the two micropatterned Si surfaces. As shown in the top image, after the transition from the Cassie-Baxter regime to Wenzel regime, the dust particles remained not only at the top, but also at the bottom of the pillars with a footprint size of about 450 μm . However, as shown in the bottom image, the dust particles remained on only a few pillars with a footprint size of about 25 μm until the end of the evaporation process. From

Fig. 6.16 Radius of droplet as a function of geometric parameters for the experimental results (*circle*) compared with the transition criteria from the Cassie-Baxter regime to Wenzel regime (*solid lines*) for two series of the micropatterned surfaces with different pitch values (Jung and Bhushan 2008a)

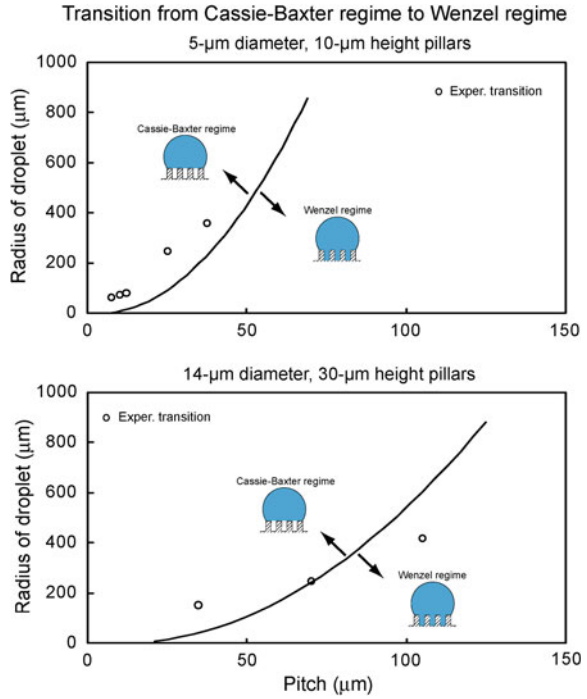


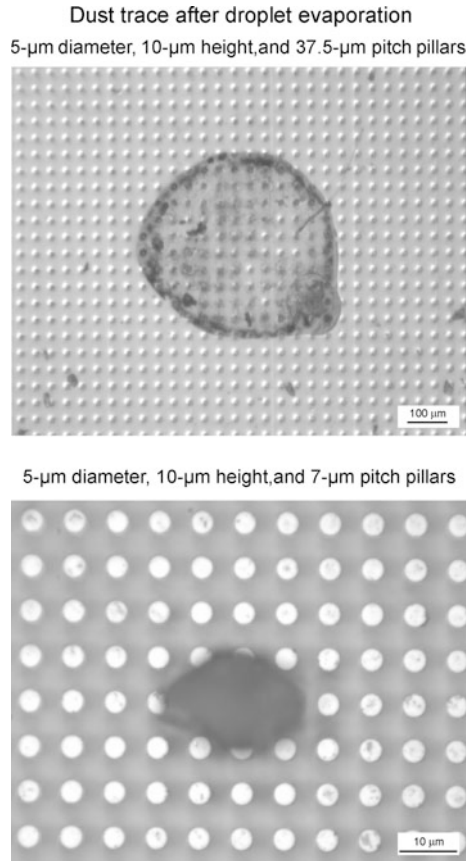
Fig. 6.16, it is observed that the transition occurs at about 300 μm radius of droplet on the 5 μm diameter and 10 μm height pillars with 37.5 μm pitch. The transition does not occur on the patterned Si surface with pitch of less than about 5 μm. These experimental observations are consistent with model predictions. In the literature, it has been shown that on superhydrophobic natural lotus, the droplet remains in the Cassie-Baxter regime during the evaporation process (Zhang et al. 2006). This indicates that the distance between the pillars should be minimized to improve the ability of the droplet to resist sinking.

6.4.4 Another Cassie-Baxter and Wenzel Transition for Different Series

Nosonovsky and Bhushan (2007a, c, d, 2008b, c) studied the data for the Cassie-Baxter and Wenzel transition with the two series of surfaces using the non-dimensional spacing factor

$$S_f = \frac{D}{P} \quad (6.10)$$

Fig. 6.17 Dust trace remained after droplet evaporation for the micropatterned surface. In the *top image*, the transition occurred at 360 μm radius of droplet, and in the *bottom image*, the transition occurred at about 20 μm radius of droplet during the process of droplet evaporation. The footprint size is about 450 and 25 μm for the *top* and *bottom images*, respectively (Jung and Bhushan 2008a)



The values of the droplet radius at which the transition occurs during evaporation plotted against the spacing factor scale well for the two series of the experimental results, yielding virtually the same straight line. Thus, the two series of micropatterned surfaces scale well with each other, and the transition occurs at the same value of the spacing factor multiplied by the droplet radius (Fig. 6.18a). The physical mechanism leading to this observation remains to be determined. However, it is noted that this mechanism is different from the one suggested by (6.4). The observation suggests that the transition is a linear one-dimensional phenomenon and that neither droplet droop (that would involve P^2/H), nor droplet weight (that would involve R^3) are responsible for the transition, but rather linear geometric relations are involved. Note that the experimental values approximately correspond to the values of the ratio $RD/P = 50 \mu\text{m}$, or the total area of the pillar tops under the droplet $(\pi D^2/4)\pi R^2/P^2 = 6200 \mu\text{m}^2$.

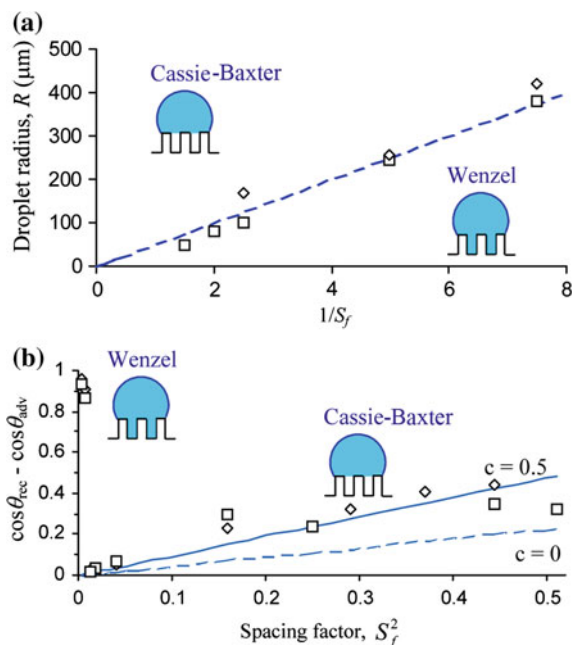


Fig. 6.18 **a** Droplet radius, R , for the Cassie-Baxter and Wenzel transition as a function of $P/D = 1/S_f$. It is observed that the transition for two series of the micropatterned surfaces takes place at a constant value of $RD/P \sim 50 \mu\text{m}$ (dashed line). This shows that the transition is a linear phenomenon. **b** The difference $\cos \theta_{\text{rec}} - \cos \theta_{\text{adv}}$ as a function of S_f for the 1st (squares) and 2nd (diamonds) series of the experiments compared with the theoretically predicted values of $\cos \theta_{\text{adv}} - \cos \theta_{\text{rec}} = (D/P)^2(\pi/4)(\cos \theta_{\text{adv}0} - \cos \theta_{\text{rec}0}) + c(D/P)^2$, where c is a proportionality constant. It is observed that when only the adhesion hysteresis/interface energy term is considered ($c = 0$), the theoretical values are underestimated by about a half, whereas $c = 0.5$ provides a good fit. Therefore, the contribution of the adhesion hysteresis is of the same order of magnitude as the contribution kinetic effects (adapted from Nosonovsky and Bhushan 2007c)

6.4.5 Contact Angle Hysteresis and Wetting/Dewetting Asymmetry

Contact angle hysteresis can be viewed as a result of two factors that act simultaneously. First, the changing contact area affects the contact angle hysteresis, since a certain value of contact angle hysteresis is inherent for even a nominally flat surface. Decreasing the contact area by increasing the pitch between the pillars leads to a proportional decrease of the contact angle hysteresis. This effect is clearly proportional to the contact area between the solid surface and the liquid droplet. Second, the edges of the pillar tops prevent the motion of the triple line. This roughness effect is proportional to the contact line density, and its contribution was, in the experiment, comparable with the contact area effect. Interestingly, the effect

of the edges is much more significant for the advancing than for the receding contact angle.

Nosonovsky and Bhushan (2007a, c, d, 2008b, c) studied the wetting of two series of micropatterned Si surfaces with different pitch values coated with PF₃ based on the spacing factor (6.10) (Fig. 6.18b). They found that the contact angle hysteresis involves two terms: the term $S_f^2(\pi/4)(\cos \theta_{adv0} - \cos \theta_{rec0})$ corresponding to the adhesion hysteresis (which is found even in a nominally flat surface and is a result of molecular-scale imperfectness), and the term $H_r \propto D/P^2$ corresponding to microscale roughness and proportional to the edge line density. Thus the contact angle hysteresis is given, based on the equation for rough surfaces (Chap. 3) and (6.10), by using $R_f = 1 + \frac{\pi DH}{P^2}$ and $f_{LA} = 1 - \frac{\pi D^2}{4P^2} = 1 - f_{SL}$ (Bhushan et al. 2007; Nosonovsky and Bhushan 2007b)

$$\cos \theta_{adv} - \cos \theta_{rec} = \frac{\pi}{4} S_f^2 (\cos \theta_{adv0} - \cos \theta_{rec0}) + H_r \quad (6.11)$$

Besides the contact angle hysteresis, the asymmetry of the Wenzel and Cassie-Baxter states is the result of the wetting/dewetting asymmetry. While the fragile metastable Cassie-Baxter state is often observed, as well as its transition to the Wenzel state, the opposite transition never happens. Using (6.2) and (6.3), the contact angle with micropatterned surfaces is given by Bhushan et al. (2007), Nosonovsky and Bhushan (2007b)

$$\cos \theta = \left(1 + 2\pi S_f^2\right) \cos \theta_0 \quad (\text{Wenzel state}) \quad (6.12)$$

$$\cos \theta = \frac{\pi}{4} S_f^2 (\cos \theta_0 + 1) - 1 \quad (\text{Cassie-Baxter state}) \quad (6.13)$$

For a perfect macroscale system, the transition between the Wenzel and Cassie-Baxter states should occur only at the intersection of the two regimes (the point at which the contact angle and net energies of the two regimes are equal, corresponding to $S_f = 0.51$). However, it is observed that the transition from the metastable Cassie-Baxter to stable Wenzel occurs at much lower values of the spacing factor $0.083 < S_f < 0.111$.

As shown in Fig. 6.19a, the stable Wenzel state (i) can transform into the stable Cassie-Baxter state with increasing S_f (ii). The metastable Cassie-Baxter state (iii) can abruptly transform (iv) into the stable Wenzel state (i). The transition point (i–ii) corresponds to equal free energies in the Wenzel and Cassie-Baxter states, whereas the transition (iv) corresponds to the Wenzel energy being much lower than the Cassie-Baxter energy. Thus, the transition (iv) involves significant energy dissipation and is irreversible (Nosonovsky and Bhushan 2007c). The solid and dashed straight lines correspond to the values of the contact angle, calculated from (6.12) to (6.13) using the contact angle for a nominally flat surface, $\theta_0 = 109^\circ$. The two series' of the experimental data are shown with squares and diamonds.

Fig. 6.19 Theoretical (solid and dashed) and experimental (squares for the 1st series, diamonds for the 2nd series) **a** contact angle as a function of the spacing factor, **b** advancing contact angle, and **c** receding contact angle and values of the contact angle observed after the transition during evaporation (blue) (adapted from Nosonovsky and Bhushan 2007c)

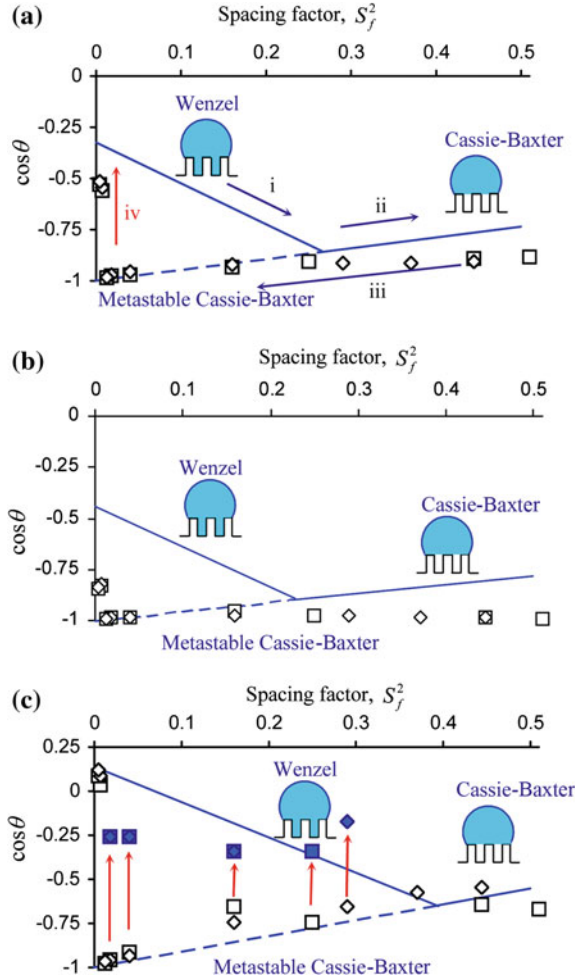


Figure 6.19b shows the values of the advancing contact angle plotted against the spacing factor (6.10). The solid and dashed straight lines correspond to the values of the contact angle for the Wenzel and Cassie-Baxter states, calculated from (6.12) to (6.13) using the advancing contact angle for a nominally flat surface, $\theta_{adv0} = 116^\circ$ (Nosonovsky and Bhushan 2007c). It is observed that the calculated values underestimate the advancing contact angle, especially for a large S_f (small distance between the pillars or pitch P). This is understandable, because the calculation takes into account only the effect of the contact area and ignores the effect of roughness and edge line density [it corresponds to $H_r = 0$ in (6.11)], while this effect is more pronounced for high pillar density (big S_f). In a similar manner, the contact angle is underestimated for the Wenzel state, since the pillars constitute a barrier for the advancing droplet.

Figure 6.19c shows the values of the contact angle after the transition took place (squares and diamonds), as it was observed during evaporation (Nosonovsky and Bhushan 2007c). For both series, the values almost coincide. For comparison, the values of the receding contact angle measured for millimeter-sized water droplets are also shown (squares and diamonds), since evaporation constitutes removing liquid, and thus the contact angle during evaporation should be compared with the receding contact angle. The solid and dashed straight lines correspond to the values of the contact angle, calculated from (6.12) to (6.13) using the receding contact angle for a nominally flat surface, $\theta_{\text{rec}0} = 82^\circ$. Figure 6.19c demonstrates a good agreement between the experimental data and (6.12) and (6.13).

In the analysis of the evaporation data of micropatterned surfaces, Nosonovsky and Bhushan (2008b) found several effects specific to the multiscale character of this process. First, they discussed the applicability of the Wenzel and Cassie-Baxter equations for average surface roughness and heterogeneity. These equations relate the local contact angle with the apparent contact angle of a rough/heterogeneous surface. However, it is not obvious what should be the size of roughness/heterogeneity averaging, since the triple line at which the contact angle is defined has two very different length scales: its width is of the molecular scale while its length is on the order of the size of the droplet (that is, microns or millimeters). They presented an argument that in order for the averaging to be valid, the roughness details should be small compared to the size of the droplet (and not the molecular size). They showed that while for uniform roughness/heterogeneity the Wenzel and Cassie-Baxter equations can be applied, for a more complicated case of non-uniform heterogeneity, the generalized equations should be used. The proposed generalized Cassie-Baxter and Wenzel equations are consistent with a broad range of available experimental data. The generalized equations are valid both in the cases when the classical Wenzel and Cassie-Baxter equations can be applied as well as in the cases when the latter fail.

The macroscale contact angle hysteresis and Cassie-Baxter and Wenzel transition cannot be determined from the macroscale equations and are governed by micro- and nanoscale effects, so wetting is a multiscale phenomenon (Nosonovsky and Bhushan 2007a, c, d, 2008b, c). The kinetic effects associated with contact angle hysteresis should be studied at the microscale, whereas the effects of adhesion hysteresis and the Cassie-Baxter and Wenzel transition involve processes at the nanoscale. Their theoretical arguments are supported by the experimental data on micropatterned surfaces. The experimental study of the contact angle hysteresis demonstrates that two different processes are involved: the changing solid-liquid area of contact and pinning of the triple line. The latter effect is more significant for the advancing than for the receding contact angle. The transition between wetting states was observed for evaporating microdroplets, and droplet radius scales well with the geometric parameters of the micropattern.

6.4.6 Contact Angle Measurements During Condensation and Evaporation of Microdroplets on Micropatterned Surfaces

To provide insight into the formation of microdroplets and detailed information about the contact angle on the micropatterned surfaces, ESEM experiments on micropatterned surfaces have been performed during condensation and evaporation. Figure 6.20 shows how water droplets grow and merge in an ESEM (Jung and Bhushan 2008a) that was used as a contact angle analysis tool. Microdroplets (with a diameter less than 1 mm) were distributed on a micropatterned surface coated with PF₃ using condensation by decreasing temperature. At the beginning, some small water droplets appeared, i.e., the water droplets at locations 1, 2, and 3 in the left image. During further condensation with decreasing temperature, the droplets at locations 1 and 3 gradually grew, while the droplets at location 2 merged together. With further condensation, the droplets at locations 1 and 2 gradually grew, while the droplets at location 3 merged together into one large droplet in the right image. In all cases, condensation was initiated at the bottom, therefore, the droplets were in the Wenzel regime.

Compared with the conventional contact angle measurement, ESEM is able to provide detailed information about the contact angle of microdroplets on micropatterned surfaces. The diameter of the water droplets used for the contact angle measurement was 10 μm , so that the size limit pointed out by Stelmashenko et al. (2001) was avoided. For a droplet size smaller than 1 μm , substrate backscattering can distort the intensity profile, such that the images are inaccurate.

As shown in Fig. 6.21, the static contact angle and contact angle hysteresis of the microdroplets on flat and micropatterned surfaces were obtained from the images using the methodology described earlier. Once the microdroplet's condensation and

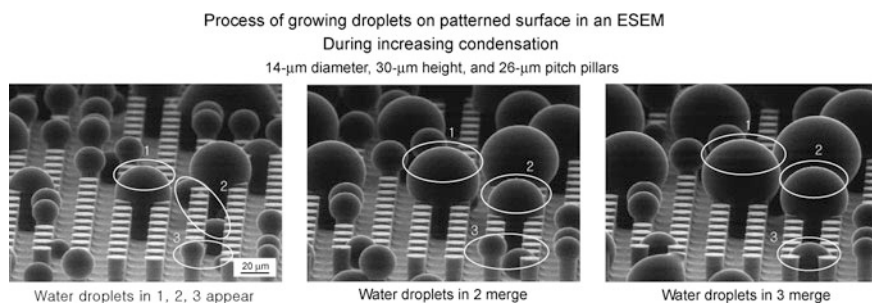


Fig. 6.20 Microdroplet (in dimensions of less than 1 mm diameter) growing and merging process under ESEM during increasing condensation by decreasing temperature. *Left image* Some small water droplets appear at the beginning, i.e. water droplets 1, 2, 3. *Middle image* Water droplets at locations 1 and 3 increase in size and water droplets at location 2 merge together to form one big droplet. *Right image* Water droplets at locations 1 and 2 increase in size and water droplets at location 3 merge together to form one big droplet (Jung and Bhushan 2008a)

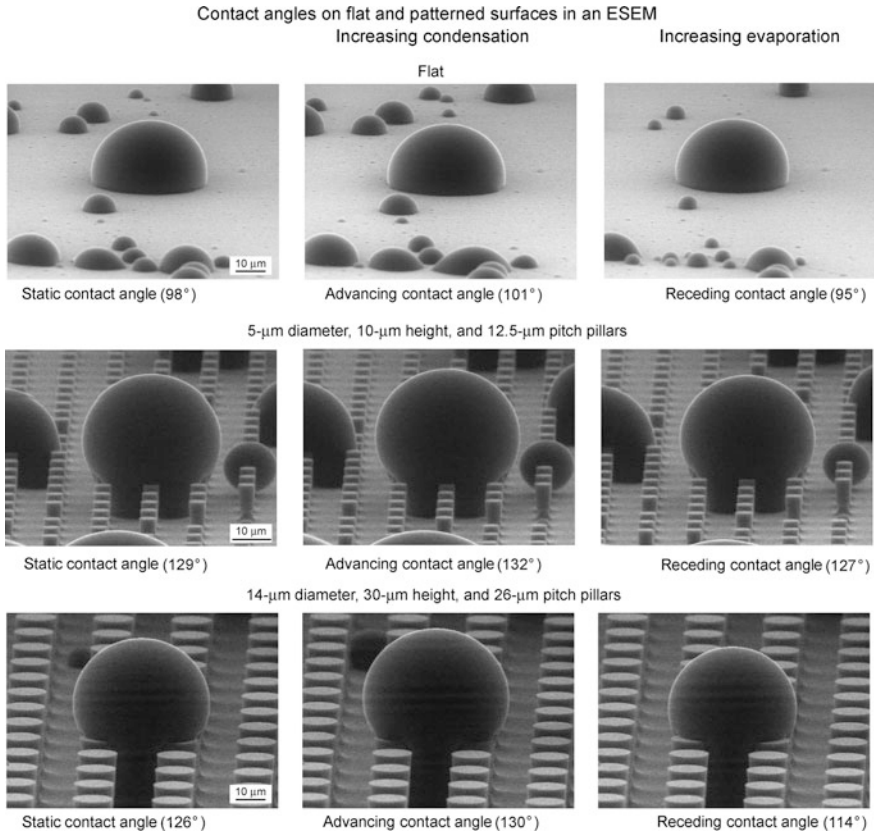
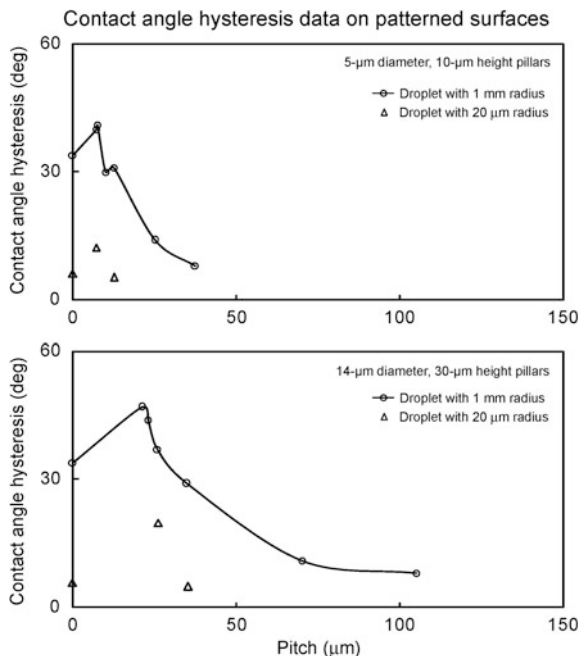


Fig. 6.21 Microdroplets on flat and two micropatterned surfaces using ESEM. Second set of images were taken during increasing condensation, and the third set of images were taken during increasing evaporation. Static contact angle was measured when the droplet was stable. Advancing contact angle was measured after increasing condensation by decreasing the temperature of the cooling stage. Receding contact angle was measured after decreasing evaporation by increasing the temperature of the cooling stage (Jung and Bhushan 2008a)

evaporation reached a dynamic equilibrium, static contact angles were determined. The flat Si coated with PF₃ showed a static contact angle of 98°. The roughness of the micropatterned surfaces coated with PF₃ increased the static contact angle compared to the flat surface coated with PF₃. Advancing and receding contact angles were measured during condensation/evaporation with decreasing/increasing the temperature of the cooling stage, and the contact angle hysteresis was then calculated (Jung and Bhushan 2008a).

Figure 6.22 shows contact angle hysteresis as a function of pitch value for the microdroplets formed in the ESEM (triangles) for two series of micropatterned Si with different pitch values coated with PF₃. Data at zero pitch correspond to a flat Si sample. The droplets with about 20 μm radii, which are larger than the pitch, were

Fig. 6.22 Contact angle hysteresis as a function of pitch value for the microdroplet with about 20 μm radius from ESEM (triangle) compared with the droplet with 1 mm radius (5 μL volume) (circle and solid lines) for two series of the micropatterned surfaces with different pitch values. Data at zero pitch correspond to a flat sample (Jung and Bhushan 2008a)



selected in order to look at the effect of pillars in contact with the droplet. These data were compared with conventional contact angle measurements with a droplet with 1 mm radius (5 μL volume) (Bhushan and Jung 2007). When the distance between pillars increased above a certain value, the contact area between the micropatterned surface and the droplet decreased, resulting in a decrease of the contact angle hysteresis. Both droplets with 1 mm and 20 μm radii showed the same trend. The contact angle hysteresis for the micropatterned surfaces with low pitch were higher compared to the flat surface, due to the effect of sharp edges on the pillars, resulting in pinning (Nosonovsky and Bhushan 2005). Contact angle hysteresis for a flat surface can arise from roughness and surface heterogeneity. For a droplet advancing forward on the micropatterned surfaces, the line of contact of the solid, liquid, and air will be pinned at the edge point until it is able to move, resulting in increasing contact angle hysteresis. The contact angle hysteresis for the microdroplet from ESEM is lower as compared to that for the droplet with 1 mm radius. The difference of contact angle hysteresis between a microdroplet and a droplet with 1 mm radius could come from the different pinning effects because the latter has more sharp edges in contact with a droplet compared to the former. The results show how droplet size can affect the wetting properties of micropatterned Si surfaces (Jung and Bhushan 2008a).

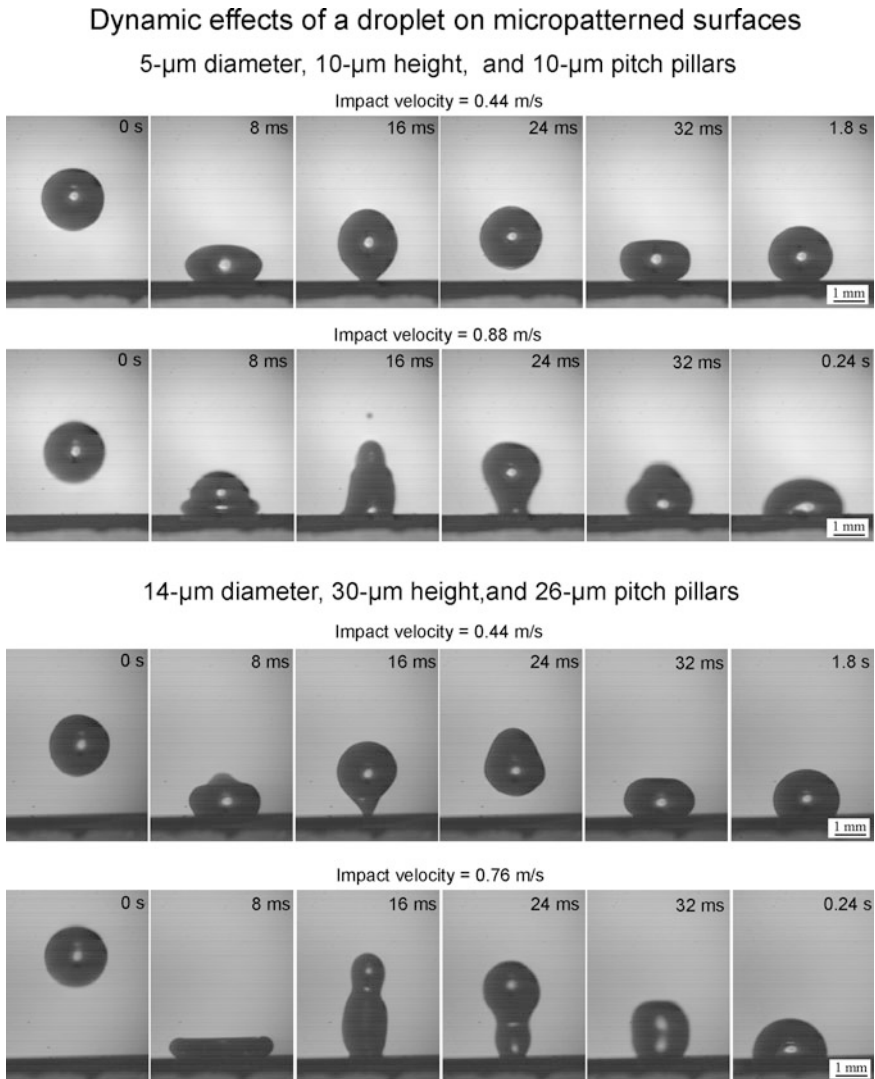


Fig. 6.23 Snapshots of a droplet with 1 mm radius hitting on two different micropatterned surfaces. The impact velocity was obtained just prior to the droplet hitting the surface. The pinning of the droplet on the surface with 5- μm diameter, 10- μm height and 10- μm pitch pillars, and on the surface with 14- μm diameter, 30- μm height and 26- μm pitch pillars occurred at impact velocity of 0.88 and 0.76 m/s, respectively (Jung and Bhushan 2008b)

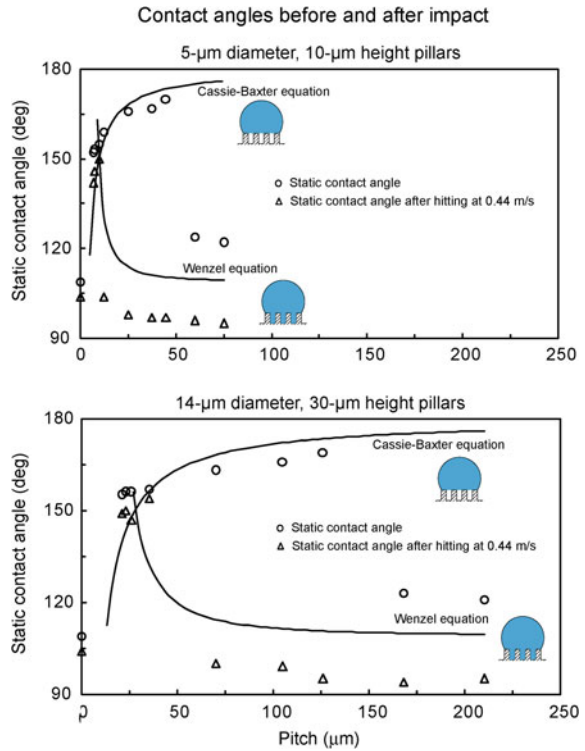
6.4.7 *Observation of Transition During the Bouncing Droplet*

Dynamic effects, such as bouncing of a droplet (e.g. rain droplets hitting the window glass), can destroy the composite interface. Based on (6.7), the relationship between the impact velocity of a droplet and geometric parameters affects the transition from the Cassie-Baxter to the Wenzel regime. Therefore, it is necessary to study the dynamic effect of droplets under various impact velocities.

Jung and Bhushan (2008b) performed bouncing droplet experiments to observe how impact velocity influences the Cassie-Baxter and Wenzel transition during the droplet hitting the surface on two different micropatterned Si surfaces with PF_3 . Figure 6.23 shows photos of a droplet with 1 mm radius hitting the surfaces. The impact velocity was obtained just prior to the droplet hitting the surface. As shown in the images in the first row for the two sets of surfaces, the droplet hitting the surface under an impact velocity of 0.44 m/s first deformed and then retracted, and bounced off the surface. Finally, the droplet sat on the surface and had a high contact angle, which suggests the formation of a solid-air-liquid interface. Next, they repeated the impact experiment by increasing the impact velocity. Bounce off did not occur, and the wetting of the surface (and possibly pinning of droplet) occurred at an impact velocity of 0.88 and 0.76 m/s, respectively. These are referred to as the critical velocity (described earlier). The second row of the two sets of images shows the droplet at the critical velocity. After the droplet hit the surface, it wetted the surface (possibly the droplet was also pinned) after the deformation of the droplet. This is because air pockets do not exist below the droplet as a result of droplet impalement by the pillars, characterized by a smaller contact angle. These observations indicate the transition from a Cassie-Baxter to a Wenzel regime.

To identify whether an interface is in a Wenzel regime or a Cassie-Baxter regime, the contact angle data in the static condition and after bounce off were plotted (Jung and Bhushan 2008b). Figure 6.24 shows the measured static contact angle as a function of pitch value for the droplet with 1 mm radius placed on the surface and for the droplet with 1 mm radius after hitting the surface at 0.44 m/s. The data are compared with predicted static contact angle values obtained using the Wenzel and the Cassie-Baxter equations with a given value of θ_0 (109°) for a smooth surface for two series' of the micropatterned surfaces. In the case of the droplet placed on the surface, as the pitch increases up to $45\ \mu\text{m}$ in series 1 and $126\ \mu\text{m}$ in series 2, the static contact angle first increases gradually from 152° to 170° . Then, the contact angle starts decreasing sharply. The increase in the contact angle occurs because of an increase in the roughness factor and the formation of composite surface (Bhushan and Jung 2007). The decrease in contact angle at pitch values higher than $60\ \mu\text{m}$ for series 1 and $168\ \mu\text{m}$ for series 2 occurs due to the transition from the composite interface to the solid-liquid interface. In the case of the droplet hitting the surface at 0.44 m/s, it is shown that the liquid-air interface can easily be destabilized due to dynamic impact on the surface with a pitch value higher than $12.5\ \mu\text{m}$ for series 1 and $70\ \mu\text{m}$ for series 2, although the droplet is in

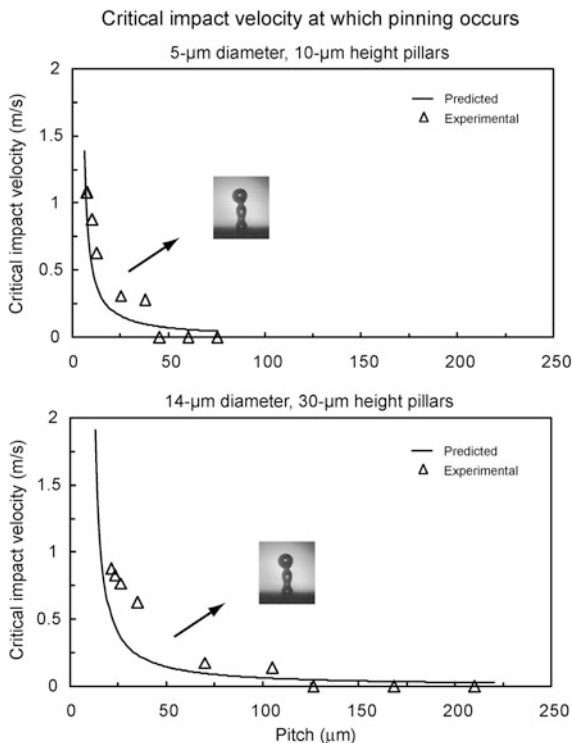
Fig. 6.24 Measured static contact angle as a function of pitch value for the droplet with 1 mm radius placed on the surface (*circles*) and for the droplet with 1 mm radius after hitting the surface at 0.44 m/s (*triangles*). The data are compared with predicted static contact angle values obtained using Wenzel and Cassie-Baxter equations (*solid lines*) with a given value of θ_0 (109°) for a smooth surface for two series of the micropatterned Si with different pitch values (Jung and Bhushan 2008b)



the Cassie-Baxter regime when it is placed on the surface. The static contact angle of the droplet after hitting at 0.44 m/s is lower than that of the droplet when placed. It can be interpreted that after hitting, the droplet contacts the bottom of the cavities between pillars and pushes out the entrapped air under the droplet, resulting in an abrupt increase of the solid-liquid surface area by dynamic impact. It will be shown in the following paragraph that the critical velocity at which wetting occurs for series 1 and series 2 samples is equal to about 0.44 m/s at pitch values larger than 12.5 and 70 µm respectively. Thus, wetting at the velocity used here is expected.

To study the validity of the transition criterion (6.7), the critical impact velocity at which wetting of the surface (possibly pinning of droplet) occurs was measured (Jung and Bhushan 2008b). For calculations, the surface tension of the water-air interface (γ) was taken at 0.073 N/m, the mass density (ρ) is 1000 kg/m³ for water, and $1 \text{ kg} \cdot \text{m/s}^2 = 1 \text{ N}$ (Adamson 1990). Figure 6.25 shows the measured critical impact velocity of a droplet with 1 mm radius as a function of pitch value. The trends were compared with the predicted curve. It was found that the critical impact velocity at which wetting occurs was in good quantitative agreement with the predictions. The critical impact velocity of the droplet decreased with the geometric

Fig. 6.25 Measured critical impact velocity of droplet with 1 mm radius as a function of pitch value (*triangles*). The data are compared with the criterion of impact velocity for the pinning of droplet (*solid lines*) for two series of the micropatterned Si with different pitch values (Jung and Bhushan 2008b)



parameter (pitch). For the surface with a small pitch, the critical impact velocity of a droplet can be large.

The energy barrier of the Cassie-Baxter and Wenzel transition can be estimated as the kinetic energy of the droplets (Nosonovsky and Bhushan 2008e). Figure 6.26 shows the dependence of the kinetic energy corresponding to the transition, E_{kin} , on $\Delta E/(A_0 \cos \theta_0)$ calculated from (6.8). It was observed that the dependence was close to linear. However, the series of smaller pillars had larger energies of transition. The value of A_0 is in the range $0.11 \text{ mm}^2 < A_0 < 0.18 \text{ mm}^2$ for series 1 and $0.05 \text{ mm}^2 < A_0 < 0.11 \text{ mm}^2$ for series 2, which is of the same order as the actual area under the droplet.

These results suggest that the energy barrier for the Cassie-Baxter and Wenzel transition is given by (6.8) and is proportional to the area under the droplet (Nosonovsky and Bhushan 2008e). For droplets sitting on the surface or evaporating, the transition takes place when the size of the barrier decreases to the value of the vibrational energy, U . The vibrational energy of the droplet is the energy associated with the vibration of the droplet due to surface waves, thermal vibration, etc. Assuming $U = \text{const}$, the proportionality of P/D and R suggests that the energy

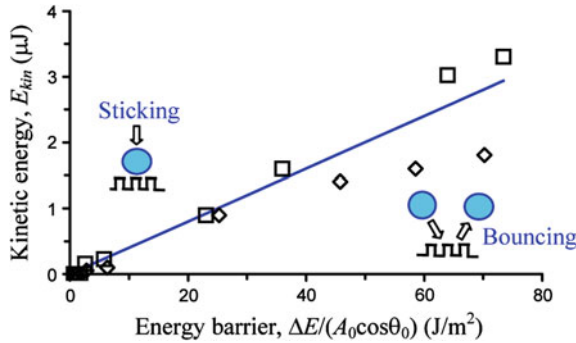


Fig. 6.26 Bouncing droplets dependency of the kinetic energy of a droplet corresponding to the regime transition upon the energy barrier calculated from (6.8) (squares for series 1 and diamonds for series 2). The fit (solid line) is shown for $A_0 = 0.12 \text{ mm}^2$ (Nosonovsky and Bhushan 2008e)

barrier is proportional to RD/P . This is indeed true, since the area under the droplet $A_0 = \pi(R \sin \theta)^2$. Substituting $\sin^2 \theta = 0.1$, $\cos \theta_0 = \cos 109^\circ = -0.33$, $\gamma_{LA} = 0.072 \text{ J/m}^2$ in (6.8) and taking the observed value $RD/P = 50 \text{ }\mu\text{m}$ yields an estimated value of the vibrational energy $U = 1.2 \times 10^{-10} \text{ J}$. The transition happens because the size of the droplet is decreased or because the pitch between the pillars that cover the surface is increased. A different way to overcome the barrier is to hit the surface with a droplet with a certain kinetic energy.

Based on Nosonovsky and Bhushan (2008e), the vibrational energy U also plays a role in overcoming energy barriers that lead to contact angle hysteresis during liquid flow (Johnson and Dettre 1964). To estimate the effect of the energy barriers on contact angle hysteresis, equations presented in Chap. 3 are used in which the difference between the advancing and receding contact angle is given by,

$$\cos \theta_{rec} - \cos \theta_{adv} = \Delta W / \gamma_{LA} \tag{6.14}$$

where ΔW corresponds to the energy barrier associated with the wetting-dewetting cycle. Assuming that this energy barrier is of the same order as the vibrational energy per contact area, $\Delta W = U/A_0$, and taking $A_0 = 0.1 \text{ mm}^2$, $\Delta W = 10^{-3} \text{ J/m}^2$ is obtained. For water ($\gamma_{LA} = 0.072 \text{ J/m}^2$), (6.14) leads to a realistic value of hysteresis on a superhydrophobic surface $\cos \theta_{rec} - \cos \theta_{adv} = 0.014$. This number provides an estimate for contact angle hysteresis in the limit of small energy barriers comparable with U . The actual values for a micropatterned surface are dependent upon the solid-liquid contact area (that provides energy barriers due to so-called adhesion hysteresis) and the density of the solid-air-liquid contact line (that provides additional pinning), and were found to be between 0.0144 and 0.440 (Bhushan et al. 2007). Thus, these showed good agreement with the value calculated based on U as the lower limit. This indicates that the value of U is relevant both for the Cassie-Baxter and Wenzel regime transition and contact angle hysteresis.

6.4.8 Summary

The presence of the Wenzel and Cassie-Baxter regimes is dependent upon the micro/nanostructure and droplet radius. Cassie-Baxter and Wenzel transition criteria have been proposed. Bhushan and Jung (2007, 2008) and Jung and Bhushan (2007, 2008a, b) proposed a transition criterion based on the pitch distance between the pillars and the curvature of the droplet governed by the Laplace equation, which relates the pressure inside the droplet to its curvature. In addition, the transition can occur by applying external pressure to the droplet, or by the impact of a droplet on the patterned surfaces (Jung and Bhushan 2008b; Nosonovsky and Bhushan 2008e). Alternatively, Bhushan et al. (2007) and Nosonovsky and Bhushan (2007c, d) found that the transition occurs at a critical value of the spacing factor, a non-dimensional parameter that is defined as the diameter of the pillars divided by the pitch distance between them for patterned surfaces and its ratio to the droplet size.

The transition criteria were validated using micropatterned surfaces with various pitch values of micropillars and droplet radii. Droplet radii were varied by performing measurements during droplet evaporation. Contact angle measurements have also been made during condensation and evaporation of droplets.

To study the dynamic effect of droplets under various impact velocities, bouncing of a droplet experiments over micropatterned surfaces have been performed. For a given micropattern geometry, as the droplet hits the surface, the droplet bounced off below a certain critical velocity. Above the critical velocity, after the droplet hits the surface, it does not bounce off and the liquid-air interface changes to the solid-liquid interface due to dynamic impact. A transition model is verified with measurement data.

6.5 Ideal Surfaces with Hierarchical Structure

It was reported earlier that a hierarchical surface is needed to develop a composite interface with high stability. The structure of an ideal hierarchical surface is shown in Fig. 6.27. The asperities should be high enough so that the droplet does not touch the valleys. As an example, for a structure with circular pillars, the following relationship should hold for a composite interface; $(\sqrt{2}P - D)^2/R = H$, (6.4). As an example, for a droplet with a radius on the order of 1 mm or larger, H on the order of 30 μm , and D on the order of 15 μm , a value of P on the order of 130 μm (Fig. 6.12) is optimum. Nanoasperities can pin the liquid-air interface and thereby prevent liquid from filling the valleys between asperities. They are also required to support nanodroplets, which may condense in the valleys between large asperities. Therefore, nanoasperities should have a small pitch to handle nanodroplets, less than 1 mm down to few nm radius. The values of H on the order of 10 nm and D on the order of 100 nm can be fabricated.

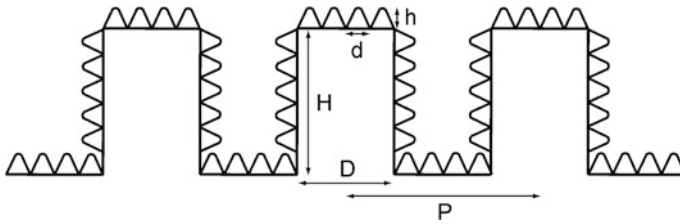


Fig. 6.27 Schematic of structure of an ideal hierarchical surface. Microasperities consist of the circular pillars with diameter D , height H , and pitch P . Nanoasperities consist of pyramidal nanoasperities of height h and diameter d with rounded tops

The structures were first fabricated using nature's route to verify that properties comparable to that of nature objects can be obtained (Sect. 6.6). Next, mechanically durable structures were fabricated guided by models and by using smart materials and fabrication techniques (Sect. 6.7).

6.6 Hierarchically Structured Surfaces with Wax Platelets and Tubules Using Nature's Route

A hierarchical structure is composed of at least two levels of structuring in different length scales. Bhushan et al. (2008a, b, 2009c, d, 2012) and Koch et al. (2009) used nature's route to create various structures. They measured contact angle, contact angle hysteresis, adhesion, and self-cleaning efficiency and compared these with that of the lotus leaf. They also performed experiments to study the dynamic effects of bouncing and vibrating droplets in order to observe their influence on transition from the composite interface to the homogeneous interface.

They fabricated surfaces with a hierarchical structure with micropatterned epoxy replicas and lotus leaf microstructure, and created a second level of structuring with wax tubules and wax platelets. Tubules and platelets are the most common wax morphologies found in plant surfaces, and exist on superhydrophobic leaves. For example, lotus and *Colocasia esculenta* leaves consist of tubule and platelet morphologies, respectively. The structures developed mimic the hierarchical structures of superhydrophobic leaves. Two steps of the fabrication process include the production of microstructured surfaces by soft lithography and the subsequent development of nanostructures on top by self-assembly of plant waxes and artificial wax components.

A two-step molding process was used to fabricate several structurally identical copies of micropatterned Si surface and lotus leaves. The technique used is a fast, precise, and low cost molding process for biological and artificial surfaces (Koch et al. 2007, 2008). The technique was used to mold a microstructured Si surface with pillars 14 μm in diameter and 30 μm in height with a 23 μm pitch (Bhushan et al. 2008a, b, 2009c, d; Koch et al. 2009), fabricated by photolithography. Before

replication of the lotus leaf, the epicuticular wax tubules were removed in areas of approximately 6 cm². For this purpose, a two-component fast hardening glue was applied on the upper side of the leaves and was carefully pressed onto the leaf. After hardening, the glue with the embedded waxes was removed from the leaf, and the procedure was repeated (Koch et al. 2009).

The replication is a two-step molding process, in which first a negative replica of a template is generated and then a positive replica is generated, as shown in Fig. 6.28a (Bhushan et al. 2009d). A polyvinylsiloxane dental wax (President Light Body[®] Gel, ISO 4823, Polyvinylsiloxan (PLB), Coltene Whaledent, Hamburg, Germany) was applied via a dispenser on the surface and immediately pressed down with a glass plate. After complete hardening of the molding mass (at room temperature for approximately 5 min), the silicon master surface and the mold (negative) were separated. After a relaxation time of 30 min for the molding material, the negative replicas were filled with a liquid epoxy resin (Epoxydharz L[®], No. 236349, Conrad Electronics, Hirschau, Germany) with hardener (Harter S, Nr 236365, Conrad Electronics, Hirschau, Germany). Specimens with microstructures were immediately transferred to a vacuum chamber at a pressure of 750 mTorr (100 Pa) for 10 s to remove trapped air and to increase resin infiltration through the structures. After hardening at room temperature (24 h at 22 °C), the positive replica was separated from the negative replica. The second step can be repeated to generate a number of replicas. The pillars of the master surface have been replicated without any morphological changes as shown in Fig. 6.28b (Bhushan et al. 2009d). The nanogrooves of a couple of hundred nm in lateral dimension present on the pillars of the master surface are shown to reproduce faithfully in the replica.

Nanostructures have been created by self-assembly of synthetic and plant waxes deposited by thermal evaporation. The alkane *n*-hexatriacontane (C₃₆H₇₄) has been used for the development of platelet nanostructures (Bhushan et al. 2008a, b, 2009d). Tubule forming waxes that were isolated from leaves of *Tropaeolum majus* (L.) and *N. nucifera*, referred to in the following as *T. majus*, and lotus, respectively, were used to create tubule structures (Bhushan et al. 2009c; Koch et al. 2009). The chemical structure of the major components of the wax forming tubule and alkane *n*-hexatriacontane are shown in Table 6.2. The complete chemistry of the plant waxes used is presented in Koch et al. (2006a). For a homogeneous deposition of the waxes and alkane, a thermal evaporation system, as shown in Fig. 6.29, has been used (Bhushan et al. 2009d). Specimens of smooth surfaces (flat silicon replicas) and microstructured replicas were placed in a vacuum chamber at 30 mTorr (4 kPa), 20 mm above a heating plate loaded with waxes of *n*-hexatriacontane (300, 500, or 1000 μg), *T. majus* wax (500, 1000, 1500, or 2000 μg), and lotus wax (2000 μg) (Bhushan et al. 2008a, b, 2009c, d; Koch et al. 2009). The wax was evaporated by heating it up to 120 °C. In a vacuum chamber the evaporation from the point source to the substrate occurs in a straight line; thus, the amount of sublimated material is equal in a hemispherical region over the point of source (Bunshah 1994). In order to estimate the amount of sublimated mass, the surface area of the half sphere was calculated by using the formula $2\pi r^2$, whereby the radius (*r*) represents the distance

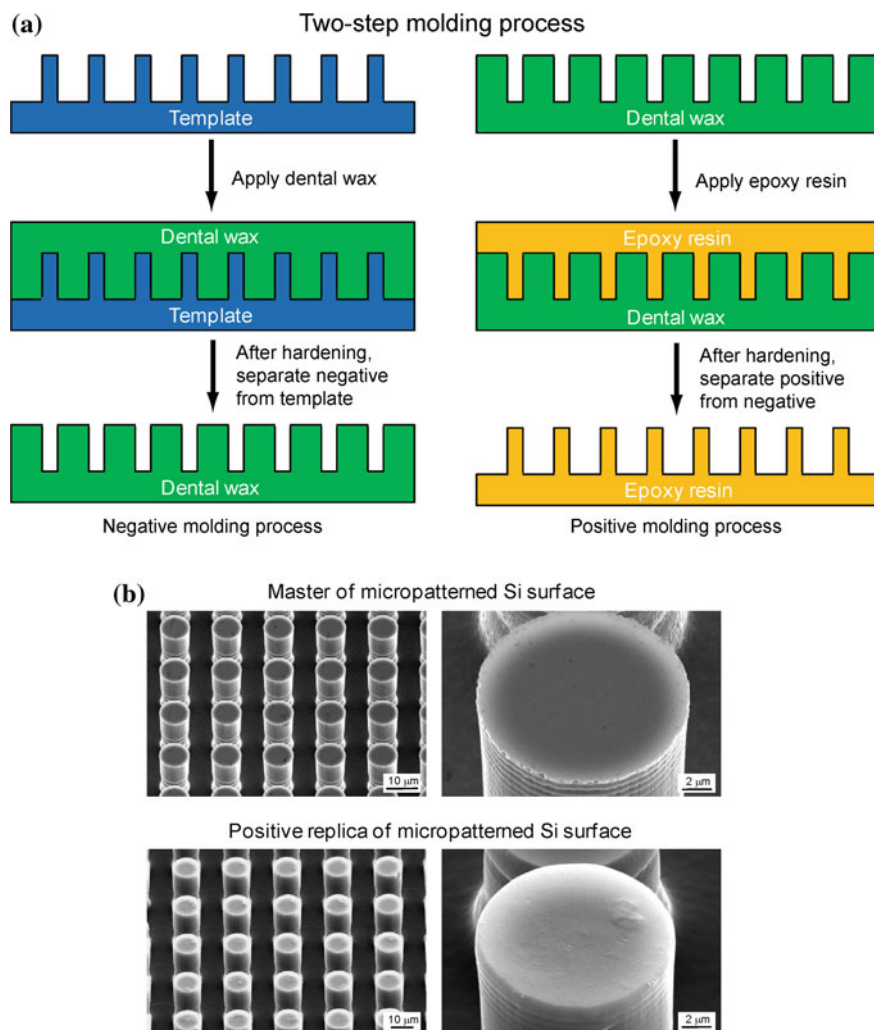


Fig. 6.28 **a** Schematic of two-step molding process used to fabricate microstructure, in which at first a negative is generated and then a positive, and **b** SEM micrographs of the master of micropatterned Si surface and positive replica fabricated from the master surface measured at 45° tilt angle (shown using two magnifications) (Bhushan et al. 2009d)

between the specimen to be covered and the heating plate with the substance to be evaporated. The amounts of wax deposited on the specimen surfaces were 0.12 , 0.2 and $0.4 \mu\text{g}/\text{mm}^2$ for *n*-hexatriacontane, and 0.2 , 0.4 , 0.6 and $0.8 \mu\text{g}/\text{mm}^2$ for *T. majus*, and $0.8 \mu\text{g}/\text{mm}^2$ for lotus waxes.

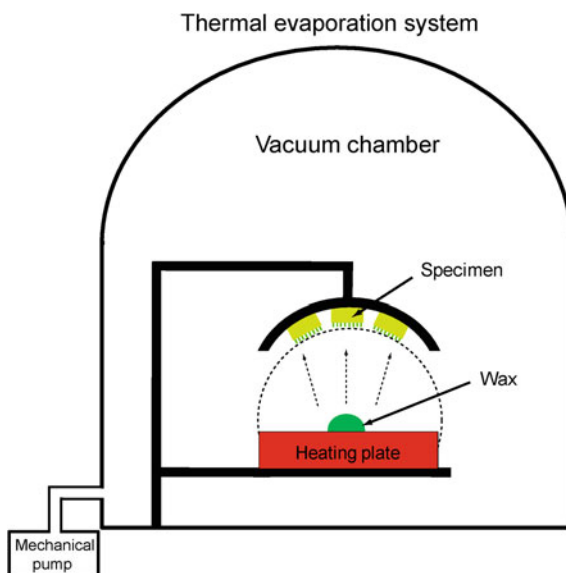
After coating, the specimens with *n*-hexatriacontane were placed in a desiccator at room temperature for three days for crystallization of the alkanes. A stable stage was indicated by no further increase of crystal sizes.

Table 6.2 Chemical structure of the major components of *n*-hexatriacontane, *T. majus*, and lotus waxes

<i>n</i> -hexatriacontane	$C_{36}H_{74}$	
<i>Tropaeolum majus</i>	Nonacosan-10-ol	$CH_3-(CH_2)_6-\overset{OH}{\underset{ }{CH}}-(CH_2)_{18}-CH_3$
	Nonacosane-4,10-diol	$CH_3-(CH_2)_2-\overset{OH}{\underset{ }{CH}}-(CH_2)_6-\overset{OH}{\underset{ }{CH}}-(CH_2)_{18}-CH_3$
Lotus	Nonacosane-10,15-diol	$CH_3-(CH_2)_6-\overset{OH}{\underset{ }{CH}}-(CH_2)_4-\overset{OH}{\underset{ }{CH}}-(CH_2)_{13}-CH_3$
	Nonacosan-10-ol	$CH_3-(CH_2)_6-\overset{OH}{\underset{ }{CH}}-(CH_2)_{18}-CH_3$

The major component is shown first (Bhushan et al. 2008a, 2009c; Koch et al. 2009)

Fig. 6.29 Schematic of thermal evaporation system for self-assembly of a wax. Evaporation from the point source to the substrate occurs over hemispherical region (dotted line) (Bhushan et al. 2009d)



For the plant waxes that are a mixture of aliphatic components, different crystallization conditions were chosen. It was reported by Niemietz et al. (2009) that an increase of temperature from 21 °C (room temperature) to 50 °C had a positive effect on the mobilization and diffusion of wax molecules, required for separation of the tubule forming molecules. It is also known that chemical ambient has an influence on the propensity of wax crystallization, thus the specimens with evaporated plant waxes (*T. majus* and lotus) were stored for three days at 50 °C in a crystallization chamber, where they were exposed to a solvent (ethanol) in vapor phase (Fig. 6.30). Specimens were placed on metal posts, and a filter paper wetted with 20 mL of the solvent was placed below the specimens. Slow diffusive loss of the solvent in the chamber was provided by placing a thin filter paper between the glass body and the lid. After evaporation of the solvent, specimens were left in the oven at 50 °C

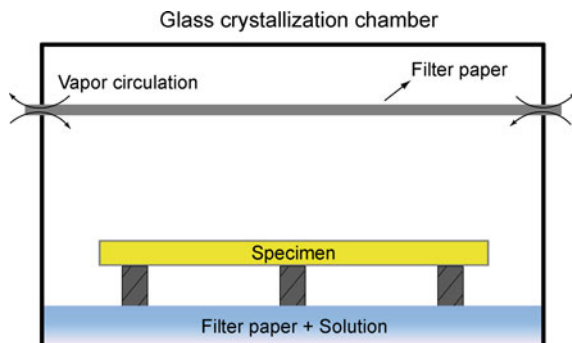
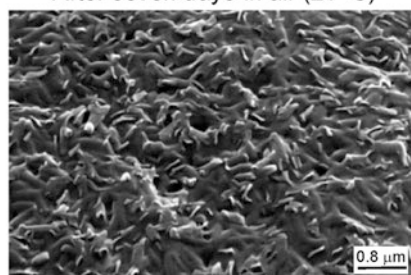


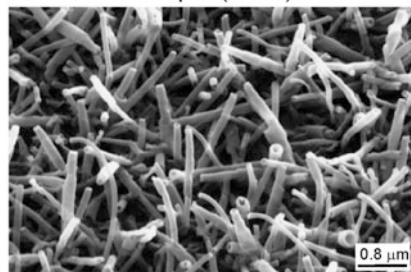
Fig. 6.30 Schematic of a glass recrystallization chamber used for tubules formation. The filter paper placed at the *bottom* of the chamber was wetted with 20 mL of the solvent, and slow evaporation of the solvent was provided by placing a thin filter paper between the glass body and the cap placed above. The total volume of the chamber is about 200 cm³ (Bhushan et al. 2009b)

Fig. 6.31 SEM micrographs of morphology of the lotus wax deposited on the flat epoxy replica surface after two treatments of specimens measured at 45° tilt angle, **a** after seven days at 21 °C (*top*), nanostructure on flat epoxy replica was found with no tubules, and **b** after seven days at 50 °C with ethanol vapor (*bottom*), tubular nanostructures with random orientation were found on the surface (Koch et al. 2009)

(a) Lotus wax deposited on the surface
Nanostructure on flat epoxy replica
After seven days in air (21° C)



(b) After seven days with ethanol vapor (50° C)



for a total of seven days. Figure 6.31 shows the nanostructures formed by lotus wax, seven days after wax deposition on flat surfaces. Figure 6.31a shows the nanostructure after storage at 21 °C; in these no tubules were grown. Figure 6.31b shows that lotus waxes exposed to ethanol vapor for three days at 50 °C formed wax

tubules. A detailed description of the nanostructure sizes and nanoroughness is given in the following.

Flat films of *n*-hexatriacontane and wax tubules were made by heating the substances above their melting point and rapidly cooling down. This procedure interrupts the crystallization and leads to smooth films (Bhushan et al. 2008a, b, 2009c, d; Koch et al. 2009).

6.6.1 Effect of Nanostructures with Various Wax Platelet Crystal Densities on Superhydrophobicity

Nanostructures with various wax platelet crystal densities were fabricated to study the effect of crystal density on superhydrophobicity. Figure 6.32a shows the SEM micrographs of a flat surface and nanostructures fabricated with various masses of *n*-hexatriacontane (Bhushan et al. 2008a). The nanostructure is formed by three-dimensional platelets of *n*-hexatriacontane, as shown in detail in Fig. 6.32b. Platelets are flat crystals, grown perpendicular to the substrate surface. They are randomly distributed on the surface, and their shapes and sizes show some variations. Some of the single platelets are connected to their neighboring crystals at their lateral ends. This arrangement leads to a kind of cross-linking of the single platelets. As shown in Fig. 6.32b, and based on additional specimens, the platelet thickness varied between 50 and 100 nm, and their length varied between 500 and 1000 nm. The self-assembly of *n*-hexatriacontane and most other long chain hydrocarbons leads to layered structures with a lamellae order. In these structures, the molecular axis is orientated parallel to the substrate surface. The growth of these layers results in an ordered, crystalline 3-D structure (Dorset et al. 1983). The created nanostructures are comparable to the wax crystal morphology found on superhydrophobic leaves, e.g., *Colocasia esculenta* (Neinhuis and Barthlott 1997) and *Triticum aestivum* (wheat) (Koch et al. 2006b). SEM micrographs of the nanostructures fabricated with three different masses of *n*-hexatriacontane show different densities of crystals. An atomic force microscope (AFM) was used to characterize the nanostructures. Statistical parameters of nanostructures [RMS height, peak to valley height, and summit density (η)] (Bhushan 2013a, b) were calculated and are presented in Table 6.3. A summit is defined as a point whose height is greater than its four nearest neighboring points above a threshold value of 10 % of RMS height to avoid measurement errors. The measurement results were reproducible within ± 5 %.

To study the effect of nanostructures with different crystal density on superhydrophobicity, static contact angle, contact angle hysteresis, tilt angle, and adhesive forces were measured (Bhushan et al. 2008a). For contact angle hysteresis, the advancing and receding contact angles were measured at the front and back of the droplet moving along the tilted surface, respectively. The data are shown in Fig. 6.33. The static contact angle of a flat surface coated with a film of *n*-hexatriacontane was 91° . It showed a contact angle hysteresis of 87° , and the droplet still adhered at a tilt

Fig. 6.32 SEM micrographs taken at 45° tilt angle (shown using two magnifications) of **a** the flat surface and nanostructures fabricated with various mass of *n*-hexatriacontane and **b** three-dimensional platelets forming nanostructures on the surface fabricated with 0.2 $\mu\text{g}/\text{mm}^2$ mass of *n*-hexatriacontane. All samples are fabricated with epoxy resin coated with *n*-hexatriacontane (Bhushan et al. 2008a)

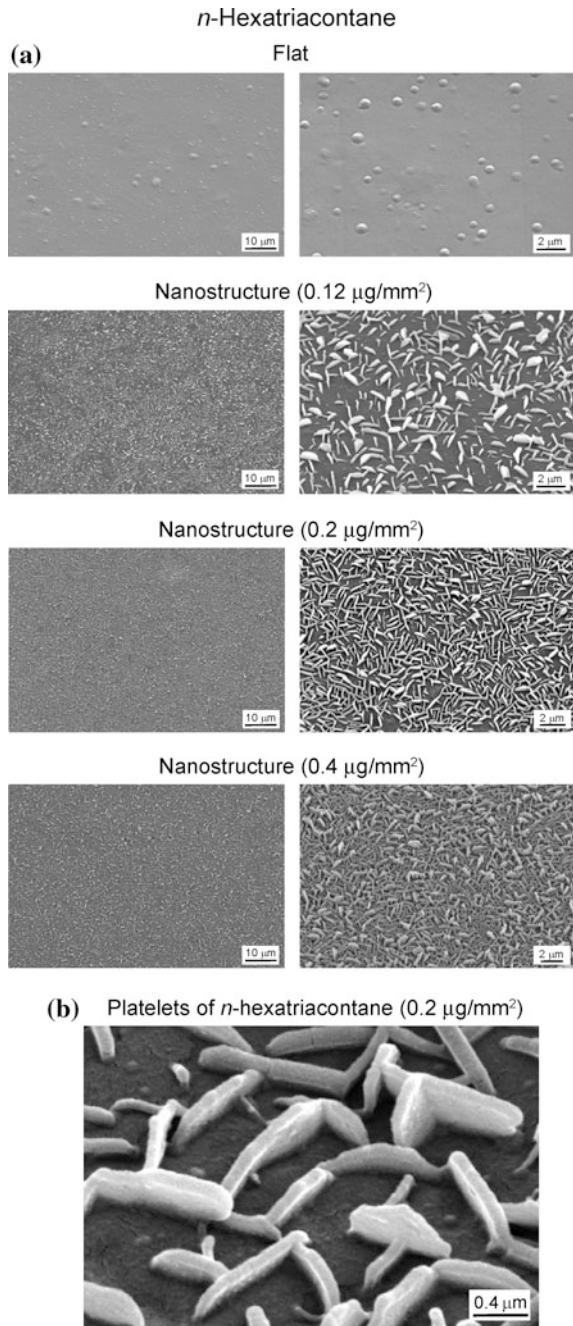


Table 6.3 Roughness statistics for a nanostructured surface measured using an AFM (Scan size $10 \mu\text{m} \times 10 \mu\text{m}$)

	RMS height (nm)	Peak to valley height (nm)	η (μm^2)
<i>n-hexatriacontane</i>			
Nanostructure (0.12 $\mu\text{g}/\text{mm}^2$)	46	522	0.78
Nanostructure (0.2 $\mu\text{g}/\text{mm}^2$)	65	663	1.39
Nanostructure (0.4 $\mu\text{g}/\text{mm}^2$)	82	856	1.73
<i>Tropaeolum majus</i> wax			
Nanostructure (0.8 $\mu\text{g}/\text{mm}^2$)	180	1570	0.57
<i>Lotus</i> wax			
Nanostructure (0.8 $\mu\text{g}/\text{mm}^2$)	187	1550	1.47

Nanostructures were fabricated with *n*-hexatriacontane, *T. majus*, and lotus waxes (Bhushan et al. 2008a, 2009c; Koch et al. 2009)

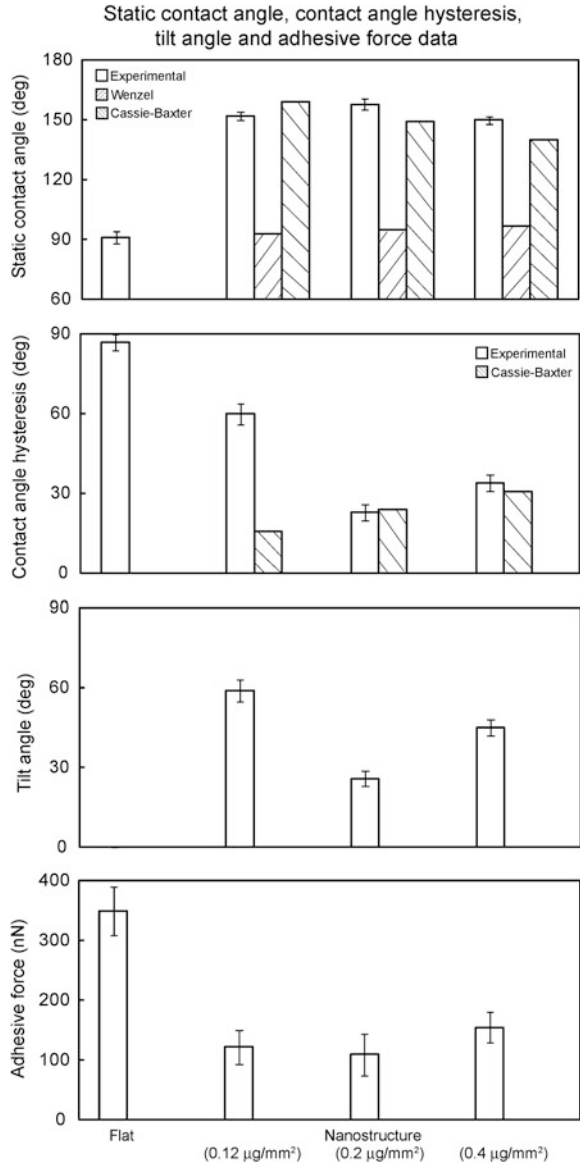
RMS – root mean square

η – summit density

angle of 90° . Nanostructuring of flat surfaces with *n*-hexatriacontane platelets creates superhydrophobic surfaces with a high static contact angle and a reduction of contact angle hysteresis and tilt angle. The values are a function of crystal density. Figure 6.34 shows a plot of static contact angle and contact angle hysteresis as a function of the mass of *n*-hexatriacontane deposited. As the mass of *n*-hexatriacontane increased, the static contact angle first increased, and the contact angle hysteresis decreased. Then, above a mass of $0.2 \mu\text{g}/\text{mm}^2$, static contact angle gradually decreased and contact angle hysteresis gradually increased with increasing mass. The highest static contact angle and lowest contact angle hysteresis are 158° and 23° at a mass of $0.2 \mu\text{g}/\text{mm}^2$. As shown in Fig. 6.33, the adhesive force measured using a $15 \mu\text{m}$ radius borosilicate tip in an AFM also shows a similar trend as the wetting properties. Adhesive forces of the nanostructured surfaces were lower than for the flat surface because the contact between the tip and surface was lower than on the flat surface, because the contact between the tip and surface was reduced by surface structuring (Bhushan 2013a, b).

To identify wetting regimes (Wenzel or Cassie-Baxter), as well as to understand the effect of crystal density on the propensity of air pocket formation for the nanostructured surfaces, roughness factor (R_f) and fractional liquid-air interface (f_{LA}) are needed. The R_f for the nanostructures was calculated using the AFM map (Burton and Bhushan 2006; Bhushan and Jung 2006). The calculated results were reproducible within $\pm 5\%$. The R_f for the nanostructured surfaces with masses of 0.12 , 0.2 , and $0.4 \mu\text{g}/\text{mm}^2$ were found to be 3.4 , 4.9 , and 6.8 , respectively. For calculation of f_{LA} of the nanostructures, only the higher crystals are assumed to come in contact with a water droplet. The fractional geometrical area of the top surface for the nanostructures was calculated from SEM micrographs with top view (0° tilt angle). The SEM images were converted to high contrast black and white images using Adobe Photoshop. The increase of contrast in the SEM image eliminates the smaller platelet structures, which were visible in the original SEM image. The higher

Fig. 6.33 Bar chart showing the measured static contact angle, contact angle hysteresis and tilt angle; also shown are calculated static contact angles obtained using Wenzel and Cassie-Baxter equations with a given value of θ_0 , and calculated contact angle hysteresis using Cassie-Baxter equation on flat surface and nanostructures fabricated with various mass of *n*-hexatriacontane. The droplet on flat surface does not move along the surface even at tilt angle of 90°. The bar chart also shows adhesive forces for various structures, measured using a 15 μm radius borosilicate tip (Bhushan et al. 2008a)



crystals led to white signals in the SEM figure. The fractional geometrical area of the top nanostructured surfaces with masses of 0.12, 0.2, and 0.4 $\mu\text{g}/\text{mm}^2$ was found to be 0.07, 0.15, and 0.24, leading to f_{LA} of 0.93, 0.85, and 0.76, respectively. The calculated results were reproducible within $\pm 5\%$. The values of static contact angle in the Wenzel and Cassie-Baxter regimes for the nanostructured surfaces were

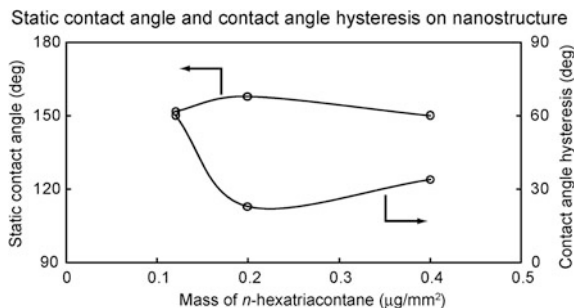


Fig. 6.34 Static contact angle and contact angle hysteresis as a function of mass of *n*-hexatriacontane deposited on nanostructures (Bhushan et al. 2008a)

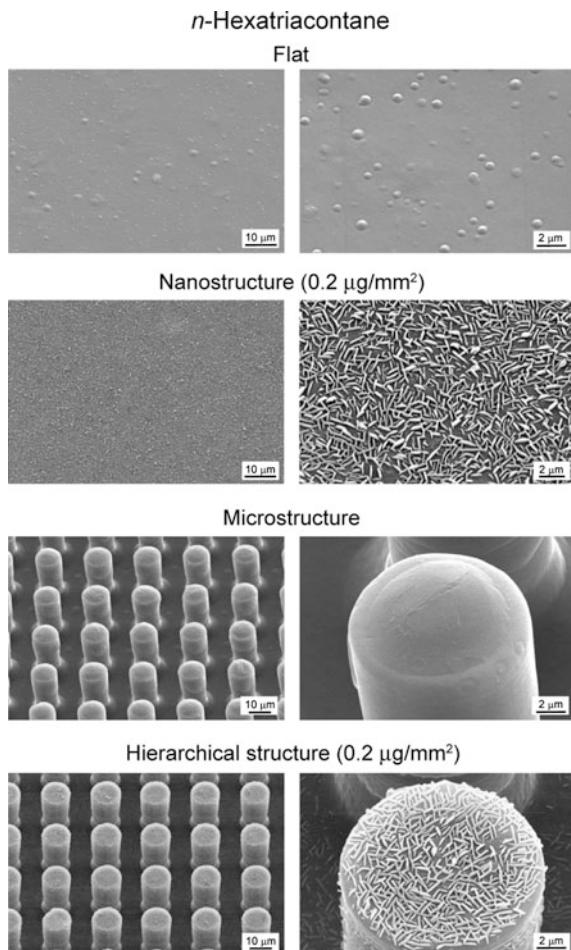
calculated using the values of R_f and f_{LA} and presented in Fig. 6.33. The values of contact angle hysteresis in Cassie-Baxter regimes for various surfaces were calculated using equations from Chap. 3. The data are presented in Fig. 6.33.

As shown in Fig. 6.33, the experimental static contact angle and contact angle hysteresis values for the two nanostructured surfaces with 0.2 and 0.4 $\mu\text{g}/\text{mm}^2$ were comparable to the calculated values in the Cassie-Baxter regime. The results suggest that a droplet on two nanostructured surfaces should exist in the Cassie-Baxter regime. However, for the nanostructured surface with 0.12 $\mu\text{g}/\text{mm}^2$, the experimental static contact angle was lower and contact angle hysteresis was higher than the calculated values in the Cassie-Baxter regime. It is believed that neighboring crystals are separated at lower crystal density and any trapped air can be squeezed out. Conversely, neighboring crystals are interconnected at higher densities and air remains trapped. At highest crystal density at a mass of 0.4 $\mu\text{g}/\text{mm}^2$, there is less open volume compared to that at 0.2 $\mu\text{g}/\text{mm}^2$, which explains a droplet static contact angle going from 158° to 150° (Bhushan et al. 2008a).

6.6.2 Effect of Hierarchical Structure with Wax Platelets on the Superhydrophobicity

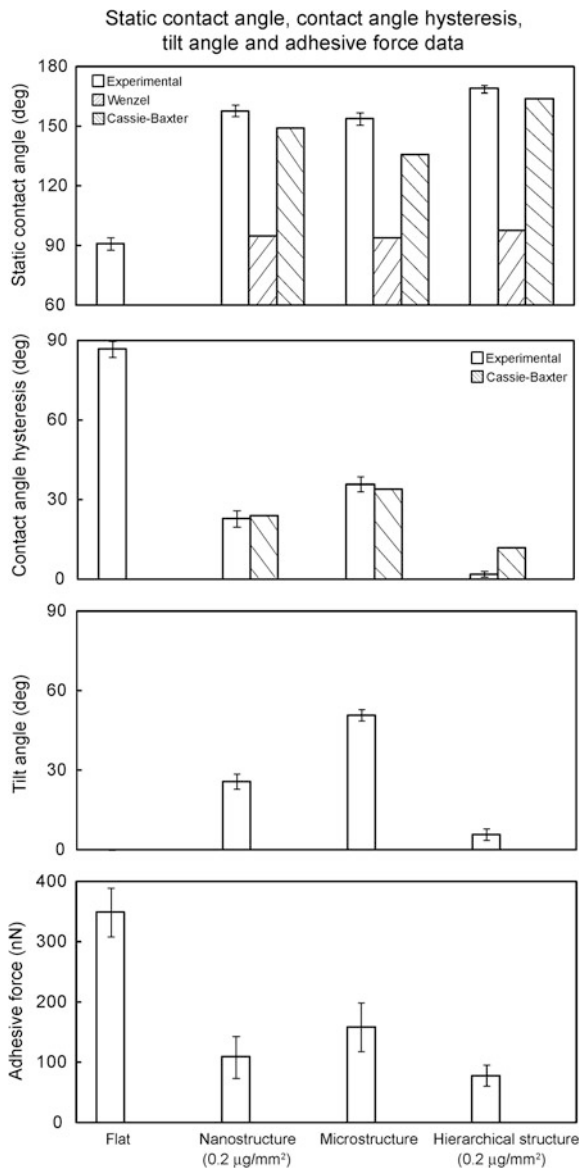
To study the influence of hierarchical structure on superhydrophobicity, Bhushan et al. (2008b, 2009d) created surfaces with *n*-hexatriacontane of 0.2 $\mu\text{g}/\text{mm}^2$. Figure 6.35 shows the SEM micrographs of a flat surface and nano-, micro-, and hierarchical structures. To study the effect of structure on superhydrophobicity, static contact angle, contact angle hysteresis, tilt angle, and adhesive forces of the four structures were measured. The data are shown in Fig. 6.36. The static contact angle of a flat surface coated with a film of *n*-hexatriacontane was 91° , and increased to 158° when *n*-hexatriacontane formed a nanostructure of platelets on it. The static contact angle on a flat specimen with a microstructure was 154° , but it increased to 169° for the hierarchical surface structure. Contact angle hysteresis and

Fig. 6.35 SEM micrographs of the flat surface, nanostructure, microstructure, and hierarchical structure measured at 45° tilt angle (shown using two magnifications). All samples are fabricated with epoxy resin coated with *n*-hexatriacontane (Bhushan et al. 2008b)



tilt angle for flat, micro-, and nanostructured surfaces show similar trends. The flat surface showed a contact angle hysteresis of 87°, and the droplet still adhered at a tilt angle of 90°. The superhydrophobic micro- and nanostructured surfaces showed a reduction of contact angle hysteresis and tilt angle, but a water droplet still needs a tilt angle of 26° and 51°, respectively, before sliding. Only the hierarchical surface structure with static contact angle of 169° and low contact angle hysteresis of 2° exceeds the basic criteria for superhydrophobic and self-cleaning surfaces (Bhushan and Jung 2008). Adhesive force measured using a 15 μm radius borosilicate tip in an AFM also showed a similar trend as the wetting properties. Adhesion force of the hierarchical surface structure was lower than that of both micro- and nanostructured surfaces because the contact between the tip and surface was lower as a result of contact area being reduced (Bhushan 2013a, b).

Fig. 6.36 Bar chart showing the measured static contact angle, contact angle hysteresis and tilt angle; also shown are calculated static contact angles obtained using Wenzel and Cassie-Baxter equations with a given value of θ_0 , and calculated contact angle hysteresis using Cassie-Baxter equation on various structures. The droplet on flat surface does not move along the surface even at tilt angle of 90° . The bar chart also shows adhesive forces for various structures, measured using a $15\ \mu\text{m}$ radius borosilicate tip (Bhushan et al. 2008b)



In order to identify wetting regimes (Wenzel or Cassie-Baxter) for the various surfaces, roughness factor (R_f) and fractional liquid-air interface (f_{LA}) are needed. The R_f for the nanostructure was described earlier. The R_f for the microstructure was calculated for the geometry of flat-top, cylindrical pillars of diameter D , height H , and pitch P distributed in a regular square array. For this case, the roughness factor for the microstructure is given by $(R_f)_{micro} = (1 + \frac{\pi DH}{P^2})$. The roughness

Table 6.4 Summary of static contact angles and contact angle hysteresis measured and calculated for droplets in the Wenzel regime and the Cassie-Baxter regime on the various surfaces with *n*-hexatriacontane using the calculated values of R_f and f_{LA} (Bhushan et al. 2008b, 2009d)

			Static contact angle (°)			Contact angle hysteresis (°)	
	R_f	f_{LA}	Measured	Calculated in Wenzel regime	Calculated in Cassie-Baxter regime	Measured	Calculated in Cassie-Baxter regime
Flat			91			87 ^a	
Nanostructure	4.9	0.85	158	95	149	23	24
Microstructure	3.5	0.71	154	94	136	36	34
Hierarchical structure	8.4	0.96	169	98	164	2	12

^aAdvancing and receding contact angles are 141° and 54°, respectively

factor for the hierarchical structure is the sum of $(R_f)_{micro}$ and $(R_f)_{nano}$. The values calculated for various surfaces are summarized in Table 6.4.

For the calculation of f_{LA} , the following assumptions are made. For the microstructure, consider that a droplet in size much larger than the pitch P contacts only the flat-top of the pillars in the composite interface, and the cavities are filled with air. For microstructure, the fractional flat geometrical area of the liquid-air interface under the droplet is given by $(f_{LA})_{micro} = \left(1 - \frac{\pi D^2}{4P^2}\right)$ (Bhushan and Jung 2008). The fractional geometrical area of the top surface for the nanostructure was described earlier. For the hierarchical structure, the fractional flat geometrical area of the liquid-air interface is given by $(f_{LA})_{hierarchical} = 1 - \left(\frac{\pi D^2}{4P^2}\right) [1 - (f_{LA})_{nano}]$. The values of contact angle hysteresis in Cassie-Baxter regimes for various surfaces were calculated using equations from Chap. 3. The values are summarized in Table 6.4.

The values of static contact angle in the Wenzel and Cassie-Baxter regimes for various surfaces were calculated using the values of R_f and f_{LA} (Table 6.4). As shown in Fig. 6.36, the experimental static contact angle values for the three structured surfaces were larger than the calculated values in the Cassie-Baxter regime. The results suggest that the droplets on three of the structured surfaces were in the Cassie-Baxter regime. This indicates that the microstructure and nanostructure surface induce air pocket formation. For the contact angle hysteresis, there is good agreement between the experimental data and the theoretically predicted values for the Cassie-Baxter regime. These results show that air pocket formation in the micro- and nanostructure decreases the solid-liquid contact (Koch et al. 2009). In hierarchically structured surfaces, the air pocket formation further decreases the solid-liquid contact, and thereby reduces contact angle hysteresis and tilt angle (Bhushan et al. 2008b, 2009d).

6.6.3 Effect of Hierarchical Structure with Wax Tubules on Superhydrophobicity

6.6.3.1 *Majus* Tubules

Figure 6.37a shows the SEM micrographs of the nanostructure and hierarchical structure fabricated with two different masses (0.6 and $0.8 \mu\text{g}/\text{mm}^2$) of *T. majus* wax (Bhushan et al. 2009c). SEM micrographs show an increase in the tubule amount on the flat and microstructure surfaces after deposition of higher masses of wax. The tubules of *T. majus* wax grown in an ethanol atmosphere are comparable to the wax morphology found on the leaves of *T. majus*. Surfaces show a homogeneous distribution of the wax mass on the specimen surfaces, and tubules provide the desired nanostructure of three-dimensional tubules on the flat and microstructure surfaces. The tubule morphology of *T. majus* wax is shown in detail in Fig. 6.37b. The tubular crystals are hollow structures, randomly oriented on the surface and embedded into an amorphous wax layer. They are randomly distributed

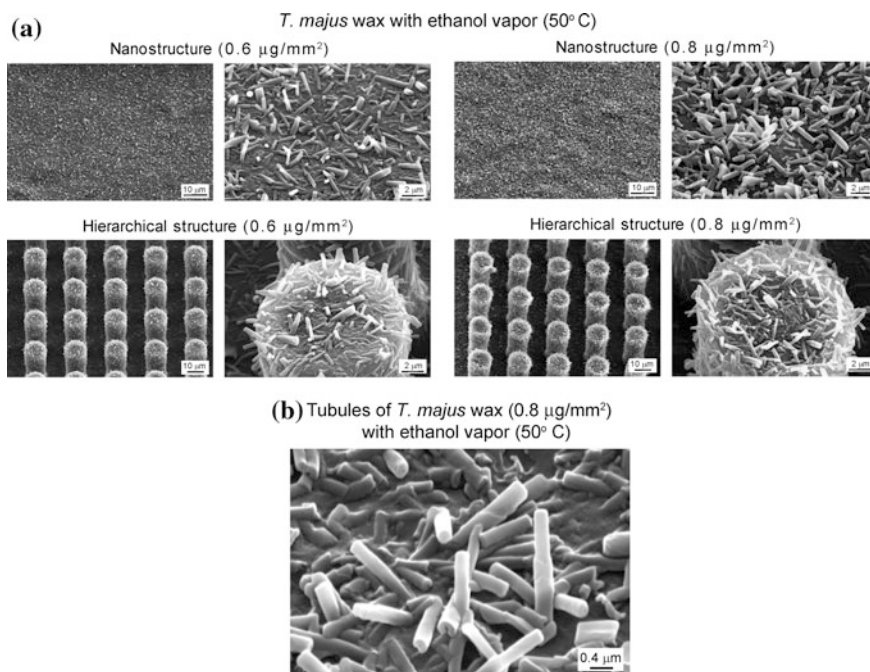


Fig. 6.37 SEM micrographs taken at 45° tilt angle (shown using two magnifications) of (a) the nanostructure and hierarchical structure fabricated with two different mass (0.6 and $0.8 \mu\text{g}/\text{mm}^2$) of *T. majus* wax after storage at 50°C with ethanol vapor and (b) three-dimensional tubules forming nanostructures on the surface fabricated with $0.8 \mu\text{g}/\text{mm}^2$ mass of *T. majus* wax after storage at 50°C with ethanol vapor (Bhushan et al. 2009c)

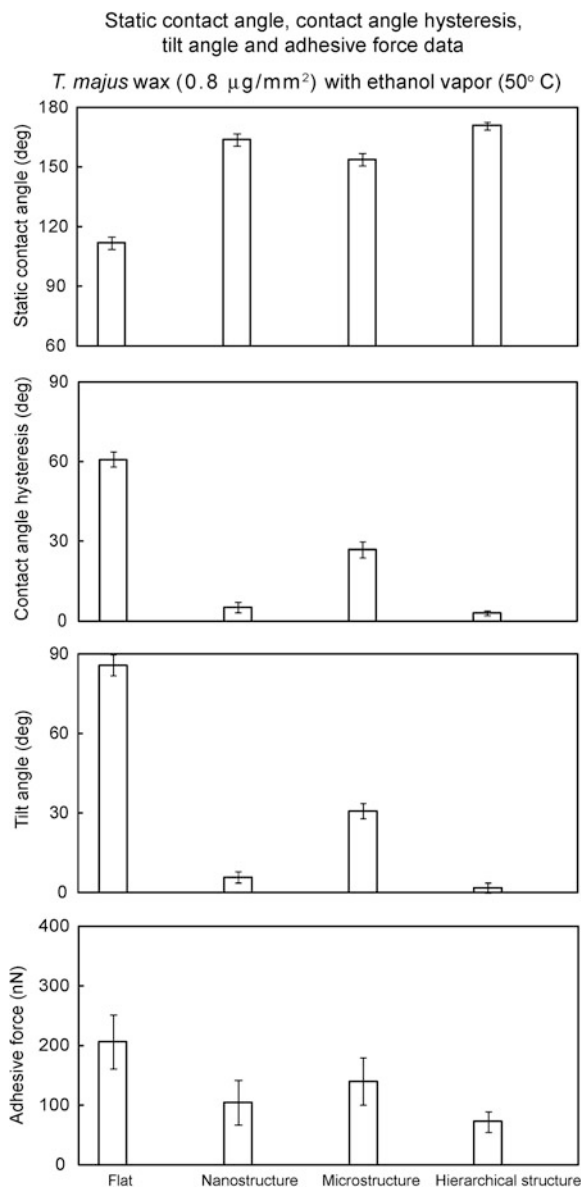
on the surface, and their shapes and sizes show some variations. As shown in Fig. 6.37b, and based on additional specimens, the tubular diameter varied between 100 and 300 nm, and their length varied between 300 and 1200 nm.

AFM was used to characterize the nanostructure fabricated using *T. majus* wax of $0.8 \mu\text{g}/\text{mm}^2$ after storage at 50°C with ethanol vapor (Bhushan et al. 2009c). Statistical parameters of the nanostructure [RMS height, peak to valley height, and summit density (η)] were calculated and are presented in Table 6.3 (Bhushan 2013a, b). A summit is defined as a point whose height is greater than that of its four nearest neighboring points above a threshold value of 10 % of RMS height to avoid measurement errors. The measurement results were reproducible within $\pm 5\%$.

To study the effect of structures with various length scales on superhydrophobicity, static contact angle, contact angle hysteresis, tilt angle, and adhesive forces of the four structures produced using *T. majus* wax were measured (Bhushan et al. 2009c). Nanostructures formed on the flat and microstructured surfaces were fabricated using *T. majus* wax of $0.8 \mu\text{g}/\text{mm}^2$ after storage at 50°C with ethanol vapor. The data are shown in Fig. 6.38. The static contact angle of a flat surface coated with a film of *T. majus* wax was 112° , and increased to 164° when *T. majus* wax formed a nanostructure of tubules on it. On the flat specimen with a microstructure on it, the static contact angle was 154° , but increased to 171° for the hierarchical surface structure. Contact angle hysteresis and tilt angle for flat, micro-, and nanostructured surfaces show similar trends. The flat surface showed a contact angle hysteresis of 61° and a tilt angle of 86° . The microstructured surface shows a reduction of contact angle hysteresis and tilt angle, but a water droplet still needs a tilt angle of 31° before sliding. As tubules were formed on the flat and microstructured surfaces, the nanostructured and hierarchical structure surfaces had low contact angle hysteresis of 5° and 3° , respectively. These properties are superior to plant leaves, including lotus leaves. Adhesive force measured using a $15 \mu\text{m}$ radius borosilicate tip in an AFM also showed a similar trend as the wetting properties. Adhesion force of the hierarchical surface structure was lower than that of micro- and nanostructured surfaces because the contact between the tip and surface was lower as a result of contact area being reduced (Bhushan 2013a, b).

To further verify the effect of hierarchical structure on the propensity of air pocket formation, Bhushan et al. (2009c) performed evaporation experiments with a droplet on a microstructure and hierarchical structure fabricated with $0.8 \mu\text{g}/\text{mm}^2$ mass of *T. majus* wax with ethanol vapor at 50°C . Figure 6.39 shows the successive photos of a droplet evaporating on the two structured surfaces. On the microstructured surface, the light passes below the droplet and air pockets can be seen. So, to begin, the droplet was in the Cassie-Baxter regime. When the radius of the droplet decreased to $425 \mu\text{m}$, the air pockets were not visible anymore, and the droplet was in the Wenzel regime. This transition resulted from an impalement of the droplet in the patterned surface, characterized by a smaller contact angle. For the hierarchical structure, an air pocket was clearly visible at the bottom area of the droplet throughout, and the droplet was in a hydrophobic state until the droplet evaporated completely. This suggests that a hierarchical structure with nanostructures prevents liquid from filling the gaps between the pillars.

Fig. 6.38 Bar chart showing the measured static contact angle, contact angle hysteresis and tilt angle on various structures fabricated with $0.8 \mu\text{m}^2/\text{mm}^2$ mass of *T. majus* wax after storage at 50°C with ethanol vapor. The bar chart also shows adhesive forces for various structures, measured using a $15 \mu\text{m}$ radius borosilicate tip (Bhushan et al. 2009c)



6.6.3.2 Lotus Tubules

Lotus wax was used for the development of nanostructures by tubule formation (Koch et al. 2009). Figure 6.40a shows the SEM micrographs of flat surfaces with the tubule nanostructure. The microstructures shown in Fig. 6.40b are the lotus leaf and the micropatterned Si replica covered with a lotus wax film. Hierarchical

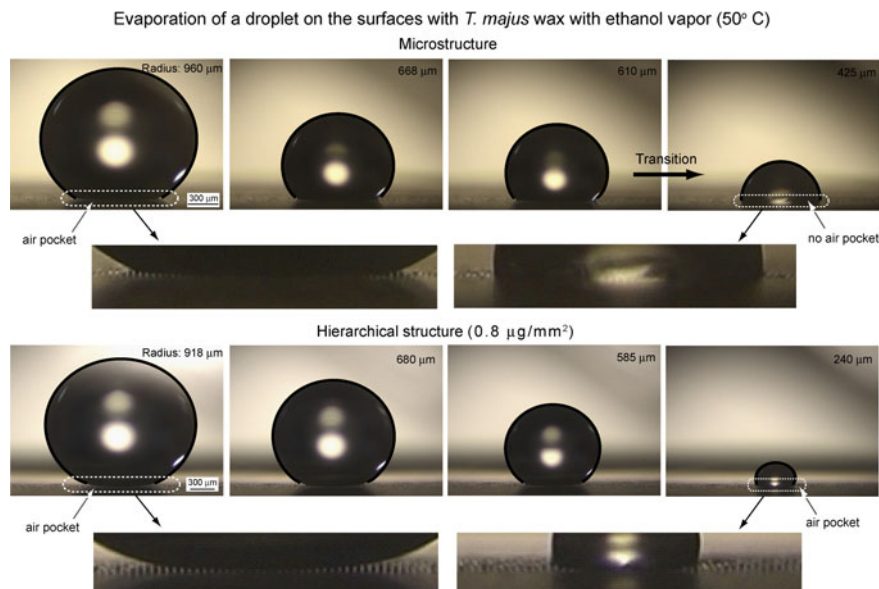
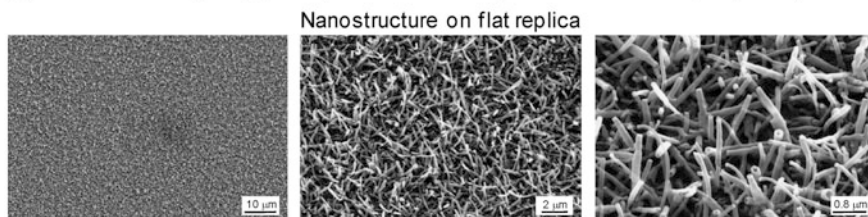


Fig. 6.39 Evaporation of a droplet on a microstructured- and hierarchically structured surfaces fabricated with 0.8 $\mu\text{g}/\text{mm}^2$ mass of *T. majus* wax after storage at 50 °C with ethanol vapor. The initial radius of the droplet was about 950 μm , and the time interval between first two photos was 180 s and between the latter was 60 s. As the radius of droplet reached 425 μm (foot print = 836 μm) on the microstructured surface, the transition from Cassie-Baxter regime to Wenzel regime occurred, as indicated by the *arrow*. On the hierarchically structured surface air pockets, visible at the *bottom* area of the droplet, exist until the droplet evaporated completely (Bhushan et al. 2009b)

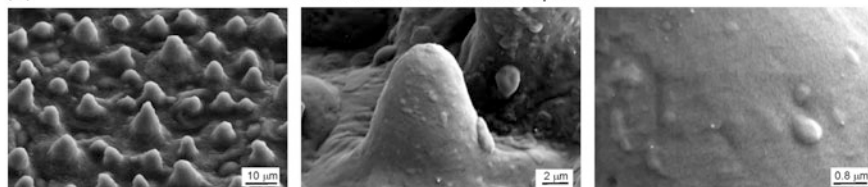
structures were fabricated with microstructured lotus leaf replicas and micropatterned Si replicas covered with a nanostructure of lotus wax tubules, as shown in Fig. 6.40c. SEM micrographs show an overview (left column), a detail in higher magnification (middle column), and a large magnification of the created flat wax layers and tubule nanostructures (right column). The grown tubules provide the desired nanostructure on flat and microstructured surfaces. The recrystallized lotus wax shows tubular hollow structures, with random orientation on the surfaces. Their shapes and sizes show only a few variations. The tubular diameter varied between 100 and 150 nm, and their length varied between 1500 and 2000 nm. Atomic force microscopy (AFM) was used to characterize the nanostructure of the lotus wax tubules. The statistical parameters of the nanostructure [RMS height, peak to valley height, and summit density (η)] were calculated and are presented in Table 6.3.

To study the effect of lotus wax tubule nanostructures on superhydrophobicity, static contact angle, contact angle hysteresis, and tilting angle were measured on flat, microstructured lotus replica, micropatterned Si replica, and hierarchical surfaces. Hierarchical surfaces were made of the lotus leaf replica and micropatterned

(a) Lotus wax ($0.8 \mu\text{g}/\text{mm}^2$) after seven days with ethanol vapor (50°C)



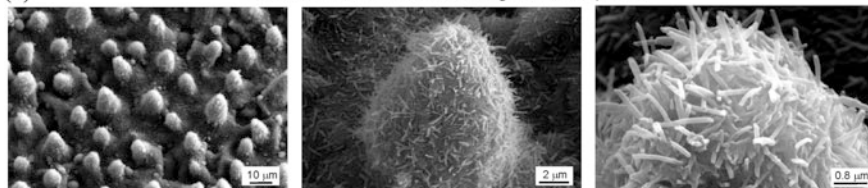
(b) Microstructure in Lotus replica



Micropatterned Si replica



(c) Hierarchical structure using Lotus replica



Hierarchical structure using micropatterned Si replica

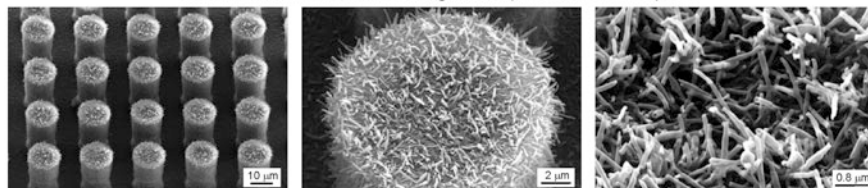
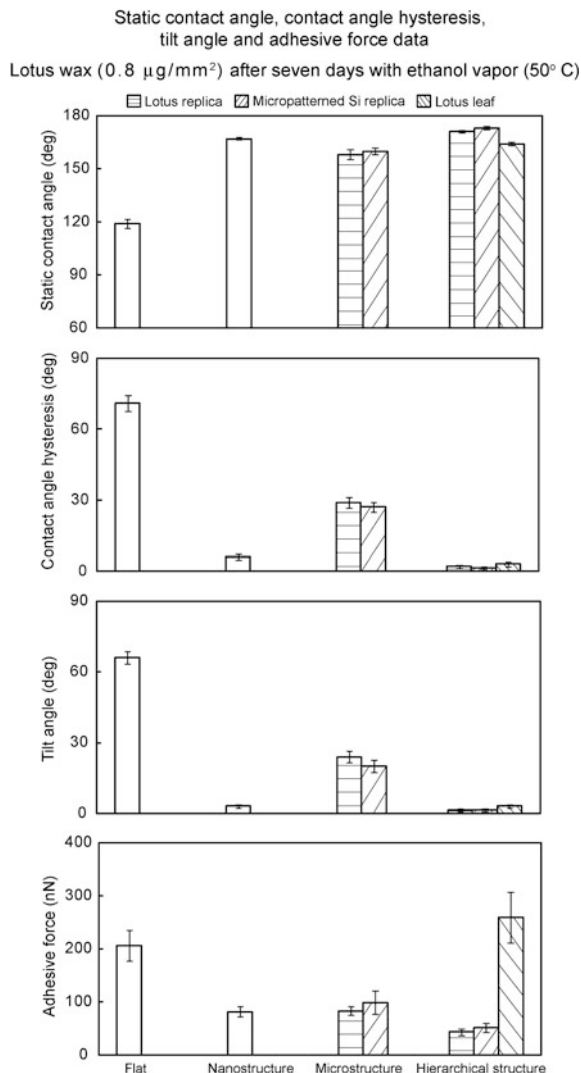


Fig. 6.40 SEM micrographs taken at 45° tilt angle (shown using three magnifications) of **a** nanostructure on flat replica, **b** microstructures in lotus replica and micropatterned Si replica, and **c** hierarchical structure using lotus and micropatterned Si replicas. Nano- and hierarchical structures were fabricated with mass $0.8 \mu\text{g}/\text{mm}^2$ of lotus wax after storage for seven days at 50°C with ethanol vapor. Flat epoxy resin and microstructure were covered with flat lotus wax (Koch et al. 2009)

Fig. 6.41 Bar chart showing the measured static contact angle, contact angle hysteresis and tilt angle on various structures fabricated with $0.8 \mu\text{g}/\text{mm}^2$ of lotus wax after storage for seven days at 50°C with ethanol vapor. The bar chart also shows adhesive forces for various structures, measured using a $15 \mu\text{m}$ radius borosilicate tip. The error bar represents ± 1 standard deviation (Koch et al. 2009)



Si replica with a nanostructure of wax tubules on top. Additionally, fresh lotus leaves were investigated to compare the properties of the fabricated structures with the original biological model.

Figure 6.41 shows that the highest static contact angles of 173° , lowest contact angle hysteresis of 1° , and tilting angle varying between 1 and 2° were found for the hierarchically structured Si replica. The hierarchically structured lotus leaf replica showed a static contact angle of 171° , and the same contact angle hysteresis (2°) and tilt angles of 1 – 2° as the hierarchical Si replica. The fresh lotus leaf surface investigated here showed a static contact angle of 164° , contact angle hysteresis of

3°, and a tilting angle of 3° which suggests that the artificial hierarchical surfaces showed higher static contact angle and lower contact angle hysteresis. Structural differences between the original lotus leaf and the artificial lotus leaf produced here are limited to a difference in wax tubules length, which are 0.5 to 1 μm longer in the artificial lotus leaf (Koch et al. 2009).

The melting of the wax led to a flat surface with a flat wax film with a much lower static contact angle (119°), a higher contact angle hysteresis (71°), and a high tilting angle of 66°. The data of a flat lotus wax film on a flat replica show that the lotus wax by itself is hydrophobic. The data demonstrate that the native, flat wax of lotus leaves, with a static contact angle of 119°, is hydrophobic and can turn superhydrophobic (167°) by increasing the surface roughness after self-assembly into three-dimensional wax tubules. The static contact angle of the lotus wax film is 119°, which is higher than that of the wax film made of *T. majus* of 112°. However, films made of *n*-hexatriacontane showed static contact angles of only 91°. SEM investigations, made directly after contact angle measurements, revealed no morphological differences between these films. Based on the chemical composition, it should be assumed that the non-polar *n*-hexatriacontane molecules are more hydrophobic than the plant waxes, which contain high amounts of oxygen atoms. At this point these differences cannot be explained by structural or chemical differences of the films, but will be of interest for further studies.

Adhesive force measured using a 15 μm radius borosilicate tip in an AFM also shows a similar trend as the wetting properties for the artificial surfaces (Fig. 6.41) (Koch et al. 2009). Adhesion force of the hierarchical surface structure was lower than that of micro- and nanostructured and flat surfaces because the contact between the tip and surface was lower as a result of the contact area being reduced. However, for the fresh lotus leaf, there is moisture within the plant material, which causes softening of the leaf, and so when the tip comes into contact with the leaf sample, the sample deforms, and a larger area of contact between the tip and sample causes an increase in the adhesive force (Bhushan 2013a, b).

6.6.4 Self-cleaning Efficiency of Hierarchically Structured Surfaces

For deposition of contamination on artificial surfaces, various structures were placed in a glass contamination chamber (Bhushan et al. 2009a). Silicon carbide (SiC) (Guillaume, Germany) particles in two different sizes ranges of 1–10 μm and 10–15 μm were used as the contaminants. The SiC particles were chosen because of their similarity in shape, sizes, and hydrophilicity to natural dirt contaminants. The number of particles per area was determined by counting them from a 280 μm × 210 μm image taken by an optical microscope with a camera before and after water cleaning.

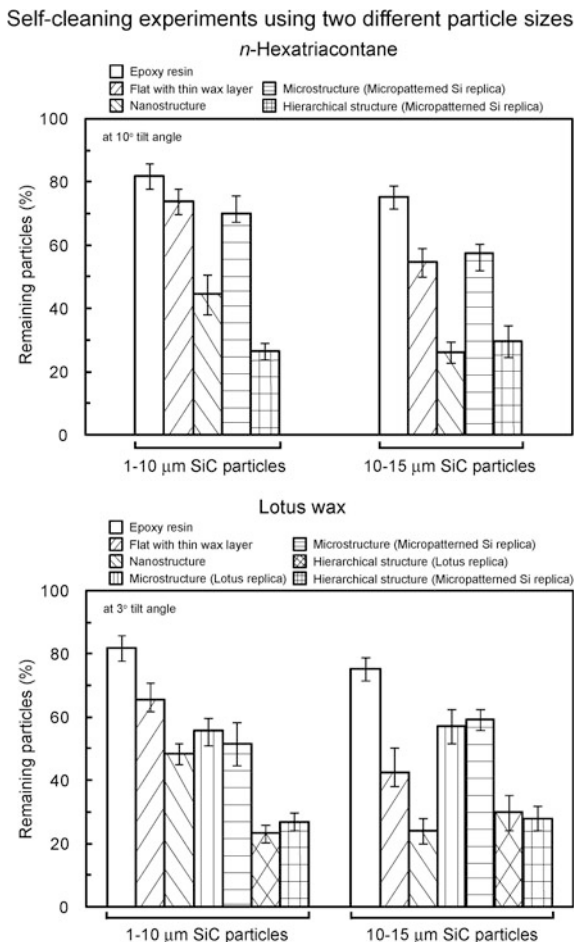
For the cleaning test, the specimens with the contaminants were subjected to water droplets of approximately 2 mm diameter, using two microsyringes (Bhushan et al. 2009a). In order to obtain a relative measure of the self-cleaning ability of hierarchical structures which exhibit the lowest contact angle hysteresis and tilt angle as compared to other structures (flat, nanostructures, and microstructures), the tilt angle chosen for the cleaning tests was slightly above the tilt angle for the hierarchical structures. Thus experiments were performed with 10° for surfaces covered with *n*-hexatriacontane and 3° for surfaces with lotus wax. The water cleaning test was carried out for 2 min (water quantity, 10 mL) with nearly zero kinetic energy of droplets. For watering with nearly zero kinetic energy, the distance between the microsyringes and surface was set to 0.005 m (nearly zero impact velocity). The chosen impact velocity represents a low value compared to a natural rain shower, where a water droplet of 2 mm diameter can reach an impact velocity of 6 m/s (measured under controlled conditions) (van Dijk et al. 2002).

The cleaning tests were performed on various surfaces with *n*-hexatriacontane and lotus wax (Bhushan et al. 2009a). The data represent the average of five different investigated areas for each experiment. Figure 6.42 shows that none of the investigated surfaces were fully cleaned by water rinsing. For lotus wax, which forms tubule nanostructures, and *n*-hexatriacontane, which forms platelet nanostructures, the same tendency of particle removal was found. With the exception of hierarchical structure on all surfaces, larger particles were removed more than small ones. Most particles (70–80 %) remained on smooth surfaces, and 50–70 % of particles were found on microstructured surfaces. Most particles were removed from the hierarchically structured surfaces, but approximately 30 % of particles remained. A clear difference in particle removal, independent of particle sizes, was only found in flat and nanostructured surfaces where larger particles were removed with higher efficiency. Observations of the droplet behavior during the movement on the surfaces showed that droplets were rolling only on the hierarchically structured surfaces. On flat, micro-, and nanostructured surfaces, the droplets first applied were not moving, but the continuous application of water droplets increased the droplet volumes and led to a sliding of these large droplets. During this, some of the particles had been removed from the surfaces. However, the rolling droplets on hierarchical structures did not collect the dirt particles trapped in the cavities of the microstructures. The data shows that hierarchical structures have superior cleaning efficiency.

6.6.5 Observation of Transition During the Bouncing Droplet

To observe how the impact velocity influences the transition from the composite solid-air-liquid interface to the homogeneous solid-liquid interface during droplet impact, Jung and Bhushan (2008b, 2009a) performed bouncing droplet experiments

Fig. 6.42 Bar charts showing the remaining particles after applying droplets with nearly zero kinetic energy on various structures fabricated using *n*-hexatriacontane and lotus wax using 1–10 μm and 10–15 μm SiC particles. The experiments on the surfaces with *n*-hexatriacontane and lotus wax were carried out on tilted stages with 10° and 3°, respectively. The error bars represent ± 1 standard deviation (Bhushan et al. 2009a)



on various surfaces with *n*-hexatriacontane and *T. majus* and lotus waxes. Figure 6.43 shows photos of a droplet of 1 mm radius hitting various surfaces fabricated with 0.2 and 0.4 $\mu\text{m}/\text{mm}^2$ of *n*-hexatriacontane after storage at room temperature. The impact velocity was obtained just prior to the droplet hitting the surface. First, on the flat surface, it was found that the droplet did not bounce off even though the impact velocity applied was up to 1.5 m/s. As shown in the images in the first row for each nano-, micro-, and hierarchically structured surface, the droplet hitting the surface under an impact velocity of 0.44 m/s first deformed and then retracted, and bounced off the surface. Finally, the droplet sat on the surface and had a high contact angle, which suggests the formation of a solid-air-liquid interface. Next, the impact experiment was repeated by increasing the impact velocity. As shown in the second row of images for the nanostructure (0.4 $\mu\text{g}/\text{mm}^2$) and microstructure, bounce off did not occur, and the wetting of the surface

Fig. 6.43 Snapshots of a droplet with 1 mm radius hitting various surfaces fabricated with 0.2 and 0.4 $\mu\text{g}/\text{mm}^2$ of *n*-hexatriacontane after storage at room temperature. The impact velocity was obtained just prior to the droplet hitting the surface. The pinning of droplet on the nanostructure with 0.4 $\mu\text{g}/\text{mm}^2$ mass, and on the microstructure occurred at impact velocities of 1.2 and 0.77 m/s, respectively (Jung and Bhushan 2009a)

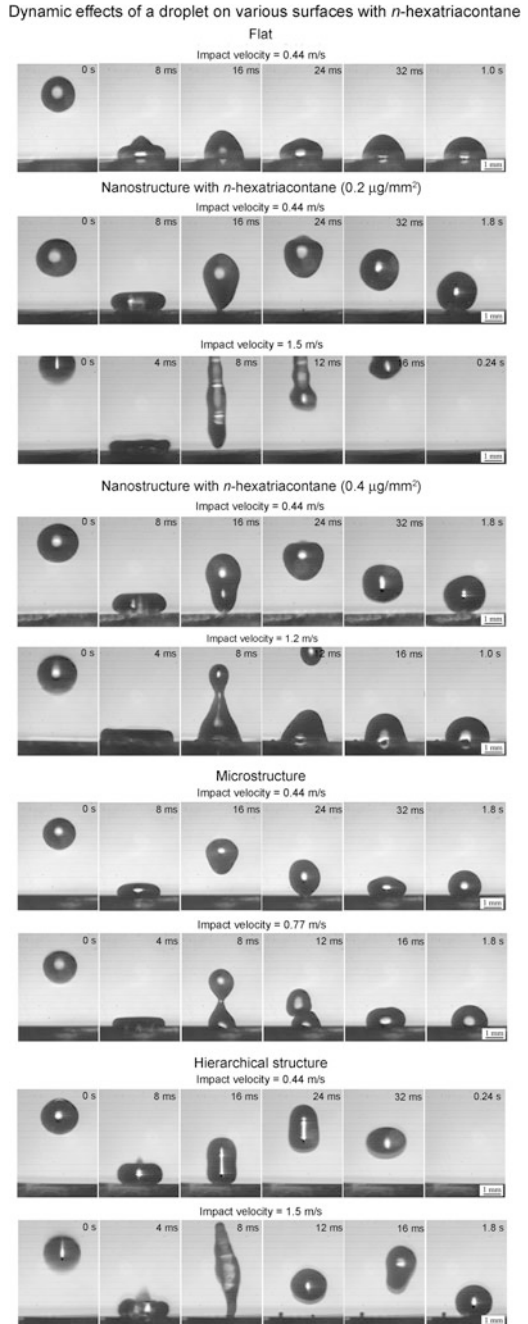
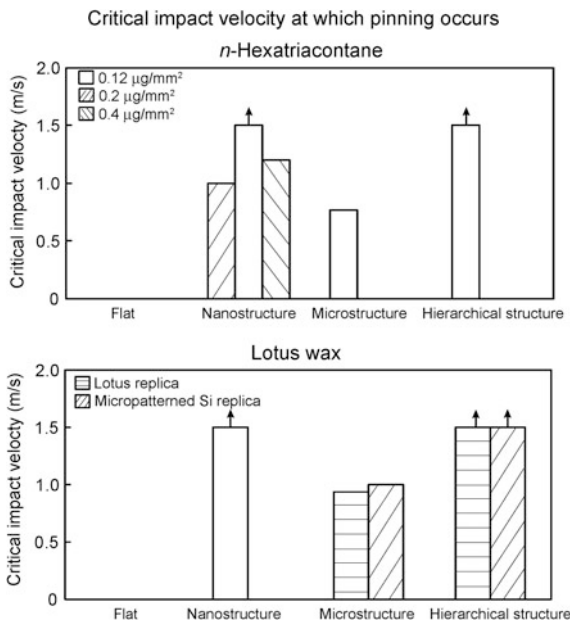


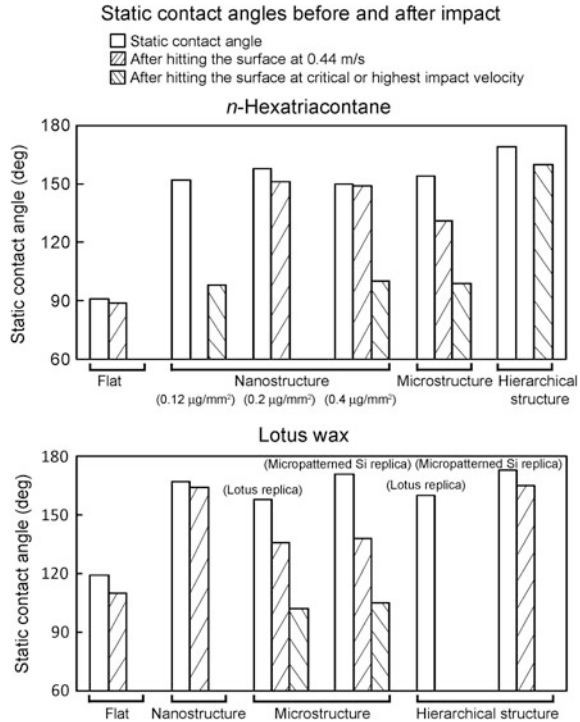
Fig. 6.44 Bar chart showing the measured critical impact velocity of a droplet with 1 mm radius at which transition occurs on various structures. The arrow indicates that the critical impact velocity can possibly be more than 1.5 m/s or the transition is not occurred (Jung and Bhushan 2009a)



(and possibly pinning of droplet) occurred at impact velocities of 1.2 and 0.77 m/s, respectively, referred to as the critical impact velocity. This is because air pockets do not exist below the droplet as a result of droplet impalement by the structures, characterized by a smaller contact angle. These observations indicate the transition from the composite interface to the homogeneous interface. However, as shown in the second row of images for the nanostructure ($0.2 \mu\text{g}/\text{mm}^2$) and hierarchical structure, during application of impact velocity up to 1.5 m/s, the bounce off always occurred and the wetting of the surface did not occur.

As shown in Fig. 6.44, the critical impact velocity of a droplet with 1 mm radius was measured on various structures on which wetting of the surface (possibly pinning of droplet) occurs (Jung and Bhushan 2009a). The arrow indicates that the critical impact velocity is more than the impact velocity used in experiments of up to 1.5 m/s. As mentioned earlier, when the mass of *n*-hexatriacontane increased, the static contact angle of the nanostructure first increased followed by a decrease at a mass of $0.2 \mu\text{g}/\text{mm}^2$. For the critical impact velocity, the same trends were found. It is believed that if neighboring crystals are separated on a sample with lower crystal density, any trapped air can be squeezed out whereas if the neighboring crystals are interconnected on a sample with higher density, air remains trapped. At the highest crystal density at a mass of $0.4 \mu\text{g}/\text{mm}^2$, there is less open volume compared to that at $0.2 \mu\text{g}/\text{mm}^2$. For all microstructures with *n*-hexatriacontane and lotus wax, the critical impact velocities of the droplet are lower than those on nano- and hierarchical structures due to the larger distance between the pillars. Further, the solid-air-liquid interface can be destabilized easily from dynamic impact on the

Fig. 6.45 Bar chart showing the measured static contact angle of a droplet on various surfaces. The contact angles of the *left bar* for each sample were measured using a droplet with 1 mm radius placed on the surface. The contact angles of the *middle and right bars* for each sample were measured using the droplet after hitting the surface at 0.44 m/s, and critical or highest impact velocity (Jung and Bhushan 2009a)



surface. Based on (6.7), the critical impact velocity of the droplet decreases with the geometric parameter (pitch). The theoretical critical impact velocity for a microstructure using (6.7) is 0.5 m/s. This value is lower than the experimental values of critical impact velocity for microstructures by about 30–50 % depending on the structured surfaces. In these experiments, while applying an impact velocity of up to 1.5 m/s on nano- and hierarchical structures with *n*-hexatriacontane (0.2 μg/mm² for nanostructure) and lotus wax, wetting of the surface did not occur. The data shows that nano- and hierarchical structures are superior to the microstructure in maintaining a stable composite solid-air-liquid interface.

To identify whether the interface is a homogeneous solid-liquid interface or a composite solid-air-liquid interface, the contact angle data in the static condition and after bounce off were measured on various surfaces, as shown in Fig. 6.45 (Jung and Bhushan 2009a). The contact angles of the left bar for each sample were measured using the droplet with 1 mm radius placed on the surface. The contact angles of the middle and right bars for each sample were measured using a droplet after hitting the surface at 0.44 m/s and critical or highest impact velocity. Missing bars mean that the droplet, after hitting the surface, bounced off without coming to sit on the surface. The static contact angle of the droplet after impact at 0.44 m/s is lower than that of the droplet when placed for all of the surfaces with *n*-hexatriacontane and lotus wax. It can be interpreted that, after hitting, the droplet pushes out

the entrapped air of the cavities between the pillars under the droplet, resulting in an abrupt increase of the solid-liquid surface area by dynamic impact. As mentioned earlier, after hitting the surface at a critical impact velocity, the contact angles were close to 90° and much lower than that of the droplet placed on the surface for the nanostructures with *n*-hexatriacontane (0.12 and $0.4 \mu\text{g}/\text{mm}^2$) and the microstructures with *n*-hexatriacontane and lotus wax. Even though the droplet is in the composite interface when it is placed on the surface, these observations indicate that the composite solid-air-liquid interface was destroyed due to dynamic impact on the surface.

6.6.6 Observation of Transition During the Vibrating Droplet

To observe how a vibrating droplet influences the transition from the composite solid-air-liquid interface to the homogeneous solid-liquid interface, Jung and Bhushan (2009a) performed vibrating droplet experiments on various surfaces with *n*-hexatriacontane and *T. majus* and lotus waxes.

6.6.6.1 Model for the Adhesion and Inertia Forces of the Vibrating Droplet

Jung and Bhushan (2009a) presented a model for vibration. In this model, they calculated expressions for adhesion force and inertia force as a function of droplet properties and operating conditions. Consider a small droplet of liquid deposited on a surface. The liquid and surface come together under equilibrium at a characteristic angle called the static contact angle θ , as shown in Fig. 6.46. When a droplet on a surface is vibrated, based on Lamb (1932), a general expression for the resonance frequency f_r of a free oscillating liquid droplet is given as,

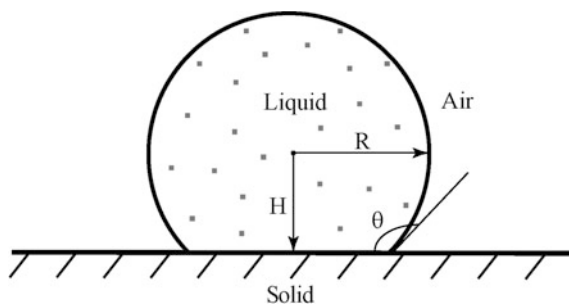


Fig. 6.46 Droplet of liquid in contact with a solid surface—contact angle θ ; radius of droplet R ; distance between the center of droplet and the solid H (Jung and Bhushan 2009a)

$$f_r = \sqrt{\frac{n(n-1)(n+2)\gamma}{3\pi\rho v}} \quad (6.15)$$

where v is the volume of the droplet, and n represents the number of modes, with 2 being the 1st mode, etc. For a spherical droplet with a radius R with the distance between the center of droplet and the solid H , the volume of droplet v is given by,

$$v = \frac{1}{3}\pi(R+H)^2(2R-H) = \frac{1}{3}\pi R^3(1-\cos\theta)^2(2+\cos\theta) \quad (6.16)$$

Experimental studies were carried out by Noblin et al. (2004) and Celestini and Kofman (2006). They showed that the frequency decreases with the volume of the droplet, and the trends are compared with a theoretical model.

When liquid comes in contact with a surface, the energy gained for surfaces coming into contact is greater than the energy required for their separation (or the work of adhesion) by the quantity ΔW , which constitutes the adhesion hysteresis (Bhushan 2003). For a surface, the difference between the two values of the interface energy (measured during loading and unloading) is given by ΔW . These two values are related to the advancing contact angle, θ_a , and receding contact angle, θ_r , of the surface. For example, a model based on Young's equation has been used to calculate the work of adhesion from contact angle hysteresis (Good 1952; Chen et al. 1991; Nosonovsky and Bhushan 2007a, 2008a),

$$\cos\theta_a - \cos\theta_r = \frac{\Delta W}{\gamma} \quad (6.17)$$

From (6.17), the dominant force (adhesion force) responsible for the separation between the droplet and surface is given by Joanny and de Gennes (1984), Lee and Laibinis (2000),

$$F_A = L\gamma(\cos\theta_a - \cos\theta_r) = 2R\sin\theta(\gamma)(\cos\theta_a - \cos\theta_r) \quad (6.18)$$

where L is the length of the triple contact line, referred to as line of contact of the solid, liquid, and air. The radius of a spherical droplet, R , depends on the contact angle and can be obtained from (6.16).

From applying vertical vibration of a droplet on a surface, the inertia force of droplet F_I is given by,

$$F_I = \rho v A \omega^2 \quad (6.19)$$

where A and ω are the amplitude and frequency of vibration, respectively. Bormashenko et al. (2007) showed that the transition occurred at a critical value of inertia force acting on the length of a triple line. However, if the inertia force of the

droplet vibrated on the surface can overcome the adhesion force between the droplet and surface, then ΔF is positive value (Jung and Bhushan 2009a),

$$\Delta F = F_I - F_A \quad (6.20)$$

The droplet can be vertically separated from the surface (bouncing off) before the composite solid-liquid-air interface is destroyed.

6.6.6.2 Vibration Study Results

A droplet on various surfaces was vibrated by varying the frequency with a sinusoidal excitation of relatively low amplitude (0.4 mm) (Jung and Bhushan 2009a). Based on (6.15), the experiments were performed in the 1st and 2nd modes ($n = 2$ and 3). Figure 6.47 shows the optical micrographs of droplets on the microstructured surface with *n*-hexatriacontane before and after vibration at an amplitude of 0.4 mm for 1st mode ($n = 2$) and 2nd mode ($n = 3$) of vibration. The frequencies for the 1st mode and 2nd mode were measured to be 86 and 208 Hz, respectively. The resonance frequencies on various surfaces were measured, and the data are summarized in Table 6.5. For comparison, the theoretical values for the two modes were calculated using (6.15). For calculations, the surface tension of the water-air interface (γ) was taken to be 0.073 N/m, the mass density (ρ) was 1000 kg/m³ for water, and the volume of the droplet (V) was 5 μ L. The theoretical values for the 1st mode ($n = 2$) and 2nd mode ($n = 3$) from (6.15) are 110 and 214 Hz, respectively. These values are similar to those of flat surfaces with *n*-hexatriacontane and lotus wax. However, with the same volume, the resonance frequencies of the structured surfaces are lower than those of flat surfaces. Celestini and Kofman (2006) showed that the resonance frequency depends on the contact angle of the structured

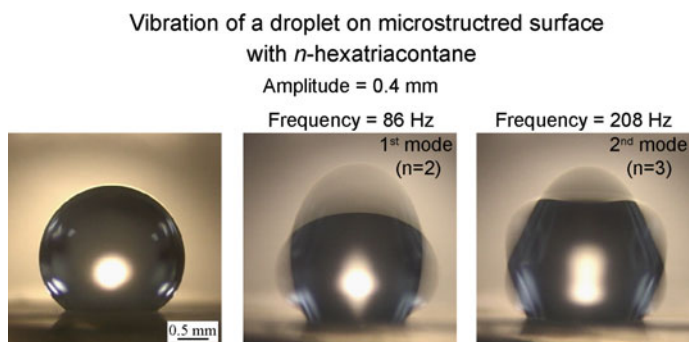


Fig. 6.47 Optical micrographs of droplets on the microstructured surface with *n*-hexatriacontane before and after vibration at amplitude of 0.4 mm for 1st mode ($n = 2$) and 2nd mode ($n = 3$) of vibration. The frequencies for 1st mode and 2nd mode were measured to be 86 and 208 Hz, respectively (Jung and Bhushan 2009a)

Table 6.5 Summary of the measured resonance frequency at the fixed amplitude value of 0.4 mm, the calculated inertia force of a vibrated droplet, and adhesive force between the droplet and surface on the various surfaces fabricated with *n*-hexatriacontane and lotus wax

	Resonance frequency (Hz)		F_A (μN)	F_I (μN) at transition or bouncing off	$\Delta F = F_I - F_A$ (μN)
	1st mode (n = 2)	2nd mode (n = 3)			
<i>n</i> -Hexatriacontane					
Flat	103	271	260 ± 3.7		
Nanostructure (0.12 $\mu\text{g}/\text{mm}^2$)	63	169	45 ± 2.2	11	-34 ± 2.2 (T)
Nanostructure (0.2 $\mu\text{g}/\text{mm}^2$)	50	147	10 ± 1.6	10	0 ± 1.6 (B)
Nanostructure (0.4 $\mu\text{g}/\text{mm}^2$)	54	149	13 ± 2.0	11	-2 ± 2.0 (B)
Microstructure	86	208	21 ± 1.7	9	-12 ± 1.7 (T)
Hierarchical structure	49	144	0.2 ± 0.06	3.6	3.4 ± 0.06 (B)
<i>Lotus wax</i>					
Flat	92	243	133 ± 3.3		
Nanostructure	47	138	0.8 ± 0.08	3.2	2.4 ± 0.08 (B)
Microstructure (Lotus replica)	63	179	14 ± 1.8	11	-3 ± 1.8 (T and B)
Microstructure (Micropatterned Si replica)	66	183	10 ± 1.6	10	0 ± 1.6 (B)
Hierarchical structure (Lotus replica)	40	139	0.1 ± 0.04	3.6	3.5 ± 0.04 (B)
Hierarchical structure (Micropatterned Si replica)	38	137	0.04 ± 0.01	2.7	2.6 ± 0.01 (B)

Positive value of ΔF means that the droplet bounced off before the transition occurred. The variation represents ± 1 standard deviation (Jung and Bhushan 2009a)

B Bouncing off; T Transition

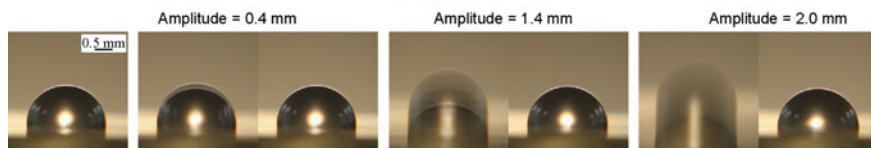
surfaces, and it decreases with increasing contact angle. The hierarchical structures with highest contact angle have the lowest resonance frequency, consistent with the results by Celestini and Kofman (2006).

To observe how the vibration of the droplet influences the transition from the composite solid-air-liquid interface to the homogeneous solid-liquid interface, Jung and Bhushan (2009a) performed vibrating droplet experiments on various surfaces with *n*-hexatriacontane and lotus wax. Figure 6.48 shows optical micrographs of droplets on various surfaces with *n*-hexatriacontane before and after vibrating at a

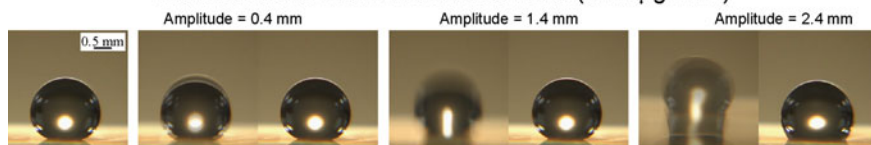
Vibration of a droplet on various surfaces with *n*-hexatriacontane

Frequency = 30 Hz

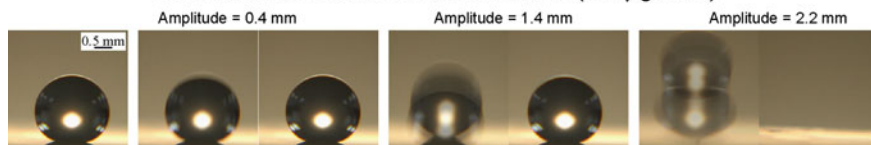
Flat



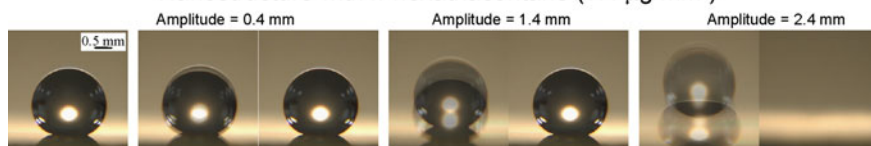
Nanostructure with *n*-hexatriacontane ($0.12 \mu\text{g}/\text{mm}^2$)



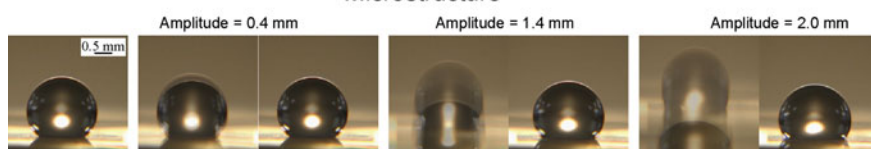
Nanostructure with *n*-hexatriacontane ($0.2 \mu\text{g}/\text{mm}^2$)



Nanostructure with *n*-hexatriacontane ($0.4 \mu\text{g}/\text{mm}^2$)



Microstructure



Hierarchical structure

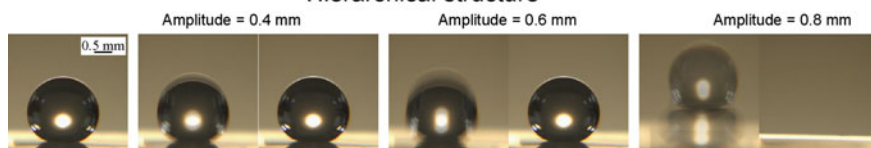


Fig. 6.48 Optical micrographs of droplets on various surfaces with *n*-hexatriacontane before and after vibrating at frequency of 30 Hz. The transition of a droplet on the nanostructure with $0.12 \mu\text{g}/\text{mm}^2$ mass of *n*-hexatriacontane and on the microstructure occurred at amplitudes of 2.4 and 2.0 mm, respectively (Jung and Bhushan 2009a)

frequency of 30 Hz, which is less than the resonance frequency for the 1st mode ($n = 2$). The vibration amplitude was increased until transition or until the droplet bounced off. First, on the flat surface, it was found that the droplet did not change much after applying vibration at amplitudes ranging from 0 to 3 mm. As shown in the images for the nanostructure ($0.12 \mu\text{g}/\text{mm}^2$) and microstructure, the static contact angles of the droplet before vibrating were 152° and 154° , respectively. After vibrating at amplitudes of 0.4 and 1.4 mm, the contact angles still had similar values (151° for nanostructure and 149° for microstructure), which suggests the formation of a solid-air-liquid interface. However, after vibrating at amplitudes of 2.4 mm for the nanostructure ($0.12 \mu\text{g}/\text{mm}^2$) and 2.0 mm for the microstructure, the static contact angles became 125° and 121° , respectively. This is because air pockets do not exist below the droplet as a result of droplet impalement by the structures, characterized by a smaller contact angle. These observations indicate the transition from the composite interface to the homogeneous interface. Observations of vibration on two nanostructures (0.2 and $0.4 \mu\text{g}/\text{mm}^2$) and a hierarchical structure showed that the transition did not occur, but the droplet started to bounce off the surface from amplitudes of 2.2, 2.4, and 0.8 mm, respectively.

The adhesive force responsible for the separation between the droplet and surface and the inertia force of a droplet vibrated on various structures were calculated to study the validity of the proposed model (6.20) (Jung and Bhushan 2009a). The adhesive force was obtained from (6.18) using static contact angle and contact angle hysteresis. The inertia forces were obtained from (6.19) using the amplitude and frequency of vibration as the transition or droplet bounce off occurred. The data are presented in Fig. 6.49 and summarized in Table 6.5. As shown in Fig. 6.48, it was observed that the transition occurred as a result of droplet impalement by the structures by increasing the inertia force of droplet on the surfaces. However, if the inertia force of the droplet vibrated on the surface can overcome the adhesion force between the droplet and surface (ΔF is positive), the droplet can be vertically separated from the surface (bouncing off) before the composite solid-liquid-air interface is destroyed. The experimental results for bouncing off of the droplet appear to have the same trend as the proposed model (6.20). It is shown that hierarchical structures have the positive value of the difference between the inertia force and adhesive force for droplet bounce off responsible for superior resistance to the dynamic effects and maintain a stable composite solid-air-liquid interface.

6.6.7 Measurement of Fluid Drag Reduction

Superhydrophobicity reduces fluid slip and drag in fluid flow (Jung and Bhushan 2010). The drag data will be presented in Chap. 10. It will be shown that fluid drag decreases with an increase in the degree of hydrophobicity.

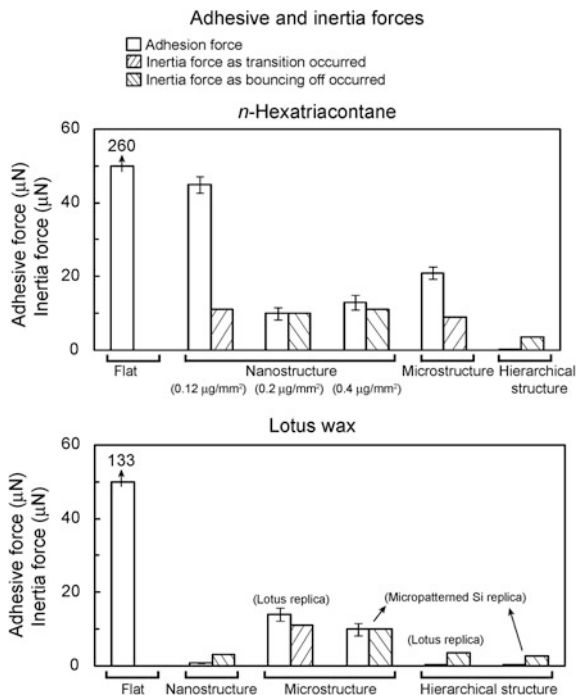


Fig. 6.49 Bar chart showing the calculated adhesive force responsible for the separation between the droplet and surface and inertia force of a droplet vibrated on various structures. The inertia forces were obtained as the transition or droplet bounce off occurred. If the inertia force of the droplet vibrated on the surface can overcome the adhesion force between the droplet and surface (ΔF is positive), the droplet can be vertically separated from the surface (bouncing off) before the composite solid-liquid-air interface is destroyed (Jung and Bhushan 2009a)

6.6.8 Summary

Hierarchically structured surfaces using nature's route were fabricated to verify that properties comparable to those of natural objects can be obtained. Various structures with two types of wax morphology with various crystal densities were fabricated for detailed analyses.

Nanostructures with different wax platelet crystal densities using *n*-hexatriacontane were deposited on a flat surface and a microstructure, and the effect of crystal density on the static contact angle, contact angle hysteresis, and air pocket formation, as well as adhesive force was studied. High density of crystals with sufficient spacing between them leads to a propensity to form air pockets resulting in a high static contact angle. In hierarchically structured surfaces, as compared to nanostructured and microstructured surfaces, the air pocket formation further increases contact angle and reduces both contact angle hysteresis and adhesive force.

The nanostructures with *T. majus* and lotus wax tubules were deposited on flat surfaces. Nanostructures were formed by wax tubules. Tubules were hollow structures and randomly oriented on the surface. The tubular diameter varied between 100 and 150 nm, and their length varied between 1500 and 200 nm. The created nanostructures were comparable to the wax crystal morphology found on the lotus leaf. The influence of these nanostructures deposited on a flat surface and a microstructure was studied on the static contact angle, contact angle hysteresis, air pocket formation, and adhesive force as well as self-cleaning efficiency. The data were compared with that of a lotus plant leaf. Hierarchically structured, followed by nanostructured, surfaces have high static contact angle, low contact angle hysteresis, and low adhesive force. These properties are superior to the lotus leaf. Evidence of air pocket formation has been reported. Self-cleaning experiments performed by deposition of contaminant particles followed by cleaning with water droplets show that hierarchical structures have superior cleaning efficiency, comparable to that of lotus leaf. To sum up, hierarchically structured surfaces using nature's route have been created and contact angles, adhesive force, and self-cleaning efficiency are comparable to that of the lotus leaf, which verifies the understanding of the mechanisms relevant to superhydrophobicity and self-cleaning in the lotus leaf.

To investigate the transition from the composite interface to the homogeneous interface on nanostructures with *T. majus* and lotus wax tubules deposited on flat surfaces and a microstructure, bouncing and vibrating droplet studies were performed. Bouncing and vibrating droplet experiments show that in hierarchically structured and nanostructured surfaces with certain crystal densities, wetting did not occur up to 1.5 m/s. In microstructured surfaces due to the larger distance between the pillars, composite interface was destroyed above a certain critical velocity in bouncing droplet experiments and above a certain inertia force of the droplet on the surfaces in vibrating droplet experiments.

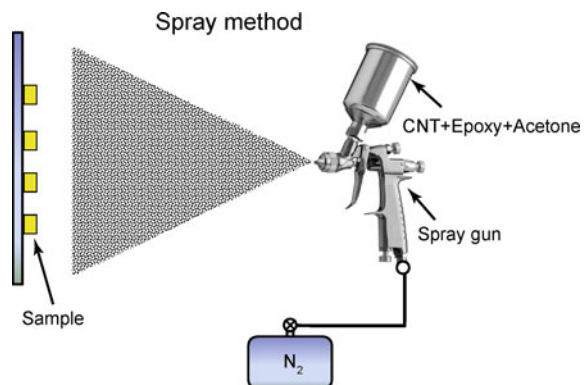
6.7 Mechanically Durable Superhydrophobic Surfaces

For commercial applications, lotus-inspired mechanically durable surfaces are needed. Two examples of hierarchically structured surfaces fabricated with CNT composites and nanoparticle composites are presented first. As a benchmark, structured surfaces with lotus wax were also prepared to compare with the durability of CNT composite structures. Then, an example of a nanoparticle composite surface with optical transparency is presented. For characterization, contact angle and contact angle hysteresis were measured. To compare the durability of the various fabricated surfaces, wear and friction studies were performed using an AFM and a ball-on-flat tribometer. Waterfall/jet tests were also conducted to determine the loss of superhydrophobicity.

6.7.1 CNT Composites

Various attempts have been made to fabricate mechanically durable structures using multi-walled CNT arrays with high mechanical strength (Lau et al. 2003; Huang et al. 2005; Zhu et al. 2005; Hong and Uhm 2006). A simpler approach is to use CNT composites. Jung and Bhushan (2009b) deposited CNT composite on flat epoxy resin and a microstructure using a spray method in order to create nano- and hierarchical structures, as shown in Fig. 6.50. CNTs were fabricated using catalyst-assisted chemical vapor deposition (CCVD) (Sun Nanotech Co Ltd, China). An iron catalyst was used to initiate growth of nanotubes using natural gas as a carbon source and Ar/H₂ as a buffer gas at 750 °C. The contact angle of individual carbon nanotubes has been reported as 60° and higher. Microstructures were fabricated using a microstructured Si surface with pillars of 14 μm diameter, 30 μm height, and 23 μm pitch by soft lithography, as described earlier (Bhushan et al. 2009b; Jung and Bhushan 2009b). The first step of deposition of the CNT composite using the spray method was to disperse the CNT into a solvent in order to maintain a uniform distribution. Acetone was used as a solvent because it does not affect surface modification and is easily vaporized in ambient conditions. The dispersion process consisted of the sonication of 200 mg the CNT in 100 mL of acetone for 4 min using a Branson Digital Sonifier with a frequency of 20 kHz at an amplitude of 80 %. During this process, the mixture was exposed to ultrasonic pressure waves in a sonifier in order to disperse the CNT into smaller aggregates. To provide strong bonding between CNT and the substrate, 200 mg EPON epoxy resin 1002F was added to the mixture of CNT and acetone, and then the mixture was sonicated for 4 more minutes. Next, the sonified mixture was poured into a spray gun and sprayed onto the specimen surfaces. The conditions for uniform deposition of the CNT on the surfaces were optimized by adjusting the concentration of CNT in the solvent. After spraying the CNT on the surfaces, the CNT composite structures were then cured at 120 °C for 3 h (above the recommended curing temperature), which is above the melting point (80–88 °C) and below the

Fig. 6.50 Schematic of spray method to deposit a mixture of CNT, epoxy, and acetone on surfaces (Jung and Bhushan 2009b)



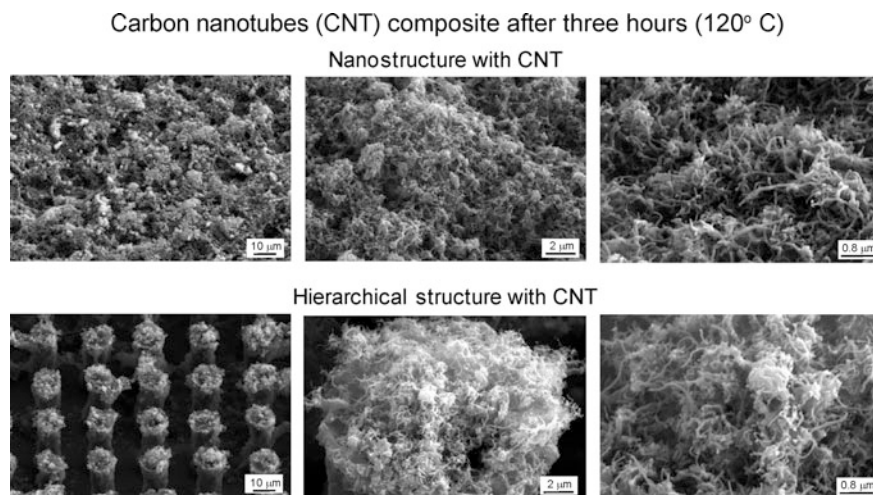


Fig. 6.51 SEM micrographs taken at 45° tilt angle, show three magnifications of nano- and hierarchical structures fabricated with CNT after 3 h at 120 °C (Jung and Bhushan 2009b)

burning point (180 °C) of EPON epoxy resin 1002F. At this temperature, the epoxy which initially covered the CNT was melted and moved to the interface between the CNT and substrates, resulting in exposed individual CNTs to provide the intended nanostructure that leads to high contact angle.

Figure 6.51 shows the SEM micrographs of nano- and hierarchical structures fabricated with CNTs (Jung and Bhushan 2009b). SEM micrographs show an overview (left column), a detail in higher magnification (middle column), and a large magnification of the nanostructures with CNT (right column). All surfaces show a homogeneous distribution of CNTs on the specimen. The CNTs were well dispersed and embedded on flat and microstructured surfaces for the desired nanostructure. The CNT diameter varied between 10 and 30 nm, and an aspect ratio varied between 160 and 200.

Lotus leaves have been the inspiration for the development of superhydrophobic and self-cleaning products. Therefore, as a benchmark for mechanical durability studies, Jung and Bhushan (2009b) used nano-, micro-, and hierarchical structures created by the self-assembly of lotus wax, with the amounts of 0.8 $\mu\text{g}/\text{mm}^2$ deposited on flat epoxy resin and microstructure by thermal evaporation as shown in Fig. 6.40.

6.7.1.1 Contact Angle

To study the effect of CNT composite structures for superhydrophobicity, Jung and Bhushan (2009b) measured the static contact angle and contact angle hysteresis on nano- and hierarchical structures with CNTs. For static contact angle and contact

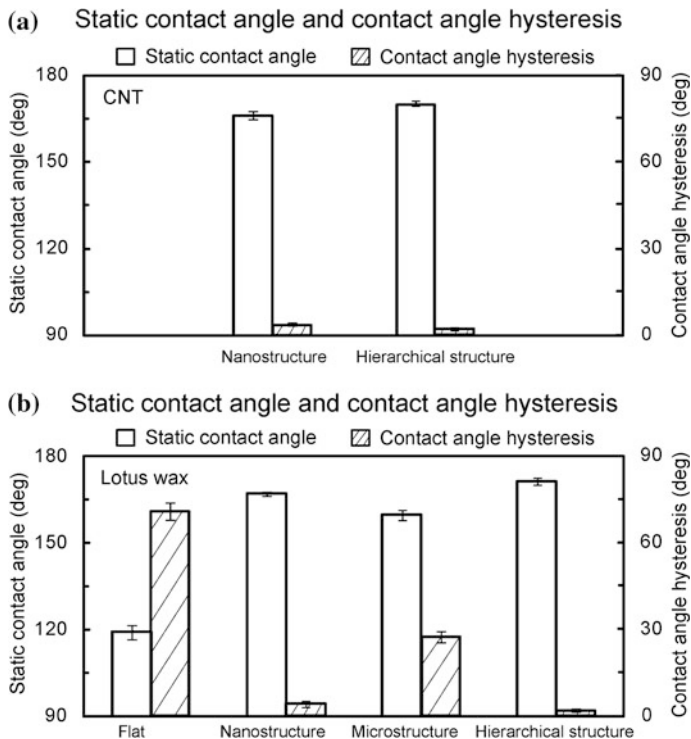


Fig. 6.52 Bar chart showing the measured static contact angle and contact angle hysteresis on **a** nano- and hierarchical structures fabricated with CNT after three hours at 120 °C, and **b** various structures fabricated with 0.8 $\mu\text{g}/\text{mm}^2$ of lotus wax after storage for 7 days at 50 °C with ethanol vapor. The error bar represents ± 1 standard deviation (Jung and Bhushan 2009b)

angle hysteresis, droplets of about 5 μL in volume (with the diameter of a spherical droplet about 2.1 mm) were deposited on the surface using a microsyringe. For contact angle hysteresis, the advancing and receding contact angles were measured at the front and back of the droplet moving along the tilted surface, respectively. Figure 6.52a shows that superhydrophobicity with a static contact angle of 166° and a contact angle hysteresis of 4° was found in the nanostructured surface with CNTs. After introducing the CNT nanostructure to the top of the micropatterned Si replica, the higher static contact angle of 170° and lower contact angle hysteresis of 2° were found for the hierarchical structures with CNTs. Both nano- and hierarchical structures created with CNTs showed superhydrophobic and self-cleaning surface, which has a static contact angle of more than 150° and contact angle hysteresis of less than 10° (Jung and Bhushan 2009b).

Figure 6.52b shows that for the hierarchical structure with lotus wax, the highest static contact angles of 173° and lowest contact angle hysteresis of 1° were found. The recrystallized wax tubules are very similar to those of the lotus leaf, but are 0.5–1 μm longer. The static contact angle is higher and the contact angle hysteresis

is lower than those reported for the lotus leaf (static contact angle of 164° and contact angle hysteresis of 3°) (Koch et al. 2009). Further, superhydrophobicity was found in the nanostructured surface with lotus wax with a static contact angle of 167° and a contact angle hysteresis of 5° . The microstructured surface with a lotus wax layer has a static contact angle of 160° , but shows a much higher contact angle hysteresis of 29° than found in hierarchical structures. Melting of the lotus wax led to a flat surface with a flat wax film and a much lower static contact angle of 119° and higher contact angle hysteresis of 71° . The data of a flat lotus wax film on a flat replica show that the lotus wax by itself is hydrophobic (Jung and Bhushan 2009b).

6.7.1.2 Durability of Various Surfaces in Waterfall/Jet Tests

To investigate the durability of the created surfaces in long-term exposure to water and how different kinetic energies of the water hitting the surface affect wetting properties, Jung and Bhushan (2009b) conducted waterfall/jet tests on the surfaces created with CNTs and lotus wax. The nano- and hierarchical structures with CNTs were exposed to water with pressure ranging from 0 to 45 kPa for 20 min. Figure 6.53 (left) shows static contact angle and contact angle hysteresis as a function of water pressure. As water pressure hitting the surfaces increased, the static contact angle and contact angle hysteresis decreased and increased slightly,

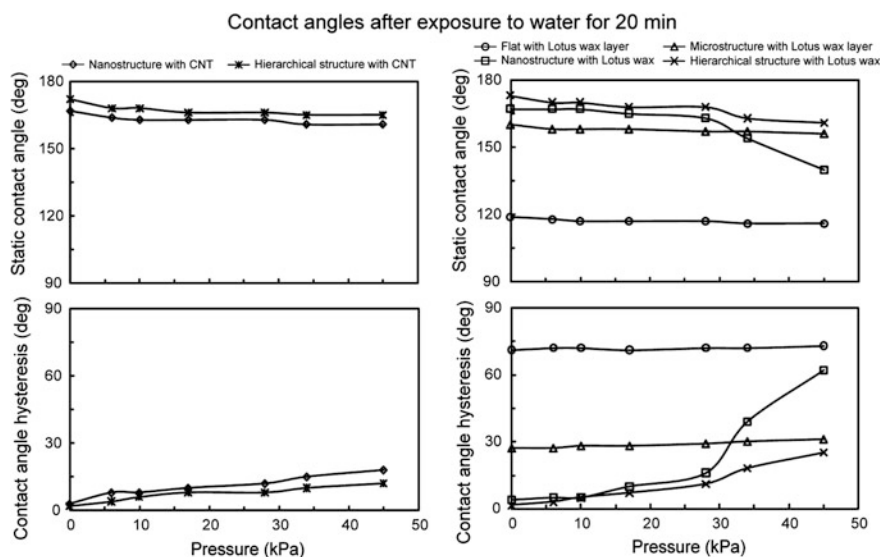


Fig. 6.53 Static contact angle and contact angle hysteresis as a function of water pressure of exposure for 20 min for the droplet with a 1 mm radius ($5 \mu\text{L}$ volume) deposited on the surfaces with CNT and lotus wax. The data are reproducible within $\pm 5\%$ (adapted from Jung and Bhushan 2009b)

respectively, but a significant change was not found on both the nano- and hierarchical structures for superhydrophobicity. It can be interpreted that there was no deformation of CNT structures due to strong bonding with the substrate. As a result, superhydrophobic CNT composite structures showed good stability of wetting properties, not only from long-term exposure to water, but also high water pressure. Jung and Bhushan (2009b) also conducted waterfall/jet tests on the flat, nano-, micro-, and hierarchical structures with lotus wax in order to compare durability of the created surfaces with CNTs and lotus wax. Figure 6.53 (right side) shows static contact angle and contact angle hysteresis as a function of water pressure exposure. As the water pressure increased up to 45 kPa, static contact angle and contact angle hysteresis remained almost constant for the flat surface and microstructure surface with lotus wax layer. However, as the water pressure increased up to 34 kPa, the static contact angle of nano- and hierarchical structures with lotus wax first decreased slightly, and then the contact angle started decreasing sharply. It was also observed that the corresponding large change in contact angle hysteresis was found above 34 kPa. As expected, it is observed that the nanostructure with lotus wax can be damaged by water with high pressure, resulting in a loss of superhydrophobicity.

6.7.1.3 Durability of Various Surfaces in AFM and Ball-on-Flat Tribometer Tests

To investigate the durability of the nanostructure fabricated using CNTs, Jung and Bhushan (2009b) conducted wear tests by creating $50 \times 50 \mu\text{m}^2$ wear scars with a $15 \mu\text{m}$ radius borosilicate ball for 1 cycle at two normal loads of 100 and $10 \mu\text{N}$ using an AFM. Figure 6.54a shows surface height maps before and after wear tests for nanostructures with CNTs. As the normal load of 100 nN was applied to the nanostructure with CNTs, the wear scar induced on the surface after the 100 nN normal load tests was not found or was very low, and it was also hard to quantify a wear depth on the nanostructure with CNTs scanned with a borosilicate ball. With increasing the normal load to $10 \mu\text{N}$, it was found that the wear depth on the nanostructure with CNTs was not significantly changed, but the morphology of the CNTs differs slightly from that before the wear test. It can be interpreted that the individual CNTs might be expected to slide or bend with the borosilicate ball applied by high normal load of $10 \mu\text{N}$ during the test process.

For comparison, Jung and Bhushan (2009b) also investigated the durability of the nanostructure fabricated using lotus wax by applying two normal loads of 100 nN and $10 \mu\text{N}$ using AFM. Figure 6.54b shows surface height maps before and after wear tests for nanostructures with lotus wax. As the normal load of 100 nN was applied to the nanostructure with lotus wax, the change in the morphology of the structured surface was observed, and a small amount of debris was generated compared to the surface before the wear test. This indicated that the wax nanostructure has weak mechanical strength, even with small loads. Increasing the normal load to $10 \mu\text{N}$, it was found that the depth of the wear mark increased, and the nanostructure with lotus wax was fully removed from the substrate. As expected,

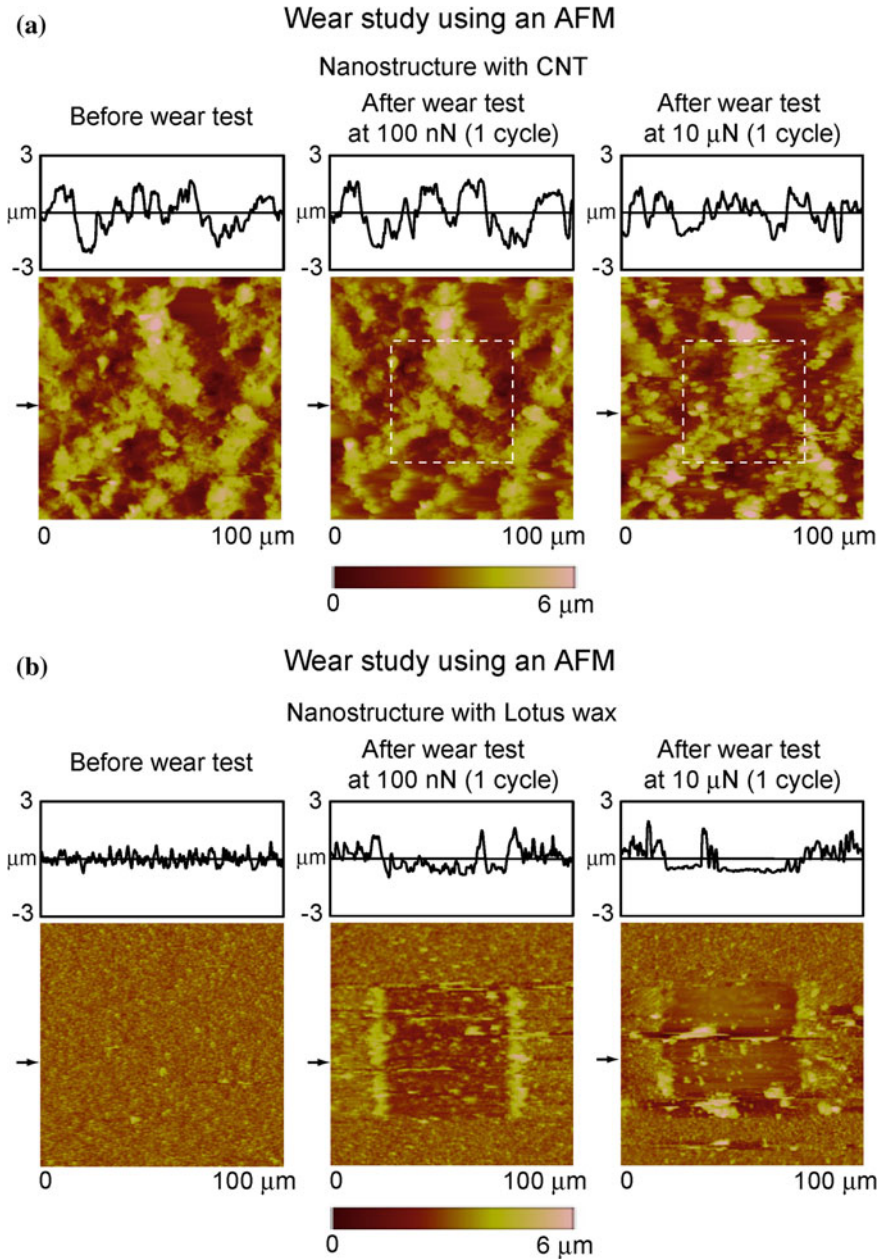
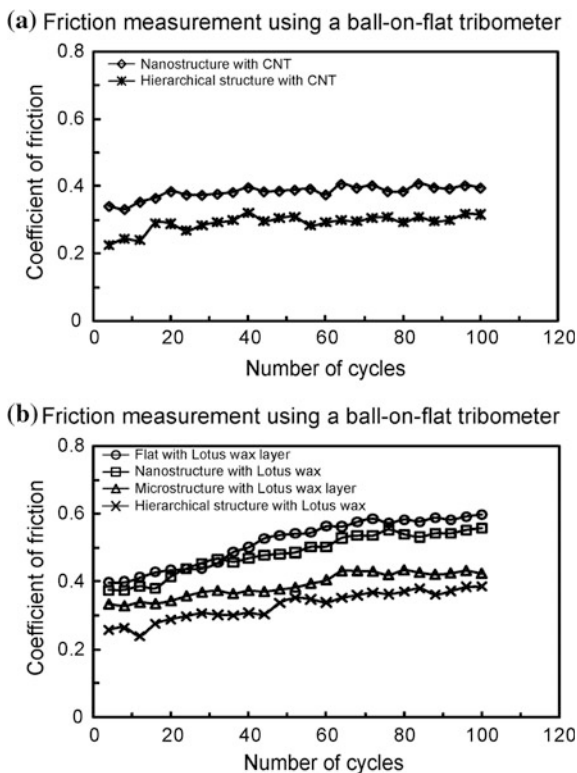


Fig. 6.54 Surface height maps before and after wear tests with a 15 μ m radius borosilicate ball at 100 nN and 10 μ N for nanostructures with **a** CNT and **b** lotus wax using an AFM (Jung and Bhushan 2009b)

Fig. 6.55 Coefficient of friction as a function of number of cycles using a ball-on-flat tribometer for the surfaces with **a** CNT and **b** lotus wax at room temperature ($22 \pm 1^\circ\text{C}$) and ambient air ($45 \pm 5\%$ RH). The data are reproducible within $\pm 5\%$ based on three measurements (Jung and Bhushan 2009b)



the nanostructure with lotus wax exhibited greater wear compared to the nanostructure with CNTs, as evidenced by debris build-up around the edge of the wear test region. The damage to the structured surface can cause the sticking of water droplets in the wear region, resulting in low static contact angle and high contact angle hysteresis.

In order to investigate the durability of structured surfaces at a high load, Jung and Bhushan (2009b) conducted conventional ball-on-flat tribometer experiments for the surfaces with CNTs. Figure 6.55a shows the coefficient of friction as a function of the number of cycles for the nano- and hierarchical structures with CNTs. The data are reproducible within $\pm 5\%$ based on three measurements. The coefficients of friction on both the nano- and hierarchical structures with CNTs first increased slightly for 20 cycles. Such a trend can be due to the elastic bending or buckling of CNTs by contacting with a sapphire ball during the beginning of scan, resulting in an increase of the contact area. During the entire experiment, the coefficient of friction value of the nano- and hierarchical structures with CNTs changed minimally, which indicates that the CNTs were not worn after 100 cycles. To investigate the change in the morphology of the surfaces after the wear test, optical microscope images were obtained before and after the wear test as shown in Fig. 6.56a. As expected, it was observed that there is no or low wear on the

Fig. 6.56 Optical micrographs before and after wear test at 10 mN (100 cycles) using a ball-on-flat tribometer for the surfaces with **a** CNT and **b** lotus wax (Jung and Bhushan 2009b)

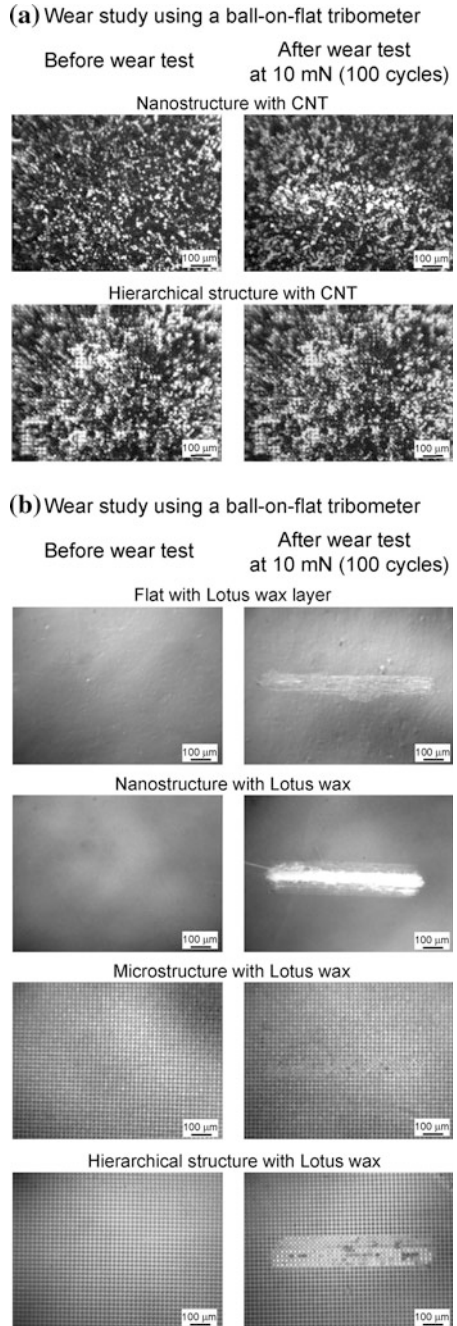


Table 6.6 Typical physical properties of various specimens and calculated contact diameters and contact stresses at three loads used in AFM and ball-on-flat tribometer measurements

	Borosilicate ball with a 15 μm radius	Sapphire ball with a 1.5 mm radius	Carbon nanotube			
Elastic modulus (GPa)	70 ^a	390 ^b	1200 ^c			
Poisson's ratio	0.2 ^a	0.23 ^b	0.2 ^d			
Bending strength (GPa)			14.2 ^c			
	Contact diameter (μm)			Mean contact pressure (GPa)		
	Borosilicate ball at 100 nN	Borosilicate ball at 10 μN	Sapphire ball at 10 mN	Borosilicate ball at 100 nN	Borosilicate ball at 10 μN	Sapphire ball at 10 mN
Carbon nanotube	0.05	0.24	6.62	0.076	0.33	0.44

It is assumed that contacts are single-asperity contact (Jung and Bhushan 2009b)

^aCallister (2000), ^bBhushan and Gupta (1991), ^cWong et al. (1997), ^dZhang et al. (2008)

nano- and hierarchical structures after wear tests. No or low wear on the CNT composite structure possibly can be due to the significant increase in the mechanical strength and wear resistance from the uniform distribution and strong bonding of CNTs on flat epoxy resin and microstructure. The elastic bending or buckling exhibited by CNTs make them exceedingly tough materials that may be absorbing some of the force at contact, acting as a compliant spring moderating the impact of the ball on the surface (Dresselhaus et al. 2000; Meyyappan 2005; Chen et al. 2006).

Contact diameters and contact stresses of CNTs at three loads used in AFM and ball-on-flat tribometer tests were calculated (Jung and Bhushan 2009b). Table 6.6 lists the physical properties of various specimens. It is assumed that contacts are single-asperity elastic contacts. For this case, the contact diameter (Bhushan 2013a, b) is given by,

$$d = 2 \left(\frac{3WR}{4E^*} \right)^{1/3} \quad (6.21)$$

where W is the total normal load, R is the asperity radius, and E^* is the effective elastic modulus. It should be noted that contact occurs on multiple asperities, and (6.21) gives an approximate value. The calculated contact diameter and contact stress are presented in Table 6.6. The deformation of CNTs appears to be elastic at the three loads applied by the borosilicate ball and sapphire ball.

In order to compare the durability of the created surfaces with CNT and lotus wax at a high load, Jung and Bhushan (2009b) conducted a wear study on the surfaces with lotus wax using a conventional ball-on-flat tribometer. As shown in Fig. 6.55b, the coefficient of friction value of the surfaces with lotus wax exhibited a gradual increase when the sliding cycle increases up to about 70 cycles, and then remains constant. This indicates that the wax nanostructure and flat wax layer could

be undergoing some wear due to weak bonding with the substrates. The change in the morphology of the surfaces with lotus wax was observed in optical microscope images as shown in Fig. 6.56b. As shown in the AFM study at low loads (Fig. 6.54b), it is observed that the flat wax layer and wax nanostructure on the flat and microstructure were fully removed from the surfaces. As a result, superhydrophobic CNT composite structures showed better mechanical durability than the structured surfaces with lotus wax to best withstand real world applications.

6.7.1.4 Summary

The hierarchical structure created with CNTs shows a high static contact angle of 170° and a low contact angle hysteresis of 2° . As a benchmark, the structures created using lotus wax were used to compare the durability of CNT composite structures. It was found that superhydrophobic CNT composite structures showed good stability of wetting properties in exposure to water. In contrast, it was observed that the nanostructure with lotus wax can be damaged by water with high pressure, resulting in the loss of superhydrophobicity. From wear and friction studies, it was found that the nanostructure with lotus wax can be damaged easily, even at a small load. However, the CNT composite structure showed high wear resistance because of the uniform distribution and strong bonding of CNTs to the flat epoxy resin and microstructure.

6.7.2 Nanoparticle Composites with Hierarchical Structure

Superhydrophobic surfaces using silica particles have been created by dropcasting, chemical deposition and sol-gel processes (Ming et al. 2005; Liu et al. 2006; Englert et al. 2006). Ebert and Bhushan (2012a) fabricated hierarchical structures resistant to mechanical wear with silica particles using a spray method. In their studies, hierarchically structured surfaces were produced by either spraying a nanoparticulate coating over a micropatterned surface or by spraying a coating with micro- and nanosized particles on a flat surface. The pitch between pillars for the micropatterns was known, and the average pitch between microparticles on a surface was determined through SEM imaging. Figure 6.57 illustrates the use of both particles and a patterned surface to form microstructures and hierarchical structures. Knowing the geometry of the particles, the transition to the Wenzel regime can be predicted to occur above a certain pitch value (Ebert and Bhushan 2012a).

6.7.2.1 Experimental Details

For samples using a micropattern as the microscale roughness, nanoparticle epoxy solution was sonicated and sprayed on the micropatterned surface. Epoxy

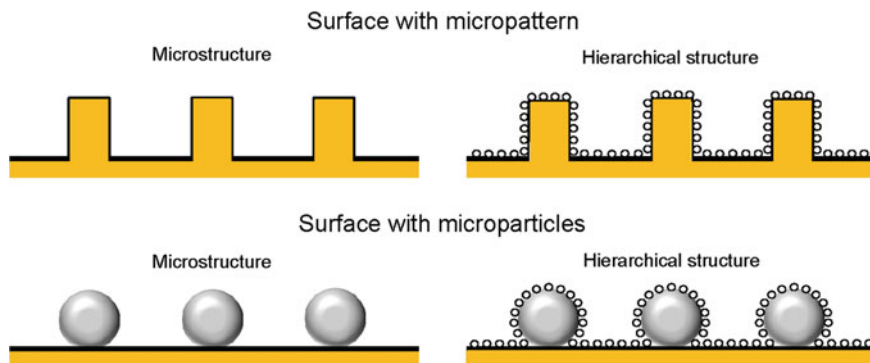


Fig. 6.57 Schematic examples of microstructured and hierarchically structured surfaces in which the microstructure is formed by both a uniform micropattern (*top*) and microparticles (*bottom*). In both cases, the hierarchical structure is achieved through addition of nanoparticles (adapted from Ebert and Bhushan 2012a)

micropatterns were fabricated by replicating a Si micropatterned surface by soft lithography. Silica nanoparticles of 10 nm (± 1 nm) and 50 nm (± 15 nm) were created through continuous flame hydrolysis of SiCl_4 , and hydrophobized through silane treatment (Evonik-Degussa Corporation, Parsippany, New Jersey). In order to spray the particles onto the surfaces, they were first dispersed uniformly in solution. 200 mg of particles were sonicated in 100 mL of acetone for 4 min with a Branson Sonifier 450A with a frequency of 20 kHz at 80 % amplitude. For strong bonding of the nanoparticles to the substrates, 200 mg of EPON epoxy resin 1002F (Hexion Specialty Chemicals, Columbus, Ohio) was then added, and the solution was sonicated for another 4 min. The dispersion of particles in solution was then sprayed onto the sample surface using a spray gun. The samples were then annealed at 120 °C for 3 h. Annealing at this temperature (above the melting point and below the burning point of EPON 1002F) was done so that the resin would melt and move to the interface between the particles and the surface.

Figure 6.58a shows the SEM micrographs of hierarchical structures with silica nanoparticles and an epoxy micropattern (Ebert and Bhushan 2012a). The hierarchical structures are shown at three magnifications: the lowest to show the pitch between pillars, the middle to show an individual pillar, and the highest to show surface nanoscale roughness.

For samples using microparticles as the microscale roughness, the microparticles were sonicated in solution in the same manner and sprayed onto flat epoxy surfaces. The hydrophobic silica microparticles (diameter = $10 \mu\text{m} \pm 5 \mu\text{m}$) were obtained as a trimethylated silica gel powder from Dow Corning (Midland, Michigan). For hierarchically structured surfaces, an additional sonication and spray of nanoparticles was performed. Surfaces of varying pitch were created by changing the concentration of microparticles in the solution (400 mg/L or 1400 mg/L). The value of the average pitch between microparticles was found by determining the number

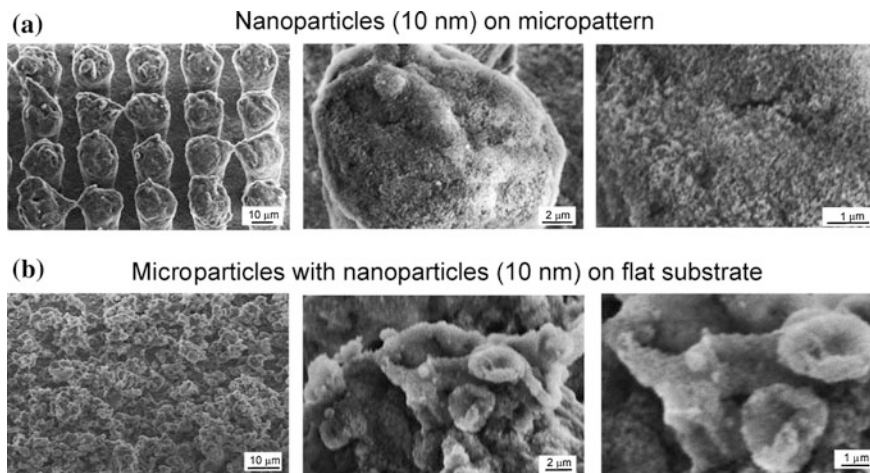


Fig. 6.58 SEM micrographs taken at 45° tilt angle showing **a** 10 nm particles on micropattern with a pitch value (P) of $23\ \mu\text{m}$ at three magnifications (*bottom*), and **b** microparticle with 10 nm particles with microparticle spray concentration of $1400\ \text{mg/L}$ with resulting average pitch value (P_{avg}) of $21\ \mu\text{m}$ (adapted from Ebert and Bhushan 2012a)

of particles in a $1\ \text{mm}^2$ area in five different locations on the sample by examining SEM images. Figure 6.58b shows the SEM micrographs of surfaces using microparticles with concentration of $1400\ \text{mg/L}$ resulting in an average pitch value (P_{avg}) of $21\ \mu\text{m}$ (Ebert and Bhushan 2012a).

6.7.2.2 Contact Angle of Surfaces Using Micropattern

Contact angle and contact angle hysteresis data for the 10 nm and 50 nm particles on flat and micropatterned surfaces are shown in Fig. 6.59 (Ebert and Bhushan 2012a). Data for the micropattern without nanoparticles is shown also for reference. In the cases of both flat and micropatterned surfaces, the difference in the data between the 10 nm and 50 nm particles was insignificant. Nanoparticles on a flat surface (nanostructure) showed a contact angle of $161^\circ (\pm 2^\circ)$ and contact angle hysteresis of $2^\circ (\pm 1^\circ)$. The contact angle and contact angle hysteresis of the epoxy micropattern alone were found to be $151^\circ (\pm 2^\circ)$ and $33^\circ (\pm 2^\circ)$, respectively. For nanoparticles on the micropattern (hierarchical structure), the highest contact angle of $168^\circ (\pm 2^\circ)$ and lowest contact angle hysteresis of $1^\circ (\pm 0.5^\circ)$ were found. The relative improvements in contact angle and contact angle hysteresis seen in the nanostructured, microstructured, and hierarchically structured surfaces are in agreement using CNTs and lotus wax, presented earlier.

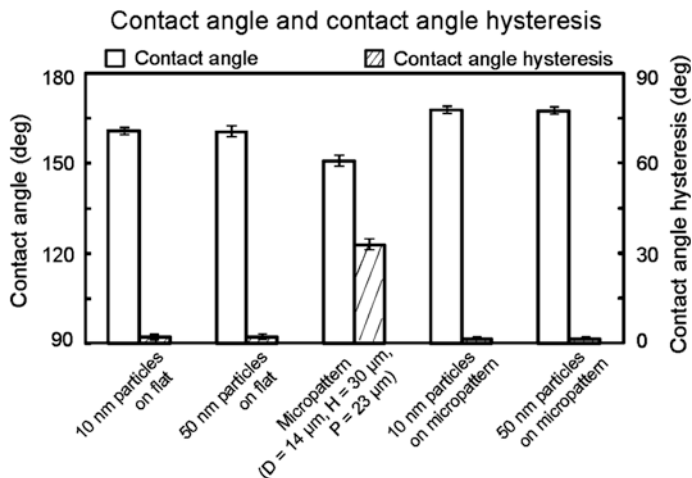


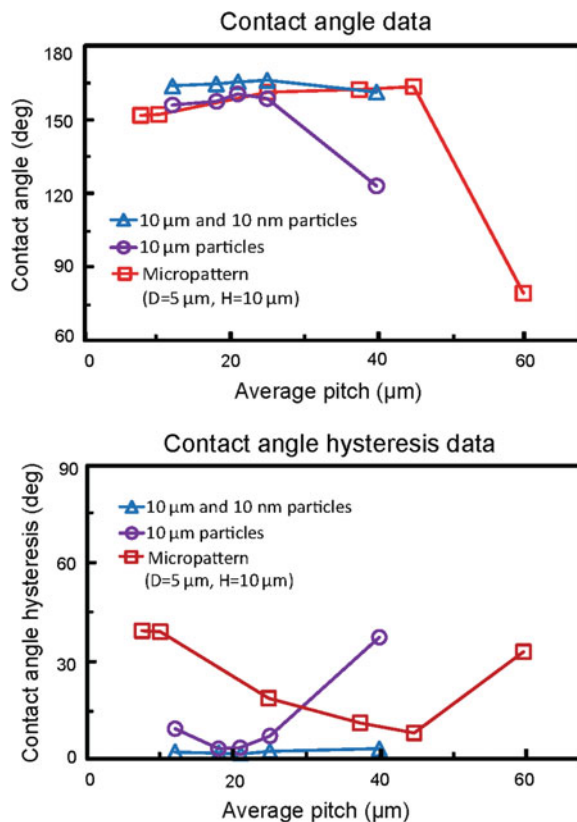
Fig. 6.59 Bar chart showing the measured static contact angle and contact angle hysteresis on nano-, micro- and hierarchically structured surfaces using both 10 and 50 nm particles. The error bars represent ± 1 standard deviation (Ebert and Bhushan 2012a)

6.7.2.3 Contact Angle of Surfaces Using Microparticles and Comparison to Micropatterns

The contact angle and contact angle hysteresis of surfaces with 10 μm particles alone on flat and 10 μm /10 nm particles combined on flat are shown in Fig. 6.60 (Ebert and Bhushan 2012a) across a range of average pitch values. In addition, the contact angle/contact angle hysteresis of epoxy micropatterns of varying pitch are shown in order to provide a comparison of the trends seen with microparticles versus micropatterns. In this comparison, micropatterns with pillars with $D = 5 \mu\text{m}$ and $H = 10 \mu\text{m}$ were used, as the size is more comparable to the microparticles. It is seen that for 10 μm particles alone on flat, the trends in contact angle and contact angle hysteresis with pitch are similar to those of the micropatterns. The micropatterns maintain a contact angle above 150° from the lowest pitch value until a sharp drop at a pitch of 60 μm . Similarly, the surfaces with microparticles show a steady contact angle above 150° , with a sharp drop at an average pitch of 40 μm . For contact angle hysteresis, the micropattern shows a steady decrease with increasing pitch, until a large increase occurs at 60 μm . For the 10 μm particles, an initial decrease is seen at low pitch, and very low contact angle hysteresis is seen until a large increase occurs, again at 40 μm .

The sudden changes in contact angle/contact angle hysteresis, occurring at a pitch of 60 μm for the micropatterns and 40 μm for the microparticles, represent the transition to the Wenzel regime. At these pitch values, the droop of the water between microstructures is enough that the water fully penetrates between them, leaving no air pockets. For the micropatterns, the value of 60 μm is close to the value predicted by (6.4) (74 μm with $D = 5 \mu\text{m}$, $H = 10 \mu\text{m}$). The transition value

Fig. 6.60 Static contact angle and contact angle hysteresis as a function of average pitch for surfaces with 10 μm particles alone and with 10 $\mu\text{m}/10\text{ nm}$ particles combined on flat. Epoxy micropattern data is also shown for comparison of microstructure behavior. Reproducibility is $\pm 1^\circ$ for CAH of 10 $\mu\text{m}/10\text{ nm}$ particles combined, $\pm 2^\circ$ for CAH of 10 μm particles and epoxy micropatterns, and $\pm 2^\circ$ for all CA data (Ebert and Bhushan 2012a)

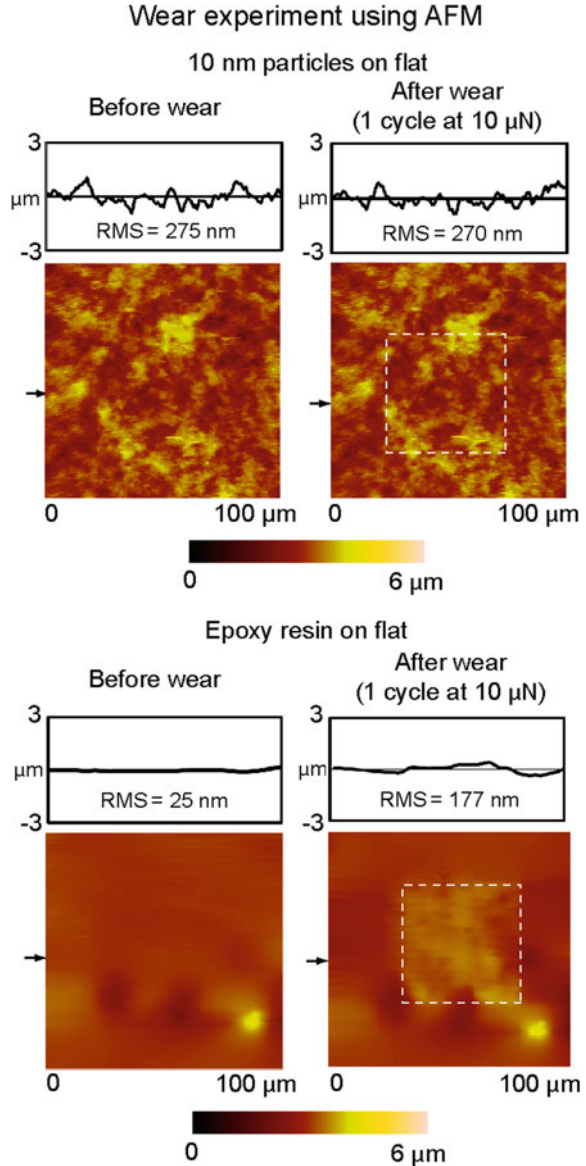


for the surfaces with 10 μm particles is expected to be different since the pitch, diameter, and height are much less uniform as compared to the micropatterns. However, the similarity of the overall trends in contact angle and contact angle hysteresis with pitch indicates that the microparticles are reasonably mimicking a micropatterned surface. In addition, the data for the 10 $\mu\text{m}/10\text{ nm}$ particles combined shows an overall increase in contact angle and decrease in contact angle hysteresis as compared to the 10 μm particles alone, indicating that the benefits of hierarchical structure can be realized using the 10 μm particles as the underlying microstructure. Contact angle as high as 166° ($\pm 2^\circ$) and contact angle hysteresis as low as 2° ($\pm 1^\circ$) were seen for these surfaces.

6.7.2.4 Durability of Various Surfaces in AFM and Ball-on-Flat Tribometer Tests

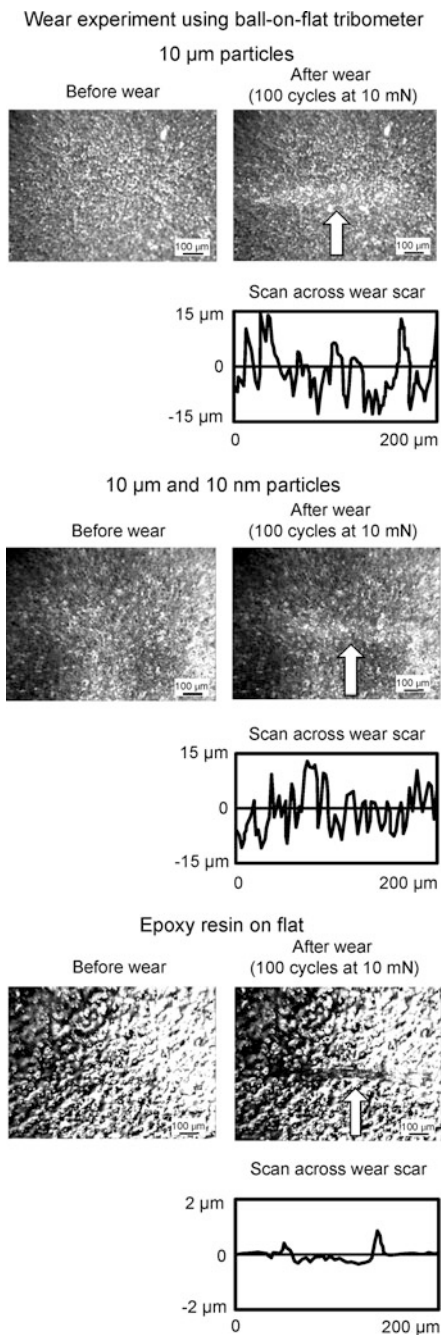
The results of the AFM wear experiment for 10 nm particles, as well as an epoxy resin, are shown in Fig. 6.61 (Ebert and Bhushan 2012a). Surface height maps

Fig. 6.61 Surface height maps and sample surface profiles (locations indicated by *arrows*) before and after AFM wear experiment with $15\ \mu\text{m}$ radius borosilicate ball at load of $10\ \mu\text{N}$ for $10\ \text{nm}$ particles on flat surface (*top*) and epoxy resin on flat surface (*bottom*). RMS roughness values for surface profiles are displayed within surface *profile boxes* (Ebert and Bhushan 2012a)



before and after the wear experiment are displayed, as well as sample scans across the middle of the image (position indicated by arrow) with RMS roughness within the wear area displayed. After 1 cycle at $10\ \mu\text{N}$ with the borosilicate ball, the morphology of the surface with $10\ \text{nm}$ particles was not significantly changed, and RMS of the sample scan within the wear area was nearly identical ($270\ \text{nm}$ after compared with $275\ \text{nm}$ before). However, the after-image for the epoxy resin

Fig. 6.62 Optical micrographs before and after wear experiment using ball-on-flat tribometer at 10 mN for 10 μm particles (*top*), 10 μm particles with 10 nm particles (*middle*), and epoxy resin on flat surface (*bottom*). Sample profiles across wear areas are shown below after-images (*arrows* indicate location of profile) (Ebert and Bhushan 2012a)



reveals some wear, as well as an overall swelling of the wear area. In addition, RMS of the sample scan increased from 25 to 177 nm within the wear area. This demonstrates that the durability of the nanoparticle-coated surfaces is superior to that of the surfaces with epoxy resin alone.

The ball-on-flat tribometer experimental results are shown in Fig. 6.62 for surfaces with 10 μm particles, 10 μm /10 nm particles combined, and an epoxy resin (Ebert and Bhushan 2012a). Before and after images as well as a scan across the wear scar are displayed for 10 μm particles on flat, 10 μm with 10 nm particles on flat, and epoxy resin on flat. After 100 cycles at 10 mN, the 10 μm particles alone showed minimal wear (mainly in the form of burnishing of the tops of particles), and a microscale roughness is preserved. The 10 μm and 10 nm particles combined show similar results of minimal wear. However, the after image of the epoxy resin reveals a well-defined groove. The scan shows buildup along the sides of the groove, and the groove depth can be seen as approximately 300 nm. Thus, the surfaces with microparticles also showed resistance to wear superior to that of the surfaces with epoxy resin alone.

6.7.2.5 Summary

Ebert and Bhushan (2012a) produced a mechanically durable, hierarchically structured surfaces exhibiting superhydrophobicity. They were produced either by spraying a nanoparticulate coating over a micropatterned surface or by spraying a coating with micro- and nanosized silica particles on a flat surface. A comparison was made between the use of microparticles and micropatterns in terms of wettability across different pitch values. Results show similar trends in CA/CAH with pitch value whether the microstructure was formed with particles or a micropattern. Hierarchical surfaces using micro- and nanoparticles exhibited a CA of $166^\circ (\pm 2^\circ)$ and a CAH of $2^\circ (\pm 1^\circ)$ at optimum pitch. For hierarchical surfaces using micropatterns with nanoparticles, a nearly identical CA of $168^\circ (\pm 2^\circ)$ and CAH of $1^\circ (\pm 0.5^\circ)$ were measured. In addition, the surfaces demonstrated wear resistance superior to the epoxy resin on multiple length scales in the AFM and tribometer experiments, showing ability to preserve both nanoscale and microscale roughness.

6.7.3 Nanoparticle Composites for Optical Transparency

For applications such as self-cleaning windows, electronic touch screens (e.g., for mobile phones, tablets, and computers), optical devices, and solar panels, high optical transparency is required, as well as mechanical durability. For example, typical requirements for an automotive windshield are visible transmittance $>70\%$, haze $<1\%$, 10,000 cycles of wiper sliding, and 250 car wash cycles; the last two requirements representing 10 years of life.

Table 6.7 Typical values for optical properties, electrical resistivity, and hardness for SiO₂, ZnO, and ITO particles (Ebert and Bhushan 2012b)

Particle	Band gap energy (band gap wavelength)	Refractive index	Hardness (GPa)	Electrical resistivity (Ω cm)	Potential benefits
SiO ₂	8.9 eV (138 nm) ^a	1.5 ^b	9 ^c	1×10^{18} d	High visible transparency, high hardness
ZnO	3.3 eV (375 nm) ^e	2.0 ^f	5 ^g	28 ^h	UV-protective effect
ITO	3.6 eV (345 nm) ⁱ	1.8 ^f	7 ^j	2×10^{-4} k	Transparent conducting oxide

^aSchneider and Fowler (1976), ^bMalitson (1965), ^cVila et al. (2003), ^dShackelford and Alexander (2001), ^eSrikant and Clarke (1998), ^fYang et al. (2006), ^gKucheyev et al. (2002), ^hNatsume and Sakata (2000), ⁱHamberg and Granqvist (1984), ^jZeng et al. (2003), ^kKim et al. (1999)

The dual requirements of superhydrophobicity and transparency pose a challenge. The surface must be sufficiently rough to obtain high CA and low CAH, but the dimensions of the roughness features must be small enough to preserve high transmittance of light. The size of surface features should not exceed roughly one quarter of the wavelength of visible light (around 100 nm or less) (Nakajima et al. 1999; Manca et al. 2009; Karunakaran et al. 2011; Ebert and Bhushan 2012b). The total coating thickness also should be less than one quarter of the wavelength of visible light.

Glass is the most common optical material for various applications, such as lenses, architectural windows, and electronic touch screens. Transparent polymers such as polycarbonate (PC) and poly(methyl methacrylate) (PMMA) also are used for wide-ranging applications, such as aircraft canopies, bullet-proof windows, solar cell panels, and many high-performance optical, electronic and medical devices.

SiO₂, ZnO, and ITO (Indium Tin Oxide) thin films are of interest for varying applications. Select properties and potential benefits of SiO₂, ZnO, and ITO are shown in Table 6.7 (Ebert and Bhushan 2012b). The three metal oxides have high transmittance for visible light due to low refractive indices (minimizing reflectance) and band gap wavelengths shorter than the visible range of 400–700 nm (minimizing visible-range absorption). SiO₂ in particular has extremely high visible transmittance. ZnO thin films can have a UV-protective effect, and have been shown to reduce photodegradation of PC (Moustaghfir, 2004). ZnO, when doped with other metals such as Al or Ga, can also be used for transparent conducting films (Noh et al. 2010; Park et al. 2010). ITO is the most commonly used material for transparent conducting films due to its combination of high visible transmittance and low electrical resistivity (Kim et al. 1999; Ederth et al. 2003; Cho et al. 2006). In addition, these particles have high hardness (Kucheyev et al. 2002; Vila et al. 2003; Zeng et al. 2003). Thus, SiO₂, ZnO, and ITO nanoparticles would seem to be suitable candidates for wear-resistant, transparent, superhydrophobic surfaces (Ebert and Bhushan 2012b).

Ebert and Bhushan (2012b) used a dip coating technique to deposit nanoparticle composite coatings on glass, PC, and PMMA substrates using SiO₂, ZnO, and ITO nanoparticles in a methylphenyl silicone resin. In order to achieve high transparency, micropatterned substrates as in a previous study were not used. The samples were characterized in terms of wettability (contact angle/contact angle hysteresis) and optical transmittance in the visible spectrum. Wear resistance experiments in sliding and using a waterjet were performed.

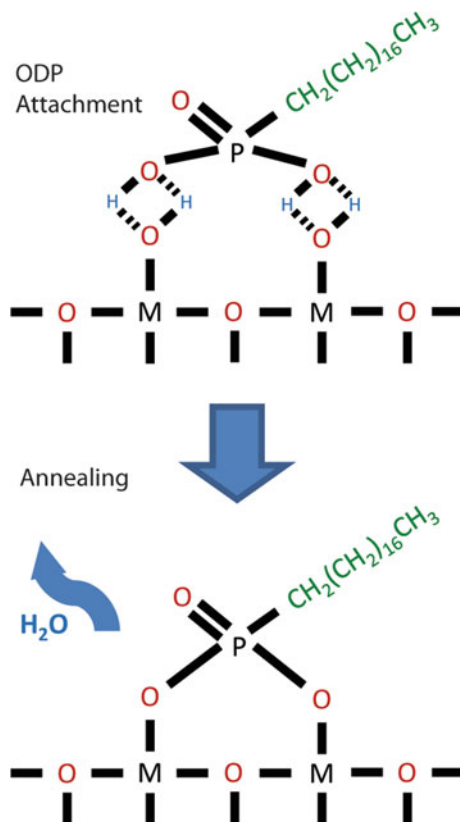
6.7.3.1 Experimental Details

Ebert and Bhushan (2012b) used soda-lime glass (2.2 mm thick), polycarbonate (Lexan, SABIC Innovative Plastics, 2.4 mm thick), and PMMA (Optix, Plaskolite Inc., 2 mm thick) to create 1 cm × 1 cm substrates. Silane-modified hydrophobic SiO₂ nanoparticles with average diameter of 55 nm (±15 nm) from Evonik Industries (AEROSIL RX 50), ZnO nanoparticles with average diameter of 70 nm (±30 nm) from Alfa Aesar (NanoTek Zinc Oxide), and ITO nanoparticles (90:10 In₂O₃:SnO₂) of average diameter 45 nm (±25 nm) from US Research Nanomaterials (US3855 Indium Tin Oxide Nanopowder) were used. Methylphenyl silicone resin was obtained from Momentive Performance Materials (SR355S Methylphenyl Silicone Resin), and was used as a binder.

The superhydrophobic SiO₂ particles obtained were already silane-modified. Conversely, the ZnO and ITO particles were not surface-modified as received. In order to hydrophobize them, they were treated in solution by octadecylphosphonic acid (ODP) (Aldrich). ODP can be used to functionalize metal oxides from hydrophilic to hydrophobic (Nishimoto et al. 2009). The process by which functionalization occurs is illustrated in Fig. 6.63 (Ebert and Bhushan 2012b). The exposed long-chain hydrocarbon tails of the ODP molecules result in a hydrophobic particle surface. Approximately 2 g of particles were added to a 100 mL ethanol solution with ODP concentration of 2 mM. The mixture was stirred vigorously for 10 min, covered, and left for 4 days at 20 °C. The solvent was then removed by evaporation, and the particles were heated at 100 °C for 1 h to improve ODP bonding and remove adsorbed water or remaining solvent.

Particles were dispersed in a 40 %/60 % tetrahydrofluorine/isopropyl alcohol (THF/IPA) (by volume) mixture to form the dip coating solution. Pure THF rapidly dissolves PC and PMMA, resulting in loss of transparency. However, if the THF concentration is low (about 5 % by volume in IPA), the visible loss can be minimized. Pure IPA unfortunately does not evaporate quickly enough to leave a homogeneous coating on the substrate. Optimal concentrations of nanoparticles in the solvent were found to be approximately 10 mg/mL for SiO₂ particles, 35 mg/mL for ZnO particles, and 50 mg/mL for ITO particles. Too low of a concentration resulted in loss of superhydrophobicity, while too high of a concentration resulted in visible agglomeration of particles on substrates, substantially reducing transparency. The nanoparticles were added to 30 mL of the THF/IPA solvent in a 100 mL glass beaker and sonicated for 4 min. Then, 150 mg of

Fig. 6.63 Schematic of hydrophobization of a generic metal oxide surface with octadecylphosphonic acid (ODP). The ODP molecule first attaches to the hydrolyzed surface via hydrogen bonds. After annealing, the ODP is strongly bonded to the metal oxide surface (Ebert and Bhushan 2012b)



methylphenyl silicone resin were added and the mixture was sonicated for an additional 4 min. In the case of silicone resin, a lower concentration resulted in poor adherence of the particles to the substrate, and a higher concentration resulted in the loss of superhydrophobicity. After sonication, approximately 10 mL of fresh solvent was added at 40 %/60 % THF/IPA ratio. Substrates were dipped into the solution and immediately removed at a speed of 10 cm/min. Coated samples were then heated at 40 °C for 10 min to remove any remaining solvent. The samples required no chemical post-treatment or modification after dip coating (Ebert and Bhushan 2012b).

6.7.3.2 Surface Roughness and Morphology

Table 6.8 presents RMS roughness, PV (peak-valley) distance, roughness factor (R_f), fractional area of liquid-area interface (f_{LA}), and coating thickness for samples with SiO_2 , ZnO, and ITO. Surfaces had nanoscale roughness formed by nanoparticles bound to the substrate with silicone resin (Ebert and Bhushan 2012b). The values of R_f and f_{LA} were calculated from AFM surface height maps (Burton and

Table 6.8 Measured roughness values (RMS and PV), coating thickness, and calculated R_f and liquid-air fractional area (f_{LA}) for samples with SiO₂, ZnO, and ITO particles (Ebert and Bhushan 2012b)

Particles on sample	RMS (nm)	PV (nm)	R_f	Coating thickness (nm)	f_{LA}
SiO ₂	58 ± 3	137 ± 5	1.5	150 ± 10	0.94
ZnO	84	191	1.8	205	0.94
ITO	45	127	1.3	135	0.91

Bhushan 2006; Ebert and Bhushan 2012b). By using the Z-height of each data point in the AFM scan matrix, the real surface area can be approximated using simple geometry. Dividing this value by the two-dimensional scan area gives R_f . Using SPIP imaging software (Image Metrology), f_{LA} was estimated. R_f and f_{LA} can be used to identify Wenzel or Cassie-Baxter wetting regimes. Coating thicknesses were measured with a Tencor[®] stylus profiler on the step formed by partially coating a substrate, and found to be nearly equal to PV distance.

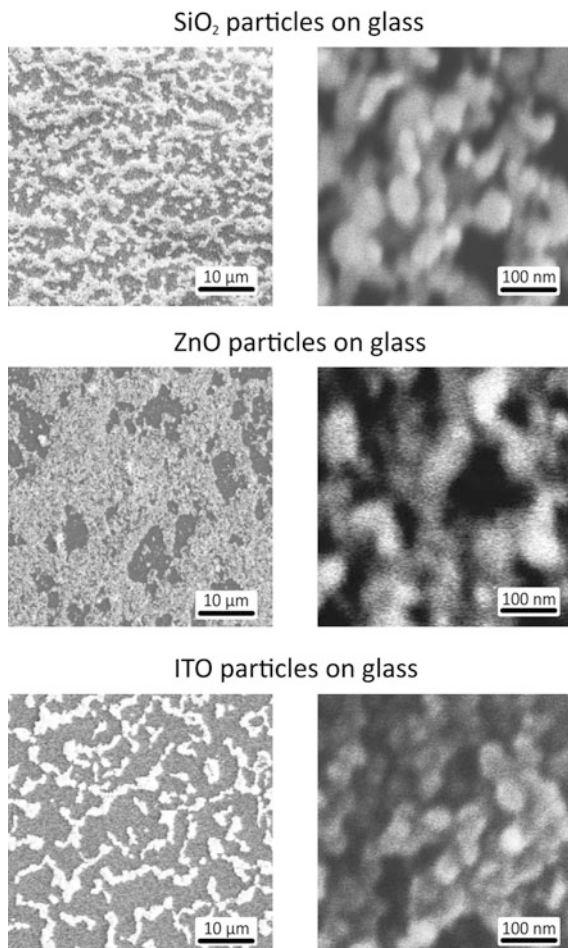
Figure 6.64 shows SEM micrographs of sample surfaces using each of the three nanoparticles on glass substrates at two magnifications (Ebert and Bhushan 2012b). At lower magnification, the particles can be seen to form islands with width on the order of a few microns. ZnO tended to cover more of the substrate, but less evenly and with larger pockets of uncoated area. ITO tended to coat the most evenly and with smallest islands. At higher magnification, individual nanoparticles can be seen forming roughness on the nanoscale, which suggests the particles are well-dispersed in solution. This multiscale roughness is desirable for superhydrophobicity.

6.7.3.3 Wettability

Contact angle and contact angle hysteresis for samples using three different nanoparticles (SiO₂, ZnO, ITO) on three different substrates (glass, PC, PMMA) are shown in Fig. 6.65 (Ebert and Bhushan 2012b). All samples exhibited superhydrophobic and self-cleaning behavior, with contact angles nearly 170° and contact angle hysteresis as low as 1° in some cases. For all three particles, contact angle was slightly higher on PC and PMMA substrates than on glass. Contact angle hysteresis was slightly higher on glass substrates, except in the case of ZnO where it was unchanged at 1°. For all substrates, the samples with ITO particles had lower contact angle and higher contact angle hysteresis than those with SiO₂ and ZnO, although self-cleaning conditions were still met (contact angle >150° and contact angle hysteresis <10°).

The f_{LA} values (shown in Table 6.8) were estimated to be 0.94, 0.94, and 0.91 for SiO₂, ZnO, and ITO samples, respectively. A lower value for ITO nanoparticles occurs because of the formation of more evenly distributed microscale islands with lower height distribution compared to SiO₂ and ZnO, possibly due in part to smaller primary particle size. The data suggests that all interfaces were in the Cassie-Baxter regime.

Fig. 6.64 SEM micrographs of SiO₂, ZnO, and ITO nanoparticle coatings on glass substrates at two magnifications each (Ebert and Bhushan 2012b)



6.7.3.4 Optical Transparency

The uncoated glass, PC, and PMMA substrates had visible-range transmittances of 92, 87, and 94 %, respectively. Transmittances of the samples are reported as percentages of the transmittance of the uncoated substrate. Figure 6.65 shows the transmittance data in the visible spectrum and Fig. 6.66 shows transmittance spectra for SiO₂, ZnO, and ITO nanoparticles on all substrates (Ebert and Bhushan 2012b). For all three particles, samples on PMMA had higher transmittance than those on PC, and PC samples had higher transmittance than those on glass, even with transmittances normalized by substrate transmittance. For all substrates, the samples with ITO particles had higher transmittance than those with silica particles, and SiO₂ samples had higher transmittance than those with ZnO. The lower transmittance of the ZnO samples likely is due to their significantly higher roughness values

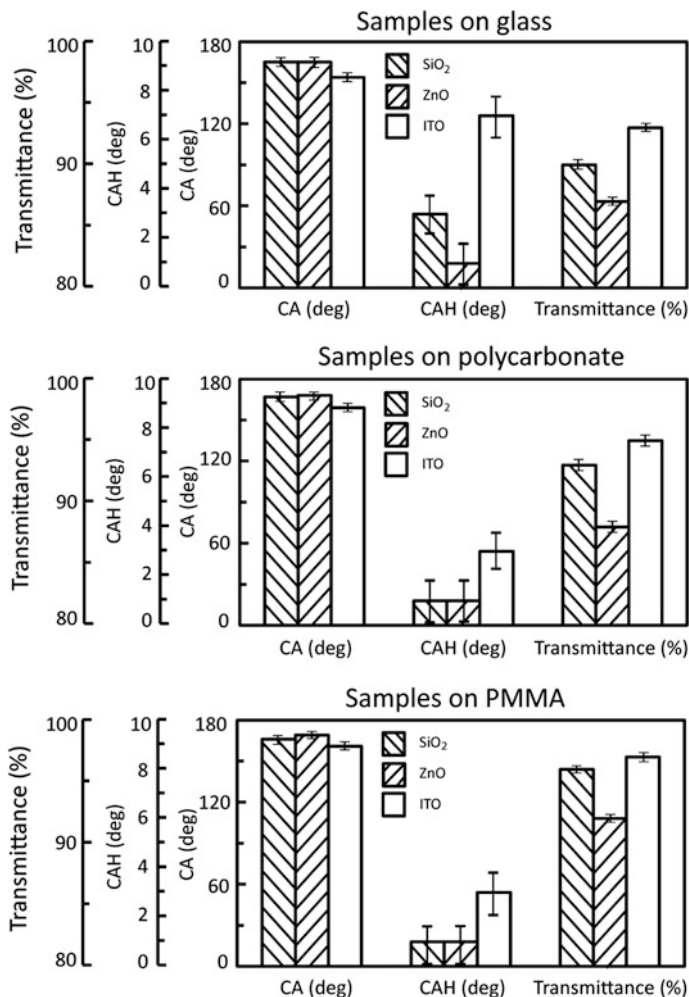
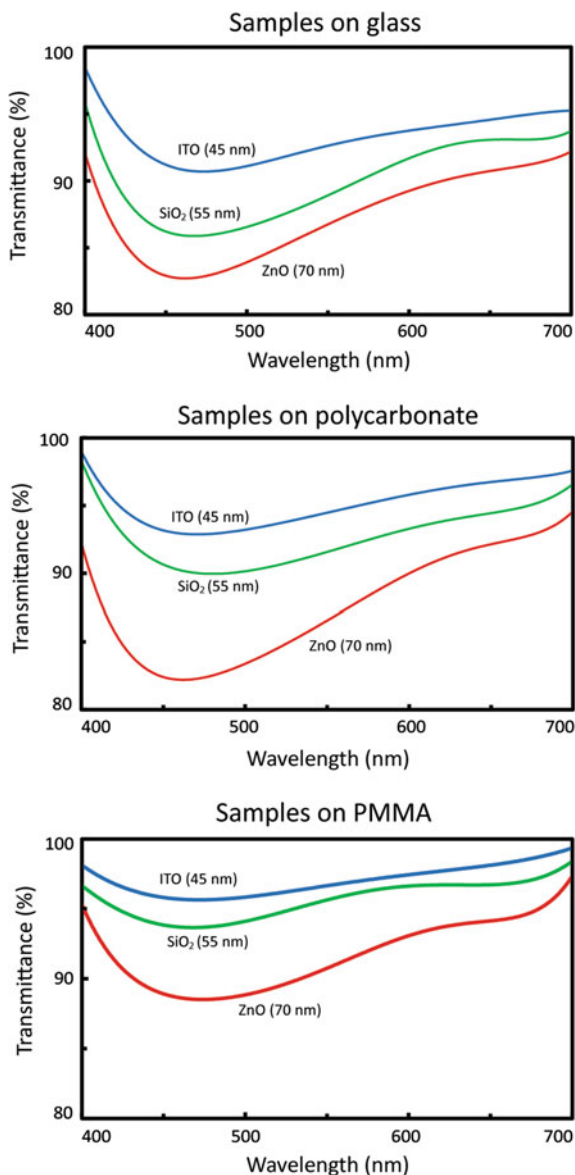


Fig. 6.65 Bar chart showing contact angle (CA), contact angle hysteresis (CAH), and visible transmittance for samples with SiO₂, ZnO, and ITO nanoparticles on glass, polycarbonate, and PMMA substrates. Error bars represent ±1 standard deviation (Ebert and Bhushan 2012b)

as compared to ITO and SiO₂. Conversely, the higher transmittance of the ITO samples likely is due to their lower roughness, comparatively. Despite somewhat less favorable values for band gap and refractive index, the ITO samples had higher transmittance than SiO₂ samples, which suggests that in this case, roughness and coating thickness, which was on the order of 100 nm, played a larger role in transmittance than did inherent optical properties of particles (Ebert and Bhushan 2012b).

Fig. 6.66 Transmittance spectra in the visible range for samples with SiO_2 , ZnO , and ITO nanoparticle coatings on glass, polycarbonate, and PMMA substrates. Data represent transmittance as a percentage of the transmittance of the uncoated substrate (Ebert and Bhushan 2012b)



ITO-coated glass, PC, and PMMA samples with deposited water droplets can be seen in Fig. 6.67, showing superhydrophobicity and high transmittance of the coatings (Ebert and Bhushan 2012b). Blue dye was added to water for visual clarity of droplets. Goniometer image of a droplet on ITO-coated glass is shown for better view of a superhydrophobic contact angle.

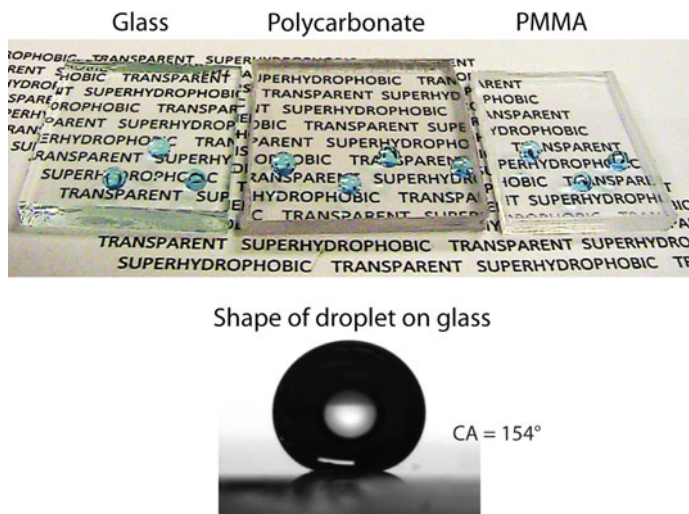


Fig. 6.67 Water droplets deposited on glass, polycarbonate, and PMMA with ITO nanoparticle coatings showing superhydrophobicity and high visible transmittance (*top*). Blue dye was added to water for visual clarity of droplets. Goniometer image of droplet is shown for glass substrate with ITO coating (*bottom*) (Ebert and Bhushan 2012b)

6.7.3.5 Wear Resistance of Samples in Sliding and Water Jet Experiments

The data from the AFM wear experiment for SiO_2 , ZnO, and ITO particles on glass, as well as silicone resin alone on glass, are shown in Fig. 6.68 (Ebert and Bhushan 2012b). Surface height maps before and after the wear experiment are displayed, as well as sample scans across the middle of the image (position indicated by arrow). Roughness values within the wear area (RMS and PV, before and after) are also displayed. Hardness of the silicone resin was measured with a microindenter (Micromet 3 Micro Hardness Tester) and found to be 1.3 GPa. The after-image of silicone resin alone reveals slight wear of the $50 \times 50 \mu\text{m}^2$ area worn by the borosilicate ball. The wear mode appears to be adhesive, as there is a fairly uniform removal of material (Bhushan 2013a, b). However, morphology was not significantly changed in the after-image for any of the three samples with nanoparticles, and RMS roughness and PV distance values remained similar. The minimal wear of the silicone resin and preservation of nearly identical roughness and surface morphology for samples indicates mechanical strength of the silicone resin, sufficient hardness of nanoparticles, and strong anchoring of particles in the silicone resin layer (Ebert and Bhushan 2012b).

The data from the water jet experiment is shown in Fig. 6.69 (Ebert and Bhushan 2012b). Samples were exposed to water jet for 20 min at each pressure ranging from 0 to 45 kPa. Contact angle and contact angle hysteresis data are displayed for silica nanoparticles as well as silicone resin alone on glass substrates. For the

Fig. 6.68 Surface height maps and sample surface profiles (locations indicated by *arrows*) before and after AFM wear experiment using 15 μm radius borosilicate ball at load of 10 μN for glass samples with silicone resin alone, SiO_2 nanoparticles, ZnO nanoparticles, and ITO nanoparticles. RMS roughness and PV distance values for surface profiles are displayed within surface *profile boxes*. Results shown are typical for all substrates (Ebert and Bhushan 2012b)

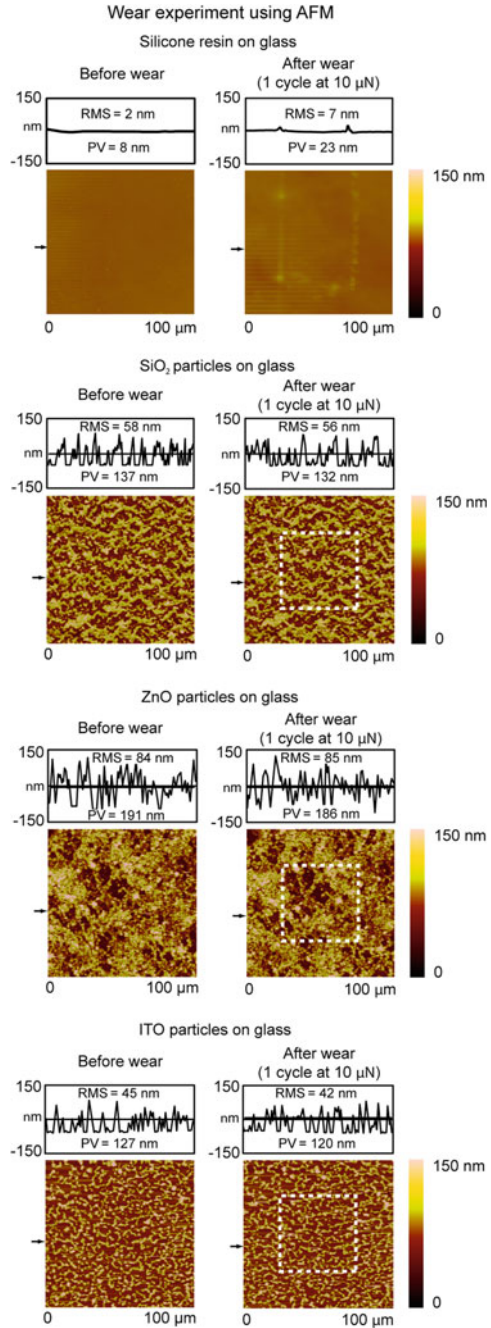
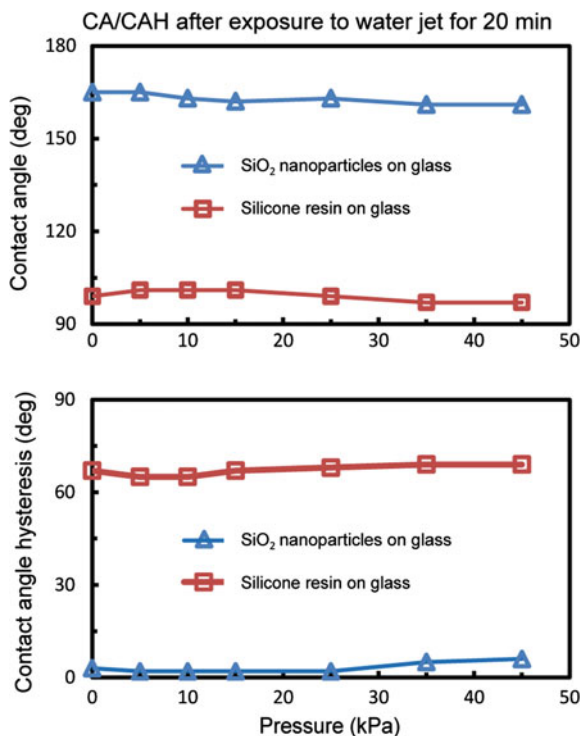


Fig. 6.69 Contact angle (CA) and contact angle hysteresis (CAH) as a function of water pressure after 20 min exposure time for samples with SiO₂ nanoparticles on glass and silicone resin alone on glass. Reproducibility is $\pm 1^\circ$ for CAH of SiO₂ nanoparticles, $\pm 2^\circ$ for CAH of silicone resin alone on glass, and $\pm 2^\circ$ for all CA data. Results shown are typical for all samples. CA $> 150^\circ$ and CAH $< 10^\circ$ were maintained in all cases (Ebert and Bhushan 2012b)



samples with SiO₂ nanoparticles, superhydrophobicity and self-cleaning properties were maintained, even at the highest pressure, with contact angle decreasing from 165° to 160°, and contact angle hysteresis increasing from 3° to 6°. At some intermediate pressures, contact angle hysteresis as low as 1° was measured. The wettability of the samples with silicone resin was likewise not significantly changed, with contact angle of 97° at 45 kPa compared to an initial value of 99°. Contact angle hysteresis for the silicone resin remained between 67° and 69° at all pressures. The results indicate wear resistance of the surfaces under impingement of water (Ebert and Bhushan 2012b).

6.7.3.6 Summary

To create transparent, superhydrophobic surfaces on glass and plastic substrates with SiO₂, ZnO, and ITO nanoparticles, Ebert and Bhushan (2012b) used a dip coating technique. ITO samples had slightly lower contact angle and slightly higher contact angle hysteresis than SiO₂, ZnO, which is likely the result of a comparatively lower liquid-air fractional area (f_{LA}). Roughness and coating thickness seemed to influence transmittance more than inherent optical properties of particles, which may be due to the proximity of roughness and thickness values to the 100 nm

threshold for visible transparency. Samples on PMMA substrates performed modestly better than those on PC and glass in terms of wettability and transmittance. However, all samples exhibited a superhydrophobic contact angle ($>150^\circ$), low contact angle hysteresis ($<10^\circ$), and high transmittance of visible light ($>90\%$ in most cases). In addition, all surfaces showed wear resistance in AFM wear and water jet experiments for potential commercial use.

6.8 Superhydrophobic Paper Surfaces

Paper with Superhydrophobic properties have been prepared by some investigators (Balu et al. 2008; Yang and Deng 2008; Obeso et al. 2013). A method proposed by Obeso et al. (2013) uses biodegradable materials for paper substrate. The method uses the precipitation of poly(hydroxybutyrate) (PHB) on the cellulose fibers of the paper using a phase separation process. Obeso et al. (2013) immersed the paper in chloroform for 6 h, to extract any possible additives soluble in the solvent. Then, the samples were immersed for 6 h in 7.5 % (w/v) solution of PHB in chloroform, followed by an immersion in a coagulation bath, formed by a mixture of 85/15 (v/v) of ethanol and water for 12 h. Finally, samples were dried at room temperature. The prepared surface exhibited a hierarchical structure with a contact angle of about 153° . They also reported that argon plasma treatment further increased the contact angle.

6.9 Closure

In this chapter, micro-, nano-, and hierarchically patterned structures were fabricated using soft lithography, photolithography, and techniques that involve the replication of micropatterns and self-assembly of hydrophobic alkanes and plant waxes. They have been characterized to validate the models and to provide design guidelines for superhydrophobic and self-cleaning surfaces. To further examine the effect of meniscus force and real area of contact, scale dependence is considered with the use of AFM tips of various radii. To investigate how the effects of spacing between pillars, droplet size, and impact velocity influence the transition, wetting, evaporation, and bouncing studies were conducted on silicon surfaces patterned with pillars of two different diameters and heights and with varying pitch values and deposited with a hydrophobic coating. In order to generate submicron droplets, an atomic force microscopy-based technique using a modified nanoscale dispensing probe was used. An ESEM study on the wetting behavior for a microdroplet with about $20\ \mu\text{m}$ radius on the micropatterned Si surfaces was carried out. Hierarchical structures using nature's route were fabricated to verify the understanding of the mechanisms relevant to superhydrophobicity and self-cleaning in the lotus leaf by comparing the superhydrophobicity and self-cleaning of fabricated surfaces and the lotus leaf.

For fabrication of mechanically durable surfaces, surfaces with carbon nanotubes and silica, zinc oxide, and indium tin oxide nanoparticles were fabricated. Superhydrophobicity, optical transparency, and wear resistance have been demonstrated. Finally, a method using biodegradable materials to produce a superhydrophobic paper is presented.

References

- Adamson A. V. (1990), *Physical Chemistry of Surfaces*, Wiley, New York.
- Balu, B., Breedveld, V., and Hess, D. W. (2008), "Fabrication of Roll-off and Sticky Superhydrophobic Cellulose Surfaces via Plasma Processing," *Langmuir* **24**, 4785-4790.
- Bartolo, D., Bouamrine, F., Verneuil, E., Buguin, A., Silberzan, P., and Moulinet, S. (2006), "Bouncing or Sticky Droplets: Impalement Transitions on Superhydrophobic Micropatterned Surfaces," *Europhys. Lett.* **74**, 299-305.
- Bhushan, B. (2003), "Adhesion and Stiction: Mechanisms, Measurement Techniques and Methods for Reduction," *J. Vac. Sci. Technol. B* **21**, 2262-2296.
- Bhushan, B. (2010), *Springer Handbook of Nanotechnology*, third ed., Springer, Heidelberg, Germany.
- Bhushan B. (2011) *Nanotribology and Nanomechanics I – Measurement Techniques, II – Nanotribology, Biomimetics, and Industrial Applications*, third ed., Springer-Verlag, Heidelberg, Germany.
- Bhushan, B. (2013a), *Principles and Applications of Tribology*, 2nd Ed., Wiley, New York.
- Bhushan, B. (2013b), *Introduction to Tribology*, 2nd Ed., Wiley, New York.
- Bhushan, B. and Blackman, G. S. (1991), "Atomic Force Microscopy of Magnetic Rigid Disks and Sliders and Its Applications to Tribology," *ASME J. Tribol.* **113**, 452-457.
- Bhushan, B. and Gupta, B. K. (1991), *Handbook of Tribology: Materials, Coatings, and Surface Treatments*, McGraw-Hill, New York.
- Bhushan, B. and Jung, Y. C. (2006), "Micro and Nanoscale Characterization of Hydrophobic and Hydrophilic Leaf Surface," *Nanotechnology* **17**, 2758-2772.
- Bhushan, B. and Jung, Y. C. (2007), "Wetting Study of Patterned Surfaces for Superhydrophobicity," *Ultramicroscopy* **107**, 1033-1041.
- Bhushan, B. and Jung, Y. C. (2008), "Wetting, Adhesion and Friction of Superhydrophobic and Hydrophilic Leaves and Fabricated Micro/nanopatterned Surfaces," *J. Phys.: Condens. Matter* **20**, 225010.
- Bhushan, B. and Jung, Y. C. (2011), "Natural and Biomimetic Artificial Surfaces for Superhydrophobicity, Self-Cleaning, Low Adhesion, and Drag Reduction," *Prog. Mater. Sci.* **56**, 1-108.
- Bhushan, B., Hansford, D., and Lee, K. K. (2006), "Surface Modification of Silicon and Polydimethylsiloxane Surfaces with Vapor-Phase-Deposited Ultrathin Fluorosilane Films for Biomedical Nanodevices," *J. Vac. Sci. Technol. A* **24**, 1197-1202.
- Bhushan, B., Nosonovsky M., and Jung, Y. C. (2007), "Towards Optimization of Patterned Superhydrophobic Surfaces" *J. R. Soc. Interf.* **4**, 643-648.
- Bhushan, B., Koch, K., and Jung, Y. C. (2008a), "Nanostructures for Superhydrophobicity and Low Adhesion," *Soft Matter* **4**, 1799-1804.
- Bhushan, B., Koch, K., and Jung, Y. C. (2008b), "Biomimetic Hierarchical Structure for Self-Cleaning," *Appl. Phys. Lett.* **93**, 093101.
- Bhushan, B., Jung, Y. C., and Koch, K. (2009a), "Self-Cleaning Efficiency of Artificial Superhydrophobic Surfaces," *Langmuir* **25**, 3240-3248.

- Bhushan, B., Jung, Y. C., and Koch, K. (2009b), "Micro-, Nano- and Hierarchical Structures for Superhydrophobicity, Self-Cleaning and Low Adhesion," *Phil. Trans. R. Soc. A* **367**, 1631-1672
- Bhushan, B., Jung, Y. C., Niemietz, A., and Koch, K. (2009c), "Lotus-like Biomimetic Hierarchical Structures Developed by the Self-assembly of Tubular Plant Waxes," *Langmuir* **25**, 1659-1666.
- Bhushan, B., Koch, K., and Jung, Y. C. (2009d), "Fabrication and Characterization of the Hierarchical Structure for Superhydrophobicity," *Ultramicroscopy* **109**, 1029-1034.
- Bhushan, B., Jung, Y.C., and Nosonovsky, M. (2012), "Hierarchical Structures for Superhydrophobic Surfaces and Methods of Making," U.S. Patent No. 8,137,751 B2, March 20.
- Bormashenko, E., Pogreb, R., Whyman, G., and Erlich, M. (2007), "Cassie-Wenzel Wetting Transition in Vibrated Drops Deposited on the Rough Surfaces: Is Dynamic Cassie-Wenzel Transition 2D or 1D Affair?" *Langmuir* **23**, 6501-6503.
- Bourges-Monnier, C. and Shanahan, M. E. R. (1995), "Influence of Evaporation on Contact Angle," *Langmuir* **11**, 2820-2829.
- Bru gnara, M., Della Volpe, C., Siboni, S., and Zeni, D, (2006), "Contact Angle Analysis on Polymethylmethacrylate and Commercial Wax by Using an Environmental Scanning Electron Microscope," *Scanning* **28**, 267-273.
- Bunshah, R. F. (1994), *Handbook of Deposition Technologies for Films and Coatings: Science, Technology and Applications*, Applied Science Publishers, Westwood, New Jersey.
- Burton, Z. and Bhushan, B. (2005), "Hydrophobicity, Adhesion, and Friction Properties of Nanopatterned Polymers and Scale Dependence for Micro- and Nanoelectromechanical Systems," *Nano Lett.* **5**, 1607-1613.
- Burton, Z. and Bhushan, B. (2006), "Surface Characterization and Adhesion and Friction Properties of Hydrophobic Leaf Surfaces," *Ultramicroscopy* **106**, 709-719.
- Callister, W. D. (2000), *Materials Science and Engineering – An Introduction*, fifth ed., John Wiley and Sons, New York.
- Celestini, F. and Kofman, R. (2006), "Vibration of Submillimeter-size Supported Droplets," *Phys. Rev. E* **73**, 041602.
- Checco, A., Guenoun, P., and Daillant, J. (2003), "Nonlinear Dependence of the Contact Angle of Nanodroplets on Contact Line Curvatures," *Phys. Rev. Lett.* **91**, 186101.
- Chen, N. and Bhushan, B. (2006), "Atomic Force Microscopy Studies of Conditioner Thickness Distribution and Binding Interactions on the Hair Surface," *J. Microsc.* **221**, 203-215.
- Chen, Y. L., Helm, C. A., and Israelachvili, J. N. (1991), "Molecular Mechanisms Associated with Adhesion and Contact Angle Hysteresis of Monolayer Surfaces," *J. Phys. Chem.* **95**, 10736-10747.
- Chen, X. H., Chen, C. S., Xiao, H. N., Liu, H. B., Zhou, L. P., Li, S. L., and Zhang, G. (2006), "Dry Friction and Wear Characteristics of Nickel/Carbon Nanotube Electroless Composite Deposits," *Tribol. Int.* **39**, 22-28
- Cho, Y.-S., Yi, G.-R., Hong, J.-J., Jang, S. H., and Yang, S.-M. (2006), "Colloidal Indium Tin Oxide Nanoparticles for Transparent and Conductive Films," *Thin Solid Films* **515**, 1864-1871.
- Choi, S. E., Yoo, P. J., Baek, S. J., Kim, T. W., and Lee, H. H. (2004), "An ultraviolet-curable mold for sub-100-nm lithography," *J. Am. Chem. Soc.* **126**, 7744-7745.
- Danilatos, G. D. and Brancik, J. V. (1986), "Observation of Liquid Transport in the ESEM," Proc. 44th Annual Meeting EMSA, 678-679
- Dorset, D. L., Pangborn, W. A., and Hancock, A. J., (1983), "Epitaxial Crystallization of Alkane Chain Lipids for Electron Diffraction Analysis," *J. Biochem. Biophys. Meth.* **8**, 29-40.
- Dresselhaus, M. S., Dresselhaus, G., and Avouris, Ph., (2000), *Carbon Nanotubes: Synthesis, Structure, Properties, and Applications*, Springer, Heidelberg, Germany.
- Ebert, D. and Bhushan, B. (2012a), "Durable Lotus-Effect Surfaces with Hierarchical Structure Using Micro- and Nanosized Hydrophobic Silica Particles," *J. Colloid Interf. Sci.* **368**, 584-591.

- Ebert, D. and Bhushan, B. (2012b), "Transparent, Superhydrophobic, and Wear-Resistant Coatings on Glass and Polymer Substrates Using SiO₂, ZnO, and ITO Nanoparticles," *Langmuir* **28**, 11391-11399.
- Ederth J., Heszler P., Hultåker A., Niklasson G. A., and Granqvist C. G., (2003), "Indium Tin Oxide Films Made from Nanoparticles: Models for the Optical and Electrical Properties," *Thin Solid Films* **445**, 199-206.
- Englert B. C., Xiu Y., and Wong C. P. (2006), "Deposition and Surface Treatment of Microparticles to Produce Lotus-Effect Surface," *11th International Symposium on Advanced Packaging Materials: Processes, Properties and Interfaces*, March 15-17, Atlanta, GA, 73-78
- Erbil, H. Y., McHale, G., and Newton, M. I. (2002), "Drop Evaporation on Solid Surfaces: Constant Contact Angle Mode," *Langmuir* **18**, 2636-2641.
- Erbil, H. Y., Demirel, A. L., and Avci, Y. (2003), "Transformation of a Simple Plastic into a Superhydrophobic Surface," *Science* **299**, 1377-1380.
- Good, R. J. (1952), "A Thermodynamic Derivation of Wenzel's Modification of Young's Equation for Contact Angles; Together with a Theory of Hysteresis," *J. Am. Chem. Soc.* **74**, 5041-5042.
- Hamberg I. and Granqvist C. G. (1984), "Band-gap Widening in Heavily Sn-doped In₂O₃," *Phys. Rev. B* **30**, 3240-3249.
- Hong, Y. C. and Uhm, H. S. (2006), "Superhydrophobicity of a Material Made From Multiwalled Carbon Nanotubes," *Appl. Phys. Lett.* **88**, 244101.
- Huang, L., Lau, S. P., Yang, H. Y., Leong, E. S. P., and Yu, S. F. (2005), "Stable Superhydrophobic Surface via Carbon Nanotubes Coated with a ZnO Thin Film," *J. Phys. Chem.* **109**, 7746-7748.
- Israelachvili, J. N. (1992), *Intermolecular and Surface Forces*, second edition, Academic Press, London.
- Joanny, J. F. and de Gennes, P. G. (1984), "A Model for Contact Angle Hysteresis," *J. Chem. Phys.* **81**, 552-562.
- Johnson, R. E. and Dettre, R. H. (1964), "Contact Angle Hysteresis," *Contact Angle, Wettability, and Adhesion, Adv. Chem. Ser.*, Vol. 43, Ed. F. M. Fowkes, pp. 112-135 American Chemical Society, Washington, D. C.
- Jung, Y. C. and Bhushan, B. (2006), "Contact Angle, Adhesion, and Friction Properties of Micro- and Nanopatterned Polymers for Superhydrophobicity," *Nanotechnology* **17**, 4970-4980.
- Jung, Y. C. and Bhushan, B. (2007), "Wetting Transition of Water Droplets on Superhydrophobic Patterned Surfaces," *Scripta Mater.* **57**, 1057-1060.
- Jung, Y. C. and Bhushan, B. (2008a), "Wetting Behavior During Evaporation and Condensation of Water Microdroplets on Superhydrophobic Patterned Surfaces" *J. Micros.* **229**, 127-140.
- Jung, Y. C. and Bhushan, B. (2008b), "Dynamic Effects of Bouncing Water Droplets on Superhydrophobic Surfaces," *Langmuir* **24**, 6262-6269.
- Jung, Y. C. and Bhushan, B. (2008c), "Technique to Measure Contact Angle of Micro/Nanodroplets using Atomic Force Microscopy," *J. Vac. Sci. Technol. A* **26**, 777-782.
- Jung, Y. C. and Bhushan, B. (2009a), "Dynamic Effects Induced Transition of Droplets on Biomimetic Superhydrophobic Surfaces," *Langmuir* **25**, 9208-9218.
- Jung, Y. C. and Bhushan, B. (2009c), "Mechanically Durable CNT-Composite Hierarchical Structures with Superhydrophobicity, Self-Cleaning, and Low-Drag," *ACS Nano* **3**, 4155-4163.
- Jung, Y. C. and Bhushan, B. (2010), "Biomimetic Structures for Fluid Drag Reduction in Laminar and Turbulent Flows," *J. Phys.: Condens. Matter* **22**, 035104.
- Karunakaran R. G., Lu C.-H., Zhang Z., and Yang S. (2011), "Highly Transparent Superhydrophobic Surfaces from the Coassembly of Nanoparticles (≤ 100 nm)," *Langmuir* **27**, 4594-4602.
- Kasai, T., Bhushan, B., Kulik, G., Barbieri, L., and Hoffmann, P. (2005), "Micro/Nanotribological Study of Perfluorosilane SAMs for Antistiction and Low Wear," *J. Vac. Sci. Technol. B* **23**, 995-1003.

- Kim, H., Gilmore, C. M., Pique, A., Horowitz, J. S., Mattoussi, H., Murata, H., Kafafi, Z. H., and Chrisey, D. B. (1999), "Electrical, Optical, and Structural Properties of Indium-Tin-Oxide Thin Films for Organic Light Emitting Devices," *J. Appl. Phys.* **86**, 6451-6461.
- Koch, K., Dommissé, A., and Barthlott, W. (2006a), "Chemistry and Crystal Growth of Plant Wax Tubules of Lotus (*Nelumbo nucifera*) and Nasturtium (*Tropaeolum majus*) Leaves on Technical Substrates," *Crystl. Growth Des.* **6**, 2571-2578.
- Koch, K., Barthlott, W., Koch, S., Hommes, A., Wandelt, K., Mamdouh, W., De-Feyer, S. and Broekmann, P. (2006b), "Structural Analysis of Wheat Wax (*Triticum aestivum*, c.v. 'Naturastar' L.): from the Molecular Level to Three Dimensional Crystals," *Planta* **223**, 258-270.
- Koch, K., Dommissé, A., Barthlott, W., and Gorb, S. (2007), "The Use of Plant Waxes as Templates for Micro- and Nanopatterning of Surfaces," *Acta Biomat.* **3**, 905-909.
- Koch, K., Schulte, A. J., Fischer, A., Gorb, S. N., and Barthlott, W. (2008), "A Fast and Low-cost Replication Technique for Nano- and High-Aspect-Ratio Structures of Biological and Artificial Materials," *Bioinsp. Biomim.* **3**, 046002.
- Koch, K., Bhushan, B., Jung, Y. C., and Barthlott, W. (2009), "Fabrication of Artificial Lotus Leaves and Significance of Hierarchical Structure for Superhydrophobicity and Low Adhesion," *Soft Matter* **5**, 1386-1393.
- Kucheyev, S. O., Bradby, J. E., Williams, J. S., and Jagadish, C. (2002), "Mechanical Deformation of Single-crystal ZnO," *J. Appl. Phys.* **80**, 956-958.
- Lafuma, A. and Quéré, D. (2003), "Superhydrophobic States," *Nature Materials* **2**, 457-460.
- Lamb, H. (1932), *Hydrodynamics*, Cambridge University Press, Cambridge, England.
- Lau, K. K. S., Bico, J., Teo, K. B. K., Chhowalla, M., Amaratunga, G. A. J., Milne, W. I., McKinley, G. H., and Gleason, K. K. (2003), "Superhydrophobic Carbon Nanotube Forests," *Nano Lett.* **3**, 1701-1705.
- Lee, S. -W. and Laibinis, P. E. (2000), "Directed Movement of Liquids on Patterned Surfaces Using Noncovalent Molecular Adsorption," *J. Am. Chem. Soc.* **122**, 5395-5396.
- Liu Y., Chen X., and Xin J. H. (2006), "Super-Hydrophobic Surfaces from a Simple Coating Method: A Bionic Nanoengineering Approach," *Nanotechnology* **17**, 3259-3263.
- Lodge, R. A. and Bhushan, B. (2006), "Surface Characterization of Human Hair using Tapping Mode Atomic Force Microscopy and Measurement of Conditioner Thickness Distribution," *J. Vac. Sci. Technol. A* **24**, 1258-1269.
- Malitson, H. (1965), "Interspecimen Comparison of the Refractive Index of Fused Silica," *J. Opt. Soc. America* **55**, 1205-1209.
- Manca M., Cannavale A., De Marco L., Aricò A. S., Cingolani R., and Gigli G. (2009), "Durable Superhydrophobic and Antireflective Surfaces by Trimethylsilanized Silica Nanoparticles-Based Sol-Gel Processing," *Langmuir* **25**, 6357-6362.
- McHale, G., Aqil, S., Shirtcliffe, N. J., Newton, M. I., and Erbil, H. Y. (2005), "Analysis of Droplet Evaporation on a Superhydrophobic Surface," *Langmuir* **21**, 11053-11060.
- Meyyappan, M. (2005), *Carbon Nanotubes – Science and Applications*, CRC Press, Boca Raton, FL.
- Ming, W., Wu, D., van Benthem, R., and de With, G. (2005), "Superhydrophobic Films from Raspberry-Like Particles," *Nano Lett.* **5**, 2298-2301.
- Moustaghfir A., Tomasella E., Rivaton A., Mailhot B., Jacquet M., Gardette J. L., and Cellier J. (2004), "Sputtered Zinc Oxide Coatings: Structural Study and Application to the Photoreception of the Polycarbonate," *Surf. Coatings Technol.* **180-181**, 642-645.
- Nakajima, A., Fujishima, A., Hashimoto, K., and Watanabe, T. (1999), "Preparation of Transparent Superhydrophobic Boehmite and Silica Films by Sublimation of Aluminum Acetylacetonate," *Adv. Mater.* **11**, 1365-1368.
- Natsume Y. and Sakata H. (2000), "Zinc Oxide Films Prepared by Sol-gel Spin-coating," *Thin Solid Films* **372**, 30-36.
- Neinhuis, C., and Barthlott, W. (1997), "Characterization and Distribution of Water-Repellent, Self-Cleaning Plant Surfaces," *Annals of Botany* **79**, 667-677.

- Niemietz, A., Wandelt, K., Barthlott, W., and Koch, K. (2009), "Thermal Evaporation of Multi-Component Waxes and Thermally Activated Formation of Nano-Tubules for Superhydrophobic Surfaces," *Prog. Org. Coat.* **66**, 221-227.
- Nishimoto S., Kubo A., Nohara K., Zhang X., Taneichi N., Okui T., Liu Z., Nakata K., Sakai H., Murakami T., Abe M., Komine T., and Fujishima A. (2009), "TiO₂-based Superhydrophobic-Superhydrophilic Patterns: Fabrication via an Ink-jet Technique and Application in Offset Printing," *Appl. Surf. Sci.* **255**, 6221-6225.
- Noblin, X., Buguin, A., and Brochard-Wyart, F. (2004), "Vibrated Sessile Drops: Transition between Pinned and Mobile Contact Line Oscillations," *Eur. Phys. J. E* **14**, 395-404.
- Noh J. H., Han H. S., Lee S., Kim D. H., Park J. H., Park S., Kim J. Y., Jung H. S., and Hong K. S. (2010), "A Newly Designed Nb-Doped TiO₂/Al-Doped ZnO Transparent Conducting Oxide Multilayer for Electrochemical Photoenergy Conversion Devices," *J. Phys. Chem. C* **114**, 13867-13871.
- Nosonovsky, M. and Bhushan, B. (2005), "Roughness Optimization for Biomimetic Superhydrophobic Surfaces," *Microsyst. Technol.* **11**, 535-549.
- Nosonovsky, M. and Bhushan, B. (2007a), "Multiscale Friction Mechanisms and Hierarchical Surfaces in Nano- and Bio-Tribology," *Mater. Sci. Eng.:R* **58**, 162-193.
- Nosonovsky, M. and Bhushan, B. (2007b), "Hierarchical Roughness Makes Superhydrophobic Surfaces Stable," *Microelectronic Eng.* **84**, 382-386.
- Nosonovsky, M. and Bhushan, B. (2007c), "Biomimetic Superhydrophobic Surfaces: Multiscale Approach," *Nano Lett.* **7**, 2633-2637.
- Nosonovsky, M. and Bhushan, B. (2007d), "Hierarchical Roughness Optimization for Biomimetic Superhydrophobic Surfaces," *Ultramicroscopy* **107**, 969-979.
- Nosonovsky, M. and Bhushan, B. (2008a), *Multiscale Dissipative Mechanisms and Hierarchical Surfaces: Friction, Superhydrophobicity, and Biomimetics*, Springer-Verlag, Heidelberg, Germany.
- Nosonovsky, M. and Bhushan, B. (2008b), "Roughness-Induced Superhydrophobicity: A Way to Design Non-Adhesive Surfaces," *J. Phys.: Condens. Matter* **20**, 225009.
- Nosonovsky, M. and Bhushan, B. (2008c), "Patterned Non-Adhesive Surfaces: Superhydrophobicity and Wetting Regime Transitions," *Langmuir* **24**, 1525-1533.
- Nosonovsky, M. and Bhushan, B. (2008d), "Capillary Effects and Instabilities in Nanocontacts," *Ultramicroscopy* **108**, 1181-1185.
- Nosonovsky, M. and Bhushan, B. (2008e), "Energy Transitions in Superhydrophobicity: Low Adhesion, Easy Flow and Bouncing," *J. Phys.: Condens. Matter* **20**, 395005.
- Obeso, C. G., Sousa, M. P., Song, W., Rodriguez-Perez, M. A., Bhushan, B., and Mano, J. F. (2013), "Modification of Paper Using Polyhydroxybutyrate to Obtain Biomimetic Superhydrophobic Substrates," *Coll. Surf. A: Physicochem. Eng. Aspects* **416**, 51-55.
- Palacio, M. and Bhushan, B. (2010), "Normal and Lateral Force Calibration Techniques for AFM Cantilevers," *Crit. Rev. Solid State Mater. Sci.* **35**, 73-104.
- Park T.-Y., Choi Y.-S., Kang J.-W., Jeong J.-H., Park S.-J., Jeon D. M., Kim J. W., and Kim Y. C. (2010), "Enhanced Optical Power and Low Forward Voltage of GaN-based Light-Emitting Diodes with Ga-doped ZnO Transparent Conducting Layer," *Appl. Phys. Lett.* **96**, 051124.
- Pompe, T. and Herminghaus, S. (2000), "Three-Phase Contact Line Energetics from Nanoscale Liquid Surface Topographies," *Phys. Rev. Lett.* **85**, 1930-1933.
- Quere, D. (2004), "Surface Wetting Model Droplets," *Nature Materials* **3**, 79-80.
- Reyssat, M., Pepin, A., Marty, F., Chen, Y., and Quere, D. (2006), "Bouncing Transitions on Microtextured Materials," *Europhys. Lett.* **74**, 306-312.
- Richard, D., Clanet, C., and Quere, D. (2002), "Contact Time of a Bouncing Drop," *Nature* **417**, 811.
- Rowan, S. M., Newton, M. I., and McHale, G. (1995), "Evaporation of Microdroplets and the Wetting of Solid Surfaces," *J. Phys. Chem.* **99**, 13268-13271.
- Schneider P. M. and Fowler W. B. (1976), "Band Structure and Optical Properties of Silicon Dioxide," *Phys. Rev. Lett.* **36**, 425-428.
- Semal, S., Blake, T. D., Geskin, V., de Ruijter, M. L., Castelein, G., and De Coninck, J. (1999), "Influence of Surface Roughness on Wetting Dynamics," *Langmuir* **15**, 8765-8770.

- Shackelford J. and Alexander W. (2001), *CRC Materials Science and Engineering Handbook*, 3rd ed., CRC Press, Boca Raton, FL p. 1716.
- Shibuichi, S., Onda, T., Satoh, N., and Tsujii, K. (1996), "Super-Water-Repellent Surfaces Resulting from Fractal Structure," *J. Phys. Chem.* **100**, 19512-19517.
- Srikant V. and Clarke D. (1998), "On the Optical Band Gap of Zinc Oxide," *J. Appl. Phys.* **83**, 5447-5451.
- Stelmashenko, N. A., Craven, J. P., Donald, A. M., Terentjev, E. M., and Thiel, B. L. (2001), "Topographic Contrast Of Partially Wetting Water Droplets in Environmental Scanning Electron Microscopy," *J. Micros.* **204**, 172-183.
- van Dijk, A. I. J. M., Bruijnzeel, L. A. and Rosewell, C. J. (2002), "Rainfall Intensity–Kinetic Energy Relationships: A Critical Literature Appraisal," *J. Hydrology* **261**, 1-23.
- Vila M., Cáceres D., and Prieto C. (2003), "Mechanical Properties of Sputtered Silicon Nitride Thin Films," *J Appl. Phys.* **94**, 7868-7873.
- Wong, E. W., Sheehan, P. E., and Lieber, C. M. (1997), "Nanobeam Mechanics: Elasticity, Strength, and Toughness of Nanorods and Nanotubes," *Science* **277**, 1971-1975.
- Yang, H. and Deng, Y. (2008), "Preparation and Physical Properties of Superhydrophobic Papers," *J. Colloid Interf. Sci.*, **325**, 588-593.
- Yang Y., Sun X. W., Chen B. J., Xu C. X., Chen T. P., Sun C. Q., Tay B. K., and Sun Z. (2006), "Refractive Indices of Textured Indium Tin Oxide and Zinc Oxide Thin Films," *Thin Solid Films* **510**, 95-101.
- Yost, F. G., Michael, J. R., and Eisenmann, E. T. (1995), "Extensive Wetting Due to Roughness," *Acta Metall. Mater.* **45**, 299-305.
- Zeng K., Zhu F., Hu J., Shen L., Zhang K., and Gong H. (2003), "Investigation of Mechanical Properties of Transparent Conducting Oxide Thin Films," *Thin Solid Films* **443**, 60-65.
- Zhang, X., Tan, S., Zhao, N., Guo, X., Zhang, X., Zhang, Y., and Xu, J. (2006), "Evaporation of Sessile Water Droplets on Superhydrophobic Natural Lotus and Biomimetic Polymer Surfaces," *Chem. Phys. Chem.* **7**, 2067-2070.
- Zhang, Y. Y., Wang, C. M., and Tan, V. B. C. (2008), "Examining the Effects of Wall Numbers on Buckling Behavior and Mechanical Properties of Multiwalled Carbon Nanotubes via Molecular Dynamics Simulations," *J. Appl. Phys.* **103**, 053505.
- Zhu, L., Xiu, Y., Xu, J., Tamirisa, P. A., Hess, D. W., and Wong C. (2005), "Superhydrophobicity on Two-Tier Rough Surfaces Fabricated by Controlled Growth of Aligned Carbon Nanotube Arrays Coated with Fluorocarbon," *Langmuir* **21**, 11208-11212.

Chapter 7

Fabrication and Characterization of Micropatterned Structures Inspired by *Salvinia molesta*

7.1 Introduction

The floating water ferns of genus *Salvinia* are of interest because of their ability to trap and hold an air film under water for up to several months (Koch et al. 2009). The ability to retain air prevents wetting and submersion. Specifically, *Salvinia molesta* has been studied because of its complex structured surface. It is an aquatic fern commonly known as giant Salvinia and is native to south-eastern Brazil. *S. molesta* is a free-floating plant that does not require soil and consists of leaves that are roughly 0.5–4 cm wide and long.

A mechanism for long-term air-retention for the floating water fern *S. molesta* has been suggested by Barthlott et al. (2010) and Hunt and Bhushan (2011). The hierarchical nature of the *S. molesta* leaf is predominantly composed of tiny eggbeater-shaped hairs, shown in Fig. 7.1. These are almost completely hydrophobic due to a coating of nanoscopic wax crystals, except for the terminal cells of each hair that lack the crystals, thus making them hydrophilic (Hunt and Bhushan 2011). These hydrophilic patches are located at the top of each hair where the individual follicles forming the egg beater shape are joined together. Due to the hydrophilic patches at the tip of each hair, *S. molesta* exhibits a pinning effect of water against the top of the hairs enabling the formation of air pockets between each hair, as shown in Fig. 7.2 (Hunt and Bhushan 2011). The combination of hydrophilic patches coupled with an inner hydrophobic coating of the *S. molesta* hairs, and the subsequent ability of *S. molesta* to pin water and retain air when submerged underwater, is referred to as the “Salvinia Effect.”

Air-retaining surfaces are of technological interest due to their ability to reduce drag when used for fluid transport, ship coatings, and other submersible industrial products in which drag is a concern. Superhydrophobic surfaces have been used to obtain the desired air film for the previously stated applications. However, the air film is shown to deteriorate in a matter of minutes (Balasubramanian et al. 2004;

Fig. 7.1 Optical micrograph of *S. molesta* leaf (Hunt and Bhushan 2011)

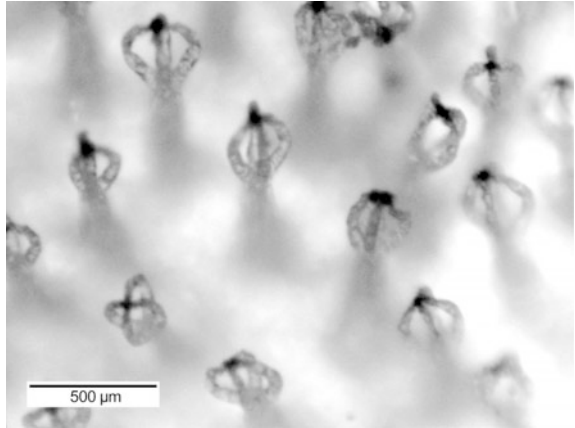
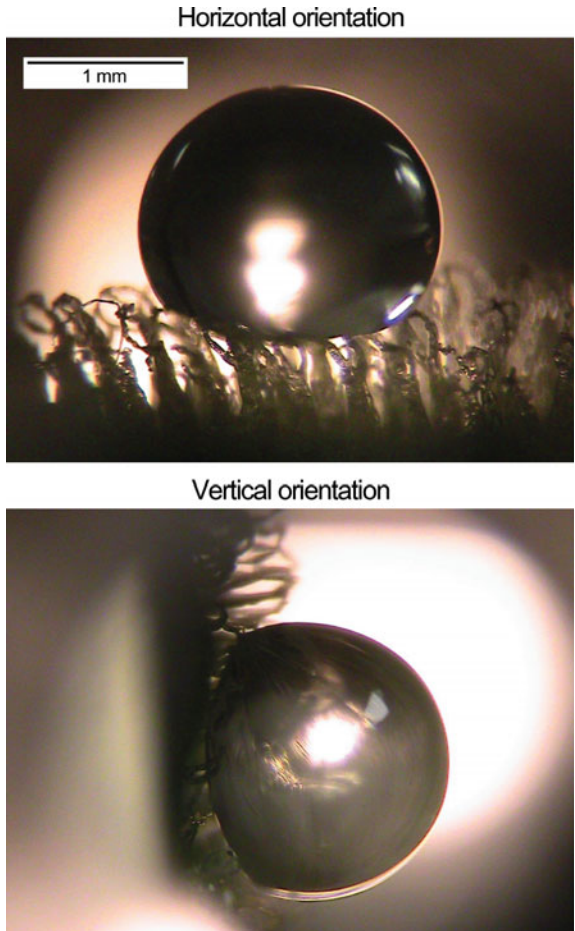


Fig. 7.2 Water droplet suspended by *S. molesta* hair at horizontal and vertical orientations demonstrating air pocket formation and water pinning at the hydrophilic tips, where the terminal cells of each *S. molesta* hair is located (Hunt and Bhushan 2011)



Choi and Kim 2006; Henocho et al. 2006; Lee and Kim 2009). Therefore, *S. molesta*'s unique ability to pin water and trap air is of importance in order to increase the durability and lifetime of air pocket formation for drag reduction in industrial use.

Hunt and Bhushan (2011) mimicked the air trapping ability of *S. molesta* to prove that a structure can be created in the lab that can mimic the behavior of the fern, as well as demonstrate microfabrication techniques that can be utilized in industry to produce such materials. To accomplish this, they created a micropattern in the lab with comparable dimensions to the *S. molesta* hairs. The micropattern was then treated with a hydrophobic coating which is then stripped away to produce a new microstructure which is hydrophobic everywhere except for the tips of the micropattern, in the same manner as the *S. molesta* hairs themselves. The new micropattern was then studied to determine air trapping ability as well as its ability to pin water in the same fashion as *S. molesta*.

7.2 Characterization of Leaves and Fabrication of Inspired Structural Surfaces

To characterize the fern hair, an optical microscope was used to image *S. molesta* as well as determine the spacing of the fern hairs (Fig. 7.1). Using the microscope images, an average hair spacing of 490 μm with a range of 250–750 μm was observed. The apparent surface area of the tip of the *S. molesta* hair where the four eggbeater-shaped hairs come to a point was observed to be on the order of 20 $\mu\text{m} \times 20 \mu\text{m}$. The height of the *S. molesta* hairs was about 2 mm.

To mimic the air trapping ability of *S. molesta*, a micropatterned surface made of epoxy (hydrophilic) was fabricated. A two-step molding technique was employed. The technique was used to create microstructures of 14 μm diameter (mimicking the surface area of the *S. molesta* hair tips) and 30 μm height with a pitch value of 26 μm . The 30 μm pillar height, while much smaller than the observed 2 mm height of the *S. molesta* hairs was selected based on the tallest pattern size readily available for the given pitch and diameter dimensions. The 26 μm pitch was selected to compensate for the lower height of the micropillars as compared to the observed height of the *S. molesta* hairs in order to reproduce the height and pitch of the fern hairs, to allow the ability to trap air.

Once epoxy replicas were created, a coating of (tridecafluoro-1,1,2,2-tetrahydrooctyl) trichlorosilane (Gelest) was then applied by a syringe to the surface of the micropatterns to impart hydrophobicity. After coating, the micropatterns were placed in a vacuum at 500 mTorr for 1 min to remove air bubbles and to assist with saturation. Next, the hydrophobic coating was removed using double sided tape to strip away the trichlorosilane from the top of the microstructures, leaving the hydrophobic coating in between the micropillars. The tape was attached to a flat surface and then lowered onto the top of the micropattern

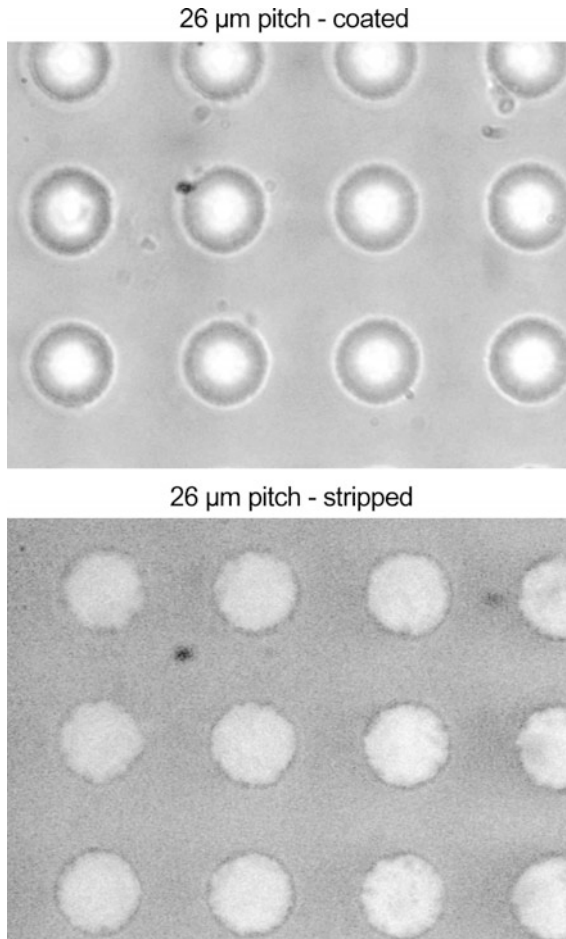


Fig. 7.3 Micropillars created in lab (14 μm diameter, 30 μm height, 26 μm pitch) coated with (tridecafluoro-1,1,2,2-tetrahydrooctyl) trichlorosilane (Gelest) and stripped away (Hunt and Bhushan 2011)

using a motor-driven arm until the surface of the micropattern came into contact with the double sided tape. This ensured that the tape stayed flat and did not bend while making contact with the tips of the micropattern. The hydrophobic coating was stripped from the tips of the micropillars, creating a microstructure which is hydrophobic with small patches at the tips of the micropillars that are hydrophilic. This was done in order to mimic the *S. molesta* hairs in which the surface of the leaf is almost completely hydrophobic, except for tiny hydrophilic patches at the tips of the fern hairs. Optical microscope imaging of the microstructure is shown in Fig. 7.3 for the coated and stripped micropillars (Hunt and Bhushan 2011).

7.3 Measurement of Contact Angle and Adhesion

7.3.1 Observation of Pinning and Contact Angle

When submerged in water, a silvery layer is visible on the surface of the *S. molesta* leaf indicating a layer of air trapped against the surface. To observe the effect that water pressure had on the ability of *S. molesta* to maintain an air layer when submerged in water, the leaf was subjected to a hydrostatic pressure test at a depth of 0.3 m under a column of water. When submerged, the fern was able to retain an air layer under a hydrostatic pressure of 3 kPa. With this result in mind, Hunt and Bhushan (2011) explored the interaction between water droplets and the micropatterns fabricated in their study to observe the micropatterns' ability to produce an air layer and pin water to its surface. This was accomplished by studying the contact angle and angle at which water will remain pinned to the surface of the micropatterns.

Results from the water contact angle test are shown in Fig. 7.4 (Hunt and Bhushan 2011). Also shown in Fig. 7.4 are the results of the tilt test used to check for water pinning at vertical orientation. The uncoated epoxy micropattern with a 26 μm pitch shows an increased contact angle of 139° . As predicted by the transition criteria discussed in Chap. 6, the interface falls within the Cassie-Baxter regime, creating air pockets between the water droplet and base of the micropattern. However, despite the higher contact angle observed on the 26 μm pitch, the water

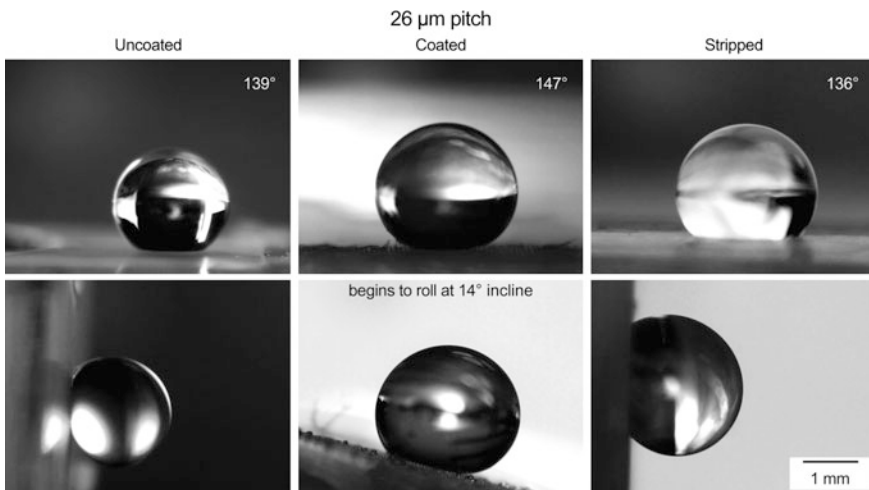


Fig. 7.4 Contact angle measurement for coated, uncoated, and stripped micropillars and samples turned to 90° vertical orientation to determine if water pinning occurs (adapted from Hunt and Bhushan 2011)

does not roll off of the epoxy microstructure due to the hydrophilic nature of the micropillars. The attraction between the micropillars and water droplet is high enough to pin the water to the surface of the microstructure at vertical orientation. This may occur possibly due to a high contact angle hysteresis of the samples (not measured). The coated 26 μm micropattern displays a contact angle of 147° and is higher than the 139° contact angle of the uncoated sample. The water begins to roll off of the 26 μm pitch at an incline of 14° . When the microstructure is stripped, the contact angle is reduced to 136° , which is on par with the uncoated 26 μm sample. As a result of stripping, water remains pinned to the surface due to the hydrophilic nature of the now-exposed tips of the micropillars. Because of the hydrophilic nature of the tips of the microstructures, the water droplet remains pinned to the surface at vertical orientation despite the hydrophobic nature of the coating between the micropillars and air pocket resulting from the interface residing in the Cassie-Baxter regime.

To summarize, the micropattern traps air at the interface of the water droplet and also has a hydrophobic coating in between the micropillars while the tips of the pillars are hydrophilic in nature, thus exhibiting the same characteristics of *S. molesta*.

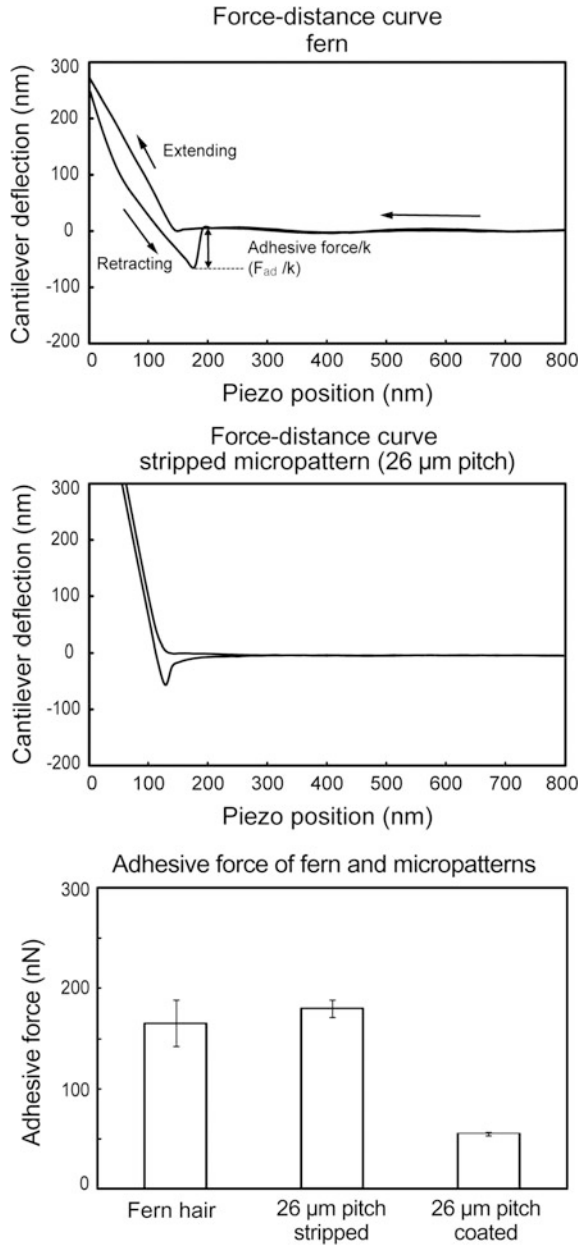
7.3.2 Adhesion

The force-distance curve resulting from the adhesion study of *S. molesta* is shown in Fig. 7.5 (top) (Hunt and Bhushan 2011). The dip in Fig. 7.5 shows a vertical tip deflection in the retracting direction of 69 nm, which is used to calculate the adhesive force (F_{ad}) by multiplying the vertical deflection of the tip by the cantilever spring constant (k) of 3 N/m. This corresponds with a resulting adhesive force of 207 nN. The force-distance curve for the stripped 26 μm micropattern is shown in Fig. 7.5 (middle). Similar to the *S. molesta* force-distance curve, a tip deflection of 67 nm is shown which corresponds with an adhesive force of 201 nN.

A comparison of the adhesive force for *S. molesta* and the 26 μm micropattern is shown in Fig. 7.5 (bottom) for both the coated and stripped micropatterns. As expected, the trichlorosilane-coated micropattern exhibits a much lower average adhesive force of 54 nN. The *S. molesta* hairs show an average adhesive force of 165 nN with a standard deviation of 47 nN, and the stripped 26 μm microstructure shows an average adhesive force of 180 nN with a standard deviation of 19 nN.

The similarity between the adhesive force of the stripped microstructure and the *S. molesta* hair is an important result because it shows that the stripped microstructure will exhibit similar surface characteristics as the *S. molesta* hair. The higher adhesive force of the stripped microstructure compared to the coated 26 μm microstructure explains why water will roll off of the coated sample at an incline of 14° whereas water will remain trapped at a vertical orientation for the stripped sample.

Fig. 7.5 Top plot shows force-distance curves for fern and stripped microstructure showing extending and retracting motion of AFM tip and illustrating adhesive force calculation. The vertical deflection of the AFM tip is given by F_{ad}/k where F_{ad} is the adhesive force between AFM tip and the surface and k is the spring stiffness of the cantilever (3 N/m). F_{ad} is calculated by multiplying the tip deflection (read from the graph) and multiplying by the spring stiffness. The bottom bar chart presents adhesive force data for fern hairs and micropillars (coated and stripped) (Hunt and Bhushan 2011)



7.4 Closure

A 26 μm pitch microstructure composed of micropillars has been created such that the surface is predominantly hydrophobic, while still having hydrophilic tips. It exhibited a comparable wetting behavior to the *S. molesta* hair. The resultant microstructure is shown to create trapped air pockets between a water droplet and microstructure base due to the water droplet residing in the Cassie-Baxter state. Additionally, the newly created microstructure has been shown to exhibit similar adhesion as the *S. molesta* hair. As a result of the similar adhesive forces, water pinning on the microstructure has been observed up to vertical orientation in the same fashion as *S. molesta* (Hunt and Bhushan 2011).

It has been shown that the Salvinia Effect of pinning water and creating air pockets at the water surface interface, as well as the necessary fabrication techniques required for such a surface, is viable through the fabrication of hydrophobic micropatterns with a predefined level of hydrophilic patches. The commercial applications for such a technology include industrial uses in which fluid transport, drag reduction, and increased buoyancy are of interest, especially in applications in which giant liquid slip has been shown to deteriorate air films created by superhydrophobic surfaces.

References

- Balasubramanian, A. K., Miller, A. C., and Rediniotis, O. K., (2004), "Microstructured Hydrophobic Skin for Hydrodynamic Drag Reduction," *AIAA J.* **42**, 411-414.
- Barthlott, W., Schimmel, T., Wiersch, S., Koch, K., Brede, M., Barczewski, M., Walheim, S., Weis, A., Kaltenmaier, A., Leder, A., and Bohn, H. F., (2010), "The Salvinia Paradox: Superhydrophobic Surfaces with Hydrophilic Pins for Air Retention Under Water," *Adv. Mater.* **22**, 2325-2328.
- Choi, C.-H., and Kim, C.-J., (2006), "Large Slip of Aqueous Liquid Flow Over a Nanoengineered Superhydrophobic Surface," *Phys. Rev. Lett.* **96**, 066001.
- Henoch, C., Krupenkin, T. N., Kolodner, P., Taylor, J. A., Hodes, M. S., Lyons, A. M., and Breuer, K., (2006), "Turbulent Drag Reduction using Superhydrophobic Surfaces," *3rd AIAA Flow Control Conf.* June 5-8, San Francisco, CA, AIAA-2006-3192.
- Hunt, J. and Bhushan, B., (2011), "Nanoscale Biomimetics Studies of Salvinia Molesta for Micropattern Fabrication," *J. Colloid Interf. Sci.* **363**, 187-192.
- Koch, K., Bhushan, B., and Barthlott, W., (2009), "Multifunctional Surface Structures of Plants: An Inspiration for Biomimetics," *Prog. Mater. Sci.* **54**, 137-178.
- Lee, C. and Kim, C.-J., (2009), "Maximizing the Giant Liquid Slip on Superhydrophobic Microstructures by Nanostructuring Their Sidewalls," *Langmuir* **25**, 12812.

Chapter 8

Characterization of Rose Petals and Fabrication and Characterization of Superhydrophobic Surfaces with High and Low Adhesion

8.1 Introduction

Unlike the lotus leaf, some rose petals (*rosea Rehd*), scallions, and garlic exhibit superhydrophobicity with high contact angle hysteresis (CAH) (Feng et al. 2008; Chang et al. 2009; Bhushan and Her 2010). While a water droplet can easily roll off the surface of a lotus leaf, it stays pinned to the surface. The different behavior of wetting between the lotus leaf and the rose petal can be explained by different designs in the surface hierarchical micro- and nanostructure. The rose petal's microstructure, and possibly nanostructure, has a larger pitch value and lower height than the lotus leaf. Therefore, the liquid is allowed to impregnate between the microstructure and partially penetrates into the nanostructure, which increases the wetted surface area. As a result, contact angle hysteresis increases with increasing wetted surface area. In the case of scallion and garlic leaves, contact angle hysteresis is high due to hydrophobic defects responsible for contact line pinning. Such superhydrophobic surfaces with high adhesion have various potential applications, such as the transport of liquid microdroplets over a surface without sliding or rolling, the analysis of very small volumes of liquid samples, and for the inside of an aircraft surface to minimize the falling of condensed water droplets onto passengers. There have been few attempts to fabricate such surfaces in the laboratory (Feng et al. 2008; Bormashenko et al. 2009; Bhushan and Her 2010; Dawood et al. 2011; Zhao et al. 2011; Zheng et al. 2011; Ebert and Bhushan 2012; Stanton et al. 2012).

Bhushan and Her (2010) have reported that rose petals can have either high or low adhesion. They studied two superhydrophobic rose petals with high and low adhesion and proposed relevant mechanisms. To verify the mechanisms, they fabricated artificial superhydrophobic surfaces using micropatterned surfaces with different pitch values coated with wax with various masses to change nanostructure density to realize high and low droplet adhesion. Bhushan and Nosonovsky (2010) have studied wetting regimes in the two kinds of rose petals.

Ebert and Bhushan (2012) fabricated mechanically durable, rose petal-effect surfaces with superhydrophobicity and high adhesion. They used micropatterned surface coated with nanoparticles bonded with an epoxy binder. Details follow.

8.2 Characterization of Two Kinds of Rose Petals and Their Underlying Mechanisms

Two kinds of rose petals with superhydrophobicity were studied by Bhushan and Her (2010). For surfaces with high adhesion, Rosa Hybrid Tea, cv. Bairage, referred to as Rosa, cv. Bairage, was studied. For surfaces with low adhesion, Rosa Hybrid Tea, cv. Showtime, referred to as Rosa, cv. Showtime, was studied. Koch et al. (2008) reported that during the measurement of real petals using SEM in a high vacuum chamber, loss of water from the cell occurred, leading to shrinkage on the hierarchical micro- and nanostructures on petals. To obtain stable samples for SEM measurement, petals were air dried (Bhushan and Her 2010). Figure 8.1 shows optical and SEM micrographs of rose petals from each variety studied. Figure 8.2a shows SEM micrographs of dahlia petal in fresh and dried condition (Koch et al. 2008). The specimen shown in the right image taken from the dried leaf shows that the loss of the water from the cells led them to shrink. Figure 8.2b demonstrates that the drying process has a great influence on the cell morphology. It is noted that the height and width of the microstructures have changed, but the number of microstructures per unit area is unchanged by shrinkage.

Figure 8.1b shows that both petals have a hierarchical structure, which means their surface structure consists of nanostructures on microstructures. The low magnification micrographs show a convex cell form with irregular cuticular folding in the central fields and parallel folding in the anticlinal field of the cells (Koch et al. 2008). It is observed that the two rose petals have different spacing (pitch value, P) and peak-to-base (P-B) height of their microstructures, and different density of nanostructures. Based on Table 8.1, to be presented later in this chapter, in the case of Rosa, cv. Showtime, the pitch value is smaller and the P-B height is larger than Rosa, cv. Bairage, which is expected to lead to a superhydrophobic surface with low adhesion (to be discussed later in this chapter).

Figure 8.3 shows optical micrographs of water droplets on the Rosa, cv. Bairage petal in the fresh state (Bhushan and Her 2010). As a water droplet is deposited on its surface, a high static contact angle (CA) (152°) is observed on the petal. When the petal is turned upside down, the water droplet does not fall off, which suggests high adhesion. In the case of a droplet on the Rosa, cv. Showtime, it also has a high static contact angle (167°), but the droplet easily rolls off the surface with a small tilt angle (6°).

Figure 8.4a shows the static contact angle and contact angle hysteresis for the superhydrophobic rose petals in fresh and dried states, and after using chloroform (Bhushan and Her 2010). Chloroform is a solvent that can be used to remove wax

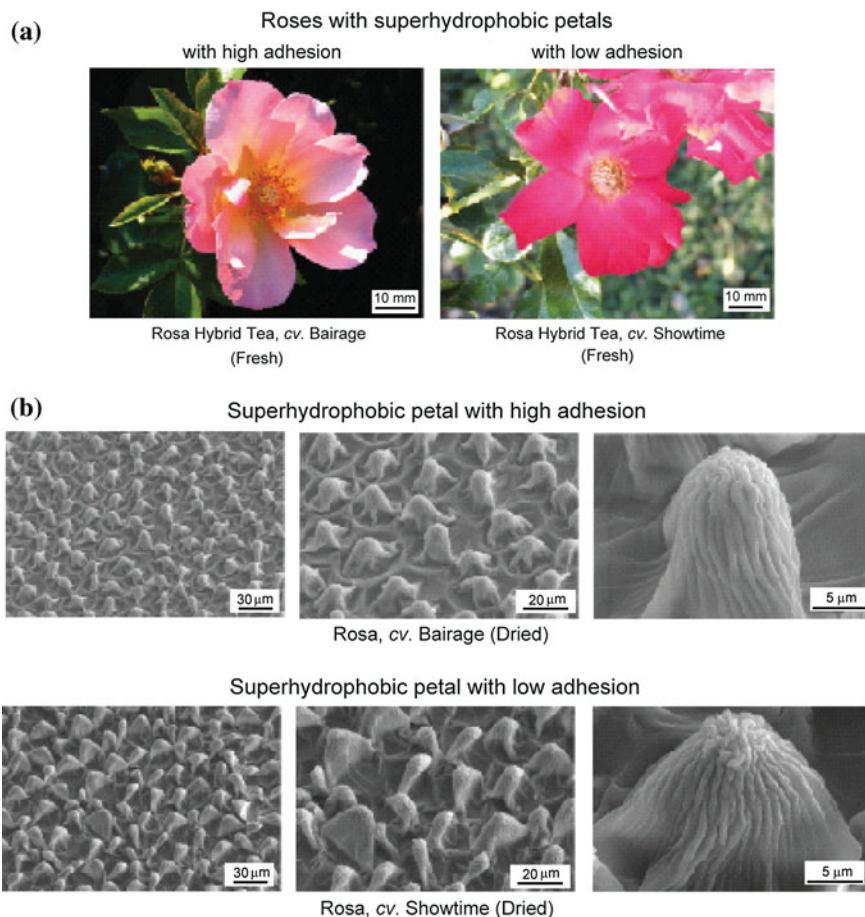


Fig. 8.1 **a** Optical micrographs and **b** SEM micrographs of two roses which have different adhesion properties on its petals—Rosa Hybrid Tea, cv. Bairage (Rosa, cv. Bairage) and Rosa Hybrid Tea, cv. Showtime (Rosa, cv. Showtime) (Bhushan and Her 2010)

compounds (Thomas et al. 1993). The contact angle reduced to less than 10° after chloroform treatment, which suggests that the two superhydrophobic rose petals have only a thin wax film (2D wax) on the surface (Koch et al. 2008). There is a small decrease in the static contact angle for both petals when they are dried. Because a fresh petal has larger microstructure than a dried petal, this gives a higher contact angle according to an equation from Chap. 3. For contact angle hysteresis, there is a decrease of about 40° on Rosa, cv. Bairage, between the fresh and dried states. Since a fresh petal has a higher P-B height of the microstructure, this may lead to a higher pinning of the water droplet, as compared to a dried leaf (McHale et al. 2004; Nosonovsky and Bhushan 2008).

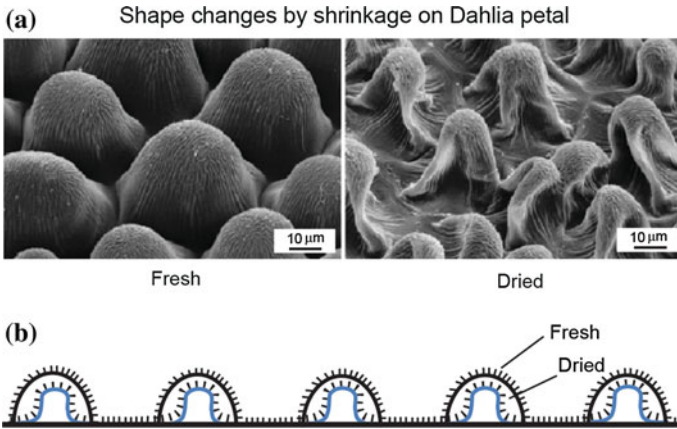


Fig. 8.2 **a** SEM micrographs of dahlia petal. These images have been taken from the same petal. *Left* is fresh and *right* is air dried (Koch et al. 2008); **b** schematic illustrations of shape changes between fresh and dried petals' hierarchical structure

Table 8.1 Microbump map statistics for rose petals with high and low adhesion measured in dried leaves using AFM (Bhushan and Her 2010)

	Peak-to-base (P-B) height (μm)	Mid-width (μm)	Peak radius (μm)	Bump density ($1/10,000 \mu\text{m}^2$)
Rosa, cv. Bairage (High adhesion)	6.8	16.7	5.8	23
Rosa, cv. Showtime (Low adhesion)	8.4	15.3	4.8	34

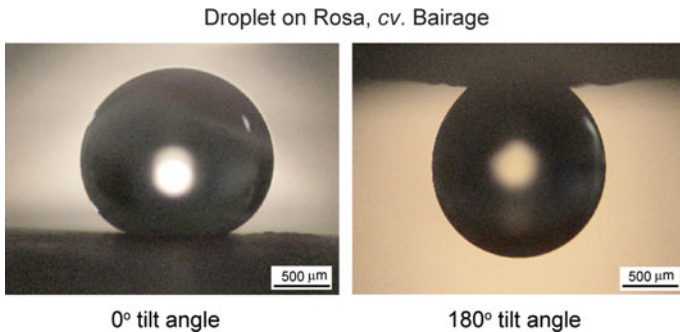


Fig. 8.3 Optical micrographs of water droplets on Rosa, cv. Bairage at 0° and 180° tilt angles. Droplet is still suspended when the petal is turned upside down (adapted from Bhushan and Her 2010)

Fig. 8.4 a Bar charts showing the static contact angle and contact angle hysteresis measured on two rose petal surfaces under fresh and dried states, and after dip into chloroform for 10 s; **b** adhesive force and coefficient of friction for both fresh and dried petals, measured using 15 μm radius of borosilicate tip (Bhushan and Her 2010)

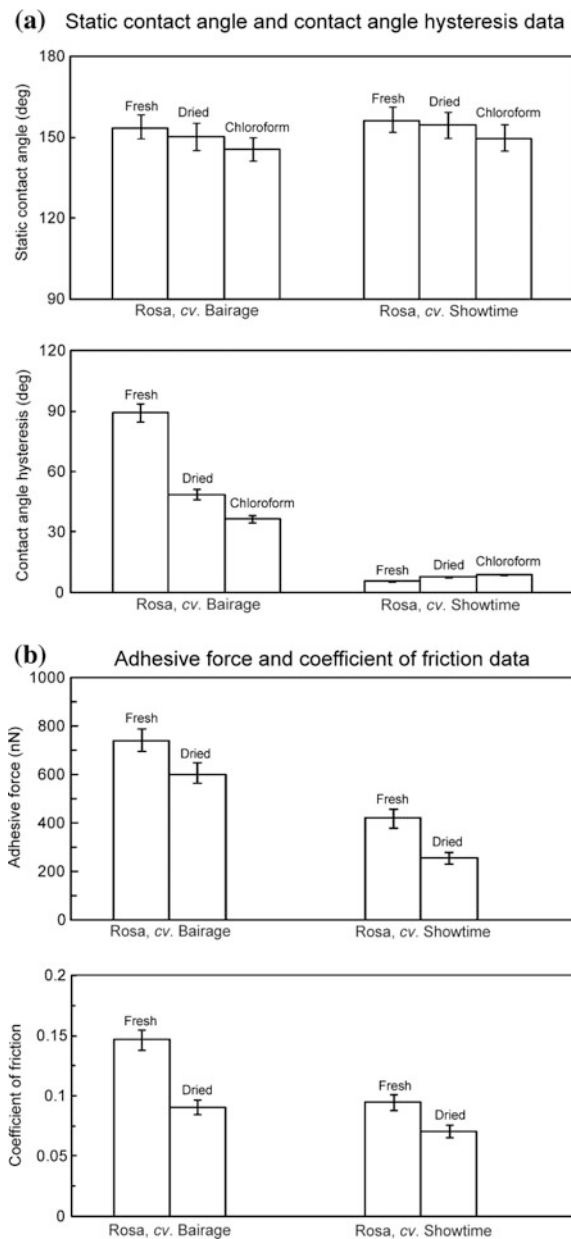


Figure 8.4b shows adhesive force measured using a 15 μm radius borosilicate tip in an AFM for fresh and dried petals (Bhushan and Her 2010). The adhesive force of the Rosa, cv. Bairage is higher than that of the Rosa, cv. Showtime. Adhesive force arises from several sources: the presence of a thin liquid film, such as an

adsorbed water layer, that causes meniscus bridges to build up around the contacting and near contacting bumps, and real area of contact and surface energy effects (Bhushan 2013). For fresh petals, there is moisture within the plant material that causes softening of the petal. When the tip comes into contact with the fresh petal sample, the sample deforms, and a larger area of contact between the tip and sample causes an increase in the adhesive force (Koch et al. 2009).

The coefficient of friction measured at a sliding velocity of $2 \mu\text{m/s}$ for the superhydrophobic surface with low adhesion is lower than that for the superhydrophobic surface with high adhesion due to the lower real area of contact between the tip and petal sample. The coefficient of friction is decreased in the dried state for both petals, since moisture on the petal leads to a higher friction force, similar to that with adhesive force results.

Figure 8.5 shows AFM topography images and 2D profiles of the surfaces for different scan sizes (Bhushan and Her 2010). The AFM has a Z-range on the order of $7 \mu\text{m}$ and cannot be used for measurements in a conventional way because of the high P-B height of rose petals. In order to compensate for the large peak-to-valley (P-V) distance, two scans were made for each height: one measurement that scans the tops of the bumps and another measurement that scans the base of the bumps. The total height of the bumps is embedded within the two scans. The two scans can be spliced together in the 2-D profile to create the full profile of the petal surface. Figure 8.5a shows the $100 \mu\text{m} \times 100 \mu\text{m}$ and $10 \mu\text{m} \times 10 \mu\text{m}$ top row surface height maps obtained using this method for the *Rosa cv. Bairage*. 2-D profiles in the right hand column take the profiles from the top scan and the bottom scan and splice them to get the total profile of the petal surface. Figure 8.5b shows the 100×100 and $10 \times 10 \mu\text{m}$ surface height maps for the *Rosa, cv. Showtime*. These AFM images for microstructure show similar morphology to that in the SEM images in Fig. 8.1b. Using the AFM surface height maps, different statistical parameters of the microstructure and nanostructure can be obtained that include P-B height, mid-width, peak radius, and bump density (inversely related to pitch). Here, mid-width is defined as the width of the bump at a height equal to half of peak to mean value. Peak radius is defined as the radius of curvature which is calculated from the parabolic curve fit of the bump. Bump density is defined as the average number of bumps in the area of $100 \times 100 \mu\text{m}^2$. These quantities for the two petals are listed in Table 8.1. From the measured data of microbumps, it is found that the superhydrophobic rose petal with high adhesion (*Rosa, cv. Bairage*) has a smaller P-B height and bump density value than those of the superhydrophobic rose petal with low adhesion (*Rosa, cv. Showtime*).

In order to understand the mechanisms for the microstructures of the two superhydrophobic rose petals with different adhesive force, Fig. 8.6 shows schematics of water droplet contact with two kinds of rose petal surfaces (adapted from Bhushan and Her 2010). Pitch value (bump density) and P-B height of microstructures are different in the two petals. On the superhydrophobic surface with low adhesion (*Rosa, cv. Showtime*), its microstructure has a smaller pitch value and a larger P-B height as compared to the superhydrophobic surface with high

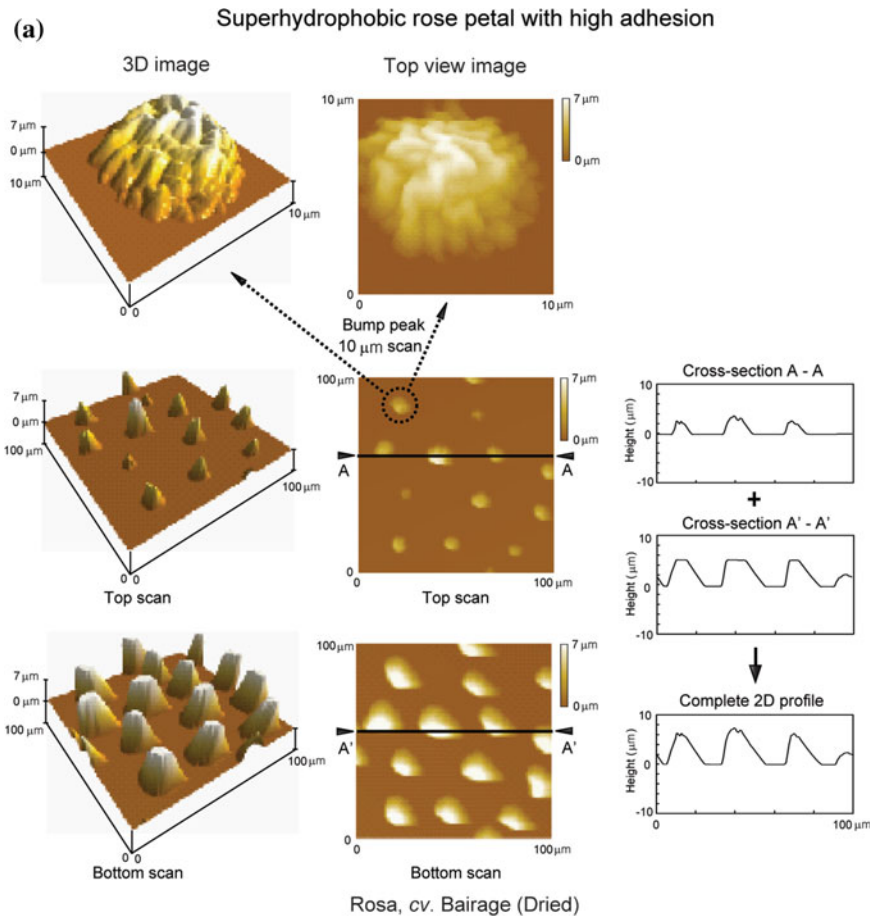


Fig. 8.5 Surface height maps and 2D profiles of **a** Rosa, cv. Bairage (dried) and **b** Rosa, cv. Showtime (dried) using an AFM. Top and bottom scans have been made using a 100 μm scan size, and the bump peak scans have made using a 10 μm scan size in tapping mode (Bhushan and Her 2010)

adhesion (Rosa, cv. Bairage). A smaller value of the ratio of pitch value (P) and P-B height (H) may develop the Cassie-Baxter regime. At a lower value of P/H , there is an increase in the propensity of air pocket formation between microstructures. Air pockets prevent the water droplet from touching the bottom and minimize the contact area between the droplet and surface. This results in high static contact angle, low contact angle hysteresis, and low adhesion (Nosonovsky and Bhushan 2008; Bhushan et al. 2009; Bhushan and Jung 2011). In the case of the superhydrophobic surface with high adhesion, large pitch value, and small P-B height, water penetrates and impregnates between the microscale features, but does not penetrate between the nanoscale features. This increases the contact area with the

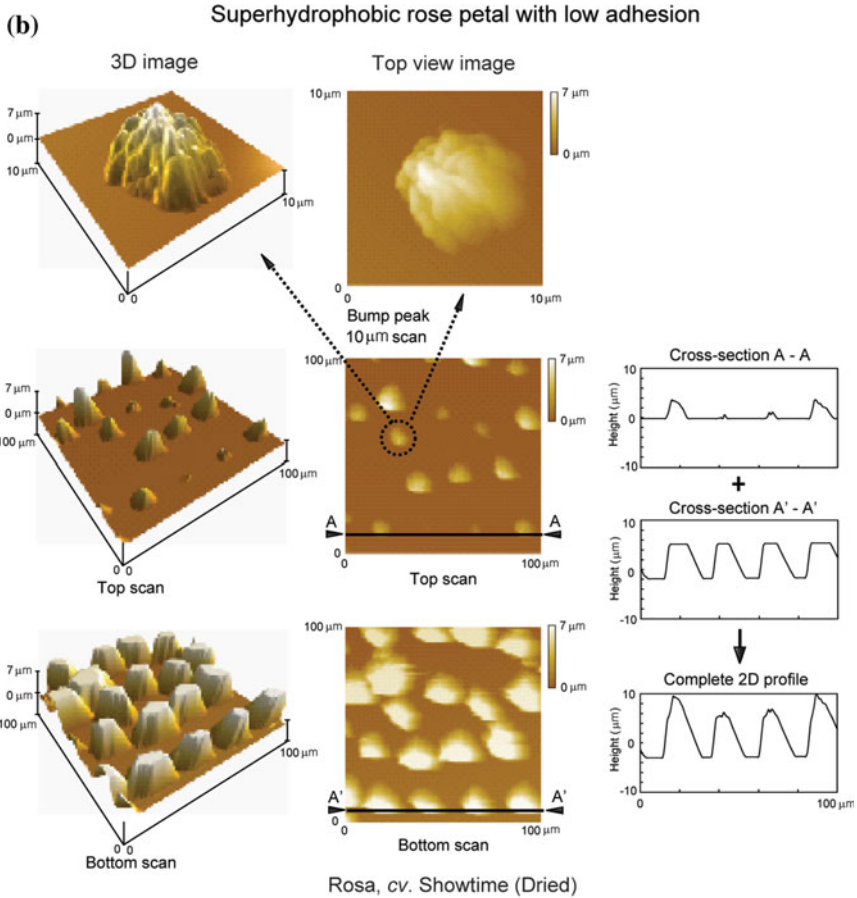


Fig. 8.5 (continued)

water droplet. This so-called mixed/impregnated wetting regime is responsible for a decrease in the static contact angle and an increase in contact angle hysteresis and high adhesion. It is noted that the mixed/impregnated regime is sometimes erroneously referred to as the Cassie-impregnated regime.

In contrast to the Wenzel regime, in which liquid fully wets a rough surface, and the Cassie-Baxter regime, in which liquid rests only on the highest asperities leaving air pockets, a droplet in the mixed/impregnated regime fully penetrates between microscale features, but is unable, or only partially able, to penetrate between nanoscale features. In this sense, the mixed/impregnated wetting regime can be thought of as an intermediate state, with liquid wetting a lower fraction of the surface than in Wenzel regime, but a higher fraction than in Cassie-Baxter regime. The penetration of microstructures and partial penetration of nanostructures causes high contact angle hysteresis (CAH) and therefore high droplet adhesion. In

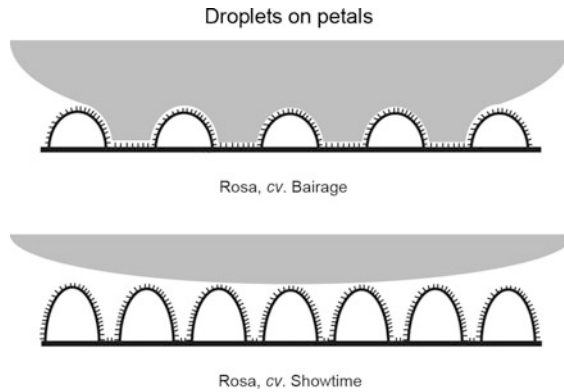


Fig. 8.6 Schematics of a water droplet contacting two rose petal surfaces. *Top* schematic shows Rosa, cv. Bairage with a superhydrophobic and high adhesion surface (mixed/impregnated wetting regime and *bottom* shows Rosa, cv. Showtime with a superhydrophobic and low adhesion (Cassie-Baxter regime) (adapted from Bhushan and Her 2010)

the Cassie-Baxter regime, the droplet has very low CAH and adhesion as a result of resting only on the tips of nanostructures and only partially drooping between microstructures.

8.3 Fabrication of Surfaces with High and Low Adhesion for Understanding of Rose Petal Effect

From the understanding of real rose petals, Bhushan and Her (2010) fabricated artificial superhydrophobic surfaces with high and low adhesion using the methodology presented earlier in Chap. 6, used for the fabrication of artificial lotus structures. In order to realize a microstructure with different pitch values, micropatterned pillars with 23 and 105 μm pitch values with the same diameter (14 μm) and height (30 μm) were used for replication. To fabricate the nanostructure with different pitch values, various masses of *n*-hexatriacontane ($\text{CH}_3(\text{CH}_2)_{34}\text{CH}_3$) (purity of >99.5 %, Sigma-Aldrich, USA) were coated on a microstructure using thermal evaporation. The nanostructure is formed by self-assembly of three-dimensional platelets of *n*-hexatriacontane. Platelets are flat crystals grown perpendicular to the surface. They are randomly distributed on the surface, and their shapes and sizes show some variation. Figure 8.7 shows selected images (Bhushan and Her 2010). When different masses (0.1 and 0.2 $\mu\text{g}/\text{mm}^2$) of wax are applied, the density of the nanostructure is changed, as shown in the bottom row of Fig. 8.7. Different pitch values and masses of wax were used to provide hierarchically structured surfaces with high and low adhesion.

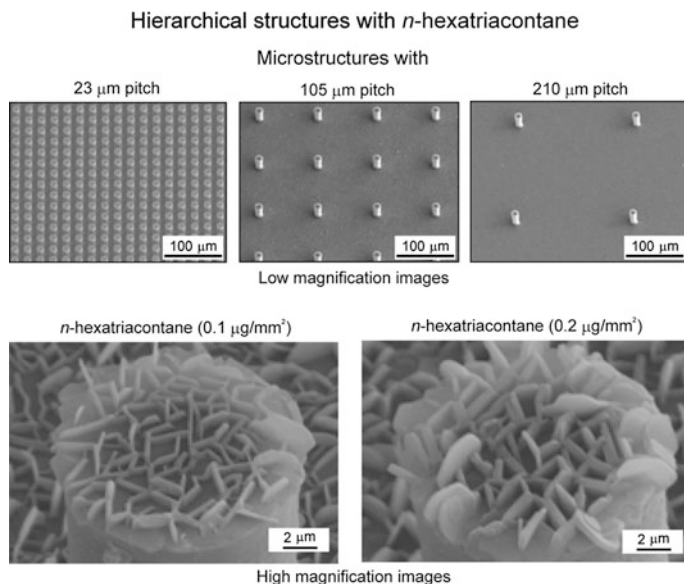


Fig. 8.7 SEM micrographs of the microstructures and nanostructures fabricated with two different masses of *n*-hexatriacontane for hierarchical structure. All images were taken at 45° tilt angle. All samples are positive replicas, obtained from negative replica with dental wax and Si micropatterned master template ($14 \mu\text{m}$ diameter and $30 \mu\text{m}$ height) fabricated with epoxy resin coated with *n*-hexatriacontane (Bhushan and Her 2010)

To identify optimized superhydrophobic surfaces with high and low adhesion, Bhushan and Her (2010) studied the static contact angle and contact angle hysteresis as a function of the mass of *n*-hexatriacontane on hierarchical structures with different pitch values as shown in Fig. 8.8a. On the surface with a $23 \mu\text{m}$ pitch value, while the mass of *n*-hexatriacontane is changed, there are only small changes in the static contact angle and contact angle hysteresis values, which means that they are always in the Cassie–Baxter wetting regime. On the surface with a $105 \mu\text{m}$ pitch value, high contact angle hysteresis (87°) with a superhydrophobic (static contact angle is 152°) state at $0.1 \mu\text{g}/\text{mm}^2$ mass of *n*-hexatriacontane is found.

To study the effect of microstructures and nanostructures with different densities on superhydrophobicity, static contact angle and contact angle hysteresis were measured on flat, nanostructured, microstructured, and hierarchically structured surfaces. All samples were coated with *n*-hexatriacontane, but the flat and microstructure samples do not have a nanostructure on top of the surface. All measurements were repeated five times, and values are presented in Fig. 8.8b, c and Table 8.2. The static contact angle and contact angle hysteresis of the flat and microstructured surfaces in regime A and B₂ were the same in both cases. These values are 92° (CA) and 86° (CAH) for flat surface and 112° (CA) and 88° (CAH) for the microstructured surface, and the droplet still adhered at a tilt angle of 90° . The highest static contact angle of 168° and lowest contact angle hysteresis of

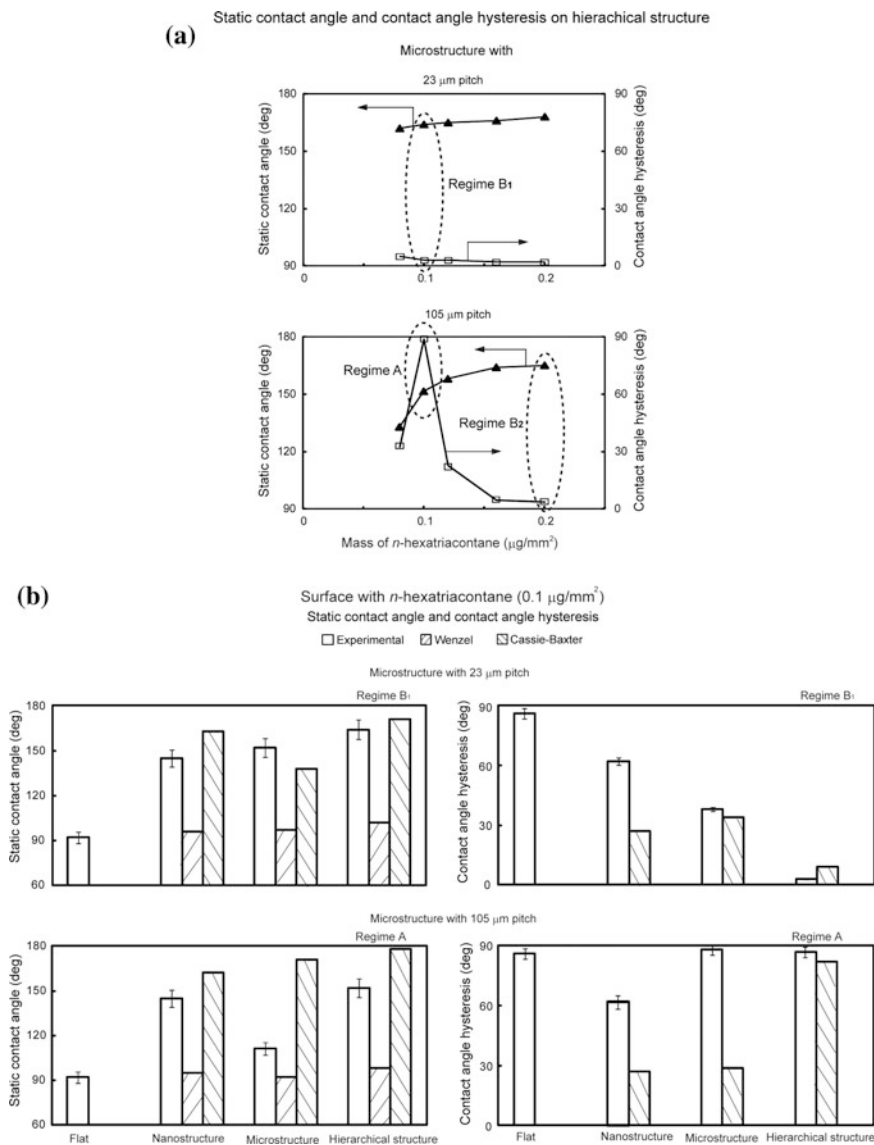


Fig. 8.8 **a** Static contact angle and contact angle hysteresis measured as a function of mass of *n*-hexatriacontane for hierarchical structures with two different pitch values (23 and 105 μm) and **b** and **c** charts showing the measured static contact angle and contact angle hysteresis, calculated contact angles obtained using the Wenzel and Cassie–Baxter equations with a given value of θ_0 , and calculated contact angle hysteresis angles using the Cassie–Baxter equation on a flat, nanostructure, microstructure and hierarchical structure fabricated. Figure 8.8b shows the comparison between regimes B₁ and A for the hierarchical structure from Fig. 8.8a, c shows comparison between regimes A and B₂ for the hierarchical structure from Fig. 8.8a (adapted from Bhushan and Her 2010)

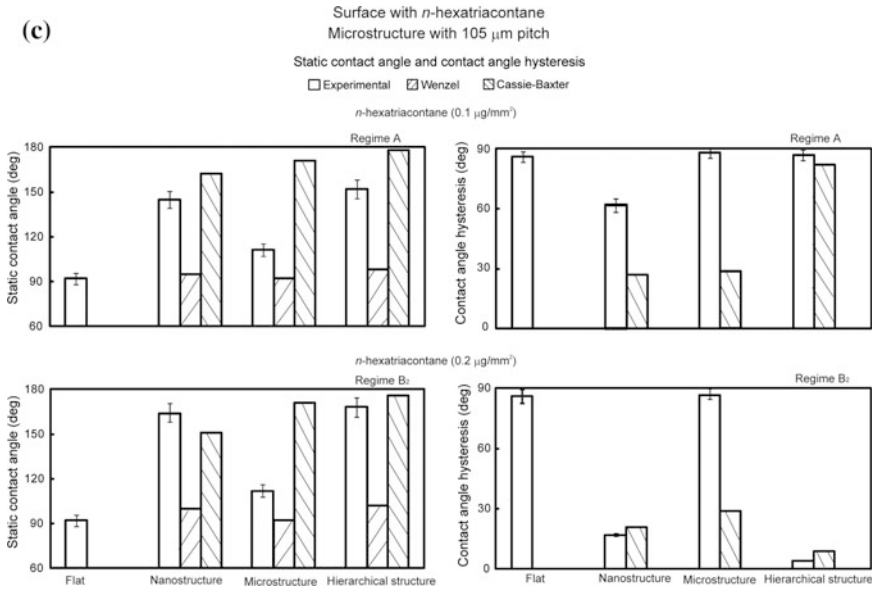


Fig. 8.8 (continued)

4° were found for the hierarchical structured surface with *n*-hexatriacontane ($0.2 \mu\text{g}/\text{mm}^2$). The nanostructured surface with *n*-hexatriacontane ($0.2 \mu\text{g}/\text{mm}^2$) showed a static contact angle of 162° and contact angle hysteresis of 17° . Static contact angle values of nanostructured and hierarchical structured surfaces changed with a decrease in the mass of evaporated *n*-hexatriacontane ($0.1 \mu\text{g}/\text{mm}^2$). The nanostructure with wax ($0.1 \mu\text{g}/\text{mm}^2$) showed a static contact angle of 145° and contact angle hysteresis of 62° . The hierarchical structure with wax ($0.1 \mu\text{g}/\text{mm}^2$) shows a static contact angle of 152° and contact angle hysteresis of 87° , and the droplet still adhered to the surface at a tilt angle of 90° or turned upside down. To compare the nanostructured surface and flat surface, melting of the wax led to a flat surface with a flat wax film and a lower static contact angle (92°) and higher contact angle hysteresis (86°).

In order to identify wetting regimes (Wenzel or Cassie–Baxter), as well as to understand the effect of microstructure and nanostructure density on the propensity of air pocket formation, a roughness factor (R_f) and a fractional liquid–air interface (f_{LA}) are needed. For the microstructured surfaces, the R_f for the microstructure was calculated for the geometry of flat-top pillars of diameter (D), height (H), and pitch value (P) distributed in a regular square array. In this case, the roughness factor for the microstructure is (Bhushan and Her 2010),

$$(R_f)_{micro} = (1 + \pi DH/P^2) \quad (8.1)$$

Table 8.2 Summary of static contact angles and contact angle hysteresis measured and calculated for droplets in Wenzel regime and Cassie-Baxter regime using the values of R_f and f_{LA} on the various surfaces produced in the laboratory (Bhushan and Her 2010)

	R_f	f_{LA}	Static contact angle (°)			Contact angle hysteresis (°)	
			Measured	Calculated using Wenzel equation	Calculated using Cassie-Baxter equation	Measured	Calculated using Cassie-Baxter equation
<i>23 μm pitch with n-hexatriacontane (0.1 μg/mm²)</i>							
Flat			92			86 ^a	
Nanostructure	2.8	0.95	145	96	163	62	27
Microstructure	3.5	0.71	152	97	138	38	34
Hierarchical structure (Regime B ₁)	6.3	0.99	164	102	171	3	9
<i>105 μm pitch with n-hexatriacontane (0.1 μg/mm²)</i>							
Flat			92			86 ^a	
Nanostructure	2.8	0.95	145	95	162	62	27
Microstructure	1.1	0.98	112	92	171	88	29
Hierarchical structure (Regime A)	3.9	0.99	152	98	178	87	82
<i>105 μm pitch with n-hexatriacontane (0.2 μg/mm²)</i>							
Flat			92			86 ^a	
Nanostructure	4.9	0.85	162	100	151	17	21
Microstructure	1.1	0.98	112	92	171	88	29
Hierarchical structure (Regime B ₂)	6.0	0.99	168	102	176	4	9

The measurement results were reproducible within $\pm 5\%$

^aAdvancing and receding contact angles are 141° and 55°, respectively

The R_f for the nanostructures was calculated using the AFM map (Burton and Bhushan 2006). The R_f for the nanostructured surfaces with masses of 0.1 and 0.2 $\mu\text{g}/\text{mm}^2$ were found to be 2.8 and 4.9, respectively. For calculation of f_{LA} , the following assumption was made. For a microstructure, consider that a droplet much larger in size than the pitch contacts only the flat-top of the pillars in the composite interface, and the cavities are filled with air. For a nanostructure, the fractional flat geometrical areas of the solid–liquid and liquid–air interfaces under the droplet are (Bhushan and Her 2010),

$$(f_{LA})_{micro} = (1 - \pi D^2 / 4P^2) \quad (8.2)$$

For calculation of the f_{LA} of nanostructures, the fractional geometrical area of the top surface for the nanostructures was calculated from top view SEM micrographs (0° tilt angle). The SEM images were converted to high contrast black and white images using Adobe Photoshop. The fractional geometrical area of the top of the

nanostructured surfaces with masses of 0.1 and 0.2 $\mu\text{g}/\text{mm}^2$ gives f_{LA} values of 0.95 and 0.85, respectively. The roughness factor for the hierarchical structure $(R_f)_{\text{hierarchical}}$ is the sum of $(R_f)_{\text{micro}}$ and $(R_f)_{\text{nano}}$. For the hierarchical structure, the fractional flat geometrical area of the liquid–air interface is,

$$(f_{LA})_{\text{hierarchical}} = 1 - (\pi D^2/4P^2)[1 - (f_{LA})_{\text{nano}}] \quad (8.3)$$

The values of contact angle hysteresis in Cassie–Baxter regimes for various surfaces were calculated using an equation from Chap. 3.

Figure 8.8b, c and Table 8.2 include the measured and calculated static contact angle and contact angle hysteresis using R_f and f_{LA} . Contact angles were calculated using the Wenzel and Cassie–Baxter equations with a given value of θ_0 and calculated contact angle hysteresis using the Cassie–Baxter equation on a nanostructure, microstructure, and hierarchical structure fabricated with two different masses of *n*-hexatriacontane. R_f and f_{LA} of the hierarchical structure are higher than those of the nano- and microstructures. These results show that air pocket formation in hierarchically structured surfaces might occur, which further decreases the solid–liquid contact and thereby reduces contact angle hysteresis.

Figure 8.8b shows the charts for surfaces with two microstructures in hierarchical structures (Regime B_1 and A defined in Fig. 8.8a). The effect of the microstructure could be explained briefly from the comparison between regime B_1 and A. Those two regimes have the same nanostructure with *n*-hexatriacontane of 0.1 $\mu\text{g}/\text{mm}^2$ and different microstructure (pitch values with 23 and 105 μm). For a microstructured surface with a 23 μm pitch value, the experimental static contact angle and contact angle hysteresis value are comparable to the calculated values in the Cassie–Baxter regime. The data suggests that this microstructured surface leads to higher propensity of air pocket formation between water droplet and the surface. Conversely, the microstructured surface with a 105 μm pitch value leads to complete wetting between water droplet and the surface. There is a good agreement between the proposed mechanism in Fig. 8.6 and the measured and calculated data in Fig. 8.8b. These results show that a larger pitch value of microstructure increases the solid–liquid contact and thereby increases the contact angle hysteresis and high adhesion.

Figure 8.8c shows the charts for surfaces with two nanostructures in hierarchical structures (Regime A and B_2 defined in Fig. 8.8a). The experimental static contact angle and contact angle hysteresis value for the nanostructured surface with *n*-hexatriacontane of 0.2 $\mu\text{g}/\text{mm}^2$ is comparable to the calculated values in the Cassie–Baxter regime. The results suggest that a droplet on the nanostructured surface should exist in the Cassie–Baxter regime. However, the experimental static contact angle was lower and contact angle hysteresis was higher for the nanostructured surface with 0.1 $\mu\text{g}/\text{mm}^2$ than the calculated values in the Cassie–Baxter regime. It is believed that the nanostructure has lower density and any trapped air can be squeezed out. Conversely, neighboring nanostructures are interconnected at higher densities, and air remains trapped. For a microstructured surface, the experimental static contact angle and contact angle hysteresis values are comparable to the calculated values in the Wenzel regime. This result shows that a

microstructured surface leads to complete wetting between the water droplet and the surface. For a hierarchically structured surface, at higher nanostructure density with a mass of $0.2 \mu\text{g}/\text{mm}^2$, the experimental static contact angle and contact angle hysteresis values are comparable to the calculated values in the Cassie–Baxter regime. However, for the hierarchically structured surface with $0.1 \mu\text{g}/\text{mm}^2$, the experimental static contact angle (152°) was lower and contact angle hysteresis (87°) was higher than the calculated values in the Cassie–Baxter regime. This surface consists of lower nanostructure density and microstructure without trapped air pockets. Hence, it is believed that the hierarchically structured surface with $0.1 \mu\text{g}/\text{mm}^2$ is between Wenzel and Cassie–Baxter regime.

Schematics of the effect of nanostructure on the propensity for air pocket formation are shown in Fig. 8.9 (regime A and B_2 in Fig. 8.8a) (Bhushan and Her 2010). When a microstructure has same the pitch value and a nanostructure has low density (regime A in Fig. 8.8a), water could penetrate between the microstructures, but it is still not completely wetted into the nanostructure, resulting in increasing static contact angle and adhesion. However, high density of nanostructure prevents the transition from Cassie–Baxter to Wenzel regime and an increased propensity for air pocket formation between micro- and nanostructures. Bhushan and Nosonovsky (2010) have considered various wetting regimes and suggested that a rose petal with high adhesion to be in the mixed/impregnated wetting regime.

Next, optical images are examined of a water droplet on surfaces in regime A, B_1 , and B_2 defined in Fig. 8.8a. Figure 8.10 shows the shape of the droplets on a

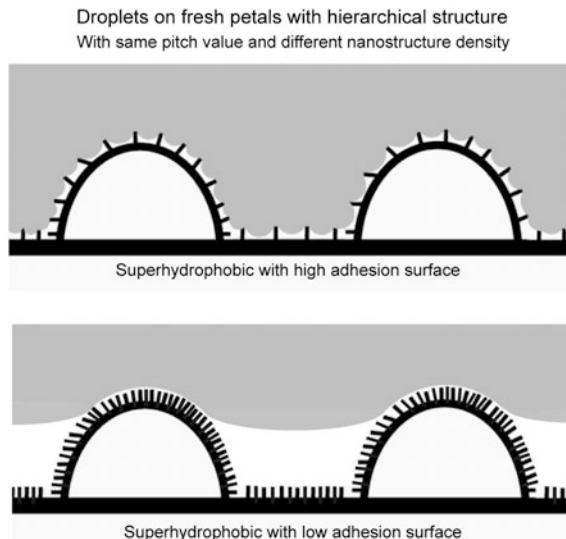
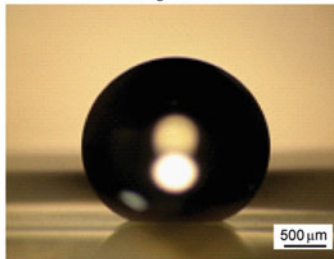
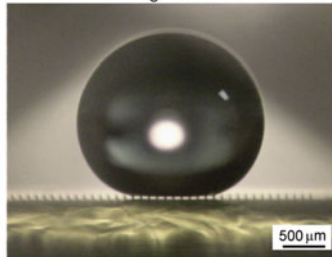
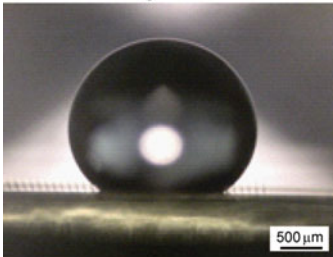


Fig. 8.9 Schematic illustrations of droplets on hierarchical structure with two nanostructures. As an example, mass of *n*-hexatriacontane changes the density of nanostructure (Regime A and B_2 in Fig. 8.8a). Nanostructures play an important role in contact formation between water and underlying substrate (Bhushan and Her 2010)

(a) Shape of droplets on hierarchical structure with 23 μm pitchHorizontal surface with *n*-hexatriacontane ($0.1 \mu\text{g}/\text{mm}^2$)Regime B₁**(b)****Shape of droplets on hierarchical structure with 105 μm pitch**Horizontal surface with different mass of *n*-hexatriacontane*n*-hexatriacontane ($0.1 \mu\text{g}/\text{mm}^2$)*n*-hexatriacontane ($0.2 \mu\text{g}/\text{mm}^2$)

Regime A

Regime B₂Inclined surface with *n*-hexatriacontane ($0.1 \mu\text{g}/\text{mm}^2$)

Regime A

vertical

upside down

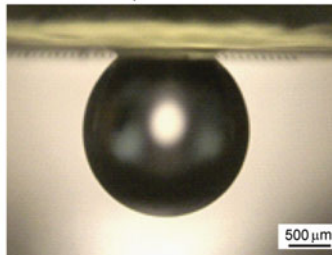
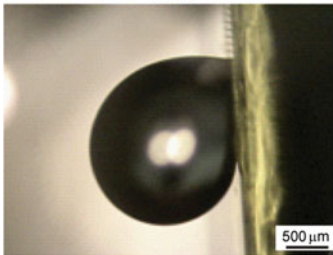


Fig. 8.10 **a** Droplet on a horizontal surface of hierarchical structure with 23 μm pitch and *n*-hexatriacontane ($0.1 \mu\text{g}/\text{mm}^2$) showing air pocket formation and **b** droplet on a hierarchical structure with 105 μm pitch and *n*-hexatriacontane ($0.1 \mu\text{g}/\text{mm}^2$) (Regime A in Fig. 8.8a) and $0.2 \mu\text{g}/\text{mm}^2$ (Regime B₂ in Fig. 8.8a) showing no air pocket and air pocket formation, respectively. Also shown is the image taken on the inclined surface with hierarchical structure with $0.1 \mu\text{g}/\text{mm}^2$ showing that droplet is still suspended (Bhushan and Her 2010)

hierarchical structure with a 23 and 105 μm pitch value (Bhushan and Her 2010). In Regime B_1 and B_2 (from Fig. 8.8a), a superhydrophobic surface with low adhesion and trapped air pockets is obtained. Figure 8.10a displays droplets on a horizontal substrate (23 μm pitch value) with *n*-hexatriacontane ($0.1 \mu\text{g}/\text{mm}^2$). Droplets on the surface (Regime B_1) have a high contact angle (164°) with low contact angle hysteresis (3°), and trapped air pockets can be seen. When *n*-hexatriacontane ($0.2 \mu\text{g}/\text{mm}^2$) is applied on a microstructure (105 μm pitch value), the droplet on the surface (Regime B_2) also reveals a high static contact angle (168°) with low contact angle hysteresis (4°) and trapped air pockets can be seen, as shown in right side of top row Fig. 8.10b. However, by applying *n*-hexatriacontane ($0.1 \mu\text{g}/\text{mm}^2$) on a surface with a 105 μm pitch value (Regime A), a superhydrophobic surface with high adhesion but with no air pocket between the microstructures was fabricated (left side of top row in Fig. 8.10b). It is observed that this surface has high adhesion since the droplet does not fall off when the substrate is vertically inclined or turned upside down (bottom row of Fig. 8.10b).

To further verify the effect of wetting states on the surfaces, evaporation experiments with a droplet on a hierarchical structure coated with two different amounts of *n*-hexatriacontane were performed (Bhushan et al. 2008). Figure 8.11 shows the optical micrographs of a droplet evaporating on two different hierarchical

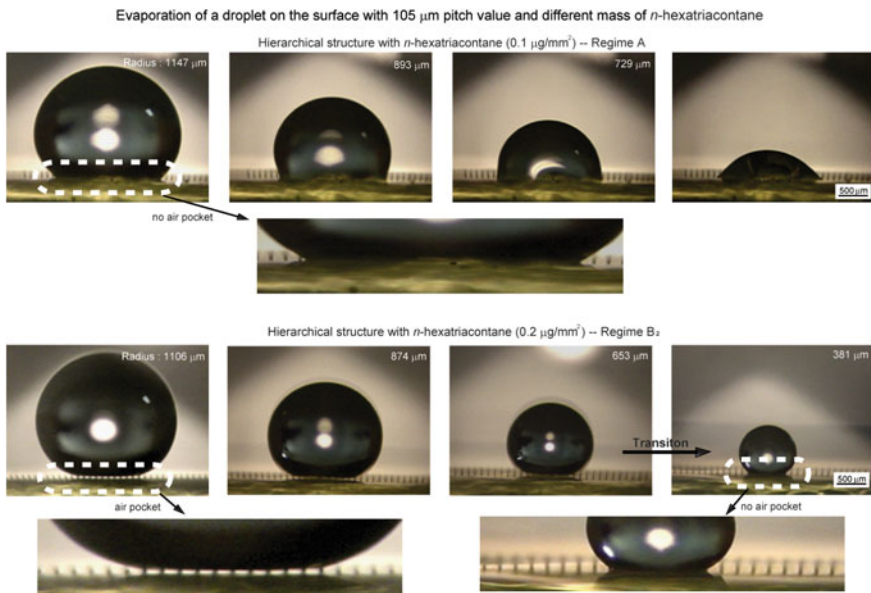


Fig. 8.11 Optical micrographs of droplet evaporation on the hierarchical structured surfaces with 105 μm pitch value. *n*-hexatriacontane ($0.1 \mu\text{g}/\text{mm}^2$) coated sample (Regime A in Fig. 8.8a) has no air pocket formed between the pillars in the entire contact area until evaporation was completed. Hierarchical structure with *n*-hexatriacontane ($0.2 \mu\text{g}/\text{mm}^2$) (Regime B_2 in Fig. 8.8a) has air pocket, and then the transition from Cassie–Baxter regime to Wenzel regime occurred (Bhushan and Her 2010)

structured surfaces (Bhushan and Her 2010). On the *n*-hexatriacontane ($0.1 \mu\text{g}/\text{mm}^2$) coated surface, an air pocket was not visible at the bottom area of the droplet. However, the droplet on the surface has a high static contact angle (152°) since the droplet still cannot completely impregnate into the nanostructure. The footprint size of the droplet on the surface has only small changes from 1820 to 1791 μm . During evaporation, the initial contact area between the droplet and hierarchically structured surface does not decrease until the droplet evaporates completely, which means complete wetting between the droplet and microstructures. For the *n*-hexatriacontane ($0.2 \mu\text{g}/\text{mm}^2$) coated surface, since light passes below the droplet, and air pockets can be seen the droplet is in the Cassie–Baxter regime at the beginning. When the radius of the droplet decreased to 381 μm , the air pockets are no longer visible. The footprint size of the droplet on the surface is changed from 1177 to 641 μm , since droplet remained on only a few pillars until the end of the evaporation process. Based on the transition criteria proposed by Bhushan and Jung (2007) and Jung and Bhushan (2008), the air pockets cease to exist below a certain ratio of the radius of the droplet to the pitch value.

To summarize, Bhushan and Her (2010) found that two species of superhydrophobic rose petals have different surface micro- and nanostructures, therefore exhibiting high and low adhesion. Both rose petals have hierarchical structures, but their spacing (pitch value) and the P-B height of the microstructure, and most likely of the nanostructure, are different from each other. Superhydrophobic rose petals with high adhesion have a smaller P-B height and bump density value (large pitch value) than those with low adhesion. For a microstructure with large pitch value and small P-B height and a nanostructure with low density, water could impregnate between microstructures (mixed/impregnated wetting regime), but it is still not completely wetted into the nanostructure, resulting in high adhesion while maintaining high static contact angle. However, a microstructure with a small pitch value, large P-B height, and a nanostructure with high density, leads to the Cassie-Baxter regime, resulting in low adhesion.

8.4 Fabrication of Mechanically Durable, Superhydrophobic Surfaces with High Adhesion

Mechanical durability of structures and surfaces are critical for applications. Ebert and Bhushan (2012) fabricated mechanically durable surfaces with superhydrophobicity and high droplet adhesion.

They created petal-effect surfaces using hydrophobic and hydrophilic nanoparticles, and examined the effects of microstructure pitch and nanostructure density. To create hierarchical structures, nanoparticles were deposited onto micropatterns with varying pitch values via a spray technique with varying particle concentration and using an epoxy binder, which is known to provide durability. The micropatterns used consisted of arrays of cylindrical micropillars with diameter of 14 μm and height of 30 μm . The pitch values used were 23, 105 and 210 μm , where pitch is

defined as the center-to-center distance between micropillars. Nanostructured surfaces were created by spraying ZnO nanoparticles with average diameter of 70 nm onto micropatterned surfaces using a spray gun. The samples were then annealed at 120 °C for 3 h. Annealing at this temperature (above the melting point and below the burning point of EPON 1002F) allowed the resin to melt and move to the interface between the particles and the surface.

In order to hydrophobize the nanoparticles, they were treated in solution by octadecylphosphonic acid (ODP) obtained from Aldrich. The samples were then heated at 100 °C for 1 h to improve ODP bonding and remove adsorbed water or remaining solvent. Durability of the samples was measured using an AFM, as described earlier.

8.4.1 Samples with Hydrophilic ZnO Nanoparticles (Before ODP Modification)

Figure 8.12 shows SEM micrographs of ZnO nanoparticles on flat and micropatterned substrates (Ebert and Bhushan 2012). The particles are shown on a flat substrate at three magnifications in Fig. 8.12a, while Fig. 8.12b shows microstructures at three pitch values along with an individual micropillar coated with nanoparticles at two different spray concentrations. Nanostructured surfaces were formed in the case of nanoparticles on flat substrate, while hierarchically structured surfaces were formed in the case of nanoparticles on microstructures.

The contact angle/contact angle hysteresis data for microstructured and flat substrates with varying nanoparticle spray concentration are displayed in Fig. 8.13 (Ebert and Bhushan 2012). At a pitch value of 23 μm , samples were superhydrophobic at all nanoparticle concentrations. Droplet adhesion was low, as contact angle hysteresis did not exceed 37° and droplets did not adhere when the surfaces were inverted. Because the pitch is relatively small, a water droplet is unable to penetrate between microstructures, and remains in the Cassie-Baxter regime with low adhesion. At pitch values of 105 and 210 μm , the contact angle is hydrophilic for lower nanoparticle concentrations, indicating that water is penetrating between microstructures and resulting in Wenzel regime wetting. At higher nanoparticle concentrations, superhydrophobic contact angles were achieved. However, in each case, the corresponding contact angle hysteresis values were low (<30°) and droplets did not adhere when inverted, indicating low adhesion. At higher nanoparticle concentration, the droplet was unable or only partially able to penetrate between microstructures, resulting in Cassie-Baxter wetting and low adhesion.

The only superhydrophobic, high adhesion state using hydrophilic particles occurred in the case of a flat substrate. At a particle spray concentration of 3000 mg/L, a superhydrophobic contact angle of 151° and high contact angle hysteresis of 71° were measured. In addition, a water droplet could remain adhered to the surface when fully inverted. The morphology of this surface can be seen in Fig. 8.12a. As the flat epoxy substrate and the nanoparticles are hydrophilic, the

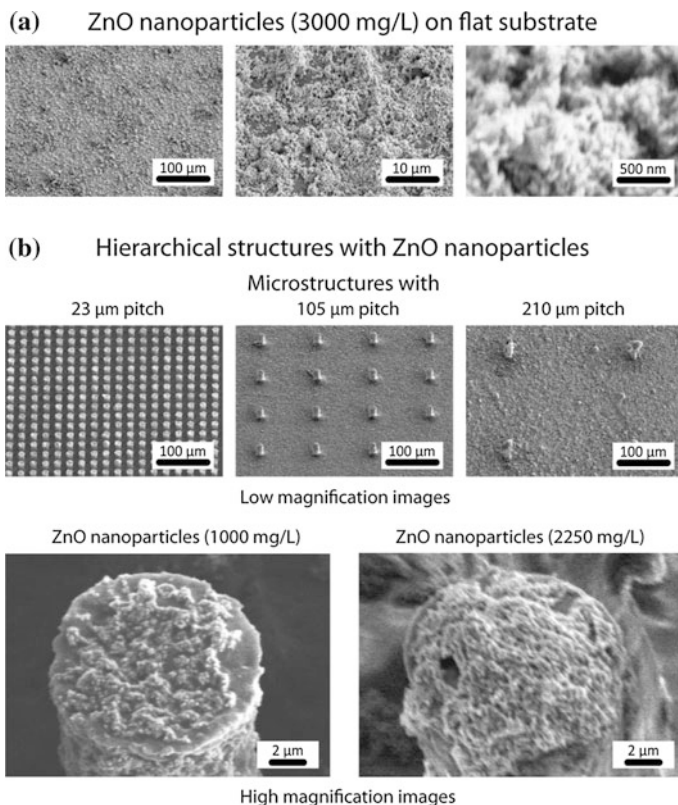


Fig. 8.12 SEM micrographs of **a** ZnO nanoparticles on flat substrate at three magnifications and **b** low magnification images of microstructures at three different pitch values, along with high magnification images of individual micropillar with two different nanoparticle spray concentrations (Ebert and Bhushan 2012)

high contact angles seen at higher concentrations are likely the result of higher roughness, leading to partial rather than full wetting of the nanostructure. This partial wetting also allows for high adhesion. However, with hydrophilic particles, it seems that the nanoscale roughness required for a superhydrophobic state with high adhesion precludes the use of a microstructure of the size used in this study, even with pitch value as high as 210 μm. With the uniform microstructures used, the high nanoscale roughness leads to Cassie-Baxter wetting and low adhesion. SEM of flat surface with 3000 mg/L ZnO nanoparticles (Fig. 8.12a) reveals microscale roughness on the order of 2–3 μm, which may provide the dual-scale roughness necessary for a mixed/impregnated state.

Table 8.3 shows measured contact angle and contact angle hysteresis values for two selected surfaces using hydrophilic nanoparticles, as well as calculated contact angle using both Wenzel and Cassie-Baxter equations (Ebert and Bhushan 2012). The contact angle of ZnO without roughness (θ_0) was assumed to be 15°

Table 8.3 Summary of measured and calculated contact angle (CA) and measured contact angle hysteresis (CAH) for selected superhydrophobic surfaces with high and low adhesion using hydrophilic ZnO nanoparticles (Ebert and Bhushan 2012)

	R_f	f_{LA}	CA measured ($^{\circ}$) ($\pm 1^{\circ}$)	CA calculated using Wenzel equation ($^{\circ}$)	CA calculated using Cassie-Baxter equation ($^{\circ}$)	CAH measured ($^{\circ}$) ($\pm 2^{\circ}$)
<i>Flat substrate with 3000 mg/L ZnO nanoparticle spray; superhydrophobic with high adhesion</i>						
Nanostructure	4.0	0.98	151	~ 0	155 ^a	71
<i>105 μm pitch with 3000 mg/L ZnO nanoparticle spray; superhydrophobic with low adhesion</i>						
Nanostructure	4.0	0.98	151	~ 0	155	71
Bare microstructure	1.1	0.98	77	79	167	72
Hierarchical structure	5.1	0.99	169	~ 0	~ 180	22

Where microstructure is used, data for hierarchical structure correspond to final samples

^aOverprediction of CA by Cassie-Baxter equation, along with high CAH, suggests mixed/impregnated wetting regime

(Zhang et al. 2010). For the surface with 3000 mg/L nanoparticles on flat substrate, the values for the resulting nanostructure are reported. For the surface with 3000 mg/L nanoparticles on microstructure with 105 μm pitch, the values for the nanostructure alone, the bare microstructure, and the resulting hierarchical structure are reported. The R_f and f_{LA} were calculated as described earlier.

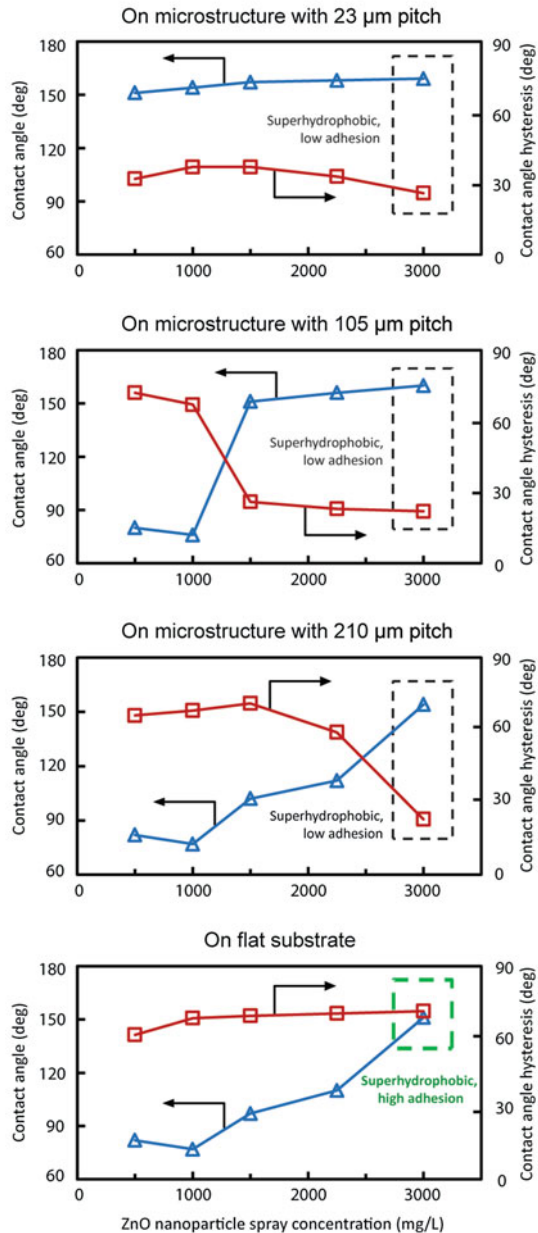
For both surfaces, R_f exceeds the value that results in a contact angle of 0° in the Wenzel regime, and the calculated contact angle can be taken as 0° . For the surface with 3000 mg/L nanoparticles on microstructure with 105 μm pitch, R_f and f_{LA} were such that the calculated Cassie-Baxter contact angle exceeds 180° , and the calculated contact angle can be taken as 180° . This over-predicts the measured value of 169° , however the low contact angle hysteresis of 22° indicates that Cassie-Baxter behavior with low adhesion is prevailing. For the surface with 3000 mg/L on flat substrate, the calculated Cassie-Baxter contact angle slightly over-predicts the measured value (155° vs. 151°). Coupled with high contact angle hysteresis of 71° and the ability of the droplet to remain adhered when inverted, this suggests a mixed/impregnated wetting regime with high adhesion. Figure 8.14 shows images of the droplet on a flat substrate with 3000 mg/L ZnO nanoparticles when it is horizontal, vertical, and upside-down (Ebert and Bhushan 2012).

8.4.2 Samples with Hydrophobic ZnO Nanoparticles (After ODP Modification)

The contact angle/contact angle hysteresis data for microstructured and flat substrates with varying nanoparticle spray concentration after modification with ODP

Fig. 8.13 Contact angle and contact angle hysteresis data on nanostructured surfaces with hydrophilic ZnO nanoparticles (before ODP modification) using microstructures with three different pitch values (23, 105, 210 μm) as well as a flat substrate. Reproducibility is $\pm 1^\circ$ for CA data and $\pm 2^\circ$ for CAH data. Low adhesion indicates CAH $> 30^\circ$, and high adhesion indicates adherence of droplet on inverted substrate (Ebert and Bhushan 2012)

Contact angle and contact angle hysteresis on nanostructured surfaces with hydrophilic ZnO nanoparticles



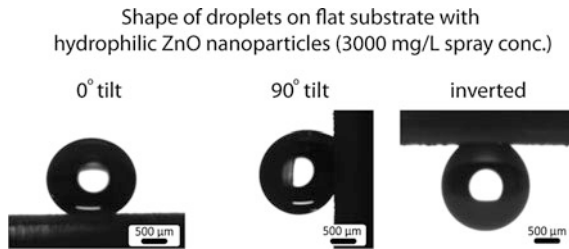


Fig. 8.14 Droplets on flat substrate with hydrophilic ZnO nanoparticles at 3000 mg/L spray concentration at 0° tilt, 90° tilt, and fully inverted, showing superhydrophobicity and high droplet adhesion (Ebert and Bhushan 2012)

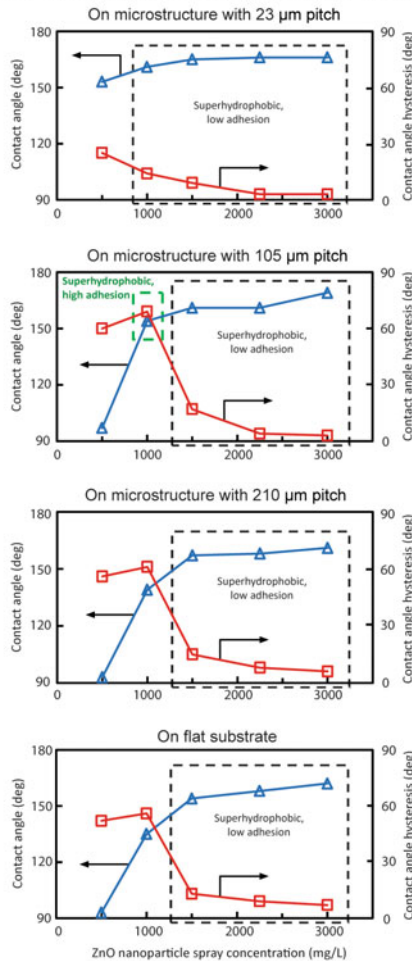
are shown in Fig. 8.15 (Ebert and Bhushan 2012). At a pitch value of 23 μm , surfaces were superhydrophobic for all nanoparticle concentrations, with contact angle hysteresis remaining below 25° and falling as low as 3° at higher concentrations. With a low pitch value of 23 μm , water was unable to penetrate the microstructure using either hydrophilic or hydrophobic particles. However, the hydrophobization of the particles provided a slight increase in contact angle and fairly substantial decrease in contact angle hysteresis. For samples on flat substrates and with microstructure pitch value of 210 μm , all surfaces with nanoparticle concentration of 1500 mg/L and above were superhydrophobic with low contact angle hysteresis (<15°). At a concentration of 1000 mg/L, both had a highly hydrophobic contact angle (135° for flat, 139° for 210 μm pitch) and high contact angle hysteresis (56° for flat, 61° for 210 μm pitch). However, in addition to not achieving superhydrophobicity, a droplet did not adhere when the surface was inverted in either case.

A superhydrophobic, high adhesion state using hydrophobic particles occurred with a nanoparticle concentration of 1000 mg/L on the microstructure with 105 μm pitch. The measured contact angle and contact angle hysteresis were 154° and 69°, respectively, and a water droplet could remain adhered to the surface when inverted. The microstructure with 105 μm pitch and an individual micropillar with nanoparticles deposited at 1000 mg/L spray concentration can be seen in Fig. 8.12b. The data indicated that with properly selected microstructure geometry and nanostructure density, a superhydrophobic, high adhesion state can be achieved with a hydrophobic nanostructure. This finding was in agreement with Bhushan and Her (2010).

Table 8.4 shows measured contact angle and contact angle hysteresis values for three selected surfaces using hydrophobic nanoparticles, as well as calculated contact angle using both Wenzel and Cassie-Baxter equations (Ebert and Bhushan 2012). The values for R_f and f_{LA} were found as described previously. The contact angle of the ODP-modified ZnO without roughness (θ_0) was taken as 103°, which was the measured contact angle value on a glass slide modified by the same ODP solution. For the surface with 105 μm pitch and 1000 mg/L nanoparticle concentration, the measured contact angle of 154° is under-predicted by the Wenzel

Fig. 8.15 Contact angle and contact angle hysteresis data on nanostructured surfaces with hydrophobic ZnO nanoparticles (after ODP modification) using microstructures with three different pitch values (23, 105, 210 μm) as well as a flat substrate. Reproducibility is $\pm 1^\circ$ for CA data and $\pm 2^\circ$ for CAH data. Low adhesion indicates CAH $> 30^\circ$, and high adhesion indicates adherence of droplet on inverted substrate (Ebert and Bhushan 2012)

Contact angle and contact angle hysteresis on nanostructured surfaces with hydrophobic ZnO nanoparticles



equation (136°) and over-predicted by the Cassie-Baxter (178°). As the contact angle hysteresis is high (69°) and the droplet could remain adhered to an inverted substrate, this suggests a mixed/impregnated wetting regime with high adhesion. For the surface with 105 μm pitch and concentration of 3000 mg/L, the measured contact angle (169°) is over-predicted, but contact angle hysteresis is extremely low (3°), indicating predominantly Cassie-Baxter behavior.

Figure 8.16 shows images of the droplet on 105 μm pitch microstructures with two different nanoparticle concentrations, leading to both high adhesion and low adhesion states. In addition, the droplet in high adhesion state is shown at vertical tilt and upside-down. For the low adhesion state, air pockets between micropillars are visible beneath the droplet.

Table 8.4 Summary of measured and calculated contact angle (CA) and measured contact angle hysteresis (CAH) for selected superhydrophobic surfaces with high and low adhesion using hydrophobic ZnO nanoparticles. Data for hierarchical structure correspond to final samples (Ebert and Bhushan 2012)

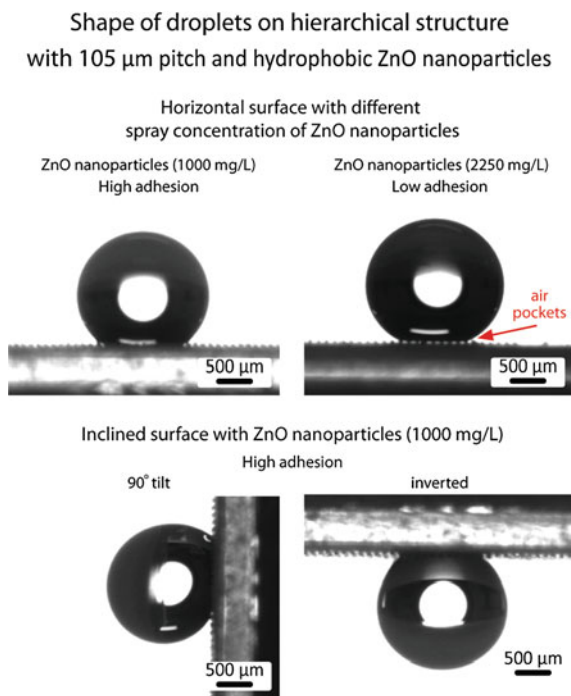
	R_f	f_{LA}	CA measured ($^{\circ}$) ($\pm 1^{\circ}$)	CA calculated using Wenzel equation ($^{\circ}$)	CA calculated using Cassie-Baxter equation ($^{\circ}$)	CAH measured ($^{\circ}$) ($\pm 2^{\circ}$)
<i>23 μm pitch with 1000 mg/L ZnO nanoparticle spray; superhydrophobic with low adhesion</i>						
Nanostructure	2.1	0.91	135	118	162	56
Bare microstructure	3.5	0.71	152	53	122	37
Hierarchical structure	4.6	0.97	161	~ 180	~ 180	14
<i>105 μm pitch with 1000 mg/L ZnO nanoparticle spray; superhydrophobic with high adhesion</i>						
Nanostructure	2.1	0.91	135	118	162	56
Bare microstructure	1.1	0.98	77	79	167	72
Hierarchical structure	3.2	0.99	154	136	178 ^a	69
<i>105 μm pitch with 3000 mg/L ZnO nanoparticle spray; superhydrophobic with low adhesion</i>						
Nanostructure	4.0	0.98	162	154	176	7
Bare microstructure	1.1	0.98	77	79	167	72
Hierarchical structure	5.1	0.99	169	~ 180	~ 180	3

^aOverprediction of CA by Cassie-Baxter equation, along with high CAH, suggests mixed/impregnated wetting regime

8.4.3 Wear Resistance in AFM Wear Experiment

The results of the AFM wear experiment for hydrophobic ZnO nanoparticles as well as the epoxy resin are shown in Fig. 8.17 (Ebert and Bhushan 2012). Surface height maps before and after the wear experiment are displayed, as well as sample scans across the middle of the image (position indicated by arrow). Root mean square roughness (RMS) and peak-valley roughness (PV) within the wear area are also displayed. Hardness of the epoxy resin was measured with a microindenter and found to be 570 MPa. The hardness of ZnO is approximately 5 GPa (Kucheyev et al. 2002). After 1 cycle at 10 μN with the borosilicate ball, the morphology of the surface with ZnO nanoparticles was not significantly changed, and RMS and PV of the sample scans within the wear area were nearly identical (455 nm after compared with 463 nm before for RMS, 1782 nm after and 1759 nm before for PV). The after-image for the epoxy resin reveals slight wear, as well as an overall swelling of the wear area, possibly due to frictional heating effects. In addition, RMS of the sample scan increased from 25 to 177 nm within the wear area, and PV increased

Fig. 8.16 Droplets on hierarchically structured surfaces microstructure pitch value of $105\ \mu\text{m}$ and two different ZnO nanoparticle spray concentrations (1000 and 2250 mg/L) resulting in superhydrophobicity with high adhesion (with 1000 mg/L) and low adhesion (with 2250 mg/L). In the case of low adhesion, air pockets are visible beneath droplet. Droplet in high adhesion state is also shown at 90° tilt and fully inverted (Ebert and Bhushan 2012)

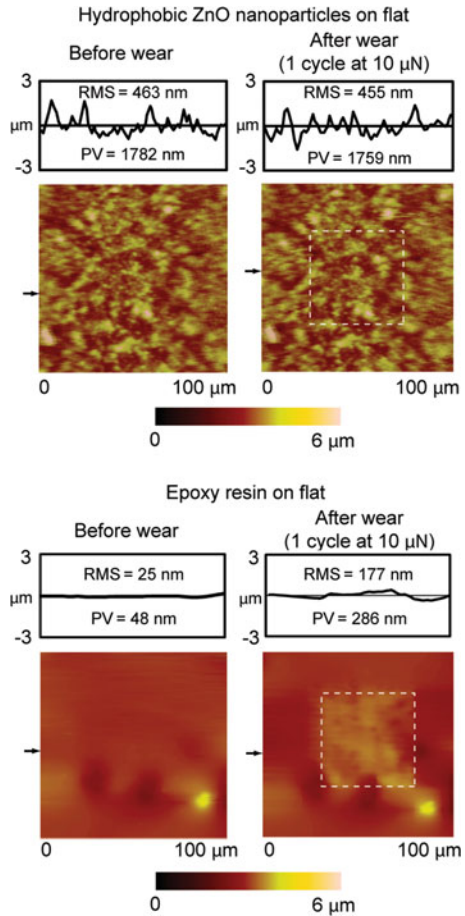


from 48 to 286 nm. However, the preservation of nearly identical roughness and surface morphology for ZnO nanoparticles and fairly minimal wear of the epoxy resin were observed.

To summarize, Ebert and Bhushan (2012) fabricated surfaces with the rose petal effect that exhibit superhydrophobicity and high droplet adhesion. They used both hydrophilic and hydrophobic nanoparticles on microstructured and flat substrates. The surfaces showed wear resistance for potential commercial use in an AFM wear experiment, indicating strong bonding of the epoxy resin and sufficient hardness of ZnO nanoparticles and resin.

When hydrophilic nanoparticles were used, the petal effect could be achieved with high nanoparticle spray concentration on a flat substrate. The high nanoparticle concentration created high surface roughness, which is necessary to obtain a superhydrophobic state using hydrophilic materials. However, the high roughness precluded the use of a microstructure of the geometry and the range of pitch values used in this study, as the roughness resulted in a predominantly Cassie-Baxter state on the microstructure with low droplet adhesion. When hydrophobic nanoparticles were used, the petal effect was achieved with significantly lower nanoparticle spray concentration on a microstructure. Increasing nanoparticle concentration or decreasing microstructure pitch resulted in a Cassie-Baxter state with low adhesion. Conversely, decreasing nanoparticle concentration or increasing microstructure pitch resulted in a loss of superhydrophobicity.

Fig. 8.17 Surface height maps and sample surface profiles (locations indicated by *arrows*) before and after AFM wear experiment using 15 μm radius borosilicate ball at load of 10 μN for glass samples with hydrophobic ZnO nanoparticles on flat substrate as well as epoxy resin alone on flat substrate. RMS roughness and PV distance values for surface profiles are displayed within surface profile boxes (Ebert and Bhushan 2012)



8.5 Closure

Unlike the lotus leaf, rose petals exhibit superhydrophobicity with either high adhesion or low adhesion. By fabricating superhydrophobic surfaces with various combinations of microstructures and nanostructures, relevant mechanisms have been proposed. Mechanically durable surfaces with high adhesion (petal effect) have been fabricated with either hydrophilic or hydrophobic materials by creating appropriate micro- and nanoscale surface structures. The hydrophilicity/hydrophobicity of material forming the nanostructure greatly affects the required nanostructure density, microstructure pitch value, and roughness necessary to achieve superhydrophobicity with high adhesion. Use of a hydrophobic nanostructure may be preferable considering that a lower surface roughness is required. A lower surface roughness may be desirable in some applications.

References

- Bhushan, B. (2013), *Introduction to Tribology*, 2nd Ed., Wiley, New York.
- Bhushan, B. and Her, E.K. (2010), "Fabrication of Superhydrophobic Surfaces with High and Low Adhesion Inspired from Rose Petal," *Langmuir* **26**, 8207-8217.
- Bhushan, B. and Jung, Y.C. (2007), "Wetting Study of Patterned Surfaces for Superhydrophobicity," *Ultramicroscopy* **107**, 1033-1041.
- Bhushan, B. and Jung, Y.C. (2011), "Natural and Biomimetic Artificial Surfaces for Superhydrophobicity, Self-Cleaning, Low Adhesion, and Drag Reduction," *Prog. Mater. Sci.* **56**, 1-108.
- Bhushan, B. and Nosonovsky, M. (2010), "The Rose Petal Effect and the Modes of Superhydrophobicity," *Phil. Trans. R. Soc. A* **368**, 4713-4728.
- Bhushan, B., Koch, K., and Jung, Y. C. (2008), "Nanostructures for Superhydrophobicity and Low Adhesion," *Soft Matter* **4**, 1799-1804.
- Bhushan, B., Jung, Y. C., and Koch, K. (2009), "Micro-, Nano- and Hierarchical Structures for Superhydrophobicity, Self-Cleaning and Low Adhesion," *Phil. Trans. R. Soc.* **367**, 1631-1672.
- Bormashenko E., Stein T., Pogreb R., and Aurbach D. (2009), "'Petal Effect' on Surfaces Based on Lycopodium: High-Stick Surfaces Demonstrating High Apparent Contact Angles," *J. Phys. Chem. C* **113**, 5568-5572.
- Burton, Z. and Bhushan, B. (2006), "Surface Characterization and Adhesion and Friction Properties of Hydrophobic Leaf Surfaces," *Ultramicroscopy* **106**, 709-719.
- Chang, F. M., Hong, S. J., Sheng, Y. J., and Tsao, H. K. (2009), "High Contact Angle Hysteresis of Superhydrophobic Surfaces: Hydrophobic Defects," *App. Phys. Lett.* **95**, 064102.
- Dawood M. K., Zheng H., and Liew T. H. (2011), "Mimicking Both Petal and Lotus Effects on a Single Silicon Substrate by Tuning the Wettability of Nanostructured Surfaces," *Langmuir* **27**, 4126-4133.
- Ebert, D. and Bhushan, B. (2012), "Wear-Resistant Rose Petal-Effect Surfaces with Superhydrophobicity and High Droplet Adhesion Using Hydrophobic and Hydrophilic Nanoparticles," *J. Colloid Interf. Sci.* **384**, 183-188.
- Feng, L., Zhang, Y., Xi, J., Zhu, Y., Wang, N., Xia, F., and Jiang, L. (2008), "Petal Effect: A Superhydrophobic State with High Adhesive Force," *Langmuir* **24**, 4114-4119.
- Jung, Y. C. and Bhushan, B. (2008), "Wetting Behavior during Evaporation and Condensation of Water Microdroplets on Superhydrophobic Patterned Surfaces," *J. Microsc.* **229**, 127-140.
- Koch, K., Bhushan, B., and Barthlott, W. (2008), "Diversity of Structure, Morphology and Wetting of Plant Surfaces," *Soft Matter* **4**, 1943-1963.
- Koch, K., Bhushan, B., Jung, Y. C., and Barthlott, W. (2009), "Fabrication of Artificial Lotus Leaves and Significance of Hierarchical Structure for Superhydrophobicity and Low Adhesion," *Soft Matter* **5**, 1386-1393.
- Kucheyev S. O., Bradby J. E., Williams J. S., and Jagadish C. (2002), "Mechanical Deformation of Single-Crystal ZnO," *J. Appl. Phys.* **80**, 956-958.
- McHale, G., Shirtcliffe, N. J., and Newton, M. I. (2004), "Contact-Angle Hysteresis on Super-Hydrophobic Surfaces," *Langmuir* **20**, 10146-10149.
- Nosonovsky, M. and Bhushan, B. (2008), *Multiscale Dissipative Mechanisms and Hierarchical Surfaces: Friction, Superhydrophobicity, and Biomimetics*, Springer-Verlag, Heidelberg, Germany.
- Stanton, M. M., Ducker, R. E., MacDonald, J. C., Lambert, C. R., and McGimpsey, W. G. (2012), "Super-hydrophobic, Highly Adhesive, Polydimethylsiloxane (PDMS) Surfaces," *J. Coll. Interf. Sci.* **367**, 502-508.
- Thomas, A. B., Donn, G. S., and Robert, Q. (1993), "Evaluation of Epicuticular Wax Removal from Whole Leaves with Chloroform," *Weed Technology* **7**, 3, 706-716.
- Zhang B., Kong T., Xu W., Su R., Gao Y., and Cheng G. (2010), "Surface functionalization of Zinc Oxide by Carboxyalkylphosphonic Acid," *Langmuir* **26**, 4514-4522.

- Zhao X. D., Fan H. M., Liu X. Y., Pan H., Xu H. Y. (2011), "Pattern-Dependent Tunable Adhesion of Superhydrophobic MnO₂ Nanostructured Film," *Langmuir* **27**, 3224-3228.
- Zheng L., Li Z., Bourdo S., Saini V., Ryerson C., and Biris A. S. (2011), "Hierarchical ZnO Structure with Superhydrophobicity and High Adhesion," *Chem. Phys. Chem.* **12**, 2412-2414.

Chapter 9

Modeling, Fabrication, and Characterization of Superoleophobic/Philic Surfaces

9.1 Introduction

Oleophobic surfaces have the potential for self-cleaning and antifouling from organic and biological contaminants both in air and underwater applications and can reduce fluid drag (Bhushan 2009). As a model surface in living nature for a liquid repellent surface in air, the upper side of the lotus leaf surface repels water (superhydrophobic) and is useful for self-cleaning and low adhesion applications (Barthlott and Neinhuis 1997; Bhushan and Jung 2011). The superhydrophobic properties of the leaf surface are achieved due to the presence of a hierarchical structure created by a microstructure formed by papillose epidermal cells covered with 3D epicuticular hydrophobic wax nanotubules, shown in Fig. 9.1a. The wax layer makes the surface hydrophobic and the hierarchical structure makes the surface superhydrophobic. This structure causes water droplets to roll off of the leaf surface and take contaminants with them to keep the leaf clean. The lower side of the lotus leaf does not contain three dimensional wax crystals (Neinhuis and Barthlott 1997), and consists of rather flat, tabular, and slightly convex papillae (Koch et al. 2009). Therefore, the bottom surface is hydrophilic, but superoleophobic in water, with a contact angle of 155° with n-hexane oil, Fig. 9.1b (Cheng et al. 2011). The lotus leaf exhibits a so-called “Janus interface” (named for the two-faced Roman god), with superhydrophobicity on the upper side, and superoleophobicity under water on the lower side (Cheng et al. 2011).

Another model surface in living nature for superoleophobicity under water is provided by sea animals such as fish (including carp and trout), which are known to be well protected from contamination by oil pollution although they are wetted by water. Fish scales are covered with oriented scales that promote anisotropic flow from head to tail (Liu et al. 2009; Bixler and Bhushan 2012b). Shark skin, which is a model for a low drag surface, is covered by small individual tooth-like scales called dermal denticles (little skin teeth) shaped like small riblets, with longitudinal grooves (aligned parallel to the local flow direction of the water) (Bixler and

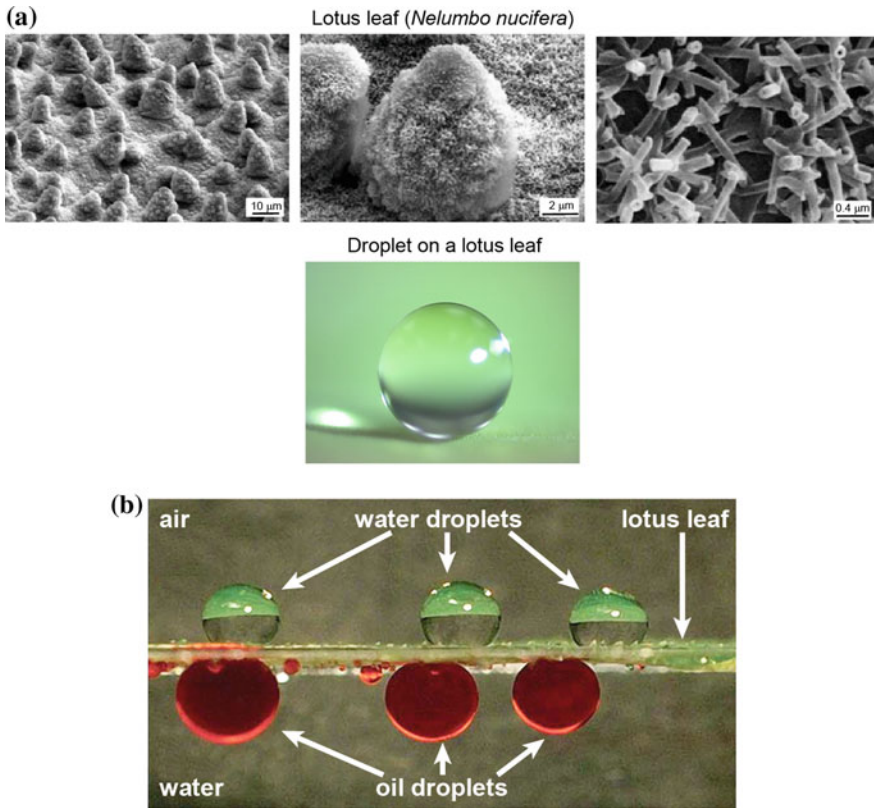
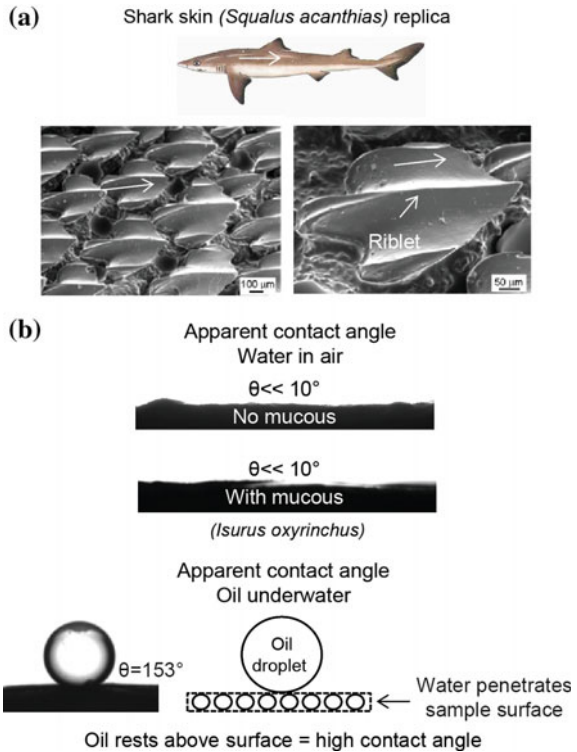


Fig. 9.1 **a** SEM micrographs (shown at three magnifications) of lotus (*Nelumbo nucifera*) leaf upper surface, consisting of microstructures formed by papillose epidermal cells covered with 3-D epicuticular hydrophobic wax nanotubules on the surface, which create hierarchical structure, and an image of water droplet sitting on lotus leaf (adapted from Bhushan et al. 2009); **b** Lotus leaf floating on water surface. Spherical water droplets on its upper side and spherical oil (n-hexane dyed *red*) droplets on the lower side in water (adapted from Cheng et al. 2011)

Bhushan 2013a). Figure 9.2a shows shark skin replica and only three ribs on each scale. It is clearly visible that the V-shaped riblets' height varies between 200 and 500 μm , and their spacing varies between 100 and 300 μm (Jung and Bhushan 2009; Dean and Bhushan 2010). The contact angle of actual shark skin using water droplets with and without mucus was $\ll 10^\circ$ (superhydrophilic) and using paraffin oil droplets under water was 153° (superoleophobic), Fig. 9.2b (Bixler and Bhushan 2013b). Their superoleophobic characteristic in water and their microstructured surfaces lead to protection from marine fouling and play a role in the defense against adhesion and growth of marine organisms, e.g., bacteria and algae (Genzer and Efimenko 2006; Bixler and Bhushan 2012a).

Hydrophilic surfaces exhibit superoleophobicity under water. For these surfaces, the underwater surface is wet by the water. In order for the underwater surface to

Fig. 9.2 a SEM micrograph of shark skin (*Squalus acanthias*) replica. The shark skin replica shows only three ribs on each scale. It is clearly visible that the V-shaped riblets' height varies between 200 and 500 μm and their spacing varies between 100 and 300 μm (adapted from Jung and Bhushan 2009); **b** Water droplet images in air and paraffin oil droplet images under water for actual shark skin (*Isurus oxyrinchus*) (Bixler and Bhushan 2013b)



become wet by oil, the water would first have to dewet the surface, which is difficult due to the very low receding angle of water on the hydrophilic surface. Thus, the hydrophilic surface exhibits superoleophobicity under water.

Model surfaces in living nature with superoleophobicity in air are rare (Brown and Bhushan 2016a). Certain species of leafhopper (Rakitov and Gorb 2013) and springtails (Hensel et al. 2013) are repellant to some low surface tension liquids. Integuments of leafhoppers (insects, *Hemiptera*, *Cicadellidae*) are coated with a thin layer of intricately structured particles known as brochosomes. They are hollow proteinaceous spheres of usually 200–700 nm diameter with honeycomb walls, Fig. 9.3a (adapted from Rakitov and Gorb 2013). The structure of brochosomal particles consists of re-entrant geometry (to be introduced later), which is repellant to water and some low surface tension liquids (diiodomethane); but is wettable with ethanol (surface tension $\sim 22 \text{ mN m}^{-1}$). Nature provides this functionality to protect these sap-sucking insects from getting trapped into water and their own liquid exudates. Springtails (*Collembola*) are wingless arthropods that survive in rain-flooded habitats. Their skin consists of mushroom-shaped profiles with cavity side-wall profiles that have characteristic overhangs. The overhanging surface structures provide re-entrant geometry, Fig. 9.3b (Hensel et al. 2013). They form a plastron, protecting them against suffocation if immersed in water and low surface tension liquids, such as alkanes and olive oil. In both cases, re-entrant geometries

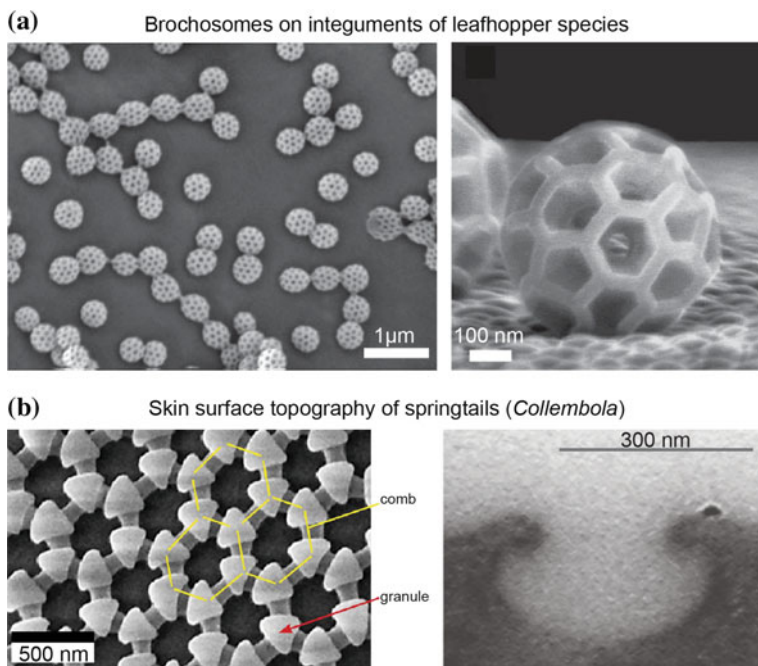


Fig. 9.3 **a** SEM micrograph of the structure of brochosomes on integuments of leafhopper species (adapted from Rakitov and Gorb 2013), and **b** SEM micrograph of the skin surface of springtail (*Orthonychiunis stachiamis*) showing granules at the intersections of the underlying comb structure (*above*) and sections through the skin, taken by TEM showing cavities with characteristic overhanging cross-sectional profiles (adapted from Hensel et al. 2013)

are responsible for the oil repellency. However, a surface found in living nature to repel very low surface tension liquids ($<30 \text{ mN m}^{-1}$) has yet to be found.

Fabrication of superoleophobic surfaces has attracted interest within the scientific community and industry for their unique characteristics, such as self-cleaning, anti-fouling, and drag reduction (Hsieh et al. 2005; Jung and Bhushan 2009; Darmanin et al. 2011; He et al. 2011; Muthiah et al. 2013; Brown and Bhushan 2015a, b, c; Wang and Bhushan 2015; Peng and Bhushan 2016). For an oleophobic surface, oil contaminants are washed away when immersed in water. This effect leads to self-cleaning that can be used against marine ship fouling (Jung and Bhushan 2009). These surfaces have a contact angle (CA) greater than 150° , combined with contact angle hysteresis (CAH) or tilt angle (TA) of 2° – 10° with oils with low surface tension on the order of 20–30 mN/m. For industrial applications, superoleophobic surfaces should be mechanically durable. In some applications, anti-smudge (finger print resistance), transparency, anti-icing, and anti-fogging properties are of interest, including windows, solar panels, electronic touch screens, and computer displays (Brown and Bhushan 2015a, b, c; Wang and Bhushan 2015; Peng and Bhushan 2016).

In this chapter, various strategies to achieve superoleophobicity in air are presented first. Then, a model advanced by Jung and Bhushan (2009) for predicting the oleophobic/philic nature of surfaces is presented. To validate the model, it has been investigated how the water and oil droplets in air and oil droplets in water influence a wetting behavior on flat surfaces, as well as micropatterned surfaces with varying pitch values. Various examples of mechanically durable superoleophobic and superoleophilic surfaces in air are presented (Brown and Bhushan 2015a, b, c; Wang and Bhushan 2015; Peng and Bhushan 2016).

9.2 Strategies to Achieve Superoleophobicity in Air

Oil repellency is more difficult to achieve than water repellency, as the surface tension of oils is much lower than that of water with surfactants as low as about 10 mN/m, Table 9.1 (Brown and Bhushan 2016a). Therefore, in order for a nanostructured surface to exhibit superoleophobicity, its surface energy should be lower than the surface tension of the oil. Fluorinated materials with low surface energy are commonly used. Nanoparticles are generally added to achieve superoleophobicity. A re-entrant geometry can be used as a way to increase the oil contact angle for a

Table 9.1 Surface tension values of selected liquids (Brown and Bhushan 2016a)

Liquid	Surface tension (mN/m)
Water ^a	71.99
Diiodomethane ^a	50.80
Ethylene glycol ^a	47.70
Rapeseed oil	~ 35
Peanut oil	~ 32
Olive oil	~ 32
Soybean oil	~ 29
Hexadecane ^a	27.05
Tetradecane ^a	26.13
Dodecane ^a	25.35
Cyclohexane ^a	24.95
Decane ^a	23.37
Methanol ^a	22.70
Ethanol ^a	22.10
Octane ^a	21.14
Hexane ^a	18.43
Pentane ^a	15.48
Silicone oils ^b	16–20
Perfluorohexane (FC-72) ^c	10

^aHaynes (2014)

^bAnonymous (2015a)

^cAnonymous (2015b)

surface with surface energy too low to repel some very low surface tension liquids (Nosonovsky and Bhushan 2008).

9.2.1 Fluorination Techniques

In the fabrication of superoleophobic surfaces in air, fluorinated coatings are most commonly used because of their low surface energy. Interaction between surfaces occurs due to polarization of molecules. Polarizability depends upon the mobility of electrons. A low polarizability signifies tightly bound electrons. Fluorine is the most electronegative element (nonpolar) on the periodic table with its small radius. Its atomic number is 9 with an electron configuration of $1s^1 2s^2 2p^5$. It consists of 5 electrons in 2p shell and only short of 1 electron. Fluorine is not easily polarized, because it wants to hold onto its 5 electrons, which are less mobile. The lack of polarizability means that fluorine is weakly susceptible to van der Waals forces and it is not easily attracted to or repelled by nearby objects. As a result, it is known to have weak intermolecular forces and therefore a lower energy.

Low adhesion of fluorinated materials can be a disadvantage as they don't adhere well to any nanoparticles or the substrates. Lack of adhesion leads to poor mechanical durability, which presents challenges. There are several popular application techniques using various fluorinated materials summarized in Fig. 9.4 (Brown and Bhushan 2016a). Details follow.

9.2.1.1 Fluoropolymers

Fluorinated polymers for low surface energy coatings are desirable as polymers. One drawback of fluoropolymers is the lack of binding to the nanoparticles which are needed to achieve superoleophobicity. To address adhesion and mechanical durability issues, hydrophilic nanoparticles may be used, which attach themselves to form a 3-D network. In another approach, the fluoropolymer can be deposited on a prefabricated substrate with the correct topography. However, if the coating is too thick, surface roughness features can be lost (Brown and Bhushan 2016a).

9.2.1.2 Fluorosilanes and Fluorothiols

Fluorosilanes are another desirable method for creating superoleophobic surfaces as they can form thin, self-assembled layers that won't conceal small topographical features. Silanes typically require $-OH$ groups on the surface (e.g., via UV/plasma) for a covalently-bonded layer to form (Wang and Bhushan 2015). However, many silanes are sensitive to moisture and form insoluble polymers in solution (Ulman 1996). When factored in with the requirement for surface activation, this can limit the use of silanes for industrial scale up.

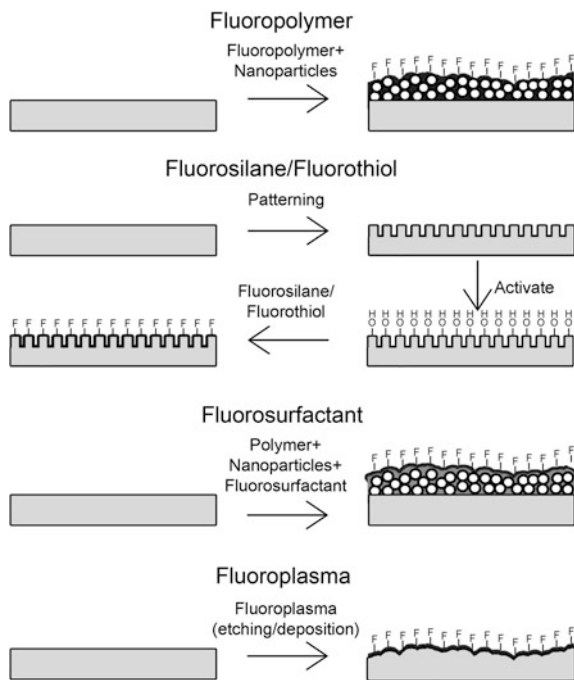


Fig. 9.4 Schematic of popular techniques for creation of fluorinated, superoleophobic surfaces. Fluoropolymer plus nanoparticles is straight-forward but mechanical durability is an issue, fluorosilane/fluorothiols are thin but require surface activation (e.g. via UV/plasma) for silanes or specific substrates (e.g. copper, silver) for thiols, fluorosurfactant layers provide a surface that repels oils but attracts water for oil–water separation but requires specific surface chemistry for bonding, and fluoroplasma accomplishes surface texturing and fluorination in one step but is difficult to scale (Brown and Bhushan 2016a)

Another species capable of forming a self-assembled, fluorinated layer are thiols. However, these display long term instability toward oxidation (Lee et al. 1998) and only assemble on specific surfaces such as silver, gold, platinum, palladium, or copper. However, durability remains a challenge (Brown and Bhushan 2016a).

9.2.1.3 Fluorosurfactants

Surfaces that repel oils also typically repel water, due to water having a higher surface tension (Table 9.1). However, it is possible to create a coating that repels oils but attracts water. This can be achieved through the use of a fluorosurfactant, which contains a high surface tension head group and a low surface tension tail group. When deposited, the fluorinated tails segregate at the air interface resulting in a low surface tension barrier that repels oils. However, when droplets of water are placed on the surface, they are able to penetrate down through the tail groups to

reach the high surface tension groups below, and thus the coating appears hydrophilic. Such surfaces can be exploited for a variety of applications, including oil–water separation and anti-fouling (Brown and Bhushan 2015a, c).

It is also possible to use fluorosurfactants to create superomniphobic surfaces where all liquids, including water, are unable to penetrate (Brown and Bhushan 2016a).

9.2.1.4 Other Fluorination Techniques

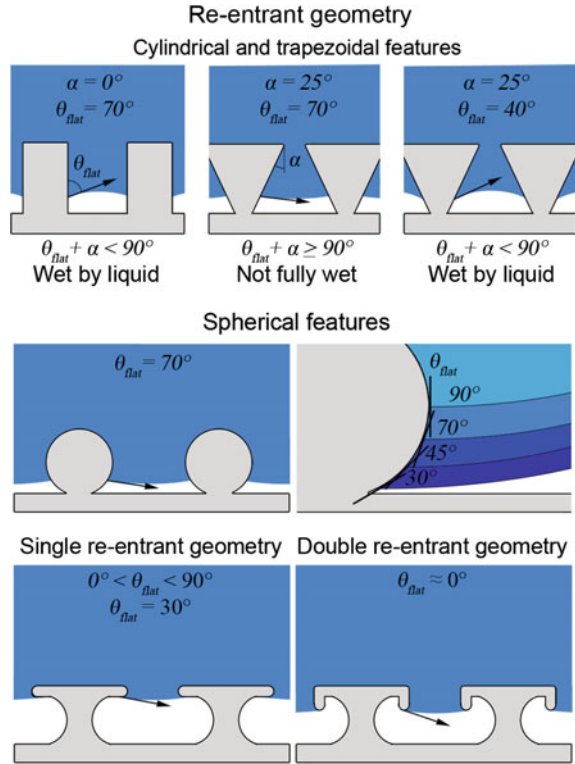
Another method of fluorination is plasma deposition. Various plasma species can be used to etch and/or fluorinate a surface for oil-repellent applications. Plasma treatments are advantageous as they can accomplish surface texturing and fluorination in one step. They also can typically treat the entire surface, regardless of geometries. However, while these may be suitable for small-scale experiments, the use of specialty conditions and chemicals may be cost prohibitive for certain applications (Brown and Bhushan 2016a).

9.2.2 *Re-entrant Geometry*

For a liquid with very low surface tension, it may not be possible to produce a surface with sufficiently low surface energy to realize a contact angle on a flat surface greater than 90° . By introducing structures with re-entrant curvatures, it is possible to achieve high contact angles, even if the contact angle on the flat surface (θ_{flat}) is less than 90° (Nosonovsky and Bhushan 2008). By pairing re-entrant geometries with low surface energy, fluorinated materials, superoleophobicity for liquids with very low surface tension can be achieved. In a re-entrant geometry, each roughness feature is wider at some point than it is at another below, creating an overhang. To repel liquids with contact angles as low as 0° , a double re-entrant geometry may be necessary (Nosonovsky and Bhushan 2008; Liu and Kim 2014; Brown and Bhushan 2016a).

Figure 9.5 shows three re-entrant geometries for demonstration. The top row shows one cylindrical surface and two trapezoidal surfaces with an inclination angle α (Brown and Bhushan 2016a, b). For two hypothetical liquids with $\theta_{flat} = 70^\circ$ and 40° , imaginary solid-liquid-air interfaces are shown for the three cases. For the case of cylindrical features with $\theta_{flat} = 70^\circ$, and the case of trapezoidal features with $\alpha = 25^\circ$ and $\theta_{flat} = 40^\circ$ ($\theta_{flat} + \alpha < 90^\circ$), the liquid-air interface is concave shaped. The Laplace pressure inside the droplet is negative, which results in a downward force, leading to fully-wetted interface. However, in the trapezoidal features with $\theta_{flat} = 70^\circ$ and $\alpha = 25^\circ$ ($\theta_{flat} + \alpha \geq 90^\circ$), the liquid-air interface is convex shaped and the net Laplace force on the interface is upward, producing a composite interface

Fig. 9.5 Three types of hypothetical re-entrant geometries covered with liquids of various contact angles. The surfaces can become wet or form a composite interface, dependent upon the surface geometry and the liquid contact angle (adapted from Brown and Bhushan 2016a)



(Cassie-Baxter regime) with a high contact angle. As long as $\theta_{flat} + \alpha \geq 90^\circ$, a liquid with $\theta_{flat} < 90^\circ$ will result in non-wetting ($\theta_{apparent} \geq 90^\circ$). The middle row in Fig. 9.5 shows structure with re-entrant curvature (spherical, cylindrical, oval, etc.), which can provide droplet contact angles $>90^\circ$ (non-wetting) for liquids with flat contact angles $<90^\circ$, since it is possible to draw tangents on the surface with liquid-air interface being convex shaped.

The bottom row in Fig. 9.5 shows single and double re-entrant geometries. The single re-entrant geometry (left) is able to support low flat angles, close to zero angle. They could theoretically support flat contact angles of 0° . However, the presence of positive pressure in the droplet means that a liquid-vapor interface shape with upward surface tension is required and it is not possible. This is possible with double re-entrant geometries (right). This geometry incorporates vertical overhangs normal to the surface in addition to the horizontal overhangs parallel to the surface found in the single re-entrant geometry (left). Tangents on the re-entrant curvature can be drawn beyond those, parallel to the flat surface and so a convex shaped liquid-air interface can be supported, even with a fully wetted liquid (Brown and Bhushan 2016a, b).

Various re-entrant geometries have been fabricated by researchers (Tuteja et al. 2008; Zhao et al. 2011; Lee et al. 2013; Liu and Kim 2014; Brown and Bhushan 2016b).

To sum up, low surface energy, fluorinated materials are popular due to their low adhesion. Fluoropolymers have the advantage of being able to form nanoparticle composites. However, durability is typically poor. Fluorosilanes, fluorothiols, and fluorosurfactants are able to produce thinner films. However, they require surface activation or specific chemistry. Finally, fluorination via plasma conditions results in good surface coverage, though such treatments require specialty chemicals and conditions not typically suitable for scale-up. In order to achieve high contact angle, even if the contact angle on the flat surface is low, even zero, re-entrant geometries can be used. A combination of fluorination and re-entrant geometry is desirable to achieve superoleophobicity, particularly for low surface energy liquids (<20 mN/m).

9.3 Model to Predict Oleophobic/Philic Nature of Surfaces

In water, if an oil droplet is placed on a solid surface in water, a three phase solid-water-oil interface exists. The nature of oleophobicity/philicity of an oil droplet in water can be determined from the values of surface energies of various interfaces and contact angles of water and oil in air. Jung and Bhushan (2009) performed experiments in a solid-water-oil interface. They found that some hydrophilic and oleophilic surfaces (solid-air-water interface and solid-air-oil interface) can switch into an oleophobic surface in water (solid-water-oil interface).

In this section, expressions are developed for CAs for various interfaces—solid-air-water, solid-air-oil, and solid-water-oil interfaces. If a water droplet is placed on a solid surface in air, the solid-air and water-air interfaces come together with a static CA, θ_w . The value of θ_w can be determined by minimizing the total energy of the system (Adamson 1990; Israelachvili 1992), and is given by Young's equation for the CA, θ_w ,

$$\cos \theta_w = \frac{\gamma_{SA} - \gamma_{SW}}{\gamma_{WA}} \quad (9.1)$$

where γ_{SW} , γ_{SA} , and γ_{WA} are surface tensions of the solid-water, solid-air, and water-air interfaces, respectively. If an oil droplet is placed on a solid surface in air, Young's equation for the CA, θ_o , can be expressed by,

$$\cos \theta_o = \frac{\gamma_{SA} - \gamma_{SO}}{\gamma_{OA}} \quad (9.2)$$

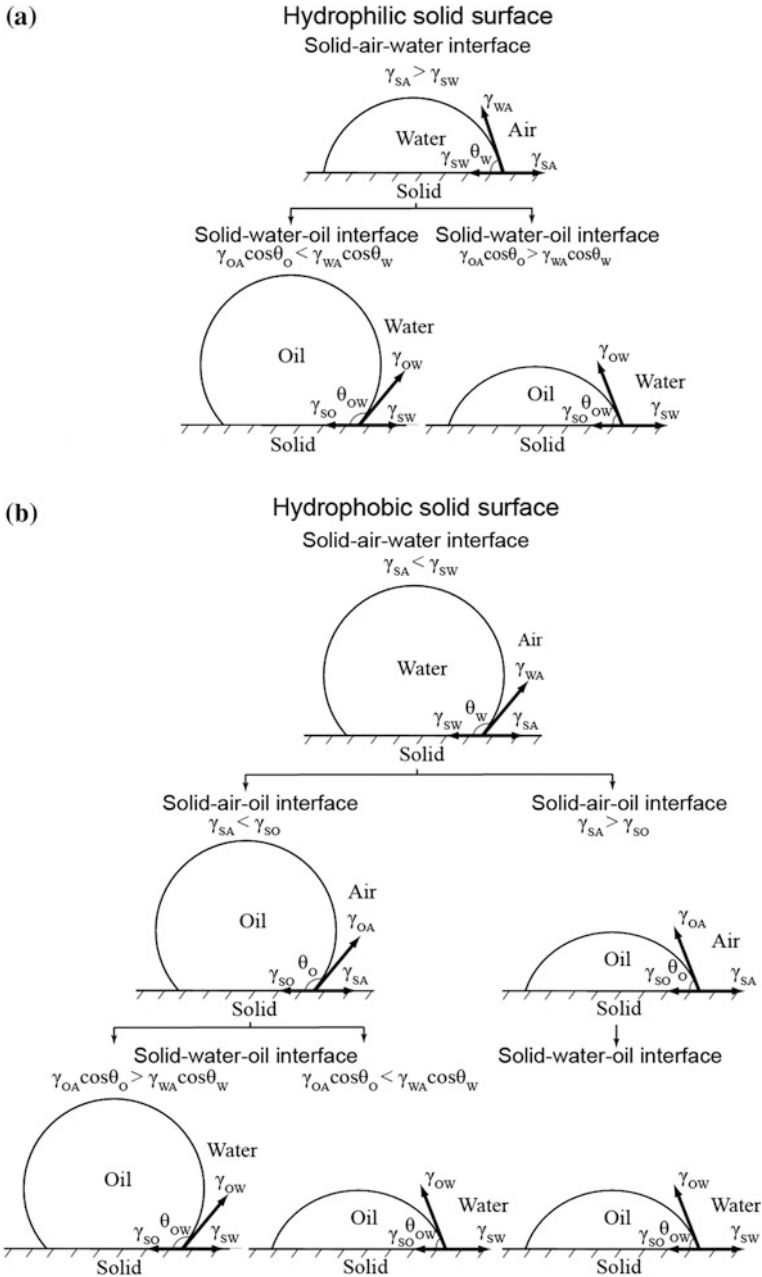


Fig. 9.6 Schematics of a droplet of liquid showing philic/phobic nature in three different phase interface on the surface— θ_w , θ_o , and θ_{ow} are static contact angles of water droplet, oil droplet, and oil droplet in water, respectively for a **a** hydrophilic solid surface, and **b** hydrophobic solid surface, and required surface properties (adapted from Jung and Bhushan 2009)

where γ_{SO} , γ_{SA} , and γ_{OA} are surface tensions of the solid-oil, solid-air, and oil-air interfaces, respectively. As predicted by (9.2), if γ_{SO} is higher than γ_{SA} , an oleophobic surface can be achieved.

To create an oleophobic surface in water, consider the solid-water-oil interface. If an oil droplet is placed on a solid surface in water, the CA of an oil droplet in water, θ_{OW} , is given by Young’s equation (Israelachivili 1992),

$$\cos \theta_{OW} = \frac{\gamma_{SW} - \gamma_{SO}}{\gamma_{OW}} \tag{9.3}$$

where γ_{SO} , γ_{SW} , and γ_{OW} are the surface tensions of the solid-oil, solid-water, and oil-water interfaces, respectively. Combining (9.1), (9.2), and (9.3), the equation for the CA, θ_{OW} , of an oil droplet in water is given by (Jung and Bhushan 2009),

$$\cos \theta_{OW} = \frac{\gamma_{OA} \cos \theta_O - \gamma_{WA} \cos \theta_W}{\gamma_{OW}} \tag{9.4}$$

As predicted by (9.4), an oleophobic surface can be created in the solid-water-oil interface on a hydrophilic surface ($\gamma_{SA} > \gamma_{SW}$) if $\gamma_{OA} \cos \theta_O$ is lower than $\gamma_{WA} \cos \theta_W$. Since the surface tension of oil and organic liquids is much lower than that of water, most hydrophilic surfaces can be made oleophobic in a solid-water-oil interface. For a surface that is hydrophobic ($\gamma_{SA} < \gamma_{SW}$) and oleophobic ($\gamma_{SA} < \gamma_{SO}$) in a solid-air-oil interface, an oleophobic surface in a solid-water-oil interface can be created if $\gamma_{OA} \cos \theta_O$ is higher than $\gamma_{WA} \cos \theta_W$ and vice versa. For a surface that is hydrophobic and oleophilic in a solid-air-oil interface, an oleophobic surface cannot be created in a solid-water-oil interface. Schematics of various cases for hydrophilic and hydrophobic surfaces and required surface properties are shown in Fig. 9.6, and the summary of surface properties required for philic/phobic nature in various interfaces is shown in Table 9.2.

Table 9.2 Summary of surface properties required for philic/phobic nature in various interfaces (Jung and Bhushan 2009)

<u>Solid-air-water interface</u>		<u>Solid-water-oil interface</u>	
Hydrophilic ($\gamma_{SA} > \gamma_{SW}$)	→	Oleophobic if $\gamma_{OA} \cos \theta_O < \gamma_{WA} \cos \theta_W$ Oleophilic if $\gamma_{OA} \cos \theta_O > \gamma_{WA} \cos \theta_W$	
<u>Solid-air-water interface</u>	<u>Solid-air-oil interface</u>	<u>Solid-water-oil interface</u>	
Hydrophobic ($\gamma_{SA} < \gamma_{SW}$)	→	Oleophobic if $\gamma_{SA} < \gamma_{SO}$	Oleophobic if $\gamma_{OA} \cos \theta_O > \gamma_{WA} \cos \theta_W$ Oleophilic if $\gamma_{OA} \cos \theta_O < \gamma_{WA} \cos \theta_W$
		Oleophilic if $\gamma_{SA} > \gamma_{SO}$	

9.4 Validation of Oleophobicity/Philicity Model for Oil Droplets in Air and Water

In this section, experiments are presented on how the oil droplets in air and in water in three phase interfaces influence wetting behavior of various surfaces.

9.4.1 Experimental Techniques

Jung and Bhushan (2009) used deionized (DI) water for the water droplet and hexadecane for the oil droplet for the measurement of the static CA in water. For analysis, the surface tensions of the water-air interface (γ_{WA}), oil-air interface (γ_{OA}), and oil-water interface (γ_{OW}) are 72 mN/m (Haynes 2014), 27.5 mN/m (Haynes 2014), and 51.4 mN/m (Tajima et al. 1980), respectively. The mass densities are 1000 and 773 kg/m³ for water and hexadecane, respectively. Water and oil droplets of about 5 μ L in volume (with radius of a spherical droplet about 1 mm) in an air environment were deposited on the specimen using a microsyringe. The process of wetting behavior of an oil droplet in water was obtained in a solid-water-oil interface system, as shown in Fig. 9.7 (Jung and Bhushan 2009). A specimen was first immersed in the water phase. Then, an oil droplet was deposited using a microsyringe from the bottom of the system, because the density of the oil (hexadecane) is lower than that of water. The image of the droplet was obtained by a digital camcorder with a 10 \times optical and 120 \times digital zoom. The images obtained were analyzed for the CA using Imagetool[®] software (University of Texas Health Science Center). The measurements were reproducible to within $\pm 2^\circ$.

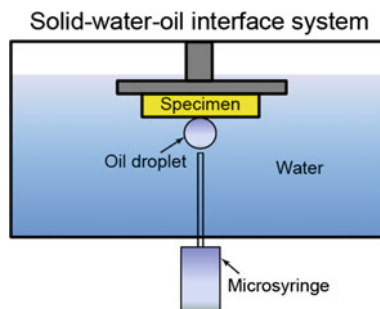


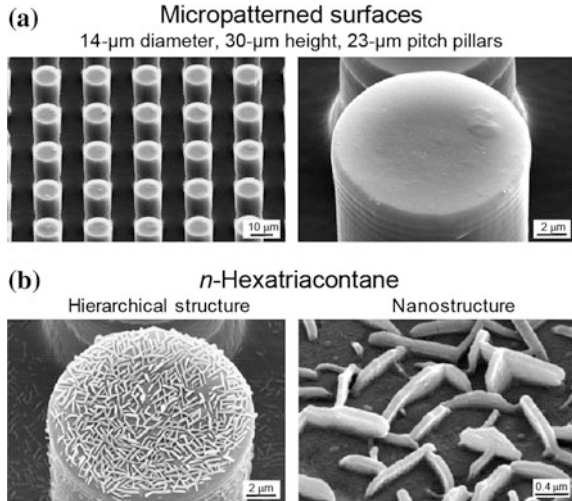
Fig. 9.7 Schematics of a solid-water-oil interface system. A specimen is first immersed in water phase, and then an oil droplet is gently deposited using a microsyringe, and the static contact angle in the system is measured (adapted from Jung and Bhushan 2009)

9.4.2 Fabrication of Oleophobic/Philic Surfaces

Micropatterned surfaces were fabricated using a two-step molding process. Microstructures were replicated using epoxy resin from master templates with varying pitch values. Master templates were created that used a flat Si surface with micropatterns fabricated by photolithography with pillars of 14 μm diameter and 30 μm height with different pitch values (21, 23, 26, 35, 70, 105, 126, 168 and 210 μm) (Jung and Bhushan 2009). To study surfaces with some oleophobicity, a surface coating that has a surface tension lower than that of oil is needed. For this purpose, Jung and Bhushan (2009) deposited *n*-perfluoroeicosane ($\text{C}_{20}\text{F}_{42}$) (268828, Sigma-Aldrich, USA) on the flat and micropatterned epoxy surfaces by thermal evaporation. The surface energy of *n*-perfluoroeicosane is 6.7 mJ/m^2 (6.7 mN/m) (Nishino et al. 1999). The specimens were mounted on a specimen holder with double-sided tape and placed in a vacuum chamber at 30 mTorr (4 kPa pressure), 2 cm above a heating plate loaded with 6000 μg *n*-perfluoroeicosane (Bhushan et al. 2009). The *n*-perfluoroeicosane was evaporated by heating it to 170 $^{\circ}\text{C}$. In a vacuum chamber, the evaporation from the point source to the substrate occurs in a straight line; thus, the amount of sublimated material is equal in a hemispherical region over the point of the source (Bunshah 1994). In order to estimate the amount of sublimated mass, the surface area of the half sphere was calculated by using the formula $2\pi r^2$, whereby the radius (r) represents the distance between the specimen to be covered and the heating plate with the substance to be evaporated. The calculated amount of *n*-perfluoroeicosane deposited on the surfaces was 2.4 $\mu\text{g}/\text{mm}^2$ (amount of *n*-perfluoroeicosane loaded on a heating plate divided by surface area) (Jung and Bhushan 2009).

Lotus leaf inspired hierarchical structures were fabricated using fabrication of microstructured surfaces by a two-step molding process with the subsequent development of nanostructures on top by self-assembly of 0.2 $\mu\text{g}/\text{mm}^2$ of *n*-hexatriacontane ($\text{C}_{36}\text{H}_{74}$), a synthetic wax, deposited by thermal evaporation, as described in Chap. 6 (Bhushan et al. 2008, 2009). Figure 9.8a shows SEM micrographs taken at a 45 $^{\circ}$ tilt angle, showing two magnifications of the micropatterned surface. Figure 9.8b shows the hierarchical structures fabricated with *n*-hexatriacontane platelets. The nanostructure is formed by three-dimensional platelets of *n*-hexatriacontane. Platelets are flat crystals, grown perpendicular to the substrate surface. The platelet thickness varied between 50 and 100 nm, and their length varied between 500 and 1000 nm. Surface energy of *n*-hexatriacontane is 31:4 mJ/m^2 (31.4 mN/m) and these surfaces are superhydrophobic and superoleophilic, as will be reported later in Fig. 9.12.

Fig. 9.8 SEM micrographs taken at a 45° tilt angle showing two magnifications of **a** the micropatterned surface, **b** hierarchical structure fabricated with three-dimensional platelets on the surface fabricated with 0.2 $\mu\text{g}/\text{mm}^2$ mass of *n*-hexatriacontane (adapted from Jung and Bhushan 2009)



9.4.3 Characterization of Oleophobic/Philic Surfaces

9.4.3.1 Wetting Behavior on Flat and Micropatterned Epoxy Surfaces

Jung and Bhushan (2009) performed experiments with water and oil droplets on hydrophilic, hydrophobic, and oleophilic surfaces in air and water to observe the wetting behavior of droplets for philic/phobic nature in air and water. Figure 9.9 shows optical micrographs of water and oil droplets in air and oil droplets in water on flat epoxy resin and micropatterned surfaces. In a solid-air-water interface with the application of a water droplet, the flat epoxy resin surface exhibited hydrophilicity and the micropatterned surface with 23 μm pitch exhibited superhydrophobicity. Jung and Bhushan (2009) reported evidence of air pocket formation between the pillars which results in a high static CA for a micropatterned surface. However, in a solid-air-oil interface with the application of an oil droplet, both surfaces exhibited oleophilicity. In the solid-water-oil interface system, in which the oil droplet sits on water trapped between the pillars, the flat epoxy resin and micropatterned surface with 23 μm pitch exhibit oleophobicity with CAs of 109° and 151°, respectively.

To study optimization of oleophobicity in the solid-air-water and solid-air-oil interfaces, the static CAs for water and oil droplets were measured on the micropatterned surfaces (Jung and Bhushan 2009). Figure 9.10 (top) shows the measured static CA as a function of pitch between the pillars for a water droplet (circle) and an oil droplet (cross) in air. The data are compared with predicted static CA values obtained using the Wenzel and Cassie-Baxter equations (Chap. 6) (solid lines) with a measured value of θ_0 for the micropatterned surfaces. In a solid-air-water interface for a water droplet, the flat epoxy resin (pitch value = 0) showed a static CA of 76°. The static CA on micropatterned surfaces is higher than

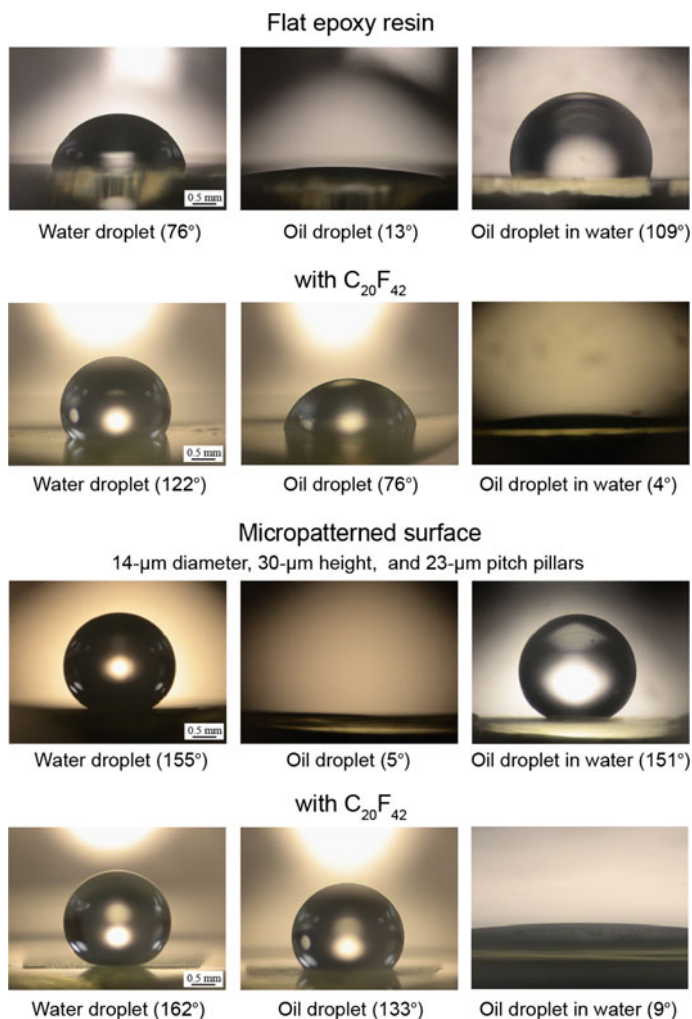
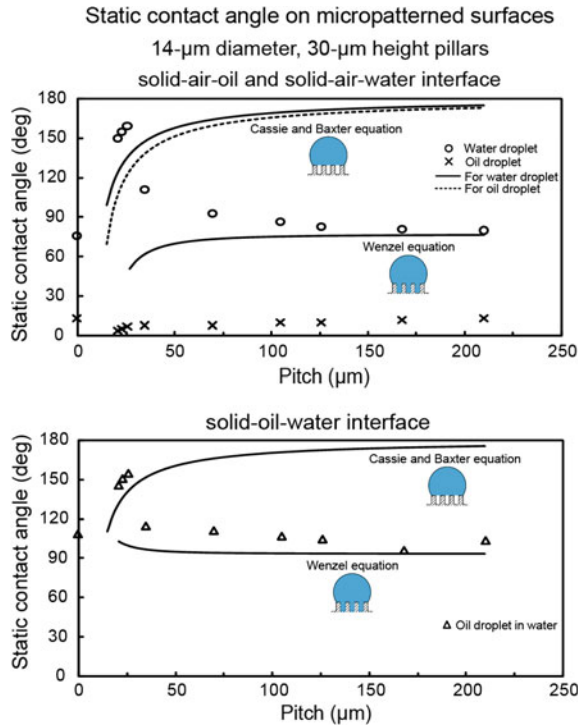


Fig. 9.9 Optical micrographs of droplets in air and under water on flat epoxy resin and micropatterned surface without and with $C_{20}F_{42}$. *Left image* A water droplet is placed on a surface in air. *Middle image* An oil droplet is placed on a surface in air. *Right image* An oil droplet is placed on a solid surface in water (adapted from Jung and Bhushan 2009)

that of the flat surfaces. CA first increases with an increase in the pitch values, then starts to drop rapidly to a value slightly higher than that of the flat surfaces. In the first portion, it jumps to a high value of 150° , corresponding to a superhydrophobic surface, and continues to increase to 160° at a pitch of $26\ \mu\text{m}$ because open air space between pillars increases with an increase in pitch. This open air space is responsible for the propensity of air pocket formation. The sudden drop at a pitch value of about $30\ \mu\text{m}$ corresponds to the transition from the Cassie-Baxter to the

Fig. 9.10 Static contact angle as a function of pitch value for water droplet (circle) and oil droplet (cross) in air (top), and oil droplet in water (triangle) (bottom) compared with predicted static contact angle values obtained using Wenzel and Cassie-Baxter equations (solid lines) with a measured value of static contact angle for the micropatterned surfaces (adapted from Jung and Bhushan 2009)



Wenzel regime. The experimental observations for the transition are comparable to the value predicted from Wenzel and Cassie-Baxter equations (Jung and Bhushan 2009).

At a solid-air-oil interface for an oil droplet, the flat epoxy resin showed a static CA of 13°. As shown in Fig. 9.10 (top), with the application of an oil droplet, all micropatterned surfaces were found to be oleophilic, and the CA was lower than that of the flat surfaces. It increases with an increase in the pitch values, as predicted from Wenzel equation. As mentioned earlier, the surface tension of the oil-air interface is very low for hexadecane. Therefore, it is observed that from (9.3) that the surface tension of solid-oil interface (γ_{SO}) is lower than that of solid-water interface (γ_{SW}), resulting in oleophilic state for all micropatterned surfaces (Jung and Bhushan 2009).

To study optimization of oleophobicity in a solid-water-oil interface, the static CAs for oil droplets in water were measured on the micropatterned surfaces (Jung and Bhushan 2009). Figure 9.10 (bottom) shows the measured static CA as a function of pitch between the pillars for an oil droplet in water (triangle). The data are compared with the predicted static CA values obtained using the Wenzel and Cassie-Baxter equations (Chap. 6) (solid lines), with a measured value of θ_0 for the micropatterned surfaces. In a solid- water-oil interface, with the application of an oil droplet, the flat epoxy resin was found to be oleophobic and had a static CA of

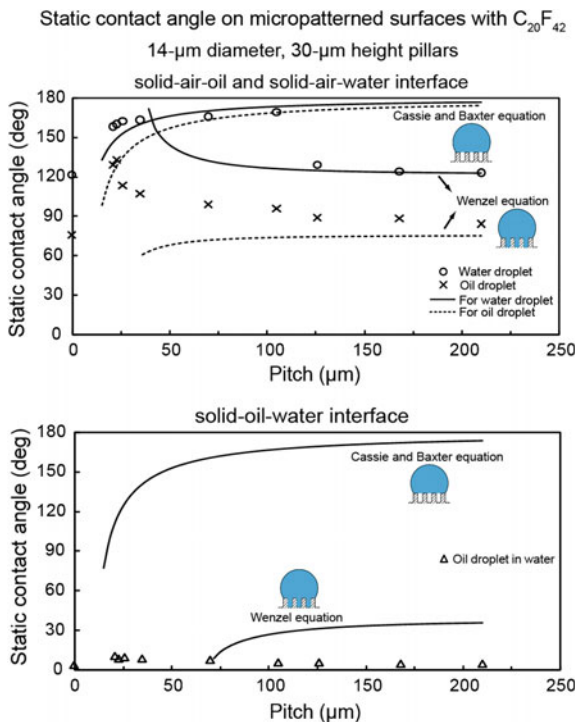
109°. The static CA of micropatterned surfaces in the solid-water-oil interface showed a similar trend to that in the solid-air-water interface. As the pitch increases up to 26 μm , the static CA first increases gradually from 146° to 155°, because the oil droplet sits on water trapped between the pillars, and open space increases with an increase in pitch. Then, the CA starts decreasing rapidly due to the transition from the Cassie-Baxter to the Wenzel regime. The experimental observations for the transition are comparable to the values predicted from Wenzel and Cassie-Baxter equations. The micropatterned surfaces studied here were either hydrophilic or hydrophobic and both were oleophilic. In the solid-water-oil interface, they were oleophobic. However, hydrophilic surfaces became oleophobic in the solid-water-oil interface because $\gamma_{OA} \cos \theta_O$ is higher than $\gamma_{WA} \cos \theta_W$ (Jung and Bhushan 2009).

9.4.3.2 Wetting Behavior on Flat and Micropatterned Surfaces with $\text{C}_{20}\text{F}_{42}$

To study surfaces with some oleophobicity, *n*-perfluoroeicosane ($\text{C}_{20}\text{F}_{42}$), which has a lower surface tension than that of oil, was deposited on the surfaces, and experiments with droplets on hydrophobic and both oleophilic and oleophobic surfaces in air were performed (Jung and Bhushan 2009). Figure 9.9 shows the optical micrographs of droplets in three different phase interfaces on a flat epoxy resin and a micropatterned surface with $\text{C}_{20}\text{F}_{42}$. In a solid-air-water interface and a solid-air-oil interface, the water droplet and oil droplet showed CAs of 122° and 76° for the flat epoxy resin with $\text{C}_{20}\text{F}_{42}$ and CAs of 162° and 133° for the micropatterned surface with 23 μm pitch with $\text{C}_{20}\text{F}_{42}$, respectively. However, in a solid-water-oil interface with the application of an oil droplet in water, both surfaces exhibited oleophilicity and had contact angles of 4° and 9°, respectively. To explain why the oleophobic surfaces in air became oleophilic in water, the theoretical values for both surfaces were calculated using (9.4). For calculations, the surface tensions of the water-air interface (γ_{WA}), oil-air interface (γ_{OA}), and oil-water interface (γ_{OW}) were taken to be 72, 27.5, and 51.4 mN/m, and the contact angles for water and oil droplets in air were taken from the measured values. The theoretical values for the flat epoxy resin and the micropatterned surface with 23 μm pitch with $\text{C}_{20}\text{F}_{42}$ are 28° and 10°, respectively. These values are similar to those from the experiments. This indicates that the oleophobic surfaces become oleophilic in water (Jung and Bhushan 2009).

To study optimization of oleophobicity in two solid-air-water and solid-air-oil interfaces, the static CAs for water and oil droplets were measured on the micropatterned surfaces with different pitch values and with $\text{C}_{20}\text{F}_{42}$ (Jung and Bhushan 2009). Figure 9.11 shows the measured static CA as a function of pitch between the pillars for a water droplet (circle) and an oil droplet (cross) in air. The data are compared with the predicted static CA values obtained using the Wenzel and Cassie-Baxter equations (Chap. 6) (solid lines) with a measured value of θ_0 for the micropatterned surfaces with $\text{C}_{20}\text{F}_{42}$. In a solid-air-water interface for the water

Fig. 9.11 Static contact angle as a function of pitch value for water droplet (*circle*) and oil droplet (*cross*) in air, and oil droplet in water (*triangle*) compared with predicted static contact angle values obtained using Wenzel and Cassie-Baxter equations (*solid lines*) with a measured value of static contact angle for the micropatterned surfaces with $C_{20}F_{42}$ (adapted from Jung and Bhushan 2009)



droplet, the flat epoxy resin with $C_{20}F_{42}$ showed a static CA of 122° . The static CA of micropatterned surfaces with $C_{20}F_{42}$ first increases from 158° to 169° with an increase in the pitch values, then drops rapidly at a pitch value of $110\ \mu\text{m}$. From comparison of the experimental data to the Wenzel and Cassie-Baxter equations, this corresponds to the transition from Cassie-Baxter to Wenzel regime. All surfaces with $C_{20}F_{42}$ had an increase in CA, and the transition took place at higher pitch value than that of the micropatterned surfaces (Fig. 9.10) (Jung and Bhushan 2009).

At a solid-air-oil interface for an oil droplet, the flat epoxy resin with $C_{20}F_{42}$ showed a static CA of 76° . As shown in Fig. 9.11, the highest CA of micropatterned surfaces with $C_{20}F_{42}$ was 133° at a pitch value of $23\ \mu\text{m}$. Then, it decreases with an increase in the pitch values, and these values are comparable with the values predicted by the Wenzel equations. The CAs of all micropatterned surfaces with $C_{20}F_{42}$ are higher than that of the flat surfaces (Jung and Bhushan 2009).

To study optimization of oleophobicity in a solid-water-oil interface, the static CAs for oil droplets in water were measured on the micropatterned surfaces with different pitch values and with $C_{20}F_{42}$ (Jung and Bhushan 2009). Figure 9.11 shows the measured static CA as a function of pitch between the pillars for an oil droplet in water (triangle). The data are compared with the predicted static CA values obtained using the Wenzel and Cassie-Baxter equations (Chap. 6) (solid lines) with a measured value of θ_0 for the micropatterned surfaces with $C_{20}F_{42}$. In a solid-

water-oil interface, the flat epoxy resin with $C_{20}F_{42}$ was oleophilic and had a static CA of 4° . All micropatterned surfaces with $C_{20}F_{42}$ were oleophilic and had CAs lower than 10° . The reason why hydrophobic and oleophobic surfaces in air became oleophilic in water can be explained from Fig. 9.6 and Table 9.2. The CA for a water droplet is higher than that for an oil droplet on all surfaces with $C_{20}F_{42}$, and the surface tension of the water-air interface (γ_{WA}) is higher than that of the oil-air interface (γ_{OA}). Therefore, it is observed that $\gamma_{WA} \cos \theta_W$ is higher than $\gamma_{OA} \cos \theta_O$, and then the surfaces become oleophilic in the solid-water-oil interface (Jung and Bhushan 2009).

9.4.3.3 Wetting Behavior on Nano- and Hierarchical Structures and Shark Skin Replica

To observe the wetting behavior of oil droplets for nano- and hierarchical structures found in lotus plant surfaces, experiments with the droplets on the surfaces in air and water were performed (Jung and Bhushan 2009). In addition, shark skin replicas without and with $C_{20}F_{42}$ coatings were tested. Shark skin is known to exhibit hydrophilicity and oleophobicity in water (Jung and Bhushan 2009).

Figure 9.12 shows the optical micrographs of water and oil droplets in air and oil droplets in water on a nanostructure and a hierarchical structure fabricated with $0.2 \mu\text{g}/\text{mm}^2$ mass of *n*-hexatriacontane. Both nano- and hierarchical structures were

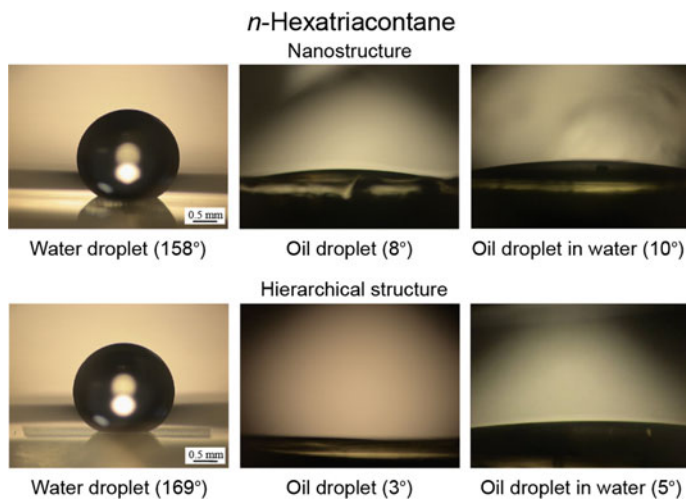


Fig. 9.12 Optical micrographs of droplets in three different phase interfaces on nanostructure and hierarchical structure fabricated with $0.2 \mu\text{g}/\text{mm}^2$ mass of *n*-hexatriacontane. *Left image* A water droplet is placed on a surface in air. *Middle image* An oil droplet is placed on a surface in air. *Right image* An oil droplet is placed on a solid surface in water (adapted from Jung and Bhushan 2009)

superhydrophobic and had a static CA of 158° and 169° in the solid-air-water interface, respectively. However, they were oleophilic in the solid-air-oil interface because the surface energy of *n*-hexatriacontane is 31.4 mJ/m^2 (31.4 mN/m) (Wu 1979), and this value is higher than that of an oil droplet (hexadecane). In the solid-water-oil interface, nano- and hierarchical structures had a static CA of 10° and 5° , respectively. Based on Fig. 9.6 and Table 9.2, both surfaces are expected to be oleophilic in solid-water-oil interface (Jung and Bhushan 2009).

To study the surface structure on an aquatic animal, experiments with water and oil droplets on shark skin replica were performed in a three phase interface (Jung and Bhushan 2009). Figure 9.13 shows the optical micrographs of water and oil droplets in air and oil droplets in water on a shark skin replica without and with $\text{C}_{20}\text{F}_{42}$. First, the shark skin replica had CAs of 89° and $\sim 0^\circ$ for water and oil droplets, respectively. After the surface was coated with $\text{C}_{20}\text{F}_{42}$, the CAs of water and oil droplets became 142° and 115° , respectively. In the solid-water-oil interface with the application of an oil droplet in water, the shark skin replica was found to be oleophobic, and had a CA of 109° . Based on (9.4), the calculated value was 59° for the oil droplet in water on a shark skin replica. This difference may come from the open space under the scales of the shark skin replica (Fig. 9.2) responsible for the propensity of trapped water pocket formation. Shark skin replica with $\text{C}_{20}\text{F}_{42}$ was oleophilic and had a contact angle of $\sim 0^\circ$. This state is the same as the micropatterned surfaces with $\text{C}_{20}\text{F}_{42}$ based on Fig. 9.6 and Table 9.2 (Jung and Bhushan 2009).

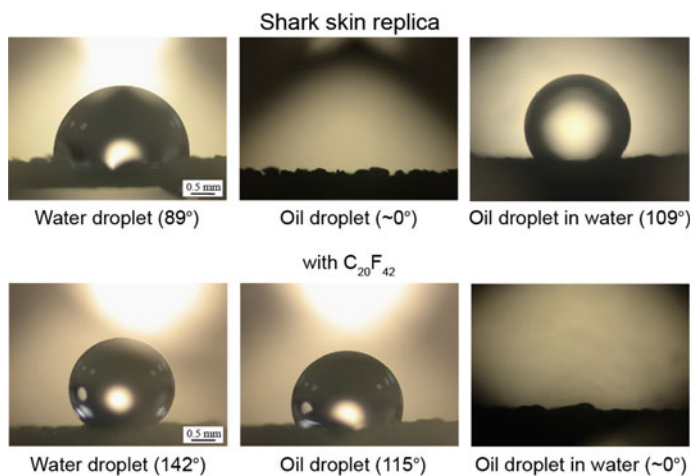


Fig. 9.13 Optical micrographs of droplets in three different phase interfaces on shark skin replica without and with $\text{C}_{20}\text{F}_{42}$. *Left image* A water droplet is placed on a surface in air. *Middle image* An oil droplet is placed on a surface in air. *Right image* An oil droplet is placed on a solid surface in water (adapted from Jung and Bhushan 2009)

9.4.4 Summary

The wetting behavior of water and oil droplets for hydrophobic/philic and oleophobic/philic surfaces in air and water was studied. In underwater applications, oleophobicity/philicity of an oil droplet in water was studied on surfaces with different surface energies of various interfaces. Additionally, CAs of water and oil droplets in air were studied. Based on the model, it was found that for a hydrophilic surface, an oleophobic surface in the solid-water-oil interface can be created if $\gamma_{OA} \cos \theta_O$ is lower than $\gamma_{WA} \cos \theta_W$. For a hydrophobic surface and an oleophobic surface in solid-air-oil interface, an oleophobic surface in solid-water-oil interface can be created if $\gamma_{OA} \cos \theta_O$ is higher than $\gamma_{WA} \cos \theta_W$.

To validate the model for predicting the oleophobic/philic nature of the surfaces, flat and micropatterned surfaces with varying pitch values were produced by soft lithography. *n*-perfluoroeicosane ($C_{20}F_{42}$) with low surface energy (6.7 mN/m) was deposited by thermal evaporation to produce superhydrophobic and oleophobic flat and micropatterned surfaces. For water and oil droplets in water in three phase interfaces, the experimental observations showed that there was a good agreement between the measured CA and the predicted values of models. It was also found that the transition from the Cassie-Baxter to the Wenzel regime can occur for hydrophobic and oleophobic micropatterned surfaces with a larger distances between pillars.

The wetting behavior of the nano- and hierarchical structures found in lotus leaf surfaces and shark skin replica was also investigated. It was found that the nano- and hierarchical structures with *n*-hexatriacontane were oleophilic due to the high surface energy of *n*-hexatriacontane. The structure of the shark skin replica showed a higher propensity for trapped water pocket formation, resulting in a higher CA than the theoretical value. In contrast, the shark skin replica with $C_{20}F_{42}$ had a CA of $\sim 0^\circ$ in the solid-water-oil interface, as predicted by the model. For self-cleaning and antifouling, an oleophobic surface can be created based on this study (Jung and Bhushan 2009).

9.5 Mechanically Durable Nanoparticle Composite Coatings for Superoleophobicity

Superoleophobic nanoparticle composite coatings have been fabricated by various investigators. Table 9.3 summarizes coatings fabricated using various resin binder, nanoparticle or substrate geometry, solvent, deposition method, substrate and coating thickness with their CA, CAH, TA values, and any mechanical durability data (adapted from Muthiah et al. 2013; Wang and Bhushan 2015).

Muthiah et al. (2013) and Wang and Bhushan (2015) were the first to develop a mechanically durable coating with anti-smudge properties and transparency. They used a dual layer approach. Wang and Bhushan (2015) used the first layer to

Table 9.3 Literature review on binder and nanoparticle systems, deposition methods and substrates used in fabrication of superoleophobic surfaces with their contact angle (CA), contact angle hysteresis (CAH), and tilt angle (TA) values and mechanical durability (adapted from Muthiah et al. 2013; Wang and Bhushan 2015)

Resin binder	Nanoparticle or substrate geometry, solvent, deposition method, substrate, coating thickness	CA (°)	Summary and comments
Fluorinated monoalkylphosphate	Anodized aluminum surface, ethanol, immersion coating (Tsujii et al. 1997)	CA (rapeseed oil) 150 CA (water) 150	A rough anodized aluminum substrate used
Fluorinated acrylic copolymer in water (Zonyl 8740 or Capstone ST-100—Dupont Co.)	TiO ₂ nanoparticles (20–50 nm), water, spray coating on Si wafer (Hsieh et al. 2005)	CA (ethylene glycol) 144 CA (water) 164	Larger P–B ratio gives higher CA
	ZnO nanoparticles (50 nm), water/acetone, spray coating on glass (Steele et al. 2009)	CA (hexadecane) 154 CAH (hexadecane) 6 CA (water) 168	P–B ratio at 3.3 yielded most superoleophobic and 1.6 yielded most superhydrophobic surfaces
Carbon nanofibers (CNF) (100 nm dia., length ~ 130 μm), water/acetone + formic acid, spray coating on glass and sand paper, 5 μm thick (Das et al. 2012)	SiO ₂ nanoparticles (30–50 nm) by sol-gel method, water, spin coating on Si wafer, 6 μm thick (Hsieh et al. 2009)	CA (ethylene glycol) 165 CAH (ethylene glycol) 3 CA (water) 168 CAH (water) 2	Based on P–B ratios, F/Si atomic ratio of 2.1 found to be best for water and ethylene glycol repellency
	SiO ₂ nanoparticles (55 nm), acetone, dual-layered coating (dip coating of fluoroacrylic and spray coating of fluoroacrylic + SiO ₂), glass (Muthiah et al. 2013)	CA (mineral oil) 164 TA (mineral oil) 9 CA (water) 164 TA (water) 5	CNF with heat transfer characteristics may find applications in fabricating icephobic surfaces
		CA (hexadecane) 147 CAH (hexadecane) 12 CA (ethylene glycol) 153 CAH (ethylene glycol) 11 CA (water) 160 CAH (water) 9	P–B ratio at 0.6 yielded most superomphobic coating Mechanically durable and anti-smudge

(continued)

Table 9.3 (continued)

Resin binder	Nanoparticle or substrate geometry, solvent, deposition method, substrate, coating thickness	CA (°)	Summary and comments
1H,1H,2H,2H-heptafluorodecyl modified polyhedral oligomeric silsesquioxane (FluoroPOSS)	FluoroPOSS, poly(methyl methacrylate) (PMMA) and Asahiklin AK-225 (consists of 3,3-dichloro-1,1,1,2,2-pentafluoropropane and 1,3-dichloro-1,1,1,2,3-pentafluoropropane), electrospinning to produce fibers (bead size 10–20 μm) (Tuteja et al. 2008)	CA _{adv} (hexadecane) 156 CAH (hexadecane) 6 TA (hexadecane) 5	A blend of hydrophilic PMMA and low energy fluoroPOSS is used to generate re-entrant surfaces
	FluoroPOSS and Asahiklin AK-225 by dip coating on Si wafer with microhooodoo re-entrant geometry (width = 10 μm, spacing = 20 μm and height = 7 μm) silanized (Tuteja et al. 2008)	CA _{adv} (hexadecane) > 150	Re-entrant geometry explored
	Electrospun coating of cross-linked PDMS/fluoroPOSS on stainless steel wire meshes, Asahiklin 225/methylformamide (Pan et al. 2013)	CA (PDMS) > 150 CAH (PDMS) 6 TA (PDMS) 1.5 CA (hexadecane) > 150 CAH (hexadecane) 5 TA (hexadecane) 1.5	Hierarchical scales of re-entrant texture Chemical resistant to various liquids
(Heptafluoro-1,1,2,2-tetrahydrodecyl) triethoxysilane (Gelest Inc.) or 1H,1H,2H,2H-perfluorodecyltriethoxysilane (Degussa Chemical Company)	Fluorinated SiO ₂ nanoparticles, isopropanol, spin coating, glass (Sheen et al. 2008)	CA (xylene) 141 CA (diiodomethane) 159 CA (water) 168	Sol-gel method was used for fabrication of fluorinated SiO ₂ nanoparticles
(Heptafluoro-1,1,2,2-tetrahydrodecyl) trimethoxysilane (Gelest Inc.) or 1H,1H,2H,2H-perfluorodecyltrimethoxysilane (Sigma-Aldrich)	SiO ₂ nanoparticles (~150 nm), acetone, saturating cotton fabrics in solution and irradiating with microwave-assisted synthetic techniques (Lovingood et al. 2013)	CA (hexadecane) 137 CA (water) 157	Repel liquid and adsorb organic vapors from liquid droplets. High

(continued)

Table 9.3 (continued)

Resin binder	Nanoparticle or substrate geometry, solvent, deposition method, substrate, coating thickness	CA (°)	Summary and comments
PTFE amorphous fluoropolymer (Teflon AF 2400—Dupont Co.)	Coaxial-electrospinning of polycaprolactam (PCL)/2,2,2-trifluoroethanol core and Teflon AF 2400/FC-75 (perfluorocarbon) sheath fibers (~2 µm in diameter) on aluminum-foil (Han and Steckl 2009)	CA (hexadecane) 138 CA (ethylene glycol) 155 CA (water) 160 CAH (water) 4 TA (water) 7	affinity for 3-hepten-2-one vapor Teflon AF 2400 is made electrospinnable by coaxial-electrospinning process using PCL
	PTFE amorphous fluoropolymer and FC-40 (perfluorocarbon) spin coating on polydimethylsiloxane (PDMS) surface with inverse-trapezoid (height = 12 µm, width = 26 µm, pitch = 40 µm) (Im et al. 2010)	CA (methanol) 135 CA (water) 153 CAH (water) 18	Transparent, flexible, re-entrant surface was explored
n-perfluoroeicosane (268828, Sigma-Aldrich)	Thermal evaporation on to micropatterned Si wafer with cylindrical pillars (diameter = 14 µm, height = 30 µm and pitch = 23 µm) (Jung and Bhushan 2009)	CA (hexadecane) 133 CA (water) 160	A model for predicting CA of water and oil droplets evaluated
1H,1H,2H,2H-Perfluorodecyltrichlorosilane (ABCR Germany)	Si nanofilaments grown on trichloromethylsilane treated glass, dry toluene, immersion coating (Zhang and Seeger 2011)	CA (decane) 163 CA (dodecane) 167 CA (hexadecane) 174	Optically transparent Stable against outdoor conditions, ozone, UV light, basic and acid
Perfluorooctanoic acid	Spray coating of copper perfluorooctanoate from perfluorooctanoic acid and copper acetate on glass, ethanol, 150 µm thick (Yang et al. 2011)	CA (dodecane) 150 CAH (dodecane) 23 CA (hexadecane) 155 CAH (hexadecane) 22	Apply to any surface Stable to high speed rotation (4000 rps).

(continued)

Table 9.3 (continued)

Resin binder	Nanoparticle or substrate geometry, solvent, deposition method, substrate, coating thickness	CA (°)	Summary and comments
Trichloro(1H,1H,2H,2H-perfluorooctyl) silane, or tridecafluoro-1,1,2,2-tetrahydrooctyltrichlorosilane, or 1H,1H,2H,2H-perfluorooctyl-trichlorosilane (Sigma-Aldrich, Gelest Inc., ABCR, or Alfa Aesar Inc.)	SiO ₂ nanoparticles (10–30 nm), spin coating of PDMS/SiO ₂ on glass and sinter to degrade PDMS, toluene, immersion coating (He et al. 2011)	CA (diiodomethane) 141 TA (diiodomethane) 6 CA (water) 153 TA (water) 6	Fragile to scratch but easy to repair by re-spray Optically transparent Thermally stable to 95 °C and stable to outdoor condition. Poor durability to ultrasonic bath damage and adhesive tape peeling
	Molecular vapor deposition on micropatterned Si wafer with cylindrical pillars (diameter = 2.7 μm, height = 7 μm and pitch = 6 μm) (Zhao et al. 2011)	CA (hexadecane) 158 TA (hexadecane) 10 CA (water) 156 TA (water) 10	Various fluorosilane coatings explored on patterned surface
	CVD of tetraethoxysilane on glass with carbon particles (40 nm) and calcination to form a silica shell first and then CVD of resin binder, ~8 μm thick (Deng et al. 2012)	CA (hexadecane) 156 TA (hexadecane) 5 CA (ethylene glycol) 160 TA (ethylene glycol) 2 CA (water) 165 TA (water) 1	Optically transparent Limited resistant to sand abrasion (5 min) and coating peeled off by adhesive tape. Thermally stable to 400 °C
	CVD of resin binder on SiO ₂ aerogel (nanoparticle network), 1–2 mm thick (Jin et al. 2013)	CA _{adv.} (mineral oil) 168 CAH (mineral oil) 38 TA (mineral oil) 10 CA _{adv.} (water) 172 CAH (water) 22	Mechanically durable to sand abrasion. After sandpaper abrasion, CAH decreased to 14

(continued)

Table 9.3 (continued)

Resin binder	Nanoparticle or substrate geometry, solvent, deposition method, substrate, coating thickness	CA (°)	Summary and comments
		TA (water) 2	for mineral oil and 1 for water
	SiO ₂ nanoparticles (55 nm), THF/IPA, dual-layered coating (dip coating of methylphenyl silicone, O ₂ plasma, and vapor deposited perfluorotrichlorosilane. (Wang and Bhushan 2015)	CA (hexadecane) 153 CAH (hexadecane) 4 CA (ethylene glycol) 165 CAH (ethylene glycol) 3 CA (water) 170 CAH (water) 2	P-B ratio of 3 yielded most superomphobic coating Mechanically durable, anti-smudge, optically transparent
Fluorinated 3,4-ethylenedioxypropylene (EDOP) monomer	Electropolymerization onto Si arrays of cylindrical micropillars (13 mm dia., 25 μm height, 40 μm distance between cylinders, photolithography and coated by gold first) (Darmanin et al. 2011)	CA _{adv} (hexadecane) 155 CAH (hexadecane) 40 TA (hexadecane) 26 CA _{adv} (sunflower oil) 155 CAH (sunflower oil) 4 TA (sunflower oil) 3	Super oil-repellency
	Electrochemical polymerization of monomer with micro/nano roughness on gold plate (Bellanger et al. 2012)	CA (hexadecane) 150 CAH (hexadecane) 22 TA (hexadecane) 11 CA (water) 157 CAH (water) 2 TA (water) 1	EDOP with different chain length found to affect surface morphology of polymer film
Fluorinated polyurethane	Fluorinated multi-walled carbon nanotubes (MWCNTs, 20–40 nm dia. and 30–50 mm length), acetone/toluene, spray coating on glass (Wang et al. 2012)	CA (hexadecane) 152 CA (water) 162	A coralline-like structure formed

(continued)

Table 9.3 (continued)

Resin binder	Nanoparticle or substrate geometry, solvent, deposition method, substrate, coating thickness	CA (°)	Summary and comments
Fluoropolymer (copolymer of ethylene, tetrafluoroethylene and perfluoromethylvinyl ether, and a cure site monomer) (Viton ETP-600S—Dupont Co.)	SiO ₂ aggregates (92 m ² /g) (fluoroalkyl-functionalized), AsahiKlin AK-225G (1,3-dichloro-1,2,2,3,3-pentafluoropropane), spray coating on Si wafer (Campos et al. 2012)	CA _{adv} (hexadecane) 155 TA (hexadecane) 25 CA _{adv} (rapeseed oil) 158 TA (rapeseed oil) 8 CA _{adv} (water) 165 TA (water) 1	Based on various particle-to-binder mass fractions, 80/20 (w/w-) yielded maximum hexadecane CA values

P-B ratio—Particle-to-binder ratio, *CVD*—Chemical vapor deposition
 Surface tension of DI water = 72.0 mN/m, ethylene glycol = 48.0 mN/m, hexadecane = 27.0 mN/m, methanol = 22.1 mN/m (Haynes 2014), mineral oils, rapeseed oil = 30–35 mN/m (Muthiah et al. 2013), sunflower oil = ~ 31 mN/m (Darmanin et al. 2011), PDMS = 20 mN/m, xylene = 29.5 mN/m (Pan et al. 2013), diiodomethane = 50.8 mN/m, dodecane = 25.4 mN/m, decane = 23.8 mN/m (Zhang and Seeger 2011)

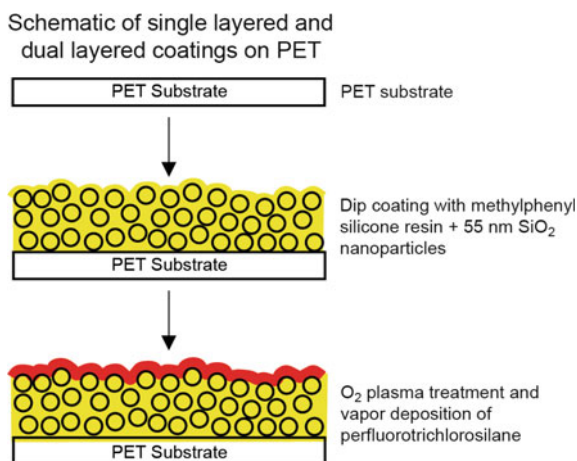
provide durability and optical transparency, and the second layer to provide superoleophobicity and anti-smudge properties. This section is based on their work.

9.5.1 Experimental Details

A dual layer coating was fabricated on polyethylene terephthalate (PET) substrate as shown in Fig. 9.14 (Wang and Bhushan 2015). PET substrate was selected because of its transparency, flexibility, low price, and light weight. These are important characteristics for various industrial applications, including smart screens for electronic display.

The first layer of a durable binder-nanoparticle nanocomposite was selected to provide mechanical durability. Methylphenyl silicone resin was selected because it is known to be durable and offer strong adhesion between nanoparticles and substrate (Ebert and Bhushan 2012). Hydrophobic SiO_2 nanoparticles with methyl groups were selected because they have high hardness to resist wear and high visible transmittance to provide transparency. Dip coating technique for application of particles was selected because it is simple, versatile, and provides a uniform coating. The second layer of a chemically active perfluorotrichlorosilane binder was selected, based on previous experience (Table 9.2) and commercial availability (He et al. 2011; Zhao et al. 2011; Deng et al. 2012; Jin et al. 2013). Fluorinated compounds generally have poor adherence, and effective attachment requires the substrates to be chemically active. Perfluorotrichlorosilane may also hydrolyze when in contact with water and this promotes its condensation. Oxygen plasma treatment was used to create active hydroxyl groups ($-\text{OH}$) at the surface of the first layer to form covalent bonds with the second layer of perfluorotrichlorosilane. Initially, it was deposited using dip and vapor deposition approaches by Wang and

Fig. 9.14 Schematic of single layer of dip coated PET and dual layer of vapor deposition of perfluorotrichlorosilane on plasma treated, dip coated PET (adapted from Wang and Bhushan 2015)



covalently attached, cross-linked polymeric layers (chemical bonding) (Wang and Bhushan 2015).

CA, CAH, and TA, surface topography, coating thickness, wear resistance on microscale and macroscale, and anti-smudge properties were measured. Liquids used for contact angle measurements included DI water with a surface tension of 72 mN/m, ethylene glycol with a surface tension of 48 mN/m, and hexadecane with a surface tension of 27 mN/m (Haynes 2014). Anti-smudge properties were measured with a homemade anti-smudge screening apparatus, a new characterization technique not described in the previous chapters (Bhushan and Muthiah 2013). The sample first was contaminated with silicon carbide (SiC, 400 mesh particle size, 357391, Sigma-Aldrich) in a glass chamber (0.3 m diameter and 0.6 m high) by blowing 1 g of SiC powder onto a sample at 10 s at 300 kPa and allowed to settle for 30 min. The contaminated sample was secured on a stage in the anti-smudge apparatus. Then, an oil (hexadecane)-impregnated microfiber wiping cloth was glued to a horizontal glass rod fixed on a cantilever (radius 0.5 mm) above the sample. As the cloth was brought in contact with the sample, the microfiber cloth rubbed the contaminated sample under a load of 5 g for 1.5 cm at a speed of about 0.2 mm/s. Photographs were taken using an optical microscope with a CCD camera (Nikon, Optihot-2). The removal and transfer of nanoparticles by the cloth was compared before and after tests.

9.5.2 Results and Discussion

Wettability of coated surfaces is presented with CA, CAH and TA, and optimization of the particle to binder (P–B) ratio of the single layer for the highest value of CA with the lowest CAH of interest (Wang and Bhushan 2015). Surface roughness and coating thickness data are reported. Wear resistance, anti-smudge properties, and transparency data are presented.

9.5.2.1 Wettability of Coated Samples

The measured CA, CAH, and TA values of water, ethylene glycol and hexadecane on coated and uncoated PET samples with their relative durability based on AFM experiment are shown in Table 9.4. The uncoated PET is hydrophilic in water and oleophilic in ethylene glycol. The uncoated PET substrate became completely wet as a hexadecane droplet was deposited with a CA close to 0°.

Single Layer Coating

In the initial experiments, for comparison, both hydrophobic and hydrophilic SiO₂ nanoparticles were used. The same procedure was followed with both types of particles. Lower CA with hydrophilic nanoparticles was obtained probably because of agglomeration of nanoparticles in the dip coating solution due to hydrogen

Table 9.4 Measured contact angle (CA), contact angle hysteresis (CAH), and tilt angle (TA) values and relative durability for coated PET samples at a particle-to-binder ratio (P-B) ratio of 3 (adapted from Wang and Bhushan 2015)

Samples	DI water (°)			Ethylene glycol (°)			Hexadecane (°)			Relative durability based on AFM experiment	Comments
	CA	CAH	TA	CA	CAH	TA	CA	CAH	TA		
PET substrate	78 ± 2	20 ± 2	>90	55 ± 2	22 ± 2	>90	~0	N/A	>90	Baseline	Hydrophilic
Single layer coating—methylphenyl silicone resin + SiO ₂											
Dip deposition of methylphenyl silicone resin + SiO ₂ (~300 nm thick)	165 ± 2	2 ± 1	2 ± 1	140 ± 3	9 ± 2	>90	~0	N/A	>90	Excellent	Superhydrophobic oleophobic/oleophilic
Single layer coating—perfluorotrichlorosilane											
Vapor deposition of perfluorotrichlorosilane (~200 nm thick)	106 ± 3	14 ± 2	>90	92 ± 4	17 ± 2	>90	76 ± 3	19 ± 2	>90	Good	Hydrophobic oleophobic/oleophilic
Dual layer coating—methylphenyl silicone resin + SiO ₂ + plasma treatment + perfluorotrichlorosilane											
Vapor deposition of perfluorotrichlorosilane (~300 nm thick)	170 ± 2	2 ± 1	1 ± 1	165 ± 2	3 ± 2	2 ± 2	153 ± 2	4 ± 2	4 ± 2	Excellent	Superhydrophobic superoleophobic

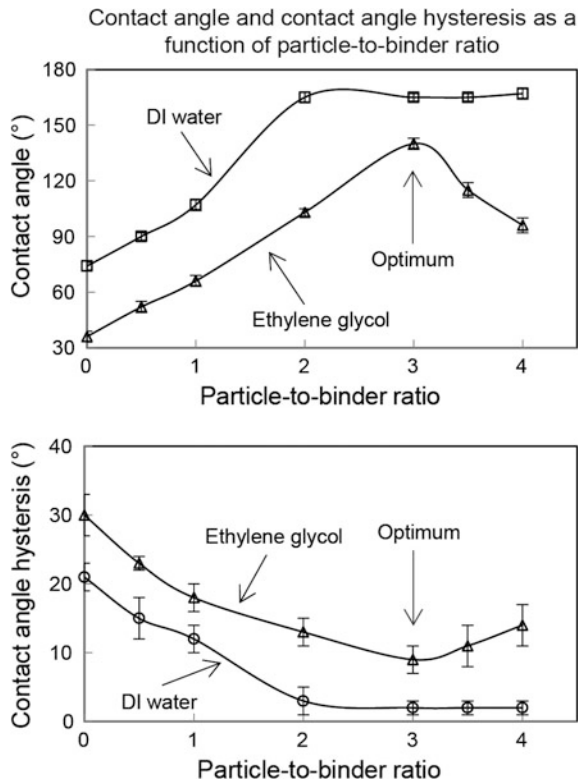
N/A—Not applicable

bonding between hydroxyl groups (–OH) resulting in a non-uniform coating. It is known that, compared with hydrophilic SiO₂, hydrophobic SiO₂ have a better dispersion and homogeneity for lack of hydrogen bonds, and better wear resistance (Jalili and Moradian 2009; Tahmasebpoor et al. 2013). Thus, hydrophobic SiO₂ was selected.

For deposition of the first layer, PET was dip coated with methylphenyl silicone resin and hydrophobic SiO₂ to provide high durability. It is known that P–B ratio affects the wettability (Muthiah et al. 2013; Wang and Bhushan 2015), and it needs to be optimized for high CA and low CAH. Figure 9.16 shows CA and CAH of water and ethylene glycol on dip coated PET at various P–B ratios (Wang and Bhushan 2015). CAs of hexadecane are close to 0° and are not shown in the figure. Dip coated PET with methylphenyl silicone resin alone showed wettability properties with CA 74° ± 2° and 36° ± 3°, CAH 21° ± 2° and 30° ± 3° for water and ethylene glycol, respectively. The data provided a baseline.

CA with water increases and CAH decreases as P–B ratio increases from 0 to 2.0, and then remains higher than 165° for P–B ratios of 2.0–4.0. This occurs because, with increasing concentration of nanoparticles, there is an increasing amount of air pockets beneath the water droplets in the Cassie-Baxter wetting

Fig. 9.16 Contact angle and contact angle hysteresis measured using droplets of water and ethylene glycol on single layer of dip coated PET as a function of particle-to-binder ratios. Lines connecting the data are to guide the eyes (adapted from Wang and Bhushan 2015)



regime, leading to a high fraction of water-air contact area for P–B ratios of 0–2.0. When the fractional area between water and air has increased to a critical point, about 0.94 at a P–B ratio of 2.0, an increase of nanoparticle concentrations does not increase the fractional water-air area (Ebert and Bhushan 2012). Thus, CA and CAH do not change (Wang and Bhushan 2015).

The ethylene glycol droplets, which have a lower surface tension (48.0 mN/m) compared with water (72.0 mN/m), behaved differently on samples with various P–B ratios. For P–B ratios of 0–3.0, the CA of ethylene glycol increases while the CAH decreases, associating with an increase of fractional contact area between ethylene glycol and air in Cassie–Baxter wetting regime. For P–B ratios of 3.0–4.0, the CA of ethylene glycol decreases while the CAH increases, associating with a decrease of fractional contact area between ethylene glycol and air. At P–B ratios less than 3.0, the addition of nanoparticles results in an increase of surface roughness, which benefits the formation of air pockets. At P–B ratios of more than 3.0, the addition of nanoparticles leads to a rather flat surface with no openings, which is not conducive to the formation of air pockets (Wang and Bhushan 2015). At a P–B ratio of 3.0, the best wettability was achieved for ethylene glycol, with a CA $140^\circ \pm 3^\circ$ and a CAH $9^\circ \pm 2^\circ$. A P–B ratio of 3.0 was selected for single layer coating.

At the selected P–B ratio, the coated surface exhibited a CA $165^\circ \pm 2^\circ$ and a CAH $2^\circ \pm 1^\circ$ for water, indicating superhydrophobicity. It exhibited a CA $140^\circ \pm 3^\circ$ and a CAH $9^\circ \pm 2^\circ$ for ethylene glycol, indicating oleophobicity. It exhibited a CA close to 0° for hexadecane, indicating superoleophilicity (Table 9.4). The lack of superoleophobicity was improved by deposition of perfluorotrichlorosilane.

In order to verify the hydrophobicity and oleophobicity of perfluorotrichlorosilane, a single layer coating was deposited by vapor deposition on PET substrate with thickness of approximately 200 nm. The CA data in Table 9.4 show that the coated surface was hydrophobic and oleophobic in ethylene glycol, but slightly oleophilic in hexadecane. The durability was good.

Dual Layer Coating with Plasma Treatment

To achieve superoleophobicity and high durability, plasma treatment of the single layer was carried out followed by vapor deposition of perfluorotrichlorosilane. After plasma treatment, the CA of water was less than 5° on the single layer coating, which suggested the introduction of (–OH) groups on the surface.

Contact angle data are presented in Table 9.4. The dual layer coating was superhydrophobic and superoleophobic in both ethylene glycol and hexadecane. The relative durability was excellent.

9.5.2.2 Surface Topography and Coating Thickness

Surface roughness data were obtained using an AFM for PET substrate, single layer coating of dip coated PET with methylphenyl silicone resin and hydrophobic SiO₂, and dual layer coating of vapor deposition of perfluorotrichlorosilane on plasma

treated, dip coated PET (Wang and Bhushan 2015). The uncoated PET was relatively smooth ($\text{RMS} = 1 \pm 0.2 \text{ nm}$, $\text{P-V} = 7 \pm 3 \text{ nm}$). Nanoscale roughness was present as a result of nanoparticles with binders on the single layer coating ($\text{RMS} = 20 \pm 2 \text{ nm}$, $\text{P-V} = 202 \pm 20 \text{ nm}$). The single layer coating after plasma treatment became rougher ($\text{RMS} = 24 \pm 2 \text{ nm}$, $\text{P-V} = 205 \pm 10 \text{ nm}$), and the dual layer coating was comparable to that of the plasma treated surface ($\text{RMS} = 26 \pm 2 \text{ nm}$, $\text{P-V} = 228 \pm 14 \text{ nm}$). In the dual layer coating, the surface roughness in combination with perfluorotrichlorosilane can produce air pockets, leading to the Cassie–Baxter wetting regime.

With a step technique using an AFM, the coating thickness of the first layer was measured to be approximately 300 nm, and the coating thickness of the second layer (vapor deposition) was also approximately 300 nm, with a total thickness of approximately 600 nm.

9.5.2.3 Wear Resistance of Coated Samples

Wear on Microscale Using AFM

AFM wear data after 1 cycle of wear at $10 \mu\text{N}$ with the borosilicate ball are shown in Fig. 9.17a for single layer of dip coated PET with methylphenyl silicone resin alone, single layer of dip coated PET with methylphenyl silicone resin and hydrophobic SiO_2 , and dual layer of vapor deposition of perfluorotrichlorosilane on plasma treated, dip coated PET (Wang and Bhushan 2015). Surface height maps and surface profiles across the middle of images (locations indicated by arrows) before and after AFM wear experiment are displayed. RMS roughness and P-V distance values for surface profiles are shown within surface profile boxes.

Wear was found on the single layer of dip coated PET with methylphenyl silicone resin alone, as observed in the surface height maps along with the change of RMS and P-V value. This is because the hardness of methylphenyl silicone resin (1.3 GPa, Ebert and Bhushan 2012) is lower than that of the composite coatings with SiO_2 particles. However, no obvious morphology change was found either on single layer of dip coated PET with methylphenyl silicone resin and SiO_2 or on dual layer of vapor deposition of perfluorotrichlorosilane on plasma treated, dip coated PET after wear. The RMS and P-V values were similar before and after wear. This demonstrated that the wear resistance of dual layer coating was superior to that of single layer of dip coated PET with methylphenyl silicone resin alone on the microscale. Wettability of the coating after wear did not change because the wear area was small (Wang and Bhushan 2015).

Wear on Macroscale Using Tribometer

The ball-on-flat tribometer data after 100 cycles of wear at 10 mN are shown in Fig. 9.17b for single layer of dip coated PET with methylphenyl silicone resin alone, single layer of dip coated PET with methylphenyl silicone resin and hydrophobic SiO_2 , and dual layer of vapor deposition of perfluorotrichlorosilane on

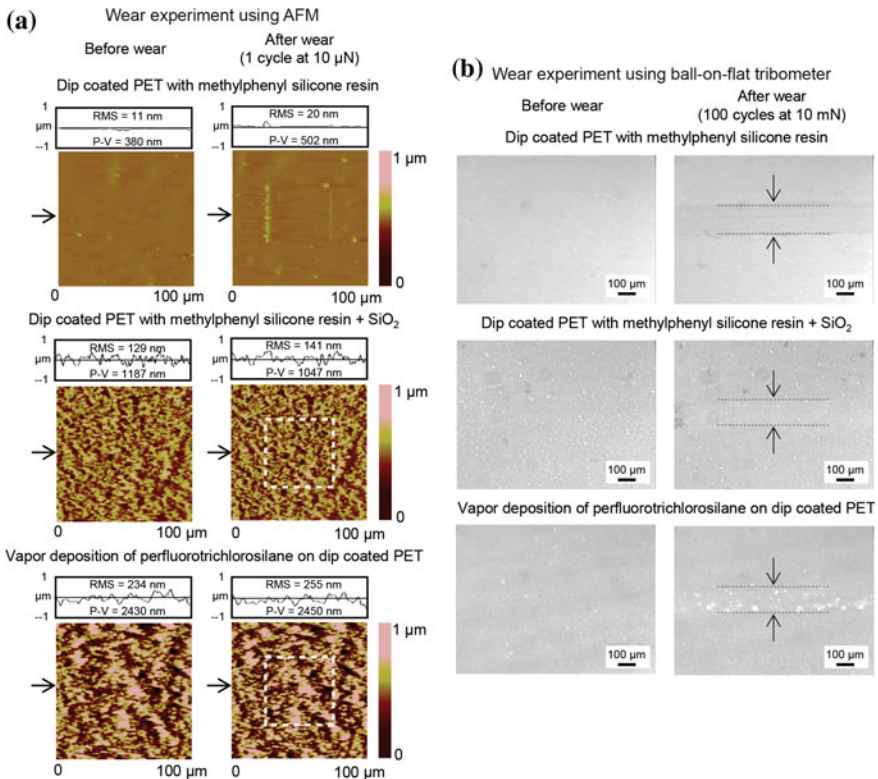
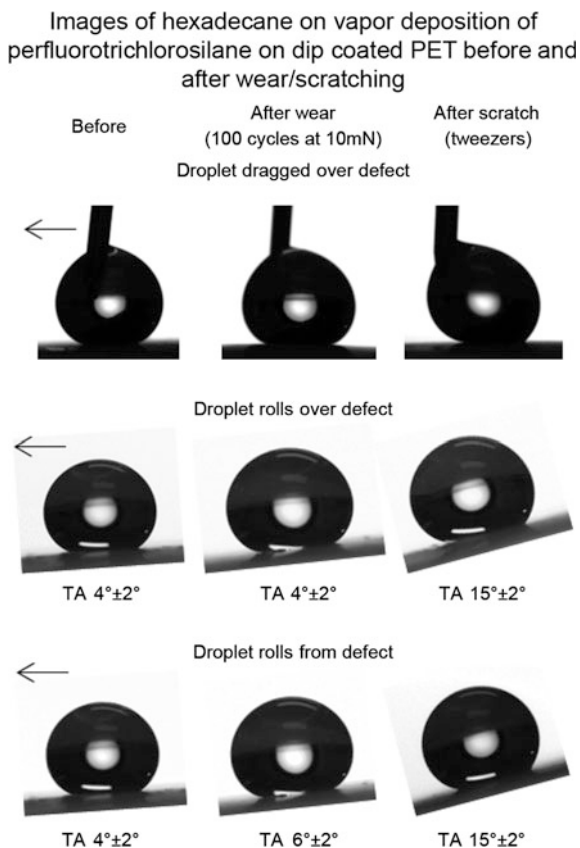


Fig. 9.17 **a** Surface height maps and sample surface profiles (locations indicated by *arrows*) of samples before and after AFM wear experiment (10.36 MPa), and **b** optical micrographs of samples before and after wear experiment using ball-on-flat tribometer (4.83 MPa) (adapted from Wang and Bhushan 2015)

plasma treated, dip coated PET. The single layer of dip coated PET with methylphenyl silicone resin alone showed a groove with maximum wear. The single layer of dip coated PET with methylphenyl silicone resin and SiO_2 displayed only burnishing, and the macroscale roughness was preserved. Although the contact pressure using the tribometer (4.8 MPa) is comparable to that of using the AFM (10.4 MPa), a higher degree of damage can be caused to the coating when multiple cycles of wear were performed, as compared to that of the AFM wear data (Wang and Bhushan 2015).

In order to identify any changes in wettability after wear, CAs and TAs were measured on the wear track. The images and TAs of hexadecane droplets on the dual layer coating after wear using ball-on-flat tribometer or scratching with tweezers are shown in Fig. 9.18 (Wang and Bhushan 2015). Droplets were dragged or tilted across the defect site in the direction of the arrows. For the coated sample before wear (left column), the droplet could be dragged freely when the sample was

Fig. 9.18 Images of hexadecane droplets on dual layer coating before and after wear/scratching. Droplets were dragged or tilted across defect site in direction of arrows. TA data are also presented (adapted from Wang and Bhushan 2015)



flat with low TA of $4^{\circ} \pm 2^{\circ}$ and the droplet rolled off at a TA of $4^{\circ} \pm 2^{\circ}$. For the coated sample after wear using ball-on-flat tribometer (center column), droplets either rolled over the defect as normal at $4^{\circ} \pm 2^{\circ}$ TA when placed to the right of the defect or rolled from the defect after tilting the sample $6^{\circ} \pm 2^{\circ}$ when placed directly over the defect. Droplets on the sample scratched by tweezers (right column) were pinned at the defect site until $15^{\circ} \pm 2^{\circ}$ TA, regardless of starting location. CAs of hexadecane droplets on all samples after wear/scratch were still greater than 150° . This indicated the superoleophobicity had been preserved after wear, although TA has been increased slightly (Wang and Bhushan 2015).

9.5.2.4 Anti-smudge Properties of Coated Samples

The optical micrographs of contaminated coatings and oil-impregnated microfiber cloth before and after smudge test on single layer of dip coated PET with methylphenyl silicone resin and SiO_2 and dual layer of vapor deposition of

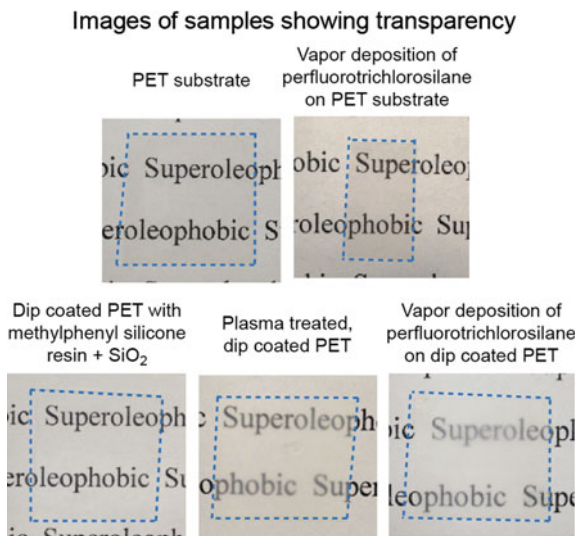
9.5.2.5 Transparency of Coated Samples

Figure 9.20 shows images of the PET substrate, the single layer of vapor deposition of perfluorotrichlorosilane on PET substrate, the single layer of dip coated PET with methylphenyl silicone resin and SiO₂, the plasma treated and dip coated PET, and the dual layer of vapor deposition of perfluorotrichlorosilane on plasma treated, dip coated PET showing transparency (Wang and Bhushan 2015). The edges of each sample are indicated with dash line. Both single layer coatings were as transparent as the uncoated PET substrate, while the dual layer coating suffered from some transparency loss. It was found that the transparency decreased after O₂ plasma treatment due to structural changes. Further, a thick, dual layer coating (approximately 600 nm) also decreased transparency. Transparency can be improved by optimization of plasma treatment parameters and a decrease in the coating thickness.

9.5.3 Summary

A superoleophobic coating was produced on PET substrates by dip coating with hydrophobic SiO₂ nanoparticles and methylphenyl silicone resin, followed by O₂ plasma treatment and vapor deposition of perfluorotrichlorosilane. Methylphenyl silicone resin was selected because it provides good adhesion between nanoparticles and substrates and is known to be durable. Hydrophobic SiO₂ nanoparticles were selected for their high hardness and high visible transmittance, and hydrophobic groups (-CH₃) can reduce agglomeration to form a uniform coating.

Fig. 9.20 Photographs of samples showing transparency. Edges of each sample are shown with dash line (adapted from Wang and Bhushan 2015)



Perfluorotrichlorosilane was selected due to its chemical activity, which could allow it to hydrolyze when in contact with hydroxyl groups ($-\text{OH}$) on a surface. During the methylphenyl silane coating process, plasma treatment was necessary to introduce hydroxyl groups ($-\text{OH}$) at the surface to form covalent bonds with perfluorotrichlorosilane to improve the durability, and increase the coverage of perfluorotrichlorosilane to achieve superoleophobicity. Water, ethylene glycol, and hexadecane were used for CA, CAH, and TA measurements (Wang and Bhushan 2015).

The dual layer coating was found to be superhydrophobic and superoleophobic to ethylene glycol and hexadecane. Wear resistance was demonstrated on both the macroscale and microscale. Anti-smudge properties were also demonstrated. The coating was transparent but some transparency was lost due to the plasma treatment and a thicker coating. This can be improved by optimization of the plasma treatment parameters and coating thickness.

9.6 Mechanically Durable Nanoparticle Composite Coatings for Superliquiphilicity and Superliquiphobicity Using Layer-by-Layer Technique

Figure 9.21 shows amphi-wettability landscape with four combinations of superliquiphilicity and superliquiphobicity, and their potential applications.

As discussed earlier, to develop oleophobic surfaces, low surface energy fluorinated coatings are needed. These coatings do not attach easily to other components in a composite and with the underlayer. Therefore, mixing of fluorinated compounds with other components in a nanocomposite in a so called “single-pot” technique does not provide a durable coating. Mechanical durability of nanocomposite coatings consisting of fluorinated compounds has been a major issue for industrial applications. Furthermore, some functionality in the fluorinated layer and/or underlayer is desirable and individual layers allow fabrication of various combinations of superliquiphilicity and superliquiphobicity.

Brown and Bhushan (2015a, b, c) used a so called “layer-by-layer” technique for water and oil superliquiphilicity and superliquiphobicity, in which components were kept separate and deposited individually. Layers of oppositely charged species were deposited one after another to create a multi-layered coating that was bound by electrostatic interaction. Many different charged species can be used to create a multi-layered coating. Thus, the technique is flexible, and various combinations can be used to realize a combination of superliquiphilicity and superliquiphobicity for a range of liquids, including water and oil.

Brown and Bhushan (2015a, b, c) used two polyelectrolyte layers with a silica nanoparticle layer in between. Nanoparticles were used to increase the roughness to realize air pocket formation. Dependent upon the deposition of a functional top layer, they were able to achieve various combinations of superliquiphilicity and

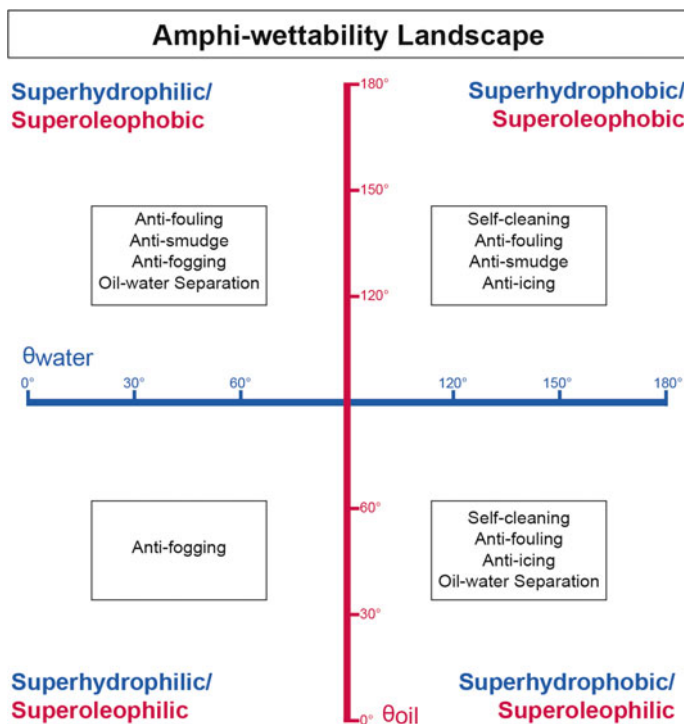


Fig. 9.21 Amphi-wettability landscape with four combinations of superliquiphilicity and superliquiphobicity

superliquiphobicity. Deposition of a separate functional layer provides correct functionality at the air interface without compromising the durability of the bulk coatings.

A variety of liquid wetting properties can be exploited for various applications. For instance, coatings that repel water (hydrophobic) are useful for self-cleaning applications (Bhushan and Jung 2011). Anti-icing surfaces are typically superhydrophobic, as supercooled droplets of water are able to roll off the cold surface before freezing and any ice formed is weakly adhered compared to hydrophilic surfaces due to an air cushion (Cao et al. 2009; Wang et al. 2013; Brown and Bhushan 2015c). Coatings that attract water (hydrophilic) are also useful for self-cleaning (Nishimoto and Bhushan 2013) and anti-fogging applications as any liquid water spreads out into a thin film, thereby cleaning the surface and maintaining transparency, respectively (Grosu et al. 2004; Cebeci et al. 2006; Brown and Bhushan 2015c). Hydrophobic surfaces have also been reported for anti-fogging applications (Sun et al. 2014). However, hydrophilic surfaces are more favorable for anti-fogging, as hydrophobic surfaces require tilting the surface for the droplets to roll off, which maintains transparency.

Table 9.5 Comparison of contact and tilt angles for water and hexadecane droplets deposited on the four layer-by-layer composite coatings (adapted from Brown and Bhushan 2015c)

Functional layer	Surface properties	Water		Hexadecane	
		Contact angle (°)	Tilt angle (°)	Contact angle (°)	Tilt angle (°)
None	Superhydrophilic/Superoleophilic	~0	N/A	~0	N/A
Silane	Superhydrophobic/Superoleophilic	161 ± 1	2 ± 1	~0	N/A
Fluorosilane	Superhydrophobic/Superoleophobic	163 ± 1	2 ± 1	157 ± 1	4 ± 1
Fluorosurfactant	Superhydrophilic/Superoleophobic	<5	N/A	157 ± 1	4 ± 1

Brown and Bhushan (2015c) produced coatings with four combinations of water and oil repellency or affinity through layer-by-layer deposition, as shown in Fig. 9.21, along with potential applications. The coating was comprised of several discrete layers that were deposited individually. A nanoparticle layer introduces roughness to enhance the surface properties of the functional layer and increase the hardness of the coating to improve durability. Intermediate polyelectrolyte layers are used to help bind the particles to the surface. The final (top) layer in the coating, referred to as the functional layer, contains the desired surface chemistry and can be easily swapped to produce a different functionality.

Table 9.5 summarizes coatings with the four possible combinations of water and oil repellency and affinity (adapted from Brown and Bhushan 2015c). In the case of the superhydrophilic/superoleophilic coating, no additional functional layer is added to leave the high surface tension polymer layer exposed. For superhydrophobic/superoleophilic coatings, a non-fluorinated silane is used to repel water but not oils, which have lower surface tensions (surface tension 20–30 mN m⁻¹). For superhydrophobic/superoleophobic coatings, a fluorinated silane is used to repel both water and oils. Finally, for superhydrophilic/superoleophobic coatings, a fluorosurfactant is used to yield the desired “flip-flop” of surface properties required. In all cases, the inclusion of a nanoparticle layer enhances the surface properties of the functional layer to result in superliquiphilic/phobic surfaces.

Brown and Bhushan (2015a, b, c) performed experiments for durability and functionality of all the coatings for a variety of applications, including anti-fogging, anti-icing, self-cleaning, anti-smudge, and oil–water separation. Details follow.

9.6.1 Experimental Details

Brown and Bhushan (2015c) deposited various coatings on a glass substrate, a substrate of interest for optical and electronic display screens applications. The four coatings described in this study are comprised of various layers deposited separately, as shown in Fig. 9.23, each of which aids the creation of a mechanically durable, functional coating. Polydiallyldimethylammonium chloride (PDDA) was chosen as

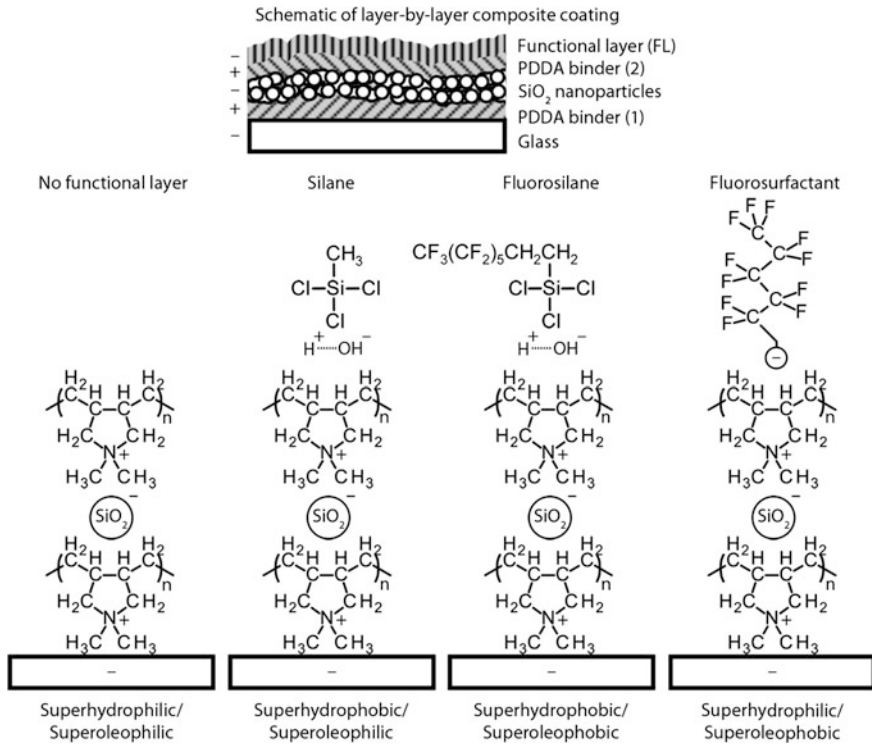


Fig. 9.23 Schematic of the four layer-by-layer composite coatings. Each layer is deposited separately. Also shown are the chemical composition and charge of each layer. The functional layer (FL) is deposited last and provides the desired surface chemistry (adapted from Brown and Bhushan 2015c)

the polymer base layer as it has a high cationic charge density, and has been shown to bind strongly to both glass substrates (Du et al. 2010; Lee and Ahn 2013) and SiO₂ nanoparticles. The specific molecular weight range (100,000–200,000) was chosen to balance mechanical properties and ease of deposition (viscosity). Untreated, hydrophilic SiO₂ nanoparticles were used to enhance the roughness of the coating. The negatively charged surface silanol groups ensure good adhesion to the positively charged polymer layers. Additionally, SiO₂ nanoparticles are known to have the high hardness (Ebert and Bhushan 2012) and wear resistance necessary for the creation of a mechanically durable coating (Bhushan 2013). Particles 7 nm in diameter were selected with the goal of creating a transparent coating. The material selected for the final, functional layer varied depending upon the desired surface properties. Two different silanes (non-fluorinated and fluorinated silanes) were selected to provide the desired repellency and for their ability to form self-assembled layers via vapor deposition. Silanes have been shown to condense on hydrophilic polymer layers in the past due to the presence of absorbed water (Xie et al. 2010). For the superhydrophilic/superoleophobic coating (“flip-flop” coating, Fig. 9.22),

a fluorosurfactant was selected for its oil repellency (low surface tension tail) and its ability to complex to a positively charged polyelectrolyte layer (high surface tension head group).

9.6.1.1 Samples

Glass slides (Fisher Scientific) cut to dimensions of 25 mm by 10 mm were used as substrates. PDDA (MW 100,000–200,000, Sigma Aldrich) was dissolved in distilled water (DS Waters of America Inc.) at various concentrations. Silica nanoparticles (NP, 7 nm diameter, Aerosil 380, Evonik Industries) were dispersed in acetone (Fisher Scientific Inc.) using an ultrasonic homogenizer (Branson Sonifier 450A, 20 kHz frequency at 35 % amplitude) at a concentration of 15 mg mL⁻¹. The fluorosurfactant solution (FL, Capstone FS-50, DuPont) was diluted with ethanol (Decon Labs Inc) so that the overall fluorosurfactant concentration was 45 mg mL⁻¹. Coatings were deposited via spray gun (Paasche) operated with compressed air at 210 kPa. The gun was held 10 cm from the glass slide at all times. First, PDDA solution (52 mg mL⁻¹, 2 mL) was spray coated and any excess was removed from the surface via bursts of compressed air from the spray gun. Second, the SiO₂ NP solution (15 mg mL⁻¹, 3 mL) was spray coated. Third, a second PDDA layer was deposited (8 mg mL⁻¹, 1 mL). After this, the samples were transferred to an oven operating at 140 °C for 1 h. Finally, the functional layer was deposited either via spray coating or vapor deposition under atmospheric conditions. For spray coating, the fluorosurfactant solution (1 mL) was spray coated and the samples were allowed to dry in air. For vapor deposition, one drop of either methyltrichlorosilane (methylsilane, Sigma Aldrich) for superhydrophobic/superoleophilic coatings or trichloro(1H,1H,2H,2H-perfluorooctyl) silane (fluorosilane, Sigma Aldrich) for superhydrophobic/superoleophobic coatings was deposited next to the samples, which were covered and left for 6 h (Brown and Bhushan 2015c).

The first layer of PDDA had a thickness of about 200 nm and acted as an anchor layer to the glass substrate. The second layer contained SiO₂ nanoparticles with a thickness of about 350 nm and acted as the roughness layer, enhancing the overall liquid–solid interactions. The third layer was a second polymer layer [PDDA (2)], with a thickness of about 50 nm, which helps to bind the nanoparticle layer, improving adhesion and mechanical durability. A final, functional layer was then deposited to provide the desired surface functionality. For the superhydrophilic/superoleophilic coating, there was no separate functional layer. For superhydrophobic/superoleophilic and superhydrophobic/superoleophobic coatings, the final layer was a silane layer with a thickness of about 25 nm, which condensed onto the hydrophilic PDDA (2) layer and provided either water- (methylsilane) or water- and oil-repellency (fluorosilane). For the superhydrophilic/superoleophobic coating, the final layer is a fluorosurfactant layer with a thickness of about 30 nm, which complexes with the positively charged PDDA (2) layer and provides the oil-repellency. Deposition of a separate functional layer ensures the correct functionality at the air

interface without compromising the durability of the bulk coating. The total coating thickness was about 630 nm (Brown and Bhushan 2015c).

9.6.1.2 Characterization Techniques

For functional characterization, wettability (CA, TA), coating thickness, macroscale and microscale wear, self-cleaning, anti-icing, anti-fogging, oil-water separation, and transparency measurements were made. Experimental details on anti-fogging, anti-icing, and oil-water separation have not been described in previous chapters, and details follow (Brown and Bhushan 2015c).

Anti-Fogging Experiment

The anti-fog characteristics of the surfaces were examined by placing the coated samples over boiling water for 5 s. The steam condensed on the coatings and was then photographed to determine the resulting transparency (Brown and Bhushan 2015c).

Anti-Icing Experiment

The anti-icing characteristics of the surfaces were examined by placing the coated samples in a freezer set at $-18\text{ }^{\circ}\text{C}$ for 2 h. The samples were tilted 10° and droplets of supercooled water ($-18\text{ }^{\circ}\text{C}$) were then dropped onto the samples from a height of 50 mm (Brown and Bhushan 2015c). Supercooled water was obtained by keeping DI water in a closed bottle in a freezer set at $-18\text{ }^{\circ}\text{C}$ for about 1 h. The pressure in the bottle prevented from freezing.

Oil–Water Separation Experiment

The superhydrophobic/superoleophilic and superhydrophilic/superoleophobic coatings were found to be suitable for oil–water separation. Stainless steel meshes (#400) were first cleaned with acetone and 2-propanol (Fisher Scientific) until they were found to be hydrophilic, then the coatings were deposited onto the meshes via spray coating. The coated meshes were then placed on top of beakers. Agitated mixtures of hexadecane and water were then poured onto the coated meshes. In separate experiments, the meshes were inclined at an angle and the oil–water mixtures were poured over them. To improve contrast, Oil Red O and Blue 1 dyes were used as oil and water dispersible dyes, respectively. The use of dyes was not found to have any effect on the performance of the coating (Brown and Bhushan 2015a, c).

9.6.2 Results and Discussion

9.6.2.1 Wettability of Coated Samples

Table 9.5 shows water and hexadecane contact angles for all four coatings (adapted from Brown and Bhushan 2015c). The superhydrophilic/superoleophilic coating

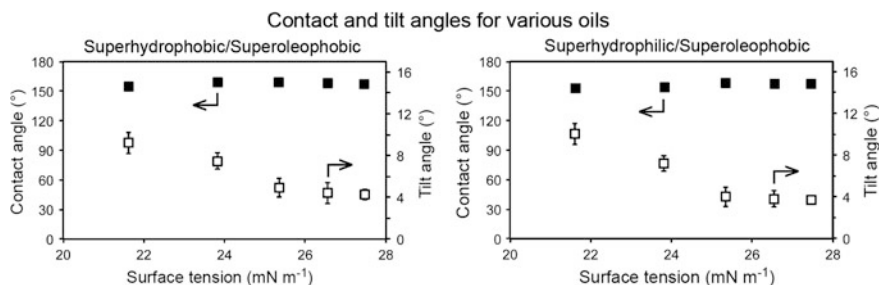


Fig. 9.24 Static contact angle and tilt angles for various liquids on the superhydrophobic/superoleophobic and superhydrophilic/superoleophobic surfaces as a function of liquid surface tension. Oils used: octane (21.14 mN/m), decane (23.37 mN/m), dodecane (25.35 mN/m), tetradecane (26.13 mN/m), and hexadecane (27.05 mN/m) (adapted from Brown and Bhushan 2015a, b)

was instantly wet by both water and oil. The superhydrophobic/superoleophilic coating was wet by oil while repelling water. The superhydrophobic/superoleophobic coating repelled both liquids. The superhydrophilic/superoleophobic coating repelled oil but was wet by water. Finally, oil repellency of both superoleophobic coatings was further tested by Brown and Bhushan (2015a, b). Figure 9.24 shows the data for two superoleophobic samples. The coatings were found to remain superoleophobic for hexadecane, tetradecane, dodecane, decane, and octane, with surface tensions of 27.05, 26.13, 25.35, 23.37, and 21.14, respectively. There was only slight increases in tilt angles for the lower chain length oils, due to their lower surface tensions (Brown and Bhushan 2015a, b).

The oil repellency of the superhydrophilic/superoleophobic coating, in addition to wetting by water, is due to the fluorosurfactant containing a low surface tension fluorinated tail and a high surface tension head group, complexed with a hydrophilic polyelectrolyte. During spray coating, the polar head group forms an electrostatic complex with the polyelectrolyte layer below and the fluorinated tails orient themselves at the air interface. Large, bulky oil molecules are trapped at this fluorinated interface while smaller water molecules can more easily penetrate down through the thin layer (ca. 30 nm) to the hydrophilic region where the surfactant head group complexes with the polyelectrolyte layer. Water droplets (5 μL) were found to immediately (less than 2 s) wet the surface, which is desirable for anti-icing, anti-fogging, and oil-water separation (Brown and Bhushan 2015c).

9.6.2.2 Wear Resistance of Coated Samples

AFM and tribometer wear experiments were used to measure wear resistance of the coatings. As an illustration, wear data for flat PDDA (with no SiO_2 nanoparticles) with a functional layer coating and a superhydrophobic/superoleophobic coating are shown in Fig. 9.25 (Brown and Bhushan 2015c). AFM images show a $100 \times 100 \mu\text{m}^2$

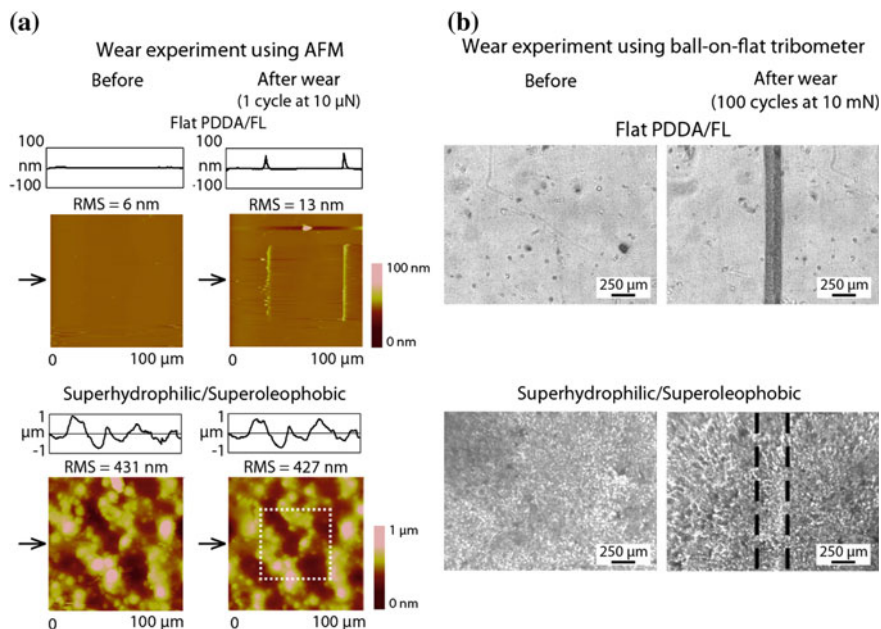


Fig. 9.25 **a** Surface height maps and sample surface profiles (locations indicated by *arrows*) before and after AFM wear experiment with 15 μm radius borosilicate ball at a load of 10 μN for flat and superhydrophilic/superoleophobic layer-by-layer composite coatings. RMS roughness values are displayed, and **b** optical micrographs before and after wear experiments using ball-on-flat tribometer at 10 mN for flat and hydrophilic/oleophobic layer-by-layer composite coatings. Similar results were obtained for the three remaining layer-by-layer composite coatings (adapted from Brown and Bhushan 2015c)

scan area with the wear location ($50 \times 50 \mu\text{m}^2$) in the center of each image. The optical images show a portion of the wear track from the tribometer experiments. For the soft PDDA/FL coating (ca. 225 nm thick), there is significant wear with both AFM and tribometer experiments, causing observable damage to the surface. In contrast, the layer-by-layer composite coating survived the AFM wear experiment with no observable defects. For the tribometer experiment, there is some noticeable burnishing to the coating. However, it is minimal when compared to the PDDA/FL coating. Higher magnification images confirmed that the layer-by-layer composite coating morphology is similar before and after the wear test, and there is no removal of the coating from the substrate. This is in contrast to the PDDA/FL coating that was completely destroyed by the wear test, revealing the substrate underneath. Similar results were found for the other three coatings investigated in their study (Brown and Bhushan 2015a, b, c). This suggests that the hard SiO_2 nanoparticle layer (underneath ca. 75 nm thick PDDA/FL layers) helps improve the durability of the coating. For both superoleophobic coatings, it was demonstrated that they are able to maintain

their oil-repellency after wear testing, with hexadecane droplets rolling over and from the wear scar with little to no impediment (Brown and Bhushan 2015a, b).

To further demonstrate the benefits of the layered structure on the mechanical durability of the coating, a fluorosurfactant-containing, superhydrophilic/superoleophobic coating was fabricated using a “one-pot” technique, where all the materials were mixed (at the same concentrations used in the layer-by-layer technique) and deposited together. This coating, which was found to be similar in terms of thickness and roughness as the layer-by-layer composite coating, was then subjected to the same ball-on-flat tribometer experiment as described above. The coating was found to have significantly poorer adhesion to the glass substrate than the layer-by-layer composite coating, most likely due to the presence of the low surface tension material throughout the coating instead of solely at the air interface, as in the layer-by-layer composite coating (Brown and Bhushan 2015c).

As far as thermal stabilities of various functional layers, methylsilane and fluorosilane exhibit thermal stabilities at 66° and 83°, respectively. The thermal stability of the fluorosurfactant layer is higher at 175 °C.

9.6.2.3 Transparency of Coated Samples

Many applications require self-cleaning and anti-smudge surfaces, as well as transparency of the coating. To test for transparency, text was placed directly behind the layer-by-layer composite coating sample, as shown in Fig. 9.26 (Brown and Bhushan 2015c). The text remained legible, suggesting that the coating displays characteristics of transparency. The transmission of visible light through the coatings, measured using a diffractive spectrometer, was found to vary between 58 and 93 % of that of uncoated glass, depending upon the wavelength and the specific coating, as shown in Fig. 9.26. The superhydrophilic/superoleophilic coating was the most transparent, with transmittance of 70–93 % over the visible spectrum. A level of 70 % visible light transmittance is acceptable for certain automotive applications (Thomsen et al. 2005). Further improvement in transparency can be made by decreasing the thickness of the nanoparticles and functional layers or reducing particle agglomeration (Brown and Bhushan 2015c).

9.6.2.4 Anti-fogging Property of Coated Samples

To measure the anti-fogging properties, all four coatings were placed directly above a source of boiling water for 5 s. The samples were then photographed to assess their transparency, as shown in Fig. 9.27 (Brown and Bhushan 2015c). Both superhydrophilic coatings were found to retain their transparency, with text remaining visible through the condensed water layer. In contrast, on the superhydrophobic coatings, the formation of discrete droplets of water results in samples that are completely opaque.

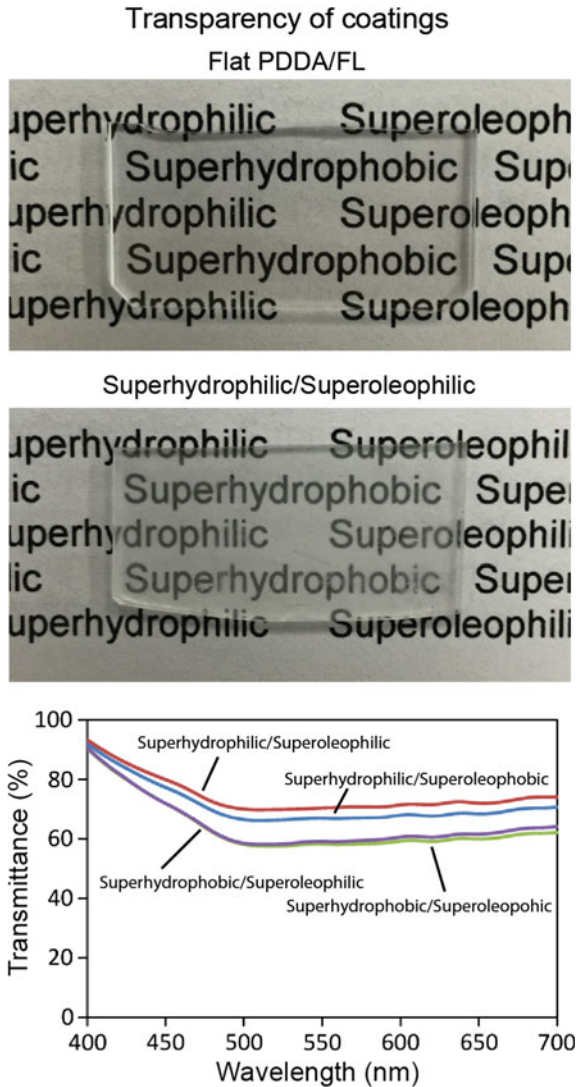


Fig. 9.26 Photographs of flat and superhydrophilic/superoleophobic layer-by-layer composite coatings. The flat coating appears transparent. Any reduction in transparency for the composite coating compared to the flat coating is due to the nanoparticles and functional layers (adapted from Brown and Bhushan 2015c)

9.6.2.5 Anti-icing Property of Coated Samples

To measure anti-icing properties, all four coatings were placed in a freezer set at $-18\text{ }^{\circ}\text{C}$ for 2 h. The samples were tilted and droplets of supercooled water were deposited onto them, as shown in Fig. 9.28 (Brown and Bhushan 2015c). On the

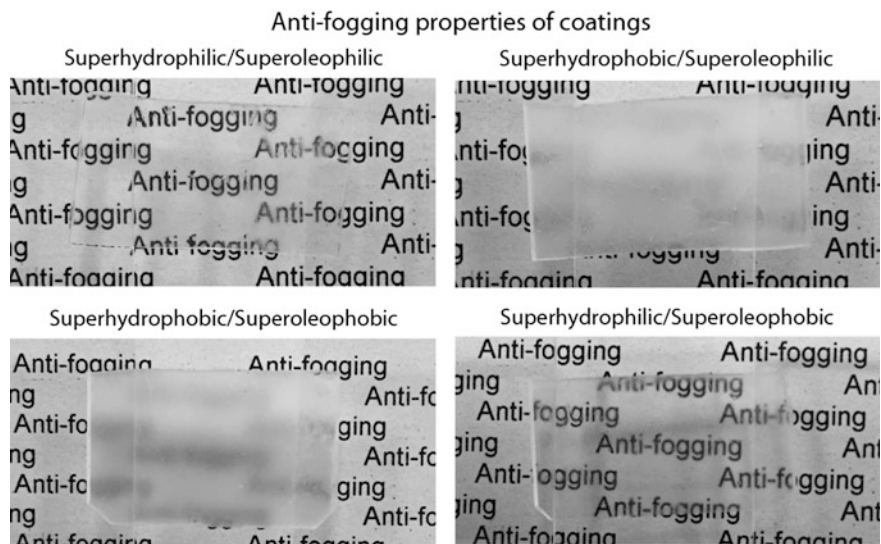


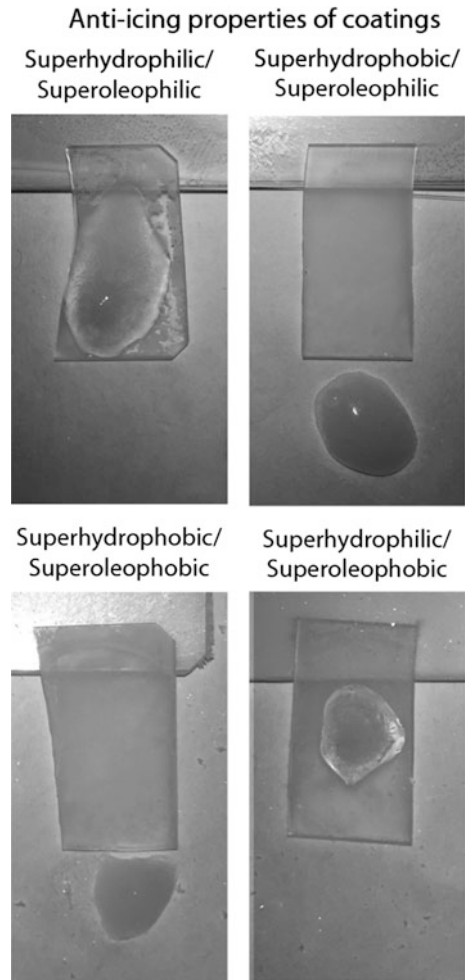
Fig. 9.27 Photographs of the four layer-by-layer composite coatings after exposure to water vapor. The hydrophilic coatings maintain transparency due to the formation of a thin water film on the surface. The hydrophobic coatings become opaque due to the formation of discrete water droplets on the surface (adapted from Brown and Bhushan 2015c)

superhydrophilic coatings, the droplets spread out and froze on the sample surface. On the superhydrophobic coatings, droplets rolled off the surface to freeze on the bottom of the freezer. This occurs because the water droplets are in the Cassie-Baxter state. The formation of a composite interface minimizes the contact with the cooled substrate and ensures a low hysteresis, so droplets can roll from the tilted surface (Brown and Bhushan 2015c).

9.6.2.6 Self-cleaning Property of Coated Samples

To measure the self-cleaning properties of two superhydrophobic coatings, the coatings were contaminated with silicon carbide particles, as shown in Fig. 9.29 (Brown and Bhushan 2015c). A stream of water droplets was then used to clean the surface. For comparison, a flat PDDA/FL coating (without SiO_2 nanoparticles) was also tested. For the superhydrophobic/superoleophilic and superhydrophobic/superoleophobic coatings, the vast majority of the particles were removed by the action of water droplets rolling across the repellent surfaces, collecting particles in the process. In contrast, the flat PDDA/FL surface remained contaminated after cleaning with water. The superhydrophobic coatings are self-cleaning due to their high water contact angle and low hysteresis. Water droplets deposited onto these samples are able to roll over the coating with little impediment, collecting fewer hydrophobic contaminants as they go (Brown and Bhushan 2015c).

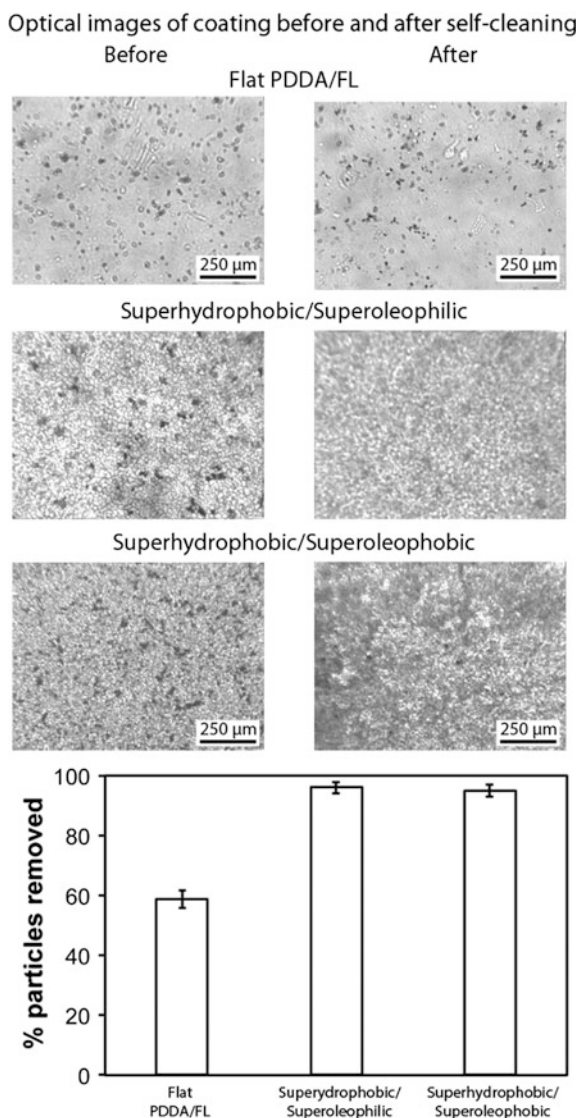
Fig. 9.28 Photographs of the four layer-by-layer composite coatings after freezing and deposition of supercooled water. The water immediately froze upon contact with the hydrophilic coatings while the droplets were able to roll off the hydrophobic coatings before freezing (adapted from Brown and Bhushan 2015c)



9.6.2.7 Anti-smudge Property of Coated Samples

To measure the anti-smudge properties of the two superoleophobic coatings, a hexadecane-soaked cloth was used to wipe the surfaces contaminated with silicon carbide, as shown in Fig. 9.30 (Brown and Bhushan 2015c). For comparison, a flat PDDA/FL coating (without SiO_2 nanoparticles) was also tested. For the superhydrophobic/superoleophobic and superhydrophilic/superoleophobic coatings, the particles were transferred to the cloth with no observable particles remaining on the surfaces. In contrast, the flat PDDA/FL surface remained contaminated after wiping with the cloth. Similar to the self-cleaning experiments with water, the anti-smudge property relies on a high contact angle and low hysteresis for the oil. The oil in the

Fig. 9.29 Optical micrographs of contaminated coatings before and after self-cleaning test on flat and the superhydrophobic layer-by-layer composite coatings. *Dark spots* on coatings and cloth indicate silicon carbide particle contaminants. Image analysis suggests a >90 % removal of particles on the two composite coatings (adapted from Brown and Bhushan 2015c)

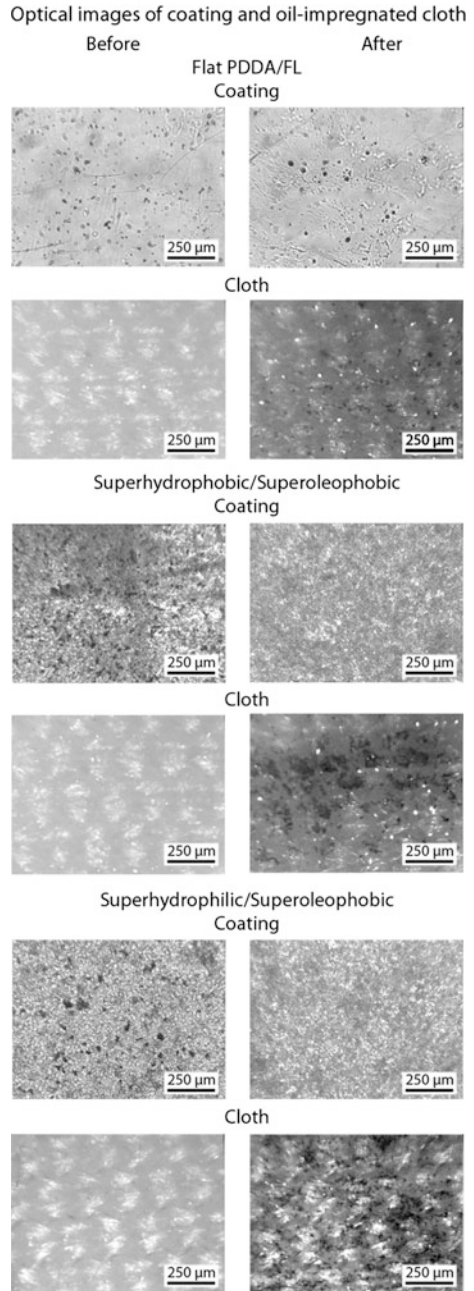


cloth is able to collect oleophilic contaminants from the surface of the coating without sticking to the surface (Brown and Bhushan 2015c).

9.6.2.8 Oil–Water Separation Ability of Coated Samples

The superhydrophobic/superoleophilic and superhydrophilic/superoleophobic coatings exhibit different responses to water and oil, and therefore are suitable

Fig. 9.30 Optical micrographs of contaminated coatings and oil-impregnated microfiber cloth before and after smudge test on flat and the superoleophobic layer-by-layer composite coatings. *Dark spots* on coatings and cloth indicate silicon carbide particle contaminants (adapted from Brown and Bhushan 2015c)



for use as oil–water separators. Agitated oil–water mixtures were poured onto coated meshes suspended over beakers, as shown in Fig. 9.31 (Brown and Bhushan 2015c). For the superhydrophobic/superoleophilic-coated mesh, the oil component of the mixture passed through, while the water remained on top. Meanwhile, for the superhydrophilic/superoleophobic-coated mesh, the opposite occurred, with the water component passing through the mesh and the oil remaining on top. In both cases, the liquid remaining on top of the coated mesh could be easily removed by tilting. Placing both the meshes on an inclined plane resulted in the simultaneous collection of oil and water in two separate beakers (Brown and Bhushan 2015c).¹

9.6.3 Summary

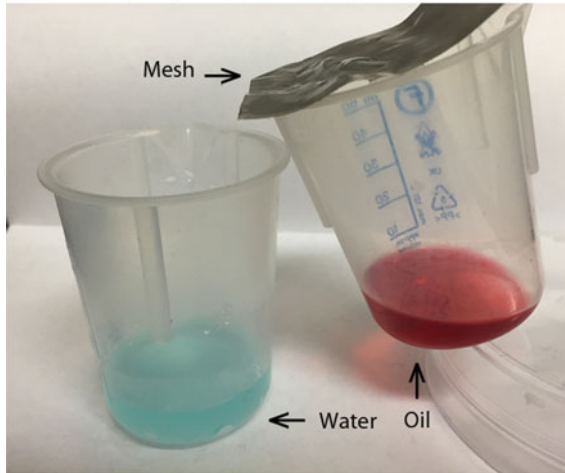
Coatings with four possible combinations of water and oil repellency and affinity were produced using a layer-by-layer technique. In this technique, the charged layer-by-layer method was used for durability, plus the addition of a functional layer on top for the desired surface properties. The superoleophobic coatings display oil contact angles of $>150^\circ$ and tilt angles $<5^\circ$ and the superhydrophobic coatings display water contact angles of $>160^\circ$ and tilt angles $<2^\circ$. One coating combines both superoleophobic and superhydrophobic properties, while others can be used to mix and match oil and water repellency and affinity (Brown and Bhushan 2015a, b, c).

The coatings were found to be mechanically durable, with micro- and macro-wear experiments not causing any considerable damage due to the hard SiO_2 nanoparticles and the electrostatic interaction between the base layers. Additionally, these surfaces were found to display characteristics of transparency, with an averaged transmission of 75 % and text remaining visible through the coating. This level of transparency is acceptable for certain automotive applications.

Superhydrophilic/superoleophilic coatings could find use in anti-fogging. Superhydrophobic/superoleophilic coatings could be used for self-cleaning, anti-fouling, anti-icing, and oil–water separation. The superhydrophobic/superoleophobic coating is suitable for self-cleaning, anti-fouling, anti-smudge, and anti-icing. Finally, the superhydrophilic/superoleophobic coating could be used for anti-fouling, anti-smudge, anti-fogging, and oil–water separation. This particular coating could be useful in anti-biofouling, where superoleophobicity, superhydrophilicity, and nanostructuring all contribute to reducing microorganism attachment. Additionally, when superhydrophobic/superoleophilic and superhydrophilic/superoleophobic coatings were applied to a porous substrate, they were found to separate oil from water.

¹For this research, authors received 2015 Institution of Chemical Engineers (UK) Global Award.

Photograph of oil-water separation
 Mesh placed on an inclined plane
 Superhydrophobic/Superoleophilic



Superhydrophilic/Superoleophobic

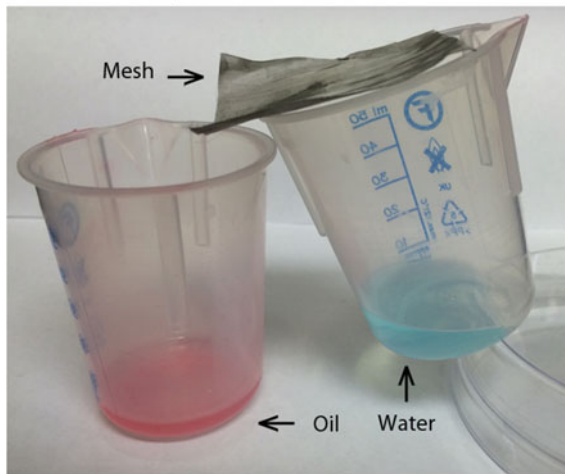


Fig. 9.31 Photographs of the hydrophobic/oleophilic and hydrophilic/oleophobic layer-by-layer composite coated stainless steel meshes acting as oil–water separators. On the superhydrophobic/superoleophilic coated mesh, water collects on top of the mesh while oil passes through. In contrast, on the superhydrophilic/superoleophobic coated mesh, water passes through the mesh while the oil remains on the top surface. Alternatively the meshes can be placed at an angle and oil and water collected simultaneously in separate beakers. Oil and water dyes used to enhance contrast (adapted from Brown and Bhushan 2015c)

9.7 Mechanically Durable Superoleophobic Aluminum Surfaces

Aluminum and its alloys present various properties, including low density, excellent heat and electrical conductivities, high specific strength, natural abundance, and good castability. They find widespread applications in aerospace, automotive industries, architecture, and household goods (Davis 1993; Hatch 1984). It is desirable to create mechanically durable superhydrophobic and superoleophobic aluminum surfaces with self-cleaning, anti-smudge, anti-fouling, and corrosion resistance properties, which can find promising applications in aircraft components, marine components, automotive components, machinery, and cooking utensils (Kaufman and Rooy 2004; Peng and Bhushan 2016).

Table 9.6 presents a summary of reported superhydrophobic/superoleophobic aluminum surfaces using various preparation methods (Peng and Bhushan 2016). Techniques, including chemical etching and anodization, have been used to produce superhydrophobic aluminum surfaces. For the chemical etching method, chemical etchants include boiling water (Ren et al. 2004; He et al. 2012), NaOH (Guo et al. 2005; Liu et al. 2013a), HCl (Qian and Shen 2005), $\text{ZnNO}_3 \cdot 6\text{H}_2\text{O}$ (Zhang et al. 2008; Lu et al. 2010), HNO_3 combined with $\text{Cu}(\text{NO}_3)_2$ (Fu and He 2008; Liu et al. 2013b), AlCl_3 combined with triethanolamine (Liu et al. 2011), $\text{La}(\text{NO}_3)_3$ (Li et al. 2014), and FeCl_3 (Maitra et al. 2014). For the anodization method, electrolytes include oxalic acid (Kim et al. 2012; Peng et al. 2014a) and mixed solutions of NaCl and fluorosilane (Song et al. 2012). In the above-mentioned papers, nanoplatelet, microstep, nanoreticula, microflower, and nanowire structures have been created to achieve superhydrophobicity.

To produce superoleophobic aluminum surfaces, either a one-step or two-step method has been used to create hierarchical structures (Peng and Bhushan 2016). In one-step techniques, superoleophobic surfaces were achieved by anodization in H_2SO_4 , followed by fluorinated monoalkylphosphate dip coating (Tsuji et al. 1997), or chemical etching in perfluorocarboxylic acid (Meng et al. 2008). There are various two-step techniques applied to fabricate superoleophobic surfaces. These include chemical etching in HCl and then in boiling water, followed by fluorosilane coating (Peng et al. 2014b); chemical etching in HCl and then in HNO_3 + $\text{Cu}(\text{NO}_3)_2$, followed by fluorosilane coating (Peng and Bhushan 2016); electrochemical etching in Na_2SO_4 combined with anodization in oxalic acid, and subsequent fluorosilane coating (Wu et al. 2009); chemical etching in HCl combined with anodization in H_2SO_4 , followed by fluorosilane coating (Barthwal et al. 2013); and electrochemical etching in NaCl combined with chemical etching in $[\text{Ag}(\text{NH}_3)_2]^+$ solution, with subsequent fluorocarbon acid coating (Song et al. 2013). These two-step techniques have been used to create the microstep structure first, followed by nanoplatelet, nanowire forest or nanoporous structure, or deposition of nanoparticles on the top of the microstep structure to form hierarchical structure, with subsequent fluoro-compound modification. Only Peng et al. (2014b) and Peng and Bhushan (2016) have reported some mechanical durability data.

Table 9.6 Literature review of superhydrophobic and superoleophobic Al surfaces with their preparation methods, properties and comments (adapted from Peng and Bhushan 2016)

Superhydrophobic Al surfaces		Preparation method	Surface structure	CA (°)	Properties and comments
Chemical etching	Boiling water (<i>one-step</i>)	Boiling water + PEI dip coating + STA dip coating (Ren et al. 2004)	Nanostructure with rms 18 nm	CA (water) 166	Decreased adhesion and friction
		Hot water + fluorosilane dip coating (He et al. 2012)	Sub microscale sharp rims and shallow floor	CA (water) 170	
	NaOH (<i>one-step</i>)	NaOH + fluorosilane dip coating (Guo et al. 2005)	Porous thickness 0.8–1 μm and pore diameters 300–600 nm	CA (water) 168	Stable for liquids with diverse pH values
	HCl (<i>one-step</i>)	NaOH + STA dip coating (Liu et al. 2013a)	Bayerite microneedle arrays	CA (water) 167 TA (water) 3	Anti-corrosive to NaCl
	ZnNO ₃ ·6H ₂ O	Mixed HCl and HF + fluorosilane dip coating (Qian and Shen 2005)	Microsteps	CA (water) 156 CAH (water) 5	
		Anodization in H ₂ SO ₄ + ZnNO ₃ ·6H ₂ O and NH ₄ NO ₃ and sodium laurate (Zhang et al. 2008) (<i>two-step</i>)	Micro-hemispherical protrusions and nanoplate like structure	CA (water) 163	Anti-corrosive to NaCl
	HNO ₃ + Cu(NO ₃) ₂ (<i>Two-step</i>)	ZnNO ₃ ·6H ₂ O and hexamethylenetetraamine + STA dip coating (Lu et al. 2010) (<i>one-step</i>)	Flower-shaped wurtzite zinc oxide microstructure and porous Zn–Al LDH	CA (water) 155 TA (water) 3	
		Mechanical roughening + mixed HNO ₃ and Cu(NO ₃) ₂ + silane dip coating (Fu and He 2008)	Microcrater-like pits and nanoreticula	CA(water) 160	
	AlCl ₃ + triethanolamine (<i>one-step</i>)	Laser roughening + HNO ₃ and Cu (NO ₃) ₂ + silane dip coating (Liu et al. 2013b)	Microcrater-like pits and nanoreticula	CA (water) 160	Keep the metal gloss and high water adhesion
		AlCl ₃ and triethanolamine + STA dip coating (Liu et al. 2011)	Flower-like microprotrusions with hundreds of nm in size	CA (water) 169 TA (water) 4	
		La(NO ₃) ₃ + fluorosilane dip coating (Li et al. 2014)	Ginkgo-leaf-like structure with 10–30 nm thickness and 100–300 nm diameter	CA (water) 160	
		FeCl ₃ + fluorosilane dip coating + PDMS coating + chlorosilane dip coating (Maitra et al. 2014)	Micropits + nanofibers	CA (water) > 160	Chemically stable under strong alkaline, acidic, and NaCl solutions; withstand water impalement and tape tests

(continued)

Table 9.6 (continued)

Superhydrophobic Al surfaces		Surface structure	CA (°)	Properties and comments
Preparation method				
Anodization (<i>one-step</i>)				
	Anodization in oxalic acid + fluorosilane dip coating (Kim et al. 2012)	Large-area nanowires	CA (water) 160	The modulus is 1000 times larger and 700 times harder than PTFE
	Anodization in mixed NaCl and fluorosilane solution (Song et al. 2012)	Microstep structure	CA (water) 166 TA (water) 1	
	Anodization in oxalic acid + fluorosilane dip coating (Peng et al. 2014a)	Large-area micro pyramids -on-nanopores structure	CA (water) 155 TA (water) 0	Chemically stable under strong acid/alkali, hot liquids etc., mechanically stable to adhesive tape and abrasion tests
<i>Superoleophobic Al surfaces</i>				
Anodization (<i>one-step</i>)				
	Anodization in H ₂ SO ₄ + fluorinated monoalkylphosphate dip coating (Tsujii et al. 1997)	Microfractal structure	CA (water) 150 CA (rapeseed oil) 150	
Chemical etching				
	Perfluorocarboxylic acid (Meng et al. 2008) (<i>one-step</i>)	Nanoflowers	CA (water) 158 CA (rapeseed oil) 155	
	HCl + boiling water + fluorosilane dip coating (Peng et al. 2014b) (<i>two-step</i>)	Microsteps and nanoplatelets structure (20–40 nm)	CA (water) 160 TA (water) 0 CA (hexadecane) 154 TA (hexadecane) 15 CA (dodecane) 152 TA (dodecane) 25	Chemically stable under strong acid/alkali, hot liquids etc., mechanically stable to adhesive tape and abrasion tests
	HCl + HNO ₃ and Cu(NO ₃) ₂ + fluorosilane dip coating (Peng and Bhushan 2016) (<i>two-step</i>)	Microsteps and nanoreticula	CA (water) 160 CAH (water) 2 CA (hexadecane) 152 CAH (hexadecane) 12 CA (ethylene glycol) 157 CAH (ethylene glycol) 5	Mechanically durable; exhibited self-cleaning and anti-smudge properties
Electrochemical etching + anodization (<i>two-step</i>)				
	Electrochemical etching in Na ₂ SO ₄ + anodization in oxalic acid + fluorosilane dip coating (Wu et al. 2009)	Microsteps and nanowires forest	CA (water) 170 TA (water) < 1 CA (hexadecane) 153 TA (hexadecane) 3 CA (silicone oil) 150 TA (silicone oil) 12	

(continued)

Table 9.6 (continued)

Superhydrophobic Al surfaces			
Preparation method	Surface structure	CA (°)	Properties and comments
Chemical etching + anodization (<i>two-step</i>)	HCl etching + anodization in H ₂ SO ₄ + fluorosilane dip coating (Barthwal et al. 2013)	CA (water) 160 TA (water) 2 CA (ethylene glycol) 158 TA (ethylene glycol) 5 CA (hexadecane) 150 TA (hexadecane) 20	Mechanical durable to Scotch tape and hardness tests
Electrochemical etching + chemical etching (<i>two-step</i>)	Electrochemical etching in NaCl + etching in [Ag(NH ₃) ₂] ⁺ solution + fluorocarbon acid dip coating (Song et al. 2013)	CA (water) 167 TA (water) 0 CA (peanut oil) 160 TA (peanut oil) 8	

CA—Contact angle, CAH—Contact angle hysteresis, TA—Tilt angle

PEI—Polyethyleneimine, STA—stearic acid, LDH—Layered double hydroxides, PDMS—Polydimethylsiloxane, PTFE—Polytetrafluoroethylene

Surface tension of DI water = 72.0 mN/m, hexadecane = 27.0 mN/m, rapeseed oil = 30–35 mN/m (Bhushan 2012), dodecane = 25.4 mN/m, silicone oil = 22.0 mN/m, ethylene glycol = 48.0 mN/m, peanut oil = 37.5 mN/m

A nanoreticula structure has been reported to facilitate air pocket formation (Fu and He 2008; Liu et al. 2013b; Peng and Bhushan 2016). In this section, based on Peng and Bhushan (2016), we present data on mechanically durable superoleophobic aluminum surfaces with combined microstep and nanoreticula structure, modified with fluorosilane to provide the ability to form air-pockets and a low surface energy. The surfaces were characterized for wettability, wear, self-cleaning, anti-smudge properties, corrosion resistance, and propensity of air pocket formation.

9.7.1 Experimental Details

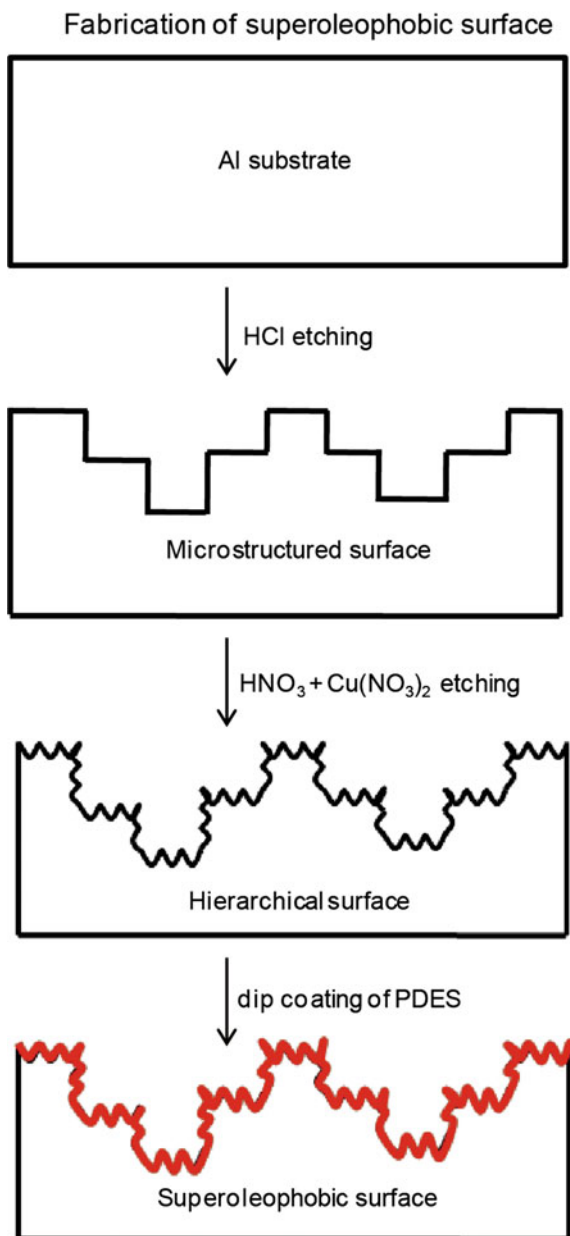
The fabrication technique for superoleophobic aluminum surfaces is shown in Fig. 9.32 (Peng and Bhushan 2016). The microstep structure was first obtained from HCl etching. Then, the microstructured surface was immersed in aqueous solutions of HNO_3 and $\text{Cu}(\text{NO}_3)_2$ to construct nanoreticula structure, in order to achieve the hierarchical structure. The hierarchical surface was modified with fluorosilane to realize superoleophobicity. Various properties of the surfaces were measured.

9.7.1.1 Sample Preparation

An aluminum plate (composition: wt 98 % Al, 0.3 % Si, 1.7 % O) was cleaned by ultrasonication in acetone, ethanol, and DI water, in sequence, before use. The cleaned plate was first immersed in 2.5 M HCl solution for 10 min at room temperature to achieve the microstep structure. Then, it was rinsed with DI water and dried. The microstructured aluminum surface was next etched in aqueous solutions of nitric acid (HNO_3 , 65 % mass fraction) (Sigma-Aldrich, # 02650) and copper nitrate trihydrate ($\text{Cu}(\text{NO}_3)_2 \cdot 3\text{H}_2\text{O}$) (Sigma-Aldrich, # 61194) with a concentration of 9.7 g/L at 80 °C for 6 min, determined by optimization for the highest CA and lowest CAH. After the two-step etching process, hierarchical structure was obtained (Peng and Bhushan 2016).

A separate nanostructured surface and microstructured surface were also fabricated, to compare with the hierarchical surface. The nanostructured surface was fabricated through one-step etching in HNO_3 and $\text{Cu}(\text{NO}_3)_2$, while the microstructured surface was obtained from one-step HCl etching. Finally, the finished samples of nanostructured, microstructured, and hierarchical surfaces were dipped into 1.0 wt% ethanol solution of [1H,1H,2H,2H-Perfluorodecyltriethoxysilane] PDES (Sigma-Aldrich, # 658758) for 2 h by dip coating technique and then cured at 100 °C for 30 min (Peng and Bhushan 2016).

Fig. 9.32 Schematic of the fabrication process of the superoleophobic hierarchical surface. The aluminum sample was etched first in HCl to get the microstep structure, then immersed in solution of HNO_3 and $\text{Cu}(\text{NO}_3)_2$ to obtain the nanoreticula structure in order to form a hierarchical surface. The hierarchical surface when modified with fluorosilane, resulting in superoleophobicity to hexadecane (adapted from Peng and Bhushan 2016)



9.7.1.2 Characterization

CA, CAH, TA, surface morphology, roughness, P-V distance, wear resistance on macroscale, self-cleaning, anti-smudge, and corrosion resistance properties were measured. Experimental details have been presented previously.

In this study, evidence of air pocket formation was also obtained. In order to assess the ability of the surfaces to trap air, the samples were photographed while submerged under water to document the formation of any plastron air layers. If a plastron air layer is formed, the surface will appear highly reflective, due to the large difference in refractive index for water and air, and the smooth interface formed between the two as the air becomes trapped by the surface roughness (Zimmerman et al. 2008; Poetes et al. 2010).

To study corrosion resistance, the electrochemical measurements were made using 3.5 wt% aqueous solution of NaCl at room temperature using an electrochemical workstation (IM6ex, Zahner, Germany) (Anonymous 1994, 2005; Peng and Bhushan 2016). These were conducted using a three-electrode configuration with saturated calomel as the reference electrode, platinum as the counter electrode, and the samples with an exposed area of 1 cm^2 as the working electrode. The potentiodynamic polarization was carried out at a scanning rate of 5 mV s^{-1} and potential-current density curves were obtained.

9.7.2 Results and Discussion

The properties of the nanostructured and microstructured surfaces, as compared to the hierarchical surface, are presented in this section.

9.7.2.1 Wettability of Coated Samples

The measured CA, CAH, and TA values for water, ethylene glycol, and hexadecane on the nanostructured, microstructured, and hierarchical surfaces before and after PDES coating are shown in Table 9.7 (Peng and Bhushan 2016). All uncoated surfaces were hydrophilic and oleophilic. Depositing a PDES coating made all surfaces superhydrophobic and two of the three nanostructured and hierarchical surfaces superoleophobic. The nanostructured surface exhibits superhydrophobicity and oleophobicity to water and ethylene glycol with CAs of $152^\circ \pm 2^\circ$ and $105^\circ \pm 2^\circ$, and CAHs of $4^\circ \pm 2^\circ$ and $12^\circ \pm 2^\circ$, respectively. Hexadecane droplets, which have a lower surface tension as compared to ethylene glycol and water, behave differently on the samples. When a hexadecane droplet wets the nanostructured surface, it shows oleophilicity, with a CA of $58^\circ \pm 2^\circ$ and CAH of $22^\circ \pm 2^\circ$. The microstructured surface exhibits superoleophobicity to water and ethylene glycol with CAs of $158^\circ \pm 2^\circ$ and $151^\circ \pm 2^\circ$, and CAHs of $2^\circ \pm 2^\circ$ and $12^\circ \pm 2^\circ$, respectively. For hexadecane, it shows only oleophobicity with a CA of

Table 9.7 Wettability summary of all samples with PDES dip coating (Peng and Bhushan 2016)

Samples	DI water (°)			Ethylene glycol (°)			Hexadecane (°)		
	CA	CAH	TA	CA	CAH	TA	CA	CAH	TA
Nanostructured surface without coating	36 ± 2	20 ± 2	>90	~4	N/A	>90	~0	N/A	>90
Nanostructured surface (with coating)	152 ± 2	4 ± 2	4 ± 1	105 ± 2	12 ± 2	>90	58 ± 2	22 ± 2	>90
Microstructured surface without coating	~0	N/A	>90	~0	N/A	>90	~0	N/A	>90
Microstructured surface (with coating)	158 ± 2	2 ± 2	2 ± 1	151 ± 2	12 ± 2	20 ± 1	142 ± 2	16 ± 2	>90
Hierarchical surface without coating	~0	N/A	>90	~0	N/A	>90	~0	N/A	>90
Hierarchical surface (with coating)	160 ± 2	2 ± 1	1 ± 1	157 ± 2	5 ± 2	5 ± 2	152 ± 2	12 ± 2	14 ± 2

N/A—Not applicable

$144^\circ \pm 2^\circ$ and CAH of $16^\circ \pm 2^\circ$. In comparison, the hierarchical surface is superhydrophobic and superoleophobic to water and ethylene glycol, as well as hexadecane, as seen by CAs of $160^\circ \pm 2^\circ$, $157^\circ \pm 2^\circ$, and $152^\circ \pm 2^\circ$, and CAHs of $2^\circ \pm 1^\circ$, $5^\circ \pm 2^\circ$, and $14^\circ \pm 2^\circ$, respectively. These results indicate that only the hierarchical structure achieves superoleophobicity to oils with low surface tension, such as hexadecane (Peng and Bhushan 2016).

9.7.2.2 Surface Morphology and Roughness of Coated Samples

Figure 9.33 shows the SEM morphological data for the nanostructured, microstructured, and hierarchical surfaces. When the aluminum plate was etched only by a mixture HNO_3 and $\text{Cu}(\text{NO}_3)_2$ solution, the aluminum surface became uneven. The high-magnification SEM image indicated that a large area of nanoreticula porous structure was formed with a nanoporous diameter about 30–40 nm.

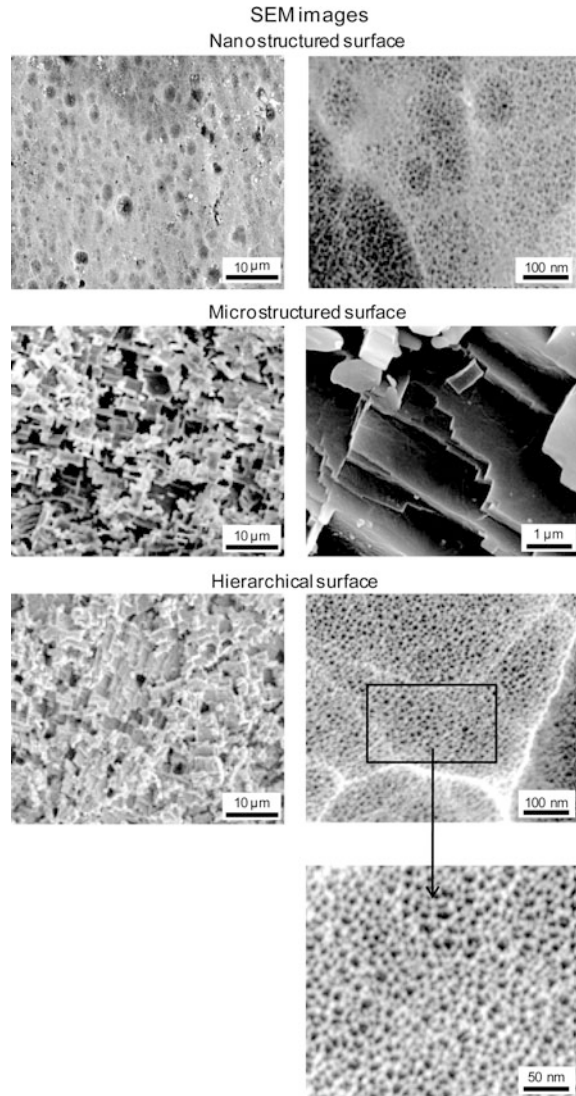
The reaction process for the formation of nanoreticula structure occurs as follows. In the chemical etchant solution of HNO_3 and $\text{Cu}(\text{NO}_3)_2$, copper nitrate precipitated into copper ions (Cu^{2+}). Copper ions reacted with electrons from the aluminum plate and reduced to copper particles (Cu), which deposited on the aluminum surface. This process resulted in the formation of micro-orifices, which in turn accelerated the erosion speed of the surrounding aluminum (Zhu 2004). Consequently, a large area of reticular porous structure was formed (Peng and Bhushan 2016).

When the aluminum plate was etched only by HCl, it resulted in a microstep structure on the surface. The low-magnification SEM image demonstrated that the surface exhibited microstep topography. As indicated by the high-magnification SEM image, the surface of each microstep was smooth. The length of the step was about 3–4 μm . A large number of dislocation defects that possess relatively higher energy exist in common crystalline metals. These dislocation sites are prone to attack by chemical etchants and dissolve first. The selective corrosion effect lead to a large number of micro-pits on the surface, and resulted in the formation of a step morphology (Qian and Shen 2005; Vander Voort 1984; Peng and Bhushan 2016).

When the two-step chemical etching process was applied on the aluminum plate, a hierarchical structure was produced. As shown in the low-magnification SEM image, the microstep structure was first formed through HCl etching. However, when the microstructured surface was further etched in mixed HNO_3 and $\text{Cu}(\text{NO}_3)_2$ solution, the microstep surface was full of the nanoreticula structure, and was no longer smooth. This variation could be observed from the high-magnification SEM images of the hierarchical surface. Higher magnification SEM images indicated that the nanoreticula diameter was about 20–30 nm (Peng and Bhushan 2016).

It should be noted that when both a smooth aluminum plate and a microstructured aluminum surface with microstep morphology are immersed in HNO_3 and $\text{Cu}(\text{NO}_3)_2$ solution, the required reaction time for forming nanoreticula structures on each surface is very different. It takes a longer etching time (about 1 h) to form nanoreticula structure on a smooth aluminum surface, while the microstructured

Fig. 9.33 Low and high-magnification SEM images of the nanostructured, microstructured, and hierarchical surfaces. The nanostructured surface shows reticular porous structure with diameter of about 20–40 nm. The microstructured surface shows smooth microstep morphology and the length of each step is about 3–4 μm . A combination of microstep and nanoreticula structure formed on the hierarchical surface. The microsteps on the hierarchical surface are no longer smooth and have a large area of nanoreticula structure (adapted from Peng and Bhushan 2016)



surface, as mentioned previously, only needs 6 min immersion time to obtain nanoreticula topography. The number of dislocation defects on the microstructured aluminum surface increased dramatically compared with the smooth aluminum plate. These dislocations were destroyed faster by chemical etchant attack, and thus, further accelerated the dissolution of surrounding aluminum, which reduced the necessary etching time (Peng and Bhushan 2016).

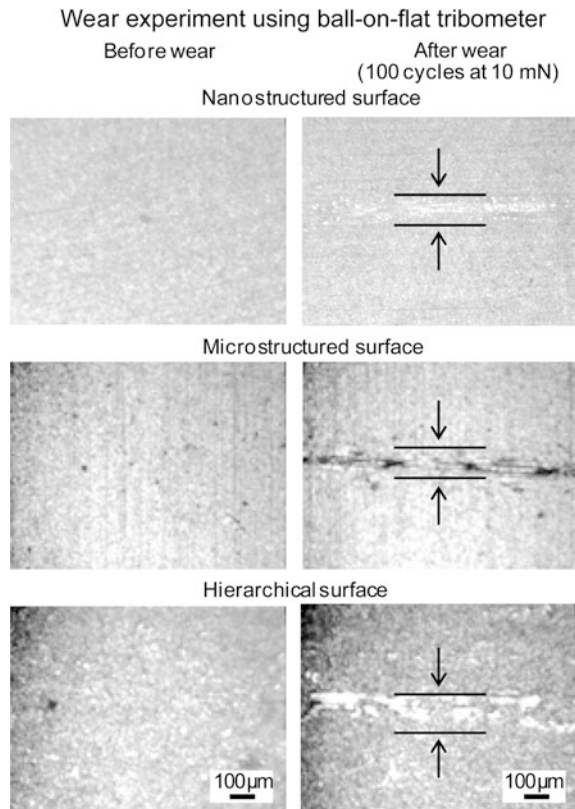
Surface roughness and P-V distance of the nanostructured, microstructured, and hierarchical surfaces were measured using a stylus profiler. RMS of 2.0 and 8.3 μm , and P-V distance of 11 and 42 μm were obtained for the nanostructured and

microstructured surfaces, respectively. The hierarchical structure achieved a rougher surface, with a RMS and P-V data of 9.6 and 49 μm , respectively (Peng and Bhushan 2016).

9.7.2.3 Wear Tests Using Tribometer

Optical images of the nanostructured, microstructured, and hierarchical surfaces before and after wear experiments using ball-on-flat tribometer are presented in Fig. 9.34 (Peng and Bhushan 2016). The wear scar is identified by two lines. The optical images show that both the nanostructured and microstructured surfaces show limited burnishing after 100 cycles of wear at 10 mN. The hierarchical surface with dual structure characteristics also shows little burnishing trace. It appears that the wear tests do not cause noticeable damage on the hierarchical surface.

Fig. 9.34 Optical images of the nanostructured, microstructured, and hierarchical surfaces before and after wear experiments using ball-on-flat tribometer at 10 mN. A sapphire ball with a radius of 1.5 mm was used and the tribometer was set into reciprocating for 100 cycles with an average linear speed of 1 mm/s. The images show very little burnishing induced on the nanostructured, microstructured, and hierarchical surfaces (adapted from Peng and Bhushan 2016)



9.7.2.4 Self-cleaning Properties

To measure self-cleaning efficiency, the nanostructured, microstructured, and hierarchical surfaces were exposed to wash experimentation. The optical images for the nanostructured, microstructured, and hierarchical surfaces before and after wash experiments are presented in Fig. 9.35. These optical images are analyzed with SPIP image software to quantify the percentage of SiC particles removed. After the wash experiment, there were still some particles remaining on the nanostructured surface, while the microstructured and hierarchical surfaces became totally clean. The histogram indicates that the self-cleaning efficiency of nanostructured, microstructured, and hierarchical surfaces are 60, 96, and 99 %, respectively. These results demonstrate that the microstructured and hierarchical surfaces present a more effective contaminant removal ability as compared to the nanostructured surface. Specially, the combination of micro-nanostructure amplifies the self-cleaning ability of the hierarchical surface, which makes the surface achieve the highest efficient particle removal ability (Peng and Bhushan 2016).

9.7.2.5 Anti-smudge Properties

Optical images of the contaminated samples and hexadecane-impregnated micro-fiber cloth before and after smudge tests on the microstructured and hierarchical surfaces are presented in Fig. 9.36 (Peng and Bhushan 2016). The nanostructured surface was not tested because of its known poor self-cleaning properties. Dark spots on the sample surface and cloth indicate silicon carbide particles. It can be seen that the cloth can only wipe a few particles on the microstructured surface, while particles on the hierarchical surface can be totally removed by the cloth. The microstructured surface can not realize anti-smudge properties, since it is unable to repel hexadecane. This demonstrates the anti-smudge properties of the hierarchical surface.

9.7.2.6 Air Pockets Measurements

In order to verify the formation of air pockets, the samples were submerged in water and photographed for any reflectivity. The optical images are shown in Fig. 9.37 (Peng and Bhushan 2016). The treated samples were found to be highly reflective under water, which indicated the formation of a plastron air layer. In contrast, the untreated surface did not become reflective under water, indicating that no air layer was formed. Air layers were present on the nanostructured, microstructured, and hierarchical surfaces. However, the air layer appeared more uniform and stable on the hierarchical surface, especially compared to the nanostructured surface. This suggests that a hierarchical structure is better at trapping air. The data suggests that reticular nanostructure is efficient in air pocket formation. As an added benefit of air pocket formation, due to the presence of these plastron layer, these surfaces could maintain a clean, reflective surface under water (Peng and Bhushan 2016).

Fig. 9.35 Optical images of the nanostructured, microstructured, and hierarchical surfaces before and after self-cleaning experiments. Silicon carbide (SiC) nanoparticles were removed partially from the nanostructured surface, while the microstructured and hierarchical surfaces become totally clean after the experiments. Particle analysis software was used to quantify the amount of particle removal (adapted from Peng and Bhushan 2016)

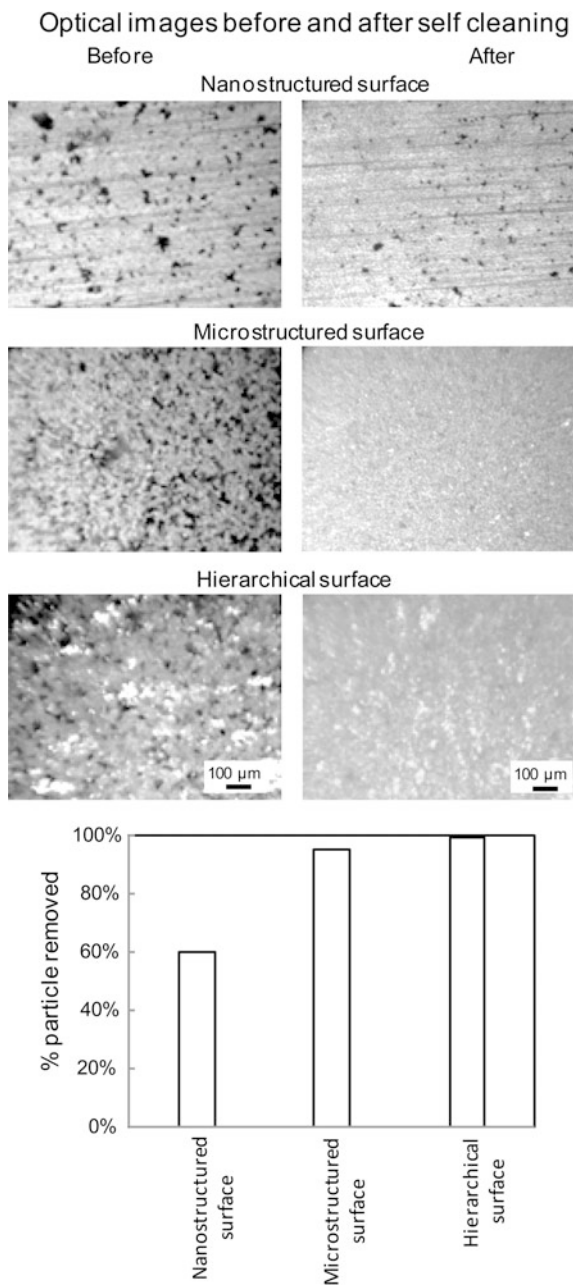
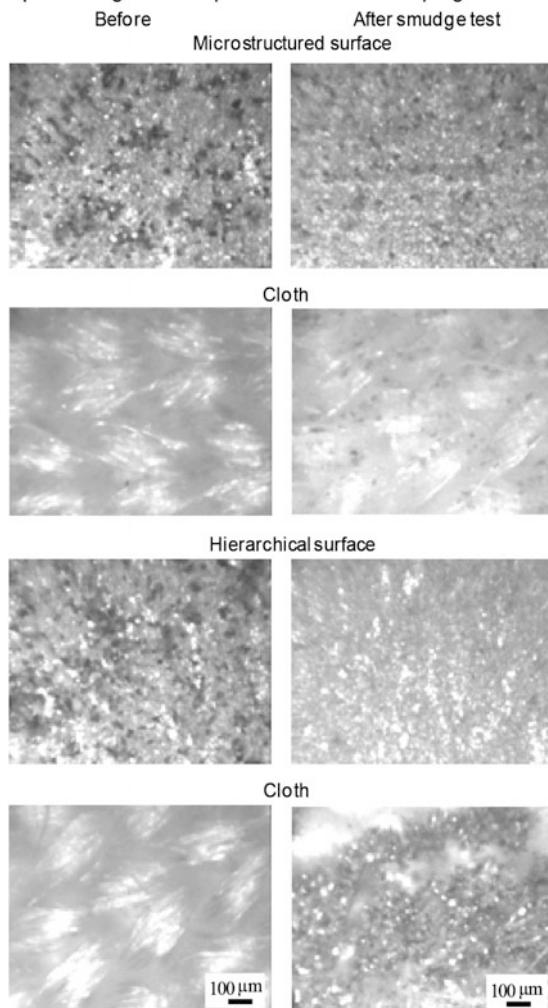


Fig. 9.36 Optical images of the contaminated samples and hexadecane-impregnated microfiber cloth before and after smudge tests on the microstructured and hierarchical surfaces. *Dark spots* on the sample surfaces are particle contaminants (400 mesh particle size by Aldrich, with sizes ranging from 10 to 15 μm). The results demonstrate that the cloth can only wipe a few particles on the microstructured surface, while particles on the hierarchical surface can be totally removed by the cloth (adapted from Peng and Bhushan 2016)

Optical images of sample surfaces and oil-impregnated cloth



9.7.2.7 Corrosion Tests

The corrosion resistance of superoleophobic aluminum surface was assessed by electrochemical experiments. The potentiodynamic polarization curves of the flat aluminum and superoleophobic aluminum surface in 3.5 wt% NaCl solutions are shown in Fig. 9.38 (Peng and Bhushan 2016). The vertical axis is electrical potential and the horizontal axis is the logarithm of current density. For each sample, as seen in Fig. 9.38 the current density decreases during cathodic reaction phase and increases during anodic reaction phase as the electrical potential is increased. The values of corrosion potential and corrosion current density can be

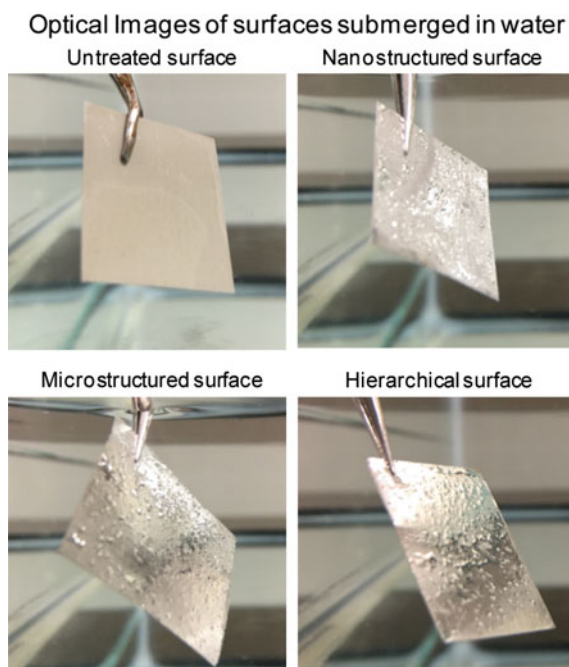


Fig. 9.37 Optical images of an untreated aluminum surface, and the nanostructured, microstructured, and hierarchical surfaces when submerged into water. The nanostructured, microstructured, and hierarchical surfaces became reflective compared with the untreated sample, indicating the formation of air layer on the surfaces. However, the air layer appeared more uniform and stable on the hierarchical surface, especially compared to the nanostructured surface, which suggests that a hierarchical structure is better at trapping air (adapted from Peng and Bhushan 2016)

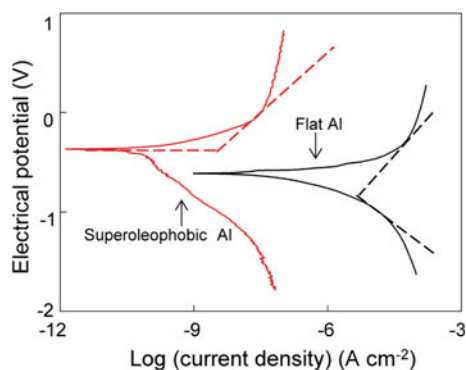


Fig. 9.38 Potentiodynamic polarization curves of the flat aluminum and superoleophobic aluminum surfaces in 3.5 wt% NaCl aqueous solution (Peng and Bhushan 2016)

calculated by the Tafel analysis, which is performed by extrapolating the linear portions of a logarithmic current density versus potential back to their intersection. The intersection point corresponds to corrosion potential and corrosion current density. Typically, a lower corrosion current density and a higher corrosion potential corresponds to a lower corrosion rate and an improved corrosion resistance (Anonymous 2005; Zhang et al. 2008). In the case of superoleophobic aluminum surface, bottom part of the curve is not smooth and only the top curve is used. By comparing the two curves, it can be observed that the corrosion potential of superoleophobic aluminum surface is higher and corrosion density is lower than that of flat Al. This indicates that the superoleophobic aluminum surface is more corrosion resistant than flat Al.

9.7.3 Summary

The microstep structure and the nanoreticula structure believed to be beneficial to trap air-pockets, were combined to form a hierarchical structure on aluminum surfaces. The microstep structure was first formed by HCl etching. Then, the nanoreticula structure was produced on top of the microstep structure through HNO_3 and $\text{Cu}(\text{NO}_3)_2$ etching. The hierarchical structure combined with subsequent fluorosilane dip coating made the surface superoleophobic to hexadecane with a CA of $152^\circ \pm 2^\circ$, CAH $14^\circ \pm 2^\circ$, and TA $14^\circ \pm 2^\circ$. The final superoleophobic aluminum surfaces were mechanically durable and exhibited self-cleaning and anti-smudge properties (Peng and Bhushan 2016).

9.8 Mechanically Durable Superoleophobic Polymer Surfaces

Polymers are used to fabricate various products. Water and oil-repellent plastic surfaces are of interest for a wide range of industrial and consumer applications such as the creation of packaging that is not fouled, reducing waste, and improving the customer experience. To achieve superoleophobicity, nanotexturing of polymer surfaces and a fluorinated layer are needed. Mechanical durability is important if these surfaces are to be feasible for application in various industries including medical, transportation, aerospace, energy, and construction. Various methods for creating nanotextured polymer surfaces typically rely on techniques such as plasma etching (Gogolides et al. 2010) or photolithography (Nie and Kumacheva 2008), top-down approaches that are expensive, time-consuming, and result in wasted material (Mijatovic et al. 2005). Alternatively, the roughness of a polymer surface can be altered through the use of nanoparticles.

Brown and Bhushan (2016b) produced superoleophobic polycarbonate through the incorporation of nanoparticles into the polymer surface. Polycarbonate is known

to undergo solvent-induced phase transformation when exposed to acetone and the resulting crystallization leads to a rough, superhydrophobic surface (Zhao et al. 2006; Cui et al. 2012). By introducing nanoparticles into the acetone solvent, polycarbonate–nanoparticle (PC–NP) composites surfaces with re-entrant geometry were created. Since the nanoparticles are only incorporated near the interface, this technique could be advantageous compared to other polymer nanocomposite fabrication techniques where nanoparticles are distributed throughout the polymer, affecting the properties of the bulk material. Roughened polymer surfaces were then fluorinated via chemical vapor deposition of a fluorosilane. Surfaces were characterized for wettability and wear resistance (Brown and Bhushan 2016b).

9.8.1 Experimental Details

To create a superoleophobic surface, polycarbonate was treated with an acetone–nanoparticle (acetone–NP) mixture. It was found that the nanoparticles become incorporated into the polymer during swelling and the subsequent polymer crystallization can be directed, Fig. 9.39 (Brown and Bhushan 2016b). By creating polymer–NP composite surfaces in this way, re-entrant geometries were achieved as the nanoparticle agglomerates were impregnated into the surface and near-surface region of the polymer. Nanoparticles incorporated deeper into the polymer would have a less pronounced effect on the surface topography.

Polycarbonate sheet (PC, Lexan 9030, SABIC Innovative Plastics IP BV) cut to dimensions of 25 by 10 mm were used throughout. Silica nanoparticles (NP, 7 nm diameter, Aerosil 380, Evonik Industries) were dispersed in acetone (Fisher Scientific Inc.) using an ultrasonic homogenizer (Branson Sonifier 450A, 20 kHz frequency at 35 % amplitude) at various concentrations, and optimized for wettability. The polycarbonate samples were immersed in the acetone–NP mixture for 5 min before being removed and allowed to dry in air. To activate the surface for silane attachment, samples were UV irradiated for 40 min (15 W, $\lambda_{\text{max}} = 254$ nm) or treated with O₂ plasma (Plasmalab System 100, Oxford Instruments) at an O₂ flow

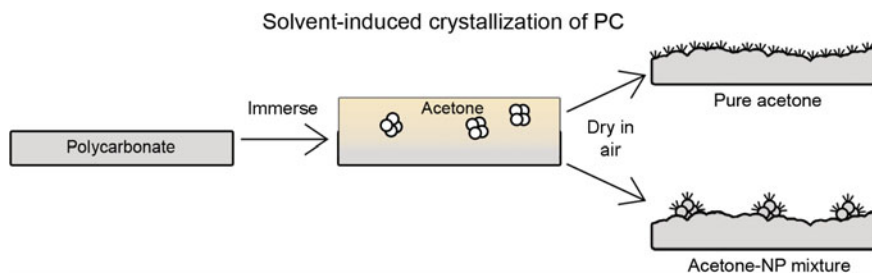


Fig. 9.39 Schematic of solvent-induced crystallization of polycarbonate using either pure acetone or an acetone–NP mixture (Brown and Bhushan 2016b)

rate of 20 sccm and a power of 40 W for 2 min. Both techniques were found to result in similar levels of activation and only UV irradiated samples are reported. Samples were fluorinated via chemical vapor deposition of a silane. One drop of trichloro(1H,1H,2H,2H-perfluorooctyl) silane (fluorosilane, Sigma Aldrich) was deposited next to the samples which were covered and left for 6 h (Brown and Bhushan 2016b).

9.8.2 Results and Discussion

The wettability and wear resistance of nanostructured surfaces are presented in this section.

9.8.2.1 Wettability of Surfaces

Untreated polycarbonate (flat PC) is found to be slightly hydrophilic with water contact angles of $76 \pm 1^\circ$, Table 9.8 (Brown and Bhushan 2016b). After immersion in acetone for 5 min followed by drying in air, the surface became opaque; suggesting crystallization of the polymer had taken place. The solvent-induced phase transformation led to a hierarchical structure of crystalline nanostructures atop micron-sized mounds, Fig. 9.40a. This roughness was sufficient to create a superhydrophobic surface with water droplets displaying contact angles of $158 \pm 1^\circ$ with low tilt angles due to the ability of the hierarchical surface to trap air and thus create a composite interface. However, due to the low contact angles for hexadecane on flat polycarbonate (ca. 12°), the acetone-treated surface is superoleophilic with hexadecane fully wetting the surface. Activation of the surface by UV irradiation followed by fluorination via silane attachment led to hexadecane angles of $76 \pm 2^\circ$ for the flat surface and $100 \pm 2^\circ$ for the acetone-treated surface, Table 9.8. This low angle is due to the lower surface tension of hexadecane being unable to support a composite interface on the hierarchical structure of the acetone-treated polycarbonate (Brown and Bhushan 2016b).

In order to create superoleophobic surfaces, nanoparticles were added to the acetone solvent used during the solvent-induced phase transformation of polycarbonate. The resulting surface was found to be dramatically different from that of the acetone-treated polycarbonate. Instead of a consistent coverage of nanostructures atop micron mounds, the nanotexturing was instead limited to discrete micron-sized spherulites, Fig. 9.40b. This is believed to be due to the presence of the nanoparticle agglomerates, which are incorporated into the surface and near-surface during polymer swelling and act as nucleation sites for polycarbonate crystallization during evaporation of the solvent. The result is re-entrant, hierarchical structures as shown in Fig. 9.41. The water contact angle of the polycarbonate-nanoparticle (PC-NP)

Table 9.8 Comparison of static contact angles and tilt angles for water and hexadecane droplets deposited on polycarbonate surfaces (Brown and Bhushan 2016b)

Surface	Water		Hexadecane	
	Contact angle (°)	Tilt angle (°)	Contact angle (°)	Tilt angle (°)
Flat PC	76 ± 1	N/A	12 ± 2	N/A
Flat PC + fluorosilane	110 ± 2	N/A	76 ± 2	N/A
Acetone treated PC	158 ± 1	3 ± 1	~0	N/A
Acetone treated PC + fluorosilane	163 ± 2	2 ± 1	100 ± 2	N/A
PC–NP composite surface	30 ± 2	N/A	~0	N/A
PC–NP composite surface + fluorosilane	165 ± 2	2 ± 1	154 ± 2	5 ± 2

composite surface was $30 \pm 2^\circ$ indicating the presence of the hydrophilic silica nanoparticle agglomerates on the surface. After UV activation and fluorosilane treatment, the surface became superhydrophobic and superoleophobic with contact angles of $165 \pm 2^\circ$ and $154 \pm 2^\circ$ for water and hexadecane respectively, Table 9.8 (Brown and Bhushan 2016b). The presence of the re-entrant, hierarchical structures enables the formation of a favorable liquid-vapor interface for lower surface tension liquids, such as hexadecane, that exhibit contact angles $<90^\circ$ on the corresponding flat surface.

In order to optimize the tilt angle of the surface, the concentration of nanoparticles in the acetone solvent was varied. An optimum hexadecane tilt angle of 5° was found on the fluorinated PC–NP composite surface resulting from an acetone–NP mixture concentration of around 8 mg mL^{-1} , Table 9.8. At this concentration, discrete spherulites were formed and their re-entrant geometry resulted in good oil repellency and a low hexadecane tilt angle (Brown and Bhushan 2016b).

9.8.2.2 Wear Resistance of Surface

The mechanical durability of the polymer-nanoparticle composite surface was investigated through the use of tribometer wear experiments and the resulting optical images, showing a portion of the wear track, are displayed in Fig. 9.42. The initial wear experiments were carried out with a load of 20 mN, however there so little observable defects found on the surface after this experiment and the coating remained oil repellent. To further test the durability of the surface, the load was increased to 45 mN. This increased load resulted in an observable wear scar, upon which hexadecane droplets were found to pin when rolled over the wear scar location. However higher magnification images confirmed that the surface features were not completely destroyed and, after re-application of the fluorosilane, the

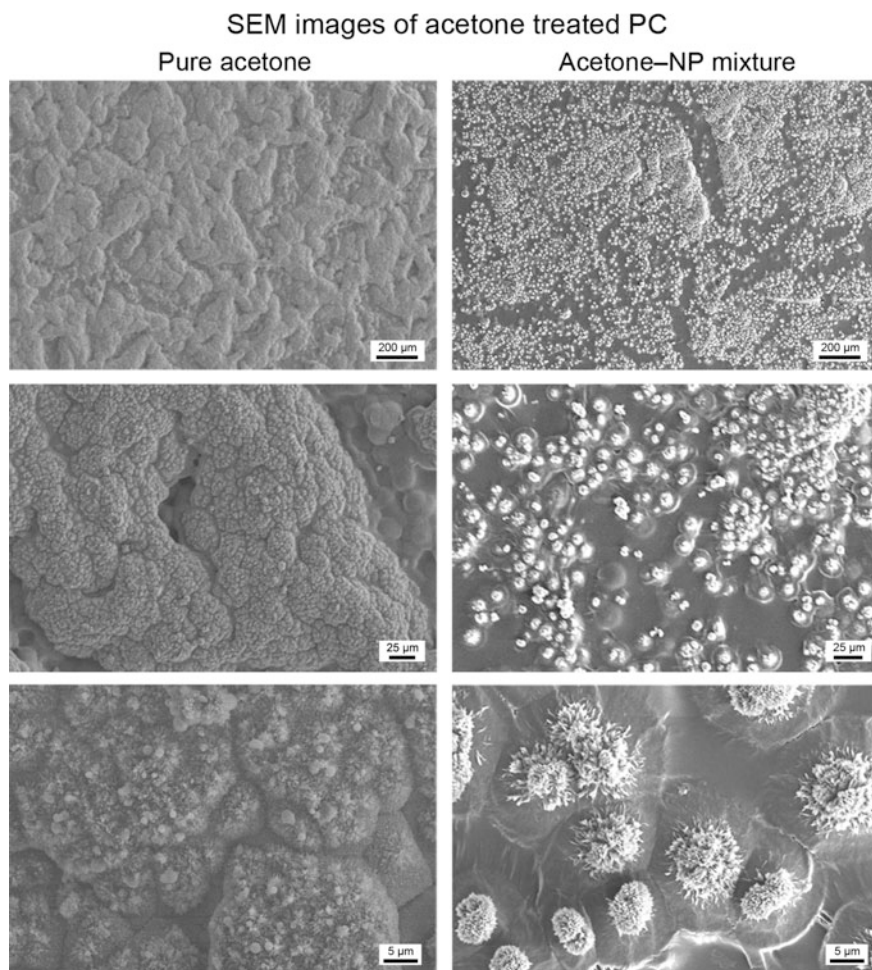


Fig. 9.40 SEM images of solvent-induced crystallization of polycarbonate using either pure acetone or an optimized acetone-NP mixture. **a** For pure acetone, the resulting surface contains good coverage of nanostructures atop micron-sized mounds. **b** For the acetone-NP mixture, the nanostructures are limited to discrete micron-sized spherulites due to the nanoparticle aggregates acting as nucleation sites for the polycarbonate crystallization (Brown and Bhushan 2016b)

surface was found to regain its oil repellency suggesting that only the low surface tension material was removed at the higher load and that any damage to the underlying polymer–nanoparticle composite structures was minimal (Brown and Bhushan 2016b). In addition, these surfaces were found to maintain their repellency towards water and oil after 6 months of storage with no noticeable degradation in their liquid repellent properties.

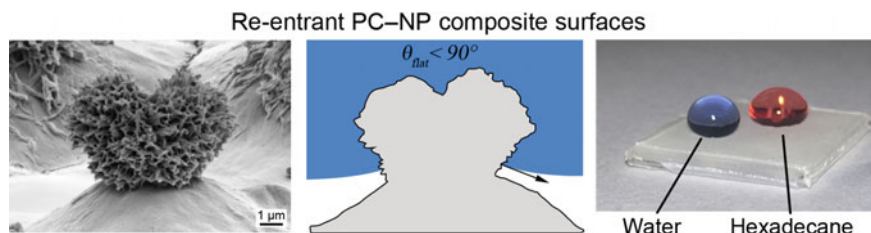


Fig. 9.41 SEM images of the PC–NP composite surface displaying re-entrant geometry. This re-entrant surface, once fluorinated, was found to be repellent towards both hexadecane and water (Brown and Bhushan 2016b)

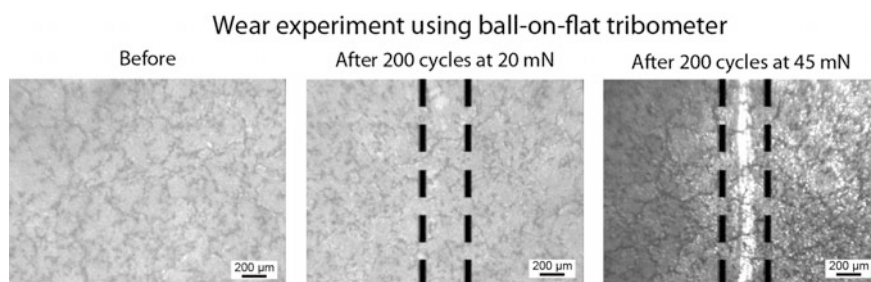


Fig. 9.42 Optical micrographs before and after wear experiments using ball-on-flat tribometer at 20 and 45 mN loadings for fluorinated PC–NP composite surfaces (Brown and Bhushan 2016b)

9.8.3 Summary

Mechanically durable, superoleophobic plastic surfaces were created through a facile method involving the impregnation of polycarbonate with silica nanoparticles during solvent-induced phase transformation. Following treatment, re-entrant structures were present on the surface due to the nanoparticle agglomerates acting as nucleation sites for polymer crystallization. After fluorosilane treatment, the surfaces displayed both high contact angles and low tilt angles for water and hexadecane. The super-repellent surfaces were found to be durable (Brown and Bhushan 2016b).

9.9 Closure

Strategies to achieve superoleophobicity in air are presented. Expressions for the surface properties for oleophobic/philic surfaces have been developed for various interfaces—solid-air-water, solid-air-oil, and solid-water-oil interfaces. A fabrication technique and characterization of mechanically durable nanoparticle composite

coatings for superoleophobicity is described. A flexible, layer-by-layer technique to develop coatings to provide a combination of mechanically durable superliquiphilicity and superliquiphobicity is then described. Finally, fabrication techniques for mechanically durable aluminum and plastic surfaces providing superoleophobicity are described.

References

- Adamson A. V. (1990), *Physical Chemistry of Surfaces*, Wiley, New York.
- Anonymous (1994), ASTM standard 3-89, (1994), Metals Test Methods and Analytical Procedures, *Annual Book of ASTM standards* (v.03.02, Wear and erosion; metal corrosion), ASTM, Philadelphia.
- Anonymous (2005), ISO 17475:2005, Corrosion of Metals and Alloys-Electrochemical Test Methods-Guidelines for Conducting Potentiostatic and Potentiodynamic Polarization Measurements. American National Standards Institute.
- Anonymous (2015a), *Silicone Fluid Technical Data*, retrieved from: http://www.shinetsusilicone-global.com/catalog/pdf/kf96_e.pdf, accessed July 26 2015.
- Anonymous (2015b), *Fluorinert™ Electronic Liquid FC-72* retrieved from: <http://multimedia.3m.com/mws/media/648920/fluorinert-electronic-liquid-fc-72.pdf>, accessed August 7 2015.
- Barthlott, W. and Neinhuis, C. (1997), "Purity of the Sacred Lotus, or Escape from Contamination in Biological Surfaces," *Planta* **202**, 1-8.
- Barthwal, S., Kim, Y. S. and Lim, S.-H. (2013), "Mechanically Robust Superamphiphobic Aluminum Surface with Nanopore-Embedded Microtexture," *Langmuir* **29**, 11966–11974.
- Bellanger, H., Darmanin, T. and Guittard, F. (2012), "Surface Structuration (Micro and/or Nano) Governed by the Fluorinated Tail Lengths toward Superoleophobic Surfaces," *Langmuir* **28**, 186–192.
- Bhushan, B. (2009), "Biomimetics: Lessons from Nature – An Overview," *Phil. Trans. R. Soc. A* **367**, 1445-1486.
- Bhushan, B. (2012), *Biomimetics: Bioinspired Hierarchical-Structured Surfaces for Green Science and Technology*, Springer-Verlag, Heidelberg, Germany.
- Bhushan, B. (2013), *Introduction to Tribology*, 2nd ed., Wiley, New York.
- Bhushan, B. and Jung, Y. C. (2011), "Natural and Biomimetic Artificial Surfaces for Superhydrophobicity, Self-Cleaning, Low Adhesion, and Drag Reduction," *Prog. Mater. Sci.* **56**, 1–108.
- Bhushan, B. and Muthiah, P. (2013), "Anti-Smudge Screening Apparatus for Electronic Touch Screens," *Microsyst. Technol.* **19**, 1261–1263
- Bhushan, B., Koch, K., and Jung, Y. C. (2008), "Nanostructures for Superhydrophobicity and Low Adhesion," *Soft Matter* **4**, 1799-1804.
- Bhushan, B., Jung, Y. C., and Koch, K. (2009), "Micro-, Nano- and Hierarchical Structures for Superhydrophobicity, Self-Cleaning and Low Adhesion," *Phil. Trans. R. Soc. A* **367**, 1631-1672
- Bixler, G. D. and Bhushan, B. (2012a), "Biofouling: Lessons from Nature," *Phil. Trans. R. Soc. A* **370**, 2381-2417.
- Bixler, G. D. and Bhushan, B. (2012b), "Bioinspired Rice Leaf and Butterfly Wing Surface Structures Combining Shark Skin and Lotus Effects," *Soft Matter* **8**, 11271-11284 (2012).
- Bixler, G.D. and Bhushan, B. (2013a), "Fluid Drag Reduction with Shark-skin Riblet Inspired Microstructured Surfaces," (Invited), *Adv. Func. Mater.* **23**, 4507-4528.
- Bixler, G. D. and Bhushan, B. (2013b), "Fluid Drag Reduction and Efficient Self-Cleaning with Rice Leaf and Butterfly Wing Bioinspired Surfaces," *Nanoscale* **5**, 7685-7710.

- Brown, P. S. and Bhushan, B. (2015a), "Mechanically Durable, Superoleophobic Coatings Prepared by Layer-by-Layer Technique for Anti-smudge and Oil-water Separation," *Sci. Rep. – Nature* **5**, 8701.
- Brown, P. S. and Bhushan, B. (2015b), "Mechanically Durable, Superomniphobic Coatings Prepared by Layer-by-Layer Technique for Self-cleaning and Anti-smudge," *J. Colloid Interf. Sci.* **456**, 210-218.
- Brown, P. S. and Bhushan, B. (2015c), "Bioinspired, Roughness-Induced, Water and Oil Super-philic and Super-phobic Coatings Prepared by Adaptable layer-by-Layer Technique," *Sci. Rep. – Nature* **5**, 14030.
- Brown, P. S. and Bhushan, B. (2016a), "Designing Bioinspired Superoleophobic Surfaces," *APL Materials* **4**, 015703.
- Brown, P. S. and Bhushan, B. (2016b), "Durable, Superoleophobic Polymer-nanoparticle Composite Surfaces with Re-entrant Geometry via Solvent-induced Phase Transformation," *Sci. Rep. – Nature* **6**, 21048.
- Brown, P. S., Atkinson, O. D. L. A. and Badyal, J. P. S. (2014) "Ultrafast Oleophobic –Hydrophilic Switching Surfaces for Antifogging, Self-Cleaning, and Oil–Water Separation," *ACS Appl. Mater. Interfaces* **6**, 7504–7511.
- Bunshah, R. F. (1994), *Handbook of Deposition Technologies for Films and Coatings: Science, Technology and Applications*, Applied Science Publishers, Westwood, New Jersey.
- Campos, R., Guenther, A. J., Meuler, A. J., Tuteja, A., Cohen, R. E., McKinley, G. H., Haddad, T. S. and Mabry, J. M. (2012), "Superoleophobic Surfaces Through Control of Sprayed-on Stochastic Topography," *Langmuir* **28**, 9834–9841.
- Cao, L., Jones, A. K., Sikka, V. K., Wu, J. and Gao, D. (2009), "Anti-Icing Superhydrophobic Coatings," *Langmuir* **25**, 12444–12448.
- Cebeci, F. Ç., Zhizhong, W., Zhai, L., Cohen, R. E., and Rubner, M. F. (2006), "Nanoporosity-Driven Superhydrophilicity: A Means to Create Multifunctional Antifogging Coatings," *Langmuir* **22**, 2856–2862.
- Cheng, Q., Li, M., Zheng, Y., Su, B., Wang, S. and Jiang, L. (2011), "Janus interface materials: superhydrophobic air/solid interface and superoleophobic water/solid interface inspired by a lotus leaf," *Soft Matter* **7**, 5948–5951.
- Cui, Y., Paxson, A. T., Smyth, K. M., and Varanasi, K. K. (2012), "Hierarchical Polymeric Textures via Solvent-induced Phase Transformation: A Single-step Production of Large-area Superhydrophobic Surfaces," *Colloids Surf. A* **394**, 8–13.
- Darmanin, T., Guittard, F., Amigoni, S., Taffin de Givenchy, E., Noblin, X., Kofman, R. and Celestini, F. (2011), "Superoleophobic Behavior of Fluorinated Conductive Polymer Films Combining Electropolymerization and Lithography," *Soft Matter* **7**, 1053–1057.
- Das, A., Schutzius, T. M., Bayer, I. S. and Megaridis, C. M. (2012), "Superoleophobic and Conductive Carbon Nanofiber/Fluoropolymer Composite Films," *Carbon* **50**, 1346–1354.
- Davis, J. R. (1993), *ASM Special Handbook, Aluminum and Aluminum Alloys*, ASM International, Materials Park, Ohio.
- Dean, B. and Bhushan, B. (2010), "Shark-Skin Surfaces for Fluid-Drag Reduction in Turbulent Flow: A Review," *Phil. Trans. Roy. Soc. A* **368**, 4775–4806.
- Deng, X., Mammen, L., Butt, H.-J. and Vollmer, D. (2012), "Candle Soot as a Template for a Transparent Robust Superamphiphobic Coating," *Science* **335**, 67–70.
- Du, X., Li, X. and He, J. (2010), "Facile Fabrication of Hierarchically Structured Silica Coatings from Hierarchically Mesoporous Silica Nanoparticles and Their Excellent Superhydrophilicity and Superhydrophobicity" *ACS Appl. Mater. Interfaces* **2**, 2365–2372.
- Ebert, D. and Bhushan, B. (2012), "Transparent, Superhydrophobic, and Wear-Resistant Coatings on Glass and Polymer Substrates Using SiO₂, ZnO, and ITO nanoparticles," *Langmuir* **28**, 11391–11399.
- Feng, L., Zhang, Z., Mai, Z., Ma, Y., Liu, B., Jiang, L. and Zhu, D. (2004), "A Super-Hydrophobic and Super-Oleophilic Coating Mesh Film for the Separation of Oil and Water," *Angew. Chem., Int. Ed.* **43**, 2012–2014.

- Fu, X. and He, X. (2008), "Fabrication of Super-Hydrophobic Surfaces on Aluminum Alloy Substrates," *Appl. Surf. Sci.* **255**, 1776–1781.
- Genzer, J. and Efimenko, K. (2006), "Recent Developments in Superhydrophobic Surfaces and Their Relevance to Marine Fouling: A Review," *Biofouling* **22**, 339–360.
- Goddard, E. D. (1986) "Polymer–Surfactant Interaction. Part II. Polymer and Surfactant of Opposite Charge," *Colloids Surf.* **19**, 301–329.
- Gogolides, E., Vlachopoulou, M., Tsoungeni, K., Vourdas, N., and Tserepi, A. (2010), "Micro and Nano Structuring and Texturing of Polymers Using Plasma Processes: Potential Manufacturing Applications," *Int. J. Nanomanuf.* **6**, 152–163.
- Grosu, G., Andrzejewski, L., Veilleux, G. and Ross G. G. (2004), "Relation Between the Size of Fog Droplets and Their Contact Angles with CR39 Surfaces," *J. Phys. D* **37**, 3350–3355.
- Guo, Z., Zhou, F., Hao, J. and Liu, W. (2005), "Stable Biomimetic Super-Hydrophobic Engineering Materials," *J. Am. Chem. Soc.* **127**, 15670–15671.
- Han, D. and Steckl, A. J. (2009), "Superhydrophobic and Oleophobic Fibers by Coaxial Electrospinning," *Langmuir* **25**, 9454–9562.
- Hatch, J. E. (1984), *Aluminum-Properties and Physical Metallurgy*, Am Soc Metals, Metals Park, Ohio.
- Haynes, W. M. (2014), *CRC Handbook of Chemistry and Physics* 95th Ed., Taylor and Francis Group, Boca Raton, FL.
- He, Z., Ma, M., Lan, X., Chen, F., Wang, K., Deng, H., Zhang, Q. and Fu, Q. (2011), "Fabrication of a Transparent Superamphiphobic Coating with Improved Stability," *Soft Matter* **7**, 6435–6443.
- He, M., Zhou, X., Zeng, X., Cui, D., Zhang, Q., Chen, J., Li, H., Wang, J., Cao, Z. and Song, Y. (2012), "Hierarchically Structured Porous Aluminum Surfaces for High-Efficient Removal of Condensed Water," *Soft Matter* **8**, 6680–6683.
- Hensel, R., Helbig, R., Aland, S., Braun, H.-G., Voig, A., Neinhuis, C. and Werner, C. (2013) "Wetting Resistance at Its Topographical Limit: The Benefit of Mushroom and Serif T Structures," *Langmuir* **29**, 1100–1112.
- Hsieh, C.-T., Chen, J.-M., Kuo, R.-R., Lin, T.-S. and Wu, C.-F. (2005), "Influence of Surface Roughness on Water- and Oil-Repellent Surfaces Coated With Nanoparticles," *Appl. Surf. Sci.* **240**, 318–326.
- Hsieh, C.-T., Wu, F.-L. and Chen, W.-Y. (2009), "Super Water- and Oil-Repellencies from Silica-Based Nanocoatings," *Surf. Coat. Technol.* **203**, 3377–3384.
- Hutton, S. J., Crowther, J. M. and Badyal, J. P. S. (2000), "Complexation of Fluorosurfactants to Functionalized Solid Surfaces: Smart Behavior," *Chem. Mater.* **12**, 2282–2286.
- Im, M., Im, H., Lee, J.-H., Yoon, J.-B. and Choi, Y.-K. (2010), "A Robust Superhydrophobic and Superoleophobic Surface with Inverse-Trapezoidal Microstructures on a Large Transparent Flexible Substrate," *Soft Matter* **6**, 1401–1404.
- Israelachvili, J. N. (1992), *Intermolecular and Surface Forces*, 2nd Edition, Academic Press, London.
- Jalili, M. M. and Moradian, S. (2009), "Deterministic Performance Parameters for an Automotive Polyurethane Clearcoat Loaded With Hydrophilic or Hydrophobic Nano-Silica," *Prog. Org. Coat.* **66**, 359–366.
- Jin, H., Tian, X., Ikkala, O. and Ras, R. H. A. (2013), "Preservation of Superhydrophobic and Superoleophobic Properties Upon Wear Damage," *ACS Appl. Mater. Interfaces* **5**, 485–488.
- Jung, Y. C. and Bhushan, B. (2009), "Wetting Behavior of Water and Oil Droplets in Three Phase Interfaces for Hydrophobicity/phillicity and Oleophobicity/phillicity," *Langmuir* **25**, 14165–14173.
- Kaufman, J. G. and Rooy, E. L. (eds.). (2004), *Aluminum Alloy Castings: Properties, Processes, and Applications*. ASM International, Materials Park, Ohio.
- Kim, Y., Lee, S., Cho, H., Park, B., Kim, D. and Hwang, W. (2012), "Robust Superhydrophilic/Hydrophobic Surface Based on Self-Aggregated Al₂O₃ Nanowires by Single-Step Anodization and Self-Assembly Method," *ACS Appl. Mater. Interfaces* **4**, 5074–5078.

- Koch, K., Bhushan, B., and Barthlott, W. (2009), "Multifunctional Surface Structures of Plants: An Inspiration for Biomimetics," *Prog. Mater. Sci.* **54**, 137-178 (2009).
- Lee, M.-T., Hsueh, C.-C., Freund, M. S. and Ferguson, G. S. (1998) "Air Oxidation of Self-Assembled Monolayers on Polycrystalline Gold: The Role of the Gold Substrate," *Langmuir* **14**, 6419–6423.
- Lee, K. K. and Ahn, C. H. (2013), "Superhydrophilic Multilayer Silica Nanoparticle Networks on a Polymer Microchannel Using a Spray Layer-by-Layer Nanoassembly Method" *ACS Applied Mater. Interfaces* **5**, 8523–8530.
- Lee, S. E., Kim, H. J., Lee, S. H., and Choi, D. G. (2013), "Superamphiphobic surface by Nanotransfer Molding and Isotropic Etching," *Langmuir* **29**, 8070-8075.
- Li, L., Wang, Y., Gallaschun, C., Risch, T. and Sun, J. (2012), "Why Can a Nanometer-Thick Polymer Coated Surface be More Wettable to Water than to Oil?" *J. Mater. Chem.* **22**, 16719–1672.
- Li, L., Huang, T., Lei, J., He, J., Qu, L., Huang, P., Zhou, W., Li, N. and Pan, F. (2014), "Robust Biomimetic-Structural Superhydrophobic Surface on Aluminum Alloy," *ACS Appl. Mater. Interfaces* **7**, 1449–1457.
- Liu, M. J., Want, S. T., Wei, Z. X., Song, Y. L. and Jiang, L. (2009), "Bioinspired Design of a Superoleophobic and Low Adhesive Water/Solid Interface," *Adv. Mater.* **21**, 665-669.
- Liu, L., Zhao, J., Zhang, Y., Zhao, F. and Zhang, Y. (2011), "Fabrication of Superhydrophobic Surface by Hierarchical Growth of Lotus-Leaf-Like Boehmite on Aluminum Foil," *J. Colloid Interface Sci.* **358**, 277–283.
- Liu, L., Feng, X. and Guo, M. (2013a), "Eco-Friendly Fabrication of Superhydrophobic Bayerite Array on Al Foil Via an Etching and Growth Process," *J. Phys. Chem.C* **117**, 25519–25525.
- Liu, T. and Kim, C. J. (2014), "Turning a Surface Super-repellant Even to Completely Wetting Liquids," *Science* **346**, 1096–1100.
- Liu, Y., Liu, J., Li, S., Liu, J., Han, Z. and Ren, L. (2013b), "Biomimetic Superhydrophobic Surface of High Adhesion Fabricated with Micronano Binary Structure on Aluminum Alloy," *ACS Appl. Mater. Interfaces* **5**, 8907–8914.
- Lovingood, D. D., Salter, W. B., Griffith, K. R., Simpson, K. M., Hearn, J. D., and Owens, J. R. (2013), "Fabrication of Liquid and Vapor Protective Cotton Fabrics," *Langmuir* **29**, 15043–15050.
- Lu, S., Chen, Y., Xu, W. and Liu, W. (2010), "Controlled Growth of Superhydrophobic Films by Sol-Gel Method on Aluminum Substrate," *Appl. Surf. Sci.* **256**, 6072–6075.
- Maitra, T., Antonini, C., auf der Mauer, M., Stamatopoulos, C., Tiwari, M. K. and Poulikakos, D. (2014), "Hierarchically Nanotextured Surfaces Maintaining Superhydrophobicity under Severely Adverse Conditions," *Nanoscale* **6**, 8710–8719.
- Meng, H., Wang, S., Xi, J., Tang, Z. and Jiang, L. (2008), "Facile Means of Preparing Superamphiphobic Surfaces on Common Engineering Metals," *J. Phys. Chem.C* **112**, 11454–11458.
- Mijatovic, D., Eijkel, J. C. T., and van den Berg, A. (2005), "Technologies for Nanofluidic Systems: Top-down vs. Bottom-up—A Review," *Lab Chip* **5**, 492–500.
- Muthiah, P., Bhushan, B., Yun, K. and Kondo, H. (2013), "Dual-Layered-Coated Mechanically-Durable Superomniphobic Surfaces With Anti-Smudge Properties," *J. Colloid Interf. Sci.* **409**, 227–236.
- Nie, Z. and Kumacheva, E. (2008), "Patterning Surfaces with Functional Polymers," *Nature Mater.* **7**, 277–290.
- Nishimoto, S. and Bhushan, B. (2013), "Bioinspired Self-cleaning Surfaces with Superhydrophobicity, Superoleophobicity, and Superhydrophilicity," *RSC Advances* **3**, 671–690.
- Nishino, T., Meguro, M., Nakamae, K., Matsushita, M., and Ueda, Y. (1999), "The Lowest Surface Free Energy Based on $-CF_3$ Alignment," *Langmuir* **15**, 4321-4323.
- Nosonovsky, M. and Bhushan, B. (2008), *Multiscale Dissipative Mechanisms and Hierarchical Surfaces: Friction, Superhydrophobicity, and Biomimetics*, Springer, Heidelberg, Germany.

- Pan, S., Kota, A.K., Mabry, J.M. and Tuteja, A. (2013), "Superomniphobic Surfaces for Effective Chemical Shielding," *J. Am. Chem. Soc.* **135**, 578–581.
- Peng, S. and Bhushan, B. (2016), "Mechanically Durable Superoleophobic Aluminum Surfaces with Microstep and Nanoreticula Hierarchical Structure for Self-Cleaning and Anti-smudge Properties," *J. Colloid Interf. Sci.* **461**, 273–284.
- Peng, S., Tian, D., Yang, X. and Deng, W. (2014a), "Highly Efficient and Large-Scale Fabrication of Superhydrophobic Alumina Surface with Strong Stability Based on Self-Congregated Alumina Nanowires," *ACS Appl. Mater. Interfaces* **6**, 4831–4841.
- Peng, S., Yang, X., Tian, D. and Deng, W. (2014b), "Chemically Stable and Mechanically Durable Superamphiphobic Aluminum Surface with a Micro/Nanoscale Binary Structure," *ACS Appl. Mater. Interfaces* **6**, 15188–15197.
- Poetes, R., Holtzmann, K., Franze, K. and Steiner, U. (2010) "Metastable Underwater Superhydrophobicity," *Phys. Rev. Lett.* **105** 166104, 1–4.
- Qian, B. and Shen, Z. (2005), "Fabrication of Superhydrophobic Surfaces by Dislocation-Selective Chemical Etching on Aluminum, Copper, and Zinc Substrates," *Langmuir* **21**, 9007–9009.
- Rakitov, R. and Gorb, S. N. (2013) "Brochosomal coats turn leafhopper (Insecta, Hemiptera, Cicadellidae) integument to superhydrophobic state," *Proc. R. Soc. B* **280**, 20122391, pp 1–9.
- Ren, S., Yang, S. and Zhao, Y. (2004), "Nano-Tribological Study on a Super-Hydrophobic Film Formed on Rough Aluminium Substrates," *Acta Mech. Sin.* **20**, 159–164.
- Saito, T., Tsuchima, Y. and Sawada, H. (2015), "Facile Creation of Superoleophobic and Superhydrophilic Surface by Using Fluoroalkyl End-Capped Vinyltrimethoxysilane Oligomer/Calcium Silicide Nanocomposites—Development of these Nanocomposites to Environmental Cyclical Type-Fluorine Recycle through Formation of Calcium Fluoride," *Colloid Polym. Sci.* **293**, 65 – 73.
- Sheen, Y., Huang, Y., Liao, C., Chou, H. and Chang, F. (2008), "New Approach to Fabricate an Extremely Super-Amphiphobic Surface Based on Fluorinated Silica Nanoparticles," *J. Polym. Sci. Part B: Polym. Phys.* **46**, 1984–1990.
- Slavov, S. V., Sanger, A. R. and Chuang, K. T. (2000), "Mechanism of Silation of Silica with Hexamethyldisilazane," *J. Phys. Chem. B* **104**, 983–989.
- Song, J., Xu, W. and Lu, Y. (2012), "One-Step Electrochemical Machining of Superhydrophobic Surfaces on Aluminum Substrates," *J. Mater. Sci.* **47**, 162–168.
- Song, J., Huang, S., Hu, K., Lu, Y., Liu, X. and Xu, W. (2013), "Fabrication of Superoleophobic Surfaces on Al Substrates," *J. Mater. Chem. A* **1**, 14783–14789.
- Sun, Z., Liao, T., Liu, K., Jiang, L., Kim, J. H., and Dou, S. X. (2014), "Fly-Eye Inspired Superhydrophobic Anti-fogging Inorganic Nanostructures," *Small* **10**, 3001–3006.
- Steele, A., Bayer, I. and Loth, E. (2009), "Inherently Superoleophobic Nanocomposite Coatings by Spray Atomization," *Nano Lett.* **9**, 501–505.
- Tahmasebpour, M., de Martín, L., Talebi, M., Mostoufi, N., and van Ommen, J. R. (2013), "The Role of the Hydrogen Bond in Dense Nanoparticle-Gas Suspensions," *Phys. Chem. Chem. Phys.* **15**, 5788–5793.
- Tajima, K., Tsutsui, T., and Murata, H. (1980), "Thermodynamic Relation of Interfacial Tensions in Three Fluid Phases," *Bull. Chem. Soc. Jpn.* **53**, 1165–1166.
- Thomsen, S. V., Hulme, R., Landa, L. & Landa, K., "High Visible Transmission and Infrared/Ultraviolet Radiation Absorption; for Automotive Windows (Windshields, Sidelites, Backlites and Sunroofs) and in Architectural Windows," US Patent 20050020430 A1, 27 Jan. 2005.
- Thünemann, A. F. and Lochhaas, K. H. (1999), "Surface and Solid-State Properties of a Fluorinated Polyelectrolyte–Surfactant Complex," *Langmuir* **15**, 4867–4874.
- Tsujii, K., Yamamoto, T., Onda, T. and Shibuichi, S. (1997), "Super Oil-Repellent Surfaces," *Angew. Chem. Int. Ed. Engl.* **36**, 1011–1012.
- Tuteja, A., Choi, W., Mabry, J. M., Mckinley, G. H., and Cohen, R. E. (2008), "Robust Omniphobic Surfaces," *Proc. Natl. Acad. Sci. U.S.A.* **105**, 18200–18205.
- Ulman, A. (1996), "Formation and Structure of Self-Assembled Monolayers," *Chem. Rev.* **96**, 1533–1554.

- Vander Voort, G. F. (1984), *Metallography: Principles and Practice*, McGraw-Hill, New York.
- Wang, Y. and Bhushan, B. (2015), "Wear-Resistant and Antismudge Superoleophobic Coating on Polyethylene Terephthalate Substrate Using SiO₂ Nanoparticles," *ACS Appl. Mater. Interf.* **7**, 743-755.
- Wang, X., Hu, H., Ye, Q., Gao, T., Zhou, F. and Xue, Q. (2012), "Superamphiphobic Coatings with Coralline-Like Structure Enabled by One-Step Spray of Polyurethane/Carbon Nanotube Composites," *J. Mater. Chem.* **22**, 9624-9631.
- Wang, Y., Xue, J., Wang, Q., Chen, Q. and Ding, J. (2013), "Verification of Icephobic/Anti-icing Properties of a Superhydrophobic Surface," *ACS Appl. Mater. Interf.* **5**, 3370-3381.
- Wu, S. (1979), "Surface-Tension of Solids-Equation of State Analysis," *J. Colloid Interf. Sci.* **71**, 605-609.
- Wu, W., Wang, X., Wang, D., Chen, M., Zhou, F., Liu, W. and Xue, Q. (2009), "Alumina Nanowire Forests Via Unconventional Anodization and Super-Repellency Plus Low Adhesion to Diverse Liquids," *Chem. Commun.*, 1043-1045.
- Xie, Y., Hill, C. A. S., Xiao, Z., Militz, H. and Mai, C. (2010) "Silane Coupling Agents used for Natural Fiber/Polymer Composites: A Review," *Composites: Part A* **41**, 806-819.
- Yang, J., Zhang, Z., Men, X., Xu, X. and Zhu, X. (2011), "A Simple Approach to Fabricate Superoleophobic Coatings," *New J. Chem.* **35**, 576-580.
- Zhang, F., Zhao, L., Chen, H., Xu, S., Evans, D. G. and Duan, X. (2008), "Corrosion Resistance of Superhydrophobic Layered Double Hydroxide Films on Aluminum," *Angew. Chem. Int. Ed.* **47**, 2466-2469.
- Zhang, J. and Seeger, S. (2011), "Superoleophobic Coatings with Ultralow Sliding Angles Based on Silicone Nanofilaments," *Angew. Chem. Int. Ed.* **50**, 6652-6656.
- Zhao, H., Law, K.-Y. and Sambhy, V. (2011), "Fabrication, Surface Properties, and Origin of Superoleophobicity for a Model Textured Surface," *Langmuir* **27**, 5927-5935.
- Zhao, N., Weng, L., Zhang, X., Xie, Q., Zhang, X., and Xu, J. (2006), "A Lotus-leaf-like Superhydrophobic Surface Prepared by Solvent-Induced Crystallization," *ChemPhysChem* **7**, 824-827.
- Zhu, Z (Ed.). (2004), *Technology of Anodizing Aluminum and Surface Treatment*, Chemical Industry Press, pp. 32-34.
- Zimmerman, J., Reifler, F. A., Fortunato, G., Gerhardt, L.-C. and Seeger, S. (2008) "A Simple, One-Step Approach to Durable and Robust Superhydrophobic Textiles," *Adv. Funct. Mater.* **18**, 3662-3669.

Chapter 10

Shark-Skin Surface for Fluid-Drag Reduction in Turbulent Flow

10.1 Introduction

Nature has created ways of reducing drag in fluid flow, evident in the efficient movement of fish, dolphins, and sharks. The mucus secreted by fish reduces drag as they move through water, protects the fish from abrasion by making the fish slide across objects rather than scrape, and prevents disease by making the surface of the fish difficult for microscopic organisms to adhere to, minimizing biofouling (Shephard 1994). Applications of drag reducing polymers has been long known. For example, by adding as little as a few hundred parts per million guar, a naturally occurring polymer, friction in pipe flow can be reduced by up to two-thirds. Other synthetic polymers are known to provide an even larger benefit (Hoyt 1975; Frings 1988). The compliant skin of the dolphin is also known to reduce drag. By responding to the pressure fluctuations across the surface, a compliant material on the surface of an object in a fluid flow has been shown to be beneficial. A drag reduction of about 7 % has been reported (Choi et al. 1997).

Fast swimming sharks also experience low drag. Lower drag is necessary for shark survival, since it allows sharks to swim faster in order to catch prey (Reif 1985; Bechert et al. 1997a; Dean and Bhushan 2010; Bixler and Bhushan 2013a). The low drag also protects against fouling as these sharks swim through water. The tiny scales covering the skin of fast swimming sharks, known as dermal denticles (skin teeth), are shaped like small riblets and aligned in the direction of fluid flow are believed to be responsible for low drag. Slower sharks are covered in dermal denticles as well, but they are not shaped like riblets and do not provide any drag reduction benefit. The shape of riblets on fast swimming sharks varies greatly, even at different locations on the same shark (Reif 1985; Dean and Bhushan 2010).

It is believed that sharks stay clean due to these microstructured riblets, flexion of the dermal denticles, and a mucous layer (Bechert et al. 1997a, 2000b; Collins and Brebbia 2004; Dean and Bhushan 2010; Bixler and Bhushan 2013a). Because low drag allows for faster movement through water, the increased fluid flow

velocity at the skin reduces microorganism settlement time and promotes antifouling (Kesel and Liedert 2007; Ralston and Swain 2009; Dean and Bhushan 2010). In addition, microorganisms larger than the spacing between riblets are unable to effectively adhere to and ultimately colonize the skin, which further promotes antifouling (Schumacher et al. 2007; Scardino 2009; Brennan et al. 2010; Bixler and Bhushan 2012a).

Low drag surfaces are of interest in both internal and external flow applications. Examples of internal flow include pipelines, catheters, and micro/nanochannels such as micro/nanofluidic based sensors. A major example of external flow is transportation—ships, airplanes, and automobiles. Low drag surfaces have been the subject of much experimentation using shark skin riblet-inspired microtextured surfaces (Dean and Bhushan 2010; Bixler and Bhushan 2013a). Experimental results indicate that shark skin inspired surfaces effectively reduce drag in open and closed channel flow. In open channel flow, drag has been measured using water (Reidy and Anderson 1988; Gillcrist and Reidy 1989; Walsh 1990a; Neumann and Dinkelacker 1991; Rohr et al. 1992; Wen et al. 2014), oil (Bechert et al. 1997b, 2000a; Buttner and Schulz 2011; Gruneberger and Hage 2011), and air (Walsh 1982; Walsh and Lindermann 1984; Bechert et al. 1985, 2000a; Wilkinson and Lazos 1988; Coustols 1989; Walsh and Anders 1989; Subaschandar et al. 1999; Viswanath 1999, 2002; Han et al. 2003; Sareen et al. 2011). Similarly, in closed channel flow, drag also has been measured using water (Reidy and Anderson 1988; Lui et al. 1990; Rohr et al. 1992; Jung and Bhushan 2010; Bixler and Bhushan 2013b), oil (Bixler and Bhushan 2013c), and air (Nitschke 1983; Enyutin et al. 1995; Bixler and Bhushan 2013b). Both drag (for open channel) and pressure drop (for closed channel) measurements characterize the efficiency of riblet drag reduction.

A variety of riblet geometries, configurations, material properties including wettability, fluid viscosity (water, oil, and air), and flow conditions (laminar and turbulent flow) have been used in experiments. Geometries include blade, sawtooth, scalloped, and bullnose geometries with continuous and segmented (aligned and staggered) configurations in water, oil, and air. Both open and closed pipes/channels with various dimensions have been used. Open channel oil experiments with metal riblets show drag reduction of nearly 10 % (Bechert et al. 1997b), while closed channel water experiments with polymer riblets show pressure drop reduction of up to 34 % (Bixler and Bhushan 2013b). Shark skin replicas have also been evaluated, and have reduced pressure drop by up to 30 % in closed channel water flow (Jung and Bhushan 2010; Bixler and Bhushan 2012b).

Larger scale drag reducing efforts have included the experimental 3 M Corp. (Minneapolis, MN) vinyl riblets, as well as the commercially available Speedo brand FastSkin[®] fabric racing swimsuit. Such riblet technology has captured the attention of the National Aeronautics and Space Administration (NASA), U.S. Department of Energy, U.S. Navy, Airbus, Boeing, and Olympic competitors. In the 1984 Los Angeles Olympics and 1987 America's Cup, 3 M riblets were applied to U.S. boats, which presumably helped to secure victories. The 2008

Beijing Olympics witnessed the benefit of the Speedo FastSkin[®] swimsuit, when American Michael Phelps broke eight Olympic records, seven world records, and won eight gold medals, the most of any athlete in any single Olympic showing. The swimsuits reduced drag up to 4 % for men and 3 % for women (Krieger 2004).

In this chapter, based on Dean and Bhushan (2010), Bixler and Bhushan (2013a, b), and Martin and Bhushan (2014, 2016), we present mechanisms of fluid drag and an overview of experimental and fluid flow modeling studies to understand the mechanisms responsible for drag reduction in shark skin and optimization of riblet geometries for low drag, followed by applications of riblets in commercial uses.

10.2 Fluid Drag Reduction

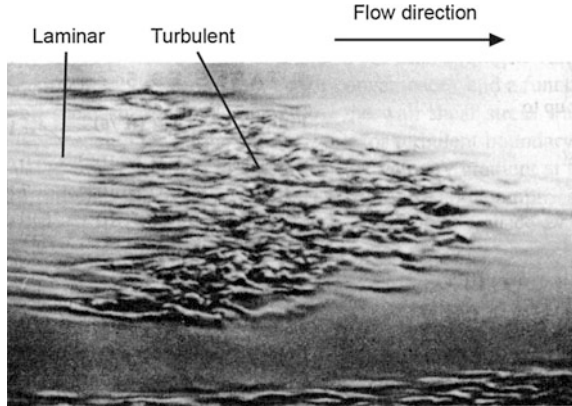
In this section, we first present mechanisms of fluid drag, which include pressure and skin friction drag, followed by the mechanisms of low drag shark skin.

10.2.1 Mechanisms of Fluid Drag

Fluid drag comes in several forms, the most basic of which are pressure drag and skin friction drag (Dean and Bhushan 2010; Bixler and Bhushan 2013a). Pressure drag is the drag associated with the energy required to move fluid out from in front of an object in the flow and then back in place behind the object. Much of the drag associated with walking through water is pressure drag, as the water directly in front of a body must be moved out and around the body before it can move forward. The magnitude of pressure drag can be reduced by creating streamlined shapes. Skin friction or viscous drag is caused by the interactions between the fluid and a surface parallel to the flow, as well as the attraction between molecules of the fluid. Skin friction drag is similar to the motion of a deck of cards sliding across a table. The frictional interactions between the table and the bottom card as well as between each successive card mimic the viscous interactions between molecules of fluid. Moving away from the surface of an object in fluid flow, each fluid layer has a higher velocity until a layer is reached where the fluid has velocity equal to the mean flow. Fluids of higher viscosity—the attraction between molecules—have higher apparent friction between fluid layers, which increases the thickness of the fluid layer distorted by an object in a fluid flow. For this reason, more viscous fluids have relatively higher drag than less viscous fluids. A similar increase in drag occurs as fluid velocity increases (Batchelor 1970; Blevins 1984; Davies 2002; Munson et al. 2012; Pritchard and Mitchell 2015).

The above discussion of friction drag assumes all neighboring fluid molecules move in the same relative direction. Figure 10.1 shows an image of the transition between laminar flow and turbulent flow, in which molecules move in swirling and cross-stream motions such that an average velocity is maintained in the direction of

Fig. 10.1 Transition between laminar and turbulent flow in fluid over a flat plate (adapted from Munson et al. 2012)



flow. Laminar and turbulent boundary layers help describe fluid flow, where turbulent boundary layers lead to higher skin friction drag. The boundary layer is the fluid layer adjacent to the surface, with the innermost layer called the viscous sublayer. In this layer, laminar flow appears smooth and orderly, while turbulent flow appears random and chaotic. Additionally, laminar flow is controlled by viscous forces between the fluid molecules, whereas turbulent flow is controlled by inertial forces. Turbulent vortices in the viscous sublayer naturally translate in cross-flow and streamwise directions, which leads to vortices intermingling and ejecting from the viscous sublayer. This movement increases momentum transfer and shear stresses, which results in higher drag (Kline et al. 1967; Munson et al. 2012). Therefore, laminar flow is preferred for low drag. However, in many real-world fluid flow applications, the boundary layers naturally transition from laminar to turbulent. This transition can be described with the dimensionless Reynolds number (Re), which is the ratio of inertial forces to viscous forces, or (Munson et al. 2012; Pritchard and Mitchell 2015):

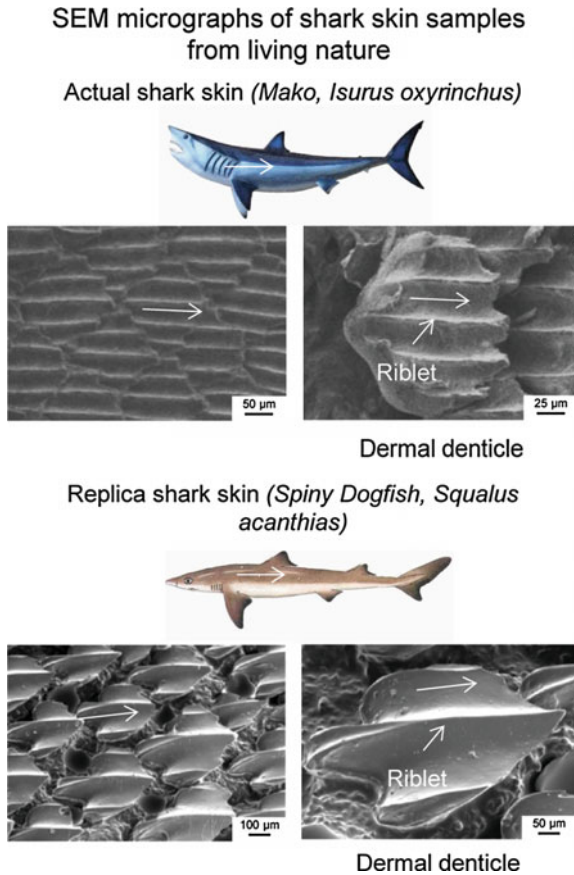
$$Re = \frac{VD}{\nu} \quad (10.1)$$

where V is the fluid mean flow velocity, D is the characteristic length which is the hydraulic diameter (for closed channel) or a distance downstream from the leading edge (for open channel), and ν the fluid kinematic viscosity. For a rectangular closed channel, $D = 4A/WP$, where A is the cross sectional area and WP is the wetted perimeter. Transition from laminar to turbulent flow depends on parameters in (10.1) as well as surface roughness and freestream disturbances, where such features may “trip” the boundary layer to become turbulent. Such transition occurs around $Re = 2300$ and fully turbulent at about $Re = 4000$ for closed channel flow. The transition occurs at $Re = 500,000$ for open channel flow over a flat plate (Munson et al. 2012; Pritchard and Mitchell 2015).

10.2.2 Shark Skin

A small amount of mucus is present on the skin of the sharks (Bechert et al. 1986). However, it is not enough to provide drag benefits, as in the case of fish. It is the microstructured skin that provides reduction in skin friction drag during turbulent flow. The skin of fast swimming sharks (such as Mako, *Isurus oxyrinchus*) is covered with scales called dermal denticles (little skin teeth), which contain specially sized and spaced riblets (microscopic grooves) oriented parallel to the swimming direction. Dermal denticles from both the mako and spiny dogfish shark species are shown in Fig. 10.2, with the flow direction indicated by arrows. The mako shark has scales with little gaps and no offsets (referred to as aligned-segmented riblets), whereas the spiny dogfish has both gaps and offsets (referred to as staggered—segmented riblets). The shape and size of the scales, as well as the number of riblets, varies between shark species. Riblets can also vary between different locations on the same shark (Reif 1985; Jung and Bhushan 2010). The scales are generally 0.2–0.5 mm in size, with the grooves spaced 30–100 μm apart.

Fig. 10.2 SEM micrographs of shark skin samples from living nature. Actual Mako (*top*) (adapted from Bixler and Bhushan 2012b) and replica spiny dogfish (*bottom*) (adapted from Jung and Bhushan 2010) shark skin micrographs are shown at two magnifications. These highlight the scales (dermal denticles) and riblets which are responsible for low drag and antifouling properties. Arrows indicate fluid flow direction



When a shark swims fast during turbulent flow, vortices form on the surface that cause high shear stresses across the entire surface, and can lead to high drag. The microstructured riblets with longitudinal grooves encourage anisotropic flow as well as control vortices on the skin naturally present in turbulent flow. The riblets lift and presumably pin any vortices generated in the viscous sublayer. The low velocity fluid in the riblet valleys causes minimal shear stress across most of the surface, which leads to lower drag. With appropriately sized riblets, for a given velocity, vortices are lifted above the surface and presumably pinned at the riblet tips. Lifting reduces the total shear stress since vortices contact just the small riblet tips (as opposed to the total surface area). Pinning is believed to reduce the cross-stream motion of fluid, which provides anisotropic flow, and ejection of vortices from the viscous sublayer, which reduces momentum transfer (Bechert et al. 1985, 1997a, b, 2000a, b; Lowrey and Harasha 1991; Luchini et al. 1991; Lee and Lee 2001; Dean and Bhushan 2010; Deyuan et al. 2011; Oeffner and Lauder 2012; Bixler and Bhushan 2013a). Turbulent vortices are also present in fluids besides water; therefore the shark skin inspired riblets are expected to provide a similar drag-reducing benefits with any fluid, such as air and oil.

10.3 Experimental Studies

Experiments have been performed on shark skin replicas and shark skin inspired artificial riblets fabricated in the lab (Jung and Bhushan 2010; Dean and Bhushan 2012; Bixler and Bhushan 2012b, 2013a, b, c, d). Such riblets represent those found on actual shark skin. However, their shape and size differ to facilitate manufacturing. The purpose of riblets is to lift and pin vortices while minimizing drag (skin friction) due to the riblets themselves. Since riblets protrude into the flow channel, the increased surface area equates to increased drag. The riblets should lift and pin the vortices, as well as encourage anisotropic flow along the surface. Such efficient flow is found by considering each valley between riblets and minimizing the wetted perimeter, since increased wetted perimeter leads to increased drag. In general, skin friction increases with higher Reynolds numbers.

To present drag data at various geometrical parameters and flow conditions, dimensionless parameters are used. These parameters are measured in wall units, where a wall unit is a parameter nondimensionalized by the wall shear stress velocity. These parameters are denoted by the $^+$ symbol, which allows for better comparison of experiments with various riblet geometries and flow conditions. As shown in (10.1), a characteristic length multiplied by mean flow velocity and divided by kinematic viscosity provides the Reynolds number, which is dimensionless. Similarly, dimensionless numbers based on riblet parameters can also be calculated. Important riblet parameters include spacing (s), height (h), and thickness (t).

The dimensionless numbers based on spacing and height of the riblets are defined as (Walsh 1982; Bechert et al. 1997b; Bixler and Bhushan 2013a):

$$s^+ = \frac{sV_\tau}{\nu} \quad (10.2)$$

$$h^+ = \frac{hV_\tau}{\nu} \quad (10.3)$$

The dimensionless number based on thickness is defined here as (Bixler and Bhushan 2013a)

$$t^+ = \frac{tV_\tau}{\nu} \quad (10.4)$$

where V_τ is the wall shear stress velocity; s^+ , h^+ and t^+ are referred to as dimensionless riblet spacing, height, and thickness parameters, respectively. Wall shear stress velocity is simply a quantity that has dimensions of velocity and is in the form that allows for different wall shear stresses to be compared (Munson et al. 2012).

Considering kinetic energy, the wall shear stress expression $\tau_o = \rho V_\tau^2$ provides the wall shear stress velocity as,

$$V_\tau = \left(\frac{\tau_o}{\rho} \right)^{1/2} \quad (10.5)$$

where ρ is the fluid mass density.

A simple force balance shows that fluid shear stress τ_o imposed on the wall of a uniform surface by the friction of the fluid in a circular pipe is equal to the friction factor multiplied with the pipe dynamic pressure (Blevins 1984; White 2006),

$$\tau_o = \frac{\rho V^2}{2} C_f \quad (10.6a)$$

where C_f is the Fanning friction factor or skin friction coefficient, and is given as

$$C_f = \frac{f}{4} \quad (10.6b)$$

A so-called Blasius formula is one of the first curve fits of the friction factor as a function of Re of air flowing in a smooth pipe in turbulent flow (White 2006),

$$C_f \sim \frac{0.0791}{Re^{1/4}} \quad (10.7)$$

Combining (10.1), (10.6a) and (10.7), the following expression is obtained for turbulent flow in a circular pipe,

$$\tau_o = 0.03955v^{1/4}\rho V^{7/4}D^{-1/4} \quad (10.8)$$

Determining optimal riblet dimensions for various flow conditions is possible by considering dimensionless parameters. For instance, the riblet spacing for a given fluid can be determined by rewriting (10.2) where $s = s^+ v/V_\tau$. This equation indicates that for a constant s^+ value, the required riblet spacing increases as kinematic viscosity ν increases or velocity decreases (Bechert et al. 1992, 1997b, 2000a).

We first provide some flow visualization studies to study drag mechanisms, followed by an overview of the various riblet geometries and various fabrication techniques used to create riblets, as well as their advantages and disadvantages. Finally, we describe the experimental procedures for open and closed channel experimentation using water, oil, and air, followed by results and discussion. Most of the data presented is based on Bixler and Bhushan (2013a, b).

10.3.1 Flow Visualization Studies

Visualizing the interaction between riblets and vortices provides insight into drag mechanisms. Figure 10.3 shows flow visualization experimental results using smoke from atomized oil burned in air, both with and without riblets, and at two different velocities (V) (Lee and Lee 2001). Flow visualization studies also have been carried out by Kline et al. (1967). The figure shows the vortices generated at two velocities V of 3 and 5 m/s for $h/s = 0.5$. These values produce s^+ values of 25.2 and 40.6, respectively, and h^+ values of 12.6 and 20.3, respectively. Vortex sizes were approximately 35–50 wall units in diameter for both cases. It was reported that $V = 3$ m/s case showed drag decreasing, whereas the $V = 5$ m/s case showed drag increasing. In the $V = 3$ m/s case, the vortex diameter was larger than s^+ , which lead to lifting the vortex, and thus lowering drag. However, for the $V = 5$ m/s case, the vortex diameter was about the same as s^+ , therefore providing less vortex lifting and leading to higher drag.

An s^+ near 15 with $h/s = 0.5$ corresponds to approximately three riblets per vortex, where vortices are believed to remain lifted and presumably pinned about the riblet tips. Both s^+ and h^+ information is useful in order to determine relationships between drag, fluid viscosity, and riblet dimensions. Such information allows for scaling riblets for drag reduction and comparing experimental results.

10.3.2 Riblet Geometries and Configurations

Shark skin dermal denticles and riblets exhibit rather complex three dimensional geometries and configurations, therefore fabrication of such microstructured

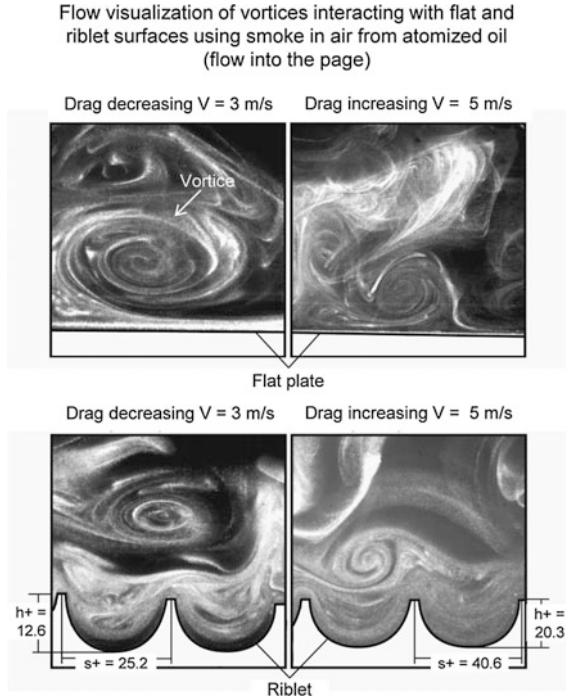


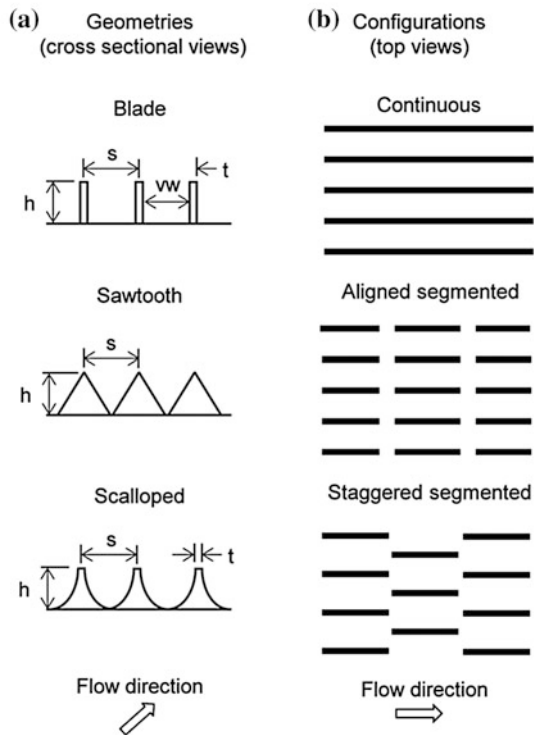
Fig. 10.3 Flow visualization images using smoke from atomized oil burned in air to study the turbulent vortices behavior with and without riblets at two velocities (adapted from Lee and Lee 2001). *Top* Images show the vortices on a flat plate with a relatively large amount of surface contact area, which leads to higher drag. *Bottom* Images show the vortices are lifted above the riblet tips, with a relatively small amount of surface contact area, which leads to lower drag. The dimensionless parameters for height (h^+) and spacing (s^+) aid in the understanding of riblet design for any flow condition. Such parameters are based on riblet spacing or height, fluid kinematic viscosity, and wall shear stress velocity

features is challenging. Additionally, in order to study the dimensional effects of riblets in fluid flow, experiments with varying sizes of relatively durable fluid-tolerant riblets are necessary. However, due to the micro-sized nature of the riblets, this poses difficulty in producing cost effective riblet samples, especially for larger sample sets. The most important characteristics of the riblets have been identified, and the samples have been fabricated for experimentation.

Riblet sizes range from species to species and from location to location on sharks. For reference, the spiny dogfish shark *Squalus acanthias* has triangular shaped riblets with a base width of 100–300 μm , summit radius of about 15 μm , height of 200–500 μm and spacing of 100–300 μm (Jung and Bhushan 2010). Using actual riblets for inspiration, simplified artificial riblet samples include various combinations of blade, sawtooth, scalloped, and bullnose geometries with continuous and segmented (aligned and staggered) configurations. It is believed that actual shark skin most closely resembles scalloped riblets with a staggered-segmented

Fig. 10.4 Typical shark skin inspired riblet geometries and configurations that have been experimentally evaluated. Shown are **a** blade, sawtooth and scalloped geometries as well as **b** continuous, aligned-segmented, and staggered-segmented configurations. Actual shark skin most closely resembles the scalloped geometry and staggered segmented configuration (Bixler and Bhushan 2013a)

Shark skin inspired riblet geometries and configurations



configuration. Schematics of simplified riblets fabricated for experimentation are illustrated in Fig. 10.4 (Bixler and Bhushan 2013a), with typical geometries and configurations. Dimensions of interest include riblet height (h), spacing (s), thickness (t), and valley width (vw); and their importance will be discussed in the results section. Drag reduction data in open and closed channel experiments, and geometries and configurations are summarized in Tables 10.1, 10.2 and 10.3 (Bixler and Bhushan 2013a).

10.3.3 Riblet Fabrication

Riblets have been fabricated with a variety of polymers and metals using various fabrication and assembly processes. Feasible riblet fabrication techniques include using metal shims (Bechert et al. 1997b), machined acrylic (Bechert et al. 1997b; Jung and Bhushan 2010; Dean and Bhushan 2012), machined aluminum (Walsh and Lindemann 1984), extruded/coextruded polymer (Marentic and Morris 1992), embossed polymer (Marentic and Morris 1992), soft lithography (Jung and Bhushan 2010; Bixler and Bhushan 2012b), photolithography (Brennan et al. 2010),

Table 10.1 Drag reduction data in open channel riblet experimentation (Bixler and Bhushan 2013a)

Fluid	Riblet design	Riblet configuration	Riblet material	Max turbulent drag reduction (%)	Reference
Water	Sawtooth	Continuous	Polymer	8	Reidy and Anderson (1988)
	Sawtooth	Continuous	Vinyl	9	Rohr et al. (1992)
	Sawtooth	Continuous	Vinyl	6	Walsh (1990a)
	Sawtooth	Continuous	Vinyl	13	Neumann and Dinkelacker (1991)
	Sawtooth	Continuous	Polymer	7	Gillcrist and Reidy (1989)
Oil	Blade, sawtooth and scalloped	Continuous	Brass and Plexiglas	9.9	Bechert et al. (1997b)
	Blade	Staggered-segmented	Brass	7	Bechert et al. (2000a)
	Blade	Continuous	Titanium and nickel	4.9	Buttner and Schulz (2011)
	Sawtooth	Continuous	Polyurethane	7.6	Gruneberger and Hage (2011)
Air	Blade	Continuous	Metal and polymer	8.5	Wilkinson and Lazos (1988)
	Blade	Staggered-segmented	Epoxy	7	Bechert et al. (2000a)
	Sawtooth, scalloped and bullnose	Continuous	Aluminum and vinyl	8	Walsh (1982)
	Sawtooth, scalloped and bullnose	Continuous	Aluminum and vinyl	8	Walsh and Lindermann (1984)

wet and dry etching (Brennan et al. 2010), grinding (Denkena et al. 2010), rolling (Hirt and Thome 2007), and laser etching (Dickinson and Proudley 1991; Bixler and Bhushan 2013b, c). In general, blade and scalloped riblets are less durable than sawtooth riblets, and continuous riblets are easier to fabricate than segmented. Embossed polymer sheets fabricated from masters appear to be a cost effective way to scale up.

Table 10.2 Drag reduction data in closed channel riblet experimentation (Bixler and Bhushan 2013a)











Fluid	Riblet design	Riblet configuration	Riblet material	Max turbulent pressure drop/drag reduction (%)	References
Water	Blade	Aligned-segmented	Acrylic	23 ^a	Jung and Bhushan (2010)
	Blade and sawtooth	Aligned-segmented and continuous	Vinyl and acrylic	22 ^a	Bixler and Bhushan (2013b)
	Sawtooth	Continuous	Vinyl	9	Rohr et al. (1992)
	Sawtooth	Continuous	Polymer	28	Reidy and Anderson (1988)
	Sawtooth	Continuous	Vinyl	7	Lui et al. (1990)
Oil	Blade	Aligned-segmented and continuous	Acrylic	7 ^a	Bixler and Bhushan (2013a)
Air	Blade	Continuous	Polymer	3	Nitschke (1983)
	Blade and sawtooth	Aligned-segmented and continuous	Vinyl and acrylic	11 ^a	Bixler and Bhushan (2013b)
	Sawtooth	Continuous	Epoxy	7	Enyutin et al. (1995)

^aMicro-sized channel

The 3 M Corp (Minneapolis, MN) produces an experimental vinyl adhesive backed riblet sheet, which has been used in some fluid drag studies. The riblet cross sectional shape consists of equilateral triangles (sawtooth geometry) (Fig. 10.4). The height (h) equals the spacing (s), which range from 44 to 150 μm . These sawtooth riblets have many advantages such as ease of installation onto large flat or curved surfaces and high durability. The sheets are reported to be either coextruded through a die capable of a patterned surface or, more likely, embossed with a negative master mold using heat and/or pressure (Marentic and Morris 1992).

In addition to riblet geometries and configurations, researchers have examined the effect of applying coatings to alter wettability properties. For instance, studies suggest that superhydrophobic surfaces exhibit lower water drag (Ou et al. 2004; Jung and Bhushan 2010; Daniello et al. 2009; Martell et al. 2009, 2010; Bhushan and Jung 2011; Bhushan 2012; Bixler and Bhushan 2012b, 2013b) and self-cleaning (Bhushan and Jung 2011; Bhushan 2012; Bixler and Bhushan 2012b) properties. These are believed to promote antifouling. One study suggests that superoleophilic as well as superoleophobic surfaces can reduce oil drag (Bixler and Bhushan 2013c). Furthermore, one study suggests that a nanostructured coating can

Table 10.3 Drag reduction data in sawtooth riblet airfoil experimentation (Bixler and Bhusan 2013a)

Reynolds number	Airfoil cross section description	Airfoil type	Sawtoothriblet size with $h = s$ (μm)	Riblets applied to longitudinal location/chord length	Strip applied to longitudinal location/chord length	Angle of attack ($^\circ$)	Max drag reduction (%)	References
17,000	Symmetrical	NACA 0012 	180	0–100 %	n/a	0	4.3	Han et al. (2003)
250,000	Symmetrical	NACA 0012 	23, 76, 152	10–100 %	n/a	0	13.3	Caram and Ahmed (1991)
530,000–790,000	Thin	LC 100D 	76, 152	20–95 %	2.5 %	0	2.7	Coustols (1989)
750,000	Thin	GAW-2 	114	12–96 %	10 %	0–6	6	Sundaram et al. (1999)
1,000,000	Symmetrical	NACA 0012 	76, 152	12–96 %	10 %	0–6	13	Sundaram et al. (1996)
1,000,000	Thin	GAW-2 	76	12–96 %	10 %	0–12	10	Subaschandar et al. (1999)
1,000,000	Thin	NACA 0012 	76	12–96 %	10 %	0–12	14	Subaschandar et al. (1999)
1,000,000	Thick	NREL S807 	114	5–100 %	5 %	0	5	Wetzel and Farokhi (1996)
1,000,000–1,850,000	Thick	DU 96-W-180 	44, 62, 100, 152	40–100 %	n/a	0	5	Sareen et al. (2011)
3,000,000	Thick	ADA-S1 	18	15–100 %	6 %	-0.5–1	10	Viswanath and Mukund (1995)

(continued)

Table 10.3 (continued)




Reynolds number	Airfoil cross section description	Airfoil type	Sawtoothribblet size with $h = s$ (μm)	Ribblets applied to longitudinal location/chord length	Strip applied to longitudinal location/chord length	Angle of attack ($^\circ$)	Max drag reduction (%)	References
3,300,000	Thin	CAST 7 	17, 23, 33, 51	15–100 %	n/a	0	3.3	Coustols and Schmitt (1990)
2,000,000–6,000,000	Symmetrical	NACA 0012 	44, 100, 152	0–100 %	5 %	0	7	Present work
4,900,000–22,300,000	n/a	Conical nose with cylindrical body 	33, 51, 76	87 % coverage	n/a	0	4	Coustols and Cousteix (1994)

Table 10.4 Summary of riblet sample dimensions (Bixler and Bhushan 2013b)

Sample set #	Material and fabrication processes	Geometry	Description ^a	Dimensions (μm)	h/s	t/s
1	Laser etched acrylic	Segmented blade L = 850 μm g = 200 μm	<i>Effect of dimensions</i>			
			Baseline	h = 127 vw = 280 t = 127	0.31	0.31
			Shallow	½ h, vw, t	0.16	0.31
			Deep	2 h, vw, t	0.62	0.31
			Narrow	h, ¾ vw, t	0.38	0.38
			Thin	h, vw, ½ t	0.37	0.18
			<i>Single versus double sided</i>			
			Shallow	½ h, vw, t	0.16	0.31
			<i>Effect of coatings</i>			
			Coated	½ h, vw, t	0.16	0.31
			Valleys coated	½ h, vw, t	0.16	0.31
2		Continuous blade L = 101 mm	Baseline	h, vw, t	0.31	0.31
3	Embossed polymer sheets supplied by 3 M Corp.	Continuous sawtooth L = 101 mm vw = 0	80 μm	h = s = t = 80	1	1
			100 μm	h = s = t = 100	1	1
			150 μm	h = s = t = 150	1	1

^aSamples are referred to as “Description (h/s, t/s)” in the chapter

improve the smoothness of milled or laser etched riblets, which may be desirable for air flow (Bixler and Bhushan 2013b).

10.3.4 Drag Measurement Techniques

In this section, we present the various methods to evaluate riblets in water, oil, and air in both open and closed channel experiments. For each of these experimental set ups, descriptions of the various drag measurement techniques are provided.

10.3.4.1 Open Channel

Measurement of drag in an open channel is conducted with water and oil channels, as well as in wind tunnels. Various methods include using force balances and wake

traverses, depending on the fluid and application. For instance, force balances measure water, oil, and air drag, whereas wake traverses measure wind tunnel airfoil drag (Caram and Ahmed 1992; Viswanath 1999). Riblets have also been evaluated on airplanes during flight tests, with riblets covering a portion of the wing and fuselage sections. Total fuel consumption is measured during the riblet flight tests in order to evaluate the total amount of drag reduction (Viswanath 1999).

A typical force balance method for open channel experimentation is illustrated in Fig. 10.5a, where flat sample plates mounted on a force balance are lowered into the moving liquid (typically water or oil) (Bixler and Bhushan 2013a). The flow rate is maintained with a flow channel set-up, as illustrated in Fig. 10.5b, with much research conducted using the so-called Berlin oil channel (Bechert et al. 1992). Propeller driven flow provides a constant current in order to measure the drag resistance force on the sample plates. The percentage drag reduction is calculated using the dimensionless expression $\Delta\tau/\tau_o$ (%), where $\Delta\tau$ is the difference between measured shear stresses on the riblet sample (τ) and the smooth (τ_o) surfaces.

Typical wake traverse and force balance methods for wind tunnel experimentation are also illustrated in Fig. 10.5a. Many experiments have been conducted with subsonic tunnels, whereas fewer with the transonic or supersonic tunnels. Accounting for compressibility effects, speed is defined as the Mach number (Ma), with subsonic ($Ma < 0.75$), transonic ($0.75 < Ma < 1.2$), and supersonic ($1.2 < Ma < 5$) designations. A transonic wind tunnel design is illustrated in Fig. 10.5b, which highlights the transverse wake probe and infrared camera locations. High pressure air in holding tanks is suddenly released into the settling chamber, which then flows across the airfoil sample at a known constant speed. Drag is measured using a traversing wake probe, which measures pressure by traversing downwind from the airfoil during experimentation. The probe measures the pressure in the airfoil wake, and when compared with a smooth airfoil is used to calculate the percentage drag reduction. The drag coefficient (C_d) is calculated with the wake integral expression using velocity calculated from the wake pressure profile (Lee et al. 1978; Barlow et al. 1999; Anderson 2010). The percentage drag reduction is calculated using the dimensionless expression ΔC_d (%), which is the difference between the drag coefficient on the riblet sample and the smooth surfaces. C_d is expressed as (White 2006),

$$C_d = \frac{F_d}{0.5\rho V^2 A_w} \quad (10.9)$$

where F_d is the drag force and A_w is the total surface area in contact with the fluid (or wetted area).

In wind tunnel experiments, riblet covered airfoils have been evaluated over a wide range of speeds and angles of attack. Military aircraft commonly experience transonic and supersonic flight. However, commercial aircraft usually cruise between Mach 0.78 and 0.9 (Barlow et al. 1999; Anonymous 2007; Anderson 2010). In the lab, achieving transonic or supersonic flow requires specialized wind tunnels that are relatively expensive to operate. The airfoil angle of attack is the

(a) Methods (a) and facilities (b) to measure open channel drag with water, oil, and air

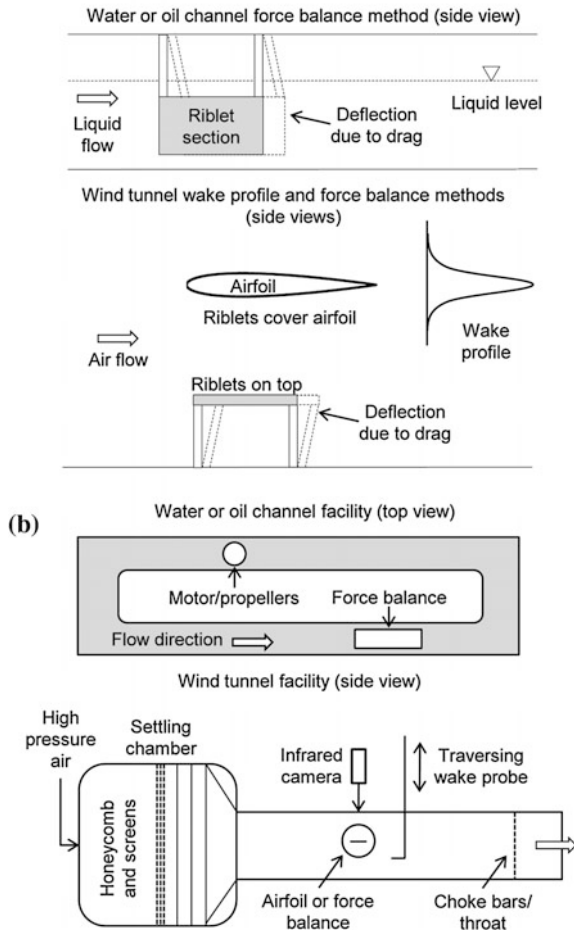


Fig. 10.5 Open channel methods and facilities to measure drag using water, oil, and air. **a** In water or oil channel flow, riblets are applied to a force balance plate that is lowered into the moving fluid (*top*). The deflection of the force balance translates into the total amount of drag. In airfoil experiments (*bottom*), the wake profile determines the total amount of drag. Drag may also be measured with riblets applied to a flat plate or airfoil using a force balance in the wind tunnel. **b** Open flow channels filled with water or oil are used with the force balance (*top*). Shown is the location of the motor and propellers that produce a constant flow. Wind tunnel schematic (*bottom*) illustrates set up for the wake traverse method. As air flows through the wind tunnel, the wake traverse lowers at a specified rate to measure the wake profile. Also shown is the infrared camera position used to visualize turbulence on the airfoil (Bixler and Bhushan 2013a)

angle between level horizontal and the chord lines. This angle varies during flight in order to maintain lift. At lower speeds, a higher angle of attack is required, and at higher speeds, a lower angle of attack is required. Experiments have been

conducted between 0° and 12° angle of attack in order to cover the majority of cruise conditions (Anonymous 2007; Anderson 2010).

A summary of conditions for open channel flat plate experiments is shown in Table 10.1 outlining the various riblet geometries, configurations, and materials that have been evaluated. Also, Table 10.3 shows wind tunnel experiments that have been conducted with various airfoils, conditions, riblet coverage, and trip strip locations. Knowing that riblets may increase drag in laminar flow, riblets were only applied in the turbulent region of an airfoil, thereby leading to improved drag reduction. Trip strips were installed in many experiments in order to force transition at a particular location (Barlow et al. 1999; Anderson 2010).

10.3.4.2 Closed Channel

Measuring drag in closed channel flow is conducted with water, oil, and air experiments using pipes and channels with both circular and rectangular cross sections. Various closed channel experiments have been conducted using riblets applied to their interiors. The fluid flows through the sample test area and the pressure difference between two points was measured with a pressure manometer. In such cases, a lower pressure drop indicates drag reduction. Apparatuses for both split round pipe and rectangular channel designs are illustrated in Fig. 10.6a (Bixler and Bhushan 2013a). Drag reduction is presented as either negative $\Delta\tau/\tau_o$ (%), where $\Delta\tau$ is the difference between shear stresses on the riblet sample surface (τ) and the smooth surfaces (τ_o), or with negative $\Delta P/P_o$ (%) values, where ΔP is the difference in pressure drop between the riblet sample (P) and the smooth (P_o) surfaces.

Generally, the greatest challenge for technology applications is affixing riblets inside of the closed channel. For larger pipes (or macro-sized closed channels), flexible sheets such as the 3 M vinyl adhesive backed riblets can be applied to the interiors. Smaller pipes (or micro-sized closed channels) must be split in order to apply the flexible 3 M riblet sheets. However, when riblets are not in the form of flexible sheets, they need to be fabricated via processes such as milling, soft lithography, or laser etching. Such fabrication generally requires flat and not curved surfaces. For applications using these fabrication techniques, the split rectangular channel design is more feasible, as it allows riblets to be applied inside the channel prior to final assembly.

During experiments, a fluid is introduced a variety of different methods depending on its viscosity and desired flow rates, as shown in Fig. 10.6b (Bixler and Bhushan 2013a). For instance, experiments with water have been conducted with both elevated bottle apparatuses (Jung and Bhushan 2010; Bixler and Bhushan 2013b), as well as syringe and gear pumps (Jung and Bhushan 2010; Dean and Bhushan 2012; Bixler and Bhushan 2013b, c). Experiments have been conducted with air flow by connecting a rotometer to a laboratory air supply (Jung and Bhushan 2010; Bixler and Bhushan 2013b) in order to achieve particular flow velocities. In the case of water and oil experiments, average flow velocity can be

(a) Methods (a) and apparatuses (b) to measure closed channel drag with water, oil, and air

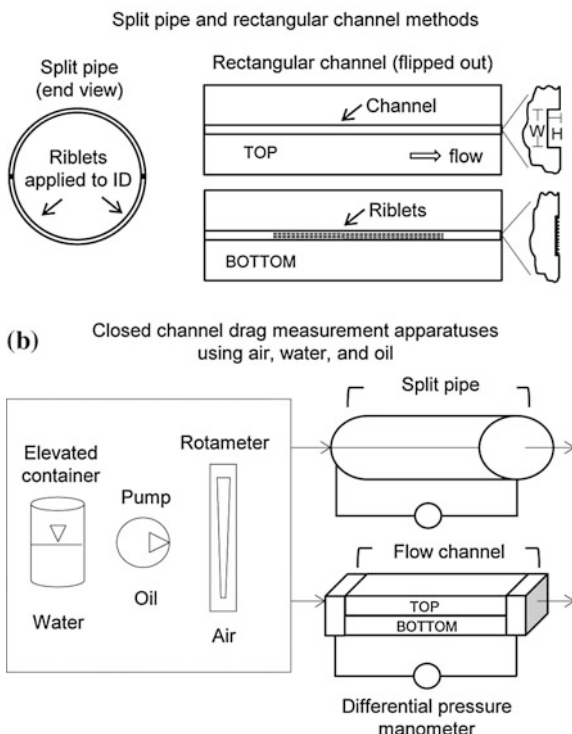


Fig. 10.6 Closed channel methods and apparatuses to measure drag using water, oil, and air. **a** Split designs are necessary in order to apply riblets inside micro-sized closed channels. *Left* Schematic shows a round split pipe, while the *right* shows a rectangular channel sandwich design. The rectangular channel allows for riblets to be fabricated on a flat surface, which may be desirable (adapted from Bixler and Bhushan 2013b). **b** Drag is determined via pressure drop reduction using closed channels lined with riblet samples. Flow is regulated with the elevated container (water), pump (water or oil), and laboratory air connected to a rotameter (air). The pressure drop is measured with a manometer connected to both ends of the flow channel. Interface views are shown highlighting the *top* and *bottom* halves that are sandwiched together (Bixler and Bhushan 2013a)

calculated from the volumetric flow rate and channel cross-sectional area. A summary of experimental closed channel conditions is shown in Table 10.2 outlining the various riblet geometries, configurations, and materials that have been evaluated. Drag is determined via pressure drop reduction, which is measured with a manometer connected to both ends of the flow channel.

Pressure drop predictions for a flat milled channel surface were made for comparison to experimental data for riblet surfaces. These predictions were made using the methodology presented in Chap. 11 on the Rice Leaf and Butterfly Wing Effect.

10.3.5 Riblet Results and Discussion

In this section, we present open and closed channel drag measurement results using water, oil, and air flow (Bixler and Bhushan 2013a). Results are discussed and compared between the various measurement techniques, riblet geometries, riblet configurations, and flow regimes. This comparison helps to provide an understanding of the data on riblet drag reduction.

Open and closed channel results can be presented similarly, including drag compared to riblet geometry and dimensions. Comparing and studying such parameters allows for the development of lessons learned in order to optimize riblets. Micro-sized closed channel results are presented with pressure drop reduction at various Reynolds numbers based on the channel dimensions. This differs from open channel results in order to account for hydraulic diameter, due to the interaction of vortices from neighboring walls (Bixler and Bhushan 2013a). Therefore both open and closed channel results are presented in forms that best represent their findings.

10.3.5.1 Open Channel

A summary of experimental results are presented in Table 10.1 for flat plate with open channel flow using water, oil, and air and Table 10.3 for wind tunnel airfoil flow. Several studies have included varying geometries and configurations. Drag reduction is presented as negative $\Delta\tau/\tau_o$ (%) and ΔC_d (%) values at various Reynolds numbers. The data indicate that properly designed riblets can reduce drag.

Flat Plate Experiments

Water channel experiments conducted at a range of s^+ values indicate maximum drag reduction of nearly 6 % using continuous sawtooth riblets on a flat plate, as shown in Fig. 10.7 (Walsh 1990a; Bixler and Bhushan 2013a). Results also show that the greatest drag reduction occurs at an s^+ of 10–15 (Walsh 1990b), which correlates well with oil channel findings presented next (Bechert et al. 1997b). Extensive research has been conducted with oil channel flow, since oil allows for larger scale riblets, which drastically eases the challenge of riblet fabrication. These experiments included blade, sawtooth, and scalloped riblet geometries with continuous and staggered-segmented configuration, all using white paraffin oil ($\nu = 1.2 \times 10^5 \text{ m}^2/\text{s}$). This research is highlighted in Fig. 10.8a, showing a wide range of h/s values that are important for determining the optimal drag reducing geometry (Bixler and Bhushan 2013a). A summary of oil channel experiments is provided in Fig. 10.8b (Bechert et al. 1997b). Figure 10.8c shows the effect of continuous and staggered-segmented configurations of blade riblets (Bechert et al. 1997b, 2000a).

Results indicate maximum drag reduction of nearly 9 % is possible with blade riblets where $h/s = 0.5$, $t/s = 0.04$, and $s^+ \approx 15$. This drag reduction further improves

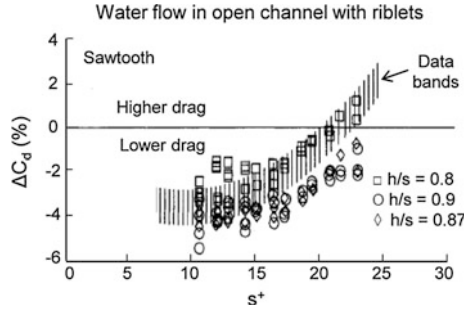


Fig. 10.7 Open channel experimental results with riblets in water flow (adapted from Walsh 1990a). Drag reduction is presented as negative ΔC_d (%) values, which is the percentage drag coefficient reduction between the smooth and riblet samples. Riblet samples with various h/s values are compared, with the maximum drag reduction near 6%. Riblets are sawtooth geometry and continuous configuration (Bixler and Bhushan 2013a)

with a lower t/s value of 0.02, where maximum drag reduction is nearly 10% (Bechert et al. 1997b). An optimum s^+ for various values of h/s suggests that a narrow range of h^+ is desirable. Furthermore, sawtooth riblets with $h/s = 0.98$ and $\alpha = 54^\circ$ provide the greatest drag reduction of nearly 6%, indicating that the smaller α is beneficial. Also, scalloped riblets with $h/s = 0.7$ provide the greatest drag reduction of nearly 7%. Results also indicate that staggered-segmented trapezoidal shaped riblets provided less drag reduction compared to continuous blade riblets (about 6 versus 10%) (Bechert et al. 1997b, 2000a). However, the staggered-segmented configuration provides drag reduction (albeit less magnitude) for a larger s^+ range, as compared to the continuous riblets.

The data presented above suggests that riblets with lower h/s values show less drag reduction but over a wider range of s^+ values (e.g. blade riblets where $h/s = 0.2-0.3$ versus $h/s = 0.5$). This is presumably due to the vortices interacting with larger area on the riblets and with each other. Previously presented flow visualization indicates that for higher flow velocity (where s^+ and h^+ increase and $h/s = 0.5$), the vortices appear not to be lifted, and shear stresses at the riblet tips are believed to increase. With constant h and increasing s values (thus lowering h/s), it is believed that the vortices fit in the riblet valleys (for instance at $h/s = 0.2-0.3$ versus $h/s = 0.5$). Furthermore, increasing h/s increases wetted surface area between the riblets, which leads to increased friction and thus drag (Bixler and Bhushan 2013a).

Choosing an optimal h/s based on the aforementioned experimental results depends on particular applications; specifically, whether or not the flow velocities are known or constant. For instance, riblets may be optimized for drag reduction over a wider range of s^+ values where flow velocity conditions are varying. Conversely, riblets may be optimized for maximum drag reduction over a smaller s^+ range, where flow velocity is relatively constant, such as aircraft at cruising speed. In addition to h/s , the t/s ratio affects drag, and a smaller ratio is desirable. Furthermore, research suggests that drag reduction is possible with sawtooth and

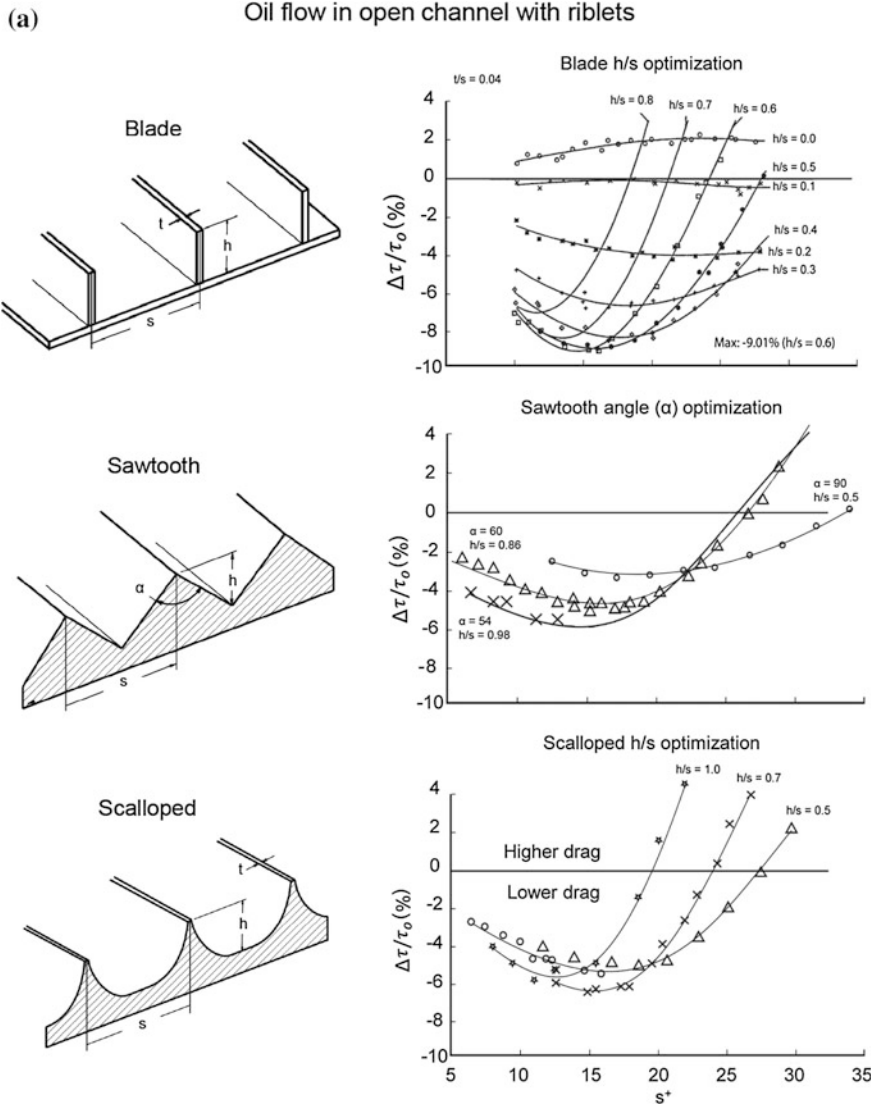


Fig. 10.8 Open channel experimental results with riblets in oil flow (adapted from Bechert et al. 1997b, 2000a). Drag reduction is presented as negative $\Delta\tau/\tau_0$ (%) values, where $\Delta\tau$ is the difference between shear stresses on the riblet sample (τ) and the smooth (τ_0) surfaces. **a** Various experiments were conducted in order to discover the optimal geometry for maximum drag reduction. Varied parameters include the riblet geometry, h/s , t/s , and s^+ , which allows for a better comparison between experiments. Oil channel experiments were conducted using white paraffin oil. **b** Maximum drag reduction results from the various blade, sawtooth, and scalloped riblets are compiled. Results indicate that the blade geometry with $h/s \approx 0.5$ and $t/s \approx 0.02$ produces the maximum drag reduction of 10 % near $s^+ \approx 15$. **c** Experimental results comparing continuous and staggered segmented blade riblets, indicating that latter configuration shows less drag reduction

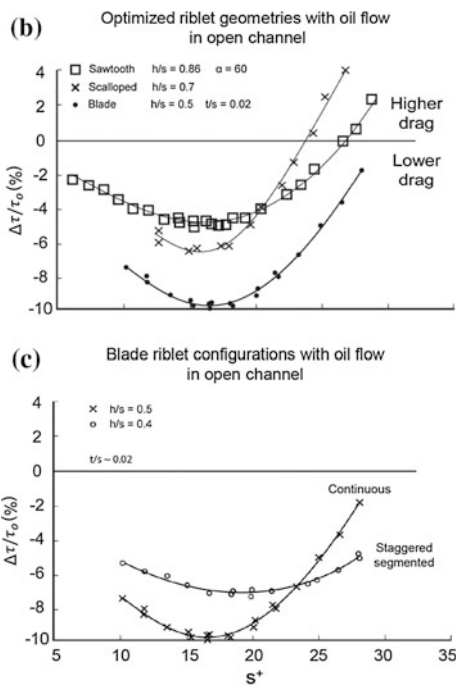


Fig. 10.8 (continued)

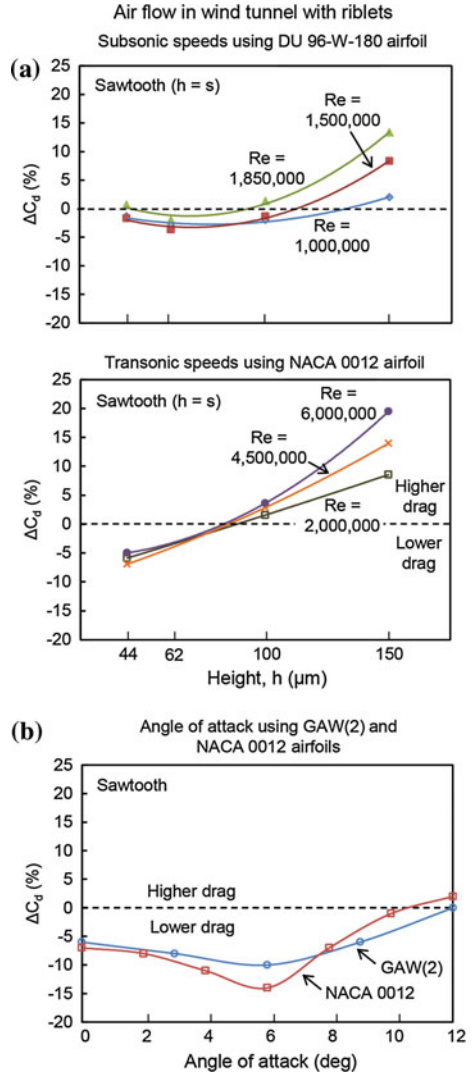
scalloped riblets, but such geometries require differing h/s values. It should be noted that the blade riblets are the most fragile, followed by scalloped and sawtooth. Therefore, clear tradeoffs are necessary when designing riblets for commercial applications (Bixler and Bhushan 2013a).

Finally, the effect of yaw angle on drag reduction on sawtooth riblets in air flow was studied by Walsh and Lindeman (1984). Yaw angle is the angle between the average flow direction and the riblet orientation. It was reported that yaw angle has a deleterious effect on the drag reduction benefit. While a small drag reduction can be seen up to a yaw angle of 15° , drag increases above a yaw angle of 30° .

Airfoil Experiments

The 3 M vinyl riblet sheets have been fabricated in large sizes that consist of continuous sawtooth riblets with various aspect ratios (to be introduced later). Many experiments have been conducted with airfoils covered with these riblet sheets in wind tunnels. Experimental results are shown in Fig. 10.9a for riblets applied to the wind turbine DU 96-W-180 airfoil (Sareen et al. 2011), as well as the aircraft wing NACA 0012 airfoil (Bixler and Bhushan 2013a). Results indicate that smaller height riblets provide the greatest drag reduction, around 2 % for the DU 96-W-180 airfoil (Sareen et al. 2011) and 7 % for the NACA 0012 airfoil (Bixler and Bhushan 2013a). Larger sized riblets and higher Reynolds numbers provide less drag

Fig. 10.9 Wind tunnel experimental results with riblets on airfoils. Drag reduction is presented as negative ΔC_d (%) values, which is the percentage drag coefficient reduction between the smooth and riblet samples. **a** Drag reduction is shown with wind turbine DU 96-W-180 (adapted from Sareen et al. 2011) and symmetrical NACA 0012 (Bixler and Bhushan 2013a) airfoils with various 3 M Corp. sawtooth riblets. The *top* and *bottom* figures show Reynolds numbers in the subsonic and transonic ranges, respectively. Maximum drag reduction is near 7% for the riblets with $h = s = 44 \mu\text{m}$ in transonic flow. **b** Riblet drag reduction is related to angle of attack, as shown with two airfoils with angles of attack up to 12° . The greatest drag reduction of nearly 14% is shown at 6° angle of attack (adapted from Subaschandar et al. 1999)



reduction, and, in some cases, the drag increases compared to the smooth airfoil. The Reynolds numbers for experiments provide a wide spectrum of subsonic ($Ma < 0.75$ with $Re = 1,000,000$) to transonic ($0.75 < Ma < 1.2$ with $Re = 6,000,000$) velocities. This allows for comparison airfoils, Reynolds numbers, and riblet sizes. An additional variable of interest is the angle of attack, shown in Fig. 10.9b using sawtooth riblets. The greatest drag reduction of nearly 14% occurs at a 6° angle of attack for the NACA 0012 airfoil (Subaschandar et al. 1999).

Boundary layer thickness can be used to describe flow over an airfoil and flat plate, and its effect on the magnitude of drag reduction. As shown in Fig. 10.10,

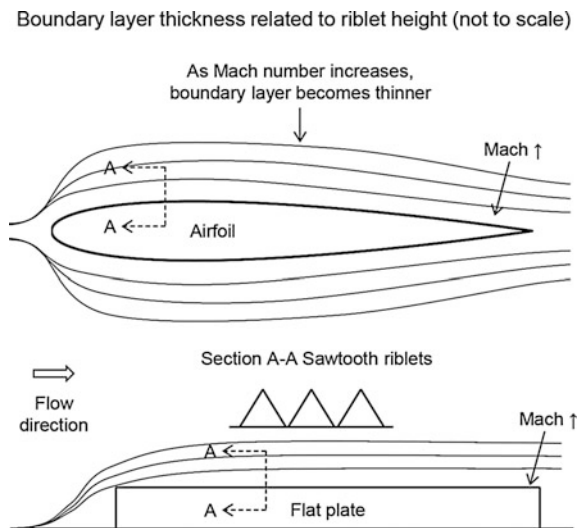


Fig. 10.10 Boundary layer thickness related to riblet height. As the Mach number increases, the boundary layer thickness decreases. It is believed for drag reduction that riblets should remain inside the viscous sublayer in order to effectively control the turbulent vortices. Shown is an illustration (not to scale) explaining the relationship (Bixler and Bhushan 2013a)

with increasing Mach number (and thus Reynolds number), the turbulent boundary layer thickness decreases. Riblets are effective by remaining inside the turbulent viscous sublayer in order to properly lift and presumably pin any vortices. However, if the riblet protrudes outside of the viscous sublayer, the increased surface area of the riblets will increase skin friction drag. Therefore, it is believed that riblets must remain within the viscous sublayer in order to provide benefit (Bixler and Bhushan 2013a).

10.3.5.2 Closed Channel

A summary of closed channel experimental results using water, oil, and air are presented in Table 10.2. Several studies have included varying geometries and configurations that have been conducted with laminar through turbulent flow. Drag reduction is presented as negative $\Delta\tau/\tau_o$ (%) or pressure drop values. Results indicate that properly designed riblets can reduce drag.

Comparison of Open and Macro-sized Closed Channels

Figure 10.11 shows a comparison of open and macro-sized closed channel results. The data show that drag reduction is similar. These results represent cases when neighboring walls are sufficiently far apart, as shown with pipe diameters approximately 25 mm or greater. However, when channel dimensions are relatively small (as shown in Fig. 10.6a with micro-sized closed channel where $H = 0.7$ mm

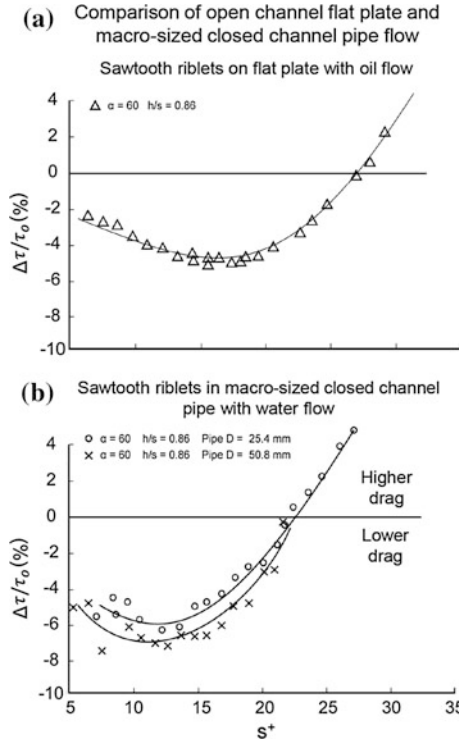


Fig. 10.11 Comparison of open channel flat plate and macro-sized closed channel pipe flow (where neighboring wall effects are assumed negligible). Drag reduction is presented as negative $\Delta\tau/\tau_o$ (%) values, where $\Delta\tau$ is the difference between shear stresses on the riblet sample (τ) and the smooth (τ_o) surfaces. Samples consist of sawtooth geometry where the angle $\alpha = 60^\circ$, as defined in Fig. 10.8a. **a** Experimental results are shown with sawtooth riblets on a flat plate (Bechert et al. 1997b) and **b** in round pipe with diameter D (Liu et al. 1990). Maximum drag reduction is similar between the presented flat plate and macro-sized pipe flow

and $W = 3.2$ mm), neighboring wall effects are believed to play an important role in riblet drag reduction. A set of experiments were conducted with such micro-sized closed channels, and results are presented in the following section.

Molded Shark Skin Replica and Machined Micro-sized Channel

Representative pressure drop data for the flat epoxy resin scales replica from the skin of the spiny dogfish (*Squalus acanthias*, *L. Squelidae*) (Fig. 10.2, bottom), along with predicted data for a hydrophilic surface, are shown in Fig. 10.12a (Jung and Bhushan 2010). A decrease in pressure drop of about 30 % in turbulent flow versus a smooth surface is observed.

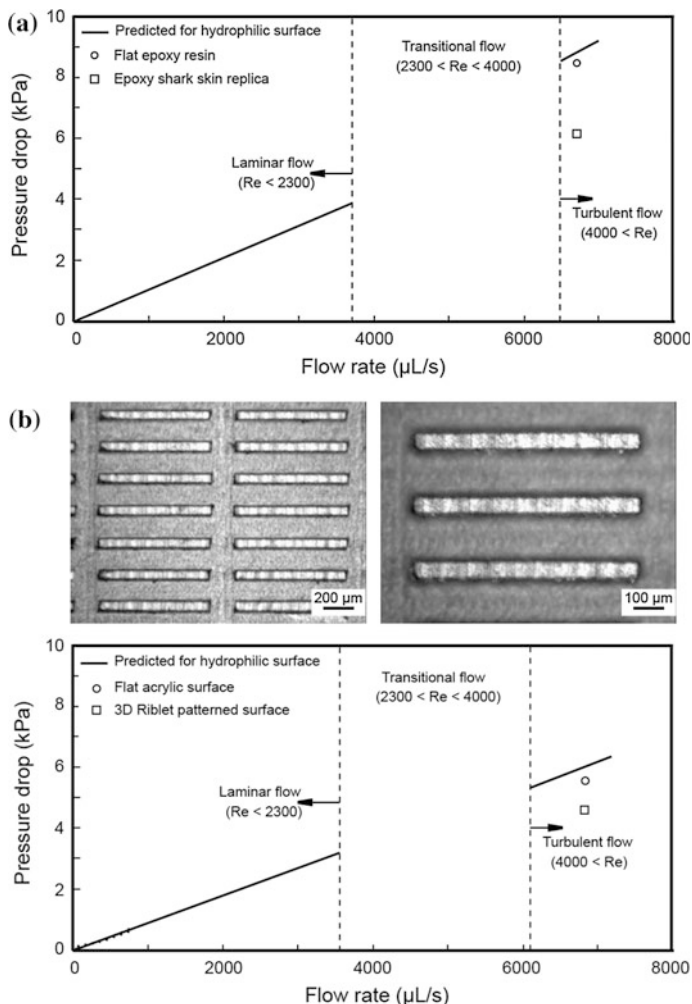


Fig. 10.12 **a** Comparison of pressure drop of water flow in a closed rectangular flow channel over flat epoxy surface and shark skin replica surface. **b** Optical microscope images (at two magnifications) showing segmented blade-type riblets machined from acrylic, and comparison of pressure drop in flow over flat acrylic surface and segmented blade type riblets. Data are compared with the predicted pressure drop for a hydrophilic surface (*solid lines*) (adapted from Jung and Bhushan 2010)

Role of Micro-sized Channel Dimensions

Closed channel experiments with various riblet geometries in water, oil, and air have been conducted (Jung and Bhushan 2010; Dean and Bhushan 2012; Bixler and Bhushan 2012b, 2013a, b, c, d). In addition to data presented here, further data are presented in Chap. 11 on the Rice Leaf and Butterfly Wing Effect. Jung and

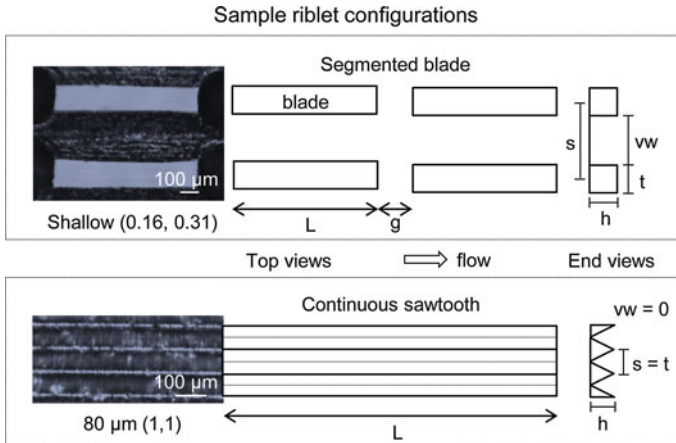


Fig. 10.13 Blade and sawtooth riblet geometries are shown on the *top* and *bottom*, respectively. Flow direction in *top views* is left to right and *end view* is into the page. Blade riblets are both segmented (*top*) and continuous (not shown); whereas sawtooth are all continuous (*bottom*). The riblet height (h), thickness (t), valley width (vw), spacing (s), and length (L) describe the geometry. Optical images show actual samples. (Bixler and Bhushan 2013b)

Bhushan (2010) and Dean and Bhushan (2012) fabricated segmented blade-type riblets on acrylic, machined using an end mill with a $130\ \mu\text{m}$ diameter bit. Representative pressure drop data for a flat acrylic sheet and machined riblets are shown in Fig. 10.12b, along with predicted data for a hydrophilic surface. A decrease of about 25 % in turbulent flow versus a smooth surface is observed.

Laser etching has been used to fabricate continuous and segmented blade-type riblets with micro-sized dimensions on cast acrylic sheets (Bixler and Bhushan 2013b). The baseline size for riblets was derived from the spiny dogfish shark *Squalus acantias*, whose riblets dimensions were provided earlier. These values served as the basis for laser-etched blade riblet samples with an expanded range of dimensions. The top image of Fig. 10.13 shows the segmented blade configuration. Sample riblet dimensions with various thicknesses (t), valley widths (vw), spacing (s), gaps (g), lengths (L), and heights (h) were selected. Blade riblet studies suggest that h/s of about 0.5, small t/s , and dimensionless riblet spacing near 15 optimizes drag reduction (Bechert et al. 1997a; Dean and Bhushan 2010). Fabrication limitations and material properties determined the minimum riblet dimensions for the segmented and continuous samples. Blade dimensions were incrementally varied to change the h/s and t/s values to fully understand their relationship in a closed channel.

A wide range of blade h/s and t/s values ($0.16 < h/s < 0.62$ and $0.18 < t/s < 0.38$) were studied with g and L held constant, and h , vw , and t varied individually; see Table 10.4 for dimensions. Samples will be referred to by their “description,” in conjunction with their h/s and t/s values. For example, the segmented blade riblet sample with $h/s = 0.31$ and $t/s = 0.31$ is called “Baseline (0.31, 0.31)” or more simply, “baseline” (Bixler and Bhushan 2013b).

Continuous sawtooth riblets (with $h = t$) were obtained from 3 M Corp. (Minneapolis, Minnesota) and inserted into the flow channel; see Table 10.4 for dimensions (Bixler and Bhushan 2013b). The bottom image of Fig. 10.13 shows the sawtooth pattern configuration.

Fabricated milled sample surfaces were hydrophilic and superoleophilic (Bixler and Bhushan 2013c). A number of studies suggest that superhydrophobic surfaces exhibit lower drag (Ou et al. 2004; Daniello et al. 2009; Martell et al. 2009, 2010; Jung and Bhushan 2010; Bhushan and Jung 2011). In order to make the surface superhydrophobic, a nanostructured coating was selected. The replica was dip-coated with a solution consisting of 50 nm (± 15 nm) hydrophobized silica nanoparticles, combined with methylphenyl silicone resin dissolved in tetrahydrofuran and isopropyl alcohol. Coated samples included completely coating the riblets and some included coating only the riblet valleys (Bixler and Bhushan 2013c).

Closed channel experiments were conducted using the experimental apparatus shown in Fig. 10.6, with varying geometries, configurations, hydrophobicity, oleophilicity, and channel dimensions with laminar through turbulent flow (Bixler and Bhushan 2013b, c). The results presented use the naming convention for samples “sample description (h/s , t/s)”. For example, the 3 M riblet sample with height and spacing equaling 44 μm is written as “44 μm (1, 1)” or more simply “44 μm sample”. The baseline blade dimensions were $h = 127 \mu\text{m}$, $v_w = 280 \mu\text{m}$, and $t = 127 \mu\text{m}$, with variations presented later in the modeling section. All samples exhibited blade geometry with the aligned-segmented configuration, except the 3 M riblets which exhibited sawtooth geometry and continuous configuration. Also, select riblet samples received a nanostructured coating (e.g. “coated” samples). Such coated samples were either superhydrophobic or superoleophilic, and were believed to improve riblet smoothness. Furthermore, the same nanostructured coating applied to replica shark skin samples indicated that the coating lowered adhesion forces (Bixler and Bhushan 2012b).

Micro-sized closed channel water and air results are presented in Fig. 10.14 and oil results (white paraffin oil with CAS 8012-95-1) in Fig. 10.15. The data are compared to the flat milled sample. Various riblet geometries and dimensions were evaluated in flows ranging from laminar to turbulent regimes. The effect of h/s and t/s , h , hydrophobicity/oleophilicity, and smoothness are shown. The Shallow sample (1/2 height) shows the most pressure drop reduction at 19 % in water and 13 % in air (Bixler and Bhushan 2013b). Due to their initial performance, these riblets received the nanostructured coating, which then produced an improved pressure drop reduction of 34 % in water and 24 % in air (Bixler and Bhushan 2013b). The 100 μm sample also reduced pressure drop by 30 % in water. In oil flow, the Narrow sample (1/4 valley width) shows the most pressure drop reduction at 9 % (Bixler and Bhushan 2013c).

From the data, we note that lower h/s values appear to provide the greatest drag reduction, although this differs from the open channel results. However with rectangular micro-sized closed channel experiments, the neighboring wall effects are believed to play a role in drag reduction. In the closed channel experiments, samples with the lowest h/s of 0.16 performed the best, presumably due to less

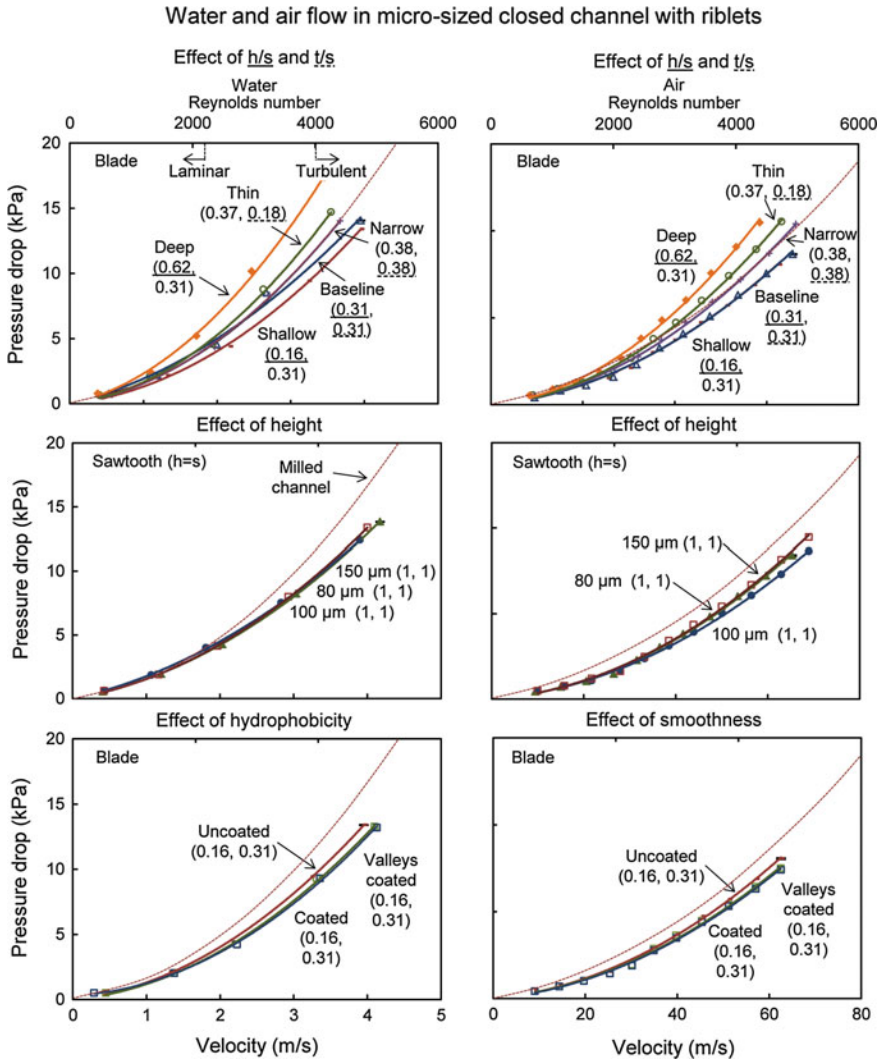


Fig. 10.14 Micro-sized closed channel experimental results with riblets in water and air flow (adapted from Bixler and Bhushan 2013b). Drag reduction is presented as pressure drops between the inlet and outlet of the channel, where lower pressure drop is desirable. Riblets of varying geometries were evaluated in laminar ($Re < 2300$) through turbulent flow ($Re > 4000$) conditions. Experiments evaluated the effect of h/s , t/s , height, hydrophobicity, and smoothness. Riblets were fabricated via laser etching, and a nanostructured coating was applied to achieve the desired hydrophobicity and smoothness. Maximum pressure drop reduction of 34 % with water was recorded for hydrophobic riblets in the turbulent regime. Flat milled channel control sample is shown for comparison. Error bars show ± 1 standard deviation

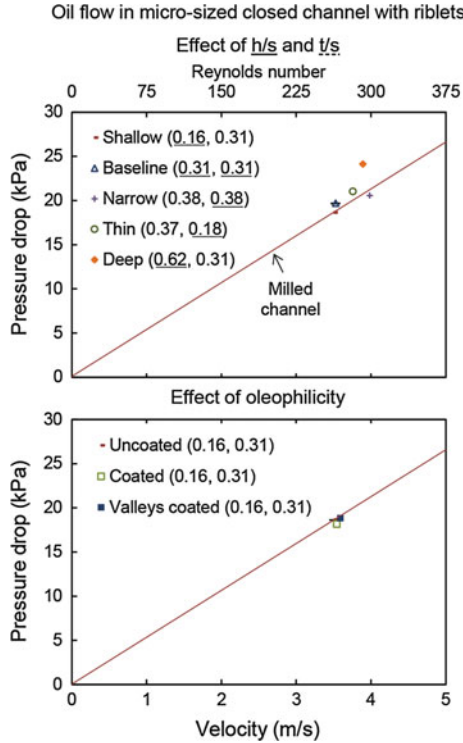


Fig. 10.15 Micro-sized closed channel experimental results with riblets in oil flow (adapted from Bixler and Bhushan 2013c). Drag reduction is presented as pressure drops between the inlet and outlet of the channel, where lower pressure drop is desirable. Riblets of varying geometries were evaluated in laminar ($Re < 375$) flow conditions. Experiments evaluated the effect of h/s , t/s , and oleophilicity. Riblets were fabricated via laser etching, and a nanostructured coating was applied to achieve the desired oleophilicity. Maximum pressure drop reduction of 9 % was recorded for the Narrow riblets. Experiments were conducted using white paraffin oil. Flat milled channel control sample is shown for comparison. Error bars show ± 1 standard deviation

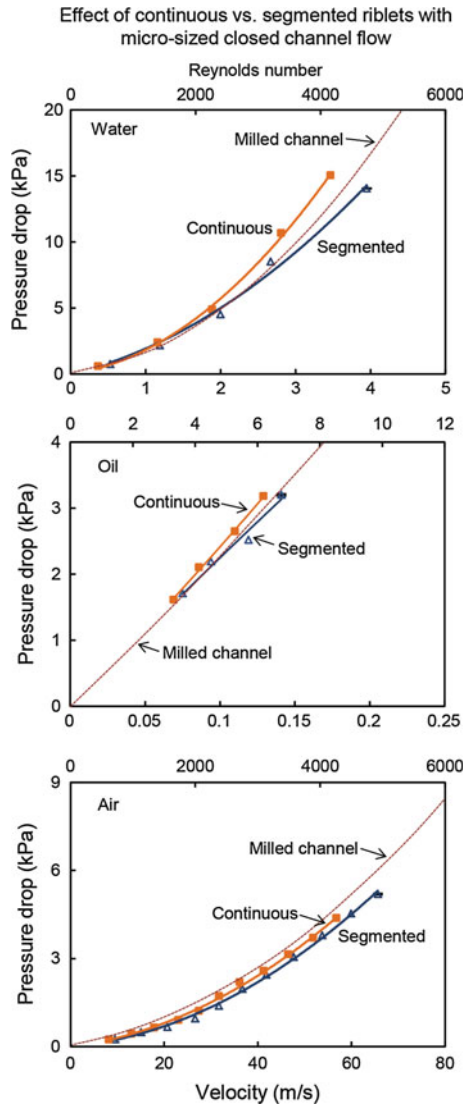
interaction between the vortices on the top and bottom of the riblet height remaining in the viscous sublayer (Bixler and Bhushan 2013a).

Understanding the differences in performance between riblet samples in water, oil, and air flow can be explained by considering the Reynolds numbers, as well as the drag reducing mechanisms. It is believed that different mechanisms are at work, mainly due to the effect of viscosity, as well as Reynolds number. For instance, where water and air flow was turbulent, the riblets are believed to lift and pin the vortices, and thus reduce drag. However, oil flow was laminar, benefitting from the so-called thin film effect that reduces skin friction at the solid-liquid interface and thereby reduces drag, to be described later in this section (Bixler and Bhushan 2013c). Additionally, it is believed that turbulent oil flow would benefit from the shark skin effect.

(a) **Continuous versus segmented riblets**

To understand the effects of riblet configurations, namely continuous and aligned-segmented configurations, a series of water, oil, and air flow experiments were conducted (Bixler and Bhushan 2013b, c). Figure 10.16 presents results from the Continuous and Baseline blade samples, representing the continuous and aligned-segmented configurations respectively. Intuitively, the Continuous sample should provide higher drag due to the increased wetted surface area. Experiments with the Continuous sample in water and oil exhibit

Fig. 10.16 Micro-sized closed channel experimental results showing the effect of continuous versus segmented blade riblets with water, oil, and air flow (adapted from Bixler and Bhushan 2013b, c). Drag reduction is presented as pressure drops between the inlet and outlet of the channel, where lower pressure drop is desirable. Riblets were evaluated in laminar ($Re < 2300$) through turbulent flow ($Re > 4000$) conditions. Results indicate that the continuous riblets increase drag with water and oil, presumably due to the increased wetted surface area, which leads to higher skin friction. Flat milled channel control sample is shown for comparison. Error bars show ± 1 standard deviation



a higher drag as compared to the Segmented sample. However, there is a decrease in drag with air, for similar Reynolds numbers in water. The continuous blades may reduce cross stream movement with air more efficiently than with segmented blades. With the lower viscosity of air, vortices rotate more easily in the channel, and the gap area between segmented blades perhaps disrupts and unpins the vortices.

(b) **Riblets on top or bottom or both sides**

To understand the effects of riblets on one side versus two sides of the closed channel and with differing micro-sized channel heights, a series of water flow experiments were conducted (Bixler and Bhushan 2013b). Such combinations included experiments with 1x channel height, 2x channel height, riblets on bottom, riblets on top, and riblets on top and bottom; all with Shallow samples. Figure 10.17 (top row) shows results from riblets on the top only and bottom only. Results indicate that riblets located on the bottom perform differently from the same riblets located on the top of the channel. The pressure drop increases by 20 % when the riblets are transferred from the bottom to the top (Bixler and Bhushan 2013b). Similar experiments were conducted to study the effect of channel height with riblets on the top or bottom. Results indicated that pressure drop with riblets on the bottom was unaffected by channel height, but pressure drop improved with topside riblets and 2x channel height.

Figure 10.17 (bottom row) shows results from riblets on both the top and bottom of the channel. Neighboring wall effects are believed to be present, since pressure drop increases with the 1x channel height as compared to the flat milled surface. In contrast, the pressure drop decreases with the 2x channel height. It is believed that the vortices from neighboring walls with the 1x channel height interact and increase drag, but the larger gap distance in the 2x channel height reduces this effect. The aforementioned effects are believed to be related to the vortices' interaction (Bixler and Bhushan 2013b).

(c) **The role of riblet wettability**

In the data presented in Figs. 10.14 and 10.15 with and without the nanostructured coating, it is observed that the nanostructured coating provided a drag reducing benefit in all fluids. In water flow, drag reduction improves with superhydrophobicity and low adhesion (Bixler and Bhushan 2012b, 2013b), in air flow with smoothness (Bixler and Bhushan 2013b), and in oil flow with superoleophilicity because of the so-called thin oil film effect. (Bixler and Bhushan 2013c). In oil, drag reduction is possible with laminar flow due to this effect. The thin oil film effect can be explained using Fig. 10.18. This model indicates that during flow, oil becomes trapped and holds stationary between the Narrow riblets, and essentially lubricates the solid-liquid interface. The lubricating effect is believed to increase slip length (b), so the flow velocity increases at the channel wall. A similar effect has been observed with the pitcher plant (*Nepenthes genus*) peristome (Koch and Barthlott 2009; Bhushan 2009).

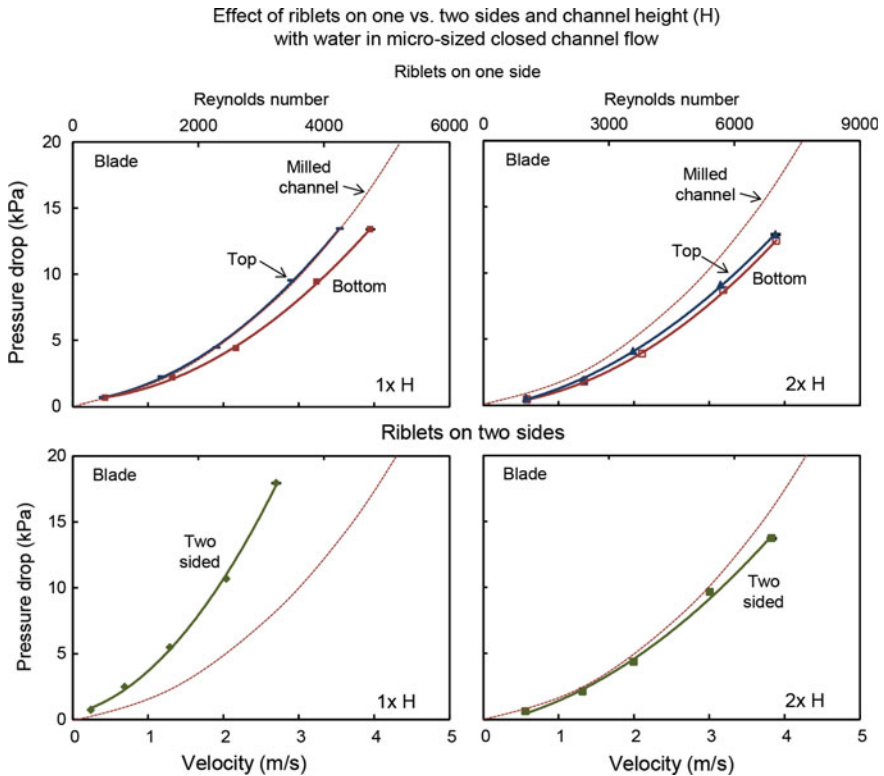


Fig. 10.17 Micro-sized closed channel experimental results showing the effect of channel height and riblets on the top, bottom, or both sides with water flow (adapted from Bixler and Bhushan 2013b). Drag reduction is presented as pressure drops between the inlet and outlet of the channel, where lower pressure drop is desirable. Riblets were evaluated in laminar ($Re < 2300$) through turbulent flow ($Re > 4000$) conditions. Results indicate that riblets on the *bottom* reduce drag more than when positioned on the top of the channel. Also, 2x channel height reduces drag, presumably due to vortices from the *top* and *bottom* moving apart (i.e. neighboring wall effects are negligible). Flat milled channel control sample is shown for comparison. Error bars ± 1 standard deviation

It has been shown that fluid slip has a direct relationship to drag. Jung and Bhushan (2010) measured pressure drop in a flow cell on hydrophilic ($CA = 76^\circ$), hydrophobic ($CA = 119^\circ$), and superhydrophobic ($CA = 173^\circ$) surfaces (used for fabrication of artificial lotus structures). Figure 10.19 shows laminar and turbulent pressure drop comparisons for these surfaces in water flow. There is no pressure drop benefit in laminar flow, whereas there is a benefit in turbulent flow. The greatest decrease in pressure drop of 33 % happens with the superhydrophobic surface, followed by 21 % with the hydrophobic surface. Reducing the strength of bonding between the fluid molecules and the surface causes a corresponding reduction in fluid drag in both laminar and turbulent regimes.

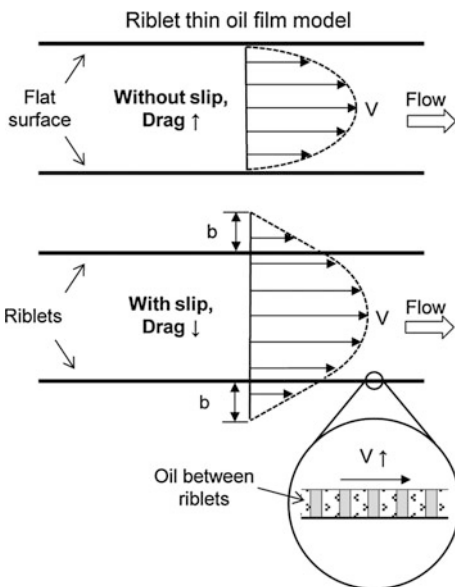


Fig. 10.18 Riblet thin-oil film model. Oil becomes trapped between appropriately sized riblets and essentially lubricates the surface. The lubricating effect is believed to increase slip length (b) during laminar oil flow, which translates into lower drag and increased flow rate (Bixler and Bhushan 2013c)

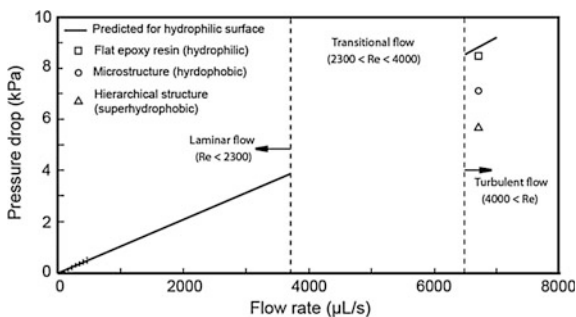


Fig. 10.19 Comparison of pressure drop of water flow in a closed rectangular channel with hydrophilic, hydrophobic, and superhydrophobic surfaces in laminar and turbulent flow regimes. Data are compared with the predicted pressure drop for a hydrophilic surface (solid lines). Decreased pressure drop in turbulent flow corresponds to decreased drag (adapted from Jung and Bhushan 2010)

10.3.6 Summary

Sharks are able to move quickly through water and remain free of fouling due to microstructured riblets covering their skin. Such riblets efficiently reduce skin

friction drag by lifting and presumably pinning naturally occurring turbulent vortices. This minimizes the effects of transverse shear stress present in turbulent flow. Lower drag translates to higher fluid flow velocity at the skin surface, so microorganisms are unable to attach and the skin remains clean. This is further facilitated with specially spaced riblets that do not allow larger microorganisms to colonize. The attempt to understand and mimic such unique shark skin structures has been the focus of many scientific studies. Commercial applications for such low drag and antifouling surfaces are plentiful, ranging from medical devices to marine vessels (Bixler and Bhushan 2013a).

A number of experiments have been performed to understand drag reduction mechanisms in shark skin. These include both open and closed channel flow, using a variety of blade, sawtooth, scalloped, and bullnose riblet geometries in continuous and segmented configurations. These have been studied with water, oil, and air in laminar through turbulent regimes. In open channel flow experiments, drag was measured with flat plates on force balances placed into water, oil, and air flows. Other experiments included airfoils in wind tunnels with drag measured by using wake traverses. In closed channel flow, drag was measured via pressure drop reduction using riblet lined micro-sized closed channels.

Riblets showed an improved drag reduction in turbulent versus laminar flow, presumably due to the lifting and pinning of vortices. Results also indicated that drag reduction improves in most cases with increasing Reynolds number (until expected plateauing). In open channel experiments, the maximum drag reduction up to 10 % has been reported (Bechert et al. 1997b). In closed channel experiments, maximum pressure drop reduction up to 34 % has been reported (Bixler and Bhushan 2013b). Experiments using water, oil, and air also indicated that properly sized riblets combined with an appropriate nanostructured coating further enhances drag reduction. Mechanisms included superhydrophobicity for water, improved smoothness for air, and superoleophilicity for oil flow.

Based on open channel and closed channel data in various fluids, producing optimal and scalable drag reducing riblets for any fluid is believed to require the following design principles: a narrow range of h^+ and s^+ , and low t , with $s^+ \approx 15$, $h/s \approx 0.5$, blade geometry, and continuous configuration. In open and closed channel flow, riblets may be scaled up according to the fluid viscosity and flow velocity, where higher viscosity and lower velocity allow for larger riblets (Bixler and Bhushan 2013a).

10.4 Fluid Flow Modeling

Various riblet geometries and configurations have been studied through modeling in closed channel flow. By modeling of continuous and sawtooth geometries, Chu and Karniadakis (1993), Choi et al. (1993), Goldstein et al. (1995) have shown drag reductions of upto 3–6 %. A drag reduction is formed by riblets lifting the

streamwise vortices formed in turbulent flow that generate transverse shear stresses. Streamwise vortices are referred to as vortices traveling in the predominant flow direction and rotating along an axis line in the streamwise direction. Continuous, blade riblets have been modelled by El-Samni et al. (2007) and Martin and Bhushan (2014, 2016) both showing a maximum drag reduction of 11 % and explained the mechanism as appropriately-sized riblets do not allow vortices to fit within the riblet valleys and bring higher velocity fluid to the wall to increase drag. Martin and Bhushan (2016) have also modeled aligned-segmented and staggered-segmented riblets and reported drag reductions of 5 and 3.3 %, respectively.

Since vortices are not generated in laminar flow, this method of drag reduction is not possible. Instead, a drag increase can result due to the greater surface area on the riblet surface (Goldstein et al. 1995). In the transitional regime, a drag reduction is possible due to the possibility of vortex structures being created; however, a drag reduction through this mechanism is best obtained through fully turbulent flow (Table 10.5).

In a study carried out by Martin and Bhushan (2016), a computational fluid dynamic (CFD) model of blade riblet structures in continuous, aligned-segmented, and staggered-segmented configurations in a closed channel flow was created in order to study the effect of riblet geometry as well as dimensions of vortices on drag reduction. The gaps and offsets in the staggered configurations were independently changed, and the resulting drag and vortex formations were compared to each other as well as to a flat surface and continuous riblet configurations. ANSYS Fluent 14.5 was used as the CFD software with the large-eddy simulation (LES) model which resolves the large scales of the flow field and filters out the small scales of the flow field chosen based on the turbulence criteria (Anonymous 2015). Details on their model and selected data follow.

Table 10.5 Summary of the static contact angles and contact angle hysteresis measured on the various surfaces (adapted from Jung and Bhushan 2010)

	Static contact angle (deg)	Pressure drop in turbulent flow (%)	Calculated slip length (μm)
<i>(a) Epoxy resin</i>			
Hydrophilic (flat epoxy resin)	76 ± 0.9	~ 0	~ 0
Hydrophobic (flat with thin Lotus wax layer)	119 ± 2.4	~ 21	~ 24
Superhydrophobic (hierarchical structure—micropatterned with thin Lotus wax layer)	173 ± 0.8	~ 33	~ 103
Shark skin replica	89 ± 1.7	~ 30	~ 35
<i>(b) Acrylic resin</i>			
Flat acrylic resin	82 ± 1.8	~ 0	–
Rib patterned surface	146 ± 1.2	~ 23	–

The variation represents ± 1 standard deviation

10.4.1 Riblet Geometry Models

The various configurations that have been analyzed are shown in Fig. 10.20, which include the continuous; aligned-segmented; and staggered-segmented configurations (adapted from Martin and Bhushan 2016). In the continuous riblets with a constant length (L), spacing, height, and thickness parameters were varied. In the segmented configurations, the spacing, height, and thickness parameters were kept constant and only the lengths (L_1), gaps (L_2), and offsets (L_3) of the riblet were modified for drag and vortex comparison.

The continuous riblet cases had two fluid parameters (velocity V and viscosity ν) and three riblet parameters (spacing s , height h , and thickness t) independently changed. Various test cases are listed in Table 10.6 (Martin and Bhushan 2016). In the table, the dimensional parameters are listed on the left and the resulting non-dimensional parameters are listed on the right. The baseline values shown in bold numbers were chosen for blank cells. The baseline value for spacing was chosen for an s^+ of 16. The baseline values for height and thickness were chosen to keep an h/s ratio of 0.5 and t/s ratio of 0.02 because h/s ratios of about 0.5 and small t/s ratios have been shown to give greater drag reductions. For the effect of velocity cases, the viscosity was held constant at $\nu = 10^{-6} \text{ m}^2\text{s}^{-1}$ (representative of water); for the effect of viscosity cases, the velocity was held constant at $V_l = 0.42 \text{ ms}^{-1}$. These values gave a baseline Reynolds number of 4180 and a ratio of $\nu/V_l = 2.38 \text{ }\mu\text{m}$. This Reynolds number is high enough for turbulent flow without becoming too large to increase mesh size and computational expense.

Fig. 10.20 Configurations for the riblet geometry cases showing continuous riblets with various spacing, and aligned-segmented and staggered-segmented styles with the various riblet gap and offset parameters (adapted from Martin and Bhushan 2016)

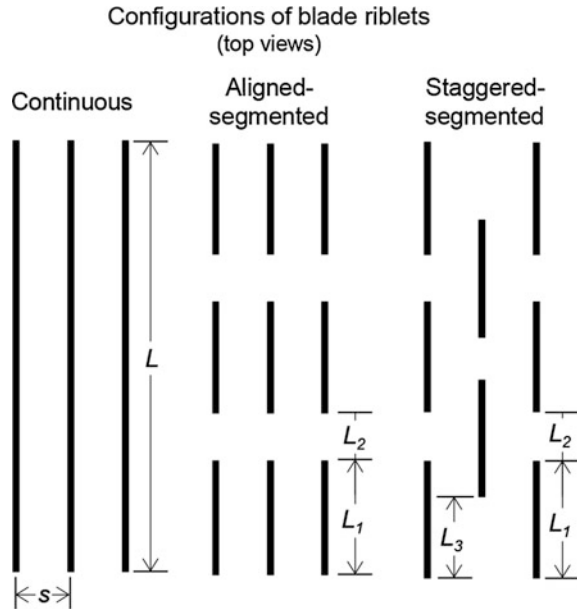


Table 10.6 Test cases for the simulations of turbulent flow over continuous riblets (Martin and Bhushan 2016)

	s (mm)	h (mm)	t (μm)	v/V_l (μm)		s^+	h^+	t^+	Number of riblets
				Varying V_l $v = 10^{-6}$ $\text{m}^2 \text{s}^{-1}$	Varying v $V_l = 0.42$ ms^{-1}				
Baseline	1.00	0.50	20.0	2.38	2.38	16.2	08.1	0.32	20
Effect of V				4.00		10.3	05.1	0.21	20
				2.38		16.2	08.1	0.32	20
				1.39		24.5	12.3	0.49	20
				0.98		32.4	16.2	0.65	20
				0.76		46.8	23.4	0.94	20
Effect of v					4.00	10.7	05.4	0.21	20
					2.38	16.2	08.1	0.32	20
					1.39	27.4	13.7	0.55	20
					0.77	46.7	23.3	0.93	20
Effect of s	0.50					08.4	08.4	0.34	40
	1.00					16.2	08.1	0.32	20
	1.50					25.3	08.4	0.34	13
	2.50					41.1	08.2	0.33	08
Effect of h		0.25				16.2	04.1	0.32	20
		0.50				16.2	08.1	0.32	20
		0.75				16.6	12.5	0.33	20
		0.75	0.22	15.0	1.20	22.9	06.7	0.46	27
		0.75	0.32	15.0	1.20	23.2	09.9	0.46	27
	0.75	0.42	15.0	1.20	23.2	13.0	0.46	27	
Effect of t			05.0			16.8	88.4	0.08	20
			10.0			17.0	08.5	0.17	20
			20.0			16.2	08.1	0.32	20
			30.0			16.6	08.3	0.50	20

Baseline values shown in bold numbers were chosen for blank cells

The values of the dimensional parameters were chosen to fulfill several requirements. First, the dimensional parameters were chosen so that the cases would cover a wide non-dimensionalized range for the parameter. In addition, the values were chosen so that s^+ of 15–20 would be in the parameter’s ranges. This range has been shown for optimal drag reduction. By centering the data on this range, it would allow for test cases on either side of this range to be investigated.

Additionally, the velocity and viscosity values were selected to show the non-dimensionalizing method is valid. By modifying the dimensional parameters and getting similar changes in drag for their non-dimensional parameters, it shows that only the non-dimensional values are important and any parameter in the equation can be modified.

To better understand the relationship between riblet height and drag, two sets of riblet height cases were created. In the first set, only the height was modified with the other parameters matching the baseline case. In the second set, all of the parameters were modified to increase the Reynolds number, center s^+ near 23, and h^+ near 10.

These continuous riblet cases were compared to the segmented riblet cases in which the length of each riblet (L_1), the gap between the riblets (L_2), and the offset between riblets (L_3) were independently changed. These cases are presented in

Table 10.7 Test cases for the simulations of turbulent flow over segmented riblets (Martin and Bhushan 2016)

Riblet geometry	$s = 1.0 \text{ mm}$, $h = 0.5 \text{ mm}$, $t = 20 \text{ }\mu\text{m}$, $\nu/V_t = 2.38 \text{ }\mu\text{m}$ for $Re = 4180$ $s^+ \approx 16$, $h^+ \approx 8$, $t^+ \approx 0.3$							
	L_1 (mm)	L_2 (mm)	L_3 (mm)	L_1^+	L_2^+	L_3^+	Drag change (%)	
Continuous blade ($L = 0.035 \text{ m}$)	∞	0	0	∞	0	0	-9	
Aligned-segmented blade	2.0	1.0	0	32	16	0	-2.1	
	4.0			67	17		-3.3	
	6.0			99	17		-4.3	
	4.0	1.0	0	67	17	0	-3.3	
				2.0	68		34	-3.6
				4.0	66		66	-3.7
				6.0	68		101	-5.0
	9.4	66	154	+5.2				
Staggered-segmented blade	4.0	1.0	0.0	67	17	0	-3.3	
			1.0	67	17	17	-3.2	
			2.0	66	17	33	-3.2	

Table 10.7 (Martin and Bhushan 2016). In the table, the dimensional and non-dimensional parameters for the riblet geometry are listed at the top. The dimensional values for the segmented geometries are shown on the left, and the resulting non-dimensional values are shown on the right. The lengths were non-dimensionalized similar to (10.1) as $L_1^+ = L_1 v_\tau / \nu$, $L_2^+ = L_2 v_\tau / \nu$, and $L_3^+ = L_3 v_\tau / \nu$, respectively.

The dimensional numbers for the various parameters were scaled up from actual riblet dimensions due to limitations with ANSYS Fluent when working with small numbers. Even with double precision, rounding errors could accumulate if actual riblet dimensions were used. Scaling up the numbers does not affect the results since only non-dimensional numbers affect the results, and this conclusion will be presented later.

In the segmented riblet cases, the spacing ($s^+ \approx 16$), height ($h^+ \approx 8$), thickness ($t^+ \approx 0.3$), and Reynolds number ($Re = 4180$) were kept constant. These cases were compared to the continuous case with these same riblet parameters. In the aligned-segmented test cases, the length of each riblet (L_1) was varied from 2 to 6 times the length of the gap between riblets (L_2) and riblet spacing because these ratios can be seen in shark scales. Also in the aligned-segmented test cases, the gap between the riblets (L_2) ranged from 1.0–9.4 mm in order to get a wide range of non-dimensional riblet gaps of 17–154. This wide range was necessary in order to examine streamwise vortices because they have a great effect on drag in riblets. In the staggered-segmented test cases, three different offsets (L_3) of 0 mm, 1 mm, and 2 mm were chosen in order to compare the effect of offset designs. These offsets were chosen to equally space the offset along the riblet length of 4 mm. The 1 mm offset would be a mirrored geometry of a 3 mm offset and so the 3 mm offset was not modeled.

10.4.2 Results and Discussion

In this section, drag data is presented for the continuous and segmented riblet configurations. This data is used to compare the different configurations and show the differences among drag changes for the different cases.

10.4.2.1 Continuous Riblets

Martin and Bhushan (2014, 2016) modeled the effect of s^+ by varying s , V , and v independently, and h^+ by varying h , s , and t independently. They showed that nondimensional parameters s^+ , h^+ , and t^+ are relevant parameters for modeling drag. These parameters can be used in the scaling up of riblet design.

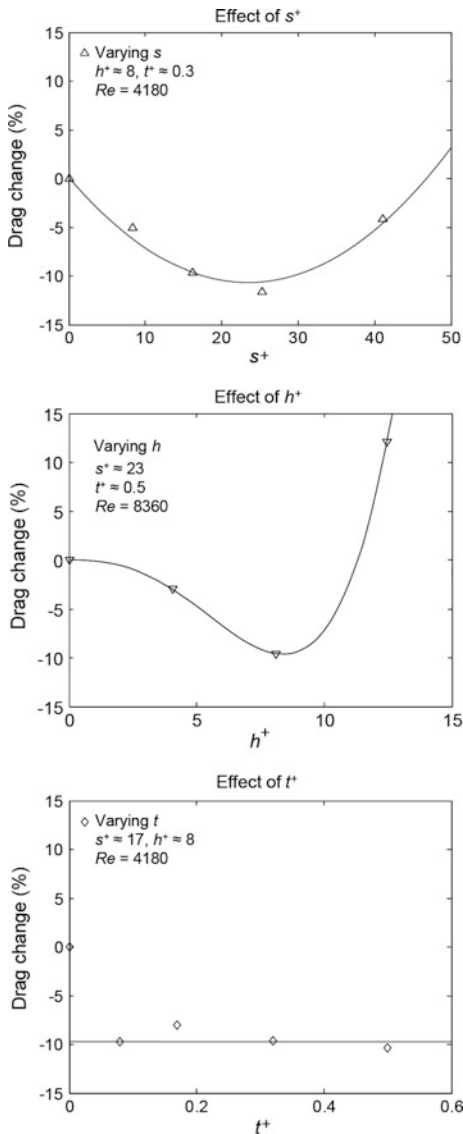
In order to understand the effect of the geometrical parameters on drag change, each parameter was individually modified and the resulting drag change was calculated. Selected results are shown in Fig. 10.21 (adapted from Martin and Bhushan 2016), where the negative drag change values indicate a drag reduction. For the varying spacing models, the maximum drag reduction was $\sim 11\%$ at $s^+ \approx 23$. When the spacing between riblets is small, more riblet peaks contact the vortices, leading to a lower drag reduction. With larger spacing, the vortices can fit within the valleys between the riblet peaks and are not lifted from the surface, leading to a drag increase. When varying only riblet height, maximum drag reduction occurred when $h^+ = 8-10$. Increasing outside of this range quickly led to a drag increasing state due to the riblets protruding too far into the higher velocity flow, or decreasing below this range led to a less efficient state due to the riblets unable to effectively repel the vortices. When the riblet thickness was modified, little drag change occurred. At much larger thicknesses, the width of the riblet valleys would decrease and the width of the riblet peaks would increase. It is expected that these changes would generate a weaker drag reduction, and eventually a drag increase.

10.4.2.2 Segmented Riblets

In order to compare continuous riblet results to segmented riblet results and better understand the riblet segmentation in sharks, various segmented riblet cases were modelled. The parameters for the length of each riblet (L_1), the gap between the riblets (L_2), and the offset between riblets (L_3) were modified independently.

The drag change data for the various models is shown in Fig. 10.22 (Martin and Bhushan 2016). In Fig. 10.22a, the aligned-segmented models were plotted for varying L_1^+ with constant L_2^+ and then also with constant L_1^+ with varying L_2^+ . In the varying L_1^+ with constant L_2^+ data set, the drag change increase as the lengths of the riblets increase. As the lengths increase, fewer gaps on the riblet surface occur leading to more of a continuous case which showed a greater drag reduction. Fewer gaps lead to less chance of burst and ejection events in the gaps. In the constant L_1^+ with varying L_2^+ data set, the drag change decreases by -5.0% at $L_2^+ = 101$ and

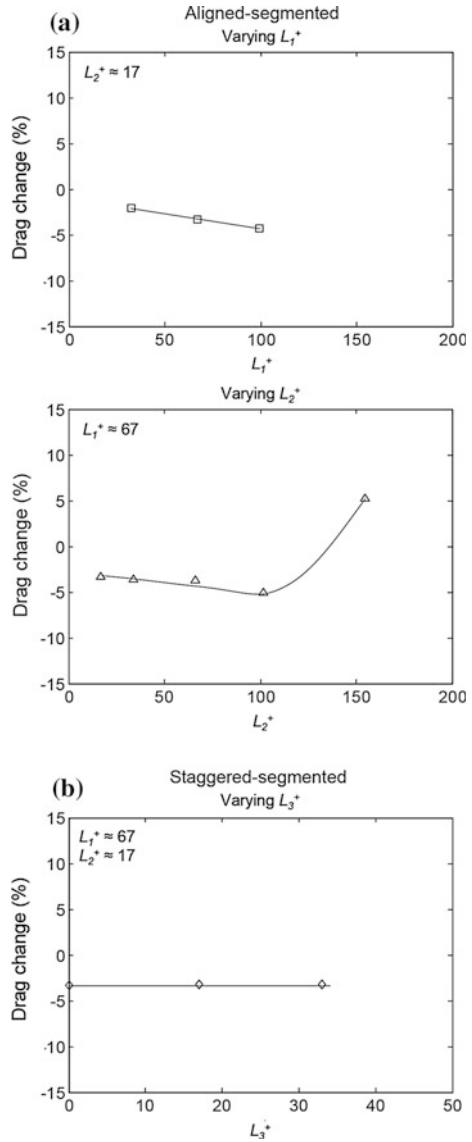
Fig. 10.21 Drag change for the various segmented models plotted against their non-dimensionalized parameter—spacing, height, and thickness. From the models with varying height, optimal height was found to be at $s \approx 20$ and $h^+ \approx 8-10$. The range of t^+ did not affect drag notably (adapted from Martin and Bhusan 2016)



then increases after that. With streamwise vortices predominately having non-dimensional lengths in the 100–200 range, once the gap becomes larger than 100 non-dimensional units, the streamwise vortex is not lifted generating a lot of drag. The staggered-segmented data set is plotted in Fig. 10.22b, showing a constant drag reduction of 3.3 %. For the values of $L_1^+ = 67$ and $L_2^+ = 17$, varying L_3^+ did not affect the drag change.

Modeling shows that aligned-segmented and staggered-segmented riblets result in drag reduction of 5.0 and 3.3 %, respectively, lower than that in the continuous

Fig. 10.22 **a** Drag change for the aligned-segmented cases. As L_1^+ increases, the riblet geometry approaches the continuous case and the drag reduction increases. As L_2^+ increases, the riblet geometry has greater gaps between the riblets, but the surface is still able to lift the streamwise vortices. The drag reduction stays constant and then increases to a drag increasing case once the gaps become on the order of the length of the streamwise vortex. **b** Drag change for the staggered-segmented cases. As L_3^+ increases, no difference in drag change is seen. It is thought that staggered-segmented riblets occur to help in ejection of contaminant particles in the riblet valleys (Martin and Bhushan 2016)



riblet configuration of 11 %. Thus it raises the question why do sharks have segmented and/or staggered riblets? It is believed that segmented riblets help the shark to swim by creating a deformable surface and/or in ejection of contaminant particles. Because each scale can individually pivot, when the shark turns, the surface of the shark becomes a deformable surface. Staggered riblets give particles a path to be removed from the surface. Aligned-segmented riblets may have less of a chance for particles to be ejected. Whereas, continuous riblets may have the least chance for

contaminants to be removed from the riblet valleys. By discouraging contaminant settlement and eventual growth, the riblet valleys in segmented configurations stay unpolluted and the drag reduction stays effective.

10.4.3 Summary

In the continuous configurations, drag reduction of approximately 10 % was reported by Martin and Bhushan (2016) when $s^+ \approx 18\text{--}25$ and $h^+ \approx 8\text{--}10$, which similar to $s^+ = 16$ and $h^+ = 8$ from Bechert et al. (1997b) and $s^+ = 18$ and $h^+ = 9$ from El-Samni et al. (2007). With these riblet dimensions, the streamwise vortices were lifted from the surface reducing the drag on the surface.

The aligned-segmented and staggered-segmented riblet configurations had maximum drag reductions of approximately 5 and 3 %, respectively (Martin and Bhushan 2016). The three parameters of riblet length, gap length, and riblet offset each changed the reported drag differently. When the lengths of the riblets increased with constant gap size, the drag reduction increased due to the configuration more closely approximating the continuous configuration. As the gap length approached 100 non-dimensional units, the drag reduction increased with the drag increasing after due to the increased odds of streamwise vortices falling into the gaps between consecutive riblets. As the riblet offset increased, no differences in drag change were observed.

Figure 10.23 summarizes the conclusions drawn from studying drag and vortex interactions on a flat surface and continuous and segmented riblet surfaces (Martin and Bhushan 2016). Figure 10.23a shows a typical streamwise vortex near a flat surface, and in Fig. 10.23b with $s^+ = 25.3$ or $s^+ = 41.2$, $h^+ = 8$, $t^+ = 0.3$, and $Re = 4180$, the vortex can be lifted or not lifted depending on the riblet spacing. As the spacing decreases below the optimum, drag reduction becomes less optimal due to vortices interacting with many riblet peaks. As the spacing increases above the optimum, drag increases due to vortices not being lifted. An example drag reduction curve for varying riblet spacing is shown in Fig. 10.23c. Figure 10.23d shows vortices on two aligned-segmented blades with different gap lengths, with $s^+ = 16$, $h^+ = 8$, $t^+ = 0.3$, $Re = 4180$, $L_1^+ = 66$, and $L_2^+ = 66$ or $L_2^+ = 154$. The figure shows that choosing a gap size smaller than the length of the streamwise vortex allows for the vortices to be lifted from the surface reducing drag in a segmented configuration, and vice versa.

Table 10.8 summarizes the effect of the continuous and segmented riblet parameters (Martin and Bhushan 2016). The riblet spacing should be around 15–20 non-dimensional units to lift the vortices with the riblet height around 8–10 non-dimensional units. If the riblets are too tall, they protrude too far into the flow and increase drag. If they are too short, they do not effectively lift the vortices, which in both cases, increases drag. Thinner riblets are better because the majority of the drag is found at the riblet peaks; however, thin riblets below a certain value do not noticeably change the drag. Riblet gaps should be less than 100 non-dimensional

Adequate spacing dimensions can lift vortices from a flat surface and lead to a drag reduction. Spacing that is too large can have vortices not lifted from the surface (shown using continuous riblets)

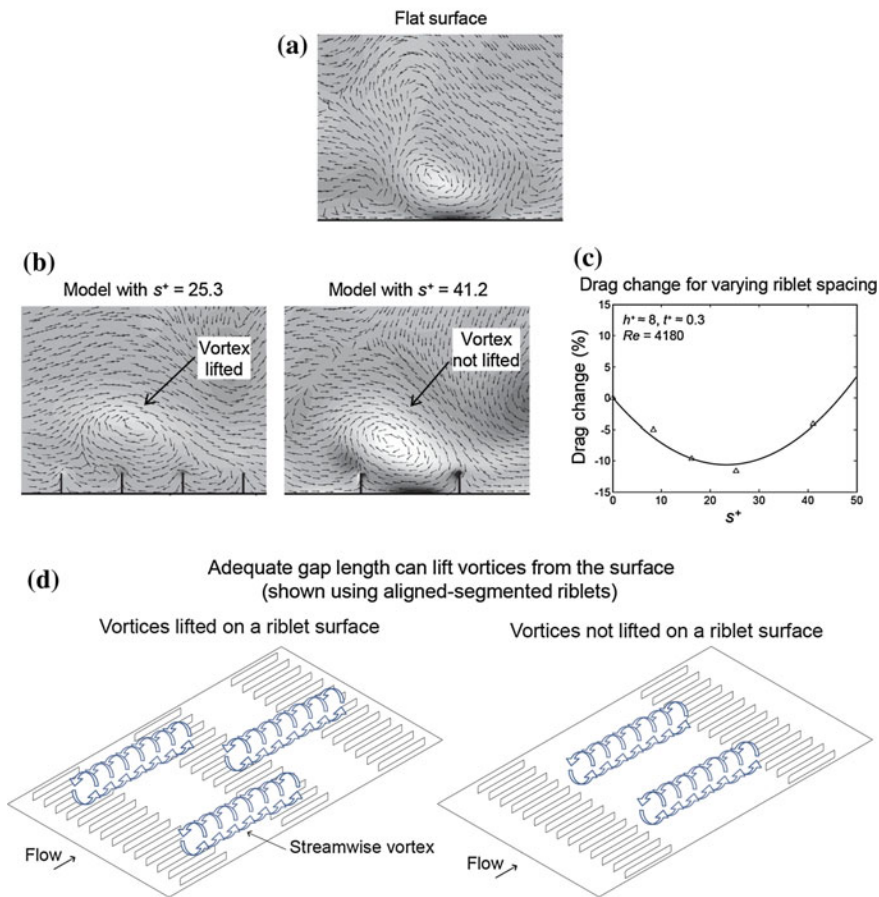


Fig. 10.23 **a** On a flat surface, vortices are near the surface and generate a lot of drag. **b** ($s^+ = 25.3$ or $s^+ = 41.2$, $h^+ = 8$, $t^+ = 0.3$ and $Re = 4180$). With adequate riblet spacing size, streamwise vortices are lifted away from the surface reducing drag and creating an overall drag reduction surface. **c** Optimal drag reduction occurred when riblet spacing was approximately 23. **d** ($s^+ = 16$, $h^+ = 8$, $t^+ = 0.3$, $Re = 4180$, $L_1^+ = 66$, and $L_2^+ = 66$ or $L_2^+ = 154$) Gaps between the riblets can be created as long as the gaps remain shorter than the common streamwise vortex lengths of 100–200 non-dimensional units (Martin and Bhushan 2016)

units to repel the streamwise vortices that predominately are 100–200 non-dimensional units long. Because continuous riblets have a greater drag reduction than aligned-segmented and staggered-segmented riblets, sharks may implement segmentation for two reasons. These configurations may help create a deformable surface for shark movement and/or in ejection of contaminant particles to keep the shark skin surface clean.

Table 10.8 Summary of effect of riblet geometry on drag (Martin and Bhushan 2016)

Parameter	Observation	Basis
<i>(a) Continuous riblet conclusions</i>		
Spacing (s^+)	Optimal riblet spacing should be around 15–20 non-dimensional units	Vortices have a diameter of 30–40 non-dimensional units. With optimal riblet spacing, these vortices can be lifted up away from the riblet surface decreasing overall drag
Height (h^+)	Optimal riblet height should be around 8–10 non-dimensional units	Riblets that are too tall protrude too far into the flow increasing drag over the entire surface. Riblets that are too short do not effectively lift the vortices away from the surface decreasing sweeps and ejections
Thickness (t^+)	Thinner riblets are better; however, at very small thicknesses, little drag differences are seen	The majority of drag occurs at the riblet peaks and with thinner riblets, there is less drag at the peaks. Most of riblet surface area comes from the spacing and height parameters, and so, thickness plays a smaller overall role in drag change
Parameter	Observation	Basis
<i>(b) Segmented riblet conclusions</i>		
Riblet gaps	Riblet gaps should be smaller than streamwise vortex lengths to increase chances of lifting vortices. Gaps should have lengths less than 100 non-dimensional units	Streamwise vortices predominately have lengths of 100–200 non-dimensional units and as gap length increases, the likelihood of a vortex fitting within the gap increases along with increasing drag
Riblet offsets	Riblet offsets by themselves have little effect on drag, but increase the chance for contaminant particles to be ejected from the channels	Riblets with offsets are still able to lift vortices from the surface decreasing sweep and ejection events associated with high drag
Observation		Why segmented?
<i>(c) Continuous versus segmented configurations</i>		
Continuous riblets have a drag reduction of approximately 10 % whereas aligned-segmented and stagger-segmented have drag reductions of approximately 5 % and 3 %		Segmented riblets may help sharks to swim by creating a deformable surface since the scales can individually pivot and/or in contaminant ejection to keep the shark clean by providing a path for particles to be removed

Notes Vortex non-dimensional diameters increase with Re —20 to 45 for Re from 2500 to 13,000. Vortex non-dimensional lengths predominately range from 100 to 200

Understanding different riblet configurations helps lead to a better understanding of the riblet mechanism which can be used as drag-reduction design principles for industrial applications in marine, medical, and industrial fields. Riblet dimensions are dependent on the component size and can range from the micro- to nanoscale.

10.5 Application of Riblets for Drag Reduction and Antifouling

Riblets provide drag reduction in fluid flow over objects where the dominant form of drag is skin friction and operates in turbulent flow. Major applications for drag reduction include transportation, fluid flow in pipelines, and other flow applications (Marentic and Morris 1992; Kennedy 1993; Davies 2002; Brostow 2008; Bhushan and Jung 2011; Deyuan et al. 2011; Bixler and Bhushan 2012a). According to the U.N. International Maritime Organization, about 90 % of worldwide goods are carried by sea-faring vessels. About 35–70 % of the energy consumed in transportation is estimated to be lost due to drag. In airplanes and automobiles, energy losses due to drag are also important. Low drag surfaces often equate to energy conservation and less fouling. For instance, in the oil industry, pipeline flow must overcome high drag due to viscous effects and sludge fouling (with Reynolds numbers reaching 1×10^5). Lower drag in pipelines reduces required pumping energy and increases flow rates. Traditionally, drag is lowered using fluid additives or improving the pipeline interior smoothness with corrosion resistant epoxy coatings (Burger et al. 1982; Brostow 2008; Martinez-Palou et al. 2011). Such coatings are most effective when sludge fouling is not present, as found with oil flowing from a well at a high temperature and velocity.

In addition to lowering drag, antifouling surfaces can reduce the spread of infectious diseases by limiting biofouling. Medical biofouling occurs in areas such as prosthetic implants, biosensors, catheters, dental implants, and medical equipment. Problems include implant rejection, malfunction of biosensors, and spread of infectious diseases (Vo-Dinh 2007; Schulz et al. 2009; Shirtliff and Leid 2009; Chan and Wong 2010). Biofouling is commonly associated with marine environments where noticeable aquatic growth appears on ships and underwater structures. This increases ship hull drag, corrosion, fuel consumption, and engine stress (Copisarow 1945; Anon 1952; Ray 1959; Melo et al. 1988; Railkin 2004). Industrial fouling occurs in areas such as power plants, water treatment systems, and food/beverage industries. Problems include pipe blockage, decreased membrane flux, contaminated water, and reduced heat exchanger efficiency (Somerscales and Knudsen 1981; Walker et al. 2000; Chan and Wong 2010).

In the mid-1980s, vinyl film sawtooth riblets were applied to boat hulls for racing (Choi et al. 1989). Both an Olympic rowing boat and an Americas Cup sailing yacht were covered with riblets during competition. Because skin friction of an airplane accounts for as much as 48 % of total drag, vinyl film riblets have also been applied on airplane wings (Han et al. 2002) and fuselage. About 70 % of the aircraft was covered with film riblets, and it provided 3 % total drag reduction. This 3 % drag reduction correlates to a similar 3 % savings in fuel costs (Bechert et al. 1997a).

Another large commercial application for riblet technologies is drag reduction in pipe flow. Sawtooth riblet film produced by 3 M has been applied inside pipes (Liu et al. 1990; Rohr et al. 1992; Enyutin et al. 1995; Koury and Virk 1995). Drag

reduction tests in pipe flow are carried out by comparing the pressure drop in a riblet lined pipe with that of a similar pipe with a smooth surface. Drag reduction data for sawtooth riblets on a flat plate are shown in Fig. 10.24a, and drag reduction data for water flow in sawtooth riblet lined pipes are shown in Fig. 10.24b. The cone angle α is shown in Fig. 10.8. As riblets are applied to the inside surface of a pipe, the riblet tips are shifted together due to the curve of the pipe wall. Consequently, the optimized s^+ range for riblets in pipe flow is lower than that for the same riblets in flow over a flat surface (Liu et al. 1990). Additionally, the decrease in s^+ suggests that an increased drag reduction in round pipes might be seen with a larger characteristic angle, α , than for flow over riblets on a flat surface.

Machining the surface or applying vinyl film riblets proves difficult for most pipes, and alternatives are being developed. Experimental application of a scratching technique to the inside surface of pipes has created a riblet-like roughness that has provided more than 5 % drag reduction benefit (Weiss 1997). Stemming from an old sailors' belief that ships sail faster when their hulls are sanded in the longitudinal direction, Weiss (1997) fabricated these riblets by using a steel brush moved through the pipeline to create a ridged surface. Studies have

Fig. 10.24 Comparison of riblet performance curves over sawtooth riblets on a flat-plate surface and inside round pipes of 25.4 and 50.8 mm diameters. Peak drag reduction for riblets in pipe flow occurs near $s^+ = 12$, which is lower than the flat plate optimal value of $s^+ = 15$. Bechert experiments were performed using oil as the test fluid, and Liu experiments were performed using water as the test fluid in an open channel (adapted from Liu et al. 1990; Bechert et al. 1997b)

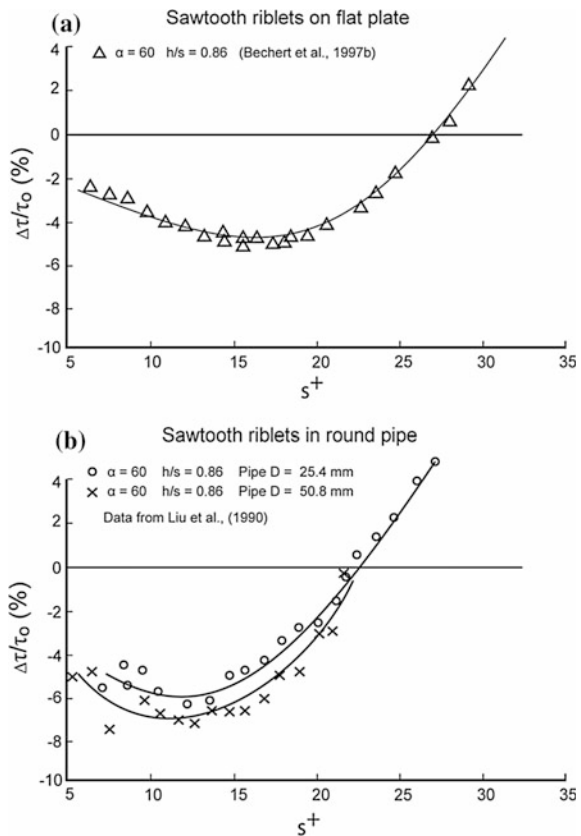
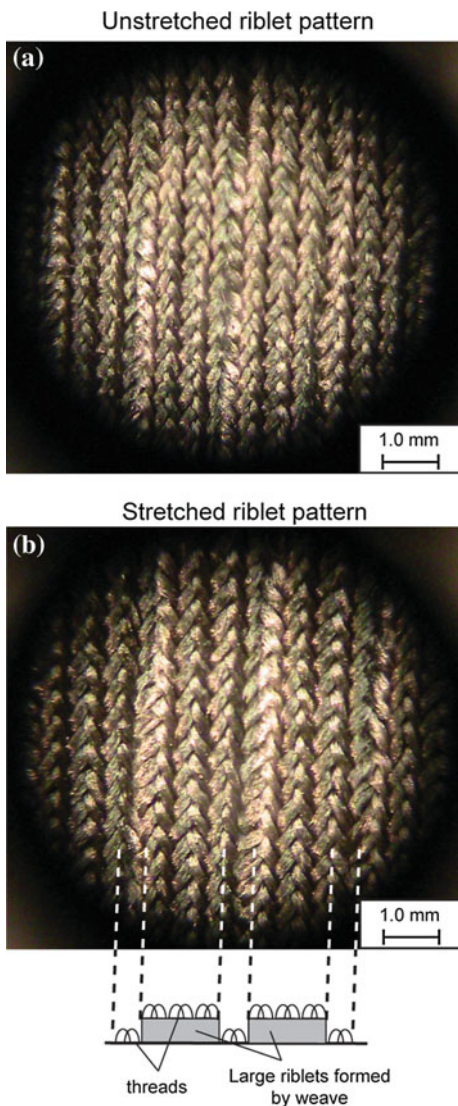


Fig. 10.25 Images of riblet geometries on **a** unstretched and **b** stretched Speedo FastSkin[®] swimsuit. **c** Schematic showing apparent hierarchical riblet structure formed by threads (Dean and Bhushan 2010)



shown as much as a 10 % reduction in fluid flow with the combined effect of cleaning the pipe and ridging the surface. Tests on a 10 mile gas pipeline section have confirmed this benefit during commercial operation (Bechert et al. 1997a).

Wind turbines are used for harnessing wind energy which is an important source for renewable energy. Riblet technology can be used on the turbine blades to reduce drag. Riblets can be either fabricated on the blades during production or vinyl film riblets could be applied on the blades.

The only presently available consumer products using riblet technology for drag reduction is competitive swimwear. The FastSkin[®] suits were introduced by Speedo

in 2004 (Krieger 2004). Speedo claimed a drag reduction of several percent in a static test compared to other race suits. However, given the compromises of riblet geometry made during manufacturing, it is hard to believe the full extent of the drag reduction. These suits were worn by American swimmer Michael Phelps in the 2008 Beijing Olympics, where he broke eight Olympic records, seven world records, and won 8 gold medals. These suits were subsequently banned by the International Swimming Federation (FINA) due to an unfair advantage of drag reduction for some swimmers.

The fabric of the FastSkin[®] swimsuits is knit and the pattern is embossed. The pattern resembles wide blade riblets, shown in Fig. 10.25. Unstretched riblets are tightly packed (Fig. 10.25a). As the fabric stretches, the riblet width and spacing increase (Fig. 10.25b). The associated decrease in h/s ratio depends on the dimensions of each swimmer's body, which is a compromising factor in the design. Riblet thickness is also a factor considered in the design.

Drag reduction is also beneficial in antifouling. Low drag and low adhesion surfaces reduce biofouling. In addition, as indicated in a later chapter, on textured surfaces, microscopic aquatic organisms have difficulty adhering to and colonizing the surface.

Manufacturing techniques for riblets must be chosen specific to their application. Vinyl film riblets are the easiest method, as application of a film to a surface requires less for work small scale application than other methods. Rolling or grinding methods of riblet application can be used for turbine blades or high volume commercially sold pieces. Laser machining, a two-step molding process using a photolithographically produced master can also be used for high volume products. Machining methods are believed to be unfavorable in most instances.

10.6 Closure

The skin of fast swimming sharks reduces drag and protects against biofouling as they swim through water. Shark skin is covered by very small individual tooth-like scales called dermal denticles (little skin teeth), ribbed with longitudinal grooves (aligned parallel to the real flow direction of water) called riblets. Longitudinal grooves encourage anisotropic fluid flow. Fluid drag in the turbulent boundary layer is in large part due to the effects of the streamwise vortices formed in the fluid closest to the surface. Turbulence in the outer boundary layers is in large part due to the translation, ejection, and twisting of these vortices. Additionally, the vortices also cause high velocities at the surface, which create large shear stresses on the surface. Riblets lift the vortices off of the surface and reduce the amount of surface area exposed to the high velocity flow. By modifying the velocity distribution, riblets facilitate a net reduction in shear stress at the surface. Fluid flow experiments and modeling have supported riblet drag reduction theories. To sum up, the microstructured riblets encourage anisotropic flow as well as control vortices on the skin naturally present in turbulent flow which reduces drag. In addition to low drag,

the spacing between these dermal denticles is such that microscopic aquatic organisms have difficulty adhering to and colonizing the surface.

Various riblet shapes have been studied experimentally for their drag reducing capabilities, but sawtooth, scalloped, and blade riblets are most common. Optimization studies have been performed by varying flow properties or riblet geometries. Drag reduction by riblet surfaces has been reported to be on the order of 10–30 % in water, air, and oil for blade type riblets. A narrow range of h^+ and s^+ and low t^+ with $s^+ \approx 15$ and $h/s \approx 0.5$, blade geometry and continuous configuration has been reported for optimal riblet design.

Fluid flow modeling of continuous and segmented riblet geometries has been carried out. In the continuous configurations, a drag reduction of approximately 10 % occurred when $s^+ \approx 18$ –25 and $h^+ \approx 8$ –10. With these riblet dimensions, the streamwise vortices were lifted from the surface, reducing the drag on the surface. Furthermore, t^+ should be low for low drag. The aligned-segmented and staggered-segmented riblet configurations had maximum drag reduction of approximately 5 and 3 %, respectively. The three parameters of riblet length, gap length, and riblet offset each changed the drag. Longer riblets were better for reducing drag. When gaps between riblets were larger than the length of streamwise vortices, drag increased due to vortices falling between consecutive riblets. Riblet offset did not have much effect. Because continuous riblets have a greater drag reduction than aligned-segmented and staggered-segmented riblets, sharks may implement segmentation for two reasons. These configurations may help create a deformable surface for shark movement and/or in ejection of contaminant particles to keep the shark skin surface clean.

Commercial applications of riblets include competition swimsuits, in which the pattern is embossed, as well as experimental applications to airplanes and boats. Drag reductions in riblet application have been accomplished, and flight applications have seen a fuel savings.

Drag reduction is also helpful in antifouling. Low drag and low adhesion surfaces reduce biofouling. Spacing between the dermal denticles is such that microscopic aquatic organisms have difficulty adhering to and colonizing the surface.

References

- Anderson, J.D. (2010), *Fundamentals of Aerodynamics*, 5th Ed., McGraw Hill, New York.
- Anonymous (1952), *Marine Fouling and its Prevention*, Woods Hole Oceanographic Institute, US Naval Institute, Annapolis, US.
- Anonymous (2007), *Pilot's Encyclopedia of Aeronautical Knowledge*, United States Federal Aviation Administration, Skyhorse, New York.
- Anonymous (2015) ANSYS® Fluent, Release 14.5, Help System, Fluent User's Guide, ANSYS, Inc.
- Barlow, J.B., Rae, W.H., and Pope, A. (1999), *Low-Speed Wind Tunnel Testing*, 3rd Ed., Wiley-Interscience, New York.

- Batchelor, G.K. (1970), *An Introduction to Fluid Dynamics*, Cambridge University Press, Cambridge.
- Bechert, D.W., Hoppe, G. and Reif, W.E. (1985), "On the Drag Reduction of the Shark Skin," Paper # AIAA-85-0546, presented at AIAA Shear Flow Control Conference, Boulder, CO, AIAA, New York.
- Bechert, D.W., Bartenwerfer, M., Hoppe, G., and Reif, W.-E. (1986), "Drag Reduction Mechanisms Derived from Shark Skin," Paper # ICAS-86-1.8.3, Vol. 2 (A86-48-97624-01), pp. 1044-1068, *Proc. 15th ICAS Congress*, AIAA, New York.
- Bechert, D.W., Hoppe, G., van der Hoeven, J.G.T. and Makris, R. (1992), "The Berlin Oil Channel for Drag Reduction Research," *Exp. in Fluids* **12**, 251-260.
- Bechert, D.W., Bruse, M., Hage, W., and Meyer, R. (1997a), "Biological Surfaces and Their Technological Application – Laboratory and Flight Experiments on Drag Reduction and Separation Control," Paper # AIAA-1997-1960, presented at AIAA 28th Fluid Dynamics Conference, Snowmass Village, CO, AIAA, New York.
- Bechert, D.W., Bruse, M., Hage, W., van der Hoeven, J. G. T. and Hoppe, G. (1997b), "Experiments on Drag Reducing Surfaces and their Optimization with an Adjustable Geometry," *J. Fluid Mech.* **338**, 59-87.
- Bechert, D.W., Bruse, M. and Hage, W. (2000a), "Experiments with Three-dimensional Riblets as an Idealized Model of Shark Skin," *Exp. Fluids* **28**, 403-412.
- Bechert, D.W., Bruse, M., Hage, W. and Meyer, R. (2000b), "Fluid Mechanics of Biological Surfaces and their Technological Application," *Naturwissenschaften* **87**, 157-171.
- Bhushan, B. (2009), "Biomimetics: Lessons from Nature – an Overview," *Phil. Trans. R. Soc.* **367**, 1445-1486.
- Bhushan, B. (2012), "Bioinspired Structured Surfaces," *Langmuir* **28**, 1698-1714.
- Bhushan, B. and Jung, Y.C. (2011), "Natural and Biomimetic Artificial Surfaces for Superhydrophobicity, Self-Cleaning, Low Adhesion, and Drag Reduction," *Prog. Mater. Sci.* **56**, 1-108.
- Bixler, G.D. and Bhushan, B. (2012a), "Biofouling Lessons from Nature," *Phil. Trans. R. Soc. A*, **370**, 2381-2417.
- Bixler, G.D. and Bhushan, B. (2012b), "Bioinspired Rice Leaf and Butterfly Wing Surface Structures Combining Shark Skin and Lotus Effects," *Soft Matter* **8**, 11271-11284.
- Bixler, G.D. and Bhushan, B. (2013a), "Fluid Drag Reduction with Shark-skin Riblet Inspired Microstructured Surfaces," *Adv. Func. Mater.* **23**, 4507-4528.
- Bixler, G.D. and Bhushan, B. (2013b), "Shark Skin Inspired Low-drag Microstructured Surfaces in Closed Channel Flow," *J. Colloid Interf. Sci.* **393**, 384-396.
- Bixler, G.D. and Bhushan, B. (2013c), "Bioinspired Micro/Nanostructured Surfaces for Oil Drag Reduction in Closed Channel Flow," *Soft Matter* **9**, 1620-1635.
- Bixler, G.D. and Bhushan, B. (2013d), "Fluid Drag Reduction and Efficient Self-Cleaning with Rice Leaf and Butterfly Wing Bioinspired Surfaces," *Nanoscale* **5**, 7685-7710.
- Blevins, R.D. (1984), *Applied Fluid Dynamics Handbook*, Van Nostrand-Reinhold, New York.
- Brennan, A.B., Baney, R.H., Carman, M.I., Estes, T.G., Feinberg, A.W., Wilson, L.H. and Schumacher, J.F.. (2010), "Surface Topographies for Non-Toxic Bioadhesion Control," United States Patent no. 7 650 848.
- Brostow, W. (2008), "Drag Reduction in Flow: Review of Applications, Mechanism, and Prediction," *J. Indust and Eng Chem* **14**, 408-416.
- Burger, E.D., Munk, W.R. and Wahl, H.A. (1982), "Flow Increase in the Trans Alaska Pipeline Through Use of a Polymeric Drag-Reducing Additive," *J. Petro Tech*, **34**, 377-386.
- Buttner, C.C. and Schulz, U. (2011), "Shark Skin Inspired Riblet Structures as Aerodynamically Optimized High Temperature Coatings for Blades of Aeroengines," *Smart Matl. and Struct.* **20**, 1-9.
- Caram, J.M. and Ahmed, A. (1991), "Effect of Riblets on Turbulence in the Wake of an Airfoil," *AIAA* **29** (11), 1769-1770.
- Caram, J.M. and Ahmed, A. (1992), "Development of the Wake of an Airfoil with Riblets," *AIAA* **30** (12), 2817-2818.

- Chan, J. and Wong, S. (eds.) (2010), *Biofouling Types, Impact and Anti-Fouling*, Nova Science Publishers, New York.
- Choi, K.S., Gadd, G.E., Pearcey, H.H., Savill, A.M., and Svensson, S. (1989), "Tests of Drag-Reducing Polymer Coated on a Riblet Surface," *Appl. Sci. Res.* **46**, 209-216.
- Choi, H., Moin, P. and Kim, J. (1993), "Direct Numerical Simulation of Turbulent Flow Over Riblets," *J. Fluid Mech.* **255**, 503-539.
- Choi, K.S., Yang, X., Clayton, B.R., Glover, E.J., Altar, M., Semenov, B.N., and Kulik, V.M. (1997), "Turbulent Drag Reduction Using Compliant Surfaces," *Proc. R. Soc A* **453**, 2229-2240.
- Chu, D. C. and Karniadakis, G. E. (1993), "A Direct Numerical Simulation of Laminar and Turbulent Flow Over Riblet-mounted Surfaces," *J. Fluid Mech.* **250**, 1-42.
- Collins, M.W. and Brebbia, C.A. (eds.) (2004), *Design and Nature II Comparing Design in Nature with Science and Engineering*, WIT Press, Southampton, UK.
- Copisarow, M. (1945), "Marine Fouling and its Prevention," *Science* **101**, 406-407.
- Coustols, E. (1989), "Behavior of Internal Manipulators: "Riblet" Models in Subsonic and Transonic Flows," Paper # AIAA-89-0963, presented at AIAA Shear Flow Conference, Tempe, AZ, AIAA, New York.
- Coustols, E. and Cousteix, J. (1994), "Performances of Riblets in the Supersonic Regime," *AIAA* **32** (2), 431-433.
- Coustols, E. and Schmitt, V. (1990), "Synthesis of Experimental Riblet Studies in Transonic Conditions," in *Turbulence Control by Passive Means* (eds. Coustols, Kluwer, Dordrecht), pp. 123-140, The Netherlands.
- Daniello, R.J., Waterhouse, N.E. and Rothstein, J.P. (2009), "Drag Reduction in Turbulent Flows over Superhydrophobic Surfaces," *Phys. Fluids* **21**, 085103.
- Davies, M. (ed.) (2002), *Standard Handbook for Aeronautical and Astronautical Engineers*, McGraw-Hill, New York.
- Dean, B. and Bhushan, B. (2010), "Shark-skin Surfaces for Fluid-Drag Reduction in Turbulent Flow: a Review," *Phil. Trans. R. Soc.* **368**, 4775-4806.
- Dean, B. and Bhushan, B. (2012), "The Effect of Riblets in Rectangular Duct Flow," *Appl. Surf. Sci.* **258**, 3936-3947.
- Denkena, B., Kohler, J. and Wang, B. (2010), "Manufacturing of Functional Riblet Structures by Profile Grinding," *CIRP J. Manuf. Sci. Tech.* **3**, 14-26.
- Deyuan, Z., Yuehao, L., Huawei, C. and Xinggang, J. (2011), "Exploring Drag-Reducing Grooved Internal Coating for Gas Pipelines," *Pipeline & Gas Journal* March, 59-60.
- Dickinson, P.H. and Proudley, G.M. (1991), "Methods of Manufacture and Surface Treatment Using Laser Radiation," United States Patent no. 4 994 639.
- El-Samni, O. A., Chun, H. H. and Yoon, H. S. (2007), "Drag Reduction of Turbulent Flow Over Thin Rectangular Riblets," *Int. J. Eng. Sci.* **45**, 436-454.
- Enyutin, G.V., Lashkov, Y.A., and Samoilova, N.V. (1995), "Drag Reduction in Riblet-Lined Pipes," *Fluid Dynamics*, **30** (1), 45-48.
- Frings, B. (1988), "Heterogeneous Drag Reduction in Turbulent Pipe Flows using Various Injection Techniques," *Rheologica Acta* **27**, 92-110.
- Gillcrist, M. C. and Reidy, L. W. (1989), "Drag Measurements on Marine Vehicles with a Riblet Surface Coating," in *Drag Reduction in Fluid Flows* (Sellin, R. and Moses, R., eds.), pp. 99-106, Ellis Horwood Publishers, Chichester, England.
- Goldstein, D., Handler, R. and Sirovich, L. (1995), "Direct Numerical Simulation of Turbulent Flow Over a Modelled Riblet-covered Surface," *J. Fluid Mech.* **302**, 333-376.
- Gruneberger, R. and Hage, W. (2011), "Drag Characteristics of Longitudinal and Transverse Riblets at Low Dimensionless Spacings," *Exp. Fluids*, **50**, 363-373.
- Han, M., Huh, J.K., Lee, S.S., and Lee, S. (2002), "Micro-Riblet Film for Drag Reduction," Proceedings of the Pacific Rim Workshop on Transducers and Micro/Nano Technologies, Xiamen, China.

- Han, M., Lim, H.C., Jang, Y.-G., Seung, S.L., and Lee, S.-J. (2003), "Fabrication of a Micro-Riblet Film and Drag Reduction Effects on Curved Objects," Paper # 0-7803-7731-1, presented at 12th International Conference on Solid State Sensors, Actuators and Microsystems, Boston, MA.
- Hirt, G. and Thome, M. (2007), "Large Area Rolling of Functional Metallic Micro Structures," *Prod. Eng. Res. Devel.* **1**, 351-356.
- Hoyt, J.W. (1975), "Hydrodynamic Drag Reduction Due to Fish Slimes," *Swimming and Flying in Nature* **2**, 653-672.
- Jung, Y.C. and Bhushan, B. (2010), "Biomimetic Structures for Fluid Drag Reduction in Laminar and Turbulent Flows," *J. Phys.: Condens. Matter* **22**, 1-9.
- Kennedy, J.L. (1993), *Oil and Gas Pipeline Fundamentals*, PennWell Books, Tulsa, Oklahoma.
- Kesel, A. and Liedert, R. (2007), "Learning from Nature: Non-Toxic Biofouling Control by Shark Skin Effect," *Comp. Biochem. Physiol. A* **146**, S130.
- Kline, S.J., Reynolds, W.C., Schraub, F.A. and Runstadler, P.W. (1967), "The Structure of Turbulent Boundary Layers," *J. Fluid Mech.* **30**, 741-773.
- Koch, K. and Barthlott, W. (2009), "Superhydrophobic and Superhydrophilic Plant Surfaces: an Inspiration for Biomimetic Materials," *Phil. Trans. R. Soc.* **367**, 1487-1509.
- Koury, E. and Virk P.S. (1995), "Drag Reduction by Polymer Solutions in a Riblet-Lined Pipe," *Appl. Sci. Res.* **54**, 323-347.
- Krieger, K. (2004), "Do Pool Sharks Really Swim Faster?" *Science* **305**, 636-637.
- Lee, S.J. and Lee, S.H. (2001), "Flow Field Analysis of a Turbulent Boundary Layer over a Riblet Surface," *Exp. Fluids* **30**, 153-166.
- Lee, J.D., Gregorek, G.M., and Korakan, K.D. (1978), "Testing Techniques and Interference Evaluation in the OSU Transonic Airfoil Facility," Paper # AIAA-1978-1118, presented at 11th Fluid and Plasma Dynamics Conference, Seattle, WA, AIAA, New York.
- Liu, K.N., Christodoulou, C., Riccius, O. and Joesph, D.D. (1990), "Drag Reduction in Pipes Lined with Riblets," *AIAA* **28** (10), 1697-1698.
- Lowrey, P. and Harasha, J. (1991), "A Preliminary Assessment of the Feasibility of using Riblets in Internal Flows to Conserve Energy," *Energy* **16**, 631-642.
- Luchini, P., Manzo, F., and Pozzi, A. (1991), "Resistance of a Grooved Surface to Parallel Flow and Cross-flow," *J. Fluid Mech.* **228**, 87-109.
- Marentic, F.J. and Morris, T.L. (1992), "Drag Reduction Article," United States Patent no. 5 133 516.
- Martell, M.B., Perot, J.B., and Rothstein, J.P. (2009), "Direct Numerical Simulations of Turbulent Flows over Drag-reducing Ultrahydrophobic Surfaces," *J. Fluid Mech.* **620**, 31-41.
- Martell, M.B., Rothstein, J.P. and Perot, J.B. (2010), "An Analysis of Superhydrophobic Turbulent Drag Reduction Mechanisms using Direct Numerical Simulation," *Phys. Fluids* **22**, 065102.
- Martin, S. and Bhushan, B. (2014), "Fluid Flow Analysis of a Shark-Inspired Microstructure," *J. Fluid Mech.* **756**, 5-29.
- Martin, S. and Bhushan, B. (2016), "Fluid Flow Analysis of Continuous and Segmented Riblet Structures," *RSC Adv.* **6**, 10962-10978.
- Martinez-Palou, R., Mosqueira, M., Zapata-Rendón, B., Mar-Juárez, E., Bernal-Huicochea, C., Clavel-López, J. and Aburto, J. (2011), "Transportation of Heavy and Extra-heavy Crude Oil by Pipeline: A review," *J or Petro Sci and Eng.* **75**, 274-282.
- Melo, L.F., Bott, T.R. and Bernardo, C.A. (eds.) (1988), *Fouling Science and Technology*, Kluwer Academic Publishers, Dordrecht, The Netherlands.
- Munson, B. R., Rothmayer, A. P., Okiishi, T. M., and Huebsch, W. D. (2012), *Fundamentals of Fluid Mechanics*, 7th Ed., Wiley, New York.
- Neumann, D. and Dinkelacker, A. (1991), "Drag Measurements on V-grooved Surfaces on a Body of Revolution in Axial Flow," *App Sci Res.* **48**, 105-114.
- Nitschke, P. (1983), "Experimental Investigation of the Turbulent Flow in Smooth and Longitudinal Grooved Pipes," *Max-Planck Institute for Stromungsforschung*, Gottingen, West Germany.

- Oeffner, J. and Lauder, G.V. (2012), "The Hydrodynamic Function of Shark Skin and Two Biomimetic Applications," *J. Exp. Biology* **215**, 785-795.
- Ou, J., Perot, B. and Rothstein, J.P. (2004), "Laminar Drag Reduction in Microchannels using Ultrahydrophobic Surfaces," *Phys. Fluids* **16**, 4635-4643.
- Pritchard, P. J. and Mitchell, J. W. (2015), *Fox and McDonald's Introduction to Fluid Mechanics, 9th Ed.*, Wiley, New York.
- Railkin, A.I. (2004), *Marine Biofouling Colonization Processes and Defenses*, CRC Press, Boca Raton, Florida.
- Ralston, E. and Swain, G. (2009), "Bioinspiration – the Solution for Biofouling Control?" *Bioinsp. Biomim.* **4**, 1-9.
- Ray, D.L. (ed.) (1959), *Marine Boring and Fouling Organisms*, University of Washington Press, Seattle.
- Reidy, L.W. and Anderson, G.W. (1988), "Drag Reduction for External and Internal Boundary Layers Using Riblets and Polymers," Paper # AIAA-1988-0138, presented at 26th AIAA Aerospace Sciences Meeting, Reno, NV, AIAA, New York.
- Reif, W. (1985), *Squamation and Ecology of Sharks*. Courier Forschungsinstitut Senckenberg, Frankfurt, Germany, **78**, 1-255.
- Rohr, J.J., Andersen, G.W., Reidy, L.W. and Hendricks, E.W. (1992), "A Comparison of the Drag-reducing Benefits of Riblets in Internal and External Flows," *Exp. in Fluids*, **13**, 361-368.
- Sareen, A., Deters, R.W., Henry, S.P. and Selig, M.S. (2011), "Drag Reduction Using Riblet Film Applied to Airfoils for Wind Turbines," Paper # AIAA-2011-558, presented at 49th AIAA Aerospace Sciences Meeting, Orlando, FL, AIAA, New York.
- Scardino, A.J. (2009), "Surface Modification Approaches to Control Marine Biofouling," in *Advances in Marine Antifouling Coatings and Technologies* (eds. Hellio, C. and Yebra, D.), pp. 664-692, CRC Press, Boca Raton, Florida.
- Schulz, M.J., Shanov, V.N. and Yun, Y. (eds.) (2009), *Nanomedicine Design of Particles, Sensors, Motors, Implants, Robots, and Devices*, Artech House, Boston.
- Schumacher, J.F., Aldred, N., Callow, M.E., Finlay, J.A., Callow, J.A., Clare, A.S. and Brennan, A.B. (2007), "Species-Specific Engineered Antifouling Topographies: Correlations between the Settlement of Algal Zoospores and Barnacle Cyprids," *Biofouling* **23**, 307- 317.
- Shephard, K.L. (1994), "Functions for Fish Mucus," *Rev. Fish Biology and Fisheries* **4**,401-429.
- Shirliff, M. and Leid, J.G. (eds.) (2009), *The Role of Biofilms in Device-Related Infections*, Springer-Verlag, Berlin.
- Somerscales, E.F.C. and Knudsen, J.G. (eds.) (1981), *Fouling of Heat Transfer Equipment*, Hemisphere Publishing Corporation, Washington.
- Subaschandar, N., Kumar, R., and Sundaram, S. (1999), "Drag Reduction Due to Riblets on a GAW(2) Airfoil," *J. of Aircraft*, **36** (5), 890-892.
- Sundaram, S., Viswanath, P.R., and Rudrakumar, S. (1996), "Viscous Drag Reduction Using Riblets on NACA 0012 Airfoil to Moderate Incidence," *AIAA* **34** (14), 676-682.
- Sundaram, S., Viswanath, P.R., and Subaschandar, N. (1999), "Viscous Drag Reduction Using Riblets on a Swept Wing," *AIAA* **37** (7), 851-856.
- Viswanath, P. R. (1999), "Riblets on Airfoil and Wings: A Review," Paper # AIAA-99-3402, presented at the AIAA 30th Fluid Dynamics Conference, Norfolk, VA, AIAA, New York.
- Viswanath, P. R. and Mukund, R. (1995), "Turbulent Drag Reduction Using Riblets on a Supercritical Airfoil at Transonic Speeds," *AIAA* **33** (5), 945-947.
- Viswanath, P.R. (2002), "Aircraft Viscous Drag Reduction using Riblets," *Prog Aerospace Sci.* **38**, 571-600.
- Vo-Dinh, T. (ed.) (2007), *Nanotechnology in Biology and Medicine*, CRC Press, Boca Raton, Florida.
- Walker, J., Surman, S. and Jass, J. (eds.) (2000), *Industrial Biofouling Detection, Prevention and Control*, Wiley, New York.
- Walsh, M.J. (1982), "Turbulent Boundary Layer Drag Reduction using Riblets," Paper # AIAA-1982-0169, presented at AIAA 20th Aerospace Sciences Meeting, Orlando FL, AIAA, New York.

- Walsh, M.J. (1990a), "Effect of Detailed Surface Geometry on Riblet Drag Reduction Performance," *J. Aircraft*, **27** (6), 572-573.
- Walsh, M. J. (1990b), "Riblets. Viscous Drag Reduction in Boundary Layers," *Progr. in Astronaut. and Aeronaut.*, **123**, 203-261.
- Walsh, M. J. and Lindemann, A.M. (1984), "Optimization and Application of Riblets for Turbulent Drag Reduction," Paper # AIAA-1984-0347, presented at AIAA 22nd Aerospace Sciences Meeting, Reno, NV, AIAA, New York.
- Walsh, M. J. and Anders, J. B., Jr. (1989), "Riblet/LEBU Research at NASA Langley," *Appl. Sci. Res.* **46**, 255-262.
- Weiss, M.H. (1997), "Implementation of Drag Reduction Techniques in Natural Gas Pipelines," presented at 10th European Drag Reduction Working Meeting, Berlin, Germany, March 19-21.
- Wen, L., Weaver, J. C., and Lauder, G. V. (2014), "Biomimetic Shark Skin: Design, Fabrication, and Hydrodynamic Function," *J. Exp. Biology* **217**, 1656-1666.
- Wetzel, K.K. and Farokhi, S. (1996), "Interaction of Riblets and Vortex Generators on an Airfoil," Paper # AIAA-1996-2428-CP, presented at the AIAA 14th Applied Aero-dynamics Conference, New Orleans, LA, AIAA, New York.
- White, F. (2006), *Viscous Fluid Flow*, 3rd ed., McGraw Hill, New York.
- Wilkinson, S.P. and Lazos, B.S. (1988), "Direct Drag and Hot-wire Measurements on Thin-element Riblet Arrays," in *Turbulence Management and Relaminarisation* (Liepman, H.W. and Narasimha, R., eds.), pp. 121-131, Springer-Verlag, Berlin.

Chapter 11

Rice Leaf and Butterfly Wing Effect

11.1 Introduction

Fluid drag reduction and antifouling are of commercial interest (Bhushan and Jung 2011; Bixler and Bhushan 2012a, 2015). Many flora and fauna flourish in living nature due to their low drag and antifouling properties, with commonly studied examples including shark skin and lotus leaves. Inspired by shark skin and lotus leaves, Bixler and Bhushan (2012b) found rice leaves and butterfly wings combine the shark skin and lotus effects. Sinusoidal grooves in rice leaves and aligned shingle-like scales in butterfly wings provide the anisotropic flow. Hierarchical structures consisting of micropapillae superimposed by waxy nanobumps in rice leaves and microgrooves on top of shingle like scales in butterfly wings provide the superhydrophobicity and low adhesion. Various studies suggest that this combination of anisotropic flow, superhydrophobicity, and low adhesion leads to improved drag reduction, self-cleaning, and antifouling (Bixler and Bhushan 2012b, 2013a, d, 2014; Bixler et al. 2014). Bixler and Bhushan (2015) provide a review and details follow.

11.2 Inspiration from Living Nature

In this section, we explain characteristics and mechanisms of lotus leaf, fish scale, shark skin, rice leaf, and butterfly wing surfaces (Bixler and Bhushan 2015).

11.2.1 Ambient Species—Lotus Effect

In the ambient environment, many surfaces including lotus leaves (Barthlott and Neinhuis 1997; Koch et al. 2008, 2009a; Nosonovsky and Bhushan 2008;

Bhushan 2009), exhibit self-cleaning superhydrophobic and low adhesion characteristics. In nature, rain droplets impact the lotus leaf surface and effectively roll off due to the water repellency. This leads to self-cleaning, where droplets collect and remove any contaminant particles. The lotus effect relies on roughness induced superhydrophobicity and low adhesion, where air pockets are present at the solid-liquid interface. Experiments with lotus effect surfaces show drag reduction in laminar (Ou et al. 2004; Jung and Bhushan 2010; Bhushan and Jung 2011) and turbulent flows (Daniello et al. 2009; Jung and Bhushan 2010; Martell et al. 2010). Additionally, self-cleaning experiments show maximum contaminant removal of 99 % for the lotus leaf replica (Bhushan et al. 2009; Bhushan and Jung 2011).

11.2.2 Aquatic Species—Shark Skin and Fish Scales Effect

In the aquatic environment, shark skin exhibits low drag and antifouling characteristics (Dean and Bhushan 2010; Bixler and Bhushan 2013b, c). Sharks are able to move quickly through water and without fouling due to microstructured riblets covering their skin. Such riblets reduce the friction drag by lifting and presumably pinning naturally occurring turbulent vortices. This minimizes the effect of transverse shear stresses present in turbulent flow. The low drag is also facilitated by the presence of anisotropic channels present in the riblets.

In addition to shark skin, certain fish (for example, rainbow trout) exhibit low drag presumably in order to navigate fast moving streams better (Bixler and Bhushan 2012b). Fish are covered with oriented scales with concentric rings overlapping that promote anisotropic flow from head to tail. Furthermore, scales are hinged, preventing motion in the opposite direction and further facilitating movement (Bixler and Bhushan 2012b). Experiments with shark skin inspired riblet and fish scale samples suggest reduced drag in laminar and turbulent flows (Bechert et al. 1997; Jung and Bhushan 2010; Bixler and Bhushan 2012b, 2013b, c). Shark skin and fish scales are also reportedly oil-repellent at the solid-water-oil interface (Liu et al. 2009; Dean and Bhushan 2010; Liu and Jiang 2011; Bixler and Bhushan 2013c).

11.2.3 Ambient Species—Rice Leaf and Butterfly Wing Effect

Bixler and Bhushan (2012b, 2013a, d, 2014) and Bixler et al. (2014) reported that rice leaves and butterfly wings combine the shark skin (anisotropic flow leading to low drag) and lotus (superhydrophobic and self-cleaning) effects. The combination of anisotropic flow, superhydrophobicity, and low adhesion is reported to reduce drag, exhibit self-cleaning, and facilitate antifouling. It is believed that since rice plants thrive in humid, marshy environments, self-cleaning prevents unwanted

fouling, which may inhibit photosynthesis (Bixler and Bhushan 2012b). Since butterflies are fragile and unable to clean their wings, these properties are critical to maintain structural coloration and flight control (Wagner et al. 1996). Figure 11.1 shows actual rice leaves and butterfly wings that exhibit unique water repellency and anisotropic flow characteristics, where droplets roll down the blade of the rice leaf and axially away from the butterfly body (Bixler and Bhushan 2012b).

Anisotropic and hierarchical structures are found on rice leaves and butterfly wings that provide the anisotropic flow, superhydrophobicity, self-cleaning, and low adhesion properties (Bixler and Bhushan 2012b). The “shark skin effect” anisotropic flow is facilitated by the longitudinal grooves with a transverse sinusoidal pattern in rice leaves and aligned shingle-like scales in butterfly wings. The “lotus effect” superhydrophobicity and low adhesion is facilitated by micropapillae superimposed by self-assembled epicuticular waxy nanobumps in rice leaves (O’Toole et al. 1979; Feng et al. 2002; Sun et al. 2005; Guo and Liu 2007; Liu and Jiang 2011) and shingle-like scales with microgrooves on butterfly wings (for example Blue Morpho didius) (Wagner et al. 1996; Zheng et al. 2007; Goodwyn et al. 2009; Sato et al. 2009; Liu and Jiang 2011; Bixler and Bhushan 2012b).

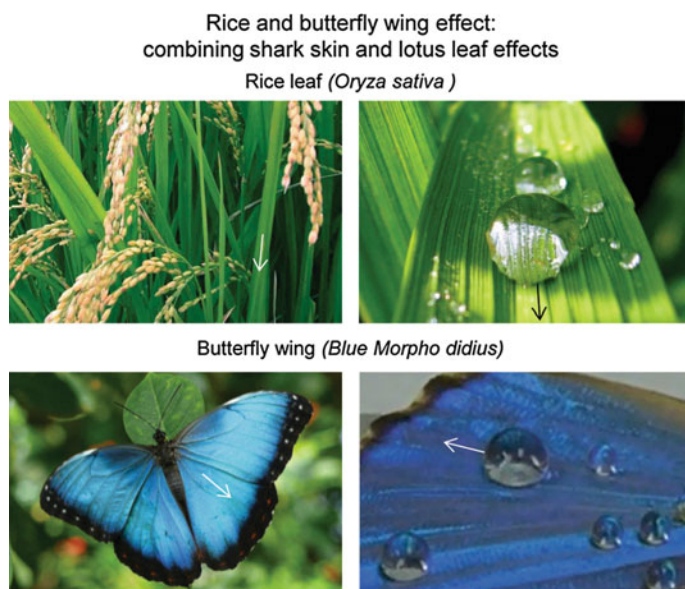


Fig. 11.1 Rice and butterfly wing effect that combines the shark skin and lotus leaf effects (adapted from Bixler and Bhushan 2013d). Shown are water droplets resting atop their superhydrophobic and low adhesion surfaces. Rice leaves contain longitudinal grooves with a transverse sinusoidal pattern and butterfly wings contain aligned shingle-like scales that provide anisotropic flow. Hierarchical structures consisting of micropapillae superimposed by waxy nanobumps in rice leaves and microgrooves on shingle-like scales in butterfly wings provide superhydrophobicity and low adhesion. This combination of anisotropic flow, superhydrophobicity, and low adhesion leads to improved drag reduction and antifouling

Ambient samples were characterized to study relevant mechanisms by Bixler and Bhushan (2012b). Replicas of rice leaves and butterfly wings, and, for comparison, fish scales and shark skin were fabricated for characterization and measurements of fluid drag by Bixler and Bhushan (2012b, 2013a, d). In addition, rice leaf inspired micropatterned replicas and embossed plastic sheets (for scaled-up manufacturing) were fabricated and tested by Bixler and Bhushan (2014). Antifouling data is presented in a separate chapter. Details are presented next on sample fabrications, followed by pressure drop measurements technique, and results and discussion (Bixler and Bhushan 2015).

11.3 Sample Fabrication

11.3.1 Actual Sample Replicas

Urethane replicas from actual samples were created using a two-step soft-lithography molding procedure (Bixler and Bhushan 2012b). Using liquid silicone, negative molds were taken after cleaning the actual samples. In the silicone molds, liquid urethane polymer was applied and cured, yielding precise positive replicas. To incorporate the lotus effect, the rice leaf and shark skin replicas received nanostructured coatings to provide superhydrophobicity; these coatings were superoleophilic. In addition, superoleophobic coatings were applied to test drag in oil flow. Such coatings were shown to exhibit both low drag and self-cleaning properties.

Superhydrophobic (superoleophilic) and superoleophobic coatings were selected for drag experiments. For the nanostructured superhydrophobic (superoleophilic) coating, a solution consisting of 50 nm (± 15 nm) hydrophobized silica nanoparticles combined with methylphenyl silicone resin dissolved in tetrahydrofuran and isopropyl alcohol was utilized (Ebert and Bhushan 2012a, b). For the nanostructured superoleophobic coating, a two-step coating system was selected (Ultra-Ever Dry[®] SE 7.6.110, Glenwood Springs, Colorado). The base and top coats were individually applied with an air spray (Bixler and Bhushan 2012b, 2013a, d). These two reported wear-resistant coatings were chosen to withstand the rigors of fluid drag experiments. As for naming conventions, the uncoated urethane rice leaf sample that received the superhydrophobic nanostructured coating was called the rice leaf replica, since it replicates actual rice leaves. Similarly, the superhydrophobic shark skin sample was the uncoated urethane shark skin sample that received the superhydrophobic nanostructured coating. Furthermore, the samples that received the superoleophobic coating were described as superoleophobic (flat), superoleophobic rice leaf, or superoleophobic shark skin. For a summary of samples and their details, see Table 11.1.

Table 11.1 A list of samples, fabrication procedures, naming conventions, and characterization techniques

Type of sample	Description	Naming convention	Characterization techniques
Actual samples	Butterfly wings, rice leaf		Surface characterization; wettability
Replicas of actual butterfly wings and rice leaf	Urethane replicas created using two-step soft lithography with actual samples	Uncoated replicas	Surface characterization, pressure drop measurements, and wettability
	Coated with superhydrophobic (superoleophilic) or superoleophobic coatings	Superhydrophobic (superoleophilic) or superoleophobic samples	
Rice leaf inspired surfaces	Rice leaf inspired silicon master created using photolithography, PDMS replica created using three-step soft lithography	Rice leaf inspired sample	Surface characterization, pressure drop measurements, and wettability
	Hot embossing used to create embossed PMMA plastic sheets from the silicon master pattern	Rice leaf inspired embossed sample	

11.3.2 Rice Leaf Inspired Surfaces

Rice leaves were used as inspiration due to relatively simple morphology. The so-called rice leaf inspired surfaces were designed and fabricated from silicon master patterns (Bixler and Bhushan 2014). Sample geometrical dimensions are based on actual rice leaf morphology shown in Table 11.2 (Bixler and Bhushan 2012b). Actual rice leaf surfaces are covered by a sinusoidal pattern of micropapillae with height 2–4 μm , diameter 2–4 μm , pitch 5–10 μm , and peak radius 0.5–1 μm (Bixler and Bhushan 2012b). Rice leaf inspired topographies shown in Fig. 11.2 were designed to include anisotropic flow and superhydrophobicity (Bixler and Bhushan 2014). The arrow indicates flow direction for maximum drag reduction and antifouling benefit. Geometrical dimensions are shown in Table 11.3 with pillar height, pillar diameter or rib width, and pitch (Bixler and Bhushan 2014). Samples 1 and 2 represent constant height pillars found in actual rice leaf patterns, whereas dual height features present in Sample 3 create a hierarchical structure designed to facilitate the anisotropic flow similar to the sinusoidal grooves in actual rice leaves. To provide additional anisotropy, Sample 4 consisting of dual height pillars and ribs was fabricated.

A microfabrication photolithographic technique was used to create silicon master patterns (Bhushan 2010). Replicas of Samples 1–4 were fabricated using silicon master patterns and soft-lithography techniques (Bixler and Bhushan 2014).

Table 11.2 Physical characterization of surface structures from actual samples (adapted from Bixler and Bhushan 2012b)

Sample	Actual Description	z-dim (μm)	x-dim/diameter (μm)	y-dim (μm)	x-spacing (μm)	Peak radius (μm)
Rice leaf (<i>Oryza sativa</i>)	Sinusoidal grooves array covered with micropapilla and nanobumps	Grooves	125–150	Full length	150–175	5–10
		Micropapillae	2–4	n/a	5–10	0.5–1
Butterfly wing (<i>Blue Morpho didius</i>)	Shingle-like scales with aligned microgrooves	Scales	30–50	100–125	50–75	n/a
		Microgrooves	1–2	100–125	1–2	0.5–1
Fish scales (<i>Oncorhynchus mykiss</i>)	Overlapping hinged scales with concentric rings	Scales	175–200	n/a	2–2.5 mm dia	n/a
		Rings	5–8	n/a	0.1–2.5 mm dia	1–1.25 mm
Shark skin (<i>Isurus oxyrinchus</i>)	Overlapping dermal denticles with triangular cross sectional riblets	Dermal denticles	75–100	135–150	150–175	1–2
		Riblets	10–15	15–25	30–50	n/a

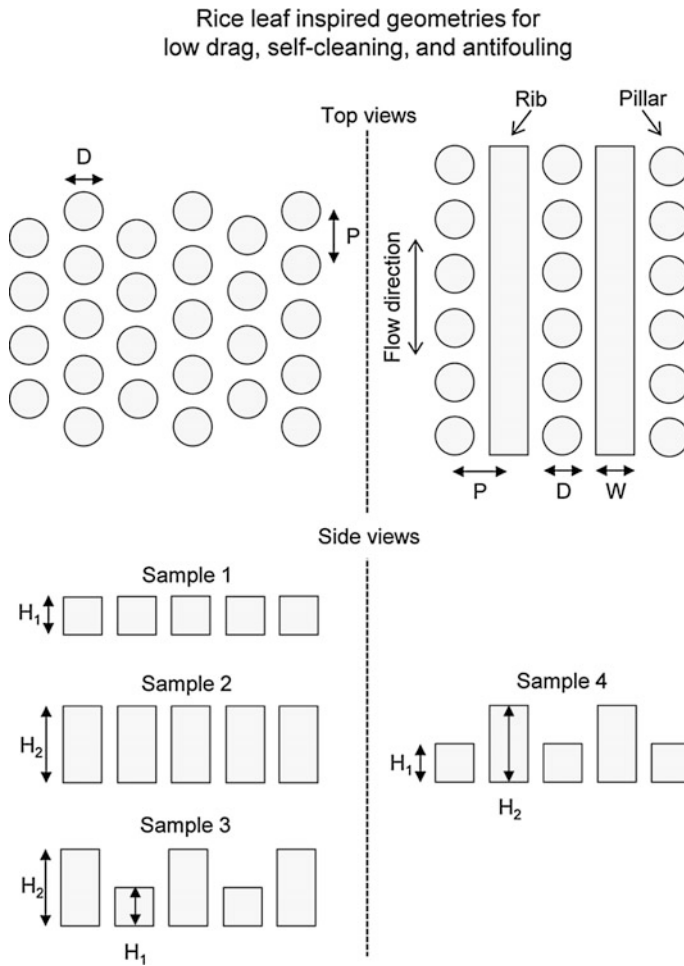


Fig. 11.2 Rice leaf inspired geometries for low drag, self-cleaning, and antifouling (adapted from Bixler and Bhushan 2014). These surfaces are reported to combine anisotropic flow, liquid repellency, and low adhesion characteristics. Pillars in *Samples 1–3* are arranged in a hexagonal array in order to maintain consistent gaps to promote antifouling. Anisotropic flow leading to lower drag is provided by the dual height pillar design of *Sample 3* and the dual height pillars and rib combination of *Sample 4*. *Samples 1 and 2* serve as the baseline samples of two consistent height pillars for comparison

Plastic sheets with micropatterns were produced using a hot embossing technique for scaled-up manufacturing. Silicon master patterns with pits (negative vs. positive features) were fabricated in order to emboss polymer films and to accurately produce master patterns. Embossing protrusions onto polymer films using master patterns is possible when the master pattern contains pits. In addition, pits are less challenging to fabricate as compared to protrusions for the dual height features (Bixler and Bhushan 2014).

Table 11.3 Geometric dimensions of rice leaf inspired samples (Bixler and Bhushan 2014)

	Description	Height (H ₁ or H ₂) (μm)	Pillar diameter (D) or rib width (W) (μm)	Pitch (P) (μm)
Sample 1	Hexagonal array of single height pillars	2	5	7
Sample 2		4		
Sample 3	Alternating rows of dual height pillars	2 and 4		
Sample 4	Alternating rows of single height pillars and ribs	2 (pillars) 4 (ribs)		

11.3.2.1 Micropatterned Replicas

Rice leaf inspired Samples 1–4 were fabricated in polydimethylsiloxane (PDMS) with a three-step soft lithography technique using silicon master patterns, Fig. 11.3 (Bixler and Bhushan 2014). PDMS was chosen due to its low surface energy which leads to high contact angle, which is believed to lower drag and increase antifouling efficiency. However, PDMS bonds well to bare silicon wafers and to itself, so therefore it was necessary to consider de-molding options for the soft lithography procedure. A hydrophilic vinyl polysiloxane dental impression material was selected to create positive master molds from the negative silicon master patterns. The positive master molds in the dental impression material were used to create negative molds in urethane material. Liquid urethane polymer was chosen due to its dimensional stability, ease of casting, ability to de-mold easily from the dental impression material, and ability to de-mold from PDMS. The negative urethane molds were used to create final positive samples in PDMS by pouring liquid PDMS and curing. Final samples were easily de-molded from the urethane negative master molds.

11.3.2.2 Hot Embossed Plastic Sheets

To demonstrate the feasibility of scaled-up manufacturing using rice leaf inspired topographies, Bixler and Bhushan (2014) fabricated embossed plastic sheets using a hot embossing procedure. Such films can be applied to flat or curved substrates, such as oil pipeline interiors, ship hulls, and aircraft bodies. Embossing polymer films were prepared using a commercial hot embossing machine in a clean room environment (Bhushan 2010). Sample 3 was selected to be embossed due to its superior drag and antifouling properties in PDMS. The hot embosser produces single-sided embossed polymer films from silicon master patterns using a combination of heat and pressure. Poly(methyl) methacrylate (PMMA) plastic sheets were selected because PMMA molds relatively easily due to its low softening temperature. These sheets were optically clear and 175 μm in thickness. The sandwich assembly shown in Fig. 11.4 consists of a 10.16 cm round silicon master pattern on

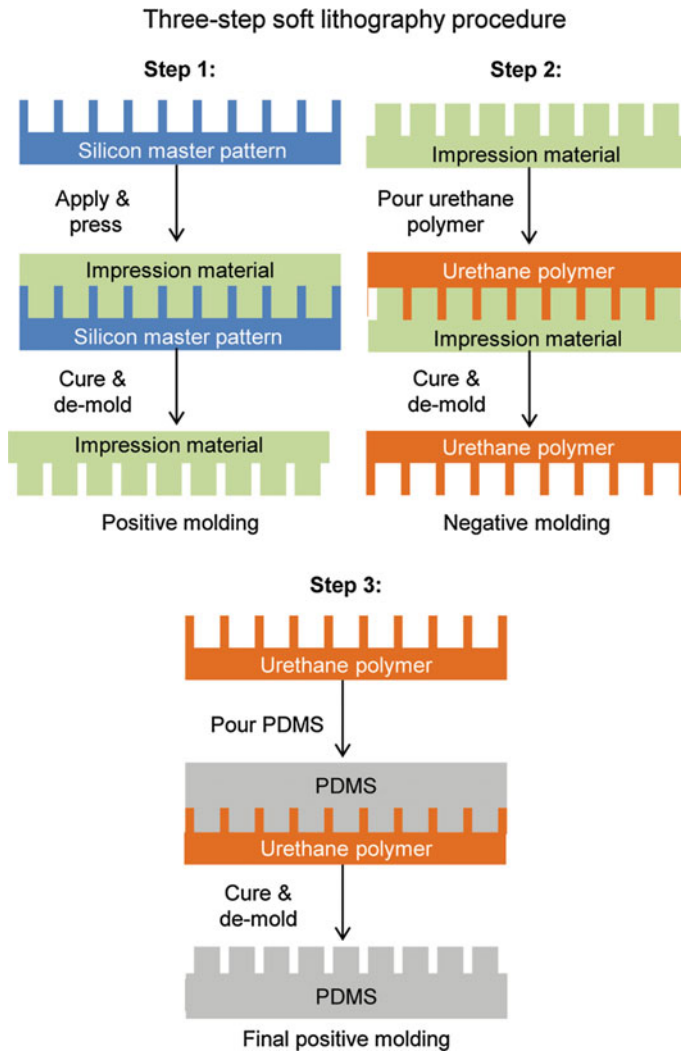
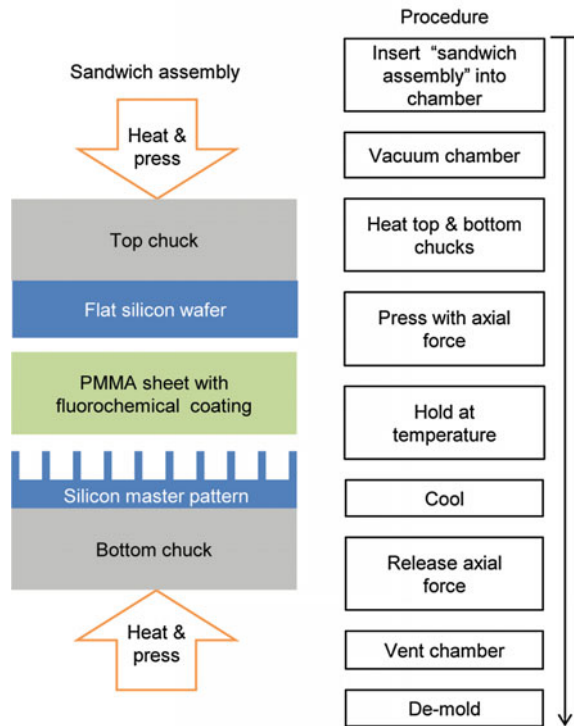


Fig. 11.3 Three-step soft lithography procedure to create samples from the silicon master patterns. The dental impression material was applied to the silicon master patterns to create positive molds (*Step 1*). Next, urethane was poured to create negative molds from the positive dental impression material molds (*Step 2*). Last, PDMS was poured to create final samples from the negative urethane molds (*Step 3*). This procedure was necessary to ensure proper de-molding and sample replication (Bixler and Bhushan 2014)

the bottom, 10.16 cm round PMMA sheet in the middle, and 10.16 cm round flat silicon wafer on the top. The PMMA film required a low surface energy coating on both sides for proper de-molding from the silicon wafers. The aqueous fluorochemical Capstone™ ST-100 was selected and diluted with deionized water.

Fig. 11.4 Hot embossing procedure using silicon master patterns and PMMA sheets (adapted from Bixler and Bhushan 2014). The sandwich assembly consisted of the negative silicon master pattern on the bottom, PMMA sheet in the middle, and flat silicon wafer on the top. The PMMA sheet requires a low surface energy fluorochemical coating for proper de-molding

Hot embossing with silicon master pattern and PMMA sheet

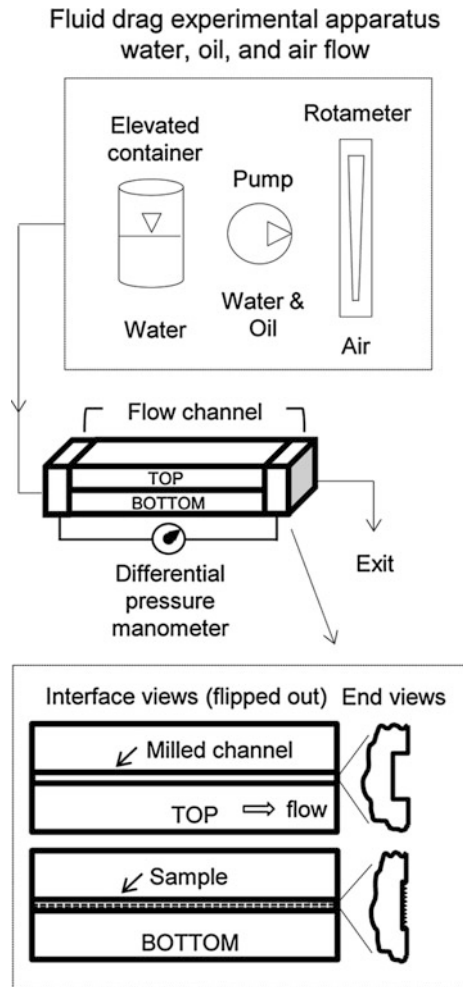


11.4 Pressure Drop Measurement Technique

For the various drag experiments by Bixler and Bhushan (2012b, 2013a, d, 2014) using replica and rice leaf inspired samples, the channel dimensions were based on hospital catheter tubes (3–5 mm diameter). A rectangular channel sandwich design was selected so that samples could be applied to one side and then sandwiched together to create a rectangular closed channel. The top side was a flat milled channel and the bottom side contained the flat PDMS replica sample. In order to measure fluid drag via pressure drop, an experimental apparatus was fabricated according to the schematic in Fig. 11.5 (adapted from Bixler and Bhushan 2013c). Experimental results have been reported for water, oil, and air (Bixler and Bhushan 2012b, 2013a, d, 2014)—using the elevated bottle, gear pump, syringe pump, and rotameter for controlled flow rates. For oil experiments, white paraffin oil was selected due to its low surface tension, chemical compatibility with samples, and low health hazard.

Prediction of pressure drop and comparison to experimental data is of interest to study parametric dependence on the pressure drop. Prediction of pressure drop of a rectangular closed channel requires use of the incompressible flow equations for

Fig. 11.5 Apparatus to measure drag via pressure drop in closed channel flow using water, oil, and air (adapted from Bixler and Bhushan 2013c). The split rectangular channel design allows for samples to be fabricated inside the channel. Interface views are shown highlighting the top and bottom halves that are sandwiched together. Flow is regulated with the elevated container (water), pumps (water or oil), and laboratory air connected to a rotameter (air). The pressure drop is measured with a manometer connected to both ends of the flow channel



straight uniform pipes. Since the Mach number is less than 0.3 for all experiments, incompressible flow equations may be used (Blevins 1984). The predicted pressure drop was calculated using the total channel cross-sectional area by Bixler and Bhushan (2012b, 2013d).

Pressure drop (Δp) between two points in a hydrophilic pipe with incompressible and fully developed flow is given by the Darcy formula (Blevins 1984; Munson et al. 2012; Pritchard et al. 2015):

$$\Delta p = \frac{\rho V^2 f L}{2D} \tag{11.1}$$

where ρ is the fluid density, V is the flow velocity, f is the Darcy-Weisenbach friction factor, L is the length between two points on a pipe, and D is the hydraulic diameter.

The friction factor is a function of the Reynolds number, Re , and relative roughness, ε/D . ε is the measure of roughness in length units. The equivalent surface roughness ε is defined as the characteristic height of sand grains that, when glued as closely together as possible on the inside of a pipe, produce the same pressure loss per unit pipe span as a test pipe of the same diameter transporting the same flow.

The Reynolds number is given by:

$$Re = \frac{VD}{\nu} \quad (11.2a)$$

where ν is the kinematic viscosity of the fluid. It is expressed also as dynamic viscosity (μ):

$$\nu = \frac{\mu}{\rho} \quad (11.2b)$$

The hydraulic diameter of a circular pipe is the diameter of the pipe. For a noncircular duct or channel, to establish an equivalent pipe diameter, the hydraulic diameter is proportional to the flow area divided by the perimeter of the surface containing the flow:

$$D = \frac{4(\text{flow area of cross section})}{\text{wetting perimeter of the cross section}} \quad (11.2c)$$

As a general rule for pipe flow, the value of Re should be less than approximately 2100 for laminar flow and greater than approximately 4000 for turbulent flow. For completeness, flow along a plate, the transition between laminar and turbulent flow, occurs at Re of approximately 500,000.

The Darcy friction factor for laminar flow in a circular pipe:

$$f = \frac{k}{Re}, \quad k = 64 \quad (11.3)$$

and it is independent of relative roughness. For a rectangular closed channel flow, a modified expression is given as (Blevins 1984),

$$k = 64 \left/ \left[\frac{2}{3} + \frac{11b}{24a} \left(2 - \frac{b}{a} \right) \right] \right. \quad \text{with } \frac{b}{a} \leq 1 \quad (11.4a)$$

Table 11.4 Fluid properties of interest (Haynes 2014)

Fluid	Density (ρ) (kg/m ³)	Kinematic viscosity (ν) (m ² /s)
Water	1000	1.034×10^{-6}
Oil	880	2.2×10^{-5}
Air	1.2	1.51×10^{-5}

and hydraulic diameter is:

$$D = \frac{2ab}{a+b} \quad (11.4b)$$

where a is the width and b is the height.

For turbulent flow, the functional dependence of the friction factor on Re and relative roughness values can only be obtained from experimental data. A Moody chart provides a plot of the Darcy friction factor as a function of the Reynolds number for the various relative roughness values for fully developed circular pipe flow (Munson et al. 2012). Various empirical relationships for the friction factor are commonly used. An approximate explicit equation for f is given by Blevins (1984):

$$f = \left[1.14 - 2 \log_{10} \left(\frac{\varepsilon}{D} + \frac{21.25}{Re^{0.9}} \right) \right]^{-2} \quad (11.5)$$

For turbulent flow in a noncircular (e.g., rectangular) duct or channel, the simplest and most general approximate method is to compute the hydraulic diameter (11.2c) for the channel of interest and use equations for a circular pipe using this hydraulic diameter in the computation of Re, relative roughness, f , and pressure drop.

Equations (11.1), (11.2a, 11.2b, 11.2c), (11.4a, 11.4b), and (11.5) were used to predict the pressure drop for the rectangular closed channels, for experiments with water, oil, and air. The channel dimensions were: $b = 1.5$ mm, $a = 3.3$ mm, $b/a = 0.45$, and $L = 102$ mm (Bixler and Bhushan 2012b, 2013a, d, 2014). Flow velocity (V) was determined by dividing the volumetric flow rate by the channel cross sectional area. In air experiments, the rotameter values were used with manufacturer provided charts to determine the flow velocity. Fluid properties of interest are presented in Table 11.4. In order to account for milled channel roughness, a roughness value ε of 0.0025 mm was used to calculate f in turbulent flow.

11.5 Results and Discussion

Surface characterization and drag data on actual, replica, and rice leaf inspired samples are presented based on Bixler and Bhushan (2012b, 2013a, d, 2014).

11.5.1 Surface Characterization

Bixler and Bhushan (2012b, 2014) examined actual, replica, and rice leaf inspired samples. Scanning electron microscope (SEM) and optical profiler images are presented for a qualitative and quantitative comparison and understanding of the relevant mechanisms. The SEM provides high resolution in the x-y direction, whereas optical profiler provides high resolution height map information in the z direction (Bixler and Bhushan 2012b).

Figure 11.6 shows the optical, SEM, and optical profiler images of an actual rice leaf, butterfly wing, fish scale, and shark skin (Bixler and Bhushan 2012b). Cylindrically tapered micropapillae on rice leaves and microgrooves on butterfly wing scales are observed (Bixler and Bhushan 2012b). Fish skin is covered by oriented scales with concentric rings overlapping and hinged such that water flow is from head to tail. Shark skin is covered by diamond-shaped dermal denticles overlapping and hinged such that the riblets are aligned in the water flow direction from head to tail (Bixler and Bhushan 2012b). A summary of the various features of interest from each sample are reported in Table 11.2.

Figure 11.7a shows SEM images of the replica samples. Figure 11.7b shows the flat, rice leaf, and shark skin samples that received the superhydrophobic and superoleophobic nanostructured coatings. As expected the rice leaf micropapillae hierarchical structure detail was not reproduced in the replica. Furthermore, the coatings increase surface nanoroughness as compared to the uncoated replicas (Bixler and Bhushan 2012b, 2013d).

Bixler and Bhushan (2012b) used optical profiler height map images to calculate the values of R_f and f_{LA} used to calculate the contact angle (CA) of samples using the Wenzel and Cassie-Baxter equations. R_f and f_{LA} values (methodology used to estimate presented in Chap. 6), along with predicted and measured CA values, are shown in Table 11.5. Data suggests that the measured and predicted values correlate with the Cassie-Baxter regime for rice leaf and butterfly wing replicas; and Wenzel regime for fish scales and shark skin. This is consistent with what is present in living nature, since rice leaves and butterfly wings are found in the ambient environment (with air pockets), whereas fish scales and shark skin are found in the aquatic environment (no air pockets) (Bixler and Bhushan 2012b).

Figure 11.8 shows SEM images of the surface structures of rice leaf inspired samples (Bixler and Bhushan 2014). Dual-height pillars are evident in images of Sample 3 along with the dual height pillars/ribs of Sample 4. Each of the sample features appears smooth and with minimal defects from the soft-lithographic process. Images of Embossed sample 3 show features have similar characteristics as with the PDMS molded Sample 3. The features appear to have been accurately reproduced for each sample with geometric dimensions as indicated in Table 11.3.

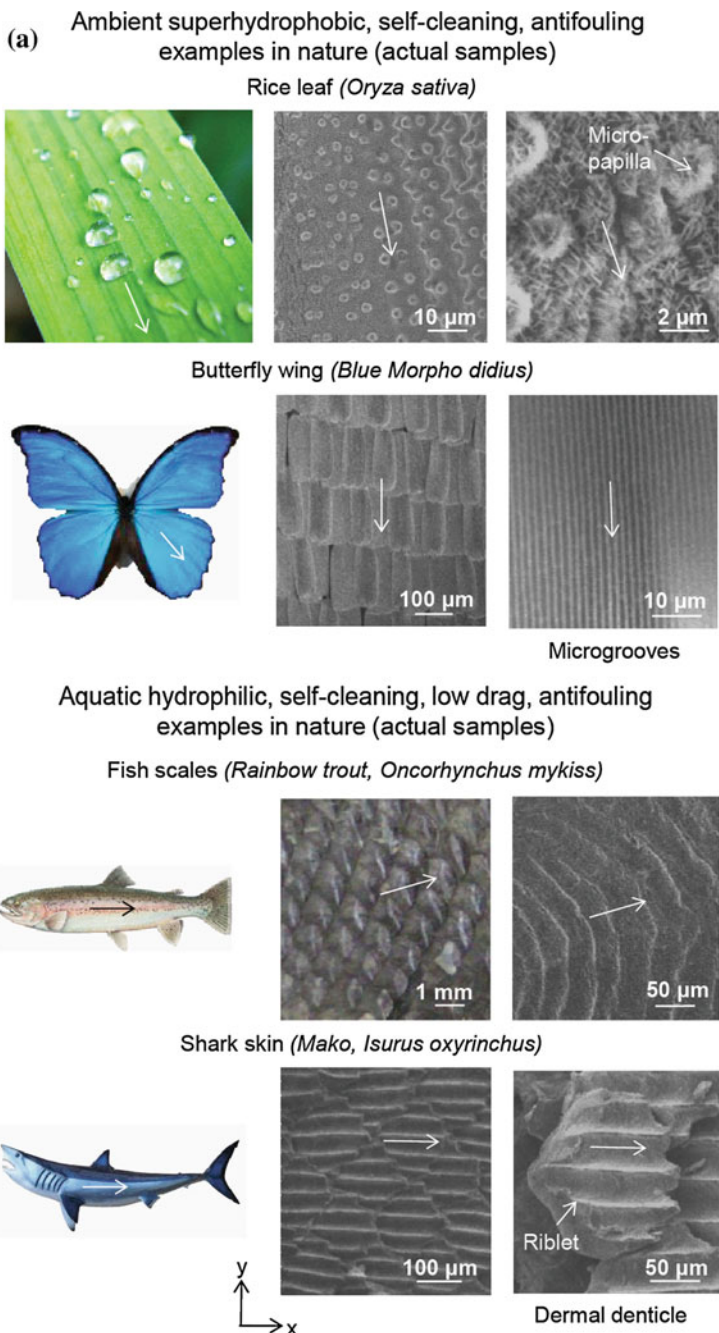


Fig. 11.6 Montage of **a** optical images and SEM images at two magnifications and **b** optical profiler images depicting actual rice leaf, butterfly wing, fish scale, and shark skin morphologies (adapted from Bixler and Bhushan 2012b). Arrows indicate the tendencies of fluid flow in transverse and longitudinal directions

(b) Ambient superhydrophobic, self-cleaning, antifouling examples in nature (actual samples)

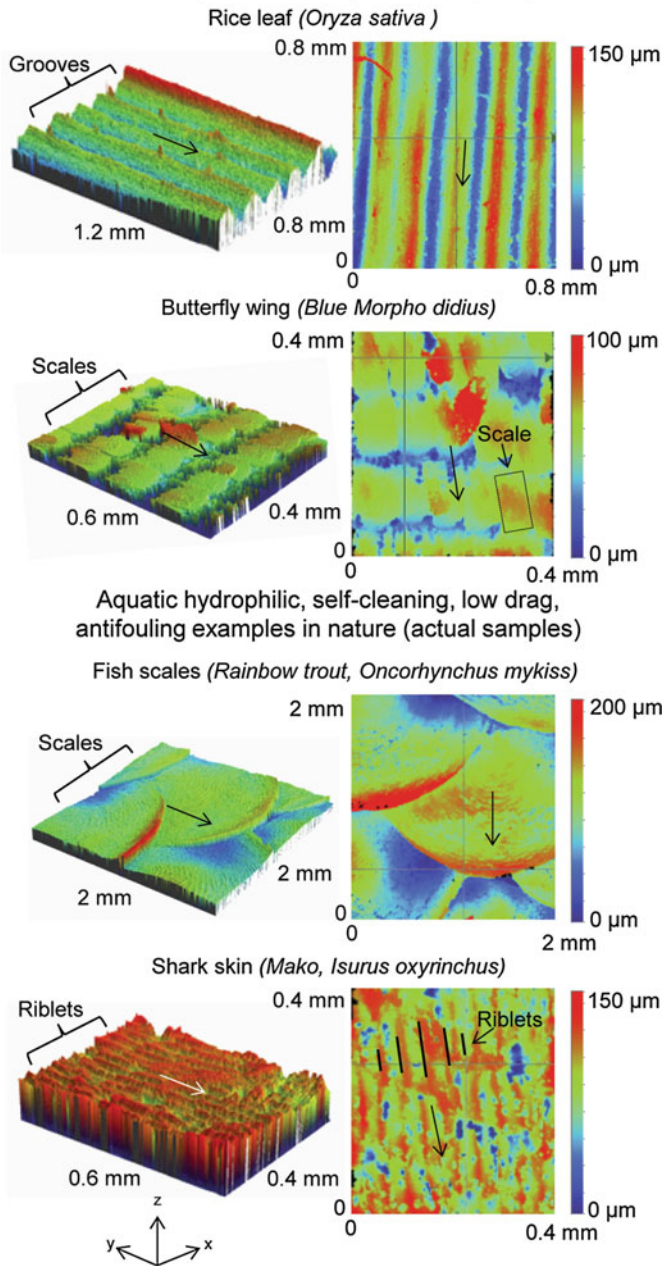
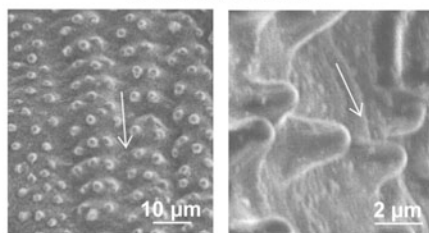


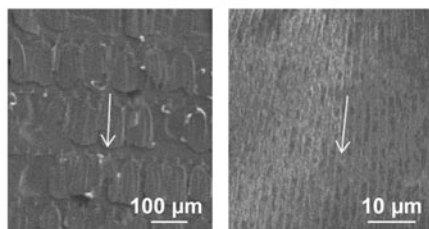
Fig. 11.6 (continued)

(a) SEM images of ambient and aquatic replica samples

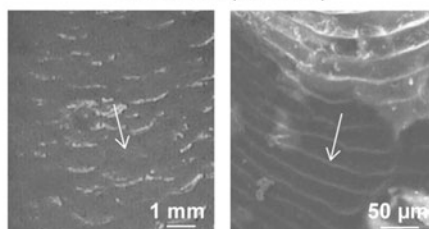
Rice leaf (urethane)



Butterfly wing (urethane)



Fish scales (urethane)



Shark skin (urethane)

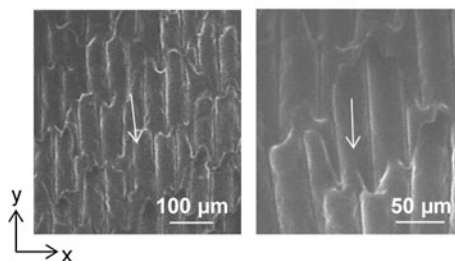


Fig. 11.7 Montage of **a** SEM images depicting rice leaf, butterfly wing, fish scale, and shark skin replica surfaces, as well as **b** flat, rice leaf, and shark skin replicas coated in superhydrophobic and superoleophobic solutions (adapted from Bixler and Bhushan 2012b, 2013d). *Arrows* indicate direction of anisotropic water droplet movement

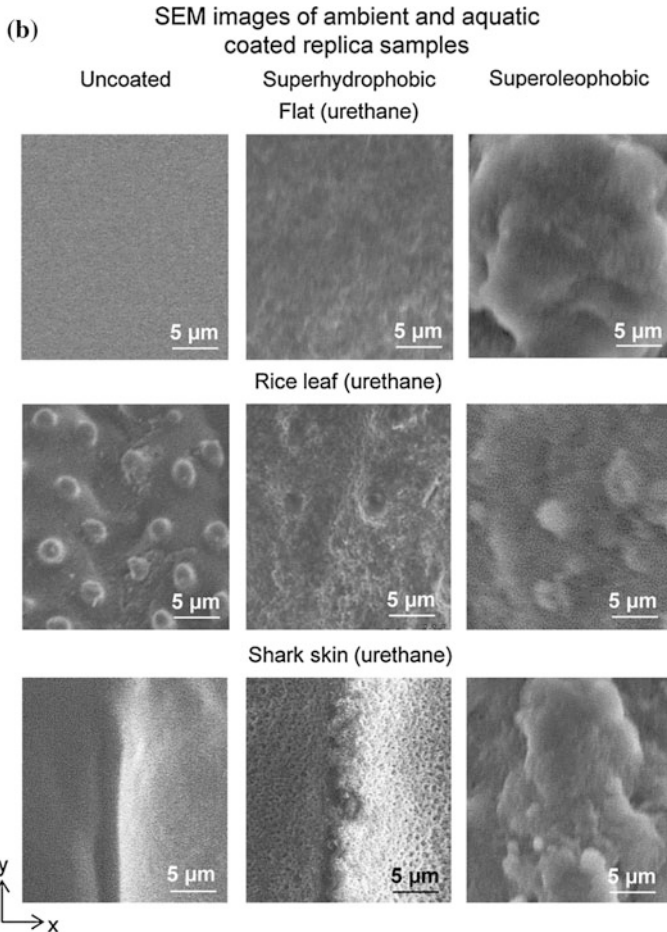


Fig. 11.7 (continued)

11.5.2 Pressure Drop Measurements

Pressure drop measurements are reported for replicas by Bixler and Bhushan (2012b, 2013a, d) and for rice leaf inspired samples by Bixler and Bhushan (2014) using water, oil, and air flow. For comparison to the flat surfaces, and as appropriate for each fluid, figures described below show data for flat channel predicted (using 11.1) and flat channel used in the split rectangular channel (milled or flat PDMS) lines. In order to account for milled channel surface roughness, friction factor values estimated from the Moody chart were selected based on the roughness value of $\varepsilon = 0.0025$ mm. Trend lines were connected through the origin in each plot.

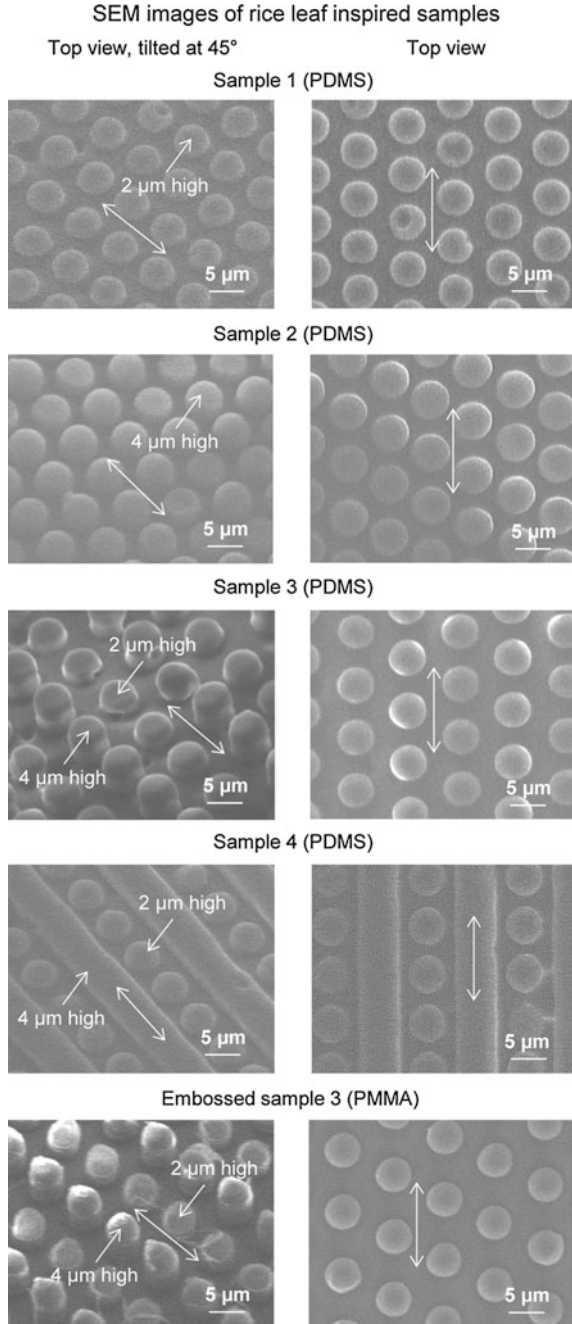
Table 11.5 Replica sample CA predictions (Bixler and Bhushan 2012b)

Sample	Actual			Replica			
	Roughness factor (R_t)	Fractional liquid-air contact area (f_{LA})	Measured CA	CA calculated using Wenzel equation	CA calculated using Cassie-Baxter equation	Measured CA (uncoated)	Measured CA (coated)
Rice leaf (<i>Oryza sativa</i>)	3.33	0.85	164 ^b	59	141 ^b	118	155 ^a
Butterfly wing (<i>Blue Morpho didius</i>)	4.41	0.93	161 ^b	48	152 ^b	84	n/a
Fish scales (<i>Oncorhynchus mykiss</i>)	1.61	0.33	58 ^a	76 ^a	99	94 ^a	n/a
Shark skin (<i>Isurus oxyrinchus</i>)	2.14	0.44	n/a	71 ^a	105	98 ^a	158

^aIndicates Wenzel regime

^bIndicates Cassie-Baxter regime

Fig. 11.8 Montage of SEM images for Samples 1–4 and Embossed sample 3 (adapted from Bixler and Bhushan 2014). Shown are images of Samples 1 and 2 with uniform height pillars arranged in the hexagonal array as well as Sample 3 with dual height pillars and Sample 4 with pillars and ribs. *Arrows* indicate direction of fluid movement for drag and self-cleaning experiments



11.5.2.1 Water Flow

Bixler and Bhushan (2013d, 2014) presented water flow data comparing the replicas, coated samples, and rice leaf inspired samples. Results are shown for experiments with low velocity laminar flow ($0 < Re < 200$) and high velocity turbulent flow ($4000 < Re < 12,500$). Calculations use the values for mass density (ρ) equaling 1000 kg m^{-3} and kinematic viscosity (ν) equaling $1.034 \times 10^{-6} \text{ m}^2 \text{ s}^{-1}$ (Haynes 2014). Samples that received the superhydrophobic and low adhesion nanostructured coating were selected based on their initial drag performance. In general, a higher pressure drop reduction is reported for the higher flow velocity conditions, where turbulent vortices are believed to be present.

Figure 11.9 shows pressure drop measurements for replica, flat, and coated samples (Bixler and Bhushan 2013d). When considering error bars, the rice leaf and butterfly wing sample pressure drops appear similar in both laminar and turbulent flow. The fish scale and shark skin sample pressure drops appear similar in laminar flow but differ in turbulent flow, with shark skin superior. In laminar water flow, the maximum pressure drop reduction of 26 % is shown with the superhydrophobic flat sample (Bixler and Bhushan 2012b). In turbulent water flow, maximum pressure drop reduction is shown with rice leaf replica and superhydrophobic shark skin at 26 and 29 %; and uncoated at 17 and 19 %, respectively (Bixler and Bhushan 2012b). The rice leaf replica benefits from anisotropic flow and low adhesion, which leads to lower drag. In addition, the superhydrophobic shark skin replica benefits from the shark skin effect combined with low adhesion, which also leads to lower drag.

Figure 11.10 shows pressure drop measurements reported for rice leaf inspired and flat samples (Bixler and Bhushan 2014). Results from the turbulent conditions indicate that Samples 1 and 2 increase the drag, and Samples 3 and 4 reduce the drag, which is believed due to anisotropic flow characteristics. In laminar flow, Sample 3 provides the greatest pressure drop reduction at 15 % (Bixler and Bhushan 2014) while in turbulent flow Embossed sample 3 provides the greatest pressure drop reduction at 23 % (Bixler and Bhushan 2012b). Sample 2 shows the greatest pressure drop increase at 13 %, presumably due to the taller pillars impeding the fluid flow and vortices translating on the pillars. Furthermore in turbulent flow, Embossed sample 3 yields more pressure drop reduction than Sample 3, with values of 23 and 12 %, respectively (Bixler and Bhushan 2014).

11.5.2.2 Oil Flow

Bixler and Bhushan (2013d, 2014) presented oil flow data comparing the replicas, coated samples, and rice leaf inspired samples. Results are shown from experiments with low velocity laminar flow ($0 < Re < 10$) and high velocity laminar flow ($0 < Re < 500$). To investigate the role of superoleophobicity on rice leaf and shark skin replicas in oil flow, a superoleophobic coating was applied in addition to a superhydrophobic (superoleophilic) coating. Calculations use the values for mass

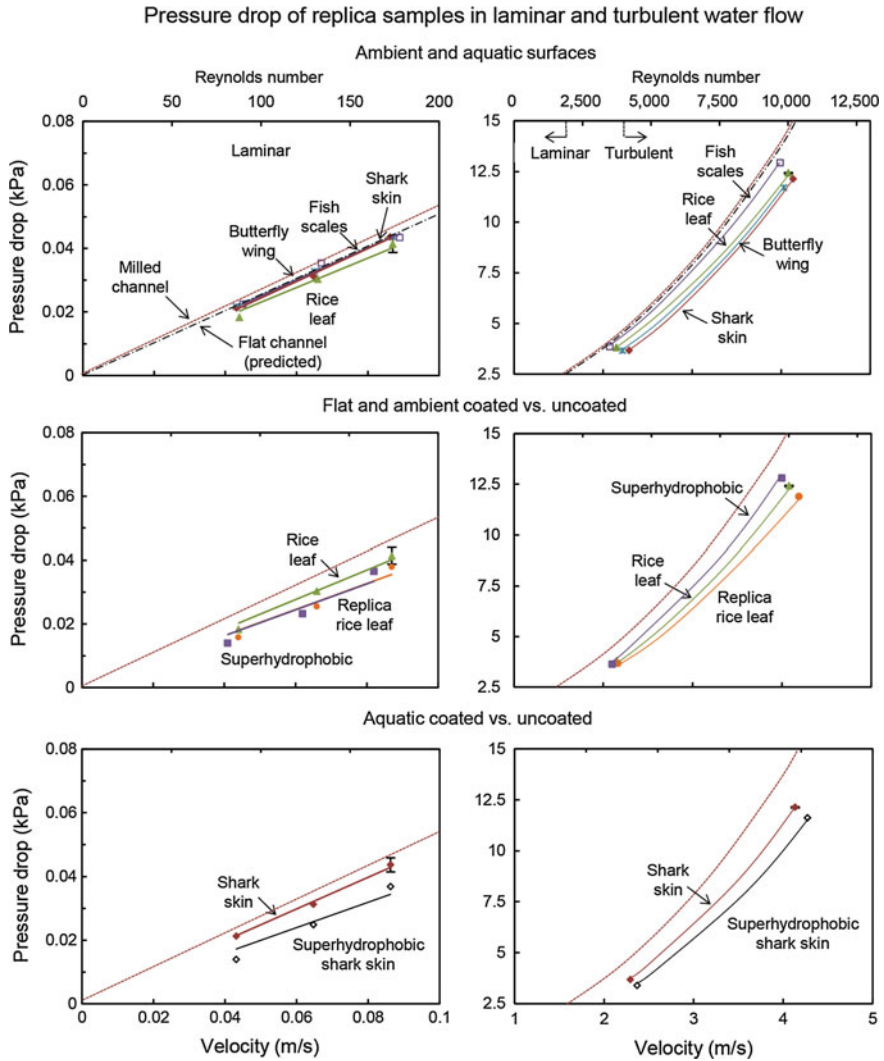


Fig. 11.9 Water pressure drop with replica samples in laminar and turbulent flows (adapted from Bixler and Bhushan 2013d). Shown are the milled channel and flat channel predicted lines as well as results for replicas of rice leaf, butterfly wing, fish scale, and shark skin surfaces, both with and without nanostructured coatings. Higher pressure drop translates into higher drag; therefore lower pressure drop is desirable. Error bars show ± 1 standard deviation, which is hardly visible in the plots

density (ρ) equaling 880 kg m^{-3} and kinematic viscosity (ν) estimated at $2.2 \times 10^{-5} \text{ m}^2 \text{ s}^{-1}$ (Haynes 2014).

Figure 11.11 shows pressure drop measurements for replica, flat, and coated samples (adapted from Bixler and Bhushan 2013d). The superoleophilic and

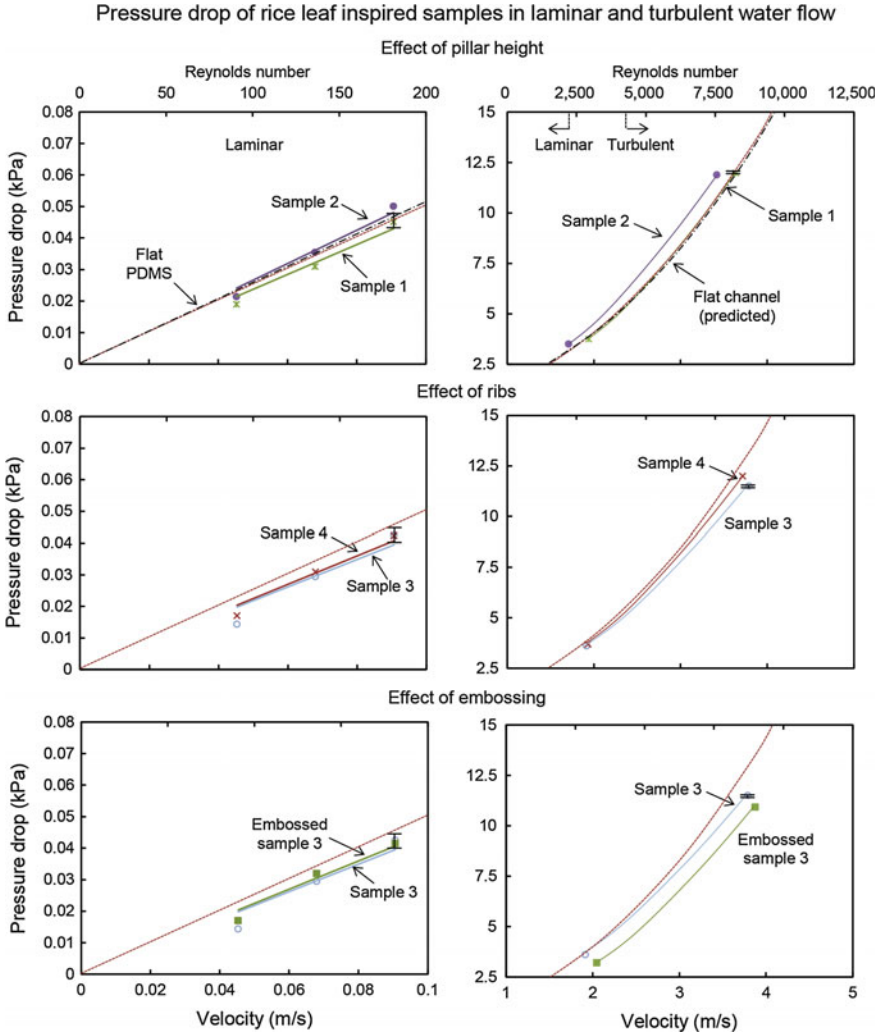


Fig. 11.10 Water pressure drop with rice leaf inspired samples in laminar and turbulent flows (adapted from Bixler and Bhushan 2014). Shown are the flat PDMS and flat channel predicted lines as well as results for Samples 1–4 and Embossed sample 3. Higher pressure drop translates into higher drag; therefore lower pressure drop is desirable. Error bars show ± 1 standard deviation, which is hardly visible in the plots

superoleophobic flat samples at high velocity show drag increases, which is presumably due to the lack of anisotropic flow control and increased surface roughness. Pressure drop reduction is detected at the high velocities for the rice leaf and butterfly wing samples. At the low and high velocities, the superoleophobic rice leaf and shark skin samples reduce drag, due to anisotropic flow and low adhesion. In addition, the superhydrophobic (superoleophilic) rice leaf replica also provides drag

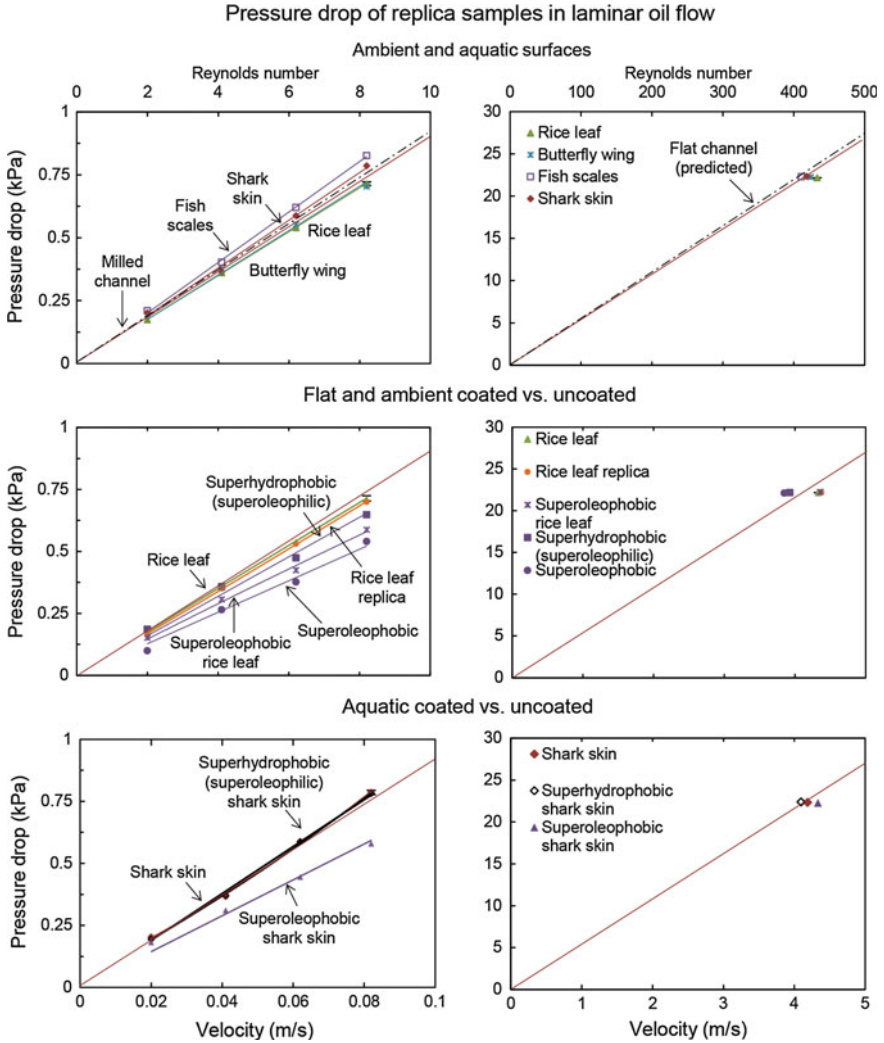


Fig. 11.11 Oil pressure drop with replica samples in laminar flow (adapted from Bixler and Bhushan 2013d). Shown are the *milled channel* and *flat channel* predicted lines. Samples include the flat control and replicas of rice leaf, butterfly wing, fish scale, and shark skin surfaces, both with and without the nanostructured superhydrophobic (superoleophilic) and superoleophobic coatings. Higher pressure drop translates into higher drag; therefore lower pressure drop is desirable. *Error bars* show ± 1 standard deviation, which is hardly visible in the plots

reduction due to the so-called thin film effect, to be described later (Bixler and Bhushan 2013a). In high velocity, maximum pressure drop reduction is shown with superhydrophobic (superoleophilic) and superoleophobic coated rice leaf and the uncoated butterfly wing replicas at 10 and 6 %, respectively (Bixler and Bhushan 2013a).

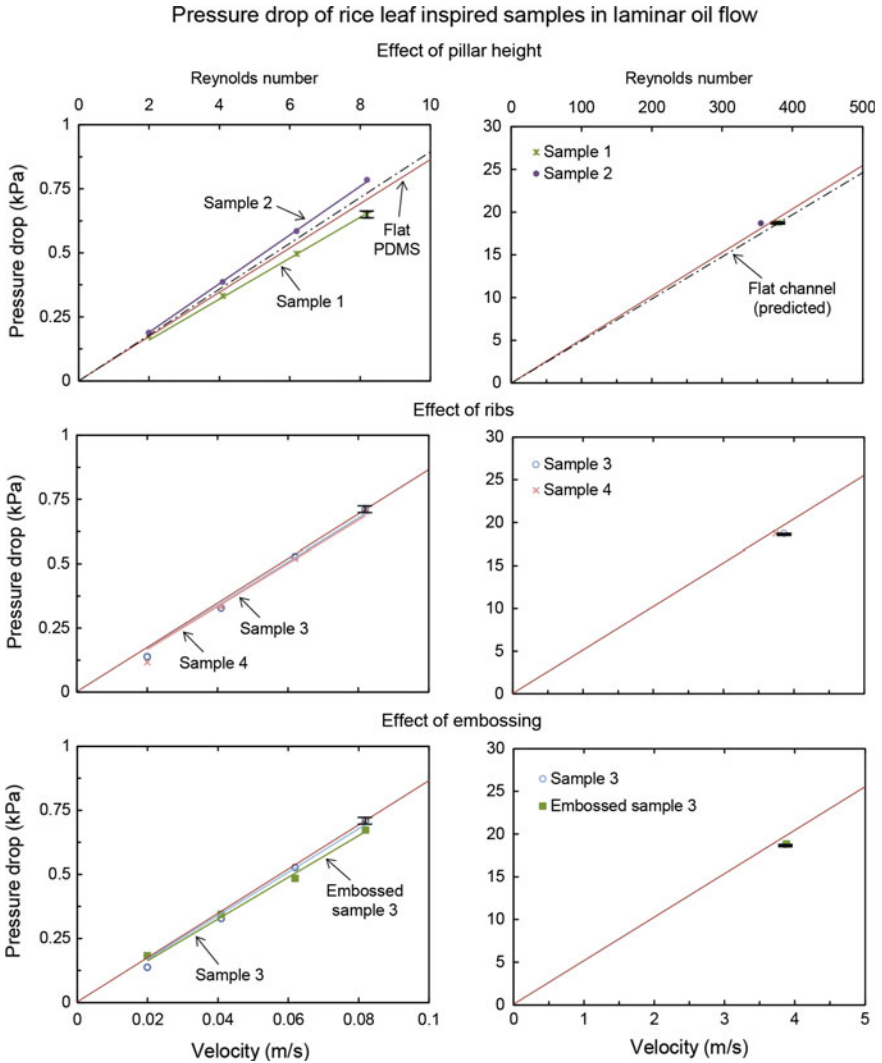


Fig. 11.12 Oil pressure drop with rice leaf inspired samples in laminar flow (adapted from Bixler and Bhushan 2014). Shown are the flat PDMS and flat channel predicted lines as well as results for Samples 1–4 and Embossed sample 3. Higher pressure drop translates into higher drag; therefore lower pressure drop is desirable. *Error bars* show ± 1 standard deviation, which is hardly visible in the plots

Figure 11.12 shows pressure drop measurements reported for rice leaf inspired and flat samples (adapted from Bixler and Bhushan 2014). A pressure drop difference is observed at high velocities when examining the effect of ribs and embossing for Samples 3 and 4. Furthermore, Samples 1, 3, 4, and Embossed sample 3 show drag reduction reportedly due to anisotropic flow (all but Sample 1)

and the thin film effect. Embossed sample 3 provides the greatest drag reduction in low and high velocity laminar flow, at 5 and 6 % pressure drop reduction, respectively. Sample 2 shows the greatest pressure drop increase at 11 %, presumably due to the taller pillars impeding the fluid flow. The so-called thin film effect (to be described later) is believed to be present in all samples except Sample 2 (Bixler and Bhushan 2014).

11.5.2.3 Air Flow

Figure 11.13 shows air flow results comparing the replicas, flat, coated samples, and rice leaf inspired samples (Bixler and Bhushan 2013d, 2014). With air, the achievable velocity range was higher as compared to the water or oil, and the higher Reynolds numbers show continued pressure drop reduction (until expected plateauing). Results are shown from experiments with laminar through high velocity turbulent air flow ($0 < Re < 5500$). Calculations use the values for mass density (ρ) equaling 1.2 kg m^{-3} and kinematic viscosity (ν) equaling $1.51 \times 10^{-5} \text{ m}^2 \text{ s}^{-1}$ (Haynes 2014).

When comparing fish scales and shark skin replicas, a smaller difference is observed in air versus water. The superhydrophobic coated rice and shark skin replicas show an improved pressure drop reduction compared to the uncoated, but this is independent of the superhydrophobicity. When comparing the best performing samples in turbulent flow, in water the superhydrophobic shark skin sample reduces pressure by 29 % ($Re = 10,000$) and in air reduces pressure by 27 % ($Re = 4200$) (Bixler and Bhushan 2012b). It is believed that the coated shark skin benefits from the shark skin effect combined with reduced surface roughness between riblets, which leads to lower drag (Bixler and Bhushan 2013c, d).

Furthermore, Samples 3 and 4, and Embossed sample 3 show pressure drop reduction, which is believed due to anisotropic flow and vortices pinned (Bixler and Bhushan 2014). Embossed sample 3 provides the greatest drag reduction in laminar and turbulent flow, at 10 and 12 % pressure drop reduction, respectively. Sample 2 shows the greatest pressure drop increase at 7 %, presumably due to the taller pillars impeding the fluid flow and vortices translating on the pillars (Bixler and Bhushan 2014).

11.5.2.4 Nondimensional Pressure Drop Model

To incorporate viscosity and density of various fluids, it is of importance to develop a nondimensional pressure drop parameter as a function of flow velocity (Re). This parameter can then be used to predict pressure drop for a variety of fluids and flow conditions.

A nondimensional pressure drop expression is developed to estimate pressure drop for various fluid flow conditions and pipe/channel dimensions (adapted from Bixler and Bhushan 2013d). The nondimensional pressure expression consists of

Pressure drop of replica and rice leaf inspired samples in laminar and turbulent air flow

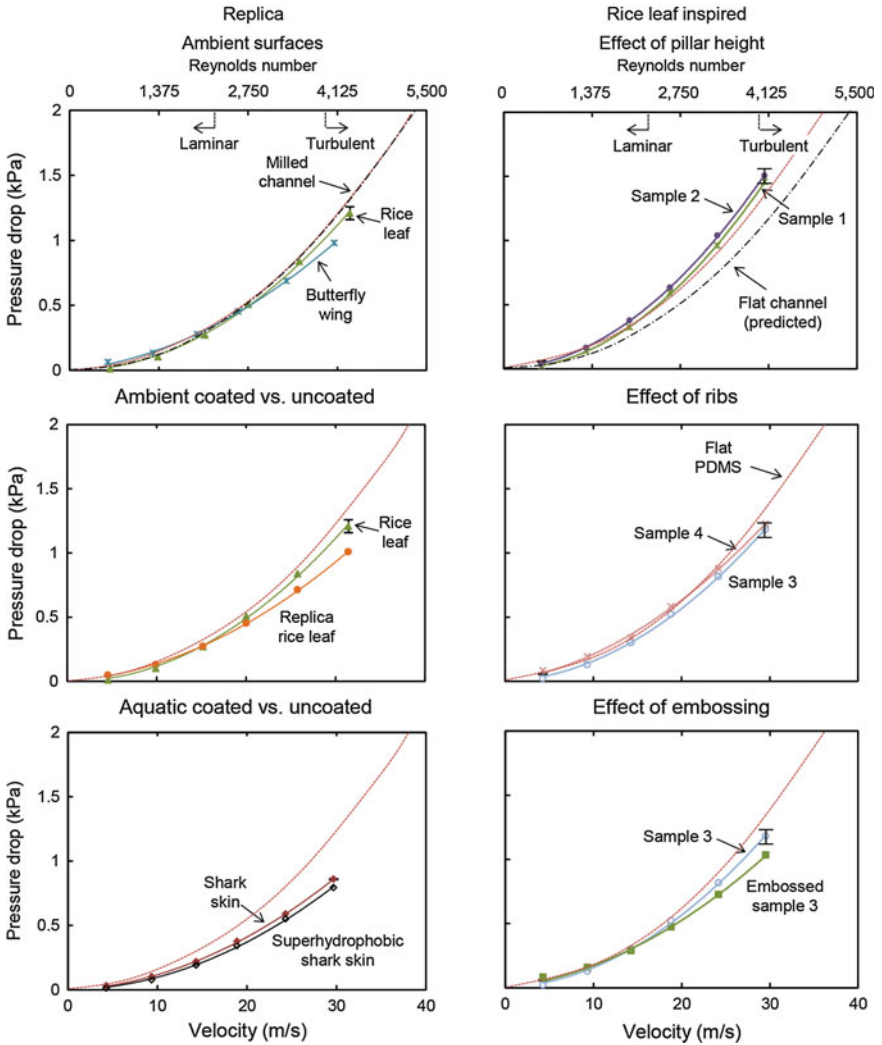


Fig. 11.13 Air pressure drop with replica and rice leaf inspired samples in laminar and turbulent flow (adapted from Bixler and Bhushan 2013d, 2014). Shown are the milled channel, flat PDMS, and flat channel predicted lines. Results are presented for replicas of rice leaf, butterfly wing, fish scale, and shark skin surfaces, both with and without the nanostructured coating, Samples 1–4, and Embossed sample 3. Higher pressure drop translates into higher drag; therefore lower pressure drop is desirable. *Error bars* show ± 1 standard deviation

two nondimensional terms. The first term, G , combines various fluid properties and pipe/channel dimensions. The second term, fRe , combines flow velocity and the friction factor, which is dependent upon the Reynolds number (flow velocity). From (11.1) to (11.5), the nondimensional pressure drop expression is given as:

$$\overline{\Delta p} = \frac{\Delta p}{G} = (fRe)Re \tag{11.6}$$

where

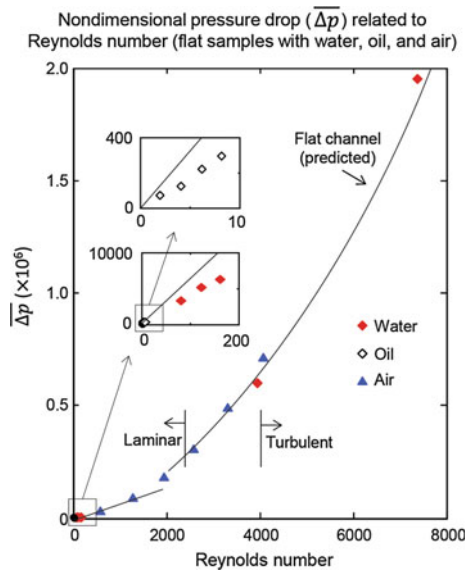
$$G = \frac{\rho L v^2}{2D^3}$$

$\overline{\Delta p}$ is equal to 64 Re for laminar flow and it needs to be calculated using Moody’s chart or (11.5) for turbulent flow.

The nondimensional pressure drop versus Reynolds numbers for a flat milled channel in water, oil, and air experiments were calculated from measured values (adapted from Bixler and Bhushan 2013d). These fluids represent a wide range of densities and viscosities found in medical, marine, and industrial applications. As stated earlier, in order to account for milled channel surface roughness, friction factor values were calculated using (11.5), based on the roughness value of $\epsilon = 0.0025$ mm.

The data for a flat milled channel in water, oil, and air experiments are shown in Fig. 11.14 (Bixler and Bhushan 2013d). The nondimensional pressure drop values for oil and air follow similar calculated linear trend lines based on water flow, with a slope change between laminar and turbulent flow. With this equation, pressure drop can be calculated for a flat surface with given fluid properties, flow conditions, and channel dimensions.

Fig. 11.14 Nondimensional pressure drop parameter related to Reynolds number. Presented are results from water, oil, and air experiments for a flat sample. This provides channel pressure drop estimations based on fluid properties, flow conditions, and channel dimensions



11.5.3 Wettability

To understand the role of CA and contact angle hysteresis (CAH) on drag, Bixler and Bhushan (2012b, 2013d, 2014) measured contact angles with actual, replica, flat control, and rice leaf inspired samples. For actual samples with water droplets in air, actual rice leaf and butterfly wing samples exhibited superhydrophobic characteristics due to Cassie-Baxter wetting. Conversely, the fish scales and shark skin showed lower contact angles, presumably due to the Wenzel wetting, see water droplet images in Fig. 11.15a (Bixler and Bhushan 2012b). With oil droplets in air, each of the actual samples exhibited superoleophilicity (Bixler and Bhushan 2013a). With oil droplets underwater, actual rice leaf and butterfly wing samples exhibited superoleophilicity; however, fish scale and shark skin samples exhibited superoleophobicity, see water droplet images in Fig. 11.15b (Bixler and Bhushan 2013d). Conceptual mechanisms of oil droplets are also shown in the figure. It is reported that the rice leaf hierarchical morphology leads to the low contact angle, and that oil penetrates into the butterfly wing open lattice microstructure. With fish scales, it is reported that a thin water layer forms between the oil droplet and the impenetrable scale surface to encourage superoleophobicity. With shark skin, water soaks into the skin and combined with the impenetrable dermal denticle microstructures produces superoleophobicity (Bixler and Bhushan 2012b, 2013a).

Figure 11.15c shows the images and contact angles of water droplets in air and oil droplets in air and under water of replica and coated samples (Bixler and Bhushan 2012b, 2013a, d). With water in air, uncoated replicas are hydrophobic, except that of butterfly wing replicas. Superhydrophobic coatings make the replicas of the rice leaf and shark skin superhydrophobic. With oil droplets in air and with a superoleophobic coating, the rice leaf becomes superoleophobic. With oil droplets underwater, oleophobic behavior is observed, except in the case of the replica of the butterfly wing.

CA and CAH data for various samples are summarized in Fig. 11.16 (adapted from Bixler and Bhushan 2013d, 2014). For actual samples at the solid-air-water interface, the rice leaf shows the highest CA = 164° and lowest CAH $\approx 3^\circ$. For comparison, maximum water contact angle of actual lotus leaves is 164° (Koch et al. 2009b). Also as expected, the coated rice leaf and shark skin replica samples exhibit a higher contact angle than the uncoated samples, showing the effectiveness of the superhydrophobic coating (Bixler and Bhushan 2012b). The superhydrophobic coating is also reported oleophilic at the solid-water-oil interface, and the superoleophobic coating is superoleophobic at the solid-air-oil interface (Bixler and Bhushan 2013d). For the rice leaf inspired samples, Samples 1–4 exhibit hydrophobic contact angles with Sample 3 the highest at 146° and Embossed sample 3 at 101° (Bixler and Bhushan 2014).

When comparing measurements from various samples, there is a noticeable difference between actual and replica samples. Using the Wenzel and Cassie-Baxter equations, predicted values along with measured data are presented in Table 11.5 (Bixler and Bhushan 2012b). A comparison shows that rice leaf and butterfly wing

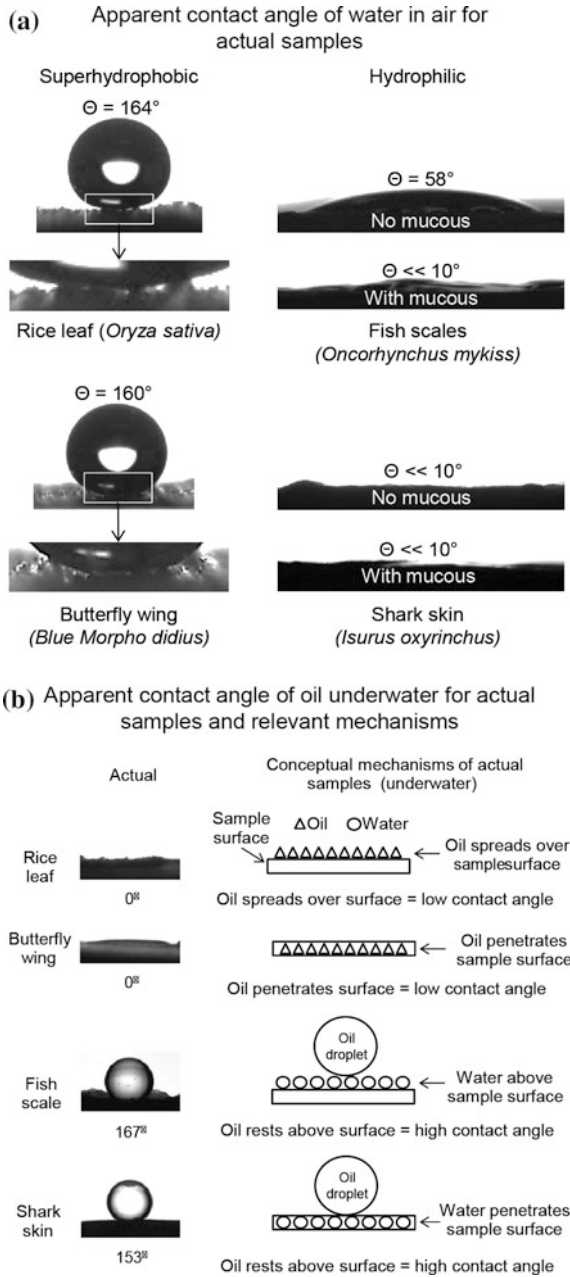


Fig. 11.15 **a** Images of water droplet in air and **b** oil droplet underwater for actual samples (adapted from Bixler and Bhushan 2012b), and **c** water droplet in air, oil droplet in air, and underwater for replica and coated samples (adapted from Bixler and Bhushan 2013d)

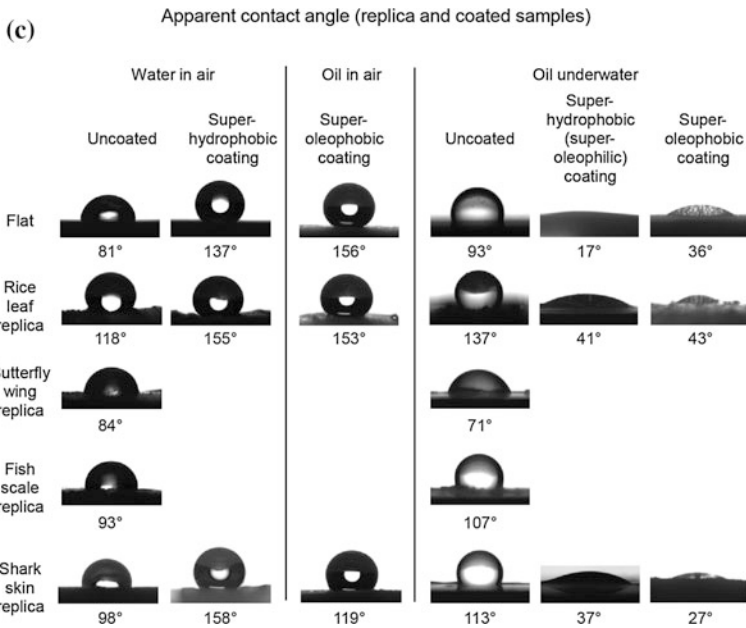


Fig. 11.15 (continued)

measurements align well with the Cassie-Baxter equation, whereas fish scales and shark skin measurements align well with the Wenzel equation. This is reportedly due to the different mechanisms at work and how the sample materials and structures differ. For instance, a low surface energy nanostructured coating was applied to rice leaf urethane replicas in order to mimic actual rice leaves; however the nanostructured morphology differs from actual rice leaves (Bixler and Bhushan 2012b, 2013a).

11.5.4 Drag Reduction Models

Drag reduction mechanisms differ for various fluids and samples under investigation with considerations given to liquid repellency, adhesion, and anisotropic flow characteristics. Drag reduction is reported to occur with superhydrophobic/superoleophobic and superoleophilic surfaces (Bixler and Bhushan 2012b, 2013a, b, c, d, 2014). In the case of water flow, superhydrophobicity and low adhesion provides the greatest drag reduction (Bixler and Bhushan 2012b). However in oil flow, the superoleophilic surfaces provide drag reduction via the thin film effect but superoleophobic surfaces perform similarly due to liquid repellency and low adhesion (Bixler and Bhushan 2013a). Anisotropy in samples also helps with drag reduction.

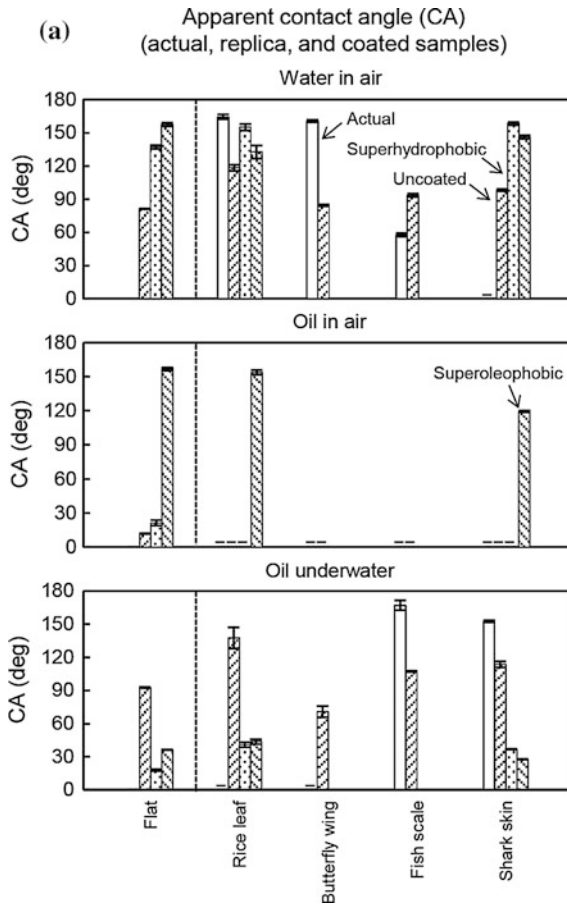


Fig. 11.16 Wettability results with water droplets and oil droplets (both in air and underwater) using actual, replica, and rice leaf inspired samples. Shown are values for apparent CA for **a** actual, uncoated replica, and coated replica samples and **b** rice leaf inspired samples (Bixler and Bhushan 2014). Also shown are values for CAH **c** actual, uncoated replica, and coated replica samples (adapted from Bixler and Bhushan 2013d) and **d** rice leaf inspired samples (Bixler and Bhushan 2014). Drag and self-cleaning efficiency improves with high CA and low CAH. Error bars show ± 1 standard deviation

Bixler and Bhushan (2013d, 2014) report that high CA and low CAH alone does not always lead to drag reduction; however, the surface must be relatively smooth for such benefit (Daniello et al. 2009; Jung and Bhushan 2010; Bixler and Bhushan 2013d). For instance, Sample 2 shows a relatively high water contact angle of 137° but also shows a drag increase in water, oil, and air. The tall pillars of Sample 2 are believed to impede fluid flow and the benefit from high contact angle is negated (Bixler and Bhushan 2014). For drag reduction, it is important to achieve high CA

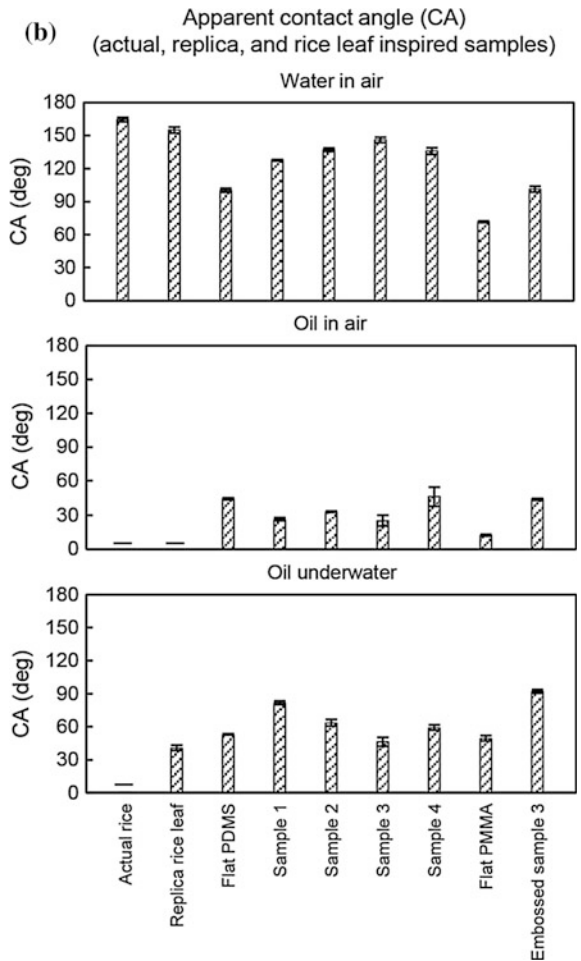


Fig. 11.16 (continued)

and low CAH with a relatively smooth surface such as the one employed with the rice leaf replica (Bixler and Bhushan 2013d).

To understand drag reducing mechanisms, conceptual simplified water flow control models were introduced for rice leaf, butterfly wing, fish scale, and shark skin (Bixler and Bhushan 2012b, 2013d). As shown in Fig. 11.17, self-cleaning rice leaves and butterfly wings easily repel water, whereas the fish scale and shark skin attract water. Furthermore, the longitudinal grooves, scales, or riblets efficiently direct fluid, which is reported to lower drag. The water droplets sit above the hierarchical surface structures of the rice leaf and butterfly wing, whereas they penetrate the surface structures of fish scales and shark skin. By staying above, the droplet can more easily roll and collect contaminants to improve antifouling

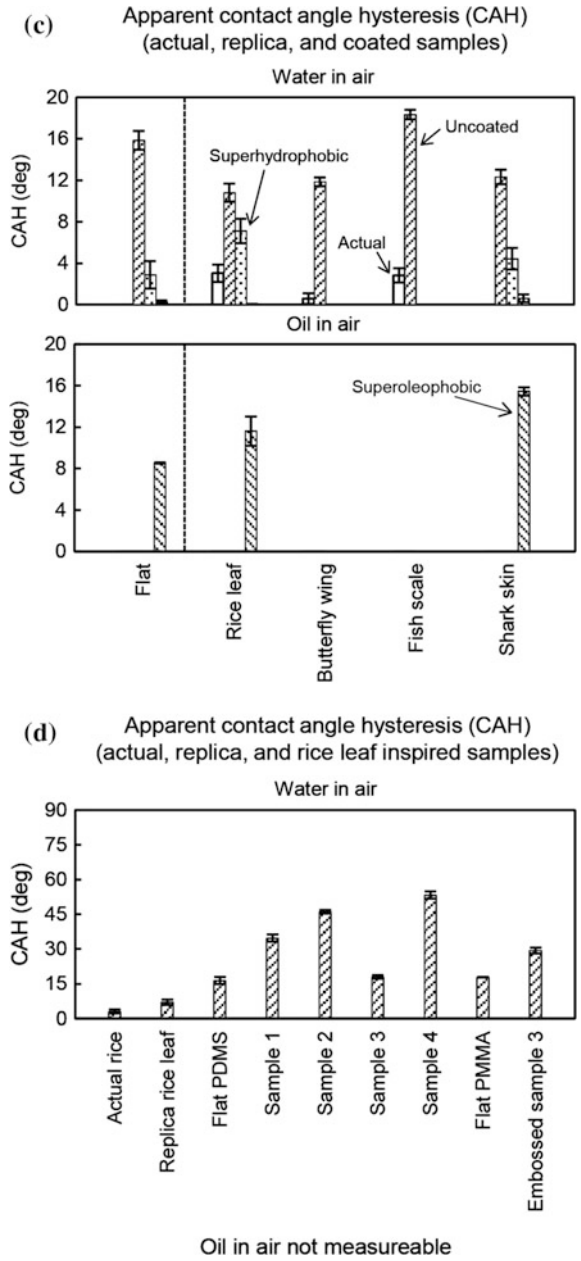


Fig. 11.16 (continued)

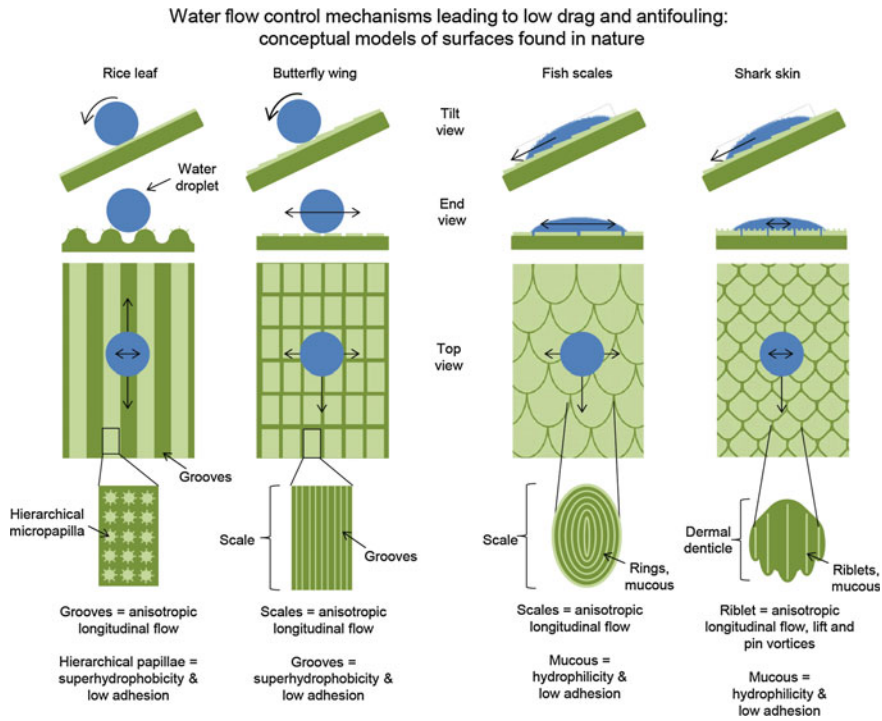


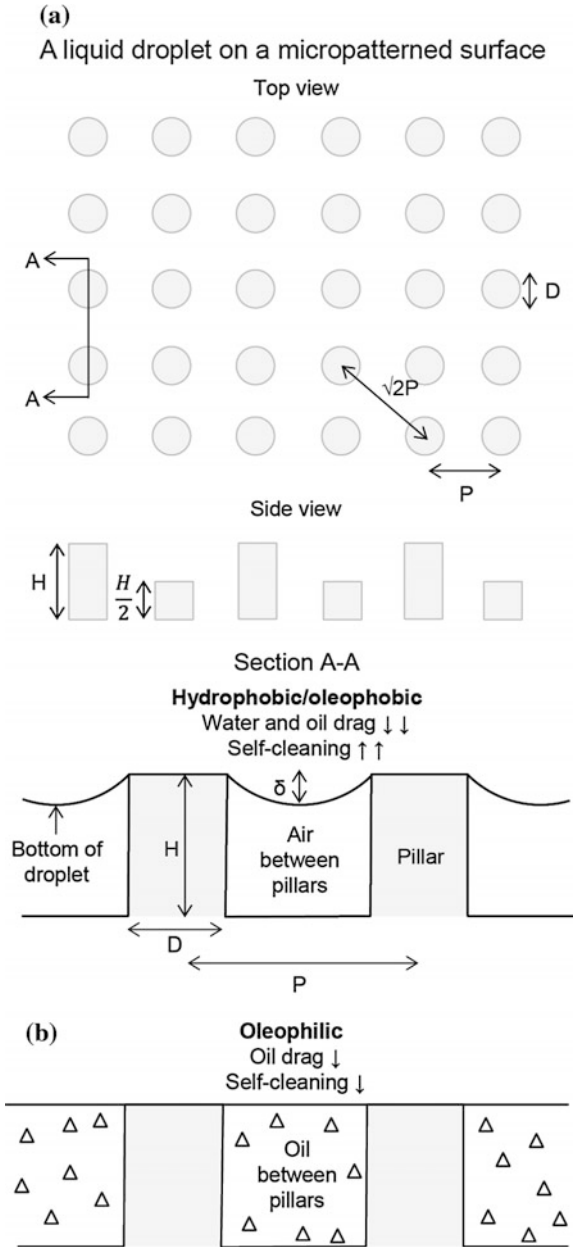
Fig. 11.17 Water flow control conceptual models of rice leaf, butterfly wing, fish scale, and shark skin (adapted from Bixler and Bhushan 2012b). Each example contains mechanisms that are believed to promote low drag, self-cleaning, and antifouling. *Arrows* indicate the tendencies of fluid flow in transverse and longitudinal directions

efficiency. Mucous found on fish scale and shark skin is believed to act as a lubricant, and further reduce drag with the lower skin friction. This also provides antifouling benefits since the water next to the fish scales and shark skin moves quickly and prevents microorganisms from attaching (Bixler and Bhushan 2012b).

It is believed that the combination of anisotropic flow, liquid repellency, and low adhesion are major contributors to drag reduction (Bixler and Bhushan 2013d, 2014). The anisotropic flow present with rice leaves and butterfly wings helps to facilitate efficient fluid movement over the surface. This control minimizes movement of fluid molecules in the viscous sublayer and thus reduces the energy losses, which leads to lower drag. A similar effect is also believed to be present with oil flow and superoleophobic surfaces (Bixler and Bhushan 2013a).

Lowering drag using the rice leaf replica and inspired micropatterned samples is demonstrated in closed channel flow for hydrophobic and oleophobic surfaces, see Fig. 11.18a. A droplet shown on two farthest apart adjacent pillars droops by a distance δ over air between pillars in the Cassie-Baxter regime (Bhushan and Jung 2011), and is given by:

Fig. 11.18 Schematic showing **a** the micropatterned surface using uniformly spaced micro-sized pillars. Drag reduction leading to self-cleaning may be achieved by either **a** hydrophobic/oleophobic or **b** oleophilic surfaces (Bixler and Bhushan 2013a)



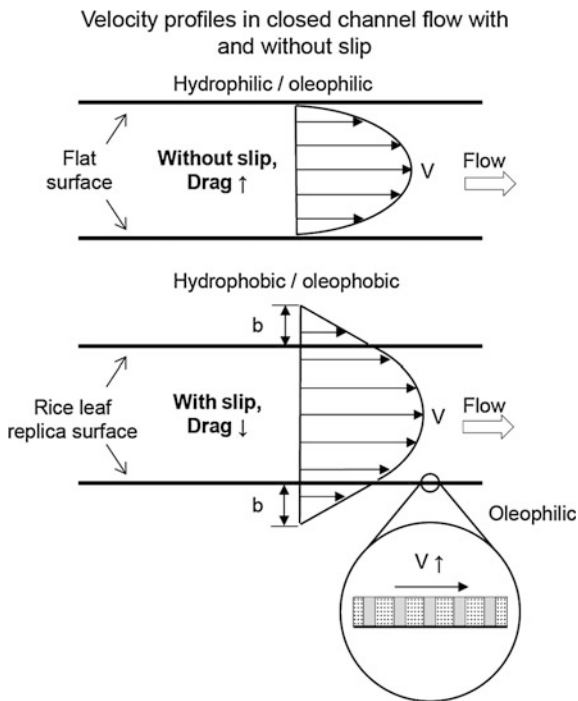
$$\delta = \left(\sqrt{2P} - D \right)^2 / R \tag{11.7}$$

where the known parameters are pitch (P), diameter (D), droplet radius (R), and uniform cylindrical pillar height (H). The liquid droplet fully penetrates the area between the pillars when $\delta \geq H$ (transitioning from Cassie Baxter to Wenzel regime). Surfaces are not wetted with liquid in the Cassie-Baxter regime if $\delta < H$. This surface is expected to work with water, oil, and air flow in laminar and turbulent regimes.

The micropatterned sample also exhibits low drag for oleophobic surfaces. In oil flow on oleophobic surfaces, oil becomes trapped and is held between the micropapillae or pillars, and facilitates oil flow, known as the thin film effect (Bixler and Bhushan 2013a, 2014). The conceptual model is shown in Fig. 11.18b. The lubricating effect is believed to increase slip length (b); therefore, the flow velocity (V) increases at the channel wall and leads to lower drag. In living nature, slippery surfaces are created by the pitcher plant (carnivorous, genus *Nepenthes*) using surface wetting, which causes insects to aquaplane into the digested area (Bhushan 2009).

Figure 11.19 shows schematically the presence of slip in hydrophobic/oleophobic surfaces and consequently drag reduction. Hydrophobic/oleophobic surfaces are known to reduce slip and have low drag (Wang and Bhushan 2010; Jing and

Fig. 11.19 A hydrophobic/oleophobic surface can increase slip length (b) during fluid flow, where higher slip translates into lower drag, increased flow rate, and thus, improved self-cleaning and antifouling. An oleophilic surface also increases the slip length (velocity, V) by the so-called thin-film effect, and translates into lower drag



Bhushan 2013). The thin film effect in oleophilic surfaces is also believed to reduce slip length and drag (Bixler and Bhushan 2013a).

11.6 Closure

Rice leaf and butterfly wing surfaces exhibit a combination of shark skin (anisotropic flow leading to low drag) and lotus leaf (superhydrophobic and self-cleaning) effects—producing the so-called rice and butterfly wing effect. To understand this effect, rice leaf and butterfly wing surfaces, and for comparison, fish scale and shark skin surfaces, were investigated and experiments were conducted with actual and replica samples. Rice leaves were used as inspiration due to relatively simple morphology and rice leaf inspired samples were fabricated with hierarchical structures. Replica and rice leaf inspired samples were fabricated using soft-lithography, photolithography, and hot-embossing techniques. Fluid drag experiments were carried out to understand the role of sample geometrical dimensions. Fluid drag is a measure of pressure drop measurements from sample lined closed channels using water, oil and air in laminar and turbulent regimes.

When examining the replica and rice leaf inspired samples, the greatest drag reduction occurs in turbulent water flow. Reportedly the maximum pressure drop reduction is shown with Embossed sample 3 and rice leaf replica at 23 and 26 %, respectively. In laminar oil flow, a 6 % pressure drop reduction is reported using the PMMA Embossed sample 3 (dual height micro-sized pillar design) as compared to 10 % with the rice leaf replica. In turbulent air flow, a 12 % pressure drop reduction is reported using the Embossed sample 3 as compared to 20 % with the rice leaf replica.

Rice leaf inspired samples are believed to provide anisotropic flow, liquid repellency, and low adhesion characteristics that lead to drag reduction. It is believed that drag reduction improves with high CA, however low CA in oil flow may create a drag reducing thin film effect. A nondimensional pressure drop equation has been developed that shows that pressure drop is directly proportional to velocity and nondimensional pressure drop is proportional to the Reynolds number.

References

- Barthlott, W. and Neinhuis, C. (1997), “Purity of the Sacred Lotus, or Escape from Contamination in Biological Surfaces,” *Planta* **202**, 1-8.
- Bechert, D.W., Bruse, M., Hage, W., and Meyer, R. (1997), “Biological Surfaces and Their Technological Application – Laboratory and Flight Experiments on Drag Reduction and Separation Control,” Paper # AIAA-1997-1960, presented at AIAA 28th Fluid Dynamics Conference, Snowmass Village, CO, AIAA, New York.

- Bhushan, B. (2009), "Biomimetics: Lessons from Nature – an Overview," *Phil. Trans. R. Soc. A* **367**, 1445-1486
- Bhushan, B. (2010), *Springer Handbook of Nanotechnology, 3rd Edition*, Springer, New York.
- Bhushan, B. and Jung, Y.C. (2011), "Natural and Biomimetic Artificial Surfaces for Superhydrophobicity, Self-Cleaning, Low Adhesion, and Drag Reduction," *Prog. Mater. Sci.* **56**, 1-108.
- Bhushan, B., Jung, Y.C. and Koch, K. (2009), "Self-Cleaning Efficiency of Artificial Superhydrophobic Surfaces," *Langmuir*, **25**, 3240-3248.
- Bixler, G.D. and Bhushan, B. (2012a), "Biofouling Lessons from Nature," *Phil. Trans. R. Soc. A* **370**, 2381-2417.
- Bixler, G.D. and Bhushan, B. (2012b), "Bioinspired Rice Leaf and Butterfly Wing Surface Structures Combining Shark Skin and Lotus Effects," *Soft Matter* **8**, 11271-11284.
- Bixler, G.D. and Bhushan, B. (2013a), "Bioinspired Micro/nanostructured Surfaces for Oil Drag Reduction in Closed Channel Flow," *Soft Matter* **9**, 1620-1635.
- Bixler, G.D. and Bhushan, B. (2013b), "Shark Skin Inspired Low-drag Microstructured Surfaces in Closed Channel Flow," *J. Colloid Interf. Sci.* **393**, 384-396.
- Bixler, G.D. and Bhushan, B. (2013c), "Fluid Drag Reduction with Shark-skin Riblet Inspired Microstructured Surfaces," *Adv. Funct. Mater.* **23**, 4507-4528.
- Bixler, G.D. and Bhushan, B. (2013d), "Fluid Drag Reduction and Efficient Self-Cleaning with Rice Leaf and Butterfly Wing Bioinspired Surfaces," *Nanoscale* **5**, 7685-7710.
- Bixler, G.D. and Bhushan, B. (2014), "Rice- and Butterfly-Wing Effect Inspired Self-Cleaning and Low Drag Micro/nanopatterned Surfaces in Water, Oil, and Air Flow," *Nanoscale*, **6**, 76-96.
- Bixler, G. D. and Bhushan, B. (2015), "Rice- and Butterfly-Wing Effect Inspired Low Drag and Antifouling Surfaces: A Review," (Invited), *Crit. Rev. in Solid State Mater. Sci.* **40**, 1-37.
- Bixler, G.D., Theiss, A., Bhushan, B., and Lee, S.C. (2014), "Anti-fouling Properties of Microstructured Surfaces Bio-inspired by Rice Leaves and Butterfly Wings," *J. Colloid Interf. Sci.*, **419**, 114-133.
- Blevins, R.D. (1984), *Applied Fluid Dynamics Handbook*, Van Nostrand-Reinhold, New York.
- Daniello, R.J., Waterhouse, N.E. and Rothstein, J.P. (2009), "Drag Reduction in Turbulent Flows over Superhydrophobic Surfaces," *Phys. of Fluids* **21**, 085103.
- Dean, B. and Bhushan, B. (2010), "Shark-skin Surfaces for Fluid-Drag Reduction in Turbulent Flow: a Review," *Phil. Trans. R. Soc. A* **368**, 4775-4806.
- Ebert, D. and Bhushan, B. (2012a), "Wear-resistant Rose Petal-effect Surfaces with Superhydrophobicity and High Droplet Adhesion Using Hydrophobic and Hydrophilic Nanoparticles," *J. Colloid Interf. Sci.* **384**, 182-188.
- Ebert, D. and Bhushan, B. (2012b), "Transparent, Superhydrophobic, and Wear-Resistant Coatings on Glass and Polymer Substrates Using SiO₂, ZnO, and ITO Nanoparticles," *Langmuir* **28**, 11391-11399.
- Feng, L., Li, S., Li, Y., Li, H., Zhang, L., Zhai, J., Song, Y., Liu, B., Jiang, L. and Zhu, D. (2002), "Super-Hydrophobic Surfaces: From Natural to Artificial," *Adv. Mater.* **14**, 1857-1860.
- Goodwyn, P.P., Maezono, Y., Hosoda, N. and Fujisaki, K. (2009), "Waterproof and Translucent Wings at the Same Time: Problems and Solutions in Butterflies," *Naturwissenschaften* **96**, 781-787.
- Guo, Z. and Liu, W. (2007), "Biomimic from the Superhydrophobic Plant Leaves in Nature: Binary Structure and Unitary Structure," *Plant Science* **172**, 1103-1112.
- Haynes, W. M. (ed.) (2014), *CRC Handbook of Chemistry and Physics, 95th Edition*, CRC Press, Boca Raton, Florida.
- Jing, D. and Bhushan, B. (2013), "Boundary Slip of Superoleophilic, Oleophobic and Superoleophobic Surfaces Immersed in Deionized Water, Hexadecane, and Ethylene Glycol," *Langmuir* **29**, 14691-14700.
- Jung, Y.C. and Bhushan, B. (2010), "Biomimetic Structures for Fluid Drag Reduction in Laminar and Turbulent Flows," *J. Phys.: Condens. Matter* **22**, 1-9.
- Koch, K., Bhushan, B., and Barthlott, W. (2008), "Diversity of Structure, Morphology, and Wetting of Plant Surfaces," (Invited) *Soft Matter* **4**, 1943-1963.

- Koch, K., Bhushan, B., and Barthlott, W. (2009a), "Multifunctional Surface Structures of Plants: An Inspiration for Biomimetics," (Invited) *Prog. Mater. Sci.* **54**, 137-178.
- Koch, K., Bhushan, B., Jung, Y.C., and Barthlott, W. (2009b), "Fabrication of Artificial Lotus Leaves and Significance of Hierarchical Structure for Superhydrophobicity and Low Adhesion," *Soft Matter* **5**, 1386-1393.
- Liu, K. and Jiang, L. (2011), "Bio-inspired Designed of Multiscale Structures for Function Integration," *Nano Today* **6**, 155-175.
- Liu, M., Wang, S., Wei, Z., Song, Y. and Jiang, L. (2009), "Bioinspired Design of a Superoleophobic and Low Adhesive Water/Solid Interface," *Adv. Mater.* **21**, 665-669.
- Martell, M.B., Rothstein, J.P. and Perot, J.B. (2010), "An Analysis of Superhydrophobic Turbulent Drag Reduction Mechanisms Using Direct Numerical Simulation," *Phys. of Fluids* **22**, 065102.
- Munson, B. R., Rothmayer, A. P., Okiishi, T. M., and Huebsch, W. D. (2012), *Fundamentals of Fluid Mechanics*, 7th Ed., Wiley, New York
- Nosonovsky, M. and Bhushan, B. (2008), *Multiscale Dissipative Mechanisms and Hierarchical Surfaces*, Springer, New York.
- O'Toole, J.C., Cruz, R.T. and Seiber, J.N. (1979), "Epicuticular Wax and Cuticular Resistance in Rice," *Physiol. Plant* **47**, 239-244.
- Ou, J., Perot, B. and Rothstein, J.P. (2004), "Laminar Drag Reduction in Microchannels Using Ultrahydrophobic Surfaces," *Phys. of Fluids* **16**, 4635-4643.
- Pritchard, P. J. and Mitchell, J. W. (2015), *Fox and McDonald's Introduction to Fluid Mechanics*, 9th Ed., Wiley, New York.
- Sato, O., Kubo, S. and Gu, Z.Z. (2009), "Structural Color Films with Lotus Effects, Superhydrophilicity, and Tunable Stop-Bands," *Acc. Chem. Res.* **42**, 1-10.
- Sun, T., Feng, L., Gao, X. and Jiang, L. (2005), "Bioinspired Surfaces with Special Wettability," *Acc. Chem. Res.* **38**, 644-652.
- Wagner, T., Neinhuis, C. and Barthlott, W. (1996), "Wettability and Contaminability of Insect Wings as a Function of Their Surface Sculptures," *Acta Zoologica* **77**, 213-225.
- Wang, Y. and Bhushan, B. (2010), "Boundary Slip and Nanobubble Study in Micro/Nanofluidics with Atomic Force Microscope," (Invited), *Soft Matter* **6**, 29-66.
- Zheng, Y., Gao, X. and Jiang, L. (2007), "Directional Adhesion of Superhydrophobic Butterfly Wings," *Soft Matter* **3**, 178-182.

Chapter 12

Bio- and Inorganic Fouling

12.1 Introduction

Fouling is generally undesirable for most applications (Bhushan 2010, 2012). Fouling includes biological fouling (commonly referred to as biofouling) and inorganic fouling. Biofouling is the accumulation of unwanted biological matter on surfaces, with biofilms created by microorganisms, and macroscale biofouling (simply called macrofouling) created by macroorganisms. Inorganic fouling is fouling that results from the accumulation of non-living particles, and includes deposits of dirt, corrosion, crystals, suspended particles, oil, and ice. The type and extent of fouling depends on the environment, inorganic deposits, and organisms. In biomedical contexts, fouling typically takes the form of biofilms (Stoodley et al. 2002; Vo-Dinh 2007; Schulz et al. 2009; Shirtliff and Leid 2009; Chan and Wong 2010), whereas marine and industrial biofouling typically includes macrofouling (Fingerman et al. 1999; Walker et al. 2000; Raikin 2004; Hellio and Yebra 2009) and inorganic fouling (Somerscales and Knudsen 1981; Bott 1988b; Pritchard 1988; Melo et al. 1988).

Bixler and Bhushan (2012) presented a review of the field. Based on the review, we start with fields susceptible to fouling, followed by biofouling and inorganic fouling formation mechanisms, antifouling strategies from nature, current prevention and cleaning techniques in antifouling, and end with bioinspired rice leaf surfaces for antifouling, based on Bixler et al. (2014).

12.2 Fields Susceptible to Fouling

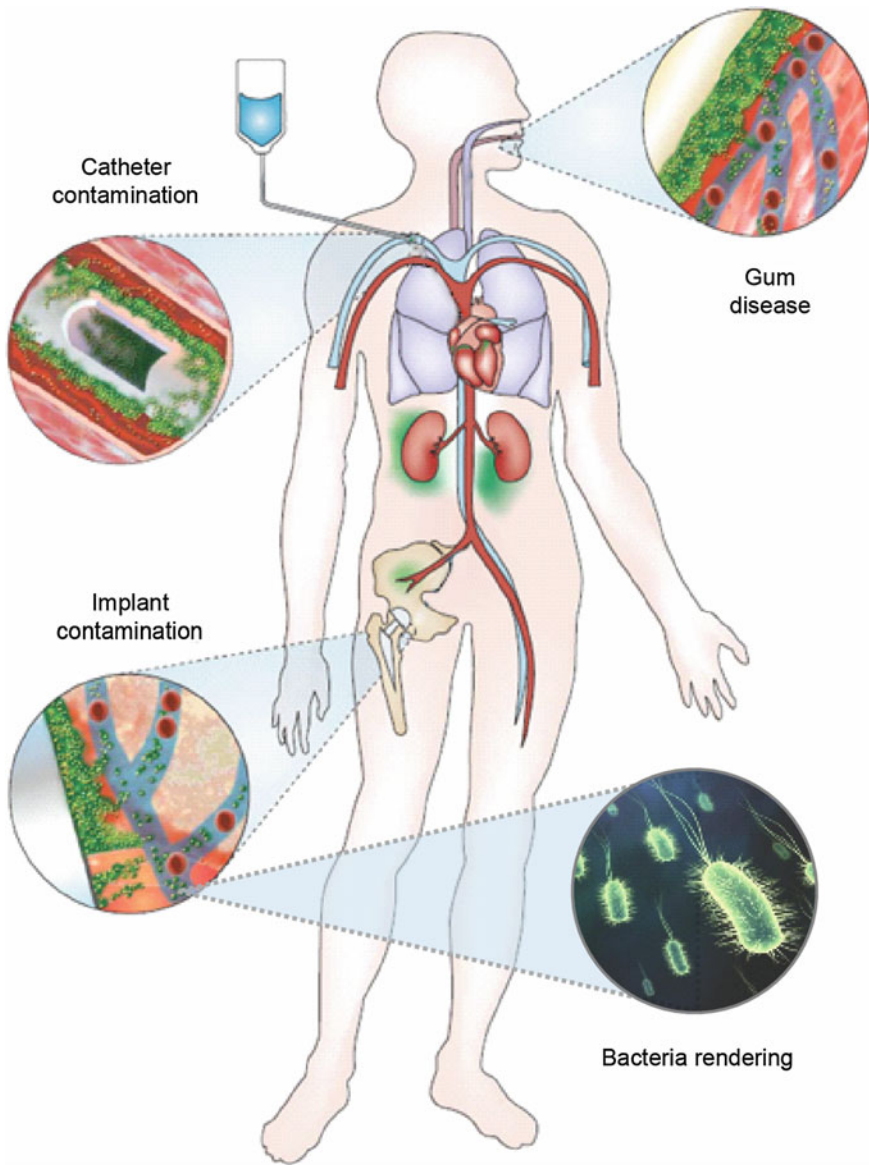
Fouling is prevalent in medical, marine, and industrial fields, causing significant health risks and loss of resources (Walker et al. 2000; Raikin 2004; Vo-Dinh 2007; Hellio and Yebra 2009). Examples of the various types and problems with fouling

Table 12.1 Fields susceptible to biofouling including common examples (adapted from Bixler and Bhushan 2012)

Type	Problems
<i>Medical</i>	
Orthopedic implant	Removal due to infection
Respirator	Ventilator associate pneumonia
Contact lens	Eye infection
Catheter	Urinary tract infections
Hemodialysis	Infectious break-outs
Teeth/dental implant	Periodontal disease, gingivitis
Biosensor	Failure from fibrous encapsulation
<i>Marine</i>	
Ship hull	Increased fuel consumption
Ship engine	Increased stress from extra drag
Marine platform	Increased marine structure load/stress/fatigue
Metal	Increased biocorrosion
<i>Industrial</i>	
Membrane	Reduced flux
Fluid flow	Frictional loss in pipes
Drinking water	Pathogens in potable water
Food, paper, and paint	Food spoilage and worker health risks
Metal cutting fluid	Filter blockage and worker health risks

are shown in Table 12.1, highlighting the many applications susceptible to biofouling and inorganic fouling (Bixler and Bhushan 2012).

Figure 12.1 shows biofouling in the human body can occur in regions such as prosthetic implants, biosensors, catheters, dental implants, and medical equipment (Bixler and Bhushan 2012). Biofouling may lead to implant rejection, malfunction of biosensors, and spread of infectious diseases (Vo-Dinh 2007; Schulz et al. 2009; Shirtliff and Leid 2009; Chan and Wong 2010). Biofilms on medical devices including a ventilation tube, needleless connector, and pacemaker wire are shown in Fig. 12.2 (Bixler and Bhushan 2012). Biofouling can also occur in marine environments where noticeable marine growth appears on ships and underwater structures. This magnifies ship drag, corrosion, fuel consumption, and engine stress (Copisarow 1945; Anonymous 1952; Ray 1959; Melo et al. 1988; Railkin 2004). Industrial biofouling occurs in areas such as power plants, water treatment systems, and food or beverage industries, as shown in Fig. 12.3 (Bixler and Bhushan 2012). Issues include pipe blockage, decreased reverse osmosis (RO) membrane flux, contaminated water, and reduced heat exchanger efficiency (Somerscales and Knudsen 1981; Walker et al. 2000; Chan and Wong 2010).

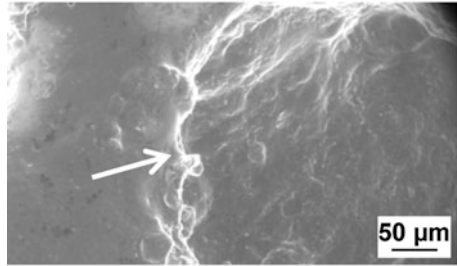


Infectious biofilms possible entrances

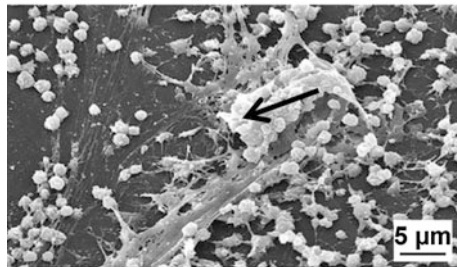
Fig. 12.1 Schematic highlighting areas and entry points of the body susceptible to infectious microorganisms leading to biofilms (Bixler and Bhushan 2012)

Fig. 12.2 Medical device biofilm examples (Bixler and Bhushan 2012). Images include a ventilation tube (*top*) (Trinidad et al. 2010), needleless connector (*middle*) (adapted from Janice Carr), and pacemaker wire (*bottom*) (Marrie and Costerton 1984). Such biofilms may lead to infections that require device removal since antibodies are often ineffective

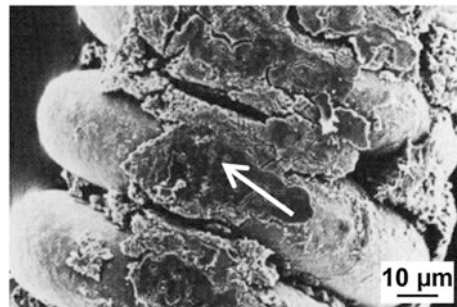
Medical biofouling SEM examples



Ventilation tube removed from patient



Needleless connector



Pacemaker wire removed from patient

Inorganic fouling creates concern in many industries with decreased performance in applications ranging from power production to consumer products. For example, the interior surface of a heat exchanger tube from a nuclear reactor is shown in Fig. 12.4 (Bixler and Bhushan 2012), and corrosion deposits are readily apparent, which leads to inefficient performance (Cunningham et al. 2008;

Industrial biofouling examples



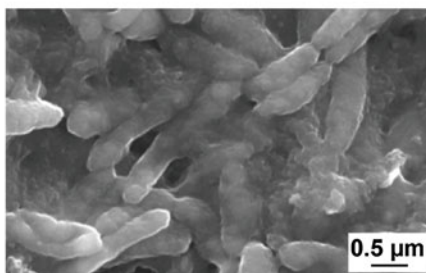
Zebra mussels in power plant pipe



Stainless tube biofilm accumulation



SEM of stainless surface from dairy industry



SEM of wastewater RO membrane

Fig. 12.3 Industrial biofouling examples (Bixler and Bhushan 2012). Zebra mussels (*Dreissena polymorpha*) clogging power plant intake pipe (*top left*) (photo courtesy of Peter Yates), biofilm accumulation in a stainless steel tube (*top right*) (Cunningham et al. 2008), biofilm (*B. cereus*) on dairy industry stainless steel plate (*bottom left*) (Simoes et al. 2010), and biofilm (*P. aeruginosa*) on reverse osmosis (RO) membrane (*bottom right*) (Herzberg and Elimelech 2007)

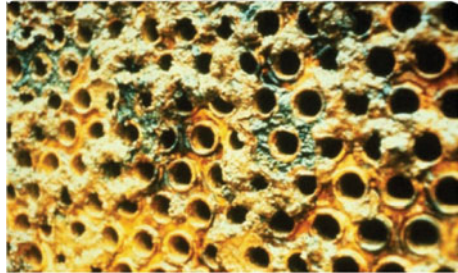
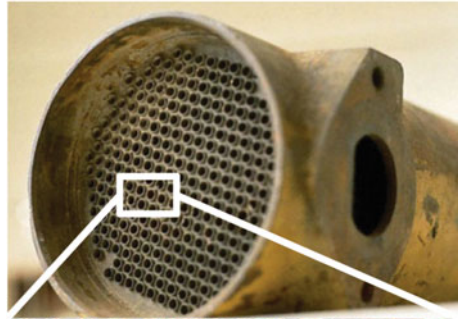
www.hcheattransfer.com). Inorganic fouling also includes undesirable fingerprints on transparent surfaces such as electronic touch screens (mobile phones, tablets, music players, GPS devices), eyeglasses, computer screens, and window glass (Wang and Bhushan 2015). Furthermore, inorganic fouling includes ice on airplane wings, helicopter blades, oil platforms, power lines, locks and dams, and wind turbines (Cao et al. 2009; Meuler et al. 2010).

12.3 Biofouling and Inorganic Fouling Formation Mechanisms

In this section, we discuss the type, formation, and morphology characteristics of biofouling and inorganic fouling (based on Bixler and Bhushan 2012). Details follow.

Fig. 12.4 Inorganic fouling examples (Bixler and Bhushan 2012). Inside of a clean nuclear power plant heat exchanger tube (*top*) compared to a fouled tube with corrosion deposits (*middle*) (Cunningham et al. 2008). Calcium carbonate crystallization fouling on the outside of a heat exchanger (*bottom*) (photo courtesy of H&C Heat Transfer Solutions, Inc.)

Inorganic fouling examples



Clean (top) fouled (bottom) power plant heat exchanger



Heat exchanger tubing with crystallization

12.3.1 Biofouling Formation

In biofilms, microorganisms adhere to one another and the substrate with an adhesive called the extracellular polymeric substance (EPS). The biofilm continues to grow and become more diverse by attracting additional microorganisms through chemical “messages”. Colonization is the process of organisms collecting and growing on a surface, and the morphology is characterized by the thickness, density, structure, composition, bioadhesive strength, and weight of fouling organisms

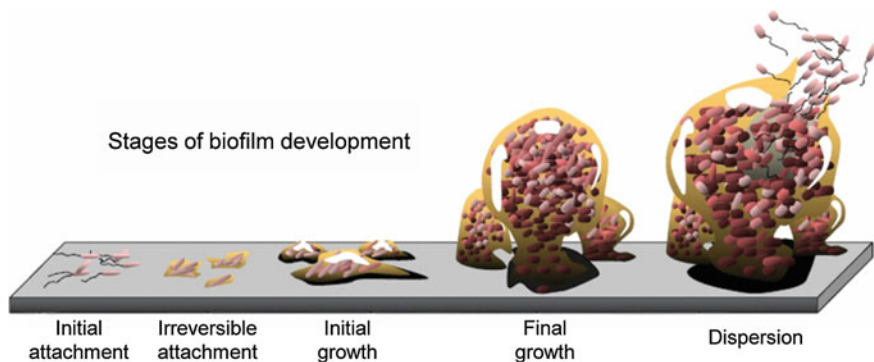


Fig. 12.5 Biofilm development process. Schematic illustrates the five stage colonization process (adapted from D. Davis)

(Marrie and Costerton 1984; Keevil et al. 1999; Flemming et al. 2000; Hellio and Yebra 2009; Chan and Wong 2010; Trinidad et al. 2010). In the marine environment, this usually starts with the formation of a biofilm that attracts larger macrofoulers (Stoodley et al. 2002; Railkin 2004; Costerton 2008; Hellio and Yebra 2009). For instance, tubeworms prefer settling on biofilms, but bryozoans and barnacles do not require a biofilm (Ralston and Swain 2009). Figure 12.5 illustrates the five-stage colonization process, which includes initial attachment, irreversible attachment, initial growth, final growth, and dispersion (adapted from D. Davis; Bixler and Bhushan 2012). Initial attachment starts the colonization process, which begins within days to a few weeks in a nutrient rich environment. The biofilm covered surface then attracts other organisms that may have been previously deterred. Initial attachment of microorganisms is reversible, but once they secrete the EPS, the bond becomes irreversible. This permanent attachment allows initial growth, final growth, and dispersion (Stoodley et al. 2002; Railkin 2004; Monroe 2007; Costerton 2008).

Biofouling growth rates depend on the organism, substrate, flow velocity, shear stress, and temperature (Griebe and Flemming 2000; Railkin 2004; Jones 2009). Organism transportation to a surface is either passive from the current or active from the propagule, juvenile, or adult organism. Active mechanisms include electrostatic repulsion, Brownian motion, turbulent pulsations, and cell outgrowths (Railkin 2004; Ralston and Swain 2009). Underwater environments are ideal for biofouling since currents deliver nutrients and carry away wastes, promoting colonization by planktonic and sessile organisms.

Tenacity of the biofouling is dependent upon bioadhesion (Stoodley et al. 2002; Railkin 2004; Monroe 2007; Costerton 2008). Bioadhesion is the adhesion strength of biofouling on a hard surface (Palacio and Bhushan 2012). This depends on the organism type, substrate, and separating fluid (Callow et al. 1986), due to influences of electrostatic forces and surface wettability (Feng and Jiang 2006; Koch and Barthlott 2009; Scardino 2009; Sheng et al. 2010). Biofilm bioadhesion is a

two-stage process, starting with the initial attachment and then the irreversible attachment. Initial attachment is controlled by a physical adhesion between the microorganism and the substrate. Also known as adsorption, the initial colonists attach to a surface through weak, reversible van der Waals bonds, which are slightly stronger than electrostatic repulsive force. Irreversible attachment is accomplished with secretion of the EPS, which exhibits a sponge-like matrix. This adhesive permanently bonds the microorganisms to one another and collectively to the surface (Flemming et al. 1999; Stoodley et al. 2002; Railkin 2004).

12.3.2 Inorganic Fouling Formation

Inorganic fouling is composed of non-biological particles that may form in addition to or independently from biofouling. Particles originate from corrosion, crystallization, suspended particles, oil, and ice. For instance, salts from aqueous solutions crystallize and deposit on surfaces. Other deposits may result from minerals found in water such as magnesium, calcium, and barium (Somerscales and Knudsen 1981; Walker et al. 2000; Chan and Wong 2010; Bixler and Bhushan 2012).

Types of inorganic fouling include particulate, freeze, and gas stream particulate. Particulate fouling occurs when suspended solid particles deposit onto a heat transfer surface (Epstein 1988). Deposition of crystals from freeze fouling occurs in locations such as cold region oil pipelines when waxy hydrocarbons contact cold pipe walls. Gas stream particulate fouling occurs in gas lines, reactors, combustion chambers, and heat exchangers. This includes mineral, organic, and inorganic particles, which are common in oil or gas combustion systems (Bott 1988a). Biofouling may initiate inorganic fouling, where biocorrosion causes the formation of corrosion particles. Such fouling is prevalent in boilers, cooling condensers, desalination plants, food processing equipment, geothermal plants, and oil production equipment (Pritchard 1988). Heat exchangers can develop hard deposits called “scale” or more porous deposits such as “sludge” (Bott 1988b).

12.3.3 Surface Factors

Biofouling and inorganic fouling depend on the surface factors such as wettability, microtexture, and contours (Fingerman et al. 1999; Railkin 2004; Vadgama 2005; Costerton 2008; Hellio and Yebra 2009; Bixler and Bhushan 2012). For instance, bryozoan and mussel larvae prefer hydrophobic surfaces (Gordon and Mawatari 1992); hydroids, bryozoans, and ascidians prefer microtextured surfaces; larvae, sponges, barnacles, ascidians, and mollusks prefer light colored surfaces; barnacles prefer convex contours; and calcareous sponges prefer concave contours (Railkin 2004).

Surface wettability influences fouler colonization, which ranges from superhydrophobic to superhydrophilic surfaces (Fingerman et al. 1999; Railkin 2004; Vadgama 2005; Costerton 2008; Helligo and Yebra 2009; Bhushan and Jung 2011). Water droplets on a hydrophobic surface will “bead up”, whilst droplets on a hydrophilic surface will spread out evenly.

Low adhesive, superhydrophobic surfaces promote contaminant removal with the application of liquid through “self-cleaning”. Sheeting action of sliding liquid on a superhydrophilic surface can promote self-cleaning, where the liquid helps collect and remove fouling and disrupt microorganism settlement (Harder and Yee 2009). In general though, microorganisms prefer to colonize hydrophilic surfaces, although some actually prefer hydrophobic surfaces. For example *Ulva linza* prefer hydrophobic surfaces, whereas *Balanus amphitrite* prefer hydrophilic surfaces. Furthermore, microorganisms such as *Ulva linza* attach more easily to hydrophobic surfaces, but experience decreased adhesive strength (Scardino 2009).

Surface microtexture influences organisms such as hydroids, bryozoans, and ascidians that seek shelter against strong currents by settling in grooves, pits, cracks, and crevices (Fingerman et al. 1999; Railkin 2004). Microorganisms prefer to settle in areas slightly larger than themselves for maximum protection and surface area contact with the substrate. The antifouling occurs when the gap between features is less than the approximate size of fouling microorganisms (Carman et al. 2006; Schumacher et al. 2007a, b; Scardino 2009; Brennan et al. 2010; Bixler and Bhushan 2012). Fewer attachment points between the microorganism and substrate translate into lower bioadhesive strength (Scardino et al. 2008). Bioadhesion is also affected by the effectiveness of EPS flowing into crevices formed by surface roughness, which depends on the adhesive viscosity. Furthermore, when adhesive only contacts the surface asperity peaks or tops of microtexture ridges, applied force to break bonds is significantly reduced (Vladkova 2008).

Several bioassay antifouling experiments have been performed with different microorganisms and microstructured surfaces—using pillars, ribs, and a combination thereof with various diameters, widths, lengths, heights, and pitches (Callow et al. 2002; Carman et al. 2006; Hoipkemeier-Wilson et al. 2004; Schumacher et al. 2007a, b; Scardino et al. 2008; Brennan et al. 2010; Bixler et al. 2014). Laboratory research suggests that samples with appropriately sized topographies prevent colonization by various microorganisms including green algae *Ulva* spores (Carman et al. 2006; Schumacher et al. 2007b), porcine cardiovascular endothelial cells (Carman et al. 2006), and *Balanus amphitrite* cyprids (Schumacher et al. 2007a). Such microorganisms have been exposed to samples and the antifouling effectiveness is determined by counting settled cells using light (Carman et al. 2006) and fluorescence microscopy (Schumacher et al. 2007b). Up to 85 % spore settlement reduction is reported with micro-sized ribs when compared to flat control samples (Carman et al. 2006). This reduction is attributed to the micro-sized feature spacing that is slightly smaller than the microorganisms under investigation. The so-called engineered antifouling microtopographies are designed to target specific microorganisms based on their shape and size (Schumacher et al. 2007a, b). Bixler et al. (2014) reported that reduction in biofouling occurs even if the micro-sized featured

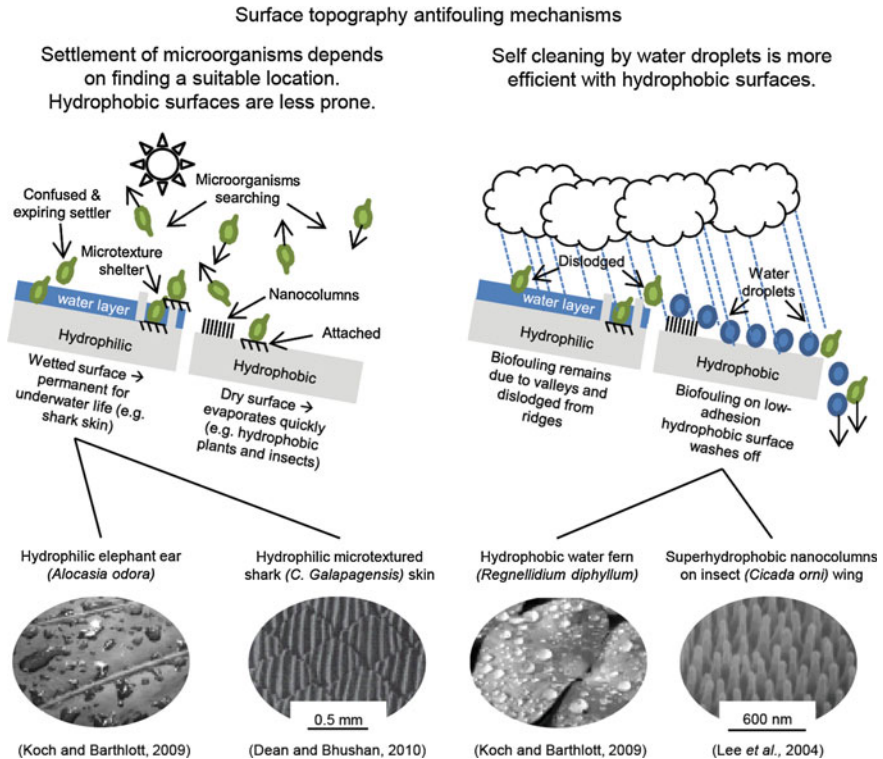


Fig. 12.6 Schematic shows surface topography antifouling mechanisms demonstrating wettability and texture properties that influence microorganism settlement and colonization (adapted from Bixler and Bhushan 2012)

spacing is larger than the microorganisms. Sharp edges of the features discourage the settling and eventual colonization of microorganisms on the surface.

Figure 12.6 shows surface topography antifouling mechanisms demonstrating wettability and texture properties that influence microorganism settlement and colonization (Bixler and Bhushan 2012). Microorganisms search for an ideal site to settle, which can depend on parameters such as wettability and texture (Scardino 2009; Feng and Jiang 2006). During the search process, microorganisms will settle, move on, or expire in the process. In general, biofouling on superhydrophobic surfaces wash off more easily (self-cleaning) as compared to superhydrophilic surfaces. Images show a variety of examples found in nature, including the hydrophilic elephant ear (*Alocasia odora*) (Koch and Barthlott 2009), microtextured shark skin (*Carcharhinus galapagensis*) (Dean and Bhushan 2010), hydrophobic water fern (*Regnellidium diphylum*) (Koch and Barthlott 2009), and superhydrophobic nanocolumns on an insect wing (*Cicada orni*) (Lee et al. 2004).

12.4 Antifouling Strategies from Living Nature

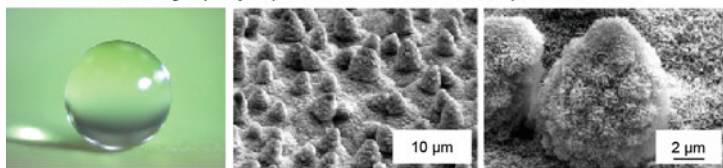
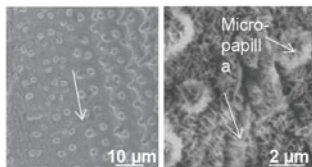
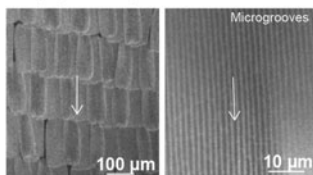
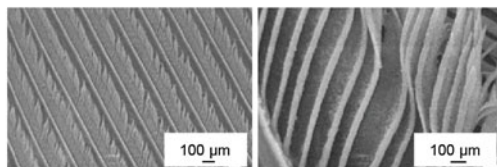
In living nature, many plants and animals thrive due to their antifouling and self-cleaning characteristics (Kesel and Liedert 2007; Koch et al. 2008, 2009; Koch and Barthlott 2009; Ralston and Swain 2009; Bhushan 2009; Bixler and Bhushan 2012). Bixler and Bhushan (2012) provide a number of examples of antifouling strategies from living nature, including a variety of both ambient and aquatic species. Common antifouling mechanisms include wettability, low drag, low adhesion, microtexture, grooming/mechanical cleaning, and chemical secretions (Bixler and Bhushan 2012).

Desirable wettability properties include superhydrophobic and superoleophobic low-adhesion self-cleaning surfaces that resist fouling, as liquids wash away contaminant particles (Bixler and Bhushan 2012). Figure 12.7a shows various superhydrophobic examples of lotus leaf, rice leaf, butterfly wings, and hydrophobic pigeon feathers. Figure 12.7b shows examples of superoleophobic-in-water fish scales and shark skin, which exhibit low drag during swimming.

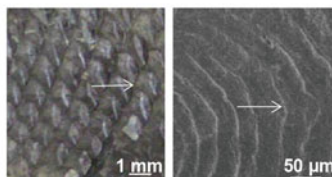
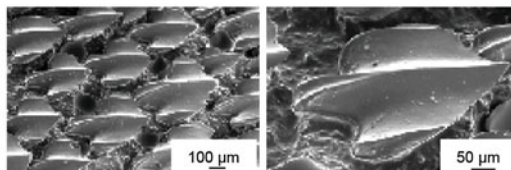
Superhydrophobic lotus leaves exhibit antifouling with self-cleaning properties (Barthlott and Neinhuis 1997; Neinhuis and Barthlott 1997). It is believed that since lotus plants thrive in humid, marshy environments, self-cleaning prevents unwanted fouling, which may inhibit photosynthesis. Lotus leaf hierarchical micropapillae, which are microbumps superimposed with low surface energy waxy nanotubules, provide superior self-cleaning properties (Barthlott and Neinhuis 1997; Bhushan et al. 2009). In nature, rain droplets impact the lotus leaf surface and effectively roll off due to the water repellency effect. This leads to self-cleaning, where droplets collect and remove any contaminant particles, Fig. 12.8a. It should be noted that many other plant species also exhibit self-cleaning properties due to superhydrophobic and low adhesion characteristics.

Fish skin and the skin of fast swimming sharks exhibit low drag, antifouling, and self-cleaning properties (Dean and Bhushan 2010; Bixler and Bhushan 2013a). Fish skin is covered by oriented scales with concentric rings overlapping and hinged such that water flow is from head to tail. Sharks exhibit low drag skin in order to swim quickly to catch prey, and that antifouling is necessary in order to maintain the low drag. Shark skin microstructured riblets on dermal denticles reduce drag and prevent biofouling, as compared to some aquatic species. For instance, whales are often covered with barnacles; however sharks remain clean, see Fig. 12.8a (Bixler and Bhushan 2012, 2013a).

Rice leaves and butterfly wings exploit a combination of antifouling properties from the shark skin and lotus leaf effects (Bixler et al. 2014; Bixler and Bhushan 2015). It is believed that since rice plants thrive in humid, marshy environments, self-cleaning prevents unwanted fouling, which may inhibit photosynthesis. Since butterflies are fragile and unable to clean their wings, these properties are critical to maintain structural coloration and flight control (Wagner et al. 1996). Hierarchical structures consisting of micropapillae superimposed by waxy nanobumps in rice leaves and microgrooves on top of single-like scales in butterfly wings provide

(a) Antifouling superhydrophobic surfaces: ambient examples from natureLotus leaf (*N. nucifera*)Rice leaf (*Oryza sativa*)Butterfly wings (*Blue Morpho didius*)

Feral Rock pigeon feathers (hydrophobic)

(b) Antifouling superoleophobic-in-water surfaces: aquatic examples from natureFish scales (*Rainbow trout, Oncorhynchus mykiss*)Shark skin (*S. acanthias*)

◀ **Fig. 12.7** Antifouling examples from nature using wettability properties. Water promotes self-cleaning on low-adhesion superhydrophobic surfaces, as shown **a** in the lotus leaf, rice leaf, butterfly wings, and pigeon feathers (hydrophobic) examples. **b** Fish scales and shark skin are superoleophobic when submerged in water, and exhibit low drag and antifouling (adapted from Bixler and Bhushan 2012, 2015)

superhydrophobicity and low adhesion exhibiting the lotus effect. Sinusoidal grooves in rice leaves and aligned, shingle-like scales in butterfly wings provide the anisotropic flow exhibiting the shark skin effect. A combination of anisotropic flow, superhydrophobicity, and low adhesion leads to drag reduction and antifouling. Due to anisotropic flow characteristics, droplets roll down the blade of the rice leaf and axially away from the butterfly body (Bixler and Bhushan 2013b, 2015). In addition, hierarchical structure reduces coverage and colonization of biofouling products (Bixler et al. 2014).

Pigeon feathers are hydrophobic and remain clean (Bormashenko et al. 2007). The feathers are formed by barbs and barbules. The hydrophobic properties of the outer feathers (pennae) are due to a combination of this complex feather microstructure and the presence of preen oil (preen wax) spread mechanically by the bird by the preening procedure. Air pockets are then trapped by the feather microstructure, responsible for hydrophobicity.

Certain microtextured surfaces resist biofouling as organisms seek ideal surface features for settlement, and may be deterred if no suitable surface is found. Various examples are shown in Fig. 12.6.

Grooming/other mechanical cleaning is the physical removal of biofouling from the host, which effectively controls slow- and fast-growing biofouling. Decapods and crustaceans groom other creatures with special brush structures for removing foulers from gills and appendages. Echinoderms and bryozoans use special structures called pedicellaria to groom macroepibionts, while crayfish depend on *Branciobdellid annelids* to feed on foulers in their gills (Bixler and Bhushan 2012).

Any physical action that prevents or removes fouling may be present in conjunction with other antifouling mechanisms, such as low drag, low adhesion and chemical secretions. Figure 12.9a illustrates a mechanical cleaning example, combining wiping with chemical secretions, as demonstrated in the human eye via the lachrymal gland secreting tears, puncta collecting tears, and eyelid wiping the cornea (Manton 2008). Chemical secretion methods range from preventing to removing biofouling. Figure 12.9b shows the red seaweed (*Delisea pulchra*), which uses a halogenated furanone to manipulate colonizing bacteria 'attraction' messages (Yen 2010). Other chemical examples include snails that leave a predatory mucous trail, antimicrobial coral egg shells, mucus on shark skin, and antifouling chemicals produced by the bacteria *Roseobacter gallaeciensis* (Bixler and Bhushan 2012). Furthermore, blood cell protein adsorption and cell adhesion are inhibited with phosphorylcholine (Bixler and Bhushan 2012).

Fig. 12.8 Shark skin and lotus leaf effects. **a** The lotus effect is illustrated with a water droplet carrying off contaminants from the lotus leaf surface (Bhushan et al. 2009). **b** Shown is biofouling on the whale and clean shark skin, even though both live in similar environments. The SEM image shows Mako shark skin microstructured riblets that provide low drag and antifouling properties (adapted from Bixler and Bhushan 2013a)

(a) Shark skin and Lotus Effects
Water droplet cleaning Lotus leaf



(b) Barnacle biofouling on Humpback Whale

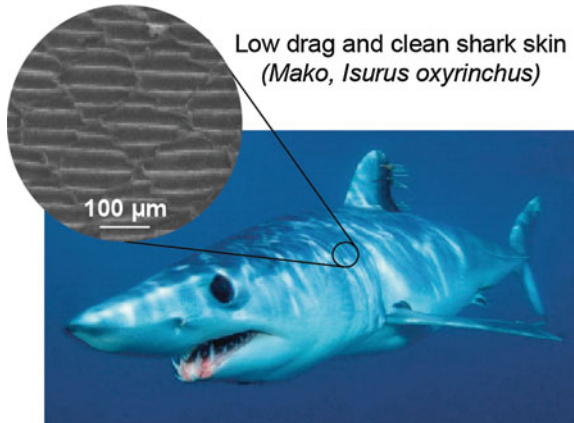
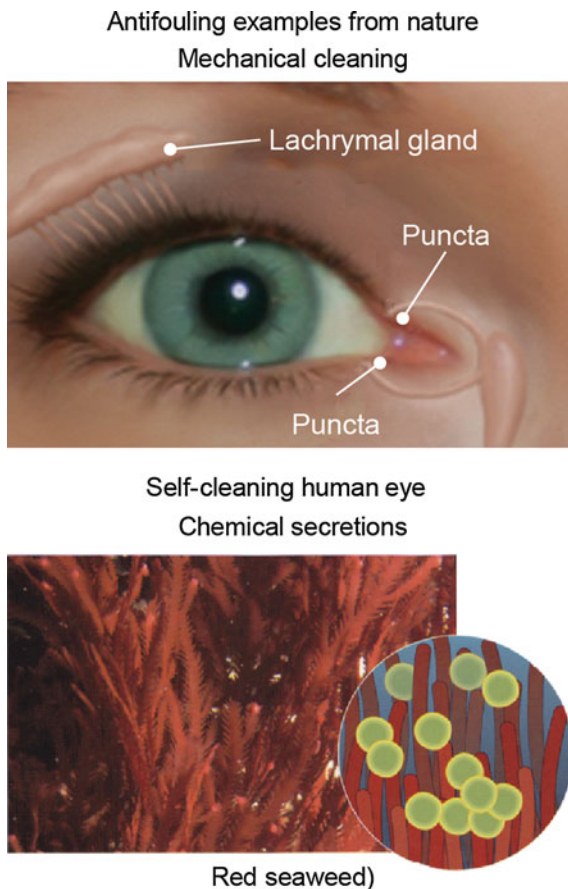


Fig. 12.9 Antifouling examples from nature using mechanical cleaning and chemical secretions. **a** Human eye combines wiping with chemical secretions to clean the cornea. **b** Red seaweed using a halogenated furanone to manipulate colonizing bacteria 'attraction' messages (Bixler and Bhushan 2012)



12.5 Antifouling: Current Prevention and Cleaning Techniques

Bixler and Bhushan (2012) report that reducing or eliminating fouling is accomplished through a variety of methods in medical, marine, and industrial applications. Common controls exist, such as microorganism resistant coatings and self-cleaning low adhesion surfaces. Improving biocompatibility can also reduce medical biofouling, since microorganisms will be less likely to target any implanted device. Details follow.

12.5.1 Prevention Techniques

Medical biofouling is of great concern for the health of patients (Bixler and Bhushan 2012). Fouling of medical devices can significantly alter the properties of the fouled

materials. Multiple coatings and anti-fouling techniques have been reported (Simoes et al. 2010), and many incorporate hydrophobic polymers with antimicrobial properties (LoVetri et al. 2010; Bixler and Bhushan 2012). Example applications include catheters, endotracheal tubes (Dror et al. 2009), and orthopedic hip implants. Superhydrophobic and low adhesion “self-cleaning” surfaces are believed to minimize protein bioadhesion, and antimicrobial surfaces reduce ambient microorganisms (Monroe 2007). Surfaces with superhydrophilic polyethylene glycol or polyethylene oxide exhibit less protein adsorption and bioadhesion (Sharma et al. 2007; Vladkova 2008). Other coating examples include self-assembled monolayers (SAMs), which are desirable since they coat surfaces with a molecularly thick biocompatible film. This is especially important for applications such as biomedical micro/nanoelectromechanical systems (BioMEMS/NEMS) (Bhushan et al. 2006; Bhushan 2010). Figure 12.10 (top left) presented by Bixler and Bhushan (2012) shows an orthopedic hip implant covered with a biocompatible coating designed to control biofouling, wear rate, and promote bone growth (Anonymous 1999; Vleugels 2006).

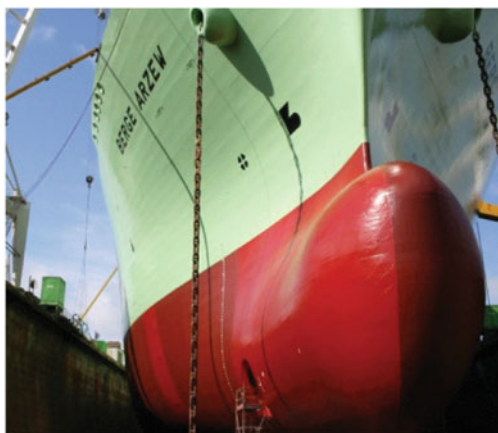
Additional medical prevention techniques include hydrophilic red blood cell plasma membranes that reduce biofouling in medical devices and other synthetic membranes (Cui and Wan 2005). For instance, Advanced Hydro[®] hydrophilic polymer coatings on water purification and filtration membranes provide a 30–50 % reduction in fouling (www.advancedhydro.net). Clean Membranes[®] utilize a “smart-comb” copolymer in ultrafiltration membranes to provide antifouling and increased permeability (www.cleanmembranes.com). Superhydrophilic and antimicrobial nanoparticles in a polyamide thin film coating provide antifouling for reverse osmosis (RO) membranes (www1.cnsi.ucla.edu). Furthermore, studies show success using titanium dioxide (TiO₂) nanoparticles as a thin film on reverse osmosis membranes to control biofouling due to the photocatalytic effects that reduce bacteria (Kim et al. 2003). Similarly, ultrafiltration membranes impregnated with antimicrobial and hydrophilic silver nanoparticles (nAg) provide antifouling benefit. Figure 12.10 (bottom) presented by Bixler and Bhushan (2012) compares such treated and untreated polysulfone ultrafiltration membranes, showing fewer *E. coli* (*Escherichia coli*) attached to the nAg membrane (Zodrow et al. 2009).

Tributyltin coatings have been efficacious in marine antifouling application, and were commonplace. Unfortunately, toxicity and other properties make tributyltin coatings unsuitable for *in vivo* use. Because of tributyltin toxicity to marine organisms, antifouling preparations containing it were banned in 2008 by the International Maritime Organization, adding urgency to the development of more environmentally friendly antifouling and foul-release coatings. As a result, many researchers have been exploring environmentally friendly methods such as new nontoxic antifouling paints and foul-release coatings (Callow 1999; Fingerman et al. 1999; Railkin 2004; Hellio and Yebra 2009). Marine foul-release coatings are nontoxic hydrophobic surfaces that promote self-cleaning. Nano/microtextured surfaces control surface energy, charge, conductivity, porosity, roughness, wettability, and friction (Clare and Aldred 2009). Hydrophobic materials such as fluoropolymers and silicone elastomers are nontoxic, adhesion resistant,

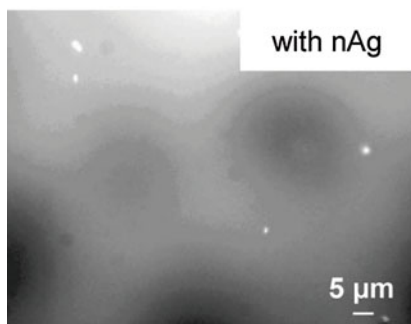
Anti-biofouling coating examples



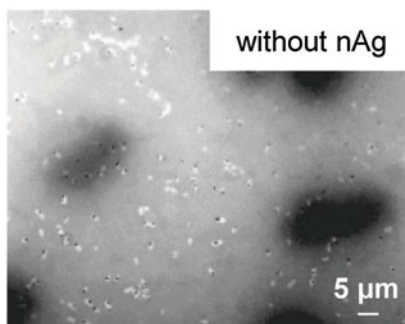
Orthopedic hip implant coating



Ship hull coating



with nAg



without nAg

Fluorescence microscope images of *E. coli* (white specs) on membranes

Fig. 12.10 Medical, marine, and industrial antifouling coating examples (Bixler and Bhushan 2012). Orthopedic hip implants are covered with biocompatible coatings designed to reduce biofouling, wear rate, and promote bone growth (*top left*) (photo courtesy of Ir Jef Vleugels). Marine foul-release organic tin-free hull coating called “Green Ocean Coating Heavy Duty” minimizes manual cleaning (*top right*) (photo courtesy of Bayer MaterialScience). Polysulfone ultrafiltration membrane treated with silver nanoparticles (nAg) shows antifouling benefit with fewer *E. coli* attached (*bottom*) (Zodrow et al. 2009)

environmentally friendly, and easy to clean (Clarkson 1999). Siloxane elastomers provide a combination of lower elastic modulus and lower surface energy, creating a hydrophobic, low-stick surface. Silicone foul-release coatings are used for some quick moving boats, but wear away over time (Vladkova 2007, 2008). Figure 12.10 (*top right*) presented by Bixler and Bhushan (2012) shows a foul-release organic tin-free hull coating called “Green Ocean Coating Heavy Duty” by

Advanced Marine Coatings, whose smoothness and hardness reduces cleaning cycles (www.bayermaterialscience.com).

Industrial antifouling is accomplished similarly to marine antifouling, with coatings that prevent and remove fouling (Bixler and Bhushan 2012). For instance, industrial heat exchanger applications utilize SAMs to reduce bioadhesive strength between foulers and a heated surface, using low surface energy hydrophobic properties. Materials such as silicon can withstand temperatures up to 200 °C whilst materials such as hexadecyl disulfide can withstand up to 225 °C. SAMs furthermore offer corrosion protection by limiting the oxygen and water diffusion at the substrate surface. This technique could be widely used for heat exchangers but needs long term durability testing (Venkatesan and Murthy 2008).

12.5.2 Self-cleaning Surfaces and Cleaning Techniques

Even though fouling prevention is the goal, in many cases fouling is not completely preventable and a surface must be cleaned. In response, several self-cleaning coatings have been developed for various applications. Bixler and Bhushan (2012) report example self-cleaning products including hydrophobic paints, roof tiles, and fabrics as well as self-cleaning hydrophilic windows and membranes. Examples are Lotusan[®] paints by Sto (www.stocorp.com), Tegotop[®] paints by Degussa (www.goldschmidt.com), Erlus Lotus[®] roof tiles (www.erlus.com), NanoSphere[®] fabrics by Schoeller Technologies (www.schoeller-textiles.com), and SunClean[®] glass by PPG Industries (www.ppg.com). Self-cleaning is demonstrated with the hydrophobic Lotusan[®] roll on and Tegotop[®] spray paints that create a microstructure surface (www.stocorp.com; www.goldschmidt.com), hydrophobic Erlus Lotus[®] roof tiles with an etched surface finish (www.erlus.com), and hydrophobic NanoSphere[®] fabrics with integrated nano particles (www.schoeller-textiles.com). Self-cleaning hydrophilic SunClean[®] glass with titanium dioxide uses the sheeting action of water to efficiently gather and remove contaminants (www.ppg.com). Figure 12.11 shows the improved cleanliness with Lotusan[®] hydrophobic self-cleaning paints on concrete and stucco (www.stocorp.com), and better clarity with the SunClean[™] hydrophilic self-cleaning glass (www.ppg.com) (Bixler and Bhushan 2012).

Physical cleaning and chemical disinfecting are often considered effective methods to remove fouling (Cologer 1984; Walker et al. 2000; Sharma et al. 2004; Hellio and Yebra 2009; Chan and Wong 2010; Bixler and Bhushan 2012). Most employ mechanical methods such as manual scrubbing to disrupt and remove the fouling. Figure 12.12 illustrates common methods of cleaning and disinfecting such as medical sterilization, chemical disinfection, high-pressure water spray, automatic brush scrubbing, and membrane cleaning techniques (Bixler and Bhushan 2012). Included are a steam sterilization medical autoclave, Listerine[®] antiseptic mouth rinse, water spray on a low-adhesion ship hull, automatic brush washing system, and microfiltration membrane using sonication, chemicals, and water backwash (Lim

Fig. 12.11 Effectiveness of anti-inorganic fouling coatings (Bixler and Bhushan 2012). Demonstrated is the improved cleanliness with Lotusan[®] hydrophobic self-cleaning paint (*top*) (www.stocorp.com), and improved clarity with the SunClean[™] hydrophilic self-cleaning glass (*bottom*) (www.ppg.com)



and Bai 2003; Bixler and Bhushan 2012). Disinfecting is commonly employed in dental applications with antiseptic mouth rinses such as Listerine[®]. For example, the active ingredient chlorhexidine attacks and reduces dental biofilm to control plaque and gingivitis in the oral cavity (Charles et al. 2004). The biofilm is reduced when the individual bacteria walls rupture (www.jjidentalprofessional.com). Mouth rinses combined with brushing and flossing increase the effectiveness, since such “mechanical methods” disrupt the biofilm (Sharma et al. 2004).

12.6 Bioinspired Rice Leaf Surfaces for Antifouling

In this section, we present data on an anti-biofouling study carried out by Bixler et al. (2014) on rice leaf inspired surfaces. The rice leaf is particularly intriguing due to its relatively simple micropapillae morphology. Bioinspired rice leaf surfaces using micro-sized pillar patterns can be produced with silicon master patterns fabricated by photolithography (Bixler and Bhushan 2014). Sample geometrical dimensions are based on actual rice leaf morphology. Actual rice leaf surfaces are covered by a

Biofouling cleaning examples Disinfecting



Sterilization



Listerine® bacteria lysis

Mechanical cleaning

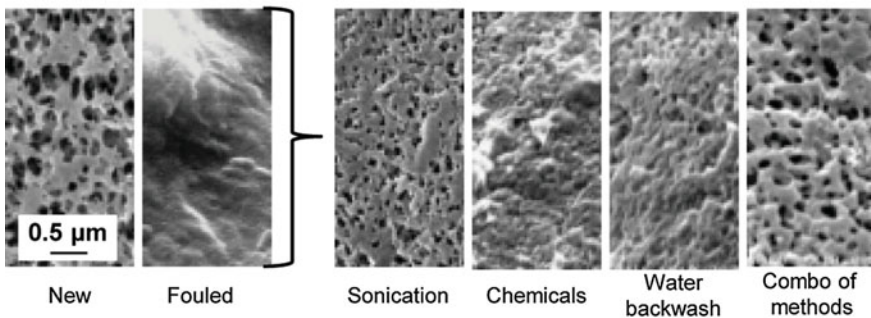


Water spray



Automatic brush

Combination of methods



SEM images comparing membrane cleaning techniques, same scale

Fig. 12.12 Medical, marine, and industrial biofouling cleaning examples (Bixler and Bhushan 2012). Steam sterilization medical autoclave (*top left*) (photo courtesy of Life Science Outsourcing), Listerine® effect on bacteria (*top right*) (adapted from Christoph Schaudinn), water spray on a low-stick ship hull (*middle left*), automatic brush washing system (*middle right*) (Willemsen 2005), and microfiltration membrane using sonication, chemicals, and water backwash (*bottom*) (adapted from Lim and Bai 2003)

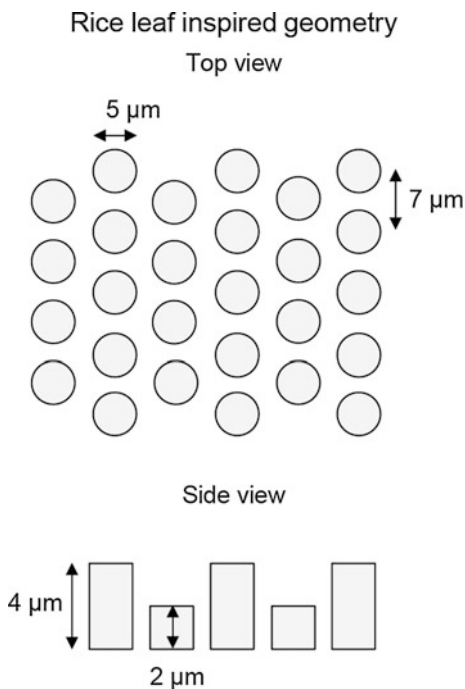
sinusoidal pattern of micropapillae with height 2–4 μm , diameter 2–4 μm , pitch 5–10 μm , and peak radius 0.5–1 μm (Bixler and Bhushan 2013b, 2015).

12.6.1 Fabrication of Micropatterned Samples

The bioinspired rice leaf surface shown in Fig. 12.13 was created to replicate the rice and butterfly wing effect, and was designed to include anisotropic flow and superhydrophobic characteristics. Samples were created using silicon master patterns and the soft-lithography technique (Bixler and Bhushan 2014). Silicon master patterns with pits (negative vs. positive features) were fabricated in order to emboss polymer films and to accurately produce master patterns. Polydimethylsiloxane (PDMS) replicas were produced from silicon master patterns using a three-step soft lithography procedure (Bixler and Bhushan 2014). PDMS (184 Silicone Elastomer by Dow Corning) was chosen due to its low surface energy property which leads to high contact angle. A nanostructured superhydrophobic coating with 50 nm hydrophobized silica nanoparticles and methylphenyl silicone resin was applied to make them superhydrophobic.

Micropatterned plastic sheets were also produced using a commercial hot embossing procedure in a clean room environment (Bixler and Bhushan 2014). The hot embosser produced single-sided embossed plastic sheets from a silicon master

Fig. 12.13 Rice leaf inspired geometry for antifouling. Shown are micropatterned surfaces with dual height pillars. Pillars are arranged in a hexagonal array in order to maintain consistent gaps to promote antifouling (adapted from Bixler and Bhushan 2014)



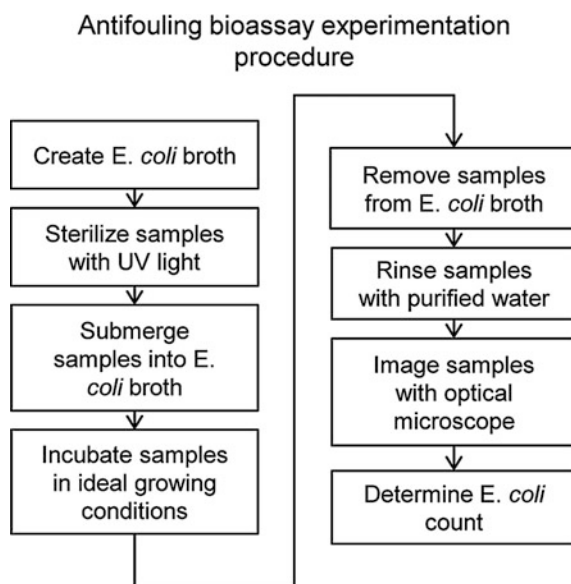
pattern using a combination of heat and pressure. Poly(methyl methacrylate) (PMMA) plastic sheets were selected, which were optically clear and 175 μm in thickness. PMMA molds relatively easily due to its softening temperature.

12.6.2 Anti-biofouling Measurements

For studies to evaluate anti-biofouling benefits, Bixler et al. (2014) considered several foulers primarily based on their size and availability. These include zoospores (*Enteromorpha*) (Callow et al. 2002) and (*Ulva linza*) (Finlay et al. 2002), proteins (Banerjee et al. 2011), *E. coli* (Ma et al. 2000), and MRSA (*Methicillin-resistant Staphylococcus aureus*) (Fletcher et al. 2007). They selected the microorganism *E. coli* due to its prevalence in the medical industry, availability, and access to facilities for safe handling. The multi-step anti-biofouling measurement process is shown in Fig. 12.14 with each process from the *E. coli* broth creation to the final counting (Bixler et al. 2014). The dimensions of single wild type *E. coli* cells were approximately 0.5–0.75 μm wide and 2 μm long. When actively growing and dividing, the cells stretch to ~ 4 μm before dividing into two cells.

The bioassay procedure began with stock solution of *E. coli* (HB2151 *E. coli* clones from The Medical Research Council, Cambridge, England) streaked onto TYE (Tryptone and Yeast Extract) dehydrated agar plates for bacterial colony growth. The plates were then placed in an incubator (Labnet, model 311 DS) at 37 °C overnight, and then stored at 4 °C until use. To prepare *E. coli* broth, a single colony was picked from streak plates and inoculated into 50 ml sterile LB (Luria Broth, Lennox from Fisher Scientific, Pittsburgh, PA) in a beveled flask. *E. coli* was grown for 16 h with

Fig. 12.14 Antifouling bioassay experimental procedure with *E. coli* cells in the laboratory. As shown, samples are sterilized, submerged into broth, placed in incubator, rinsed to remove loose cells, and imaged with oil immersion light microscope to determine cell counts (Bixler et al. 2014)



shaking at 250 rpm at a temperature of 37 °C. After incubation, *E. coli* solution was diluted to 1/100 and 1/10 into sterile LB broth and placed on ice until use.

Bixler et al. (2014) placed the flat control sample (PDMS), a replica sample (PDMS) and an embossed sample (PMMA) in the bottom of a sterile, polystyrene culture dish and sterilized for 10 min via ultraviolet exposure (30W T8 Hot Cathode Germicidal Sterilamp fluorescent light bulb, Philips TUV30W G30T8 360164). *E. coli* broth was added to the culture dish until all samples were covered and then incubated at 37 °C for either 2 or 4 h. The aforementioned concentrations and incubation times were determined from trial and error with samples to achieve an appropriate level of *E. coli* growth. The goal was to visually determine a difference at 1000× magnification between flat control and other samples under investigation.

After incubation, samples were removed from *E. coli* broth and rinsed at a 45° angle. Rinsing removed any unattached *E. coli* from the surface prior to imaging. An auto-pipette (Pipet-Aid from Drummond Scientific, Broomall, PA) was clamped and held on a stand over the rinsing station with a liquid fall height (distance between pipette tip end and sample) of 7 cm. Samples were rinsed with 10 ml of sterile PBS at a flow rate of approximately 2 ml/s, and then immediately placed onto a glass microscope slide with a glass cover slip on top. Using a light microscope and CCD camera (Nikon, Diagnostics Instruments, Inc.), a 140 μm by 140 μm area of each sample was imaged and flat samples analyzed with image processing software (SPIP 5.1.11, Image Metrology A/S, Horshølm, Denmark). Images were collected with a 100× oil immersion objective lens for a total magnification of 1000×. For flat control samples, image processing software (SPIP 5.1.11, Image Metrology A/S, Horshølm, Denmark) was utilized to determine total coverage area of *E. coli*. For the samples, the *E. coli* was manually counted five times in circular areas 35 μm in diameter using two samples within the same bioassay.

12.6.3 Anti-inorganic Fouling Measurements

To understand the anti-inorganic fouling effectiveness of the samples, self-cleaning experiments were conducted (Bixler and Bhushan 2014). These experiments included contaminating samples, employing a wash technique, and determining the percentage of inorganic particles removed. Depositing contaminate particles on the tilted (45°) replicas involved a glass contamination chamber (0.3 m in diameter and 0.6 m high). A tray containing 0.2 g of hydrophilic silicon carbide (SiC) contaminants (400 mesh particle size by Aldrich, with sizes ranging from 10 to 15 μm) was placed in the top chamber with an air hose directed in the center. These particles were chosen because of their similar properties to natural dirt (shape, size, and hydrophilicity). Contaminants were blown with laboratory air for 10 s at 300 kPa, and then allowed to settle for 30 s before the separator panel was removed.

After 30 min, the samples were removed and subjected to pre-wash experiment particle analysis. Using a light microscope and CCD camera, a 280 μm by 210 μm area of each sample was imaged and analyzed with SPIP image processing

software. This process was performed before and after each wash experiment. Wash experiments consisted of exposing the tilted (45°) replicas to water droplets falling from a specified heights and drip rates (total duration of 2 min using 10 mL water). Droplet velocity was approximately 5.6 m/s at a height of 0.4 m. This translates into pressures of 4000 Pa.

12.6.4 Results and Discussion

Anti-biofouling

To understand the antifouling effectiveness of the various samples, Bixler et al. (2014) conducted a series of bioassay experiments. Figure 12.15 shows light microscope images of the *E. coli* colonized on a flat sample at two magnifications (Bixler et al. 2014). As shown, the *E. coli* are long cylindrically shaped microorganisms and tend to cluster in groups and align themselves from head to tail.

Figure 12.16a shows light microscope images of flat PDMS samples at the two concentrations and two incubation times (with *E. coli* highlighted by the SPIP software) (Bixler et al. 2014). Figure 12.16b shows the tabulated results of percentage coverage area of the *E. coli* on the surfaces for 1/100 and 1/10 concentrations at 2 and 4 h incubation time. The greatest coverage occurs at the higher incubation time as *E. coli* growth occurs exponentially over time. Furthermore, as expected, the lower concentration does not provide as much coverage area, however the differences are within 10 % for both incubation times.

Figure 12.17 shows light microscopic images of the flat PDMS control sample, replica sample, and the embossed sample. Antifouling is determined by counting the total number of *E. coli* on the flat control samples and comparing that to the other samples, with results reported in percentage *E. coli* reduced coverage. Figure 12.18 shows the percentage reduced coverage compared to the flat control samples. As anticipated due to the discontinuities of the various surfaces, patterned samples provided antifouling benefits. In general, the antifouling benefit is greater with the 2 h incubation duration as compared to the 4 h duration. It is believed that

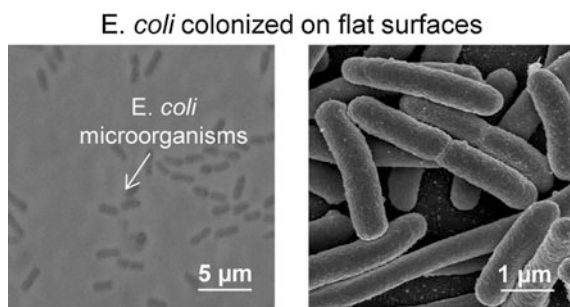
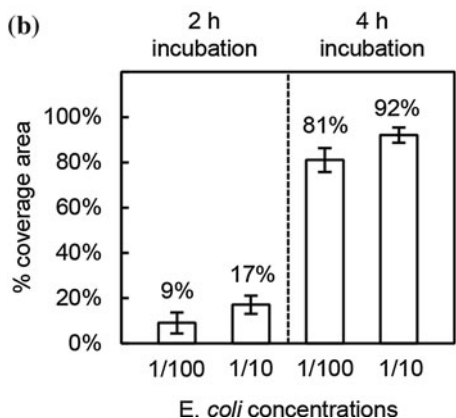
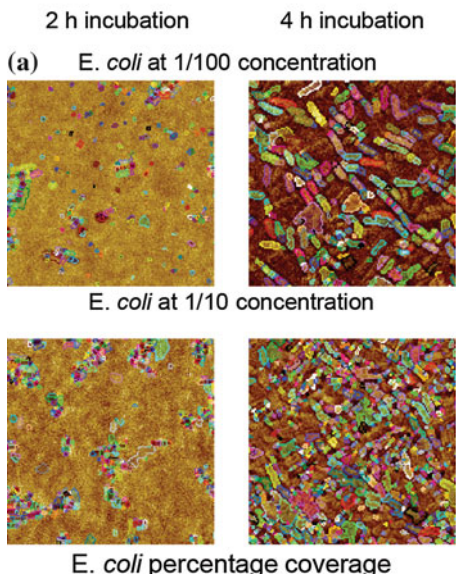


Fig. 12.15 Images of *E. coli* on flat surfaces after the bioassay procedure (Bixler et al. 2014) and at a higher magnification (adapted from www.universityofcalifornia.edu)

Fig. 12.16 a Light microscope images of flat PDMS control samples and **b** percent coverage area after *E. coli* bioassay with two concentrations and two incubation times. *E. coli* covers the majority of the surface after 4 h in ideal growing conditions. This baseline serves to compare the replica sample and embossed sample when calculating percentage reduced coverage (adapted from Bixler et al. 2014)

Light microscope images after bioassay with flat PDMS



the longer duration leads to more significant coverage, and the features provide less overall benefit. It should be noted that the replica sample and embossed sample performed similarly, indicating minimal differences between samples fabricated from PDMS or PMMA.

Anti-inorganic Fouling

To understand the anti-inorganic fouling effectiveness of the various samples, Bixler and Bhushan (2014) conducted a series of self-cleaning wash experiments. Figure 12.19 presents the before and after images for flat PDMS and PMMA

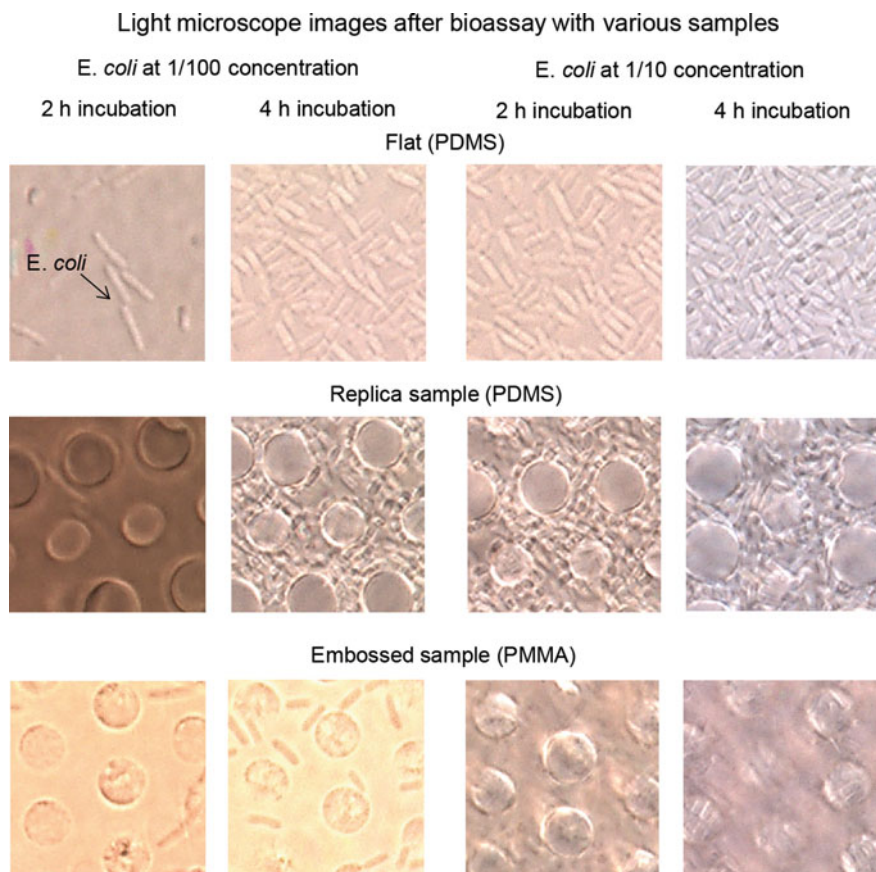
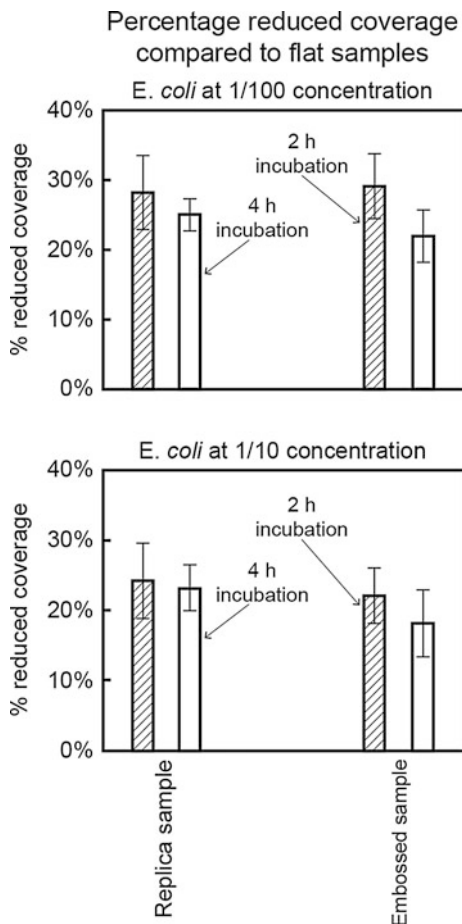


Fig. 12.17 Light microscope images using oil immersion techniques at 1000 \times magnification of samples after bioassay experiments using *E. coli*. Images of flat PDMS, the replica sample, and the embossed sample are shown with two *E. coli* concentrations and two incubation times. Long and narrow cylindrically shaped objects are the *E. coli*. Antifouling analysis was conducted using the images and particle analysis software to quantify effectiveness (adapted from Bixler et al. 2014)

control samples, the replica sample, and the embossed sample (Bixler and Bhushan 2014). These images were used with SPIP imaging software to quantify the percentage of particles removed. Figure 12.20 shows self-cleaning data for wash experiments. Self-cleaning is more evident with a patterned sample and an embossed sample; as compared to flat samples (Bixler and Bhushan 2014). To understand wettability of samples, Bixler and Bhushan (2014) made contact angle measurements. They measured contact angle (CA) and contact angle hysteresis (CAH) values. The replica sample was found to be superhydrophobic ($\sim 150^\circ$) with low CAH, whereas the embossed sample was hydrophobic ($\sim 101^\circ$). High CA and low CAH is believed to amplify the self-cleaning abilities of the samples, as it is believed that the droplets are able to roll and collect the particles after impact.

Fig. 12.18 Anti-biofouling results from *E. coli* bioassay experiments. Results are presented for flat PDMS, the replica sample, and the embossed sample. The percentage reduced coverage is calculated from the flat PDMS control samples. It is believed that antifouling efficiency improves with high CA and low CAH. Error bars show ± 1 standard deviation (adapted from Bixler et al. 2014)



12.6.5 Anti-biofouling and Anti-inorganic Fouling Mechanisms

Bixler et al. (2014) presented conceptual models to describe anti-biofouling mechanisms. Figure 12.21 shows schematic illustrations of colonization of microorganisms exposed to flat and patterned samples. Microorganisms are unable to effectively colonize patterned morphology as well as they can on the flat control sample. If the length of the microorganism is larger than the pillar spacing, they cannot invade the spacing and instead land on top of the pillars. If the length of the microorganism is smaller than the spacing, as is the case with *E. coli*, the sharp edges of the pillars are believed to discourage the settling and eventual colonization of microorganisms on the surface. The edges provide an inconvenient landing zone for settlement, and thus the microorganism must continue the search for an ideal

Light microscope images from anti-inorganic fouling wash experimentation

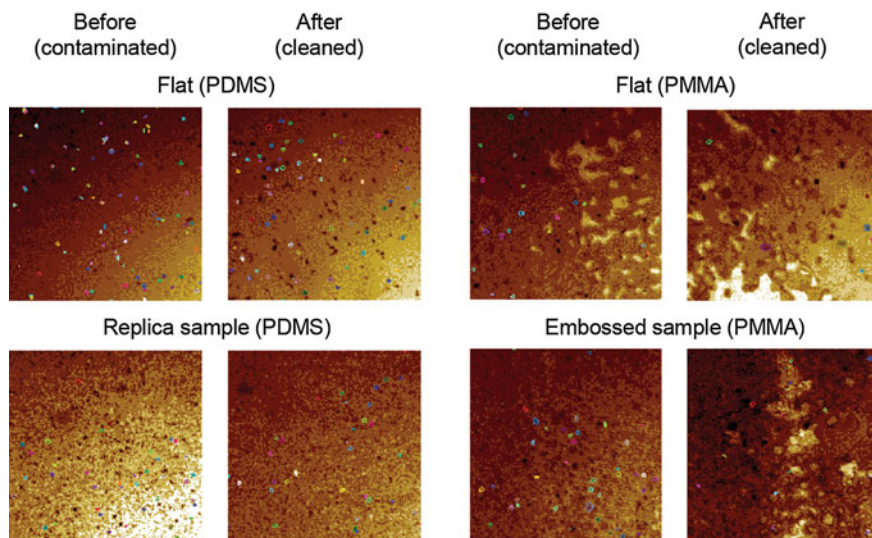


Fig. 12.19 Light microscope images of samples before and after anti-inorganic fouling wash experimentation, with specs representing silicon carbide (SiC) particles (Bixler and Bhushan 2014). Results are presented for flat PDMS and PMMA, the replica sample, and the embossed sample. Self-cleaning analysis was conducted using the images and particle analysis software to quantify particle removal

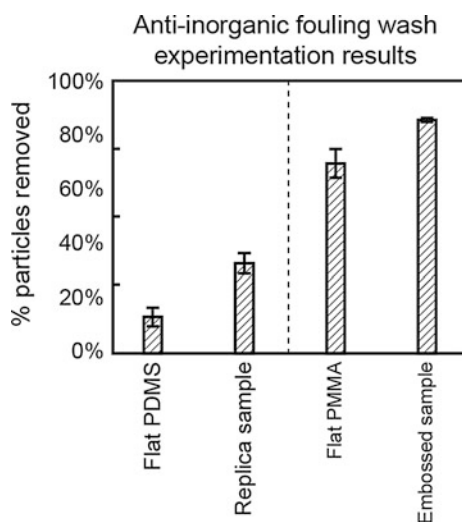


Fig. 12.20 Anti-inorganic fouling wash experimentation results (adapted from Bixler and Bhushan 2014). Results are presented for flat PDMS, replica sample, flat PMMA sample, and embossed sample. The embossed sample shows the greatest self-cleaning efficiency followed by the replica sample. Micropatterned samples are superior in self-cleaning efficiency compared to their respective flat samples. Error bars show ± 1 standard deviation

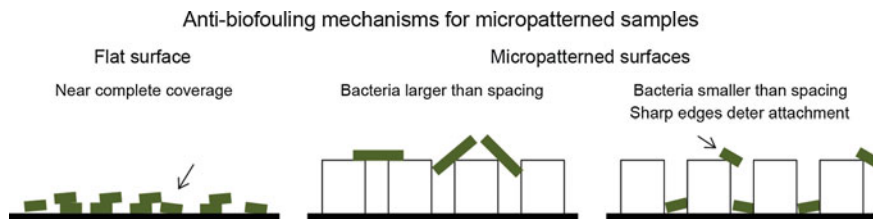
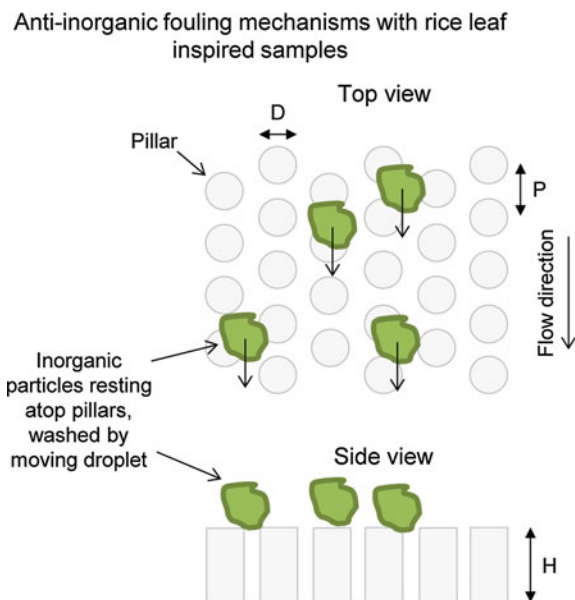


Fig. 12.21 Conceptual models of anti-biofouling mechanisms with micropatterned samples. Shown are colonization on flat and micropatterned surfaces. If the length of the microorganism is larger than the pillar spacing, it cannot invade the spacing and instead it land on top of the pillars. If the length of the microorganism is smaller than the spacing, microstructured discontinuities and sharp edges are believed to discourage colonization—where they may expire in the process of searching for an ideal landing site

location to colonize. It is believed during this process that many *E. coli* that do not attach remain metabolically active throughout the experiment or others may expire. In many cases, the *E. coli* may be able to settle in clusters and around the bases of the pillars, which provide multiple attachment points of contact.

When the microorganism concentrations are low and the incubation times are short, only a few microorganisms are able to colonize the sample surface. However, when the concentrations are high and the incubation times are long, the microorganisms eventually will cover over the pillars and create a biofilm. Nevertheless, the discontinuities found with the sharp edged micro sized pillars are demonstrated to provide antifouling benefit and extend the time at which a particular surface becomes colonized.

Fig. 12.22 Anti-inorganic fouling mechanisms with rice leaf inspired samples (adapted from Bixler and Bhushan 2014). Model shown utilizes uniformly spaced micro-sized single height pillars in a hexagonal array. Inorganic fouling may be washed away in fluid flow via self-cleaning



An illustration of anti-inorganic fouling mechanisms is shown in Fig. 12.22 (Bixler and Bhushan 2014). The schematic shows that foulers may be removed from a surface by water droplets or fluid flow when the rice and butterfly wing effect is present. Such a pattern is believed to encourage self-cleaning and directional fluid control, which is believed to provide antifouling benefit.

To summarize, there are a number of examples of micropatterned surfaces in the literature that show that, if the micro-sized feature spacing is slightly smaller than the microorganisms, they exhibit anti-biofouling. The data presented in this section shows that even if the spacing is larger, they exhibit anti-biofouling.

12.7 Closure

In this chapter, biofouling and inorganic fouling are introduced. Next, fields susceptible to fouling are summarized, followed by biofouling and inorganic fouling formation mechanism, antifouling strategies from living nature, current prevention and cleaning techniques for antifouling, and ends with demonstrations of the use of bioinspired rice leaf surfaces for anti-fouling. The data shows that micropatterned surfaces facilitate antifouling.

References

- Anonymous (1952), *Marine Fouling and its Prevention*, Woods Hole Oceanographic Institute, US Naval Institute, Annapolis, Maryland.
- Anonymous (1999), Why Is Titanium the Metal of Choice for Medical Applications from Head to Toe? International Titanium Association, Boulder, Colorado.
- Banerjee, I., Pangule, R.C., and Kane R.S. (2011), "Antifouling Coatings: Recent Developments in the Design of Surfaces That Prevent Fouling by Proteins, Bacteria, and Marine Organisms," *Adv. Mater.* **23**, 690-718
- Barthlott, W. and Neinhuis, C. (1997), "Purity of the sacred lotus, or escape from contamination in biological surfaces," *Planta* **202**, 1-8
- Bhushan, B. (2009), "Biomimetics: Lessons from Nature – an Overview," *Phil. Trans. R. Soc. A* **367**, 1445-1486
- Bhushan, B. (2010), *Springer Handbook of Nanotechnology*, 3rd Edition, Springer, New York.
- Bhushan, B. (2012), *Encyclopedia of Nanotechnology*, Vol. 1-4, Springer, New York.
- Bhushan, B. and Jung, Y.C. (2011), "Natural and Biomimetic Artificial Surfaces for Superhydrophobicity, Self-Cleaning, Low Adhesion, and Drag Reduction," *Prog. Mater. Sci.* **56**, 1-108
- Bhushan, B., Hansford, D. and Lee, K.K. (2006), "Surface modification of silicon and polydimethylsiloxane surfaces with vapor-phase-deposited ultrathin fluorosilane films for biomedical nanodevices," *J. Vac. Sci. Technol. A* **24**, 1197-1202
- Bhushan, B., Jung, Y.C. and Koch, K. (2009), "Micro-, nano- and Hierarchical Structures for Superhydrophobicity, Self-cleaning and Low Adhesion," *Phil. Trans. Roy. Soc. A* **367**, 1631-1672
- Bixler, G.D. and Bhushan, B. (2012), "Biofouling Lessons from Nature," *Phil. Trans. R. Soc. A* **370**, 2381-2417

- Bixler, G.D. and Bhushan, B. (2013a), "Fluid Drag Reduction with Shark-skin Riblet Inspired Microstructured Surfaces," *Adv. Funct. Mater.* **23**, 4507-4528.
- Bixler, G.D. and Bhushan, B. (2013b), "Fluid Drag Reduction and Efficient Self-Cleaning with Rice Leaf and Butterfly Wing Bioinspired Surfaces," *Nanoscale* **5**, 7685-7710.
- Bixler, G.D. and Bhushan, B. (2014), "Rice- and Butterfly-Wing Effect Inspired Self-Cleaning and Low Drag Micro/nanopatterned Surfaces in Water, Oil, and Air Flow," *Nanoscale* **6**, 76-96
- Bixler, G. D. and Bhushan, B. (2015), "Rice- and Butterfly-Wing Effect Inspired Low Drag and Antifouling Surfaces: A Review," (Invited), *Crit. Rev. Solid State Mater. Sci.* **40**, 1-37
- Bixler, G. D., Theiss, A., Bhushan, B., and Lee, S. C. (2014), "Anti-fouling Properties of Microstructured Surfaces Bio-inspired by Rice Leaves and Butterfly Wings," *J. Colloid Interf. Sci.* **419**, 114-133
- Bormashenko, E., Bormashenko, Y., Stein, T., Whyman, G., and Bormashenko, E. (2007), "Why Do Pigeon Feathers Repel Water? Hydrophobicity of Pennae, Cassie-Baxter Wetting Hypothesis, and Cassie-Wenzel Capillary-induced Wetting Transition," *J. Colloid Interf. Sci.* **311**, 212-216.
- Bott, T.R. (1988a), "Crystallization of Organic Materials," in *Fouling Science and Technology* (eds. Melo, L.F., Bott, T.R. and Bernardo, C.A.), pp. 275-280, Kluwer Academic Publishers, Dordrecht, The Netherlands.
- Bott, T.R. (1988b), "Crystallization Fouling – Basic Science and Models," in *Fouling Science and Technology* (eds. Melo, L.F., Bott, T.R. and Bernardo, C.A.), pp. 251-260, Kluwer Academic Publishers, Dordrecht, The Netherlands.
- Brennan, A.B., Baney, R.H., Carman, M.I., Estes, T.G., Feinberg, A.W., Wilson, L.H. and Schumacher, J.F. (2010), "Surface Topographies for Non-Toxic Bioadhesion Control," United States Patent no. 7 650 848
- Cao, L., Jones, A.K., Sikka, V.K., Wu, J. and Gao, D. (2009), "Anti-Icing Superhydrophobic Coatings," *Langmuir* **25**, 12444-12448
- Callow, M.E. (1999), "The Status and Future of Biocides in Marine Biofouling Prevention," in *Recent Advances in Marine Biotechnology* (eds. Fingerman, M., Nagabhushanam, R. and Thompson, M.F), pp. 109-126, Science Publishers, Enfield, New Hampshire.
- Callow, M.E., Pitchers, R.A. and Milne A. (1986), "The Control of Fouling by Non-Biocidal Systems," in *Algal Biofouling* (eds. Evans, L.V. and Hoagland, K.D), pp. 145-158, Elsevier Science Publishers, Amsterdam.
- Callow, M.E., Jennings, A.R., Brennan, A.B., Seegert, C.E., Gibson, A., Wilson, L., Feinberg, A., Baney, R., and Callow, J.A. (2002), "Microtopographic Cues for Settlement of Zoospores of the Green Fouling Alga *Enteromorpha*," *Biofouling* **18**, 237-245
- Carman, M.L., Estes, T.G., Feinburg, A.W., Schumacher, J.F., Wilkerson, W., Wilson, L.H., Callow, M.E., Callow, J.A. and Brennan, A.B. (2006), "Engineered Antifouling Microtopographies—Correlating Wettability with Cell Attachment," *Biofouling* **22**, 11–21
- Chan, J. and Wong, S. (eds.) (2010), *Biofouling Types, Impact and Anti-Fouling*, Nova Science Publishers, New York
- Charles, C.H., Mostler, K.M, Bartels, L.L. and Mankodi, S.M. (2004), "Comparative Antiplaque and Antigingivitis Effectiveness of an Chlorhexidine and an Essential Oil Mouth Rinse: 6-Month Clinical Trial," *J Clin Periodontal* **31**, 878-884
- Clare, A.S. and Aldred, N. (2009), "Surface Colonization by Marine Organisms and its Impact on Antifouling Research," in *Advances in Marine Antifouling Coatings and Technologies* (eds. Hellio, C. and Yebra, D.), pp. 46-79, CRC Press, Boca Raton, Florida.
- Clarkson, N. (1999), "The Antifouling Potential of Silicone Elastomer Polymers," in *Recent Advances in Marine Biotechnology* (eds. Fingerman, M., Nagabhushanam, R. and Thompson, M.F), pp. 87-108, Science Publishers, Enfield, New Hampshire.
- Cologer, C.P. (1984), "Six Year Interaction of Underwater Cleaning with Copper Based Antifouling Paints on Navy Surface Ships," *Nav. Eng. J.* **96**, 200–208
- Copisarow, M. (1945), "Marine Fouling and its Prevention," *Science* **101**, pp. 406-407
- Costerton, J.W. (ed.) (2008), *Springer Series on Biofilms*, Springer-Verlag, Berlin.

- Cui, Z. and Wan, Y. (2005), "Biofouling in Membrane Separation Systems," in *Surfaces and Interfaces for Biomaterials* (ed. Vadgama, P.), pp. 493-544, CRC Press, Boca Raton, Florida.
- Cunningham, A.B., Lennox, J.E. and Ross, R.J. (2008), *Biofilms in Industrial Environments*. Retrieved June 27, 2011, from http://biofilmbook.hypertextbookshop.com/public_version/contents/contents.html
- Dean, B. and Bhushan, B. (2010), "Shark-skin Surfaces for Fluid-Drag Reduction in Turbulent Flow: a Review," *Phil. Trans. R. Soc. A* **368**, 4775-4806
- Dror, N., Mandel, M., Hazan, Z. and Lavie, G. (2009), "Advances in Microbial Biofilm Prevention on Indwelling Medical Devices with Emphasis on Usage of Acoustic Energy," *Sensors* **9**, 2538-2554
- Epstein, N. (1988), "Particulate Fouling of Heat Transfer Surfaces: Mechanisms and Models," in *Fouling Science and Technology* (eds. Melo, L.F., Bott, T.R. and Bernardo, C.A.), pp. 143-164, Kluwer Academic Publishers, Dordrecht, The Netherlands.
- Feng, X. and Jiang, L. (2006), "Design and Creation of Superwetting/Antiwetting Surfaces," *Adv. Mater.* **18**, 3063-3078
- Fingerman, M., Nagabhushanam, R. and Thompson, M.F. (eds.) (1999), *Recent Advances in Marine Biotechnology*, Science Publishers, Inc., Enfield, New Hampshire.
- Finlay, J.A., Callow, M.E., Schultz, M.P., Swain, G.W., and Callow, J.A. (2002), "Adhesion Strength of Settled Spores of the Green Alga *Enteromorpha*," *Biofouling* **18**, 251-256
- Fletcher, J.T., Finlay, J.A., Callow, M.E., Callow, J.A., and Ghadiri, M.R. (2007), "A Combinatorial Approach to the Discovery of Biocidal Six-Residue Cyclic L-alanine Peptides Against the Bacteria Methicillin-Resistant *Staphylococcus aureus* (MRSA) and *E. coli* and the Biofouling Algae *Ulva linza* and *Navicula perminuta*," *Chem. Eur. J.* **13**, 4008-4013
- Flemming, H.C., Wingender, J., Moritz, R., Borchard, W. and Mayer, C. (1999), "Physio-chemical Properties of Biofilms – A Short Review," in *Biofilms in the Aquatic Environment* (eds. Keevil, C.W., Godfree, A., Holt, D. and Dow, C), pp. 1-12, The Royal Society of Chemistry, Cambridge.
- Flemming, H.C., Szewzyk, U. and Griebe, T. (eds.) (2000), *Biofilms Investigative Methods and Applications*, Technomic Publishing Co., Lancaster, Pennsylvania.
- Gordon, D.P. and Mawatari, S.F. (1992), *Atlas of Marine-fouling Bryozoa of New Zealand Ports and Harbours*, Miscellaneous Pub, New Zealand Oceanographic Institute.
- Griebe, T. and Flemming, H.C. (2000), "Rotating Annular Reactors for Controlled Growth of Biofilms," in *Biofilms Investigative Methods and Applications* (eds. Flemming, H.C., Szewzyk, U. and Griebe, T.), pp. 1-22, Technomic Publishing Co, Inc., Lancaster, Pennsylvania.
- Harder, T. and Yee, L.H. (2009), "Bacterial Adhesion and Marine Fouling," in *Advances in Marine Antifouling Coatings and Technologies* (eds. Hellio, C. and Yebra, D.), pp. 113-131, CRC Press, Boca Raton, Florida.
- Hellio, C. and Yebra, D. (eds.) (2009), *Advances in Marine Antifouling Coatings and Technologies*, CRC Press, Boca Raton, Florida.
- Herzberg, M. and Elimelech, M. (2007), "Biofouling of reverse osmosis membranes: Role of biofilm-enhanced osmotic pressure," *J. of Membrane Science* **295**, 11-20
- Hoipkemeier-Wilson, L., Schumacher, J.F., Carman, M.L., Gibson, A.L., Feinberg, A.W., Callow, M.E., Finlay, J.A., Callow, J.A., and Brennan, A.B. (2004), "Antifouling Potential of Lubricious, Micro-engineered, PDMS Elastomers against Zoospores of the Green Fouling Alga *Ulva (Enteromorpha)*," *Biofouling* **20**, 53-63
- Jones, G. (2009), "The Battle Against Marine Biofouling: a Historical Review," in *Advances in Marine Antifouling Coatings and Technologies* (eds. Hellio, C. and Yebra, D.), pp. 19-45, CRC Press, Boca Raton, Florida.
- Keevil, C.W., Godfree, A., Holt, D. and Dow, C. (eds.) (1999), *Biofilms in the Aquatic Environment*, The Royal Society of Chemistry, Cambridge, UK.
- Kesal, A. and Liedert, R. (2007), "Learning from Nature: Non-Toxic Biofouling Control by Shark Skin Effect," *Comp. Biochem. Physiol. A* **146**, S130

- Kim, S.H., Kwak, S.Y., Sohn, B.H. and Park, T.H. (2003), "Design of TiO₂ nanoparticle self-assembled aromatic polyamide thin-film-composite (TFC) membrane as an approach to solve biofouling problem," *J. of Membrane Science* **211**, 157-165
- Koch, K. and Barthlott, W. (2009), "Superhydrophobic and Superhydrophilic Plant Surfaces: an Inspiration for Biomimetic Materials," *Phil. Trans. R. Soc.* **367**, 1487-1509
- Koch, K., Bhushan, B., and Barthlott, W. (2008), "Diversity of Structure, Morphology, and Wetting of Plant Surfaces," (Invited) *Soft Matter* **4**, 1943-1963.
- Koch, K., Bhushan, B., and Barthlott, W. (2009), "Multifunctional Surface Structures of Plants: An Inspiration for Biomimetics," (Invited) *Prog. Mater. Sci.* **54**, 137-178.
- Lee, W., Jin, M.K., Yoo, W.C. and Less, J.K. (2004), "Nanostructuring of a Polymeric Substrate with Well-Defined Nanometer-Scale Topography and Tailored Surface Wettability," *Langmuir* **20**, 7665-7669
- Lim, A.L. and Bai, R. (2003), "Membrane fouling and cleaning in microfiltration of activated sludge wastewater," *J. Membrane Sci.* **216**, 279-290
- LoVetri, K., Gawande, P.V., Yakandawala, N. and Madhyastha S. (2010), "Biofouling and Anti-fouling of Medical Devices," in *Biofouling Types, Impact and Anti-Fouling* (eds. Chan, J. and Wong, S.), pp. 105-128, Nova Science Publishers, New York.
- Ma, H., Bowman, C.N., and Davis, R.H. (2000), "Membrane fouling reduction by backpulsing and surface modification," *J. Membrane Sci* **173**, 191-200
- Marrie, T.J. and Costerton, J.W. (1984), "Morphology of Bacterial Attachment to Cardiac Pacemaker Leads and Power Packs," *J. Clin. Microbiol.* **19**, 911-914
- Melo, L.F., Bott, T.R. and Bernardo, C.A. (eds.) (1988), *Fouling Science and Technology*, Kluwer Academic Publishers, Dordrecht, The Netherlands.
- Menton, D. (2008), "The Seeing Eye," *AnswersMagazine.com*, July-Sept. 76-79.
- Meuler, A.J., Smith, J.D., Varanasi, K.K., Mabry, J.M., McKinley, G.H., Cohen, R.E. (2010), "Relationships between Water Wettability and Ice Adhesion," *ACS Appl. Mat. Interf.* **2**, 3100-3110
- Monroe, D. (2007), "Looking for Chinks in the Armor of Bacterial Biofilms," *PLoS Biol* **5**, 2458-2461
- Neinhuis, C. and Barthlott, W. (1997), "Characterization and Distribution of Water-repellent, Self-cleaning Plant Surfaces," *Annals of Botany* **79**, 667-677
- Palacio, M.L.B. and Bhushan, B. (2012), "Bioadhesion: A Review of Concepts and Applications," (Invited), *Phil. Trans. Royal Soc. A* **370**, 2321-2347
- Pritchard, A.M. (1988), "Deposition of Hardness Salts," in *Fouling Science and Technology* (eds. Melo, L.F., Bott, T.R. and Bernardo, C.A.), pp. 261-274, Kluwer Academic Publishers, Dordrecht, The Netherlands.
- Railkin, A.I. (2004), *Marine Biofouling Colonization Processes and Defenses*, CRC Press, Boca Raton, Florida.
- Ralston, E. and Swain, G. (2009), "Bioinspiration – the Solution for Biofouling Control?" *Bioinsp. Biomim.* **4**, 1-9
- Ray, D.L. (ed.) (1959), *Marine Boring and Fouling Organisms*, University of Washington Press, Seattle.
- Scardino, A.J. (2009), "Surface Modification Approaches to Control Marine Biofouling," in *Advances in Marine Antifouling Coatings and Technologies* (eds. Hellio, C. and Yebra, D.), pp. 664-692, CRC Press, Boca Raton, Florida.
- Scardino, A.J., Guenther, J., and de Nys, R. (2008), "Attachment point theory revisited: the fouling response to a microtextured matrix," *Biofouling* **24**, 45-53
- Schulz, M.J., Shanov, V.N. and Yun, Y. (eds.) (2009), *Nanomedicine Design of Particles, Sensors, Motors, Implants, Robots, and Devices*, Artech House, Boston.
- Schumacher, J.F., Aldred, N., Callow, M.E., Finlay, J.A., Callow, J.A., Clare, A.S. and Brennan, A.B. (2007a), "Species-Specific Engineered Antifouling Topographies: Correlations between the Settlement of Algal Zoospores and Barnacle Cyprids," *Biofouling* **23**, 307- 317

- Schumacher, J.F., Carman, M.L., Estes, T.G., Feinberg, A.W., Wilson, L.H., Callow, M.E., Callow, J.A., Finlay, J.A., and Brennan, A.B. (2007b), "Engineered antifouling Microtopographies – effect of feature size, geometry, and roughness on settlement of zoospore of the green alga *Ulva*," *Biofouling* **23**(1), 55-62
- Sharma, N., Charles, C.H., Lynch, M.C., Qaqish, J., McGuire, J.A., Galustians, J.G. and Kumar, L.D. (2004), "Adjunctive Benefit of an Essential Oil-Containing Mouth Rinse in Reducing Plaque and Gingivitis in Patients Who Brush and Floss Regularly," *J American Dental Assoc* **135**, 496-504
- Sharma, S., Popat, K.C. and Desai, T.A. (2007), "Design and Biological Applications of Nanostructured Poly(Ethylene Glycol) Films," in *Nanotechnology in Biology and Medicine Methods, Devices, and Applications* (ed. Vo-Dinh, T.), pp. 39-1, CRC Press, Boca Raton, Florida.
- Sheng, X., Ting, Y.P. and Pehkonen, S.O. (2010), "Force Measurements of Bacterial Adhesion to Metals Using Cell Probe in Atomic Force Microscopy," in *Biofouling Types, Impact and Anti-Fouling* (eds. Chan, J. and Wong, S.), pp. 129-154, Nova Science Publishers, New York.
- Shircliff, M. and Leid, J.G. (eds.) (2009), *The Role of Biofilms in Device-Related Infections*, Springer-Verlag, Berlin.
- Simoës, M., Simoës, L.C. and Vieira, M.J. (2010), "A Review of Current and Emergent Biofilm Control Strategies," *LWT – Food Science and Technology* **43**, 573-583
- Somerscales, E.F.C. and Knudsen, J.G. (eds.) (1981), *Fouling of Heat Transfer Equipment*, Hemisphere Publishing Corporation, Washington.
- Stoodley, P., Sauer, K., Davies, D.G. and Costerton, J.W. (2002), "Biofilms as Complex Differentiated Communities," *Annu. Rev. Microbiol.*, **56**, 187–209
- Trinidad, A., Ibanez, A., Gomez, D., Garcia-Berrocal, J.R. and Ramierz-Camacho, R. (2010), "Application of Environmental Scanning Electron Microscopy for Study of Biofilms in Medical Devices," *Microscopy: Science, Technology, Applications and Education*, **1**, 204-210
- Vadgama, P. (ed) (2005), *Surfaces and Interfaces for Biomaterials*, CRC Press, Boca Raton, Florida.
- Venkatesan, R. and Murthy, P.S. (2008), "Macrofouling Control in Power Plants", in *Springer Series on Biofilms* (ed. Costerton, J.W.), pp. 265-290, Springer-Verlag, Berlin.
- Vladkova, T. (2007), "Surface Engineering for Non-Toxic Biofouling Control," *J. Univ. Chem. Technol. Metallurgy* **43**, 239-256
- Vladkova, T. (2008), "Surface Modification Approach to Control Biofouling", in *Springer Series on Biofilms* (ed. Costerton, J.W.), pp. 135-162, Springer-Verlag, Berlin.
- Vleugels, I.R. (2006), "Multi-Functional Coating Solution," *Euprofile, Public Service Review: European Union* **18**, 1-2
- Vo-Dinh, T. (ed.) (2007), *Nanotechnology in Biology and Medicine*, CRC Press, Boca Raton, Florida.
- Wagner, T., Neinhuis, C. and Barthlott, W. (1996), "Wettability and Contaminability of Insect Wings as a Function of Their Surface Sculptures," *Acta Zoologica* **77**, 213-225
- Walker, J., Surman, S. and Jass, J. (eds.) (2000), *Industrial Biofouling Detection, Prevention and Control*, Wiley, New York.
- Wang, Y. and Bhushan, B. (2015), "Wear-Resistant and Antismudge Superoleophobic Coating on Polyethylene Terephthalate Substrate Using SiO₂ Nanoparticles," *ACS Appl. Mater. Interf.* **7**, 743-755
- Willemsen, P. (2005), "Biofouling in European Aquaculture: is there an easy solution," TNO Industrial Technology.
- Yen, J. (2010), "Marine Dynamics," *Bulletproof Feathers How Science Uses Nature's Secrets to Design Cutting-Edge Technology* (Allen, R., Ed.), pp. 22-43, University of Chicago Press, Chicago.
- Zodrow, K., Brunet, L., Mahendra, S., Li, D. and Zhang, A. (2009), "Polysulfone ultrafiltration membranes impregnated with silver nanoparticles show improved biofouling resistance and virus removal," *Water Research* **43**, 715-723

Chapter 13

Gecko Adhesion

13.1 Introduction

The leg attachment pads of several animals are capable of attaching to and detaching from a variety of surfaces and are used for locomotion, even on vertical walls or across the ceiling (Gorb 2001; Bhushan 2007). These include many insects, spiders, and lizards. Biological evolution has led to the optimization of their leg attachment systems. This dynamic attachment ability is referred to as reversible adhesion or smart adhesion (Bhushan et al. 2006). Many insects (e.g., beetles and flies) and spiders have been the subject of investigative interest. However, the attachment pads of geckos have been the most widely studied because they have the highest body mass and exhibit the most versatile and effective adhesive known in nature. Therefore, this chapter will be concerned primarily with gecko adhesion.

There are over 1000 species of geckos (Kluge 2001; Han et al. 2004) that have attachment pads of varying morphology (Ruibal and Ernst 1965). However, the Tokay gecko (*Gekko gekko*) native to south-east Asia, has been the main focus of scientific research (Hiller 1968; Irschick et al. 1996; Autumn 2006) because of its size and availability. The Tokay gecko is the second largest gecko species, reaching lengths of approximately 0.3–0.4 m and 0.2–0.3 m for males and females, respectively. They have a distinctive blue or gray body with orange or red spots and can weigh up to 300 g (Tinkle 1992).

Almost 2500 years ago, the ability of the gecko to “run up and down a tree in any way, even with the head downwards,” was observed by Aristotle (Aristotle/Thompson 1918, Book IX, Part 9). Even though the adhesive ability of geckos has been known since the time of Aristotle, little was understood about this phenomenon until the late nineteenth century when the microscopic hairs covering the toes of the gecko were first noted. In the 1950s, electron microscopy enabled scientists to view the complex hierarchical morphology that covers the skin on the

gecko's toes. Scientific studies have been conducted to determine the factors that allow the gecko to adhere to and detach from surfaces at will, including surface structure (Ruibal and Ernst 1965; Russell 1975, 1986; Williams and Peterson 1982; Schleich and Kästle 1986; Irschick et al. 1996; Autumn and Peattie 2002; Arzt et al. 2003); the mechanisms of adhesion (Wagler 1830; Simmermacher 1884; Schmidt 1904; Hora 1923; Dellit 1934; Ruibal and Ernst 1965; Hiller 1968; Gennaro 1969; Stork 1980; Autumn et al. 2000, 2002; Bergmann and Irschick 2005; Huber et al. 2005b); and adhesion strength (Hiller 1968; Irschick et al. 1996; Autumn et al. 2000; Arzt et al. 2003; Huber et al. 2005a, b). Modeling the gecko attachment system as a system of springs (Bhushan et al. 2006; Kim and Bhushan 2007a, b, c, 2008) has provided valuable insight into adhesion enhancement. van der Waals forces are widely accepted in literature as the dominant adhesion mechanism used by hierarchical attachment systems. Capillary forces created by humidity naturally present in the air can further increase the adhesion force generated by the spatulae (Kim and Bhushan 2008). Both experimental and theoretical work supports these adhesion mechanisms.

There is great interest among the scientific community to study further the characteristics of gecko feet. It is hoped that this information could be applied to the production of micro/nanosurfaces capable of recreating the adhesion forces generated by these lizards (Bhushan 2007). Common man-made adhesives such as tape or glue involve the use of wet adhesives that permanently attach two surfaces. However, replication of the characteristics of gecko feet would enable the development of a superadhesive surface capable of clean, dry adhesion. They have the potential for use in everyday objects such as adhesive tapes, fasteners, and toys and in high technology, such as microelectronic and space applications. These structures also can be used in prosthetics and surgical masks, and can bind to components in microelectronics without the high heat associated with various soldering processes. These structures will never dry out in a vacuum—a common problem in aerospace applications. Replication of the dynamic climbing and peeling ability of geckos could find use in the treads of wall-climbing robots.

This chapter first introduces various hairy attachment systems. Then, it introduces the Tokay Gecko and its construction, and some details on adhesion, peeling, and self-cleaning mechanisms. The next section describes the attachment mechanisms, followed by adhesion measurements and data, adhesion modeling, and adhesion data base of fibrillar structures. The last section presents various fabrication techniques to create structures in the lab.

13.2 Hairy Attachment Systems

There are generally two kinds of attachment pads. The first kind are relatively smooth pads, so-called arolia and euplantulae, which are soft and deformable and are found in some amphibians, such as tree frogs, torrent frogs, cockroaches,

grasshoppers, and bugs. They are able to attach to and move over wet or even flooded environments without falling (Federle et al. 2006). Tree frog toe attachment pads consist of a hexagonal array of flat-topped epidermal cells about 10 μm in size separated by approximately 1 μm wide mucus-filled channels. The flattened surface of each cell consists of submicron array of nanopillars or pegs of approximately 100–400 nm diameter. The toe pads are made of an extremely soft, nonhomogeneous material. The epithelium itself has an effective elastic modulus of about 15 MPa, equivalent to silicone rubber. The pads are permanently wetted by mucus secreted from glands that open into the channels between epidermal cells. They attach to mating surfaces by wet adhesion (Federle et al. 2006). They are capable of climbing on wet rocks even when water is flowing over the surface (Barnes et al. 2002). During walking, squeezing of the mucus glands is expected to occur rapidly. Torrent frogs can resist sliding even on flooded surfaces. The surface of their toe pad is similar to that of tree frogs, with some changes in the structure to handle the large flow of water (Ohler 1995).

The second kind of attachment pads are the hairy types, which consist of long, deformable setae, and are found in many insects (e.g., beetles, flies), spiders, and lizards. The microstructures used by beetles, flies, spiders, and geckos have similar structures and can be seen in Fig. 13.1a. As the size (mass) of the creature increases, the radius of the terminal attachment elements decreases. This allows a greater number of setae to be packed into an area, increasing the linear dimension of contact and the adhesion strength. Arzt et al. (2003) determined that the density of the terminal attachment elements, ρ_A , per m^{-2} strongly increases with increasing body mass, m , in g. In fact, a master curve can be fitted for all the different species (Fig. 13.1b),

$$\log \rho_A = 13.8 + 0.669 \cdot \log m \quad (13.1)$$

The correlation coefficient of the master curve is equal to 0.919. Beetles and flies have the largest attachment pads and the lowest density of terminal attachment elements. Spiders have highly refined attachment elements that cover its legs. Geckos have both the highest body mass and greatest density of terminal elements (spatulae). Spiders and geckos can generate high dry adhesion, whereas beetles and flies increase adhesion by secreting liquid stored generally within a spongy layer of cuticle and delivered at the contacting surface through a system of porous channels (Gorb 2001; Arzt et al. 2003; Kesel et al. 2003). Note that in the smooth attachment system discussed earlier, the secretion is essential for attachment.

Peattie and Full (2007) have revisited the scaling of terminal attachment elements with the body mass using a phylogenetic approach. In their work, a larger set of species (81) over a wider range of body mass and setal morphology were considered. They found that fiber morphology is better predicted by evolutionary history and adhesion mechanism (dry or wet) than by body mass.

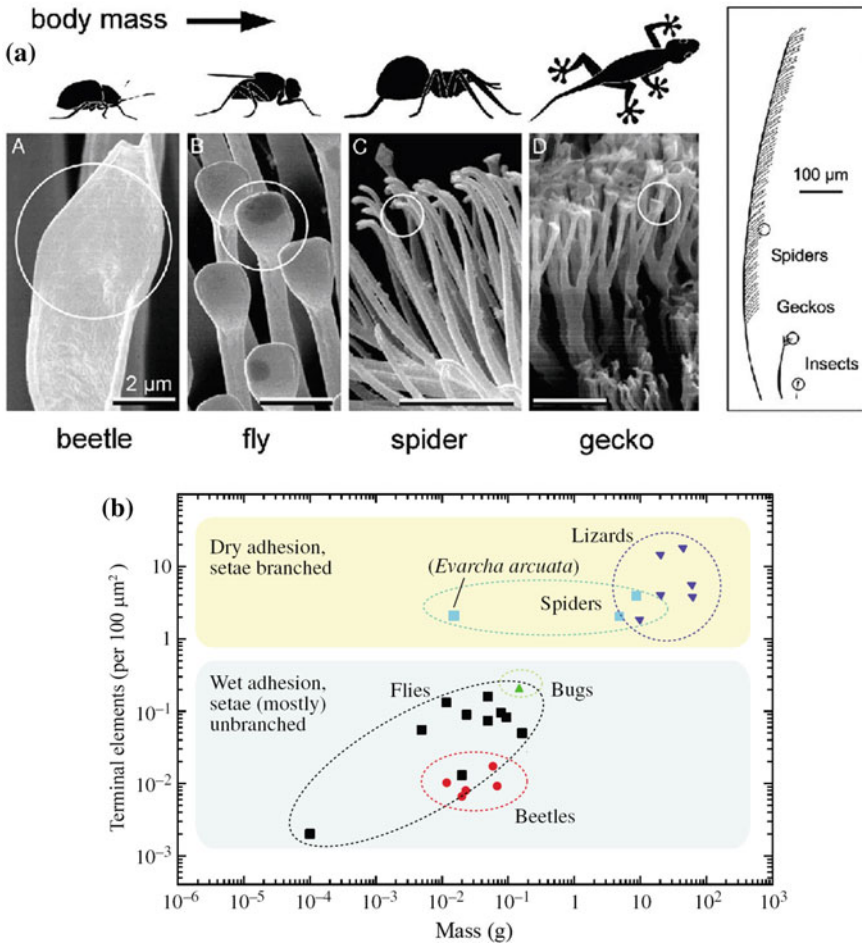


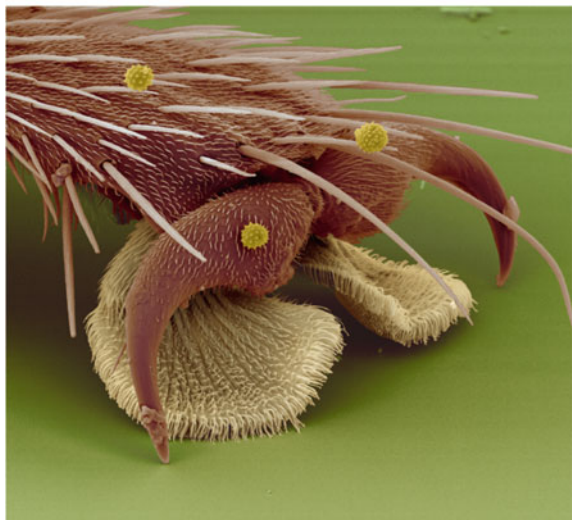
Fig. 13.1 **a** Terminal elements of the hairy attachment pads of a beetle, fly, spider, and gecko shown at two different scales (Arzt et al. 2003), and **b** the dependence of terminal element density on body mass (Federle 2006). Data are from Arzt et al. (2003) and Kesel et al. (2003)

Figure 13.2 shows the scanning electron micrographs (SEM) of the end of the legs of two flies—the fruit fly (*Drosophila melanogaster*) and the syrphid fly. The fruit fly uses setae with flattened tips (spatulae) on the two hairy rods for attachment to smooth surfaces and two front claws for attachment to rough surfaces. The front claws are also used for locomotion. The syrphid fly uses setae on the legs for attachment. In both cases, fluid is secreted at the contacting surface to increase adhesion.

Fig. 13.2 SEM micrographs of the end of the legs of fruit fly (*Drosophila melanogaster*) and syrphid fly (Gorb 2001)



End of the legs of fruit fly (*Drosophila melanogaster*)



End of the leg of syrphid fly

13.3 Tokay Gecko

13.3.1 Construction of Tokay Gecko

The explanation for the adhesion properties of gecko feet can be found in the surface morphology of the skin on the toes of the gecko. The skin is comprised of a complex hierarchical structure of lamellae, setae, branches, and spatulae (Ruibal and Ernst 1965). Figure 13.3 shows various SEM micrographs of a gecko foot, showing the hierarchical structure down to the nanoscale. Figure 13.4 shows a schematic of the structure, and Table 13.1 summarizes the surface characteristics. The gecko attachment system consists of an intricate hierarchy of structures beginning with lamellae, soft ridges 1–2 mm in length (Ruibal and Ernst 1965) that are located on the attachment pads (toes) that compress easily so that contact can be made with rough bumpy surfaces. Tiny curved hairs known as setae extend from the lamellae with a density of approximately 14,000 per square millimeter (Schleich and Kästle 1986). These setae are typically 30–130 μm in length, 5–10 μm in diameter (Ruibal and Ernst 1965; Hiller 1968; Russell 1975; Williams and Peterson 1982), and are composed primarily of β -keratin (Maderson 1964; Russell 1986)

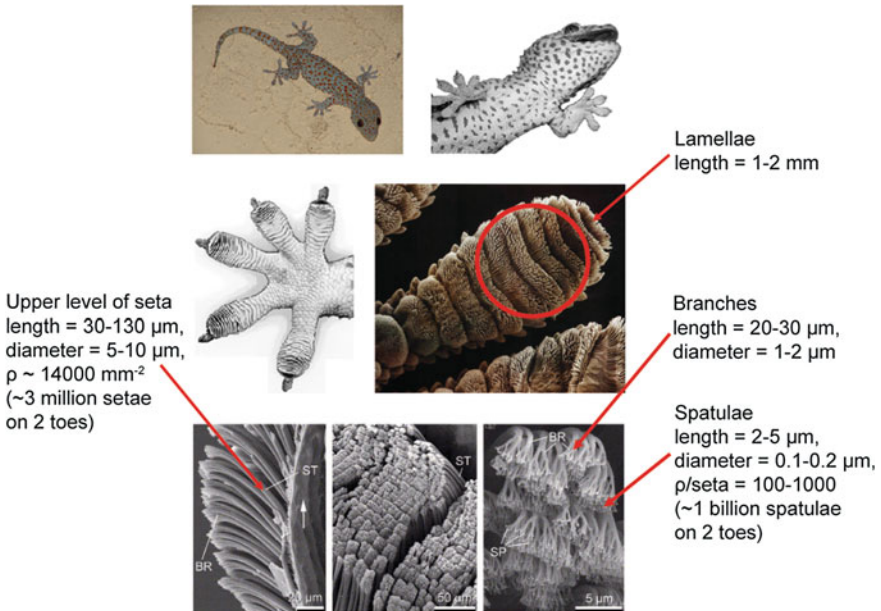


Fig. 13.3 The hierarchical structures of a Tokay gecko foot: a gecko foot (Autumn et al. 2000) and a gecko toe (Autumn 2006). The two feet with an area of 220 mm^2 consist of about three million setae on their toes that branch off into about three billion spatulae. Scanning electron microscope (SEM) micrographs of the setae and the spatulae are shown in the *bottom row* (Gao et al. 2005). *ST* seta, *SP* spatula, *BR* branch

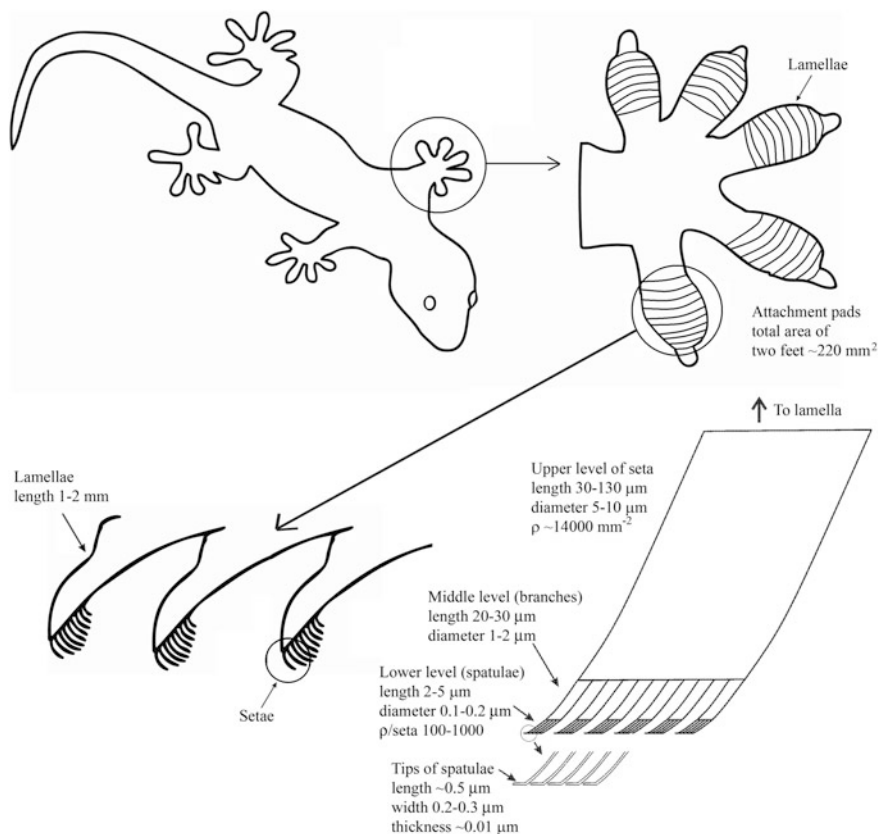


Fig. 13.4 Schematic drawings of a Tokay gecko including the overall body, one foot, a cross-sectional view of the lamellae, and an individual seta. ρ represents number of spatulae

with some α -keratin component (Rizzo et al. 2006). Each seta divides into branches that separate into spatulae, with 100 to 1000 total spatulae per seta (Ruibal and Ernst 1965; Hiller 1968). The spatulae are typically 2–5 μm in length with a diameter of 0.1–0.2 μm (Ruibal and Ernst 1965), and they form the points of contact with the surface. The tips of the spatulae are approximately 0.2–0.3 μm in width (Ruibal and Ernst 1965), 0.5 μm in length, and 0.01 μm in thickness (Persson and Gorb 2003) and garner their name from their resemblance to a spatula.

The attachment pads on two feet of the Tokay gecko have an area of about 220 mm^2 . About three million setae on their toes that branch off into about three billion spatulae on two feet can produce a clinging ability of about 20 N (vertical force required to pull a lizard down a nearly vertical (85°) surface) (Irschick et al. 1996) and allow them to climb vertical surfaces at speeds over 1 m/s with the capability to attach and detach their toes on the order of 10 ms. In isolated setae, a 2.5 μN preload yielded adhesion of 20–40 μN , and thus the adhesion coefficient,

Table 13.1 Physical dimensions of fibrillar structures on Tokay gecko feet and measured adhesive force data. Young's modulus of surface material, keratin = 1–20 GPa^{a,b}

Component	Size	Density	Adhesive force
Seta	30–130 ^{c,f} /5–10 ^{c,f} length/diameter (μm)	~ 14,000 ^{h,i} setae/mm ²	194 μN ^j (in shear) ~ 20 μN ^j (normal)
Branch	20–30 ^c /1–2 ^c length/diameter (μm)	–	–
Spatula	2–5 ³ /0.1–0.2 ^{c,g} length/diameter (μm)	100–1000 ^{c,d} spatulae per seta	–
Tip of spatula	~ 0.5 ^{c,g} /0.2–0.3 ^{c,f} /~ 0.01 ^g length/width/thickness (μm)	–	11 nN ^k (normal)

^aRussell (1986); ^bBertram and Gosline (1987); ^cRuibal and Ernst (1965); ^dHiller (1968); ^eRussell (1975); ^fWilliams and Peterson (1982); ^gPersson and Gorb (2003); ^hSchleich and Kästle (1986); ⁱAutumn and Peattie (2002); ^jAutumn et al. (2000); ^kHuber et al. (2005a)

which represents the strength of adhesion as a function of preload, ranges from 8 to 16 (Autumn et al. 2002).

13.3.2 Adhesion Enhancement by Division of Contacts and Multilevel Hierarchical Structure

Typical rough, rigid surfaces are able to make intimate contact with a mating surface only over a very small portion of the perceived apparent area of contact. In fact, the real area of contact is typically two to six orders of magnitude less than the apparent area of contact (Bhushan 2011, 2013a, b). Autumn et al. (2002) proposed that divided contacts serve as a means for increasing adhesion. The surface energy approach can be used to calculate adhesion force in a dry environment in order to calculate the effect of division of contacts. If the tip of a spatula is considered as a hemisphere with radius, R , adhesion force of a single contact, F_{ad} , based on the so-called JKR (Johnson-Kendall-Roberts) theory (Johnson et al. 1971) is given as,

$$F_{ad} = \frac{3}{2} \pi W_{ad} R \quad (13.2)$$

where W_{ad} is the work of adhesion (units of energy per unit area). Equation (13.2) shows that the adhesion force of a single contact is proportional to a linear dimension of the contact. For a constant area divided into a large number of contacts or setae, n , the radius of a divided contact, R_1 , is given by $R_1 = R/\sqrt{n}$ (self-similar scaling) (Arzt et al. 2003). Therefore, the adhesion force of (13.2) can be modified for multiple contacts such that,

$$F'_{ad} = \frac{3}{2} \pi W_{ad} \left(\frac{R}{\sqrt{n}} \right) n = \sqrt{n} F_{ad} \quad (13.3)$$

where F'_{ad} is the total adhesion force from the divided contacts. Thus the total adhesive force is simply the adhesion force of a single contact multiplied by the square root of the number of contacts.

For contact in a humid environment, the meniscus (or capillary) forces further increase the adhesion force (Bhushan 2011, 2013a, b). The attractive meniscus force (F_m) consists of a contribution by both Laplace pressure and surface tension; discussed later in this chapter (Orr et al. 1975; Bhushan 2013b). The contribution by Laplace pressure is directly proportional to the meniscus area. The other contribution is from the vertical component of surface tension around the circumference. This force is proportional to the circumference, as is the case for the work of adhesion (Bhushan 2013b). Going through the analysis presented earlier, one can show that the contribution from the component of surface tension increases with splitting into a larger number of contacts. It increases linearly with the square root of the number of contacts n (self-similar scaling) (Bhushan 2007; Cai and Bhushan 2007, 2008).

$$(F'_m)_{surface\ tension} = \sqrt{n} (F_m)_{surface\ tension} \quad (13.4a)$$

where F'_m is the force from the divided contacts, and F_m is the force of an individual contact. This component of meniscus force is significant if the meniscus radius is very small and the contact angles are relatively large.

During separation of two surfaces, a viscous force, F_v , needs to be applied. F_v of the divided contacts is given as (Cai and Bhushan 2007, 2008),

$$F'_v = F_v/n \quad (13.4b)$$

where F'_v is the force from the divided contacts, and F_v is the force of an individual contact.

The models just presented only consider contact with a flat surface. Multilevel hierarchical structure of the gecko provides compliance and conformability to rough surfaces in order to achieve high adhesion. The flexibility of the body provides conformability at the cm scale. Several toes on the feet provide conformability independently at the several mm scale. Lamellae on the bottom surfaces of the toes provide conformability at the mm scale. The setae on the lamellae provide conformability at the several μm scale. The tips of the setae are divided into spatulae which provide conformability at the few to several hundred nm scale. To summarize, on natural rough surfaces the compliance and adaptability of the hierarchical structure of gecko setae allows for greater contact with a natural rough surface than a non-branched attachment system (Sitti and Fearing 2003; Bhushan et al. 2006; Kim and Bhushan 2007a, b, c, 2008). Modeling of the contact between gecko setae and rough surfaces is discussed in detail in Sect. 13.6.

Table 13.2 Young's modulus of gecko skin and other materials for comparison

Material	Young's modulus
β -keratin, mostly present in gecko skin	1–20 GPa
Steel	210 GPa
Cross-linked rubber	1 MPa
Consumer adhesive tape (uncrosslinked rubber)	1 kPa

Material properties also play an important role in adhesion. A soft material is able to achieve greater contact with a mating surface than a rigid material. Although gecko skin is primarily comprised of β -keratin, a stiff material with a Young's modulus in the range of 1–20 GPa (Russell 1986; Bertram and Gosline 1987), the effective modulus of the setal arrays on gecko feet is about 100 kPa (Autumn et al. 2006a), which is approximately four orders of magnitude lower than the bulk material. Young's modulus of the gecko skin is compared with that of various materials in Table 13.2. Humans have selected a relatively soft and compliant material for consumer adhesive tape to increase the contact area for high adhesion. Nature has selected a relatively stiff material for the setae to avoid clinging to each other. The non-orthogonal attachment angle of the seta increases the bending stiffness, and the division of contacts and hierarchical structure provide high adhesion. By combining optimal surface structure and material properties, nature has created an evolutionary superadhesive.

13.3.3 Peeling

Although geckos are capable of producing large adhesion forces, they retain the ability to remove their feet from an attachment surface at will by peeling action. The orientation of the spatulae facilitates peeling. Autumn et al. (2000) were the first to experimentally show that the adhesion force of gecko setae is dependent on the three-dimensional orientation as well as the preload applied during attachment (see later in the chapter). Because of this, geckos have developed a complex foot motion during walking. First, the toes are carefully uncurled during detachment. The maximum adhesion occurs at an attachment angle of 30°—the angle between a seta and mating surface. The gecko is then able to peel its foot from surfaces one row of setae at a time by changing the angle at which its setae contact a surface. At an attachment angle greater than 30°, the gecko will detach from the surface. Two diagonally opposite feet participate in the movement.

Shah and Sitti (2004) determined the theoretical preload required for adhesion as well as the adhesion force generated for setal orientations of 30°, 40°, 50°, and 60°. Consider a solid material (elastic modulus, E , Poisson's ratio, ν) to make contact with the rough surface described by,

$$f(x) = H \sin^2\left(\frac{\pi x}{\lambda}\right) \quad (13.5)$$

where H is the amplitude, and λ is the wavelength of the roughness profile. For a solid adhesive block to achieve intimate contact with the rough surface, neglecting surface forces, it is necessary to apply a compressive stress, σ_c (Jagota and Bennison 2002),

$$\sigma_c = \frac{\pi EH}{2\lambda(1 - \nu^2)} \quad (13.6)$$

Equation (13.6) can be modified to account for fibers oriented at an angle, θ . The preload required for contact is summarized in Fig. 13.5a. As the orientation angle decreases, so does the required preload. Similarly, adhesion strength is influenced by fiber orientation. As seen in Fig. 13.5b, the greatest adhesion strength occurs at $\theta = 30^\circ$.

Gao et al. (2005) created a finite element model of a single gecko seta in contact with a surface. A tensile force was applied to the seta at various angles, θ , as shown in Fig. 13.5c. Maximum adhesion again occurs at an angle of 30° . For forces applied at an angle of less than 30° , the dominant failure mode was sliding. In comparison, the dominant failure mode for forces applied at angles greater than 30° was detachment. This verifies the results of Autumn et al. (2000) that detachment occurs at attachment angles greater than 30° .

Tian et al. (2006) studied the attachment and detachment process in detail. Schematics of various configurations are shown in Fig. 13.6. In their natural configuration, shown in Fig. 13.6a, the spatula pads are at an angle of about 30° to the seta shaft and are approximately normal to the spatula shafts. This corresponds to a weak adhesion force. When geckos roll their toes inward and grip them, shown in Fig. 13.6b, the pulling angle θ_s of the seta shaft to the substrate will range from 0 to 30° , whereas the pulling angles θ of the spatula shafts to the substrate will range from 0 to 90° . Pulling in of the toes leads to smaller θ and θ_s , with a larger number of spatulae in contact with the substrate. This results in both higher friction and adhesion at the seta shaft. During the rolling out of the toes to detach from a substrate, shown in Fig. 13.6c, the setae move back to their initial free state with $\theta_s \sim 30^\circ$ and $\theta \sim 90^\circ$.

Pesika et al. (2007) developed a tape-peeling model based on the geometry of the peeling zone. They considered geometrical changes within the peel zone. The increased radius of curvature, R , increases the length of the peel zone, which in turn increases the peel force, F , in the peel direction. Figure 13.7a shows a schematic of the peel zone for two peel regimes: peel angles between cases I and II (constant peel-zone regime) and between cases II and III (variable peel-zone regime). In the constant peel-zone regime, the geometry of the peel zone (i.e., length of the peel zone and the curvature of the tape backing) remains constant while the peel angle, θ , is changed. In contrast, in the variable peel-zone regime, the length of the peel zone and curvature of the tape backing both increase as the peel angle, θ , is

Fig. 13.5 Contact mechanics results for the effect of fiber orientation on **a** preload required for contact, and **b** adhesive pressure for roughness amplitudes ranging from 0 to 2500 nm (Shah and Sitti 2004). **c** Finite element analysis of the adhesive force of a single seta as a function of pull direction (Gao et al. 2005)

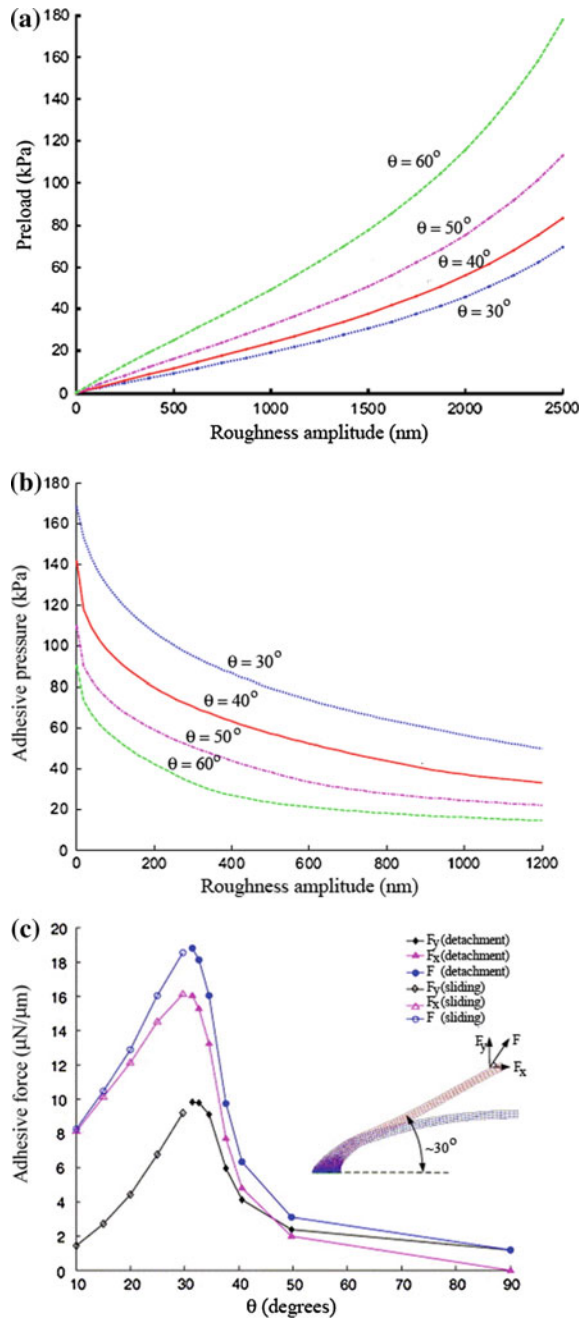


Fig. 13.6 Sketches of attachment and detachment of a single seta by **a** approaching the substrate, **b** rolling (or gripping) in, and **c** rolling (or peeling) out of the toes. The image in **c left** is from the left back foot (Tian et al. 2006)

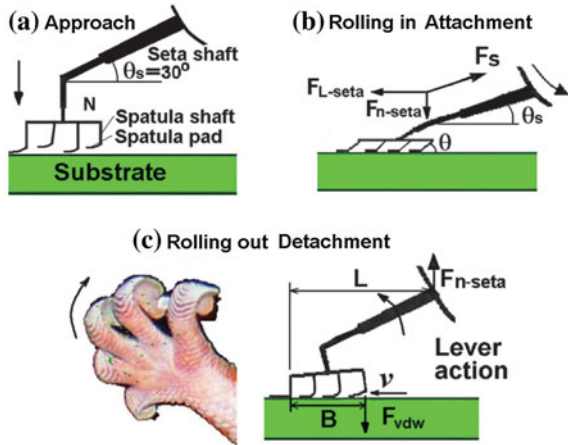
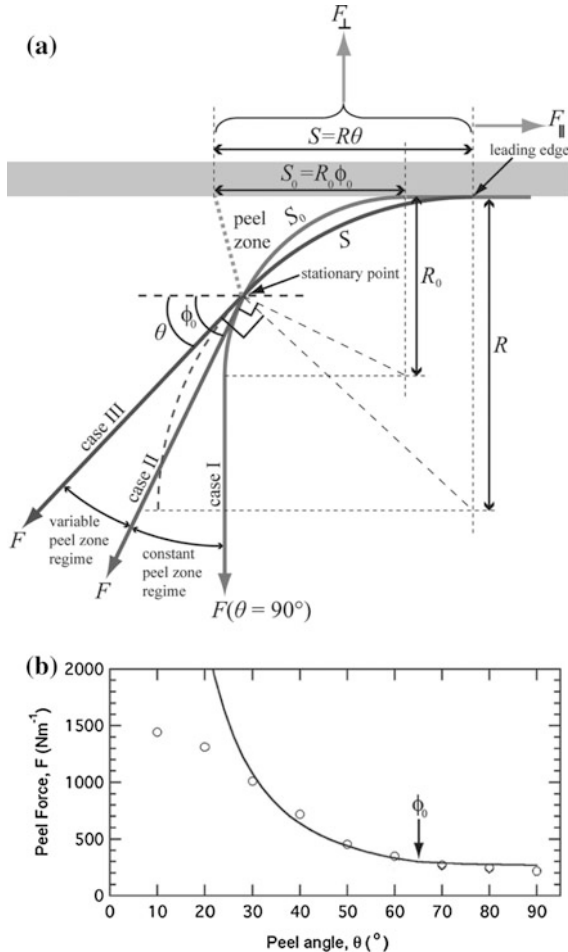


Fig. 13.7 a Schematic illustration of the peel zone showing the two peel regimes: constant peel-zone regime and variable peel-zone regimes, and **b** plots of predicted (solid line) and measured (data for a tape) peel force, F , as a function of peel angle, θ (Pesika et al. 2007)



changed. Figure 13.7b shows a plot of predicted value of peel force, F , as a function of the peel angle, θ . During detachment, θ increases, resulting in a lower peel force (Fig. 13.5c). The measured peel force for a model tape over glass surface as a function of peel angle is also plotted. The measured data correlate well with the predicted values.

13.3.4 Self Cleaning

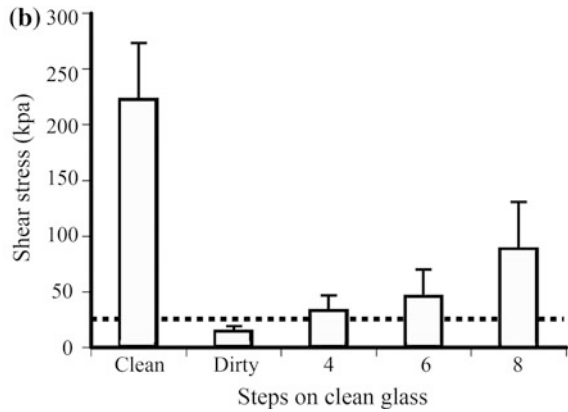
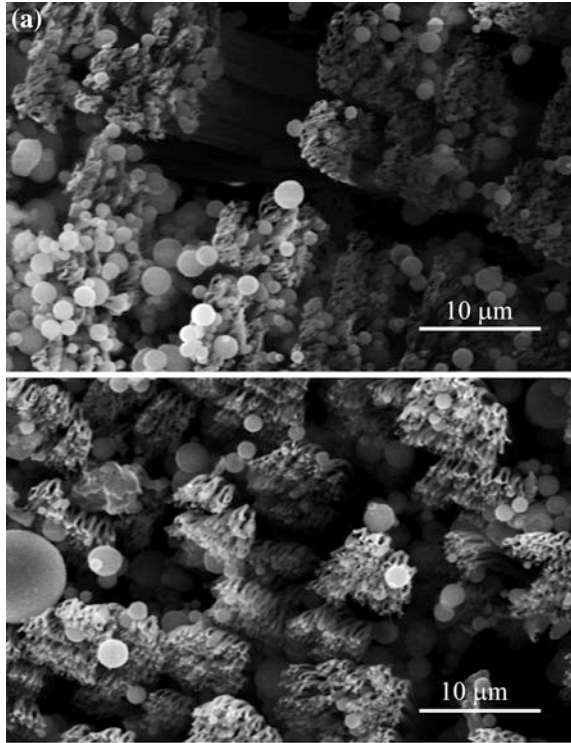
Natural contaminants (dirt and dust) and man-made pollutants are unavoidable and have the potential to interfere with the clinging ability of geckos. Particles found in the air are typically less than 10 μm in diameter, while those found on the ground can often be larger (Hinds 1982; Jaenicke 1998). Intuitively, it seems that the great adhesion strength of gecko feet would cause dust and other particles to become trapped in the spatulae, and that they would have no way of being removed without some sort of manual cleaning action on behalf of the gecko. However, geckos are not known to groom their feet like beetles (Stork 1983), nor do they secrete sticky fluids to remove adhering particles like ants (Federle et al. 2002) and tree frogs (Hanna and Barnes 1991), yet they retain adhesive properties. One potential source of cleaning is during the time when the lizards undergo molting, or the shedding of the superficial layer of epidermal cells. However, this process only occurs approximately once per month (Van der Kloot 1992). If molting were the sole source of cleaning, the gecko would rapidly lose its adhesive properties as it was exposed to contaminants in nature (Hansen and Autumn 2005).

Hansen and Autumn (2005) tested the hypothesis that gecko setae become cleaner with repeated use—a phenomenon known as self-cleaning. The cleaning ability of gecko feet was first tested experimentally by applying 2.5 μm radius silica-alumina ceramic microspheres to clean setal arrays. Figure 13.8a shows the setal arrays immediately after dirtying and after five simulated steps. It is noted that a significant fraction of the particles has been removed after five steps. The maximum shear stress that these “dirty” arrays could withstand was measured using a sensor. After each step that the gecko took, the shear stress was once again measured. As seen in Fig. 13.8b, after four steps, the gecko foot was clean enough to withstand its own body weight.

In order to understand this cleaning process, substrate-particle interactions must be examined. The interaction energy between a dust particle, a wall, and spatulae can be modeled as shown in Fig. 13.9 (Hansen and Autumn 2005). The interaction energy between a spherical dust particle and the wall, W_{pw} , can be expressed as (Israelachvili 1992),

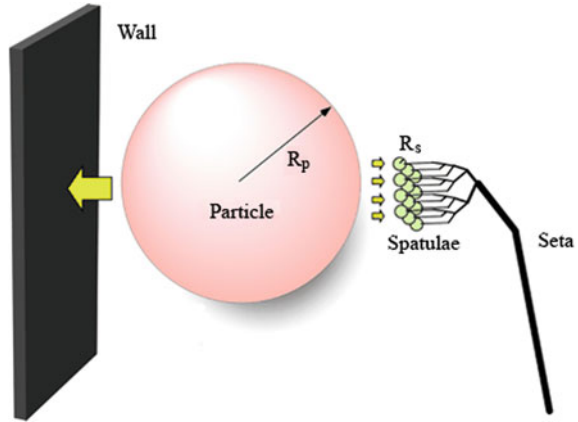
$$W_{pw} = \frac{-H_{pw}R_p}{6D_{pw}} \quad (13.7)$$

Fig. 13.8 **a** SEM image of spatulae after dirtying with microspheres (*top*) and after five simulated steps (*bottom*), **b** mean shear stress exerted by a gecko on a surface after dirtying. The *dotted line* represents sufficient recovery to support weight by a single toe (Hansen and Autumn 2005)



where p and w refer to the particle and wall, respectively. H is the Hamaker constant, R_p is the radius of the particle, and D_{pw} is the separation distance between the particle and the wall. Similarly, the interaction energy between a spherical dust particle and a spatula, s , assuming that the spatula tip is spherical is (Israelachvili 1992),

Fig. 13.9 Model of interactions between gecko spatulae of radius R_s , a spherical dirt particle of radius R_p , and a planar wall that enable self-cleaning (Hansen and Autumn 2005)



$$W_{ps} = \frac{-H_{ps}R_pR_s}{6D_{ps}(R_p + R_s)} \quad (13.8)$$

The ratio of the two interaction energies, Z , can be expressed as

$$Z = \frac{W_{pw}}{W_{ps}} = \left(1 + \frac{R_p}{R_s}\right) \frac{H_{pw}D_{ps}}{H_{ps}D_{pw}} \quad (13.9)$$

When the energy required to separate a particle from the wall is greater than that required to separate it from a spatula ($Z > 1$), self-cleaning will occur. For small contaminants ($R_p < 0.5 \mu\text{m}$), there are not enough spatulae available to adhere to the particle. For larger contaminants, the curvature of the particles makes it impossible for enough spatulae to adhere to it. As a result, Hansen and Autumn (2005) concluded that self-cleaning should occur for all spherical spatulae interacting with all spherical particles.

13.4 Attachment Mechanisms

When asperities of two solid surfaces are brought into contact with each other, chemical and/or physical attractions occur. The force developed that holds the two surfaces together is known as adhesion. In a broad sense, adhesion is considered to be either physical or chemical in nature (Bikerman 1961; Zisman 1963; Houwink and Salomon 1967; Israelachvili 1992; Bhushan 1996, 2010, 2011, 2013a, b). Chemical interactions such as electrostatic attraction charges (Schmidt 1904), as well as intermolecular forces (Hiller 1968) including van der Waals and capillary forces, have all been proposed as potential adhesion mechanisms in gecko feet. Others have hypothesized that geckos adhere to surfaces through the secretion of

sticky fluids (Wagler 1830; Simmermacher 1884), suction (Simmermacher 1884), increased frictional force (Hora 1923), and microrinterlocking (Dellit 1934).

Through experimental testing and observations conducted since the mid 1800s, many potential adhesive mechanisms have been eliminated. Observation has shown that geckos lack any glands capable of producing sticky fluids (Wagler 1830; Simmermacher 1884), ruling out the secretion of sticky fluids as a potential adhesive mechanism. Furthermore, geckos are able to create large adhesive forces normal to a surface. Since friction only acts parallel to a surface, the attachment mechanism of increased frictional force has been ruled out. Dellit (1934) experimentally ruled out suction and electrostatic attraction as potential adhesive mechanisms. Experiments carried out in vacuum did not show a difference between the adhesive force at low pressures compared to ambient conditions. Since adhesive forces generated during suction are based on pressure differentials, which are insignificant under vacuum, suction was rejected as an adhesive mechanism (Dellit 1934). Additional testing used X-ray bombardment to create ionized air in which electrostatic attraction charges would be eliminated. It was determined that geckos were still able to adhere to surfaces in these conditions, and therefore, electrostatic charges could not be the sole cause of attraction (Dellit 1934). Autumn et al. (2000) demonstrated the ability of a gecko to generate large adhesive forces when in contact with a molecularly smooth SiO₂ microelectromechanical system (MEMS) semiconductor. Since surface roughness is necessary for microrinterlocking to occur, it has been ruled out as a mechanism of adhesion. Two mechanisms, van der Waals forces and capillary forces, remain as the potential sources of gecko adhesion. These attachment mechanisms are described in detail in the following sections.

13.4.1 *van der Waals Forces*

van der Waals bonds are secondary bonds that are weak in comparison to other physical bonds such as covalent, hydrogen, ionic, and metallic bonds. Unlike other physical bonds, van der Waals forces are always present, regardless of separation. They are effective from very large separations (~ 50 nm) down to atomic separation (~ 0.3 nm). The van der Waals force per unit area between two parallel surfaces, f_{vdW} , is given by (Hamaker 1937; Israelachvili and Tabor 1972; Israelachvili 1992),

$$f_{vdW} = \frac{H}{6\pi D^3} \quad \text{for } D < 30 \text{ nm} \quad (13.10)$$

where H is the Hamaker constant, and D is the separation between surfaces.

Hiller (1968) showed experimentally that the surface energy of a substrate is responsible for gecko adhesion. One potential adhesion mechanism would then be van der Waals forces (Stork 1980; Autumn et al. 2000). Assuming van der Waals forces to be the dominant adhesion mechanism used by geckos, the adhesion force of a gecko can be calculated. Typical values of the Hamaker constant range from

4×10^{-20} to 4×10^{-19} J (Israelachvili 1992). In calculation, the Hamaker constant is assumed to be 10^{-19} J, the surface area of a spatula is taken to be 2×10^{-14} m² (Ruibal and Ernst 1965; Williams and Peterson 1982; Autumn and Peattie 2002), and the separation distance between the spatula and contact surface is estimated to be 0.6 nm. This equation yields the force of a single spatula to be about 0.5 μ N. By applying the surface characteristics of Table 13.1, the maximum adhesion force of a gecko is 150–1500 N for varying spatula density of 100–1000 spatulae per seta. If an average value of 550 spatulae/seta is used, the adhesion force of a single seta is approximately 270 μ N, which is in agreement with the experimental value obtained by Autumn et al. (2000), which will be discussed later in this chapter.

Another approach to calculate adhesion force is to assume that spatulae are cylinders that terminate in hemispherical tips. By using (13.2) and assuming that the radius of each spatula is about 100 nm and that the surface energy is expected to be 50 mJ/m² (Arzt et al. 2003), the adhesive force of a single spatula is predicted to be 0.02 μ N. This result is an order of magnitude lower than the first approach calculated for the higher value of A . For a lower value of 10^{-20} J for the Hamaker constant, the adhesive force of a single spatula is comparable to that obtained using the surface energy approach.

Several experimental results favor van der Waals forces as the dominant adhesive mechanism, including temperature testing (Bergman and Irschick 2005) and adhesion force measurements of a gecko seta with both hydrophilic and hydrophobic surfaces (Autumn et al. 2000). This data will be presented later in this chapter.

13.4.2 Capillary Forces

It has been hypothesized that capillary forces that arise from liquid mediated contact could be a contributing or even the dominant adhesive mechanism used by gecko spatulae (Hiller 1968; Stork 1980). Experimental adhesion measurements (presented later in this chapter) conducted on surfaces with different hydrophobicities and at various humidities (Huber et al. 2005b) as well as numerical simulations (Kim and Bhushan 2008) support this hypothesis as a contributing mechanism. During contact, any liquid that wets or has a small contact angle on surfaces will condense from vapor in the form of an annular-shaped capillary condensate. Due to the natural humidity present in the air, water vapor will condense to liquid on the surface of bulk materials. During contact this will cause the formation of adhesive bridges (menisci) due to the proximity of the two surfaces and the affinity of the surfaces for condensing liquid (Zimon 1969; Fan and O'Brien 1975; Phipps and Rice 1979).

In the adhesion model with capillarity by Kim and Bhushan (2008), the tip of the spatula in a single contact was assumed as spherical; see Fig. 13.10. The total

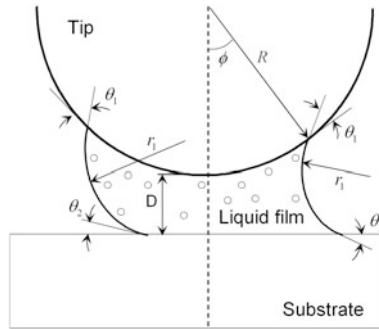


Fig. 13.10 Schematic of a sphere on a plane at distance D with a liquid film in between, forming menisci. In this figure, R is the tip radius, ϕ is the filling angle, θ_1 and θ_2 are contact angles on sphere and plane, respectively, and r_1 and r_2 are the two principal radii of the curved surface in two orthogonal planes (Kim and Bhushan 2008)

adhesion force between a spherical tip and a plane consists of the capillary force and the solid-to-solid interaction. Capillary force can be divided into two components: the Laplace force F_L and the surface tension force F_s , such that the total capillary force F_c ,

$$F_c = F_L + F_s \quad (13.11)$$

The Laplace force is caused by the pressure difference across the interface of a curved liquid surface (Fig. 13.10) and depends on the pressure difference multiplied by the meniscus area, which can be expressed as (Orr et al. 1975),

$$F_L = -\pi\kappa\gamma R^2 \sin^2 \phi \quad (13.12)$$

where γ is the surface tension of the liquid, R is the tip radius, ϕ is the filling angle, and κ is the mean curvature of the meniscus. From the Kelvin equation (Israelachvili 1992), which is the thermal equilibrium relation, the mean curvature of the meniscus can be determined as,

$$\kappa = \frac{\Re T}{V\gamma} \ln\left(\frac{p}{p_o}\right) \quad (13.13)$$

where \Re is the universal gas constant, T is the absolute temperature, V is the molecular volume, p_o is the saturated vapor pressure of the liquid at T , and p is the ambient pressure acting outside the curved surface (p/p_o is the relative humidity). Orr et al. (1975) formulated the mean curvature of a meniscus between a sphere and a plane in terms of elliptic integrals. The filling angle ϕ can be calculated from the expression just mentioned and (13.13) using the iteration method. Then, the Laplace force is calculated at a given environment using (13.12).

The surface tension of the liquid results in the formation of a curved liquid-air interface. The surface tension force acting on the sphere is (Orr et al. 1975),

$$F_s = 2\pi R\gamma \sin \phi \sin(\theta_1 + \phi) \quad (13.14)$$

where θ_1 is the contact angle on the sphere.

Hence, the total capillary force on the sphere is

$$F_c = \pi R\gamma \{2 \sin \phi \sin(\theta_1 + \phi) - \kappa R \sin^2 \phi\} \quad (13.15)$$

The effect of capillarity on gecko adhesion results will be presented later in this chapter.

13.5 Adhesion Measurements and Data

Experimental measurements of the adhesion force of a single gecko seta (Autumn et al. 2000) and single gecko spatula (Huber et al. 2005a) have been made. The effect of the environment, including temperature (Losos 1990; Bergmann and Irschick 2005) and humidity, (Huber et al. 2005b) has been studied. Some of the data has been used to understand the adhesion mechanism used by the gecko attachment system—van der Waals or capillary forces. The majority of experimental results point towards van der Waals forces as the dominant mechanism of adhesion (Autumn et al. 2000; Bergmann and Irschick 2005). Some research suggests that capillary forces can be a contributing adhesive factor (Huber et al. 2005b; Kim and Bhushan 2008).

13.5.1 Adhesion Under Ambient Conditions

Two feet of a Tokay gecko are capable of producing about 20 N of adhesive force with a pad area of about 220 mm² (Irschick et al. 1996). Assuming that there are about 14,000 setae per mm², the adhesion force from a single hair should be approximately 7 μN. It is likely that the magnitude is actually greater than this value because it is unlikely that all setae are in contact with the mating surface (Autumn et al. 2000). Setal orientation greatly influences adhesive strength. This dependency was first noted by Autumn et al. (2000). It was determined that the greatest adhesion occurs at 30°. In order to determine the adhesion mechanism(s) used by gecko feet, it is important to know the adhesion force of a single seta. Hence, the adhesion force of gecko foot-hair has been the focus of several investigations (Autumn et al. 2000; Huber et al. 2005a).

13.5.1.1 Adhesion Force of a Single Seta

Autumn et al. (2000) used both a microelectromechanical (MEMS) force sensor and a wire as a force gauge to determine the adhesion force of a single seta. The MEMS force sensor is a dual-axis atomic force microscope (AFM) cantilever with independent piezoresistive sensors which allows simultaneous detection of vertical and lateral forces (Chui et al. 1998). The wire force gage consisted of an aluminum bonding wire that displaced under a perpendicular pull. Autumn et al. (2000) discovered that setal force actually depends on the three-dimensional orientation of the seta, as well as the preloading force applied during initial contact. Setae that were preloaded vertically to the surface exhibited only one-tenth of the adhesive force ($0.6 \pm 0.7 \mu\text{N}$) compared to setae that were pushed vertically and then pulled horizontally to the surface ($13.6 \pm 2.6 \mu\text{N}$). The dependence of the adhesion force of a single gecko spatula on perpendicular preload is illustrated in Fig. 13.11. The adhesion force increases linearly with the preload, as expected (Bhushan 1996, 2013a, b). The maximum adhesion force of a single gecko foot-hair occurred when the seta was first subjected to a normal preload and then slid $5 \mu\text{m}$ along the contacting surface. Under these conditions, adhesion force measured $194 \pm 25 \mu\text{N}$ (~ 10 atm adhesive pressure).

13.5.1.2 Adhesive Force of a Single Spatula

Huber et al. (2005a) used atomic force microscopy to determine the adhesion force of an individual gecko spatulae. A seta with four spatulae was glued to an AFM tip. The seta was then brought in contact with a surface and a compressive preload of 90 nN was applied. The force required to pull the seta off of the surface was then measured. As seen in Fig. 13.12, there are two distinct peaks on the graph—one at 10 nN and the other at 20 nN. The first peak corresponds to one of the four spatulae adhering to the

Fig. 13.11 Adhesive force of a single gecko seta as a function of applied preload. The seta was first pushed perpendicularly against the surface and then pulled parallel to the surface (Autumn et al. 2000)

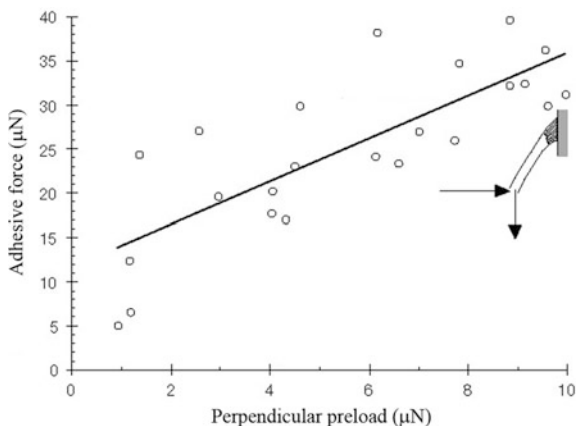
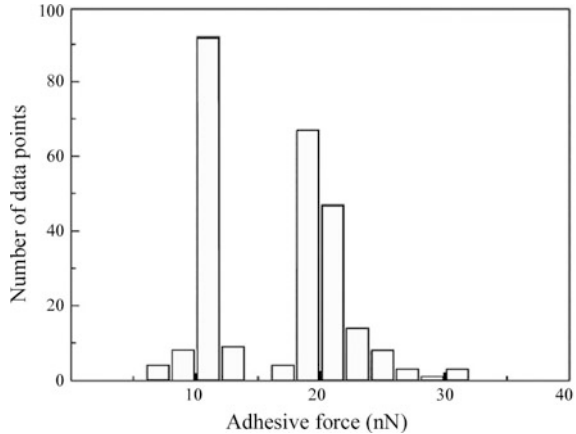


Fig. 13.12 Adhesive force of a single gecko spatula. The peak at 10 nN corresponds to the adhesive force of one spatula and the peak at 20 nN corresponds to the adhesive force of two spatulae (Huber et al. 2005a)

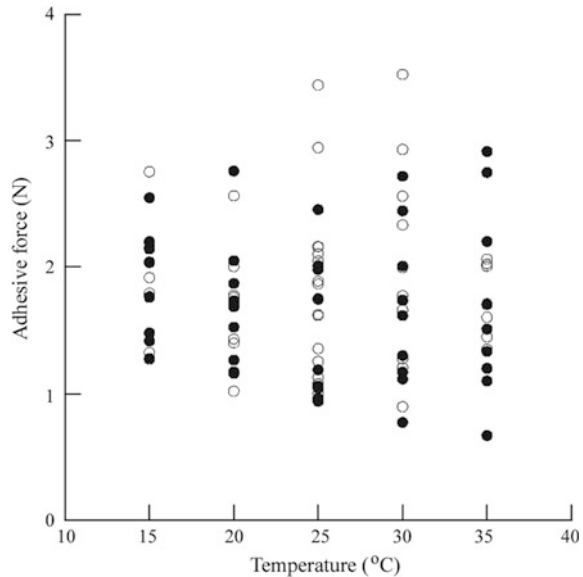


contact surface while the peak at 20 nN corresponds to two of the four spatulae adhering to the contact surface. The average adhesion force of a single spatula was found to be 10.8 ± 1 nN. The measured value is in agreement with the measured adhesive strength of an entire gecko (on the order of 10^9 spatulae on a gecko).

13.5.2 Effects of Temperature

Environmental factors are known to affect several aspects of vertebrate function, including speed of locomotion, digestion rate, and muscle contraction. As a result, several studies have been completed to investigate environmental impact on these functions. Relationships between the environment and other properties such as adhesion are far less studied (Bergmann and Irschick 2005). Only two known studies exist that examine the effect of temperature on the clinging force of the gecko (Losos 1990; Bergmann and Irschick 2005). Losos (1990) examined the adhesion ability of large live geckos at temperatures up to 17 °C. Bergmann and Irschick (2005) expanded upon this research for body temperatures ranging from 15 to 35 °C. The geckos were incubated until their body temperature reached a desired level. The clinging ability of these animals was then determined by measuring the maximum exerted force by the geckos as they were pulled off a custom-built force plate. The clinging force of a gecko for the experimental test range is plotted in Fig. 13.13. It was determined that variation in temperature is not statistically significant in the adhesion force of a gecko. From these results, it was concluded that the temperature independence of adhesion supports the hypothesis of clinging as a passive mechanism (i.e. van der Waals forces). Both studies only measured the overall clinging ability on the macroscale. There have not been any investigations into the effects of temperature on the clinging ability of a single seta on the microscale, and therefore testing in this area would be extremely important.

Fig. 13.13 Adhesive force of a gecko as a function of temperature (Bergmann and Irschick 2005)



13.5.3 Effects of Humidity

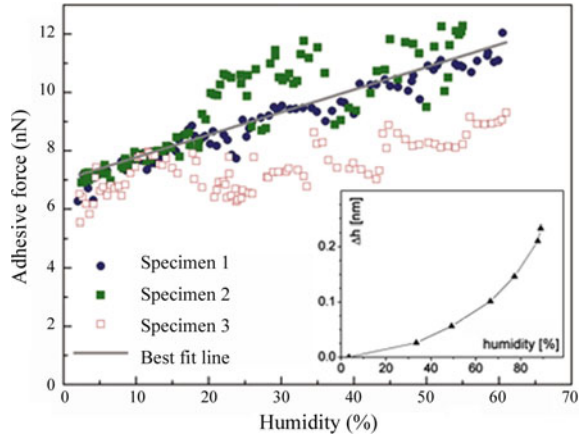
Huber et al. (2005b) employed similar methods to Huber et al. (2005a) (discussed previously in this chapter) in order to determine the adhesive force of a single spatula at varying humidity. Measurements were made using an AFM placed in an air-tight chamber. The humidity was adjusted by varying the flow rate of dry nitrogen into the chamber. The air was continuously monitored with a commercially available hygrometer. All tests were conducted at ambient temperature.

As seen in Fig. 13.14, even at low humidity, adhesion force is large. An increase in humidity further increases the overall adhesion force of a gecko spatula. The pull-off force roughly doubled as the humidity was increased from 1.5 to 60 %. This humidity effect can be explained in two possible ways: (1) by standard capillarity or (2) by a change of the effective short-range interaction due to absorbed monolayers of water. In other words, the water molecules increase the number of van der Waals bonds that are made. Based on this data, van der Waals forces are the primary adhesion mechanism, and capillary forces are a secondary adhesive mechanism.

13.5.4 Effects of Hydrophobicity

To further test the hypothesis the capillary forces play a role in gecko adhesion, the spatular pull-off force was determined for contact with both hydrophilic and hydrophobic surfaces. As seen in Fig. 13.15a, the capillary adhesion theory predicts

Fig. 13.14 Humidity effects on spatular pull-off force (*inset*). The increase in water film thickness on a Si wafer with increasing humidity (Huber et al. 2005b)



that a gecko spatula will generate a greater adhesion force when in contact with a hydrophilic surface as compared to a hydrophobic surface. However, the van der Waals adhesion theory predicts that the adhesion force between a gecko spatula and a surface will be the same regardless of the hydrophobicity of the surface (Autumn et al. 2002). Figure 13.15b shows the shear stress of a whole gecko and adhesive force of a single seta on hydrophilic and hydrophobic surfaces. The data shows that the adhesion values are the same on both surfaces. This supports the van der Waals prediction of Fig. 13.15a. Huber et al. (2005b) found that the hydrophobicity of the attachment surface had an effect on the adhesion force of a single gecko spatula as shown in Fig. 13.15c. These results show that adhesion force has a finite value for a superhydrophobic surface, and increases as the surface becomes hydrophilic. It is concluded that van der Waals forces are the primary mechanism, and capillary forces further increase the adhesion force generated.

13.6 Adhesion Modeling of Fibrillar Structures

With regard to the natural living conditions of the animals, the mechanics of gecko attachment can be separated into two parts: the mechanics of adhesion of a single contact with a flat surface, and an adaptation of a large number of spatulae to a natural, rough surface. Modeling of the mechanics of adhesion of spatulae to a smooth surface, in the absence of meniscus formation, was developed by Autumn et al. (2002), Jagota and Bennison (2002) and Arzt et al. (2003). As discussed previously in this chapter, the adhesion force of multiple contacts F'_{ad} can be increased by dividing the contact into a large number (n) of small contacts, while the nominal area of the contact remains the same, $F'_{ad} \sim \sqrt{n}F_{ad}$. However, this model only considers contact with a flat surface. On natural, rough surfaces, the

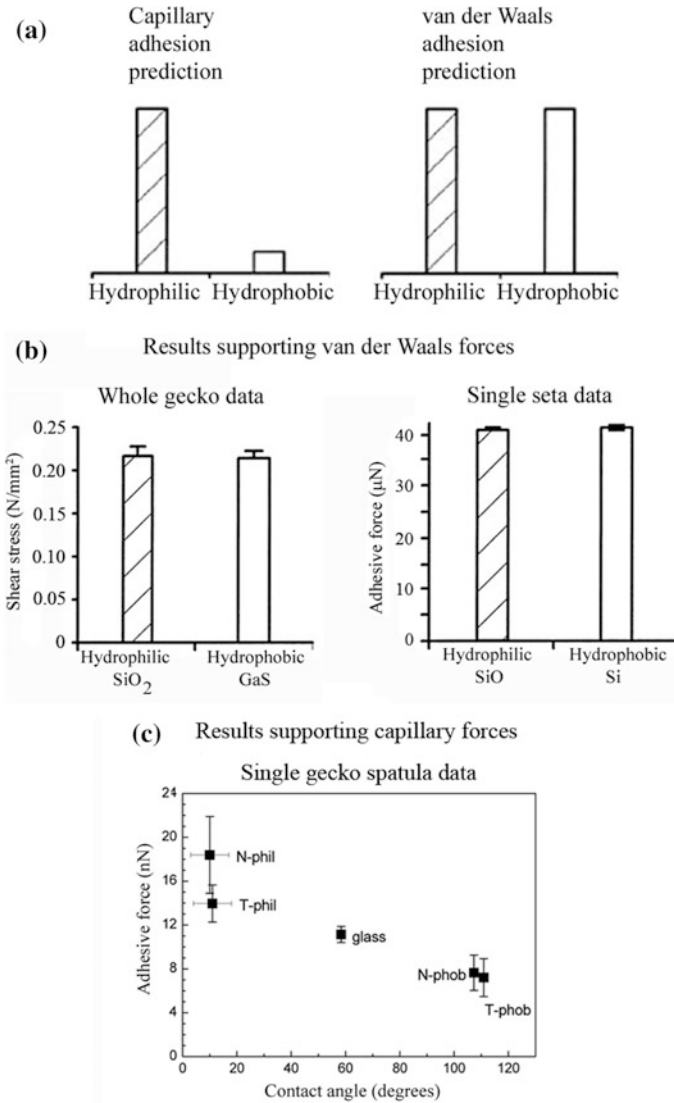


Fig. 13.15 **a** Capillary and van der Waals adhesion predictions for the relative magnitude of the adhesive force of gecko setae with hydrophilic and hydrophobic surfaces (Autumn et al. 2002). **b** Results of adhesion testing for a whole gecko and single seta with hydrophilic and hydrophobic surfaces (Autumn et al. 2002) and **c** results of adhesive force testing of a single gecko spatula with surfaces with different contact angles (Huber et al. 2005b)

compliance and adaptability of setae are the primary sources of high adhesion. The hierarchical structure of gecko setae allows for a greater contact with a natural, rough surface than a non-branched attachment system (Sitti and Fearing 2003).

Table 13.3 Geometrical size, calculated stiffness, and typical densities of branches of seta for Tokay gecko (Kim and Bhushan 2007a)

Level of seta	Length (μm)	Diameter (μm)	Bending stiffness ^a (N/m)	Typical density (#/mm ²)
III upper	75	5	2.908	14×10^3
II middle	25	1	0.126	–
I lower	2.5	0.1	0.0126	$1.4\text{--}14 \times 10^6$

^aFor elastic modulus of 10 GPa with load applied at 60° to spatula long axis

Bhushan et al. (2006) and Kim and Bhushan (2007a, b, c, 2008) have approximated a gecko seta in contact with random rough surfaces using a hierarchical spring model. Each level of springs in their model corresponds to a level of seta hierarchy. The upper level of springs corresponds to the thicker part of gecko seta, the middle spring level corresponds to the branches, and the lower level of springs corresponds to the spatulae. The upper level is the thickest branch of the seta. It is 75 μm in length and 5 μm in diameter. The middle level, referred to as a branch, has a length of 25 μm and a diameter of 1 μm . The lower level, called a spatula, is the thinnest branch with a length of 2.5 μm and a diameter of about 0.1 μm (Table 13.3). Autumn et al. (2000) showed that the optimal attachment angle between the substrate and a gecko seta is 30° in the single seta pull-off experiment. This finding is supported by the adhesion models of setae as cantilever beams (Shah and Sitti 2004; Gao et al. 2005) (see Sect. 13.3.3 for more details). Therefore, θ was fixed at 30° in the studies by Bhushan et al. (2006) and Kim and Bhushan (2007a, b, c, 2008) presented below.

13.6.1 Single Spring Contact Analysis

In their analysis, Bhushan et al. (2006) and Kim and Bhushan (2007a, b, c, 2008) assumed the tip of the spatula in a single contact to be spherical. The springs on every level of hierarchy have the same stiffness as the bending stiffness of the corresponding branches of seta. If the beam is oriented at an angle θ to the substrate and the contact load F is aligned normal to the substrate, its components along and tangential to the direction of the beam, $F \cos \theta$ and $F \sin \theta$, give rise to bending and compressive deformations, δ_b and δ_c , respectively, as (Young and Budynas 2001),

$$\delta_b = \frac{F \cos \theta l_m^3}{3EI}, \quad \delta_c = \frac{F \sin \theta l_m}{A_c E} \quad (13.16)$$

where $I = \pi R_m^4/4$ and $A_c = \pi R_m^2$ are the moments of inertia of the beam and the cross-sectional area, respectively, and l_m and R_m are the length and the radius of seta branches, respectively, and m is the level number. The net displacement, δ_\perp normal to the substrate, is given by,

$$\delta_{\perp} = \delta_c \sin \theta + \delta_b \cos \theta \quad (13.17)$$

Using (13.16) and (13.17), the stiffness of seta branches, k_m , is calculated as (Glassmaker et al. 2004),

$$k_m = \frac{\pi R_m^2 E}{l_m \sin^2 \theta \left(1 + \frac{4l_m^2 \cot^2 \theta}{3R_m^2}\right)} \quad (13.18)$$

For an assumed elastic modulus, E , of seta material of 10 GPa with a load applied at an angle of 60° to the spatulae long axis, Kim and Bhushan (2007a) calculated the stiffness of every level of seta, as given in Table 13.3.

In the model, both the tips of a spatula and the asperity summits of the rough surface are assumed to be spherical with a constant radius (Bhushan et al. 2006). As a result, a single spatula adhering to a rough surface was modeled as the interaction between two spherical tips. Because β -keratin has a high elastic modulus (Russell 1986; Bertram and Gosline 1987), the adhesion force between two round tips was calculated according to the Derjaguin-Muller-Toporov (DMT) theory (Derjaguin et al. 1975) as,

$$F_{ad} = 2\pi R_c W_{ad} \quad (13.19)$$

where R_c is the reduced radius of contact. It is calculated as $R_c = (1/R_1 + 1/R_2)^{-1}$, where R_1 and R_2 are the radii of contacting surfaces. When $R_1 = R_2$, $R_c = R/2$. The work of adhesion, W_{ad} , is then calculated using the following equation for two flat surfaces separated by a distance, D , (Israelachvili 1992),

$$W_{ad} = -\frac{H}{12\pi D^2} \quad (13.20)$$

where H is the Hamaker constant which depends on the medium between the two surfaces. Typical values of the Hamaker constant for polymers are $H_{air} = 10^{-19}$ J in the air and $H_{water} = 3.7 \times 10^{-20}$ J in the water (Israelachvili 1992). For a gecko seta, which is composed of β -keratin, the value of H is assumed to be 10^{-19} J. The works of adhesion of two surfaces in contact separated by an atomic distance $D \approx 0.2$ nm is approximately equal to 66 mJ/m² (Israelachvili 1992). By assuming that the tip radius, R , is 50 nm, using (13.19), the adhesion force of a single contact is calculated as 10 nN (Kim and Bhushan 2007a). This value is identical to the adhesion force of a single spatula measured by Huber et al. (2005a). This adhesion force is used as a critical force in the model for judging whether the contact between the tip and the surface is broken or not during pull-off cycle (Bhushan et al. 2006). If the elastic force of a single spring is less than the adhesion force, the spring is regarded as having been detached.

13.6.2 The Multi-level Hierarchical Spring Analysis

In order to study the effect of the number of hierarchical levels in the attachment system on attachment ability, models with one (Bhushan et al. 2006; Kim and Bhushan 2007a, b), two (Bhushan et al. 2006; Kim and Bhushan 2007a, b) and three (Kim and Bhushan 2007a, b) levels of hierarchy were simulated (Fig. 13.16). The one-level model has springs with length $l_I = 2.5 \mu\text{m}$ and stiffness $k_I = 0.0126 \text{ N/m}$.

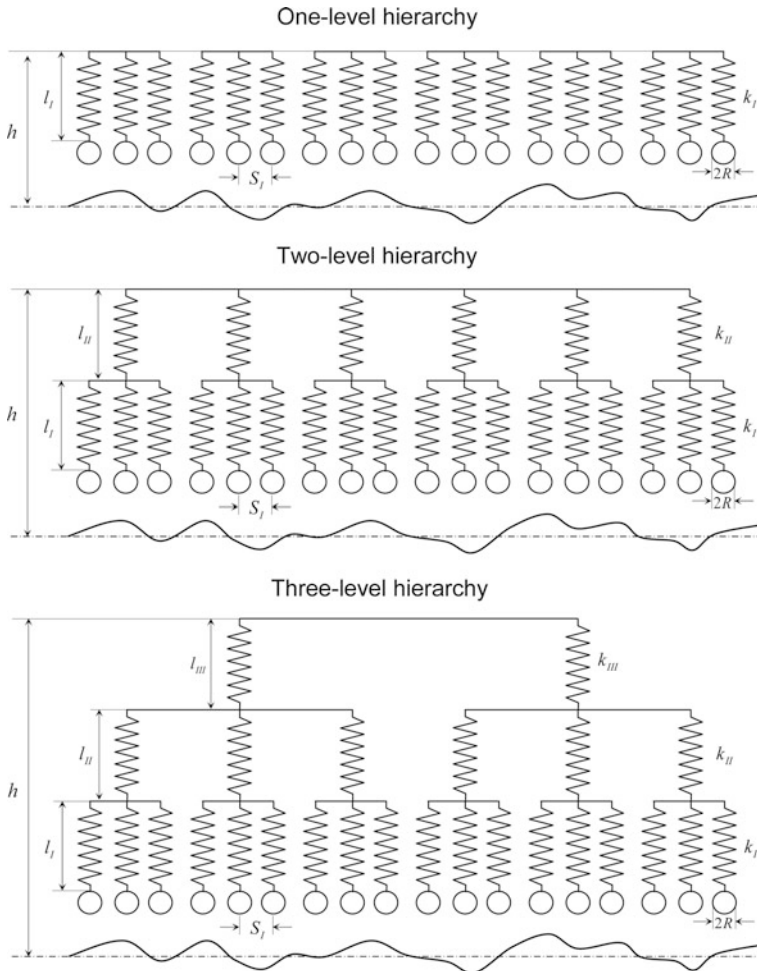


Fig. 13.16 One-, two-, and three-level hierarchical spring models for simulating the effect of hierarchical morphology on interaction of a seta with a rough surface. In this figure, l_I, II, III are lengths of structures, s_I is space between spatulae, k_I, II, III are stiffnesses of structures, I, II , and III are level indexes, R is radius of tip, and h is distance between upper spring base of each model and mean line of the rough profile (Kim and Bhushan 2007a)

The length and stiffness of the springs in the two-level model are $l_I = 2.5 \mu\text{m}$, $k_I = 0.0126 \text{ N/m}$ and $l_{II} = 25 \mu\text{m}$, $k_{II} = 0.126 \text{ N/m}$ for levels *I* and *II*, respectively. The three-level model has additional upper level springs with $l_{III} = 75 \mu\text{m}$, $k_{III} = 2.908 \text{ N/m}$ on the springs of the two-level model, which is identical to gecko setae. The base of the springs and the connecting plate between the levels are assumed to be rigid. The distance S_j between the neighboring structures of level *I* is $0.35 \mu\text{m}$, obtained from the average value of measured spatula density, $8 \times 10^6 \text{ mm}^{-2}$, calculated by multiplying $14,000 \text{ setae/mm}^2$ by an average of 550 spatula/seta (Schleich and Kästle 1986) (Table 13.3). A 1:10 proportion of the number of springs in the upper level to that in the level below and the same proportion from mid-level to bottom level was assumed (Bhushan et al. 2006). This corresponds to one spring at level *III* which is connected to ten springs on level *II*, and each spring on level *II* is connected with ten springs on level *I*. The number of springs on level *I* considered in the model is calculated by dividing the scan length ($2000 \mu\text{m}$) with the distance S_I ($0.35 \mu\text{m}$), which corresponds to 5700.

The spring deflection Δl was calculated as,

$$\Delta l = h - l_0 - z \quad (13.21)$$

where h is the position of the spring base relative to the mean line of the surface; l_0 is the total length of a spring structure, which is $l_0 = l_I$ for the one-level model, $l_0 = l_I + l_{II}$ for the two-level model, and $l_0 = l_I + l_{II} + l_{III}$ for the three-level model; and z is the profile height of the rough surface. The elastic force F_{el} arisen in the springs at a distance h from the surface was calculated for the one-level model as (Bhushan et al. 2006),

$$F_{el} = -k_I \sum_{i=1}^p \Delta l_i u_i \quad u_i = \begin{cases} 1 & \text{if contact} \\ 0 & \text{if no contact} \end{cases} \quad (13.22)$$

where p is the number of springs in level *I* of the model. For the two-level model, the elastic force was calculated as (Bhushan et al. 2006),

$$F_{el} = - \sum_{j=1}^q \sum_{i=1}^p k_{ji} (\Delta l_{ji} - \Delta l_j) u_{ji} \quad u_{ji} = \begin{cases} 1 & \text{if contact} \\ 0 & \text{if no contact} \end{cases} \quad (13.23)$$

where q is the number of springs in level *II* of the model. For the three-level model, the elastic force was calculated as (Kim and Bhushan 2007a),

$$F_{el} = - \sum_{k=1}^r \sum_{j=1}^q \sum_{i=1}^p k_{kji} (\Delta l_{kji} - \Delta l_{kj} - \Delta l_j) u_{kji} \quad u_{kji} = \begin{cases} 1 & \text{if contact} \\ 0 & \text{if no contact} \end{cases} \quad (13.24)$$

where r is the number of springs in level *III* of the model. The spring force when the springs approach the rough surface is calculated using either (13.22), (13.23), or (13.24) for one-, two- and three-level models, respectively. During pull-off, the same equations are used to calculate the spring force. However, when the applied load is equal to zero, the springs do not detach due to the adhesion attraction, given by (13.19). The springs are pulled apart when pull-off force is equal to adhesion force at the interface. The adhesion force is the lowest value of elastic force F_{el} when the seta has detached from the contacting surface.

The adhesion energy is calculated as,

$$W_{ad} = \int_{\bar{D}}^{\infty} F_{el}(D)dD \quad (13.25)$$

where D is the distance that the spring base moves away from the contacting surface. The lower limit of the distance \bar{D} is the value of D where F_{el} is first zero when the model is pulled away from the contacting surface. Also although the upper limit of the distance is infinity, in practice, the $F_{el}(D)$ curve is integrated to an upper limit where F_{el} increases from a negative value to zero. Figure 13.17 shows the flow chart for the calculation of the adhesion force and the adhesion energy employed by Kim and Bhushan (2007a).

The random rough surfaces used in the simulations were generated on a computer (Bhushan 2013a, b). Several natural (sycamore tree bark and siltstone) and artificial (drywall, wood, laminate, steel, aluminum, and glass) surfaces were chosen to determine the surface parameters of typical rough surfaces that a gecko might encounter. Two-dimensional profiles of surfaces were obtained using a stylus profiler for two scan lengths: 80 μm , which is approximately the size of a single gecko seta, and 2000 μm , which is close to the size of a gecko lamellae (Bhushan et al. 2006). Surface roughness parameters (root mean square (RMS) amplitude σ and correlation length β^*) for scan lengths of 80 and 2000 μm , are presented in Table 13.4. The roughness parameters are scale dependent; therefore, adhesion values also are expected to be scale dependent. As the scan length was increased, the measured values of RMS amplitude and correlation length both increased. At a scale length of 80 μm (size of seta), the roughness amplitude does not exceed 5 μm , while at a scale length of 2000 μm (size of lamella), the roughness amplitude is as high as 30 μm . This suggests that setae should adapt to surfaces with roughness on the order of several microns, while lamellae should adapt to roughness on the order of tens of microns. The skin of the gecko should adapt to larger roughness values. The range of values of σ from 0.01 to 30 μm and a fixed value of $\beta^* = 200 \mu\text{m}$ were used for modeling the contact of a seta with random rough surfaces. The chosen range covers values of roughnesses for relatively smooth, artificial surfaces to natural, rough surfaces.

Fig. 13.17 Flow chart for the calculation of the adhesion force (F_{ad}) and the adhesion energy (E_{ad}) for three-level hierarchical spring model. In this figure, F_n is an applied load, k_I, k_{II}, k_{III} and l_I, l_{II}, l_{III} are stiffnesses and lengths of structures, Δl_{kji} , Δl_{ki} , and Δl_k are the spring deformations on level I, II , and III , respectively, i, j , and k are spring indexes on each level, f_i is the elastic force of a single spring, and f_{ad} is the adhesion force of a single contact (Kim and Bhushan 2007a)

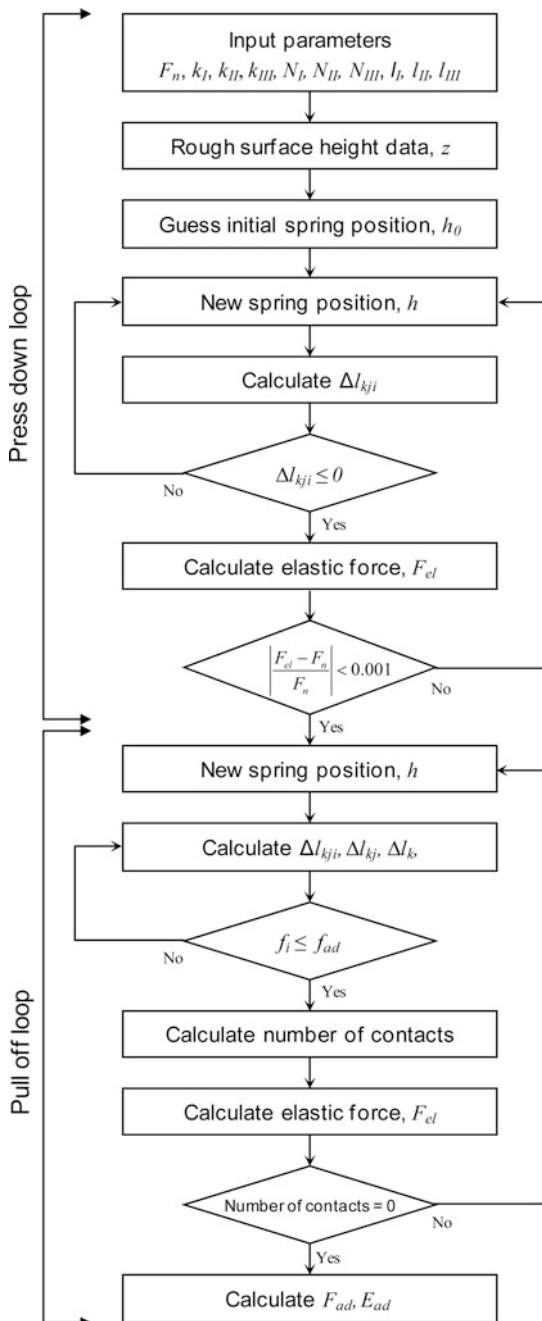


Table 13.4 Scale dependence of surface parameters σ and β^* for rough surfaces at scan lengths of 80 and 2000 μm (Bhushan et al. 2006)

Scan length	80 μm		2000 μm	
	σ (μm)	β^* (μm)	σ (μm)	β^* (μm)
Sycamore tree bark	4.4	17	27	251
Siltstone	1.1	4.8	11	268
Painted drywall	1	11	20	93
Wood laminate	0.11	18	3.6	264
Polished steel	0.07	12	0.40	304
Polished 2024 aluminum	0.40	6.5	0.50	222
Glass	0.01	2.2	0.02	152

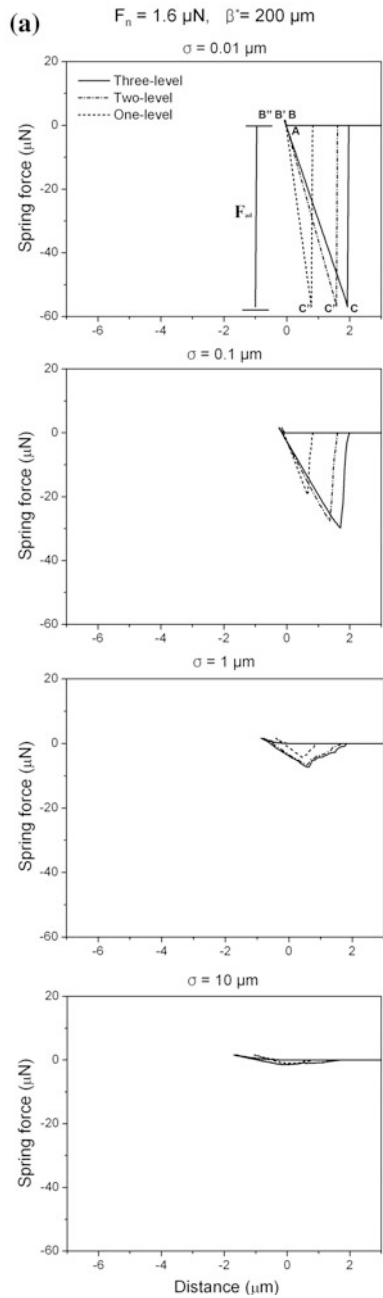
13.6.3 Adhesion Results of the Multi-level Hierarchical Spring Model

The multi-level hierarchical spring model was developed by Kim and Bhushan (2007a). They obtained various useful results are presented next. Figure 13.18a shows the calculated spring force–distance curves for the one-, two- and three-level hierarchical models in contact with rough surfaces of different values of RMS amplitude σ , ranging from $\sigma = 0.01 \mu\text{m}$ to $\sigma = 30 \mu\text{m}$ at an applied load of 1.6 μN , which was derived from the gecko's weight. When the spring model is pressed against the rough surface, contact between the spring and the rough surface occurs at point A. As the spring tip presses into the contacting surface, the force increases up to point B, B', or B''. During pull off, the spring relaxes, and the spring force passes an equilibrium state (0 N). Tips break free of adhesion forces at point C, C', or C'' as the spring moves away from the surface. The perpendicular distance from C, C', or C'' to zero is the adhesion force. The data show that adhesion forces for various levels of hierarchy are comparable when in contact with a smooth surface. However, the adhesion force for the three-level model is the largest when in contact with a rough surface. Thus, multilevel hierarchy facilitates adaptability to various rough surfaces.

Adhesion energy stored during contact can be obtained by calculating the area of the triangle during the unloading part of the curves (13.25). Using the spring force-distance curves, Kim and Bhushan (2007a) calculated the adhesion coefficient, the number of contacts per unit length, and the adhesion energy per unit length of the one-, two-, and three-level models for an applied load of 1.6 μN and a wide range of RMS roughness (σ), as seen in the left graphs of Fig. 13.18b. The adhesion coefficient, defined as the ratio of pull-off force to applied preload, represents the strength of adhesion with respect to the preload. For the applied load of 1.6 μN , which corresponds to the weight of a gecko, the maximum adhesion coefficient is about 36 when σ is smaller than 0.01 μm . This means that a gecko can generate enough adhesion force to support 36 times its bodyweight. However, if σ is increased to 1 μm , the adhesion coefficient for the three-level model is reduced to

Fig. 13.18 a Force-distance curves of one-, two-, and three-level models in contact with rough surfaces with different σ values for an applied load of 1.6 μN . **b** The adhesion coefficient, the number of contacts, and the adhesion energy per unit length of profile for one- and multi-level models with an increase of σ value (*left figures*), and relative increases between multi- and one-level models (*right side*) for an applied load of 1.6 μN . The value of k_{III} in the analysis is 2.908 N/m (Kim and Bhushan 2007a)

The effect of multi-level hierarchical structure



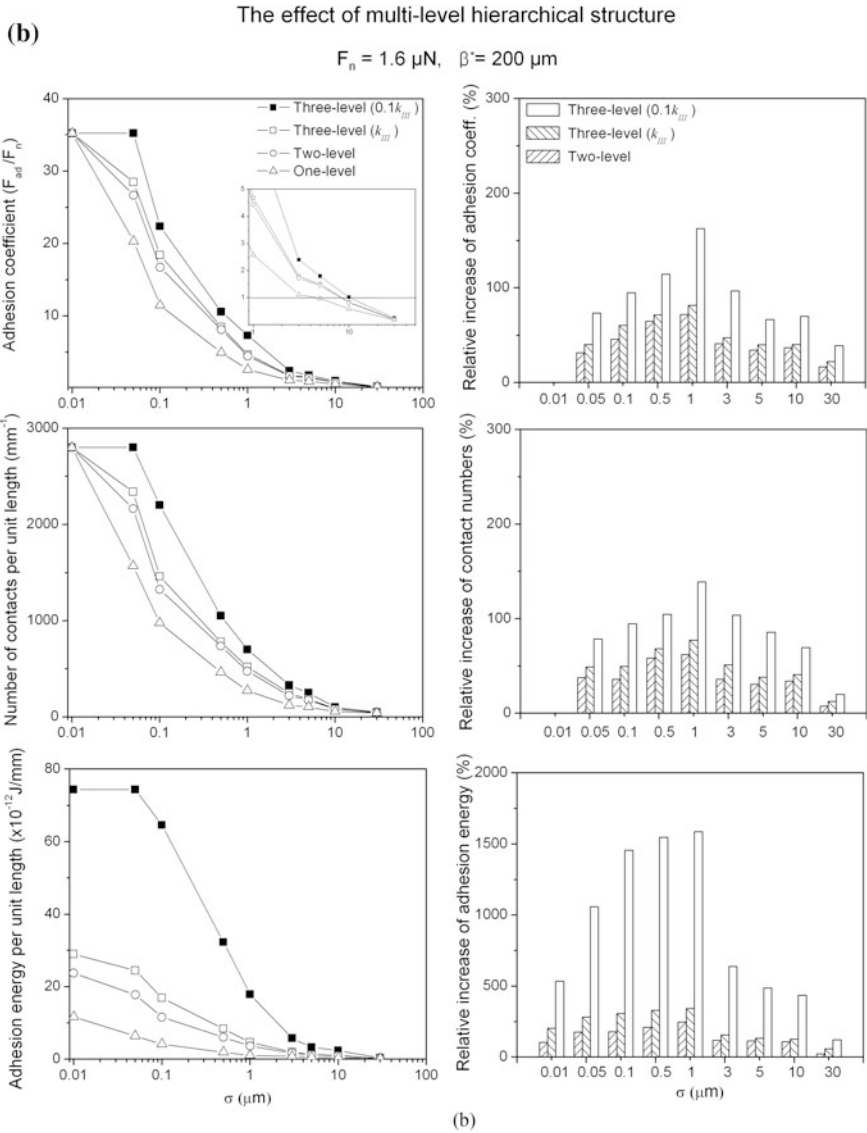


Fig. 13.18 (continued)

4.7. It is noteworthy that the adhesion coefficient falls below 1 when the contacting surface has an RMS roughness σ greater than $10 \mu\text{m}$. This implies that the attachment system is no longer capable of supporting the gecko’s weight. Autumn et al. (2000, 2002) showed that in isolated gecko setae contacting with the surface of a single crystalline silicon wafer, a $2.5 \mu\text{N}$ preload yielded adhesion of $20\text{--}40 \mu\text{N}$

and thus a value of adhesion coefficient of 8–16, which supports the simulation results of Kim and Bhushan (2007a).

Figure 13.18b (top left) shows that the adhesion coefficient for the one-level model is lower than that for the three-level model, but that there is only a small difference between the values of the two- and three-level models. In order to show the effect of spring stiffness in the three-level model, another model used springs in level *III* with stiffness that was ten times smaller than the stiffness of the original level *III* springs used. The data are presented in Fig. 13.18b. It can be seen that the three-level model with a third level stiffness of $0.1 k_{III}$ has a 20–30 % higher adhesion coefficient than the three-level model. The results also show that the trends in the number of contacts are similar to that of the adhesive force. The study also investigated the effect of σ on adhesion energy. It was determined that the adhesion energy decreased with an increase of σ . For a smooth surface with $\sigma = 0.01 \mu\text{m}$, the adhesion energies for the two- and three-level hierarchical models are 2 times and 2.4 times larger than that for the one-level model, respectively, but adhesion energy decreases rapidly at surfaces with σ greater than $0.05 \mu\text{m}$. Further, in every model adhesion energy finally decreases to zero at surfaces with σ greater than $10 \mu\text{m}$. The adhesion energy for the more compliant three-level model is 2–3 times higher than that for the original three-level model.

In order to demonstrate the effect of the hierarchical structure on adhesion enhancement, Kim and Bhushan (2007a) calculated the increases in the adhesion coefficient, the number of contacts, and the adhesion energy of the two- and three-level models, as well as the three-level with $0.1 k_{III}$ model, relative to the one-level model. These results are shown in the right side of Fig. 13.18b. It was also found that for the two- and three-level models, the adhesion coefficient increases slowly with an increase of σ , and has maximum values of about 70 and 80 % at $\sigma = 1 \mu\text{m}$, respectively, and then decreases for surfaces with σ greater than $3 \mu\text{m}$. The condition at which a significant enhancement occurs is related to the maximum spring deformation, which is the applied load divided by the spring stiffness. If the maximum spring deformation is greater than 2–3 times larger than the σ value of the surface roughness, a significant adhesion enhancement occurs. The more compliant three-level model shows significant adhesion enhancement. The relative increase of the adhesion coefficient and adhesion energy for that model was the highest at $\sigma = 1 \mu\text{m}$.

Figure 13.19 shows the variation of adhesion force and adhesion energy as a function of applied load for both one- and three-level models contacting a surface with $\sigma = 1 \mu\text{m}$. It is shown that as the applied load increases, the adhesion force increases up to a certain applied load and then has a constant value, whereas, adhesion energy continues to increase with an increase in the applied load. The one-level model had a maximum value of adhesion force per unit length of about $3 \mu\text{N}/\text{mm}$ at the applied load of $10 \mu\text{N}$, and the three-level model had a maximum value of about $7 \mu\text{N}/\text{mm}$ at the applied load of $16 \mu\text{N}$. However, the adhesion coefficient continues to decrease at higher applied loads because adhesion force is constant even if the applied load increases.

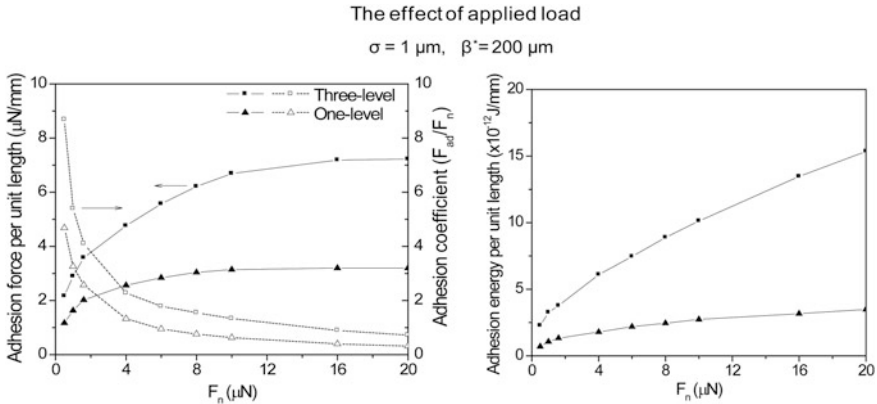


Fig. 13.19 The adhesion force, adhesion coefficient, and adhesion energy as a function of applied loads for both one- and three-level models contacting with the rough surface (Kim and Bhushan 2007a)

The simulation results for the three-level model, which is closest to actual gecko setae, presented in Fig. 13.18 show that roughness reduces the adhesion force. At a surface with σ greater than $10 \mu\text{m}$, the ratio of the adhesion force to the gecko weight indicates that it cannot support itself. However, in practice, a gecko can cling or crawl on the surface of ceiling with higher roughness. Kim and Bhushan (2007a) did not consider the effect of lamellae in their study. The authors stated that the lamellae can adapt to the waviness of a surface while the setae allow for the adaptation to micro- or nano-roughness and expect that adding the lamellae of gecko skin to the model would lead to higher adhesion over a wider range of roughness. In addition, their hierarchical model considers deformation normal to the surface and the motion of seta. It should be noted that the measurements of adhesion force of a single gecko seta made by Autumn et al. (2000) demonstrated that a load applied normal to the surface was insufficient for an effective attachment of seta.

Finally, in order to determine the effects of spring stiffness and the number of springs on the adhesion enhancement of a multi-level hierarchical model, one- and three-level models with four different spring stiffnesses and three different numbers of springs were analyzed by Kim and Bhushan (2007b). The stiffness k_I was taken equal to 0.0126 N/m , as before. Other stiffnesses, k_{II} and k_{III} , were normalized with respect to k_I . The three-level model with $k_{III}/k_I = 100$ and $k_{II}/k_I = 10$ has similar stiffness values to gecko's seta presented in Table 13.3 and used in the previous example (Figs. 13.18 and 13.19). The left part in Fig. 13.20 shows the adhesion coefficient, the number of contacts and adhesion energy per unit length for the one- and three-level models with four different spring stiffnesses as a function of σ value for an applied load of $1.6 \mu\text{N}$. Trends as a function of σ are the same as observed previously in Fig. 13.18b. For the case of $k_{III} = k_{II} = k_I$, one gets the highest value of adhesion coefficient of 36 on a rough surface, and it remains high up to σ value of

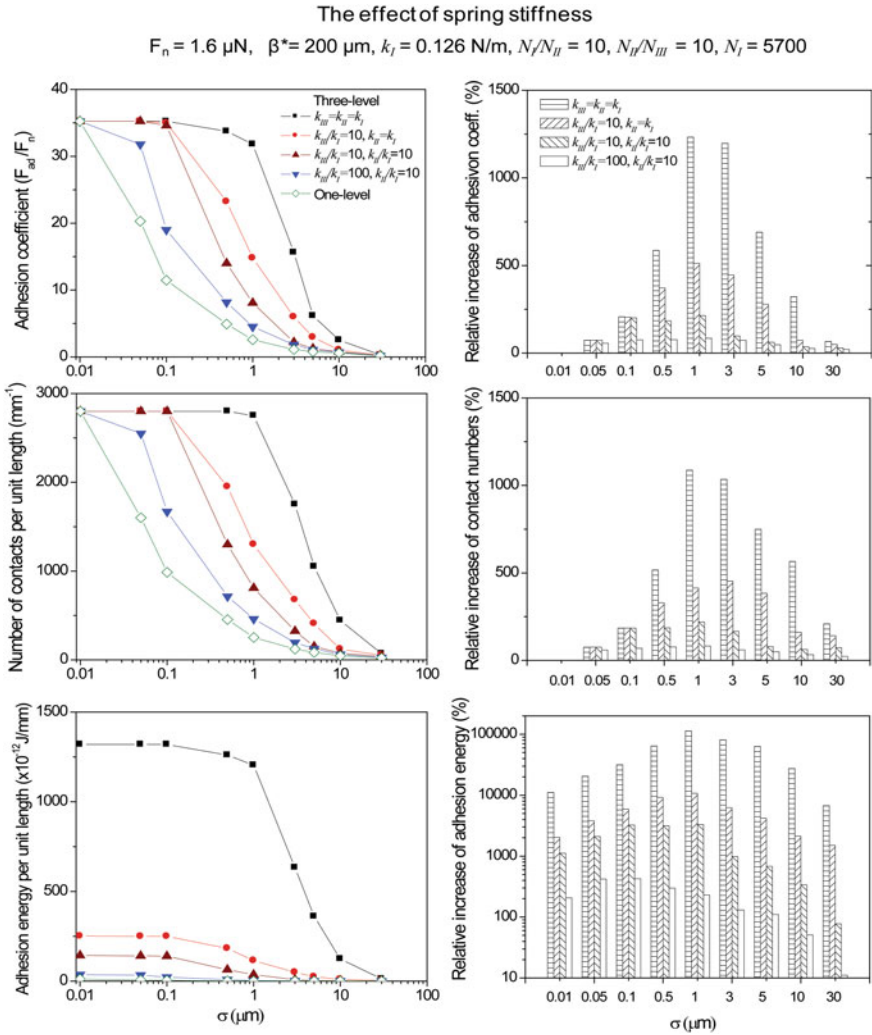


Fig. 13.20 The adhesion coefficient, the number of contacts, and the adhesion energy per unit length of profile for one- and three-level models with different spring stiffnesses as a function of σ value (*left figures*), and relative increases between one- and three-level models (*right figures*) for an applied load of $1.6 \mu\text{N}$ (Kim and Bhushan 2007b)

about $1 \mu\text{m}$, and then it starts to decrease. As the stiffness values of k_{II} and k_{III} increase, the adhesion coefficient starts to decrease at lower values of σ , and it decreases rapidly with an increase in σ . The number of contacts and adhesion energy per unit length as a function of σ have trends similar to that of adhesion coefficient. The right part in Fig. 13.20 shows relative increases between one- and three-level models. The trends are the same as discussed earlier.

For the effect of the number of springs, three different cases of the number of springs in the upper level to that in the lower level were considered. The three-level model with $N_I/N_{II} = 10$ and $N_{II}/N_{III} = 10$ is closest to the actual gecko's setae (discussed earlier). Figure 13.21 shows the adhesion force, adhesion coefficient, and adhesion energy as a function of applied loads for one- and three-level models with different numbers of springs contacting the rough surface. The variation of the number of springs on each level affects the equivalent stiffness of the model. As the number of springs on the lower level increases, the equivalent stiffness decreases. The figure shows that the three-level model with $N_I/N_{II} = 100$ and $N_{II}/N_{III} = 10$ gives the largest adhesion force and adhesion energy among every model, because the equivalent stiffness is lowest.

To sum up, multi-level hierarchical structures with more compliant springs and at an increasing applied load are beneficial to gecko adhesion enhancement. Furthermore, for significant adhesion enhancement, the maximum spring deformation should be two to three times larger than the σ value of the surface roughness.

13.6.4 Capillary Effects

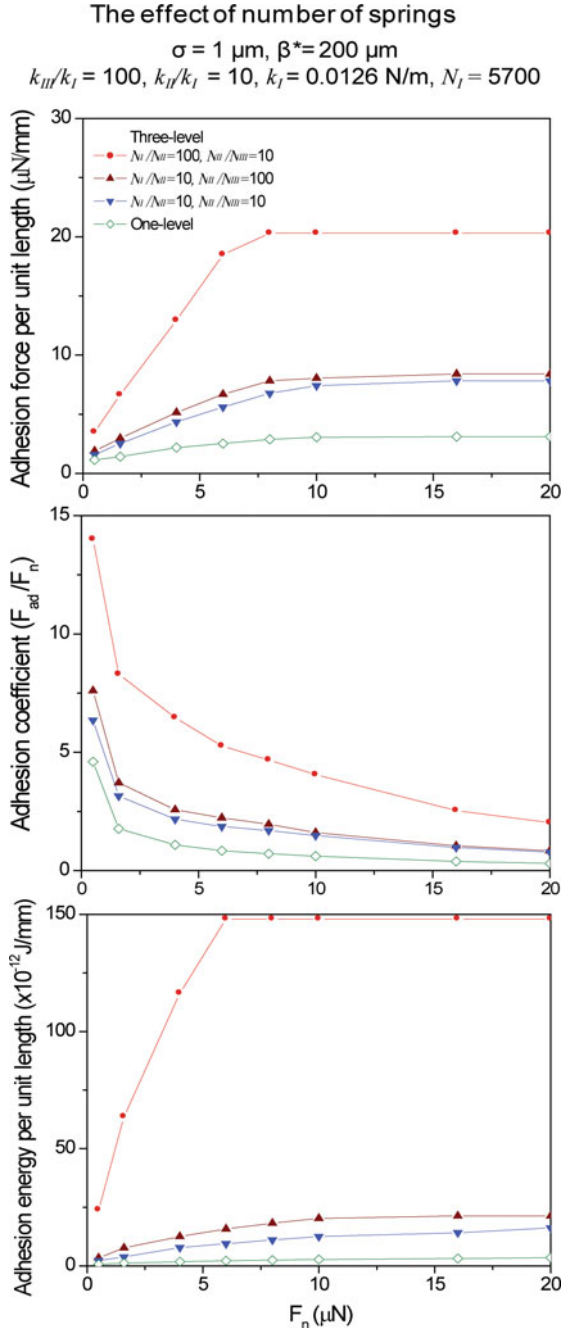
Kim and Bhushan (2008) investigated the effects of capillarity on gecko adhesion by considering capillary force as well as the solid-to-solid interaction. The Laplace and surface tension components of the capillary force are treated the same as earlier in this chapter. The solid to solid adhesive force was calculated by DMT theory according to (13.19) and will be denoted as F_{DMT} .

The work of adhesion was calculated by (13.20). Kim and Bhushan (2008) assumed typical values of the Hamaker constant to be $H_{air} = 10^{-19}$ J in the air and $H_{water} = 6.7 \times 10^{-19}$ J in the water (Israelachvili 1992). The works of adhesion of two surfaces in contact separated by an atomic distance $D \approx 0.2$ nm (Israelachvili 1992) are approximately equal to 66 mJ/m² in air and 44 mJ/m² in water. Assuming tip radius R is 50 nm, the DMT adhesion forces F_{DMT} of a single contact in air and in water are $F_{DMT}^{air} = 11$ nN and $F_{DMT}^{water} = 7.3$ nN, respectively. As the humidity increases from 0 to 100 %, the DMT adhesion force will take a value between F_{DMT}^{air} and F_{DMT}^{water} . To calculate the DMT adhesion force for the intermediate humidity, an approximation method by Wan et al. (1992) was used. The work of adhesion W_{ad} for the intermediate humidity can be expressed as,

$$W_{ad} = \int_D^{\infty} \frac{H}{6\pi h^3} dh = \int_D^{h_f} \frac{H_{water}}{6\pi h^3} dh + \int_{h_f}^{\infty} \frac{H_{air}}{6\pi h^3} dh \quad (13.26)$$

where h is the separation along the plane. The water film thickness at a filling angle ϕ is h_f , which can be calculated as,

Fig. 13.21 The adhesive force, adhesion coefficient, and adhesion energy as a function of applied loads for one- and three-level models with different number of springs contacting with the rough surface (Kim and Bhushan 2007b)



$$h_f = D + R(1 - \cos \phi) \quad (13.27)$$

Therefore, using (13.19), (13.26), and (13.27), the DMT adhesion force for the intermediate humidity is given as,

$$F_{DMT} = F_{DMT}^{air} \left\{ 1 - \frac{1}{(1 + R(1 - \cos \phi)/D)^2} \right\} + F_{DMT}^{water} \left\{ \frac{1}{(1 + R(1 - \cos \phi)/D)^2} \right\} \quad (13.28)$$

Finally, Kim and Bhushan (2008) calculated the total adhesion force F_{ad} as the sum of (13.15) and (13.28),

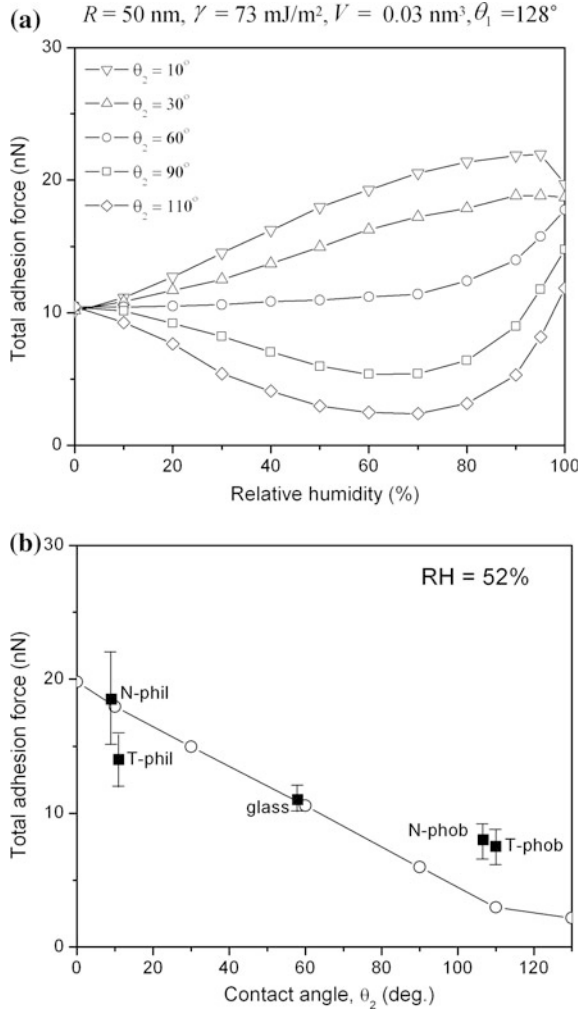
$$F_{ad} = F_c + F_{DMT} \quad (13.29)$$

Kim and Bhushan (2008) then used the total adhesion force as a critical force in the three-level hierarchical spring model discussed previously. In the spring model for gecko seta, if the force applied upon spring deformation is greater than the adhesion force, the spring is regarded as having been detached. To simulate the capillary contribution to adhesion force for a gecko spatula, Kim and Bhushan (2008) set the contact angle on a gecko spatula tip θ_1 equal to 128° (Huber et al. 2005b). It was assumed that the spatula tip radius $R = 50$ nm, the ambient temperature $T = 25$ °C, the surface tension of water $\gamma = 73$ mJ/m², and molecular volume of water $V = 0.03$ nm³ (Israelachvili 1992).

Figure 13.22a shows the total adhesion force as a function of relative humidity for a single spatula in contact with surfaces with different contact angles. Total adhesion force decreases with an increase in the contact angle on the substrate, and the difference of total adhesion force among different contact angles is larger in the intermediate humidity regime. As the relative humidity increases, total adhesion force for the surfaces with contact angles less than 60° has a higher value than the DMT adhesion force not considering wet contact, whereas with the value above 60° , total adhesion force has lower values at most relative humidities.

The simulation results of Kim and Bhushan (2008) are compared with the experimental data by Huber et al. (2005b) in Fig. 13.22b. Huber et al. (2005b) measured the pull off force of a single spatula in contact with four different types of Si wafers and glass at a temperature of 25 °C and relative humidity of 52 %. According to their description, wafer families “N” and “T” in Fig. 13.22b differ by the thickness of the top amorphous Si oxide layer. The “Phil” type is the cleaned Si oxide surface that is hydrophilic with a water contact angle $\approx 10^\circ$, whereas the “Phob” type is covered by a hydrophobic monolayer with a water contact angle $> 100^\circ$. Glass has a water contact angle of 58° . Huber et al. (2005b) showed that the adhesion force of a gecko spatula rises significantly for substrates with increasing hydrophilicity (adhesive force increases by a factor of two as mating surfaces go from hydrophobic to hydrophilic). As shown in Fig. 13.22b, the simulation results of Kim and Bhushan (2008) closely match the experimental data of Huber et al. (2005b).

Fig. 13.22 a Total adhesion force as a function of relative humidity for a single spatula in contact with surfaces with different contact angles. **b** Comparison of the simulation results of Kim and Bhushan (2008) with the measured data obtained by Huber et al. (2005b) for a single spatula in contact with the hydrophilic and the hydrophobic surfaces (Kim and Bhushan 2008)



Kim and Bhushan (2008) carried out adhesion analysis for a three-level hierarchical model for gecko seta. Figure 13.23 shows the adhesion coefficient and number of contacts per unit length for the three-level hierarchical model in contact with rough surfaces with different values of the RMS amplitude σ ranging from $\sigma = 0.01 \mu\text{m}$ to $\sigma = 30 \mu\text{m}$ for different relative humidities and contact angles of the surface. It can be seen that for a surface with contact angle $\theta_2 = 10^\circ$, the adhesion coefficient is greatly influenced by relative humidity. At 0% relative humidity the maximum adhesion coefficient is about 36 at a value of σ smaller than $0.01 \mu\text{m}$, compared to 78 for 90% relative humidity with the same surface roughness. As expected, the effect of relative humidity on increasing the adhesion coefficient decreases as the contact angle becomes larger. For hydrophobic surfaces, relative

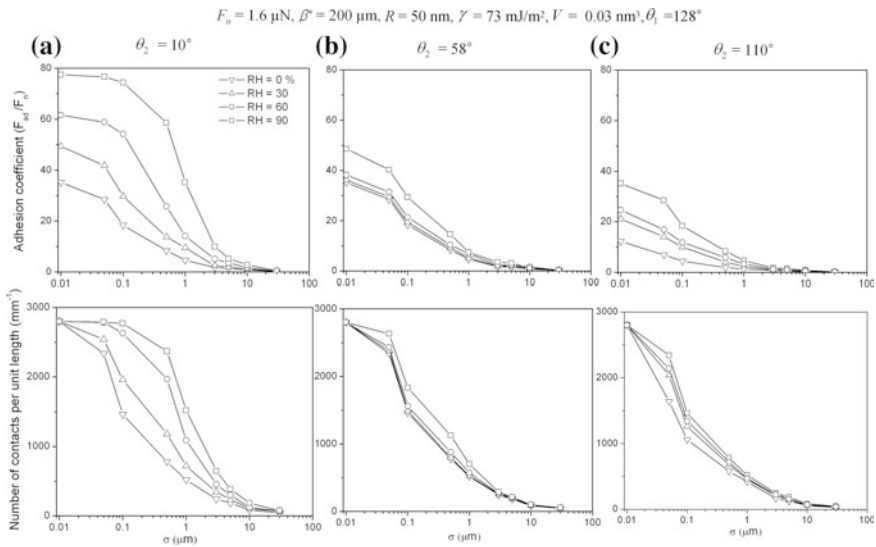


Fig. 13.23 The adhesion coefficient and number of contacts per unit length for three-level hierarchical model in contact with rough surfaces with different values of root mean square amplitudes σ and contact angles for different relative humidities (Kim and Bhushan 2008)

humidity decreases the adhesion coefficient. Similar trends can be noticed in the number of contacts. Thus, the conclusion can be drawn that hydrophilic surfaces are beneficial to gecko adhesion enhancement.

13.7 Adhesion Data Base of Fibrillar Structures

As it relates to the design of biomimetic structures, the mechanics of adhesion between a fibrillar structure and a rough surface has been a topic of investigation by many researchers (Jagota and Bennison 2002; Persson 2003; Sitti and Fearing 2003; Glassmaker et al. 2004, 2005; Gao et al. 2005; Yao and Gao 2006; Kim and Bhushan 2007b, c). Kim and Bhushan (2007c) developed a convenient, general, and useful guideline for understanding biological systems and for improving the attachment of fibrillar structures. This adhesion database was constructed by modeling the fibers as oriented cylindrical cantilever beams with spherical tips. The authors then carried out numerical simulations of the attachment system in contact with random rough surfaces considering three constraint conditions: buckling, fracture, and sticking of the fiber structure. For a given applied load, roughnesses of contacting surface, and fiber material, a procedure to find an optimal fiber radius and aspect ratio for the desired adhesion coefficient was developed.

The model developed by Kim and Bhushan (2007c) is used to find the design parameters for fibers of a single-level attachment system capable of achieving

desired properties—high adhesion coefficient and durability. The design variables for an attachment system are as follows: fiber geometry (radius and aspect ratio of fibers, tip radius), fiber material, fiber density, and fiber orientation. The optimal values for the design variables to achieve the desired properties should be selected for fabrication of a biomimetic attachment system.

13.7.1 Fiber Model

The fiber model developed by Kim and Bhushan (2007c) consists of a simple idealized fibrillar structure with a single-level array of micro/nano beams protruding from a backing as shown in Fig. 13.24. The fibers are modeled as oriented cylindrical cantilever beams with spherical tips. In Fig. 13.24, l is the length of fibers, θ is the fiber orientation, R is the fiber radius, R_t is the tip radius, S is the spacing between fibers, and h is the distance between the upper spring base of each model and mean line of the rough profile. The end terminal of the fibers is assumed to be a spherical tip with a constant adhesion force.

13.7.2 Single Fiber Contact Analysis

Kim and Bhushan (2007c) modeled an individual fiber as a beam oriented at an angle θ to the substrate, with the contact load F aligned normal to the substrate. The net displacement normal to the substrate can be calculated according to (13.16) and (13.17). The fiber stiffness ($k = F/\delta_{\perp}$) is given by (Glassmaker et al. 2004),

$$k = \frac{\pi R^2 E}{l \sin^2 \theta \left(1 + \frac{4R^2 \cot^2 \theta}{3R^2}\right)} = \frac{\pi R E}{2\lambda \sin^2 \theta \left(1 + \frac{16\lambda^2 \cot^2 \theta}{3}\right)} \quad (13.30)$$

where $\lambda = l/2R$ is the aspect ratio of the fiber, and θ is fixed at 30° .

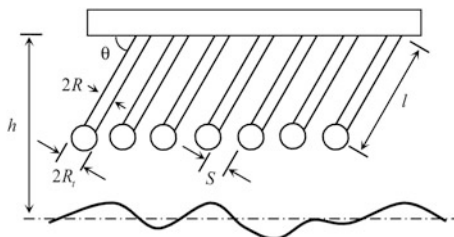


Fig. 13.24 Single-level attachment system with oriented cylindrical cantilever beams with spherical tip. In this figure, l is the length of fibers, θ is the fiber orientation, R is the fiber radius, R_t is the tip radius, S is the spacing between fibers, and h is distance between base of model and mean line of the rough profile (Kim and Bhushan 2007c)

Two alternative models dominate the world of contact mechanics—the Johnson-Kendall-Roberts (JKR) theory (Johnson et al. 1971) for compliant solids, and the Derjaguin-Muller-Toporov (DMT) theory (Derjaguin et al. 1975) for stiff solids. Although gecko setae are composed of β -keratin with a high elastic modulus (Russell 1986; Bertram and Gosline 1987) which is close to the DMT model, in general the JKR theory prevails for biological or artificial attachment systems. Therefore the JKR theory was applied in the subsequent analysis of Kim and Bhushan (2007c) to compare the materials with wide ranges of elastic modulus. The adhesion force between a spherical tip and a rigid flat surface is thus calculated using the JKR theory as (Johnson et al. 1971),

$$F_{ad} = \frac{3}{2}\pi R_t W_{ad} \quad (13.31)$$

where R_t is the radius of spherical tip, and W_{ad} is the work of adhesion [calculated according to (13.24)]. Kim and Bhushan (2007c) used this adhesion force as a critical force. If the elastic force of a single spring is less than the adhesion force, they regarded the spring as having been detached.

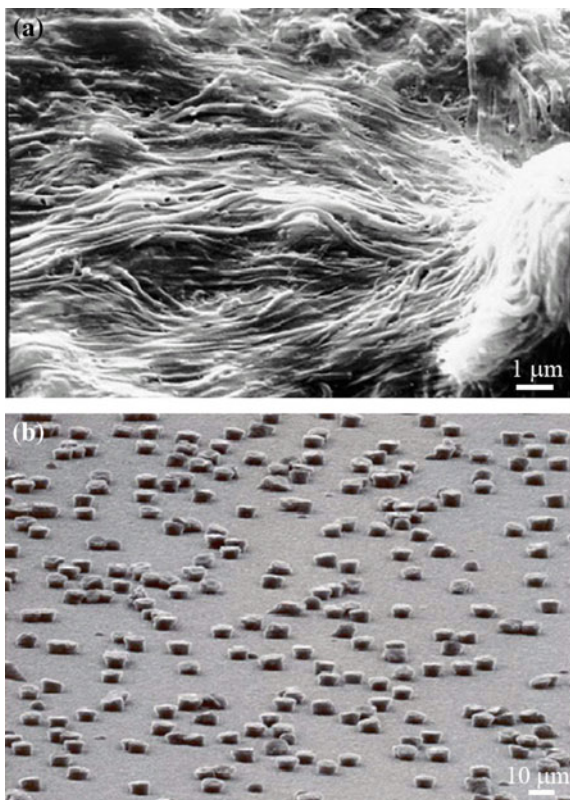
13.7.3 Constraints

In the design of fibrillar structures, a trade-off exists between the aspect ratio of the fibers and their adaptability to a rough surface. If the aspect ratio of the fibers is too large, they can adhere to each other or even collapse under their own weight as shown in Fig. 13.25a. If the aspect ratio is too small (Fig. 13.25b), the structures will lack the necessary compliance to conform to a rough surface. Spacing between the individual fibers is also important. If the spacing is too small, adjacent fibers can attract each other through intermolecular forces, which will lead to bunching. Therefore, in their analysis, Kim and Bhushan (2007c) considered three necessary constraints to the allowed geometry: buckling, fracture, and sticking of fiber structure.

13.7.3.1 Non-buckling Condition

A fibrillar interface can deliver a compliant response while still employing stiff materials because of bending and micro-buckling of fibers. Based on classical Euler buckling, Glassmaker et al. (2004) established a stress-strain relationship and a critical compressive strain for buckling, ε_{cr} , for the fiber oriented at an angle, θ , to the substrate,

Fig. 13.25 SEM micrographs of **a** high aspect ratio polymer fibrils that have collapsed under their own weight and **b** low aspect ratio polymer fibrils that are incapable of adapting to rough surfaces (Sitti and Fearing 2003)



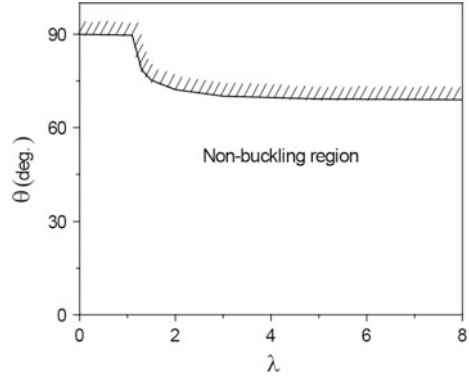
$$\varepsilon_{cr} = -\frac{b_c \pi^2}{3(A_c l^2 / 3I)} \left(1 + \frac{A_c l^2}{3I} \cot^2 \theta \right) \tag{13.32}$$

where A_c is the cross-sectional area of the fibril, and b_c is a factor that depends on boundary conditions. The factor b_c has a value of 2 for pinned-clamped micro-beams. For fibers having a circular cross section, ε_{cr} is calculated as,

$$\varepsilon_{cr} = -\frac{b_c \pi^2}{3(4I^2 / 3R^2)} \left(1 + \frac{4I^2}{3R^2} \cot^2 \theta \right) = -b_c \pi^2 \left(\frac{1}{16\lambda^2} + \frac{\cot^2 \theta}{3} \right) \tag{13.33}$$

In (13.33), ε_{cr} depends on both the aspect ratio, λ , and the orientation, θ , of fibers. If $\varepsilon_{cr} = 1$, which means the fiber deforms up to the backing, buckling does not occur. Figure 13.26 plots the critical orientation, θ , as a function of aspect ratio for the case of $\varepsilon_{cr} = 1$. The critical fiber orientation for buckling is 90° at λ less than 1.1. This means that buckling does not occur, regardless of the orientation of the fiber, at λ less than 1.1. For λ greater than 1.1, the critical fiber orientation for buckling decreases with an increase in λ , and has a constant value of 69° at λ greater than 3.

Fig. 13.26 Critical fiber orientation as a function of aspect ratio λ for non-buckling condition for pinned-clamped micro-beams ($b_c = 2$) (Kim and Bhushan 2007c)



Kim and Bhushan (2007c) used a fixed value at 30° for θ , because the maximum adhesive force is achieved at this orientation, and buckling is not expected to occur.

13.7.4 Non-fiber Fracture Condition

For small contacts, the strength of the system will eventually be determined by fracture of the fibers. Spolenak et al. (2005) suggested the limit of fiber fracture as a function of the adhesion force. The axial stress σ_f in a fiber is limited by its theoretical fracture strength σ_{th}^f as,

$$\sigma_f = \frac{F_{ad}}{R^2 \pi} \leq \sigma_{th}^f \quad (13.34)$$

Using (13.31), a lower limit for the useful fiber radius R is calculated as,

$$R \geq \sqrt{\frac{3R_t W_{ad}}{2\sigma_{th}^f}} \approx \sqrt{\frac{15R_t W_{ad}}{E}} \quad (13.35)$$

where the theoretical fracture strength is approximated by $E/10$ (Dieter 1988). The lower limit of fiber radius for fiber fracture by the adhesion force depends on elastic modulus. By assuming $W_{ad} = 66 \text{ mJ/m}^2$ as stated earlier, Kim and Bhushan (2007c) calculated the lower limits of fiber radius for $E = 1 \text{ MPa}$, 0.1 GPa and 10 GPa to be $0.32 \text{ }\mu\text{m}$, $0.032 \text{ }\mu\text{m}$ and $0.0032 \text{ }\mu\text{m}$, respectively.

The contact stress cannot exceed the ideal contact strength transmitted through the actual contact area at the instant of tensile instability (Spolenak et al. 2005). Kim and Bhushan (2007c) used this condition (13.34) to extract the limit of tip radius, R_t ,

$$\sigma_c = \frac{F_{ad}}{a_c^2 \pi} \leq \sigma_{th} \quad (13.36)$$

where σ_c is the contact stress, a_c is the contact radius, and σ_{th} is the ideal strength of van der Waals bonds, which equals approximately W_{ad}/b , where b is the characteristic length of surface interaction. Based on the JKR theory, for the rigid contacting surface, a_c at the instant of pull-off is calculated as,

$$a_c = \left(\frac{9\pi W_{ad} R_t^2 (1 - \nu^2)}{8E} \right)^{1/3} \quad (13.37)$$

where ν is Poisson's ratio. The tip radius can then be calculated by combining (13.36) and (13.37) as,

$$R_t \geq \frac{8b^3 E^2}{3\pi^2 (1 - \nu^2)^2 W_{ad}^2} \quad (13.38)$$

The lower limit of tip radius also depends on elastic modulus. Assuming $W_{ad} = 66 \text{ mJ/m}^2$ and $b = 2 \times 10^{-10} \text{ m}$ (Dieter 1988), the lower limits of tip radius for $E = 1 \text{ MPa}$, 0.1 GPa , and 10 GPa are calculated as $6 \times 10^{-7} \text{ nm}$, $6 \times 10^{-3} \text{ nm}$, and 60 nm , respectively. In this study, Kim and Bhushan (2007c) fixed the tip radius at 100 nm , which satisfies the tip radius condition throughout a wide range of elastic modulus up to 10 GPa .

13.7.4.1 Non-sticking Condition

A high density of fibers is also important for high adhesion. However, if the space S between neighboring fibers is too small, the adhesion forces between them become stronger than the forces required to bend the fibers. Then, fibers might stick to each other and get entangled. Therefore, to prevent fibers from sticking to each other, they must be spaced apart and be stiff enough to prevent sticking or bunching. Several authors (e.g., Sitti and Fearing 2003) have formulated a non-sticking criterion. Kim and Bhushan (2007c) adopted the approach of Sitti and Fearing (2003). Both adhesion and elastic forces will act on bent structures. The adhesion force between two neighboring round tips is calculated as,

$$F_{ad} = \frac{3}{2} \pi R'_t W_{ad} \quad (13.39)$$

where R'_t is the reduced radius of contact, calculated as $R'_t = (1/R_{t1} + 1/R_{t2})^{-1}$; R_{t1} and R_{t2} are the radii of contacting tips. In the case of similar tips, $R_{t1} = R_{t2}$, and thus $R'_t = 2/R_t$.

The elastic force of a bent structure can be calculated by multiplying the bending stiffness ($k_b = 3\pi R^4 E/4l^3$) by a given bending displacement δ as,

$$F_{el} = \frac{3\pi R^4 E \delta}{4l^3} \quad (13.40)$$

The condition for the prevention of sticking is $F_{el} > F_{ad}$. By combining (13.39) and (13.40), a requirement for the minimum distance S between structures, which will prevent sticking of the structures, is given as (Kim and Bhushan 2007c),

$$S > 2\delta = 2\left(\frac{4W_{ad}l^3}{3ER^3}\right) = 2\left(\frac{32W_{ad}\lambda^3}{3E}\right) \quad (13.41)$$

The constant 2 takes into account the two nearest structures. Using distance S , the fiber density, ρ , is calculated as,

$$\rho = \frac{1}{(S + 2R)^2} \quad (13.42)$$

Equation (13.42) was then used to calculate the allowed minimum density of fibers without sticking or bunching. In (13.41), it is shown that the minimum distance, S , depends on both the aspect ratio λ and the elastic modulus E . A smaller aspect ratio and higher elastic modulus allow for greater packing density. However, fibers with a low aspect ratio and high modulus are not desirable for adhering to rough surfaces due to lack of compliance.

13.7.5 Numerical Simulation

The simulation of adhesion of an attachment system in contact with random rough surfaces was carried out numerically. In order to conduct 2D simulations, it is necessary to calculate applied load F_n as a function of applied pressure P_n as an input condition. Using ρ calculated by non-sticking condition, Kim and Bhushan (2007c) calculated F_n as,

$$F_n = \frac{P_n p}{\rho} \quad (13.43)$$

where p is the number of springs in the scan length L , which equals $L/(S + 2R)$.

Fibers of the attachment system are modeled as one-level-hierarchy elastic springs (Fig. 13.16) (Kim and Bhushan 2007c). The deflection of each spring and the elastic force that arises in the springs are calculated according to (13.21) and (13.22), respectively. The adhesion force is the lowest value of elastic force F_{el} when the fiber has detached from the contacting surface. Kim and Bhushan (2007c)

used an iterative process to obtain optimal fiber geometry—fiber radius and aspect ratio. If the applied load, the roughness of contacting surface, and the fiber material are given, the procedure for calculating the adhesion force is repeated iteratively until the desired adhesion force is satisfied. In order to simplify the design problem, fiber material is regarded as a known variable. The next step is constructing the design database. Figure 13.27a shows the flow chart for the construction of adhesion design database, and Fig. 13.27b shows the calculation of the adhesion force that is a part of the procedure to construct an adhesion design database.

13.7.6 Results and Discussion

Figure 13.28 shows an example of the adhesion design database for biomimetic attachment systems consisting of single-level cylindrical fibers with an orientation angle of 30° and spherical tips of $R_t = 100$ nm constructed by Kim and Bhushan (2007c). The minimum fiber radius calculated by using non-fiber fracture condition, which plays a role of lower limit of optimized fiber radius, is also added on the plot. The plots in Fig. 13.28 cover all applicable fiber materials from soft elastomer material, such as poly(dimethylsiloxane) (PDMS), to stiffer polymers, such as polyimide and β keratin. The dashed lines in each plot represent the limits of fiber fracture due to the adhesion force. For a soft material with $E = 1$ MPa in Fig. 13.28a, the range of the desirable fiber radius is more than $0.3 \mu\text{m}$ and that of the aspect ratio is approximately less than 1. As elastic modulus increases, the feasible range of both fiber radius and aspect ratio also increase as shown in Fig. 13.28b, c. In Fig. 13.28, the fiber radius has a linear relation with the surface roughness on a logarithm scale.

If the applied load, the roughness of contacting surface, and the elastic modulus of a fiber material are specified, the optimal fiber radius and aspect ratio for the desired adhesion coefficient can be selected from this design database. Adhesion databases are useful for understanding biological systems and for guiding the fabrication of biomimetic attachment systems. Two case studies (Kim and Bhushan 2007c) are discussed below.

Case study I: Select the optimal size of fibrillar adhesive for a wall climbing robot with the following requirements:

- Material: polymer with $E \approx 100$ MPa
- Applied pressure by weight < 10 kPa
- Adhesion coefficient ≈ 5
- Surface roughness $\sigma < 1 \mu\text{m}$

The subplot of adhesion database that satisfies the requirement is at the second column and second row in Fig. 13.28b. From this subplot, any values on the marked line can be selected to meet the requirements. For example, fiber radius of $0.4 \mu\text{m}$ with an aspect ratio of 1 or fiber radius of $10 \mu\text{m}$ with an aspect ratio of 0.8 satisfies the specified requirements.

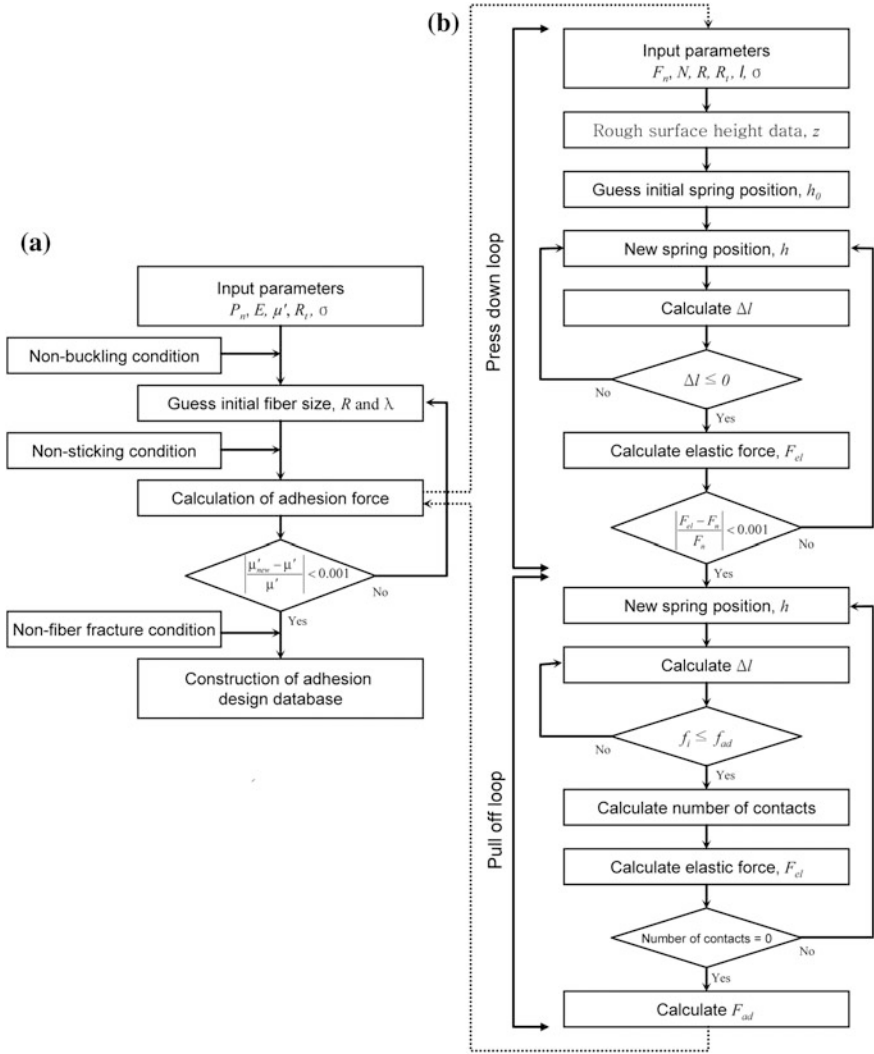


Fig. 13.27 Flow chart for **a** the construction of adhesion design database and **b** the calculation of the adhesion force. In this figure, P_n is the applied pressure, E is the elastic modulus, μ' is the adhesion coefficient, R_t is the tip radius, σ is root mean square amplitude, R is the fiber radius, λ is the aspect ratio of fiber, F_n is the applied load, N is the number of springs, k and l are stiffness and length of structures, Δl is the spring deformation, f_1 is the elastic force of a single spring, and f_{ad} is the adhesion force of a single contact (Kim and Bhushan 2007c)

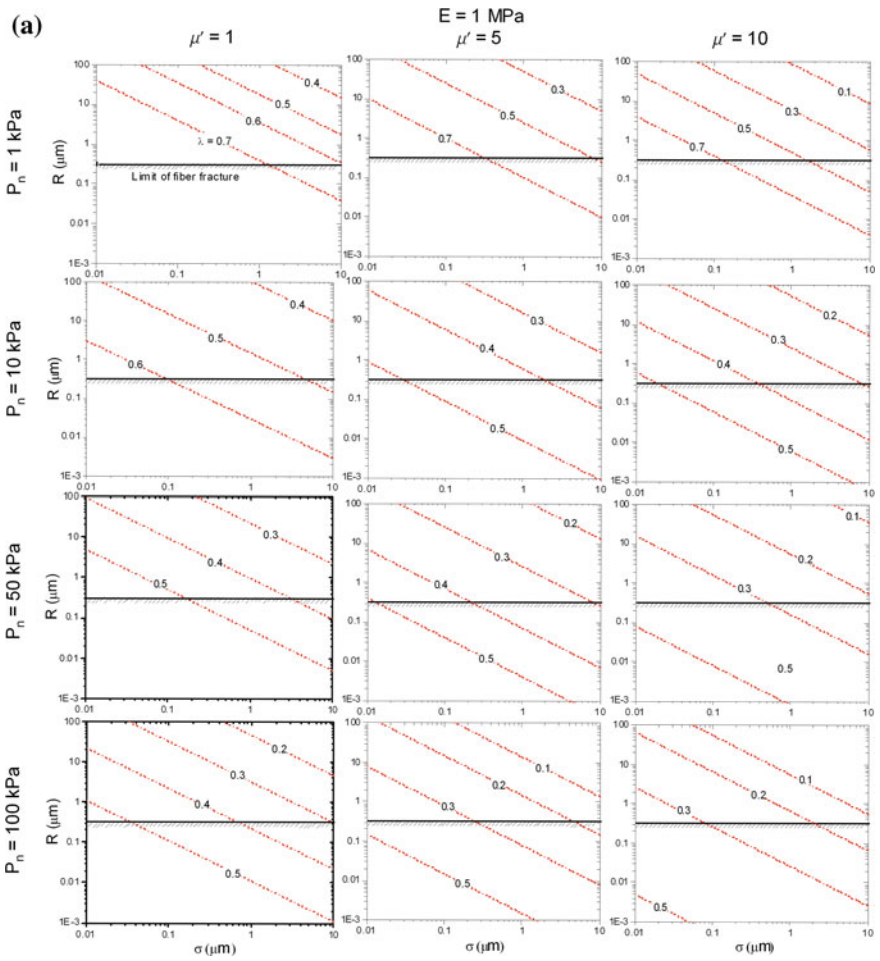


Fig. 13.28 Adhesion design database for biomimetic attachment system consisting of single-level cylindrical fibers with orientation angle of 30° and spherical tips of 100 nm for elastic modulus of **a** 1 MPa, **b** 100 MPa, and **c** 10 GPa (Kim and Bhushan 2007c). The *solid lines* shown in **b** and **c** correspond to the cases I and II, respectively, which satisfy the specified requirements (Kim and Bhushan 2007c)

Case study II: Compare with adhesion test for a single gecko seta (Autumn et al. 2000, 2002)

- Material: β -keratin with $E \approx 10$ GPa
- Applied pressure = 57 kPa ($2.5 \mu\text{N}$ on an area of $43.6 \mu\text{m}^2$)
- Adhesion coefficient = 8 to 16
- Surface roughness $\sigma < 0.01 \mu\text{m}$

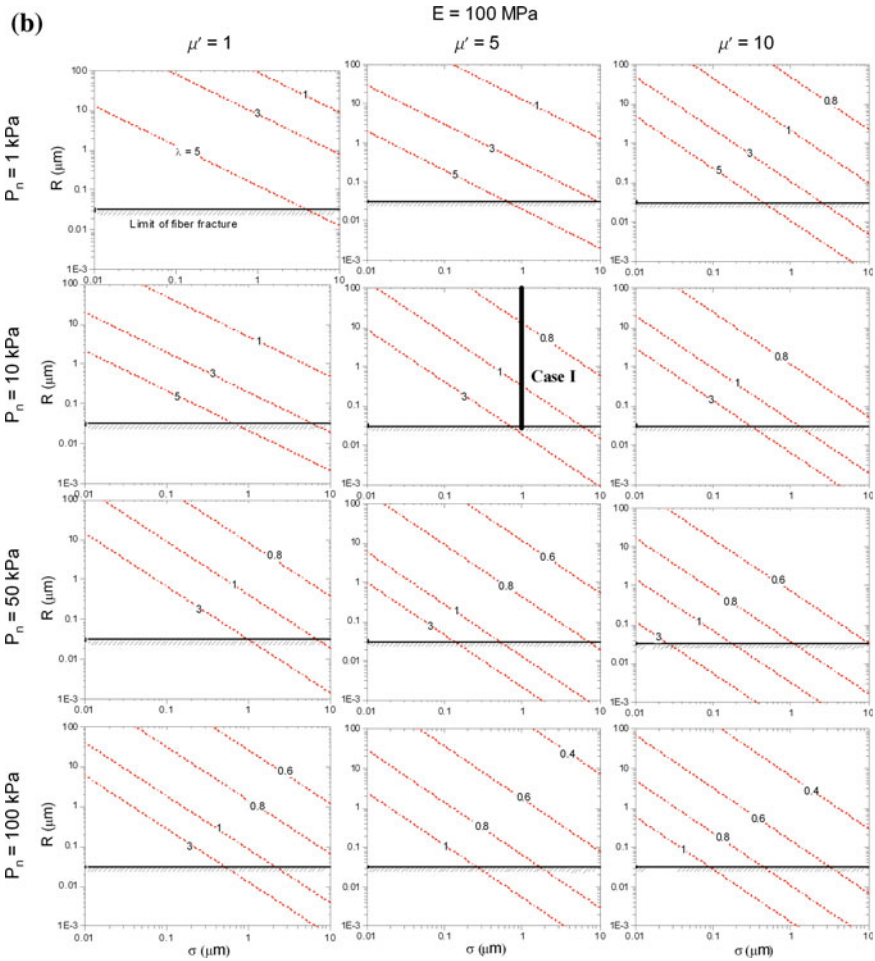


Fig. 13.28 (continued)

Autumn et al. (2000, 2002) showed that in isolated gecko setae contacting the surface of a single crystalline silicon wafer, a 2.5 μN preload yielded adhesion of 20–40 μN and thus a value of adhesion coefficient of 8–16. The region that satisfies the above requirements is marked in Fig. 13.28c. The spatulae of gecko setae have an approximate radius of 0.05 μm with an aspect ratio of 25. However, the radius corresponding to $\lambda = 25$ for the marked line is about 0.015 μm . This discrepancy is due to the difference between a simulated fiber model and a real gecko setae model. Gecko setae are composed of a three-level hierarchical structure in practice, so higher adhesion can be generated than in a single-level model (Bhushan et al. 2006; Kim and Bhushan 2007a, b). Given the simplification in the fiber model, this simulation result is very close to the experimental result.

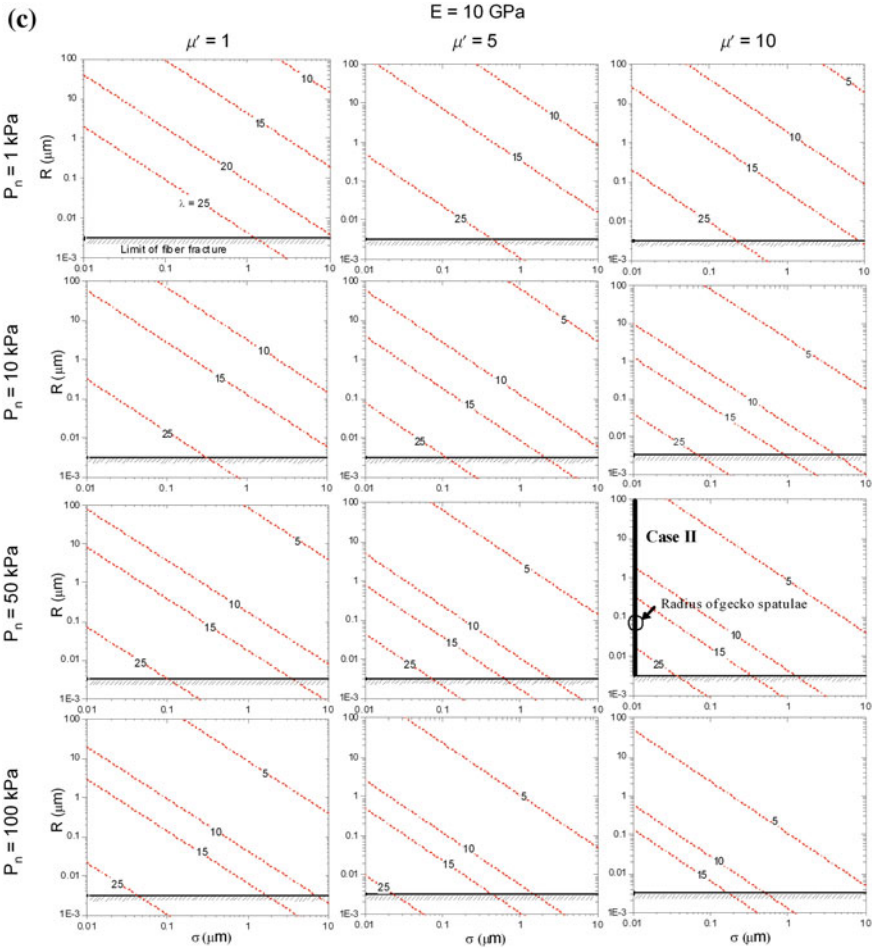


Fig. 13.28 (continued)

13.8 Fabrication of Gecko Skin-Inspired Structures

Based on the studies reported in the literature, the dominant adhesion mechanism used by gecko attachment systems appears to be van der Waals forces. The hierarchical structure involving complex divisions of the gecko skin (lamellae-setae-branches-spatulae) enable a large number of contacts between the gecko skin and mating surface. As shown in previous calculations, the van der Waals adhesive force for two parallel surfaces is inversely proportional to the cube of the distance between two surfaces. These hierarchical fibrillar microstructured surfaces would be capable of reusable dry adhesion and would have uses in a wide range of applications from everyday objects such as adhesive tapes, fasteners, toys,

microelectronic and space applications, and treads of wall-climbing robots. The development of nanofabricated surfaces capable of replicating this adhesion force developed in nature is limited by current fabrication methods. Many different techniques have been used in an attempt to create and characterize bio-inspired adhesive tapes. Attempts are being made to develop climbing robots using gecko inspired structures (Autumn et al. 2006b; Daltorio et al. 2007; Aksak et al. 2008; Cutkosky and Kim 2009).

13.8.1 Single Level Roughness Structures

A soft, compliant fibrillar structure is desirable in order to enable more fibrils to be in close proximity to a mating surface to increase van der Waals forces. Sitti and Fearing (2003) and Cho and Choi (2007) used nanoporous anodic alumina and polycarbonate membranes, as a template to create polymeric nanofibers. Geim et al. (2003) created arrays of polyimide nanofibers using electron-beam lithography and dry etching in oxygen plasma (Fig. 13.29a (left)). By using electron-beam lithography, thermal evaporation of an aluminum film, and lift-off, an array of nanoscale aluminum disks were prepared. These patterns were then transferred in the polyimide film by dry etching in oxygen plasma. A 1 cm² sample was able to create 3 N of adhesive force under the new arrangement. This is approximately one-third the adhesive strength of a gecko. They fabricated a Spiderman toy (about 0.4 N) with a hand covered with molded polymer nanohairs, Fig. 13.29b. They demonstrated that it could cling to a glass plate. Bunching of the nanohairs (as described earlier) if they are closely spaced was determined to greatly reduce the both the adhesive strength and durability of the polymer tape. The bunching can be clearly seen in Fig. 13.29a (right). Therefore, an optimal geometry is required.

Gorb et al. (2007) and Bhushan and Sayer (2007) characterized two polyvinylsiloxane (PVS) samples from Gottlieb Binder Inc., Holzgerlingen, Germany: one consisting of mushroom-shaped pillars (Fig. 13.30a), and the other an unstructured control surface (Fig. 13.30b). The structured sample is inspired by the micropatterns found in the attachment systems of male beetles from the family chrysomelidae and is easier to fabricate. Both sexes possess adhesive hairs on their tarsi. However, males bear hair extremely specialized for adhesion on the smooth surface of female's covering wings during mating. The hairs have broad flattened tips with grooves under the tip to provide flexibility. The mushroom shape provides a larger contact area. The structured samples were produced at room temperature by pouring two-compound polymerizing PVS into the holed template lying on a smooth glass support. The fabricated sample was comprised of pillars that are arranged in a hexagonal order to allow maximum packing density. They were approximately 100 μm in height, 60 μm in base diameter, 35 μm in middle diameter, and 25 μm in diameter at the narrowed region just below the terminal contact plates. These plates were about 40 μm in diameter and 2 μm in thickness at the lip edges. The adhesion force of the two samples in contact with a smooth, flat

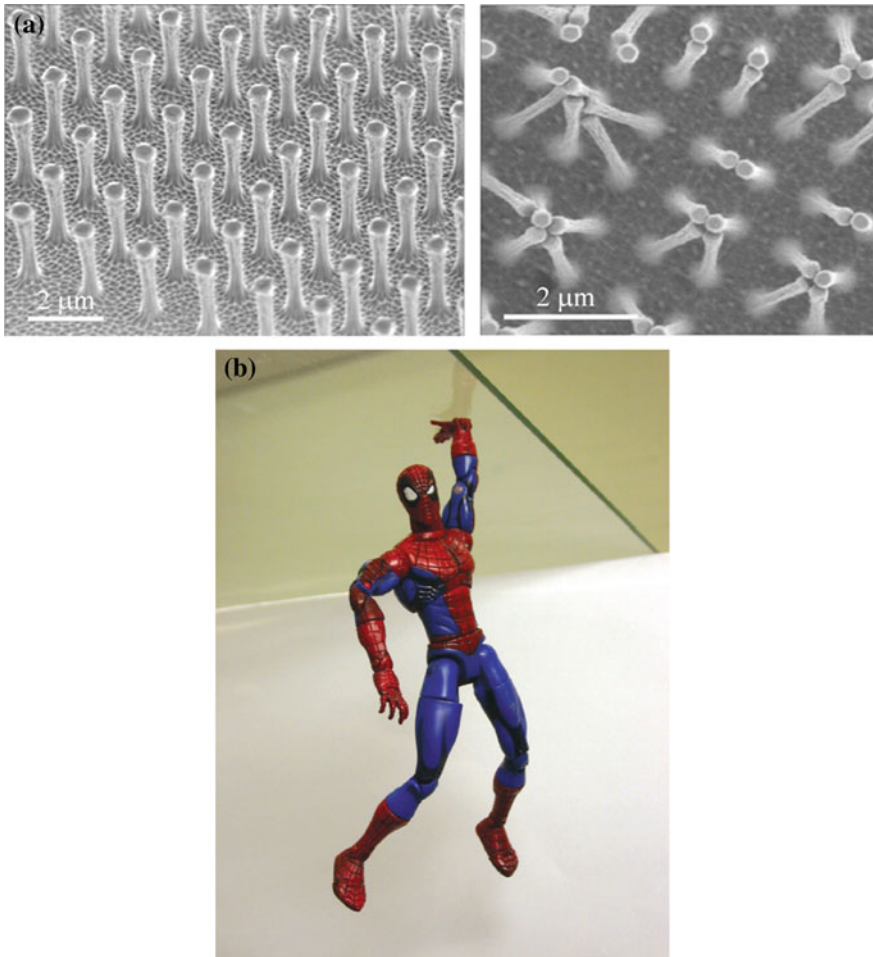
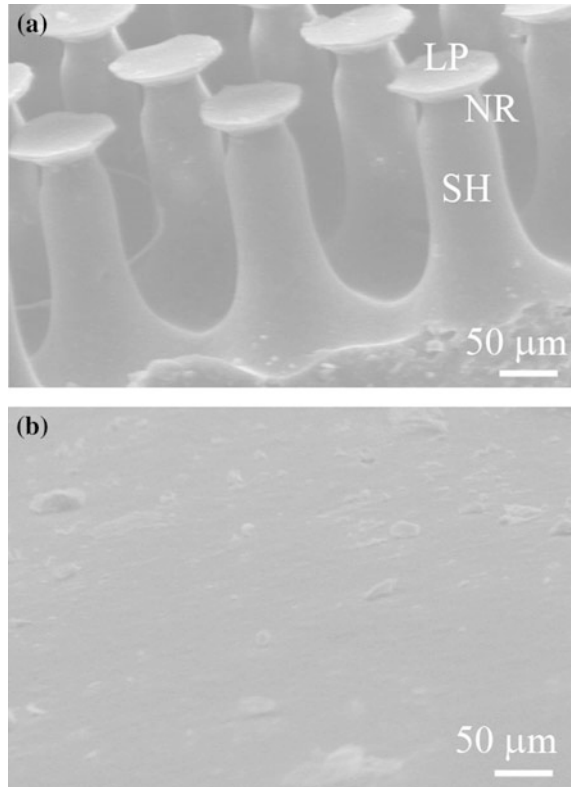


Fig. 13.29 **a** (*left*) An array of polyimide nanohairs and (*right*) bunching of the nanohairs, which leads to a reduction in adhesive force. **b** A Spiderman toy (about 0.4 N) with a hand covered with the molded polymer nanohairs, clinging to a glass plate (Geim et al. 2003)

glass substrate was measured by Gorb et al. (2007) using a microtribometer. Results revealed that the structured specimens featured an adhesion force more than twice that of the unstructured specimens. The adhesion force was also found to be independent of the preload. Moreover, it was found that the adhesive force of the structured sample was more tolerant to contamination compared to the control, and it could be easily cleaned with a soap solution.

Bhushan and Sayer (2007) characterized the surface roughness, friction force, and contact angle of the structured sample and compared the results to an unstructured control. As shown in Fig. 13.31a, the macroscale coefficient of kinetic friction of the structured sample was found to be almost four times greater than the

Fig. 13.30 SEM micrographs of the **a** structured and **b** unstructured PVS samples. *SH* shaft, *NR* neck region, *LP* lip (Bhushan and Sayer 2007)



unstructured sample. This increase was determined to be a result of the structured roughness of the sample, and not the random nanoroughness. It is also noteworthy that the static and kinetic coefficients of friction are approximately equal for the structured sample. It is believed that the divided contacts allow the broken contacts of the structured sample to constantly recreate contact. As seen in Fig. 13.31b, the pillars also increased the hydrophobicity of the structured sample, in comparison to the unstructured sample, as expected due to increased surface roughness (Wenzel 1936; Burton and Bhushan 2005; Bhushan and Jung 2011). A large contact angle is important for self-cleaning (Nosonovsky and Bhushan 2008), which agrees with the findings of Gorb et al. (2007) that the structured sample is more tolerant of contamination than the unstructured sample.

To demonstrate the potential of the mushroom-shaped microstructure for real, macroscopic applications, the structure-covered foil was glued with its back to a 20 cm × 20 cm poly(methyl methacrylate) (PMMA) plate with a handle bar. The adhesive performance was tested on a glass plate firmly attached to the ceiling. This device was able to support the weight of a human being, shown in Fig. 13.32.

Directed self-assembly has been proposed as a method to produce regularly spaced fibers (Schäffer et al. 2000; Sitti 2003). In this technique, a thin liquid

Fig. 13.31 a Coefficients of static and kinetic friction for the structured and unstructured samples slid against magnetic tape with a normal load of 130 mN.
b Water contact angle for the structured and unstructured samples (Bhushan and Sayer 2007)

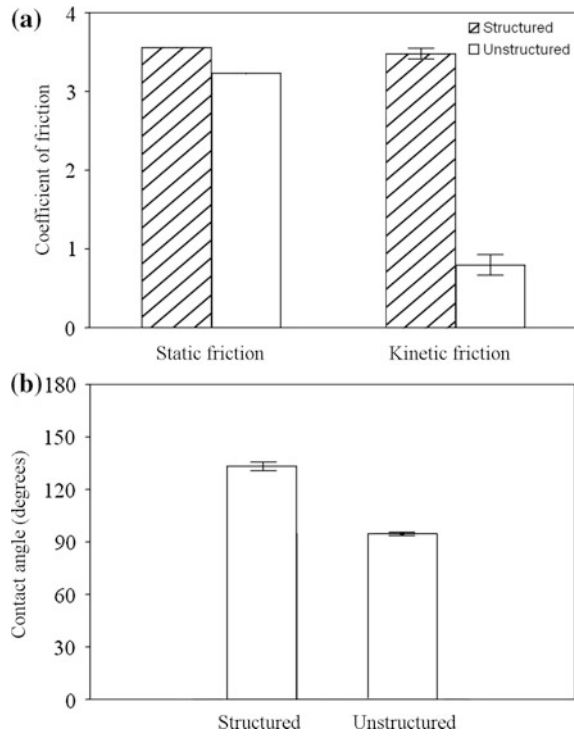


Fig. 13.32 Photograph of a man attached to the glass ceiling by a 20 cm × 20 cm PMMA plate covered by the mushroom-shaped adhesive microstructure (Heepe et al. 2012)



polymer film is coated on a flat conductive substrate. As demonstrated in Fig. 13.33, a closely spaced metal plate is used to apply a DC electric field to the polymer film. Due to instabilities on the film, pillars will begin to grow until they are touching the upper metal plate. Self-assembly is desirable because the components spontaneously assemble, typically by bouncing around in a solution or gas phase until a stable structure of minimum energy is reached.

Vertically-aligned multiwalled carbon nanotubes (MWCNT) have been used to create nanostructures on polymer surfaces. Yurdumakan et al. (2005) used chemical vapor deposition (CVD) to grow vertically-aligned MWCNT that are 50–100 μm in length on quartz or silicon substrates. The sample with MWCNT site facing up was then dipped in PMMA solution. After the polymerization, PMMA-MWCNT sheets were peeled off from the silicon substrate. The MWCNTs were exposed from the silicon-facing side of the PMMA matrix by etching the top 25 μm with a solvent. SEM images of the MWCNT grown on a silicon substrate as well as transferred into a PMMA matrix and then exposed on the surface can be seen in Fig. 13.34. On a nanoscale, the MWCNT surface was able to achieve adhesive forces two orders of magnitude greater than those of gecko foot-hairs. These structures provided high adhesion on the nanometer level and were not capable of producing high adhesion forces on the macroscale, because they are not compliant. Ge et al. (2007) and others have fabricated nanostructures by transferring micropatterned, vertically-aligned MWCNT arrays onto flexible polymer tape. They reported high adhesion on the macroscale. They also performed peeling experiments. Durability of the adhesive tape is an issue as some of the nanotubes can detach from the substrate with repeated use. Qu et al. (2008) measured adhesion on vertically-aligned MWCNT arrays on Si substrate and reported high adhesion on the nanoscale.

Davies et al. (2008) fabricated mushroom-headed microfibers made of PDMS. In one of the fabrication strategies, a silicon wafer with a thickness that defined the stalk length was obtained, and the masks with mushroom-head features were first used to pattern one side of the silicon wafer with resist. Features were etched to a

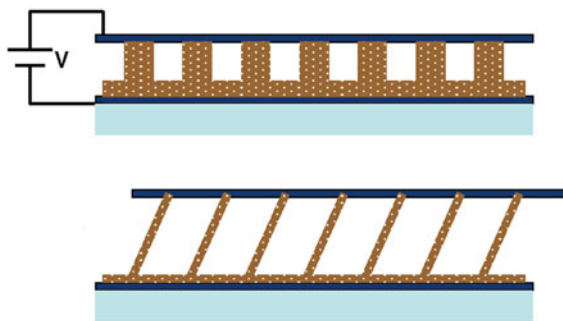


Fig. 13.33 Directed self-assembly based method of producing high aspect ratio micro/nanofibers (Sitti 2003)

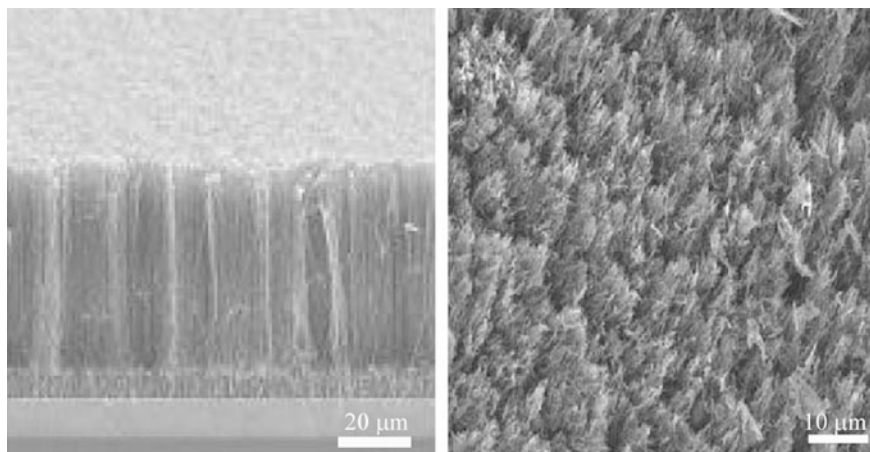


Fig. 13.34 Multi-walled carbon nanotube structures: *left* grown on silicon by chemical vapor deposition, *right* transferred into a PMMA matrix, and then exposed on the surface after solvent etching (Yurdumakan et al. 2005)

depth equal to that of the thickness of the mushroom head. Next, the smaller diameter mask was used to pattern the other side of the wafer, which was then etched to produce holes through the entire thickness of the wafer, meeting mushroom headed cavities. This mold was first coated in a fluorocarbon release agent. A PDMS solution was then spun onto this mold and cured to produce mushroom headed microfibers. The resulting casting comprising of stalks and mushroom heads was then pulled through the mold in a single peeling process. To create angled microfiber arrays found in biological attachments using photolithography, Aksak et al. (2007) simply varied the ultraviolet (UV) exposure angle by tilting the wafer during exposure. The fibers were formed at a nonperpendicular angle to the substrate surface (Fig. 13.35a). This master template of angled SU-8 fibers was then used to form many copies of the fiber arrays from curable polyurethanes by molding. They reported that angled fibers exhibited reduced adhesion compared to similar vertical fibers due to a peeling moment. However, angled fibers are favored in biological attachment systems. Murphy et al. (2007) modified angled fiber arrays by adding soft spherical and spatula shaped tips via dipping in a liquid polymer of interest (Fig. 13.35b). To add tips to the fibers, the fiber array sample attached to a micropositioning stage was dipped into a liquid polyurethane layer and retracted, retaining some of the liquid polymer on the tips of the fibers. To form spherical tips, the sample was placed with the fibers facing up and allowed to cure. To form spatula tips, the fiber sample was placed onto a smooth low energy surface and then peeled away after curing. They reported very high adhesion of these fibers with soft tips because of increased contact area.

del Campo et al. (2007a, b) fabricated pillar arrays with controlled 3D tip geometries resembling those found in biological attachments. The fabrication

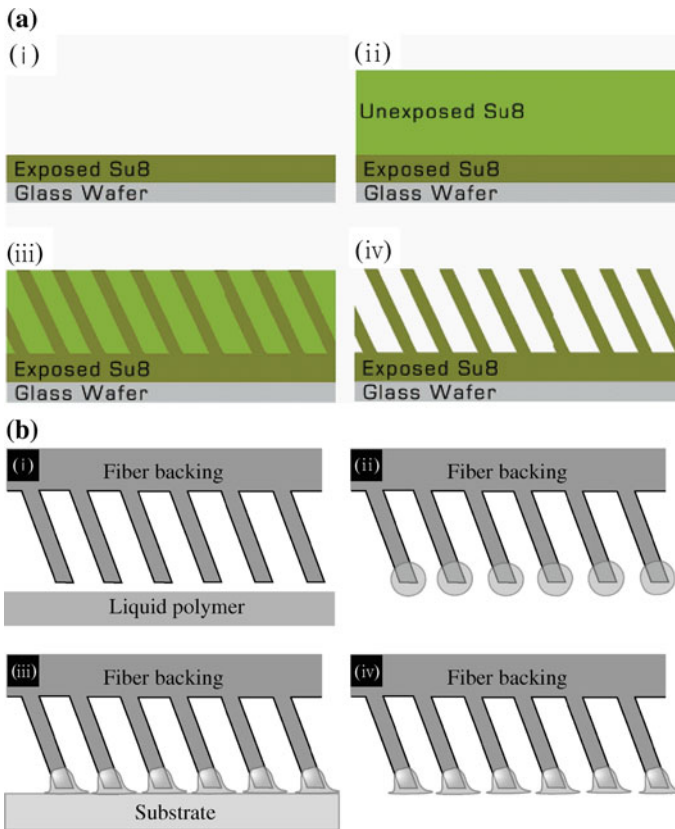


Fig. 13.35 **a** The process steps of the polymer fiber orientation: (i) a thin layer of SU-8 is spun on a glass substrate, then exposed and cured; (ii) a thicker layer of SU-8 is spun that will become the fibers; (iii) the thick layer is patterned with UV exposure by tilting the wafer; and (iv) the SU-8 photoresist is developed, leaving the desired angled fiber array (Aksak et al. 2007). **b** Fiber tip fabrication process: (i) bare fibers are aligned with a layer of liquid polymer; (ii) the fibers are dipped into the liquid and retracted; (iii) the fibers are brought into contact with a substrate; and (iv) the fibers are peeled away from the substrate after curing (Murphy et al. 2007)

strategy was based on complete or partial soft molding on 2D masters made by lithography with elastomeric precursors followed in some cases by inking and microprinting steps. The patterned master with high-aspect-ratio cylindrical holes was produced by photolithography using SU-8 photoresist films. The SU-8 masters were filled with elastomeric precursors (PDMS supplied as Sylgard 184 by Dow Corning) to produce arrays of cylindrical pillars (Fig. 13.36a). Arrays of pillars with spherical and spatular tips were obtained by inking the Sylgard 184-structured substrates in a thin film of Sylgard 184 precursor. Curing of arrays in upside-down orientation yielded hemispherical tips as a consequence of gravity and surface tension acting on the fluid drop (Fig. 13.36b). Alternatively, the inked stamp can be

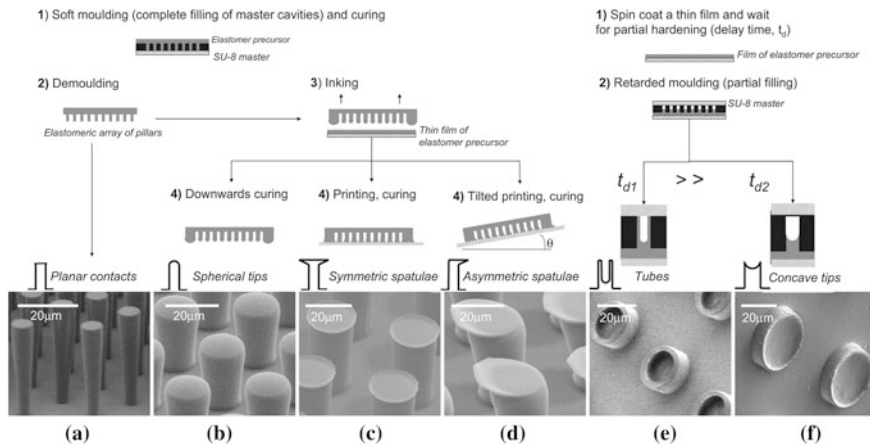


Fig. 13.36 The fabrication strategies and SEM images showing examples of the pillar arrays obtained with controlled 3D tip geometries (del Campo et al. 2007a)

pressed against a flat substrate and then cured. This leads to pillars with a flat roof (Fig. 13.36c). The roof can be symmetric or asymmetric depending on the tilt of the substrate during curing (Fig. 13.36c, d). They also used silicones used for dental impressions. These materials possess higher initial viscosities and faster crosslinking kinetics than Sylgard 184, which results in incomplete cavity filling. By soft moulding these materials after selected delay times after mixing, arrays of tubes and pillars with concave tips (Fig. 13.36e, f) were obtained. They performed adhesion tests on various geometries against a sapphire sphere. They reported that shape of pillar tip affects the contact area and adhesion behavior. Figure 13.37 shows the pull-off strength data as a function of tip radius for various tip geometries. For a given tip radius, pillars with flat punch geometry have significantly higher adhesion than spherical contacts. Pillars with mushroom tips have the highest adhesion.

13.8.2 Multi-level Hierarchical Structures

The aforementioned fabricated surfaces only have one level of roughness. Although these surfaces are capable of producing high adhesion on the micro/nanoscale, they are not expected to produce large scale adhesion due to a lack of compliance and bunching.

del Campo and Greiner (2007) fabricated a hierarchical structure by two-level photolithography. Figure 13.38 shows a schematic of the process and an example of two-level SU-8 patterns obtained.

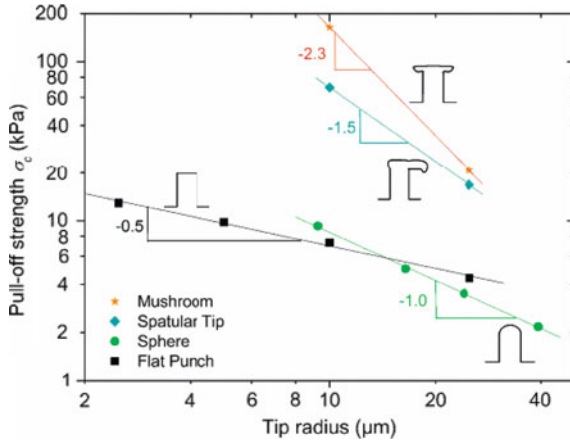
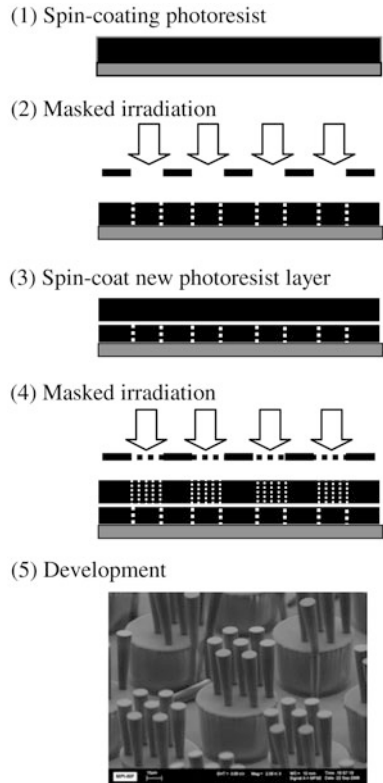


Fig. 13.37 Tip radius dependence of the pull-off force for flat, spherical, spatular, and mushroom-like contacts at a preload of 1 mN. In the case of spherical tips, the radius corresponds to the tip radius. For all other geometries, the pillar radius is used (del Campo et al. 2007b)

Fig. 13.38 Layer-by-layer structuring method and example of fabricated hierarchical structure with SU-8. Base pillars have 50 μm diameter and 40 μm height and the top pillars have 9 μm diameter and 35 μm height (del Campo and Greiner 2007)



Palacio et al. (2013) fabricated two-level hierarchically structured superhydrophobic surfaces made of polyethylene using two-stacked porous polycarbonate membranes as template. Bhushan and Lee (2012) and Lee and Bhushan (2012) fabricated one level, two-level, and three-level hierarchically structured superhydrophobic surfaces made of polypropylene using one, two, or three stacked porous polycarbonate membranes as a template, respectively, Fig. 13.39. By changing the density and diameter of the nanofibers, surfaces with either the lotus effect or gecko effect could be achieved. Figure 13.40 shows the SEM micrographs of selected micro-, nano-, and hierarchical structures made from polypropylene (Lee and Bhushan 2012). Figure 13.41 shows the contact angle and contact angle hysteresis data (Lee and Bhushan 2012). It can be seen that all structures surfaces are superhydrophobic governed by air pocket formation on the surfaces. Figure 13.42 shows the adhesive force data (Lee and Bhushan 2012). The oriented fibers of 100 and 600 nm diameter and hierarchical structure exhibited the gecko effect (high adhesion) due to their high fiber densities and large contact areas. Conversely, the random fibers of 50 nm and the oriented fibers of 5 and 14 μm diameter exhibited the lotus effect due to their smaller fiber density. They used a soft, conventional adhesive to coat fiber ends to provide added adhesion.

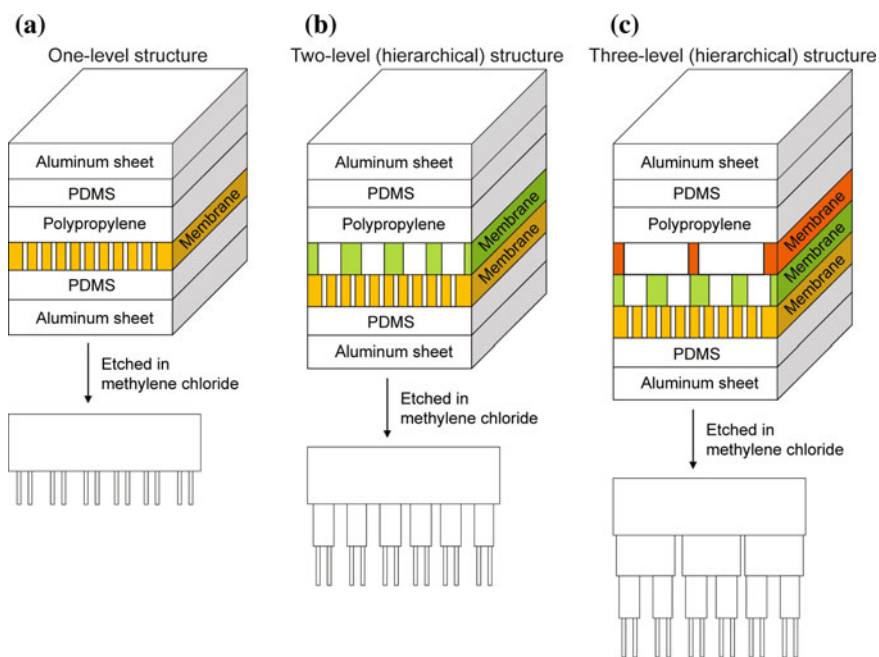


Fig. 13.39 Sample fabrication processes for **a** the one-level, **b** the two-level, and **c** the three-level fiber structures using one, two, and three polycarbonate membranes in the stack, respectively. After heating the stacks in an oven, the membranes are etched using methylene chloride to obtain the fibrillar samples (Bhushan and Lee 2012)

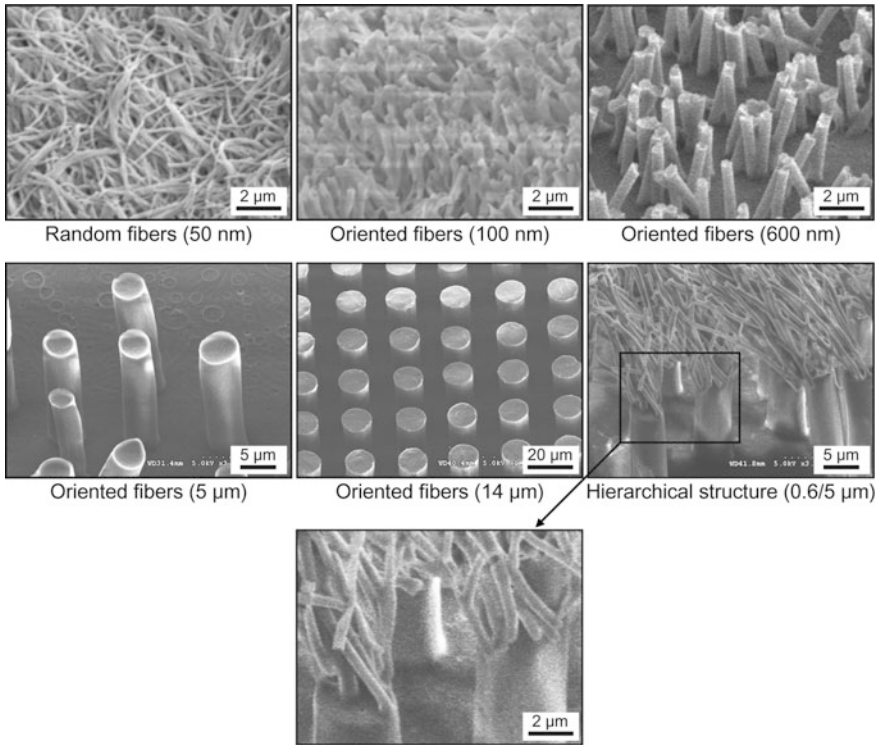


Fig. 13.40 SEM images for samples. The one layer structure of 50 nm diameter random fiber, 100 and 600 nm oriented fibers, 5 and 20 μm diameter oriented fibers, and the two layer structure of 600 nm diameter with 5 μm diameter oriented fibers are shown (Lee and Bhushan 2012)

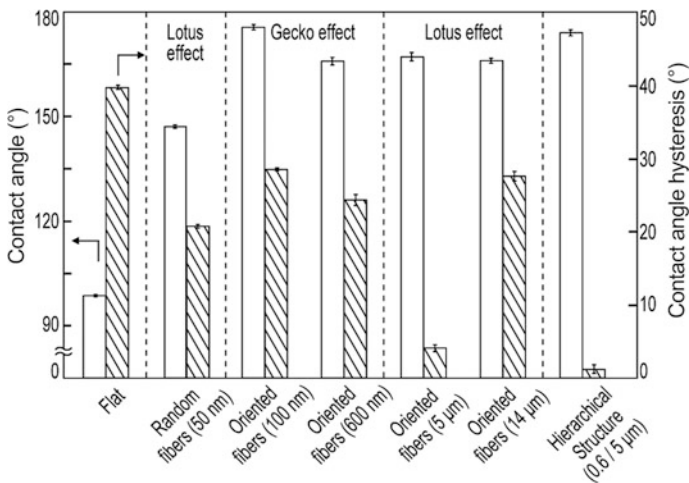
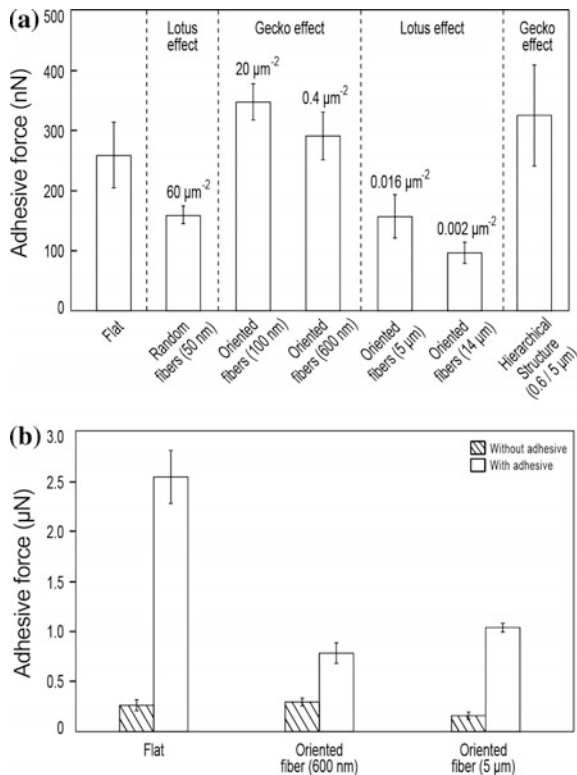


Fig. 13.41 The measured CAs and CAHs on all the one- and two-layered samples (Lee and Bhushan 2012)

Fig. 13.42 a Adhesive force on all the one- and two-layered samples measured using the $30\ \mu\text{m}$ diameter tip. The values above each bar are the number of fibers in unit area (μm^2). The measurements were performed at a temperature of $21\ ^\circ\text{C}$ and 45–55 % relative humidity, and **b** adhesive force of the fibers with and without the adhesive applied to the samples (Lee and Bhushan 2012)



Northern and Turner (2005) created a two-level compliant structure by employing a microelectromechanical based approach. The multiscale structures consisted of arrays of organic-looking photoresist nanorods (organorods), $\sim 2\ \mu\text{m}$ tall and 50–200 nm in diameter (comparable in size to gecko spatulae) (Fig. 13.43a); atop photolithographically defined $2\ \mu\text{m}$ thick SiO_2 platforms 100–150 μm on a side (Fig. 13.43b). The platforms of various geometries are supported by single high aspect ratio pillars down to $1\ \mu\text{m}$ in diameter and with heights up to $\sim 50\ \mu\text{m}$ (Fig. 13.43c). The structures were fabricated out of 100 mm single-crystal wafers using standard bulk micromachining techniques. An array of four-fingered platform structures is shown in Fig. 13.43d. Adhesion testing was performed using a nanorod surface on a solid substrate and on the two-level structures. They reported that adhesive pressure of the two-level structures was about four times higher than that of the surfaces with only one level of hierarchy.

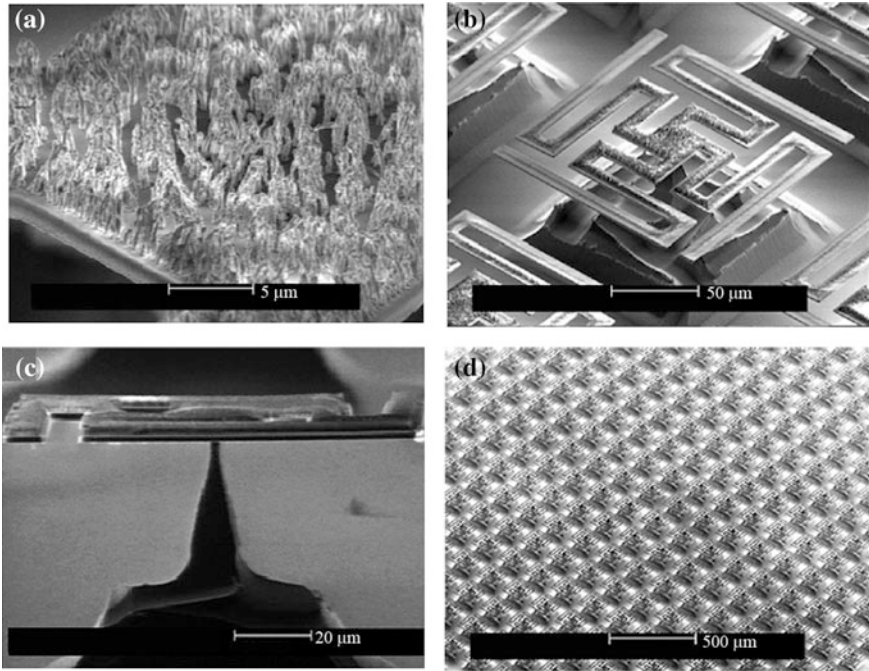


Fig. 13.43 Two-level fabricated adhesive structure composed of **a** organorods atop, **b** silicon dioxide platforms. The platforms are supported by **c** support pillars. **d** This structure was repeated multiple times over a silicon wafer (Northen and Turner 2005)

13.9 Closure

The adhesive properties of geckos and other creatures, such as flies, beetles and spiders, are due to the hierarchical structures present on each creature's hairy attachment pads. Geckos have developed the most intricate adhesive structures of any of the aforementioned creatures. The attachment system consists of ridges called lamellae that are covered in microscale setae that branch off into nanoscale spatulae, about three billion spatulae on two feet. The so-called division of contacts provide high dry adhesion. Multiple level hierarchically structured surface construction plays an important role in adapting to various rough surfaces, bringing the spatulae in close proximity with the mating surface. These structures, as well as material properties, allow the gecko to obtain a much larger real area of contact between its feet and a mating surface than is possible with a non-fibrillar material. Two feet of a Tokay gecko have about 220 mm² of attachment pad area on which the gecko is able to generate approximately 20 N of adhesion force. Although capable of generating high adhesion forces, a gecko is able to detach from a surface at will—an ability known as smart adhesion. Detachment is achieved by a peeling motion of the gecko's feet from a surface.

Experimental results have supported the adhesion theories of intermolecular forces (van der Waals) as a primary adhesion mechanism and capillary forces as a secondary mechanism, and have been used to rule out several other mechanisms of adhesion including the secretion of sticky fluids, suction, and increased frictional forces. Atomic force microscopy has been employed by several investigators to determine the adhesion strength of gecko foot hairs. The measured values of the lateral force required to pull parallel to the surface for a single seta (194 μN) and adhesive force (normal to the surface) of a single spatula (11 nN) are comparable to the van der Waals prediction of 270 μN and 11nN for a seta and spatula, respectively. The adhesion force generated by seta increases with preload and reaches a maximum when both perpendicular and parallel preloads are applied. Although gecko feet are strong adhesives, they remain free of contaminant particles through self-cleaning. Spatular size, along with material properties, enables geckos to easily expel any dust particles that come into contact with their feet.

A three-level hierarchical model for a gecko lamella consisting of setae, branches, and spatulae has brought more insight into adhesion of biological attachment systems. One-, two- and three-level hierarchically structured spring models for simulation of a seta contacting with random rough surfaces were considered. The simulation results show that the multi-level hierarchical structure has a higher adhesion force as well as higher adhesion energy than the one-level structure for a given applied load, due to better adaptation and attachment ability. It is concluded that the multi-level hierarchical structure produces adhesion enhancement, and this enhancement increases with an increase in the applied load and a decrease in the stiffness of springs. The condition at which a significant adhesion enhancement occurs appears to be related to the maximum spring deformation. The result shows that significant adhesion enhancement occurs when the maximum spring deformation is two to three times larger than the σ value of surface roughness. For the effect of applied load, as the applied load increases, adhesion force increases up to a certain applied load, and then has a constant value, whereas, adhesion energy continues to increase with an increase in the applied load. For the effect of spring stiffness, the adhesion coefficient increases with a decrease in the stiffness of springs. The hierarchical model with more compliant springs can generate higher adhesion enhancement in the lower applied load. For the effect of the number of springs, as the number of springs on the lower level increases, the equivalent stiffness decreases. Therefore, the three-level model with larger number of springs on the lowest level gives larger adhesion force and energy. Inclusion of capillary forces in the spring model shows that the total adhesion force decreases as a substrate becomes more hydrophobic (increase in the contact angle of water). The difference of total adhesion force among different contact angles is larger in the intermediate humidity regime. In addition, the simulation results match the measured data for a single spatula in contact with both the hydrophilic and the hydrophobic surfaces, which further supports van der Waals forces as the dominant mechanism of adhesion and capillary forces as a secondary mechanism.

There is a great interest among the scientific community to create surfaces that replicate the adhesion strength of gecko feet. These hierarchical fibrillar

microstructured surfaces would be capable of reusable dry adhesion, and would have uses in a wide range of applications from everyday objects such as adhesive tapes, fasteners, toys, microelectronics, and space applications, to the treads of wall-climbing robots. In the design of fibrillar structures, it is necessary to ensure that the fibrils are compliant enough to easily deform to the mating surface's roughness profile, yet rigid enough to not collapse under their own weight. Spacing between the individual fibrils is also important. If the spacing is too small, adjacent fibrils can attract each other through intermolecular forces which will lead to bunching. The adhesion design database developed by Kim and Bhushan (2007c) serves as a reference for choosing design parameters.

Nanoindentation, molding, self-assembly, carbon nanotube arrays, and lithography are some of the methods that have been used to create fibrillar structures. The limitations of current machining methods on the micro/nanoscale have resulted in the majority of fabricated surfaces consisting of only one level of hierarchy. Bunching, lack of compliance, and lack of durability are some of the problems that may arise with the aforementioned structures. Multilevel compliant systems have been created using molding, photolithography, and a microelectromechanical based approach. Inspired by work on adding tips to the fibrillar structures, the end of the fibers could be modified to enhance adhesion. For example, a soft adhesive could be used to coat fiber ends to provide added adhesion by conventional adhesives.

Fibrillar structures show great promise in the creation of adhesive structures. Some of the structures have been incorporated into the design of treads of climbing robots.

References

- Aksak, B., Murphy, M. P., and Sitti, M. (2007), "Adhesion of Biologically Inspired Vertical and Angled Polymer Microfiber Arrays," *Langmuir* **23**, 3322-3332.
- Aksak, B., Murphy, M. P., and Sitti, M. (2008), "Gecko Inspired Micro-Fibrillar Adhesives for Wall Climbing Robots on Micro/Nanoscale Rough Surfaces," *Proc. 2008 IEEE Conf. on Robotics and Automation*, Pasadena, CA, pp. 3058-3063.
- Aristotle, *Historia Animalium*, trans. Thompson, D.A.W. (1918), <http://classics.mit.edu/Aristotle/history_anim.html>.
- Arzt, E., Gorb, S. and Spolenak, R. (2003), "From Micro to Nano Contacts in Biological Attachment Devices," *Proc. Natl. Acad. Sci. USA* **100**, 10603-10606.
- Autumn, K. (2006), "How Gecko Toes Stick," *Am. Scientist*, **94**, 124-132.
- Autumn, K. and Peattie, A. M. (2002), "Mechanisms of Adhesion in Geckos," *Integr. Comp. Biol.* **42**, 1081-1090.
- Autumn, K., Liang, Y. A., Hsieh, S. T., Zesch, W., Chan, W. P., Kenny, T. W., Fearing, R. and Full, R. J. (2000), "Adhesive Force of a Single Gecko Foot-Hair," *Nature*, **405**, 681-685.
- Autumn, K., Sitti, M., Liang, Y.A., Peattie, A.M., Hansen, W.R., Sponberg, S., Kenny, T.W., Fearing, R., Israelachvili, J.N. and Full R.J. (2002), "Evidence for van der Waals Adhesion in Gecko Setae," *Proc. Natl. Acad. Sci. USA* **99**, 12252-12256.
- Autumn, K., Majidi, C., Groff, R.E., Dittmore, A., and Fearing, R. (2006a), "Effective Elastic Modulus of Isolated Gecko Setal Arrays," *J. Exp. Biol.* **209**, 3558-3568.

- Autumn, K., Dittmore, A., Santos, D., Spenko, M., and Cutkosky, M. (2006b), "Frictional Adhesion, a New Angle on Gecko Attachment," *J. Exp. Biol.* **209**, 3569-3579.
- Barnes, W. J. P., Smith, J., Oines, C., and Mundl, R. (2002), "Bionics and Wet Grip," *Tire Technol. Int.* **2002**, 56-60.
- Bergmann, P.J. and Irschick, D. J. (2005), "Effects of Temperature on Maximum Clinging Ability in a Diurnal Gecko: Evidence for a Passive Clinging Mechanism?" *J. Exp. Zool.* **303A**, 785-791.
- Bertram, J. E. A. and Gosline, J. M. (1987), "Functional Design of Horse Hoof Keratin: The Modulation of Mechanical Properties through Hydration Effects," *J. Exp. Biol.* **130**, 121-136.
- Bhushan, B. (1996), *Tribology and Mechanics of Magnetic Storage Devices, second ed.*, Springer-Verlag, New York.
- Bhushan, B. (2007), "Adhesion of Multi-Level Hierarchical Attachment Systems in Gecko Feet," *J. Adhesion Sci. Technol.* **21**, 1213-1258.
- Bhushan, B. (2010), *Springer Handbook of Nanotechnology, third ed.*, Springer-Verlag, Heidelberg, Germany.
- Bhushan B. (2011) *Nanotribology and Nanomechanics I – Measurement Techniques, II – Nanotribology, Biomimetics, and Industrial Applications, third ed.*, Springer-Verlag, Heidelberg, Germany.
- Bhushan, B. (2013a), *Principles and Applications of Tribology, 2nd Ed.*, Wiley, New York.
- Bhushan, B. (2013b), *Introduction to Tribology, 2nd Ed.*, Wiley, New York.
- Bhushan, B. and Jung, Y. C. (2011), "Natural and Biomimetic Artificial Surfaces for Superhydrophobicity, Self-Cleaning, Low Adhesion, and Drag Reduction," *Prog. Mater. Sci.* **56**, 1-108.
- Bhushan, B. and Lee, H., "Fabrication and Characterization of Multi-level Hierarchical Surfaces," *Faraday Discussion* **156**, 235-241 (2012).
- Bhushan, B. and Sayer, R. A. (2007), "Surface Characterization and Friction of a Bio-Inspired Reversible Adhesive Tape," *Microsyst. Technol.* **13**, 71-78.
- Bhushan, B., Peressadko, A. G., and Kim, T. W. (2006) "Adhesion Analysis of Two-Level Hierarchical Morphology in Natural Attachment Systems for 'Smart Adhesion'," *J. Adhesion Sci. Technol.* **20**, 1475-1491.
- Bikerman, J. J. (1961), *The Science of Adhesive Joints*, Academic, New York.
- Burton, Z. and Bhushan, B. (2005), "Hydrophobicity, Adhesion, and Friction Properties of Nanopatterned Polymers and Scale Dependence for Micro- and Nanoelectromechanical Systems," *Nano Letters* **5**, 1607-1613.
- Cai, S. and Bhushan, B. (2007), "Effects of Symmetric and Asymmetric Contact Angles and Division of Menisci on Meniscus and Viscous Forces during Separation," *Philos. Mag.* **87**, 5505-5522
- Cai, S. and Bhushan, B. (2008), "Meniscus and Viscous Forces During Separation of Hydrophilic and Hydrophobic Surfaces with Liquid Mediated Contacts," (invited) *Mater. Sci. Eng. R* **61**, 78-106.
- Cho, W. K. and Choi, I. S. (2007), "Fabrication of Hairy Polymeric Films Inspired by Geckos: Wetting and High Adhesion Properties," *Adv. Func. Mater.* **18**, 1089-1096.
- Chui, B. W., Kenny, T. W., Mamin, H. J., Terris, B. D. and Rugar, D. (1998), "Independent Detection of Vertical and Lateral Forces with a Sidewall-Implanted Dual-Axis Piezoresistive Cantilever," *Appl. Phys. Lett.* **72**, 1388-1390.
- Cutkosky, M. R. and Kim, S. (2009), "Design and Fabrication of Multi-Materials Structures for Bio-Inspired Robots," *Phil. Trans. R. Soc. A* **367**, 1799-1813.
- Dalton, K. A., Gorb, S., Peressadko, A., Horchler, A. D., Ritzmann, R. E., and Quinn, R. D. (2007), "A Robot that Climbs Walls using Micro-Structured Polymer Adhesive," *Proc. 30th Annual Meeting of the Adhesion Society*, pp. 329-331.
- Davies, J., Haq, S., Hawke, T., and Sargent, J. P. (2008), "A Practical Approach to the Development of a Synthetic Gecko Tape," *Int. J. Adhesion and Adhesives* **29**, 380-390.
- del Campo, A. and Greiner, C. (2007), "SU-8: A Photoresist for High-Aspect-Ratio and 3D Submicron Lithography," *J. Micromech. Microeng.* **17**, R81-R95.

- del Campo, A. Greiner, C., Alvares, I., and Arzt, E. (2007a), "Patterned Surfaces with Pillars with Controlled 3D Tip Geometry Mimicking Bioattachment Devices," *Adv. Mater.* **19**, 1973-1977.
- del Campo, A., Greiner, C. and Arzt, E. (2007b), "Contact Shape Controls Adhesion of Bioinspired Fibrillar Surfaces," *Langmuir* **23**, 10235-10243.
- Dellit, W. D. (1934), "Zur Anatomie und Physiologie der Geckozehne," *Jena. Z. Naturwissen*, **68**, 613-658.
- Derjaguin, B. V., Muller, V. M., and Toporov, Y. P. (1975), "Effect of Contact Deformation on the Adhesion of Particles," *J. Colloid Interface Sci.* **53**, 314-326.
- Dieter G. E. (1988), *Mechanical Metallurgy*, McGraw Hill, London.
- Fan, P. L. and O'Brien, M. J. (1975), "Adhesion in Deformable Isolated Capillaries," *Adhesion Science and Technology*, ed. Lee, L. H., **9A**, 635, Plenum, New York.
- Federle, W., (2006) "Why are So Many Adhesive Pads Hairy?" *J. Exp. Biol.* **209**, 2611-2621.
- Federle, W., Riehle, M., Curtis, A. S. G. and Full, R. J. (2002), "An Integrative Study of Insect Adhesion: Mechanics of Wet Adhesion of Pretarsal Pads in Ants," *Integr. Comp. Biol.* **42**, 1100-1106.
- Federle, W., Barnes, W. J. P., Baumgartner, W., Drechsler, P., and Smith, J. M. (2006), "Wet but Not Slippery: Boundary Friction in Tree Frog Adhesive Toe Pads," *J. R. Soc. Interf.* **3**, 689-697.
- Gao, H., Wang, X., Yao, H., Gorb, S. and Arzt, E. (2005), "Mechanics of Hierarchical Adhesion Structures of Geckos," *Mech. Mater.* **37**, 275-285.
- Ge, L., Sethi, S., Ci, L., Ajayan, M., and Dhinojwale, A. (2007), "Carbon Nanotube-based Synthetic Gecko Tape," *PNAS* **104**, 10792-10795.
- Geim, A. K., Dubonos, S. V., Grigorieva, I. V., Novoselov, K. S., Zhukov, A. A. and Shapoval, S. Y. (2003), "Microfabricated Adhesive Mimicking Gecko Foot-Hair," *Nat. Mater.* **2**, 461-463.
- Gennaro, J. G. J. (1969), "The Gecko Grip," *Nat. Hist.* **78**, 36-43.
- Glassmaker, N. J., Jagota, A., Hui, C. Y. and Kim, J. (2004), "Design of Biomimetic Fibrillar Interfaces: 1. Making Contact," *J. R. Soc. Interface* **1**, 23-33.
- Glassmaker, N. J., Jagota, A. and Hui, C. Y. (2005), "Adhesion Enhancement in a Biomimetic Fibrillar Interface," *Acta Biomaterialia* **1**, 367-375.
- Gorb, S. (2001), *Attachment Devices of Insect Cuticles*, Kluwer, Dordrecht, Netherlands.
- Gorb, S., Varenberg, M., Peressadko, A. and Tuma, J. (2007), "Biomimetic Mushroom-Shaped Fibrillar Adhesive Microstructures," *J. Royal Soc. Interf.* **4**, 271-275.
- Hamaker, H. C. (1937), "London van der Waals Attraction between Spherical Bodies," *Physica*, **4**, 1058.
- Han, D., Zhou, K., and Bauer, A. M. (2004), "Phylogenetic Relationships among Gekkotan Lizards Inferred from C-mos Nuclear DNA Sequences and a New Classification of the Gekkota," *Biol. J. Linn. Soc.* **83**, 353-368.
- Hanna, G. and Barnes, W. J. P. (1991), "Adhesion and Detachment of the Toe Pads of Tree Frogs," *J. Exper. Biol.* **155**, 103-125.
- Hansen, W. R. and Autumn, K. (2005), "Evidence for Self-Cleaning in Gecko Setae," *Proc. Natl. Acad. Sci. USA* **102**, 385-389.
- Heepe, L., Kovalev, A. E., Varenberg, M., Tuma, J., and Gorb, S. N. (2012), "First Mushroom-Shaped Adhesive Microstructure: A Review," *Theoretical *pp1. Mech. Lett.* **2**, 014008
- Hiller, U. (1968), "Untersuchungen zum Feinbau und zur Funktion der Haftborsten von Reptilien," *Z. Morphol. Tiere*, **62**, 307-362.
- Hinds, W. C. (1982), *Aerosol Technology: Properties, Behavior, and Measurement of Airborne Particles*, Wiley, New York.
- Hora, S. L. (1923), "The Adhesive Apparatus on the Toes of Certain Geckos and Tree Frogs," *J. Asiat. Soc. Beng.* **9**, 137-145.
- Houwink, R. and Salomon, G. (1967), "Effect of Contamination on the Adhesion of Metallic Couples in Ultra High Vacuum," *J. Appl. Phys.* **38**, 1896-1904.
- Huber, G., Gorb, S. N., Spolenak, R. and Arzt, E. (2005a), "Resolving the Nanoscale Adhesion of Individual Gecko Spatulae by Atomic Force Microscopy," *Biol. Lett.* **1**, 2-4.

- Huber, G., Mantz, H., Spolenak, R., Mecke, K., Jacobs, K., Gorb, S. N. and Arzt, E. (2005b), "Evidence for Capillarity Contributions to Gecko Adhesion from Single Spatula and Nanomechanical Measurements," *Proc. Natl. Acad. Sci. USA* **102**, 16293-16296.
- Irschick, D. J., Austin, C. C., Petren, K., Fisher, R. N., Losos, J. B. and Ellers, O. (1996), "A Comparative Analysis of Clinging Ability Among Pad-Bearing Lizards," *Biol. J. Linn. Soc.* **59**, 21-35.
- Israelachvili, J. N. (1992), *Intermolecular and Surface Forces*, 2nd edition, Academic, San Diego.
- Israelachvili, J. N. and Tabor, D. (1972), "The Measurement of van der Waals Dispersion Forces in the Range of 1.5 to 130 nm," *Proc. R. Soc. Lond. A.* **331**, 19-38.
- Jaenicke, R. (1998), "Atmospheric Aerosol Size Distribution," *Atmospheric Particles*, R.M. Harrison and R. van Grieken, eds., pp. 1-29, Wiley, New York.
- Jagota, A. and Bennison, S. J. (2002), "Mechanics of Adhesion through a Fibrillar Microstructure," *Integr. Comp. Biol.* **42**, 1140-1145.
- Johnson, K. L., Kendall, K. and Roberts, A. D. (1971), "Surface Energy and the Contact of Elastic Solids," *Proc. R. Soc. Lond. A.* **324**, 301-313.
- Kesel, A. B., Martin, A. and Seidl, T. (2003), "Adhesion Measurements on the Attachment Devices of the Jumping Spider *Evarcha arcuata*," *J. Exp. Biol.* **206**, 2733-2738.
- Kim, T. W. and Bhushan, B. (2007a), "The Adhesion Analysis of Multi-Level Hierarchical Attachment System Contacting with a Rough Surface," *J. Adhesion Sci. Technol.* **21**, 1-20.
- Kim, T. W. and Bhushan, B. (2007b), "Effect of Stiffness of Multi-Level Hierarchical Attachment System on Adhesion Enhancement," *Ultramicroscopy* **107**, 902-912.
- Kim, T. W. and Bhushan, B. (2007c), "Optimization of Biomimetic Attachment System Contacting with a Rough Surface," *J. Vac. Sci. Technol. A* **25** 1003-1012.
- Kim, T. W. and Bhushan, B. (2008), "The Adhesion Model Considering Capillarity for Gecko Attachment System," *J. R. Soc. Interf.* **5**, 319-327.
- Kluge, A. G. (2001), "Gekkotan Lizard Taxonomy," *Hamadryad* **26**, 1-209.
- Lee, H. and Bhushan, B. (2012), "Fabrication and Characterization of Hierarchical Nanostructured Smart Adhesion Surfaces," *J. Colloid Surf. Sci.* **372**, 231-238.
- Losos, J. B. (1990), "Thermal Sensitivity of Sprinting and Clinging Performance in the Tokay Gecko (*Gekko gekko*)," *Asiat. Herp. Res.* **3**, 54-59.
- Maderson, P. F. A. (1964), "Keratinized Epidermal Derivatives as an Aid to Climbing in Gekkonid Lizards," *Nature* **203**, 780-781.
- Murphy, M. P., Aksak, B., and Sitti, M. (2007), "Adhesion and Anisotropic Friction Enhancement of Angled Heterogeneous Micro-fiber Arrays with Spherical and Spatula Tips," *J. Adhes. Sci. Technol.* **21**, 1281-1296.
- Northen, M. T. and Turner, K. L., (2005), "A Batch Fabricated Biomimetic Dry Adhesive," *Nanotechnology*, **16**, 1159-1166.
- Nosonovsky, M. and Bhushan, B. (2008), *Multiscale Dissipative Mechanisms and Hierarchical Surfaces: Friction, Superhydrophobicity, and Biomimetics*, Springer-Verlag, Heidelberg, Germany.
- Ohler, A. (1995), "Digital Pad Morphology in Torrent-living Ranid Frogs" *Asiatic Herpetological Res.* **6**, 85-96.
- Orr, F. M., Scriven, L. E., and Rivas, A. P. (1975), "Pendular Rings between Solids: Meniscus Properties and Capillary Forces," *J. Fluid. Mech.* **67**, 723-742.
- Palacio, M. L. B., Bhushan, B., and Schrick, S. R. (2013), "Hierarchical Nanostructured Polymers for Reversible Adhesion in Biomedical Applications," *Materials Letters* **92**, 409-412.
- Peattie, A. M. and Full, R. J. (2007), "Phylogenetic Analysis of the Scaling of Wet and Dry Biological Fibrillar Adhesives," *Proc. Natl. Acad. Sci. USA* **104**, 18595-18600.
- Persson, B. N. J. (2003), "On the Mechanism of Adhesion in Biological Systems," *J. Chem. Phys.* **118**, 7614-7621.
- Persson, B.N.J. and Gorb, S. (2003), "The Effect of Surface Roughness on the Adhesion of Elastic Plates with Application to Biological Systems," *J. Chem. Phys.* **119**, 11437-11444.

- Pesika, N. S., Tian, Y., Zhao, B., Rosenberg, K., Zeng, H., McGuiggen, P., Autumn, K., and Israelachvili, J. N. (2007), "Peel-Zone Model of Tape Peeling Based on the Gecko Adhesive System," *J. Adhesion* **83**, 383-401.
- Phipps, P. B. P. and Rice, D. W. (1979), "Role of Water in Atmospheric Corrosion," *Corrosion Chemistry, ACS Symposium Series Vol. 89* (ed. by G. R. Brubaker and P. B. P. Phipps), pp. 235-261, American Chemical Society, Washington, D.C.
- Qu, L., Dai, L., Stone, M., Xia, Z., and Wang, Z. L. (2008), "Carbon Nanotube Arrays with Strong Shear Binding-On and Easy Normal Lifting-Off," *Science* **322**, 238-242.
- Rizzo, N., Gardner, K., Walls, D., Keiper-Hrynko, N., and Hallahan, D. (2006), "Characterization of the Structure and Composition of Gecko Adhesive Setae," *J. Royal Soc. Interf.* **3**, 441-451.
- Ruibal, R. and Ernst, V. (1965), "The Structure of the Digital Setae of Lizards," *J. Morphol.* **117**, 271-294.
- Russell, A. P. (1975), "A Contribution to the Functional Morphology of the Foot of the Tokay, *Gekko gekko*," *J. Zool. Lond.* **176**, 437-476.
- Russell, A. P. (1986), "The Morphological Basis of Weight-Bearing in the Scansors of the Tokay Gecko," *Can. J. Zool.* **64**, 948-955.
- Schäffer, E., Thurn-Albrecht, T., Russell, T.P. and Steiner, U. (2000) "Electrically Induced Structure Formation and Pattern Transfer," *Nature*, **403**, 874-877.
- Schleich, H. H. and Kästle, W. (1986), "Ultrastrukturen an Gecko-Zehen," *Amphibia Reptilia*, **7**, 141-166.
- Schmidt, H. R. (1904), "Zur Anatomie und Physiologie der Geckopfote," *Jena. Z. Naturwissen* **39**, 551.
- Shah, G. J. and Sitti, M. (2004), "Modeling and Design of Biomimetic Adhesives Inspired by Gecko Foot-Hairs," *IEEE Int. Conf. on Robotics and Biomimetics*, 873-878.
- Simmermacher, G. (1884), "Untersuchungen uber Haftapparate an Tarsalgliedern von Insekten," *Zeitschr. Wissen Zool.* **40**, 481-556.
- Sitti, M. (2003), "High Aspect Ratio Polymer Micro/Nano-Structure Manufacturing using Nanoembossing, Nanomolding and Directed Self-Assembly," *Proc. IEEE/ASME Advanced Mechatronics Conf.* **2**, 886-890.
- Sitti, M. and Fearing, R. S. (2003) "Synthetic Gecko Foot-Hair for Micro/Nano Structures as Dry Adhesives," *J. Adhesion Sci. Technol.* **17**, 1055-1073.
- Spolenak, R., Gorb, S. and Arzt, E., (2005), "Adhesion Design Maps for Bio-Inspired Attachment Systems," *Acta Biomaterialia* **1**, 5-13.
- Stork, N. E. (1980), "Experimental Analysis of Adhesion of *Chrysolina polita* on a Variety of Surfaces," *J. Exp. Biol.* **88**, 91-107.
- Stork, N. E. (1983), "A Comparison of the Adhesive Setae on the Feet of Lizards and Arthropods," *J. Nat. Hist.*, **17**, 829-835.
- Tian, Y., Pesika, N., Zeng, H., Rosenberg, K., Zhao, B., McGuiggen, P., Autumn, K., and Israelachvili, J. (2006), "Adhesion and Friction in Gecko Toe Attachment and Detachment," *Proc. Nat. Acad. Sci. U. S. A.* **103**, 19320-19325.
- Tinkle, D. W. (1992), "Gecko," *Encyclopedia Americana*, edited by M. Cummings, Vol. 12, 359, Grolier, U.K.
- Van der Kloot, W. G. (1992), "Molting," *Encyclopedia Americana*, edited by M. Cummings, Vol. 19, 336-337, Grolier, U.K.
- Wagler, J. (1830), *Naturliches System der Amphibien*, J. G. Cotta'schen Buchhandlung, Munich.
- Wan, K. T., Smith, D. T. and Lawn, B. R. (1992), "Fracture and Contact Adhesion Energies of Mica-Mica, Silica-Silica, and Mica-Silica Interfaces in Dry And Moist Atmospheres," *J. Am. Ceram. Soc.* **75**, 667-676.
- Wenzel, R. N. (1936), "Resistance of Solid Surfaces to Wetting by Water," *Ind. Eng. Chem.* **28**, 988-994.
- Williams, E. E. and Peterson, J. A. (1982), "Convergent and Alternative Designs in the Digital Adhesive Pads of Scincid Lizards," *Science* **215**, 1509-1511.
- Yao, H., and Gao, H. (2006), "Mechanics of Robust and Releasable Adhesion in Biology: Bottom-Up Designed Hierarchical Structures of Gecko," *J. Mech. Phys. Solids*, **54**, 1120-1146.

- Young, W. C. and Budynas, R. (2001) *Roark's Formulas for Stress and Strain, seventh ed.* McGraw Hill, New York.
- Yurdumakan, B., Raravikar, N. R., Ajayan, P. M. and Dhinojwala, A. (2005), "Synthetic Gecko Foot-Hairs from Multiwalled Carbon Nanotubes," *Chem. Comm.* 3799-3801.
- Zimon, A. D. (1969), *Adhesion of Dust and Powder*, translated from Russian by M. Corn, Plenum, New York.
- Zisman, W. A. (1963), "Influence of Constitution on Adhesion," *Ind. Eng. Chem.* **55** (10), 18-38.

Chapter 14

Structure and Mechanical Properties of Nacre

14.1 Introduction

Many biological organisms exhibit unique chemical and physical properties (Lowenstam and Werner 1989). They often use components that contain both inorganic and organic compounds with complex structures, and are often hierarchically organized, ranging from nano- to meso-levels. The hierarchical structure provides a high tolerance against defects at all length scales. Most biological materials are multifunctional and often tend to have self-healing abilities (Vincent 1991; Ratner and Bryant 2004). In two-component biological materials, such as bones, teeth, and abalone shells, the mineral component provides high mechanical strength and the organic component hinders crack propagation, which increases fracture toughness responsible for high durability (Meyers et al. 2006). A biomineral system, which has been much investigated, is the inner layer of abalone, called nacre

Abalone, from the family *Haliotidae* and the genus *Haliotis*, are edible marine gastropod mollusks (Abbott et al. 2000). The shells of abalones are convex, with a rounded to oval shape. The spiral shell has two or three whirls, resembling an ear. The thick, inner layer of the shell is called “nacre”, or “mother-of-pearl”, and is highly iridescent with color variations including silvery white, pink, red, and deep blues, greens, and purples, making the shells attractive as decorative objects. The flesh (muscle) of abalones can create a pearl from the nacre, similar to the way an oyster makes a pearl, though the pearls are very rare and irregularly shaped. Additionally, the abalone meat is eaten as a food.

The nacre of abalone is exceptionally strong, with high hardness and fracture toughness (Meyers et al. 2006, 2008, 2011; Barthelat et al. 2006, 2007; Barthelat 2010; Sun and Bhushan 2012). The shell strength is needed to adapt to the living conditions to protect their soft bodies from predators, rocks, or debris.

The nacre composite is comprised of a layered structure of hard aragonite platelets (a crystallographic form of CaCO_3). These platelets are about 0.5 μm thick

arranged in a brick-and-mortar microstructure with a 20–50 nm thick organic matrix interlayer (proteins and polysaccharides) that serves as the glue between the single platelets, as shown in Fig. 14.1 (Meyers et al. 2011). This composite is a hierarchically organized structure, starting at the nano-level with a 20–30 nm thick organic layer, proceeding with single crystals of the aragonite polymorphs of CaCO_3 , consisting of bricks 0.5 μm thick with 10 μm lateral dimensions (microstructure), and finishing with layers approximately 0.3 mm thick (mesostructure). Although the organic matrix in nacre is only 5 wt%, it plays an important role in spatial and chemical control of crystal nucleation and growth. In the event of an impact, the viscoelastic layer deflects cracks, the tiles slide instead of shattering, and the proteins absorb the energy, responsible for high fracture toughness. The fracture toughness of nacre is $3.3\text{--}9 \text{ MPa}\sqrt{\text{m}}$, which about three to nine times greater than that of monolithic aragonite (about $1 \text{ MPa}\sqrt{\text{m}}$) (Jackson et al. 1988; Sarikaya et al. 1989; Gunnison et al. 1991). To sum up, the tiles provide the high hardness and the layered structure provides resistance to impact and fracture.

Nacre is of commercial interest due to its exceptional mechanical properties (Ratner and Bryant 2004; Podsiadlo et al. 2005, 2007; Cartwright and Checa 2007; Bonderer et al. 2008; Chen et al. 2008; Bhushan 2009; Luz and Mano 2009; Liu and Jiang 2011; Meyers et al. 2011; Yourdkhani et al. 2011; Sun and Bhushan 2012). A review of the characteristics of the hierarchical structure and mechanical

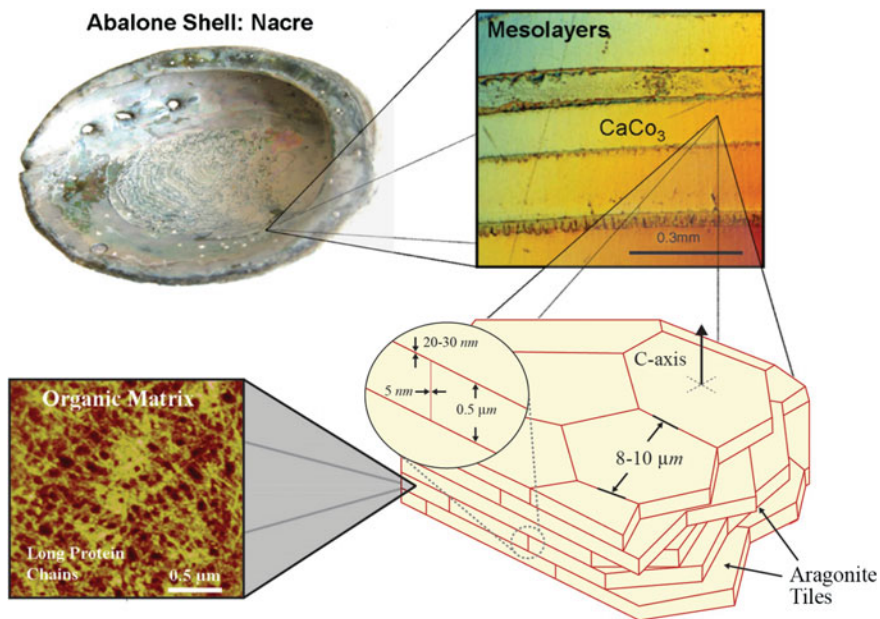


Fig. 14.1 The hierarchy of nacre—the inner layer of an abalone shell. Clockwise from *top left*: entire shell; mesostructure with mesolayers; microstructure with aragonite tiles; nanostructure showing organic interlayer comprising 5 wt% of overall shell (adapted from Meyers et al. 2006)

properties of nacre, toughening mechanisms, and the latest developments in bioinspired composites has been presented by Sun and Bhushan (2012). Details follow.

14.2 Hierarchical Structure

Nacre has a complex hierarchical architecture that spans over five length scales from nanoscale to macroscale. This characteristic of structural materials is also found in bone, teeth, and various biological microorganisms (Bhushan 2009). Figure 14.2 shows the five hierarchical levels found in abalone nacre (Meyers et al. 2011):

- Level I is the molecular structure of the chitin fibers that are the structural components of the intertile organic layers and of the atomic crystalline structure of the aragonite (which might incorporate nanosized islands).
- Level II is composed of the mineral bridges between tiles, with a diameter of 20–60 nm. It also comprises the sandwich structure of the organic intertile layer, with a core consisting of a random dispersion of chitin fibrils and a thickness equal to the length of the mineral bridges (~ 20 nm).
- Level III are the well-recognized hexagonal tiles, with lateral dimensions of 10 μm and thickness of 0.5 μm . These tiles are generally hexagonal, with a distribution of dimensions.
- Level IV are the mesolayers, which are characterized by a thick organic layer (~ 200 μm) separating tile assemblages with approximately 0.1–0.3 mm.
- Level V is the entire structure that, because of its architecture (dome shape, thickness distribution, etc.) is optimized for strength and toughness.

14.2.1 Columnar and Sheet Structure

The precise geometric arrangement of the tiles is one of the important reasons for the robust mechanical behavior of nacre (Currey 1977). There are two different mineralization types of nacre on the microscale: columnar nacre, found, for example, in *Gibbula umbilicalis* (gastropods), and sheet nacre, found, for example, in *Nucula nitidosa* (bivalves), shown in Fig. 14.3a (Wang et al. 2001). Nacres are “columnar nacre” or “sheet nacre” depending on the stacking mode of the tablets, as shown in Fig. 14.3b (Wang et al. 2001). Columnar nacre has tablets of rather uniform size with coinciding centers that determine the nucleation site of the overlying tablet. In sheet nacre, deposition takes place over most of the inner surface of the shell, and the tablets are stacked in a “brick wall” pattern, spanning the interface between underlying tablets.

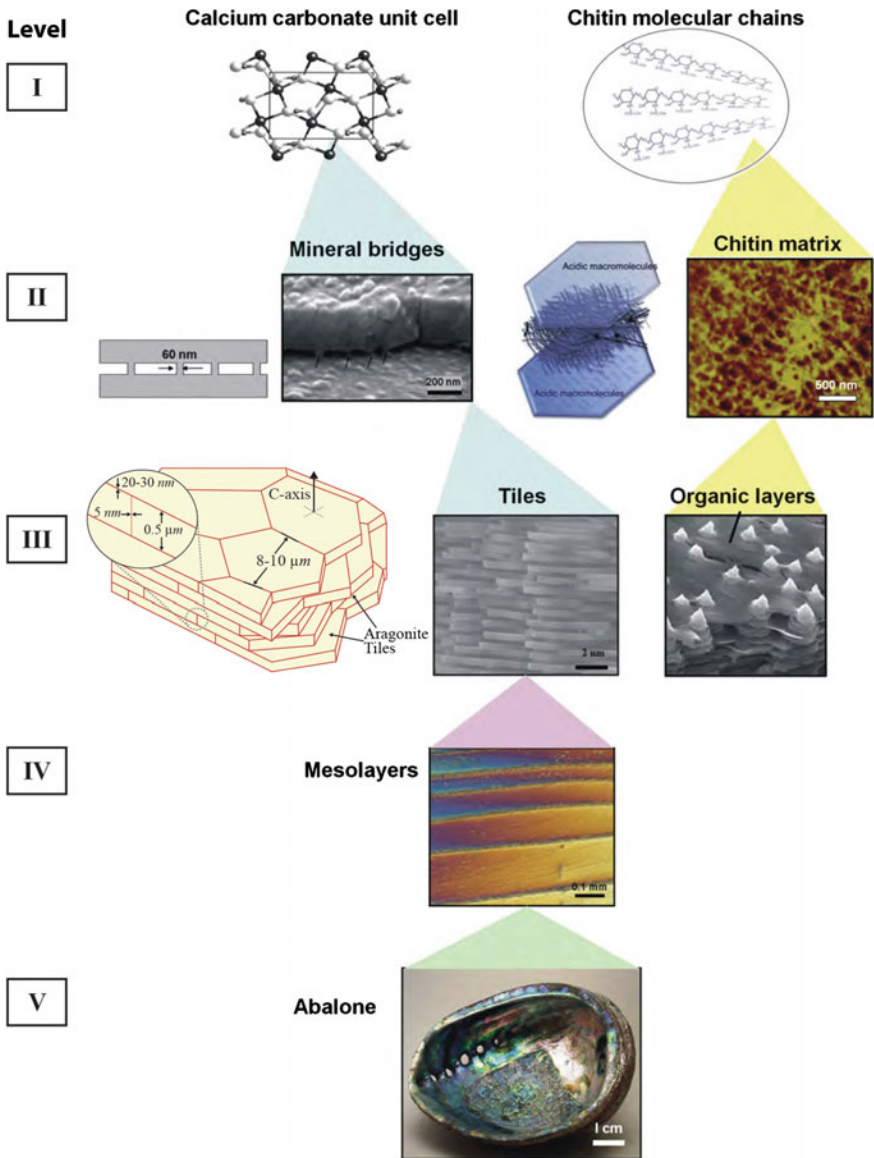


Fig. 14.2 Hierarchical structure (5 levels) of the red abalone nacre from nano, micro, meso, to structural length scales (adapted from Meyers et al. 2011)

In columnar nacre, from the top view, the polygonal tablets form neighboring layers that overlap in such a manner that the inter-tablet boundaries form tessellated bands perpendicular to the lamellae boundaries, shown in Fig. 14.3c–e (Barthelat et al. 2007).

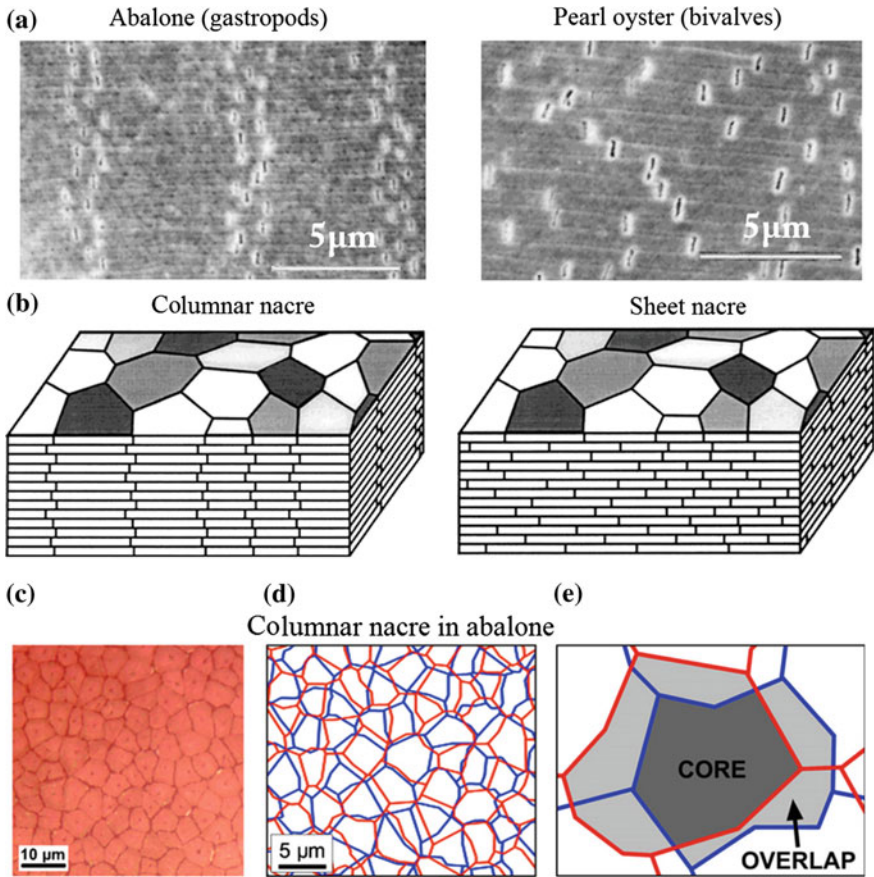


Fig. 14.3 SEM images of deformation bands by tensile test of **a** abalone (gastropods), showing four vertical dilatation bands and pearl oyster (bivalves), the separations are randomly dispersed, and **b** schematic illustrations of columnar nacre/abalone and sheet nacre/pearl oyster. Polygonal aragonite tablets are adhered into a lamellar structure by a thin organic interlayer. In columnar nacre, the intertablet boundaries are correlated into a tessellated arrangement (Wang et al. 2001). **c** Optical image of the cleaved surface shows a Voronoi like tiling of the tablets within one layer in red abalone nacre from top view; **d** reconstitution of the arrangement of the tablets from one layer to the next, and **e** core and overlap areas in the tablet arrangements (Barthelat et al. 2007) (adapted from Sun and Bhushan 2012)

14.2.2 Mineral Bridges

The existence of mineral bridges connecting individual tablets was first demonstrated by Schäffer et al. (1997), and later confirmed by others. They proposed that the mineral bridges improve the mechanical properties of the organic matrix layers

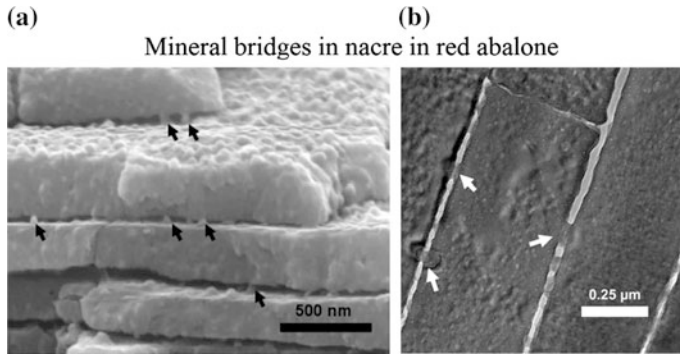


Fig. 14.4 TEM images of red abalone nacre cross-section showing **a** mineral bridges between tile interfaces, and **b** mineral bridges between tablets of neighboring layers shown by *arrows* (Lin et al. 2008). These mineral bridges are also found in bivalves

and prevent crack extension in nacre (Song et al. 2002; Barthelat et al. 2006; Cartwright and Checa 2007; Lin et al. 2008; Checa et al. 2011).

Mineral bridges represent the continuation of mineral growth in the *c*-axis from a preceding layer of tiles. They protrude through the growth-arresting layers of proteins, creating sites on the covering organic layer where mineralization can continue, shown in Fig. 14.4 (Lin et al. 2008). To directly observe mineral bridges between individual tablets, nacre was fractured in tension parallel to the direction of growth (Song et al. 2002, 2003). In Fig. 14.4a, arrows mark the location of remaining mineral bridges, while a gap between tile layers clearly can be seen to exist in the absence of the organic matrix. Figure 14.4b provides further evidence of mineral bridge formation, in that the aragonite surrounding individual mineral bridge seems to have semicircular bands emanating from the bridge. Meyers et al. (2008) have reported that these mineral bridges are responsible for high tensile strength in the direction perpendicular to the layer plane.

14.2.3 Polygonal Nanograins

On the nanoscale, polygonal nanograins have been observed on the aragonite tablets that are the basic building blocks in nacre (Li et al. 2004). High-resolution transmission electron microscopy (TEM) micrographs (from top view) of a tablet show nanograins about 3–10 nm in size, Fig. 14.5a (Barthelat et al. 2006). These nanograins provide a ductile nature to the microstructure (Schäffer et al. 1997). The deformability of the aragonite tablets is relevant to the nacre's high fracture toughness.

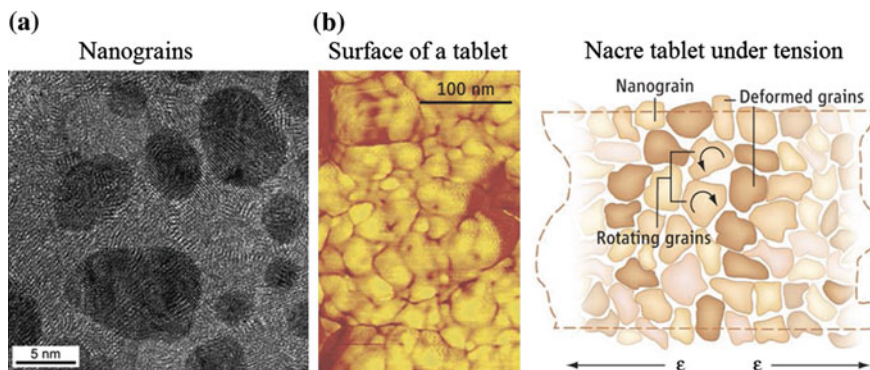


Fig. 14.5 **a** High-resolution TEM images (face-on view) of a tablet from the nacreous layer of a red abalone specimen showing nanograins about 3–10 nm in size (Barthelat et al. 2006). **b** (Left) AFM image of surface nanograins on an individual nacre platelet from California red abalone and (right) schematic of nanograin rotation and deformation under tension (Li et al. 2006; Ortiz and Boyce 2008) (adapted from Sun and Bhushan 2012)

In situ atomic force microscopy (AFM) allows for observation of the nanogranular texture of the aragonite tablets during mechanical deformation. Nanograin rotation and deformation occur, facilitated by the existence of the biopolymer spacing between the nanograins. This will contribute to energy dissipation in the nacre, as shown in Fig. 14.5b (Li et al. 2006; Ortiz and Boyce 2008). The water present at the nanograin interfaces may facilitate the viscoelastic deformations of nacre (Verma et al. 2007).

14.2.4 Inter-Tile Toughening Mechanism

Toughening mechanisms and their guide to materials synthesis are of interest. Currey (1977) mentioned several toughening mechanism: plastic deformation ahead of the crack tip, crack deflection, crack blunting, and tablet pullout. A significant mechanism of toughening is crack deflection at both the meso- and microscale, shown in Fig. 14.6a (Meyers and Chawla 2008). Figure 14.6b shows cracks that are deflected at each soft protein layer. The viscoelastic glue (organic material) provides a crack-deflection layer, such that cracks have difficulty propagating through the composite of layers of CaCO_3 (Meyers and Chawla 2008). The toughness of this laminated composite is vastly superior to that of a monolithic material, in which the crack would be able to propagate freely, without barriers. Figure 14.6 shows the two levels of the structure engaging in this mechanism: (a) mesolayers provide crack deflection, (b) at a smaller scale the tile layers force cracks in a tortuous path.

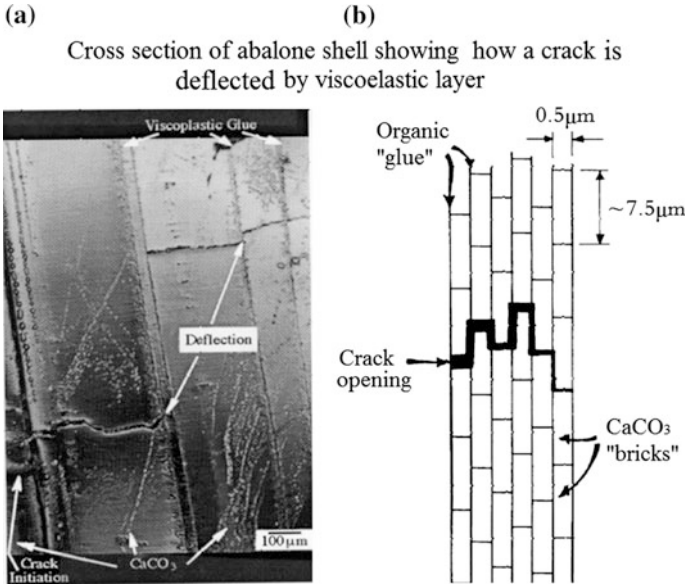


Fig. 14.6 **a** Cross-section of abalone shell showing how a crack, starting at the left is deflected by viscoplastic layer between calcium carbonate lamellae; **b** Schematic drawing showing arrangement of calcium carbonate in nacre, forming a miniature “brick and mortar” structure (Meyers and Chawla 2008)

14.3 Mechanical Properties

Experimental data show that the nacre exhibits high strength and fracture toughness because of its structure (Meyers et al. 2006; Barthelat et al. 2007; Meyers et al. 2011; Wang et al. 2012). Currey (1977) was the first to perform measurements of mechanical properties of nacre from a variety of bivalves, gastropods, and cephalopods. He suggested that the geometry of the tablets and the arrangement is optimized for mechanical properties and energy absorption. This was followed by Jackson et al. (1988) who studied nacre from the shell of a bivalve mollusk, *Pinctada*, and found that the water absorbed in the organic matrix of nacre plays a role in its mechanical response.

Mechanical properties of various nacles reported in the literature are summarized by Sun and Bhushan (2012). The compressive and ultimate tensile strengths of nacre with respect to various loading directions are shown in Fig. 14.7 (Meyers et al. 2008). The compressive strengths are larger than the tensile strengths in both perpendicular and parallel directions. The tensile and shear stress-strain curves of nacre under both ambient (dry conditions) and hydrated (soaked in water)

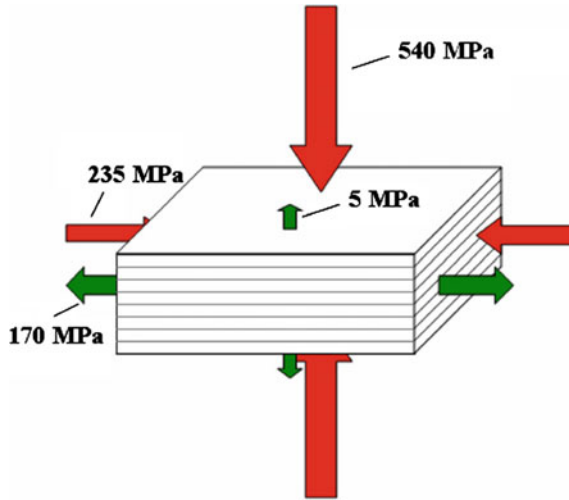


Fig. 14.7 Compressive and ultimate tensile strengths of nacre under different loading directions (Meyers et al. 2008)

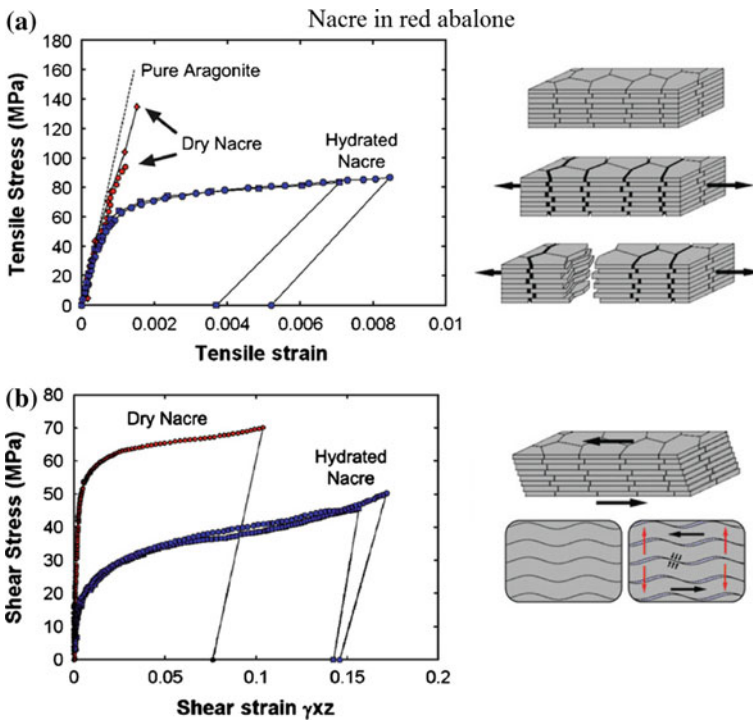


Fig. 14.8 **a** Tensile and **b** shear stress-strain curves for nacre in red abalone and schematic of lamellar tile structures showing associated deformation modes. Tablet waviness generates resistance to sliding, accompanied by lateral expansion (*vertical arrows*) (Barthelat et al. 2007)

conditions, are presented in Fig. 14.8a and b, showing some ductility at the macroscale (Barthelat et al. 2007). In tension, the behavior of dry nacre is similar to that of pure aragonite, and it failed in a brittle fashion. It showed that dehydrated nacre loses its strength. On the other hand, it demonstrated that the organic materials (5 wt%) are essential to nacre. After an initial linear response comparable to dry nacre, hydrated nacre showed a region of larger inelastic strains starting at a stress of 70 MPa. While this mechanism can easily be envisioned in simple shear, it is less obvious in tension, as tablet sliding only occurs in the tablet overlap areas. Jackson et al. (1988) concluded that water affects the elastic modulus and tensile strength by reducing the shear modulus and shear strength of the organic matrix. The toughness is enhanced by water, which plasticizes the organic matrix, resulting in greater crack blunting and deflection abilities.

Figure 14.9 shows the compression stress-strain curves for abalone nacre representing interlamellar shear, measured both in monotonic loading and with loading/unloading loops (Wang et al. 2001). The insert indicates that the lamellae boundaries are orientated at 45° to the loading axis; the unloading/reloading measurements reveal hysteresis, indicative of internal friction and viscoelasticity (Sun and Bhushan 2012).

Because of large statistical variations in the strength of ceramics, Weibull distribution is used. Menig et al. (2000) measured the compressive strength of red abalone and found considerable variation in results. Weibull analysis of abalone nacre in quasi-static and dynamic compressive loading with loading parallel and perpendicular to layered structure are shown in Fig. 14.10 (Menig et al. 2000).

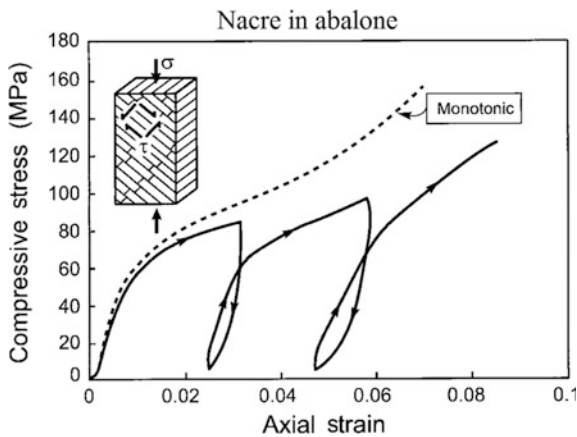


Fig. 14.9 Compression stress-strain curves for nacre in abalone representing interlamellae shear, measured both in monotonic loading and with loading/unloading loops. The *insert* indicates that the lamellae boundaries are orientated at 45° to the loading axis (Wang et al. 2001)

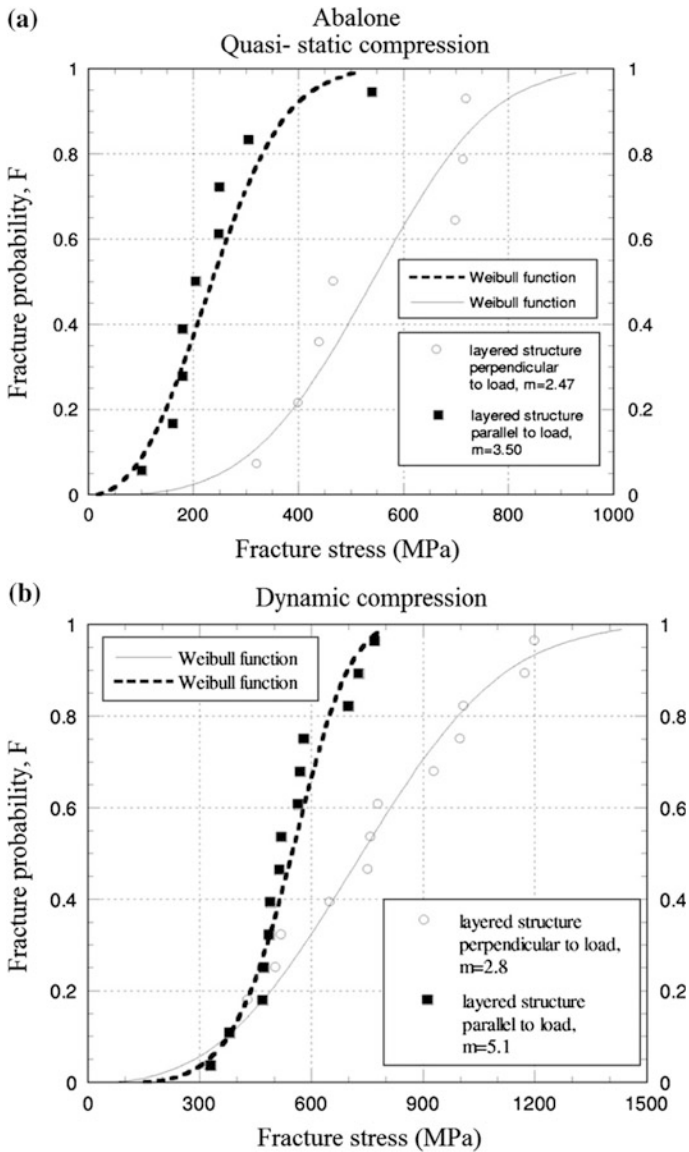


Fig. 14.10 Weibull plots of abalone nacre in abalone in: **a** quasi-static, and **b** dynamic compressive loading (Menig et al. 2000)

In the figure, m is the Weibull shape parameter, or Weibull modulus, which is an inverse measure of the distribution width; that is, a high value of m corresponds to a narrow distribution (Wachtman 1996). With failure probabilities of 50 %, the

abalone nacre is stronger with layers perpendicular to the loading direction. The dynamic strength of abalone is approximately 50 % higher than its quasi-static strength. In tension perpendicular to the direction of the layers, the parameter m was found to be 1.6 (Meyers et al. 2008), as compared to that found in compressive tests of 2.47. This relative similarity is in stark contrast to the strength of 5 MPa found in tension tests, which is dramatically smaller than the strength of 540 MPa found in compressive tests.

Fracture toughness of nacre has been measured by various researchers (Sun and Bhushan 2012). Fracture toughness of $3.3\text{--}9\text{ MPa}\sqrt{m}$ has been reported by Jackson et al. (1988), Sarikaya et al. (1989), and Gunnison et al. (1991).

The nanomechanical properties of soaked and dry nacre surfaces have been studied using nanoindentation experiments (Sun and Bhushan 2012). Mohanty et al. (2006) reported the dynamic nanomechanical behavior of nacre, and showed that the aragonite platelets are viscoelastic in nature and can absorb energy. Polished red abalone nacre samples' elastic modulus was found to be between 60 and 80 GPa and nanohardness perpendicular to the tablet lamella was found to be between 2 and 4 GPa (Li et al. 2004). They also reported that there is plastic deformation in the indented region. For *Trochus Niloticus* nacre, the reported values of elastic modulus and nanohardness perpendicular to the tablet lamella were between 114 and 143 GPa and between 9.7 and 11.4 GPa for freshly cleaved samples, and between 101 and 126 GPa and between 3.6 and 8.7 GPa for artificial seawater soaked samples, respectively (Bruet et al. 2005). Images of the indents revealed extensive plastic deformation with a clear residual indent and surrounding pileup. Compared with these values, the elastic modulus value of single tablet was 79 GPa (Barthelat et al. 2006) which is close to that of monolithic aragonite (81 GPa). The organic layer between the layers of aragonite tablets has been shown to exhibit elastic modulus values between 2.8 and 15 GPa (Katti and Katti 2001; Barthelat et al. 2006). This suggests that the softer interfaces and structure of tablets have an effect on overall mechanical properties of nacre.

14.4 Bioinspired Structures

The mimicking of nacre is focused on its various aspects: (1) structure, including laminated structure, hierarchical structure, brick-like structure, or organic and inorganic multilayered structure (brick-and-mortar structure), (2) manufacturing process, which means mimicking its mineralization process, and (3) components, mimicking its 5 wt% organic with inorganic materials for producing artificial nacre (Sun and Bhushan 2012). These design concepts and fabrication methods have been used with various nonmetallic materials and polymers for enhancing or improving their original mechanical properties.

Table 14.1 Fracture toughness values for various refined ceramic materials that were bioinspired from nacre (Sun and Bhushan 2012)

Bioinspired nacre structural materials	Scale	Fracture toughness ($\text{MPa}\sqrt{m}$)	References
Al/Al–Si	μm	5.5–10	Deville et al. (2006)
$\text{Al}_2\text{O}_3/\text{Al–Si}$	μm	40	Lin et al. (2009), Launey et al. (2010)
$\text{Al}_2\text{O}_3/\text{PMMA}^a$	μm	30	Munch et al. (2008)
$\text{Al}_2\text{O}_3/\text{TiO}_2$	mm	12	Bueno and Baudin (2009)
$\text{SiC}/\text{Al}_2\text{O}_3\text{–Y}_2\text{O}_3$	mm	14	Zhang and Krstic (1995)
$\text{Si}_3\text{N}_4/\text{BN}$	mm	28	Wang et al. (2000)

^aPolymethyl methacrylate (PMMA)

Based on fabrication methods, bioinspired structures can be considered from two different points of views: hierarchical structure (top-down) and self-assembled nanocomposite (bottom-up) (Deville et al. 2008). Wang et al. (2012) summarized various fabrication methods in six categories: conventional methods for bulk ceramic materials, freezing casting, layer-by-layer deposition, electrophoretic deposition, mechanical assembly, and chemical self-assembly.

Table 14.1 shows some refined ceramic materials that consist of bioinspired structure from nacre. The fracture toughness of bioinspired composite materials is equal to or larger than that of natural nacre. The bioinspired structures from nacre have also been applied to composite films (Rubner 2003; Tang et al. 2003; Zhang et al. 2004, 2006; Deville et al. 2006; Podsiadlo et al. 2008). Nacre-inspired paper has been fabricated with a light weight, shape-persistence, tunable mechanical properties, and heat and fire-shielding capabilities (Walther et al. 2010).

As an example, polymethyl methacrylate (PMMA) tablets were generated that exhibit unique mechanisms, Fig. 14.11a (Barthelat and Zhu 2011). Progressive tablet locking, strain hardening, and spreading of large deformations over large volumes were all achieved in this material. Stiff and brittle tablets are arranged in a columnar fashion with well-defined overlap and core regions, and interfaces between the tablets maintain cohesion over long sliding distances. Waviness on the tablets is used to generate strain hardening and spread deformations and reinforcements in the core regions. The expected behavior in tension of such composite is shown in Fig. 14.11b. The dovetails are critical to generate progressive locking, and the stresses involved in this mechanism are shown in Fig. 14.11c. The resulting material, shown in Fig. 14.11d, consisted of seven layers and was composed of eight columns of tablets.

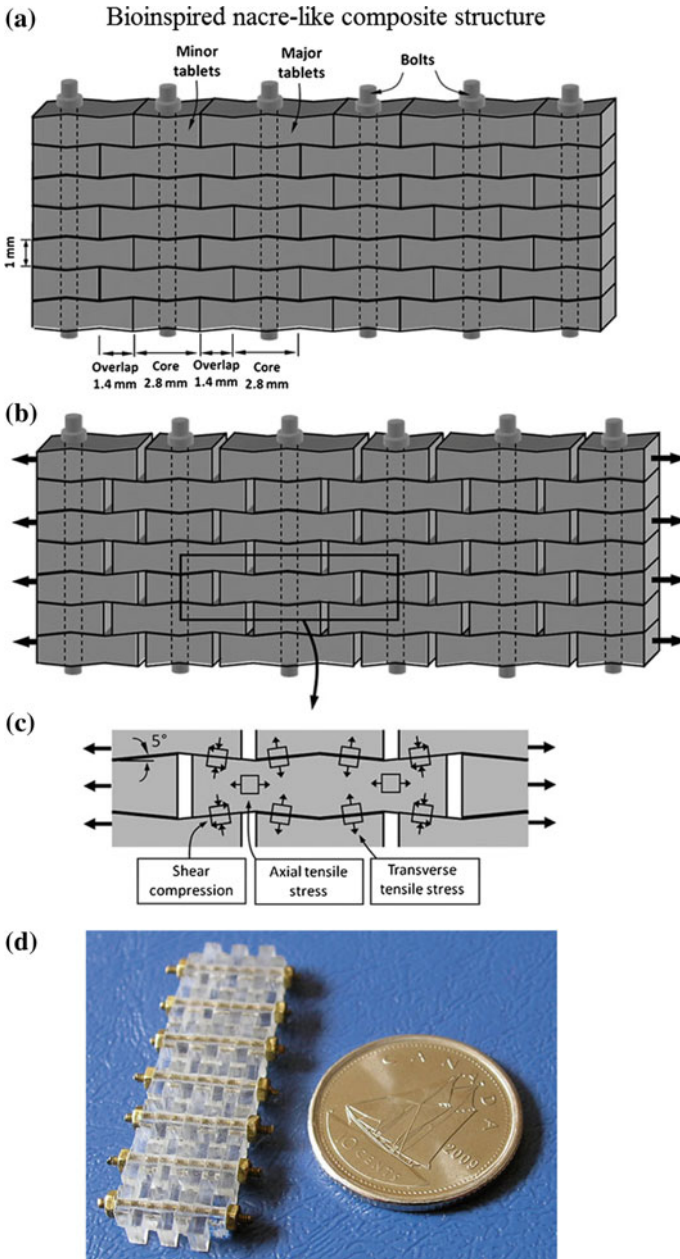


Fig. 14.11 Overview of the nacre-like composites: **a** schematic with dimensions; **b** under tension tablets slide with progressive locking; **c** some of the stresses involved in progressive locking; **d** actual composite after assembly (Barthelat and Zhu 2011)

14.5 Closure

Nacre, also called mother of pearl, is the iridescent inner layer of a shell. Nacre is composed of 95 wt% aragonite (a crystallographic form of CaCO_3) tiles stacked like bricks with a 5 wt% organic materials (proteins and polysaccharides) interlayer. It consists of hierarchical, organized structure that spans over multiple length scales from nanoscale to mesoscale. It starts at the nano-level, with a 20–30 nm thick organic layer, proceeding with simple crystals of the aragonite polymorph of CaCO_3 , consisting of bricks with dimensions of 0.5 μm in thickness and 10 μm lateral dimensions (microstructure), and finishing with 0.3 mm thick layers (mesostructure). It includes columnar architecture and sheet tiles, mineral bridges, and polygonal nanograins. Crack deflection and interlocking bricks exhibit a remarkable combination of stiffness, low weight, and strength. Nacre exhibits high fracture toughness, greater than that of monolithic aragonite, because of its structure: a soft protein interlayer deflects crack trajectories. A combination of high fracture toughness and high strength and hardness found in nacre have attracted an interest by researchers for the development of laminated composite materials, molecular self-assembly, and biomineralization.

References

- Abbot, R., Tucker, D., and Peter, S. (2000), *Compendium of Seashells, 4th Ed.*, Odyssey Publishing, El Cajon, California.
- Barthelat, F. (2010), "Nacre from Mollusk Shells: A Model for High-performance Structural Materials," *Bioinspir. Biomim.* **5**, 035001-1-8.
- Barthelat, F. and Zhu, D. J. (2011), "A Novel Biomimetic Material Duplicating the Structure and Mechanics of Natural Nacre," *J. Mater. Res.* **26**, 1203-1215.
- Barthelat, F., Li, C.M., Comi, C. and Espinosa, H. D. (2006), "Mechanical Properties of Nacre Constituents and Their Impact on Mechanical Performance," *J. Mater. Res.* **21**, 1977-1986.
- Barthelat, F., Tang, H., Zavattieri, P. D., Li, C. M. and Espinosa, H. D. (2007), "On the Mechanics of Mother-of-Pearl: A Key Feature in the Material Hierarchical Structure," *J. Mech. Phys. Solids* **55**, 306-337.
- Bhushan, B. (2009), "Biomimetics: Lessons from Nature- An Overview," *Phil. Trans. R. Soc. A* **367**, 1445-1486.
- Bonderer, L. J., Studart, A. R. and Gauckler, L. J. (2008), "Bioinspired Design and Assembly of Platelet Reinforced Polymer Films," *Science* **319**, 1069-1073.
- Bruet, B. J. F., Qi, H. J., Boyce, M. C., Panas, R., Tai, K., Frick, L., and Ortiz, C. (2005), "Nanoscale Morphology and Indentation of Individual Nacre Tablets from the Gastropod Mollusc *Trochus niloticus*," *J. Mater. Res.* **20**, 2400-2419.
- Bueno, S. and Baudin, C. (2009), "Design and Processing of a Ceramic Laminate with High Toughness and Strong Interfaces," *Compos. Part A* **40**, 137-143.
- Cartwright, J. H. E. and Checa, A. G. (2007), "The Dynamics of Nacre Self-assembly," *J. R. Soc. Interface* **4**, 491–504.
- Checa, A. G., Cartwright, J. H. E., Willinger, M. G. (2011), "Mineral Bridges in Nacre," *J. Struct. Biol.* **176**, 330-339.
- Chen, R. F., Wang, C. A., Huang, Y. and Le, H. R. (2008), "An Efficient Biomimetic Process for Fabrication of Artificial Nacre with Ordered-Nano Structure," *Mater. Sci. Eng. C* **28**, 218-222.

- Currey, J. D. (1977), "Mechanical Properties of Mother of Pearl in Tension," *Proc. R. Soc. Lond. B* **196**, 443-463.
- Deville, S., Saiz, E., Nalla, R. K., and Tomsia, A. P. (2006), "Freezing as a Path to Build Complex Composites," *Science* **27**, 515-518.
- Deville S., Saiz E., and Tomsia A. P. (2008), "Using Ice to Mimic Nacre: From Structural Applications to Artificial Bone," in: *Handbook of Biomineralization: Biomimetic and Bioinspired Chemistry*, Behrens P. and Bäuerlein E. (Eds.), John Wiley & Sons, Ltd, Weinheim, Germany.
- Gunnison K. E., Sarikaya M., Liu J. and Aksay I. A. (1991), "Structure-mechanical Property Relationships in a Biological Ceramic-polymer Composite: Nacre," *MRS Proc.*, **255**, 171-184.
- Jackson, A. P., Vincent, J.F.V. and Turner, R.M. (1988), "The Mechanical Design of Nacre," *Proc. R. Soc. Lond. B* **234**, 415-440.
- Katti, D. R. and Katti, K. S. (2001), "3D Finite Element Modeling of Mechanical Response in Nacre-based Hybrid Nanocomposites," *J. Mater. Sci.* **36**, 1411-1417.
- Launey, M. E., Munch, E., Alsem, D. H., Saiz, E., Tomsia, A. P., and Ritchie, R. O. (2010), "A Novel Biomimetic Approach to the Design of High-performance Ceramic-metal Composites," *J. R. Soc. Interface* **7**, 741-753.
- Li, X. D., Chang, W. C., Chao, Y. J., Wang, R. and Chang, M. (2004), "Nanoscale Structural and Mechanical Characterization of a Natural Nanocomposite Material: The Shell of Red Abalone," *Nano Lett.* **4**, 613-617.
- Li, X. D., Xu, Z. H. and Wang, R. Z. (2006), "In Situ Observation of Nanograin Rotation and Deformation in Nacre," *Nano Lett.* **6**, 2301-2304.
- Lin, A. Y. M., Chen, P. Y. and Meyers, M. A. (2008). "The Growth of Nacre in the Abalone Shell," *Acta Biomater.* **4**, 131-138.
- Lin, T. H., Huang, W. H., Jun, I. K., and Jiang, P. (2009), "Bioinspired Assembly of Colloidal Nanoplatelets by Electric Field," *Chem. Mater.* **21**, 2039-2044.
- Liu, K. S. and Jiang, L. (2011), "Bio-inspired Design of Multiscale Structures for Function Integration," *Nano Today* **6**, 155-175.
- Lowenstam, H. A. and Weiner, S. (1989), *On Biomineralization*, Oxford University Press, New York.
- Luz, G. M. and Mano, J. F. (2009), "Biomimetic Design of Materials and Biomaterials Inspired by the Structure of Nacre," *Phil. Trans. R. Soc. A.* **367**, 1587-1605.
- Menig, R., Meyers, M. H., Meyers, M. A. and Vecchio, K. S. (2000), "Quasi-static and Dynamic Mechanical Response of *Haliotis rufescens* (Abalone) Shells," *Acta mater.* **48**, 2383- 2398.
- Meyers, M. A. and Chawla, K. K. (2008), *Mechanical Behavior of Materials*, Cambridge University Press, New York.
- Meyers, M. A., Lin, A. Y. M., Seki, Y., Chen, P. Y., Kad, B. K., Bodde, S. (2006), "Structural Biological Composites: An Overview," *JOM*, July, 35-41.
- Meyers, M. A., Chen, P. Y., Lin, A.Y.M. and Seki, Y. (2008), "Biological Materials: Structure and Mechanical Properties," *Prog. Mater. Sci.* **53**, 1-206.
- Meyers, M. A., Chen, P. Y., Lopez, M. I., Seki, Y. and Lin, A.Y.M. (2011), "Biological Materials: A Materials Science Approach," *J. Mech. Behav. Biomed. Mater.* **4**, 626-657.
- Mohanty, B., Katti, K. S., Katti, D. R. and Verma, D., 2006, "Dynamic Nanomechanical Response of Nacre," *J. Mater. Res.* **21**, 2045-2051.
- Munch, E., Launey, M. E., Alsem, D. H., Saiz, E., Tomsia, A. P., and Ritchie, R. O. (2008) "Tough Bio-inspired Hybrid Materials," *Science* **322**, 1516-1520.
- Ortiz, C. and Boyce, M. C. (2008), "Bioinspired Structural Materials," *Science* **319**, 1053-1054.
- Podsiadlo, P., Paternel, S., Rouillard J. M., Zhang, Z. F., Lee, J., Lee, J. W., Gulari, L. and Kotov, N. A. (2005), "Layer-by-layer Assembly of Nacre-like Nanostructured Composites with Antimicrobial Properties," *Langmuir* **21**, 11915-11921.
- Podsiadlo, P., Kaushik, A. K., Arruda, E. M., Waas, A. M., Shim, B. S., Xu, J. D., Nandivada, H., Pumphlin, B. G., Lahann, J., Ramamoorthy, A. and Kotov, N. A. (2007), "Ultrastrong and Stiff Layered Polymer Nanocomposites," *Science* **318**, 80-83.

- Podsiadlo, P., Kaushik, A. K., Shim, B. S., Agarwal, A., Tang, Z., Waas, A. M., Arruda, E. M. and Kotov, N. A. (2008), "Can Nature's Design be Improved Upon? High Strength, Transparent Nacre-like Nanocomposites with Double Network of Sacrificial Cross Links," *J. Phys. Chem. B* **112**, 14359-14363.
- Ratner, B. D. and Bryant, S. J. (2004), "Biomaterials: Where We Have Been and Where We are Going," *Annu. Rev. Biomed. Eng.* **6**, 41-75.
- Rubner, M. (2003), "Synthetic Sea Shell," *Nature* **423**, 925-926.
- Sarikaya, M., Gunnison, K. E., Yasrebi, M. and Aksay, I. A. (1989), "Mechanical Property-Microstructural Relationships in Abalone Shell," *MRS Proc.*, **174**, 109.
- Schäffer, T. E., IonescuZanetti, C., Proksch, R., Fritz, M., Walters, D. A., Almqvist, N., Zaremba, C. M., Belcher, A. M., Smith, B. L., Stucky, G. D., Morse, D. E. and Hansma, P. K. (1997), "Does Abalone Nacre Form by Heteroepitaxial Nucleation or by Growth Through Mineral Bridges?," *Chem. Mater.* **9**, 1731-1740.
- Song, F., Zhang, X. H. and Bai, Y. L. (2002), "Microstructure and Characteristics in the Organic Matrix Layers of Nacre," *J. Mater. Res.* **17**, 1567-1570.
- Song, F., Soh, A. K. and Bai, Y. L. (2003), "Structural and Mechanical Properties of the Organic Matrix Layers of Nacre," *Biomater.* **24**, 3623-3631.
- Sun, J. and Bhushan, B. (2012), "Hierarchical Structure and Mechanical Properties of Nacre: A Review," *RSC Advances* **2**, 7617-7632.
- Tang, Z. Y., Kotov, N. A., Magonov, S. and Ozturk, B. (2003), "Nanostructured Artificial Nacre," *Nature Mater.* **2**, 413-418.
- Verma, D., Katti, K. and Katti, D. (2007), "Nature of Water in Nacre: A 2D Fourier Transform Infrared Spectroscopic Study," *Spectrochim. Acta A Mol. Biomol. Spectrosc.* **67**, 784-788.
- Vincent, J. F. V. (1991), *Structural Biomaterials*, Princeton University Press, Princeton, NJ.
- Wachtman, J. B. (1996), *Mechanical Properties of Ceramics*, Wiley-Interscience, New York.
- Walther, A., Bjurhager, I., Malho, J.-M., Ruokolainen, J., Berglund, L. and Ikkala, O. (2010), "Supramolecular Control of Stiffness and Strength in Lightweight High-performance Nacre-mimetic Paper with Fire-shielding Properties," *Angew. Chem. Int. Ed. Engl.* **49**, 6448-6453.
- Wang, C. A., Huang, Y., Zan, Q. F., Guo, H., and Cai, S. Y. (2000), "Biomimetic Structure Design – A Possible Approach to Change the Brittleness of Ceramics in Nature," *Mater. Sci. Eng. C* **11**, 9-12.
- Wang, J. F., Cheng Q. F. and Tang, Z. Y. (2012), "Layered Nanocomposites Inspired by the Structure and Mechanical Properties of Nacre," *Chem. Soc. Rev.* **41**, 1111-1129
- Wang, R. Z., Suo, Z., Evans, A. G., Yao, N. and Aksay, I. A. (2001), "Deformation Mechanisms in Nacre," *J. Mater. Res.* **16**, 2485-2493.
- Yourdkhani, M., Pasini, D. and Barthelat, F. (2011), "Multiscale Mechanics and Optimization of Gastropod Shells," *J. Bionic Eng.* **8**, 357-368.
- Zhang, L. and Krstic, V. D. (1995), "High Toughness Silicon Carbide/Graphite Laminar Composite by Slip Casting," *Theor. Appl. Fract. Mech.* **24**, 13-19.
- Zhang, S. M., Zhang, J. W., Zhang, Z. J., Dang, H. X., Liu, W. M. and Xue, Q. J. (2004), "Preparation and Characterization of Self-assembled Organic-Inorganic Nacre-like Nanocomposite Thin Films," *Mater. Lett.* **58**, 2266-2269.
- Zhang, X., Liu, C. L., Wu, W. J. and Wang, J. F. (2006), "Evaporation-induced Self-assembly of Organic-inorganic Ordered Nanocomposite Thin Films that Mimic Nacre," *Mater. Lett.* **60**, 2086-2089.

Chapter 15

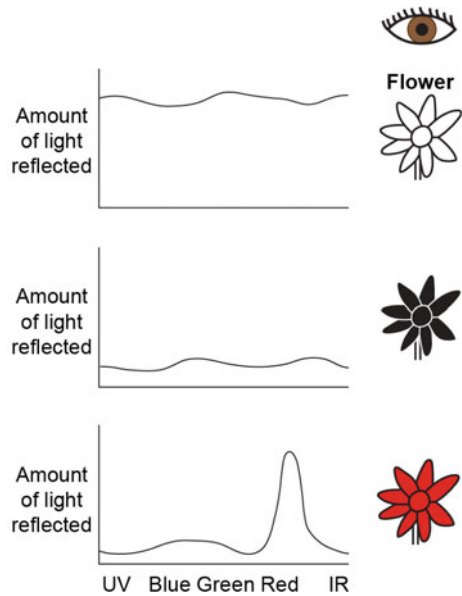
Structural Coloration

15.1 Introduction

In living nature, flora and fauna produce color through pigments, bioluminescence, or structural coloration (Booth 1990). Biological pigments, or simply pigments, are substances produced by living organisms, which produce color resulting from selective light adsorption and reflection of a specific light wavelength. These include plant and flower pigments, such as green pigment chlorophyll used by plants for photosynthesis. Many biological structures contain pigments such as melanin in skin, eyes, fur, and hair. Bioluminescence is the production and emission of visible light by a living organism. It occurs widely in marine organisms, as well as in some fungi, bacteria, and terrestrial invertebrates, such as fireflies. Structural coloration is the production of color by selective light reflection by nanostructured surfaces with features of the same scale as incident visible light wavelengths (Fox 1976; Kinoshita 2008; Kinoshita et al. 2008; Sun et al. 2013; Yu et al. 2013). While pigments degrade and their colors fade over time, structural coloration can persist for long periods, even after the death of the organism.

Upon reflection of white light, a specific wavelength range in the visible spectrum creates a specific color. If an object reflects all wavelengths of white light, it is perceived as white and if it absorbs all light, it is perceived as black. However, if an object reflects some fraction of the wavelength of visible light, it produces color, Fig. 15.1 (adapted from Glover and Whitney 2010). Selective reflectance and absorption of incident light in the visible light region at viewing angle can change the resulting color. Structural colors often appear iridescent, meaning that the color changes where the angle of view or the angle of illumination changes (Ghiradella and Butler 2009). Some structural colors can be non-iridescent as well (Shawkey et al. 2009).

Fig. 15.1 Color is a result of light reflected by an object at a viewing angle, as illustrated by three special cases of light reflection (adapted from Glover and Whitney 2010)



Structural coloration occurs in various flora and fauna in living nature. Figure 15.2 shows a montage of photographs of structural coloration in plants and animals, both over the land and underwater, including insects, birds, mollusks, sea mouse, and fish (adapted from Sun et al. 2013). It should be noted that perceived color is not only a result of structural color, but is also sometimes combined with pigment (Yu et al. 2013). As an example, peacock tail feathers are pigmented brown, but their structure makes them appear blue, turquoise, and green, and often they appear iridescent. In some species, coloration changes occur to provide various functionalities, such as camouflage, predation, signal communication, and sex choice.

Thomas Young first explained structural coloration using wave interference in 1803. He described iridescence as the result of interference between reflections from thin film surfaces, combined with refractions as light enters and leaves the films. By the invention of electron microscopy in the 1950s, researchers were able to study nanostructures of surfaces, and it led to further understanding of structural coloration mechanisms. The most common mechanisms of structural colors are film interference, diffraction grating, light scattering, and photonic crystals (Land 1972; Fox 1976; Srinivasarao 1999; Parker 2000, 2004; Vukusic and Sambles 2003; Prum 2006; Kinoshita 2008; Kinoshita et al. 2008; Doucet and Meadows 2009; Vigneron and Simonis 2010; Sun et al 2013; Yu et al. 2013). Biological colors are mainly derived from film interference, which includes thin-film and multi-film interference. The diffraction grating mechanism is found in, for example, seed shrimp, mollusk *Haliotis glabra*, and the flower *Hibiscus trionum*. Examples of light scattering include colors produced by brilliant iridescent butterfly wing scales and avian

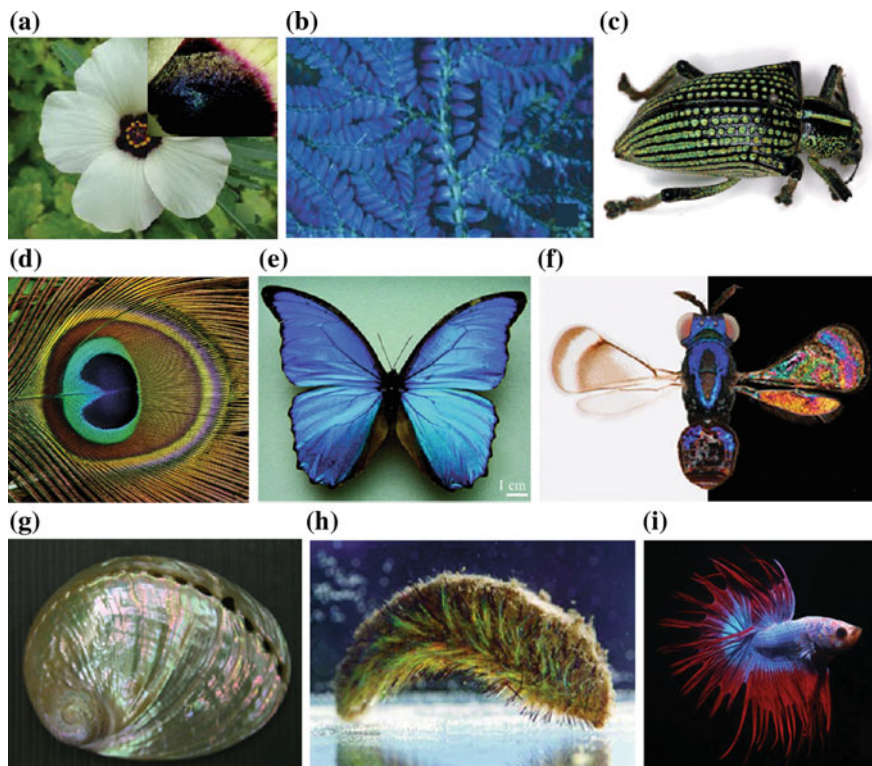


Fig. 15.2 Montage of photographs of structural colorations in living nature. **a** Base of *H. trionum* petal, showing iridescence overlying red pigment; **b** Blue iridescence in the fern-like tropical understory plants of the genus *Selaginella*; **c** The diamond weevil beetle, *Entimus imperialis*, with the black elytra where numerous pits are studded with yellow-green scales; **d** The brilliant iridescent colors of the male peacock's tail feathers; **e** Broad blue dorsal wing color of blue butterfly *Morpho rhetenor*; **f** composite image of *Closterocerus coffeellae* (Hymenoptera, insect) showing the dramatic effect of changing background reflections on wing interference pattern visibility. The left side wing displays its pigmentation pattern against a light reflecting white background whereas the right side wing displays its wing interference pattern reflection against a light absorbing black background; **g** The polished shell of the mollusk, nacre of *Haliotis glabra* has beautiful iridescent colors; **h** hollow nanofiber bristles of *Aphrodita aculeata* (a species of Sea mouse) reflect light in yellow, red and green to warn off predators; **i** Siamese fighting fish (*Betta splendens*), the males have more attractive colors and fins (adapted from Sun et al. 2013)

feather barbules, such as the peacock's tail. Examples of photonic crystal structures include the opal colors in beetles and iridescent spines in the sea mouse.

Structural coloration is of interest in applications in science, technology, and visual arts as it does not require the use of chemicals, and represents a green solution. Various structural surfaces have been fabricated for commercial applications.

Based on a review by Sun et al. (2013), we present an introduction to physical mechanisms of structural colors, lessons from living nature, followed by bioinspired fabrication and applications.

15.2 Physical Mechanisms of Structural Colors

Thin film interference occurs when incident light waves are reflected by the upper and lower surfaces of a thin film interface and form a new wave. Multi-film interference occurs in multi-layered films. A diffraction grating is an optical component with periodic structure that splits and diffracts light into several beams traveling in different directions. Scattering refers to the dispersal of a light beam into a range of directions as a result of reflection from a surface. Scattering includes both coherent and incoherent scattering. It should be noted that some scattering produces non-iridescent structural colors because of its origin in the irregularity of a structure. Photonic crystals have periodic structures, and are defined as a medium with a refractive index that varies in space periodically. The purpose of this periodic structure is to control the scattering of an incident illumination.

Figure 15.3 shows schematics of physical mechanism of structural colors in nature: thin-film and multi-film interference, diffraction grating, coherent and incoherent scattering, and photonic crystals [one-dimensional (1-D), two-dimensional (2-D) and three-dimensional (3-D)].

Sometimes different physical mechanisms combine to produce perceived color (Kinoshita et al. 2008). For example, in the *Morpho* butterfly, a multi-film interference was found in the vertical direction and diffraction grating in the horizontal direction (Vukusic et al. 1999; Kinoshita et al. 2002; Berthier et al. 2006).

15.2.1 Film Interference

Film interference in nature includes thin-film and multi-film interference (Sun et al. 2013). Thin-film interference occurs where light is reflected and interferes from the upper and lower boundaries of the film (Fig. 15.3a) (Parker 2000). The reflectivity of a thin, non-absorbing layer of thickness d with refractive index n , bound by two semi-infinite media with refractive indices, can be determined theoretically. This is done by summation over the amplitudes of all the light beams that leave the layer in reflection. Note that these beams may have incurred multiple reflections within the layer. The well-known example of color caused by thin film interference is the iridescent soap bubble.

Light waves traveling from low refractive index media toward higher index media undergo a 180° phase change on reflection. There is no phase change in the opposite case. In Fig. 15.3a, at normal incidence, when a light wave of wavelength λ travels from air of refractive index 1, to another index medium n (>1), a phase change of 180° occurs in the ray labeled 1. Upon reflection from the bottom of the film, the ray labeled 2 undergoes no phase change with respect to the incident wave, but travels an extra distance $2d$, before the waves combine. For constructive interference,

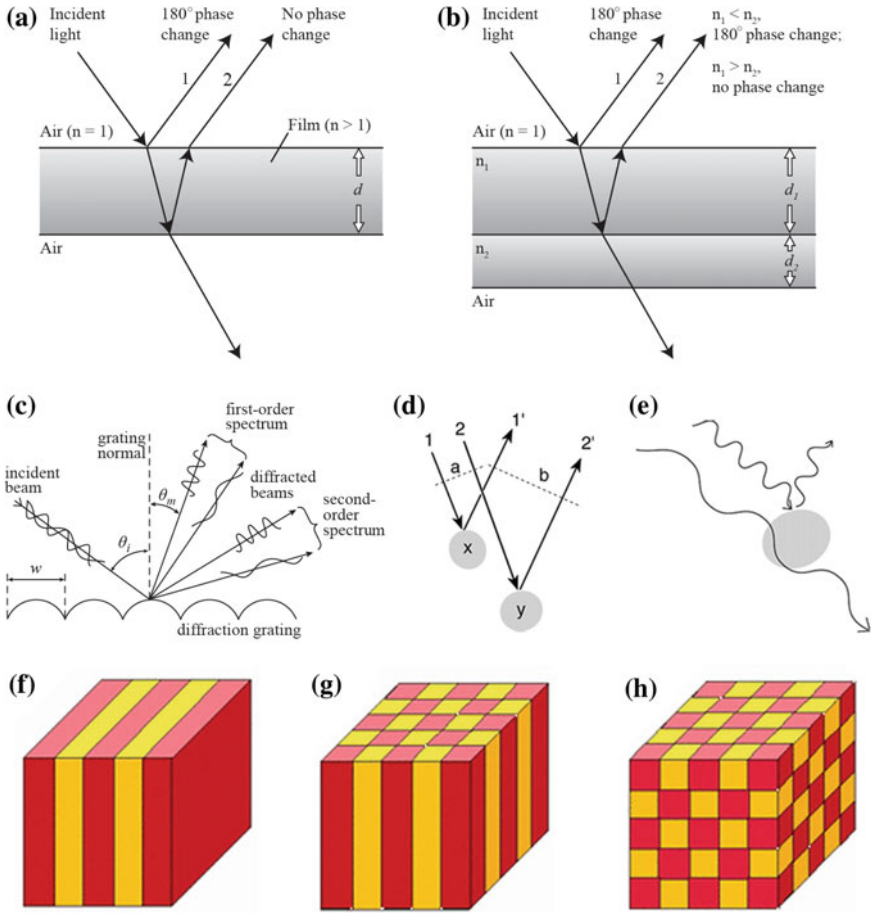


Fig. 15.3 Structural colors arise via **a** Thin-film interference. Many of the light beams that contribute to the overall reflectivity of a thin-film incur multiple reflections in the layer, which determine their final amplitude when they leave the layer; **b** multi-film interference; **c** diffraction grating dividing white light into spectra, rays scattered from different points on the grating interfere either constructively or destructively (Parker 2009); **d** and **e** coherent and incoherent scattering; and **f–h** photonic crystals: one-, two- and three- (1-D, 2-D, 3-D) dimensional photonic crystals, and the colors represent materials with different refractive indices (adapted from Joannopoulos et al. 2008)

$$2nd = \left(m + \frac{1}{2}\right)\lambda \tag{15.1}$$

Based on refractive indices of various media, if two phase change reversals occur, then

$$2nd = m\lambda \quad (15.2)$$

Multi-film interference occurs in multi-layered films. Consider two layers with thicknesses d_1 and d_2 , and refractive indices n_1 and n_2 , respectively, shown in Fig. 15.3b. At normal incidence, for $n_1 < n_2$, two phase reversals occur and constructive interference occurs when

$$2(n_1d_1 + n_2d_2) = m\lambda \quad (15.3a)$$

For multiple layers, if an even number of phase reversals occur,

$$2njdj = m\lambda \quad (15.3b)$$

where j represents the respective layers and m is a positive integer.

For two layers, if $n_1 > n_2$, then one phase reversal occurs and

$$2(n_1d_1 + n_2d_2) = \left(m + \frac{1}{2}\right)\lambda \quad (15.4a)$$

For multiple layers, if an odd number of phase reversals occur,

$$2njdj = \left(m + \frac{1}{2}\right)\lambda \quad (15.4b)$$

At $m = 0$, (15.4b) simplifies to $n_jd_j = \lambda/4$; hence, a quarter-wave stack is ideal for multilayer arrangements for high reflectivity.

15.2.2 Diffraction Gratings

Diffraction grating is a surface which is periodically corrugated in some direction along the surface (Palmer and Loewen 2005; Vigneron and Simonis 2010; Sun et al. 2013). The physics of a diffraction grating is the same as that involved in a periodic multilayer stack, except for the orientation of the periodicity. Figure 15.3c shows that light may be deviated from the direction of its simple transmission or reflection when it interacts with a periodic surface consisting, for example, of a series of parallel grooves. For this deviation to happen, the light that is diffracted from the successive grooves should be out of phase by integral values of 2π . This occurs when, for a given direction of propagation, the optical path difference via successive grooves is $m\lambda$, where m is an integer known as the diffraction order and λ is the wavelength. This may be expressed by the grating equation:

$$2w(\sin \theta_i - \sin \theta_m) = m\lambda \quad (15.5)$$

where θ_i and θ_m are the angles of incidence and diffraction, respectively, and w is the period (Fig. 15.3c).

According to 15.5, a diffraction grating occurs where constructive interference for different wavelengths is fulfilled under different angles. This constructive interference is what gives rise to the coloration. Diffraction gratings are particularly common in butterflies and the ostracod (seed shrimp) *Euphilomedes carcharodonta*.

15.2.3 Scattering

Light scattering is the deflection of a ray from the direction of its straight path, either by irregularities in the propagation medium or on the surface with which the ray interacts. Deviations from the conventional reflection due to irregularities is referred to as scattering (Land 1972; Sun et al. 2013). The simplest classifications of light scattering are coherent scattering and incoherent scattering. Coherent scattering involves interference, reinforcement, thin-film reflection, and diffraction. Incoherent scattering includes Rayleigh, Tyndall, and Mie scattering (Prum and Torres 2003). With coherent scattering there is a phase relationship between incoming and scattered waves, which constructively reinforce each other. Color is produced in terms of the phase interactions among these light waves as they are scattered by multiple scattering objects (Fig. 15.3d). With incoherent scattering, there is no phase relationship among the scattered waves. Instead, color is produced as a result of differential scattering of wavelengths by individual scattered rays (Fig. 15.3e).

In nature, light scattering is the most common mechanism for production of blue coloration. This coloration can be as a result of either coherent or incoherent scattering. The common mechanism for the production of iridescent colors in nature is coherent scattering of light waves.

15.2.4 Photonic Crystals

Photonic crystals are structures periodic in 1-D, 2-D, or 3-D ordered, sub-wavelength lattices. They can control the propagation of light in the manner that atomic crystals control electrons (Fig. 15.3f–h) (Joannopoulos et al. 2008; Thylén et al. 2004; Vigneron and Simonis 2010; Kolle 2011; Sun et al. 2013). The defining feature of a photonic crystal is the periodicity of dielectric material along one axis or more. Photonic crystals may be regarded as a special case of a composite, built from two materials with different refractive indices, characterized by a

refractive index invariant under the spatial translations of a crystalline lattice. A 1-D photonic crystal is merely the thin-film interference described earlier.

15.2.5 Coloration Changes

A change in structures will result in coloration changes. This is found in organisms for camouflage, predation, signal communication and sex choice (Sun et al. 2013). When a substance is illuminated with white light, we see a specific color if the reflected light has a wavelength in the range of 380–770 nm, which is the visible light range. Different wavelengths within that range result in different color perceptions by the human eye: 770–622 nm is perceived as red; 622–597 nm as orange; 597–577 nm as yellow; 577–492 nm as green; 492–455 nm as indigo, and 455–350 nm as purple. Therefore, a change of wavelength will lead to the perception of color change.

Figure 15.4a–c illustrates that the variations of d , θ , and n , results in color changes in cephalopods (expansion and compression of extracellular space between protein platelets), neon tetra fish (tilting protein platelets), and beetle cuticles (changing refractive index of a porous layer by absorbing liquid), respectively (adapted from Fudouzi 2011).

For the underlying mechanism of 3-D photonic crystals, the color also depends on the refractive index, tilting angle, and distance between the cubic close packing (CCP) (111) planes. The reflected wavelength λ is expressed by the combining of the Bragg equation with the Snell law (adapted from Fudouzi 2004)

$$\lambda = 2d_{111}\sqrt{n_{\text{eff}}^2 - \sin^2\theta_0} \quad (15.6)$$

Here, d_{111} is the interplanar spacing of the CCP (111) planes, n_{eff} is the average refractive index, and θ_0 is the angle of incidence. From (15.6), the structural color can be changed by controlling three parameters: d_{111} , n_{eff} and θ_0 . In 3-D photonic crystals, a simpler method to induce color change is by changing d_{111} . Figure 15.4d–f shows three structure types of colloid-based soft materials, which exhibit tunable structural color by diffracting visible light: opal composite (3-D close-packed) (Fig. 15.4d), inverse opal (Fig. 15.4e) and non-close-packed colloidal crystal embedded in a soft material, typically a hydrogel (Fig. 15.4f), they all can change color by adjusting the value of d_{111} (Fudouzi 2011). Opal composite (3-D close packed) has an elastomer that plays an important role in the reversible tuning of the colloidal crystal lattice, as shown in Fig. 15.4d. Using opal as a template, an inverse opal structure can be produced, which exhibits porous morphology and tunable color as shown in Fig. 15.4e. Figure 15.4f shows a colloidal crystal embedded in a poly (N-isopropylacrylamide) hydrogel; its lattice spacing is tuned by the temperature-induced phase transition in the hydrogel (Sun et al. 2013).

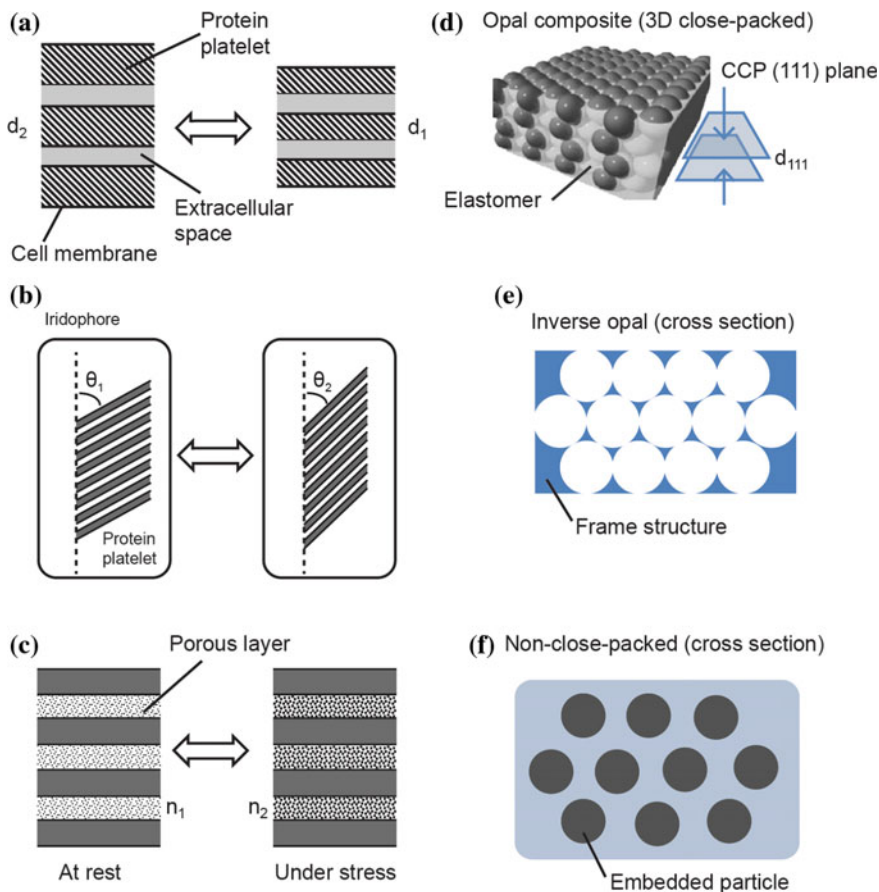


Fig. 15.4 Coloration changes mechanisms in living creatures: multi-film interference (a–c): **a** expansion and compression of extracellular space between protein platelets in cephalopods, **b** tilting protein platelet in the iridophore of neon tetra fish, **c** changing refractive index of a porous layer by absorbing liquid onto the beetle shell; photonic crystals structures by diffracting visible light (d–f): **d** opal composite made of 3D close-packed colloidal spheres bonded by an elastomer, **e** inverse opal made of a soft-material frame structure—here opal acts as a template for the soft material, **f** non-close-packed colloidal crystal embedded in a soft material, typically a hydrogel (adapted from Fudouzi 2011)

15.3 Lessons from Living Nature

Structural color exists in a number of animals and plants. The micro- or nano-structures are responsible for the color in form, such as hair, fur, scales, filaments, skin, barbules, shells, and exoskeletons. We present various lessons from nature based on various physical mechanisms.

15.3.1 Film Interference

Film interference is most common for structural color in nature. Some examples are presented in Table 15.1 (Sun et al. 2013). The color caused by the thin-film interference exists in the transparent wings of *Closterocerus coffeellae* (a hymenoptera wasp) (Shevtsova et al. 2011). The wings of some houseflies act as a single thin-film and appear to have different colors as a result of difference in the thickness of the layer. This provides a change in the color observed from unidirectional, polychromatic light (Parker 2000). Some birds' iridescence originates from thin-film reflectors, such as satin bowerbirds (Doucet et al. 2006), rock dove (Yoshioka et al. 2007), and blue-black grassquit (Maia et al. 2009). The two-color (green and purple) switching iridescence of the neck feather of the rock dove occurs very suddenly by only slight shifting of the viewing angle (Yoshioka et al. 2007). An iridescent blue color leaf is caused by a physical effect, thin-film interference (Héban and Lee 1984; Graham et al. 1993). Two examples of plants that exhibit film interference are the neotropical ferns *D. nodosa* and *T. elegans*. In *D. nodosa*, multiple layers of cellulose and helicoidal arrangement of microfibrils create the structural basis for the film that produces the perceived blue color. In *T. elegans*, remarkably uniform thickness and arrangement of grana in specialized chloroplasts adjacent to the adaxial wall of the adaxial epidermis creates the structural basis for the film that produces this fern's perceived colors (Graham et al. 1993).

Multi-film interferences in beetles can be located at different layers within the integument: epicuticle, exocuticle, and endocuticle (Seago et al. 2009; Sun et al. 2013). In the case of the jewel beetle (Fig. 15.5a) and leaf beetle, where the epicuticle region consists of a high reflector due to a multilayer, the outer epicuticle mainly contributes to the reflection, which is essentially insensitive to the polarization (Kinoshita and Yoshioka 2005). Many scarab beetles have exocuticular reflectors: layers of chitin fibrils are laminated with protein, structured as parallel bars, and stacked with a rotation of each layer. This results in a helical structure that only reflects circular waves of inverse chirality. Insect cuticle is secreted in phases, which gives rise to nanostructured multilayers that create brilliant body colors (Stavenga 2009). Butterflies and moths are prolific examples of multi-film interference (Yoshioka and Kinoshita 2007).

Film interference used by animals to produce structural colors are also used by plants (Glover and Whitney 2010), such as marble berry *Pollia condensata* fruits (Fig. 15.5b). The brilliant, pixelated color is caused by Bragg reflection of helicoidally stacked cellulose microfibrils that form multilayers in the cell walls of the epicarp (Vignolini et al. 2012). In plants, multilayers are found predominantly in shade-plant leaves, suggesting a role either in photoprotection or in optimizing capture of photosynthetically active light (Glover and Whitney 2010).

Multi-film interferences widely exist in fish (Lythgoe and Shand 1989; Nagaishi et al. 1990; Nagaishi and Oshima 1992; McKenzie et al. 1995; Kinoshita and Yoshioka 2005; Yoshioka et al. 2011), mollusks (Brink et al. 2002; Brink and van der Berg 2005), saphrinid copepods (Chae and Nishida 1994), swimming crab

Table 15.1 Examples of film interference in living nature (Sun et al. 2013)

	Variety	Species	Color	References
Thin-film interferences	Bird	Satin bowerbirds	Iridescent color	Doucet et al. (2006)
		Rock dove	Green and purple	Yoshioka et al. (2007)
		Blue-back grassquit	UV-reflecting iridescent color	Maia et al. (2009)
	Marine animal	Fishes	Blue, turquoise, green, copper, gold, or platinum	Amiri and Shaheen (2012)
	Plant	Leafs	Iridescent blue	Hébant and Lee (1984), Graham et al. (1993)
	Insect	Butterflies	Iridescent color	Ghiradella (2010)
		Months	Iridescent color	Ghiradella (2010)
		Hymenoptera	Vivid color interference	Shevtsova et al. (2011)
		Diptera	Vivid color interference	Shevtsova et al. (2011)
	Multi-film interferences	Insect	Beetles	Iridescent green; blue-violet iridescence; gold; jewel;
Dragonflies			Blue	Prum et al. (2004)
Bees			Blue	Fung (2005)
Damselfly			Green	Vukusic et al. (2004)
Moths			Iridescent color	Mason (1927), Lippert et al. (1959), Ghiradella (1984)
Butterflies			Iridescent color; reflect yellow and blue light to combine green	Vukusic et al. (2000), Vukusic and Sambles (2003), Yoshioka and Kinoshita (2004), Wilts et al. (2009), Ghiradella (2010)
Plant		Fruits	Iridescent blue color with green and purple/red speckles	Vignolini et al. (2012)
Marine animal		Fish	Silver; red; iridescent color	Lythgoe and Shand (1989), Nagaishi et al. (1990),

(continued)

Table 15.1 (continued)

	Variety	Species	Color	References
				Nagaishi and Oshima (1992), McKenzie et al. (1995)
		Mollusk	Iridescent color	Brink et al. (2002), Brink and van der Berg (2005)
		Sapphirinid copepods	Iridescent color	Chae and Nishida (1994)
		Decapods	Iridescent color	Parker et al. (1998)
		Clam shrimps	Iridescent color	Parker (2000)
		Tanaidacea	Iridescent color	Parker (2000)
		Squid	Iridescent color	Sutherland et al. (2008), Mäthger et al. (2009)
	Bird	Male Lawes' parotia	Yellow-orange, blue-green	Stavenga et al. (2010)

Ovalipes decapods (Parker et al. 1998), *Limnadia* clam shrimp (Spinicaudata) and *Tanais tennicornis* (Tanaidacea; Parker 2000), and squid (Sutherland et al. 2008; Mäthger et al. 2009). In Fig. 15.5c, the iridescent cells under a blue stripe in neon tetra fish, each cell contains two rows of parallel platelets of guanine crystals, which move like a Venetian blind. A few stacks of these periodically arranged light-reflecting platelets result in the multilayer optical interference phenomena (Kinoshita and Yoshioka 2005; Yoshioka et al. 2011).

Figure 15.6a, b shows the breast-plate plumage of the male Lawes' parotia bird (*Parotia lawesii*), which combines thin film and multi-film interference to produce dramatic color changes during its courtship displays, thereby achieving much larger and more abrupt color changes than is possible with ordinary iridescent plumage (adapted from Stavenga et al. 2010). This combination of coloration mechanisms within a single feather is unique to the parotia breast-plate plumage. Melanin multi-layers within the barbules give a yellow-orange reflection, while the cortex acts as an enveloping thin-layer reflector producing bluish side beams.

Sun et al. (2013) reviewed the literature on the structural color of butterfly scales, with exemplary optics in nature. The beautiful colors in different species of butterflies, sometimes even within one species, are produced by various mechanisms. Figure 15.7 presents a diagrammatic view of a fragment together with some of the more common variants on this form (adapted from Ghiradella 2010). As shown in Fig. 15.7a, the ridges can be taller so that their lamellae form a stack of thin-films that collectively form a multi-film interference mirror or "multi-film reflector". This mechanism is responsible for such structural colors as the brilliant blues of the *Morpho* butterfly and others, the ultraviolet reflection in certain male Pierid butterflies, and the greens in some Papilionid butterflies (*Euploea desfresnes*, *Colias eurytheme* male). In Fig. 15.7b, the scale lumen form a 2-D photonic crystal that may channel or direct incoming light, for example, to reflective structures within the

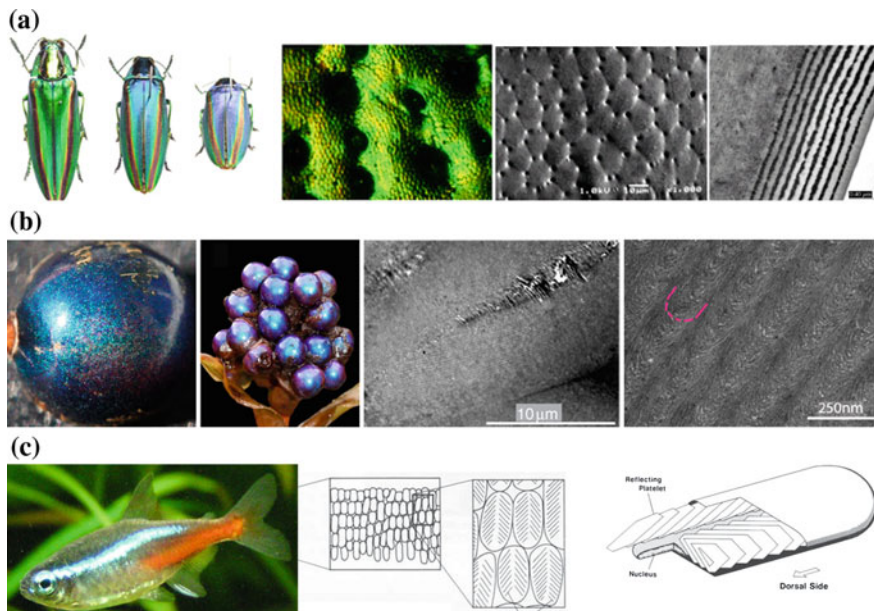


Fig. 15.5 Some examples of multi-film interference in nature. **a** Dorsal and ventral views of the Japanese jewel beetle (*Chrysochroa fulgidissima*) at various viewing angles, and microstructures of surface and cross-section by SEM (scanning electron microscope) and TEM (Kinoshita and Yoshioka 2005). **b** Photographs of marble berry *Pollia condensata* fruits which blue color is not uniform have a brilliant pixelated iridescent appearance with green and purple/red speckles. The diameter of each fruit is about 5 mm. TEM of a single thick-walled cell is multilayer structure and the cellulose microfibrils that constitute the thick cell wall. The red lines highlight the twisting direction of the microfibrils (Vignolini et al. 2012) **c** Iridescent cells under a blue stripe in neon tetra fish (body length = 30 mm). Each cell contains two rows of parallel platelets of guanine crystals which move like a Venetian blind. An iridophore of the neon tetra contains a few stacks of periodically arranged light-reflecting platelets, which can cause multilayer optical interference phenomena (Kinoshita and Yoshioka 2005; Yoshioka et al. 2011) (adapted from Sun et al. 2013)

interior of the scale. These act as a long-pass optical filter, and together with variable multi-film reflection, determine the blue-green wing coloration of Papilionid butterflies of the nireus group, such as *Papilio bromius*, *P. epiphorbas*, *P. nireus*, *P. oribazus* and *P. zalmoxis* (Ghiradella 2010; Trzeciak et al. 2012). Figure 15.7c shows that the reflective system on the ridges can “rock back,” so that it is the microribs that are serving as the multi-film interference; the lamellae may or may not still be present (*Trogonoptera brookianus*). Microribs can run from ridge to ridge, essentially obliterating the scale lumen; such scales typically have a “satiny” sheen (*Lamproptera curiosa*), as shown in Fig. 15.7d. Figure 15.7e shows that the window structure can be modified into “pores and plates,” although not so regular as to qualify as a 2-D photonic crystal (*Colias eurytheme* male, *Colias eurytheme* butterflies). As shown in Fig. 15.7f, the scale lumen may be filled with laminae that act as thin-film mirrors (*Urania ripheus*, *Papilio sp.* butterflies).

Fig. 15.6 The breast-plate plumage of male Lawes' parotia bird (*Parotia lawesii*) produces dramatic color changes from **a** yellow-orange to **b** blue-green when viewed from fronto-parallel to oblique alter the positioning of barbules on the feather tips (adapted from Stavenga et al. 2010)

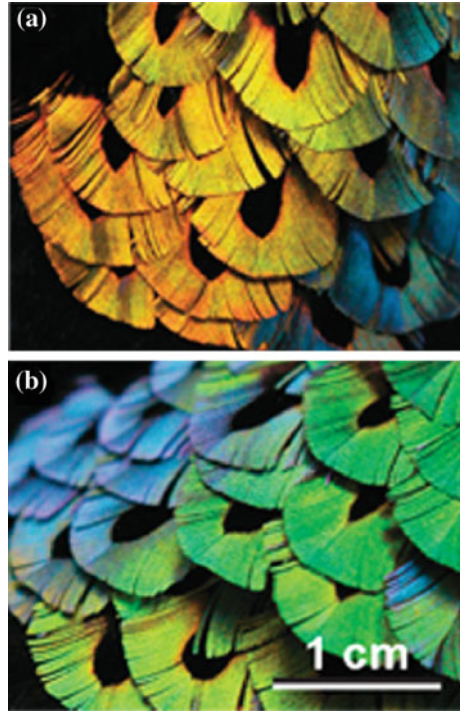


Figure 15.7g shows that the scale lumen may contain iridescent 3-D photonic crystals (*Thecla herodotus*, *Mitoura grynea*, *Parides sesostris*, *Teinopalpus imperialis* butterflies).

15.3.2 Diffraction Grating

The diffraction grating approach for structural color is common in invertebrates (Parker 2000; Sun et al. 2013). *Morpho* butterflies are perhaps one of the most strikingly colored butterflies. Most species have two distinct layers of different scales: larger cover scales and smaller ground scales arranged alternately in rows (Biró and Vigneron 2010; Tamáska et al. 2013). One layer is in the basal scales, which form a multi-film interference vertically (arrays of chitin that are shaped like Christmas trees and sprout at the scales' outward surface) and a diffraction grating horizontally (the parallel branches of each "tree" act as another kind of diffraction grating which may reflect up to 80 % of the incident blue light). The other layer is the ridges of the cover scales, which are wider than those of the basal scales, and serve to diffract and broaden the angle over which the blue color is visible. Its function is to produce synergistically novel visual effects (Vukusic et al. 1999; Kinoshita et al. 2002; Berthier et al. 2006). The *Lamprolenis nitida* butterfly hindwing, shown in

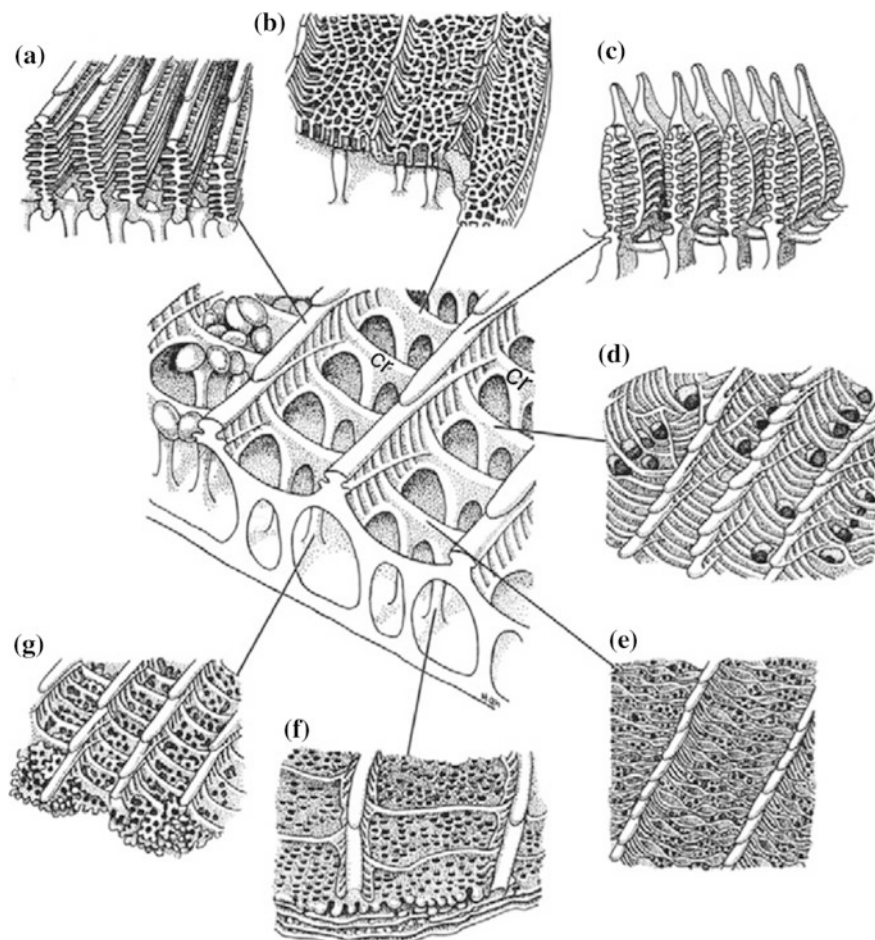


Fig. 15.7 Possible structural variations on a generic scale in butterflies. **a** The ridges can become taller than usual and their lamellae stack up to produce a series of thin-films that act as multi-film interference mirrors. **b** The window regions may display a series of fine alveoli that form in essence a 2-D photonic crystal with associated optical properties. **c** The ridge structure can “rock back” so that the lamellae are now vertical and it is the microribs that are acting as the reflective multilayers. **d** The microribs can extend across from ridge to ridge and essentially close the windows. **e** The region between the ridges may be filled with a “plates and pores” structure that we take to be essentially a variant of the 2-D photonic crystal structure shown in **(b)**. **f** The scale interior, or *lumen*, can be filled with stacks of laminae that form a second type of multi-film interference mirror. **g** The scale interior can be filled with a lattice that is effectively a form of 3-D photonic crystal, again with associated optical properties (adapted from Ghiradella 2010)

Fig. 15.8a, is capable of emitting two distinct patterns of iridescence in different directions by separate components on the same scale. These were found to originate from first order blazed diffraction gratings formed by different scale nanostructures angled with respect to the scale surface (Ingram et al. 2008).

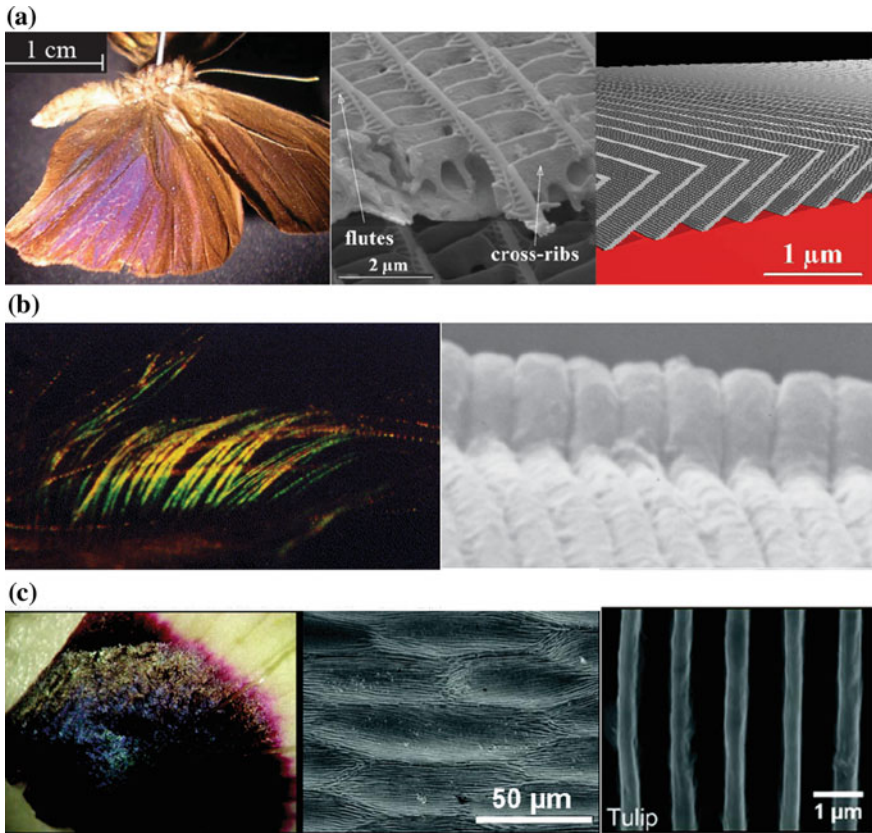


Fig. 15.8 Examples of diffractive structures in nature. **a** A photograph showing the violet observable when illuminating the male *Lamprolenis nitida* butterfly hindwing at 60° (left), an SEM showing the cross-ribs are roughly rectangular slabs, making an angle of approximately 30° with the plane of the scale indicating the position of the cross ribs and flutes (middle), model of the blazed grating (right) (Ingram et al. 2008); **b** a diffraction grating in the seed-shrimp (ostracod crustacean) *Azygocypridina lowryi*, all spectral colors can be observed with varying angle, periodicity is 600 nm (Parker 1995, 2004); **c** Base of flower *Hibiscus trionum* petal, showing iridescence overlying red pigment (left), SEM of flower *H. trionum* petal, half spanning the pigmented (heavily striated longitudinally toward the petal base) epidermis (middle), top view showing striations on the petal surface of flower *Tulipa kolpakowskiana*, resembling a line grating with a periodicity of 1.2–0.3 μm (right) (adapted from Whitney et al. 2009)

Some polychaete worms also produce iridescence through diffraction gratings (Parker 2000). Iridescence is particularly common on the setae or setules (hairs) of Crustacea, such as on certain first antennal setules of male ‘seed shrimp’ (*Myodocopina ostracods*, Crustacea) (Parker 1995). Here, the grating is formed by the external surface of juxtaposed rings with walls circular in cross section. The width of the rings, and consequently the periodicity of the grating, is about 700 nm in *Azygocypridina lowryi* (a species of ostracod crustacean), shown in Fig. 15.8b

(Parker 1995, 2004). Diffraction grating is also found in plants. For iridescence in flowers of the *Hibiscus trionum*, *Tulipa* species, shown in Fig. 15.8c, and *Mentzelia lindleyi*, the overlying cuticle of the petal epidermal cells produces a series of long, ordered ridges. The periodicity of the ridges acts as a diffraction grating, and splits the light reflecting from the surface into component wavelengths (Whitney et al. 2009).

15.3.3 Scattering

Special white colors exist in beetles' cuticles (Vukusic et al. 2007; Seago et al. 2009; Luke et al. 2010). All white colors in beetles are structural, arising from non-ordered, broadband, or Mie scattering of incident light by nanoscale particles. Structural whiteness is created by having a light scattering material that scatters all incident wavelengths equally.

Examples of incoherent scattering include the perception of blue sky, blue smoke, blue ice, and blue snow (Prum and Torres 2003). For example, so-called Rayleigh scattering results in a blue color and a red color when the system is viewed in transmission (Parker 2000). Although most structural color in animals is produced by coherent light scattering, the blue coloration in many amphibians is attributed to incoherent scattering, shown in Fig. 15.9a (Bagnara et al. 2007). The blue color in some other animals has also been thought to be caused by incoherent scattering, such as the giant blue swallowtail butterfly (*Papilio zalmoxis*) (Huxley 1976), dragonflies and damselflies (Odonata) (Mason 1926), and avian skin.

Figure 15.9b shows TEM micrographs of structurally colored facial caruncles of male yellow-bellied asity bird *Neodrepanis hypoxantha*. It shows that the tissues are substantially nanostructured at the appropriate spatial scale to scatter visible light coherently (Prum et al. 1999). These results confirm that the nanostructure of the collagen arrays determines the colors that are coherently scattered by these tissues.

Well-known examples of coherent scattering include the structural colors produced by brilliant iridescent butterfly wing scales and avian feather barbules, such as the peacock's tail (Fox 1976; Ghiradella 1991). Iridescence occurs if changes in the angle of observation or illumination affect the mean path length of scattered waves. Such a change will affect the phase relationships among the scattered waves and which wavelengths are constructively reinforced after scattering (Prum and Torres 2003). The fluorescent blue colors seen in many fish, for example, the coral reef damselfish and surgeonfish *Paracanthurus hepatus*, are the products of coherent light scattering (Bagnara et al. 2007). Similar phenomena were also found in plants. Iridescent blue leaf coloration is found in various plants and comes from a physical effect: constructive interference of reflected blue light (Gould and Lee 1996; Lee 1997).

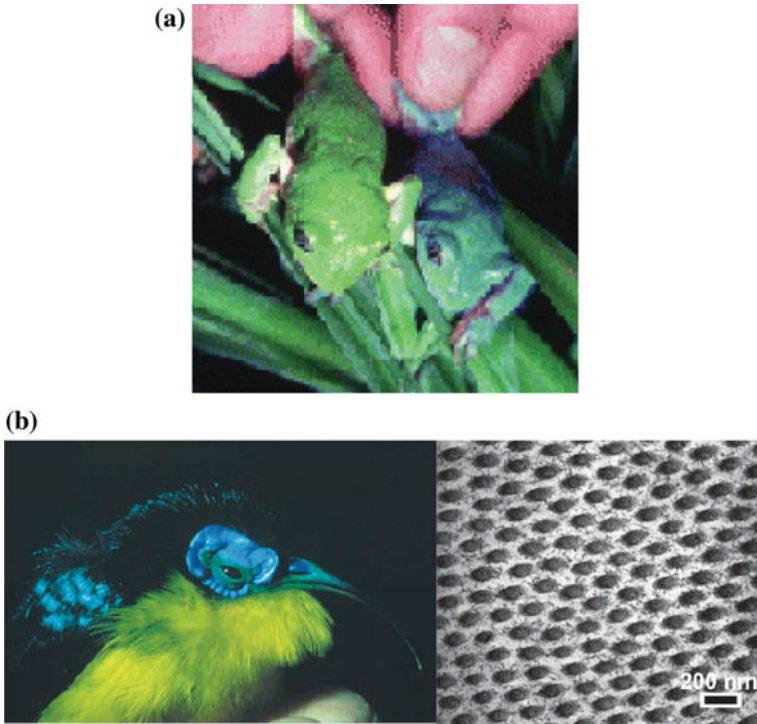


Fig. 15.9 **a** Blue coloration in amphibians; young sibling male frogs of *P. dacnicolor* (Bagnara et al. 2007). The *green* individual is normal for the species, while the *blue* frog is one of only a few that was produced from this spawning. **b** Structurally colored facial caruncles of male asities bird (*Neodrepanis hypoxantha*). TEM micrograph shows the nanostructure of a nearly hexagonal array of collagen fibers in light *blue caruncle* tissue (Prum et al. 1999)

15.3.4 Photonic Crystals

Natural photonic crystals are defined as a medium with a refractive index that varies in space periodically (Vigneron and Simonis 2010). Typical examples of 2-D and 3-D photonic crystals were first found in the sea mouse *Aphroditidae Polychaeta* (Parker et al. 2001) and the opal-analogue of a weevil species (Parker et al. 2003), respectively. Photonic crystals have been revealed in marine animals, insects, and birds (Hadley 1979; McClain et al. 1985; Aizenberg et al. 2001; Mähnger et al. 2003; Vigneron et al. 2007; Kinoshita et al. 2008; Eliason and Shawkey 2010; Colomer et al. 2012). 2-D and 3-D photonic crystals are more common in marine animals, birds, insects (beetle, butterfly), and plants, shown in Table 15.2 (Sun et al. 2013).

The beautiful iridescent feathers of some birds are due to 2-D photonic crystals incorporated on the surfaces of their barbules, for example, peacock tail feathers shown in Fig. 15.10a (Durrer 1962; Yoshioka and Kinoshita 2002; Zi et al. 2003). It was found that the cortex in differently colored barbules of peacock feathers is

Table 15.2 Examples of photonic crystals in living nature (Sun et al. 2013)

	Variety	Species	Color	Structure	References
2-D photonic crystal	Marine animal	Marine worm	Iridescent color	Tubular structures containing hexagonally packed hollow cylindrical channels	Parker et al. (2001), Trzeciak and Vukusic (2009)
		Comb-jellyfish	Iridescent	Tightly packed arrays of cilia	Welch et al. (2005, 2006), Welch and Vigneron (2007)
		Brittlestar	Color-change	Double-lens arrays	Aizenberg et al. (2001), Aizenberg and Hendler (2004)
		Glass sponge	Fiber-optical characteristics	Lattice-like skeleton of fused siliceous spicules and a crown-like organization of basalial at the base.	Sundar et al. (2003), Aizenberg et al. (2004)
	Bird	Peacock	Iridescent	Lattice arrays of solid rods	Durrer (1962), Yoshioka and Kinoshita (2002), Zi et al. (2003)
		Magpie	Black, yellowish-green iridescent	Air-filled circle melanin granules	Vigneron et al. (2006), Lee et al. (2010)
		Crow	Black	Solid circle melanin granules rods	Lee et al. (2010, 2012)
3-D photonic crystal	Insect	Beetle	White; opal; orange scale; green iridescence; rows of brilliant spots; yellow and blue bands; greenish-white; mixed blue and violet colors; bright white	Solid array of transparent spheres with hexagonal close-packing order; face-centered cubic; concave spots with diamond-type scale; ordered periodic 3D-lattice; face-centered-cubic array of spheres; bags containing agglomerated spheres; random	Parker et al. (2003), Welch et al. (2007), Galusha et al. (2008, 2010), Wilts et al. (2012), Vigneron and Simonis (2012), Pouya et al. (2011), Colomer et al. (2012), Simonis and Vigneron (2011), Lafait

(continued)

Table 15.2 (continued)

Variety	Species	Color	Structure	References
			network of interconnecting cuticular filaments	et al. (2010), Vukusic et al. (2007), Luke et al. (2010)
	Butterfly	Blue dorsal color, matt pea green ventral color; the matte black with blue shining	Gyroid-type; a chitinous matrix with regularly arrayed air-holes; shingles on a roof; elongated; deep zigzag ending	Ghiradella (1984, 1998, 2010), Wilts et al. (2011), Berthier et al. (2006), Biró et al. (2007), Welch and Vigneron (2007), Poladian et al. (2009), Zhang et al. (2009), Saranathan et al. (2010)
Plant	Edelweiss flowers	White	Hollow tubes with a series of parallel striations around the external surface	Vigneron et al. (2005)

responsible for coloration as it contains a 2-D photonic crystal structure. In the blue, green, and yellow barbules, the lattice structure is nearly square, whereas in the brown barbule it is a rectangular lattice. The only differences are the lattice constant (rod spacing) and the number of periods (melanin rod layers) along the direction normal to the cortex surface (Zi et al. 2003). The black-billed magpie bird *Pica pica* is not exactly a black-and-white bird; in fact, it has yellowish-green iridescent feathers forming a long tail, and bluish reflections on the dark areas of the wings, shown in Fig. 15.10b (Vigneron et al. 2006; Lee et al. 2010). For a yellowish-green feather, the structural model is a homogeneous block of keratin and melanin (refractive index 2) which contains a hexagonal lattice of parallel air channels. For the bluish reflections on the dark areas of the wing, the barbule cross section shows the cortex surrounding the central core, while the cortex is a thin-film of keratin and melanin containing cylindrical air holes, regularly distributed.

The 3-D photonic crystals have been found in some beetle species, as well as in butterflies (Ghiradella 1984, 1998, 2010; Berthier et al. 2006; Biró et al. 2007; Welch and Vigneron 2007; Poladian et al. 2009; Zhang et al. 2009; Saranathan et al. 2010; Wilts et al. 2011). Structurally colored butterfly scales are extremely diverse in nanostructure and in optical function (Saranathan et al. 2010).

Photonic crystals are also found in plants (Lee 1997; Vigneron et al. 2005). The hairs of edelweiss flowers (*Leontopodium nivale subsp. alpinum*) are hollow tubes with a series of parallel striations around the external surface that act as a 3-D photonic crystal. Through diffraction effects, the hairs absorb the majority of the

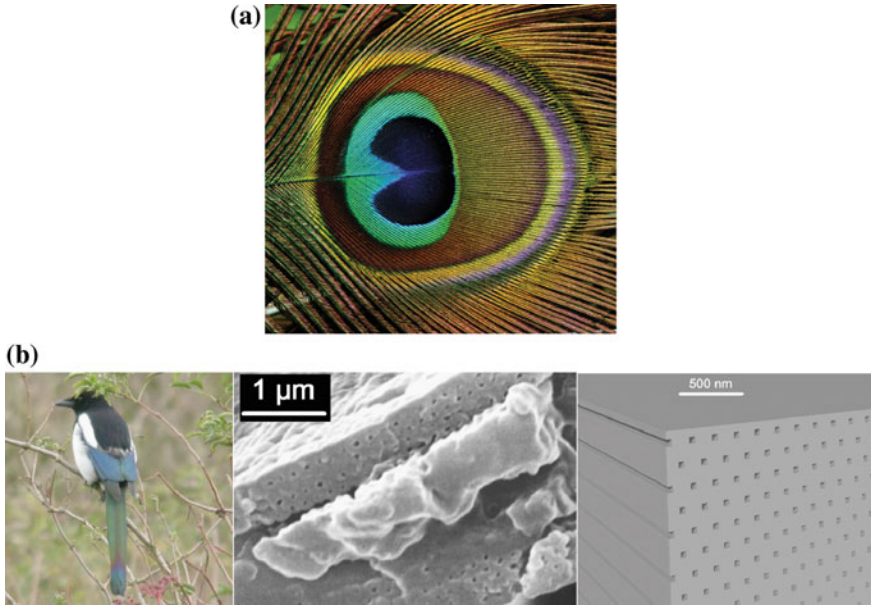


Fig. 15.10 **a** Male peacock's tail feathers with iridescent blue feathers forming an "eye" surrounded by orange and neon green rings, finishing with long, iridescent yellowish-green fringe, and **b** the black-billed magpie bird *Pica pica* with yellowish-green iridescent feathers forming a long tail, and bluish reflections on the dark areas of the wings (left), cross section of a barbule of a yellowish-green tail feather showing the cortex surrounding the central core, the cortex is a thin-film of keratin and melanin containing cylindrical air holes, regularly distributed (middle), model of the structure (right) (adapted from Vigneron et al. 2006)

UV light, effectively acting as an efficient sun-block that shield the covered living cells from harmful ultraviolet radiations (Vigneron et al. 2005).

15.3.5 Coloration Changes

The adaptive values of color change are usually regarded as camouflage, predation, signal communication, conspecific recognition, and reproductive behavior (Liu et al. 2009). That is color changes are triggered by excitement, stress, mate choices, or to prevent water from evaporating, which is found in fish, cephalopods, and insects. Some examples are presented in Table 15.3 (Sun et al. 2013).

Coloration change includes reversible and non-reversible changes (Seago et al. 2009). The former can occur via change in pigment, microstructure, or a combination of these (pigment color produced by the selective absorption of natural light and the structural color produced by the interactions of natural light with microstructures) (Liu et al. 2009). Non-reversible structural color change co-occurs with aging (Seago et al. 2009), such as pupa of a large tree nymph butterfly (*Idea*

Table 15.3 Examples of coloration change found in biological animals (Sun et al. 2013)

Species		Normal color	Changed color	Trigger reasons	References
Fish	Damselfish <i>Chrysiptera cyanea</i>	Blue	Ultraviolet	Stressful conditions	Kasukawa et al. (1986), Kasukawa and Oshima (1987), Oshima and Fujii (1987)
	Paradise whiptail <i>Pentapodus paradiseus</i>	Blue	Red	Stress	Mäthger et al. (2003)
	Neon tetra <i>Paracheirodon innesi</i>	Blue	Violet, yellow	Excited or under stress	Yoshioka et al. (2011)
Cephalopod	Squid <i>Loligo pealeii</i>	Iridescence	Disruptive pattern	Agonistic encounters, camouflage	Mäthger et al. (2009)
Bird	Mourning dove <i>Zenaida macroura</i>	Iridescence	More chromatic	Water	Shawkey et al. (2011)
	Male bird of paradise Lawes' parotia <i>Parotia lawesii</i>	Yellow-orange	Blue-green	Attract female	Stavenga et al. (2010)
Beetle	Tortoise beetles <i>Charidotella egregia</i>	Red	Golden	Stress	Vigneron et al. (2007)
	Hercules beetles <i>Dynastes hercules</i>	Khaki-green	Black	With humidity level increases at night for better camouflage; thermoregulation	Hinton and Jarman (1973), Rassart et al. (2008), Kim et al. (2010)
	Desert beetles <i>Cryptoglossa verrucosa</i>	Bluish-white	Black	Prevent water from evaporating	Hadley (1979), McClain et al. (1985)
	Beetles <i>Tmesisternus isabellae</i>	Golden	Red	Not clear	Liu et al. (2009)
	Beetle <i>Hoplia coerulea</i>	Blue	Green	Conspecific sex choice recognition	Rassart et al. (2009)
	Manuka beetle <i>Pyronota festiva</i>	Green	Purple, blue, orange, red or brown	Camouflage	De Silva et al. (2005)
	Tiger beetle <i>Cicindela</i>	Interference colors	Nearly to rock or soil condition	Camouflage	Schultz and Rankin (1985)
Butterfly	Lepidoptera	Iridescence		Camouflage	Tamáška et al. (2013), Berthier et al. (2007), Otaki (2008), Liu et al. (2010)

leuconoe), which color changes from yellow to gold within two days after pupation (Kinoshita and Yoshioka 2005).

There is another mechanism of coloration changes. Hydration levels can cause a variation in the thickness of the multilayer stack, thus changing the refractive index of porous layers (Seago et al. 2009). In ordered photonic crystals, color changes can be induced by relative gas/vapor concentration variations in a mixed atmosphere (Mouchet et al. 2012). There are color changes in elytra of some species of beetles that are related to humidity and microstructures, such as nanosized holes in the layer (3-D porous structure) of hercules beetles *Dynastes hercules* (Hinton and Jarman 1973; Rassart et al. 2008; Kim et al. 2010), a chirped multilayer reflector in tortoise beetles *Charidotella eregia* (Vigneron et al. 2007), multilayer in the scale interior of the longhorn beetles *Tmesisternus isabellae* (Liu et al. 2009), a stack of repeated corrugated layers (a 2-D photonic crystal) in beetles *Hoplia coerulea* (Rassart et al. 2009), and the “wax filaments” meshwork in desert beetles *Cryptoglossa verrucosa* (LeConte) (Hadley 1979).

15.4 Bioinspired Fabrication and Applications

Structural colors have high brightness and do not fade. They have the iridescent effect, polarization effect, and UV effect, and pigment colors do not have these characteristics. The understanding of the mechanisms of production of structural colors has inspired scientists and engineers to develop various optical coatings, paints, cosmetics, textiles, and anti-counterfeiting devices (Parker and Townley 2007; Vigneron et al. 2007; Forster et al. 2010; Vukusic 2010; Sun et al. 2013). Some researchers are reproducing natural structures with the highest possible degree of fidelity. Others are extracting new principles from structures found in the living world and implementing those using different materials and different structural solutions (Biró and Vigneron 2010). The design concepts and reproduction methods have been used in various nonmetallic materials and polymers for enhancing or improving their original properties.

Diffraction gratings are used to produce various optical effects. They are responsible for the metallic-like colored holograms found on credit cards or foil-type wrapping paper, and they also appear on stamps and banknotes since they can be difficult to forge (Parker 2004).

The iridescent effect of blue butterfly wings have been reproduced (Sun et al. 2013). For example, Watanabe et al. (2005) fabricated *Morpho* butterfly wing surfaces by focused ion beam chemical vapor deposition (FIB-CVD), shown in Fig. 15.11a, left. The quasi-structure was 2.60 mm in height, 0.26 mm in width, 20 mm in length, and had a 0.23 mm grating pitch. The shape and size were nearly the same as *Morpho* butterfly scales. The brilliant blue reflection from the quasi-structure was observed for a wide range of incident light angles, shown in Fig. 15.11a, right. In another fabrication of *Morpho* butterflies, a dielectric multilayered nanostructure on the stepped quartz was fabricated by electron beam

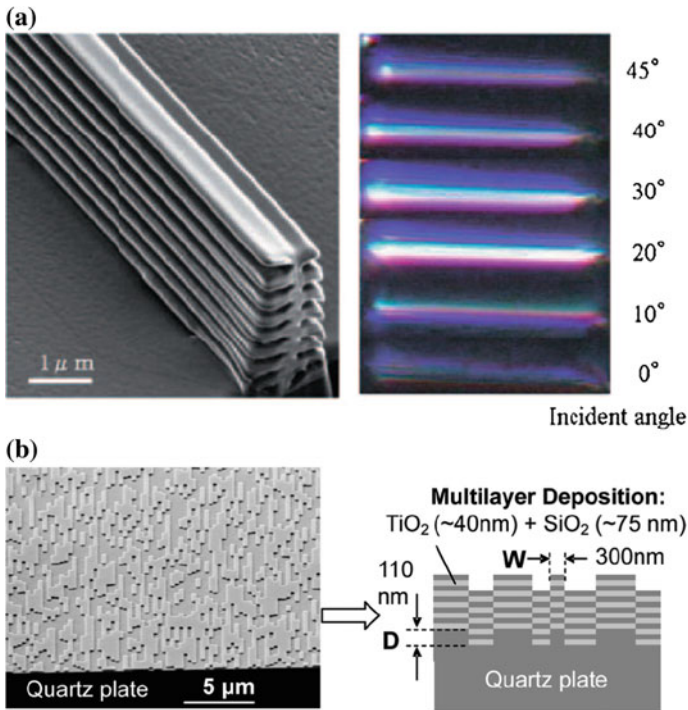


Fig. 15.11 **a** *Morpho*-butterfly-scale quasi-structure fabricated by FIB-CVD: (left) Secondary-ion microscopy image of the imitation of the *Morpho*-butterfly scale; (right) Optical microscope images of the structure observed with a 5° – 45° incidence angle of white light (Watanabe et al. 2005); **b** *Morpho*-blue fabricated by electron beam lithography and dry etching: (left) SEM image of a quasi-1-D pattern on a quartz substrate; (right) followed by deposition of $\text{TiO}_2/\text{SiO}_2$ multilayer on the nano-pattern (adapted from Saito et al. 2009)

lithography and dry etching, a simple and conventional technique in the semiconductor industry (Saito et al. 2009). To produce the desired surface pattern, conventional electron beam lithography and dry etching were applied to quartz substrates, shown in Fig. 15.11b, left. Next, step-by-step electron-beam-assisted deposition of seven bilayers of TiO_2 (high refractive index layer, ~ 40 nm thickness) and SiO_2 (low refractive index layer, ~ 75 nm thickness) was carried out, as shown in Fig. 15.11b, right.

15.5 Closure

Flora and fauna found in living nature exhibit vivid colors, some produced by structural coloration. Structural colors have iridescent, polarization, and UV effects that are not found in pigment colors. A review of the physical mechanisms and

species found in nature with structural colors produced by film interference, diffraction grating, scattering, and photonic crystals are presented. The special functions of color changes in some animals serve as camouflage, predation, signal communication, sex selection, and reproductive behavior. Some examples of bioinspired fabrication and applications are presented.

References

- Aizenberg, J. and Hendler, G. (2004), "Designing Efficient Microlens Arrays: Lessons from Nature," *J. Mater. Chem.* **14**, 2066–2072.
- Aizenberg, J., Tkachenko, A., Weiner, S., Addadi, L. and Hendler, G. (2001), "Calcitic Microlenses as Part of the Photoreceptor System in Brittlestars," *Nature* **412**, 819–822.
- Aizenberg, J., Sundar, V. C., Yablon, A. D., Weaver, J. C. and Chen, G. (2004), "Biological Glass Fibers: Correlation between Optical and Structural Properties," *PNAS* **101**, 3358–3363.
- Amiri, M. H. and Shaheen, H. M. (2012), "Chromatophores and Color Revelation in the Blue Variant of the Siamese Fighting Fish (*Betta splendens*)," *Micron* **43**, 159–169.
- Bagnara, J. T., Fernandez, P. J. and Fujii, K. (2007), "On the Blue Coloration of Vertebrates," *Pigment Cell Res.* **20**, 14–26.
- Berthier, S., Charron, E. and Boulenguez, J. (2006), "Morphological Structure and Optical Properties of the Wings of *Morphidae*," *Insect. Sci.* **13**, 145–158.
- Berthier, J., Boulenguez, J. and Balint, Z. (2007), "Multiscaled Polarization Effects in *Suneve coronata* (Lepidoptera) and Other Insects: Application to Anti-Counterfeiting of Banknotes," *Appl. Phys. A* **86**, 123–130.
- Biró, L. P. and Vigneron, J. P. (2010), "Photonic Nanoarchitectures in Butterflies and Beetles: Valuable Sources for Bioinspiration," *Laser Photonics Rev.* **5**, 27–51.
- Biró, L. P., Kertész, K., Vértessy, Z., Márk, G. I., Bálint, Z., Lousse, V. and Vigneron, J. P. (2007), "Living Photonic Crystals: Butterfly Scales- Nanostructure and Optical Properties," *Mater. Sci. Eng. C* **27**, 941–946.
- Booth, C. L. (1990), "Evolutionary Significance of Ontogenetic Colour Change in Animals," *Biol. J. Linn. Soc.* **40**, 125–163.
- Brink, D. J. and van der Berg, N. G. (2005), "An Investigation of Green Iridescence on the Mollusc *Patella granatina*," *J. Phys. D: Appl. Phys.* **38**, 338–343.
- Brink, D.J., van der Berg, N.G. and Botha, A.J. (2002), "Iridescent Colors on Seashells: An Optical and Structural Investigation of *Helcion pruinosus*," *Appl. Opt.* **41**, 717–722.
- Chae, J. and Nishida, S. (1994), "Integumental Ultrastructure and Color Patterns in the Iridescent Copepods of the Family Sapphirinidae (Copepoda: Poecilostomatoida)," *Mar. Biol.* **119**, 205–210.
- Colomer, J. F., Simonis, P., Bay, A., Cloetens, P., Suhonen, H., Rassart, M., Vandenberg, C. and Vigneron, J. P. (2012), "Photonic Polycrystal in the Greenish-White Scales of the African Longhorn Beetle *Prosopocera lactator* (Cerambycidae)," *Phys. Rev. E* **85**, 011907.
- De Silva, L., Hodgkinson, I., Murray, P., Wu, Q., Arnold, M., Leader, J. and McNaughton, A. (2005), "Natural and Nanoengineered Chiral Reflectors: Structural Color of Manuka Beetles and Titania Coatings," *Electromagnetic* **25**, 391–408.
- Doucet, S. M. and Meadows, M. G. (2009), "Iridescence: A Functional Perspective," *J. R. Soc. Interface* **6**, S115–S132.
- Doucet, S. M., Shawkey, M. D., Hill, G. E. and Montgomerie, R. (2006), "Iridescent Plumage in Satin Bowerbirds: Structure, Mechanisms and Nanostructural Predictors of Individual Variation in Colour," *J. Exp. Biol.* **209**, 380–390.
- Durrer, H. (1962), "Schillerfarben Beim Pfau (*Pavo cristatus* L.)," *Verhand. Naturforsch. Ges. Basel* **73**, 204–224.

- Eliason, C.M. and Shawkey, M.D. (2010), "Rapid, Reversible Response of Iridescent Feather Color to Ambient Humidity," *Opt. Express*, **18**, 21284–21292.
- Forster, J. D., Noh, H., Liew, S. F., Saranathan, V., Schreck, C. F., Yang, L., Park, J. G., Prum, R. O., Mochrie, S. G., O'Hern, C. S., Cao, H. and Dufresne, E. R. (2010), "Biomimetic Isotropic Nanostructures for Structural Coloration," *Adv. Mater.* **22**, 2939-2944.
- Fox, D.L. (1976), *Animal Biochromes and Structural Colours*, University of California Press, London, UK.
- Fudouzi, H. (2004), "Fabricating High-Quality Opal Films with Uniform Structure over a Large Area," *J. Colloid Interface Sci.* **275** 277-283.
- Fudouzi, H. (2011), "Tunable Structural Color in Organisms and Photonic Materials for Design of Bioinspired Materials," *Sci. Technol. Adv. Mater.* **12**, 064704.
- Fung, K. K. (2005), "Photonic Iridescence of a Blue-Banded Bee," *Microscopy and Microanalysis* **11**, 1202-03.
- Galusha, J. W., Richey, L. R., Gardner, J. S., Cha, J. N. and Bartl, M. H. (2008), "Discovery of a Diamond-Based Photonic Crystal Structure in Beetle Scales," *Phys. Rev. E* **77**, 050904.
- Galusha, J. W., Jorgensen, M. R., and Bartl, M. H. (2010), "Diamondstructured Titania Photonic-bandgap Crystals from Biological Templates," *Adv. Mater.* **27**, 107–110.
- Ghiradella, H. (1984), "Structure of Iridescent Lepidopteran Scales: Variations on Several Themes," *Ann. Entomol. Soc. Am.* **77**, 637-645.
- Ghiradella, H. (1991), "Light and Color on the Wing: Structural Colors in Butterflies and Moths," *Appl. Optics* **30**, 3492-3500.
- Ghiradella, H. (1998), "Hairs, Bristles and Scales," In: *Microscopic Anatomy of Invertebrates* (ed. F.W. Harrison and M. Locke), Wiley-Liss Inc., New York.
- Ghiradella, H. (2010), "Insect Cuticular Surface Modifications: Scales and Other Structural Formations," In: *Advances in Insect Physiology: Insect Integument and Colour* (Casas, J. and Simpson, S. J., eds.), Elsevier, London, Vol. 38, pp. 135-180.
- Ghiradella, H. and Butler, M. (2009), "Many Variations on a Few Themes: A Broader Look at Development of Iridescent Scales (And Feathers)," *J. R. Soc. Interface* **6**, S243-S251.
- Glover, B. J. and Whitney, H. M. (2010), "Structural Colour and Iridescence in Plants: The Poorly Studied Relations of Pigment Colour," *Ann. Bot.* **105**, 505-511.
- Gould, K. S. and Lee, D. W. (1996), "Physical and Ultrastructural Basis of Blue Leaf Iridescence in Four Malaysian Understory Plants," *Am. J. Bot.* **83**, 45-50.
- Graham, R. M., Lee, D. W. and Norstog, K. (1993), "Physical and Ultrastructural Basis of Blue Iridescence in Two Neotropical Ferns," *Am. J. Bot.* **80**, 198-203.
- Hadley, N.F. (1979), "Wax Secretion and Color Phases of the Desert Tenebrionid Beetle *Cryptoglossa verrucosa* (LeConte)," *Science* **203**, 367-369.
- Hariyama, T., Takaku, Y., Hironaka, M., Horiguchi, H., Komiya, Y. and Kurachi, M. (2002), "The Origin of the Iridescent Colors in *Coleopteran elytron*," *Forma* **17**, 123-132.
- Hariyama, T., Hironaka, M., Takaku, Y., Horiguchi, H. and Stavenga, D. G., 2005, "The Leaf Beetle, the Jewel Beetle, and the Damsel; Insects with a Multilayered Show Case," In: *Structural Color in Biological Systems—Principles and Applications*, (Kinoshita, S. and Yoshioka, S., Eds.), Osaka University Press, Osaka, Japan.
- Hébat, C. and Lee, D. W. (1984), "Ultrastructural Basis and Developmental Control of Blue Iridescence in *Selaginella* Leaves," *Am. J. Bot.* **71**, 216-219.
- Hinton, H. E. and Jarman, G. M. (1973), "Physiological Colour Change in the Elytra of the Hercules Beetle, *Dynastes Hercules*," *J. Ins. Physiol.* **19**, 533-549.
- Huxley, J. (1976), "Coloration of *Papilio zalmoxis* and *P. Antimachus*, and Discovery of Tyndall Blue in Butterflies," *Proc. R. Soc. Lond. B Biol. Sci.* **193**, 441-453.
- Ingram, A. L., Lousse, V., Parker, A. R. and Vigneron, J. P. (2008), "Dual Gratings Interspersed on a Single Butterfly Scale," *J. R. Soc. Interface* **5**, 1387-1390.
- Jewell, S. A., Vukusic, P. and Roberts, N. W. (2007), "Circularly Polarized Colour Reflection from Helicoidal Structures in the Beetle *Plusiotis boucardi*," *New J. Phys.* **9**, 99.
- Joannopoulos, J. D., Johnson, S. G., Winn, J. N. and Meade, R. D. (2008), *Photonic Crystals: Molding the Flow of Light*, Second Ed., Princeton University Press, Princeton, NJ.

- Kasukawa, H. and Oshima N. (1987), "Divisionistic Generation of Skin Hue and the Change of Shade in the Scalycheek Damselfish, *Pomacentrus lepidogenys*," *Pigment Cell Res.* **1**,152-157.
- Kasukawa, H., Oshima, N. and Fujii, R. (1986), "Control of Chromatophore Movements in Dermal Chromatic Units of Blue Damselfish-II. The Motile Iridophore," *Comp. Biochem. Physiol. C.* **83**, 1-7.
- Kattawar, G. (1994), "A Search for Circular Polarization in Nature," *Opt. Photon. News* **5**, 42-43.
- Kim, J. H., Moon, J.H., Lee, S. Y. and Park, J. (2010), "Biologically Inspired Humidity Sensor Based on Three-Dimensional Photonic Crystals," *Appl. Phys. Lett.* **97**, 103701.
- Kinoshita, S. (2008), *Structural Colors in the Realm of Nature*, World Scientific Publishing Co., Singapore.
- Kinoshita, S. and Yoshioka, S. (2005), "Structural Colors in Nature: The Role of Regularity and Irregularity in the Structure," *Chem. Phys. Chem.* **6**, 1442-1459.
- Kinoshita, S., Yoshioka, S. and Kawagoe, K. (2002), "Mechanisms of Structural Colour in the Morpho Butterfly: Cooperation of Regularity and Irregularity in an Iridescent Scale," *Proc. R. Soc. Lond. B* **269**, 1417-1421.
- Kinoshita, S., Yoshioka, S. and Miyazaki, J. (2008), "Physics of Structural Colors," *Rep. Prog. Phys.* **71**, 076401.
- Kolle, M. (2011), *Photonic Structures Inspired by Nature*, Springer-Verlag, Heidelberg, Germany.
- Kurachi, M., Takaku, Y., Komiya, Y. and Hariyama, T. (2002), "The Origin of Extensive Colour Polymorphism in *Plateumaris sericea* (Chrysomelidae, Coleoptera)," *Naturwissenschaften* **89**, 295-298.
- Lafait, J., Andraud, C., Berthier, S., Boulenguez, J., Callet, P., Dumazet, S., Rassart, M. and Vigneron, J. P. (2010), "Modeling the Vivid White Color of the Beetle *Calothyrsa margaritifera*," *Mater. Sci. Eng. B* **169**, 16-22.
- Land, M. F. (1972), "The Physics and Biology of Animal Reflectors," *Prog. Biophys. Mol. Biol.* **24**, 77-106.
- Lee, D. W. (1997), "Iridescent Blue Plants," *Am. Sci.* **85**, 56-63.
- Lee, E., Lee, H., Kimura, J. and Sugita, S. (2010), "Feather Microstructure of the Black-Billed Magpie (*Pica pica sericea*) and Jungle Crow (*Corvus macrorhynchos*)," *J. Vet. Med. Sci.* **72**, 1047.
- Lee, E., Miyazaki, J., Yoshioka, S., Lee, H. and Sugita, S. (2012), "The Weak Iridescent Feather Color in the Jungle Crow *Corvus macrorhynchos*," *Ornithol. Sci.* **11**, 59-64.
- Lippert, W., Gentil, K., and Morphol, Z. (1959), "Über Lamellare Feinstrukturen Bei Den Schillerschuppen Der Schmetterlinge Vom Urania- And Morpho-typ," *Oekol. Tiere* **48**, 115-122.
- Liu, F., Yin, H. W., Dong, B. Q., Qing, Y. H., Zhao, L., Meyer, S., Liu, X. H., Zi, J. and Chen, B. (2008), "Inconspicuous Structural Coloration in the Elytra Of Beetles *Chlorophila obscuripennis* (Coleoptera)," *Phys. Rev. E* **77**, 012901.
- Liu, F., Bong, B.Q., Liu, X. H., Zheng, Y. M. and Zi, J. (2009), "Structural Color Change in Longhorn Beetles *Tmesisternus isabellae*," *Opt. Express* **17**, 16183-16191.
- Liu, F., Wang, G. B., Jiang, L. P. and Dong, B. Q. (2010), "Structural Colouration and Optical Effects in the Wings of *Papilio peranthus*," *J. Opt.* **12**, 065301.
- Luke, S. M., Hallam, B. T. and Vukusic, P. (2010), "Structural Optimization for Broadband Scattering in Several Ultra-Thin White Beetle Scales," *Appl. Opt.* **49**, 4246-4254.
- Lythgoe, J. N. and Shand, J. (1989), "The Structural Basis for Iridescent Colour Changes in Dermal And Corneal Iridophores In Fish," *J. Exp. Biol.* **141**, 313-325.
- Maia, R., Caetano, J. V. O., Bao, S. N. and Macedo, R. H. (2009), "Iridescent Structural Colour Production in Male Blue-Black Grassquit Feather Barbules: The Role of Keratin and Melanin," *J. R. Soc. Interface* **6**, S203-S211.
- Mason, C. W. (1926), "Structural Colors in Insects. I," *J. Phys. Chem.* **30**, 383-395.
- Mason, C. W. (1927), "Structural Colors in Insects-II," *J. Phys. Chem.* **31**, 321-354.
- Mäthger, L. M., Land, M. F., Siebeck, U. E. and Marshall, N. J. (2003), "Rapid Colour Changes in Multilayer Reflecting Stripes in the Paradise Whiptail, *Pentapodus paradiseus*," *J. Exp. Biol.* **206**, 3607-3613.

- Mähger, L. M., Denton, E. J., Marshall, N. J. and Hanlon, R. T. (2009), "Mechanisms and Behavioural Functions of Structural Coloration in Cephalopods," *J. R. Soc. Interface* **6**, S149-S163.
- McClain, E., Seely, M.K., Hadley, N.F. and Fray, V. (1985), "Wax Blooms in Tenebrionid Beetles of the Namib Desert: Correlations with Environment," *Ecology* **66**, 112-118.
- McKenzie, D. R. and Large, M. (1998), "Multilayer Reflectors in Animals using Green and Gold Beetles as Contrasting Examples," *J. Exp. Biol.* **201**, 1307-1313.
- McKenzie, D. R., Yin, Y. and McFall, W. D. (1995), "Silvery Fish Skin as an Example of A Chaotic Reflector," *Pro. Mathem. Phys. Sci.* **451**, 579-584.
- Mouchet, S., Deparis, O. and Vigneron, J. P. (2012), "Unexplained High Sensitivity of the Reflectance of Porous Natural Photonic Structures to the Presence of Gases and Vapors in the Atmosphere." In: *Nanophotonics IV, Proc. SPIE* **8424**, 842425.
- Nagaishi, H. and Oshima, N. (1992), "Ultrastructure of the Motile Iridophores of the Neon Tetra," *Zool. Sci.* **9**, 65-75.
- Nagaishi, H., Oshima, N. and Fujii, R. (1990), "Light-Reflecting Properties of the Iridophores of the Neon Tetra, *Paracheirodon innesi*," *Comp. Biochem. Physiol.* **95A**, 337-341.
- Neville, A. C. and Caveney, S. (1969), "Scarabaeid Beetle Exocuticle as an Optical Analogue of Cholesteric Liquid Crystals," *Biol. Rev.* **44**, 531-562.
- Oshima, N. and Fujii, R. (1987), "Mobile Mechanisms of Blue Damselfish (*Chrysiptera cyanea*) Iridophores," *Cell Motil. Cytoskel.* **8**, 85-90.
- Otaki, J. M. (2008), "Physiologically Induced Color-Pattern Changes in Butterfly Wings: Mechanistic and Evolutionary Implications," *J. Insect Phys.* **54**, 1099-1112.
- Palmer, C. and Loewen, E. (2005), *Diffraction Grating Handbook*, Sixth Ed., Newport Corporation, New York.
- Parker, A. R. (1995), "Discovery of Functional Iridescence and its Coevolution with Eyes in the Phylogeny of *Ostracoda* (Crustacea), *Proc. R. Soc. London, Ser. B.* **262**, 349-355.
- Parker, A. R. (2000), "515 Million Years of Structural Colour," *J. Opt. A: Pure Appl. Opt.* **2**, R15-R28.
- Parker, A. R. (2004), "A Vision for Natural Photonics," *Phil. Trans. R. Soc. Lond. A* **362**, 2709-2720.
- Parker, A. R. (2009), "Natural Photonics for Industrial Inspiration," *Philos. Transact. A Math. Phys. Eng. Sci.* **367**, 1759-1782.
- Parker, A. R. and Townley, H. E. (2007), "Biomimetics of Photonic Nanostructures," *Nat. Nanotechnol.* **2**, 347-353.
- Parker, A. R., McKenzie, D. R. and Ahyong, S. T. (1998), "A Unique Form of Light Reflector and the Evolution of Signalling in *Ovalipes* (Crustacea: Decapoda: Portunidae)," *Proc. R. Soc. Lond. B Biol.* **265**, 861-867.
- Parker, A. R., McPhedran, R. C., McKenzie, D. R., Botten, L. C. and Nicorovici, N. A. (2001), "Photonic Engineering: Aphrodite's Iridescence," *Nature* **409**, 36-37.
- Parker, A. R., Welch, V. L., Driver, D. and Martini, N. (2003), "Structural Colour: Opal Analogue Discovered in a Weevil," *Nature* **426**, 786-787.
- Poladian, L., Wickham, S., Lee, K. and Large, M. C. J. (2009), "Iridescence from Photonic Crystals and Its Suppression in Butterfly Scales," *J. R. Soc. Interface* **6**, S233-S242.
- Pouya, C., Stavenga, D. G. and Vukusic, P. (2011), "Discovery of Ordered and Quasi-Ordered Photonic Crystal Structures in the Scales of the Beetle *Eupholus magnificus*," *Opt. Express* **19**, 11355-11364.
- Prum, R.O. (2006), "Anatomy, Physics, and Evolution of Structural Colors," In: *Bird Coloration: Mechanisms and Measurements* (Hill, G. E., and McGraw, K. J., eds.) Harvard University Press, Boston.
- Prum, R. O. and Torres, R. H. (2003), "A Fourier Tool for the Analysis of Coherent Light Scattering by Bio-Optical Nanostructures," *Integr. Comp. Biol.* **43**, 591-602.
- Prum, R. O., Torres, R., Kovach, C., Williamson, S., and Goodman, S. M. (1999), "Coherent Light Scattering by Nanostructured Collagen Arrays in the Caruncles of the Malagasy Asities (Eurylamidae: aves)," *J. Exp. Biol.* **202**, 3507-3522.

- Prum, R. O., Cole, J. A., and Torres, R. H. (2004), "Blue Integumentary Structural Colors in Dragonflies (Odonata) are not Produced by Incoherent Tyndall Scattering," *J. Exp. Biol.* **207**, 3999–4009.
- Rassart, M., Colomer, J. F., Tabarrant, T., and Vigneron, J. P. (2008), "Diffractive Hygrochromic Effect in the Cuticle of the Hercules Beetle *Dynastes hercules*," *New J. Phys.* **10**, 033014.
- Rassart, M., Simonis, P., Bay, A., Deparis, O. and Vigneron, J. P. (2009), "Scale Coloration Change following Water Absorption in the Beetle *Hoplia coerulea* (Coleoptera)," *Phys. Rev. E* **80**, 031910.
- Saito, A., Miyamura, Y., Ishikawa, Y., Murase, J., Akai-Kasaya, M. and Kuwahara, Y. (2009), "Reproduction, Mass-Production, and Control of the Morpho-Butterfly's Blue," In: *Advanced Fabrication Technologies for Micro/Nano Optics and Photonics II* (Suleski, T. J., Schoenfeld, W. V., and Wang, J. J., Eds.), *Proceedings of SPIE* **7205**, 720506.
- Saranathan, V., Osuji, C. O., Mochrie, S. G. J., Noh, H., Narayanan, S., Sandy, A., Dufresne, E. R. and Prum, R. O. (2010), "Structure, Function, and Self-Assembly of Single Network Gyroid (I4132) Photonic Crystals in Butterfly Wing Scales," *PNAS* **107**, 11676-11681.
- Schultz, T. D. and Rankin, M. A. (1985), "The Ultrastructure of Epicuticular Interference Reflectors of Tiger Beetles (Cicindela)," *J. Exp. Biol.* **117**, 88-110.
- Seago, A. E., Brady, P., Vigneron, J. P. and Schultz, T. D. (2009), "Gold Bugs and Beyond: A Review of Iridescence and Structural Colour Mechanisms in Beetles (Coleoptera)," *J. R. Soc. Interface* **6**, S165-S184.
- Sharma, V., Crne, M., Park, J. O. and Srinivasarao, M. (2009), "Structural Origin of Circularly Polarized Iridescence in Jeweled Beetles," *Science* **325**, 449-451.
- Shawkey, M. D., Morehouse, N. I. and Vukusic, P. (2009), "A Protean Palette: Colour Materials and Mixing in Birds and Butterflies," *J. R. Soc. Interface* **6**, S221–S231.
- Shawkey, M. D., D'Alba, L., Wozny, J., Eliason, C., Koop, J. A. and Jia, L. (2011), "Structural Color Change following Hydration and Dehydration of Iridescent Mourning Dove (*Zenaida macroura*) Feathers," *Zool.* **114**, 59-68.
- Shevtsova, E., Hansson, C., Janzen, D. H. and Kjærandsen, J. (2011), "Stable Structural Color Patterns Displayed on Transparent Insect Wings," *PNAS* **108**, 668-673.
- Simonis, P. and Vigneron, J. P. (2011), "Structural Color Produced by a Three-Dimensional Photonic Polycrystal in the Scales of a Longhorn Beetle: *Pseudomyagrus waterhousei* (Coleoptera: Cerambycidae)," *Phys. Rev.* **83**, 011908.
- Srinivasarao, M. (1999), "Nano-Optics in the Biological World: Beetles, Butterflies, Birds, and Moths," *Chem. Rev.* **99**, 1935-1961.
- Stavenga, D. G. (2009), "Surface Colors of Insects: Wings and Eyes," In: *Functional Surfaces in Biology* (Gorb, S. N., ed.), Springer, Netherlands.
- Stavenga, D. G., Leertouwer, H. L., Marshall, N. J., and Osorio, D. (2010), "Dramatic Colour Changes in a Bird of Paradise Caused by Uniquely Structured Breast Feather Barbules," *P. Roy. Soc. B* **278**, 2098-2104.
- Sun, J., Bhushan, B., and Tong, J. (2013), "Structural Coloration in Nature," *RSC Advances* **3**, 14862- 14899.
- Sundar, V. C., Yablou, A. D., Grazul, J. L., Ilan, M. and Aizenberg, J. (2003), "Fiber-Optical Features of a Glass Sponge," *Nature* **424**, 899-900.
- Sutherland, R. L., Mäthger, L. M., Hanlon, R. T., Urbas, A. M. and Stone, M. O. (2008), "Cephalopod Coloration Model. I. Squid Chromatophores and Iridophores," *JOSA A* **25**, 588-599.
- Tamáška, I., Kertész, K., Vértesy, Z., Bálint, Z., Kun, A., Yen S. H. and Biró, L. P. (2013), "Color Changes upon Cooling of Lepidoptera Scales Containing Photonic Nanoarchitectures," *Key Engineering Materials* **543**, 18-21.
- Thylén, L., Qiu, M. and Anand, S. (2004), "Photonic Crystals—A Step Towards Integrated Circuits for Photonics," *Chem. Phys. Chem.* **5**, 1268-1283.
- Trzeciak, T. M. and Vukusic, P. (2009), "Photonic Crystal Fiber in the Polychaete Worm *Pherusa sp.*," *Phys. Rev. E* **80**, 061908.

- Trzeciak, T. M., Wilts, B. D., Stavenga, D. G., and Vukusic, P. (2012), "Variable Multilayer Reflection together with Long-Pass Filtering Pigment Determines the Wing Coloration of Papilionid Butterflies of the *Nireus* Group," *Opt. Express* **20**, 8877-8890.
- Vigneron, J. P. and Simonis P. (2010), "Structural Colours," *Adv. Insect Physiol.* **38**, 181-218.
- Vigneron, J. P. and Simonis, P. (2012), "Natural Photonic Crystals," *J. Phys. B Condensed Matter.* **20**, 4032-4036.
- Vigneron, J. P., Colomer, J. F., Vigneron, N. and Lousse, V. (2005), "Natural Layer-by-layer Photonic Structure in the Squamae of *Hoplia coerulea* (Coleoptera)," *Phys. Rev. E* **72**, 061904.
- Vigneron, J. P., Colomer, J. F., Rassart, M., Ingram, A. L., and Lousse, V. (2006), "Structural Origin of the Colored Reflections from the Black-Billed Magpie Feathers," *Phys. Rev. E* **73**, 021914.
- Vigneron, J. P., Pasteels, J. M., Windsor, D. M., Vértessy, Z., Rassart, M., Seldrum, T., Dumont, J., Deparis, O., Lousse, V., Biró, L. P., Ertz, D. and Welch, V. (2007), "Switchable Reflector in the Panamanian Tortoise Beetle *Charidotella egregia* (Chrysomelidae: Cassidinae)," *Phys. Rev. E* **76**, 031907.
- Vigneron, J. P., Rassart, M., Simonis, P., Colomer, J. F., and Bay, A. (2009), "Possible Uses of the Layered Structure Found in the Scales of *Hoplia coerulea* (Coleoptera)," In: *Biomimetics and Bioinspiration* (Martín-Palma, R. J. and Lakhtakia, A., eds.), Proc. of SPIE **7401**, 74010B.
- Vignolini, S., Rudall, P. J., Rowland, A. V., Reed, A., Moyroud, E., Faden, R. B., Baumberg, J. J., Glover, B. J. and Steiner, U. (2012), "Pointillist Structural Color in *Pollia* Fruit," *Proc. Natl. Acad. Sci. USA* **109**, 15712-15715.
- Vukusic, P. (2010), "An Introduction to Bio-Inspired Design," *Contact Lens Spectrum* <http://www.clspectrum.com/printarticle.aspx?articleID=104164>.
- Vukusic, P. and Sambles, J. R. (2003), "Photonic Structures in Biology," *Nature* **424**, 852-855.
- Vukusic, P., Sambles, J. R., Lawrence, C. R. and Wootton R. J. (1999), "Quantified Interference and Diffraction in Single *Morpho* Butterfly Scales," *Proc. R. Soc. Lond. B* **266**, 1403-1411.
- Vukusic, P., Sambles, J. R. and Lawrence, C. R. (2000), "Colour Mixing in Wing Scales of a Butterfly," *Nature* **404**, 457.
- Vukusic, P., Wootton, R. J. and Sambles, J. R. (2004), "Remarkable Iridescence in the Hindwings of the Damselfly *Neurobasis chinensis chinensis* (Linnaeus) (Zygoptera: Calopterygidae)," *Proc. R. Soc. Lond. B* **271**, 595-601.
- Vukusic, P., Hallam, B. and Noyes, J. (2007), "Brilliant Whiteness in Ultrathin Beetle Scales," *Science* **315**, 348.
- Watanabe, K., Hoshino, T., Kanda, K., Haruyama, Y. and Matsui, S. (2005), "Brilliant Blue Observation from a Morpho-Butterfly-Scale Quasi-Structure," *Jap. J. Appl. Phys.* **44**, L48-L50.
- Welch, V. and Vigneron, J. (2007), "Beyond Butterflies—The Diversity of Biological Photonic Crystals," *Opt. Quantum Electron.* **39**, 295-303.
- Welch, V., Vigneron, J. and Parker, A. (2005), "The Cause of Colouration in the Ctenophore *Beroë cucumis*," *Curr.Biol.* **15**, R985-R986.
- Welch, V., Vigneron, J. P., Parker, A. and Lousse, V. (2006), "Optical Properties of the Iridescent Organ of the Comb-Jellyfish *Beroë cucumis* (Ctenophora)," *Phys. Rev. E* **73**, 041916.
- Welch, V., Lousse, V., Deparis, O., Parker, A. and Vigneron, J. P. (2007), "Orange Reflection from a Three-Dimensional Photonic Crystal in the Scales of the Weevil *Pachyrhynchus congestus pavonius* (Curculionidae)," *Phys. Rev. E* **75**, 041919.
- Whitney, H. M., Kolle, M., Andrew, P., Chittka, L., Steiner, U. and Glover, B. J. (2009), "Floral Iridescence, Produced by Diffractive Optics, Acts as a Cue for Animal Pollinators," *Science* **323**, 130-133.
- Wilts, B. D., Leertouwer, H. L., and Stavenga, D. G. (2009), "Imaging Scatterometry and Microspectrophotometry of Lycaenid Butterfly Wing Scales with Perforated Multilayers," *J. R. Soc. Interface* **6**, S193-S202.
- Wilts, B. D., Piriš, P., and Stavenga, D. G. (2011), "Spectral Reflectance Properties of Iridescent Pierid Butterfly Wings," *J. Comp. Physiol. A Neuroethol. Sens. Neural. Behav. Physiol.* **197**, 693-702.

- Wilts, B. D., Michielsen, K., De Raedt, H., and Stavenga, D. G. (2012), "Hemispherical Brillouin Zone Imaging of a Diamond-Type Biological Photonic Crystal," *J. R. Soc. Interface* **9**, 1609-1614.
- Yoshioka, S. and Kinoshita, S. (2002), "Effect Of Macroscopic Structure in Iridescent Color of the Peacock Feathers," *Forma* **17**, 169-181.
- Yoshioka, S. and Kinoshita, S. (2004), "Wavelength-Selective and Anisotropic Light-Diffusing Scale on the Wing of the *Morpho* Butterfly," *Proc. Biol. Sci.* **271**, 581-587.
- Yoshioka, S. and Kinoshita, S. (2007), "Polarization-Sensitive Color Mixing in the Wing of the Madagascan Sunset Moth," *Opt. Express* **15**, 2691-2701.
- Yoshioka, S., Nakamura, E. and Kinoshita, S. (2007), "Origin of Two-Color Iridescence in Rock Dove's Feather," *J. Phys. Soc. Japan* **76**, 013801.
- Yoshioka, S., Matsuhana, B., Tanaka, S., Inouye, Y., Oshima, N. and Kinoshita, S. (2011), "Mechanism of Variable Structural Colour in the Neon Tetra: Quantitative Evaluation of the Venetian Blind Model," *J. R. Soc. Interface* **8**, 56-66.
- Yu, K.L., Fan T.X., Lou, S. and Zhang, D. (2013), "Biomimetic Optical Materials: Integration of Nature's Design for Manipulation of Light," *Prog. Mater. Sci.* **58**, 825-873.
- Zhang, W., Zhang, D., Fan, T., Gu, J., Ding, J., Wang, H., Guo, Q. X. and Ogawa, H. (2009), "Novel Photoanode Structure Templated from Butterfly Wing Scales," *Chem. Mater.* **21**, 33-40.
- Zi, J., Yu, X., Li, Y., Hu, X., Xu, C., Wang, X., Lui, X. and Fu, R. (2003), "Coloration Strategies in Peacock Feathers," *Proc. Natl. Acad. Sci. USA* **100**, 12576-12578.

Chapter 16

Outlook

Biomimetics, or more accurately, biological inspiration, allows engineers and scientists to develop materials and devices of commercial interest by taking inspiration from nature. Functionality of biological materials and surfaces result from a complex interplay between surface morphology and physical and chemical properties. In nature, hierarchical structures with dimensions of features ranging from the macroscale to the nanoscale are extremely common and provide properties of interest.

There is significant interest in eco-friendly materials and surfaces for a large number of applications. Nature uses commonly found materials that provide functionality of interest. These materials and surfaces are eco-friendly and are being leveraged for various commercial applications. This recognition has led to “Green Science and Technology”, a term used for the first time in this book. As an example, this author has made efforts to popularize the term “Green Tribology.” Biologically-inspired green surfaces are serving the interests of both commercial viability and environmental sensitivity.

This emerging field of biomimetics, or bioinspiration, is highly interdisciplinary, and has attracted biologists, physicists, chemists, materials scientists, and engineers, as well as inspired artists, architects, and other non-scientists. The cross fertilization of ideas is providing progress at a fast pace if the number of research papers and symposia on this topic is any guide. The major emphasis on nanoscience and nanotechnology science in the early 1990s has provided the impetus for mimicking nature using nanofabrication techniques for commercial applications.

There are a large number of flora and fauna with properties of commercial interest. Functionalities of interest found in living nature include molecular scale devices, superhydrophobicity, self-cleaning, drag reduction in fluid flow, antifouling, superhydrophilicity, energy conversion and conservation, reversible adhesion, aerodynamic lift, high mechanical strength in materials and fibers, biological self-assembly, anti-reflection, structural coloration, thermal insulation, self-healing, and sensory aid mechanisms.

We find these functionalities in various objects and species from living nature. These include bacteria, plants, insects/spiders/lizards/frogs, aquatic animals, birds, seashells/bones/teeth, spider webs, moth eyes, and the fur and skin of polar bears.

These functionalities and the development of surfaces from them are important for basic research and various applications. These include self-cleaning windows, windshields, exterior paints for buildings, shipping vessels, utensils, roof tiles, textiles, solar panels, antifouling membranes for desalination and water purification, fluid flow reduction, and climbing robots.

There are various applications still needing nature's functionalities, and research is ongoing. Oleophobic surfaces have the potential for self-cleaning and antifouling from biological and organic contaminants both in air and underwater applications. This could lead to drag reduction in oil pipelines or other commercial applications.

This book provides a useful guide for the research and development of bioinspired artificial surfaces. Various flexible and low-cost techniques are described for the fabrication of hierarchically structured surfaces. A proper control of roughness constitutes the main challenge in producing a reliable hierarchical surface. The fabrication of complex structures with high durability is key to commercial exploitation.

Index

A

- Adhesion measurement, *Salvinia molesta*, 210–211
 - Adhesive force, 110–111
 - AFM tests, surfaces durability in, 174–179
 - Ambient species, lotus effect, 383–384
 - Anti-biofouling, 446–447
 - Antifogging, 26, 288, 291–292
 - Antifouling, 6, 17, 27–29, 433–441
 - anti-biofouling, 446–447
 - mechanisms, 449–452
 - anti-inorganic fouling, 447–449
 - mechanisms, 449–452
 - bioinspired rice leaf surfaces for, 441–452
 - anti-biofouling measurements, 444–445
 - anti-inorganic fouling measurements, 445–446
 - micropatterned samples, fabrication, 443–444
 - cleaning techniques, 437–441
 - chemical disinfecting, 440
 - cleaning techniques, 440–441
 - physical cleaning, 440
 - self-cleaning surfaces, 440–441
 - prevention techniques, 437–440
 - hydrophobic materials in, 438
 - for medical devices, 437–438
 - silicone foul-release coatings, 439
 - tributyltin coatings in, 438
 - strategies from living nature, 433–437
- Anti-icing experiment, 288
 - Anti-icing property, 292–293
 - Anti-inorganic fouling, 447–449
 - measurements, 445–446
 - Aquatic species, shark skin and fish scales effect, 384

- Arolia, 458
- Art & architecture, 12–16
- Attachment mechanisms, Tokay gecko, 472–476

B

- Ball-on-flat tribometer tests, surfaces durability in, 174–179
- Berlin oil channel, 342
- Bioarchitecture, 12–16
 - Biodiversity, 2
- Biofouling, 423–452. *See also* under Antifouling
 - anti-biofouling measurements, 444–445
 - fields susceptible to, 423–427
 - formation mechanisms, 427–432
 - medical biofouling, 437
 - surface factors, 430–433
- Bioinspiration, 14–15
- Biomimetics, 12–16
- Biornametics, 13
- Bouncing droplet studies, 100
- Bouncing droplet, transition during, 132–135, 157–162
- Butterfly wing effect, 383–420
 - drag reduction models, 413–420
 - pressure drop measurement technique, 392–411
 - air low, 408
 - nondimensional pressure drop model, 408–410
 - oil flow, 403–408
 - surface characterization, 396–400
 - water flow, 403
 - sample fabrication, 386–392
 - actual sample replicas, 386–387

- hot embossed plastic sheets, 390–392
 - micropatterned replicas, 390
 - wettability, 411–413
- C**
- Capillary forces, 474–476
 - Laplace force, 474
 - surface tension force, 474
 - Cassie equations, 37–49
 - Cassie impregnating wetting regime, 29
 - Cassie-Baxter and Wenzel transition, 55–59
 - criteria, 114–116
 - for different series, 122–125
 - Cassie-Baxter equations, 37–49
 - applicability range of, 45–49
 - limitations of, 42–45
 - Cassie-Baxter regime, 29
 - Chemical bath deposition (CBD), 91
 - Chemical vapor deposition (CVD), 89–90
 - CNT composites, 170–179
 - AFM tests, surfaces durability in, 174–179
 - ball-on-flat tribometer tests, surfaces durability in, 174–179
 - contact angle, 171–173
 - waterfall/jet tests, surfaces durability in, 173–174
 - Colonization, 428
 - Composite interface stability, 51–55
 - Computational fluid dynamic (CFD) model, 363
 - Contact angle (CA), 35–36, 108–109, 171–173, 411
 - CNT composites, 171–173
 - definition, 35–37
 - Cassie-Baxter equations, 37–49
 - composite interface stability, 51–55
 - heterogeneous interfaces, 37–49
 - hierarchical structure with convex surfaces, role of, 51–55
 - homogeneous interfaces, 37–49
 - Wenzel equation, 37–49
 - for liquid in contact with a rough surface, modeling, 35–60
 - of surfaces
 - using microparticles, 182–183
 - using micropattern, 181–182
 - Contact angle hysteresis (CAH), 25, 49–51, 97, 124–127, 411
 - Contact angle measurements
 - during condensation and evaporation of microdroplets, 128–131
 - hydrophilic leaf surfaces, 66–79
 - Salvinia molesta*, 209–211
 - superhydrophobic leaf surfaces, 67–69
 - Convex surfaces, hierarchical structure with, 51–55
 - Cubic close packing (CCP) (111) plane, 556
 - Cuticle, 64
- D**
- Darcy formula, 393
 - Darcy-Weissenbach friction factor, 394
 - Deposition methods, 89
 - Derjaguin-Muller-Toporov (DMT) theory, 483, 500
 - Diffraction grating, 562–565
 - Disjoining pressure, 44
 - 2-D photonic crystal, 567
 - Drag reduction models, 413–420
 - Droplet evaporation
 - studies, 100
 - transition during, observation, 118–122
 - Dupré equation, 35
- E**
- Engineered antifouling, 431
 - Environmental scanning electron microscope (ESEM), 98
 - Epidermis cells, 64
 - Euplantulae, 458
 - Evaporation studies using ESEM, 101
 - Extracellular polymeric substance (EPS), 428
- F**
- Fibonacci numbers, 7–12
 - Fibrillar structures
 - adhesion modeling of, 498–509. *See also under* Gecko adhesion
 - adhesion data base of, 480–498. *See also under* Gecko adhesion
 - Film interference, 552–554, 558–562
 - Fish scales effect, 384
 - Flat epoxy surfaces, wetting behavior on, 257–260
 - with $C_{20}F_{42}$, 260–262
 - Flat plate experiments, 346–349
 - Flat surface, wetting of, 27
 - ‘Flip-flop’ surface property, 284
 - Fluid drag reduction measurement, 167–168
 - Fluid flow modeling, 362–372
 - for shark-skin surface in turbulent flow, 362–372
 - continuous riblets, 367

- riblet geometry models, 364–366
 - segmented riblets, 367
 - Fluid-drag reduction, 329–332. *See also under* Shark-skin surface
 - mechanisms of fluid drag, 329–330
 - shark skin, 331–332
 - Fluorination techniques, 248–250
 - fluoropolymers, 248
 - fluorosilanes, 248–249
 - fluorosurfactants, 249–250
 - fluorothiols, 248–249
 - plasma deposition, 250
 - Focused ion beam chemical vapor deposition (FIBCVI), 571
 - Fogging, 26
 - Fouling, 423–452. *See also* Antifouling; Biofouling; Inorganic fouling
 - Freeze fouling, 430
- G**
- Gas stream particulate fouling, 430
 - Gaseous secondary electron detector (GSED), 101
 - Gecko adhesion, 457–524. *See also* Tokay gecko
 - adhesive force of a single spatula, 477–478
 - fibrillar structures, adhesion data base of, 498–509
 - constraints, 500–502
 - fiber model, 499
 - non-buckling condition, as constraint, 500–502
 - non-fiber fracture condition, 502–504
 - non-sticking condition, 503–504
 - numerical simulation, 504–505
 - single fiber contact analysis, 499–500
 - fibrillar structures, adhesion modeling of, 480–498
 - adhesion energy, 486
 - capillary effects, 494–498
 - multi-level hierarchical spring analysis, 484–488
 - multi-level hierarchical spring model, 488–494
 - single spring contact analysis, 482–483
 - hairy attachment systems, 458–461
 - humidity effects on, 479
 - hydrophobicity effects on, 479–480
 - measurements and data, 476–480
 - temperature effects on, 478–479
 - under ambient conditions, 476
 - Gecko skin-inspired structures, fabrication of, 509–522
 - multi-level hierarchical structures, 517–522
 - single level roughness structures, 510–517
 - Golden Ratio, 7–12
 - Golden Rectangle, 7–9, 11
 - ‘Green Ocean Coating Heavy Duty’, 439
 - Green science, 2
- H**
- Hairy attachment systems, 458–461
 - Hamaker constant, 483
 - Heterogeneous interfaces, 37–49
 - Hierarchical roughness, 4, 77–79
 - Hierarchical structures
 - with convex surfaces, role of, 51–55
 - and shark skin replica, wetting behavior on, 262–264
 - surface, wetting of, 27
 - Hierarchically structured lotus-like surfaces, 97–198. *See also* Mechanically durable superhydrophobic surfaces fabrication and characterization of, 97–198
 - adhesion, 99
 - adhesive force, 110–111
 - bouncing droplet studies, 100
 - contact angle, 108–109
 - contact angle, 99
 - droplet evaporation studies, 100
 - dynamic contact angles, 99
 - evaporation studies using ESEM, 101
 - experimental techniques, 99–106
 - hierarchically structured surfaces with wax platelets and tubules, 137–169
 - ideal surfaces with hierarchical structure, 136–137
 - microdroplet condensation using ESEM, 101
 - nanoparticle composites with hierarchical structure, 179–183. *See also individual entry*
 - static contact angles, 99
 - submicron droplet effect on contact angle, 109–110
 - submicron droplets, generation of, 101–104
 - superhydrophobic paper surfaces, 197
 - surface roughness, 99
 - transmittance measurements, 106
 - vibrating droplet studies, 100
 - waterfall/jet tests, 104–105

- wear and friction tests, 105–106
- Hierarchically structured surfaces, 137–169
 - with wax platelets and tubules, 137–169
 - bouncing droplet, transition during, 157–162
 - fluid drag reduction measurement, 167–168
 - hierarchical structure effect with wax tubules on superhydrophobicity, 150–156
 - hierarchically structured surfaces,
 - self-cleaning efficiency of, 156–157
 - two-step molding process, 137–139
 - vibrating droplet, adhesion and inertia forces of, 162–164
 - vibrating droplet, transition during, 162–167
 - wax platelet crystal densities on superhydrophobicity, nanostructures effects of, 142–146
- Hierarchically structured surfaces, self-cleaning efficiency of, 156–157
- High adhesion surfaces, 28–29
- Homogeneous interfaces, 37–49
- Hydrophilic leaf surfaces, characterization, 66–79
 - adhesion, using AFM, 71–77
 - adhesive force and friction, 76–77
 - contact angle measurements, 67–69
 - experimental techniques, 66–67
 - friction using AFM, 71–77
 - hierarchical roughness role, 77–79
 - SEM micrographs, 67
 - surface characterization
 - using AFM, 71–77
 - using optical profiler, 70–71
 - surface characterization, 72–76
- Hydrophilic ZnO nanoparticles, 231–233
- I**
- Icephobicity, 26
- Ideal surfaces with hierarchical structure, 136–137
- Indium tin oxide (ITO) electrode, 91
- Inorganic fouling, 423–452
 - anti-inorganic fouling measurements, 445–446
 - anti-inorganic fouling, 447–449
 - fields susceptible to, 423–427
 - formation, 430
 - freeze fouling, 430
 - gas stream particulate fouling, 430
 - particulate fouling, 430
 - surface factors, 430–433
- Inspiration from living nature, 383–386
 - ambient species, 383–386
 - lotus effect, 383–384
 - rice leaf and butterfly wing effect, 384–386
 - aquatic species, shark skin and fish scales effect, 384
- Inspired structural surfaces, 205–212. *See also under* *Salvinia molesta*
- Inter-tile toughening mechanism, 537–538
- J**
- ‘Janus interface’, of lotus leaf, 243
- Johnson-Kendall-Roberts (JKR) theory, 464, 500
- K**
- Kelvin equation, 475
- L**
- Laplace force, 474
- Large-eddy simulation (LES) model, 363
- Layer-by-layer (LBL) technique, 282–297
 - mechanically durable nanoparticle composite coatings using, 282–297
 - anti-fogging experiment, 288
 - anti-fogging property of coated samples, 291–292
 - anti-icing experiment, 288
 - anti-icing property of coated samples, 292–293
 - anti-smudge property of coated samples, 294–295
 - characterization techniques, 288–289
 - experimental details, 285–288
 - oil-water separation ability of coated samples, 295–297
 - oil-water separation experiment, 288
 - self-cleaning property of coated samples, 293–294
 - transparency of coated samples, 291
 - wear resistance of coated samples, 289–291
 - wettability of coated samples, 288–289
 - self-assembly technique, 91
- Liquid in contact with a rough surface, modeling, 35–60. *See also under* Contact angle (CA)
- Lotus effect surfaces in nature, 6, 17, 30, 63–84, 383–384. *See also*

- Hierarchically structured lotus-like surfaces; Hydrophilic leaf surfaces;
 - Microstructured lotus-like surfaces;
 - Nanostructured lotus-like surfaces;
 - Superhydrophobic leaf surfaces
- nanofabrication techniques for, 85–93.
 - See also individual entry*
- plant leaves, 63–66
- self-cleaning approaches, 79–82
 - superhydrophilicity, 79–80
 - superhydrophobicity, 79–80
 - superoleophobicity, 79–80
- Lotus tubules, 152–156
- Low adhesion/drag reduction surfaces, 27–28
 - Low drag, 6, 12, 17
- M**
- Macroscopic contact angle hysteresis, 127
- Majus* tubules, 150–152
- Mechanically durable superhydrophobic surfaces, 169–197. *See also* CNT composites
 - AFM tests, surfaces durability in, 183–186
 - ball-on-flat tribometer tests, surfaces durability in, 183–186
 - morphology, 189–190
 - nanoparticle composites for optical transparency, 186–197
 - optical transparency, 191–194
 - sliding and water jet experiments, wear resistance of samples in, 194–196
 - surface roughness, 189–190
 - wettability, 190–191
- Mechanically durable superoleophobic aluminum surfaces, 299–314
 - air pockets measurements, 310
 - anti-smudge property, 310
 - characterization, 305
 - corrosion tests, 312–314
 - experimental details, 303–305
 - sample preparation, 303
 - roughness, 307–309
 - self-cleaning property, 310
 - surface morphology, 307–309
 - wear tests using tribometer, 309
 - wettability, 305–307
- Mechanically durable superoleophobic polymer surfaces, 314–319
 - experimental details, 315–316
 - wear resistance of surface, 317–319
 - wettability of surfaces, 316–317
- Mechanically durable surface, 230–239
- Micro/nanoroughened surfaces, creating, 86
- Microdroplet condensation using ESEM, 101
- Microelectromechanical systems (MEMS), 26, 477
- Micropattern, contact angle of surfaces using, 181–182
- Micropatterned epoxy surfaces, wetting behavior on, 257–260
 - with C₂₀F₄₂, 260–262
- Micropatterned polymers, 106–111
- Micropatterned Si surfaces, 111–135
 - Cassie-Baxter and Wenzel transition criteria, 114–116
 - Cassie-Baxter and Wenzel transition for different series, 122–125
 - condensation and evaporation of, contact angle measurements during, 128–131
 - contact angle hysteresis, 124–127
 - droplet evaporation, transition during, observation, 118–122
 - macroscopic contact angle hysteresis, 127
 - pitch value effect on transition, 116–118
 - transition during bouncing droplet, observation, 132–135
 - wetting/dewetting asymmetry, 124–127
- Microstructure surface, wetting of, 27
- Microstructured lotus-like surfaces, 97–198.
 - See also* Micropatterned Si surfaces
- fabrication and characterization of, 97–198
 - adhesion, 99
 - adhesive force, 110–111
 - bouncing droplet studies, 100
 - contact angle, 108–109
 - contact angle, 99
 - droplet evaporation studies, 100
 - dynamic contact angles, 99
 - evaporation studies using ESEM, 101
 - experimental techniques, 99–106
 - microdroplet condensation using ESEM, 101
 - static contact angles, 99
 - submicron droplet effect on contact angle, 109–110
 - surface roughness, 99
 - transmittance measurements, 106
 - vibrating droplet studies, 100
 - waterfall/jet tests, 104–105
 - wear and friction tests, 105–106
- Mineral bridges, 535–536
- Mother-of-pearl. *See* Nacre
- Multi-level hierarchical spring analysis, 484–488
- Multi-level hierarchical spring model, 488–494
- Multiwalled carbon nanotube (MWCNT), 90, 514

N

- Nacre, 531–545
 bioinspired structures, 542–544
 hierarchical structure (top-down), 543
 self-assembled nanocomposite (bottom-up), 543
 hierarchy of, 532–542
 columnar structure, 533–535
 inter-tile toughening mechanism, 537–538
 mineral bridges, 535–536
 polygonal nanograins, 536–537
 sheet structure, 533–535
 structure, 533
 mechanical properties, 538
 structure and mechanical properties, 531–545
- Nano structures and shark skin replica, wetting behavior on, 262–264
- Nanodevices, 2, 16
- Nanoelectromechanical systems (NEMS), 26
- Nanofabrication, 18
- Nanofabrication techniques for lotus-like structures, 85–93
 micro/nanoroughened surfaces, creating, 86
 one-level structure, roughening to create, 86–90
 materials, 87
 pros and cons of, 88
 techniques, 87
 one-level structures, coatings to create, 90–91
 two-level (hierarchical) structures, methods to create, 92–93
 Nanomaterials, 2, 16
- Nanoparticle composites for optical transparency, 186–197
- Nanoparticle composites with hierarchical structure, 179–183
 contact angle of surfaces, 181–182
 using microparticles, 182–183
 using micropattern, 181–182
 experimental details, 179–181
- Nanopatterned polymers, 106–111
- Nanoscale dispensing (NADIS) probe, 102–103
- Nanoscience, 18
- Nanostructure surface, wetting of, 27
- Nanostructured lotus-like surfaces, 97–198.
See also Micropatterned Si surfaces fabrication and characterization of, 97–198.
See also Micropatterned polymers; Nanopatterned polymers
 adhesion, 99
 adhesive force, 110–111
 bouncing droplet studies, 100
 contact angle, 99, 108–109
 droplet evaporation studies, 100
 dynamic contact angles, 99
 evaporation studies using ESEM, 101
 experimental techniques, 99–106
 microdroplet condensation using ESEM, 101
 static contact angles, 99
 submicron droplet effect on contact angle, 109–110
 submicron droplets, generation of, 101–104
 surface roughness, 99
 transmittance measurements, 106
 vibrating droplet studies, 100
 waterfall/jet tests, 104–105
 wear and friction tests, 105–106
 Nanotechnology, 17–18
- Natural superhydrophobic surfaces, 27–29
- Natural superoleophobic self-cleaning surfaces, 29
- Nature, lessons from, 2–7
- Nondimensional pressure drop model, 408–410
- Non-fiber fracture condition, 502–504
- ‘Non-flip-flop’ surface property, 284
- Nosonovsky-Bhushan equation, 46
- n*-perfluoroeicosane (C₂₀F₄₂), 260–262
- O**
- Octadecyl- trichlorosilane (OTS), 86
- Oil-water separation experiment, 288
- Oleophobic/philic nature of surfaces, 252–254
- Oleophobic/philic surface, 30
- Oleophobicity/philicity model, 255–264
 flat epoxy surfaces, wetting behavior on, 257–260
 hierarchical structures and shark skin replica, wetting behavior on, 262–264
 micropatterned epoxy surfaces, wetting behavior on, 257–260
 nano structures and shark skin replica, wetting behavior on, 262–264
 oleophobic/philic surfaces, characterization, 257–263
 for oil droplets in air and water, validation, 255–264
 experimental techniques, 255
 oleophobic/philic surfaces fabrication, 256–257
 two-step molding process, 256
- One-level structure

- coatings to create, 90–91
- roughening to create, 86–90
- ‘One-pot’ technique, 291
- Optical transparency
 - nanoparticle composites for, 186–197
 - superhydrophobic surfaces, 191–194
- P**
- Particulate fouling, 43
- Perfluorodecyltriethoxysilane (PFDTES), 86, 107–109
- Perfluorooctanesulfonate (PFOS), 89
- Photonic crystals, 555–559
 - 2-D photonic crystal, 567
 - 3-D photonic crystal, 567
- Pitch value effect on transition, 116–118
- Plant leaves, 63–66
- Plasma deposition, 250
- Plasma enhanced chemical vapor deposition (PECVD), 90
- Poly(acrylic acid) (PAA) multilayer, 91
- Poly(allylamine hydrochloride) (PAH) multilayer, 91
- Poly(dimethylsiloxane) (PDMS), 92
- Poly(ethylene terephthalate) (PET), 89
- Poly(methyl methacrylate) (PMMA), 106–109, 187, 390–392, 444, 512
- Poly(tetrafluoroethylene) (PTFE), 89
- Polycarbonate (PC), 187
- Polydiallyldimethylammonium chloride (PDDA), 285
- Polydimethylsiloxane (PDMS), 107, 390, 443
- Polyethylene terephthalate (PET), 271
- Polygonal nanograins, 536–537
- Polymethylmethacrylate (PMMA), 86, 543
- Poly-styrene (PS), 106–107
- Polyurethane acrylate (PUA) resin, 106–107
- Polyvinylsiloxane (PVS), 510
- Pressure drop measurement technique, 392–411
- R**
- Re-entrant geometry, 250–252
 - double re-entrant geometry, 251
 - single entrant geometry, 251
- Reversible adhesion, 3–5, 457
- Reynolds number, 394
- Rice leaf effect, 383–420
 - drag reduction models, 413–420
 - pressure drop measurement technique, 392–411
 - air low, 408
 - nondimensional pressure drop model, 408–410
 - oil flow, 403–408
 - surface characterization, 396–400
 - water flow, 403
- sample fabrication, 386–392
 - actual sample replicas, 386–387
 - hot embossed plastic sheets, 390–392
 - micropatterned replicas, 390
 - rice leaf inspired surfaces, 387–390
 - wettability, 411–413
- Rose petals characterization with high and low adhesion, 213–239
 - mechanically durable surface, 230–239
 - mechanisms, 214–221
 - surfaces fabrication, 221–230
- S**
- Salvinia molesta*, micropatterned structures
 - inspired by, 205–212
 - adhesion measurement, 209–211
 - characterization of, 205–212
 - contact angle measurement, 209–211
 - fabrication of, 205–212
 - leaves, 207–208
- Self cleaning, 3–6, 11, 17–18, 64, 79–82, 470–472
 - efficiency of hierarchically structured surfaces, 156–157
 - superhydrophilicity, 79–80
 - superhydrophobicity, 79–80
 - superoleophobicity, 79–80
- Shark skin effect, 384
- Shark-skin surface for fluid-drag reduction in turbulent flow, 327–377. *See also* Fluid-drag reduction; Fluid flow modeling
 - drag measurement techniques, 341–345
 - closed channel, 344–345
 - open channel, 341–344
 - experimental studies, 332–362
 - flow visualization studies, 334
 - riblet fabrication, 336–341
 - riblet geometries and configurations, 334–336
 - riblet results and discussion, 346–362
 - airfoil experiments, 349–351
 - closed channel, 351–361
 - continuous versus segmented riblets, 358
 - flat plate experiments, 346–349
 - machined micro-sized channel, 352–353

- micro-sized channel dimensions, role of, 353–361
- molded shark skin replica, 352–353
- open and macro-sized closed channels, comparison, 351–352
- open channel, 346–351
- riblet wettability, 359
- riblets on top or bottom or both sides, 359
- riblets application for drag reduction and antifouling, 373–376
- Single entrant geometry, 251
- Single fiber contact analysis, 499–500
- Single layer coating, 273–276
- Single spring contact analysis, 482–483
- ‘Single-pot’ technique, 282
- Sliding experiments, wear resistance of samples in, 194–196
- Smart adhesion, 457
- Static contact angle, 36
- Stiction, 25
- Stream particulate fouling, 430
- Structural coloration, 3–4, 6, 12, 18, 549–573
 - bioinspired fabrication and applications, 571–572
 - lessons from living nature, 557–571
 - coloration change found in biological animals, 570
 - coloration changes, 569–571
 - diffraction grating, 562–565
 - film interference, 558–562
 - multi-film interferences, 558–559
 - photonic crystals, 566–569
 - scattering, 565–566
 - thin-film interferences, 559
 - in living nature, 550
 - physical mechanisms, 552–557
 - coherent scattering, 553
 - coloration changes, 556–557
 - diffraction grating, 554–555
 - film interference, 552–554
 - incoherent scattering, 553
 - multi-film interference, 553
 - photonic crystals, 555–556
 - scattering, 555
 - thin-film interference, 553
- Submicron droplets
 - effect on contact angle, 109–110
 - generation of, 101–104
- Superhydrophilicity, for self-cleaning, 79–80
- Superhydrophobic leaf surfaces,
 - characterization, 66–79
 - adhesion, using AFM, 71–77
 - adhesive force and friction, 76–77
 - contact angle measurements, 67–69
 - experimental techniques, 66–67
 - friction using AFM, 71–77
 - hierarchical roughness role, 77–79
 - SEM micrographs, 67
 - surface characterization
 - using AFM, 71–77
 - using optical profiler, 70–71
 - surface characterization, 72–76
- Superhydrophobic paper surfaces, 197
- Superhydrophobic surfaces fabrication and characterization with high and low adhesion, 230–239
 - hydrophilic ZnO nanoparticles, 231–233
 - before ODP modification, 231–233
 - after ODP modification, 233–237
 - wear resistance in AFM wear experiment, 237–239
- Superhydrophobicity, 3–6, 17, 142–146
 - hierarchical structure effect with wax tubules on, 150–156
 - Majus* tubules, 150–152
 - lotus tubules, 152–156
 - for self-cleaning, 79–80
 - wax platelet crystal densities nanostructures
 - effects of, 142–146
- Superoleophobic/philic surfaces, 243–320.
 - See also* Mechanically durable superoleophobic aluminum surfaces; Mechanically durable superoleophobic polymer surfaces; Oleophobicity/philicity model; Superoleophobicity
 - characterization of, 243–320
 - fabrication, 243–320
 - mechanically durable nanoparticle composite coatings, 282–297
 - using layer-by-layer technique, 282–297. *See also individual entry*
 - modeling, 243–320
 - oleophobic/philic nature of surfaces, 252–254
- Superoleophobicity, 29, 264–281
 - coated samples, wettability of, 273–276
 - dual layer coating with plasma treatment, 276
 - single layer coating, 273–276
 - mechanically durable nanoparticle composite coatings for, 264–281
 - anti-smudge properties of coated samples, 279–280
 - experimental details, 271–273
 - surface topography and coating thickness, 276–277

- transparency of coated samples, 281
 - wear on macroscale using tribometer, 277–279
 - wear on microscale using AFM, 277
 - wear resistance of coated samples, 277–279
 - for self-cleaning, 79–80
 - Superoleophobicity in air, 247–252
 - re-entrant geometry, 250–252
 - single entrant geometry, 251
 - double re-entrant geometry, 251
 - strategies to achieve, 247–252
 - fluorination techniques, 248–250.n
 - See also individual entry*
 - Super-philic/phobic surfaces,
 - roughness-induced, 23–30
 - applications, 25–26
 - natural superhydrophobic surfaces, 28–29
 - natural superoleophobic self-cleaning surfaces, 29
 - wetting states, 23–24
 - Super-phobic surface, wetting hysteresis for, 56
 - Surface tension force, 474
- T**
- Tetramethylsilane (TMS), 89
 - ‘The apparent contact angle’, 44
 - Thin film effect, 406
 - Thin oil film effect, 359
 - Tokay gecko, 462–472
 - adhesion enhancement, 464–466
 - by division of contacts and multilevel hierarchical structure, 464–466
 - attachment mechanisms, 472–476
 - capillary forces, 474–476
 - construction of, 462–464
 - peeling, 466–470
 - self cleaning, 470–472
 - van der Waals forces, 473–474
 - Tolman’s length, 44
 - Transmittance measurements, 106
 - Tribometer, 309
 - Two-level (hierarchical) structures, methods to create, 92–93
- V**
- Van der Waals forces, 473–474
 - Vibrating droplet
 - adhesion and inertia forces of, 162–164
 - transition during, 162–167
- W**
- Water jet experiments, wear resistance of samples in, 194–196
 - Waterfall/jet tests, 104–105
 - surfaces durability in, 173–174
 - Wear and friction tests, 105–106
 - Wear resistance in AFM wear experiment, 237–239
 - Wear tests using tribometer, 309
 - Wenzel equation, 37–49
 - applicability range of, 45–49
 - limitations of, 42–45
 - Wenzel regime, 29
 - Wettability
 - superhydrophobic surfaces, 190–191
 - Wetting states, 23–24
 - flat surface, 27
 - hierarchical structure surface, 27
 - microstructure surface, 27
 - nanosurface surface, 27
 - Wetting/dewetting asymmetry, 124–127
- Y**
- Young’s equation, 254